

FLUID-DYNAMIC LIFT

Practical Information on
AERODYNAMIC and HYDRODYNAMIC LIFT

by

SIGHARD F. HOERNER Dr.-Ing. habil

Co-author and Editor

HENRY V. BORST

SECOND EDITION

Published by

Mrs. Liselotte A. Hoerner

1985

AUTHOR'S PREFACE

Between the years of 1945 and 1950, the author consolidated his aerodynamic experience (since 1930) as a researcher, wind-tunnel experimenter, designer and as a pilot (in organizations such as Junkers and Messerschmitt) by writing "Aerodynamic Drag". After augmenting his knowledge through the numerous publications pouring out after that time, he then wrote and published "Fluid-Dynamic Drag" (1958), second edition 1965. On the basis of this book he was asked by the U.S. Navy's Office of Naval Research, whether he could and would write a text on "lift". Thus encouraged and aided by Contract Nonr-3196(00), the author set out writing "Fluid-Dynamic Lift".

The number of available publications and technical reports dealing with aerodynamic lift, may now be between 10 and 20,000. It soon became obvious that not all of these could be evaluated. To reduce the amount of effort and complexity, the author restricted the subject to subsonic speeds. Even then, it was found impossible to study all of the remaining, say 10,000 sources of information. However, not all of the published information is worth reading. Possibly 50% of it is obsolete, unnecessary, repetitious, and some of it is misleading. If the author did not use all of the useful results available, there is a point of view given as advice by the late Hugo Junkers to his engineers. He told them, when studying and developing something new, not to look up what others had done and found in the same field. New ideas, aspects and conclusions may thus be reached, without interference by premature and/or erroneous judgements by others. The best way of using existing information seems to be to take indisputable facts, and to explain and accept them in spite of conclusions and theoretical indications to the contrary. To be sure, it is the author's intent to find the "truth" about the many aspects of fluid-dynamic lift. However, as a French research professor (Ourisson, Ecole Normale Supérieure in Paris) has said, "the search for truth is influenced by one's idea of what the truth must be". In this respect, the author never accepts what theory says it "must" be. Emphasis is placed upon the deviations from theoretical predictions, although any theoretical analysis is gratefully used as soon as it consistently agrees with experimental results. In particular, theory can thus be used to extrapolate available statistical data.

After completion of this text, the author wishes to thank and/or to acknowledge the help of those, without whom the book could not have been written; among them Cdr. H.B. Keller and Mr. Ralph C. Cooper of the Office of Naval Research, Mr. G.L. Desmond at the Bureau of Weapons, the Office of Scientific Research of the U.S. Air Force, the NACA or NASA (where most of the technical reports came from) and the librarians of the American Institute of Aeronautics and Astronautics.

S. Hardy F. Hoerner

New York City
January 1967

THE AUTHOR studied mechanical engineering at the Institute of Technology in München (Dipl.Ing.), he earned a degree as Dr.-Ing. in aerodynamics at the Institute of Technology in Braunschweig, and he obtained a degree as Dr.-Ing.habil. from the TH Berlin. He served at one time as research assistant at the Deutsche Versuchsanstalt für Luftfahrt (DVL, near Berlin), as aerodynamicist in the Fieseler Corporation (working on the first STOL airplane, the "Stork") and later for a time as head of design aerodynamics in the Junkers A.G. He was then research aerodynamicist at the Messerschmitt A.G. After World War II, the author was invited to come to the United States, where he worked in aerodynamics at Wright Field, Ohio. For some years he has been acting as specialist for aerodynamics and hydrodynamics in the field of naval architecture at Gibbs & Cox, Inc., New York City.

CO-AUTHOR'S PREFACE

The task of completing this book was undertaken to fulfil an important technical need, as did the book, "Fluid-Dynamic Drag". Upon reviewing the available material and notes of the late Dr. Hoerner on the subject of lift, we felt that his valuable and extensive work should be made available to the engineering community.

In working with Dr. Hoerner's data, we have considered and incorporated recent technological advances and developments. In compiling and completing his work we have attempted to maintain his standards and technical excellence. His notes, completed chapters and extensive library provided the basic material needed to do this, and also have helped to preserve his ideas and expertise. Although considerable work had been done on the subject by Dr. Hoerner extensive studies and analysis were necessary to meld the vast store of material into a complete and useful book.

This book has been written for both the practicing engineer and the student. It is designed so that the physical aspects of the problem can be understood as well as to provide solutions. The book is not just a collection of data but brings together and integrates the material to form as complete a picture as possible. The many sources of data used are given to provide material for any desired expanded studies.

Many people have cooperated in providing new sources of data for this book, including the many scientists of NASA. Without their extensive help this book could not have been completed in its present form. We also want to thank Mrs. Hoerner for giving us the opportunity to complete the work of her late husband on the subject and for making available his extensive library, notes and data. Special thanks are also given to Mr. Ralph C. Cooper of the Office of Naval Research for his support in the final consummation of this work.

Although the basic and underlying work of the late Dr. Hoerner on fluid dynamic lift was done over a period of many years, the remaining chapters were written and the final review was completed during the last two years. It is hoped that this book fills an existing technical gap and will be useful over many years as an engineering resource.

Wayne, Pennsylvania
June, 1975

Henry V. Borst

This 1985 second edition differs from the preceding one as follows: a number of misprints and some errors have been eliminated. New material has been added on cascade flow in Chapter II and in Chapter III new data on winglets and endplates. The improvements possible in section maximum lift with small changes in the upper surface contour are given in Chapter IV. Also in Chapter XII the theoretical characteristics of ducted fans has been expanded along with the effect of rotation on blade section characteristics.

Wayne, Pennsylvania
April 1985

Henry V. Borst

THE CO-AUTHOR graduated in aeronautical engineering from Rensselaer Polytechnic Institute in Troy, New York. He worked for the Curtiss Wright Corporation on research projects for many years and became Chief of Aerodynamics. During this time advanced work on propulsion systems was done and two new VTOL aircraft were developed, the X-100 and the X-19 for which he holds the basic patent. Later he joined the Vertol Division of the Boeing Company becoming Director of Preliminary Design. During his career he has written many technical papers of aerodynamics. He now heads the Henry V. Borst and Associates of Wayne, Pennsylvania, aeronautical consultants to government and industry.

TABLE OF CONTENTS

(pages are numbered by chapters)

CHAPTER I – GENERAL INFORMATION ON FLUID DYNAMICS AND AIRPLANES

1. HISTORY OF AIRPLANE AERODYNAMICS

heavier than air, aerodynamic theory,	
wind tunnels	1-1
high Reynolds numbers	1-2
mathematics, aviation	1-3

2. GLOSSARY OF TERMS

airfoil, wing	1-3
aerodynamic center, mean aerodynamic chord,	
lift angle, forces	1-4
vortex, irrotational, potential flow,	
momentum, pressure	1-5
stagnation point, negative pressure,	
pressure distribution, hydrodynamics,	
other terms	1-6
similarity laws, metric system	1-7

3. NOMENCLATURE

directions	1-7
angle of attack, positive/negative values	1-8

4. PHYSICAL PROPERTIES OF FLUIDS

(A) Characteristics of Atmospheric Air 1-8

sea-level constants, dynamic pressure, function	
of altitude, viscosity of the air	1-8
Speed of sound, humidity	1-9
fog, rain, icing, wind	1-10

(B) Physical Properties of Water 1-11

the compressibility, dynamic pressure, viscosity	
of water, water tunnels	1-11
cavitation, cavitation number	1-12

5. CONSIDERATION OF SIZE AND SPEED OF VEHICLES

squire-cube law	1-13
froude number, hydrofoil boats, lift coefficient	1-13
STOL, high altitude	1-14
control, dynamic stability, advanced vehicles	1-15

6. AIRPLANE PERFORMANCE

takeoff, climb and descent, takeoff figure of merit,	
high speed, drag and lift	1-16
speeds	1-17
landing, evaluation of KC-135, takeoff,	
for climbing	1-7
endurance, range, propeller-driven airplanes	1-18

CHAPTER II – LIFT CHARACTERISTICS OF FOIL SECTIONS

1. GEOMETRY AND GENERAL

airfoils, early sections	2-1
modern sections, systematic series	2-2
testing techniques	2-4
flow deflection	2-5

2. THE MECHANISM OF CIRCULATION IN FOIL SECTIONS

circular cylinder	2-5
lifting line, circulation, foil sections,	
elliptical sections	2-6
trailing edge, reversed 0012	2-7
lift coefficient, sharp leading edges	2-8
nose radius, influence of thickness,	
strut section	2-9
trailing-edge angle, blunt trailing edges	2-10
influence of friction	2-11
section shape, "efficiency"	2-12
roughness, Reynolds number, b'layer transition	2-13
practical construction	2-14

3. INFLUENCE OF SECTION CAMBER ON LIFT

camber lines, zero-lift angle	2-14
design $C_{L\alpha}$, pressure distributions,	
symmetrical flow	2-15
optimum lift, thickness ratio, "laminar"	
foil sections	2-16

4. LOW REYNOLDS NUMBER

turbulence effects, thickness ratio and camber	2-17
--	------

5. CHARACTERISTICS OF SPECIFIC AIRFOILS

concave pressure distribution	2-18
general aviation – airfoils	2-19
sailplanes, surface roughness, cascades	2-20

6. PITCHING-MOMENT CHARACTERISTICS	
center of lift, zero-lift moment	2-21
reflexed camber, helicopter blades, aerodynamic center	2-22
section thickness, trailing wedge angle, beveled trailing edge	2-23
vertical position of the AC, thickness ratio	2-24

CHAPTER III — THE LIFT OF STRAIGHT WINGS

1. APPLIED LIFTING-LINE THEORY

vortex sheet, trailing vortex	3-1
roll-up, rectangular wings, downwash, induced angle, lift angle, lifting surface	3-2
round wings, dihedral	3-3
induced drag	3-4

2. INFLUENCE OF SHAPE ON PLAIN WINGS

lift distribution	3-4
tapered planform, rectangular wings	3-5
foil-section thickness, tapered wings	3-6
round planforms	3-7
rear corner, U shape, tip drag	3-8

3. WINGS WITH END PLATES

basic principle	3-9
area ratio, shape of plates, canted plates, lift and drag	3-10
drag due to lift, maximum lift	3-11
single end plates, wing-tip tanks, alpha flow	3-12
inboard plates, cambered span	3-13
bent-up tips, addendum	3-14

CHAPTER IV — MAXIMUM LIFT AND STALLING

1. THEORETICAL AND DEMONSTRATED LEVELS OF MAXIMUM LIFT

theoretical maximum lift coefficient $C_{L_{max}}$	4-1
--	-----

2. THE PHYSICAL MECHANISM OF STALLING

types of lift stall, thin (sharp) leading edge	4-2
separation bubble — long type	4-3
boundary layer transition, bubble bursting, trail edge stalling	4-4
circular arc sections	4-5
zero lift angle of attack, rounding of leading edge	4-6

3. CORRELATION PROCEDURES OF TEST DATA

wind tunnel test conditions	4-7
variation of "f", low-turbulence tunnels, tunnel corrections	4-8
effective camber in wind tunnels, aspect ratio	4-9

4. MAXIMUM LIFT AS A FUNCTION OF SHAPE AND REYNOLDS NUMBER

principles	4-9
stall type prediction, $C_{L_{max}}$ as a function of nose shape	4-10
sharp leading edges, effect of camber	4-11
camber ratio, nose camber, critical Reynolds number	4-12
high Reynolds number	4-14
theoretical analysis, thickness ratio	4-15
high-speed airfoil sections, influence of nose radius	4-16
Mach number effects on $C_{L_{max}}$	4-17
efficiency of airfoils	4-18

5. INFLUENCE ON SURFACE ROUGHNESS

maximum-lift divergence, permissible roughness	4-19
roughness in wind tunnels, roughness in full-scale operation	4-20
stimulation of turbulence, type of stalling, airfoil thickness, cambered sections, corrugated surface	4-21
ice formation	4-22

6. AIRFOIL CHARACTERISTICS ABOVE STALL

correlation of theory, fully stalled wings	4-23
--	------

7. DYNAMIC EFFECTS

fluctuations of lift, dynamic lift stall	4-24
--	------

8. STALLING OF STRAIGHT WINGS

planform	4-26
--------------------	------

CHAPTER V — CHARACTERISTICS OF TRAILING-EDGE WING FLAPS

1. LIFT CHARACTERISTICS IN TWO-DIMENSIONAL FLOW

1. GENERAL

analysis	5-1
types of flaps, experimental results, forces and moments	5-2

2. LIFT CHARACTERISTICS OF PLAIN FLAPS

flap deflection, flap-chord ratio	5-5
round corner, stream turbulence	5-6

3. LIFT CHARACTERISTICS OF SPLIT FLAPS

flow pattern, zap flap, split flap forward	5-7
lift-curve slope, full scale airplane, perforated flaps	5-8
airfoil-section shape	5-9
trailing-wedge angle, plain flaps	5-10

4. LIFT CHARACTERISTICS OF SLOTTED FLAPS

single-slotted flaps, external flaps	5-11
Fowler flaps, chord extension	5-12
extended slot lip	5-14

II. PERFORMANCE OF WINGS WITH FLAPS**1. CHARACTERISTICS IN THREE-DIMENSIONAL FLOW**

limits of circulation, "base" drag	5-14
part-span flaps	5-15
outboard flaps, lift distribution	5-16

2. PERFORMANCE DURING TAKEOFF AND CLIMB

flow pattern	5-16
thick wing sections, thrust available, figure of merit-t.o., takeoff characteristics	5-17
flap selection for takeoff, part-span flaps, induced drag	5-18

3. MAXIMUM LIFT DURING LANDING

landing characteristics	5-19
full-span flaps, critical angles	5-20
flaps with gaps, split flaps, slot-in flaps, double and triple slotted flaps, Dornier flap	5-21
Reynolds number, the thickness ratio	5-22
nose radius, part-span flaps	5-23

4. POWER-ASSISTED WING FLAPS

rotating cylinder, rotating flap, boundary-layer suction	5-24
jet-augmented flaps	5-25
blowing over flaps, equivalent rag	5-26
slot size, flap size, the jet flap	5-27
the momentum coefficient, jet-flap theory, wing span	5-29
lift due to momentum, jet angle, loss of momentum, "short" jet flaps	5-30
jet slot, fuselage, part-span jet sheet	5-31
ground effect	5-32
efficiency, drag due to lift	5-33

III. MOMENTS AND LOADS OF AND DUE TO FLAPS**1. WING PITCHING MOMENTS**

simple flaps	5-34
Fowler flaps, split flaps forward, zap flaps	5-35
extended lip flaps, double-slotted flaps, part-span flaps	5-36
swept wings, jet flaps, performance	5-37
ground effect	5-38

2. LOADS OF AND DUE TO FLAPS

pressure distribution, theory, split flap, slotted flaps	5-39
flap load, chord force	5-40
load across the span	5-41

3. FLAP HINGE MOMENTS

simple flaps, zap flaps, slotted flaps	5-42
Fowler flaps, gap pressure	5-43

CHAPTER VI — LEADING-EDGE HIGH-LIFT DEVICES**1. INFLUENCE OF SLOTS AND SLAT ON LIFT**

principle	6-1
fixed slots, drag, auxiliary airfoils	6-2
Maxwell slat	6-3
Reynolds number, slat size	6-4
design rules, loss of lift	6-5
pitching moments, combination with trailing-edge flap	6-6
combined pitching moments, pressure distributions	6-7
slat forces, line of force, inclination, kinematics	6-8
slot pressure, sliding slats	6-9
stall control, span ratio	6-10

2. LEADING-EDGE OR NOSE FLAPS

nose shape, leading-edge camber, flap theory	6-11
stalling angle, hinged noses, optimum flap angle	6-12
Reynolds number, leading and trailing edge flaps, sharp leading edges, maximum lift	6-13
comparison with slat, Kruger flap, nose radius	6-14
stalling, pitching moments	6-15
camber, drag, pressure distribution	6-16
flap forces, hinge moments	6-17

3. BOUNDARY LAYER CONTROL NEAR THE LEADING EDGE

(a) Control Through Turbulence or Vortex Generation; laminar separation, transition, vortex generators	6-18
increasing lift	6-19

(b) Boundary-layer Control by Suction:

nose-shape	6-19
leading-edge slot, distributed suction	6-20
lift increments, porous materials, pressure required, stalling	6-21
cambered airfoil, nose flap, trailing flap, power required	6-22
takeoff	6-23

(c) Boundary-layer Control by Blowing; round

airfoil, comparison	6-23
combined blowing, momentum required, ground proximity, stalling	6-24
pitching moments, blowing from the knee	6-25
takeoff, slot design	6-26
horizontal tail, rotating cylinder, high-lift combinations	6-27
blowing around leading edge	6-28

CHAPTER VII – INFLUENCE OF COMPRESSIBILITY AT SUBSONIC SPEEDS

1. PRINCIPLES OF COMPRESSIBLE FLUID FLOW

the speed of sound	7-1
impact pressure, Prandtl-Glauert rule, critical velocity	7-2
critical Mach number	7-3

2. INFLUENCE OF COMPRESSIBILITY ON AIRFOIL SECTIONS

Prandtl-Glauert factor	7-3
angle of attack, the minimum pressure	7-4
leading edge, divergence	7-5
pitching moment, pitching due to lift, sharp leading edges	7-6

3. STRAIGHT WINGS AS USED IN HIGH-SPEED AIRPLANES

lift angle, smaller aspect ratios	7-7
lifting bodies, tail surfaces	7-8
control flap, wing flaps, critical lift	7-9

4. LIFT ABOVE THE CRITICAL MACH NUMBER

flow around the leading edge, supersonic expansion, shock stall	7-10
minimum lift, "supersonic" pattern, center of lift, pitching down, pitchup	7-11
approaching $M = 1$, transonic flight	7-12

CHAPTER VIII – HYDRODYNAMIC LIFT

1. FULLY SUBMERGED LIFTING CHARACTERISTICS

Reynolds number, rudders	8-1
wall gap, roll-stabilizing fins, submarines	8-2
control flaps, rudder torque	8-3
fairing, foil section, hull wake	8-4
astern, slipstream, course stability	8-5

2. CHARACTERISTICS OF LIFTING HYDROFOILS

surface waves, induced drag, biplane theory	8-6
circulation	8-7
lift angle, drag due to lift, small aspect ratios, non-linear lift, hydroskis, struts	8-8
end plates, end struts	8-9
control flaps, surface-piercing	8-10
lift angle	8-11

3. CHARACTERISTICS OF HYDROFOIL BOATS

benefits, size and speed	8-11
wave pattern, downwash	8-12
wave angle, wave downwash, roach	8-13
typical hydrofoil boat, three foils, main foil, takeoff	8-14
size-speed-submergence, hull lift	8-15
surface-piercing, turning, lateral foil forces	8-16
strut forces, limitations, interference	8-17

CHAPTER IX – CHARACTERISTICS OF AIRPLANE CONTROL SURFACES

1. GEOMETRY OF CONTROL FLAPS

definitions, flap chord	9-1
-----------------------------------	-----

2. LIFTING CHARACTERISTICS OF FLAPS

horizontal tail surface	9-1
control effectiveness, theory, chord ratio	9-2
aspect ratio, wing shape	9-3
flap-span ratio	9-4

3. PITCHING MOMENTS DUE TO FLAPS

flap/chord ratio, comparison with camber	9-4
thickness ratio, moment due to lift, center of pressure	9-5

4. HINGE MOMENTS OF PLAIN CONTROL FLAPS

definitions, derivatives, hinge moment due to lift	9-6
hinge moment due to flap, hinge moments of landing flaps, example, stick-free condition	9-7
stick-free stability	9-8

5. INFLUENCE OF ASPECT RATIO AND FORM

influence of aspect ratio	9-8
induced angle, reversal of hinge moments	9-9
sweepback, hinge moments, plan-form shape	9-10

6. INFLUENCE OF FLAP-SECTION SHAPE

section thickness	9-10
trailing-wedge angle	9-11
hinge moments, stick-free characteristics	9-12
beveled trailing edges, pressure distribution, flow pattern	9-13
flap camber, "S" type moments	9-14

7. OVERHANGING-NOSE BALANCE

definitions, example	9-14
overhand length	9-15
lifting characteristics, hinge moments, characteristics at $\alpha = \text{zero}$	9-16
nose shape	9-17
stick-free characteristics, hinge gaps, influence on lift	9-18
covered balance, pressure differential	9-19
cover plates, internal efficiency, horn-type balance, hinge-moment	9-20
guards	9-21

8. CONTROL-FLAP CHARACTERISTICS AT HIGHER DEFLECTION ANGLES

critical flap angle	9-21
auxiliary foil, lift-curve slope, flap effectiveness	9-22
pitching moment, hinge moments	9-23

9. CHARACTERISTICS OF CONTROL TABS

mechanics of trailing edge tabs	9-23
hinge moment, trim tabs, effectiveness, linked-tab balance	9-24
reduction of hinge moments, boosting hinge moments, leading tab	9-25
stick-free condition, flap size, servo control	9-26
reduction of torque, fully-movable tail	9-27
tab-hinge moments, balance of tab torque, linked servo system, spring-tab control	9-28
control forces	9-29

CHAPTER X – ROLL CONTROL OF AIRPLANES**1. CHARACTERISTICS IN ROLL**

design requirements, flap type ailerons	10-2
part-span flaps	10-3
rolling moment due to aileron deflection, part-span ailerons	10-4
aspect ratio	10-5
tunnel testing, aileron effectiveness, rolling velocity, helix angle, rolling effectiveness	10-6
sweepback, internal force, stick force	10-7
differential linkage, nose balance, slotted ailerons	10-8
yawing moment, the “Frise” aileron, stick-force coefficient	10-9
stick-force slope, rigging-up	10-10
tab balancing, spring-tab ailerons, effectiveness	10-11
control moment, full-span wing flaps	10-12
trailing-edge deflection, duplex flap, split-flap aileron	10-13

2. CHARACTERISTICS OF SPOILERS

definition, mechanism, thin foil sections	10-14
solid spoiler flaps	10-15
rake-type spoiler, chordwise location, slot-lip aileron	10-16
effectiveness as a function of lift, helix angle	10-18
spoilers in presence of wing flaps, flap flow	10-19
induced yawing moments, parasite drag	10-20
combination with aileron flap, spoiler and plain flap, spoiler span, flight testing	10-21
jet spoiler	10-22

3. INFLUENCE OF COMPRESSIBILITY UPON LATERAL CONTROL

Prandtl Glauert factor, hinge moments, spoilers, critical Mach number	10-22
---	-------

CHAPTER XI – LONGITUDINAL STABILITY CHARACTERISTICS OF AIRPLANES**1. FUNDAMENTALS OF LONGITUDINAL STABILITY**

parameters involved	11-1
notation, the signs, static stability, balance	11-2
basic stability equation, free moment, dynamic longitudinal stability	11-3

2. LONGITUDINAL CHARACTERISTICS OF WING-FUSELAGE COMBINATIONS

stream curvature, aerodynamic chord, tapered wings	11-4
wing moment, lift due to fuselage, cross flow	11-5
moment due to fuselage	11-6
wing interference, upwash/downwash, fuselage shape	11-7
the flying boat hull, fillets, fuselage ducts	11-8
stalling	11-9

3. HORIZONTAL TAIL CHARACTERISTICS

cross flow, fuselage interference	11-9
load distribution	11-10
surface roughness	11-11
statistical evaluation, fuselage shape	11-12
effective tail length, horizontal tail contribution, free elevator, general method	11-13
“V” tail, sidewash	11-14
tail size	11-15

4. CHARACTERISTICS OF WING DOWNWASH

mechanism of downwash	11-15
trailing system, downwash due to circulation, rolling up, final downwash	11-16
combined downwash, variation in vertical plane	11-17
fuselage downwash interference, wing roots	11-18
wing-root fillets, cut-outs	11-19

5. SIMPLE AIRPLANE CONFIGURATIONS

moment due to tail, neutral point, high wing	11-20
wing wake	11-21
low horizontal tail, vertical position of tail	11-22
“T” tail	11-23
“T” tail at high angles, aspect ratio	11-24
big fuselages, tail contributions	11-25
X-15, long fuselage, zero-lift moment	11-26
taper ratio, across the span	11-27

6. CHARACTERISTICS OF CANARD CONFIGURATIONS

canard principles	11-27
tandem configuration, stability, control	11-28
canard analysis, basic configuration, canard effectiveness, stability contributions	11-29
stalling, aspect ratio	11-30
full scale experience, high-speed configurations, supersonic airplane	11-31
improve longitudinal characteristics, fuselage length	11-32
interference, delta canard	11-33

7. CHARACTERISTICS OF TAILLESS CONFIGURATIONS

stability of airfoil, wing sweep, wing flaps,	
swept-forward	.11-34
conclusion	.11-35

CHAPTER XII – PROPULSION LIFT AND STABILITY**1. LIFT OF PROPULSION SYSTEMS**

lift – thrust characteristics, rotors and	
propellers	12-2
induced flow—upwash	12-4
propeller lift and thrust, propeller and rotor	
moments, normal force V/STOL aircraft	12-5
ducted propeller or fan lift, lip stall ducted fans	12-6
duct moments, lift engines, engine lift turbofans	
and turbojets	12-7

2. INFLUENCE OF PROPELLER SLIPSTREAM ON WINGS

slipstream characteristics – propellers	12-9
propeller slipstream – thrust effects, lift due	
to slipstream, propeller wing lift, propeller jet	
effect on wing lift	12-10
turning effectiveness, total wing propeller lift	12-11

3. SLIPSTREAM EFFECTS OF DUCTED PROPELLER AND FAN ENGINE ON WINGS

turbine engine definitions, ducted propeller wing	
lift	12-12
wing lift with turbo jet engines	12-13
lift with underslung engines, propulsion lift	
engines over wing	12-14
wing lift interaction with external jet	12-15

4. SLIPSTREAM EFFECTS ON TAIL SURFACES

slipstream flow field, tail load distribution	12-16
dynamic pressure at the tail	12-17
horizontal tail span, dynamic pressure effects,	
vertical variation	12-18
downwash angle	12-19
fuselage + wing + propeller, wing roots	12-20
jet propulsion, downwash due to jet	12-21
jet engine effects on tail surfaces, aft mounted	
engine tail interference	12-22
slipstream effects of wing mounted engines	12-24

CHAPTER XIII – DIRECTIONAL CHARACTERISTICS OF AIRPLANES**I. GENERAL**

reference, yawing	13-1
yaw moments, notation, static stability	13-2

II. YAW MOMENTS OF FUSELAGES

basic moments, fineness ratio	13-2
lateral force, roughness	13-3
location of force, shape, analysis, ducts,	
lateral ducts	13-4
fuselage forward, engine nacelles	13-5
airplane configurations	13-6

III. VERTICAL TAIL CHARACTERISTICS**1. FUSELAGE INTERACTION**

aspect ratio	13-6
cylindrical fuselage, fuselage force, fuselage	
diameter	13-7
fuselage length	13-8

2. INFLUENCE OF WING AND HORIZONTAL STABILIZER ON VERTICAL TAIL

sidewash	13-9
horizontal tail interference, influence of	
canopy, end-plate effect, fuselage wake	13-10
load distribution, horizontal tail position,	
“T” tail	13-11
“V” tail, “V” derivatives	13-12
area required, “Y” tail, pitching moment	13-13

3. YAW MOMENT ARMS

vertical tail volume, yaw moment, moment arm	13-14
fuselage shape, fins on top of wing	13-15
twin tails	13-16

IV. INFLUENCE OF PROPULSION**1. MOMENT DUE TO FORCES IN THE PROPELLER**

tractor propeller, pusher propeller	13-17
-------------------------------------	-------

2. INFLUENCE OF THE SLIPSTREAM UPON THE VERTICAL TAIL

sidewash	13-18
dynamic pressure	13-19
wing flaps	13-20
inverted flight, jet propulsion	13-21
flow separation	13-22

V. CHARACTERISTICS AT HIGHER ANGLES OF YAW

fuselage	13-22
displacement, slipstream, tail stalling, dorsal fins	13-23
airplane configuration	13-24
propeller moment	13-25
twin propellers, pair of slipstreams, opposite-rotation	13-26

VI. DIRECTIONAL CONTROL OF AIRCRAFT

design requirements, rudder control, analysis	13-27
sideslipping, flight testing, lateral force	13-28
yaw moment, inopporative engine	13-29
yaw moment	13-30

CHAPTER XIV – LATERAL STABILITY CHARACTERISTICS OF AIRPLANES

Static stability, components, nomenclature, derivative notation	14-1
systems of reference, stability axis	14-2

1. FORCES AND MOMENTS OF STRAIGHT WINGS

lift of sideslipping wings	14-2
lateral forces, component of lift	14-3
rolling moments, aspect ratio	14-4
yawing moment	14-5

2. LATERAL CHARACTERISTICS DUE TO DIHEDRAL

lift differentials, lateral force	14-5
small aspect ratios, rolling moment, yawing moment	14-6
numerical results	14-7
part-span dihedral, influence of wing flaps	14-8

3. LATERAL CHARACTERISTICS OF SWEEP WING

lift differential, rolling moment	14-8
yawing moment, component due to lift	14-9

4. INFLUENCE OF FUSELAGE ON ROLLING MOMENT

flow pattern	14-10
analysis, fuselage/wing size, shape of fuselage, dihedral, influence of wing flaps	14-11

5. THEORY – DYNAMIC LATERAL STABILITY

basic equations, rolling derivatives, damping in roll	14-12
lateral force due to rolling, yawing derivatives, dynamic stability	14-13
spiral stability, lateral oscillation	14-14
“Dutch” roll, lateral directional stability – high angles	14-15

6. LATERAL DIRECTIONAL FLYING QUALITIES

pilot ratings, aircraft handling qualities	14-16
--	-------

CHAPTER XV – LIFT OF SWEEP WINGS

1. PRINCIPLES OF SWEEP-WING FLOW

geometry	15-1
sheared wing, cross-flow principle	15-2
yawed airfoil	15-3
direction of flow, sideslipping	15-4

2. LIFT OF SWEEP WINGS

wing center, lift distribution	15-4
taper ratio	15-5
forward sweep, induced angle	15-6
drag due to lift, lift angle	15-7
neutral angle of sweep, influence of fuselage	15-8
aspect ratio	15-9
cranked wings, end plates, vertical fins	15-10
engine nacelles, tip tanks-swept wings	15-11
control flaps	15-12
ground effect	15-13

3. INFLUENCE OF COMPRESSIBILITY ON SWEEP WINGS

angle of sweep, lift angle	15-14
larger angles of sweep, aspect ratio, critical Mach number	15-15
center of a swept wing	15-16
wing roots, contouring	15-17
fuselage interference, critical lift	15-18
forward sweep, engine nacelles	15-19
high-speed performance	15-20

CHAPTER XVI – STALLING OF SWEEP WINGS (PITCHING, ROLLING AND YAWING)

Definitions	16-1
-----------------------	------

1. DEFINITIONS AT HIGH ANGLES OF SIMPLE SWEEP WINGS

maximum lift – swept wings	16-2
wing tip flow, boundary layer flow	16-3
influence of section stall, aspect ratio	16-5
critical angle of sweep, drag at maximum lift	16-6
longitudinal stability, lateral stability, stall of swept forward wings	16-7
fuselage interference	16-8
dynamic stall, prediction of swept wing stall	16-9

2. SWEEP WING MODIFICATIONS FOR STALL

twist and camber modification	16-11
boundary layer fences, inverse taper	16-12
positive wing taper, leading edge extensions	16-13

3. COMPRESSIBILITY EFFECTS

buffeting	16-15
---------------------	-------

4. HIGH LIFT DEVICES FOR SWEEPED WINGS

wing loading, design for high $C_{L\alpha}$	16-17
leading edge slat	16-18
leading edge flaps, trailing edge flaps, typical	
high lift devices – swept wings	16-19

5. DEEP STALL

basic cause	16-20
deep stall prevention, mechanical warning devices	16-21

CHAPTER XVII – CHARACTERISTICS OF SMALL ASPECT RATIO WINGS**1. BASIC LIFT CURVE SLOPE**

flow mechanism, lifting surface	17-1
slender wings	17-2
lift curve slope, effective span, higher aspect ratios	17-3
round tip wings	17-4

2. NON-LINEAR LIFT COMPONENT

basic flow, cross flow, theory	17-5
two components of lift, end plate effect	17-6
non-linear component, leading-edge suction	17-7

3. CHARACTERISTIC DATA

circular planform, ellipsoid, the discus, streamline body	17-8
flap characteristics, horizontal tail surfaces	17-9
ring wings	17-10
aspect ratio	17-11
effects of yaw	17-12

4. COMPRESSIBILITY

lift at $M < 1$	17-12
non-linear lift, transonic range	17-13
supersonic range	17-14

5. MAXIMUM LIFT

theoretical maximum	17-14
variation of $C_{L\alpha}$ with aspect ratio	17-15
type of stall	17-16

CHAPTER XVIII – CHARACTERISTICS OF DELTA WINGS**1. CHARACTERISTICS OF DELTA WINGS**

geometry	18-1
--------------------	------

2. FLOW CHARACTERISTICS

leading-edge vortices, flow pattern	18-2
vortex pair, vortex breakdown	18-3
lift variation, 60° delta wings, lift to $\alpha = 90^\circ$	18-4

3. ANALYTICAL ANALYSIS

potential flow lift	18-6
vortex lift, theory, leading-edge suction analogy, vortex lift to total lift	18-7
delta-low aspect ratio wing analysis, the aerodynamic center	18-8

4. CONFIGURATION VARIABLES

aspect ratio, planform shape, potential flow lift	18-9
vortex lift, leading-edge shape, circulation lift – leading-edge shape, vortex lift – leading-edge shape	18-10
camber	18-11
double delta wings	18-12
wing + bodies	18-13
delta–point flying last	18-14

5. VORTEX BREAKDOWN – WING STALL

effect on lift, vortex breakdown position, slender wings	18-15
--	-------

6. HIGH LIFT AND CONTROL DEVICES

plain flaps, split flaps, double slotted flaps	18-16
part span flaps, aileron	18-17
antisymmetric deflection	18-18

7. COMPRESSIBILITY EFFECTS – DELTA WINGS

subsonic compressibility effects, lift at supersonic speeds	18-19
---	-------

8. PARAWINGS

geometric characteristics, lift characteristics, longitudinal moment, lift-drag characteristics	18-20
---	-------

CHAPTER XIX – LIFTING CHARACTERISTICS OF STREAMLINE BODIES

Geometry	19-1
--------------------	------

1. LIFT DUE TO CIRCULATION

theory	19-1
elliptical cones, delta wings	19-2
Mach number, lateral forces, load distribution	19-3
viscous lift, edges	19-4
vortex pair, lift = $f(\text{drag})$	19-5
square cross section, parabolic bodies	19-6
boundary layer	19-7

2. CROSS FLOW FORCE

circular cylinder, cross flow	19-9
transition	19-10
pyramidal shape, drag	19-11
airship hull	19-12
equivalent wing	19-13

3. THE LONGITUDINAL MOMENTS OF STREAMLINE BODIES

theory, streamline bodies, pressure distribution	19-13
elliptical cross section, experimental results, ducts	19-15
ducted body	19-16
neutral point, zero moment, cylindrical streamline bodies, nose shape	19-17
afterbody, cylindrical middle body, cross section, seaplane float, curvature, camber	19-18

4. STABILITY OF STREAMLINE BODIES

static stability	19-19
boat tail, streamline bodies	19-20
thickness ratio, neutral points	19-21
wedge shape	19-22
dorsal fins, tail fins	19-23
fin size, ring surface, airship	19-24
tail fins, stability	19-25

5. CONTROL OF STREAMLINE BODIES

flap theory, airplane ski, bent-up trailing edge	19-26
radio-controlled bomb, airship rudder	19-27
“Akron”, turning	19-28

CHAPTER XX – LIFT OF AIRPLANE CONFIGURATIONS

1. CONFIGURATION TYPES

general aviation aircraft	20-2
transport aircraft, military aircraft	20-4
special aircraft	20-5
sailplane design, hang gliders, variable geometry configurations	20-6

2. VARIOUS WING ARRANGEMENTS

tip-to-tip coupled, biplane	20-7
effective aspect ratio, lift distribution	20-8
multiplanes, ring foil	20-9
ground effect, induced effect	20-10
landing flaps, ram wings	20-11
tandem wings, tandem wings – refueling	20-12
canard arrangement	20-13

3. LIFT OF WING-BODY COMBINATIONS

alpha flow, body lift	19-14
wing with body, fuselage shape	20-15
fillets, displacement, engine nacelles, induced drag	20-16

4. INTERRUPTIONS OF SPAN

with longitudinal gap	20-17
horizontal tail, influence of fuselage cutouts	20-18
	20-19

5. TOTAL AIRCRAFT LIFT

stalling speed	20-19
stalling characteristics, desired stall characteristics	20-20
prediction of aircraft maximum lift	20-21
maximum lift build up, effect of flap design	20-22

CHAPTER XXI – LIFT OF BLUNT BODIES

1. IN TWO-DIMENSIONAL FLOW

flat plate	21-1
circular cylinders, unsteady lift	21-2
lateral motion, splitter plates, magnus force	21-3
power and drag, cylinders with flaps, two-dimensional shape variations, non-circular cylinders	21-4
wedge shape sections	21-5
round corners, thick airfoil	21-6

2. THREE-DIMENSIONAL DRAG BODIES

plates	21-6
bodies of revolution, parachutes	21-7
cross parachute, steerable parachutes, man in free fall	21-8
radar screens	21-9
half sphere, gliding, cones	21-10
rotating spheres	21-11

3. LIFT IN GROUND VEHICLES

automobile lift	21-12
-----------------	-------

4. LIFT FORCES ON STRUCTURES

ambient wind characteristics, fastest mile wind, hurricanes, tornados	21-13
lift in structure design, tall buildings, towers, stacks	21-14

LIST OF SYMBOLS	Z-1
-----------------	-----

ABBREVIATIONS	Z-3
---------------	-----

INDEX	Z-4
-------	-----

CHAPTER I — GENERAL INFORMATION ON FLUID DYNAMICS AND AIRPLANES

As in "Fluid-Dynamic Drag", this first chapter is intended to be some introduction as to the physical principles involved in the flow of fluids, and about airplanes in particular. The chapter also presents necessary and/or useful information on conventional definitions and physical properties. In doing so, duplication of the "general" chapter in "Fluid-Dynamic Drag" (1) has been minimized.

I. HISTORY OF AIRPLANE AERODYNAMICS

During the last decade or so, interest and effort in the United States have largely been shifted from aeronautics to astronautics (from atmospheric to space flight). Except for the deeds of the Wright Brothers (17 December 1903), and their own experiences as airline passengers, not all of our aerospace engineers may know much about the art of aerodynamic airplane design.

Heavier Than Air. We will not bother you with Leonardo da Vinci (1452 to 1519) or the balloonists (since 1783), not to mention kites (which may be 1000's of years old) or birds (22) at that. The most prominent among the "modern" aerodynamic experimenters was Otto Lilienthal (2,b). Between 1891 and 1896, he made some 2000 gliding flights, down the side of a hill. Samuel P. Langley (then Director of the Smithsonian Institution) flew a steam-powered model airplane in 1896; and one with a gasoline engine in 1903. During all this time, stabilizing tail surfaces were used; and it is the Frenchman Penaud, who is reported to have invented the elevator, and to have combined it with the control of a rudder in a "stick" (1872 or 1876). The Wright Brothers invented the aileron, by warping the ends of their wings.

Aerodynamic Theory in modern form, may have begun with Newton (Professor of Mathematics, 1642 to 1727). However, the largest steps forward have been the concept of the limited boundary layer (1904) promoted by Ludwig Prandtl (1875 to 1953) and his induced-drag formulation (before 1918). An equally famous aerodynamic scientist was Theodore von Karman (1881 to 1962) particularly known for his work on turbulent skin friction and in gasdynamics (3,e). Others instrumental in the development of modern knowledge in the field of fluid dynamics, listed in (1) have been:

Will Froude	(1810 to 1879)	dynamic Froude similarity
Osborne Reynolds	(1842 to 1912)	similarity of viscous flow
N. E. Joukovsky	(1847 to 1921)	airfoil-section theory
F. W. Lanchester	(1868 to 1945)	flight mechanics

Still others are acknowledged in (2,d).

Wind Tunnels. Experiments, by means of arms rotating models through the air (Lilienthal) or by moving them through water (towing tanks) were undertaken before 1900. Then came a period, particularly characterized by Gustave Eiffel (1832 to 1923) where wind tunnels (6) were built and used to find empirical forces such as the lift of wings. Then, persons such as Prandtl and his many associates tried to analyze the potential flow around wings. Subsequently, hundreds of wind tunnels such as in (4,d) proved that the theories were not quite right. As a consequence, 1000's of tunnel investigations were undertaken. In fact, full-scale tunnels were built, at least in France and in the United States (6,c), where real airplanes could be tested, to finally arrive at the truth of aerodynamic forces and moments. However, all tunnels are limited in size, speed, pressure, temperature, quality of the stream, or at least half of these parameters. Theory and/or empirical calibration, is therefore required to "correct" the findings obtained in wind tunnels:

- (2) History of aerodynamic airplane development:
 - a) History of Flight, American Heritage (Simon & Schuster) 1962.
 - b) Lilienthal, "Vlgeflug als Grundlage der Fliegekunst", Berlin 1889.
 - c) Octave Chanute, "Progress in Flying Machines", 1894
 - d) Hunsaker and Doolittle, To 1958, NACA Last Annual Rpt (1958).

(1) Hoerner, "Fluid-Dynamic Drag", 1958 and 1965 Editions, published by the author

a) Turbulence (6,g). The flow of air in a wind tunnel is more or less turbulent. The acoustic noise from the fan driving the stream of air, is already sufficient to precipitate turbulence in an otherwise laminar boundary layer, in particular around the nose of an airfoil section.

b) Stimulation of boundary layer turbulence (by stream turbulence or by surface roughness on the model) is very often desirable to produce at least qualitatively, flow pattern and forces as at higher Reynolds numbers.

c) Induced Angle. Elaborate methods have been developed and "verified" to account for the influence of the tunnel walls (or the absence of them) upon the induced angle of attack of wings.

d) Blockage. When placing an obstacle within a duct (such as the test section of a wind tunnel) a pressure drop necessarily develops, from a higher level (ahead of the model) to a lower level (behind the model). Not only drag, but also lift is thus affected.

While all these considerations are of little or no consequence, within the range of smaller lift coefficients and larger tunnels, they can be problematic at higher coefficients (including $C_{L\alpha}$) and particularly in regard to the longitudinal (pitching) moment.

(3) Theoretical advancement of aerodynamics:

- a) Prandtl, Necrology, see Journal Aeron Sciences 1953 p 779.
- b) Lanchester, "Aerodynamics", London 1907; and "Aeronautics", 1908.
- c) Prandtl, "Essentials of Fluid Dynamics", Trans New York 1952.
- d) The aerodynamic center of airfoils and/or wings was established by v.Mises (1917 and 1920) and quoted or repeated by Munk (1922), Glauert (3,f), Durand (3,i), and Theodorsen (NACA Rpt 383 and 411).
- e) Dryden, Karman's Contributions, Astronautics Aerospace Engg July 1963.
- f) Glauert, "Aerofoil and Airscrew Theory", Cambridge 1926.
- g) Schlichting, "Boundary Layer Theory" (1951, 1965), McGraw Hill 1955.
- i) Durand, 6 volumes of "Aerodynamic Theory", 1934/36/43.

(4) Experimental fluid dynamics (wind tunnels):

- a) Otto Lilienthal, Rotating Arm, see reference (2,b).
- b) Flachsbarth, History of Experimental Fluid-Dynamics (from the Greeks to past 1900), Volume IV-2 of Wien-Harms "Handbook Experimentalphysik" (1932).
- c) Eiffel, Recherches de l'Air et l'Aviation, Paris 1910 and 1914.
- d) Ergebnisse AVA Gottingen, Volumes I (1920) II (1923) III (1927) IV (1934).
- e) Lewis: "The model test may be considered as an analogue type of computer", stated in Transactions SNAME 1954 p 431.
- f) Schulz, Design and Use of Tunnels, Luftfahrttechnik 1958 p 105.
- g) Hoerner, Design and Operation of a Water Tunnel, Fieseler Rpts 1939.

High Reynolds Numbers. Researchers such as Eiffel and Prandtl started out with R'numbers (on wing chord) around 10^5 . We now have test results up to 10^7 . In the quest for higher Reynolds numbers, the speeds of wind tunnels have been increased over the years (this leads to compressibility effects), the size has been increased up to 240 m^2 ($= 2500 \text{ ft}^2$) test-cross-section area (which results in expensive and hard to manage facilities), and the tunnel pressure has been increased in a few installations (thus increasing the air density in the Reynolds number). The last method leads to a very interesting phenomenon. As pointed out in chapter V of "Fluid-Dynamic Drag", the permissible surface roughness of the wing models to be investigated, is among others $k \sim 1/\rho$. So, for a tunnel pressure of 10 at (instead of one at) that size is only 1/10 of that in atmospheric air (provided that temperature and speed are the same). Besides the British Compressed Air Tunnel, an extreme example is or was the NACA's Variable Density Tunnel. For a maximum pressure of 20 atmospheres, at a speed of 8 m/s ($= 26 \text{ ft/sec}$) the maximum permissible "sand" grain size is in the order of 0.01 mm. For comparison, this is between the optimum possible painted, and the average paint-sprayed surface of airplanes. Of course, a metal surface can be polished down to a grain size of one micron ($= 1/1000$ of a mm). However, erosion by dust particles usually present in wind tunnels, can be expected to produce roughness much larger than one micron during the testing of a model. In fact, the tunnel discussed is no longer listed as active in (6,d). We are tempted to use the many published results from that tunnel, however. In conclusion, a little better thinking can be more important than a lot of "fruitless air blowing" (quoted from Munk, J. Aeron Sci 1938 p 241). To say the least, test conditions have to be judged when using wind-tunnel results. One can also say that applied fluid dynamics is to some degree an art (rather than a science); and in the words of Philip von Doepf (Junker's last chief aerodynamicist), "the air is a beast", meaning that we must always be prepared for an unexpected result.

Aviation. Since the days of Lilienthal and the Wright Brothers, aviation has grown from a possible 30 people involved, at one and the same time, to more than 30,000 members of the American Institute of Aeronautics and Astronautics alone. The number of employees of the big airplane (and space) companies may be above 100,000 each. The number of airplanes produced during WW II was in the order of 300,000. The number of passenger miles is now in excess of 40 billion per year. In the words C.S. Gross (Lockheed Aircraft Corporation) all this may only be the beginning of atmospheric aviation. It is possible that now after reaching the moon (and finding nothing there but clues as to the nature of the Universe), that technological interest will really return to safe and low cost mass transportation from New York to London or San Francisco as well as other nearby cities.

Mathematics. Ever since Newton (around 1700), mathematics have been a useful tool in the exploration of fluid dynamics. It must be said, however, that Newton's theory of particle flow (although correct at the boundary of outer space, see chapter XIX of "Fluid-Dynamic Drag") was erroneous as far as atmospheric airplanes are concerned. This did not prevent civil engineers from applying results of that theory in building codes, for a period of 200 years. Contrary to the belief of many, Einstein was originally and primarily a physicist (with imagination). He had to learn and use mathematics, however, as a tool to bring order and system into his theories. Today we have computers speeding up the work not only of mathematics, but also of your supermarket. This book only uses high-school mathematics. The point is to encourage the designer of airplanes (and similar contraptions) to think in terms of force, power, moment, equilibrium, as the Wright Brothers, or men such as Ludwig Prandtl, did. Instead of depending on the results for computer studies, the engineer should in many cases study the problem and conduct the necessary simple calculations to obtain answers. This is important as many of the computer programs are long and complex with only the initial programmer and the engineers involved able to understand the program, its limitations and results. By conducting his own calculations and knowing the many assumptions and empirical data, the background necessary to apply the computer programs is obtained with a much better understanding of the results. The computer programs then become extremely valuable and, with proper testing, lead to the best overall solution. In conclusion, a sound combination of analysis (mathematics), experience and experiment will lead to the most satisfactory engineering results.

- (5) The most important research reports come from:
 - a) National Advisory Committee for Aeronautics (since 1915).
 - b) National Aeronautics and Space Administration (since 1959).
 - c) British Aeronautical Research Council; Brit Info Service New York City.
- (6) Characteristics and description of wind tunnels:
 - a) Prandtl, Wind-Tunnel Design, in Wien-Harms Handbook Vol IV-2 (1932).
 - b) Hoerner, Survey of European Tunnels, Z.VDI 1936 p 949.
 - c) DeFrance, Full-Scale Wind Tunnel, NACA Rpt 459 (1933).
 - d) Schaefer, Wind Tunnels at Langley Field, NASA TM X-1130 (1965).
 - e) Hoerner, Spheres and Turbulence, Lufo (March 1935) p 42; NACA TM 777.
 - f) Hoerner, TH Brunswick Wind Tunnel, Luftf Forschung 1937 p 36.
 - g) Schuh, Tunnel Turbulence and Noise Measured, ARC RM 2905 (1957).
 - h) Anon, National Wind-Tunnel Summary, NASA and Defense Department (1961), available from U.S. Department of Commerce.

2. GLOSSARY OF TERMS

There are some comparatively recent publications available (9,a) listing and defining aero-space terms. In the following are some of them referring to lifting airplanes.

An Airfoil (British "aerofoil") is usually meant to be a rectangular wing model, used to determine lifting characteristics of particular airfoil or wing sections. There may be some doubt whether the airfoil has a leading edge or a "nose". The latter evidently comes from the two-dimensional thinking (on paper) in terms of airfoil-section shapes. One also talks about "points" along the surface. So there is some confusion between 2- and 3-dimensional terms.

Wing. It seems that birds have a pair of wings, while an airplane has only one. This wing has a pair of "panel", however. Wings used to be straight; they are swept now, that is in high subsonic speed airplanes. The shape preferred in super-hypersonic flight is the "delta" wing. The most important geometric characteristic of wings is their aspect ratio

$$A = b/\bar{c} = b^2/S = S/\bar{c}^2 \quad (1)$$

where \bar{c} = (mean aerodynamic chord) = S/b .

S = wing area

b = wing span

Aerodynamic Center. In Europe, there were many decades where the pitching moment was measured and defined about the leading-edge "point". Since theoretically the lift can be expected to be centered at $1/4$ of the chord, that is at $x = 0.25 c$, it became customary, however, to indicate the moment about this point. While in the European definition, the coefficient may thus be C_m in the order of $-0.25 C_L$ (indicating that the lift would cause the airfoil to pitch down, about the leading edge) — the coefficient may be $C_{m/a} = (+ \text{ or } -0.01) C_L$, for example, thus indicating that the lift force is centered at a point ($0.01 C_L$) ahead or aft of the quarter-chord point. There is also a point on or near the chord of every airfoil (or a transverse axis in every airplane without a horizontal tail) about which the moment coefficient C_m is constant (when increasing the lift coefficient). This point is the aerodynamic center (3,d); see Chapter II on airfoils.

- (7) Biot (a friend of vonKarman), "Drowning in Complexity", Mech Engg 1963 p 26; says that engineering "ability is intuitive, resembling artistic talent", while "formal knowledge rather than understanding, is not favorable to creative talent".

Mean Aerodynamic Chord. Considering a wing with an arbitrary plan-form shape, the mean aerodynamic chord is that of "an imaginary rectangular wing that would have pitching moments the same as those of the actual airfoil or combination of airfoils" (such as a biplane). The "mac" is geometrically defined by

$$c = (2/S) \int_0^{b/2} c^2 dy \quad (2)$$

In case of a swept wing, the spanwise position is of great importance. It is normally assumed that the lift distribution be elliptical. The load is then concentrated at

$$y = (4/3\pi) b/2 = 0.424 (b/2) \quad (3)$$

from the centerline. Of course, the lateral center is "always" somewhere else. In particular, in rectangular and/or swept-back wings it is outboard of 0.424. It would therefore be just as well to determine the aerodynamic center as a geometrical point as in figure 2 in Chapter XI.

Lift Angle. Lift as a function of the angle of attack is usually given in form of the derivative $(dC_L/d\alpha)$. However, in wings with finite span, the angle required to produce a certain lift coefficient consists of at least 2 components. Including the influence of longer chords and the proximity of the ground (in airplane wings) or the water surface (in hydrofoils), there are at least 2 more additional terms of the angle of attack to be taken into account. It is therefore logical to use what we call the "lift angle", namely the derivative $(d\alpha/dC_L) = (d\alpha/dC_L)_1 + (d\alpha/dC_L)_2$ and so on. The equations describing lift are thus simplified, and each component can be treated individually.

Forces. As shown in figure 1, in the wind-tunnel system, the normal-force coefficient of a wing is

$$C_N = C_L \cos \alpha + C_D \sin \alpha \quad (4)$$

where the second term is usually quite small. However, in the longitudinal (or chordwise) direction, the two components of the longitudinal force

$$C_X = C_D \cos \alpha - C_L \sin \alpha \quad (5)$$

are of equal importance. In fact, if $C_D = 0.01$ for example, a $C_L = (dC_L/d\alpha) \sin \alpha \approx 4(0.0025)$ is sufficient to make $C_X = \text{zero}$. The corresponding values are $\alpha = 0.05 \approx 3^\circ$, and $C_L = 0.2$. In other words, at larger angles of attack, C_X turns negative, which means directed forward along the wing chord. — It might sometimes also be necessary to consider the resultant of the components. This "total" force corresponds to

$$C_R = C_L^2 + C_D^2 \quad (6)$$

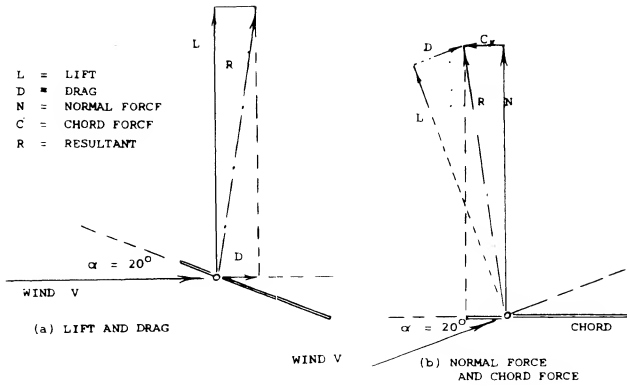


Figure 1. Aerodynamic forces and their components in an airfoil section (or of an airplane).

and it should not be confused with the normal force, of a wing for example. As shown in the illustration that force can also be split up into the normal force (equation 4) and a longitudinal or tangential component.

A Vortex has a strength of circulation

$$\Gamma = w2r \quad \text{in (m}^2/\text{s)} \quad (7)$$

This means that $(wr) = \text{constant}$, and $w \sim 1/r$. The circumferential speed w thus varies with the radius r in the same manner as that of a planet or satellite. Theoretically, therefore, $w \rightarrow \infty$ in the center of the vortex. In reality, viscosity produces a rotating core, where $w \sim r$. The circulation of a wing is

$$\Gamma = 0.5C_L V_\infty = w2r\pi \quad (8)$$

and this circulation is maintained in the pair of trailing vortices. We obtain the speed ratio

$$V/w = 4\pi(r/c)/C_L \quad (10)$$

Since formation and diameter of that core is a matter of viscosity and the disturbance (separation) of the flow at the lateral edges of a wing, experimental results are better than any estimates. In this respect, see Chapter III.

Irrotational is a flow, and particularly that in a vortex, where the air particles move in the manner as the cars in a Ferris wheel (G.W.G. Ferris, engineer, 1859 to 1896). It is difficult, however, to "tie in this analogy with the mathematics of the flow". Indeed, it does not seem to be of any practical consequence whether the molecules rotate about their own axes. It is emphasized, however, that any rotational flow involves losses of energy, through turbulent mixing and possibly by way of flow separation. Might "irrotational" be a misnomer, insofar as absence of viscosity would be more important?

Potential Flow. In contradistinction to a streamline, a streamtube is something real. The constant volume flow of air which it is carrying, is its "stream function" Q in (m^3/s). In theoretical analysis, the tube is said to gain the

$$\text{potential} = (Q/S)x = Vx \quad \text{in } (m^2/s) \quad (11)$$

This quantity can be visualized as that of a mass travelling upward at the speed V , thus gaining potential energy. In any direction normal to a streamline, the potential is constant. In the direction of the streamline the stream function, is constant, while the potential may be said to be a level, the variation of which produces a speed differential. All this applies only to "irrotational" flow, as explained above. When, under conditions of no loss of momentum, the diameter of a streamtube increases, the velocity decreases, and the rate of gain of the potential decreases accordingly. However, the rate increases again, when the velocity increases, for example as a consequence of a negative pressure gradient.

The Momentum of a solid body moving at the speed V , is

$$\text{momentum} = \text{mass (speed)} \quad \text{in } (kg \text{ m/s}) \quad (12)$$

It is an indication for the inherent energy of that body, or the work which the mass can produce when stopped. Thus

$$\begin{aligned} \text{work} &= \text{energy} = \text{momentum (speed)} \\ \text{in } (N\cdot m) &= (kg\cdot m^2/s^2) \end{aligned} \quad (13)$$

In a stream of air, we do not have a finite mass. Rather, in case of a propeller or a jet engine, we have a mass flow in kg/s . The thrust produced is

$$\begin{aligned} T &= (\text{mass flow}) (\text{added speed}); \\ \text{in } N &= (kg\cdot m/s^2) \end{aligned} \quad (14)$$

In the case of a lifting wing, momentum is transferred onto the passing stream of air by adding a vertical component of velocity. Momentum is thus added, not in the direction of flow, but essentially at a right angle to it. Accordingly, lift is proportional to the vertical or downwash velocity w

$$L \sim (\text{mass flow}) w; \quad \text{in } N = (kg\cdot m/s^2) \quad (15)$$

Pressure. Various types of pressure in fluid-dynamic flow are explained in "Fluid-Dynamic Drag". Because of their importance, the following is added (or repeated) at this point. Absolute pressures, such as $p = 2116 \text{ lb/ft}^2$, or $= 1010 \text{ N/m}^2$, as in the ambient standard atmosphere at sea level, are often used in gasdynamics (at supersonic speed). Within the range of subsonic aerodynamics, pressure *differences* are usually considered. An example for such a differential is the "gage" pressure in the tires of an automobile, measured against the atmosphere. Of course, lift is the result of pressure differences between the upper and lower side of a wing; and it would not make any difference whether the pressures involved would be measured as absolute or relative quantities. In a wind tunnel, for example, it is more convenient and accurate, however, to measure them as gage pressures, that is as positive or negative quantities as against the ambient (atmospheric or tunnel) pressure. To be correct, the pressure coefficient should thus be written as

$$C_p = (p - p_a)/q = \Delta p/q \quad (16)$$

where "a" indicates "ambient" or "atmosphere", and Δp = pressure differential.

Stagnation Point. Strictly, an airplane may only have one point (at the nose of the fuselage) where the air particles really come to rest. No doubt, a configuration with a swept-forward wing will have a minimum of three such points. For practical purposes, a straight leading edge would have a stagnation "line", however. In incompressible fluid flow, the pressure increment at the stagnation point is the "dynamic" pressure

$$q = 0.5 \rho V^2 \quad (17)$$

In spite of its name, this pressure is thus basically a static pressure differential; namely between that at a stagnation point (where velocity = zero) and the ambient level. At higher speeds in gases, the pressure at the point is higher, however, than according to equation (17), because of compressibility of the fluid or air used, and on account of an increase in its temperature. That pressure is called the impact pressure. The dynamic pressure must then be considered to be a dynamic potential of the stream of air against an obstacle; and all coefficients (at least in subsonic aerodynamic flow) are still referred to that pressure. One practical reason for doing so, is skin-friction, the coefficient of which reduces with the Mach number (because of increasing temperature and increasing density within the boundary layer). Another reason is the fact that the value of negative pressure coefficients does not increase in proportion to that of the stagnation pressure. The only place where forces et cetera, are found to be proportional to the impact pressure, is in hypersonic gas dynamics.

- (8) General and varied information on applied aerodynamics:
 a) Goldstein, "Modern Developments Fluid Dynamics", London 1938.
 b) Eck, "Technische Stromungslehre", Springer 1941 and 1961.
 c) Thwaites, "Incompressible Aerodynamics", Clarendon Oxford 1960.

"Negative" Pressure. One of the discoveries of experimenters such as Lilienthal (before 1900) was the fact that "suction" over the upper side of a properly cambered airfoil contributes more to lift than the "positive" pressure at the lower side. Of course, in absolute terms, pressure at the upper side was simply more lower, than that at the lower side was higher. This balance of pressures can be dramatized when thinking of a pump in a farm-yard. When moving the plunger up, it does not exactly draw water up. Rather, the piston tries to create a vacuum; and the atmospheric pressure pushes the water up *from below*. In fact, when the waterlevel in the well is more than some 10 m or 34 below the pump, no water can be pumped at all. A similar thing happens in hypersonic flow (at $M \rightarrow \infty$) where the pressure on the upper side of a wing is zero (vacuum) and "all" of the lift is produced by positive pressure at the lower side.

"Pressure Distribution" generally indicates the distribution of static pressure over the upper and lower surfaces of a wing, plotted particularly in chordwise direction. In contradistinction, the term "load distribution", for example along the span of a wing, indicates that of the normal force which is equal to the pressure differential between lower and upper side. For the sake of correlation with the sides of airfoil sections, their pressure distributions are usually plotted with the negative pressure coefficients developing along the upper section side up, and the positive values on the lower side down. This procedure could be made mathematically perfect when plotting $(V_+/V)^2 = 1 - C_{p+}$, where (+) indicates the specific location. For $V_+ = V$, we then find $C_{p+} = 0$; or for $(V_+/V)^2 = 0$, we have $C_{p+} = +1$.

Hydrodynamics. The term "hydrodynamics" is used in aerodynamics, to indicate that compressibility is absent or negligibly small. There are devices, however, actually used in water, producing "lift" in a manner at least similar to that of wings in air. In ships and boats, we have rubbers, fins, control surfaces (in submarines) and finally hydrofoils. As far as their fluid-dynamic characteristics are the "same" as in air, a chapter of this book is devoted to their presentation. Since "lifting" characteristics in water can also be different or limited (by cavitation or ventilation), another chapter is added describing these effects.

Other Terms, explained in chapter I of "Fluid-Dynamic Drag" are:

Boundary layer, developing along surfaces;
Circulation around wings, as in equation (8);
Compressibility in air flow, at higher speeds;
Downwash, developing behind wings;
Induced angle of attack, in wings;
Rotation, as in the core of a vortex;
Separation and Wake Flow, associated with pressure drag;

Streamlines and Streamtubes, forming a flow pattern;
Turbulence, developing in boundary layers;
Vortex, lifting and trailing, as mentioned above;
Vorticity, in viscous fluid flow, equivalent to "rotation".

Similarity Laws. Many fluid-dynamic similarity laws are needed to correlate model test results with full scale tests. The more common parameters used are Reynolds number, the ratio of the inertia forces in the fluid to the viscous forces, and Mach number, the ratio of the velocity of the body to the velocity of sound. The following additional correlating parameters are explained in "Fluid-Dynamic Drag" and are also of importance:

- Lift, drag and movement non-dimensional coefficients
- Cavitation Number in water
- Froude Number, at the surface of the water.

Regarding the various laws of similarity, there may be conditions where at least two of them are involved at the same time (such as Reynolds and Mach number). There are, on the other hand, areas where one or the other is not important (such as compressibility in water). We have to be sure, however, that we do not cross critical boundaries, between different modes of fluid behavior (such as the critical Mach number, or the number of incipient cavitation).

Metric System. The atomic physicist Edward Teller is reported to have said that "the United States may lose the space race by an inch". Meanwhile, the U.S. Army is measuring distance in meters, NASA's space laboratories are using the metric system, and the Bureau of Standards has adopted it. The metric system is thus generally used in this book. Conversion factors and constants may be found in (10,a), which is readily available as well as many other sources.

- (9) Regarding aeronautical terminology, see:
 - a) Adams, Aeronautical Dictionary, NACA (1959).
 - b) Books such as Diehl (20,b) and Wood (20,c) (20,h).
 - d) Wenzelberger, Mechanical Analogy, Award Paper IAS Student Conference (1957).
 - e) NAVAER (Operations) Flight Manual (1957); reproduced by Fed Aviation Agency.
 - f) Nayler, Dictionary Aeronautical Engg, Philosophical Library New York.
- (10) The international system of units (SI):
 - a) Mechtley, International System of Units, NASA SP-7012 (1964). Available Superintendent of Documents, U.S. Government Printing Office, Washington, D.C. 20402.
 - b) Hamilton, "Going Metric", The Engineer 1966 p 150.
 - c) Miller, Calibration in Hotshot Tunnel, NASA TN D-3278 (1966).
 - d) See also "The Standard Atmosphere" under (11,e).

3. NOMENCLATURE

For convenience, symbols as used throughout this text, are listed at the very end of the book. In this manner, the meaning of any one symbol can easily be found, without searching through this first chapter.

Directions. There are two geometric systems considered and used in airplane aerodynamics.

a) Body axes (as in part (a) of figure 2) could logically be used by a pilot flying in an airplane; and they are used when analyzing motions of airplanes. It should be noted that x is positive forward from the CG, and Z positive in the down direction (where the airplane tends to fall). According to standard notation roll angle ψ and moment "L" are positive in right-hand screwdriver direction.

b) In a wind tunnel, the geometric system is defined by the direction of the airflow (as in part (b) of figure 2). Lift L and drag D as produced by that flow are positive in their common sense. Fortunately, the angles of pitch (of attack) and or roll are defined positive in the same directions in the two systems.

The difference between the two systems is shown in figure 2. In part (a) the airplane moves forward and sideways (sideslipping) in positive directions. In part (b) of the illustration, the airplane is stationary (suspended in a wind tunnel) and set at an angle of yaw. The wind direction is positive. About the vertical axis, the angle of "sideslip" is defined to be positive when the airplane moves to the right (starboard) side. This definition is opposite to the angle of yaw under (b), where the airplane is turned to the right, so that the wind comes from the left. Nevertheless, the corresponding moment is still the "yaw moment" as under (a). The corresponding angle is the angle of yaw. Regarding the sign, the aerodynamic engineer is primarily interested in whether the yaw moment helps turning when deflecting the ailerons or not. Thus the positive direction as in system (a) conveys the right meaning, while a negative yaw moment can also be called "adverse", even if by definition, it is positive in system (b). The same combination of signs for roll and yaw moments goes for a motion initiated by rudder deflection. — Since in this text, forces and moments, rather than motions, are primarily considered, the wind-tunnel system (b) is predominantly used. As in general usage, some inconsistencies (some mixup between the two systems of reference) seem to be unavoidable, however. — There is still another direction used in aerodynamic language. According to Webster, down — and upstream indicate a direction, rather than a location. To identify the ends of a fuselage, one should, therefore, use the words forward and aft or rear; or in case of wing edges, leading and trailing.

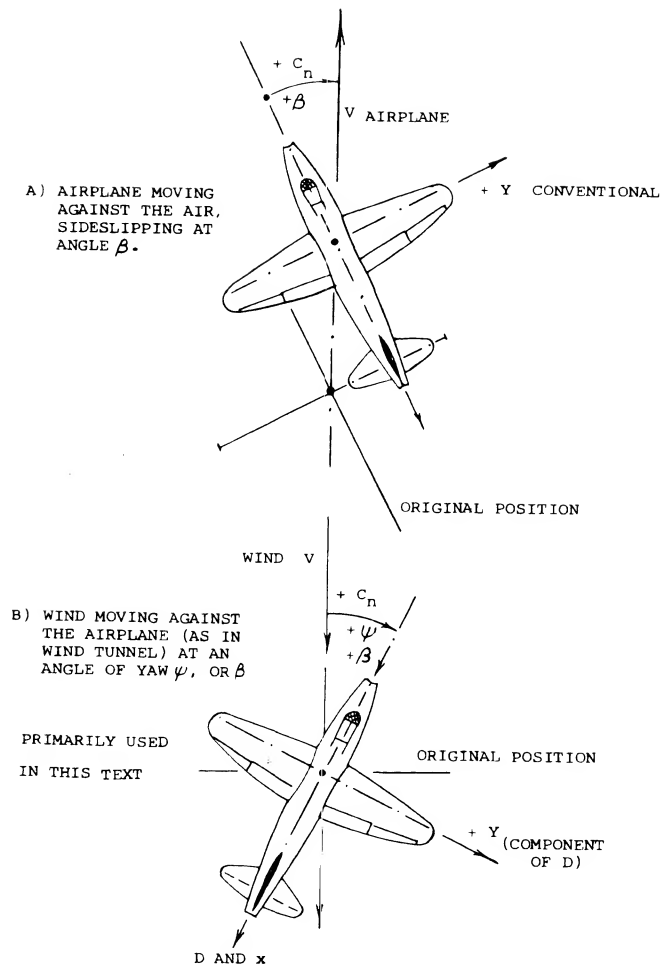


Figure 2. Systems of axes, forces, moments, used in analysis and presentation of aerodynamic characteristics of airplanes.

- (11) Physical properties of air as a function of altitude:
 - a) Values by International Civil Aviation Organization (1952), NACA Rpt 1235.
 - b) Atmospheric properties are presented at length in (20,c) (20,h).
 - c) Properties are presented in chapters I & XIX of "Fluid-Dynamic Drag".
 - d) Information on viscosity is found in chapter I of "Fluid-Dynamic Drag".
 - e) Minzner, US Standard Atmosphere 1962, US Government Printing Office.
 - f) Density Variations, Army R&D Labs Monmouth Rpt 2393 (1963); AD-425,913.
 - g) Valley, "Handbook Geophysics and Space", McGraw-Hill 1965.
- (13) Regarding various types of pressure see:
 - a) Aiken, Pressures and Airspeeds, NACA Rpt 837 (1946).
 - b) Atmospheric, as a function of altitudes, see (11,a,b,e).
 - c) The pressure p in figure 4 is of importance for the performance of engines.

Angle of Attack. In the two systems discussed, the angle of attack or pitch has one and the same sign. A British synonym is "incidence". In the United States, however, the angle of incidence (or that of setting) is meant to be that of the wing (or horizontal-tail) chord against the fuselage. Corresponding to the sign of these angles, positive when "nose-up" and when increasing the lift, the longitudinal or pitch moment is automatically called positive when tending to increase the angle of attack. As a consequence, longitudinal stability in terms of (dC_m/dC_L) or $(dC_L/d\alpha)$, has a negative sign when the airplane is stable. — Still another longitudinal angle is that of attitude, that is the angle of the airplane axis against the horizontal. The angle of climb or of gliding is included in this angle.

Positive/Negative Values. For the aerodynamic engineer, there are various considerations where the sign of a parameter is in doubt. We see in figure 2 that in one system of reference, drag is positive, while in the other, thrust is positive. Also, which one is positive, lift or weight = g (mass)? Regarding the induced angle of attack, we can write

$$C_L = 2\pi(\alpha_2 - \alpha_i);$$

$$\text{or } C_L = (dC_L/d\alpha)(\alpha_2 + \alpha_i) \quad (18)$$

where α_2 = two-dimensional or sectional angle. In a similar manner, it can be argued whether the angle of downwash behind a wing is positive or negative. Certainly, this angle is down in the wind system, but the foil requires an additional positive angle of attack. In all such examples, we have action and reaction, or the compensation of fluid-dynamic forces or moments by "static" ones. The problems can be resolved by accepting absolute values of the many dimensions involved; and the typical engineer is doing that daily, without even thinking about it. The sign of a quantity becomes critical, however, when pitching one force (for example) against another one, or when adding quantities (such as lift and weight, for example).

4. PHYSICAL PROPERTIES OF FLUIDS

Properties such as density and viscosity are presented in chapters I and XIX of "Fluid-Dynamic Drag". Some of them are presented here again, in revised form.

(A) Characteristics of Atmospheric Air

Air is the most important element for fluid-dynamic motion. Its properties are simple and consistent within the range of subsonic (and transonic) speeds and up to altitudes in the order of 90 km.

Sea-Level Constants. Many examples of air flow (such as takeoff and landing of airplanes, for example) take place near the ground, or at sea level. For such operations, a standard atmosphere (11) has been adopted by international convention, averaging conditions in the temperate zones of the earth:

temperature (15° C)	T_o	= 288.1	°K
pressure (760 mm Hg)	p_o	= $1.01(10)^5$	N/m
mass density (equation 19)	ρ	= 1.225	kg/m
kinematic viscosity $(\mu/\rho)_o$	ν_o	= $1.46/10^5$	m ² /s
speed of sound	a_o	= 340.3	m/s
gravity acceleration	g	= 9.807	m/s ²

The temperature at the freezing point of water (where $T = 0^\circ \text{C}$) is $T = 273.15^\circ \text{K}$, and at the boiling point under sea-level pressure, = 100°C , or = 373.15°K .

Dynamic Pressure. The mass density of air is essentially

$$\rho(\text{kg/m}^3) = p(\text{N/m}^2) / 'R' T (^\circ \text{K}) \quad (19)$$

where 'R' = gas constant = $8314/29 = 290$ (N-m/kg-°K), up to some 90 km altitude, in one of its many definitions. In standard sea-level air, it happens to be that

$$\rho_o = g/8 = 1.225 \text{ (kg/m}^3\text{)} \quad (20)$$

as listed above. The dynamic pressure $q = 0.5 \rho V^2$ at sea level is accordingly

$$q_o = (V, \text{m/s})^2 / 2.45 = (V, \text{kts})^2 / 9.3$$

$$\text{in (N/M}^2\text{) or (kg/m-s}^2\text{)} \quad (21)$$

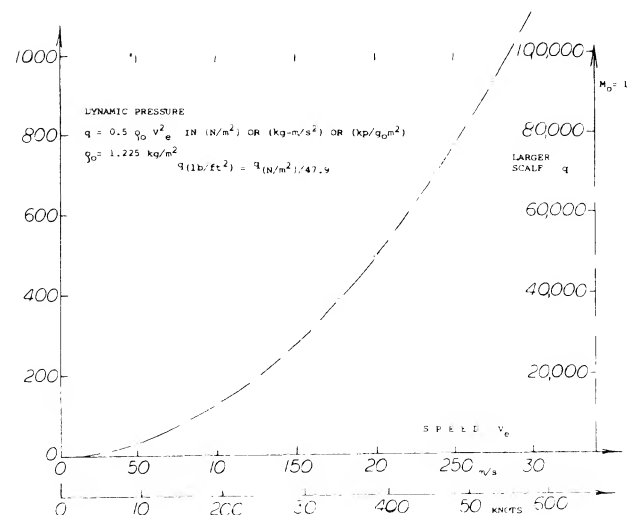


Figure 3. Standardized dynamic pressure, as a function of indicated, or effective sea-level speed.

This pressure is plotted in figure 3. Of course, there is some variation between the seasons of the year. As we all know, temperature at the ground may be 15 °C lower during a winter day, and 15 °C higher on a summer day. Atmospheric density may thus be 5% higher or lower. Also considering a possible variation of the barometric pressure in the order of + or -3%, the total variation of density and dynamic pressure at sea level as in figure 3, could be + or - 8%.

Function of Altitude. Aviation is not confined to sea-level operation. In fact, modern airliners cruise at altitudes around 10 km, not to mention the supersonic transporter SST which will do it at some 20 km. Values of temperature and density ratios, standardized for the temperate zones of the earth, are plotted in figures 4 and 5. It is seen how temperature reaches a value assumed to be constant, at $Z = 11$ km. Density at this altitude is down to about 30% of that at sea level, which could be said to mean that the drag of an airliner be reduced to the same 30%. What is said above regarding temperature and density deviations from the average or standard values at sea level, does not mean, however, that the same differentials would also be found at altitude (11,f), let alone higher altitudes, that is above some 30 km. It is also not correct to assume that the same differences as at sea level, between the equator and the poles of the earth, would also prevail at those altitudes. In fact, temperatures can be warmer at times and locations where they are expected to be colder, and vice versa.

Viscosity of the Air. The dynamic or physical or absolute viscosity in standard sea-level air is

$$\mu_o = 1.79/10^5 \quad (\text{m}^2/\text{s}) \quad (22)$$

For all practical purposes covered in this book, this type of viscosity is independent of pressure. As plotted in chapter I of "Fluid-Dynamic Drag", it increases with temperature, however. For subsonic speeds (that is, between $T = 170$ and 500°K) the viscosity of air varies in good approximation, as

$$\mu \sim T^{0.76} \quad (23)$$

By combination with the density, the kinematic viscosity $\nu = \mu/\rho$ is obtained (in m^2/s). Under standard sea-level conditions (see tabulation above) the non-dimensional Reynolds number is then approximately

$$R_\ell = V\ell/\nu \approx V\ell 7(10)^4 \quad (24)$$

where ℓ is a suitable length such as the mean aerodynamic wing chord in particular. Of course, at altitude, the absolute viscosity has to be reduced as per equation (23), while the density reduces as in figure 4. For example, as Z above 11 km,

$$\mu = (0.75)^{0.76} \mu_o = 0.805 \mu_o \quad (25)$$

Considering the density at 11 km to be 30% of that at sea level, we obtain a kinematic viscosity

$$\nu = (0.805/0.30)\nu_o = 2.7 \nu_o$$

for that particular altitude. The important result is that the Reynolds number $R_\ell \sim 1/\nu$, reduces considerably with altitude for a given airplane when flying at the same speed, that is to $1/2.7 = 37\%$, for example at 11 km. When flying at the same dynamic pressure (which means essentially at the same lift, drag and thrust) the speed at 11 km is increased to $(1/0.3) = 1.8$ times that at sea level. The Reynolds number is then $(1.8/2.7) = 0.67$ times that at sea level.

The Speed of Sound is generally

$$a' = \sqrt{dp/d\rho} = \sqrt{k'R'T} \quad (26)$$

where $k = c_p/c_v = 1.4 = \text{constant}$ in atmospheric air up to some 100 km, and ' R ' = gas constant as above. For standard sea-level temperature, the sonic velocity is

$$a' \approx 340 \text{ (m/s)} \approx 660 \text{ knots} \quad (27)$$

Throughout the troposphere, the speed of sound reduces according to

$$a' = 20\sqrt{T(^{\circ}\text{K})} \quad \text{in (m/s)} \quad (28)$$

Disregarding a tiny decrease of $g = \text{acceleration due to gravity}$, the standardized speed of sound remains constant above $Z = 11$ km, see figure 5:

$$a' = 0.867 a'_o = 0.867 (340.3) = 297 \text{ (m/s)}$$

For practical purposes, we might memorize this speed to be 1% less than $= 300 \text{ m/s}$.

- (14) Intensity and characteristics of rain, fog, icing:
- a) Brun, Impingement of Water Droplets on 65-208, 65-212, 65AO(04 to 12)% Airfoils at $\alpha = 4^\circ$, NACA TN 2952 and 3047 (1953).
 - b) Brun and Dorsch, On Bodies, NACA TN 2903, 3099, 3147, 3153, 3410 (1953/55).
 - c) Kriebel and Lundberg, Drag in Particle-Laden Gas Flow, 4 Rpts (1962) for Defense Atomic Supply Agency by Stanford Res Institute; AD-291,178.
 - d) Shifrin, Microstructure of Fog, NASA Trans TT F-317 (1964).
 - e) Preston, Ice Formation and Airplane Performance NACA TN 1598 (1948).
 - f) Gray, Aerodynamic Penalties by Ice on Airfoils, NASA TN D-2166 (1964).

Humidity. The amount of water "solved" in atmospheric air is usually small (less than 1% by weight, before vaporizing). Since vapor is lighter than air, the density is reduced (14,f). For example, in standard sea-level condition, 100% vapor humidity reduces density by 0.6%. Humidity has other effects upon the air, such as upon temperature as a function of altitude. More dramatic results are fog, clouds, rain, snow and icing.

Fog. As stated in (14,d) fog particles are between 4 and 15 microns in diameter; and there are at least 50 droplets in one cm^3 . The mass ratio is then found to be in the order of $2/10^5$, which is negligibly small. However, fog reduces visibility to such a degree that even automobiles get into serious accidents.

Rain. Modern airplanes are designed to operate in a common rate of rainfall. As reported in (14,a,b) most rain drops are in the 0.5 to 1.0 mm size range. Their average falling velocity is estimated (see chapter III of "Fluid-Dynamic Drag") to be in the order of 4 m/s relative to the air, which is 2% of 400 knots of airplane speed, for example. A usual rainfall is said to accumulate between 1 and 2 mm per hour at the ground. The mass content of water in air is then in the order of $1/10^4$. In "heavy rain", this content may be tenfold (1 per 1000), and in a cloudburst 100-fold, making the mass ratio equal to 1%. Really small drops would likely be more or less directed by the airflow around a wing, while typical rain drops may directly impact upon the upper and the frontal areas. Consequences are as follows:

- Due to water adhering to the surface, the increase of the weight of an airplane is estimated to be a small fraction of 1%.
- The vertical mass flow of droplets possible impinging upon the wing from above, during a "heavy" rain, might be

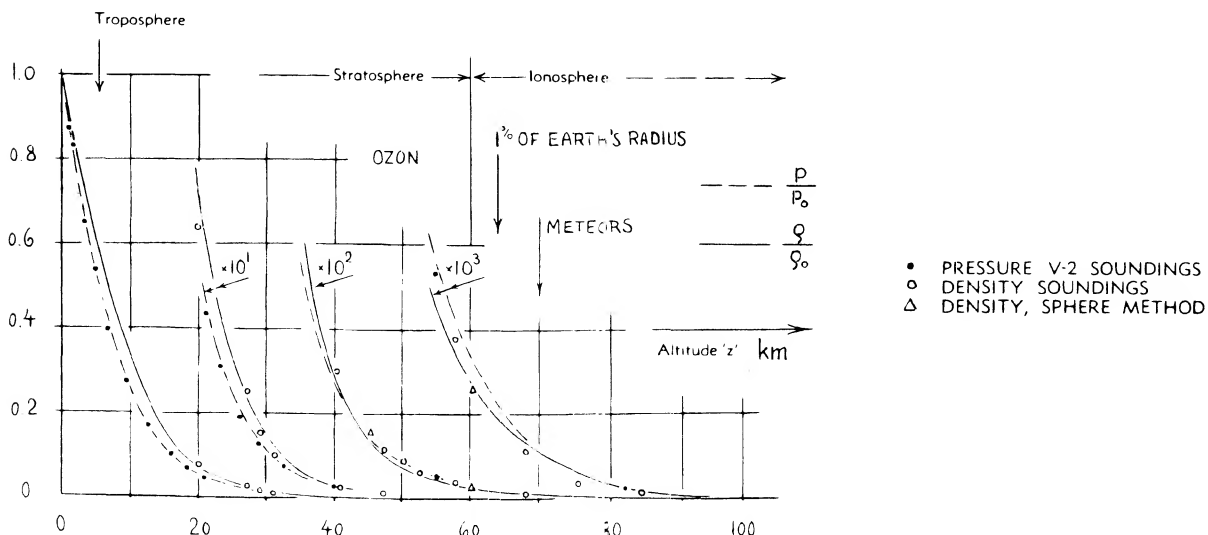


Figure 4. Standardized reduction of atmosphere pressure and mass density, as a function of altitude.

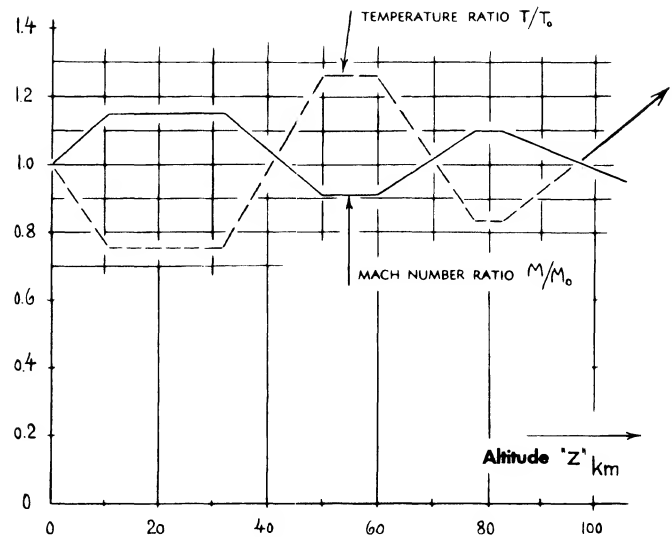


Figure 5. Standardized variation of temperature and Mach number, up to 100 km of altitude, presented in the form of ratios.

$$(dm/dt) = w \rho_a / 1000 \quad (\text{kg/m}^2 \text{ s}) \quad (29)$$

where m = mass per unit wing area and $(1/1000)$ as above. For the velocity $w = 4 \text{ m/s}$, and an air density $\rho_a = 1 \text{ kg/m}^3$, the impact pressure of the rain drops might then be

$$(dm/dt) w g = 16(9.81)/1000 \approx 0.16 \quad (\text{kg-s/m}^2) = (\text{N/m}^2)$$

By comparison, the mass loading of an airplane is between 150 and 300 kg/m^2 or a weight loading of 1500 to 3000 N/m^2 (or 35 to 70 lb/ft^2). The impact of rain considered, would thus not be of any importance.

- In regard to drag, rain drops will more or less impinge upon the frontal area of an airplane. This type can thus be treated as a free-particle flow (similar to the Newtonian type as described in "Fluid-Dynamic Drag").

Assuming that the rain drops captured by the frontal area S_f of an airplane, lose half of their momentum (that they are accelerated to $\frac{1}{2}$ the airplane's speed V) we obtain

$$\Delta D = 0.5 V^2 \rho_w S_f (m_w/m_a) \quad (\text{kg-m/s}^2) = N \quad (30)$$

where "w" indicates water and "a" = air. Assuming an effective (capturing) frontal area ratio $S_f/S = 0.1$, the incremental drag coefficient may then be

$$\Delta C_D = (S_f/S) (\rho_w/\rho_a) (m_w/m_a) \quad (31)$$

For a constant $(m_w/m_a) = 0.1\%$, as in "heavy rain", the result is $\Delta C_D = 0.08$. This would be as much as the airplane's original drag at $C_L = 1$. According to (14,c) it seems, however, that a portion of the rain drops larger than assumed above, is diverted by the air flow around the wing, for example.

Icing. The formation (deposit) of ice upon the frontal areas of an airplane (such as the leading edge around the stagnation line) can increase weight and drag appreciably. At cruising speed, drag increments up to 80% are reported in (14,e), while the propeller efficiency may be reduced 10 or even 20%.

Wind profiles (velocity w or dynamic pressure q_w as a function of altitude Z above ground) are plotted in chapter IV of "Fluid-Dynamic Drag", up to altitudes Z between 25 and 250 m. Similar data are reported in (15,a). It appears that in properly developed steady wind over a plane unobstructed surface (such as an airfield) the variation is approximately

$$w_z/w_i = (Z_z/Z_i)^{1/n} \quad ; \quad \text{or} \quad q_{wz}/q_{wi} = (Z_z/Z_i)^{2/n} \quad (32)$$

where n between 6 and 8. At "higher" Reynolds numbers, distributions within turbulent boundary layers usually correspond to $w \sim Z^{1/7}$. Behind obstacles (such as buildings at the edge of an airport) there is a deficiency of speed. As shown in (15,b) a gradient much stronger than that indicated by $n = 6$ or 8, may then be found above the level of those obstructions. Regarding the climb-out performance of airplanes, any positive gradient will help. It seems, however, that when landing into a strong wind (and possibly over an obstacle) the negative gradient can be dangerous. While reducing the airplane speed, thus increasing the lift coefficient, the wind velocity also reduces, thus possibly leading to wing stalling at angles of attack beyond that for C_{Lx} . Airplanes are thus operated at lift coefficients approximately 70% of the maximum to allow for turbulent velocity conditions and control inputs.

(B) Physical Properties of Water

There are "lifting" devices used in water such as rudders and hydrofoils. Properties of water are presented in "Fluid-Dynamic Drag". They are here given again, in metric units.

The Compressibility of water $d\rho/dp$, measured in $(\text{kg/m}^3)/(\text{N/m}^2) = (\text{kg/mN}) = (\text{s/m})^2$, is very small in comparison to that in air. As a consequence, the speed of sound 'a' = $\sqrt{dp/d\rho}$ is in the order of 1440 m/s (4700 ft/sec, 2800 kts) in comparison to 340 m/s (1117 ft/sec, 660 kts), in sea-level air. For example, it takes more than 7 hours for an explosion, say at the coast of Japan, to be "heard" in San Francisco (over a distance of almost 5000 sea miles, or 9000 km). It would only be less than 2 hours, however, to detect the same disturbance by sonar. For comparison, the travel time is in the order of 10 hours by subsonic jet airplane (if non-stop at $M = 0.8$), and less than 3 hours by Supersonic Transport (at 2000 mph, approaching $M = 3$).

Dynamic Pressure. The density of sea water is some 840 times that of sea-level air. For all practical purposes, this density can be considered to be constant (to be independent of temperature and pressure):

$$\rho \text{ (fresh water)} = 1000 \text{ kg/m}^3$$

In average (Atlantic) sea water, with a salinity in the order of 3.5% (16,c), the density is higher:

$$\rho \text{ (sea water)} = 1025 \text{ kg/m}^3 \quad 2.0 \text{ lb-sec/ft}$$

Corresponding to these densities, the dynamic pressure is

$$q = 500 \text{ g V}^2 \quad \text{in } (\text{N/m}^2) \text{ or } (\text{kg-m-s}^{-2}) \quad \text{in fresh water} \quad (33)$$

$$q = 513 \text{ g V}^2 \quad \text{in } (\text{N/m}^2) \text{ or } (\text{kg-m-s}^{-2}) \quad \text{in sea water} \quad (34)$$

Using ρ as above, we also obtain conveniently:

$$q = 500 (V \text{ m/s})^2 \text{ in } (\text{kp/m}^2) \quad \text{in fresh water} \quad (35)$$

$$* q = (V, \text{ft/sec})^2 \quad \text{in } (\text{lb/ft}^2) \quad \text{in sea water} \quad (36)$$

$$q = 0.97 (V^2) \quad \text{in } (\text{lb/ft}^2) \quad \text{in fresh water} \quad (37)$$

Equation (37) is plotted in figure 6 in fresh water expecting that the metric system will be accepted last, in the field of naval architecture.

(15) Characteristics of atmospheric wind:

- Lettau, "Exploring Atmosphere's First Mile", Pergamon 1957; also "Wind" in chapter 5 of "Handbook of Geophysics", MacMillan 1960.
- Stearns, "Atmospheric Boundary Layer", Univ Wisconsin (1964); AD-611, 209.
- Am Meteorological Soc, Wind for Aerospace Vehicles, Bull 11 (1964) p 720.

The Viscosity of water, needed for the computation of the Reynolds number, is plotted in chapter I of "Fluid-Dynamic Drag", in the form of $\nu = \mu/\rho$. At the standard temperature of 15°C, the kinematic viscosity is between (1.16 in fresh and 1.13 in sea water)/10⁵ (ft²/sec), which is between (1.08 and 1.05)/10⁶ (m²/s). Contrary to that in air, this viscosity reduces as temperature is increased, that is roughly as

$$\nu = \mu/\rho \sim 1/T^6 \quad (38)$$

Water Tunnels (17). The high density of water makes it possible to obtain high Reynolds numbers in a tunnel built in the same form as that of an ordinary wind tunnel. For example, in a comparatively large, but low-speed wind tunnel we may have:

c	=	1	m	wing chord
V	=	40	m/s	air speed
q	=	100	kp/m ²	dynamic pressure
R _c	=	2.8	(10) ⁶	Reynolds number

For operational reasons, the size of a water tunnel might be restricted. We could obtain the following, however:

c	=	0.5	m	wing chord
V	=	10	m/s	water speed
q	=	50000	kp/m ²	dynamic pressure
R	=	4.3	(10) ⁶	Reynolds number

As in equation (38) the viscosity of water reduces as temperature is increased. Therefore, when increasing the absolute temperature from the standard 288° K to 316 K, that is from 15° C to 43° C (which is only 4° C more than our blood temperature) the Reynolds number in the water tunnel suggested, can be doubled. A number R_c approaching 10⁷ could thus be obtained. For many purposes, we just do not need such high R-numbers; and at a speed, say of 2 m/s the most instructive flow patterns could easily be produced in water by adding a suitable substance. To make the water tunnel still more attractive, its low power requirement is mentioned. For a one meter squared test cross section, the power is approximately

$$\text{power} = 0.5 q V \approx 0.25 \rho V^3 / 1000 = V^3 / 4 \quad \text{kwatt}$$

For V = 10 m/s, that would be 250 kwatt; and for 2 m/s, only 2 kwatt.

(16) Physical properties and characteristics of water:

- See for example in Transactions INA (London) 1953 p 358.
- See in chapter I of "Fluid-Dynamic Drag".
- The salinity in the Dead Sea is 22%. The corresponding density ratio as against fresh water is estimated to be 1.26.

Cavitation is vaporization (boiling) due to reduced pressure. Fundamentals and examples of cavitation are presented in chapter X of "Fluid-Dynamic Drag". Really pure water (distilled, in a pure container) may not cavitate at all. However, all kinds of microscopic impurities (such as cosmic dust, particles remaining in drinking water after filtering, tiny air bubbles in the interface of sea water, or plankton) will "always" provide the nuclei needed to start a vapor bubble. The critical pressure at which water at a temperature of 15° C begins to turn into gas (vapor) is less than 0.016 of the atmospheric pressure (= 33 lb/ft² = 1600 N/m²). So, for practical purposes, we may as well say the vapor pressure p_v is zero.

The **Cavitation Number** indicates the tendency of the ambient flow to cavitate, when meeting an obstacle:

$$\sigma = (p_a - p_v)/q \approx p_a/q \quad (39)$$

where q = dynamic pressure, and p_a = ambient pressure. At standard sea-level pressure ("at" the surface of open sea water) the coefficient of that pressure (p_a - p_v) = 2116 - 33 = 2083 lb/ft², is

$$\sigma = (p_a - p_v)/q = 2090/(V, \text{ft/sec})^2 = 195/(V, \text{m/s})^2 \quad (40)$$

For each unit of submergence "h" (below the free water surface) we have to add a

$\Delta p/q$	=	64 lb/ft ²	for each foot of sea water
$\Delta p/q$	=	1000 kp/m ²	for each meter of fresh water

5. CONSIDERATION OF SIZE AND SPEED OF VEHICLES

Dimensions, weight or mass, cruising speed and density of the medium through which they move, all have an influence upon the geometrical design of dynamically lifted vehicles and their operational qualities.

Square-Cube Law. The volume (weight, mass) of a body grows in proportion to the cube of its linear dimension ℓ , while its significant area is only $S \sim (\ell)^2$. As an example, we may compare the frontal area of a motorcycle (with 1 passenger) with that of a bus (with 50 passengers) or a railroad train (with 500 passengers). It can be found that the aerodynamic drag, roughly proportional to frontal area, is "very" high per passenger for the motorcycle, and "very" low per passenger for the train. Aerodynamic efficiency of these land vehicles, thus increases with their size. In the case of an airplane, the significant area is that of the wing (lifting the vehicle), while the volume is the equivalent of its mass, figure 7. Therefore, the mass grows "faster" with size ' ℓ ', than the areas of its lifting, stabilizing and controlling surfaces.

Froude Number. In the hydrodynamic design of ships, the Froude number is used to establish similarity between towing-tank tests and full-scale operation, primarily in regard to wave pattern and wave resistance in calm water (19). The square of this number is the ratio between the inertial or wave-producing forces involved, and the weight (due to gravity) of water and/or vessel. Thus:

$$F_n^2 = \rho_w V^2 l^2 / \gamma_w l^3 = V^2 / g l \quad (41)$$

where $\rho_w = \gamma_w / g$, γ_w = weight per unit volume ($v = l^3$) of the water displaced by the ship's hull (displaced volume of water). Note that the vehicle's weight is $W = \gamma_w (l^3)$, where γ (subscript v) is equal to that of the water (subscript w).

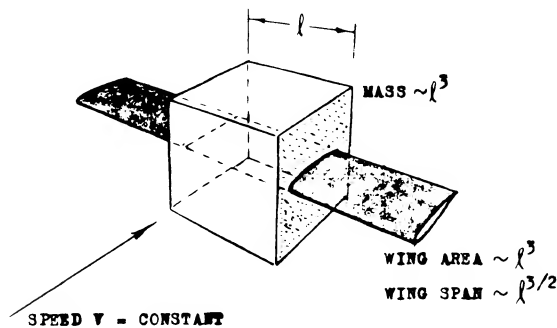


Figure 7. Demonstration of the influence of size and speed upon the relative dimensions of wing and volume of airplanes or hydrofoil boats.

- (17) Water tunnels, some of them used for "aerodynamic" investigations:
- See author's description and results in Fieseler Rpts (1939, 1940).
 - Hoerner, Fieseler Water Tunnel, Yearbk D Lufo 1943 (not distributed).
 - Drescher, Water Tunnels of the AVA, Yearbk D Lufo 1941 p I-714.
 - Ross-Robertson, 4-Foot Tunnel Penn University, Trans SNAME 1948 p 5.
 - Brownell, Variable Pressure Tunnel, DTMB Rpt 1052 (1956); see also description of tunnels in TMB Rpt 1856 (AD-607, 773).
- (18) Introduction of Froude number in this book, based upon:
- Gabrielli and von Karman (Mech Engg 1950 p 775, or J.ASNE 1951 p 188).
 - Davidson (Stevens ETT TM 97 & Note 154, 1951; also SNAME Bulletin 1955).
 - Hoerner, Consideration of Size-Speed-Power in Hydrofoil Craft, SAE Paper 522-B (1962); reprinted in Naval Engineers Journal 1963 p 915.
 - Froude, Collected Papers and Memoir, Inst Nav Architects (London) 1955.
- (19) Consideration of dynamic stability:
- Braun, Static Stability, Ringbuch Luftfahrttechnik I-B-6 (1940).
 - Jones, Airplane Dynamics, in Volume V of Durand (3.1).
 - Rodgers, Neutral Point, AIAA J. Aircraft 1965 p 33 and 352.
 - Carlson (Wright-Patterson AF Base), Analysis of Stability and Control of Lockheed C-5A Airplane, Astronautics & Aeronautics 1965 p 60.

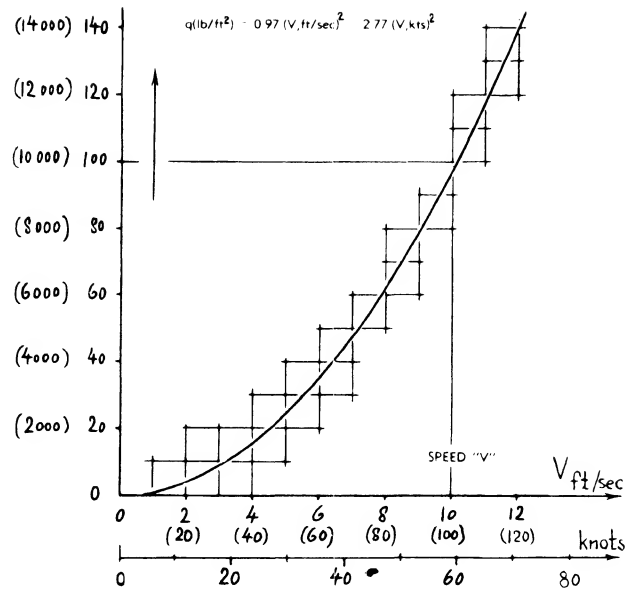


Figure 6. Dynamic pressure in fresh water (equation 37) as a function of speed.

Hydrofoil Boats. In a boat supported above the water, by "wings" running below the surface, weight or "load" is concentrated upon comparatively small foils. The density of these foils in terms of W/S , or m/S (in kg/m^2) is "very" high. Neglecting the comparatively small surface waves left behind these boats when "flying", the inertial forces are now fluid-dynamic lift (and induced drag). The Froude number may be written in the form of

$$(V^2/gl) \quad \text{or} \quad (V_k^2/\sqrt{\Lambda}) \quad \text{or} \quad (V_k/\sqrt[3]{\Lambda})$$

where k is indicating speed in knots, and Λ = weight of the craft in long tons (representing its mass). These numbers have a definite influence upon the geometric configuration of hull and foils. Since it is desirable to limit the foil span to the dimension of the hull's beam, the following similarity numbers are statistically found:

$$\begin{aligned} (V/\sqrt[3]{\Lambda}) &= \text{for configurations with 3 foils} \\ &= \text{for "wing" plus stabilizing foil} \\ &= \text{for a pair of foils in tandem} \end{aligned}$$

While it is possible to make a boat with 3 foils very small, there is an upper limit to the size of operationally feasible hydrofoil boats. The size (span) of the foils required, simply outgrows that of the hull (beam). For a speed below 50 knots, therefore, the largest boat practicable may be in the order of 400 long tons (some 400 metric tons).

Lift Coefficient. When comparing airplanes with each other, interpretation of the Froude number is as follows. The fluid-dynamic force (lift) acting upon the "vehicle" is proportional to $(\rho V^2 S)$, while the number reflects weight and/or mass forces of the vehicle (subscript "v"):

$$(F_L^2) = (\rho_a V^2 S) / (m/g) = (\rho_a / \rho_v) V^2 / g l \quad (42)$$

where the significant area $S = l^2$ is that of the wing. The subscript 'a' indicates 'ambient', while ρ_v is the density of the airplane (in kg/m³). This type of Froude number thus contains a density ratio. The mass density of a conventional airplane may be $m/V = 200$ (kg/m³), in comparison to 1000 for water, and roughly 1.0 for air (at an altitude of 7 km). The density ratio for an airplane is in the order of 200, accordingly. To support the craft by means of aerodynamic lift, the speed in $(\rho V^2 l^2)$ has to be much higher than that of a hydrofoil boat, say between 200 and 800, instead of 40 knots, for example. Equation (42) can now be rewritten as

$$(m/g) / (\rho_a V^2 S) = W / \rho_a V^2 S = 2 C_L \quad (43)$$

In other words, the lift coefficient

$$C_L = 2(W / \rho_a V^2 S) = 2 / F_L^2 \quad (44)$$

is the equivalent of a Froude number. Table 1 has been prepared, containing characteristics of several typical, but extremely different lift-supported vehicles (including birds). It can tentatively be assumed that all of them fly (cruise, climb, keep aloft) at the "same" lift coefficient, say between 0.3 and 0.7.

STOL — airplanes necessarily need to have exceptionally high lift coefficients (possibly up to 8). One example is included in Table 1 on "size and speed". Structurally, such aircraft must be expected to be limited in size (wing area and span). High lift coefficients are obtained by trailing edge flaps, by propeller-slipstream deflection, and finally by direct application of thrust (as in helicopters, for example). Figure 8 demonstrates how in helicopters, VTOL and STOL aircraft lift is ideally produced, by deflecting a stream tube of air or by direct downward deflection.

TABLE I

Table I, average characteristics (in rough and round numbers) of various lift-supported "vehicles", including birds.

	m	= mass	(kg)		ρ_v	= m/l^3	kg/m ³				
	S	= wing area	(m ²)		V_k	= speed	knots				
	b	= Span	(m)		Δ_t	= weight	l'tons				
“vehicle”	W(kp)	b(m)	S(m ²)	(m)	W/S	V_k	$V_k/\sqrt{\Delta_t}$	V(m/s)	C _L	ρ_v/ρ_a	F_L^2
buzzard (22)	1	1	0.2	0.4	4	18	90	9	0.7	8	3
albatross (22)	8	3	1	1	8	33	130	17	0.5	8	4
small airplane	1,000	10	20	4	50	130	200	65	0.4	11	9
STOL airplane	5,000	20	35	6	140	40	3	21	5.0	20	4
fighter airplane	8,000	18	18	4	440	520	370	260	0.2	160	10
C5-A airplane	250,000	60	600	22	420	480	190	240	0.3	50	10
hydrofoil boat	100,000	10	25	5	4000	40	19	20	0.3	1	8

(F_L^2) is as in equation 42. Note that numerically, $W(kp) = m(kg)$. The "huge" airplane is assumed cruising at an altitude of 10 km, where air density is less than half of that at sea level. The hydrofoil boat is "flying" in (or above) water, where density is a 1000 times that of atmospheric air at an altitude of 2 km.

High Altitude means low density. The value of density at 10 km (30,000 ft, where airliners obtain their longest range) is roughly 40% of that at sea-level. Similarity in the geometric design (wing area in comparison to fuselage dimensions) of two airplanes, one designed for low, and the other for high altitude (say 20 km as the SST, where density is only some 7% of that at sea level) can only be maintained when keeping the Froude number as per equation (42) constant. A larger airplane will statistically have to be designed for a higher speed; and when flying at higher altitude, the speed has to be higher again. These considerations lead to supersonic cruising speeds (as in the SST).

Control. High lift coefficients are usually produced by part-span flaps, while the tail surfaces and particularly the ailerons of an airplane, remain unchanged. Considering a rolling STOL, similar to that in the "size-speed" table, but flying at $C_L = 0.8$ for example, the control 'power' corresponds to the low value $F_R^2 = 2.5$. Control effectiveness would thus be only $\frac{1}{4}$ that of the fighter airplane. It can also be said that the control surfaces, or their area ratio (control/wing) should be 4 times as high to obtain the same result as with the fighter. The low Froude numbers of the birds as in the table, suggest that they have a highly effective automatic control system, in the form of feel, instant reaction and muscles serving as actuators. They also have variable areas in their wings and tails; and they can twist all surfaces to a degree not found in conventional man-made airplanes.

Dynamic Stability. The motions of an airplane, resulting from the combination of fluid-dynamic forces (such as in the tail surfaces, for example) and forces arising in the masses of the craft as a consequence of acceleration (and deceleration) determines the dynamic characteristics (19). The term in the equations of motions accounting for these forces is the relative density, or the ratio of the mass of the vehicle to that of the fluid affected. Therefore, the Froude number as in equation 42 could directly be used when determining dynamic stability. For example, oscillatory motions of an airplane will be "similar" to those of a properly built wind-tunnel model, when the Froude number is kept constant. On the basis of the F'numbers in Table 1, it can also be expected that a fighter-type airplane can be very stable.

Advanced Vehicles. Table 1 in this section only presents examples of birds, airplanes and a hydrofoil boat. In reality, there is a wide range of size and speed in each category of vehicle, depending among others, upon power or thrust installed. For example, a fighter airplane is designed for high speed; its Froude number is particularly high, accordingly. Nevertheless, there are statistical trends evident; the average lift coefficient decreases as the size is increased; the Froude number increases as the speed is increased. The speed-size relation is not usually considered when designing an airplane. Power available and speed are

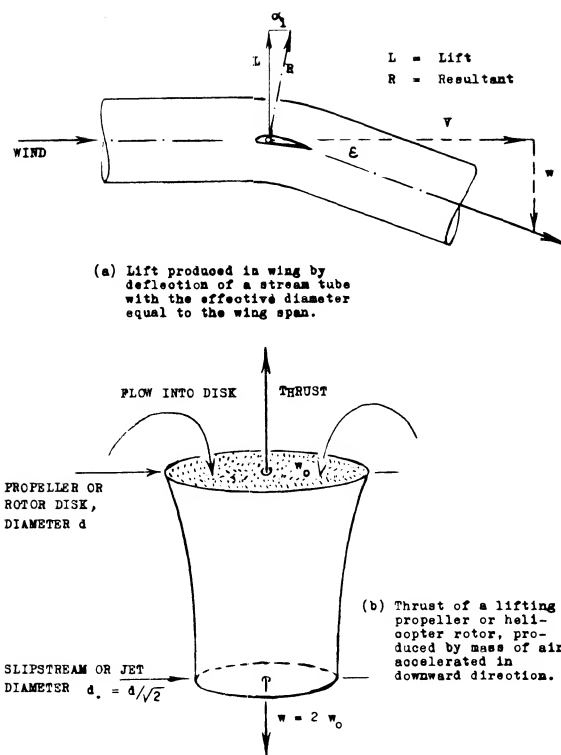


Figure 8. The origin of lift:

- a) produced in a wing by deflecting a streamtube of air,
- b) produced by a fan, propeller or helicopter rotor.

a matter of specifications for a particular type of airplane required. To produce this aircraft, is then a matter of structural design, engine development, the introduction of new materials. For example, the increase of maximum lift from $C_{Lx} = 1.5$ (say around 1930) to 7.5 as in STOL airplanes (around 1960 or 1965) is made possible by elaborate structural innovations, such as triple-slotted wing flaps and tilting wing-engine-propeller combinations.

- (20) Calculation of airplane performance:
 - a) Oswald, Performance Formulas and Charts, NACA Rpt 408 (1932).
 - b) Diehl, in "Engineering Aerodynamics", Ronald New York, 1928 to 1936.
 - c) Wood, "Technical Aerodynamics", McGraw-Hill (1935, 1947) by author (1955).
 - d) Perkins-Hage, "Airplane Performance Stability Control", Wiley 1949.
 - e) Dommasch, "Airplane Aerodynamics", Pitman 1951.
 - f) Wood, "Aircraft Design", Johnson Publishing (Boulder, Colo.) 1963.
 - g) Breguet, Endurance (1921); see J.Aeron Sci 1938 p 436; see (b).
- (21) Characteristics and Performance of KC-135 (Boeing 707):
 - a) Vancey, KC-135 Flight Tests, Edwards AF Base TR-1958-26; AD-152, 257.
 - b) Tambor, Flight Tested Lift and Drag, NASA TN D-30 (1960).

It is not yet clear where the consideration of size and speed similarity (or dissimilarity) can be of practical value. One example in this respect seems to be the control of aircraft. In very high altitudes (low air density, as in NASA's more or less ballistic X-15) and/or at low speeds (as in STOL airplanes) aerodynamic devices are no longer sufficient. Suitably located gas jets, coupled with automatic sensing and actuating devices, therefore, have to be used. An awareness of the influence of size, speed, density; and, of course, the anticipation of limitations or difficulties such as supersonic effects (or cavitation in water) may prepare the designer for the effort in research and development required, before proceeding with the construction of any advanced vehicle, or the introduction of a new mode of lift-supported transportation.

6. AIRPLANE PERFORMANCE

Methods of performance determination, such as finding the takeoff distance and rate of climb are not the purpose of this book. To point up the significance of certain aerodynamic characteristics that influence the design and selection of the various components of the airplane, some important principles of performance are presented, however. These will include the primary design flight conditions of the airplane such as takeoff, cruise, high speed and landing. For more complete analysis of aircraft performance there are many excellent sources available (20).

Takeoff. The takeoff performance of an airplane, field length and distance over an obstacle, is directly influenced by the thrust, weight, C_{Lx} and drag. To accelerate the aircraft to the takeoff speed, high thrust to weight ratios are needed with a low drag to lift ratio. The speed at takeoff is a function of the maximum lift at the selected flap angle and the wing loading. In the case of large aircraft the rules for safety effectively determine the takeoff distance. As a result, the rate of climb with one failed engine at takeoff speed may be specified and be the determining factor. This is discussed in Chapter VI and determines the lift drag ratio at takeoff as well as the takeoff flap angle setting. The flap angle setting then establishes the lift coefficient at the takeoff speed which is usually

$$C_L \text{ (at takeoff)} = C_{Lx} / 1.44 \quad (45)$$

where C_{Lx} is maximum lift coefficient, the airplane in the takeoff configuration with the flaps at the proper angle and the landing gear down.

Climb and Descent. The rate of climb or descent is dependent on the difference in power available or required, the weight, velocity and the drag. Thus

$$w_c = (T - D) V / W \quad (46)$$

Equation 46 shows that a high lift drag ratio is required for a high rate of climb. High rates of descent are obtained at low lift drag ratios and at low or negative thrust conditions. Thus drag spoilers and thrust reversers are sometimes used to achieve high descent rates.

Takeoff Figure of Merit. Since both the distance and steepness of climb after takeoff are important the relative performance can only be judged by a factor that takes both the C_L for takeoff and the rate of climb into effect. This may be done by finding the maximum rate of climb after takeoff at a minimum flight speed. Since for a given engine

$$w_c / V = T / W - D / L = C_{Tx} - C_D / C_L \quad (47)$$

since V at takeoff is $V \sim \sqrt{C_L}$ we can establish a figure of merit for takeoff as

$$FM_{to} \sim C_{Tx}^2 / C_L^3 \quad (48)$$

When the FM_{to} is a minimum the angle of climb is a maximum. This factor gives an initial indication of the relative performance of different systems.

High Speed is basically made possible by reducing the drag coefficient of an airplane increasing thrust and by flying at higher altitude (in air with lower density). There are some effects, however, resulting from lift to be mentioned here:

- a) Leading-edge devices such as slats in particular, are likely to precipitate turbulent boundary-layer flow, because of the gaps and sheet-metal edges left when closed.
- b) Not only the gaps of the trailing-edge flaps and ailerons, but also the arms or tracks supporting, and the devices deflecting them, are bound to contribute to drag.
- c) A twisted wing can have a considerable amount of induced drag, even at zero total lift.
- d) The horizontal tail surface may be loaded down at high speed, thus producing its own double trailing-vortex system, and making a higher lift coefficient necessary in the wing.
- e) When flying at higher altitude, lift and induced-drag coefficients are necessarily increased. The induced drag (in newtons or pounds) might remain unchanged, however.

(22) Lifting characteristics of birds:

- a) Lilienthal, "Bird Flight and Aviation", Translation London 1911.
- b) Holst and Kuchemann, Probleme des Tierfluges, Naturwissenschaften 1941 p 348.
- c) Holst and Zimmer, Vogelflug, J. Ornithology 1943 p 371 & 406.

Drag and Lift. An airplane operating characteristics are determined according to its mass or weight, thrust or drag, and speed. So, while in the rest of this book almost nothing but coefficients are presented, ratios and meters per second are plotted as for example in figure 10. Drag consists of two components. The first, the “viscous” or “parasite” drag is essentially proportional to the dynamic pressure $q = 0.5 \rho V^2$. Thus

$$D_o = C_{Dov} S (0.5 \rho V^2) \sim \rho V^2 \sim V_e^2$$

In order to be independent of altitude and density, the “equivalent” airspeed is useful, that is the value “indicated” by an airspeed indicator calibrated for sea level density.

$$V_e = V \sqrt{\rho/\rho_o} ; V_e^2 = V^2 (\rho/\rho_o) = (2W/\rho_o S)/C_L \quad (49)$$

where $(2W/\rho_o S) = \text{constant}$ for a given airplane in steady flight, without fuel consumption (and disregarding compressibility). The dynamic pressure is then

$$q = 0.5 \rho_o V_e^2 = V_e^2 / 16$$

$$\text{in } (\text{kg/m-s}^2) = (\text{N/m}^2)$$

where ρ_o has a standard value (– in kg/m^3 , as in figure 3) and V_e in m/s. The second component of drag is that due to lift. The major portion of this drag is the induced drag. To account for some viscous drag originating as a consequence of lift, Oswald (20,a) has introduced a span-efficiency factor which we will designate by a . The drag due to lift:

$$D_i = W^2 / \pi q a b = K (m/V_e b)^2 \quad (50)$$

in $(\text{N} = \text{kg-m/s}^2)$

where $m = \text{mass of the airplane (in kg)}$. As a rule of thumb, $\Delta C_D = 0.01 C_L^2$, so that for $A = 6$, $\Delta C_D / C_{Di} = 20\%$. For statistical purposes, then $a = 1/1.2$, and

$$K = 2 g^2 / \pi \rho_o a = 60 = \text{constant} \quad (51)$$

in $(\text{m}^5/\text{kg-s}^4)$

Speeds. In terms of the indicated or equivalent speed, the lift of an airplane is

$$L = \{W\} = m g = C_L q S = C_L 0.5 \rho_o V_e^2 S \quad (52)$$

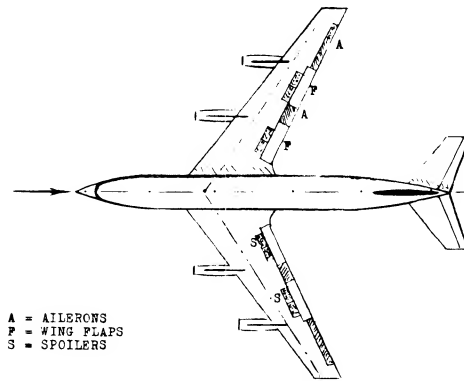
The speed corresponding to a given lift coefficient is accordingly:

$$V = \sqrt{(2g/\rho)(m/SC_L)} = 4 \sqrt{\text{gm/SC}} \quad \text{in (m/s)} \quad (53)$$

where (m/S) in $(\text{kg/m}^2) = \text{mass loading of the airplane and } \sqrt{2g/\rho_o} = 4 \sqrt{g} = \text{constant, in } (\text{m}^4/\text{s}^2 - \text{kg})$. Considering now a sailplane in calm air (without any supporting up-wind) its “effective” (reduced to sea level) sinking velocity w (in vertical direction) is essentially

$$w \sqrt{\rho/\rho_o} = \sqrt{2W/\rho_o S (C_D^2/C_L^3)} = \sqrt{(2/g \rho_o) (m/S) (C_D/C_L^{3/2})} \quad (54)$$

Disregarding any possible influence of Reynolds and Mach numbers, all of the right side of this equation is given for a particular airplane configuration. The sinking velocity is found in part (b) of figure 10.



b = 131 ft	mean chord = 20 ft
S = 2433 ft ²	horizontal tail = 500 ft ²
A = 7.1 -	angle of sweep = 35 deg
W = 100 kip	completely empty
W = 300 kip	with maximum load
δ = 30 deg	flaps during takeoff
T = 11000 lb	continuous rated thrust
at sea level for each of 4 Pratt & Whitney J-57 (1957)	
B ₀ = 3 to 6 × 10 ⁷	in flight up to 36,000 ft

Figure 9. Planform view and principle data of the USAF KC-135 tanker airplane (prototype of the Boeing 707 airliner) as of 1958 (21).

Landing. The minimum landing speed of an airplane depends on the maximum lift coefficient that can be developed. Since the stopping distance after landing is influenced by the touch down speed, it is desirable to have wing systems that produce as high a C_{Lx} as possible. Although drag is important in case of an aborted landing, lower lift drag ratios are acceptable with high values of C_{Lx} as high levels of power and lower weights are usually encountered during landing, see Chapter VI.

Thus the landing speed will be some factor, say 1.2 times the stalling speed which is

$$V_L = 1.2 (295W/\sigma S_W C_{Lx})^{1/2} \quad (55)$$

Where V_L is the landing speed in knots and W the landing weight.

Evaluation of KC-135. We are now in a position to derive drag and lift of an airplane and its equivalent velocities (in m/s) either from flight tests or from given drag and lift coefficients. Performance data of the Air Force's KC-135 tanker (refuelling airplane, prototype of the Boeing 707) are available (26). We are using the flight-tested results, to explain the aerodynamic principles of performance. Dimensions and data of the airplane (as in 1958) are listed in figure 9. We have assumed $W = 200,000$ lb, and a combined constant thrust of 40,000 lb. Evaluation of the data particularly in (21,a) indicates an extrapolated $C_{D0} = 0.013$, and a $dC_D/dC_L^2 = 0.053$. The span efficiency factor is $a = 0.84$, for "clean" condition (flaps neutral, landing gear in). The extrapolated minimum drag coefficient is $C_{D0} = 0.013$, so that approximately

$$C_D = 0.013 + 0.054 C_L^2$$

Results are plotted in figure 10, in form of force ratios and equivalent speeds.

Takeoff. In case of the KC-135, 30° of flap deflection are recommended for takeoff. A corresponding (D/L) function is shown in part (c) of figure 10. It is seen, however, that after leaving the ground, neutral flaps (and a retracted landing gear) provide a much higher rate of climb.

For Climbing, excess thrust is required. The fastest climb (that is the highest vertical velocity w) is obtained at the speed where $(D/L) = \text{minimum}$, or $(L/D) = \text{maximum}$ (as in part (a) of the illustration). We may be interested, however, in a steep (rather than a fast) climb, say over an obstacle (such as a building). The minimum thrust required to do this for a "clean" airplane corresponds to the minimum of the sinking speed as in part (b) of figure 10. According to equation (55) the optimum speed of lift coefficient is defined by a minimum of the parameter

$$(C_D/C_L^{3/2}); \text{ or } (C_D^2/C_L^3);$$

$$\text{or } (C_D^{2/3}/C_L) \quad (56)$$

Reasonable numbers are obtained when using (C_L^3/C_D^2) . In case of the KC-135, we find at $V_e = 100$ m/s, a value of 212.

Range. The sailplane mentioned above will travel farthest when gliding along the lowest possible angle, indicated by the tangent from the origin of graph (b). The point found is at the same speed where $L/D = \text{maximum}$, as in part (a) of figure 10. However, in a powered airplane, the miles of distance flown per unit weight of fuel burned, has to be considered. The tangent as in part (c) indicates an optimum speed of 150 m/s, for a $C_L = 0.29$, in the example of the KC-135. Here as in the case of endurance, it has to be taken into account, however, that the weight of the airplane reduces considerably (possibly to half) as the end of the flight is approached (20.g).

Endurance (the number of hours staying aloft with a given supply of fuel) is maximum at the speed where the sinking speed is minimum. This point corresponding again to a minimum of the parameters in equation (56), is found in part (b) of the illustration.

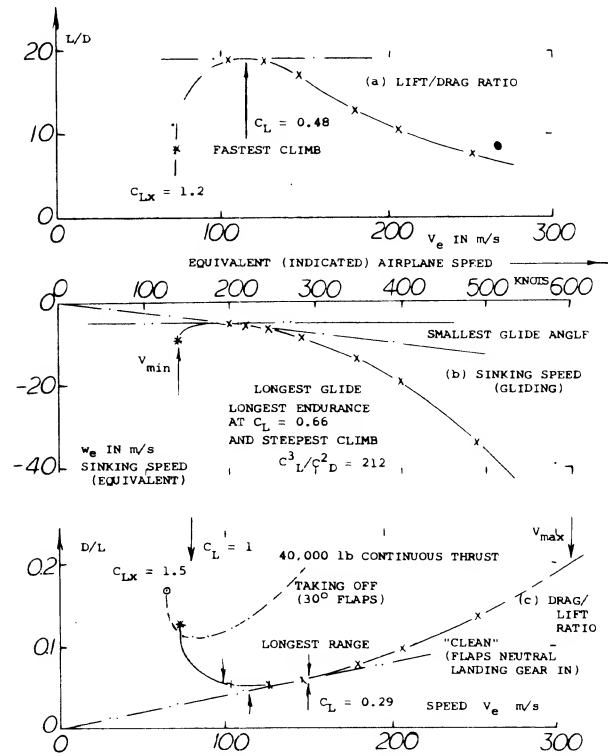


Figure 10. Flight-tested performance (lift and drag) of the USAF KC-135 tanker airplane (21) prototype of the Boeing 707 airplane.

Propeller-Driven Airplanes may have constant engine power available. Even assuming a variable-pitch, constant-speed propeller, neither net power nor thrust are constant, however. Qualitatively, performances are as follows:

- During the takeoff run, propeller efficiency increases, possibly to near maximum, while thrust reduces.
- Assuming constant efficiency and constant net power in terms of $(T V)$, maximum climb velocity depends upon excess power (rather than thrust). The corresponding speed V is, therefore, lower than that of a same-size jet-powered airplane.
- Regarding range, a minimum of $(\text{power times time})/(\text{speed times time}) = (D V)/V = D$ has to be found. This will be at the speed where $(D/W) = \text{minimum}$.
- Both in jet- and in propeller-driven airplanes, maximum altitude (ceiling) and minimum turning circle will approximately be obtained for the point where (C_D^2/C_L^3) is minimum.

CHAPTER II — LIFT CHARACTERISTICS OF FOIL SECTIONS

The basic element of every wing or control surface and that of "vanes" and propeller blades, id est of all "lifting" devices (in air or in water), is the foil section. Lift- and pitching- moment characteristics of such sections, in two-dimensional fluid flow, are presented as follows, as a function of shape, skin friction and Reynolds number.

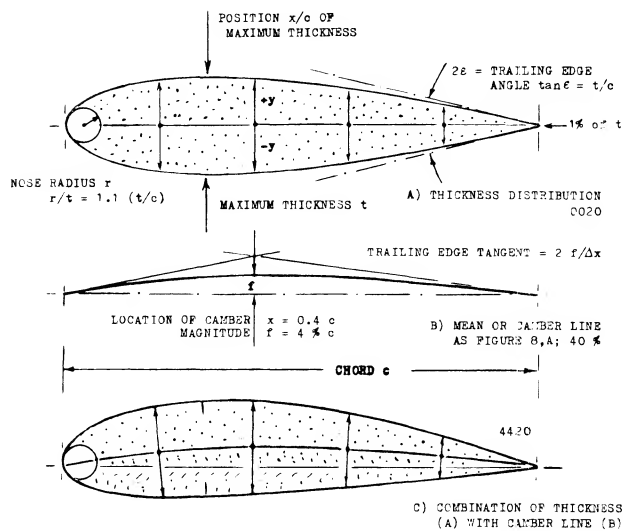


Figure 1. Basic geometry of airfoil sections shown by the example of 0020/4420.

1 GEOMETRY AND GENERAL

Before we can evaluate available experimental and other information, we will consider the geometrical shape of foil sections. We will also discuss methods and limitations of testing foil sections.

AIRFOILS, or aerofoils as the British say, are more or less flat surfaces producing or experiencing lift (or "lateral" forces) in a direction essentially normal to their plane. They have usually a more or less round "nose" or leading edge, and a comparatively slender wedge-like afterbody, ending in a sharp trailing edge. Figure 1 shows the geometric elements of such a section; namely chord and mean or camber line, thickness and thickness location, camber and camber location. Regarding shape, there is a nose radius; and a trailing-edge "wedge" angle to be considered. Any section can thus be fairly well defined by listing the various dimensions in terms of the chord.

EARLY SECTIONS. Within the framework above, there is an endless variety of shapes that can be designed and tried. In fact, during the last 50 or more years, thousands of sections have been tested, and a smaller number of them have been used in the actual building of airplanes. Early researchers developed wing sections completely by empirical methods, imitating, for example, those of birds. The sections investigated by Lilienthal (2,a) in the past century, and many of those tested by Eiffel (2,b) during the first decade of this century, were comparatively thin, and cambered. They are completely obsolete now, although they are evidently suitable for birds (at Reynolds numbers below 10^5). A few of these sections can still be found in (7,a); one of them is included in figure 2. As flying was progressing from just "hovering" at maximum L/D , thin sections used in biplanes, were straightened to accommodate higher forward speeds.

- (1) Practical information on foil sections and their mechanics can be found in engineering books, such as:
 - a) Diehl, "Engineering Aerodynamics", Ronald 1936.
 - b) Prandtl, "Führer Strömungslehre", 1942; "Essentials of Fluid Dynamics", London & New York 1952.
 - c) Goldstein, "Developments in Fluid Dynamics", 1938.
 - d) Schlichting, "Boundary Layer Theory", Mc-Graw-Hill.
 - e) Wood, "Aircraft Design", Author Uni Colorado, 1963.
 - f) Pope, "Wing and Airfoil Theory", McGraw-Hill.
- (2) Early investigations of wing sections:
 - a) Lilienthal, "Vogelflug/Fliegekunst", Berlin 1889.
 - b) Eiffel, "La Résistance de l'Air et l'Aviation"; and "Nouvelles Recherches...", Paris 1910, 1919.
 - c) Munk (& others), Systematic Tests, Tech Berichte der Fliegertruppen Vol I (1917) and Vol II (1918).
- (3) McLaren, "Wright Flyer", Aero Digest July 1953.
- (4) Theory and tunnel testing of Joukowsky sections:
 - a) Joukowsky, Zeitschr Flugtech Motorluft 1910, p 281; also in his "Aérodynamique", Paris 1916.
 - b) AVA Göttingen, 36 Foils, Erg III & IV (1927/32).
 - c) Glauert, Generalized Family, ARC RM 911 (1924).
 - d) ARC, Series Tested, RM 1241 (1929) & 1870 (1939).

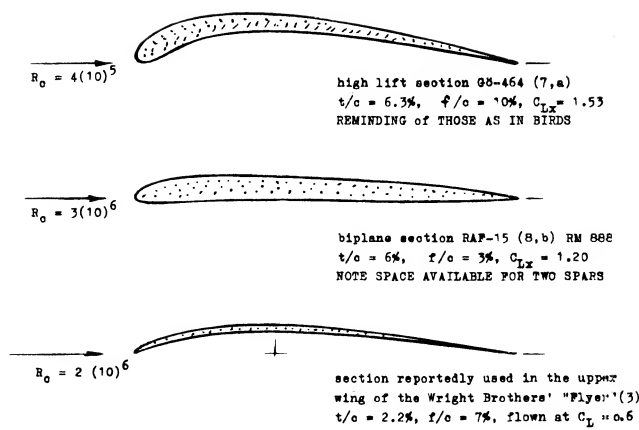


Figure 2. Examples of early wing sections.

MODERN SECTIONS. Roughly between 1915 and 1925, sections were developed, as particularly reported in (7), eventually to be used in cantilevered monoplane wings. The most successful of these sections, such as G8-535 (a famous sailplane shape) or the Clark-Y repeatedly tested by the NACA (32,a) in thickness ratios between 6 and 22% (31,e) or the British RAF-34, had a thickness ratio in the order of 12%, a thickness location around 30% and some camber; see figure 3. The first systematic series of sections named after Joukowski (4,a) who established the mathematical method of producing their shape and predicting their circulation, is similar in shape to those first sections. A number of 36 of these "theoretical" sections were tested at Göttingen (7,a) at $R_c = 4(10)^5$, with thickness ratios between 6 and 36%, and with camber ratios between zero and 20%. As shown in figure 4, the tail end of these sections (in their original form) is very thin, the leading edge is round, with the maximum thickness in the vicinity of but 25% of the chord.

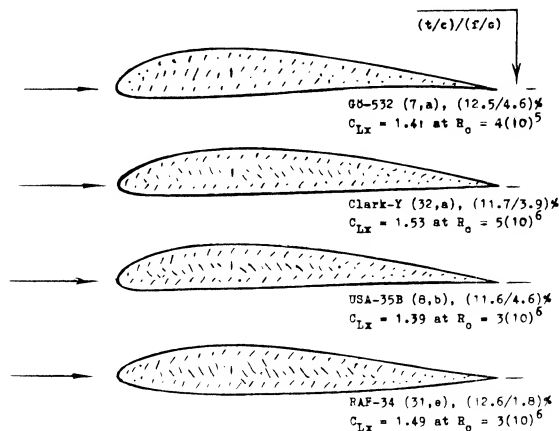


Figure 3. A selection of wing sections developed between 1910 and 1925, suitable in the design of cantilever monoplane wings.

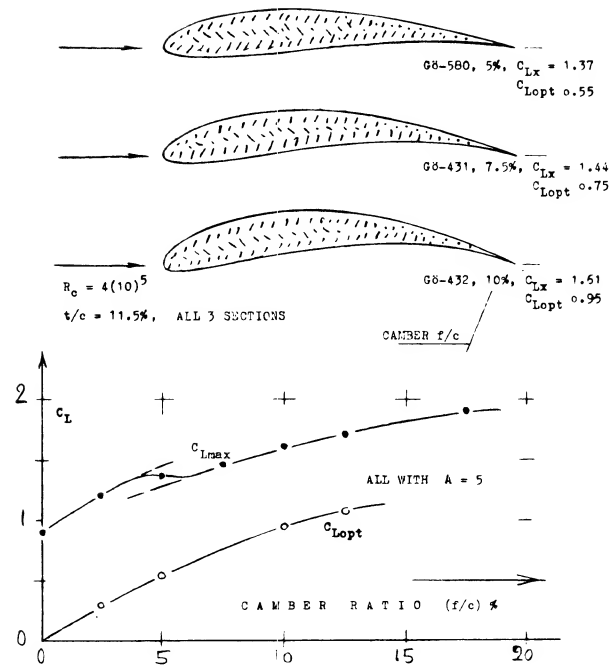


Figure 4. Representative sections of the Joukovsky series, tested at the AVA (7,a).

SYSTEMATIC SERIES. To establish some order, several series (families) of practical foil sections have been developed, by systematic variation of their geometry.

(a) The so-called 4-digit series was published by the NACA (31,a) in 1933, intended to be used in practical design and construction of airplane wings. The maximum thickness in this family is located at 30% of the chord (see figure 6) thus reflecting the earlier empirical result that such sections are most efficient, at the moderate speeds then considered. Thickness ratios tested (first in the very turbulent Variable Density Tunnel) are between 3 and 25%, later extended to 35% (32,c). Camber ratios are up to 7%, with locations between 20 and 70% of the chord (see figure 25). Selected shapes of this series are shown in figure 5.

An example of this series is

2 4 1 2 — thickness $t/c = 12\%$
 | camber location at 0.4 chord
 camber ' f ' = 2% of the chord

The 4-digit series was later modified (37) as to nose radius and location of the maximum thickness by adding numbers, as for example:

2412-34 — location at 0.4 chord
 | indicating the nose radius

As to the nose radius, 'O' indicates zero

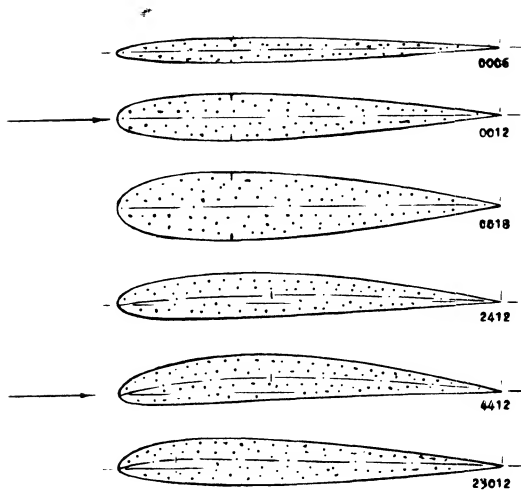


Figure 5. A selection of foil sections in the NACA 4-digit series, including 23012 which can be considered to be a modification of that series.

radius, '3' (as in the example) $1/4$ original size, '6' as in the original 4-digit section, and '9' three times the original radius.

(b) After disappointing experimentation with reflexed camber lines (8) the 5-digit series was developed at the NACA (33). By making the mean line perfectly straight, aft of 0.2 or so of the chord, the pitching moment C_{m0} was reduced to "nothing." Regarding thickness distribution, this series is the "same" as the 4-digit type above. The most famous of the family is the

2 3 0 1 2 — thickness $t/c = 12\%$
 |
 twice the camber location at 0.15 chord
 design lift coefficient = 0.2

It must be noted that the geometric camber is replaced by the theoretical "design" lift coefficient (see figure 27).

Figure 6. Thickness distribution (shape) of several NACA systematic series of airfoil sections.

- (5) British information on airfoil sections:
 - a) Pankhurst, NPL Catalogue, ARC C'Paper 81 (1952).
 - b) Experimental results are found in (36).
 - c) Nonweiler, Survey, Aircraft Engg 1956 (July).
- (6) Riegels, "Aerodynamische Profile", München 1958; Theory & Experimental Results Over Past 30 Years. Also "Aerofoil Sections", Butterworth (1961).
- (7) A variety of wing sections can be found in:
 - a) Ergebnisse AVA Göttingen, 4 volumes (1920/32).
 - b) Louden, Collection of Foils, NACA TR 331 (1929).
 - c) ARC/RAF-34, RM 1071, 1146, 1087, 1635, 1708, 1771.
 - d) Characteristics of airfoil sections from all over the earth, at lower R numbers collected in NACA T Rpts 93, 124, 182, 244, 286, 315 (1920 to 1929).

(c) Another modification of the 4-digit series was introduced by the Germans (34), adding digits to indicate nose radius and thickness location much in the same manner as under (a) above. Example:

0012 - 0.55 40—thickness location 0.4 c
 |
 one half original nose radius

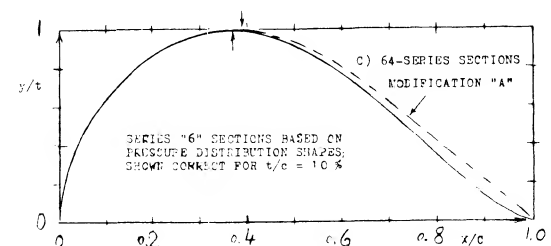
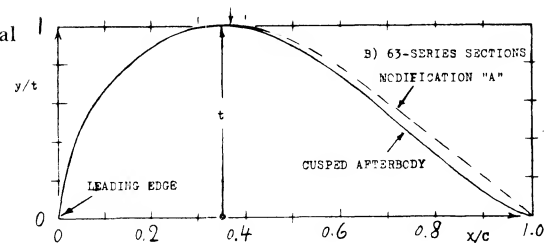
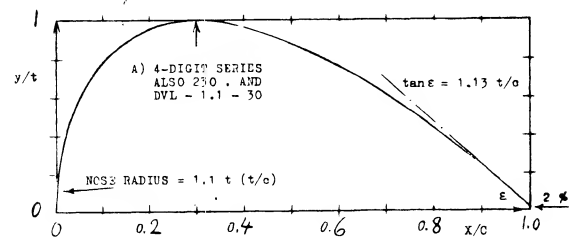
Nose radii were tested between

$$r c/t^2 = 0.275 \text{ and } 1.10 = (r/t)/(t/c) \quad (1)$$

where 1.10 indicates the original nose shape of the 4-digit series, and 0.275 one quarter of that; see figure 7.

(d) With the advent of higher speeds, it became necessary to vary the position of the maximum thickness. Two things are expected to be obtained by moving the thickness back to between 40 and 50% (and by reducing the nose radius at the same time); preservation of laminar flow (lower drag) and postponement of the critical speed (Mach number) brought on by compressibility. An example of the most-widely used so-called 6-series sections (38,b) of the NACA is

6 4 - 2 1 2 — thickness ratio 12%
 |
 design lift coefficient $C_L = 0.2$
 location of minimum pressure at 0.4 c
 NACA series designation for such sections



FLOW DEFLECTION. As far as airplane wings are concerned, their flow pattern is never two-dimensional. Because of the limitation of their span, the flow of fluid gets more or less permanently deflected by such wings so that the sections are actually exposed to a curved stream of air. As a consequence, their characteristics such as pitching moment due to camber in particular, must be expected to vary as a function of the aspect ratio. In closed wind tunnels, floor and ceiling more or less resist any deflection (up or down) of the stream by a lifting foil. On the other hand, investigation of wings or airfoils in open-jet wind tunnels (where the stream of air gets too much deflected) can lead to errors opposite in sign to those in closed tunnels. Statistical experience such as in (6) indicates that lift-curve slopes in the NACA two-dimensional closed tunnel set-up (38) are somewhat too high, while those from the open-jet DVL tunnel (34) are somewhat too low. Reduced to two-dimensional condition, the differentials are in the order of plus/minus 5%. We have in the graphs given preference to results obtained from airfoils with $A = 5$ or 6. In other words, we will deal with average wings and not with sections, in the end results.

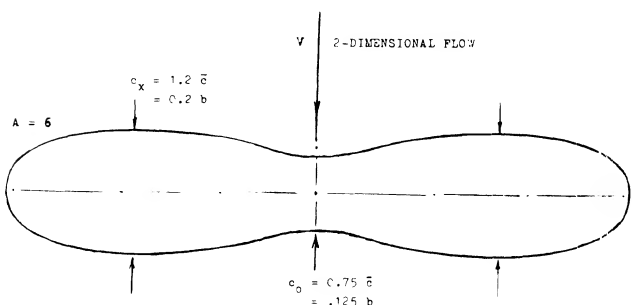


Figure 10. Planform of a wing (9) designed so that it experiences, along center line, two-dimensional flow (no downwash).

- (8) Reflexed foil sections for airplane wings:
 - a) Defore, In V'Density Tunnel, NACA TN 388 (1931).
 - b) Jacobs, "M" Series Foils, NACA Rpt 532 & 628.
 - c) 23012 (figure 5) considered to be reflexed?
 - d) 2-R-12 Sections in VD Tunnel, NACA TR 460.
 - e) Moscow, 'B' Airfoils, CAHI Rpt 903 (1923).
 - f) British RAF-34 (figure 3), ARC RM 1771 (1936).
 - g) For supercritical M'Numbers, NACA T'Rpt 947.
- (9) Fage, Lift and Drag = $f(A)$, ARC RM 903 (1923).
- (10) For example, $a = 4$ (as in the 64 Series of NACA airfoil sections) means that at design lift, pressure due to camber remains at its minimum plateau up to $x = 0.4 c$.
- (11) Flow pattern and mechanics of vortices:
 - a) Betz, About Vortex Systems, NACA TM 767.
 - b) Newman, Trailing Vortex, Aeron Quart 1959 p 149.

2. THE MECHANISM OF CIRCULATION IN FOIL SECTIONS

The lift produced by a finite-span airfoil, such as a plate for example, or an airplane wing, can physically be understood as the upward reaction to a downward deflection of a tube or cylinder of fluid having a diameter equal to the span of the lifting element. In a foil section (in two-dimensional flow) there is no permanent deflection. Therefore, lift or normal force produced, must rather be explained as the result of circulation.

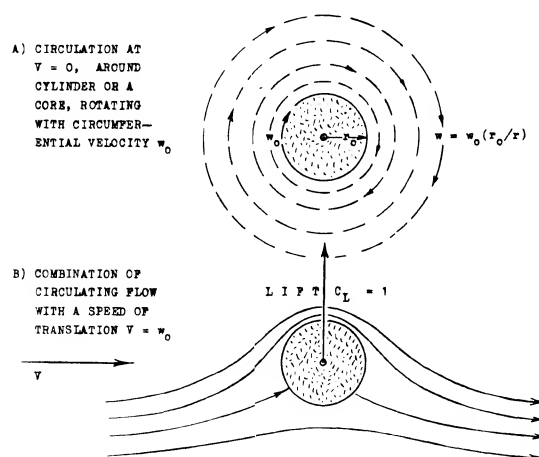


Figure 11. Theoretical flow pattern of circulation around circular cylinder or vortex core. At each and every point, the local velocity and direction corresponds to the geometrical sum of $(V + w)$.

CIRCULAR CYLINDER. Circulation can best be understood by considering the circular cylinder as in figure 11. There are several methods of leading a certain portion of the air flow over the top, one of which is rotation, thus producing the so-called Magnus force to be discussed further in the chapter dealing with "blunt bodies". At this point, we will only make the statement that a "circulating" motion "around" the cylinder is set up by rotation. More fluid passes over the upper and less under the lower side; and the average velocity is increased and decreased, respectively. According to Bernoulli's basic law, the static pressure along the surface of the body is thus reduced on the upper or suction side, and it is increased on the lower or pressure side. The result is a lifting force, i.e. a resultant of the pressure distribution the direction of which is normal (vertical or lateral, as it may be) to that of the basic stream of fluid and/or to the axis of the cylinder. The configuration as in the illustration thus yields a lift coefficient $C_L \approx 1.4$, while the theoretical limit for the flow pattern as in figure 11, would be $C_L = 4\pi \approx 12.6$.

LIFTING LINE. When reducing the diameter of the Magnus cylinder mentioned above, we finally arrive at a "rotating line." Together with the surrounding circulating (but not rotating) field of flow, that line represents a vortex (11), and since it develops lift (if restrained to remain at, or if "bound" to its location) that vortex is a "lifting line." The flow pattern of this line, as that of any other vortex, is characterized by the circumferential velocity

$$w \sim 1/r; \text{ or: } (w r) = \text{constant} \quad (2)$$

where r = radial distance of the fluid particle considered. As ' r ' increases, ' w ' reduces (eventually approaching zero). On the other hand, when approaching the center of the vortex, the velocity ' w ' theoretically approaches infinity. Actually, there is always a core within which viscosity (11,b) slows down the circulating motion, reducing it to rotation (similar to that of a solid cylinder as in figure 11,a).

THE CIRCULATION of the lifting line considered is

$$\Gamma = w 2 r \pi \quad \text{in (m}^2/\text{s)} \quad (3)$$

where $(2 r \pi)$ = circumference of the circle with the radius ' r ' at which the velocity is ' w '. When going around the lifting line, or around a rotating cylinder, or around a lifting foil by a 1000 different ways, we arrive at the

integral representing the same circulation as above:

$$\Gamma = \int w ds \quad \text{in (m}^2/\text{s)} \quad (4)$$

where ' s ' = length of the way once around. This circulation represents the lift produced by any lifting device, or by any section of a wing, around which the integral is taken.

FOIL SECTIONS, as used in wings or anything similar in flatness such as a plate for example, are not lines; in fact, only a mathematician can produce lift by means of a line. To understand the function of a wing section, we might say that at an angle of attack, the pressure side "leans" against the oncoming flow, thus forcing a certain volume of air to go around the usually rounded leading edge (nose), from the lower to the upper or suction side. Along the inclined and possibly cambered upper side, the stream of fluid is then lead down again. The airfoil is thus a device which forces certain stream tubes to go over the top. Theoretically this is not so certain, however. In an ideal, completely non-viscous fluid, the flow would pass around the trailing edge, from the lower to the upper side, and from the stagnation point near the leading edge, around the nose, to a corresponding rear stagnation point, at the upper side, near the trailing edge. The resultant lift would be zero, while there would be a "positive" pitching moment, tending to turn the foil to higher angles of attack.

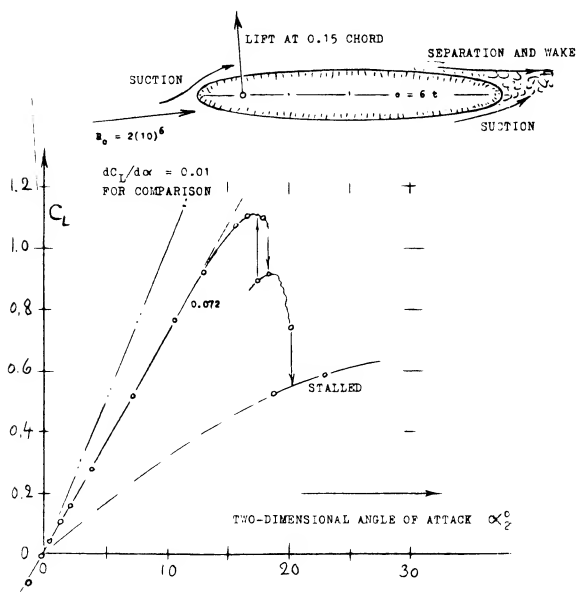


Figure 12. Lifting characteristics of a round-edged, id est elliptical section.

ELLIPTICAL SECTIONS. To illustrate this flow pattern, the lift of an elliptical section having a trailing edge as round as the leading edge, is presented in figure 12. Disregarding some secondary variations of the $C_L(\alpha)$ function, it can be said that the lift-curve slope is simply reduced in comparison to that of a conventional airfoil section. The flow is evidently separated from the round trailing end; and the two separation "points" move, together with the wake, steadily around the end from the pressure towards the suction side, as the angle of attack is increased. Consideration of the pitching moment gives some more insight into the flow pattern. At $R_c = 2(10)^6$, the center of lift is in the vicinity of 15% of the chord (strong suction forces along the upper side of the section nose, in combination with flow along the convex lower side, possibly to the very end of the section). The lift-curve slope as shown is the minimum. Since separation is a function of boundary layer conditions, the characteristics of the

section in figure 13 vary with Reynolds number. The lift-curve slope increases slightly as that number is increased. As the number is reduced below 10^6 , the slope increases also; and it reaches values very considerably above those of conventional foil sections, probably as a consequence of early laminar separation from the lower side, in combination with attached flow around nose and suction side (reattachment after laminar separation). This flow pattern is confirmed, at R_c between (3 and 6) 10^5 , by C_D between 0.05 and 0.02 (which means C_{D_0} up to 0.3), by a location of the lift force in the vicinity of 30% of the chord, and by a maximum coefficient $C_{L_{\alpha}}$ approaching 1.0. - As shown in figure 13, the lift or normal force of elliptical sections reduces with their thickness ratio. Naturally, at $t/c = 1$, that is for a circular cylinder, lift (or lateral force) is zero.

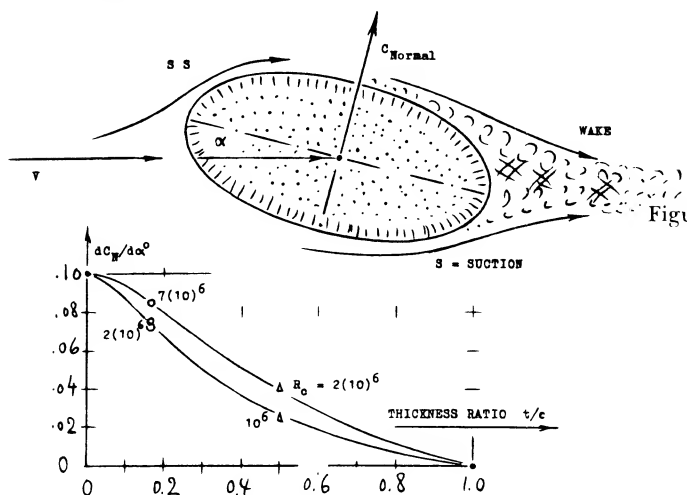


Figure 13. Lift of elliptical sections at Reynolds numbers as indicated, as a function of their thickness or rounding ratio.

TRAILING EDGE. In the case of an essentially sharp trailing edge (as we find it in all practical wing sections) the velocity of the particles around that edge would have to be infinite (or at least extremely high), so that it is obvious that skin friction (boundary layer losses) in any realistic fluid would be equally high. At any rate, it is a fact, that the flow does not get around any sharp trailing edge (20) so that the position of this edge controls the circulation around the rest of the foil section. Adopting the empirical fact, in the mathematical treatment of lift, the trailing edge is assumed to be the rear stagnation point; and this assumption is named after the two scientists (17) who first introduced and used it, the Kutta-Joukowski condition. The resultant flow field around a foil section is the deformed equivalent of a lifting-line vortex. As in the rotating cylinder, there is a circulating motion around the section, caused by the sharp trailing edge in combination with an angle of attack. Position and direction of that edge primarily determine the strength of the circulation produced.

REVERSED 0012. After what is said about round and sharp edges, the lift of the 0012 section as in figure 14 should be expected to be very poor when reversing the direction of flow or flight. Surprisingly enough, the section tested has a lift-curve slope not only as high as in the conventional direction, but even slightly higher. There is first the leading-edge flow. As found in many tests with flat plates, a sharp leading edge is "no" obstacle for the flow to get around, and to continue (after a small local separation) along the suction side. To explain the increased lift-curve slope, we may suggest two possible reasons. One is that the round but separated trailing edge acts like a blunt edge (to be discussed later). The other reason may be found in the volume (displacement) of foil plus wake. Increased velocities might thus help to produce higher lift. Of course, the maximum lift coefficient of the section with the sharp edge leading, is but 0.8, in comparison to 1.3 in the conventional direction. - Testing conventional airfoil sections in reverse direction, is not as useless as it may seem at first. In the rotors of helicopters flying at higher speeds, it is quite possible that the in-board portions of the blades are moving against the air, with their sharp edges first.

- (12) Characteristics of elliptical sections:
 - a) Williams, Elliptical in CAT, ARC RM 1817 (1937).
 - b) Polhamus, Non-Circular, NASA TR R-46 (1959).
 - c) Dannenberg, "Airfoil" w/Suction, NACA TN 3498. (1955).
 - d) Gregory, Thick with Suction, ARC RM 2788 (1953).
- (13) Characteristics of sharp-nosed sections:
 - a) Daley, 6% Thick Sections, NACA TN 3424 (1955).
 - b) DVL, Double-Arc Sections, see (6) or (34,c).
 - c) Solomon, Double Wedge, NACA RM A1946G24.
 - d) Critzos, 0012 to $\alpha 180^\circ$, NACA TN 3361, 3241.
 - e) Lift in reversed flow similar to that in (d) for 2212, Ybk D Lufo 1938 p I-90 (NACA TM 1011).
 - f) Lock, Symmetrical Also Reversed, ARC RM 1066 (1926).
 - g) Polhamus, Drag Due to Lift, NACA TN 3324 (1955).
 - h) Williams, 4 Circular Arc Foils, ARC RM 2301 (1946).
 - i) Note that flow does go around leading edge ("no" boundary layer yet), to considerable degree.
- (14) In a manner related to that of maximum lift (see the chapter on this subject) the lift-curve slope is also affected (usually increased) by stream turbulence. For example (as reported by Millikan, CIT, around 1939) $dC_L/d\alpha$ of 2412 increases from 0.094 (for 0.3% turbulence) to 0.105 (for 5.3% turbulence) at $R_c = 1.4 (10)^6$.

LIFT COEFFICIENT. In applied aerodynamics, the term "circulation" is not used very much. The lift 'L' referred to the lifting area 'S', and to the dynamic pressure 'q' of the fluidflow, is represented by the non-dimensional coefficient

$$C_L = L/qS = 2 \Gamma/cV \quad (5)$$

while the circulation producing the lift, is

$$\Gamma = C_L c V/2 \quad \text{in (m}^2/\text{s)} \quad (6)$$

As a function of the angle of attack ' α ', the lift of a flat and thin plate (in two-dimensional flow) corresponds theoretically to

$$C_L = 2 \pi \sin \alpha \quad (7)$$

At small angles, the lift-curve slope is

$$dC_L/d\alpha = 2\pi; \quad dC_L/d\alpha^\circ = 2\pi^2/180 \approx 0.11 \quad (8)$$

and the "lift angle" (15) is:

$$d\alpha/dC_L = 0.5/\pi; \quad \text{or} \quad = 90/\pi^2 = 9.1^\circ \quad (9)$$

This function means that an angle in the order of 9° is theoretically required, in two-dimensional flow, to produce a lift coefficient equal to unity, through the use of a plate or any thin airfoil shape.

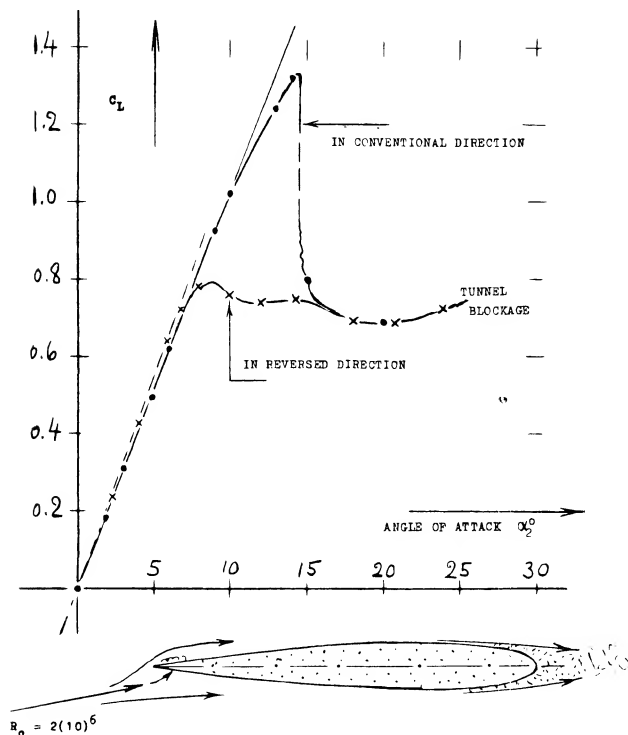


Figure 14. Lifting characteristics of 0012 section in reversed flow (12.d).

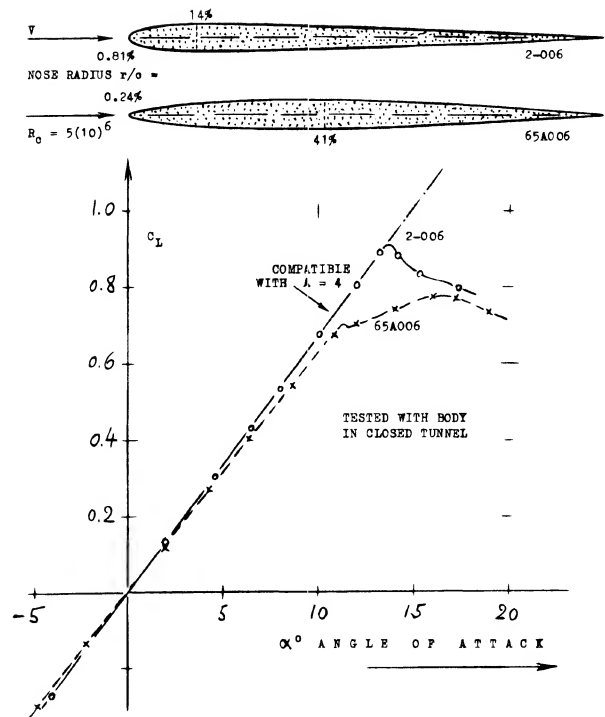


Figure 15. Lift of two 6% thick foil sections, differing in nose radius, tested in tapered wings with $A = 4$, on fuselage body (29).

SHARP LEADING EDGES. We have mentioned (in connection with the reversed 0012 in figure 14) that a sharp leading edge can very well produce a high lift curve slope. Theoretically, evaluated from (13,g), the loss of lift, when losing the leading-edge suction peak, is

$$\Delta C_L = -(0.25/\pi^2) \times C_L^3 \quad (10)$$

This would be 2.5% at $C_L = 1$, and it would be "nothing" at small lift coefficients. We have evaluated lift-curve slopes as a function of the leading edge radius ratio (r/c) for the 4-digit sections (31,c) as well as for a series of more or less sharp-nosed 6% sections (13,g). The conclusion is, that in a 6% section, about 5% is actually lost when making the leading edge perfectly sharp, as in a double wedge section, for example (having the same location of maximum thickness). This much is indicated in figure 21 as an increase of the lift angle at $t/c \rightarrow 0$. Sharp-nosed sections (with a certain trailing-edge angle) can also display a lift deficiency (non-linearity) near zero or symmetrical lift coefficient. The losses of momentum at the sharp l'edge evidently cause an accumulation near the trailing edge. For example, double-wedge or double-arc sections as in (13,a,c) not thicker than 6%, already show the non-linearity.

THE NOSE RADIUS of a foil section is a function of thickness ratio and thickness location. One can change the radius, however, according to equation (1). As an example, lift and drag of a 6% section are shown in figure 15. There are evidently losses of momentum in the flow when getting around the leading edge of a thin airfoil. The difference in the lift-curve slope of the two shapes tested, is some 7%. The optimum size of the nose radius will also be a function of surface roughness and Reynolds number (see later), and of the Mach number (see the chapter on "compressibility"). The maximum lift coefficient must also be considered when selecting a radius for the leading edge; see "maximum lift and stalling".

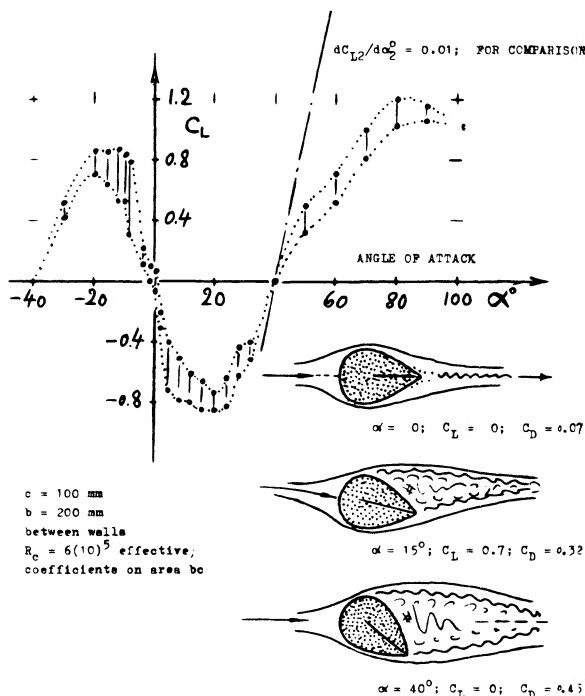


Figure 16. Lift of the extremely thick foil or strut section 0070, tested (18) to an angle of 90°. The lower and upper points plotted, correspond to the time-dependent fluctuations of the separated flow pattern. R'number above critical.

INFLUENCE OF THICKNESS. Thickness means displacement. As a consequence, average fluid-flow velocities along the sides of foil sections are generally increased over those past a thin plate; and their lift-curve slope is theoretically expected to increase with the thickness ratio. As an extreme, we may again consider the circular cylinder. Assuming that we would manage by means of boundary layer control around the rear side, to displace the stagnation points from zero (at the forward side) and from 180° (at the rear side) both down toward 90° (at the lowest point), without losing any momentum, its lift curve slope would be $dC_L/d\alpha = 4\pi$, rather than $= 2\pi$, as in thin foil sections. In theory, therefore, the lift angle (15) reduces (as shown in figure 21) as a function of the thickness ratio.

STRUT SECTION. "Streamline" sections, suitable to be applied in struts or in propeller blades near the hub, have usually higher thickness ratios than conventional foil sections. As an extreme example, the lift coefficient of an 0070 section (18) is presented in figure 16. The lift-curve slope at small angles of attack is strongly negative (!) up to $\alpha \approx 20^\circ$. The flow pattern proves that negative lift is the result of flow separation from the upper side of the section. As a consequence of the well-attached flow along the negatively cambered lower side of the section, suction develops there, thus producing negative lift. As the angle of attack is increased, the lower side eventually produces predominantly positive pressures and a correspondingly positive lift. Also note that the maximum lift coefficient at $\alpha = 90^\circ$, fluctuating between 1.0 and 1.2, corresponds to suction forces developing around the section's nose. - It is shown in (22,b) how the lift function of an airfoil with $t/c = 68\%$, is almost perfectly linear, with a blunt trailing edge (see later). It can also be found in Chapter III of "Fluid-Dynamic Drag," that the maximum lift of a section with $t/c = 40\%$, is increased from $C_{Lx} = 0.8$ to 1.15, when blunting the trailing edge to $h = 0.4 t$. Again, lift as a function of the angle of attack is practically linear. It may not be desirable, however, to have much lift or lateral force in a "strut." The best method to keep such forces down, is to provide a well-rounded trailing edge.

- (15) For "lift angle" ($d\alpha/dC_L$) see the "wing" chapter.
- (16) NACA airfoil sections, other than '6' series:
 - a) See NACA Wartime Report L-345.
 - b) '16' Series, TN 976, 1546, 2951; TR 763 & 2951.
- (17) W. M. Kutta (Bavaria, 1911); N. E. Joukovsky (Zhukovskij) "father of Russian aviation" (1847/1921).
- (18) Lift (and drag) of the 0070 section, tested by the author, in the two-dimensional water tunnel of Fieseler Aircraft Corporation, 1939.
- (20) Influence of the trailing-edge angle:
 - a) Williams, Cuff Sections, ARC RM 2457 (1951).
 - b) See chapter "characteristics of control devices".
 - c) DVL, Modified 0015 and 0018, see (34,c).
 - d) Hoerner, 0070 in Water Tunnel, not published (18).
 - e) Batson, 0015 Modified, ARC RM 2698 (1943).
 - f) Beasley, Lift Reduction, AD-455,356; see (27,d).
- (21) The 63 and 64 series sections have almost exclusively been tested in closed two-dimensional tunnels. There results have been disregarded in this text to a large degree. The value of the (38) data is found in the comparison of the foil sections tested, with each other.

TRAILING-EDGE ANGLE. The shape of all so-called streamline sections (designed for subsonic speeds) is such that the afterbody is more slender than the forebody. Flow separation is avoided or postponed in this manner. Figure 17 presents the lift coefficient of a foil section with thickness location at 40% of the chord. In combination with a thickness ratio of 18%, a trailing-edge angle (included by upper and lower side) of approximately 30° is thus obtained. As a consequence, when rotating the foil out of zero angle of attack, the boundary layer (id est its thickness, but not the material itself) switches from one side to the other. The growth at (and possibly some separation from) the upper side, and the suction of the attaching flow at the negatively cambered lower side, are so strong, that a negative lift-curve slope is produced at angles between plus and minus 1.5° . The positive lift-curve slope (above $\alpha \approx 1.5^\circ$) is almost equal to that of the same type of section with the thickness located at 30% of the chord. The later figure 33 includes a different example of trailing "wedge" angle on a comparatively small beveled portion of the chord. While any of the "wild" effect as in figure 17, is not evident, the lift-curve slope near zero lift, is noticeably reduced. Such an effect of the "wedge" angle is particularly known in control surfaces where effectiveness and hinge moment are both a direct function of that angle (as explained in the chapter on "control surfaces"). In figure 18, it is shown how the lift-curve slope (of symmetrical sections, around $\alpha = 0$) reduces, and the "switching" angle (defined in figure 17) increases, as a

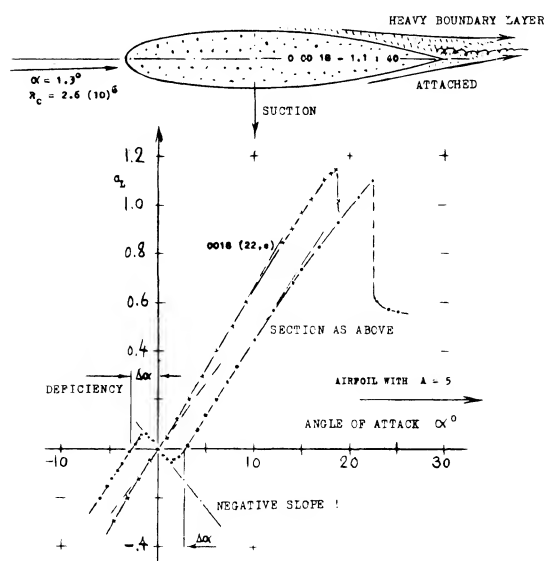


Figure 17. Lift as a function of angle of attack of a section having a large trailing-edge angle.

function of the trailing wedge angle (or of the half angle ϵ). At $\tan \epsilon$ between 0.3 and 0.4 (that is between 16° and 22°) the slope of the lift seems suddenly to switch from positive to negative. Here again, the Reynolds number (affecting boundary-layer conditions) must be expected to have an influence. As seen in (20,a) for example, "switching" and negative lift-curve slope are not obtained at smaller R'numbers (below 10^6). Since delay and switching do not take place in round-ended (elliptical) sections, it can be concluded that a sharp trailing edge (with a certain wedge angle) is necessary for producing the flow pattern described.

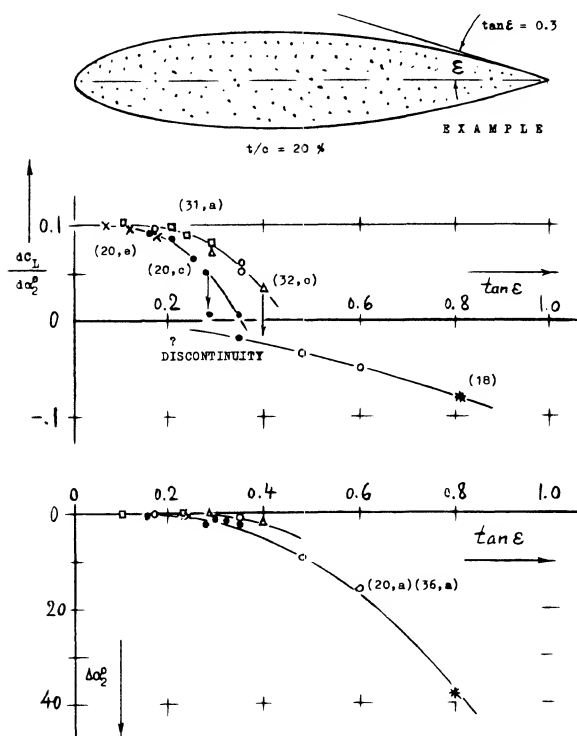


Figure 18. Lift-curve slope and "switching" angle of thick foil sections as a function of the trailing-edge angle as defined in the graph.

BLUNT TRAILING EDGES have an effect upon section characteristics which is precisely opposite to that of large trailing wedge angles. In fact, the angle included by upper and lower side is naturally reduced when thickening the trailing edge. Figure 19 presents an example where an 0018 airfoil was shortened by cutting off 5% of the chord from the trailing edge. Results of blunt edges similar to this one are generally as follows:

(a) Any weakness of the lift-curve slope in the range of small angles of attack (if any) can be cured by making the trailing edge thick and blunt. This may again be important for control surfaces such as ailerons.

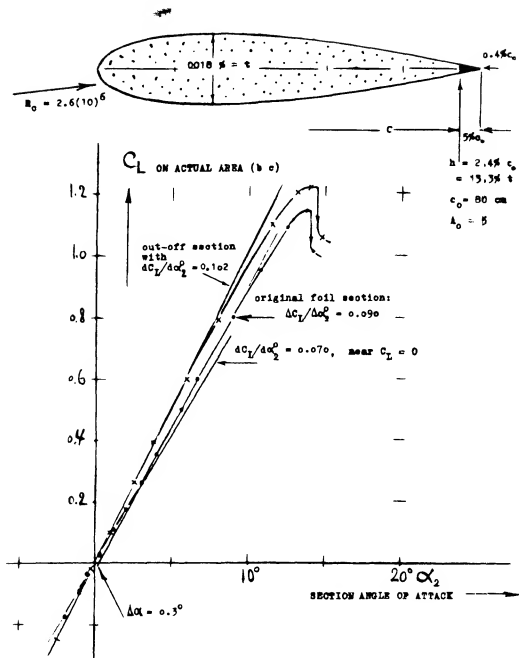


Figure 19. Lift of an 0018 airfoil with and without a blunt trailing edge (22,c), produced by cutting off from that edge. The angle of attack is reduced to 2-dimensional conditions by analysis.

(b) The lift curve slope is somewhat increased above that of the same section having a conventional sharp trailing edge. In the case of figure 19, the slope (reduced to two-dimensional condition) is a full 10% increased over that of the original section. If considering lift (id est, L/q of the wing as tested) rather than the coefficient (referred to span times chord shortened from the trailing edge), we still obtain 5% more lift for the section with the blunt edge than for the sharp-edged original section.

- (22) Airfoil sections with blunt trailing edge:
 - a) Smith-Schaefer, Cut-Off 0012, NACA TN 2074 (1950).
 - b) AVA, Cut-Off Air-foil, Ergebnisse III (7,a).
 - c) Swaty, 0018 Cut-Off, Yearbk D Lufo 1940 p 1-58.
 - d) Engelhardt, Wake Survey Behind Thick Trailing Edges, Aerody Lab TH München Rpt 4/1944.
 - e) Okamoto, Aeron Inst Tokyo University Rpt 131.
- (23) Strut sections with blunt trailing edges:
 - a) Barlow, Propeller Shanks, NACA T Rpt 852 (1946).
 - b) Strut Sections, Junkers Tunnel Rpt S.1943/85.
 - c) See "pressure drag" in "Fluid-Dynamic Drag".
- (24) Correlation of lift-curve slope as a function of the trailing-edge angle, as in (9), confirms the fact that sections with cusped (concave) afterbody distinctly differ from straight or convex shapes.
- (25) Presentation of Airfoil-section theory:
 - a) Munk, Wing Section Theory, NACA TR 191 (1924).
 - b) Glauert, "Elements Foil Theory", Cambridge 1926.
 - c) Theodorsen, Arbitrary, NACA TR 383,411,452.

(c) The maximum lift coefficient of the section in figure 19 is noticeably increased. However, if considering C_{Lx}/C_{Dmin} as a figure of merit for a wing, the test does not show any advantage of the blunt-edged (102) over the original section (142). It is only when thickening (rather than cutting off from) the trailing edge, thus keeping the ratio $t/c = \text{constant}$, that a very small improvement of the figure of merit (143), can be found (23,c) for the type of section as in the illustration, for a very modest thickness ratio of the trailing edge (in order of $h/c = 0.5\%$, or $h/t = 3\%$). Full-scale, this might be 1 cm; but the edge should be sharp to be of benefit.

Results of another foil section are shown in figure 20. When cutting off a small piece of the trailing edge, the boundary layer accumulation as indicated in the illustration is evidently cut down too, so that the slope of the lift coefficient (referred to the reduced area) increases, to a certain maximum as shown. For similar results on 0012 see (22,a).

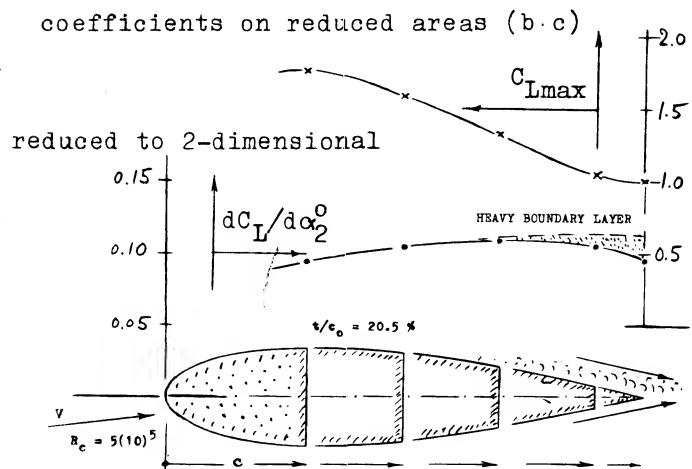


Figure 20. Influence of cutting off from the trailing edge upon the sectional lifting characteristics of the foil section GÖ-490; (7,a) (22,b).

INFLUENCE OF FRICTION. In reality, the lift angle is never as low as predicted by theory (equation 9), not even in sections with "optimum" thickness and shape. Because of skin friction and boundary layer growth along the suction side of lifting foil sections, the angle necessary to produce a certain lift coefficient is larger than according to circulation theory. The growth (displacement) of the B'layer is usually of such a nature, however, than the straightness of the $C_L(\alpha)$ function is preserved for practical purposes, for all but the higher thickness ratios, within the range of

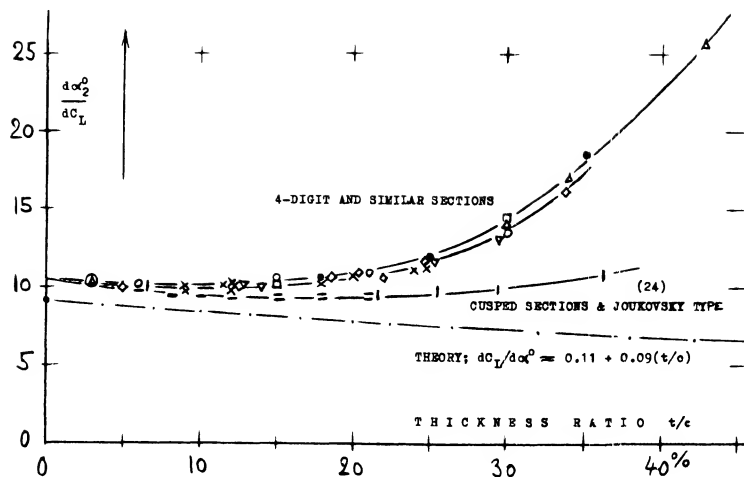


Figure 21. The lift angle of airfoil sections as a function of their thickness ratio (15).

- NACA, 0025/35 IN FST (32, c)
- ARC, 0015/30, 3(10)⁶ (36, a)
- △ FROM VARIOUS OTHER SOURCES
- ◇ AVA, AT 4(10)⁵ & 3(10)⁶ (6)
- NACA, IN VDT, 3(10)⁶ (31, c)
- ▽ ARC STRUTS AT 3(10)⁵ (36, c)
- × DVL (HOERNER), CLARK-Y (34)
- NACA 63/64 IN 2 DIMENS (38)
- | AVA, JOUKOVSKY SERIES (4, b)

lift coefficients excepting those approaching the maximum. Sectional lift angles are plotted in figure 21, as a function of the thickness ratio. It is seen that the theoretical prediction mentioned above, whereby the lift-curve slope should increase with the thickness ratio (so that the lift angle would reduce), does only come true, say up to $t/c = 10\%$. The boundary-layer growth and the theoretical influence of thickness evidently cancel each other to a large degree, so that the lift angle in the range of t/c between 0 and 12 or 15%, comes out as a more or less constant value in the order of

$$(d\alpha^{\circ}/dC_L)_2 = 10^{\circ} \quad (11)$$

Where the subscript '2' indicates conditions in two-dimensional flow (id est at $A = \infty$).

SECTION SHAPE. Although there seems to be an influence of testing technique (14), conclusions as to the influence of section shape upon the lift angle in figure 21, are as follows:

(a) Sections with cusped (concave) afterbody contour (such as the 63 and 64 series, in particular) have the highest lift-curve slopes (21) and they maintain a lift angle slightly below 10° , possibly up to $t/c = 30\%$ (20, e).

(b) All "conventional" sections (such as the 4-digit series) with convex afterbody contour and trailing-wedge angles of corresponding magnitude, display a reduction of their lift-curve slope) above $t/c = 10$ or 12% .

(c) Roughness, even if only applied in form of a stimulation strip near the leading edge, increases the lift angle of sections, particularly within the range of higher thickness ratios.

"EFFICIENCY." The loss of lift of a foil section as against potential theory, can be interpreted as an effective reduction of the wing chord ' c ' = \tilde{a} c. Consequently, in two-dimensional flow, in comparison to thin-plate theory (equation 20):

$$C_L = 2 \tilde{a} \pi \sin \alpha_2 ; \quad dC_L/d\alpha_2 = 2 \tilde{a} \pi ;$$

$$d\alpha_2/dC_L = 0.5/\tilde{a} \pi \quad (12)$$

The commonly used airfoil sections have efficiency factors (30) in the order of $\tilde{a} = 0.9$. At higher thickness ratios as in figure 21, $(d\alpha/dC_L)$ increases considerably. Formation of a heavy boundary layer at (and eventually flow separation from) the suction side, displace the outer flow, away from the trailing edge so that the circulation becomes progressively reduced. Theory has tried analysis of this effect; in fact, one author (27) has gone so far as to predict the circulation of a certain foil section from a boundary-layer survey taken at the trailing edge.

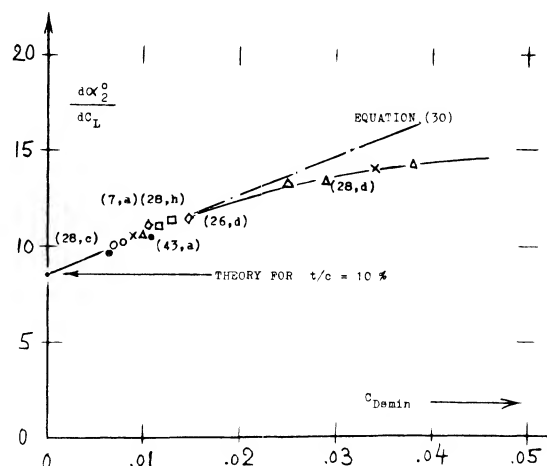


Figure 22. Lift angle (15) of foil sections as a function of minimum drag (friction and roughness).

ROUGHNESS. The section-drag coefficient increases with the thickness ratio. Skinfriction can also be increased, above that as for smooth surface condition, by roughness. Figure 22 presents $d\alpha/dC_L$ of various "conventional" foil sections having thickness ratios between 12 and 17%, as a function of their minimum section drag coefficient (as tested at small lift coefficients). The lift angle increases considerably; a value twice as high as that for smooth condition, is not impossible, provided that skin friction is sufficiently increased by surface roughness and/or other "obstacles." For practical purposes, the slope of the lift angle in figure 22 might be approximated by

$$\Delta(d\alpha/dC_L) = 180 C_{D_{\min}} \quad (13)$$

- (26) Influence of skin friction on lift, experimental:
 - a) Betz, Lift/Drag, ZFM 1932 p 277; NACA TM 681.
 - c) See results function of Reynolds number (40).
 - d) Batson, B'layer at Tr'edge, ARC RM 2008, 1998
- (27) Analysis of lift as a function of drag:
 - a) Weinig, Lift Deficiency, Lufo 1938 p 383.
 - b) Stüper, Lift f(Drag), ZFM 1933 p 439.
 - c) Preston, Boundary Layer, ARC RM 2725 (1953).
 - d) Beasley, Lift Reduction Due BL, ARC RM 3442
- (28) Influence of surface roughness on lift:
 - a) Wieselsberger, Ringbuch IA9 (Durand IV p 19).
 - b) See Ergebnisse AVA Göttingen III (1926) p 112.
 - c) Jones, 0012 & RAF-34 roughness, ARC RM 1708.
 - d) Hoerner, 0012 in Wat'Tunnel, unpublished (1939).
 - e) Hooker, Surface Roughness, NACA TN 457 (1933).
 - f) Muttray, On Joukowsky Sections, NACA TM 768.
 - g) Bradfield, With Metal Gauze, ARC RM 1032 (1926).
 - h) Wood, Corrugated Surface, NACA T Rpt 336 (1929).
- (29) Maki, 64A010 Modifications, NACA TN 3871 (1956).
- (30) Neely, 44(12 to 24) A = 8 to 12, NACA TN 1270.
- (31) Airfoils with A = 6 in NACA V'Density Tunnel:
 - a) Jacobs, 78 Related Sections, T Rpt 460 (1933).
 - b) Jacobs, Function of R'number T Rpt 586 (1937).
 - c) Jacobs, Various Corrections, T Rpt 669 (1939); this report is the best of the series.
 - e) Pinkerton, Various Sections, T Rpt 628 (1938).
 - f) Jacobs, 23012 Type, see references (33,b,c).
- (32) Airfoils with A = 6, in NACA Full-Scale Tunnel:
 - a) Silverstein, Clark-Y Airfoil, T Rpt 502 (1934); section named after Colonel V E Clark (1886 to 1943).
 - b) Goett; 0009, 0012, 0018 Airfoils, TR 647 (1939).
 - c) Bullivant, 0025 & 0035 Foils, TR 708 (1941).
- (33) Investigations and results on 23012 airfoils:
 - a) Jacobs, FS and V'Dens Tunnels, TR 530 (1935).
 - b) Jacobs, in V'Density Tunnel, NACA T Rpt 537.
 - c) Jacobs, Foil Series in VDT, NACA Rpt 610 (1937).
 - d) NACA, with Flaps, T'Rpts 534 (1935), 664 (1939).
 - e) ARC, in CAT, RM 1898 (1937); RM 2151 (1945).
 - f) Doetsch, In DVL Tunnel, Ybk D Lufo 1939 p I-88.
- (34) Airfoils as tested in the "large" DVL wind tunnel:
 - a) Doetsch and Kramer, Lufo 1937 p 367 and 480; also Ybk D Lufo 1937 p I-69, 1939 p I-88, 1940 p I-182.
 - b) Hoerner, Clark-Y Series, DVL Rpt Jf 208/3 (1940); also in small tunnel, ZWB FB 65 (1934).
 - c) Collection of DVL Results, ZWB FB 1621 (1943).
 - d) For DVL (and other) results see also ref (6).
 - e) Pressure Distributions, Ringb Luftf Tech LA,11.

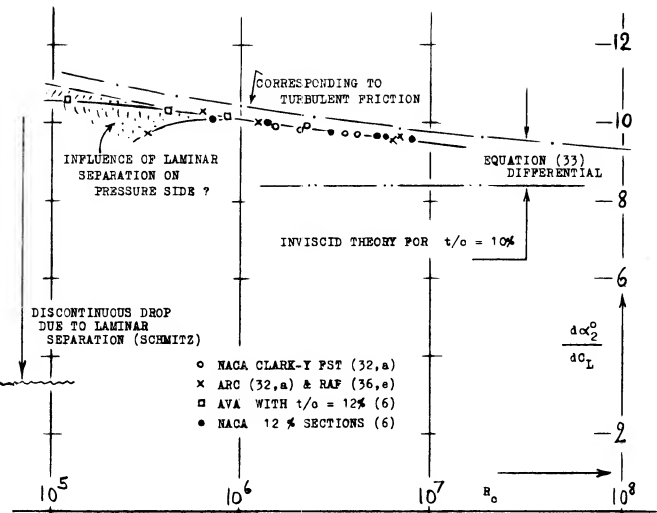


Figure 23. The lift angle (15) of airfoil sections as a function of Reynolds number, affecting their skin friction drag.

REYNOLDS NUMBER. Combining the last equation with a function expressing the section-drag coefficient for fully turbulent B'layer flow:

$$C_{D_{\min}} \approx 0.1/R^{1/6} \quad (14)$$

we can predict the variation of the lift angle at higher Reynolds numbers to be

$$\Delta(d\alpha/dC_L) \approx 200 (t/c)/R^{1/6} \quad (15)$$

Some experimental results (reduced to two-dimensional condition) as plotted in figure 23, confirm this expression at R'numbers above 10^6 . Below that number, serious variation can take place (due to B'layer transition) the character of which seems to depend upon the particular shape of the section nose.

B' LAYER TRANSITION. Growth and flow condition of the boundary layer are a function of the Reynolds number (and of wind-tunnel turbulence). The character of the B'layer, whether laminar or turbulent, also depends upon the angle of attack. As a consequence, the $C_L(\alpha)$ function is not always completely straight. Transition from laminar to turbulent B'layer flow may, for example, make the lift-curve slope slightly irregular, particularly at smaller R'numbers. We have, wherever this seems to take place, in the many graphs in this text, indicated discontinuities in the $C_L(\alpha)$ function by not fairing a line through them, but by leaving the experimental results as discontinuous as they are found.

PRACTICAL CONSTRUCTION (44). The boundary layer developing along the chord of foil sections, can be disturbed (made heavier) by skin irregularities (protuberances) due to fabrication. A different effect is deformation of section shape. Portions of helicopter blades were tunnel-tested (44,a). These blades consist of a solid nose section and a fabric-covered afterbody supported by ribs (with spacings equal to 1/3 of the chord). As a consequence of pressure distribution (due to lift) the fabric deforms itself. Because of porosity (leakage) there may also be a negative pressure inside. In helicopter blades, positive pressures may also develop inside, caused by centripetal acceleration. The experimental results as in figure 24 show:

(a) When the fabric is bulging, the lift-curve slope is reduced, probably because of trailing-edge angle and increased drag.

(b) For a negative inside pressure of 100 lb/ft (at an estimated dynamic pressure of the same but positive order) the sides of the foil section are somewhat hollow. As a consequence of reduced trailing-wedge angle, the lift-curve slope is as high as that of a smooth and solid 0012 section.

(c) In samples where the fabric tension is not very high, a deformation takes place in such a manner that the pressure side becomes somewhat hollow, and the suction side bulging. The resultant section camber, increasing with the lift coefficient, produces a particularly high lift curve slope, in the order of 0.12 as tested in a closed-type tunnel between walls (21).

(d) The maximum lift coefficient varies corresponding to the lift-curve slope.

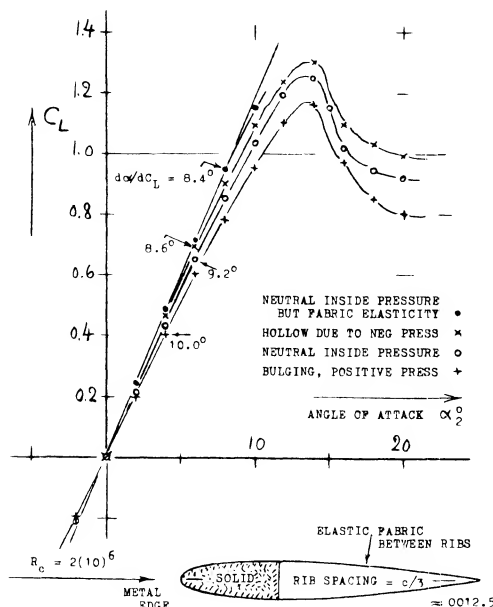


Figure 24. Lift characteristics of practical-construction helicopter blades, as tested in a tunnel, between walls (43,a).

C. INFLUENCE OF SECTION CAMBER ON LIFT

In subsonic aerodynamics nearly all wing sections designed for the production of lift have a cambered mean line. The shape of the mean line selected influences the chordwise lift distribution, the zero lift angle, the lift at an angle of attack of zero, the lift at the maximum lift drag ratio and the maximum lift coefficient. The type of mean line used depends on the airfoil series type, and its application.

CAMBER LINES. Mean lines used in the most widely known families of wing sections, are shown in figure 8. These lines are characterized primarily by the location of their tops (in % of foiled chord) and by their camber ratio f/c (see figure 1). Although circular arcs are not really used in conventional foil sections, their geometry lends itself to analysis. In particular, the angle at the edges, as in the sketch (figure 27) of such a mean line is

$$\tan \gamma = 2 f/x$$

where x = distance between f and trailing or leading edge.

ZERO-LIFT ANGLE. In two-dimensional flow, the "symmetrical" lift coefficient (see equation 21) for a circular-arc mean line (with $x = c/2$) is obtained at zero angle of attack. In terms of the angle at the trailing edge, the perturbation or circulation velocity at that edge is

$$w = V\gamma; \Gamma = w 2 (c/2) \pi = \pi c V\gamma \quad \text{in (m}^2/\text{s)} \quad (16)$$

so that the lift coefficient due to camber (at $\alpha = 0$) is:

$$C_{L_0} = \Gamma / (c V) = \pi \gamma = 4 \pi f/c \quad (17)$$

The angle of attack necessary to reduce the C_L due to camber to zero, corresponds to $d\alpha_2/dC_L = 0.5/\pi$. Therefore, in a section with circular-arc camber, this angle is theoretically

$$\alpha_0 = -2f/c = -(360/\pi) f/c = -1.15(f/c)\% \quad \text{degrees} \quad (18)$$

Zero-lift angles are plotted in figure 25, as a function of camber location. Since the angle is related to the tangent to the camber line at the trailing edge, foil sections of the 230 type, having a straight camber line over most of their afterbody, show less negative zero angles than the more evenly cambered 4-digit sections. Foil shapes with thickness ratios exceeding 12%, have zero angles somewhat smaller (less negative) than those shown in the graph, for t/c between 6 and 12%. The angle of zero lift also increases (to somewhat more negative values) as the camber ratio is increased above a few percent.

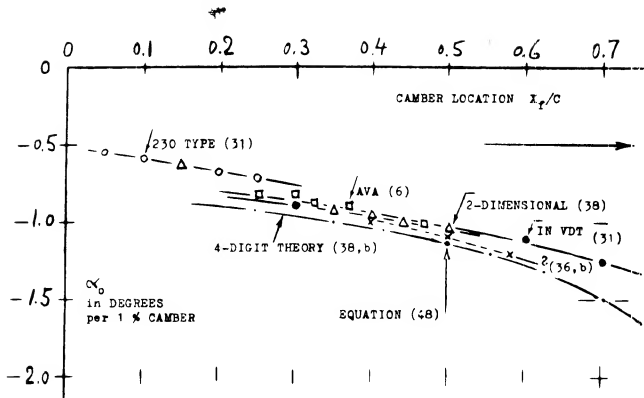


Figure 25. Angle of attack for zero lift, for camber ratios up to 2 or 3%, as a function of the location of camber along the section chord.

Design C_{Li} . The maximum camber, f , of NACA 1 and 6 series airfoils is generally given in terms of C_{Li} , the design C_{Li} , and can be found from the equation

$$f/c \% = 5.515 C_{Li} \quad (18a)$$

From equations 18, 18a the angle for zero lift is

$$\alpha = -6.34 C_{Li} \quad (18b)$$

- (35) Airfoils tested in DVL High-Speed Tunnel:
 - a) Göthert, In High-Speed Tunnel, ZWB FB 1490.
 - b) Göthert, Symmetrical Sections, ZWB FB 1505/06.
 - c) Göthert, Cambered Sections, ZWB FB 1910 (6 Vol).
- (36) Airfoil sections reported by British ARC:
 - a) Jones, 0015 and 0030 in CAT, RM 2584 (1952).
 - b) Hilton, 18 Sections High Speed, RM 2058 (1942).
 - c) Williams, Strut Sections, RM 2457 (1951).
 - d) See also references (5) (6) (7,c) (28,c) (40,b).
 - e) ARC, Investigations in the Compressed Air Tunnel, RM 1627 (R'number), 1635 (RAF-34), 1717 (RAF-69-89), 1771 (airscrew sections), 1772 (RAF-34), 1870 (Joukowsky), 1898 (23012), 2151 (23012 wing), 2301 (circular-arc backs), 2584 (0015 — 0030).
 - f) Pankhurst, Aerofoil Catalogue, ARC RM 3311 (1963).
- (37) Modifications of the NACA 4-digit series:
 - a) A modification as to thickness location is presented by Stack, "Tests at High Speed", NACA TR 492 (1934); also found in TR 610.
 - b) Elimination of cusped contour, . . . Loftin, "A" Series, NACA TR 903 (1948); also TN 1591 & 1945.
- (38) Foil sections tested in two dimensions by NACA:
 - a) Doenhoff, Low-Turbulence Press Tunnel, TR 1283.
 - b) Abbott & von Doenhoff, Collection, TR 824 (1945); also "Wing-Section Theory", McGraw Hill 1949.
 - c) Loftin, At Very High R'Numbers, TN 1945 (1949) & Rpt 964 (1950); also RM L8L09 with 34 sections.
 - d) See also reports in reference (37,b).
 - e) Loftin, Modified 64-010 Section, TN 3244 (1954).
 - f) McCullough, 0006/7/8 in Tunnel, TN 3524 (1955).
 - g) 64-X10 Sections, TN 2753,2824,1945,3871; R 824,903.

PRESSURE DISTRIBUTIONS are shown in figure 26, for one and the same lift coefficient, one around a straight, and the other for a cambered foil section. The sharp suction peak found at and above the leading edge of the symmetrical section, is avoided by cambering the edge into the oncoming flow. Doing this (between 1910 and 1920, or so) simple imagination was applied, with the idea of helping the flow to get around the edge (from the lower to the upper side). Meanwhile, it has been discovered that under certain conditions, suction peaks do as follows:

they prevent laminar separation, making the B'layer turbulent; they do not necessarily cause cavitation in hydrofoils; they may even be desirable at higher sub-sonic speeds.

Nevertheless, some small amount of camber, say $f/c = (1 \text{ or } 2)\%$ can successfully be used in the design of wings.

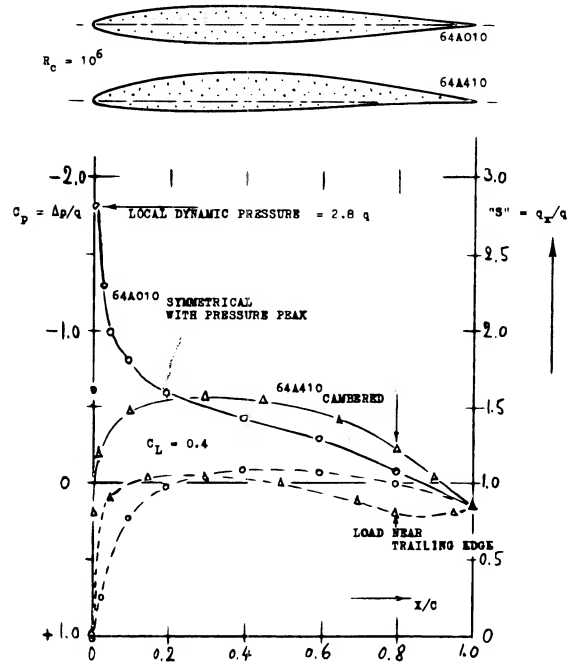


Figure 26. The pressure distribution of a properly cambered, in comparison to that of a symmetrical airfoil section (53,e).

SYMMETRICAL FLOW. Pursuing the original idea of camber, it is possible to "optimize" the shape for a certain lift coefficient by giving the section such a camber that the flow passes smoothly along both sides of the leading edge, without going around that edge. We will call this condition "symmetrical", that is in regard to the local flow past the leading point of the camber line. For circular-arc camber (at 50% of the chord) the sym-

metrical lift coefficient is expected to be as in equation (17) so that

$$C_{L_{sym}} = 4\pi f/c = 0.126 (f/c)\% \quad (19)$$

For camber positions between 30 and 40% of the chord, camber required to make the leading-edge flow symmetrical, must be expected to be slightly smaller than corresponding to this equation. However, in wings with finite span, stream curvature reduces the effective camber by

$$\Delta(f/c) = -(0.25/\pi) C_L/A \quad (20)$$

For practical purposes (with A in the order of 6) the "symmetrical" lift coefficient for commonly used foil sections, is therefore, approximately

$$C_{L_{sym}} = 0.115 (f/c)\% \quad (21)$$

This function is confirmed in figure 27, by results obtained from pressure-distribution tests. Selecting the center of the "bucket" formed by their drag coefficient, "symmetrical" lift coefficients can also be obtained for laminar-type foil sections (21).

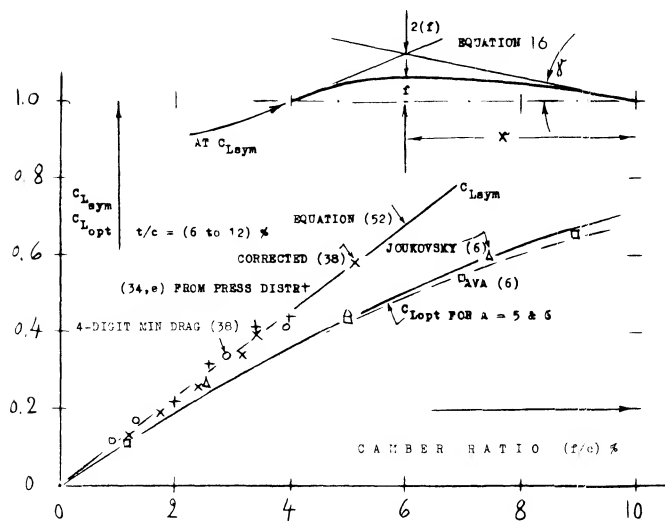


Figure 27. Symmetrical and optimum lift coefficients as a function of camber, for airfoil sections with t/c between 6 and 12%.

OPTIMUM LIFT coefficients are meant to indicate a minimum of the section-drag coefficient. In "ordinary" foil sections such minimum is not very well defined. Figure 27 leaves no doubt, however, that the optimum are lower than the symmetrical coefficients. As camber is increased, $C_{L_{opt}}$ more and more deviates from and below the straight line as for symmetrical flow (equation 52). A sufficient amount of camber is thus found to reduce the viscous or sectional component of drag, that is at and around a certain lift coefficient (such as $C_L = 0.3$ or 0.4 , at which an airplane may cruise from New York to Europe).

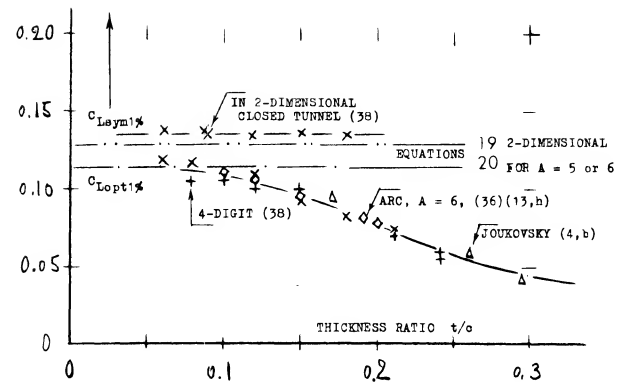


Figure 28. Symmetrical and optimum lift coefficients per percent of camber (for camber ratios up to 2 or 3%) as a function of thickness ratio.

THICKNESS RATIO. Figure 28 shows the value of the optimum lift coefficient per 1% camber, as a function of the thickness ratio. It is seen that $C_{L_{opt}}$ as determined on the basis of section-drag readings, reduces considerably at higher thickness ratios. This result can be explained by the fact that in cambered sections, the weakest part of the boundary layer is near the trailing edge (where the layer is heavy and the pressure gradient positive, thus favoring separation). As a consequence, minimum section drag (and possibly a symmetrical flow pattern) is obtained at lift coefficients smaller than theoretically expected.

"LAMINAR" FOIL SECTIONS are discussed in Chapter VI of "Fluid-Dynamic Drag". Among the shapes under (d) in section (A), the '64' series (with maximum thickness at 38% of the chord) represents a tentatively effective, yet conservative type of laminar-flow sections. To really obtain the benefit of a section drag coefficient as low as 0.004 (which is half of that of a 4-digit section) certain requirements have to be observed. (a) A minimum thickness (say $t/c = 10\%$) is needed to maintain a favorable pressure gradient. (b) The surface has to be kept as smooth as possible. (c) The low-drag "bucket" should be around the cruising lift coefficient. — When giving a '64' section the optimum or the symmetrical camber, the "bucket" moves from zero lift to the design lift coefficient, without losing any or much of its size. For example, the 64-210 section (38,b) is found to have a low drag coefficient at C_L between 0.1 and 0.3. The $\Delta C_L = 0.2$ is almost doubled (that is, to 0.4) when using $t/c = 12\%$, even at a design lift coefficient $C_{Li} = 0.4$, as in 64-412.

4. LOW REYNOLDS NUMBER

The operating Reynolds number is very low for model aircraft wings, birds, bugs and other devices such as wings and propellers used on high altitude remote piloted vehicles. Typical values have been listed (41,c) as

Butterfly Wing	R = 7,000
Small model airplane	R = 20,000
Large model airplane	R = 200,000
Albatross	R = 200,000
RPV Propeller blade chord	R = 60,000 to 200,000

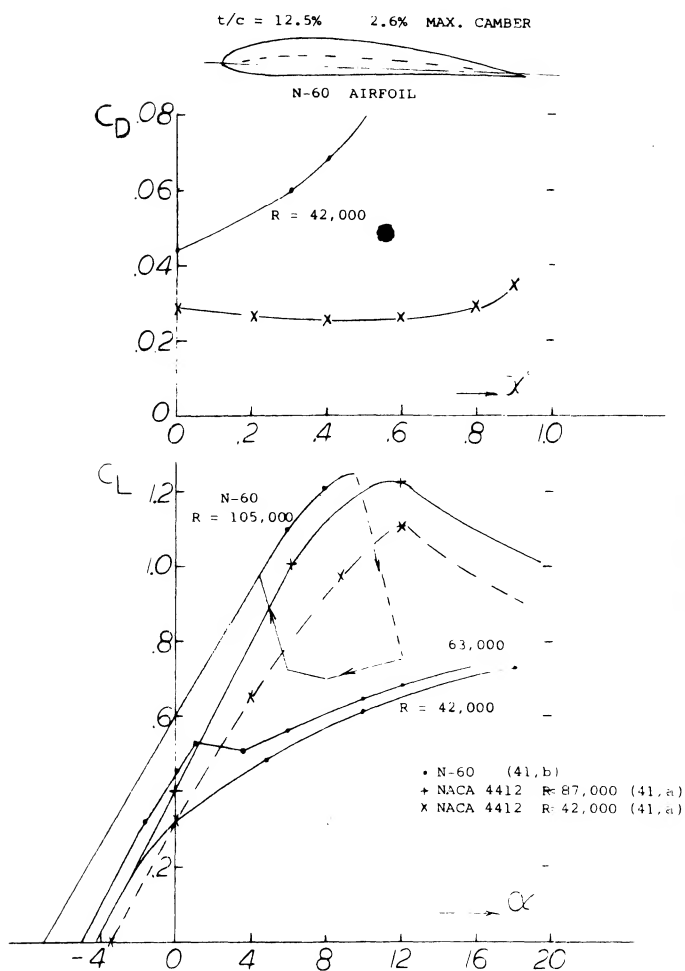


Figure 29. Lift comparison at low Reynolds number, low and high turbulence tunnels.

(39) Airfoil sections, function of Reynolds number:

- Jacobs, Tested in VDT, NACA T Rpt 586 (1937).
- Relf, In the British CAT, ARC RM 1706 (1936).
- See results in references (32,a) (38,c).
- Jacobs, Thick Sections in VDT, T Rpt 391 (1931).
- Pinkerton, 4412 Press Distribution, NACA TR 613.
- AVA Göttingen, Ergebnisse III (1920) p 58.

Turbulence Effects. Airfoil test data at low Reynolds number is limited to that obtained by early investigators and for use in conjunction with model airplanes. The systematic airfoil investigations run in the highly turbulent VDT (41,a) are considered to be questionable because of the effect of turbulence on the boundary layer. Compared to the data of (41,a) the low Reynolds number data of (41,b) run in a low turbulence tunnel show at $R < 100,000$ higher levels of drag, lower values of $C_{L_{max}}$ and a lift hysteresis after stall, as illustrated on figure 29. The reduction of drag obtained at $R < 1.0^5$ was anticipated by the work of (41,b).

Thickness Ratio and Camber. For the best performance at low Reynolds numbers the thickness ratio should be low and camber high, whereas at $R > 1.0^5$ the higher thickness distribution of a Clark Y or similar airfoil gives better performance, figure 30. This may explain the type of wing section found in nature and the shape preferred by the early investigators. Airfoils with high thickness ratios have much lower values of $C_{L_{\alpha}}$ as shown on figure 31. Here, increasing the thickness ratio from 12 to 20% reduced $C_{L_{\alpha}}$ by one-half. The test in the VDT indicated that large gains can be made by making the flow turbulent. A wire in front of the airfoil can be expected to give the desired flow at low Reynolds numbers.

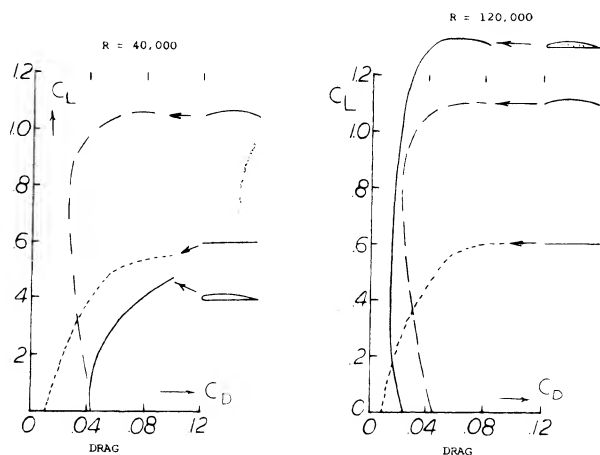


Figure 30. Lift-drag characteristics of thin sections at low turbulence and Reynolds number.

(40) Airfoil Development Theory

- Ayers, Supercritical Aerodynamics, A & A Aug 1972.
- Stevens Math Model for Two dimensional Multi-Component Airfoils, NASA CR-1843, 1971.

(41) Low Reynolds number data

- Jacobs, Airfoil Section Characteristics, NACA 586.
- Schmitz, Aerodynamics of the Model Airplane, Part 1, Airfoil Measurements, N70-39001.
- Jones, R.T., Behavior of Airfoils at Low Reynolds Numbers, Unpublished.

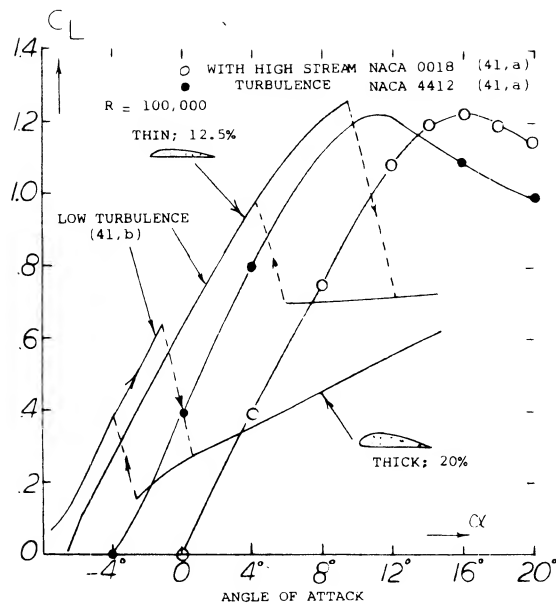


Figure 31. Lift at $R = 100,000$ for high and low turbulence at $t/c - 12$ to 20% .

5. CHARACTERISTICS OF SPECIFIC AIRFOILS

The generalized characteristics and parametric analysis of airfoils given above is suitable for initial studies of configurations and developing an overall understanding. For specific applications the characteristics of the specific airfoil to be used are needed operating at Reynolds and Mach numbers as near the actual condition as possible. While there have been great strides in the development and use of airfoil theory with high speed computer (40,a,b), actual test results are still preferred for final analysis. The use of the computer has resulted in a new series of airfoils which give important improvements in performance for wings, rotors and any other air-moving device. Since the lift characteristics of two dimensional airfoils are necessary for design of all types of wings the characteristics of specific airfoils and specialized operating conditions will be considered in this section considering only two dimensional airfoil characteristics eliminates the three dimensional characteristics which are covered in the chapters on the various wing types.

(42) High Lift, Low Drag Airfoils

- Wortmann, The Quest for High Lift, AIAA 74-1018.
- Nash-Webber, Motorless Flight Research, NASA CR-2315.
- Althaus, Stuttgarter Profilkatalog I, U of Stuttgart 1972.
- Liebeck, Airfoils for High Lift, J of A/C Oct 1973.
- Hicks, Optimizing Low-Speed Airfoils, NASA TM X-3213

(43) High Performance Airfoils for General Aviation

- McGhee, Characteristics of a 17% Airfoil, NASA TND-7428.
- Wentz, Fowler Flap System, NASA CR-2443.

FLUID DYNAMIC LIFT

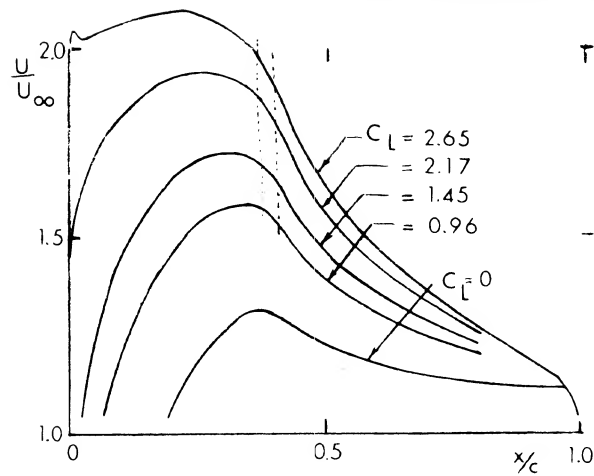


Figure 32. Relative velocity distribution for an airfoil designed high C_{Lx} (FX 74-CL 5 - 140). Dotted lines enclosed observed length of laminar separation bubble.

Concave Pressure Distribution. Since the development of the laminar airfoil sections (38,b) a need for higher critical Mach number, improved C_{Lx} and lower drag has existed. To satisfy this need new airfoils have been developed by a number of investigators including Whitcomb, Wortman, Liebeck and others (42). In the development of these airfoils, theoretical methods were used to obtain the pressure distribution as well as the prediction of separation of turbulent boundary layer. As discussed in (42,a) the maximum lift is determined by the interaction of the upper surface pressure distribution and the boundary layer. A turbulent boundary layer is needed to obtain the necessary pressure recovery. This is achieved by a concave pressure distribution with a more or less flat forward part, as illustrated on figure 32. The lift characteristics of such an airfoil illustrated in figure 33 show $C_{Lx} = 2.38$ and $L/D_x = 140$ and a $C_L^{1/5}/C_D$ of 200 at $R = 10^6$. The L/D for the "concave" pressure airfoils are compared with the 6 series on figure 34 as a function of Reynolds number and prove the value of the design approach.

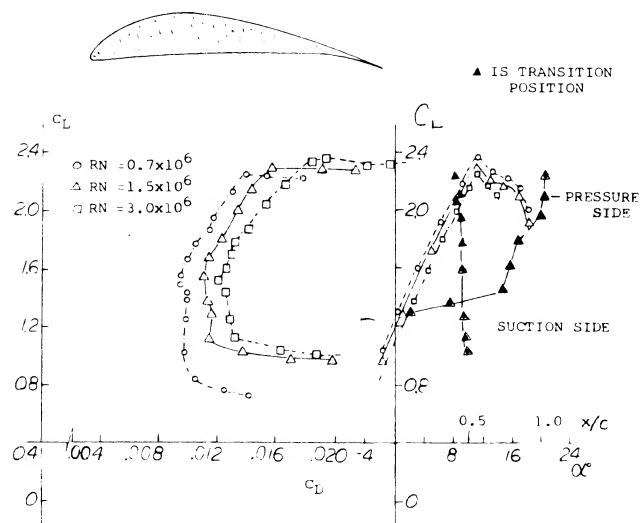


Figure 33. Drag polar of FX 74-CL5-140 for Reynolds number 1.0, 1.5 and 3.0 (10^6).

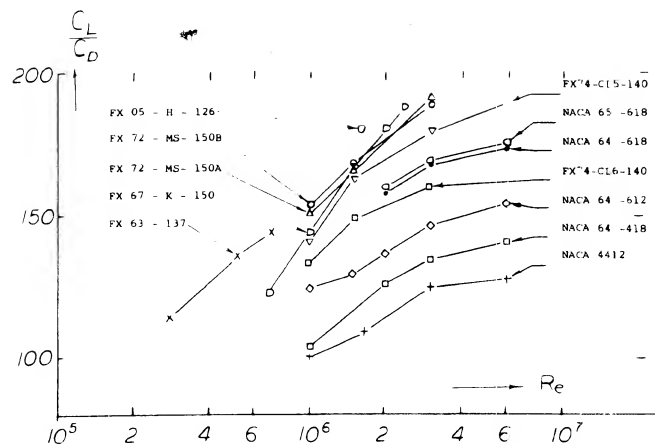


Figure 34. Lift-drag ratio comparisons for NACA 6 and 4 digit airfoils with high performance FX airfoils.

General Aviation – Airfoils. Airfoils suitable for general aviation aircraft should have a gentle stall characteristic, low drag and fairly high thickness ratios for an improved structure and thus a reduction of wing weight. Based on the general design concepts for low drag supercritical airfoils, a new airfoil was designed using the computer study of (40,a,b) and wind tunnel tests (43,a). The test data of the NASA GA(W)-1, Whitcomb airfoil indicated important improvements of the drag and $C_{L\alpha}$ characteristics, figure 35, thus validating the theoretical approach. The application of this airfoil with flaps (43,b) shows that a maximum lift coefficient of 3.8 can be achieved with a 30% chord Fowler flap, no leading edge devices and no blowing.

The GA(W)-1 airfoil tested with a flat under surface (43,b) resulted in a loss of $C_{L\alpha}$ and with an increase of drag, and illustrates the importance of the cusp on the overall design. Reduction of the lift curve slope illustrated on figure 36 was corrected by vortex generators. Although the drag was also reduced at the higher lift coefficients, the L/D_{α} was not improved.

SURFACE ROUGHNESS. As stated in (38,b) "dust particles adhering to the 'oil' left on airfoil surfaces by fingerprints may be expected to cause transition" on laminar-type sections. In realistic operation of engine-powered airplanes, there is plenty of grease, scratches, dust, insects, corrosion of metal and/or erosion of painted surfaces, to precipitate turbulent boundary-layer flow. To account for these possibilities, it is a standard wind-tunnel procedure in (38) to investigate foil sections, and in particular the laminar-type sections, not only in a perfectly smooth condition, but also with a turbulence stimulating strip of carborundum grains (0.01 inch size) spread on both sides over the first 8% of the wing chord (which is $c = 24$ inches). The consequences of applying this type of roughness, at $R_N = 6(10)^6$, are primarily:

- a reduction of maximum lift, say by 20%,
- a reduction of the lift-curve slope by a few %,
- elimination of the laminar low-drag "bucket".

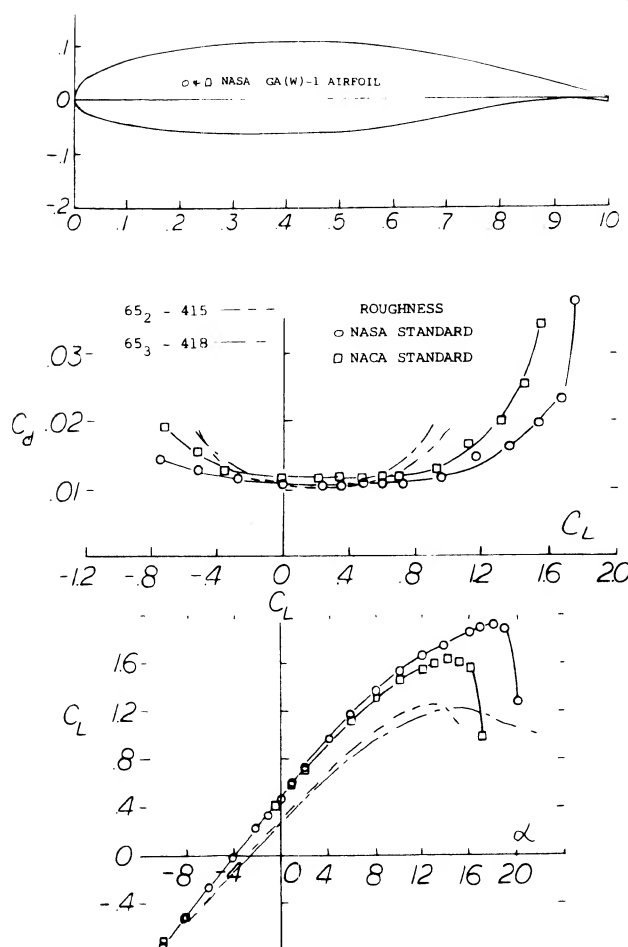


Figure 35. Thick airfoils of the Whitcomb type for General Aviation, GA(W)-1 and corresponding NACA 6 series.

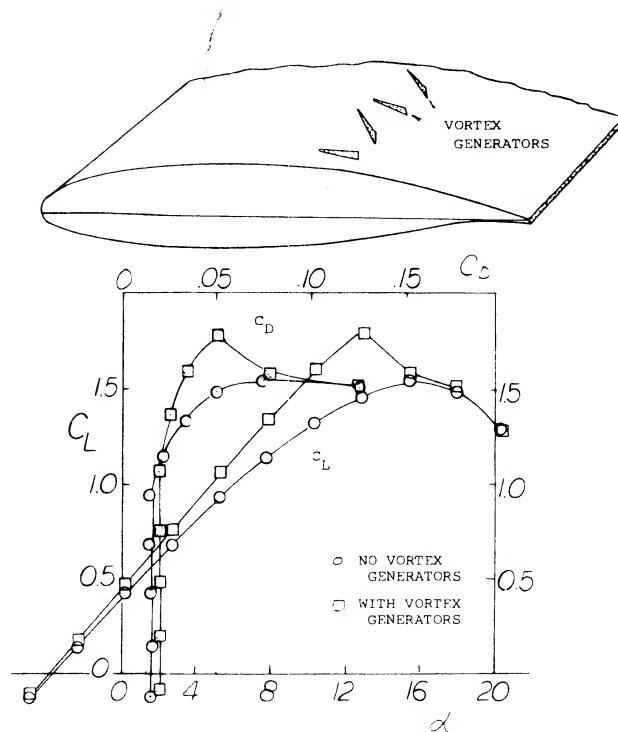


Figure 36. Effect of vortex generators on the performance of the GA(W)-1 airfoil.

SAILPLANES. As pointed out in (48,a) design conditions for the wing of a sailplane are different from those for a powered aircraft: (a) The aspect ratio is "very" high, in the order of 20 or 25, for glide performance. (b) The Reynolds number is comparatively low, between 1(10) when circling (around 50 mph, at $C = 0.8$) and 2(10) when cruising (at $V = 100$ mph, and $C = 0.2$), (c) Absence of engine vibration and noise. — These three considerations call for, and make possible, the use of comparatively thick and cambered laminar-type airfoil sections. A large selection of airfoils suitable for sailplanes is given in (42,a,c). The characteristics of a typical high performance airfoil is on figure 33.

CASCADES: In those applications such as propellers and axial flow compressors, the airfoils effectively follow one another and so operate as a cascade, figure 37. The function of the cascade of airfoils is to create a pressure rise. If the cascade is operating between walls where the axial velocity does not change the pressure rise is developed as a result of the turning of the flow by the cascade. When the spacing between the airfoils is large compared to the airfoil chord, low solidity, and the sections are between walls the lift and drag characteristics approach that of the two dimensional airfoil. When the solidity is high however there is a interaction between the airfoil sections and the overall characteristics of the sections change. Cascade airfoil tests are conducted to determine the performance of the sections as a function of stagger angle, solidity and airfoil type. Because of the limited scope of the cascade airfoil data it is desirable to determine corrections for the application of two dimensional airfoil data to cascade conditions.

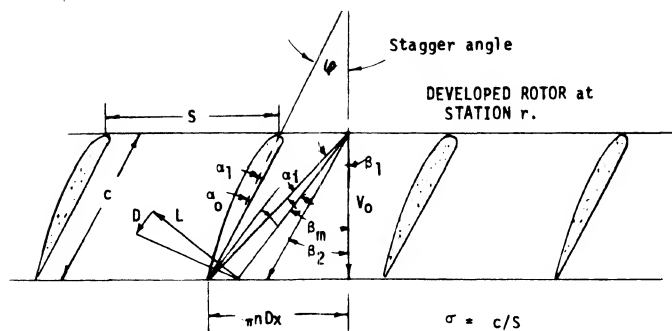


Figure 37. Cascade airfoils and velocity triangle.

Airfoil data is applied in the design of propellers by determining the angle required to correct the three dimensional conditions of the propeller to the two dimensional flow conditions of the airfoil (49e). These angle corrections account for the loading, the blade number, operating condition and span condition including tip effects. In the case of a rotor operating between walls the angle correction for applying two dimensional airfoil data can be determined from the equation

$$\sigma C_L = 2 \cos(\beta_i - \alpha_i) (\tan \beta_i - \tan(\beta_i - 2\alpha_i)) \quad (22)$$

where σ = the blade solidity = $cB/\pi x D = c/s$

C_L = operating lift coefficient - 2/d

ψ = inlet stagger angle

α_i = induced angle of attack

The two dimensional angle of attack is found from the equation

$$\alpha = \beta_i - \psi - \alpha_i$$

Here α_i is the angle between the rotor blade chord line and the inlet vector, figure 37. In the application of the above equations the lift and drag coefficients are determined from the two dimensional airfoil data at the angle of attack of α . The lift and drag is calculated from these coefficients using the mean velocity vector W to find the dynamic pressure. Good agreement between the cascade test data and σC_L calculated with equation 22 is obtained for all section cambers and stagger angles up to camber solidities of 1.5

The cascade data (49,f) indicates the lift curve slope decreases with increasing solidity and inlet angle. Based on these data the slope of the lift curve of the two dimensional airfoil, m , becomes, m' , when operating in a cascade and is found from the equation

$$m' = m(1 + \sigma(.00645\beta_i - .2352 - .3121\sigma + .05859\sigma^2))$$

(44) Results on practical-construction airfoils:

- a) Tetervin, Helicopter Blades, NACA W Rpt L-643.
- b) Doetsch, Waviness 23012, Ybk D Lufo 1939 p 1-88.
- c) NACA, TN 428 (fabric), 457 (irregularities), 461 (rivet heads), 724 (rib stitching); 1932.
- d) Quinn, Practical Construction, NACA T Rpt 910.

(45) Mechanism of, and penalties due to icing:

- a) Gelder, Droplet Impingement, NACA TN 3839.
- b) Bosoden, Aerodyn Characteristics, NACA TN 3564.
- c) Gray, Penalties (Summary), NASA TN D-2166 (1964).

(46) At negative angles (negative camber):

- a) NACA, In Variable Density Tunnel, TN 397 & 412.
- b) AVA Göttingen, Ergebnisse III (1927) p 78, 79.
- c) Williams, RAF-34 in CAT, ARC RM 1772 (1937).

(47) NACA "H" sections, for helicopter blades:

- a) Stivers, Several Sections, W'Rpt L-29 (1946).
- b) Schaefer, Between 9 and 15% Thick, TN 1922 (1949).
- c) Stivers, 8-H-12 Section, TN 1998 (1949).

(48) "Laminar" airfoils for sailplanes:

- a) Carmichael, Thick Foils, "Soaring" 1958 (Nov/Dec).
- b) Wortman, Laminar Profiles, ZFW 1957 (May).

(49) Cascades of foils, vanes, blades:

- a) Kröber, Ingenieur Archiv 1932 p 516.
- b) Patterson, Duct Corners, ARC RM 1773 (1936).
- c) ARC, Tests, RM 1768; Analysis, RM 2095 & 2920.

(49) Cascades of foils, vanes, blades, propellers

- e) Borst, High and Intermediate Solidity Fans, NASA CR 3063.
- f) Emery, et al, Cascade tests NACA 65 sections, NACA TN 1368.

6. PITCHING-MOMENT CHARACTERISTICS

The center of lift of a thin and straight foil section is theoretically at 25% of the chord. Actually, the boundary layer changes this condition somewhat and as soon as there is camber involved, the mechanism of longitudinal moment is different altogether.

CENTER OF LIFT. The longitudinal or pitching moment is designated to be positive when it tends to increase the angle of attack. The moment is generally made up of two components:

$$C_{m_s} = M/qSc = C_{m_0} + C_L(dC_{m_s}/dC_L) \quad (22)$$

where the dots ($\dot{}$) indicate that the reference point is at the leading edge. The quotient C_m/C_L indicates the “center of pressure”, id est the point along the section chord at which the resultant lift force is acting. The derivative

$$dC_m/dC_L = x/c \quad (23)$$

indicates the "aerodynamic center" of the foil section. When taking the moment about this point, the coefficient $C_{m_{ac}}$ is equal to C_{m_o} and constant (within the operational range of the lift coefficient). To demonstrate what equation (22) means in terms of foil and force geometry, *figure 39* was prepared, showing location and direction of total forces (composed of lift and drag) of one particular cambered section. We see that the location of the resultant force is far back on the wing chord at lift coefficients below 0.1. This tendency corresponds to $C_{m_o} = -0.04$ of the section used. The force then moves forward along the chord, as the lift coefficient is increased, approaching the "aerodynamic center" corresponding to dC_m/dC_L . The displays in part (A) of *figure 39* has a practical advantage (and it was used in the early years of airplane and/or biplane design for that reason). There is a particular point (or a narrow region) below the foil section where most of the force lines shown, meet and cross each other. When placing the CG of an airplane in that point, wing moments are near zero over most of its speed range (except for very high speeds where the moment corresponding to C_{m_o} predominates). Modern analysis of longitudinal stability and control is based upon equation (22) however.

ZERO-LIFT MOMENT. For positive amounts of camber, the component C_{m0} (in equation 22) is always negative. This means that the bent-down trailing edge tries to lift that edge up, in a manner similar to that of a wing- or control flap. The value of C_{m0} increases in proportion to the camber ratio (f/c); and *figure 30* shows how the coefficient per 1% of camber, varies as a function of camber position. Tested values do not agree with the theoretical functions. The deviation increases, as the thickness ratio is increased above some 12%. Results in the graph are not very consistent. After ruling out theoretical functions and the VDT data, one may say, however, that the most widely used foil sections have a zero-lift moment roughly corresponding to

$$C_{m0} = (0.05 \text{ to } 0.06) (x/c) (f/c)\% \quad (24)$$

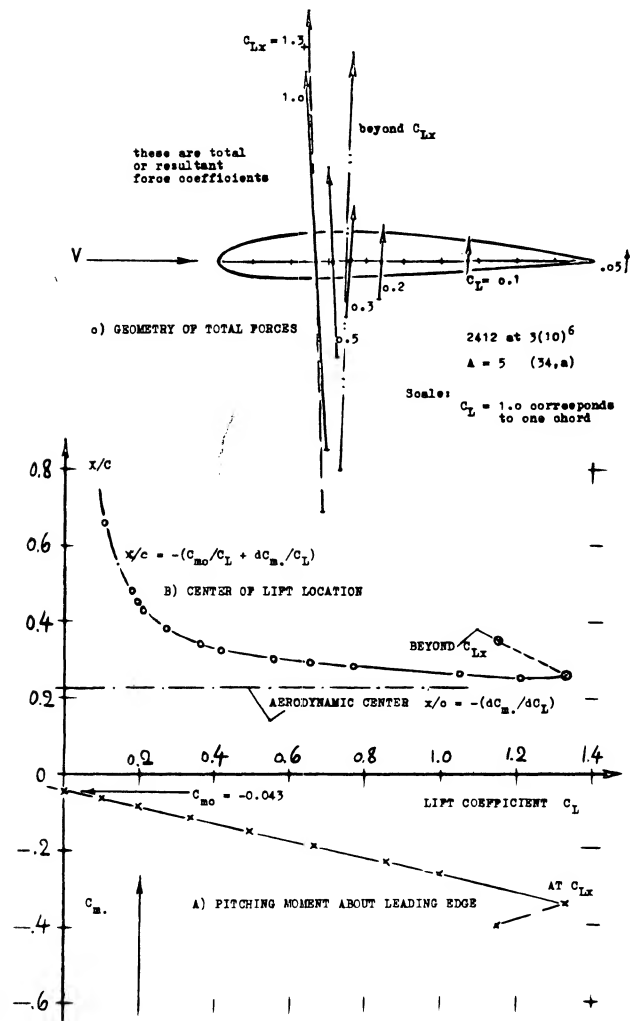


Figure 39. Geometry of resultant forces, and pitching moment of a particular cambered foil section (34,a) as a function of lift coefficient.

REFLEXED CAMBER. Any pitching moment at zero lift is undesirable because it produces structural strain in, and elastic twisting of the wings of an airplane when diving (or when at maximum speed). To reduce the value of C_{m0} , reflexed camber lines were thus investigated (8). The idea was, to camber the section nose into the oncoming flow, while at the same time a bent-up trailing edge would compensate for that camber, thus reducing the pitching moment to "nothing". Experiments in various places confirmed that the moment was reduced as desired. The trailing edge is very important, however, in producing circulation. As a consequence, higher angles of attack (measured against the chord line) are required to obtain a certain lift coefficient, when bending the trailing edge up. In short, the sections developed, were not very efficient as to (L/D) and maximum lift. A better solution was found in the 23012 type sections (33) where most of the mean line is straight, while camber is concentrated near the leading edge (around 15% of the chord, see figure 8). Figure 40 proves that C_{m0} is reduced to roughly half of what it is in other sections having the same location of camber, and to a small fraction of that in "conventional" sections.

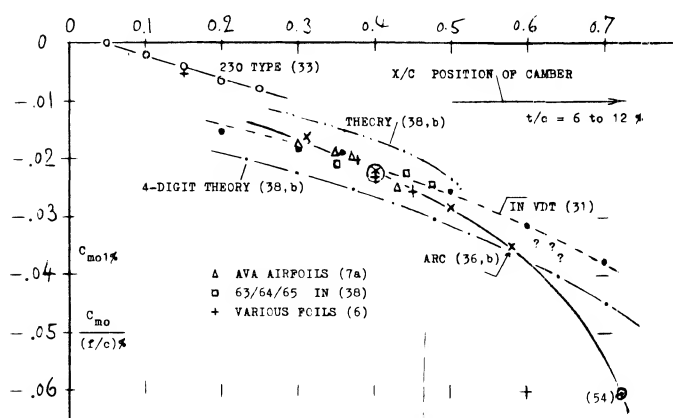


Figure 40. Pitching moment at zero lift caused by camber, as function of camber location.

- (50) Pitching moment of control surface sections:
- Lockwood, Bevelled Edge, NACA W'Rpt L-666.
 - Influence of control gaps, see (a) & NACA TR 868.
 - Trailing edge, NACA TN 1296 & 3174; T'Rpt 803.
 - Regarding shape, . . . ARC RM 2008,2184,2256,2506.
- (52) See for example, and in particular (38,b).

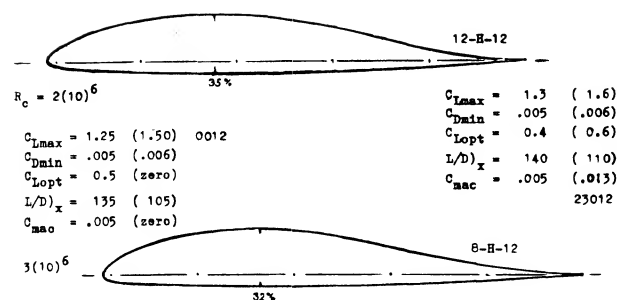


Figure 41. Shape and performance data of two reflexed foil sections, specifically designed (47) for helicopter blades.

HELICOPTER BLADES. Reflexed sections (without twisting moments) are of interest in the design of rotor blades. A series of 6 such sections varying in thickness and camber, are described in (47). Shape and characteristics of two of them are shown in figure 41. Both of them are "better" than the 0012 or 23012 sections, data for which are listed in parentheses, "for most of the flight conditions" of the helicopter considered. The fact that lift = f (angle) is not exactly linear, is the consequence of the tail shape and of the drag coefficient varying around C_{Lopt} . As intended, the pitching moment is small, taken around the aerodynamic center. The reflexion is around 80% of the chord. Camber (near 1/3 of the chord) is between 3 and 4%. The aerodynamic center is 1% or 2% more aft than in conventional sections; more lift is produced around the leading edge.

AERODYNAMIC CENTER. In symmetrical sections, the due-to-lift component in the second term of equation (22) is expected to be all of the pitching moment. This moment is equal to lift times moment arm x . In a cambered section, the derivative dC_{m0}/dC_L (always negative) indicates the "aerodynamic center", id est the point about which $C_m = C_{m0} = \text{constant}$; thus :

$$x/c = -dC_{m0}/dC_L \quad (25)$$

where x = distance (considered to be positive) behind the leading edge. The aerodynamic center is usually evaluated (53,a) from wind-tunnel tests, and tabulated for the many foil shapes investigated. Another point about which the pitching moment can be taken, is the aerodynamic center theoretically expected for zero thickness ratio, id est the quarter point of the chord. Since this point is not necessarily the aerodynamic center, there usually remains a derivative, and the differential of the location is

$$\Delta x/c = -dC_{m/4}/dC_L \quad (26)$$

where the '4' indicates the quarter-chord point. Since the aerodynamic center is at that point only by coincidence, we prefer to define the pitching moment about the leading edge. This type of moment is

$$dC_{m0}/dC_L = (dC_{m/4}/dC_L) - 0.25 \quad (27)$$

IN OPEN WIND TUNNELS:
 × ARC, 2 SOURCES (36)
 + DVL, 3 SOURCES IN (6)
 Δ NACA, F'SCALE TU (32)
 / OPEN, W' A=6 (28,h)

IN CLOSED WIND TUNNELS:
 • NACA, V'DENSI TU (31)
 ○ 4-DIGIT, 2-DIM'L (38)
 † 63/64 MODIFIED A (37)

CUSPED (CLOSED) JOUKOVSKY
 ~ 63/64 2-DIM'L (38)
 □ AVA, JOUKOVSKY (4,b)

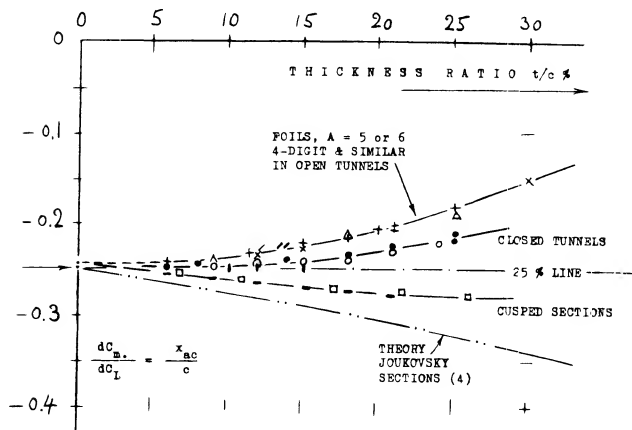


Figure 42. Pitching moment due to lift, indicating the aerodynamic center (or the neutral point) as a function of thickness ratio.

SECTION THICKNESS. Theory expects the distance x in equation (25) to grow with the section thickness ratio. However, as shown in figure 32, the aerodynamic center is in reality, usually somewhat ahead of 25%; and it does not move downstream as the thickness ratio is increased. As a consequence of momentum losses in the boundary layer, at the suction side, near the trailing edge, a high angle of attack is obviously required to obtain a certain lift coefficient. The deficient amount of lift is then produced near the leading edge, so that a positive differential of the pitching moment is obtained. Through the same mechanism, we must also expect that the aerodynamic center will be shifted further ahead when increasing skin friction (section drag coefficient) through surface roughness.

TRAILING WEDGE ANGLE. It is pointed out in section (b) of this chapter, how much shape and thickness of the trailing edge affects the lift-curve slope. The same and an even more pronounced influence is found in regard to the pitching moment:

(a) On the basis of investigations in (53,c) it can be said:

$$\Delta(dC_m/dC_L) = + 0.004 \varepsilon^\circ = + 0.23 \tan \varepsilon \quad (60)$$

where $\varepsilon = 1/2$ trailing-wedge angle.

(b) It can be concluded that

$$\Delta(dC_{m0}) \approx + 2(\tan \varepsilon)(\tan \gamma) \approx 8(\tan \varepsilon)(f/c) \quad (61)$$

where γ as in figure 27.

BEVELED TRAILING EDGE. Several modifications of a control flap forming the trailing edge of a foil section are illustrated in figure 43. It is seen in particular, that the aerodynamic center (represented by dC_m/dC_L) moves forward, when beveling the edge. Note that $dC_L/d\alpha$ is reduced at the same time. The effect of beveling is, of course, a function not only of the bevel angle but also of the length of the beveled (chamfered) portion of the chord. Expressing this length by the "thickness" of the edge as defined in figure 44, a very good correlation (50,a) is obtained of experimental results.

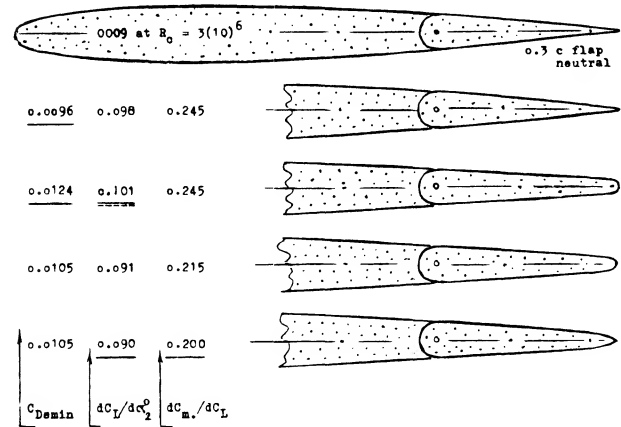


Figure 43. Influence of trailing-edge modifications (50,a), upon the pitching moment of an 0009 section.

VERTICAL POSITION OF THE AC. As pointed out before, the aerodynamic center is a point of reference for which $C_m = \text{constant}$. As explained, the location is usually somewhat ahead of 25% of the chord. Figure 45 shows that the point is also somewhat above the section's chord line. In terms of equation (53) this means that the variation of $C_m(C_L)$ is not necessarily a straight line. It is usually possible, however, to find a point somewhat above the chord line for which dC_m/dC_L is constant, at least over the "useful" range of the lift coefficient, id est excluding higher angles of attack, approaching the stall. Consider in this respect the pitching moment including a component due to the tangential force:

$$C_{m0} = C_{m0} - (x/c)C_N + (z/c)C_T \quad (30)$$

(53) Investigation of camber and pitching moment:

- Thompson, Aerody Center, J Aeron Sci 1938 p 138.
- ARC, Determination of C_L and C_m , RM 1914 (1944).
- Purser, Trail-Edge Angle, NACA W Rpt L-664
- McCullough, 4 10% Sections, NACA TN 2177 (1950).
- Stivers, 4 Airfoil Sections, NACA TN 3162.

(54) Loftin, 66-210 Camber, NACA TN 1633.

where C_N = normal-force coefficient (primarily C_L) and C_T = tangential-force coefficient. By differentiating this equation against C_N , and setting the derivative equal to zero, the location of the aerodynamic center 'AC' can be obtained (53). It should be noted that $C_T \approx C_{D_s} - C_L \sin \alpha$. Assuming that the section drag coefficient be constant, the divergence of a tested $C_m(C_L)$ function from a straight line, is found (1,b) to be $\Delta C_m \sim C_L^2$. The height 'z' of the AC above the chord line (measured in the direction normal to the zero lift line) is then approximately

$$z/c = -7 \Delta C_m / C_L^2 \quad (64)$$

where ΔC_m = deviation in the range of small and intermediate lift coefficients.

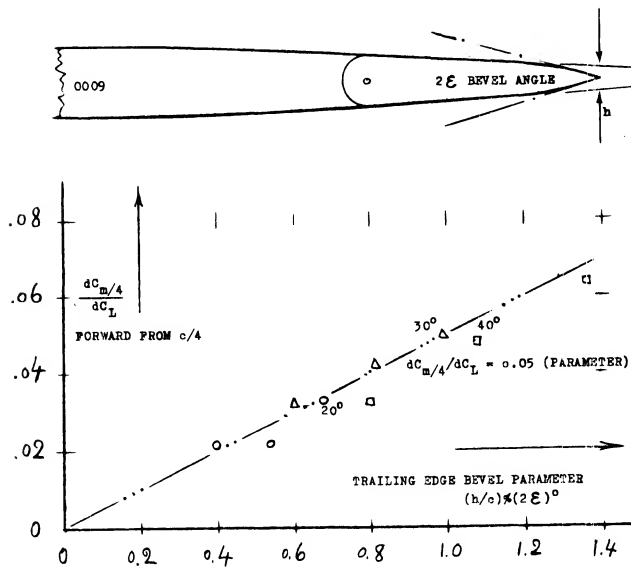


Figure 44. Correlation (50,a) of experimental (dC_m/dC_L) values against a trailing-edge bevel parameter.

THICKNESS RATIO. Since the two-dimensional testing method (38) is the only one yielding negative values for z/c , we are inclined to disregard these results (21). We can then say that according to figure 45, z/c increases with the thickness ratio. The boundary layer developing toward the trailing edge, seems to be responsible for this result. Necessarily, the height 'z' has to change from above to below the chord line in symmetrical sections, between C_L = plus and minus 0.1, or so. The boundary layer accumulation (and/or separation) switches accordingly, as explained before in connection with figures 17 and 18. By comparison, the variation of z/c with the camber ratio f/c , as found in (31) is very small. It should be noted, however, that the 5-digit sections (with $t/c = 12\%$) also listed in (31) exhibit z/c values more than twice as high as those reported for the 4-digit airfoils.

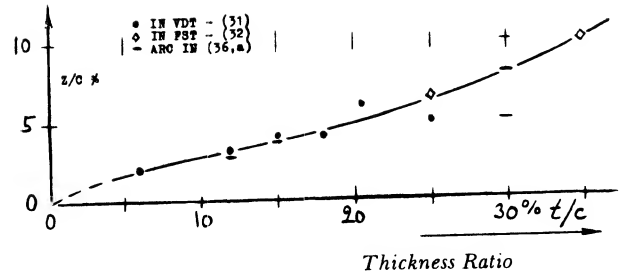


Figure 45. Vertical position of the aerodynamic center for various types of foil sections.

WING ICING and its aerodynamic penalties are reported in (45). Typical conditions are as follows:

- | | |
|---------------------|----------------------|
| (a) icing rate | $h/t = 3 \text{ mm}$ |
| (b) for $h/c = 1\%$ | $\Delta C_D = 0.01$ |
| (c) at $C_L = 0.6$ | $\Delta C_D = 0.02$ |
| loss of lift (c) | $\Delta C_L = -0.1$ |
| pitching moment | $\Delta C_m = 0.02$ |

The rate (a) is per minute of time 't'. As in (b) the ice accumulates "in" the stagnation point of the 0011 section (45,b) at zero angle of attack, to the thickness 'h'. The same can be expected for a cambered section when flying at $C_{L_{sym}}$. In case (c) there is a considerable flow around the leading edge. As a consequence, ice deposits itself not only forward, but also upward of the edge, thus forming a ridge across the high-speed flow of air. The maximum section-drag coefficient thus observed (in climbing flight condition) is in the order of 0.04, the loss of lift corresponds to $\Delta C_L = -0.2$, and the pitch-up moment to $\Delta C_m = +0.04$. The time used in these tests, was in the order of 't' = 10 minutes, the chord of the 0011 airfoil was $c = 2.1 \text{ m}$. With the help of these data, consequences of icing can be estimated for the wing of a real airplane. The combination of insufficient power or thrust, with reduced longitudinal stability can be dangerous.

CHAPTER III — THE LIFT OF STRAIGHT WINGS

Aerodynamic lift is primarily utilized to “lift” airplanes into the air and to keep them aloft. The device which nature has evolved for this purpose (as in birds) and which man has successfully developed to sizes not available in nature, is “the” wing. Lifting characteristics of various shapes of essentially straight wings are treated in this chapter.

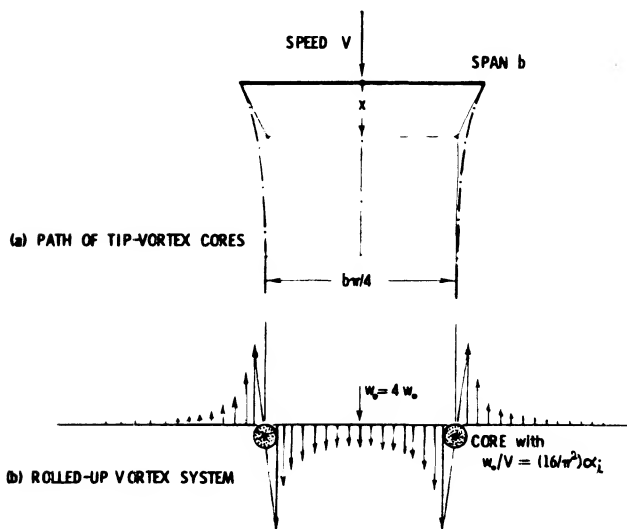


Figure 1. Vortex pattern behind lifting line (2) and/or wings (3).

- (1) Principles and results of lifting-line theory:
 - a) Prandtl's Wing Theory, Nachrichten Königliche Gesellschaft Wissenschaften 1918 p 451, 1919 p 107.
 - b) Glauert, "Elements of Aerofoil and Airscrew Theory", Cambridge University Press, 1926 and 1948.
 - c) Account of Lanchester's work given by Prandtl "Generation of Vortices", Paper RAS London, 1927.
- (2) Analysis of trailing wing vortices:
 - a) Wetmore, Hazard For Aircraft, NASA TN D-1777; also Astronautics/Aeronautics, Dec 1964 p 44.
 - b) Kaden, Roll-Up Analysis, Ing Archiv 1931 p 140.
 - c) McCormick, Vortex Sheet, Penn U A'Engg 1965.
 - d) See AIAA J. 1963 p 1193; Aeron Quart 1965 p 302.
 - e) Mechanism of vortices (cores) by Newman, Aeron Quart 1959 p 149; Schaefer, J. Fluid Mech 1959 p 241.
 - f) Squire, Viscous Analysis, Imp Coll London (1954).

A. APPLIED LIFTING-LINE THEORY

One of the most useful tools in the aerodynamic design of airplanes is the lifting-line wing theory, first published in 1918 (1,a). Practical results and limitations are presented as follows.

VORTEX SHEET (3). As explained in the chapter dealing with the characteristics of "airfoil sections", lift is the result of a "bound vortex" or "lifting line". In wings with finite span, the circulation around this line does not discontinue at the ends or tips. Immediately behind the line, a vortex sheet with a more or less uniform downward velocity 'w' leaves the wing. As a consequence of the pressure difference between lower and upper side of the lifting surface, a certain flow is caused *around* the lateral edges, thus starting a pair of strong trailing vortices. The vortex sheet immediately begins to roll itself up into these vortices; and it eventually passes all of its vorticity into the pair shown in part (b) of figure 1. Note that the sheet also contains the viscous wake (boundary layer) of the wing. The "dead" air rolls "into" the trailing vortices together with the vorticity. It is not correct, however, to assume, that the viscous wake would be sucked into the vortex cores. More information on shape and location of the vortex sheet is given in "longitudinal stability".

TRAILING VORTEX. The structure of a vortex is described in the "general" chapter. The size (diameter) of the viscous core depends upon viscosity and upon the disturbance (separation) of the flow at the edge from which it originates. For example, in chapter VII of "Fluid-Dynamic Drag", the diameter of a core starting from a rounded lateral edge is seen to be $d_c = 0.05c$, where c = chord length of a rectangular wing, with $A = 3$, at $C_L = 0.6$. As reported in (2,c) the diameter is proportional to C_L ; and it is a function of scale (Reynolds number). As measured in flight (at $R_c = 3(10)^6$, and $C_L = 0.75$) the diameter was found to be 10% of the wing-tip chord, while in a wind-tunnel test at $R_c = 2(10)^5$ it was about twice as large. At a distance behind the trailing edge $x = c$, where these tests were performed, the pressure within the viscous core is in the order of $C_p = -1$. The diameter grows with distance. For example, flight tests (3,c) indicate for a wing with $A = 6$, at $C_L = 0.9$, a core diameter $d = 0.2b$, at $x = 25b$.

ROLL-UP. As observed in wind-tunnel tests, the tip vortices start forming at the corner of the leading edge (if there is one, as in rectangular or tapered wings). Theoretically (for elliptical lift distribution across the span) the final distance between the vortex centers is $b_{\chi}/b = \pi/4$. As indicated in (2,b) the distance x as defined in part (a) of figure 1, is

$$x/b = 0.1 A/C_L = 0.1/C_{Lb} \quad (0)$$

where $C_{Lb} = L/qb$. As derived in (16,a) the distance from the lifting line where the roll-up is "completed", is approximately

$$x/b = k/C_{Lb} \quad (1)$$

where $k = 0.4$, for "essentially" rolled-up condition; and $k = 0.9$, indicating that 99% of the vorticity is concentrated in a pair of non-viscous cores. Nominally, the diameter of these cores is $d = b(2/3)$. For example, for $C_L = 1$, and $A = 5$, and $C_{Lb} = 0.2$, the 99% rolled-up distance is $x = 4.5b$, or $x = 22c$. However, at or beyond this distance, dissipation takes over. Nevertheless, as pointed out in (2,a) the vortices generated by a transport plane with $W = 300,000$ lb, and $b = 43$ m, flying at $C_L = 1.2$ (climbing) corresponding to $V = 160$ kts, still persist after more than 2 minutes, at a distance behind the aircraft of 10 km (!). In this manner, such an airplane leaves behind a disturbance with up and down velocities up to plus/minus 3 or 4 m/s. Another airplane, flying into this wake, can then encounter angle-of-attack differentials in the order of plus/minus 2 or 3°, and local lift differentials in the half wings, up to plus/minus 15%. A smaller airplane hitting the center of a vortex, might even be rolled over.

RECTANGULAR WINGS. Most analyses consider elliptical lift distribution. For sharp or square-ended rectangular wings, experimental evidence such as in figure 10, suggests a vortex span in the order of $b_l = 0.9b$. It seems that the lateral edges of such a planform are a continuation of the bound vortex, thus making this shape more effective and efficient than predicted by the "chordless" theory. In fact, when assuming the lateral edges to be end plates (see later) reasonable answers are obtained for induced angle and effective aspect ratio (equation 2).

DOWNWASH. An integral part of the flow pattern behind a lifting wing is a permanent downward deflection (downwash) of the affected stream of air. Lift can thus be understood as the result of that deflection. In wings with an elliptical distribution of lift or load along the span, the affected stream is equal in magnitude (but it is not identical) to that contained in a cylinder having a diameter equal to the wing span 'b'. Considering an airplane in level flight, we may visualize this cylinder as being deflected so that it assumes the downward velocity 'w'. Behind the airplane, the cylinder is thus inclined against the horizontal at the downwash angle $\varepsilon = w/V$, until it finally meets the ground. There, the momentum

imparted by the airplane upon the cylinder of air, is transferred onto the earth in the form of pressure. In this manner, the airplane may thus be considered as being supported from the ground.

INDUCED ANGLE. At the location of wing or lifting line, the average angle of deflection is but one half of that of the assumed cylinder at a sufficiently great distance behind the wing. The angle at the wing is called "induced" (4). The *minimum* of the induced angle is theoretically found for elliptical distribution of the lift over the wing span:

$$\alpha_i = L/q\pi b^2 = C_L/\pi A_i \quad (2)$$

where A_i denotes the effective aspect ratio as explained later. This angle has to be added to that required in two-dimensional flow (as shown in the chapter on "airfoil sections") to develop a certain lift coefficient.

LIFT ANGLE. The lift-curve slope of an airfoil in two-dimensional flow is theoretically $dC_L/d\alpha_2 = 2\pi$. Instead of this slope, it is more convenient, however, in practical applications of lifting-line theory, to use the reciprocal value $d\alpha/dC_L$ which shall be called the "lift angle". Including the induced component, this angle is (in larger aspect ratios)

$$d\alpha/dC_L = 1/(2\tilde{a}\pi) + 1/(\pi A_i) \quad (3)$$

where subscript '2' denotes the angle in 2-dimensional flow. For conventional foil sections in undisturbed flow, the factor ' \tilde{a} ' is in the order of 0.9. Using this value, equation (3) can be written in degrees, roughly as

$$d\alpha/dC_L = 10 + (19/A_i) \approx 10 + (20/A) \quad (4)$$

where '19' and '20' are somewhat larger than the theoretical minimum $(180/\pi^2) = 18.3^\circ$. This equation, representing lifting-line theory, is primarily applicable to wings with short chords, that is, with high aspect ratios $A = b/\bar{c} = b^2/S$, where the average chord $\bar{c} = S/b$. Accordingly, the function is seen in figure 2, adequately describing the lift angle of rectangular and/or moderately tapered wings, with sharp or square lateral edges, up to $1/A = 0.15$, or down to $A = 7$.

"LIFTING SURFACE". A wing is not a "line". The chord has a certain influence upon the magnitude of the lift angle. As explained in the "small-aspect-ratio" chapter, a long chord appears not only in the form of a small ratio, but also in a three-dimensionality of the airfoil section used. On the basis of experimental results (9) in figure 2, the additional lift angle of the section, is

$$\Delta(d\alpha_2^0/dC_L) = 9/A^2 \quad (5)$$

Summing up, the lift angle of efficient wings is

$$d\alpha/dC_L = 10 + (9/A^2) + (20/A) \quad (6)$$

This equation describes rectangular and moderately tapered plain wings with sharp or square lateral edges.

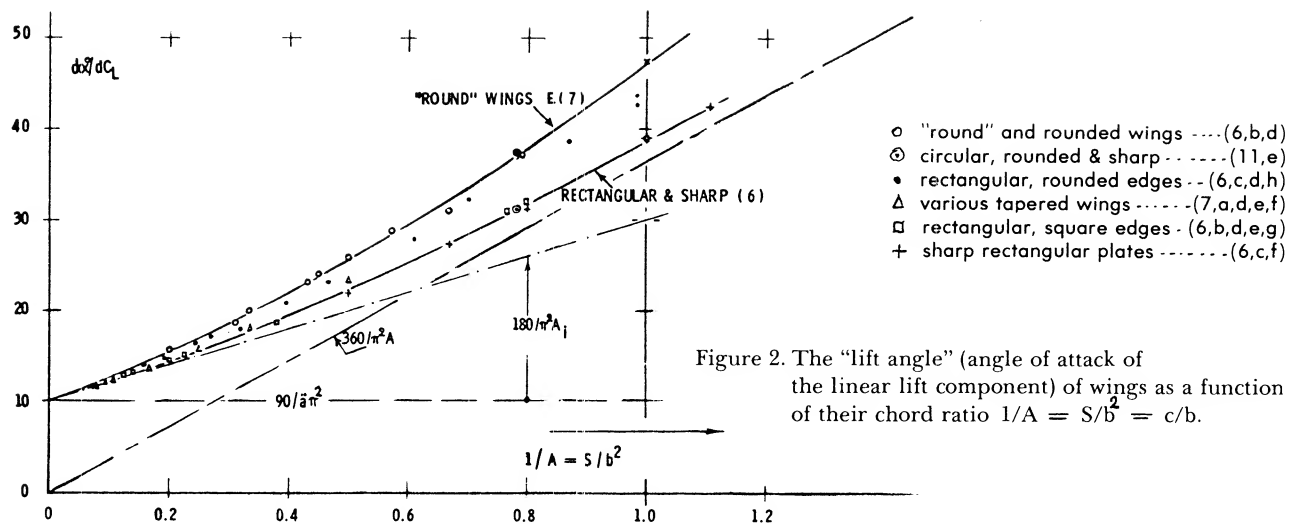


Figure 2. The "lift angle" (angle of attack of the linear lift component) of wings as a function of their chord ratio $1/A = S/b^2 = c/b$.

- (3) Regarding rolling-up trailing wing-tip vortices:
 - a) Bird, Visualization, J Aeron Sci 1952 p 481.
 - b) Hoerner, Tunnel Tests, see (13,a,b,f).
 - c) Kraft, Flight Tests, NACA TN 3377 (1955).
 - d) Shape of vortex sheet behind delta and swept wings, see NACA TN 3175 (1954) & 3720 (1956).
 - e) Vortex Wakes, RAE TN Aero 2649, and ARC CP 79.
 - f) ARC, Flight Tests, CP's 282,489,795 (1954/65).
- (4) The word "induced" refers to an analogy to the magnetic field around a wire carrying electric current. Glauert: "induced velocity at any point corresponds to magnetic force due to current".
- (6) Systematic investigations of rectangular wings:
 - a) Series of Wings, Service Technique No. 83.
 - b) Göttingen, Rectangular, Ergebnisse I, III & IV.
 - c) Winter, Plates and Wings Short Span, Forschung 1935 p 40 & 67; Translation NACA T'Memo 798.
 - d) Zimmerman, Various Shapes, NACA Rpt 431 (1932); also Circular, TN 539 (1935); J A Sci 1935 p 156.
 - e) Higgins, In VD Tunnel, NACA T'Rpt 275 (1927).
 - f) Wadlin, Hydrodynamics of Rectangular Plates, NACA TN 2790, 3079 & 3249, or T'Rpt, 1246 (1955).
 - g) Scholz, Forschung Ing'Wesen 1949/50 p 85.
 - h) Brebner, Various Wings, RAE Rpt 65236 (1965).
 - i) Bussmann, 0015 Wings, ZWB T'Berichte 1944 p 245.
- (7) Lifting characteristics of tapered wings:
 - a) Anderson, Investigation of 22 Tapered Wings, NACA TR 572 & 627 (1936/38); also T'Rpt, 665 (1939).
 - b) Junkers Wind-Tunnel Results, about 1941.
 - c) Truckenbrodt, Delta Wings, ZFW 1956 p 236.
 - d) Allen, 3 Tapered on Fuselage, NACA RM A53C19.
 - e) NACA; $A = 8, 10, 12$, TN 1270 and 1677 (1947/48).
 - f) Wolhart, $A = 2$ to 6, NACA TN 3649 (1956).
 - g) King, Taper Ratio Series, NACA TN 3867 (1956).
- (8) Distribution of lift across the wing span:
 - a) Multhopp, Calculation of Distribution Across Wing Span, Lufo 1938 p 153 (Transl ARC No. 8516).
 - b) DeYoung, Arbitrary Plan Form, NACA Rpt 921.
 - c) Schrenk, Simple Procedure, Luftwissen 1940, p 118; English translation, NACA T'Memo 948.
 - d) Hafer, Improvement of (c), Luftwi 1944 p 12.
 - e) Laporte, Examination of (c), J A Sci 1955 p 787.
- (9) We do not agree with the widely used formulation (12,a) whereby the angle as in equation (5) is in the order of $\Delta(d\alpha/dC_L) = 8/A$.

"ROUND" WINGS are meant to have rounded lateral edges and/or to be rounded in the planform (see later) of the wing "tips". As a consequence of some flow *around* the lateral edges, not only the effective aspect ratio, but also the effective wing area is reduced. To properly formulate these effects would be complex. The experimental results in figure 2, suggest, however, as an upper limit:

$$d\alpha/dC_L = 10 + (12/A^2) + (25/A) \quad (7)$$

It is not certain that the last term of this equation represents induced drag only. In fact, when A reduces by ΔA to A_i , the effective area can be assumed also to be reduced, thus increasing the sectional angle of attack required. Equations (6) and (7) demonstrate that the components of the angle of attack can be added to each other. In the case of wind-tunnel tests and/or in the presence of the ground, the correction of the angle of attack caused by the boundaries of the fluid space, presents another angle-of-attack component. For those who wish to think in terms of lift-curve slope, equation (3) transforms into

$$dC_L/d\alpha = 2\ddot{a}\pi/(1 + 2\ddot{a}/A_i) \quad (8)$$

where $(2\ddot{a}\pi) =$ lift-curve slope of the foil section used (as in two-dimensional flow). Transformation of equations (6) and (7) would be complex.

DIHEDRAL is the academic word for what we can also call "V" shape. Lifting-line theory as described in this section, has one final application in such wings. As pointed out in (14,a) when raising the tips of a straight wing (thus reducing the span), each wing panel approximately maintains induced characteristics, in the plane *normal* to the panel, equal to those of the original straight wing. The lift of a panel (in vertical direction) is equal to (normal force) times $(\cos\Gamma)$. Since the angle of attack is measured in the wing's plane of symmetry, the lift angle α_L of a dihedral

wing is expected to be

$$d\alpha/dC_L = (0.5/\pi \cos^2 \Gamma) + (1/\pi A_p \cos^2 \Gamma) \quad (9)$$

where 'p' indicates that the reference area is the sum of the panel areas, S_p , and $A_p = 2s/c = 4s^2/S_p$, where s = span of a panel, $= 0.5b$. As confirmed by the experimental results on a "V" shaped tail surface in figure 3, lift then reduces in proportion to $\cos^2 \Gamma$. The lateral force derivative of the surface is shown in the chapter on "directional stability and control".

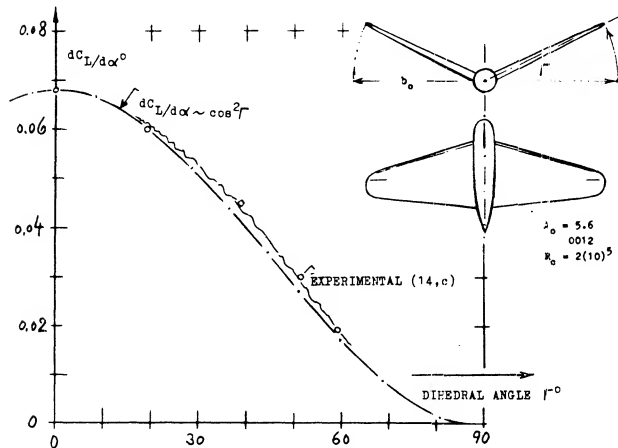


Figure 3. The lift coefficient (based on sum of panel areas) of a "V" tail surface, as tested (14,c) and as calculated (14,a) as a function of the dihedral angle.

INDUCED DRAG. Referring the lift coefficient of a dihedral wing to the projected planform area $S = b \bar{c}$, it is found that $C_L = C_{Np}$, where 'p' indicates that the normal force is still referred to the panel area. Equation (9) then changes into

$$d\alpha/dC_L = (0.5/\pi \cos^2 \Gamma) + (1/\pi A \cos^2 \Gamma) \quad (10)$$

Defining now $A = b/\bar{c}$, the induced lift angle is

$$d\alpha_i/dC_L = S/\pi b^2 \quad (11)$$

where S = projected area, as above. - For a dihedral angle of 6° (as possibly used in the wings of conventional airplanes) the increment is expected to be only in the order of 1%. However, "V"-shaped tail surfaces have been used in place of the conventional tail assembly, with dihedral angles in the order of 30° . Comparing such a surface with a straight horizontal tail having the same span, equation 11 predicts that induced angle and induced drag will remain unchanged. A more correct analysis (14,b) indicates the very small decrease as shown in figure 21. For example, at $\Gamma = 30^\circ$, the reduction (when keeping $b = \text{constant}$) is in the order of 4%.

B. INFLUENCE OF SHAPE ON PLAIN WINGS

The wings of airplanes are not anything close to lifting lines. They are composed of panels with a certain chord and thickness distribution, planform and shape. The influence of these parameters on lift is described as follows.

LIFT DISTRIBUTION. Figure 4 shows the lift distribution of three different planform shapes. It should be noted in particular:

- (a) the elliptical wing has a constant C_L and a uniform induced angle of attack.
- (b) the rectangular wing has a somewhat more uniform distribution in newtons or pounds, while downwash is somewhat shifted from the center to the wing tips.
- (c) the highly tapered (triangular) wing is loaded in the center, while the lift coefficient reaches comparatively high values near the tips.
- (d) Wings with lateral edges show peaks at these edges, not predicted by theory, but nevertheless real.

There are elaborate methods (8) available for computing lift distribution across the span of any given planform. We would like to mention here, only a simple procedure approximately indicating spanwise distribution. According to (8,c,d) the load (in newtons or pounds) of a plane wing is distributed in such a manner as to form the mean between geometrical chord length and the elliptical shape. To find the distribution, it is thus sufficient to draw a half circle with the span as diameter, to plot the chord distribution in a scale so that the resultant planform area is equal to that of the half circle, and to take at a number of stations the mean between chord distribution and half circle.

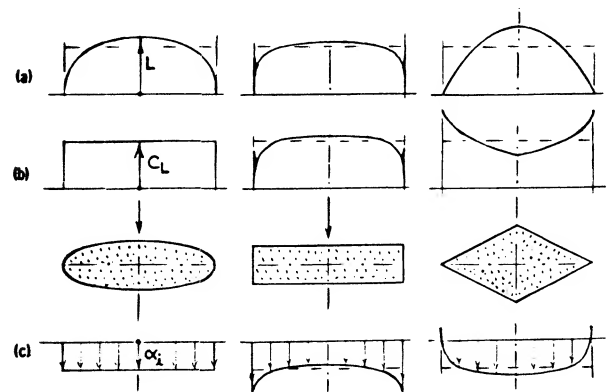


Figure 4. Distribution across the span of four different wing plan-form shapes, of local lift coefficient, lift as a force, and induced angle.

Figure 6. Experimental results (7,d) indicating the induced characteristics of a rectangular and two tapered wings.

TAPERED PLAN FORM. The simple lifting-line theory (equation 3) represents a minimum and thus optimum of the induced angle, obtained for elliptical load distribution. Theory expects that any deviation from this distribution results in a certain increase of the average or effective value of this angle-of-attack component. There are correction factors available, indicating the additional amount of induced angle for rectangular and tapered wing planforms. The theoretical correction can be presented in the form of the differential

$$(d\alpha_i^0/dC_L) = k \sqrt[3]{\bar{a}/A} \quad (12)$$

where A/\bar{a} = effective aspect ratio and $\bar{a} = 0.9$, for conventional airfoil sections. This function is an interpolation (by this author) of analysis (1,b)(10,b), applicable between $A = 4$ and 15. The factor K , as plotted in figure 5, is in theory smallest for taper ratios around 0.3. In fact, reference (10,b) predicts that the lift-curve slope of such wings is 99% of the theoretical as for elliptical load distribution. By comparison, the influence of fuselage and engine nacelles (see the chapter on "airplane configurations") can be much larger.

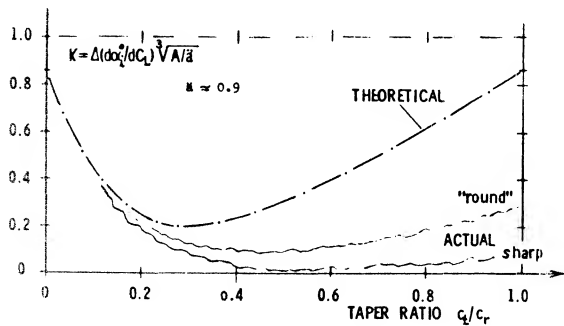
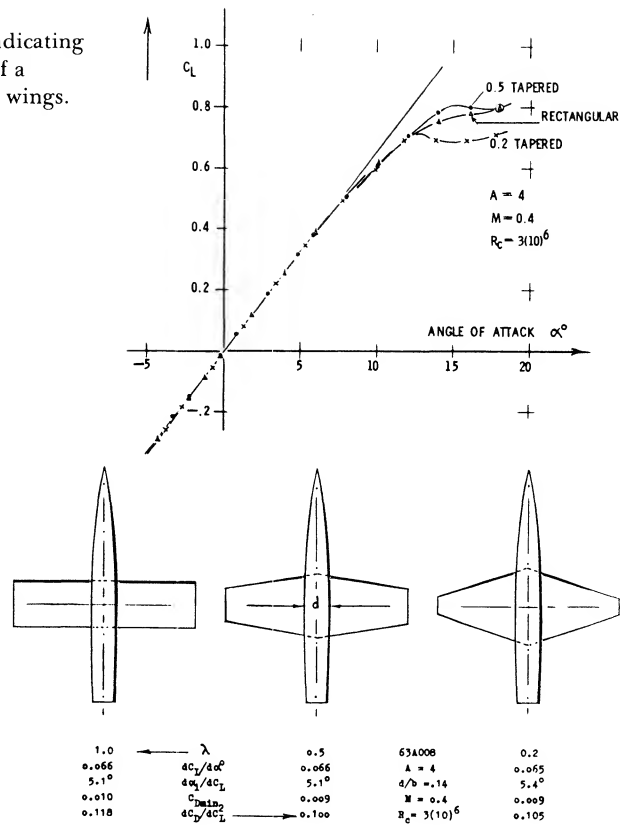


Figure 5. Factor k , theoretically needed in equation (5) to indicate the additional induced angle of attack, as a function of the taper ratio.

- (10) Influence of plan form on induced angle, theory:
 a) Glauert, ARC RM 723 (1922); "Elements Aerofoil Theory", Cambridge 1926; quoted in Durand Vol II.
 (b) Hueber, Character of Tapered Wings, Zts Flugt Motorluftsch 1933 p 249 & 269, and Lufo 1938 p 218.
 c) Plan-form corrections for the induced drag, as presented in "Fluid-Dynamic Drag", are different and somewhat smaller than for the induced angle.
 d) Reissner, Minimum Wing Drag, J A Sci 1940 p 114.



RECTANGULAR WINGS are expected by theory (figure 5) to be less efficient than elliptical or tapered wings. Tunnel tests on a set of three tapered wings are presented in figure 6. It takes a microscope to determine the differences in the lift-curve slope; and it may be said at this point that the selection of a plan form for the design of an airplane usually depends upon considerations other than the induced angle, such as structural or stalling. At any rate, the tabulation shows that . . . the moderately tapered wing has the lowest drag-due-to-lift derivative, and that the rectangular wing (with square lateral edges) has the smallest lift angle. There are many other results showing that rectangular wings with sharp lateral edges are very efficient in producing lift. Figure 7 demonstrates, for example, that the sharp-edged rectangular form is nearly as efficient as the elliptical wing of the same aspect ratio. Theory as in figure 5, is thus not confirmed (to be discussed later). When evaluating the induced angle of a rectangular wing, it must be considered that the effective area varies (reduces) together with the effective aspect ratio. If, for example, A reduces by $\Delta A = \Delta b/c = -0.1$, then the area reduces by $\Delta S = -\Delta b/b = -(\Delta b/c)/A$. As a consequence, the first two terms in equation (6) have to be increased. In equation (7) this is primarily done by the addition of $(5/A)$ in the third term. In the case of figure 7, it is seen that when adding the fairings to the lateral edges, the induced characteristics remain unchanged. Comparing, however, a wing with rounded edges (e) on the basis of equal aspect ratio and of area including the added caps, it is found that $\Delta A = -0.12$, and that the effective area is reduced by 2.5%.

FOIL-SECTION THICKNESS evidently helps the flow to get around the lateral edges. Figure 8 presents a possibly extreme example. A 25% thick rectangular wind-tunnel airfoil was tested both with and without round fairings added to the lateral edges. Based on one and the same area (without the end caps) the wing without fairings is slightly more effective, as far as *lift* is concerned. Note that the due-to-lift drag derivative also favors the wing without the fairings, while the zero-lift drag coefficient of this wing is, of course, higher than that of the wing with rounded lateral edges. A simple assumption would be that the flow passes around the half-circular end caps to a degree as though they were not present. The fact that the original square-ended wing has a 3% higher lift-curve slope, might then be explained by a more outward location of the tip vortex, as in shape (1) in figure 10. Regarding drag, the two wings in figure 8 compare as follows:

$$\begin{aligned} C_{D_{\min}} &= 0.0102, \quad dC_D/dC_L^2 = 0.062, & \text{square edges} \\ C_{D_{\min}} &= 0.0085, \quad dC_D/dC_L^2 = 0.067, & \text{with end caps} \end{aligned}$$

For practical purposes, we thus find:

$$\Delta b/c = -(t/c) = \Delta A \quad (13)$$

A rectangular wing with rounded lateral edges thus behaves, regarding its induced angle of attack and the effective area, roughly as though the end caps were not present (12,c). As in figure 8, the lift-curve slope (with C_L based on rectangular area) is usually slightly less than that of the wing without the tip fairings; see also (13,e).

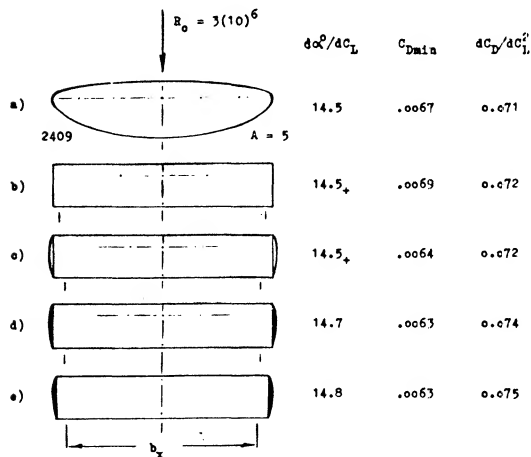


Figure 7. Characteristics of three wing shapes (11,a)
 (a) ideal elliptical wing,
 (b) rectangular with sharp lateral edges,
 (d) rectangular with end caps added.

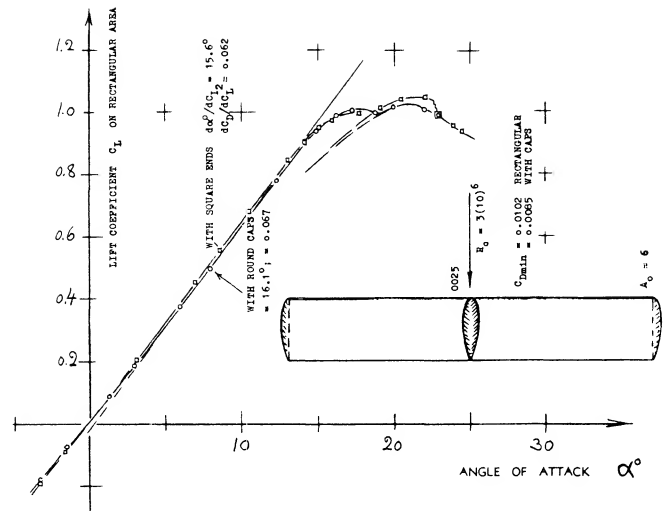


Figure 8. Characteristics of a 25% thick rectangular airfoil; tested (13,g) with and without round fairings at the lateral edges.

TAPERED WINGS. We may assume that the rounding effect be proportional to the chordwise dimension of the edge, indicated in tapered wings by the ratio $c(\text{tip})/c(\text{root}) = \lambda$. Since the effect is also proportional to (t/c) at the wing tips, equation (13) holds for tapered wings when using for c and t the dimensions at the tips. We have evaluated the theoretical function as in figure 5 and equation (10) for $A = 5.5$. The result is plotted in figure 9, in the form of $\Delta A = A_i - A$, where A_i = effective aspect ratio. A number of experimental points (some of which obtained in direct comparison to an elliptical plan form) clearly show the beneficial influence of lateral edges, particularly when they are sharp or square. Our final conclusion from experiments and analysis presented, is that the classical statement pronouncing the elliptical as the optimum plan form shape, is a "myth", particularly when it comes to designing and fabricating a wing. Famous airplanes such as the Heinkel-70 and the "Spitfire" did have costly elliptical wings. Our graphs show, however, that a tapered wing can have at least the same aerodynamic effectiveness. Another argument against the elliptic plan form is offered in (10,d). The angle of the viscous or section drag is $\alpha_s = C_{D_s}/C_L$. Since in a real airplane, C_L and (t/c) are highest at the roots of the wing, C_{D_s} and α_s are larger there, than in the outboard portions of the panels. If minimum drag is expected for $\alpha_i + (\alpha_s/2) = \text{constant}$ across the span, the optimum plan form is somewhere between elliptical and rectangular. Finally, it can be said that the "best" wing may not be optimum for an airplane, with a fuselage (see "airplane configurations") and with a horizontal tail surface exposed to the downwash coming from the center or the roots of the wing (see "longitudinal stability").

“ROUND” PLANFORMS. In wing sections, a physical (so called Kutta-Joukowski) assumption is necessary to fix the trailing edge as the point where the flow components coming from the two section sides, meet each other (in a rear “stagnation point”). A similar, never mentioned but equally necessary assumption, is that the tips of a finite-span wing coincide with the ends of the lifting line. As explained above, this is not true in the case of well-rounded lateral edges, as in figure 8 for example. In a similar manner, wing “tips” with well-rounded *plan form* shape result in an effective aspect ratio which is smaller than the geometrical one. The path of the trailing vortex is shown in figure 10, for three different tip shapes of a basically rectangular wing, with $A = \text{constant} = 3$. According to equation (1) the roll-up distance (say behind the quarter-chord line) is in the order of $x/c = 10$, for $C_L = 0.6$. The path of the tip vortex was traced to only one chord downstream from the trailing edge in the investigation discussed. The location of the vortex at this distance may permit, however, to estimate the reduction of the “vortex span” of the shapes tested, in comparison to that of the basic rectangular wing. Values of ΔA , evaluated from experimental results of $d\alpha/dC_L$ of various shapes, were found to be proportional to the lateral displacement ($\Delta y/c$) as defined in figure 10. Assuming

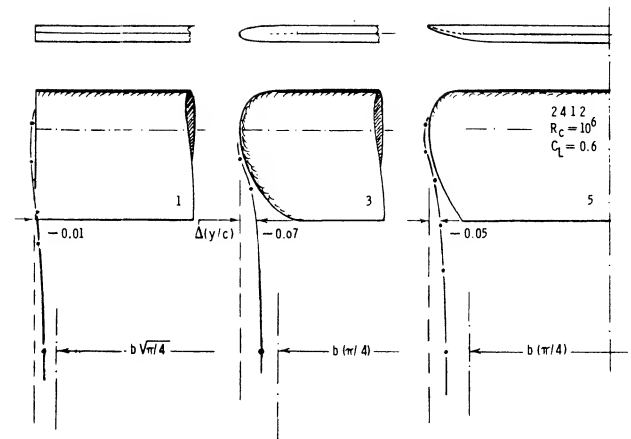


Figure 10. Location and path of the trailing vortex originating along the lateral edge of a basically rectangular wing, having an aspect ratio $A = 3$, as found (13,f) for six different wing-tip shapes.

that the volume of air affected (deflected) by the wing be proportional to the square of the vortex span b_i , the average induced angle may be expected to correspond to

$$A_i = A + \Delta A = (b + \Delta b)^2/S = A + 2(\Delta b/c) \quad (14)$$

For shapes (1) and (3) substitution of $2(\Delta y/c)$ for $(\Delta b/c)$ leads by way of equations (4) and (6), correctly to the lift angles as tested. Doing this, it is not assumed that the effective area would be reduced.

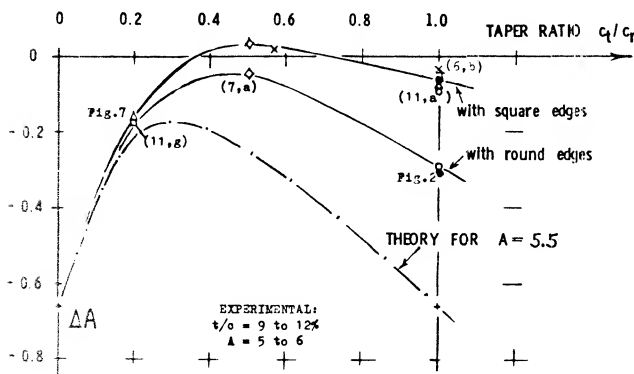


Figure 9. Differential ΔA of the effective aspect ratios of tapered wings having a geometrical ratio $A = 5$ to 6, as a function of their taper ratio.

- (11) Plan form and induced angle, experimental:
a) Doetsch, Rectangular/Elliptical, Ybk D Lufo 1940.
b) Ergebnisse AVA Göttingen, Vol I (1921) p 63.
c) Göthert, Control Surfaces, Ybk D Lufo 1940, 542.
d) Silverstein, H-Tail Collection, NACA T'Rpt 688.
e) Circular Wings, see Yearbk D Lufo 1939 p I-152, and Zimmerman in NACA Tech Note 539 (1935).
f) Hansen, 5 Elliptical, Ybk D Lufo 1942 p I-160.
g) Purser, Various Wing Shapes, NACA TN 2445 (1951).
h) Knight, Various at $R = 2(10^5)$, NACA TR 317 (1929).

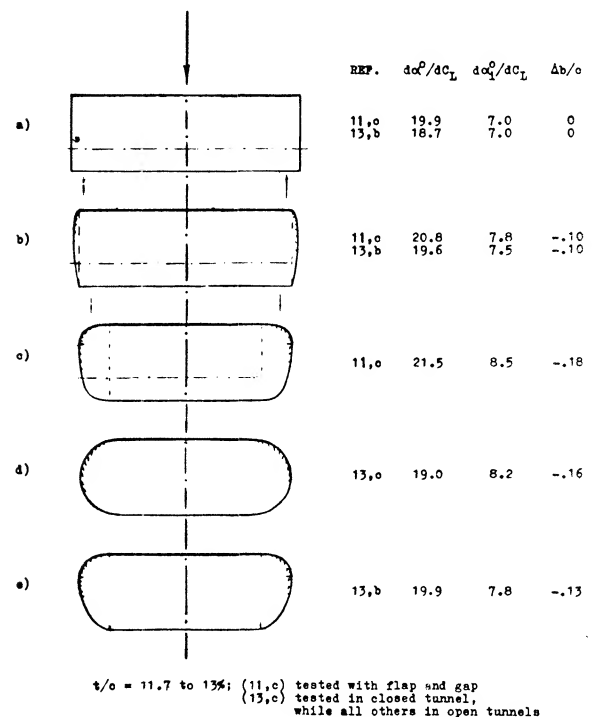


Figure 11. Reduction of the effective aspect ratio of “round” wings as against the sharp-edged rectangular shape having the same aspect ratio $A = 3$.

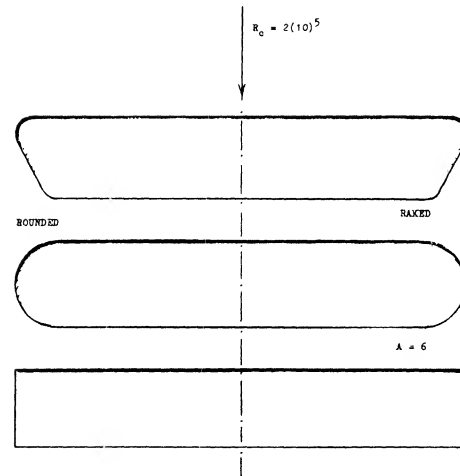
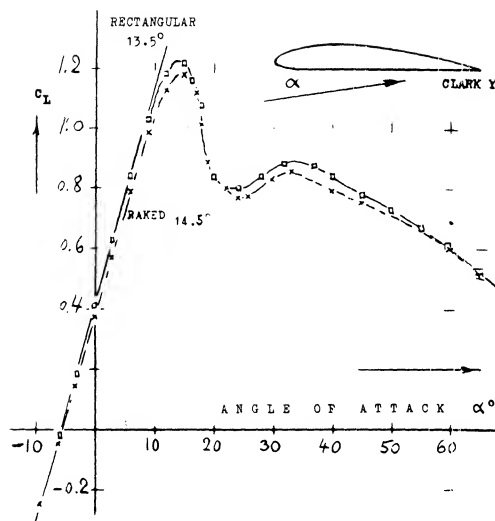


Figure 12. Comparison of a basically rectangular wing with $A = 6 = \text{constant}$, for three different planform shapes of the ends or tips (11, h).

REAR CORNER. Some more “round” planform shapes are shown in figure 11. Here and in figure 12, it is seen that cutting away from the rear corners of the plan form is particularly harmful in reducing lift-curve slope and effective aspect ratio. For conventional thickness ratios (between 11 and 13% as tested), $\Delta b/c$ reaches values, as against the sharp-edged rectangular wing having the same aspect ratio, roughly between -0.2 and -0.3 , for round or cut-away shapes. This reduction is larger than that for rounded lateral edges (preserving rectangular planform) where $\Delta b/c$ is between -0.10 and -0.14 , for the thickness ratios investigated. Such values are to be used to modify the sectional as well as the induced angle required to produce a certain lift coefficient. Accounting for the loss of useful span of the round or raked, and rounded two tip shapes in figure 12, only by way of an effective aspect ratio, values of $\Delta A = -0.4$ and -0.5 are found, in comparison to rectangular and square-edged Wing.

“U” SHAPE. Wing ‘5’ in figure 10 is very effective, despite the fact that the vortex span is somewhat small by comparison (19). It was found, however, that the trailing vortex is located at a level some 6% of the wing chord higher than in the case of other wing ends tested. The bent-up tips seem to serve as a low type of end plates (see later). Taking the 6% as measured (which are equal to 0.5 (t/c) of the foil section used) it can be assumed that the wing tips impose upon the vortex sheet a “U” shape with an equivalent end-plate height $h/b = 0.06/A = 2\%$. According to equation (25) the corresponding increment of the effective aspect ratio is $\Delta A = 2(0.02) = 0.04$. This much helps, but it

is not yet enough to explain the performance of shape ‘5’. It is suggested that the clean flow around the wing tip, as shown in Chapter VII of “Fluid-Dynamic Drag”, may be responsible, (a) for the complete preservation of the effective area, (b) for minimum parasitic drag due to lift, and (c) possibly for a more favorable roll-up process in the wing’s vortex wake. These arguments are supported by trying the opposite, id est adding drag.

TIP DRAG. As reported in (15) a pair of spheres (as in ball bearings) was attached to the lateral edges of the horizontal-tail-surface model as in figure 13. When writing the well-known equation for the induced angle in the form of

$$d\alpha_i / dC_{Lb} = 1/\pi \equiv 180/\pi^2 = 18.3^\circ \quad (15)$$

where $C_{Lb} = L/qb$, an angle is found which is independent of the aspect ratio $A = b/c$. In the experiment, it was found that

$$\begin{aligned} \Delta\alpha / \Delta C_L &= 19.0^\circ, & \text{for the plain wing tips,} \\ \Delta\alpha / \Delta C_L &= 19.8^\circ, & \text{with the spheres attached.} \end{aligned}$$

The effective aspect ratio is thus $A_i = (19/19.8)A = 0.96 A$. The reduction caused by the spherical obstacles (15.b) is $\Delta A = -0.04 A$, which is $\Delta A = -0.14$, for $A = 3.7$. In other words, a strip of $\Delta b/c = \Delta A/4 = 0.035$, is effectively cut-off from each lateral edge of the rectangular wing, when disturbing the flow along and around the edges. When eliminating a similar disturbance by means of the “clean” tip shape ‘5’, the superior performance of this type of edge can be understood (19).

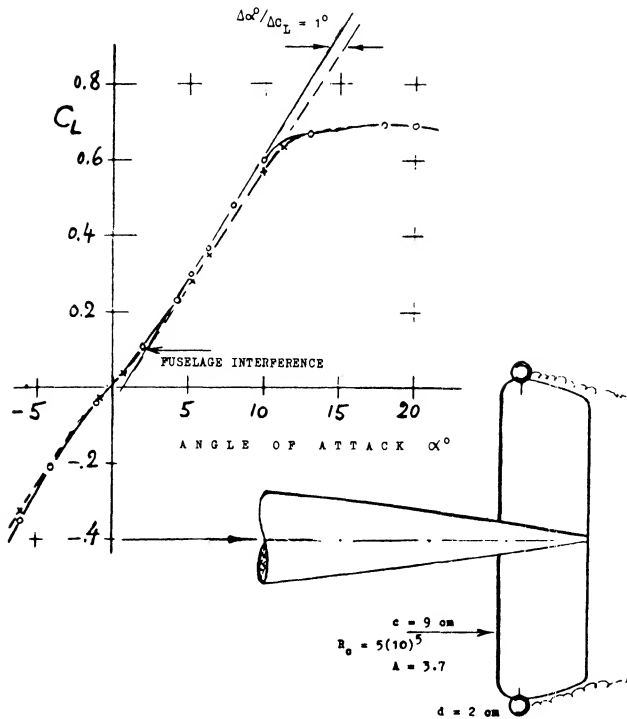


Figure 13. Experiment (15) demonstrating the influence of a pair of obstructions (spheres) upon the lift of a horizontal tail surface.

(12) Small-aspect-ratio considerations:

- a) Jones, NACA TN 817 and T'Rpt 835 (1946); also in "High-Speed Aerodynamics" Vol VI of Princeton Series.
- b) Bartlett, Lateral Edges, J Aeron Sci 1955 p 517.
- c) This result agrees with the concept in (a) and (b) whereby any "retracting" parts of lateral edges, behind maximum span, do not contribute to lift.

(13) Influence of tip shape on wing characteristics:

- a) Hoerner, Fieseler Water-Tunnel Rpt 16 (1939).
- b) Kesselkaul, Tests of Wings with Various Lateral-Edge Shapes, Inst Aircraft Des Braunschweig, 1941.
- c) Zimmerman, Small A' Ratios, NACA TN 539 (1935).
- d) Hoerner, Aerodynamic Shape of Wing Tips, USAF AMC Tech Rpt 5752 (Wright Field 1949).
- e) Goett, Rounded Edges, NACA T'Rpt 647 (1939).
- f) Hoerner, Tip Vortex Measurements Behind 6 Wing Shapes, ZWB UM 7815 (Messerschmitt Rpt TB-92/1943).
- g) Bullivant, 0025 and 0035, NACA T'Rpt 708 (1941).
- h) Experiments similar to (b) and (f) by Valensi in Publ Sci Tech Ministère de l'Air, 1938 No. 128.

(14) Characteristics of wings with dihedral shape:

- a) Purser-Campbell, Experimental Verification of Vee-Tail Theory and Analysis, NACA Rpt 823 (1945).
- b) Dätwyler, Mitteilung Aerody Inst TH Zürich, 1934.
- c) Schade, "V" Tail Forces, NACA TN 1369 (1947).

(15) Engelhardt, Influence of Fuselage Upon Horizontal Tail, Rpt Aerody Lab TH Munchen (1943).

C. WINGS WITH END PLATES

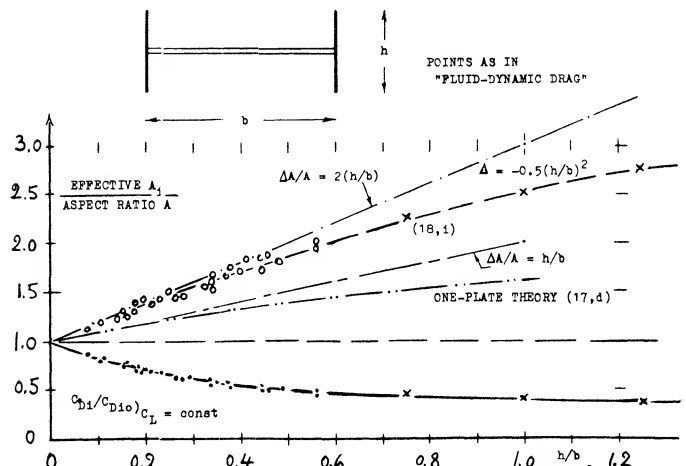
End plates have found little application on airplane wings until recently when the winglet and/or tip sails have been applied to reduce the induced drag, the drag due to lift. As the induced drag of a wing is a large part of the total a device that can reduce this component is of importance. In considering such devices the improvement obtained must be weighed against that possible with an increase in the wing aspect ratio. With the available theoretical and experimental data the relative merits of wing and plates, winglets and similar devices can be found. The theoretical and experimental characteristics of the various types of end plates are presented as follows.

BASIC PRINCIPLES. The objective of adding wing end plates is to control the flow at the wing tip and to reduce the induced angle of attack and thus the induced drag. In some ways this is analogous to the operation of a wing between the walls in a wind tunnel and thus eliminating the three dimensional effects leading to the induced drag loss. Thus the addition of end plates would be in the limit a wing with the drag characteristics of a two dimensional section, an infinite aspect ratio wing. In any case when adding a pair of end plates, figure 14, the effective span is increased. Theory (17) considers a lifting line with an elliptical loading which is bent up at both ends. The results of this can be approximated in terms of an effective aspect ratio

$$A_i = A + \Delta A, \text{ where}$$

$$\Delta A/A \approx k h/b \quad (16)$$

Figure 14 shows that this equation is confirmed, using $k = 1.9$, up to $h/b = 0.4$. Note that this type of effective A' ratio can be used both to calculate induced drag or the lift-curve slope. With the data given on figure 14 it does not matter whether the plates are attached nearer to the leading or trailing edge of the wing. Note that the effect of end plates is also obtained in swept wings (18,e) and essentially to the same degree as straight wings.



WINGS WITH AND WITHOUT END PLATES. The characteristics of wings with end plates and the wing with the plates used to extend the wing and so increase its aspect ratio is given on figure 15. As shown in figure 15, **B DRAG**, the drag of the wing with the end plates is less than the wing without them only above $C_L^2 = .3$. This is evidently a major reason for the fact that end plates are not usually applied in the design of airplanes. Aerodynamically, it is much more profitable to add end plates to the wing span thus gaining aspect ratio as well as lift-producing area. To demonstrate this point, we have analytically determined the $C_D(C_L^2)$ function for the enlarged wing as shown on figure 15. Based on the original area of the wing, we then find a reduction of the drag/lift ratio, for example at $C_L = 0.9$, as against the original plane wing, twice as large as that obtained by means of the end plates. Below that lift coefficient, the wing with the enlarged span is clearly superior to the wing with end plates.

MAXIMUM LIFT. The end-plated wing in figure 15, shows an increase of the maximum lift coefficient from 1.1 to 1.2. The increment is 9%, while the enlargement of wetted area is almost 40%. Here again, a wing increased in span by adding the end-plate areas, is superior, resulting in a $C_{Lx} = 1.38 (1.09) = 1.5$. Of course, a larger span may be structurally undesirable. However, end plates at the wing tips are not desirable either. As a rule, therefore, end plates are used in the design of aircraft only under conditions where they may perform another function, in addition to improving the lift of the device to which they are attached. Such a case is for example a tailless airplane with a swept-back wing, where a pair of end plates serve in place of the vertical tail to provide directional stability and control. Another application of end plates can be found in hydrofoil boats, Chapter VIII where the span of a submerged wing may be limited to the dimension of the beam of the craft. End plates are also used in ground effect vehicles.

Although end plates do produce an increase in the effective aspect ratio which reduces the drag at very high lift coefficients only slight reductions in drag are obtained when operating at or near the cruise lift coefficients. At the cruise conditions the viscous and interference drag increments associated with the end plates are nearly as great as the reduction of the induced drag due to the effective increase in aspect ratio. While considerable testing has been done with wing end plates it is apparent from figure 15 that the optimum design had not been developed. If the wing span cannot be changed, the use of wing tip devices may be desirable. To develop an optimum wing tip configuration for this purpose it is necessary to examine the flow field in which the end plate must operate and then find the tip device required to give the desired performance.

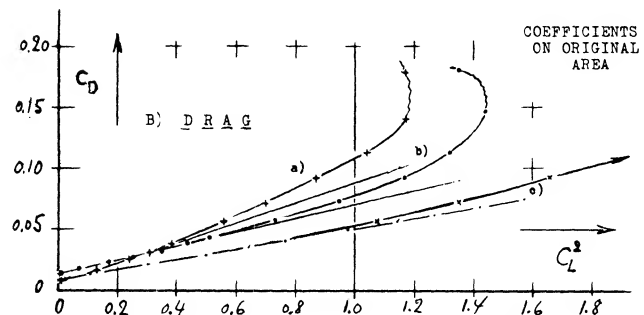
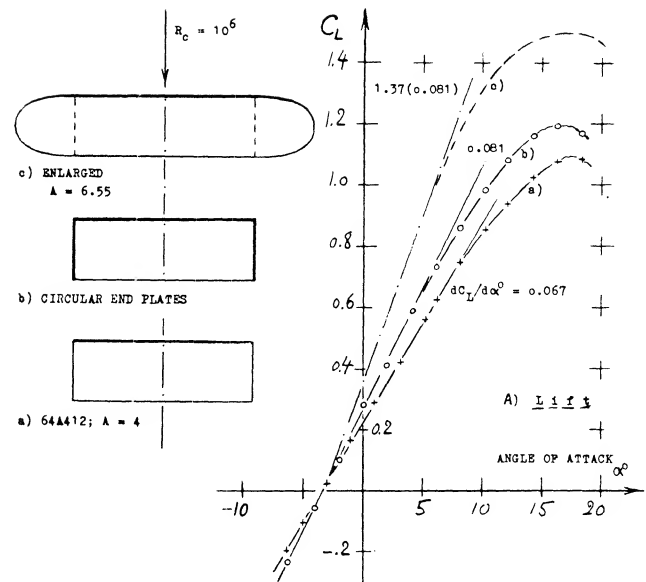


Figure 15 Lift and drag of a rectangular wing

- (a) plain, as tested (18,b).
- (b) with circular end plates.
- (c) calculated with enlarged span.

WING TIP FLOW FIELD. Detailed measurements of the velocity field at wing tips as influenced by the tip vortex have been made by a number of investigators, (16). Tests show that a main vortex forms over the wing surface as illustrated on figure 16. Between the main vortex and the wing tip a small secondary vortex is also formed as shown. At any station in the streamwise direction the rotational velocity increases linearly with radius from the core center until the core diameter is reached. Then the velocity decreases as a direct function of the radius. Typical velocity distributions from (16,a) are given on figure 17 as a function of wing span station from the tip and the vertical distance showing these characteristics. The core radius reaches a maximum at the wing trailing edge and then decreases in size with downstream location until it again becomes larger starting at an axial distance of four wing spans downstream, figure 18. The location of the vortex core is inboard and above the wing tip as illustrated on figure 18. The variation of the axial velocity maxima and the circumferential velocity maxima as a function of the streamwise distance from the trailing edge is given on figure 20.

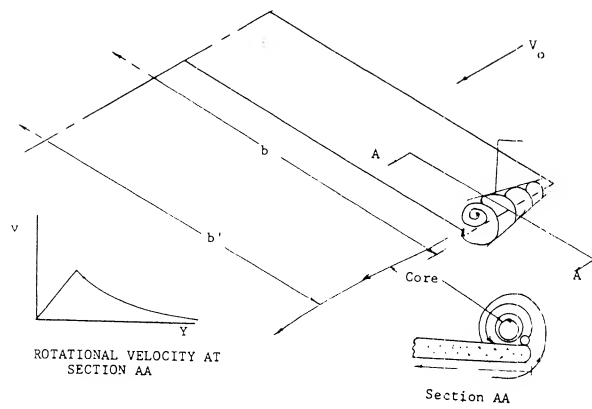


Figure 16. Detailed characteristics of a wing tip vortex.

The characteristics of the wing tip flow given on figures 16 to 20 were obtained from tests given in (16,a) for a rectangular wing of A'ratio of 5.33. The decrease of velocity with increasing radius from the core center shown on figure 16 is a function of the wing span, aspect ratio and operating lift coefficient. Theory is available (16,b,c) for calculating the induced velocity produced by the wing tip vortices at the downstream station where the trailing vortices are rolled up, figure 20. At a distance r from the vortex core center the rotational velocity v_t of the rolled up vortex can be found from the equations

$$\frac{v_t}{V_0} = \frac{C_{L0}}{\pi^2 AR} \left[\frac{6r}{b} - 9 \left(\frac{r}{b} \right)^2 \right] ; 0 < \frac{r}{b} < \frac{1}{3} \quad (17)$$

$$\frac{v_t}{V_0} = \frac{C_{L0}}{\pi^2 AR} \frac{b}{r} ; \frac{r}{b} > \frac{1}{3} \quad (18)$$

where C_{L0} = the lift coefficient at the wing center
 b = wing span
 V_0 = free stream velocity

A comparison of the measured tangential velocity with that calculated using equations 17, 18 is given on figure 17. Here the velocity ratio at the wing trailing edge is very nearly the same as the value calculated at two chord lengths downstream where the vortices are rolled up. Although equations 17 and 18 were developed for the case where the vortices are completely rolled up it appears that to the first approximation they can be corrected using the data given on figure 20. This is done by multiplying the calculated velocity ratio of equations 17 and 18 by k equation 19.

$$k = u @ x/c = 2 / u @ x/c = x \quad (19)$$

(16) Characteristics of wing tip vortices:

- Chigier, et al Tip Vortices Velocity AHS 27 Forum May '71
- Betz, Behavior of Vortex Systems, NACA TM 713, 1933
- Donaldson, The Aircraft Vortex Problem ARAP No. 155 1971
- Donaldson, Vortex Wake Conventional A/C, AGARD No. 204
- Spreiter, et al Rolling up Trailing Vortex J.A. Sci. Jan. '51
- Grow, Effects of Wing on Tip Vortex J of A/C May 1968
- Corsigli, Hot-Wire Wing Tip Surveys J of A/C Dec. 1973
- Russow Rolled-Up Structure Vortices, J of A/C Nov. 1973
- McCormick, et al, Structure trailing vortices J A/C Jan. '69

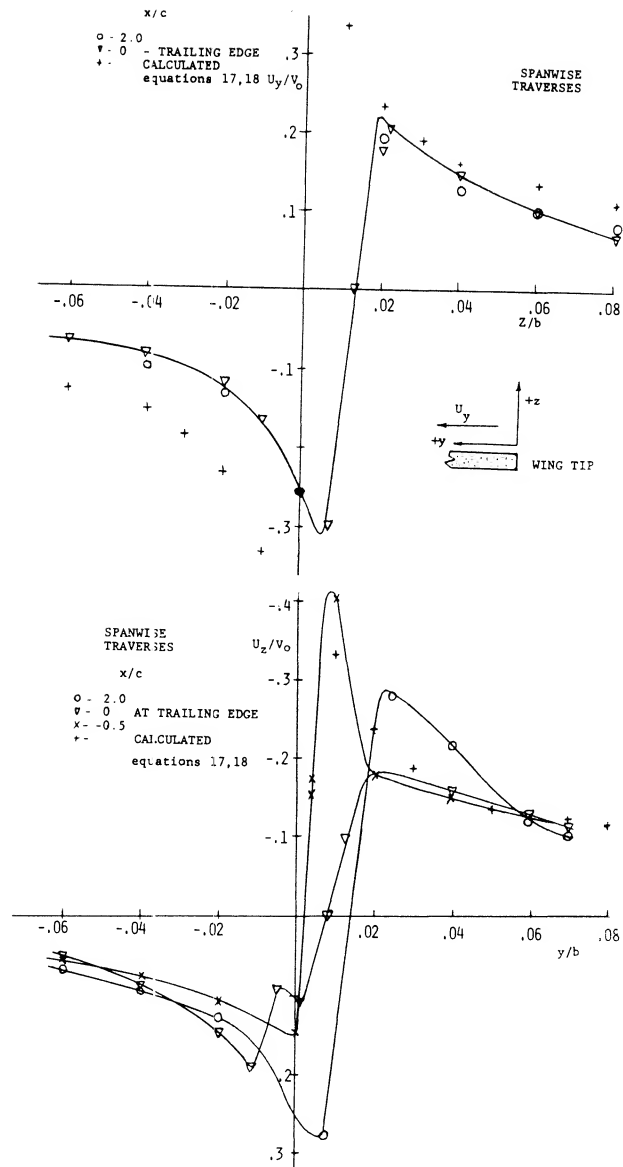


Figure 17. Circumferential velocity of the tip vortex.

(a) Vertical distribution
 (b) Span distribution

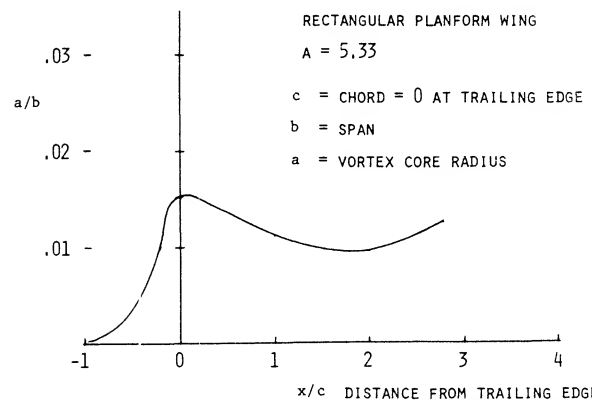


Figure 18. Vortex core radius as function of downstream distance.

(17) Available theoretical results on end plates:

- Ergebnisse AVA Göttingen Vol III (1927) p 18.
- Mangler, Theoretical Analysis of End Plates, Lufo 1937 p 564 (NACA T Memo 856) and 1939 p 219.
- Küchemann, On Swept Wings, ARC CP 104 (1951).
- Rotta, Plate at One End, Ing Archiv 1942 p 119.
- Weber, Loads & Inboard Plates, ARC RM 2960 (1956).

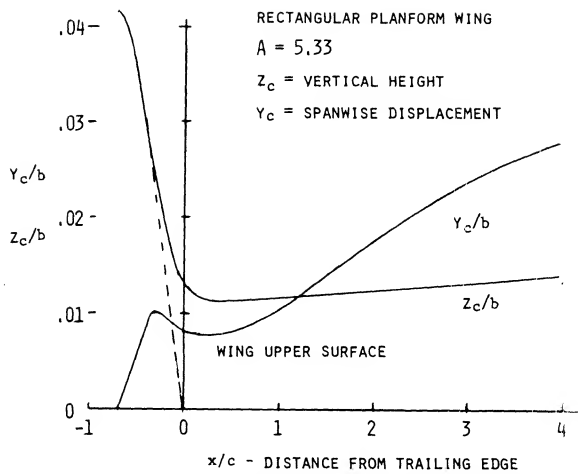


Figure 19. Normal and spanwise displacement of vortex centerline.

INDUCED DRAG RECOVERY. According to theory (16,b,c,d) all the swirl energy in the trailing vortex system is trapped within a distance from the centerline of the wing and for a considerable distance outboard. However, as indicated by theory and test the major portion of the rotational energy occurs within a very small radius. This is confirmed by (16,c) where it was shown that 54% of the vorticity is within a radius up to 0.1 of the wing span should be of sufficient size to obtain high energy recovery and a corresponding reduction of the induced drag. Devices that can be used to recover the energy of the tip vortex of a wing thus do not have to be large. Some of the devices that have been considered for this purpose are shown on figure 21 (18,n) and include winglets tip sails, fixed tip vanes and rotating propellers.

WINGLETS. Of the wing end plate devices considered the winglet appears to be the most effective for reducing the induced drag and effectively increasing the aspect ratio. Results of test data (18,k,l) show that using winglets the induced drag is decreased as much as 30% depending on the lift coefficient, figure 22. The winglets tested have the best performance at a wing lift coefficient of 0.5. It would be expected that a change in configuration could shift the C_L for best recovery up or down.

The design and analysis of winglets is involved and complex due to the mutual interaction with the wing surface and the exact solution is not available (18,k). However, by assuming the tip vortex is only affected by the main wing the performance of winglets can be estimated by relatively simple methods. This is done by finding the local flow conditions at a series of winglet stations using equations 17 to 19 and the methods previously given. Knowing the flow conditions the force coefficients are found and resolved in the flight direction to find the change relative to the entire wing.

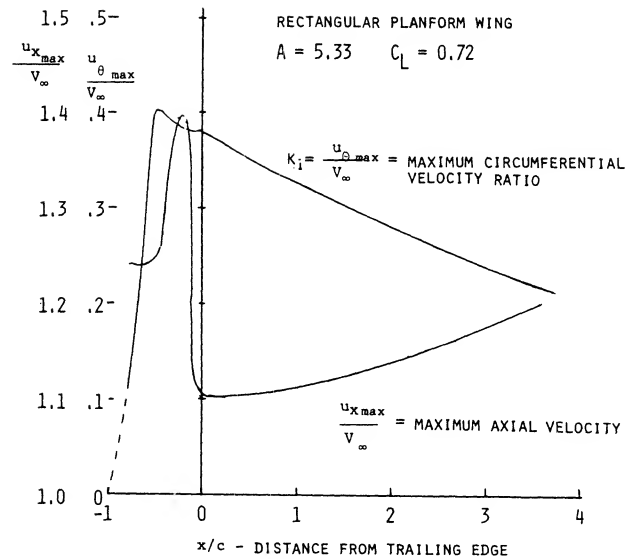


Figure 20. Variation of axial velocity maxima and circumferential velocity maxima as a function of streamwise distance.

Consider a winglet mounted at the tip of a wing, figure 23, at any station r on the winglet the effective axial velocity, V_E , is influenced by the sweep of the leading edge and the angle of attack so

$$V_E = V_L \cos(\alpha + \Theta) \quad (20)$$

where α = the main wing angle of attack
 Θ = the angle of the winglet leading edge
 V_L = the local axial velocity

The true velocity relative to the airfoil section W , is

$$W = V_E^2 + v^2 \quad (21)$$

The rotational velocity v produced by the tip vortex is determined using equations 17 to 20. The apparent angle of attack at any wing tip station is, section AA, figure 23.

$$\alpha_a = \phi_0 + i \quad (22)$$

where α_a = apparent wing angle = $\tan v/V_E$
 i = winglet section incidence

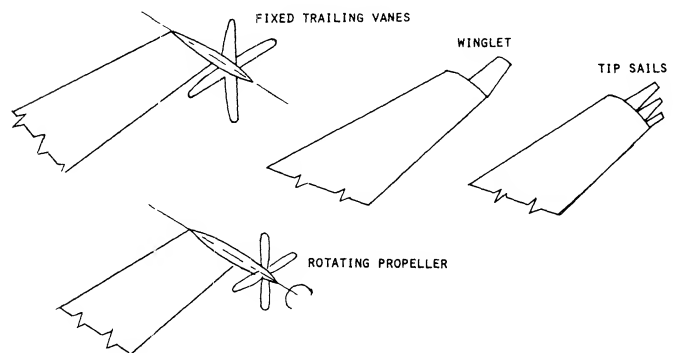


Figure 21. Wing tip vortex energy drag recovery devices.

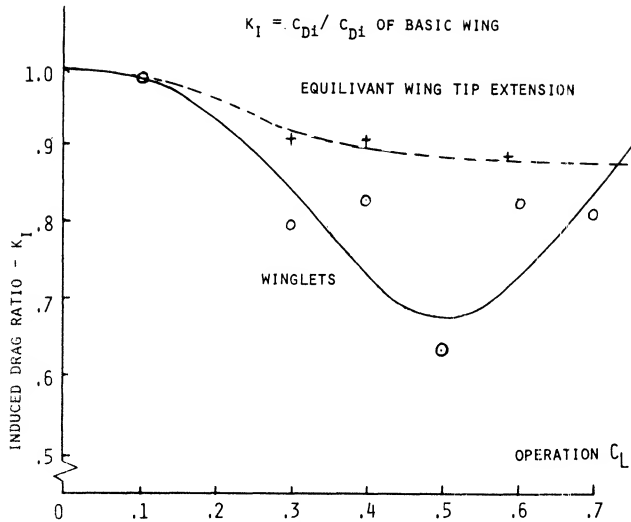


Figure 22. Comparison of induced drag ratio of wing with extended tip to that of a wing with winglets.

The lift and drag coefficients developed on the winglet can be found by assuming it is operating as a simispan wing due to the reflection plane characteristics of the main wing. Thus, knowing the effective aspect ratio of the winglet the lift angle and operating C_L can be found using equations 2 and 22. The drag coefficient is determined from standard data and the resultant force coefficient found from the equation

$$C_R = C_{LW} / \cos \gamma' \quad (23)$$

where $\gamma' = \tan C_{DW} / C_{LW}$

As shown on section AA figure 23 the resultant force coefficient resolved in the direction of flight gives a change in the drag coefficient of the basic wing equal to

$$\Delta C_D = \frac{2}{S} \int_0^{b/2} \frac{C_R \sin(\phi_0 - \gamma') W c' db'}{V_o^2} \quad (24)$$

where S = area of the basic wing
 $b'/2$ = the span of the winglet
 c' = the chord of the winglet

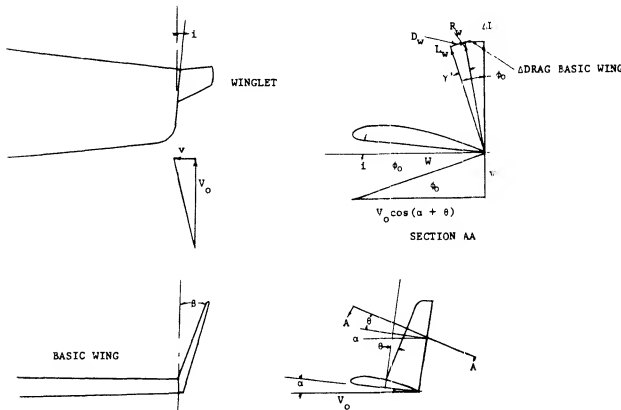


Figure 23. Relation of winglet to basic wing with flow condition and force vectors.

If the angle of the winglet relative to a line normal to the wing is the increase of lift on the basic wing is

$$\Delta C_L = \frac{2}{S} \int_0^{b/2} \frac{C_R \cos(\phi + \gamma') \sin \beta W^2 c' db'}{V_o^2} \quad (25)$$

Based on the above approach the drag reduction and the lift increase is in good agreement with the available test data.

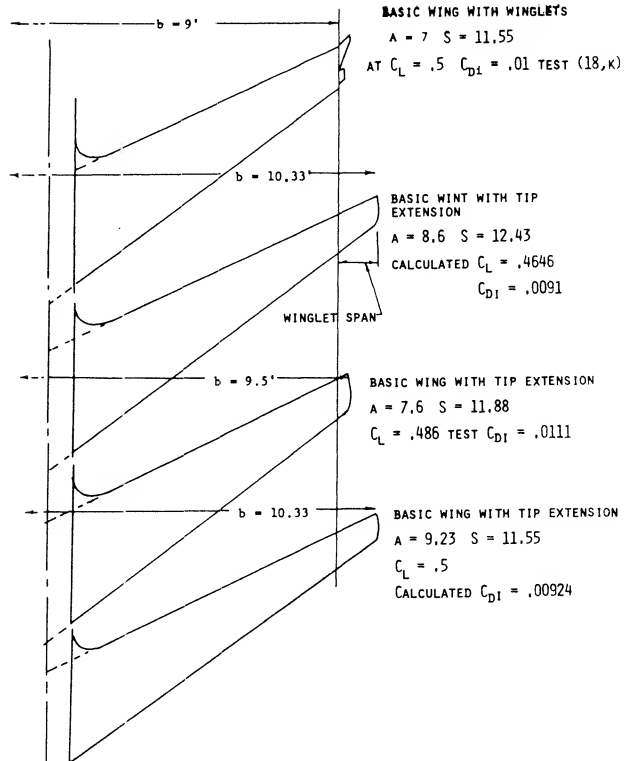


Figure 24. Comparison of performance of wings with and without winglets.

WINGLET PERFORMANCE AND APPLICATION.

Just as in the case of wings with end plates the application and performance advantages of winglets are dependent on the configuration of the wing, its aspect ratio and the total area. If the wing span is increased by the height of the winglet and the area held constant then as is shown in figure 24 the winglets have no performance advantage. Further if the wing span is increased with a corresponding increase in wing area the operating C_L will decrease along with the induced drag and this along with the aspect ratio increase will give improved performance compared with the wing with winglets. Also if a wing tip extension is used that gives the same wing root bending moment as a wing with winglets there appears to be no performance advantage with the winglets. However, if a winglet is used on a wing there is a decrease in the induced drag of the order of 20% compared to the wing alone. Based on the above, figure 24 it appears that winglets are useful for increasing the performance of an existing wing but if a new wing configuration is to be designed the use of winglets will give little improvement.

Single End Plates, placed at only one end of a wing (17, d) have an effect which is roughly half of that of a pair of plates; id est, for small height ratios (up to $h/b = 0.2$), the maximum increase in effective aspect ratio is theoretically slightly less than

$$\Delta A/A = h/b \quad (18)$$

A plate on one side has a definite limit, however, as to its effect. As the height ratio approaches infinity, the effective A_i ratio is no more than doubled, while a *pair* of plates yields $A_i = \infty$. The function for a one-side plate plotted in figure 14 can be approximated by

$$A/\Delta A = (1 - (b/h)^{4/3})^{3/4} \quad (19)$$

Note that the ratios are reversed in this equation. As a practical example of "single" end plates, a vertical tail surface is shown in "Fluid-Dynamic Drag" with a horizontal surface placed on top (serving as end plate). $A_i/A = 1.5$, is thus obtained for the fin.

Wing-Tip Tanks (detachable or disposable) have become standard equipment in certain types of military airplanes (to extend their range). They are not really end plates. There is an end-plate effect involved, however. Three specific effects of tip tanks can be stated:

- (a) Tip tanks usually extend beyond the lateral edge; they may thus increase area and aspect ratio.
- (b) They can be expected to permit the flow, laterally to get around them, to a certain degree.
- (a) Because of their height (equal to their diameter) and/or regarding their displacement, tip-mounted tanks have an effect similar to end plates.

A number of wind-tunnel tests is available (20) presenting the lift of wings or wing-body combinations, including a pair of tip tanks. Analyses as in (21) do not take into account the rolling-up of the wing-tip vortices. We will assume that the flow gets around each tank as far as qualitatively shown in *figure 19*, so that the span is effectively reduced at each wing tip, as against that between the outer sides of the tanks by $\Delta b = -r$, where r = maximum radius of the tanks. Thus, for the two tanks $\Delta b = -d$, and $\Delta A = -d/c$. Definition of the effective wing area with and without the tanks is problematic. Using lifting-line principles, exact knowledge

is not necessary, however. Assuming the height of the "plates" representing the tanks, to be $h = d$, equation (25) indicates $\Delta A/A = 1.9(d/b)$. Depending upon the manner in which the tanks are attached (possibly as in figure 19) we then have 3 steps to consider, the geometrical increment of span and aspect ratio when adding the tanks, the effective reduction due to flow around the tanks, and the increment $\Delta A = \Delta b/c$, due to end-plate effect. Using equations (6) and (7) we then obtain approximately:

$$d\alpha^2/dC_L = 10/(1 + d/b) + 20/A(1 + 2d/b) \quad (20)$$

A tank with $d = t$, may not really have an end-plate effect. It can be assumed, however, that the portion of the tank protruding ahead of the leading edge of the wing, will produce the α flow as explained in the "airplane configuration" chapter, that is on the inboard side. Even a tank with $d = t$, can thus be expected to have an effect similar to end plates. "Lift-angle" differentials due to tip tanks have been evaluated from available wind-tunnel tests (20). As seen in figure 19, equation (20) agrees with the experimental points. Of course, any end-plate effect will be reduced, and the drag due to lift will be increased, when attaching the tanks to the wing tips in a crude manner (leaving a gap, for example).

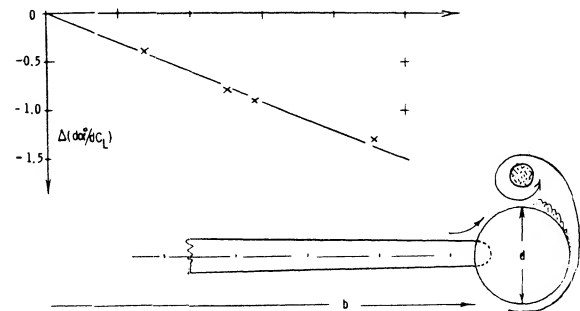


Figure 19. Statistical evaluation of the influence of wing-tip tanks on the "lift angle" of conventional wings.

ALPHA FLOW. It can be argued that tank bodies are neither plates nor capable of producing circulation. We can indeed speculate that the mechanism through which they affect the wing, is different from that of end plates. It is thus suggested that the " 2α " cross flow, as explained in the chapter on "airplane configurations", increases the lift on the wing tips. This can only be true when the tanks protrude forward from the wing's leading edge. In this respect, tanks typical for fighter airplanes, have a length about twice the chord of the wing tips. Their influence upon the adjacent portions of the wing is, therefore, similar to that of a fuselage upon the wing roots.

(18) Experimental results end plates and winglets

- a) NACA Technical Rpts 201 and 267 (1927).
- b) Riley, End-Plate Shape, NACA TN 2440 (1951).
- c) Clements, Canted Plates, Aeron Eng Rev July 1955.
- d) See due-to-lift chapter in "Fluid-Dynamic Drag".
- e) Riebe, On 45° Swept Wing, NACA TN 2229 (1950).
- f) Wadlin, On Hydrofoil, NACA RM L1951B13.
- g) Bates, H-Tail Surfaces, NACA TN 1291 (1947).
- h) CAHI (Moscow) Technical Rpt 58 (around 1930).
- i) Halliday, Very Large Plates, ARC CP 305 (1956).
- k) Riley, Vertical With Horizontal Tail, NACA Rpt 1171.
- j) Roberts, Drag Planer Wings USAACLABS TR 65-79
- k) Whitcomb, Design and tests Winglets, NASA TN D-8260, 1976
- l) Kirkman, Effectiveness Devices Tests, NASA CR-2202, Dec. '73
- m) Flechner, Second-Generation winglets, NASA TN D 8264 1976
- n) Wentz, Wing-Tip devices N76 11012, July '75

INBOARD PLATES. End plates have also been investigated in positions inboard the wing tips. Results are presented in the "due-to-lift" chapter of "Fluid-Dynamic Drag". Results of a more recent analysis (17,e) are plotted in figure 20. Because of viscous interference in the four corners of such combinations (particularly on the upper side) the actual effect is much smaller, however, than theoretically predicted. For comparison, we have calculated a function, assuming that the outboard portions of the wing panels would be ineffective (as a consequence of "complete" flow separation). Real results may be expected to fall inbetween the two lines shown. Pylon- or strut-supported fuel tanks, say at $1/2$ of the half-span of an airplane, can be considered also to be inboard end plates. As tested in (22,a) a 1% reduction of induced angle and induced drag can be found for a pair of tanks at 0.64 of the half-span, with a strut length (measured to the center of the tanks) of almost 5% of the wing span.

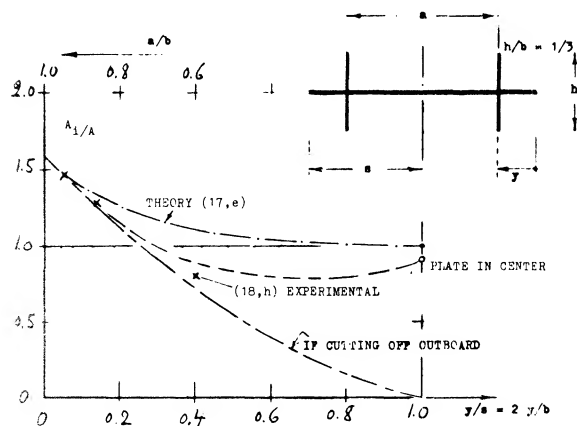


Figure 20. The effective aspect ratio of a wing when moving a pair of end plates inboard.

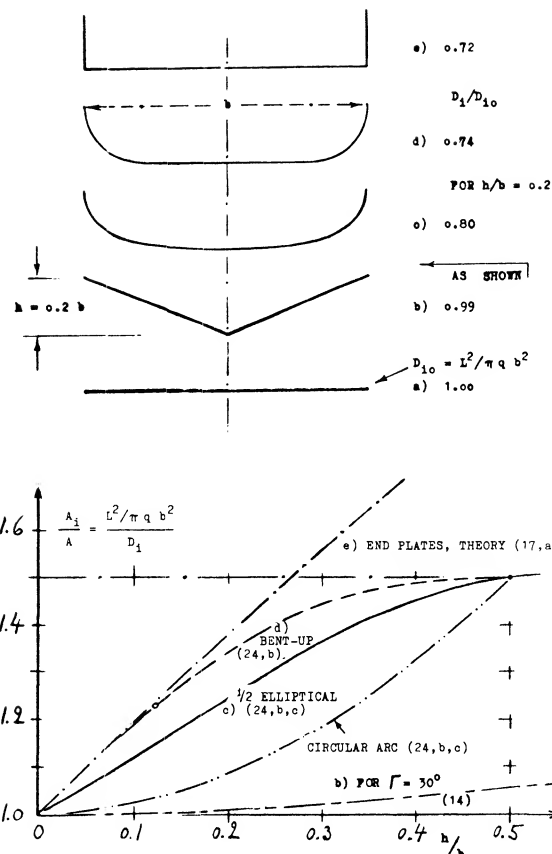


Figure 21. The effective aspect ratio of wings cambered in spanwise direction (24, b, c).

Cambered Span. The original induced-flow theory (1) applies to plane wings. A reanalysis (24) including shapes extending geometrically into the third dimension, points out possibilities of improving the efficiency of wings whose span 'b' (straight line between the tips) might be restricted. As shown in figure 21, the effective aspect ratio increases, meaning that induced angle and induced drag decrease, when cambering in spanwise direction. In comparison to a dihedral wing having the same height ratio, the half-elliptical shape proves to be much more efficient. Of course, as in the case of end plates, the increased "wetted" area of cambered-span wings has to be taken into account when considering their "total" efficiency (in terms of L/D). Except for (a) all of the references under (24) deal with a reduction of the induced drag corresponding to A_1/A as in chapter VII of "Fluid-Dynamic Drag". For practical purposes, we may assume that the induced angle of end-plated wings is one and the same for drag as for lift, expressed by:

$$d\alpha/dC_L = dC_D/dC_L^2 \quad (21)$$

Optimum lift distributions studied in (24) are essentially elliptical.

- (20) Influence of tip tanks on wing characteristics:
a) Howard, North American Aviation Rpt NA-1947-755.
b) NACA. Wind-Tunnel Tests, RM A5F02, L8J04, L9J04.
c) Fahl, Characteristics, RAE TN Aero-2085 (1950).
(21) Analysis of wing-tip tanks:
a) Hartley, Analysis, ARC C'Paper 147 (1952).
b) Weber, Wing and Body, ARC RM 2889 (1957).
c) Robinson, Loading, NACA RM L1953B18.
(22) Pylon-supported tanks or engine nacelles:
a) Pepper, Fuel Tanks, NACA W'Rpt L-371 (1942).
b) RAE, On Swept Wing, ARC RM 2951 (1952).
(24) Cone (NASA) re-analysis of induced flow:
a) Vortex Sheet Deformation, TN D-657 (1961).
b) Induced Drag of Bent-Up Wing Tips, R-139 (1962).
c) Wings With Cambered Span, Rpt R-152 (1963).
d) Bending Moments of Wings as in (c), TN D-1505.

Bent-Up Tips. The result of equation (26) or figure 14, is also included in figure 21. End plates are seen to be more efficient than any continuous spanwise camber leading to the same height ratio. Up to $h/b = 0.1$, wing tips bent-up in the form of a quarter circle (24.b) are equally efficient, however. For example for $A = 5$, the corresponding bending radius would be $1/2$ of the chord of a rectangular wing. As shown in chapter VIII of "Fluid-Dynamic Drag", the interference drag in the corner of an 0010 airfoil bent up (or down) 90° , using a radius not larger than $r = 2t$, or $= 0.2c$, is already zero (at zero lift). How large drag and loss of lift might be, say at the cruising lift coefficient of an airplane, can only be determined by experiment. It is suggested, however, that with a bending radius between $(0.2c)$ and $(0.1b)$ as in the example above, interference would be small, and the effectiveness of a bent-up tip as an end plate would be high (might be the same as theoretically predicted). It is also expected that any bent-down wing tips (or suitably profiled end plates) would not have much of an interference drag.

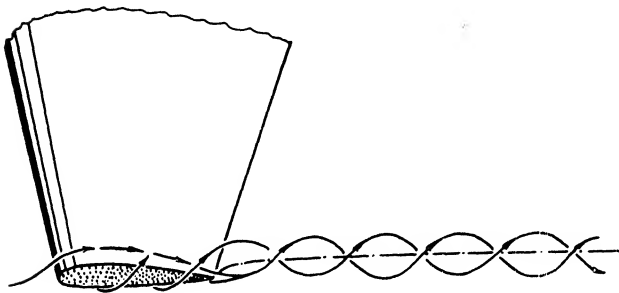


Figure 22 Flow pattern past a wing tip, drawn on the basis of flow observations in a water tunnel (7,a).

Trailing-Vortex Hazard. As discussed in the beginning of this chapter, the characteristics of the trailing vortex, figure 22 and Chapter XI, and its strength determine the hazard effects of large aircraft on other airplanes flying in the vicinity. These hazard effects are especially severe when there is a large spread in gross weight between the aircraft (25,a,c,d). It is thus desirable to alleviate the hazard by reducing the strength or breaking up the trailing vortices. The strength of the trailing vortices depends on the wing loading and thus in the far wake would be the same if all the energy is concentrated in the rolled up tip vortex. Thus, changes in distribution would be expected to have a small effect in alleviating the hazard. The use of part span trailing edge wing flaps, however, does apparently reduce the hazard by a change in lift distribution at a distance of 180 wing chords downstream (25,b). This is probably due to a reduction of the strength of the tip vortex by the generation of second vortex at the flap outboard edge. If the vortex at the flap outboard edge does not combine with the tip vortex, use of flaps may be a practical method of reducing the trailing-vortex hazard in the vicinity of airports.

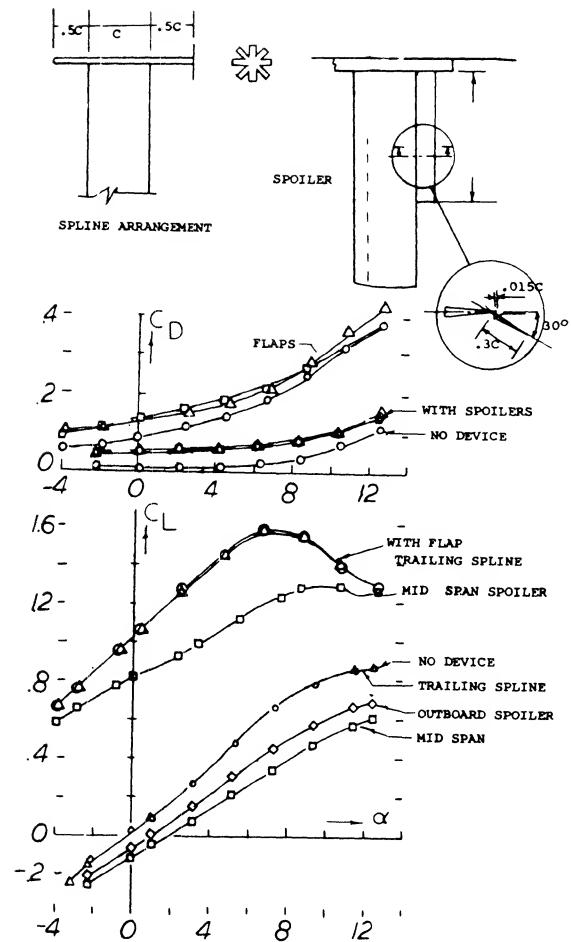


Figure 23. Effects of changes of lift distribution and trailing edge spoiler on lift and drag of a wing.

A second way of reducing the problem of trailing vortices is by breaking up the rotational energy. To accomplish this a trailing spline as illustrated on figure 23 was tested as well as a spoiler. These devices were designed to break up the vortex and did show an improvement to 100 chords downstream; however, the improvement died out at the downstream distances corresponding to 180 chord lengths. It appears that such devices should be designed to take out the rotational velocity of the vortex to be effective. The trailing spline did not effect the lift of the wing but did increase the drag as shown on figure 23.

25. T Wing trailing-vortex hazard
 - a) McGowan, Trailing Vortices of Transport Aircraft, NASA TN-D-829.
 - b) Croom, Trailing-vortex Hazard Alleviation Devices, NASA TN LX-3166.
 - c) Orloff, Vortex Measurements — Swept Wing Transport, JofA/C June 1974.
 - d) Brashers, Aircraft Wake Vortex Transport Model, J of A/C May 1974.
 - e) Chigier, Vortexes in Aircraft Wakes, Sci Amer, March 1974.
 - f) Donaldson, Vortex Wakes of Conventional A/C, AGARD-AR-204

CHAPTER IV — MAXIMUM LIFT & STALLING

The wing area required for a given application is influenced largely by the maximum lift and stalling characteristics of the airfoil sections used. Because of the possibility of mishaps in the event of stalling, the factors effecting the maximum lift and stall of wings are of great importance. The stalling characteristics of airfoils also affects the design of helicopter rotors as well as other types of propulsive devices.

The maximum lift of a wing is defined as that value obtained when a further increase in the section angle of attack gives zero or a negative increase of lift. An airfoil can have two or more values of maximum lift but generally only the first is of importance. A wing is said to stall when as a result of a further increase of the angle of attack there is a loss of lift.

The maximum lift of a wing depends on parameters such as:

- Airfoil section shape
- Operating conditions such as Mach number and Reynolds number
- Wing planform, and twist
- Auxiliary devices such as flaps, slots, etc.
- Influence of the fuselage and propulsion system
- The type of application; that is, fixed wings, helicopter rotors, etc.

The absolute magnitude of maximum lift in the case of wings is generally not as important as the type of stall encountered. A wing with very high maximum lift can stall abruptly, losing a major portion of its lift for a small increase in angle of attack above stall with dangerous consequences. Such a wing would not be as useful for flight as a wing, having a lower C_{Lx} with a more gentle stall. Thus maximum lift and stalling are of primary importance in the application of wings and airfoils. In this chapter only the characteristics of straight wings and single element airfoils will be covered in detail; items such as flaps, slats, sweep and low aspect ratio wings and their influence on maximum lift will be discussed in chapters V, VI and XVI.

1. THEORETICAL AND DEMONSTRATED LEVELS OF MAXIMUM LIFT

An overview of the theoretical values of maximum lift compared to demonstrated levels is desirable before examining the detailed maximum lift characteristics of single element airfoils and wings.

Theoretical Maximum Lift Coefficient C_{Lx} . Theory (1) shows that $C_{Lx} = 1.94A$ but can be no greater than 4π . Thus the C_{Lx} of a two-dimensional wing is 4π . The maximum lift is set by the physical ability of the airfoil to produce circulation. With actual wings and the use of high lift devices the maximum lift coefficient achieved is much less than the theoretical maximum. As shown on figure 1 the maximum lift coefficient demonstrated for a single element airfoil is only 1.5 to 1.6, or 10% of the value theoretically possible. Even with flaps, slats and blowing the demonstrated level of C_{Lx} (figure 1) is only approximately 30% of the ideal. The addition of forced circulation brings the demonstrated level of C_{Lx} reasonably near

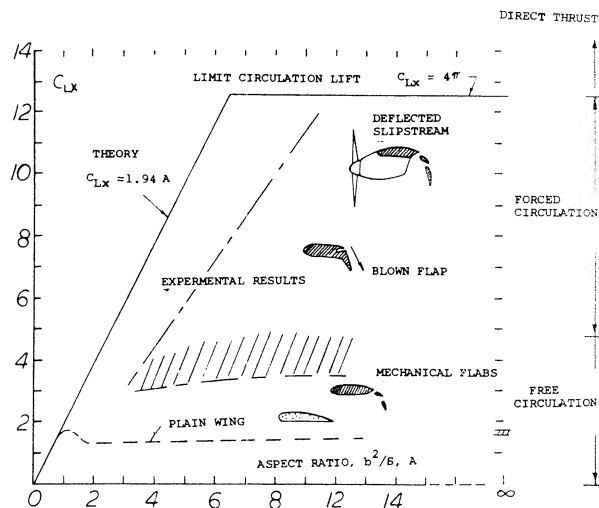


Figure 1. Potential maximum lift as a function of aspect ratio—demonstrated and theoretical.

- (1) Maximum Lift
a) Cone, D. D. Theory NASA TN D-657

the ideal. In this case, however, power is required which could have been used directly to supply lift! Based on the large spread between the theoretical value and the actual demonstrated values of maximum lift, especially in the case of single element airfoils, it would appear that there is considerable room for improvements of this type.

2. THE PHYSICAL MECHANISM OF STALLING

The stall of an airfoil depends on the section shape, thickness ratio and the operating Reynolds number. The flow along the pressure side of the airfoil section is of little importance with regard to maximum lift. On the other hand, as the angle of attack is increased the flow past the suction side develops:

- a) A negative peak in the pressure distribution at or near the leading edge
- b) A strong positive pressure gradient between the negative pressure peak and the trailing edge
- c) A growth of the boundary layer thickness along the chord.

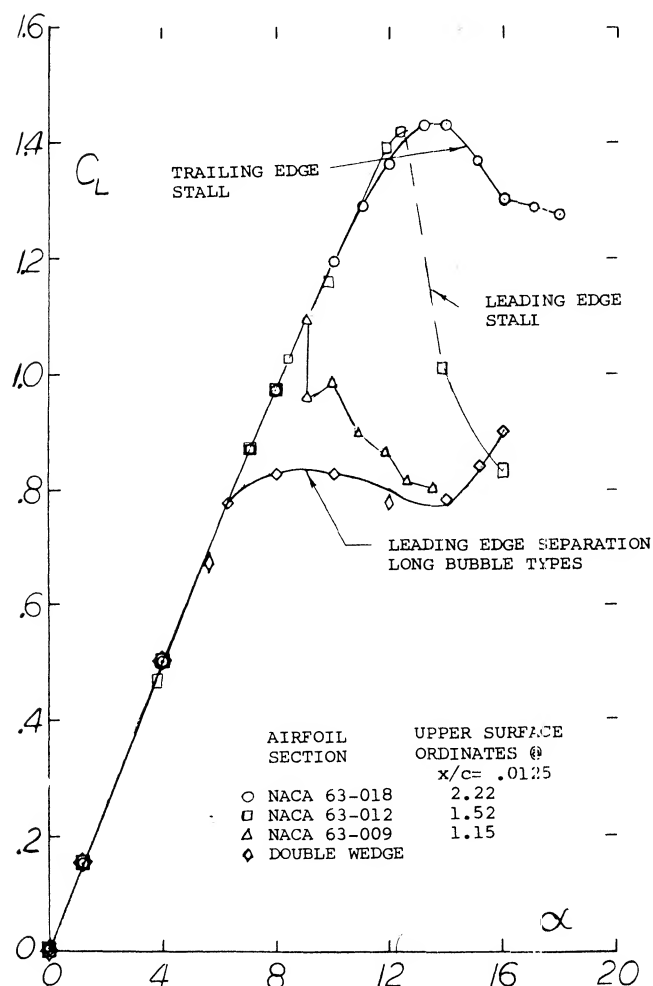


Figure 2. Types of airfoil stall Reynolds number 5.8×10^6 , TN 2502.

With an increasing angle of attack of the section the flow on the suction side of the airfoil develops two weak spots where boundary layer separation is to be expected:

- 1) At the leading edge where the flow must go around the nose section with a corresponding loss of momentum
- 2) Near the trailing edge where an increase in the boundary layer thickness takes place.

Stalling (loss of lift due to flow separation) will originate in one of the two locations, or in both concurrently.

Types of Lift Stall. The lift stall encountered by an airfoil as a result of separation has been classified into three different types:

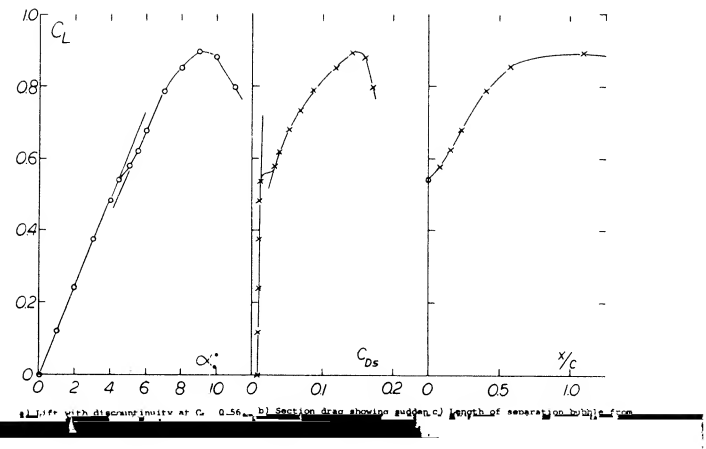
- 1) Leading Edge Separation — Long Bubble Type. This is a gradual stalling of thin sections from a more or less sharp edge by way of a laminar separation bubble and reattachment.
- 2) Leading Edge Separation — Short Bubble Type. Sudden stall is encountered with round nose zero or low camber sections with so-called bubble bursting.
- 3) Trailing Edge Separation. Gentle stalling from separation at the trail edge is experienced with this type. As the stall increases the separation progresses forward from the trail edge.

Each of the above types of stall has a distinct behavior as characterized by the variation of lift as a function of angle of attack, figure 2.

The lift characteristics of a double wedge section, figure 2, illustrates leading edge stall of the long bubble type. Here the variation of lift with α is linear nearly to the maximum and then rounds and continues flat. When leading edge separation of the short bubble type is encountered the lift remains linear to the stall and then drops suddenly as illustrated by the NACA 63-009 section, figure 2. Trailing edge separation is encountered typically with thicker, more rounded nose airfoils, such as the NACA 63-018 type also shown on figure 2.

Thin (Sharp) Leading Edge. The reason for the leading edge separation of the long bubble type is explained by considering the pressure distribution for the wedge section operating at $\alpha = 6^\circ$, figure 3. The flow does get around its sharp leading edge up to angles of attack for a lift coefficient in the order of $C_L = 0.7$. The mechanism through which this is possible, is as follows: Corresponding to the small distance between stagnation point (at the lower side) and leading edge, the boundary layer arriving at that edge, is very thin. The Reynolds number of the flow at the leading edge is also very small. Taking into account the strong negative pressure gradient between stagnation point (where $C_p = +1$) and the leading edge (where C_p possibly = -10) the boundary layer flow

must certainly be assumed to be laminar; and since it is laminar, the flow "around" a sharp leading edge must be expected to separate "immediately". As confirmed by several special investigations (2), laminar separation does take place. However, after separating, the inside surface of the fluid forming the contour of the separated space, turns turbulent. As shown in figure 3, the boundary layer (the sheet of air adjacent to the bubble) then expands in volume because of mixing with the "dead" material in the separated space, thus reducing the size of that space, until the outer flow (including the now thickened boundary layer) re-attaches itself to the upper surface of the plate at some distance behind the leading edge. The presence of the separated space is recognized (as in figure 2) in the



Boundary Layer Transition. At higher Reynolds numbers (above 2 or 3 times 10^5) it can be assumed that laminar separation and the formation of the bubble are reduced, and that re-attachment of the flow is facilitated by camber and thickness (nose radius). The whole bubble mechanism still persists, however, at least under certain conditions, in round-nose sections, although the size and development of the separation bubble may be very limited, and as a consequence the magnitude of the $C_{L\alpha}$ is different. For example, in the 64A010 section reported in (2,b) the chordwise dimension of the bubble is but 0.5% of the chord at $C_L = 1.0$. For practical purposes, the sequence of such minimal separation plus "immediate" re-attachment, obtained within the first 1% of the chord, simply constitutes the transition of the boundary layer from the laminar to the turbulent type of flow. Such transition is susceptible to stream turbulence (as in certain wind tunnels) and to variations of the Reynolds number (3). The maximum lift coefficient increases, therefore, due to turbulence as well as to increasing the Reynolds number. Airfoil sections of this type are very numerous. Among them are the symmetrical NACA 0012 to 0021 shapes, and most of the sections with modest thickness and camber dimensions such as the NACA 2409, 23012, and 64-212.

Bubble Bursting. Leading edge separation of the short bubble type is encountered when the angle of attack of a section is further increased without a further growth of the separation bubble in fact, as documented in (2,b,c,d), the length of the very small bubble (found at higher Reynolds numbers) reduces as the angle of attack is increased. In this condition, the lift continues to grow, essentially along a straight line versus the angle of attack, with hardly any losses. Figure 2 demonstrates this type of lift function very well for the NACA 63-009 airfoil section. However, without any warning, upon reaching a critical condition in which the bubble is strained too much, "complete" separation takes place from near the leading edge. As noted in (2,a) the bubble thus "bursts" into separation (re-attachment fails suddenly). The lift coefficient drops at the same instant, from a maximum to a level which seems to be of the same type as in a stalled thin airfoil section.

Trail Edge Stalling. After eliminating (by using a round nose, increased thickness and/or camber) the flow near the leading edge as the weakest part of the circulating motion of the fluid, another weak region soon develops near the trailing edge. For example, consider the pressure distribution of a 4% cambered airfoil section shown in figure 5,a. On the suction side, three pressure distributions are superimposed:

- (a) a component due to thickness
- (b) a distribution representing lift due to camber
- (c) a peaked contribution due to flow around the nose

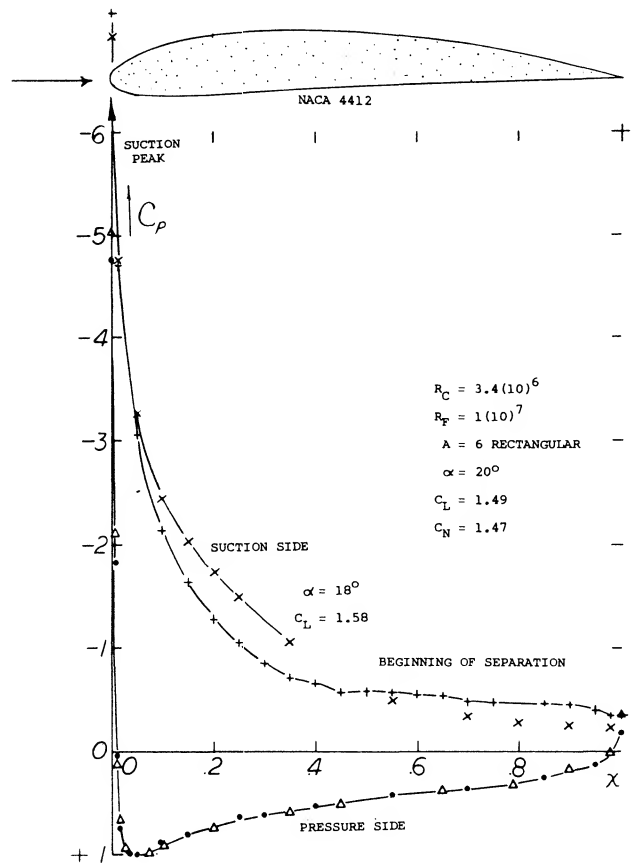


Figure 5. Lifting characteristics of a 4412 section tested (4,e) (5) on the center line of an A = 6 airfoil in the VDT tunnel at $R_f = 4(10)^6$.

a) pressure distribution at an angle of attack slightly beyond that for $C_{L\alpha}$.

Evaluation of (5,b) roughly yields the ratio of the maximum local velocity "w", at the nose of average symmetrical foil sections:

$$w/V \approx 1 + 2 t/c + 0.2 C_L / (r/t) \quad (1)$$

where r/t , the ratio of lead edge radius to thickness, may be between (0.5 and 2.0) t/c . Maximum speed w , maximum dynamic pressure q and the minimum pressure coefficient can be estimated using this equation. Both items

- (3) Regarding the strong effect of transition and/or R -number upon the elimination of laminar-type separation, the mechanism of the drag of spheres may be consulted as described (for example) in Chapter III of "Fluid-Dynamic Drag".

(a) and (b) above produce a positive pressure gradient approaching the trailing edge. Under the influence of this gradient, the boundary layer grows considerably; and at the trailing edge will have a total thickness δ which can roughly be described by

$$\delta/c = 5 C_f + k (C_L)^n \quad (2)$$

where C_f = skin friction drag coefficient, n possibly = 2, k in the order of 10, and $C_f = 0.03$, depending on the thickness and shape of the section used. After growing so much, the boundary layer reaches a critical condition (where it cannot keep moving against the pressure) so that a gradual accumulation of boundary layer material and a corresponding separation of the outer flow from the surface of the foil section take place. The circulation then stops growing with the angle of attack; the lift reaches a maximum.

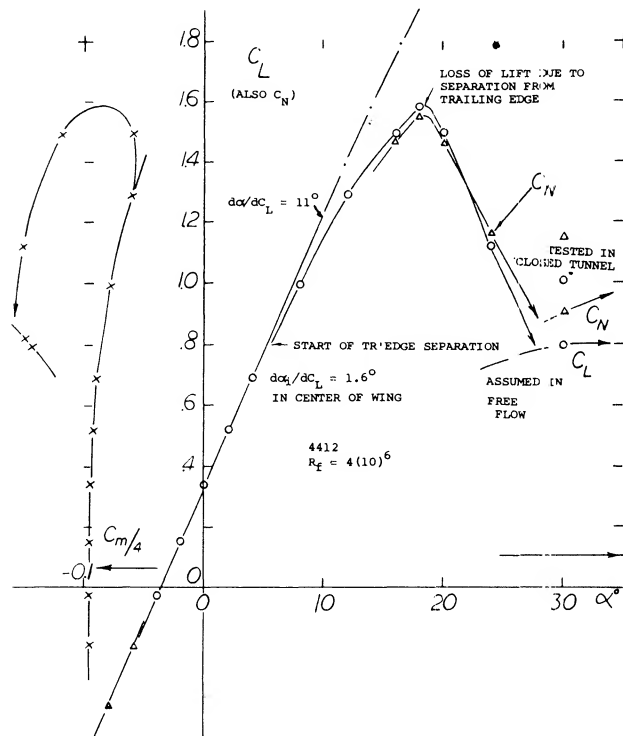


Figure 5. b) C_L (and C_N) integrated from pressure distributions on center line of $A = 6$ airfoil.

As shown in figure 5,b, the NACA 4412 airfoil displays a rounding-over lift function. Thus, *before* reaching its maximum, the lift coefficient diverges from the straight line indicating the beginning of flow separation from the trailing edge. Upon increasing the angle of attack beyond that for C_{Lx} , the lift decreases gradually (and without discontinuity) eventually reducing (at very high angles of attack) to a level or a function corresponding to "full" separation. It should be emphasized that separation in sections of this kind, proceeds from the trailing edge toward the leading edge; and that stalling from the leading edge is only obtained at the very high angles mentioned.

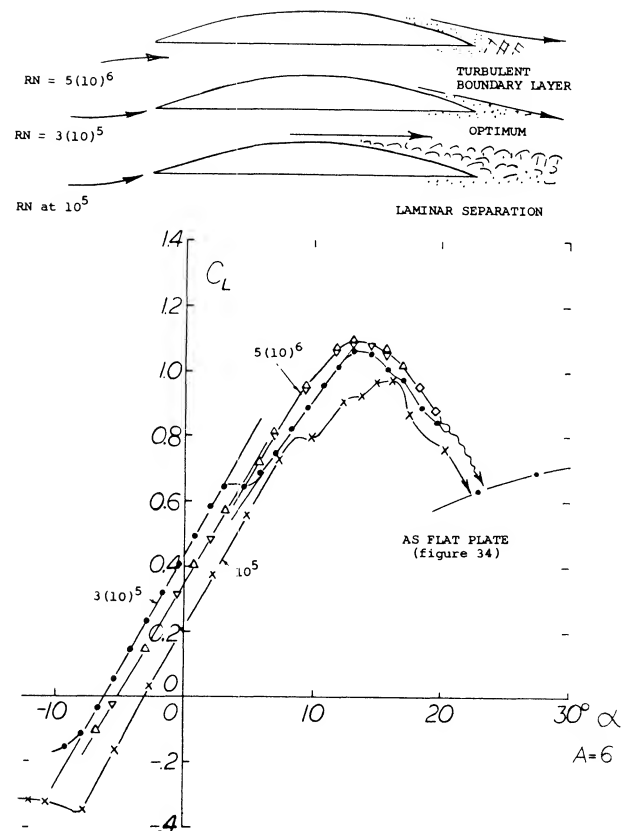


Figure 6. Lift characteristics and mechanism of stalling of a 10% circular-arc section as tested (6,d) at three different Reynolds numbers, in the British Compressed Air Tunnel ($A = 6$).

Circular Arc Sections. The mechanism and details of trailing-edge stalling have not been studied as much as leading-edge stalling. Some further insight can be gained, however, by considering the data for the circular-arc section shown in figure 6. The well-defined characteristics of essentially sharp-edged plates change to a degree as a sufficient amount of thickness is added, particularly in the form of an arched "back". Keeping the lower side flat, their camber ratio is equal to $\frac{1}{2}$ the thickness ratio. With maximum thickness located at 50% of the chord such sections have a considerable trailing edge "wedge" angle "at" the suction side, easily leading to separation from that edge. In other words, thickness, camber and the location of these two at 50% of the chord, combine to make the flow along the suction side comparatively sensitive and weak as it approaches the trailing edge. Specific characteristics of the circular arc section of figure 6 are as follows:

(a) At a Reynolds number of but 10^5 (in the comparatively turbulent CA'tunnel) laminar-type separation seems to take place from the minimum-pressure point at or somewhat ahead of the 50% chord point. At this condition the minimum drag coefficient is 0.02, confirming separation.

(b) At $R_c = 3(10)^5$ and the angle for minimum drag the lift coefficient is 0.575, which is equal to the potential flow theory $C_{Lsym} = 0.575$, as in figure 27, of Chapter II, for $f/c = 0.5$. The drag coefficient ($C_{DS} = 0.008 = \text{minimum}$) obviously confirms that the flow is fully attached and we have the condition of symmetrical flow.

(c) Upon increasing the Reynolds number above $3(10)^5$, the lift coefficient for minimum drag reduces slowly; and becomes $C_{Lo} = 0.46$ at $5(10)^6$. An increase of skin friction more turbulent along the upper side of the section ($C_{DS} = 0.009$) is evidently responsible for reduced boundary-layer momentum approaching the trailing edge. As a consequence, pressure recovery is somewhat deficient, and circulation and lift are somewhat reduced.

Zero-Lift Angle of Attack. The lift-curve slopes shown in figure 6 are practically the same at all three Reynolds numbers considered. However, the zero-lift angle of attack varies from -3° at a Reynolds number of 10^5 , up to a maximum of -60° at $RN = 3 \times 10^5$, and slowly down again to -5° at $RN = 5(10)^6$. This variation of the zero lift angle corresponds to that of the skin-friction drag coefficient, down from the laminar separated value at 10^5 , to a minimum part laminar and part turbulent value in the vicinity of $3(10)^5$, and somewhat up again to a mostly turbulent level at $5(10)^5$. We can also make the prediction that skin friction would decrease again, and that lift would increase again, upon increasing Reynolds number above about 10^7 , provided that neither surface roughness nor compressibility would interfere. It should be noted that all these variations are a consequence of beginning trailing edge stalling. The report (6,d) from which the results in figure 6 are taken, also contains data on circular-arc sections with different thickness ratios (while f/c always = 0.5 t/c). Sections with ratios $t/c = 15$ and 20% show the variations as discussed above in stronger form, while a 5% section does not show much of a variation at all.

Rounding of Leading Edge. The report (6,d) also gives an explanation for the fact that sharp-edged circular arc sections (as frequently used in marine propellers) do have the same efficiency as similar sections with rounded noses where, and if, used at lift coefficients close to C_{Lsym} . However, when using the section of figure 6, at a lift coefficient of 1.0, the section-drag coefficient of a suitability rounded foil shape (with r/c between 1 and 2%) is but half ($C_{DS} \approx 0.017$) of that of the original sharp-edged section ($C_{DS} = 0.038$) at $R_c = 4(10)^6$. Rounding also has an effect upon the maximum lift coefficient of the sections tested at Reynolds numbers above $(2 \text{ or } 3) 10^6$. When rounded, the 10% section (as in figure 6) thus exhibits a maximum $C_{Lx} = 1.55$, at $R = 4(10)^6$, rather than ≈ 1.10 as at lesser Reynolds numbers, or as in the original condition (with sharp leading edge).

3. CORRELATION PROCEDURES OF TEST DATA

From the discussion of the types and mechanism of stalling it is apparent that it is a separation phenomenon within the boundary layer, and thus the airfoil shape and operating Reynolds will have a large influence on the results. Because of this the test conditions, including tunnel turbulence, also affect the results. Since we are interested in the application of airfoils in free air conditions, the consideration of wind tunnel turbulence must be made before satisfactory results concerning shape and R'number can be presented. It will then be possible to correlate the results between various tunnels and will provide a reliable basis for comparisons with any newly developed theories.

Also important in the application of wind tunnel test results are the test conditions with regard to wall location if the test section is open or closed jet. Airfoils tested between walls will give two-dimensional results that must be corrected for application to a three dimensional wing. The use and correlation of such data requires that the airfoil has been tested with ends sealed as this can influence the results, especially with regard to C_{Lx} . Data published before 1950 were often influenced by end leakage problems, and caution must be exercised in their use.

- (4) Airfoil sections as a function of R'number:
 - a) Jacobs, In VDT, NACA T Rpt 586 (1937).
 - b) Relf, In the British CAT, ARC RM 1706 (1936).
 - c) See references (7,a) (11,c).
 - d) Jacobs, Thick Sections in VDT, T Rpt 391 (1931).
 - e) Pinkerton, 4412 Pressure Distribution, NACA TR 613 (1938).
 - f) AVA Gottingen, Ergebnisse III (1920) p. 58.
 - a) Pinkerton, 4412 Distribution, NACA T Rpt 613.
 - b) Kochanowsky, Theoretical, Ybk D Lufo 1940 p. I-72.
 - c) Schrank, Collection of Data, Ringbuch Luft Tech, Rpt IA11 (1938).

- (5) Pressure distribution around foil sections:
 - a) Pinkerton, 4412 Distribution, NACA T Rpt 613.
 - b) Kochanowsky, Theoretical, Ybk D Lufo 1940 p I-72.

- (6) Maximum lift of sharp-edged sections:
 - a) Thin Plates and Circular Arcs, Erg TV AVA Gottingen.
 - b) Doetsch, Modified Biconvex, Ybk D Lufo 1940 p. I,54.
 - c) Circular-Arc Foil Sections, Bull Serv Tech Aeron (Belgium) 15 (1935).
 - d) Williams, Circular-Back Foils, ARC RM 2301 (1946).
 - e) See also references under (35).
 - f) Williams, 5% Biconvex in CAT, ARC RM 2413 (1950).

Wind Tunnel Test Conditions. Stream turbulence, found in many wind tunnels, considerably increases the $C_{L\alpha}$ of most of the commonly used sections. This type of turbulence can be of practical interest, such as the case of propeller slipstream effects on a wing. Figure 7 presents the maximum lift coefficient of a given airfoil section as tested in several wind tunnels having different degrees of stream turbulence. Turbulence evidently affects the transition of the boundary layer from laminar to turbulent flow so that the bubble bursting previously described is postponed to higher lift coefficients. In this manner, turbu-

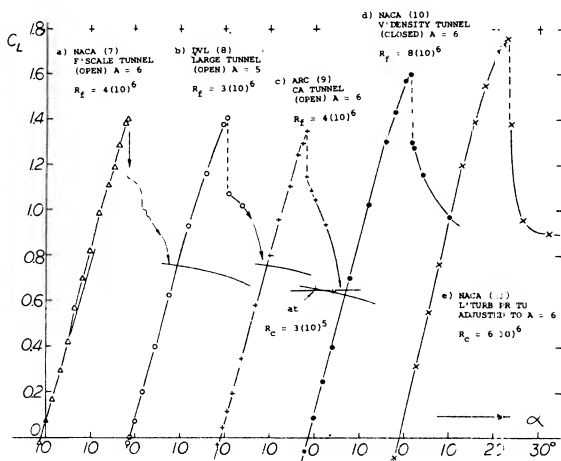


Figure 7. Lift function of 23012 airfoils as tested in wind tunnels differing in Reynolds number, degree of stream turbulence and stream deflection. Comparison in different tunnels:

a) FST and DVL, same type tunnels, same result, including reduced L'curve slope to $C_{L\alpha} = 0.4$ or 0.5 (must have b'layer reason).
 b) Turbulent VDT does *not* show variation of L'curve slope; $C_{L\alpha}$ = increased because of turbulence; but type of stall preserved. For same R'number = $8(10)^6$, the Low-Turbulence Pressure Tunnel (38) indicates $C_{L\alpha} = 1.79$, caused by effective camber.
 c) In the 2-dimensional Low-Turbulence Tunnel, $C_{L\alpha}$ is increased to a lesser degree by R'number ($C_{L\alpha}$ is tested in that tunnel as 1.61, at $3(10)^6$). Effective camber (as against $A = 6$) is $3.3(1.61) = 5.5\%$. Figure 14 suggests a corresponding maximum increase $C_{L\alpha} = 0.15$.

lence does something which is otherwise only obtained by increasing the Reynolds number. Consequently, a method for correlating wind tunnel data with free stream conditions has been proposed (12,a). This method consists of multiplying the actual Vc/τ by a so-called turbulence factor "F", in order to obtain the effective number $R_F = "F" R_c$. The turbulence factor suggested to be used is

$$"F" = (10) / R_{crit} \quad \text{where } k \approx 4, \text{ and} \quad (3)$$

where R_{crit} = Reynolds number of a sphere used to calibrate the particular wind tunnel, at the speed where the drag coefficient of that sphere passes through the point where either $C_D = 0.3$, or where the pressure at the rear side of the sphere (12,b) is equal to the ambient pressure in the test section of the tunnel. The most turbulent tunnel is the NACA's Variable Density Tunnel (13) where " F " ≈ 2.7 (in its rebuilt condition, since 1929, see NACA TR 416), corresponding to root-mean square velocity fluctuations in the order of 2% of the tunnel

- (9) Airfoil sections tested by British ARC:
 - a) Jones, 0015 and 0030 in CAT, RM 2584 (1952).
 - b) Hilton, 18 Sections High Speed, RM 2058 (1942).
 - c) Williams, Strut Sections, RM 2457 (1951).
 - d) See also references (5) (28,c) (40,b), (7,c), Chapter II.
 - e) ARC, Investigations in the Compressed Air Tunnel, RM 1627 (R'number), 1635 (RAF-34), 1717 (RAF-69+89), 1771 (Airscrew sections), 1772 (RAF-34), 1870 (Joukowski), 1898 (23012), 2151 (23012 wing), 2301 (circular-arc backs), 2584 (0015 + 0030).
- (10) Investigations and results on 23012 airfoils:
 - a) Jacobs, in FS and V'Density Tunnels, Rpt 530 (1935).
 - b) Jacobs, in V'Density Tunnel, NACA T Rpt 537 (1935).
 - c) Jacobs, Airfoil Series in VDT, NACA Rpt 610 (1937).
 - d) NACA, with Flaps, Rpt 534 (1935) & 664 (1939).
 - e) ARC, In CAT, RM 1898 (1937); also RM 2151 (1945).
 - f) Doetsch, In DVL Tunnel, Ybk D Lufo 1939 p. I-88.
 - g) The foil section 23012 (figure 7) is outstanding in regard to maximum lift (see figure 19). The tested $C_{L\alpha}$ corresponds to that of other sections having 4% camber, while 23012 has only 1.8%. The pitching moment coefficient due to camber is but -0.01 , which is $\sim 1/5$ of that of the corresponding conventionally cambered section. Unfortunately, 23012 is not considered to be desirable at higher speeds.
- (11) Foil sections tested in two dimensions by NACA:
 - a) Doenhoff, Low-Turbulence Pressure Tunnel, T Rpt 1283.
 - b) Abbott & von Dornhoff, Collection of Data, T Rpt 824. (1945); also "Wing-Section Theory", McGraw Hill 1949.
 - c) Loftin, At Very High R'Numbers, TN 1945 (1949) & Rpt 964 (1950); also RM L8L09 with results on 34 sections.
 - d) See also reference (37,b).
 - e) Loftin, 64-010 modified, TN 3244 (1954).
 - f) McCullough, 0006/7/8 in Ames Tunnel, TN 3524 (1955).
 - g) NACA, 64-x10 sections, TN 2753, 2824, 1945, 3871; T Rpt 824, 903.

speed. Modern tunnels such as the NACA's special low-turbulence tunnels (having fluctuations below 0.1%) would have factors only slightly above unity. Although there are strong reservations against using the turbulence factor, the following values are for a number of the more important wind tunnels:

wind tunnel	type	stream dim. ft	V, ft/sec	c, ft	R _c	"f"
NACA, VDT (*)	closed	5 ft ϕ	75	0.4	3 (10)	2.7
Full-Scale Tunnel	open	30x60	100	6.0	4 (10)	1.1
Low T Pressure TDT	closed	3x7.5	250	2.0	6 (10)	1.0
AVA, 2.25 m Diameter	open	7.4 ϕ	30	0.7	4 (10)	1.2
DVL, "Large" Tunnel	open	16x23	130	2.6	3 (10)	1.1
ARC-NPL-CAT (*)	open	6 ft ϕ	80	0.7	4 (10)	2.1

(*) variable-density or compressed-air tunnels with up to 10 and 25 at as operating pressure.

The airfoil chords, speeds and Reynolds numbers listed indicate typical, or possible, testing conditions in each tunnel.

Variation of "f": Stream turbulence most certainly helps the flow pattern past typical airfoil sections to get qualitatively above the critical phase (to be discussed later) between $R_c = (1 \text{ and } 2)10^5$. However, any quantitative agreement of $C_{L\alpha}$ values thus obtained (7,a) (10,a) (12,a) only applies to a particular group of foil sections (of the sharp edge bursting-bubble type of stalling). Comparison of VDT results of sections such as the 0006 to 0015, 2412, 23012, 4412 to 21, Clark Y and RAF-34 with maximum lift coefficients obtained in low-turbulence tunnels, extrapolated to zero turbulence, suggests "f" factors between 2.8 and 3.4 for that particular tunnel (rather than 2.7 as recommended). The factor does not "work", on the other hand, for cambered and thicker sections (with typical trailing-edge type stalling) such as Gö 387, 23015, 2415 to 21. In other words, the factor is not uniform. In its form as per equation (3) it only represents the degree of turbulence. A really reliable correction factor should also take into account the specific influence of

the turbulence on the individual section shape. Since the critical Reynolds number of the sphere reduces as the tunnel speed is reduced (see Chapter X of "Fluid-Dynamic Drag"), it must also be suspected that the turbulence factor (in constant-pressure tunnels) varies approximately as

$$"f" \sim 1/\sqrt[n]{R} \quad (4)$$

where $n \approx 4$ in the carefully designed tunnels, $n \approx 3$ in average-quality test streams, and $n \approx 2$ in very turbulent conditions (14). This influence of speed can be considerable when investigating one and the same airfoil section at different Reynolds numbers, obtained by varying the tunnel speed.

Low-Turbulence Tunnels. It is reported in (12,e) that the turbulent fluctuations in the TDT facility increase with the operating speed from 0.02 to 0.15%. This variation is opposite to that indicated by equation (4). It seems that the source of turbulence in this elaborately designed tunnel is acoustic (from the fan; power and blade frequency of which increase with speed). It is also mentioned in (12,e) that turbulence reduces as the operating pressure is increased. In terms of the Reynolds number, this trend is again opposite to that in other tunnels where the Reynolds number is varied by means of tunnel speed. In conclusion, tunnels built to a low turbulence level do not seem to follow equation (4). After all this introduction, it certainly must be clear that a realistic presentation of $C_{L\alpha}$ values as a function of effective Reynolds number is problematic. We have applied turbulence factors similar to those listed above to the graphs of this text wherever this seemed to improve correlation of results from different sources. Regarding the variation of "f" with speed (equation 4), factors different from (that is, larger than) the "standard" values have only been used wherever this seemed to eliminate obvious discrepancies. All this is somewhat arbitrary. It is believed, however, that the $C_{L\alpha}$ functions thus obtained are more realistic than those presented to date in any other place.

Tunnel Corrections. The dimensions of the wind stream provided in wind tunnels are limited by reasons of economy (size and power of the installations). Corrections for the limited diameter of an open jet or the restraining walls in closed-type test sections have routinely been applied before presenting the lift and drag results. Since this is not a text on testing techniques, we will not go into the details of such corrections. There is one aspect, however, for which there is usually no correction applied; and that is the curvature (in contradistinction to deflection) of the stream of air passing through the tunnel. This curvature is caused by the interaction of the lift of the airfoil model

(12) Influence of stream turbulence:

- a) Platt, Turbulence Factors, NACA T Rpt 558 (1936).
- b) Dryden, Turbulence Companion of R'Number, J A Sci 1934 p. 67; also Wind Tunnel Turbulence, NACA T Rpts 320, 342, 392, 581 (1929/37).
- c) Milliken, Turbulence Aircraft Engg 1933 p. 169; Maximum Lift, ASME Trans 1934 p. 815.
- d) Hoerner, Influence on Spheres, Lufo 1935 p. 42 (NACA Memo 777).
- e) Dryden, Low-Turbulence Tunnels, T Rpt 940 (1949).
- f) Jacobs, NACA VDT Tunnel, T Rpt 416 (1932).

tested with the boundaries or walls of the test section. For wings of aspect ratios of 5 or 6, this effect causes a change in the effective camber ratio (discussed below) on the order of

$$\Delta(f/c)_T = -0.2\% C_{LX} \quad (5)$$

where the + sign is for closed, and the - sign for open tunnel test operations. For example, for $C_{LX} = 1.5$, the difference is $\Delta(f/c) = -0.3\%$. No direct attempt has been made, however, in the graphs presented later, to correct for this effect.

Effective Camber in Wind Tunnels. In wings of finite aspect ratio, the flow past the sections is deflected in the longitudinal direction, corresponding to the induced angle of attack. In comparison with two-dimensional conditions, the leading edge of a wing is, therefore, at a higher local angle of attack than the trailing edge, by the value of α_i . This effectively reduces the amount of camber of the airfoil as installed on the three dimensional wing. In terms of effective section camber, the difference may then be

$$\Delta(f/c)\% = -25 \alpha_i = -2.5 C_L / \pi A \quad (6)$$

For example, at an aspect ratio $A = 6$, the difference is $-1.3\% C_L$, which is in the order of -2% at C_{LX} . When testing such an airfoil in an open-throat wind tunnel flow conditions are also affected, as indicated by equation (5). On the other hand, when investigating an airfoil model in a two-dimensional closed-type wind tunnel, final downwash is prevented. The floor of the tunnel produces an effect similar to the "ground" discussed in the Chapter III, and the ceiling of the test section doubles that effect. Conditions in the NACA's two-dimensional tunnels (11) appears to increase effective camber of foil sections in comparison with those of airfoils in free flow. For aspect ratios between 5 and 6, the camber change is

$$(f/c)\% \approx (1.4 + 0.2) C_L = 1.6\% C_L \quad (7)$$

where the second term indicates the wall effect similar to equation (5). For a value of $C_{LX} = 1.3$, a difference in effective camber on the order of 2% (1) is thus found between tunnel and free flight. This conclusion is substantiated by comparing maximum lift coefficients obtained at the same effective Reynolds number: (a) in the Low-Turbulence Pressure Tunnel (11), and (b) on finite-span wings having the same foil sections tested in the same tunnel (11,b), or in different tunnels (7) (10). One example (15) is included in figure 7. Since airfoil sections are "always" used in three-dimensional devices (such as wings in particular), two-dimensional results obtained from testing airfoils between the walls in closed-type test sections do not appear to be realistic. We have, therefore, primarily

evaluated test data for airfoils on wings having finite aspect ratios of 5 or 6. However, quite a number of test points from (11), corrected (that is, increased) in effective camber to free flight conditions of an airplane wing by adding camber as per equation (7), have been included in the various graphs. All such results were evaluated for, and are classified by, their effective camber ratio.

Aspect Ratio. It is repeated at this point that all maximum lift coefficients presented in the various graphs (unless otherwise noted) are those, or are meant to represent those, of rectangular wings of aspect ratio between 5 and 6 (rather than of airfoil sections). Using equation (6), it can be estimated that the maximum lift coefficient of the wing sections represented in figure 14 varies as a function of the effective camber ratio, roughly corresponding to

$$d(\Delta C_{LX})/d(1/A) \approx -0.5 \quad (8)$$

The difference between a wing with $A = 5$ in free flow, and a foil section in two-dimensional tunnel flow, is then $C_{LX} \approx -0.05$. That is, the C_{LX} of an airfoil with $A = 5$ or 6 is less than that of the foil section in a two-dimensional stream. By that amount on the other hand, see (15).

4. MAXIMUM LIFT AS A FUNCTION OF SHAPE AND REYNOLDS NUMBER

As previously noted, the airfoil shape and the operating Reynolds number strongly influence maximum obtainable lift. Also influenced is the variation of C_L with angle of attack or the type of stall encountered by the airfoil. These characteristics are a function of the type of boundary layer and its thickness variation along the chord.

Principles. Analysis of boundary layer development along the suction side is very involved. The methods available for predicting the value of the maximum lift coefficient, say as a function of section shape, are lengthy and involved and require the use of high speed computers, yet are not completely reliable. For this reason, statistical information are presented in this section to provide an insight of the available data. Certain guiding principles can be stated, however, and it can be said that C_{LX} depends:

- a) on the sum of the momentum losses incurred along the suction side
- b) on the values of the skin friction drag coefficient
- c) on the location of the boundary layer transition point along the suction side

Boundary layer transition and drag coefficient are both a function of Reynolds number and of surface roughness. Momentum losses are, of course, a function of shape (as explained to some degree in the "stalling" section). Transition from laminar to turbulent boundary layer flow can be strongly affected by wind-tunnel turbulence, or it can be brought about on purpose by stimulation (surface roughness around the leading edge).

Stall Type Prediction. It is useful to determine the type of stall that will be encountered. Prior to discussing the effects of airfoil shape and Reynolds number in terms of the individual parameters. For airfoils such as the NACA four and five digit types, as well as the NACA 6 series, the type of stall encountered is a function of the Reynolds number and the vertical ordinate at the 0.0125% chord, (see figure 8). This curve applies for smooth airfoils and shows the effects of camber and leading edge radius on the type of stall. Note the importance of leading edge radius and the secondary effects of Reynolds number.

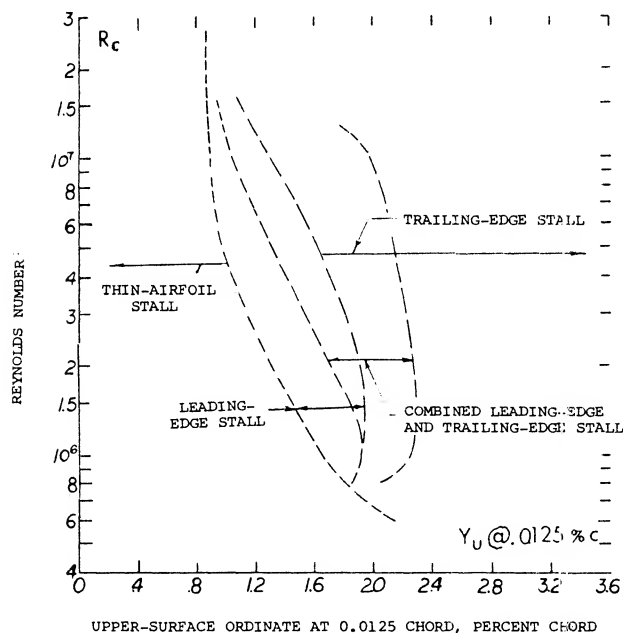


Figure 8. Low speed airfoil stalling characteristics correlated to Reynolds number and upper surface ordinate at 0.0125 chord station.

Figure 8 is a generalized curve and does not predict the stall type for all airfoils. One notable example is the NACA 23xxx series which have blunt leading edges so that the upper surface ordinate at 0.0125% chord is high, indicating trailing edge stall. However, the stall shown in figure 7 for the 23011 section is sudden and sharp, indicating leading edge stall. In spite of this problem, figure 8 is useful in the majority of cases.

- (13) Airfoils with $A = 6$ in NACA V'Density tunnel:
- Jacobs, 78 Related Sections, T Rpt 460 (1933)
 - Jacobs, Function of R'number, T Rpt 586 (1937).
 - Jacobs, Various Corrections, T Rpt 669 (1939); this report is the best of the series.
 - Pinkerton, Various Sections, T Rpt 628 (1938).
 - Jacobs, 23012 Type, see references (10,b,c).

C_{LX} As a Function of Nose Shape. As previously indicated, the flow at the leading edge is critical with regard to separation, and therefore maximum lift. This is illustrated by considering symmetrical airfoils in which case the flow about the leading edge is a function of forebody shape, or in this case nose radius (see equation 1).

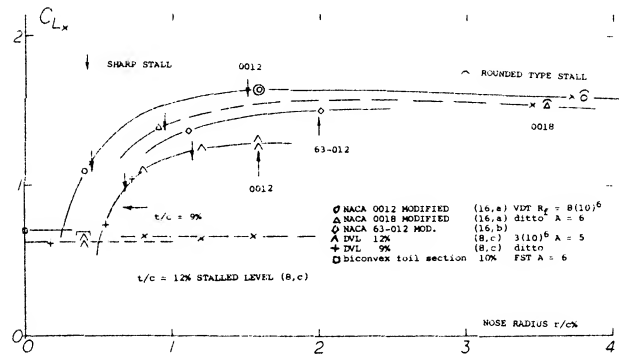


Figure 9. Maximum lift of symmetrical airfoil sections, as a function of their nose radius ratio r/c .

Maximum lift coefficients are plotted versus the nose radius ratio in figure 9. The optimum radius (yielding the peak maximum lift coefficient) is found to be between 1.5 and 2.0% of the chord; and it seems this size radius applies to all thickness ratios between 6 and 18%, results of which are plotted. Nose radii on this order are provided in the NACA 0012 and 63-012 airfoils. From figure 9 it would therefore appear to be advisable to double the nose radius of 4-digit foil sections having thickness ratios between 6 and 9% to improve C_{LX} , while it might do no harm to reduce the radius in sections which are thicker than 15%. Note, however, that camber should also be considered in connection with the nose radius. An extreme example of increased nose radius is shown in figure 10. While C_{LX} is duly increased, C_{Dmin} may also be increased, particularly in comparison with a same-thickness airfoil section providing there is some laminarization of the flow, such as the NACA 65-006 for example. As a consequence the parameter of merit, C_{LX}/C_{Dmin} , of the highly round-nose section is not in any way higher than a comparable 63/64/65 series section.

- Suppose there is a turbulence factor reported, presumably correct for the tunnel's "cruising" speed, and the tunnel is used at $1/8$ of that speed. Corresponding to $\sqrt[3]{8} = 2$, the factor should then be doubled; and when the factor was 1.5, for example, it should be 3 for the low speed assumed.
- The C_{LX} value in two-dimensional flow can be expected to be some 6% higher than the average in a wing with $A = 6$. However, the boundary layer along the lateral walls in a two-dimensional tunnel can be suspected to cause some reduction of the average maximum lift tested.
- Influence on stalling of section nose modifications:
 - Modification of 4-Digit Sections, see (13,a,3)
 - Kelly, 63-012 Section, NACA TN 2228 (1950).
 - Doetsch, Symmetrical Sections, see (8,a).
 - Maki, 64A010 Modifications, TN 3871 (1956).
 - Racisz, Round-Nose 6% Section, NACA RM L53J29.

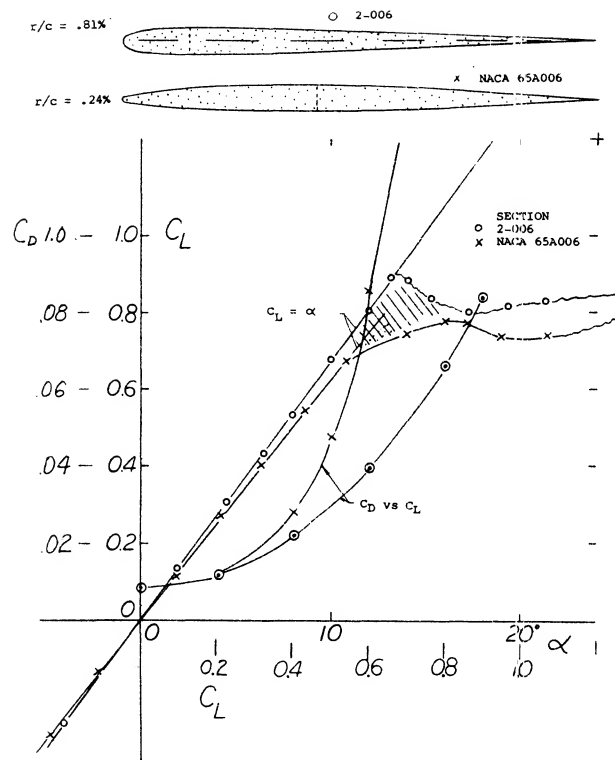


Figure 10. Lift and drag of two 6% thick airfoil sections differing in nose radius, tested in $A = 4$ tapered wings, on fuselage body at $R_c = 5(10)$ in a closed tunnel (16,e).

Sharp Leading Edges. As explained by the thin-airfoil stall mechanism, boundary-layer transition can be precipitated by a sharp leading edge. This is evidently so in flat, and/or cambered plates, at Reynolds numbers below 10^5 (see figure 11). In that range, such plates, and/or very thin and/or sharp-edged foil sections, develop much higher maximum lift coefficients than any conventional (round-nosed) airfoil shapes. This fact seems to be the reason and/or the explanation why insects and some birds do have thin and possibly sharp-edged wings (12). Birds may also have some turbulence-stimulating roughness (fuzz) which could be particularly useful along the upper side of the leading edge. The jib of a small sailboat also seems to fall into the range below the critical Reynolds number, at least in light breezes, and certainly when trying to get out of a calm. In other words, the shape of a sail stretched from a wire or a reinforced seam, is an optimum, at least below $R_c = 10^5$. Another example where a sharp leading edge has a beneficial effect is the circular-arc section (as frequently used in marine propeller blades) when used at lower Reynolds numbers.

- (17) A variety of wing sections can be found in:
- Ergebnisse AVA Gottingen, 4 volumes (1920/32).
 - Louden, Collection of Foils, NACA T Rpt 331 (1929).
 - ARC, RAF-34, RM 1071, 1087, 1146, 1635, 1708, 1772 (1927/37).
 - Characteristics of airfoil sections from all over the world, at lower or intermediate R numbers, have been collected and presented in NACA T Rpts 93, 124, 182, 244, 286, 315 (1920 to 1929).

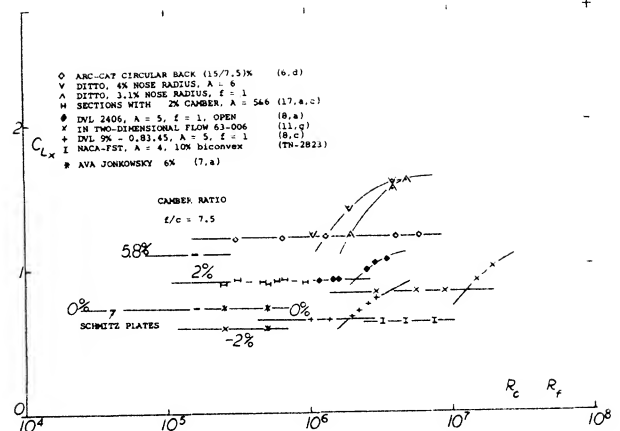


Figure 11. Maximum lift of rectangular airfoils as a function of Reynolds number, (A) sections with sharp leading edges.

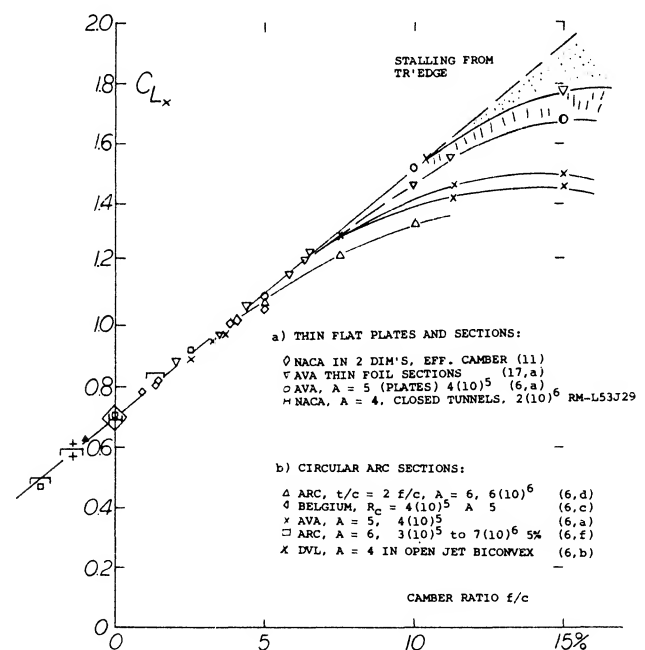


Figure 12. Maximum lift coefficient of sharp-edged sections as a function of their camber ratio:

- thin plates, tested in $A = 5$
- circular-back airfoils in $A = 6$
- biconvex and double-wedge sections.

Effect of Camber. Where camber is used, stalling and C_{Lx} become a function of the section-nose curvature between the leading edge and the upper (suction) side. This curvature is related to the nose radius, r/c , and the camber ratio, f/c , and increases with f/c . The flow around the leading edge of a thin plate can obviously be facilitated by bending the section "nose" into the oncoming flow. At higher Reynolds numbers, laminar separation and the bubble-plus-re-attachment mechanism might then be minimized. For thin sharp-edge sections and airfoil sections, the C_{Lx} increase is given as a function of camber ratio on figure 12. For practical purposes, the values reached seem to be independent of the Reynolds number, providing that the leading edge is reasonably thin (and the camber not too high).

Camber Ratio. No distinction has been introduced in all graphs presented with regard to the location of maximum camber along the chord. The differences in maximum lift for airfoil sections having their maximum camber located between 30 and 50% of the chord are comparatively small. The main effect of camber is the actual amount of camber. This is illustrated by a few experimental points obtained from a two-dimensional wind-tunnel set-up (11) plotted against camber ratio figures 13 and 14. After adjustment to $A = 5$ or 6 according to equation (7). Characteristics of thin airfoils, with $t/c = 6$ and 9% are presented in figure 13. It is seen that for camber ratios between plus and minus 1% their maximum lift coefficients reduce to the fully stalled level indicated by a straight line connecting points obtained at very high angles of attack (on the order of 30°). The practical use of thin and cambered sections in airplanes is limited by structural considerations. For certain other applications, such as turning vanes in ducts or turbines, they may profitably be used at lift coefficients compatible with their camber ratio. Airfoil shapes with thickness ratios of

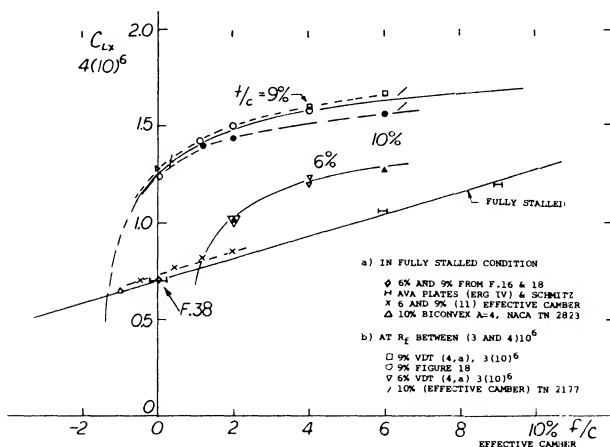


Figure 13. Maximum lift coefficient of airfoils having thickness ratios of 6 and 9% respectively, as a function of their camber ratio:

a) in fully stalled condition.

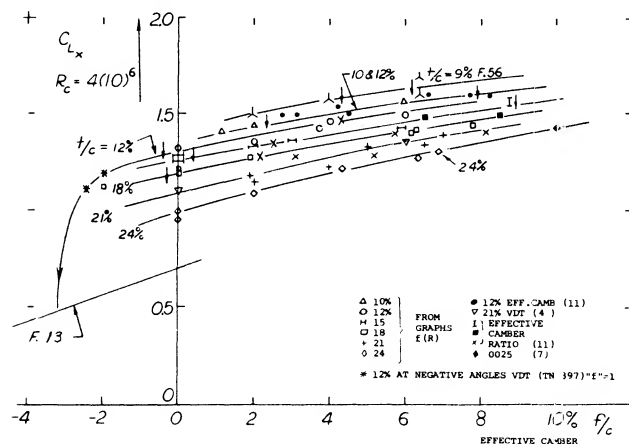


Figure 14. Maximum lift coefficient of airfoils having thickness ratios between 12 and 24%, tested at $R_c = 4(10)^6$, as a function of their camber ratio.

12%, and above, represented in figure 14, fall entirely above the stalled level indicated in figure 13. Their maximum lift coefficients grow steadily as a function of camber, to the highest effective camber ratios tested, on the order of 10%.

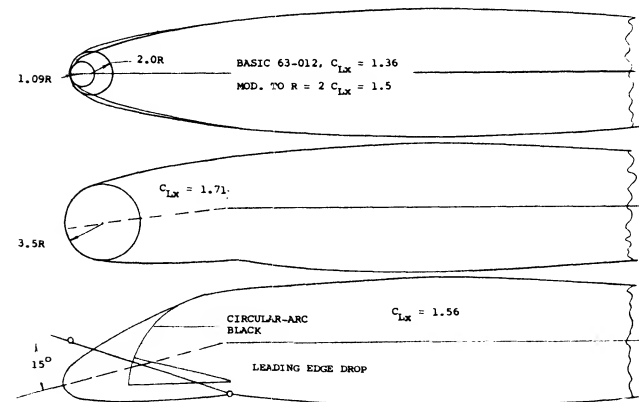


Figure 15. Several leading-edge (nose) modifications tried (16,b) on 63-012 foil section to improve maximum lift (and stalling). $R_c = 4.9(10)^6$.

Nose Camber. The NACA 63-012 section as tested between walls (16,b) at $R_c = 5(10)^6$ and $M = 0.18$, stalls suddenly from $C_{Lx} = 1.36$, exhibiting violent buffeting and shaking at angles of attack beyond stalling as would be predicted from figure 8. By increasing the nose radius from 1.1% of the chord to 2%, C_{Lx} is increased to 1.50; the sudden type of stalling still remains, however. An attempt was, made therefore, to remedy the situation by pulling down (i.e., drooping) the section nose using nose camber in the form shown in figure 15. Again, C_{Lx} is increased; but the type of stalling is still sudden, of the thin airfoil bubble bursting type. Pressure distributions show that stalling takes place on reaching $C_{pmin} = -10$. It therefore appears that behavior at and beyond C_{Lx} can only be made gentle when stalling occurs from the trailing edge; and that can be done only by camber plus thickness.

Critical Reynolds Number. The Operating Reynolds number is an important parameter affecting the maximum lift coefficient of airfoils, since it, along with the shape, is a factor which determines the position of airflow separation and thus C_{Lx} . As shown on figure 16, the maximum lift coefficients of all but very thin airfoils increase sharply in the vicinity of $R_c = 10^5$. This is the critical Reynolds number range where the boundary layer flow turns turbulent so that the laminar-type separation from the suction side disappears. Airfoils such as the NACA 0009 also have the same critical change of flow pattern, but at a higher R_c (see figure 16). Because of shape (no camber), transition from the laminar to the turbulent boundary layer is

x	AVA JOUKOWSKY INTERPOL 9%, $f = 1.2$	(17,a)
H	GO-358 (10.5/6)% BETWEEN END PLATES, $f = 1.2$	(4,f)
▽	ARC-CAT (8.6/4.0)% $A = 6$, $f = 2.5$	(9,e)
H	DVL 2409, $A = 5$, $f = 1.1$	(8,a)
-	DVL 2309, $A = 5$, $f = 1$	(8,a)
◇	AVA GO-622 (8/2.2)% $A = 5$, $f = 1.5$	(19)
+	RAF-28 (9.7/1.8)% DUPLEX (7,c) and CAT, $f = 1$	(4,b)
•	NACA-FST 0009, $A = 6$, $f = 1.0$ & 1.2	(7,b)
C	DVL 0009, $A = 5$, $f = 1.0$ & 1.1	(8,a)
□	NACA 64-210 $A = 6$ WING, $f = 1$	(TN 2753)
▲	63 and 64-009, EFF CAMBER 1.8%	(11,g)
△	0008 in 2-DIMENSIONAL FLOW 1.7%	(11,f)
x	DVL 9% - 0.83, 40, $A = 5$, $f = 1$	(8,c)
+	DVL 9% - 0.83, 45, $A = 5$, $f = 1$	(8,c)
•	DVL 9% - 0.55, 40, $A = 5$, $f = 1$	(8,c)
—	FULL-SCALE T, $A = 4$, 10% BICONVEX	(TN 2823)
•	RAF-34 IN ARC (10/1.5)% $f = 2$	(9,e)

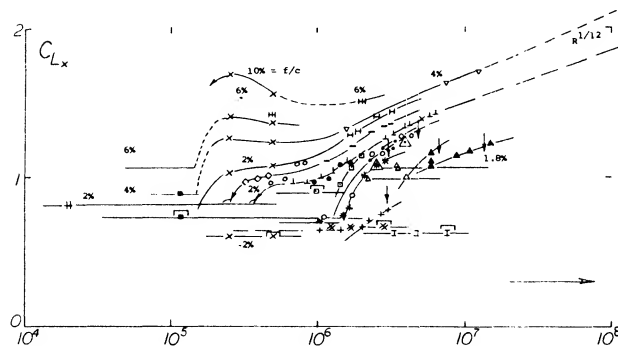


Figure 16. Maximum lift of rectangular airfoils as a function of Reynolds number, (C) sections with $t/c = 8$ to 10%.

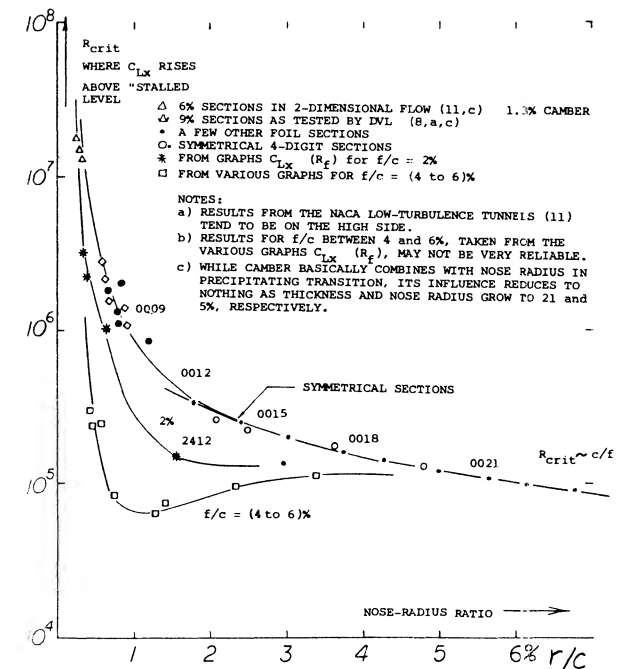


Figure 17. Critical Reynolds number of airfoil sections, where flow attaches to the suction side so that the maximum lift coefficient rises above the subcritical stalled level, as a function of the nose-radius ratio.

delayed to a Reynolds number which is roughly 10 times as high as for most of the other sections having thickness ratios and/or nose-radius ratios larger than the NACA 0009 section. The airfoil nose-radius ratio is thus an important influence with regard to the critical Reynolds number of the section, figure 17. Note that the sections with the smallest curvature tend to have the highest critical Reynolds numbers for the strong increase of C_{Lx} .

x	AVA JOUKOWSKY 11.5%, $A = 5$, $f = 1.2$	(17,a)
■	AVA GO-358 (10.5/6)% BETWEEN END PLATES, $f = 1$	(4,f)
▽	SCHMITZ N60 (12.4/4)% $f = 1.1$	(20,a)
△	NACA-VDT 6412/4412, $f = 2.9$, $A = 6$	(13,b)
+	DVL 23012, $A = 5$, $f = 1$ IN OPEN TUNNEL	(8,b)
◇	DVL CLARK-Y (11.7/3.9)% $A = 5$, $f = 1$	(7,a)
•	NACA-FST CLARK-Y, $A = 6$, $f = 1$	(7,a)
x	0012 IN 2-DIMENSIONAL, EFF CAMBER 3%	(11,c)
▲	ARC-CAT (12.9/6)% $A = 6$, $f = 2$	(9,e)
◆	ARC-CAT CLARK-YH (11.7/3.1)% $f = 1$	(9,e)
+	AVA GO-796 (12/3.7)% BETWEEN WALLS, $f = 1.2$	(19)
—	NACA 23016/09 TAPERED WING	(TN 1299)
H	GALCIT 2412, $A = 6$, $f = 1.2$ to 2.4 (T RPT 558)	(12,c)
□	DVL 2412, $A = 5$, $f = 1$	(8,a)
▽	ARC RAF-34 (12.6/1.8)% $f = 1.8$	(17,c)&(4,b)
+	NACA FST 0012, $A = 6$, $f = 1.1$	(7,b)
•	0012, $A = 5$, $f = 1.1$	(8,a)
◇	DVL 12% - 1.1, 40, $A = 5$, $f = 1.1$	(8,c)
+	ARC-CAT 0012, $A = 6$, $f = 2$ to 3	(4,b)
-	AVA GO-459 (12.5/0)% $A = 5$, $f = 1$ & 1.5	(17,a)
+	DVL 0012 - 0.83, 35, $A = 5$, $f = 1$	(8,c)
+	DVL 1.1, 35, 11.4 - 0.55, 43, $A = 5$, $f = 1$	(8,c)
△	SCHMITZ N60R (12.4/3)% $A = 5$	(20,a)
✓	DITTO, FULLY STALLED C_{Lx} , $f = 1$	(20,a)

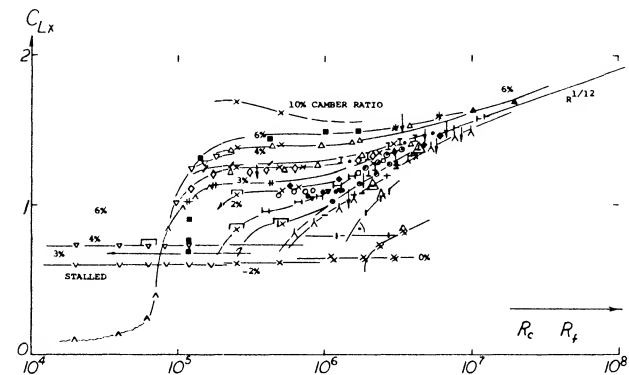


Figure 18. Maximum lift of rectangular airfoils as a function of Reynolds number, (D) sections with t/c 12%.

- (18) Lift coefficients are rather low in insects (below 0.1).
- (19) Riegels, "Aerodynamische Profile", Munchen 1958; review of theory and experimental results over the past 30 years, a catalog of airfoil sections.
- (20) Airfoils at very small R 'numbers:
 - a) Schmitz, Aerodynamik des Flugmodells, Berlin 1942 & Duisburg 1952; Small R 'Numbers, Ybk WGL 1953 p. 149.
 - b) Muesmann in AVA Tunnel, 1956, quoted in (19).
- (21) See in Chapter II of "Fluid-Dynamic Drag". The reduction of maximum lift observed in "well-rounded" foil sections also corresponds with the fact that the drag coefficient of a sphere increases again after the critical drop at $R_d = 4(10)^5$; see Chapter III of "Fluid-Dynamic Drag".
- (22) Theory and tests of Joukowski sections:
 - a) Joukowski, Zeitschr Flugtech Motorluft 1910 p. 281; also in "Aerodynamique", Paris 1916.
 - b) AVA Gottingen, 36 Sections, Erg III & IV (1927/32).
 - c) Glauert, Generalized Family, ARC RM 911 (1924).
 - d) ARC, Series Tested, RM 1241 (1929) & 1870 (1939).

High Reynolds number. Reynolds numbers in the range of 10^6 to 10^7 represent airplanes operating at minimum flying speed at takeoff or landing. The variation of C_{LX} of airfoils in this range of Reynolds number and down to 10^5 are given in figures 16 and 18 to 22. The principle characteristics for this range are:

(a) Thin plates and airfoil sections up to 3% thickness continue to have essentially constant maximum lift coefficients, corresponding to thin-foil type stalling.

(b) Thin airfoil sections (between $t/c = 5$ and 10%) display a basic increase in C_{LX} as their camber ratio is increased from zero to 2% (as in figure 16). Their flow pattern at the angle of attack where $C_L = \text{maximum}$ changes from more or less separated (as in thin airfoil stalling) to almost fully attached. The Reynolds number and/or camber ratio at which the change takes place, can be very sensitive to the test conditions.

(c) As seen in figures 16 and 18, in the vicinity of $R_c = 10^6$, all sections with moderate thickness (between 8 and 12%) and small camber (between 0 and 2%) have a marked tendency for increasing maximum lift coefficient as a function of Reynolds number. This is caused by an improved flow around their noses as the transition to turbulent flow within the boundary layer moves farther toward the leading edge.

(d) All highly cambered and/or thicker airfoil sections (that is, all sections with well rounded noses) do not present "any" difficulties to the flow around the leading edge. Since their maximum lift coefficient is a function of the momentum remaining within the boundary layer

when arriving at the trailing edge, the C_{LX} of these thicker sections depends on the average skin-friction drag coefficient along their upper (suction) side. For Reynolds numbers approaching 10^7 that drag coefficient increases (21) as a consequence of boundary layer transition. As seen, particularly in figures 20 and 21, the maximum lift coefficient of this group of sections is therefore lower in the vicinity of $R_c = 10^6$, reaching a minimum somewhere between $R_c = 10^6$ and 10^7 .

GO JOUKOWSKY INTERPOLATED (17,a)
 ARC-CAT (16.8/7.6)% $f = 1$ (9,e)
 NACA 23018 in 2-DIMENSIONAL FLOW, $f/c = 5\%$ (11,a)
 NACA 4418 in 2 DIMENSIONS (6.3%) (11,a)
 DVL C1-Y-18 (18/6.3)% $A = 5$ (8,b)
 AVA GO 390 BETWEEN WALLS $f = 1.2$ (4,f)
 2-DIMENSIONAL 63-018, $f/c = 2.3\%$ (11,c)
 DVL 2418, $A = 5$, $f = 1$ (8,a)
 NACA 0018 - FULL SCALE T, $f = 1.1$, $A = 6$ (7,b)
 DVL 0018, $A = 5$, $f = 1$ (8,a)
 DVL 18 - 1.1, 40, $A = 5$, $f = 1$ (8,c)

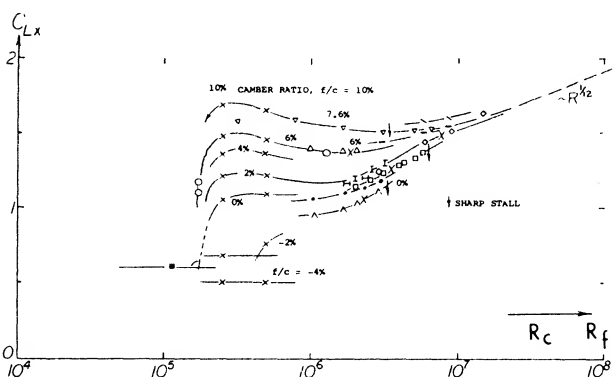


Figure 20. Maximum lift of rectangular airfoils as a function of Reynolds number, (F) sections with t/c 18%.

NACA 24 & 4412 in 2 DIM'S, EFF CAMBER 4.6/6/6% (11,a)
 AVA JOUKOWSKY INTERPOLATED $f = 1.2$ (17,a)
 2-DIMENSIONAL 63 & 64-215, EFF CAMBER 3.5% (11,g)
 ARC-CAT GO-387 (14.9/5.9)% $f = 1$ (4,b)
 AVA, GO-361 (16.3/4.1)% $f = 1.2$ (4,f)
 AVA, GO-624 (16/4.8)% $A = 5$, $f = 1$ (11,a)
 AVA, GO-797 (16/5.1)% BETWEEN WALLS $f = 1.2$ (19)
 4215, TECHN WOOD FLOTA 1937 No. 11/12 (4,b)
 RAF-48 (15/3)% IN CAT, $f = 1$ (4,b)
 RAF (15/1.8)% DUPLEX TU $A = 6$, $f = 1$ (17,c)
 DVL 2415 $A = 5$, $f = 1$ (8,a)
 DVL 0012 OPEN TUNNEL (8,a)
 ARC-CAT 0015 WITH $f = 1$ and 2 (9,a)
 DVL 15 - 1.1, 40, $a = 5$ (8,c)
 DVL 15 - 0.55, 40 & 45, $f = 1.1$ (8,c)

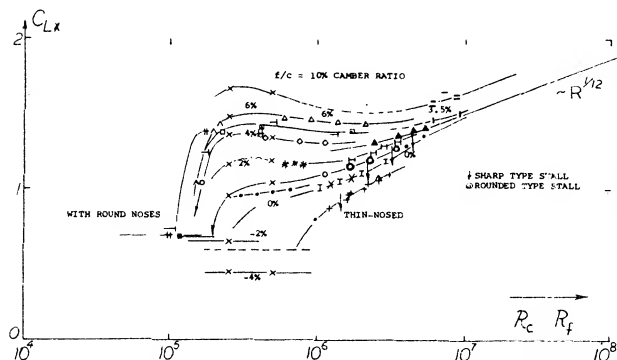


Figure 19. Maximum lift of rectangular airfoils as a function of Reynolds number, (E) sections with t/c 15%.

AVA JOUKOWSKY INTERPOLATED (22,b)
 AVA GO-390 (21/8.8)% $f = 1$, $A = 5$ (17,a)
 NACA 2421, 4421, 23021 EFFECTIVE CAMBER (11,a)
 AVA GO-798 (20/6.5)% BETWEEN WALLS $f = 1$ (19)
 DVL GO-625 (20/6.5)% $f = 1$, $A = 5$ (8,c)
 SCHMITZ GO-625 (20/6.5)%, $f = 1$ (4,e)
 NACA 63, 64-021 2-DIMENSIONAL (2%) (11,a)
 NACA-VDT 6321 $f = 1$, $A = 6$ (4,d)
 CAT, RAF-69 (21/1.9)% $f = 1$ (9,a)
 RAF-34-20 (20/1.8)% DUPLEX TUNNEL $f = 2$ (11,c)
 DVL 0021 and 2421, $f = 1.1$ (8,a)
 NACA-VDT 0021, $f = 1$ and 2 (13)
 DITTO IN ORIGINAL OPEN TUNNEL $f = 2.7$ (4,d)
 NACA (21/8.8)% IN OPEN TUNNEL $f = 2.7$ VDT (4,d)
 NACA (21/6)% IN OPEN TUNNEL $f = 2.7$ VDT (4,d)

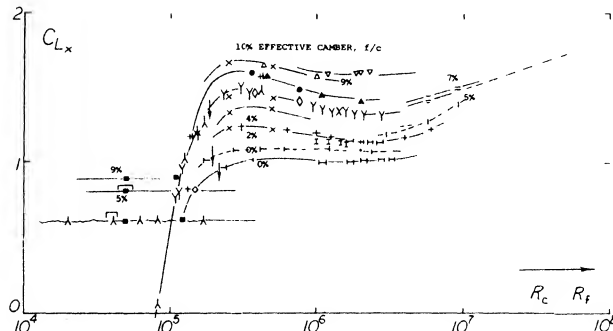


Figure 21. Maximum lift of rectangular airfoils as a function of Reynolds number, (G) sections with t/c 20 and 21%.

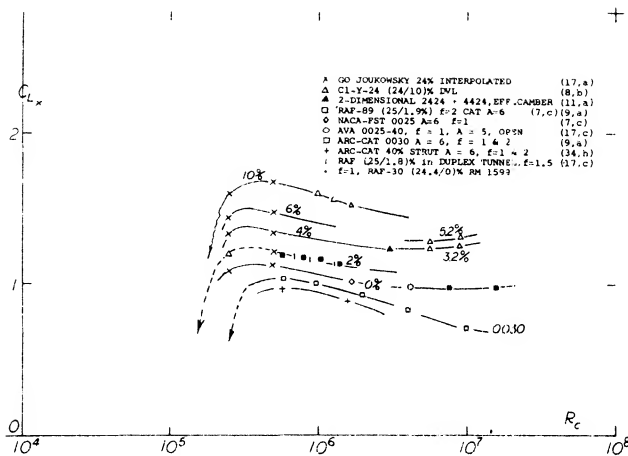


Figure 22. Maximum lift of rectangular airfoils as a function of Reynolds number, (H) sections with t/c equal to and above 24%.

The different types of stalling discussed before also result in different trends (gradients) of C_{LX} . Sections exhibiting the thin-foil type of stalling have essentially constant maximum lift coefficients. The sudden leading-edge type stalling is accompanied by a usually steep increase of C_{LX} as a function of Reynolds number. Real trailing-edge stalling grows slowly as a function of Reynolds number, so that the maximum lift coefficient reduces for higher camber ratios, as seen in most of the graphs presented. Regarding the flying qualities of an airplane near C_{LX} , the round-top type of stalling is, of course, more desirable than a sharp stall from a high peak. It can also be argued that a gently stalling airfoil section will have a "useable" maximum lift coefficient equal to its maximum, while a thinner and/or less cambered section with a dangerous sharp type of stalling would always have to be kept sufficiently below the maximum. The various phases marked in all the graphs permit selection of airfoil sections, not only as to efficiency but as to behavior.

Theoretical Analysis. An early theory for analyzing the boundary layer around the leading edge of an airfoil is presented in (23). This theory permits calculation of the maximum lift coefficient as a function of Reynolds number and/or stream turbulence for moderately thick and cambered air-foil sections. The theory appears to be accurate, however, only at Reynolds numbers where stalling is produced by separation (bubble bursting) near the leading edge.

- (23) Theoretical analysis of maximum lift and separation:
- a) vonKarman and Millikan, Analysis of Maximum Lift, J RAS July 1935; also J Appl Mech 2,A,21 (1935).
 - b) Howarth, Theory, Proc Roy Soc London A.868 (1935) p. 558.
 - c) Math Model, Stevens, W.A. et al, NASA CR-1843.
 - d) Evans & Mort, Sudden Stall, NASA TND-85.

In the case where stalling is caused by trail edge separation the maximum lift coefficient is a result of a balance between the kinetic and potential energies of the boundary layer flow. The potential flow energy is represented by the pressure increase between the minimum-pressure point and the trailing edge. Thus for a section with moderate camber and a well rounded leading edge the stalling can be determined as a function of the kinetic energy in the boundary layer. Since the kinetic energy in the boundary layer is a function of Reynolds number and increases as skin friction decreases, it can be speculated that

$$C_{LX} \sim 1/\sqrt{C_f} \quad R \sim R^n \quad (9)$$

where $n = 0.5$ ($1/6$) = $1/12$, and $1/6$ is equal to the average exponent when the drag coefficient is turbulent. Based on the above equation it would appear that the maximum lift coefficient should continue to increase above $R_c = 10^7$. In making such extropolation of the test data it should be noted that any increase in Reynolds number is usually a result of an increase in speed and the following must be considered:

- (a) the influence of surface roughness (see section 4)
- (b) the effects of compressibility as measured by Mach number.

With the use of high speed computers the theoretical methods have been extended (23,c) to allow the calculation of C_{LX} for any combination of conditions operating at low Mach numbers. Such procedures have led to the development of advanced airfoils as discussed in Chapter II with an increase of C_{LX} equal to 20%.

Thickness Ratio. Practical applications, with regard to maximum lift, such as airplane wings, require consideration of Reynolds numbers in the vicinity of $R_c = 10^7$. Since only a few systematic investigations have been extended to that Reynolds number, we have rather plotted the more complete data for $R_f = 4(10)^6$ in figure 23, as a function of thickness ratio. The critical change of the flow pattern described for the Reynolds number of $4(10)^6$ will also apply at Reynolds Numbers in the vicinity of $R_c = 10^7$. The maximum lift coefficient is seen to increase "suddenly" for camber ratios between 0 and 2% at t/c between 5 and 8%. Below $t/c = 8$ or 9%, (and below 2 or 4% camber) the sections exhibit thin-foil stalling. Peak values of the maximum lift coefficients are then obtained in sections with t/c in the vicinity of 10%. Judging by the large number of experimental results available, a thickness ratio of $t/c = 12\%$ is evidently considered to be most efficient. While somewhat thinner sections may, at full-scale Reynolds numbers, be superior in the fluid-dynamic aspect, structural considerations tend to make a 12%

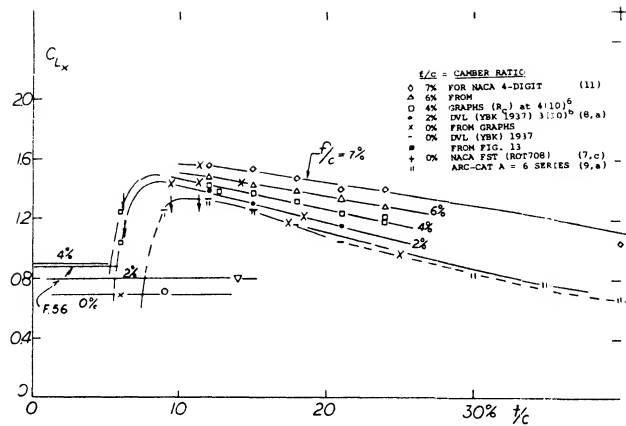


Figure 23. Maximum lift coefficient of various types of airfoils, at $R_L = 4(10)^6$, as a function of their thickness ratio. Primarily 4-digit type foil shapes.

thickness ratio more attractive, at least within the range of moderately high subsonic speeds. Sections with $t/c = 0$ and 10% have frequently been investigated. As a compromise between aerodynamic and structural effectiveness. For example, the NACA 0009 has often been proposed as a shape to be used in the design of tail surfaces for higher-speed airplanes. Maximum lift characteristics of most of these sections are as described under (c) of the previous section. As the thickness ratio is increased to 18% (as sometimes used in the wing-root sections of big but low-speed airplanes) and above that ratio, the maximum lift coefficient reduces gradually. By employing proportionately higher camber ratios, it is possible, however, to keep the C_{LX} at 1.4. Their stalling characteristics are very gentle. Unfortunately, however, thick and highly cambered sections are not suitable for high-speed applications due to their low critical Mach number. Also they have correspondingly high pitching moments, which tend to be too large with regard to structural strength and rigidity (torsion).

High-Speed Airfoil Sections. It has previously been stated that the position of the maximum camber point is not very important with regard to maximum lift, at least not between 30 and 50% of the chord. In contrast, position of maximum thickness has some influence, particularly when a nose radius change is coupled with that position. This is usually the case with laminar-type airfoil sections and/or in sections particularly designed for high-speed applications (at higher subsonic Mach numbers). In particular, the NACA 63 and 64 series sections (11) have ratios $(r/t)/(t/c) = 0.75$ and $= 0.72$, respectively, while the 4-digit (and similar lower-speed sections) have a radius parameter of 1.10. When evaluating maximum lift of the 63 and 64 series sections, the complication of effective camber is encountered again. Results taken from (11) have been transformed (using equation 7) and interpolated where necessary, so that they represent sectional conditions (24) as in wings with A between 5 and 6.

Influence of Nose Radius. In keeping with what is said above regarding their nose radius ratio, the experimental results of 63 and 64 series airfoils are more or less different from the corresponding graphs representing 4-digit and similar foil shapes:

(a) Because of the comparatively small nose radius, the increase of C_{LX} versus thickness ratio, as in figure 24, is considerably delayed in comparison to that in figure 23. See figure 17.

(b) For the same reason, the 63 and 64 type sections in figure 25, exhibit C_{LX} values which are considerably lower than those in figure 14, particularly in the range of smaller and smallest camber ratios.

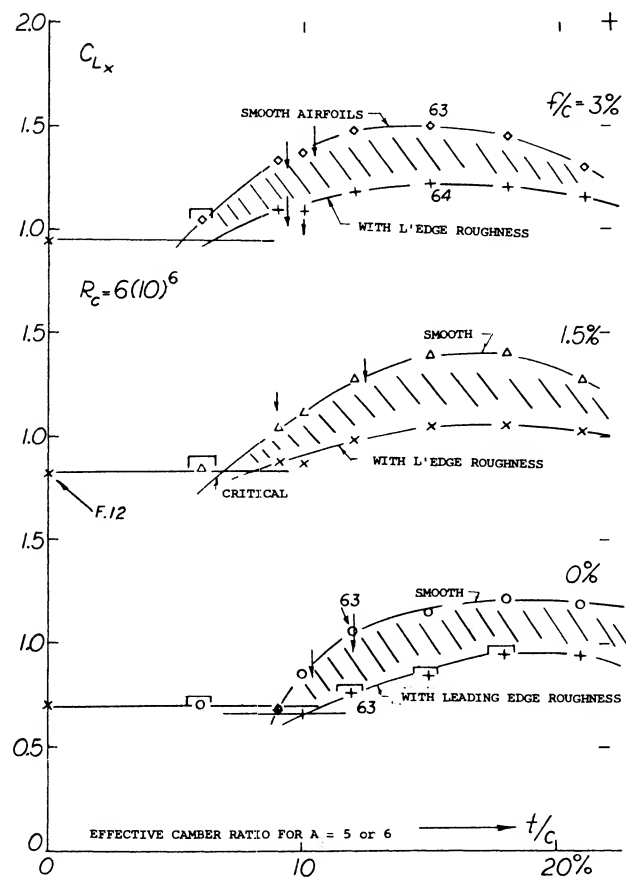


Figure 24. Maximum lift coefficient of 63 and 64 series airfoils as tested (11) at $R_L = 6(10)^6$, as a function of their thickness ratio, grouped as to their camber ratio effective for A between 5 and 6 (see equation 7).

(24) The difference in effective camber (between 2-dimensional tunnel and an airplane wing having an aspect ratio of, say 6,) is considerable at lift coefficients above unity. Characteristics at small lift coefficients are affected to a much lesser degree.

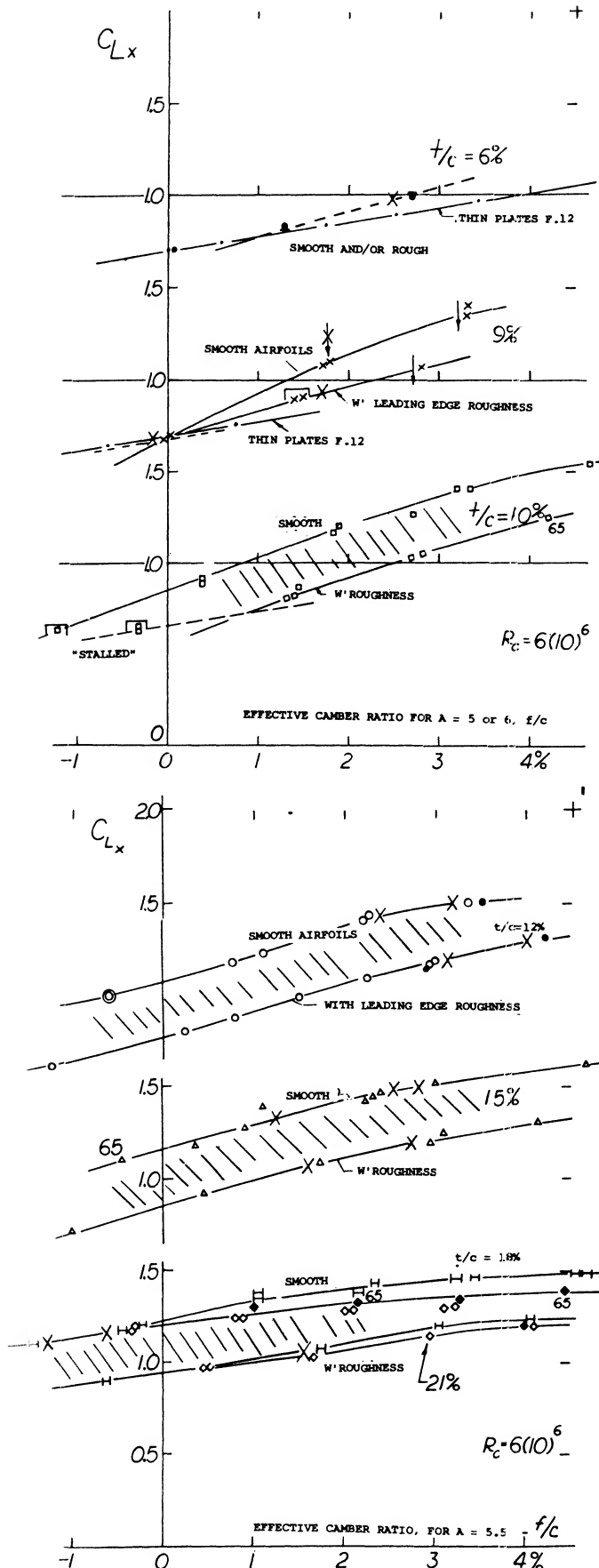


Figure 25. a) Maximum lift coefficient of 63 and 64 series airfoils as tested (12) at $R_c = 6(10)^6$, as a function of their camber ratio effective for wings with A between 5 and 6 (see equation 7).

In conclusion, comparison on the basis of nose radius ratio r/c (rather than thickness ratio) would bring about a more favorable correlation between the two major types of airfoil sections. Characteristics of 12% thick symmetrical sections are included in figure 9, accordingly. At the lower end of the nose-radius scale, we recognize the effect of the critical change (transition) within the boundary-layer flow around the section nose. Stalling of these high-speed sections is comparatively sudden sometimes showing large hysteresis loops. Of course, the drop of the lift coefficient is aggravated by the fact that the sections in figure 9 are all without camber (geometrically, that is).

Mach Number Effects on C_{Lx} . The operating Mach number has a large influence on the maximum lift coefficient of an airfoil. The change in C_{Lx} is caused by the formation of shock waves in those regions on the airfoil where the local Mach number exceeds 1.0. The shock wave pattern formed depends on the boundary layer type. As the pressure increases on passing through the shock wave, the lift on the suction side of the airfoil is reduced and a reduction of C_{Lx} is encountered.

Two regions are important with regard to the formation of the shock waves:

- (1) the area around the nose of the airfoil and
 - (2) the area toward the trailing edge on the suction side.
- On blunt nose airfoils operating at high lift coefficients the local Mach number of 1 can be exceeded at free stream as low as $M_\infty = .25$ (25,a). On the first tenth of the chord on blunt airfoils standing shock waves are formed similar to the more well known shocks on the aft section of the airfoil, except their size is an order of magnitude less. The familiar lambda type shock with a weak forward shock and pressure plateau as illustrated in figure 26 is formed with a laminar boundary layer. With a turbulent boundary layer the single shock with a strong pressure rise and an expanding bubble is formed at the nose (25,b). These shock waves interact with the boundary layer causing separation and a reduction of C_{Lx} as illustrated in figure (27).

(25) Mach Number Effects on Max. Lift.

- a) Fitzpatrick, & Schneider, NACA TN2753.
- b) Aerodynamics Dept. Annual Report 1971, RAE TR 72073.
- c) Cleary, Complete Wings, NACA WR L-514.
- d) Wilson & Horton, NACA RM L-53C20.
- e) Racisz, S., NACA TN 2824.
- f) Stivers, L., NACA TN 3162.
- g) Summers, J.L., NACA TN 2096.

- h) Hicks, et al, Forward contour modes 64-212 foil NASA TM-3293
- i) Hicks & Schairer Upper surfaces modes 63-215, NASA TM-78503
- j) Hicks, Mods to an NACA 65-(.82).099) airfoil, NASA TM-85855

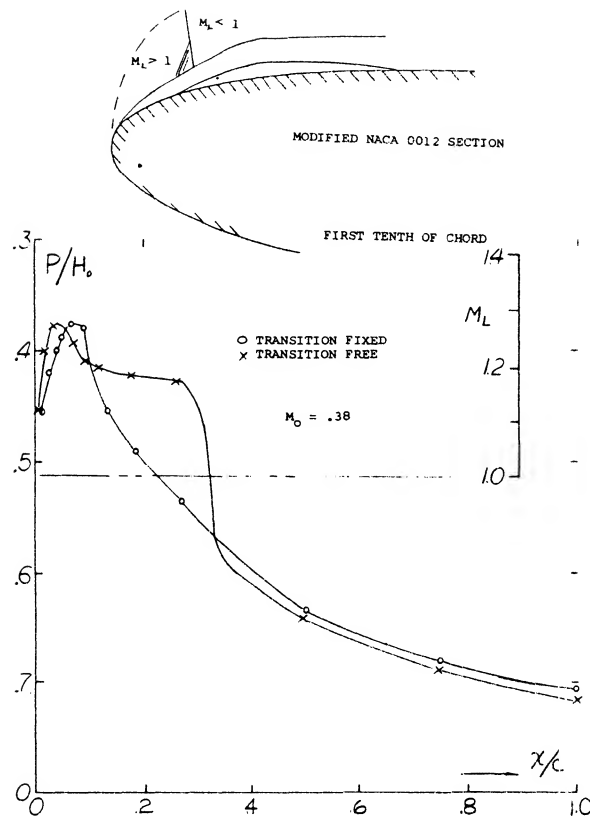


Figure 26. Pressure and local Mach number distribution at maximum lift (25,b).

The variation of C_{LX} with Mach number with the NACA 64-210, 64-410, 64A-610 airfoils are examples where separation due to leading edge shock wave reduces lift, figure 27. With an airfoil such as the NACA 64-010 where leading edge separation already takes place the formation of a shock would not influence the variation of C_{LX} with Mach number.

At Mach numbers in the transonic range the C_{LX} is influenced by the formation of shock waves at speeds above the critical. After reaching a minimum, C_{LX} will increase and approach the theoretical value shown on figure 27 which is described by the equation at $M > 1.0$

$$C_{LX} = .5 p_s - p_R \quad (10)$$

where p_s is the stagnation point pressure and p_R is the rear surface pressure corresponding to vacuum.

The negative peak pressure toward the leading edge of the airfoil leading to the lambda type shock wave and lift stall shown in figure 26 can be eliminated at the lower Mach numbers by recontouring the upper surface as indicated on figure 26a. This change (25,h,i,j) reduced the local Mach number below one thus eliminating separation with the result that the airfoil can operate at a much higher angle of attack and C_L before stall occurs. This characteristic is shown on figure 26a and shows a large increase of C_L from 1.33 to 1.6 and a stall angle increase from 10 to 15 for a NACA 65 - (.82 .099) airfoil, (25,j).

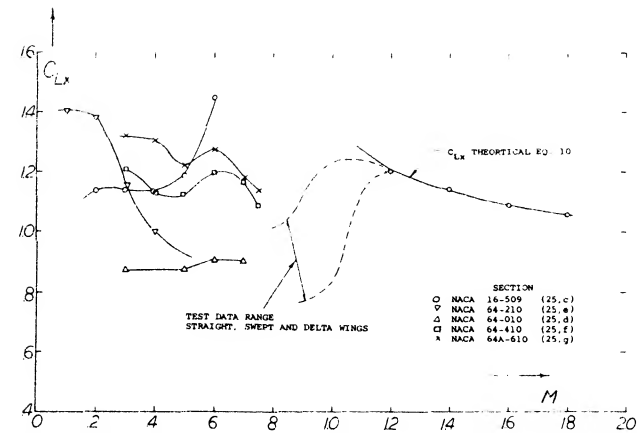


Figure 27. Influence of Mach number on maximum lift.

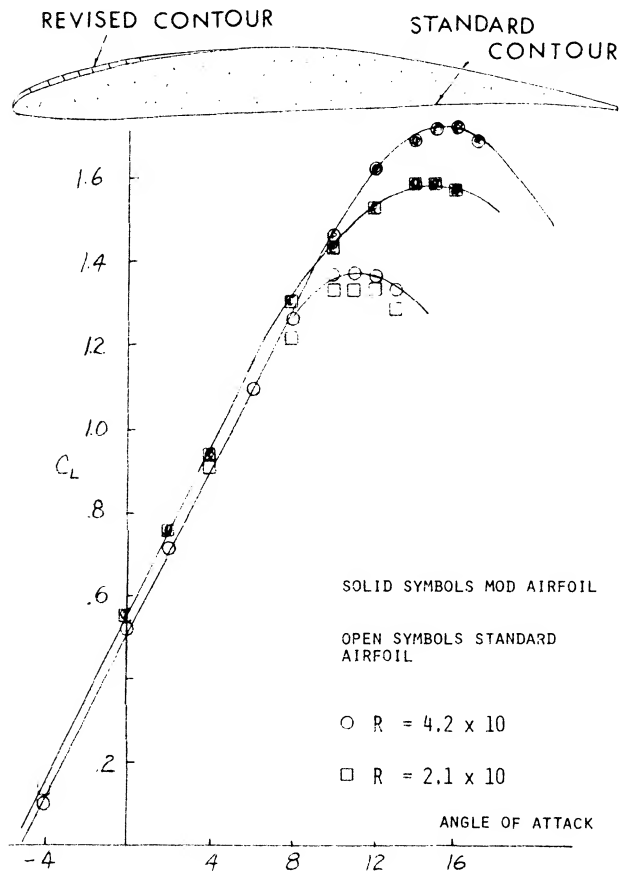


Figure 26a. Lift of an airfoil modified to eliminate shock stall relative to standard. NACA 65 (.82)(.099) airfoil.

- (26) Structural roughness (imperfections):
 - a) Jacobs, Protuberances, NACA T Rpt 446 (1933).
 - b) Hood, Surface Irregularities, TN 695 (1939).
 - c) Wood, Corrugated Surface, NACA Rpt 336 (1929).
 - d) See Also references under (27).
- (27) Characteristics of practical-construction airfoils:
 - a) Tetervin, Helicopter Blades, NACA W Rpt L-643 (1944).
 - b) Doetsch, Waviness on 23012, Ybk D Lufo 1939 p. I-88.
 - c) NACA, TN 428 (fabric-covered), 457 (irregularities), 461 (rivet heads), 724 (rib stitching).
 - d) Quinn, Practical Construction, NACA T Rpt 910.

5. INFLUENCE OF SURFACE ROUGHNESS

The consequences of increased skin friction, caused by surface roughness, as to lift-curve slope, are explained in the section on "circulation", Chapter II. The basic influence on pitching moment is mentioned in connection with figure 32. In the following, roughness will be considered as it affects the maximum lift of airfoil sections and/or airplane wings.

Surface roughness can be local such as at a particular chordwise station of an airfoil, or uniformly distributed over the surface, such as a rough coat of paint, for example. On the lower (pressure) side, roughness tends very slightly to increase the lift at a certain angle of attack. Roughness on the suction side on the other hand, reduces lift and maximum lift coefficient, particularly in well-rounded sections where a gentle type stalling takes place from the trailing edge. As an example of the effect of distributed roughness, figure 28 shows the lift function of an NACA 0012 airfoil tested at $RN = 6(10)^6$, both in the perfectly smooth condition and after coating the surface uniformly with grains of carborundum. The lift-curve slope is reduced (see figure 28) and the maximum lift is cut down from 1.48 to 1.07.

Maximum-Lift Divergence. As explained, for example in "Fluid-Dynamic Drag", one consequence of uniformly distributed and closely packed sand-type roughness in the turbulent boundary layer is the fact that the skin-drag coefficient C_f is independent of the Reynolds number and assumes a constant value. As demonstrated in figure 29, the maximum lift coefficient of completely rough airfoil sections is also constant above a certain limiting Reynolds number. Below this Reynolds number, the airfoil behaves as though it were perfectly smooth. Figure 30 shows how the maximum lift coefficient reduces as a function of the roughness grain size. A comparatively small but permissible grain size should apply to this graph too.

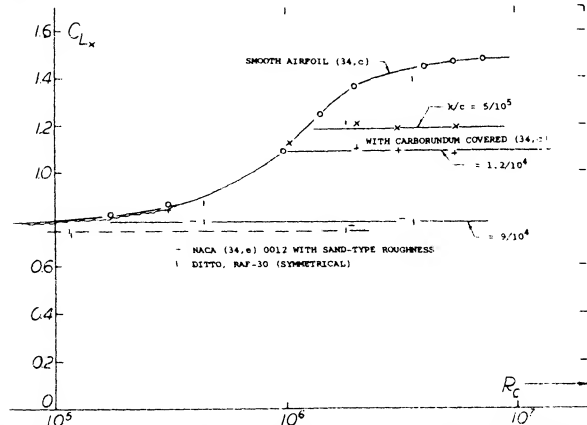


Figure 29. Maximum lift coefficient as tested on 0012 airfoils with $A = 6$, as a function of R -number:

- smooth wind-tunnel models,
- completely covered with carborundum grains.

Permissible Roughness. As explained in "Fluid-Dynamic Drag", the permissible roughness size in a turbulent boundary layer approximately corresponds to the grain Reynolds number

$$R_k = w k / \nu = R_c (w/V)(k/c) \approx 120 \quad (11)$$

where k = grain diameter and w = local velocity at the spot where the roughness is located. Using equation (1) we can estimate that the NACA 0012 section as in figure 28 and 29, may have a maximum local velocity (somewhere at or above the nose) corresponding to $w/V \approx 3$ at $C_{Lx} = 1.2$ as in graph at R_c somewhat above 10^6 . For the grain size ratio $k/c = 5/10^5$, we thus obtain a critical Reynolds number

$$R = 120 (10)^5 / (3.5) = 8(10)^5 \quad (12)$$

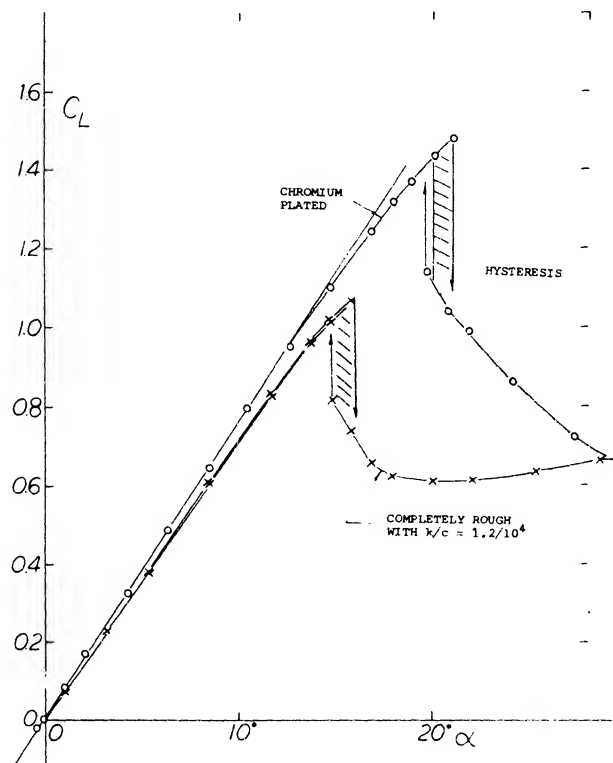


Figure 28. Lift of an 0012 airfoil tested in $A = 6$ in the CATunnel (34,c) at $R = 6(10)^6$, in smooth and carborundum covered condition.

This estimate does not agree with the actual divergence Reynolds number $1.2(10)^6$ as in figure 29. When carrying out the calculation for the re-attachment point (at which the local velocity is lower), satisfactory agreement is expected to be found, however. Now, Extrapolating the results of figure 29 yields

$$k/c \approx 1 / ((1 + 2 C_{Lx}) R_c) \quad (13)$$

and we tentatively find a permissible grain size ratio k/c below $1/10^5$ at $R_c = 4(10)^6$ where $C_{Lx} = 1.45$, as in figure 30.

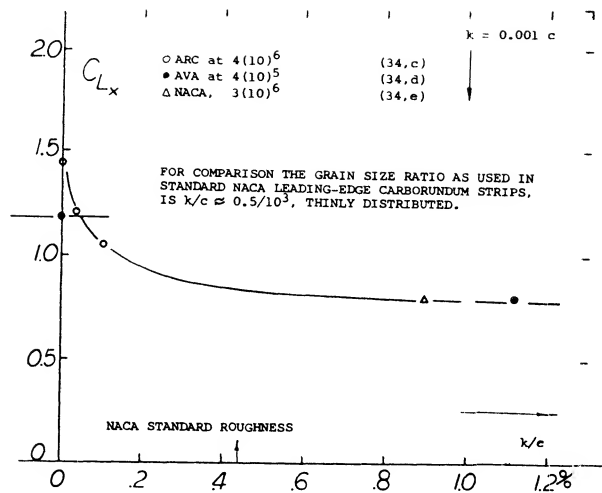


Figure 30. Maximum lift coefficient of 0012 airfoils (as in figure 29) as a function of the roughness grain size ratio.

Roughness in Wind Tunnels. The influence of roughness on C_{Lx} has an important implication with regard to the results obtained in either high-speed or pressurized wind tunnels. Consider in particular the NACA's Variable Density and the British Compressed Air Tunnels operating at 20 and 25 ats, respectively, while testing standard airfoil models having but 5 and 8 inches chord length. At a maximum Reynolds number (as in the CAT of $R_c = 7(10)^6$) the permissible roughness ratio for an airfoil section at $C_{Lx} = 1.5$ is found (for an assumed velocity ratio of $w/V = 2$) to be in the order of

$$k/c = 120 / (2(7) \times 10^6) \approx 1/10^5 \quad (14)$$

The corresponding grain size k is below $1/10^4$ inch or 0.1 mills, or in the order of ≈ 2 microns. This roughly represents the surface roughness of "finished" metal. There is evidence such as in (11,c) where tests of NACA 63 and 64 series sections (with a chord $c = 2$ ft) up to $R_c = 2.5(10)^7$ show that C_{Lx} stops increasing in certain sections (see figure 31, a, b, c) between $R_c = 10^6$ and 10^7 . While it seems to be routinely possible to produce model surfaces sufficiently smooth for this condition, there are reports from other high-speed tunnels indicating that it is a real problem to prevent "sandblasting" of the

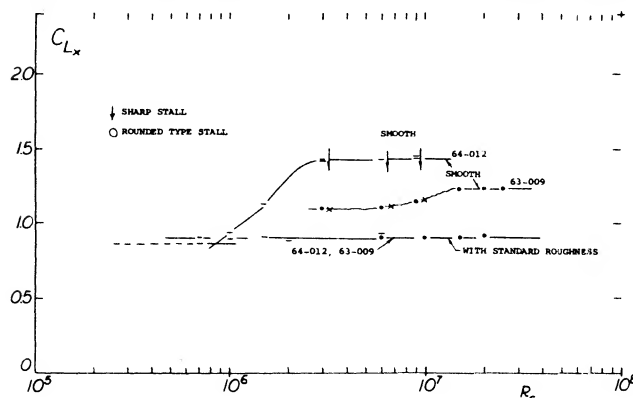


Figure 31. a) Maximum lift coefficient of two dimensional airfoil sections, NACA 64-012, 63-009 (11), with and without standard roughness.

models by dirt originating in, or "seeping" into, the tunnel. In conclusion, wherever wind-tunnel tests show maximum lift coefficients leveling off upon approaching $R_c = 10^7$, it may be suspected that surface roughness is the cause, unless influenced by compressibility.

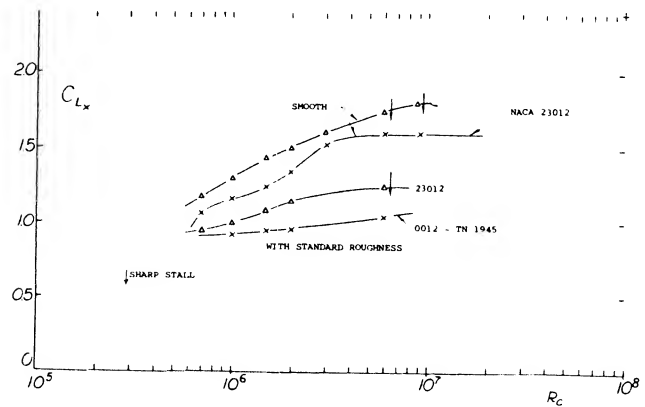


Figure 31. b) Maximum lift coefficient of two dimensional airfoil sections, NACA 23012 and 0012 (11), with and without standard roughness.

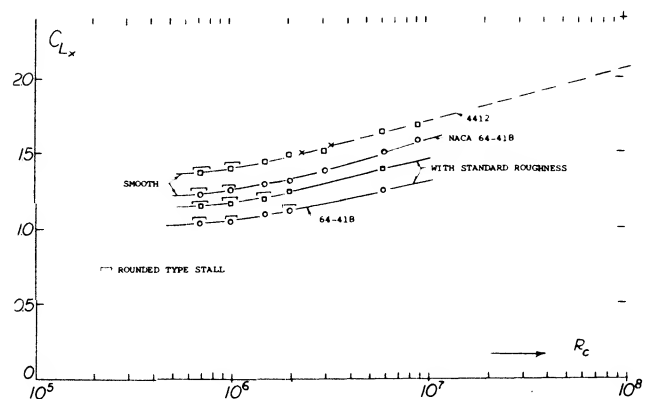


Figure 31. c) Maximum lift coefficient of two dimensional airfoil sections, NACA 4412 and 64-418 (11), with and without standard roughness.

Roughness in Full-Scale Operation. The above method for estimating the permissible roughness grain size can also be applied to full-scale airplane operation. Consider, for example, flow conditions at the suction side near the leading edge of a wing. At lift coefficients above unity the critical local velocity at this point is increased to about 2 times the airplane's air speed. When flying at 100 knots (for example, takeoff or landing) the maximum local speed is thus in the order of 200 knots (or 340 ft/sec). The permissible grain size of sand-type roughness is then in the order of 0.6 milli-inch, while paint in aircraft mass production may have a grain size of 1 milli-inch. If it is not the paint, dust and/or insects picked up by the airplanes or the ground or in flight can easily make the nose of the wing section sufficiently rough, so as to affect its maximum lift coefficient in the manner as shown in figures 28 and 29. Note also, that in a turbulent boundary layer the permissible grain size is a function of speed, and not of wing or aircraft dimensions.

Stimulation of Turbulence. In the practical operation of high-speed airplanes (such as fighters) it is known that the qualities of laminar-type wing sections deteriorate rapidly by picking up dust, mud and insects. To simulate this condition, the sections investigated particularly in (11) were (in addition to their smooth condition) routinely tested with a turbulence-stimulating strip of thinly spread carborundum grains placed over the first 8% of the chord (both on the upper and lower sides). The grain size used was 0.011 inch, equal to somewhat less than $5/10^4$ of the chord. Consequences of this type of stimulation with regard to lift, are:

- (a) Some reduction of the lift-curve slope (up to about 10% in higher thickness ratios).
- (b) A reduction of maximum lift of as much as 25% depending on shape and thickness ratio.

Efficiency of Airfoils. The efficiency of airfoil sections can be measured by the ratio C_{LX} / C_{Dmin} . In high-speed sections, the C_{Dmin} is expected to be low (say in the order of 0.005) corresponding to an appreciable percentage of laminar boundary layer flow. However, when judging the efficiency of an airplane, the drag coefficient of the complete craft should be considered rather than that of the wing only.

Type of Stalling. Maximum lift coefficients of several airfoil sections, tested with “standard” leading-edge roughness, are plotted in figure 31 as a function of the Reynolds number. Three different groups of airfoil sections were found as to the influence of the roughness strip upon the magnitude of C_{LX} .

- (a) Figure 31,a shows that in symmetrical (and comparatively sharp-nosed sections) the rise of the maximum lift coefficient above the thin-foil level is prevented by roughness. Note that in the smooth condition the two sections shown each end up at a higher but constant level, suggesting that the “natural” roughness of their “smooth” surface is dictating that level.
- (b) The majority of all airfoil sections belongs to the leading-edge stalling group as in figure 31,b. Their maximum lift coefficient is considerably reduced by the roughness strip, the amount growing with the Reynolds number.
- (c) The influence of nose roughness on the maximum lift of the sections shown in figure 31,c is to produce a more or less constant reduction. It seems that all sections with typical or exclusive trailing-edge stalling (highly cambered sections, with higher thickness ratios) belong to this group. It appears that the carborundum strip takes away a specific amount of momentum from the suction-side boundary layer, thus reducing pressure recovery at the trailing edge.

Airfoil Thickness. The size of the “standard” turbulence stimulation strip used by the NACA (11) is arbitrary. All that the strip tests give in regard to maximum lift is a qualitative indication of the influence of roughness around the nose on the magnitude of C_{LX} . Figure 24 shows that the C_{LX} of sections below 6% or 8% or 10% may not be sensitive to roughness. Sections with thickness ratios between 12% and above 20% can, on the other hand, be very much affected by leading-edge roughness, particularly in effective camber ratios between 0% and 3% (which means all sections used in high-speed airplanes).

Cambered Sections. Figure 25 illustrates the variation of the maximum lift coefficient of the NACA 63 and 64 series sections (11) as a function of effective camber ratio and shows that:

- (a) Sections up to $t/c = 6\%$ do not exhibit much of an influence of leading-edge roughness.
- (b) The influence of roughness increases systematically as the thickness ratio is increased to 9%, 10% and 12%.
- (c) The 12% and 15% thick sections show practically constant differentials of maximum lift due to standard roughness;

$$\Delta C_{LX} \approx -0.3.$$

The data given in figure 25 shows little difference in the maximum lift coefficient of NACA 63 and 64 series sections in the smooth model condition.

Corrugated Surface. Early Junkers aircraft used corrugated sheet metal as a properly stiffened skin for cantilevered monoplane wings. At speeds in the order of 200 mph it was thought that drag may not be too critical while light-weight construction did provide high payload fractions and/or range. To evaluate the effects of a corrugated surface three Clark-Y wing models were tested (26,c) at $R_c = 2(10)^6$ with the following results:

- (a) smooth airfoil with $A = 6$; $C_{LX} = 1.22$.
- (b) with corrugations placed on top of contour; $C_{LX} = 1.25$.
- (c) with corrugations cut into the model; $C_{LX} = 1.26$.

Although drag is generally somewhat increased, the maximum lift coefficient is surprisingly enough not reduced. It must, therefore, be postulated that the corrugations have some “stabilizing” effect on the flow past the suction side, reminiscent of the influence of vortex generators (see Chapter V). This effect is particularly present at angles of attack some 8° above that for C_{LX} of the $A = 6$ airfoils tested.

Ice Formation. When flying at temperatures below freezing, rain may be deposited, particularly on the leading edge of wings, in the form of ice. Figure 32 presents one example of such deposits, tested (28,a) at $R_C = 4(10)$. In comparison to the smooth NACA 2212 section, $C_{L\alpha}$ is reduced from 1.3 to below 1.0. Not only is the maximum lift of an airplane flying in icing weather reduced but its drag and its weight also grow simultaneously so that eventually it may no longer be possible to keep the craft flying. Ice coatings may be mechanically removed by inflating rubber "boots" (28,b) placed upon (built into) the wing leading edge. Of course, such devices are bound to reduce lift (lift-curve slope) and maximum lift coefficient to a degree, even when not in operation. Naturally, all the types of roughness discussed also increase the section drag, (a) because of stimulation of turbulence and (b) because of their own addition to skin drag (See Chapter V of "Fluid-Dynamic Drag").

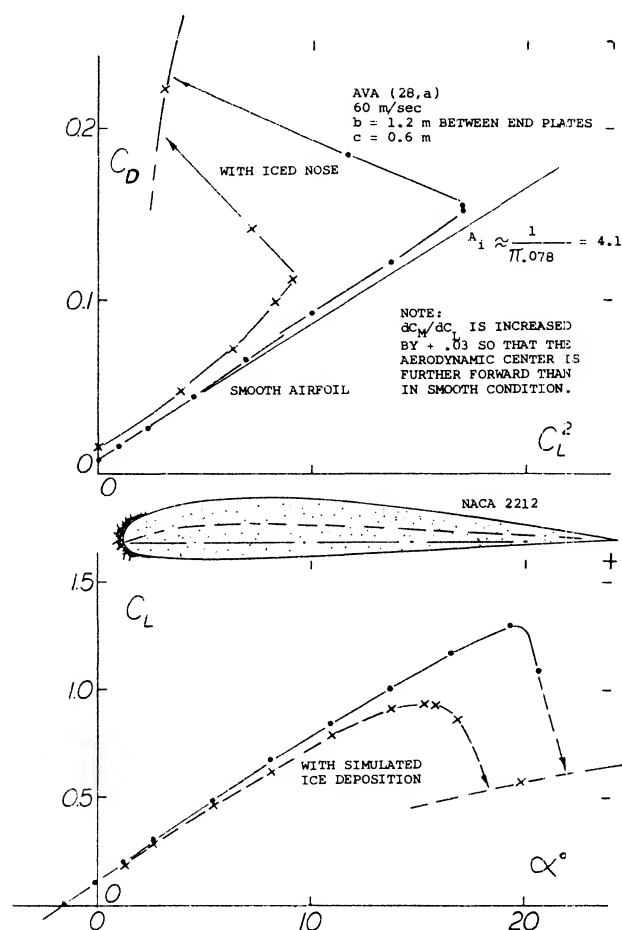


Figure 32. Example for lift and drag of a 2212 airfoil, tested (28,a) between end plates, with and without simulated ice formation around the leading edge.

- (28) Influence of roughness caused by icing:
a) Gerhardt, (AVA), Ybk D Lufo 1940 p. 1,575.
b) Bowden, Ice Formation, NACA TN 3564 (1955).
c) Gray, 65-212 Airfoil, NACA TN 2962 (1953).

6. AIRFOIL CHARACTERISTICS ABOVE STALL

The characteristics of airfoils operating at angles of attack above stall are of importance in analyzing airplane off-design conditions and helicopter rotors operating at high forward speeds where reverse flow can be encountered. Normally airfoils operate in the range of angle of attack from near zero at zero C_L to angles 10 to 20 degrees above that, and produce a maximum lift coefficient in the range of 1.0 to 1.6 plus. Upon increasing the angle of attack above $C_{L\alpha}$, the flow detaches (separates), more or less suddenly, from the suction or upper side of the airfoil. After reaching its maximum C_L will drop to a value of 0.8 to 1.0 and then increases again as the angle of attack is further increased. This latter increase in lift is caused by a combination of the impact pressure on the lower surface together with some scavenging effect of the outer flow along the boundaries of the wake originating from the upper side. The scavenging results in a negative pressure differential, or suction, on the upper surface. Finally, the whole aggregate will result in some circulation. All this amounts to the fact that lift is derived from changes in momentum in the fluid flow, both in the direction of motion (drag) and in a direction normal to that motion.

The two dimensional characteristics of airfoils in the angle of attack range of 0 to 180 degrees are given in figure 33 for NACA 0012, 0015 and 63A-012 airfoils (29,a, c). The results for all the 12% thick airfoils agree closely. Above an angle of 20 degrees indicating that shape has little effect on the lift variation at high angle. The results given in figure 33 also indicate that:

(a) After stalling, the resultant force acting on the airfoil section is essentially normal to the chord line.

(b) Lift reaches a second maximum at $\alpha \approx 45^\circ$ with a value on the order of $C_L = 1.0$.

(c) Together with the drag at 45° (corresponding to $C_D \approx 1.0$) the normal force at that angle amounts to $C_N \approx \sqrt{2} \approx 1.4$.

(d) At $\alpha = 90^\circ$ $C_N = C_D \approx 1.8$. The normal force thus reaches a maximum at this angle of attack, in a manner similar to the theoretical lift coefficient.

(e) Lift is approximately zero at 90° ; and the drag coefficient is 1.8, which is similar to that of a flat plate ($C_D \approx 1.95$).

(f) At angles of attack between 90° and 180° , the sharp trailing edge becomes a leading edge, while the round leading edge has to perform as a trailing edge. The variation of the drag and lift coefficients in this region is similar to that between 0° and 90° .

The two dimensional airfoil data presented on figure 33 was obtained primarily for use in helicopter rotor analysis. However, definition of the flow conditions required for correcting these data for their use in rotor analysis are not yet available. Testing of various airfoils on actual rotors is recommended (29) to account for all the variables, since the effects of three dimensional flow are of great importance. Three dimensional flow due to leakage may account for the difference between the NACA 0015 and 0012 airfoil data of figure 33.

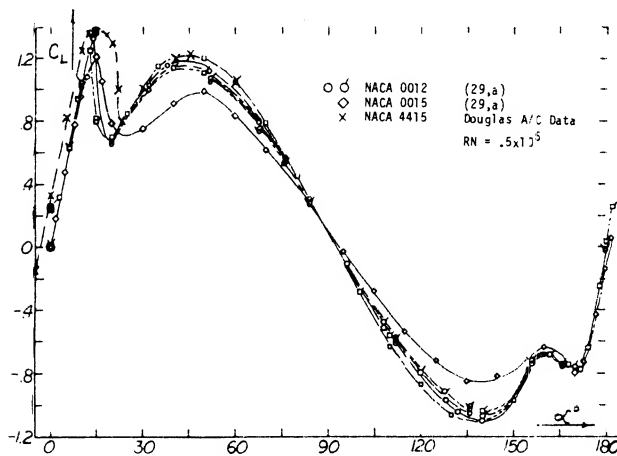


Figure 33. Variation of lift coefficient for angles of attack 0 to 180 degrees.

Correlation of Theory. Analysis of the experimental results presented in figure 33 is as follows. First, multiply the theoretical lift function (30) given as equation (15) by $\cos \alpha$

$$C_L = 2\pi' \sin \alpha \quad (15)$$

to account for the loss of suction around the round leading edge of the section. We must next reduce the constant term 2π , to account for the loss of circulation due to separation. The test lift coefficients are thus approximately represented by

$$C_L = (1.8 \text{ to } 2.0) \sin \alpha \cos \alpha \quad (16)$$

- (29) Lift at High Angles of Attack $0-180^\circ$:
 a) Critzos, NACA 0012, $\alpha=0$ to 180° , NACA TN 3361.
 b) Helicopter Model Blade Stall, J of AHS, Jan 1972.
 c) Sike and Gorenberg, 63A, $\alpha=0$ to 180° AVLABS TR 65-28, AD 619153

from the geometry, we also obtain

$$C_D = (1.8 \text{ to } 2.0) \sin^2 \alpha \quad (17)$$

$$C_N = (1.8 \text{ to } 2.0) \sin \alpha \quad (18)$$

Fully Stalled Wings. In the range of small Reynolds numbers (roughly below $R_c = 10^5$) the boundary layer flow past rounded section noses stays completely laminar; separation follows at zero angle of attack from a theoretically traceable point on the upper side of the section, the location of which is independent of the Reynolds number, but dependent upon the angle of attack. As a consequence, the flow completely separates from the suction side and the lift is mainly due to the pressure forces on the lower side. This type of lift also reaches a maximum as the angle of attack is sufficiently increased; and the maximum lift coefficient is essentially independent of Reynolds number.

Experimental points representing fully stalled (separated) conditions are plotted in figure 34. The maximum lift coefficient is between 0.6 and 0.7, at an angle of attack (for airfoils with $A = 5$ or 6) in the vicinity of 40° . It seems that the influence of Reynolds number in the range below 10^5 to above 10^6 is small in this range of fully stalled flow. At angles of attack below 60° , the highest values tested belong to cambered and round-nosed sections, while the lowest values are formed at negative angles of attack (simulating negative camber). Also, the stalled values of lift coefficients measured in closed wind tunnels are somewhat higher, and lower in open-jet-type tunnels.

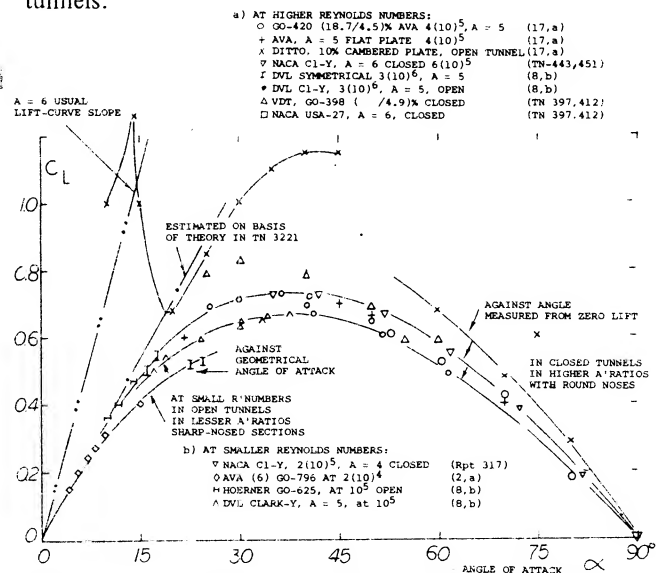


Figure 34. Lift coefficient of rectangular airfoils with A between 5 and 6, as tested at larger angles of attack and/or below $R^5 = 10$, id est in fully stalled (separated) condition.

- (30) Airfoil and Wing Theory:
 a) Hemke, P.E., Prentice Hall, N.Y. 1946.
 b) Sivells and Neely, NACA TN 1269.
 c) Soule & Anderson, Design Charts Stalling Tapered Wings NACA TR 703.

7. DYNAMIC EFFECTS

Fluctuations of Lift. Lifting characteristics as obtained from wind-tunnel tests, and in the form as presented in tunnel reports, are misleading insofar as the lift at and around $C_{L\alpha}$ is sometimes not as steady as it appears. Speeds in air are so high, and the inertia and the damping of the wind-tunnel balances are large enough, so that a time-averaged values of lift and other forces and moments are recorded. A particular characteristic of fluid-dynamic testing in water (in a water tunnel or towing tank) is, on the other hand, the fact that the speeds required to obtain a certain Reynolds number are but a fraction (possibly a few percent) of those in wind tunnels. As a consequence, fluctuations of lift can "easily" be read from the balance. Lift as a function of the angle of attack from a water tunnel test at 2.4 m/sec = 6 ft/sec is plotted in figure 35 for two foil sections. Quoting from (31), the lift of the NACA 0012 section fluctuates "at" $C_{L\alpha}$, irregularly up and down as indicated in the illustration. The cambered and round-nosed section Go-387, displays similar (if lesser) fluctuations at angles of attack beyond $C_{L\alpha}$, over an extended range of that angle. The frequency "f" of these fluctuations as tested, is between 0.2 and 1.0 per second which, at a speed of 2.4 m/sec, leads to the non-dimensional value of

$$f c/V = \text{between } 0.03 \text{ and } 0.16 \quad (19)$$

Dynamic Lift Stall. When a wing or a two-dimensional airfoil approaches the stall angle at a significant rate, such as might be encountered with a sudden pull-up of the airplane, the angle of attack for stall and the maximum lift coefficient are increased (32,a) as compared to the steady state flow case. When the dynamic change of angle of attack reverses the flow on the airfoil the lift does not revert to the value encountered at the lower angles, but will fall below these values. This results in lift coefficients below the values for the steady state case and causes a hysteresis loop as illustrated in figure 36. This tendency for a lift overshoot and a hysteresis loop is encountered in almost any dynamic situation of airfoils, and is especially important in the designs of helicopter, propeller and compressor blades as it may lead to stall flutter. Stall flutter of a blade can result in very high values of torsional stress as well as undesirable vibrations.

The dynamic lift overshoot is also important in the operation of an aircraft, since a sudden pull-up can produce an effective sudden stall even if the wing is one which displays a gentle type stall under steady state conditions. This may cause difficulties, especially under emergency conditions.

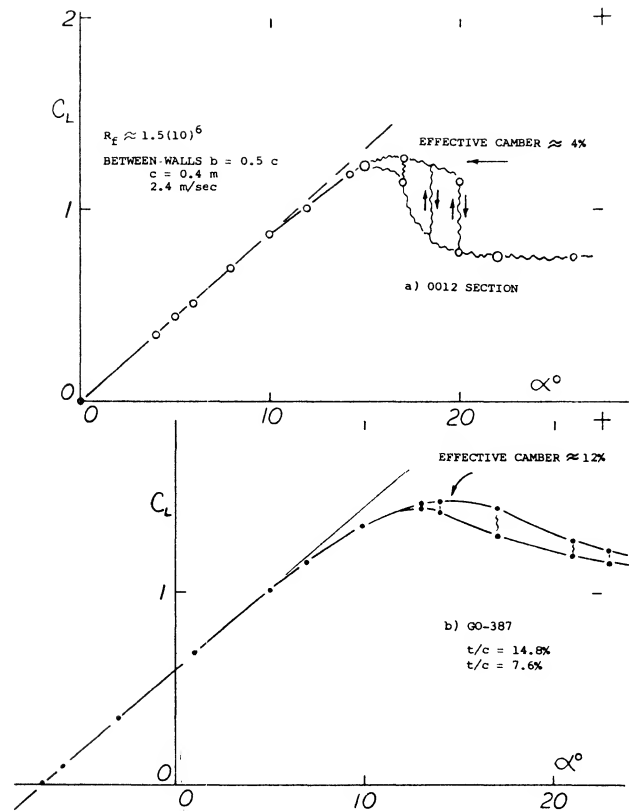


Figure 35. Lift as tested in a water tunnel (31) showing fluctuations in the vicinity of the maximum coefficient.

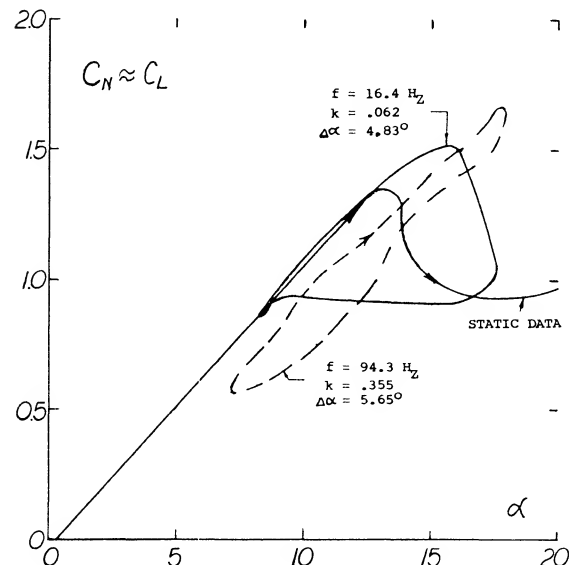


Figure 36. Frequency effect on hysteresis loop for oscillation airfoil (32,i).

- (31) Investigation of foil sections in a water tunnel.
a) Hoerner, 0012 and Go-387, Fieseler W'Tunnel Rpt 3 (1939).

The dynamic lift overshoot is caused by a delay of the adverse pressure gradient, allowing the airfoil to support greater lift than during the steady state case. The oscillating airfoil derives lift from the frequency induced normal velocity and the effects of the change in the rate of angle of attack (32,b). The frequency induced velocity normal to the airfoil effectively results in an increase in the section camber as α increases and a corresponding decrease as α is reduced. Thus, the rate of change of angle of attack, $\dot{\alpha}$, effectively increases and decreases the angle of attack compared to the static case. Since a certain amount of time is required for the boundary layer to build up, separation is delayed and the airfoil responds to the dynamic angle of attack change without stall, also contributing to the lift overshoot (32,c).

The combination of the q and the $\dot{\alpha}$ effects influences the shape of the hysteresis loop which is a function of the reduced frequency defined by (32,d)

$$k = c\omega/V \quad \text{or} \quad c\omega/V_0 \quad (20)$$

where ω is the oscillation frequency, c is the mean aerodynamic chord and c is the 2-dimensional chord length. The reduced frequency is thus a measure of the rate of change of oscillation with respect to the free stream velocity. The reduced frequency given in equation (20) is normally considered applicable only for incompressible flow cases. For the compressible flow case at Mach numbers below the critical the reduced frequency will be

$$k = c\omega/V_0 \sqrt{1-M^2} \quad (21)$$

where M is the free stream Mach number.

The maximum lift coefficient overshoot, $\Delta C_{L,d}$, due to the dynamic condition at which it occurs, $\Delta \alpha_d$, is a function of the section shape, Reynolds number, type of stall and the reduced frequency. Test data (32,f) indicates that for a given level of reduced frequency $\Delta C_{L,d}$ reduces with increasing camber and, although $C_{L,\alpha}$ under static conditions changes with Reynolds and Mach numbers, the lift overshoot is not effected. Under dynamic conditions, however, the level of turbulence increases with the reduced frequency which could give higher values of $\Delta C_{L,d}$ than would be predicted by dynamic effects alone. This, along with the turbulence in the propeller slipstream may explain the large difference between the test data of (32,a) and (32,g), figure 37.

The basic shape of the dynamic lift curve through stall is dependent on the type of stall in the same way as airfoils operating at steady state conditions, figure (38). Thus, trailing edge stall will tend to yield a more rounded stall shape than leading edge stall. The reduced frequency and the type of motion effect the stalling, and it appears the stall becomes sharper as the frequency increases figure 38.

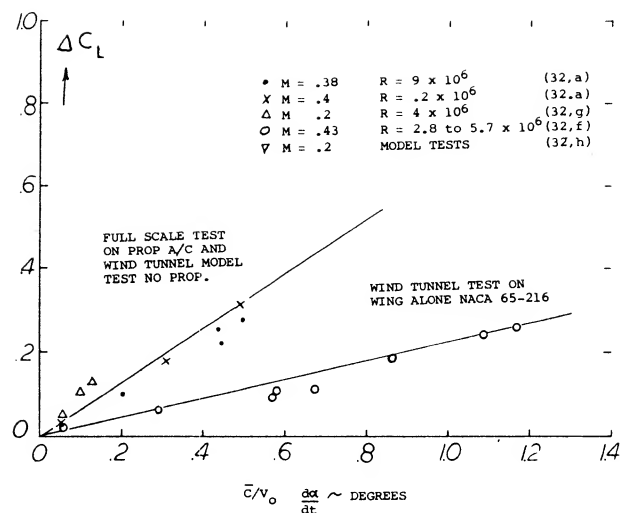


Figure 37. Lift increase due to dynamic change of angle of attack.

The shape of the lift hysteresis curve, figure 36, depends on the airfoil shape, reduced frequency, the initial angle and angle of attack range of the test. If the initial angle of attack and change is below the static stall angle the hysteresis loop will be very small and on the static lift curve slope. However, if the initial angle and increment allow the static stall angle to be exceeded the loop can be large as shown on figure 36.

From figure 37 the lift overshoot can be estimated as a function of the pitch rate velocity and mean aerodynamic chord. The considerable scatter in the test data is caused by changes in section, turbulence and Reynolds number which influence the basic maximum lift of the section.

Although many experimental investigations of dynamic lift stall have been undertaken (32), it is desirable to have a means for predicting the angle overshoot and the shape of the hysteresis loop as a function of the instantaneous angle of attack from the available static airfoil data. An approximate method based on the concept of induced camber, attached flow phase lag and reduced frequency (32,d) appears to give a good first approximation.

(32) Dynamic Lift Stall:

- a) Gadeberg, B.L., Dynamic Aircraft Stall, NACA TN 2525.
- b) Ericsson, L.E., J of Aircraft, Vol 4 No. 5, 1967.
- c) Moore, F.K., Lift Hysteresis — Boundary Layer, NACA TN 1291.
- d) Ericsson, L.E. & Reding, J.P., J.A/C, Vol 8 No. 8 & Vol 8 No. 7.
- e) Halfman, R.L., Johnson, H.C. & Haley, S.M., NACA TN 2533.
- f) Conner, F., Willey, C. and Twomey, W., NASA CR 321.
- g) Davis and Sweberg, NACA TN 1639.
- h) Harper, P., Rate Change on $C_{L,\alpha}$, NACA TN 2061.
- i) Liiva, Jaan, Unsteady Lift, J.Aircraft, Vol. 6, No. 1.

8. STALLING OF STRAIGHT WINGS

The stalling of a wing occurs when the more or less linear function of lift with angle of attack comes ultimately to an end. At this angle where the lift is no longer linear, the flow of the air separates from the suction side and the wing stalls. The stalling of a three dimensional wing is dependent on all the factors discussed in this chapter including the section shape, angle of attack, Reynolds number, Mach number and the planform shape. The stalling of the wing is dependent on the local angle of attack of the sections as effected by both geometrical and induced flow characteristics. Thus, the aspect ratio and shape of the planform are of primary importance. The stalling characteristics of low aspect ratio, delta, and swept wings are complex and, therefore, are covered in separate chapters.

Plan Form. As mentioned in Chapter III, the local lift coefficient of a rectangular wing is highest at the center; stalling, therefore, begins here. On the other hand, in a highly tapered wing, stalling is bound to start at and near the wing tips. Since it is desirable to have a wing display a gradual stall and maintain lateral control, a wing that stalls inboard first is desired. For this reason, reduction of wing-tip stalling is often attempted by twisting the wing so that the effective angle of attack is smaller at the tip than the root. This procedure ("washout") is often supplemented by the use of slots, etc., see Chapter VIII.

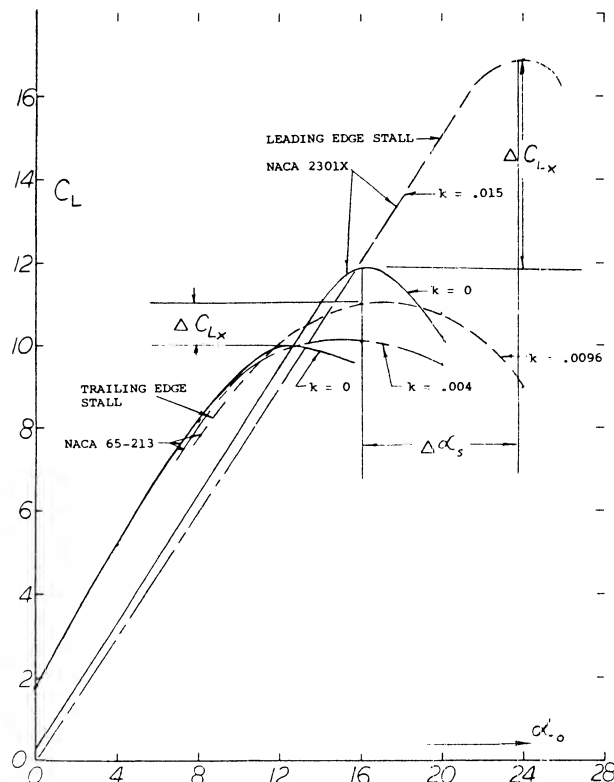


Figure 38. Lift coefficient and angle of attack overshoot from static stall due to dynamic effects (32,d).

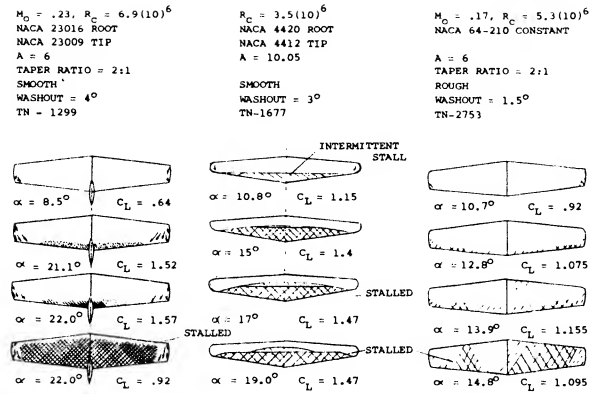


Figure 39. Examples of the stall progression of straight wings differing in aspect ratio and section type.

A typical flow pattern for a tapered wing showing the progression of stall with increasing angle is shown on figure 39. It will be noted that the aspect ratio 6 wing using NACA 23 xxx series airfoils (33,a) develops stall near the trailing edge, and that there is a cross flow from the wing tip. Also, after the maximum lift coefficient has been exceeded the wing tips are still not completely stalled. For the aspect ratio 10 wing with the same type of sections (33,b) stall proceeds in the same manner as the AR = 6 wing. The stall pattern shown would be expected since both wings are built with the tips washed out to obtain this pattern.

In both cases the wings with NACA 23 xxx section exhibited an abrupt stall even though the stall appears to start at the trailing edge. Sharp stall would not be predicted from figure 8, but appears to be a characteristic of the 23 xxx airfoils and is seen in the two dimensional airfoil data (11,b). For wings using NACA 64 and the four digit series the stall is more gradual and of the type that would be predicted using figure 8. The prediction of these characteristics of plane wings is accurate using two-dimensional airfoil data for the proper operating condition of Mach number and Reynolds number and the lifting line theory (30).

- (33) Straight & Taper Wing Stall:
 - a) Mach and Reynolds No. Effects, NACA TN 1299.
 - b) High-Aspect-Ratio Tapered Wings, NACA TN 1677.
 - c) Compressibility Effects, NACA TN 1877.
 - d) Tapered Wings, NACA WR L-311.
- (34) Influence of surface roughness on maximum lift:
 - a) Williams, Thick Sections in CAT, ARC RM 2457 (1951).
 - b) Hoerner, Survey, Ringbuck-Lufo Rpt IA9 (1937).
 - c) Jones, 0012 and RAF-34 in CAT, ARC RM 1708 (1936).
 - d) AVA Gottingen, Ergebnisse III² (1927) p 112.
 - e) Hooker, Airfoils w/Roughness, NACA TN 457 (1933).
 - f) See also references under (28).
- (35) Characteristics of sharp-nosed sections:
 - a) Daley, 6% Thick Sections, NACA TN 3424 (1955).
 - b) DVL, Double-Arc Sections, see (8,c) or (19).
 - c) Solomon, Double Wedge, NACA RM A6G24.
 - d) Polhamus, Drag Due to Lift, NACA TN 3324 (1955).

CHAPTER V — CHARACTERISTICS OF TRAILING-EDGE WING FLAPS

Flaps deflected downward from the trailing edges of wings, are primarily used to increase lift so that the landing speed can be reduced. They may also be used to improve performance during takeoff and when climbing. Available information on high-lift flaps is essentially statistical in nature. It is attempted in the following, to present the trailing edge flap characteristics as a function of pertinent parameters and to find methods of evaluation, beginning with two-dimensional sections and ending with configurations as they are used in operational airplanes.

I. LIFT CHARACTERISTICS IN TWO-DIMENSIONAL FLOW

Wing flaps as used in airplanes, are three-dimensional devices, limited in span, usually interrupted by the fuselage and interfered with by nacelles and propeller slipstreams (if any). The two-dimensional flow characteristics of flaps are the basis, however, from which more complicated configurations can be understood.

1. GENERAL

The problems connected with the design and analysis of trailing-edge flaps, in two-dimensional flow, are as follows:

- lack of, or complexity of theoretical methods,
- the amount of lift added by deflection of flaps,
- pitching moments affecting longitudinal trim,
- load distribution and hinge moments,
- stalling characteristics of flaps and airfoils,
- influence of Reynolds number on maximum lift,
- drag associated with the production of lift.

Analysis. The lift of thin airfoil sections correspond to $C_L = 2 \pi \sin \alpha$. Maximum lift is thus “expected” at $\alpha = 90^\circ$, where practically all of that lift would be generated “at” the leading edge, by way of suction. The maximum lift coefficient would be in the order of $C_{Lx} = 6$. Deflection of a trailing-edge flap has two advantages: it reduces the need for higher angles of attack, and it gives the airfoil section “camber”, thus postponing flow separation from the upper side. Disregarding boundary-layer control (such as by suction) flow separation is evidently so strong at the larger angles of deflection needed that analytical efforts have been considered to be useless (1,e). However, with the use of high speed computation it is expected that methods will be developed to find the performance of wings with flaps (2,g). Lift is generated in a wing, by deflecting a “tube” of the oncoming stream. To understand the mechanism of a trailing-edge flap, one may assume that the deflection corresponds to the direction into which the tail of the air foil section is pointing, or to which a not-too-small flap is deflected. Referring to Chapter IX, it may be said that (taking into account boundary layer effects) roughly:

$$d\alpha / d\delta = C_L / C_{L\alpha} \approx (c_f / c)^n ; 8 < 15^\circ \quad (1)$$

where n decreases from 0.7 at $c_f / c = 0.1$, to 0.6 at $c_f / c = 0.3$. This means that at a chord ratio $c_f / c = 0.2$, for example, a deflection of the flap by 10_f , produces almost the same lift increment as the airfoil or wing at an angle of attack of 5° . Equation 1 can only be used at small angles of flap deflection (say, up to 15°) as they may be used during takeoff and climbing of airplanes. Substantially to increase the maximum lift of a wing, much larger flap angles are required. Replacing the deflection angle δ by its sine, and $d\alpha / d\delta$ by $\sin \delta$, we tentatively obtain

$$\Delta C_L = 2 \pi \sin(\alpha + \delta(d(\sin \alpha) / d(\sin \delta))) \quad (2)$$

For $\alpha = 0$, it may then be true that

$$(\Delta C_L) = 2 \pi \sin(\delta^* (\sin \delta / \delta)(d\alpha / d\delta)) \quad (3)$$

Tentatively again, it is assumed that $d(\sin \alpha)/d(\sin \delta) = d\alpha/d\delta$ as plotted in figure 2 of Chapter IX. For example, for $d\alpha/d\delta = 0.5$, as for $c_f/c = 0.20$ or 0.25 , we thus obtain a maximum

$$(\Delta C_L)_x \approx 0.9 (2\pi) \sin(0.5 \cdot 0.64 \cdot 90)^\circ = 2.7$$

These equations produce a flat maximum at $\delta = 90^\circ$ which seems to be compatible with experimental results on flaps with boundary-layer control by suction. However, flow separation (on plain and split flaps), boundary-layer and circulation losses (on slotted flaps) and increased or "super-circulation" (in particular when blowing over flaps) are bound to bring about negative or positive deviations from any simple theoretical formulation.

Types of Flaps. As illustrated in figure 1, a number of trailing-edge flaps have been developed, tested and used:

- a) The ordinary or plain type (similar to control flaps) is rarely used as a landing flap. As mentioned above, the flow separates easily from the suction side. Maximum lift is not spectacular, drag is high because of separation and the wake is not necessarily stable.
- b) Through the use of boundary layer control (suction) the separation from the plain flap can be eliminated. Characteristics would then be similar to those under (e).
- c) The split flap was for many years used in the design of airplanes, particularly of fighters. This type is considered structurally simple. In terms of performance the lift is comparatively high and the drag connected with the "dead" space behind the flap, is evidently tolerable or even desirable during the landing operation.
- d) The Zap flap (named after its inventor E.F. Zap) is a kinematic variation of the split type. Forces (moments) required for deflection are reduced, and maximum lift is increased (on account of an effective increase of wing chord).
- e) The simple slotted flap (first or predominantly promoted by Handley Page) postpones separation to some 45° of deflection. Lift is increased, and drag is reduced.
- f) The "external" flap (developed and used at one time by Junkers) can be considered to be a slotted flap, with a very long and flat entrance.
- g) The supply of "fresh" air through a slot can be replaced and considerably increased by blowing over the deflected flap.
- h) Shape of and flow through a slot are improved when extending the upper lip and translating the flap accordingly.

i) The Fowler flap (named after H.D. Fowler), combines the slotted feature as in (e) with an increase of the effective geometric airfoil chord; similar to (h).

j) The ultimate in variable geometry are double-, triple-, or multiple-slotted devices, combining and fully utilizing the characteristics as under (e) and (i).

All of these types of trailing-edge flaps (and some similar devices) are discussed in this chapter.

Experimental Results. Wind-tunnel tests are usually carried out between $Re = 4(10)^5$ and possibly $6(10)^5$. For a landing speed, say of 120 knots, and an assumed wing chord of 10 ft, the Reynolds number is in the order of $Re = 10^7$. Realistic simulation of full-scale conditions in wind tunnels thus seems to be possible. However, because of the particularly high lift coefficients tested, tunnel corrections are comparatively large; and it seems that these corrections (developed for lift coefficients, say up to unity) are no longer sufficient. It is shown in Chapter II that pitching moments due to camber as tested in the NACA two-dimensional setup (between walls in a closed test section) are evidently out of line. Although the procedure for correction lift-curve slope (2,b) includes a term corresponding to C_m , it is suspected that this term is no longer adequate considering the extreme amounts of "camber" introduced by trailing-edge flap deflection. Another reason for the high lift increments observed in closed-type tunnels seems to be blockage by larger flap deflections and by the comparatively very large wakes (2,d) trailing from certain types of flaps. Corrected experimental results obtained in open-jet wind tunnels, exhibit, on the other hand, comparatively smaller lift increments due to flaps. This is possibly because of the curved deflection of the tunnel stream. We have corrected (2,c) some of the data evaluated and presented in this chapter to levels believed to be realistic.

Forces and Moments. When using trailing-edge flaps (at modest angles of deflection) during takeoff and when climbing, their performance efficiency (in terms of D/L or L/D) is most important. We will see what can be accomplished when using trailing-edge flaps for this purpose. — Loads due to flaps and on flaps are a justified concern of structural engineering. Pressure or load distributions, and the magnitude of the hinge moments due to deflection, will be presented. — Pitching moments due to flaps are a necessary evil connected with any successful type of trailing-edge flaps. It will be seen what their magnitude is, and how it can be reduced by three-dimensional "tailoring" of a wing.

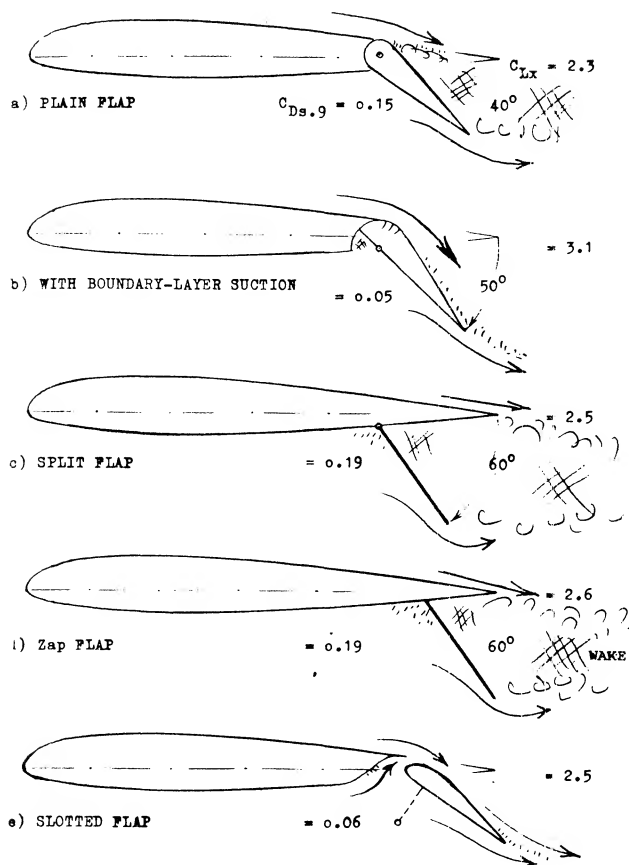


Figure 1 - continued. $C_{Ds,9}$ = D'coefficient at $0.9 C_{L\alpha}$.

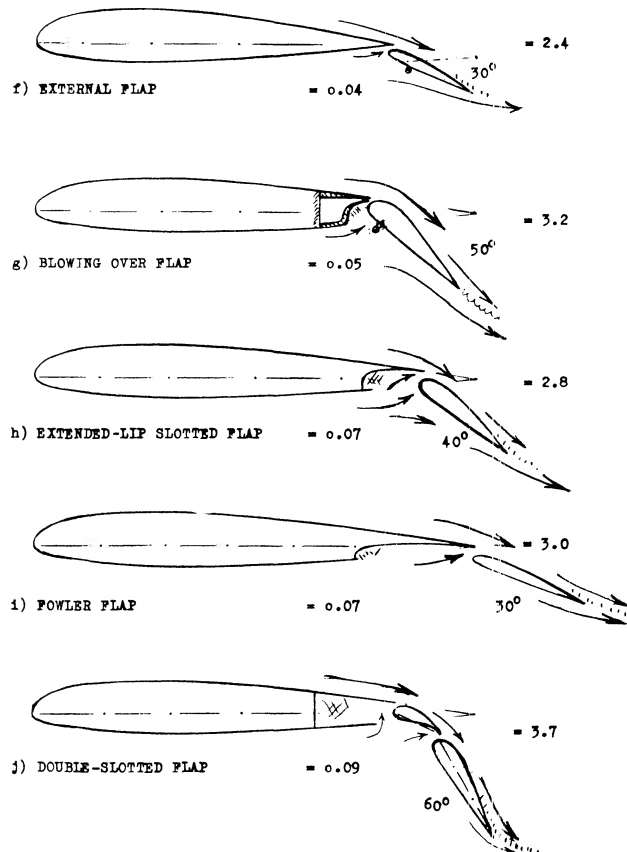


Figure 1. Principal types of trailing-edge flaps, at an angle of deflection considered suitable in the landing operation of airplanes. The force and moment coefficients are estimated average values in two-dimensional flow, for 25% flap-chord ratio.

(1) Theoretical analysis of wing flaps:

a) Theoretical analysis applies primarily to small angles of deflection, and is as such treated in the "control-devices" chapter.

b) For some extension of analysis to higher angles of deflection, see (13,b).

c) Walz, Pressure Distribution Including Wake, Ybk D Lufo 1940 p I-265.

d) Walz, Analysis of $C_{L,max}$ German ZWB FB 1769 (1943); Cornell Trans 1951.

e) Some results of (c) and (d) are shown by Reigels in "Aerodynamische Profile", Oldenbourg Munich 1958. Assuming wake or dead space behind a sufficiently deflected flap to have a certain size and shape, it is possible (c) to "predict" pressure distribution, forces and moments using potential theory. Of course, these characteristics have to be known first from experiments, before the agreement as shown can be obtained.

f) Davenport, Limits of Circulation in Three-Dimensional Flow, J A'Space Sci 1960 p 959. Earlier work on the subject by Helmbold & McCormick is referenced.

g) Stevens Mathematical Model for 2D Multi-Component Airfoils NASA CR-1843.

(2) Correction of wind-tunnel results:

a) It is not the purpose of this text to investigate wind-tunnel techniques. There is some difference, however, in the lift-curve slopes as reported for the two-dimensional setup (between walls) as in (13,a) and as derived from wings tested at $A = 5$ or 6 in open-jet tunnels such as in (13,b).

b) Procedures for correcting closed-tunnel results are reported in (13,a); see also Allen, Wall Interference NACA TRpt 782 (1944).

c) As shown in Chapter II, the lift-curve slope depends upon parameters such as thickness ratio and skin friction (Reynolds number). Restricting ourselves to moderately thick and "conventional" airfoil sections, statistical experience seems to indicate that increments (ΔC_L) as tested in the NACA two-dimensional tunnels are too high (possibly by 4%), while those evaluated from the DVL open-jet tunnel are too low (possibly by 4%). Results in the various graphs of this chapter have been corrected accordingly.

d) Consider that the section-drag coefficient of an airfoil with 60° split flap is in the order of $C_{Ds} = 0.15$, in comparison to less than 0.01 for the plain foil. As a consequence, blocking should have an effect upon lift due to flaps.

e) An example for blocking is NACA TN 3797 where an airfoil with 4.5 ft chord is tested between the walls of a closed tunnel which is 10 ft high, with a 30% plain flap deflected up to 70° . The increment for that angle is stated to be $(\Delta C_L) = 1.8$, which is some 25% more than we would expect according to figure 3.

2. LIFT CHARACTERISTICS OF PLAIN FLAPS

Ordinary or plain flaps are similar in shape to control flaps, elevators and/or rudders as described in Chapter IX.

Lift Increment (ΔC_L). Figure 2 presents the lift coefficient of a flapped wing as a function of its angle of attack α as well as of the flap angle δ . The effect of the flap deflection is to displace the $C_L(\alpha)$ function by more or less a constant amount of ($\Delta\alpha$). At constant lift coefficient, such ($\Delta\alpha$) values can be considered to be independent of the wing aspect ratio. The ratio ($\Delta\alpha/\delta$) could thus be utilized to indicate the flap effectiveness. At the large deflection angles used during landing, C_L does not vary in linear proportion to the angle δ , however. A statistical evaluation is, therefore, needed. Using the angle-of-attack displacement stated above, the lift due to flap deflection corresponds to $\Delta C_L = d\alpha (dC_L/d\alpha)$, where the lift-curve slope ($dC_L/d\alpha$) = $1/(d\alpha/dC_L)$ and the "lift angle" roughly:

$$\Delta\alpha^\circ/dC_L \approx 10 + 20/A \quad (6)$$

as discussed in Chapter III. To eliminate the second term (containing the aspect ratio A) that term is simply subtracted from the "lift angle" as tested. The result is a two-dimensional lift differential due to flap deflection, indicated by

$$(\Delta C_L) \approx \Delta\alpha^\circ / ((d\alpha^\circ/dC_L) - (20/A)) \quad (7)$$

A graphical procedure for the evaluation of this type of (ΔC_L) is indicated in figure 2,a. As discussed above, results from the modern "two-dimensional" closed wind-tunnel setups (2,c) have been "corrected" corresponding to $\Delta(d\alpha/dC_L) = +0.4^\circ$.

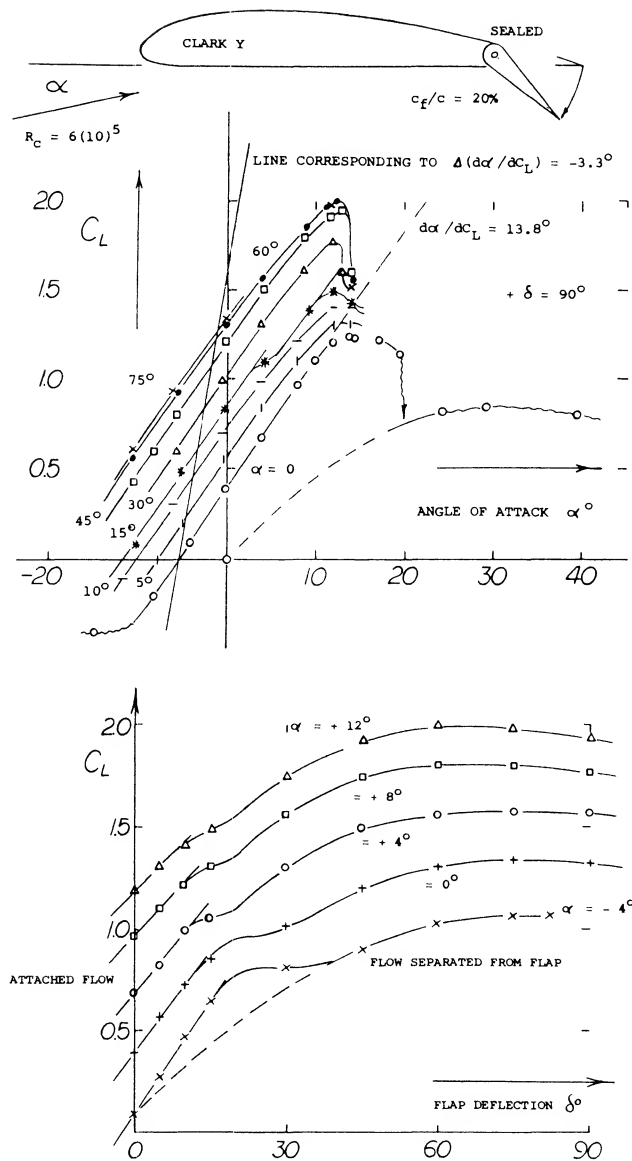


Figure 2. Lift of a flapped rectangular model wing with $A = 6$, tested (10,a) in a closed wind tunnel:

Part a) as a function of the angle of attack α .

Part b) as a function of the flap angle δ .

(3) Summary and review of trailing-edge flaps:

- a) Cahill; Data on Trailing-Edge Devices, with 58 references, with emphasis on slotted flaps; NACA TRpt 938 (1949).
 - b) Wenzinger, Summary as of 1939, SAE Journal 1939 p 161.
 - c) Serby, Review of Full-Scale Landing Flaps, ARC RM 1821 (1937).
 - d) Kruger, High Lift Devices, ZWB UM 3025 (1943) and Tech Berichte 1944 p 461.
 - e) See in Riegels, "Aerodynamische Profile", Oldenbourg 1958.
 - f) Young, Characteristics of Flaps, ARC RM 2622 (1947), with 138 references (theory, flap types, pressure distribution, downwash, swept wings).
- (4) NACA Investigation of Fairchild airplane in full-scale tunnel and in flight:
 - a) Dearborn, With Fowler Flaps, TN 578 (1936).
 - b) Dearborn, With Zap Flap and Ailerons, TN 596 (1937).
 - c) Reed, With External-Airfoil Flaps, TN 604 (1937).
 - d) Silverstein, Maximum Lift Without Flaps, NACA TRpt 618 (1938).
 - (5) Soule, Discussion of the Minimum Horizontal Tail Surface Required for Airplanes With Flaps; NACA TN 597 (1937).

Flap Deflection. Values of (ΔC_L) are plotted in figure 3 as a function of the flap angle. As any plain-type flap is deflected from zero, its (ΔC_L) value increases first according to $d\alpha/\delta = f(c_f/c)$. Between $\delta = 10$ and 20° the flow will separate on the upper side of the airfoil. The actual flap angle for separation depends on the influence of Reynolds number, foil thickness ratio, flap-chord ratio, angle of attack " α " and the size of the gap around the nose of the flap. After an interval in the order of 10° , the increment (ΔC_L) again increases, at a reduced and no longer linear rate, which is similar in character, to $\sin \delta$. The increment (ΔC_L) due to flaps usually reduces somewhat as the angle of attack, or the basic lift coefficient is increased. We have generally evaluated flap effectiveness starting at $\alpha = 0$, or at the angle of attack where the airfoil section used, see figure 2. At angles around $\delta = 60^\circ$, the increment usually reaches a maximum. Any increase of the deflection angle above this limit, gives only a small increase of C_L . For landing near C_{Lx} , for example a high angle of attack would be combined with a large flap angle. The increment (ΔC_L) will then be somewhat smaller than indicated in figure 3.

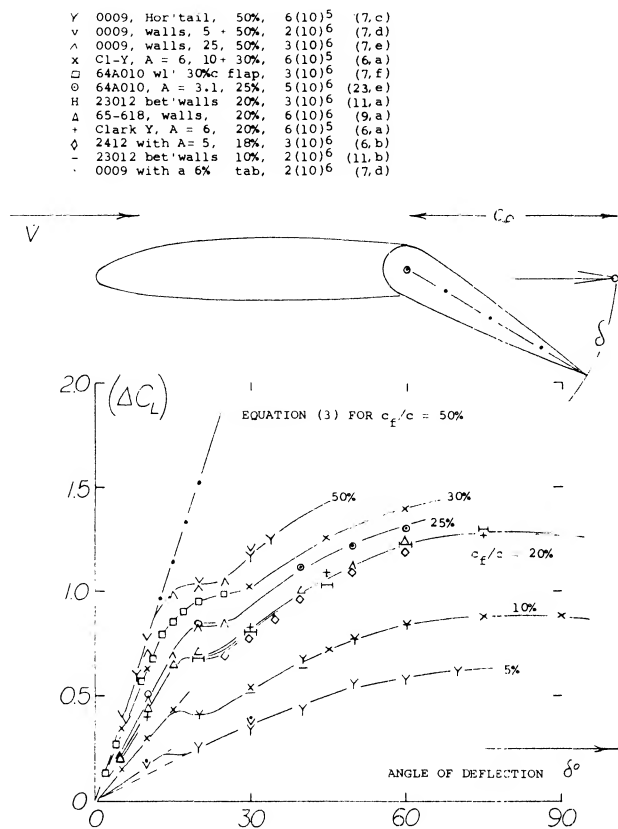


Figure 3. Lift increments (ΔC_L) in two-dimensional flow, of plain flaps deflected from conventional foil sections, at Reynolds numbers between $6(10)^5$ and $6(10)^6$.

Flap-Chord Ratio. The effectiveness of plain flaps increases as a function of the c_f/c ratio. As shown in figure 4, this increase is similar to

$$(\Delta C_L) \sim \sqrt{c_f/c} \quad (8)$$

Referred to the flap area indicated by the flap chord c_f effectiveness is highest in small chord ratios, and decreases rapidly as the ratio is increased. In the design of airplanes, chord ratios in the order of 20% for plain flaps have evidently been found to be most economical or practical, producing a comparatively large increment of lift with a limited structural penalty.

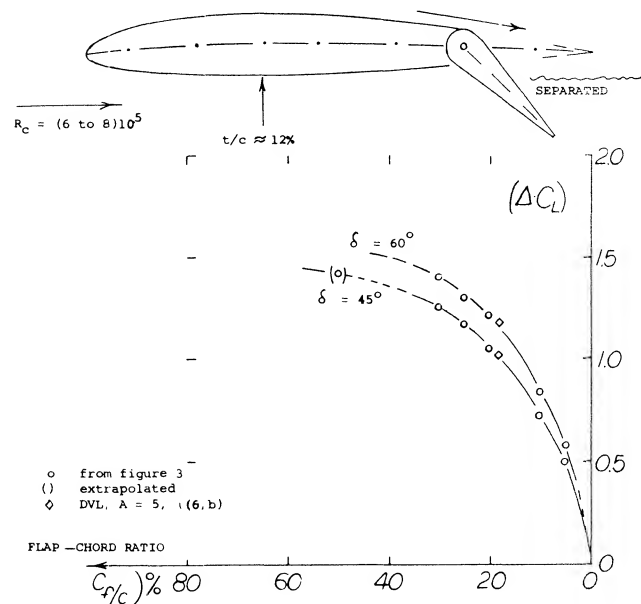


Figure 4. Lift increments of plain flaps (as in figure 3) as a function of their flap-chord ratio.

- (6) Wind-tunnel investigation of simple wing flaps:
 - a) Wenziner, Ordinary and Split Flaps on Various Wings Having $A = 6$, at $R_c = 6(10)$ NACA TRpt 554 (1936).
 - b) Bausch-Doetsch, Rectangular 2412 Wing With Flap and Tab in DVL Open-Jet Wind Tunnel, Yearbk D Lufo 1940 p I-182.
- (7) Investigations of plain control flaps:
 - a) Dods, Nine Related Straight and Swept Horizontal Tails, NACA TN 3497 (1955).
 - b) Bryant, Evaluation of Control-Flap Characteristics for Small Deflections, with 19 references; ARC RM 2730 (1955).
 - c) Gothert, Two Series of Airfoils With Flaps and Tabs Tested to $\delta = 40^\circ$ in Open-Jet Tunnel, Yearbk D Lufo 1940 p I-542.
 - d) NACA, 0009 Foil Section Between Walls With 30, 50, 80% Flaps and With Tabs, TNotes 759, 734, 761 (1939/1940).
 - e) Spearman, 0009 Section with 25 and 50% Control Flaps, NACA TN 1517 (1948).
 - f) Crane, 66-216 Airfoil With Flap and Tab, NACA TRpt 803 (1944).

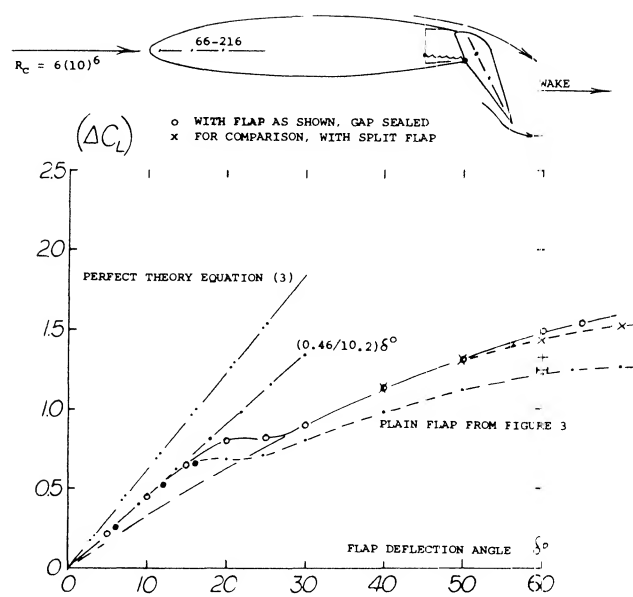


Figure 5. Lift increment of a plain flap (18,a) providing a well rounded shape when deflected.

Round Corner. With the larger radius made possible with the hinge located on the lower side as in figure 5, it would be expected that the flow would go further around the corner without separation than in a conventional plain flap, such as in figure 2 for example. Direct evidence for an improvement at deflections between 30 and 60° is not available. Two things can be seen however, in figure 5, the angle of incipient separation is raised from $\delta = 15^\circ$ to 20° ; and the lift increment (ΔC_L) keeps rising above $\delta = 60^\circ$. Other factors contributing to the increase of lift over that of plain control-type flaps such as in figure 3, are:

- the internal seal, preventing flow through the gap,
- the thickness ratio $t/c = 16\%$, in comparison to $\approx 12\%$,
- the 66-series section, in comparison to "old" shapes.

At any rate, the high effectiveness of the flap in figure 5 at larger angles of deflection is due to several factors as well as the greater radius.

- (8) Influence of stream turbulence:
- Abbott, 23012 Rectangular Wing With Plain and Split Flaps in the Variable-Density Tunnel, NACA TRpt 661 (1939).
 - Morris, Flight Investigation Regarding the Effect of Vortex Generators on Flap Effectiveness, NACA TN 3536 (1955).

Stream Turbulence. The NACA's Variable-Density Wind Tunnel is known to have a very turbulent stream of air, see Chapter IV. Results obtained for a 20% chord plain flap (8,a) are interesting in regard to the influence of turbulence upon the effectiveness of that type of flap. For $\delta = 60^\circ$, the lift increment is:

$$(\Delta C_L) = 1.42 \text{ for the plain flap}$$

$$= 1.27 \text{ for a same-size split flap}$$

Comparison with the results in figure 3 shows that the lift is some 25% higher with plain flaps. The fact that the split flap does not exhibit an increased increment (see figure 6) proves that the phenomenon is not the result of tunnel interference. Thus, the conclusion is that stream turbulence helps the flow somewhat go around the bend of the plain flap. A reduction of turbulent separation, by way of "mixing" can also be produced by means of so-called turbulence generators small pieces of sheetmetal set at an angle of yaw on the upper side of wings, ahead of trailing-edge flaps. Flight tests (8,b) indicate the following:

- Generators do not have a detectable effect at larger angles of flap deflection.
- In climbing flight, with a flap angle of 19° , performance is slightly improved.

H	23012, WALLS, 20 + 40%,	3(10) ⁶ (10, b)
Δ	23012, WALLS, 10 + 30%,	3(10) ⁶ (10, b)
Λ	23012, BET' WALLS, 20%,	3(10) ⁶ (11, a)
+	23012, WITH A = 6, 20%,	8(10) ⁶ (8, a)
x	23012, WITH A = 6, 20%,	6(10) ⁶ (6, a)
\	65-212, BET WALLS 20%,	6(10) ⁶ (10, c)
o	0012, WITH A = 6, 20%,	3(10) ⁶ (10, a)
v	23012, WALLS, 5 & 10%,	3(10) ⁶ (15, b)
v	AVA GOTTINGEN, 5, 10, 20%,	1932 (10, f)

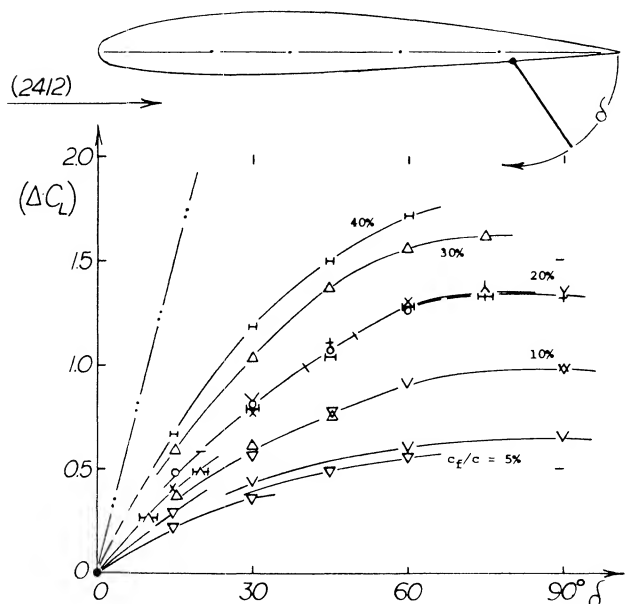


Figure 6. Lift increments (ΔC_L) of split flaps deflected from conventional foil sections with t/c around 12%, at Reynolds numbers between $6(10)^5$ and $6(10)^6$.

3. LIFT CHARACTERISTICS OF SPLIT FLAPS

Split flaps have been used for many years in fighter-type airplanes as a simple device for increasing their glide-path angle and reducing landing speed.

Flow Pattern. At higher angles of deflection, the flow pattern past split flaps is very similar to that of plain flaps. As a consequence, lift as a function of flap angle as in figure 6, is similar to that as in figure 3; that is, above $\delta \approx 25^\circ$. In a similar manner, the lift increments in figure 7, for constant angles of deflection, are almost as high as those in figure 4. Referring to the theoretical "analysis" in the first section of this chapter, equation 3 can be applied to interpolate lift increments using $\delta/2$ and $\sin(\delta/2)$. Figure 7 reveals, however, that split flaps are somewhat superior to plain flaps. The straight upper side of the airfoil section evidently leads the flow right to the trailing edge, while past a plain flap the flow is exposed to interference (mixing) with the highly turbulent "dead" space. Another advantage of the split type might also be a more stable wake pattern; the separation points are clearly fixed.

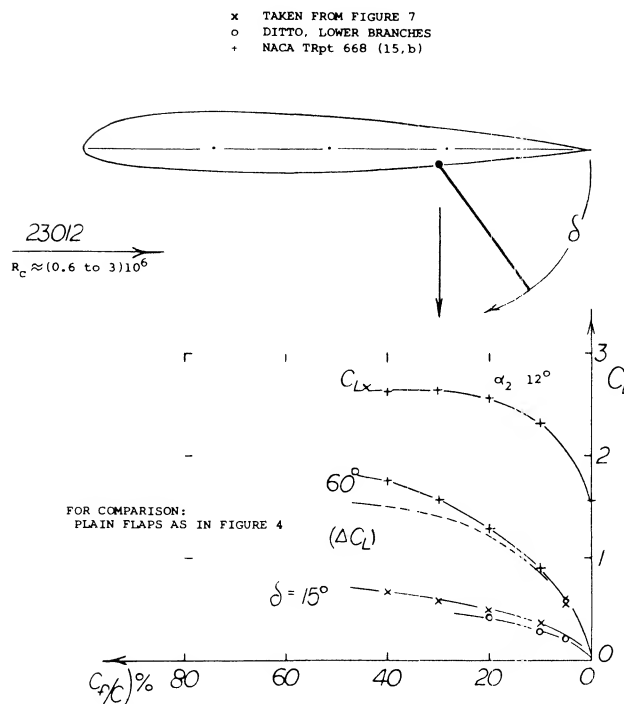


Figure 7, Lift increments as in figure 6, as a function of flap-chord ratio.

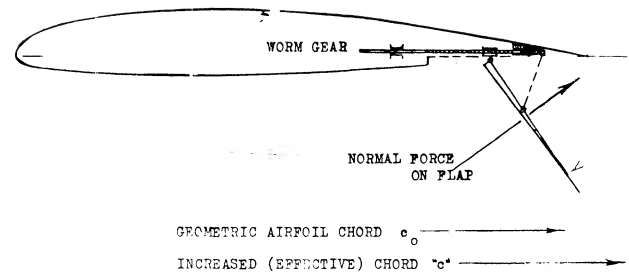


Figure 8, Mechanism of the Zap-type split flap.

Zap Flap. A linkage system is shown in figure 8, through which the split flap can be moved back when deflecting, or be deflected when moving its pivot point back. The advantages are a reduction of actuation forces and an increase of effective wing chord. The corresponding increment of lift may be found in figure 9, as a function of the distance of translation. Assuming that it would be correct to say that in figure 7, the increment increases as $(\Delta C_L) \sim \sqrt{c_f/c}$, it may also be stated that

$$(\Delta C_L) \sim \sqrt{c_z/c_0} \sqrt{c_f/c_0} \quad (10)$$

However, as we will see below, the lift-curve slope increases also corresponding to the effective chord length ($c + \Delta x$). A more basic formulation, therefore, is necessary.

Split Flap Forward. As shown later, the nose-down pitching moments due to trailing-edge wing flaps are large. To reduce them and possibly to make it practical to use split flaps as glide brakes it has been tried to locate such flaps more forward. In figure 9, lift characteristics are shown of a split flap for various flap positions "x" along the lower side of a rectangular wing. Considering the most "stable" range, say at α around 8° , extrapolation of the straight-line lift coefficients to $C_L = \text{zero}$, leads to an approximately common angle of attack. For the 20% flap, this angle corresponds to $\Delta \alpha \approx -15^\circ$, as measured against that for the plain foil section. Such common angles are also found in (12,b) for flap angles different from 60° and for chord ratios other than 20%.

- (9) Investigation of perforated (brake) flaps:
 - a) Purser, Split Flaps on 23012 Wing, NACA W Rpt L-445 (1941).
 - b) Purser, Brake Flaps 33% Perforated, NACA W Rpt L-415 (1943).

Airfoil-Section Shape. Split flaps can easily be attached to wind-tunnel models. This was evidently the inducement for testing routinely (13) various airfoil sections with a standardized 20% and 60° split flap. Such tests are considered to indicate the forebody response to trailing-edge flaps in general, corresponding to thickness ratio and other shape parameters. Evaluation of (13,a) shows that camber between 0 and 4% of the chord has practically no influence on the increment (ΔC_L). One of the parameters describing shape is the location of maximum thickness. The due-to-flap increment increases as this location "x" is moved back along the chord. Thus as tested at $R_c = 6(10)^6$ (with roughness strips added near the leading edge):

20%, 60° SPLIT FLAPS

63-012	x/c = 33%	(ΔC_L) = 1.25
64-012	= 37%	= 1.29
65-012	= 41%	= 1.34
66-012	= 46%	= 1.37

The nose radius of a certain foil section is indicated by

$$r/t = K t/c$$

where $K = 1.1$ for NACA 4-Digit sections, or $K = 0.76$ for the 63 Series, decreasing to 0.70 for the 65 Series. The radius thus varies as

$$r/c = K (t/c)^2 \quad (13)$$

It is seen in figure 12, that when plotted against r/c , certain families of airfoil sections show approximately the same ΔC_L , lift-due-to-flap values. The increment (ΔC_L) increases from 1.25 for sharp-edged sections, to a possible maximum of 1.8 at radius ratios above $r/c = 6\%$. Since the nose radius increases in proportion to the square of the section thickness, it can be argued that according to theory (see Chapter II) that the lift-curve increases with the thickness ratio. For the maximum represented in the graph ($t/c = 24\%$) the increment would be some 19%. The desirable effect of the high leading edge radius illustrates the importance of protecting the leading edge from separation so that high values of $C_{L\alpha}$ can be obtained both with and without flaps. This is further discussed in the next chapter on leading edge devices.

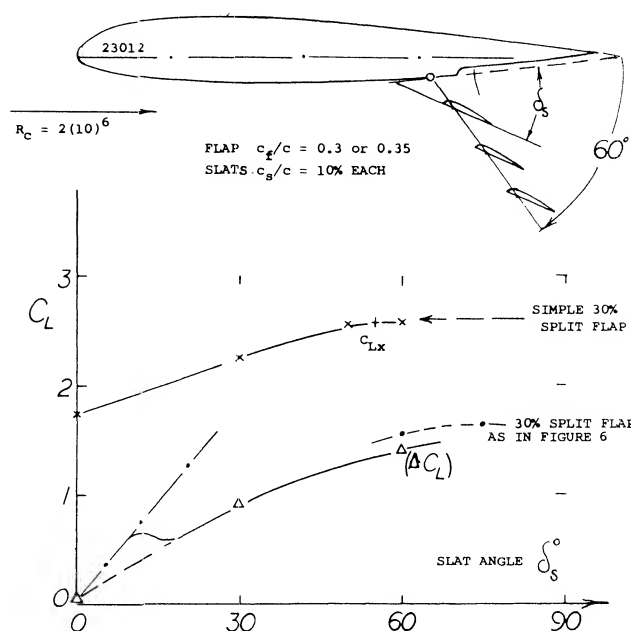


Figure 10. Lift increment of a venetian-blind type split flap (20,c).

(11) Discussion and characteristics of Zap flaps:

- Weick, Split Flap Moved to Rear, NACA TN 422 (1932).
- Joyce, Discussion of Zap Flaps, Trans ASME 1934 p 193.
- Serby, Balancing of Flaps, Aircraft Engineering 1937 p 292.
- Dearborn, Fairchild Airplane with Zap Flap, NACA TN 596 (1937).
- Jones, Full-Scale Flight Tests, ARC RM 1741 (1936).
- Practical Discussion, "Flight" Supplement 27 July and 31 Aug 1933.

(12) Characteristics of split flaps moved forward:

- Wenzinger, 23012 Wings With Split Flaps, NACA TN 661 (1938).
- Wallace, Fairchild Airplane With Split Flaps in Full-Scale Tunnel, also flap loads and downwash, NACA TN or TRpt 539 (1935).
- The Schrenk flap (15,f) is also investigated in the CAT, ARC RM 1636.

(13) Influence of airfoil shape on flap effectiveness:

- Abbott-vonDoenhoff-Stivers, Airfoil Data, NACA TRpt 824 (1945).
- DVL, Collection of Berlin Airfoil Data, ZWB FB 1621 (1943).
- Loftin, Modified 4-Digit Sections, NACA TN 1591 (1948).
- Loftin, 15 Airfoil Sections, NACA TN 1945 (1949).
- Loftin, 6A-Series Airfoil Sections, NACA TRpt 903 (1948).

(14) The flow pattern of slotted flaps:

- Hoerner, Wing Flaps, Fieseler Water Tunnel Rpt 11 (1939).
- Petrikat, Landing Flaps, Fieseler Water Tunnel Rpt 19 (1940).

Trailing-Wedge Angle. The family of airfoil sections reported on in (13,b) shows variations of the nose radius without changing other parameters such as thickness and afterbody shape in (13,a). The results obtained for these variations do not correlate on the basis as in figure 11. Besides the thickness ratio, the trailing-wedge angle, see Chapters II and IX, seems to be the most important parameters. Consider a split flap deflected from the lower side, by a certain constant angle such as 60° , the location of its trailing edge in relation to that of the airfoil, evidently changes as a function of the wedge angle. The edge of the flap moves down as the angle is increased; and its effective chord length may also be considered to be increased. In comparison with a very thin section, the 4424 airfoil included in figure 11, thus has a 27% longer effective flap chord. Based on figure 7, the lift increment might then be expected to be some 13% higher. We have used the section thickness at 80% of the chord as a measure for the trailing-wedge angle. As shown in figure 12, the lift increment due to the standard 20% and 60° split flap increases with the wedge angle, roughly from 1.2 to 1.6 and higher, depending on Reynolds number and wedge shape.

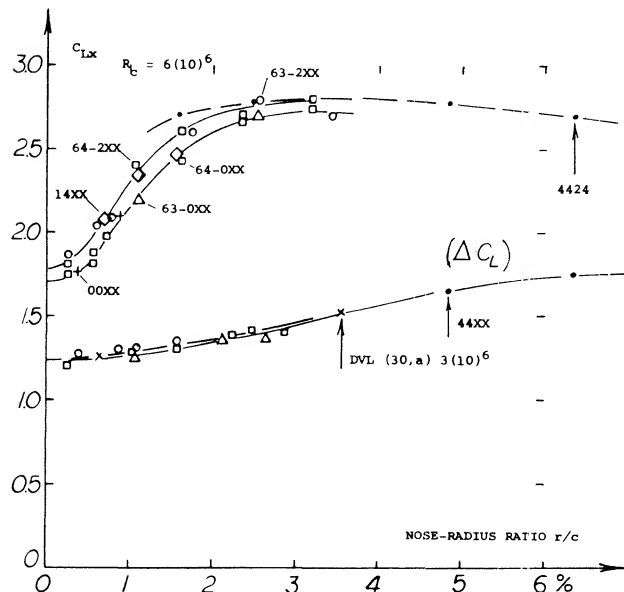


Figure 11. Lift increment in two-dimensional flow due to standard 20% and 60° split flap, as function of the nose-radius ratio.

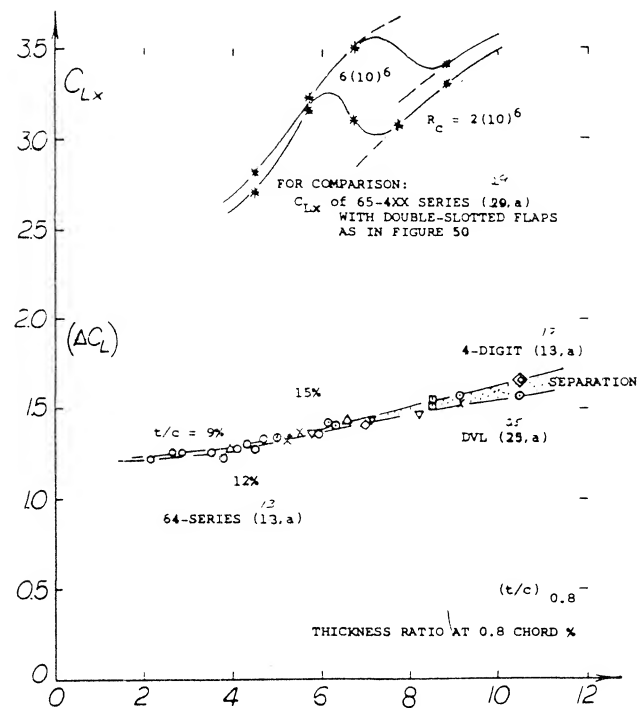


Figure 12. Lift increment in two-dimensional flow due to standard 20% and 60° split flap, as a function of the trailing-wedge angle (thickness ratio at 80% of the foil chord).

Plain Flaps. The influence of the trailing-wedge angle as for split flaps, does not necessarily hold for other types of flaps such as conventional plain flaps. Figure 13 presents the example of an aileron flap and a tab, attached to a 66-216 airfoil section. From what is said in Chapter IX on control devices it is clear that at small angles of deflection, the thin-edged flaps have greater effectiveness. Both the aileron and the tab show each some 25% higher (ΔC_L) values for the cusped section shape. Considering higher angles of deflection (tested to 25° only) where the flow is no longer attached to the back of the flap, the configuration as in figure 13, indicates increments higher by

17% for the aileron,

19% for the tab flap,

when using the concave shape. These variations are contrary to those found for split flaps. There are two reasons to be considered. Plain flaps, with their hinge point located on section center line, do not grow effectively longer when deflected. Also, the geometrical angle of the flap at the lower side and near the trailing edge, is somewhat larger for the cusped than for the straight-sided shape.

(15) Wind-tunnel investigation of slotted flaps:

- a) Wenzinger, 23012 With Various Shapes, NACA TRpt 664 (1939).
- b) Wenzinger, 23012 With Flaps and Tabs, NACA TRpt 679 (1939).
- c) Harris, 23012 Airfoil With 40% Flap, NACA TN 715 (1939).

4. LIFT CHARACTERISTICS OF SLOTTED FLAPS

To postpone flow separation from the back of deflected flaps, boundary-layer control by means of a slot, opening ahead of the flap nose has been found useful.

Single-Slotted Flaps. In a systematic investigation of slot shapes (15,a) the one designated as “2-h” (with a somewhat extended upper lip) was found to provide the highest lift—combined with the lowest drag coefficients. To obtain the optimum positions shown in figure 14, a complicated kinematic system is required; simple rotation about a suitable hinge point is not optimum for all angles of attack and of deflection encountered during takeoff, climb and when landing an airplane. Lift increments both for fixed hinge point and for optimum positions, are indicated in figure 14. These increments are appreciably higher than those for plain or split flaps (in figures 3 and 6, respectively). However, there is a limit above $\delta = 40^\circ$, where separation evidently takes place. Other flaps of the slotted type, shown in figure 15, show a deterioration of their performance, already at $\delta = 30$ or 35° . As a function of their chord ratio, there are not many results available; they are included in figure 19.

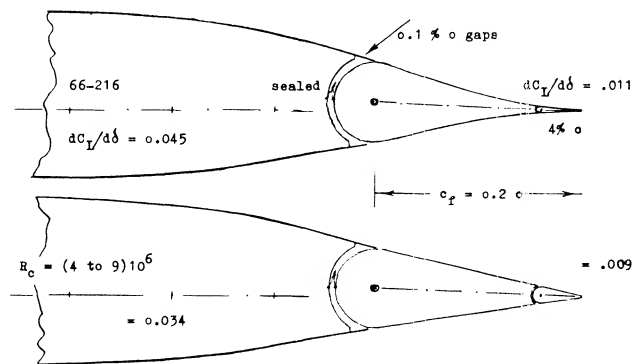


Figure 13. Lifting characteristics of a plain flap and a tab, for two different shapes of the trailing edge of the airfoil section used.

External Flaps. It has been mentioned (under “flow pattern”) that a way of substantially improving the performance of flap slots, is to make their entrance long and flat. In the extreme, this design procedure leads to the “external” flap, developed at one time by Junkers (17,e) under the name of Doppelflügel (double wing). As suggested in figure 1, structural strength necessitates a larger thickness ratio of the “main” airfoil section. The combination of main airfoil and flap must be considered to be the lifting wing. Characteristics of such a wing with $A = 6$, are presented in figure 16. The fact that tests in the NACA’s Variable-Density Tunnel produce a high lift-curve slope (at $\alpha = -2^\circ$) may be attributed to the turbulence level in that facility. The flow past the flap breaks down between 30 and 40° deflection. In aerodynamic respect, the external flap can also be considered to be a Fowler-type.

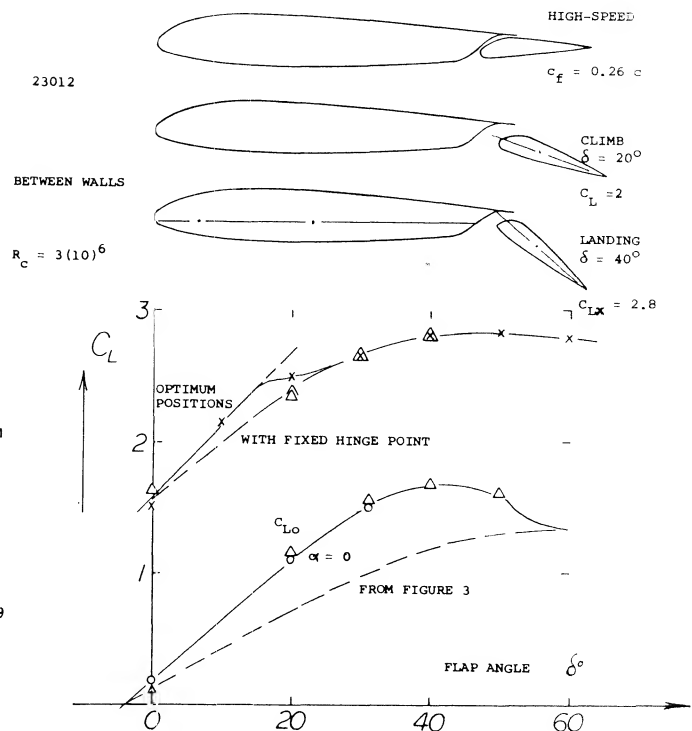


Figure 14. Optimum slotted flap “2-h” as tested in (15,a).

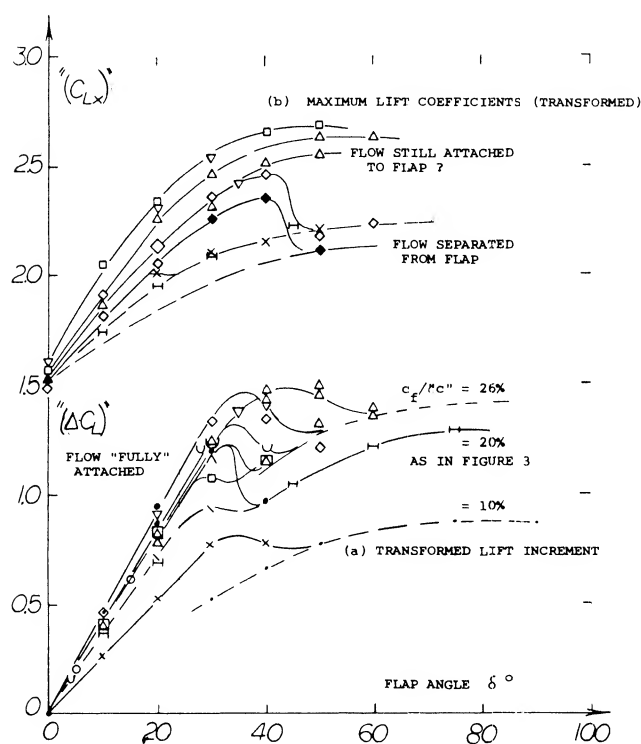
(16) Particularly thick airfoils with flaps:

- Wenzinger, 23021 With Slotted Flaps, NACA TRpt 677 (1939).
- Duschik, 23021 With 40% Slotted Flap, NACA TN 728 (1939).
- Recant, 23030 Airfoil With Various Slotted Flaps, NACA TN 755 (1940).
- Harris, Pressure Distribution With Slotted and Split Flap, NACA TRpt 718.
- Harris, 23012/30 Airfoils With Slotted Flaps, NACA TRpt 723 (29,a) (1941).
- Wenzinger, 23012/30 Airfoils With Split Flaps, NACA TRpt 668 (15,b) (1939).

(17) Characteristics of external flaps:

- Wenzinger, 23012 Airfoil Between Walls, NACA TRpt 614 (1938).
- Reed, Fairchild Airplane With 23015 Wing, NACA TN 604 (1937).
- Platt; 23012 Airfoil, Also With Roll Control, NACA TRpt 541 (1935).
- Platt; 23012 and 21 Wings, also in VDT Tunnel, NACA TRpt 573 (36).
- Billeb, Junkers Doppelflügel, Luftwissen January 1935; Translation in “The Aeroplane” 1935 p 269.
- Bradfield, Junkers Type Ailerons, ARC RM 1583 (1934).

Fowler Flaps. A breakthrough in the aerodynamic design of wing flaps invented by H.D. Fowler. This flap combines: a highly efficient slot opening with an effective increase of wing chord. When retracted, the Fowler flap is hidden within the contour of the airfoil section, with only a small gap left (if any at all) on the lower side. Translation and deflection of this type of flap poses some engineering problems, of course. For one thing, the flap has to be moved along tracks; and these tracks are likely to protrude from under and beyond the trailing edge of the basic wing. Also, when effectively increasing the wing chord, the lift-curve slope increases (with the lift coefficient still based upon the original chord). This increase is shown in figure 17.



LEGEND FOR FIGURE 15/ SLOTTED FLAPS:

- a) SINGLE SLOTTED FLAPS:
- | | | |
|------------------------------|----------|--------|
| 23012, WALLS, SINGLE SLOTTED | 26%/1.08 | (15,c) |
| 23012, WALLS, SINGLE SLOTTED | 40%/1.1 | (15,c) |
| 23012, WALLS, SINGLE SLOTTED | 10%/1.0 | (15,b) |
| 23012, WALLS, SINGLE SLOTTED | 26%/1.08 | (15,a) |
| DITTO, OPTIMUM FLAP "2-h" | 26%/1.08 | (15,a) |

- b) EXTENDED-LIP SLOTTED FLAPS:
- | | | |
|----------------------------------|---------|--------|
| 23012, END PLATES, EXTERNAL FLAP | 20%/1.0 | (17,a) |
| 66-(1.5)16, A 6, FOWLER FLAP | 30%/1.3 | (23,d) |
| 23012, WALLS, EXTENDED LIP | 30%/1.2 | (18,a) |
| DITTO, REAL FOWLER FLAP | 30%/1.3 | (18,a) |
| 23012, EXTERNAL FLAP, A 6 | 20%/1.2 | (17,c) |
| 63-420, WALLS, TRANSLATING FLAP | 25%/1.1 | (18,a) |

- c) FOR COMPARISON:
- | | | |
|--------------------------|---------|--------|
| 23012, WALLS, PLAIN FLAP | 20%/1.0 | (15,a) |
|--------------------------|---------|--------|

ALMOST ALL THE FLAPS ARE TESTED AT $R_c = 2$ or $3 \cdot 10^6$.
RESULTS ARE TRANSFORMED TO THE EFFECTIVE CHORD
LENGTH "c" BY DIVIDING THROUGH THE RATIOS LISTED.

Figure 15. Lift increments (ΔC_L) and maximum lift coefficients of various slotted flaps in two-dimensional flow, as function of their angle of deflection.

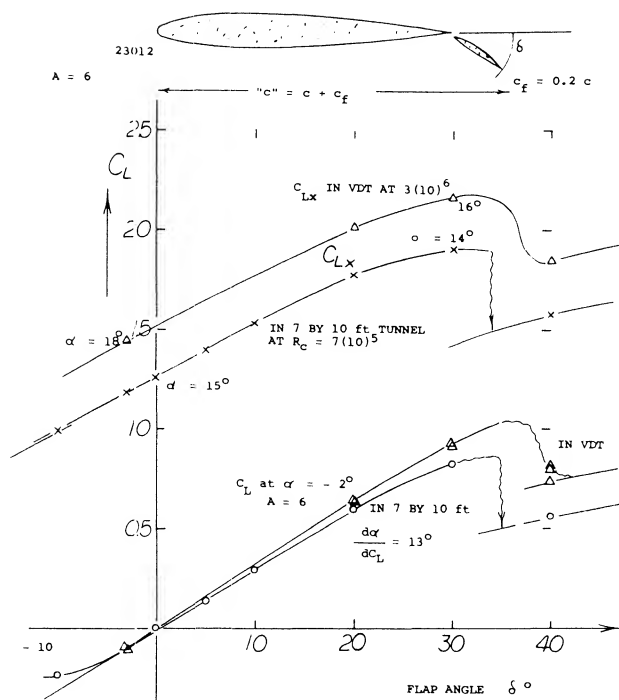


Figure 16. Example (17) of an external flap (Doppelflügel) as part of a rectangular wing with an aspect ratio of $A = 6$.

Chord Extension. It can be assumed that the lift-curve slope ($dC_L/d\alpha$) grows in proportion to $(c + \Delta x)$, where Δx = chordwise translation of the flap when deflecting and extending. Lift characteristics can thus be reduced to those of an airfoil section having the chord " c " = $(c + \Delta x)$, and a flap-chord ratio

$$c_f/"c" = 1/((c/c_f) + (\Delta x/c_f)) \quad (17)$$

Even the original simple slotted flaps have a small translation to the rear when deflected to a suitable position. For the ideal (fully extended) Fowler flap, the translation is $\Delta x = c_f$. We thus obtain:

an effective foil chord

$$"c" = c + \Delta x = c(1 + c_f/c),$$

an effective flap-chord ratio

$$c_f/"c" = (c_f/c)/(1 + c_f/c)$$

an effective lift coefficient

$$"C_L" = C_L/(1 + c_f/c)$$

Using this type of transformation, we can treat these flaps in the same manner as simple slotted flaps (assumed to have no translation). Lift increments " (ΔC_L) " and maximum coefficients " C_{Lx} " for Fowler flaps are thus included in figure 15.

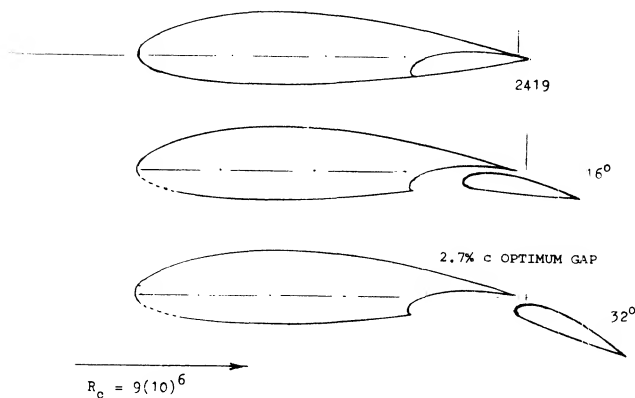
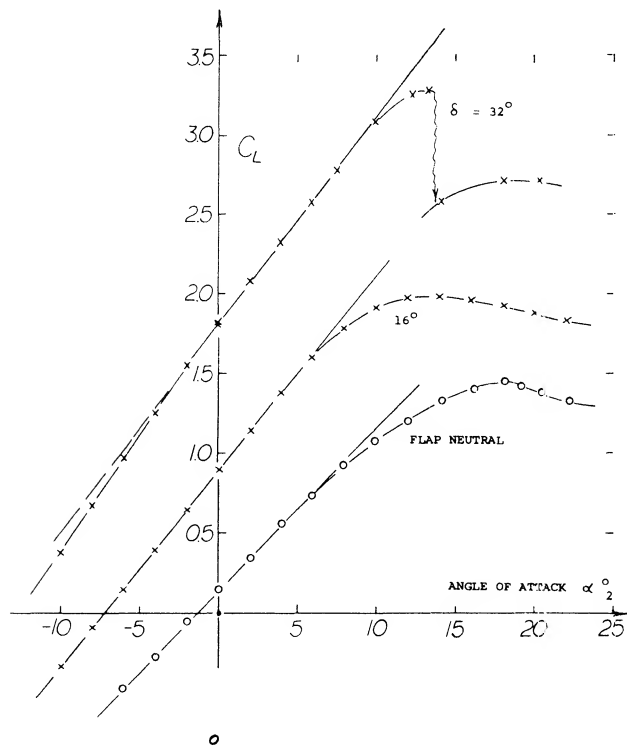


Figure 17. Example for a 30% Fowler flap, tested (20.g) between walls, in three positions.

(18) Characteristics of slotted flaps with extended lip:

- Lowry, 23012 Airfoil With 3 Flaps, NACA TN 803 (1941).
- Loftin, 65-(1.5)13 Airfoil With Flap, NACA W Rpt 746 (1946).
- Cahill, 65-210 Airfoil With 4 Flaps, NACA TN 1191 (1947).

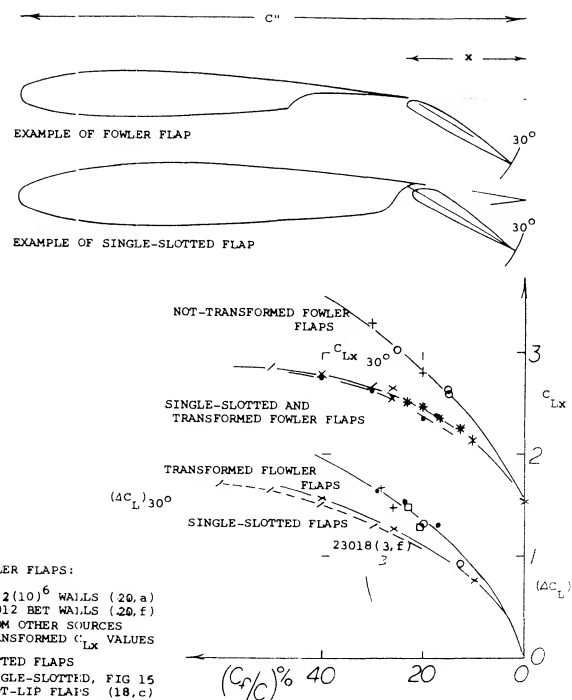


Figure 18. Examples for slotted flaps with extended lips and corresponding translation, tested (18,c) between walls at $\delta = 40^\circ$ each, in optimum position.

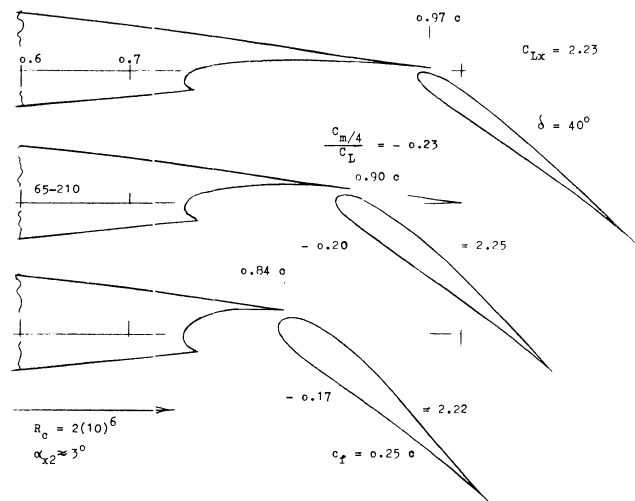


Figure 19. Lift characteristics of all types of slotted flaps as a function of their chord ratio. It must be noted that the standard increment (ΔC_L) is plotted in transformed manner, while the maximum coefficients C_{Lx} are indicated in conventional form.

(19) Flaps for takeoff

- Wimpress, Short takeoff and landing for aircraft, A&A Feb. 1966
- Title 14 -- Aeronautics and Space, Code of Federal Regulations 1974

Extended Slot Lip. Fowler flaps have the disadvantage of producing large nose-down pitching moments. It is possible, however, to go "half" way, such as in the extended-lip flaps shown in figure 18. Using the transformation explained above, their lift coefficients are also included in figure 16; and all types of slotted flaps are evaluated in figure 19 as a function of their chord ratio. Extended-lip flaps reach a critical angle, at δ between 30° and 45° , where flow separation takes place. There is evidence, however, to the effect that these flaps are superior to the simple type, at $\delta = 30^\circ$. At this angle, their lift increment is some 20% higher than that of the simple flaps. It is assumed that the long and flat slot entrance, made possibly by translation, produces a better flow through the slot with consequent better boundary layer control on the upper side. There are similar critical angles and/or lift coefficients found in the maximum lift coefficients. After separation, the "viscous" drag is higher, but $C_{L\alpha}$ resumes rising after a dip, in a manner similar to that of airfoils with plain or split flaps as in figures 3 and 6, respectively.

II. PERFORMANCE OF WINGS WITH FLAPS

In conventional airplanes, landing flaps seldom cover the entire wing span as the wing tips have to be reserved for ailerons. As a consequence the performance of wings with flaps is somewhat different from that given for two-dimensional sections in the first section of this chapter.

1. CHARACTERISTICS IN THREE-DIMENSIONAL FLOW

In wings with finite span the induced angle of attack and the induced drag have important effects upon the performance of flaps.

Limits of Circulation. Any lifting wing deflects a stream tube of air with an effective diameter approximately equal to its span. In engineering language the corresponding downwash angle at the "lifting line" corresponds to the second term in

$$d\alpha^\circ/dC_L \approx 10 + 20/A \quad (20)$$

where $20 = 180/\pi^2 = 18.2^\circ$, plus some 10% accounting for non-elliptical distribution across the span and other effects (such as round tip shape, for example). When using wing flaps, producing maximum lift coefficients above 3, at an angle of attack approaching 30° , equation 20 may no longer be adequate. First, theory shows that $C_L = 2\pi \sin\alpha$ in two dimensional flow. This leads to the first term of equation 20 or $10 \approx 180/2\pi^2 \cdot 0.9$ where 0.9 accounts for boundary-layer losses of circulation. Using the sine for $\alpha = 30^\circ$ we find a reduction of lift by almost 5%, in two-dimensional flow. At any rate, it is clear that equation (20) cannot be used for lift coefficients approaching the simple theoretical limit for plain airfoils, of $C_L = 2\pi$, see Chapter IV as we can obtain for example, when using airfoils and flaps with boundary-layer control. Theoretical limits of circulation have been considered; and they are summarized in Chapter IV and (1,f). It is believed that the maximum (average across the span) circulation obtainable corresponds to

$$C_{L\lim} \approx 1.9 A \quad (22)$$

Considering "powered" lift such as in the jet flap, the circulation component of lift (but not the jet-reaction force) may be expected to conform to this equation as discussed later in conjunction with figure 39.

"Base" Drag. Behind flaps with separated flow pattern there is a negative base-type pressure. Tests reveal that the magnitude of this pressure behind split flaps deflected 60° , corresponds to the coefficients.

$$C_p = -0.55 \text{ in two-dimensional flow} \\ \text{(between walls)}$$

$$= -0.60 \text{ in wings with full-span} \\ \text{split flaps}$$

$$= -0.45 \text{ in wings with part-span} \\ \text{split flaps}$$

So, there is a difference in drag due to flaps installed on finite wings. Assuming that the negative pressure has some boundary-layer controlling effect upon the upper side of the airfoil, there is also a possibility that in part-span flaps, quantities such as (ΔC_L) and $C_{L\alpha}$ are somehow lower than in two-dimensional conditions. The negative pressure in full-span split flaps may be explained by tip vortex suction.

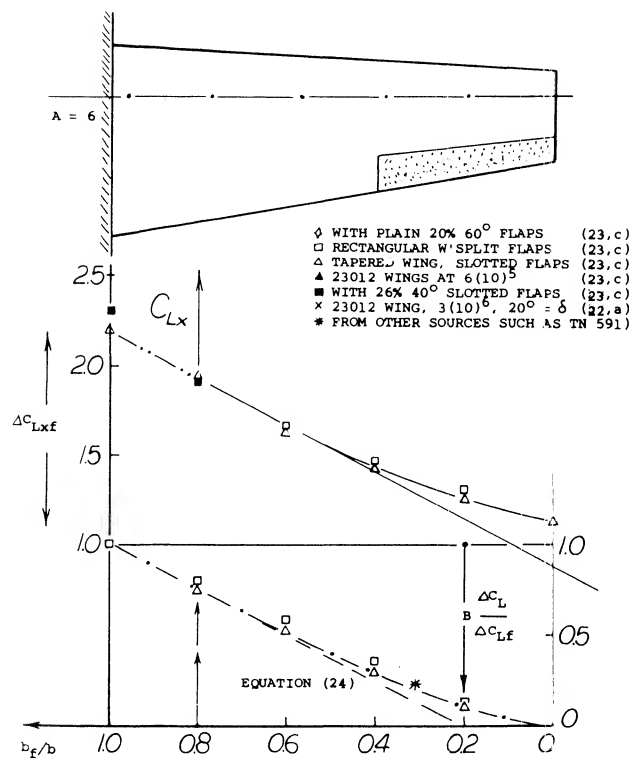
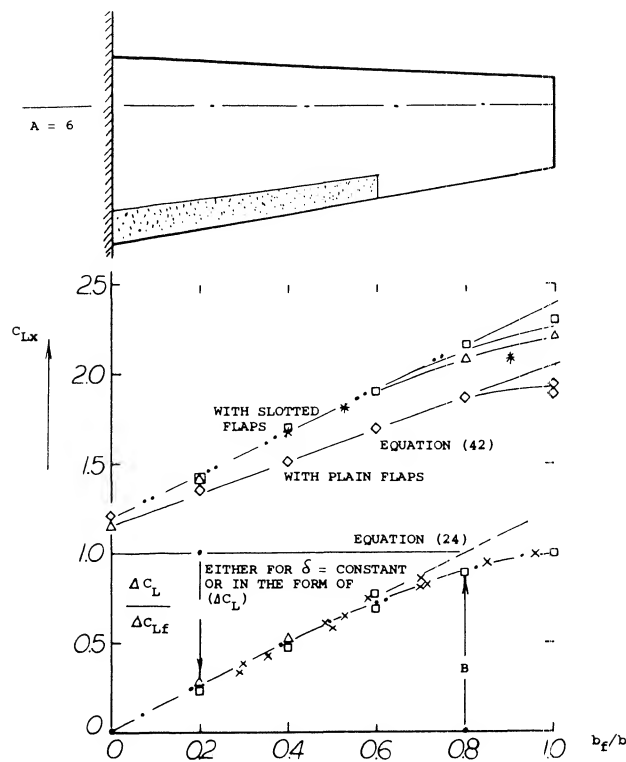


Figure 20. Lifting characteristics of wings with part-span trailing-edge flaps.

Part (a) – Inboard (landing) flaps.

Part (b) – Outboard flaps (ailerons).

Part-Span Flaps. Figure 20 shows how the overall lift of a wing is reduced as a function of the flap-span ratio. Since the presence of the fuselage usually makes it impossible to deflect wing flaps in the very center of the airplane, a function is also included showing how lift decreases when cutting away from the center. Flaps are usually used up to some 0.6 of each half span; and the cutout due to fuselage may amount to 0.1 b . The resultant lift increment of an airplane as derived from the graph, may be some 70% of the two-dimensional values found in the first section of this chapter. This influences the performance in three ways:

- the optimum average lift coefficient is reduced,
- the optimum flap deflection is reduced,
- the induced drag of the wing is increased.

The induced drag will be considered under “takeoff” and “climb”. The results of part-span analysis (23,c) are plotted in figure 20. The subscript “f” indicates values for a wing with full-span flaps. The ratio $\Delta C_L / \Delta C_{Lf}$ can be evaluated for constant angle of attack such as $\alpha = \text{zero}$. For small angles of deflection:

$$\Delta C_L / \Delta C_{Lf} = C_{L\delta} / C_{L\delta f} \quad (23)$$

where $C_{L\delta} = dC_L / d\delta$. Theory is well confirmed by experimental points. Variations of the function with platform (taper ratio) and/or aspect ratio are predicted to be small. For flap-span ratios up to 0.5 halfspan, it can be written:

$$\Delta C_L / \Delta C_{Lf} \approx 1.25 (b_f / b) \quad (24)$$

(20) Characteristics of Fowler and similar flaps:

- Wenzinger, Pressure Distributions 20 to 40% Flaps, NACA TRpt 620 (1938).
- Platt; Wing Including Loads, Downwash, Takeoff; NACA TRpt 534 (1935).
- Wenzinger, Venetian-Blind Flaps, NACA TRpt 689 (1940).
- Wenzinger, 23012 Airfoil With Auxiliary Tabs, NACA TRpt 679 (1939).
- H.D. Fowler, Variable Lift, “Western Flying”, Nov 1931 p 31.
- Harris, 23012 Airfoil With 2 Flaps, NACA W Rpt L-441 (1940).
- Fullmer, Foil Sections for Lockheed “Vega”, NACA W Rpt L-681 (1945).

(21) Rettie, Velocity Around Airfoil Nose, ARC RM 3027 (1957).

Outboard Flaps. The results in part (b) of figure 20, gives the influence of a fuselage on the performance of outboard flaps. It might tentatively be assumed that the loss of lift is

$$(\Delta C_L / \Delta C_{L_f}) = (b - b_f) / b \quad (25)$$

where $b - b_f$ = flap cutout in the center of the wing. For determining maximum lift, a similar equation might be used.

Lift Distribution. The problem with part-span wings, is the fact that optimum conditions (providing maximum L/D) in the flapped and the plain parts of the span may not be obtained at one and the same angle of attack. For the modest angle of deflection $\delta = 20^\circ$, the lift increment due to an average flap is already $\Delta C_L \approx 0.7$ ($\Delta C_L \approx 0.7$), while the difference in the optimum coefficient between flapped and plain parts of the wing, only amounts to $\Delta C_L \approx 0.2$. Thus, a compromise must be accepted and the optimum angle of flap deflection may only be in the order of 10° , rather than 30 or even 40° as suggested by two-dimensional flap investigations. In fact, all the disturbances and interruptions of the lift distribution by supporting and actuating devices, by the fuselage and by engine nacelles, make the more advanced wind-tunnel results questionable, particularly as far as flight performance is concerned.

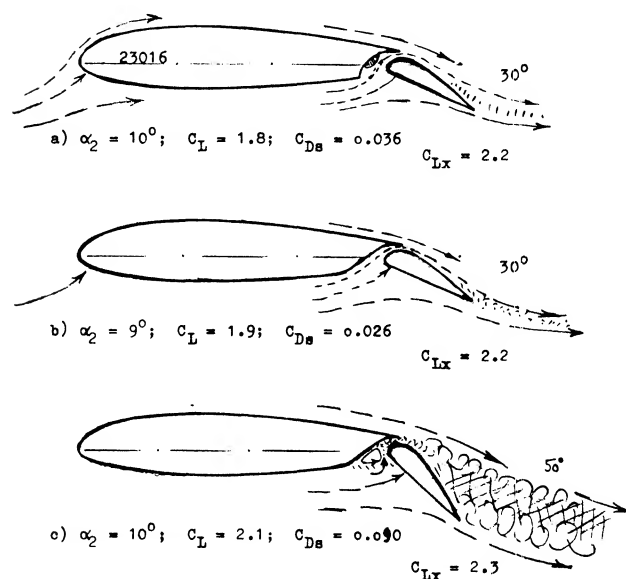


Figure 21. Examples for the flow pattern past slotted-flap configurations as observed in a water tunnel at Re_f above 10^6 .

2. PERFORMANCE DURING TAKEOFF AND CLIMB

Although flaps are usually designed for the landing condition, higher lift coefficients will also make possible improved performance during takeoff and climb. At these conditions drag becomes an important consideration as the performance is determined by the level of excess thrust. Thus, for improved takeoff and climb performance it will be found that flaps with higher levels of C_{Lx} and lift drag ratio are needed.

Flow Pattern. To determine the best flap configuration, it is desirable to understand the flow pattern in and around the flap. Unfortunately, when watching wind-tunnel tests one sees very little. Examination of the drag- and lift forces as tested, and sometimes pressure distributions, will give some indication of the actual flow pattern. For example, flow separation from the upper side of the flap shows up in reduced lift, increased drag and (if tested) in higher hinge moments. However, some investigations of slotted flaps have been undertaken (14) in a water tunnel where the flow pattern was visible while measuring forces and moments at the same time. Some results are presented in figure 21.

a) In neutral flap position, there is a stationary small vortex within the slot entrance. Such a vortex consumes little energy, provided that the outlet of the slot is effectively closed (sealed).

b) For the slot shape as shown, the flow separates around the bend of the entrance. As long as this separation is only local, an efficient nozzle flow may develop, as long as the flow remains essentially attached to the upper side of the flap.

c) A bad example of a flow pattern is shown for a deflection angle of 50° . Separation is "complete" within the slot as well as on the upper side of the flap.

Optimum or acceptable slot and flap shapes are discussed below. However, the only straight-forward way of making a single-slotted flap really efficient is to give it a long and flat entrance. In a way, this is done in the case of the Fowler flap (to be discussed later).

Thick Wing Sections. For a certain period of time, sections with thickness ratios in the order of 20% were used. It seems that someone put together the facts

that minimum drag of thick sections (when tested on smooth wind-tunnel models) is not much higher than that of wings with conventional thickness ratios,

that very high aspect ratios may result in low induced drag and long range,

that thick wings could be used to store fuel, as in long-range airplanes.

It was therefore found justified to spend money on the tunnel testing of airfoil sections up to $t/c = 30\%$ such as in (16c,e,f). It is interesting to see to what limits one can go in aerodynamic shape. To increase the maximum lift coefficient of such sections, slotted flaps have been tried (15,d,e,f). The general characteristics of their performance are given in figure 22. The choice of the flap type for these thick sections can be evaluated from a comparison of C_{Lx} and L/D @ $C_L = .9 C_{Lx}$. Based on this the double slotted type is superior because of the reduced separation and drag.

Thrust Available. The takeoff and climb performance is directly a function of the excess thrust available as shown by equation

$$w_c = (T/W - D/W)V = (T/W - 1/(L/D))V$$

Since the thrust available is here considered to be fixed, the thrust required must be determined and minimized for best performance. The excess thrust is the difference in that available and the total drag. On the ground the drag includes the ground rolling friction, the "parasitic" or

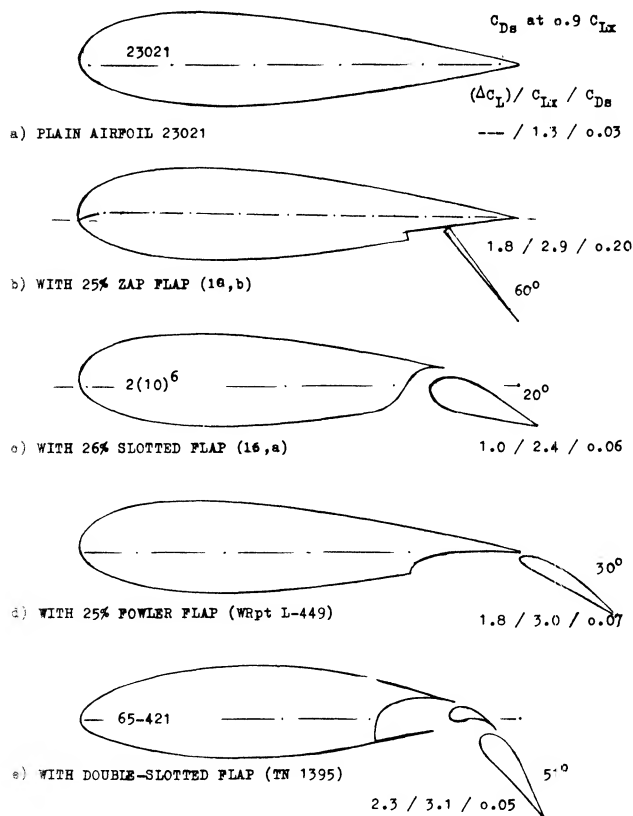


Figure 22. Lifting characteristics of 21% thick airfoil sections, tested between walls at $R_c = 2(10)^6$, equipped with various types of flaps.

viscous components, the ideal induced drag and that induced component due to the non-elliptical loading. When considering flap performance during takeoff and climb, the drag increase due to deflection and the non-elliptical loading are of primary concern. Also of importance is the maximum lift coefficient at the flap setting being considered.

Figure of Merit-T.O. In Chapter I a figure of merit was given for evaluating configuration with respect to the takeoff and climb performance. The peak climb angle is obtained when C_D^2 / C_L^3 , the figure of merit, is a minimum. The drag coefficient corresponds to the total at the C_L selected. While the value of C_D^2 / C_L gives a rough idea of the relative merit of a system it does not indicate the full capability, as the C_L is not known for the system. A better procedure is to relate the performance to C_{Lx} and the operating rules governing takeoff.

Takeoff Characteristics. The performance at takeoff in terms of field length and maximum gross weight is governed by safety considerations and the corresponding operating rules and regulations (19,a,b). These considerations generally lead to a requirement of a minimum rate of climb after takeoff with the flaps and landing gear in the takeoff configuration. The rate of climb required must usually be met with the critical engine inoperative. Where the case where power is fixed equation can be rewritten in terms of the lift drag ratio required

$$L/D_r = 1/(T/W - w_c / V) \quad (26)$$

At the L/D_r given in equation 26 the airplane is generally required to operate at a speed 20% above the stalling speed. This means that the operating C_L is $1/1.44 C_{Lx}$ for the flaps and landing gear in the takeoff configuration. Thus the takeoff speed is effected by two considerations: the L/D ratio and the C_{Lx} . If the flap angle could be changed during takeoff improved performance would be possible, but this is not allowed by the rules and is generally impractical as the pilot work load during a failure is too high.

(22) Theoretical analysis of part-span wing flaps:

- Pearson, Spanwise Load Distribution, NACA TRpt 585 (1937) and 665 (1939).
- Sivells, Distribution on Straight Wings, NACA TN 2283 (1951).
- DeYoung, Symmetric Span Loading, NACA TRpt 921 (1948) and 1071 (1952).
- Falkner, Calculation of Loading, ARC RM 1910 (1943); see also RM 2661 (1945).
- Diederich, Span-wise Lift Distribution, NACA TRpt 1228 (or TN 3014) 1955. (23)

Flap Selection for Takeoff. Flaps are usually thought of as devices for improving the maximum lift coefficient and are thus selected for reducing the landing distance. On most conventional powered jet aircraft, however, the field length needed for takeoff is generally longer than that required for landing. Thus, the flap system should be designed to give peak takeoff performance as well as minimum landing distance. Based on the concept of operating at a C_L that results in the L/D needed to give the required rate of climb at takeoff, the best flap configuration and operating angle can be found. This requires determining the lift drag ratio for the complete airplane as a function of flap angle when operating at a $C_{L\delta} = C_{Lx} / 1.44$. The choice of the best flap type and angle for takeoff can be determined from plots such as illustrated on figure 24. On figure 24,a the lift drag characteristics of the total airplane are given as a function of flap angle for various types of flap configurations with NACA 6 series sections (13,a). The lift coefficient corresponding to the flap angles is given on figure 24,b for the same section. Based on a given L/D required to satisfy the climb requirements the lift coefficient at takeoff can be determined for the given system from figure 25. The flap angle is then found from figure 24,a at the same lift drag ratio and flap type. From these figures the best flap system is obtained when at the L/D . Based on the data given on figure 24 the double slotted flap is the best of these considered as it generates the highest coefficient for any given lift drag ratio.

Part-Span Flaps have been mentioned above. In a rectangular wing, a modest inboard flap deflection can be expected to reduce the induced drag during climb (28,e), making the lift distribution more elliptical. In conventionally tapered wings, the induced drag is likely to be increased. There are elaborate methods available (22) for the determination of load distribution across the span. An approximate procedure of estimating the corresponding variation of the induced drag is presented in Chapter VII of "Fluid-Dynamic Drag". Another such method is as follows.

Induced Drag. An analysis of *elliptical* wings with part-span flaps is presented by Young (5,f). For practical purposes it can be said that

$$C_{Di} = (C_L^2 / \pi A) + K(\Delta C_L)^2 \quad (33)$$

where C_L = coefficient of total lift, and $\Delta C_L = (\Delta C_L) S_f / S$, where (ΔC_L) = increment due to flap in two-dimensional flow as in various graphs of this chapter. The factor K is approximately as follows:

$$K = 0.17 (1 - (b_f/b))^2 \quad \text{for inboard flaps}$$

$$= 0.21 (1 - (b_f/b))^2 \quad \text{including a 0.1 b cut-out}$$

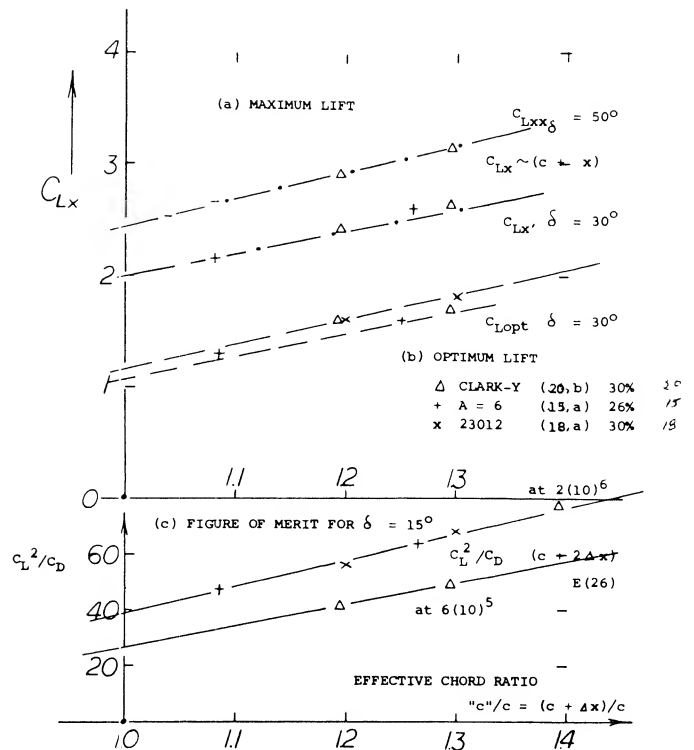


Figure 23. Performance of extended-lip slotted flaps (including Fowler flaps) as a function of their translation.

where b_f is measured between the ends of the flaps. For example, for $b_f/b = 0.5$, the factor K is ≈ 0.04 , and ≈ 0.05 when including 10% cut-out due to the fuselage. It is interesting to note that for a given combined geometric flap span (not including the cut-out) the minimum induced drag of elliptical wings is obtained for a cut-out in the order of 10% of the span. As mentioned before, the increments due to flaps, particularly in rectangular wings, are different from those of the elliptical ones stated in this paragraph. We will assume, however, that the basic lift distribution may be close to elliptical, as it actually is in average tapered wings.

3. MAXIMUM LIFT DURING LANDING

Besides stability and control, the primary requirement for landing is high lift to reduce the speed at touchdown. This, of course, is accomplished by increasing the maximum lift coefficient of the airplane. In fact, trailing-edge wing flaps were invented and developed as "landing flaps".

Landing Characteristics. The lifting system needed to give the best landing performance is chosen in a manner similar to that used to find the best configuration for takeoff. For landing, however, the highest C_{Lx} possible is of importance as this reduces the speed at touchdown and makes possible a shorter landing roll. Since the glide slope is proportional to the drag lift ratio, high drag during

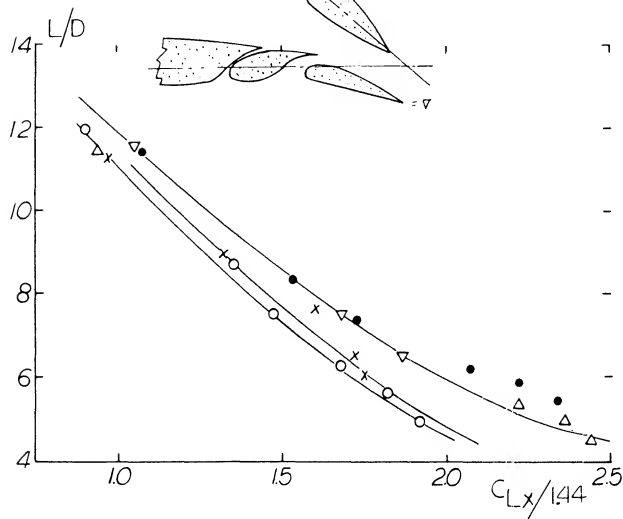
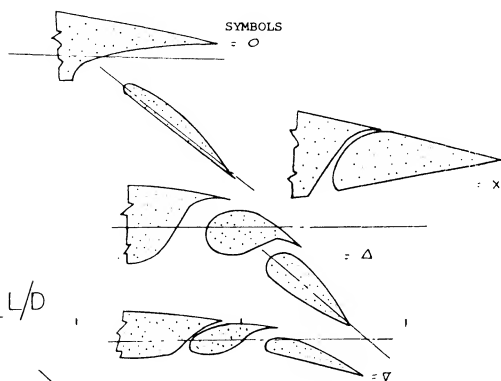
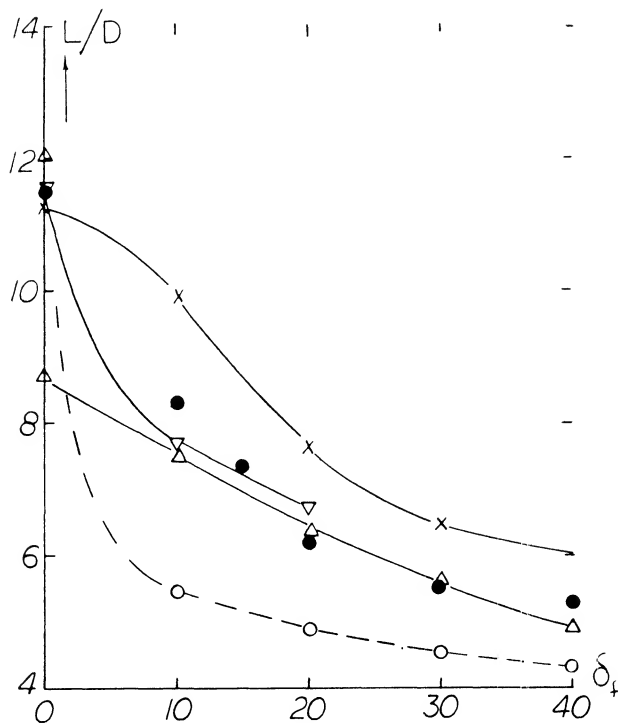


Figure 24. Selection of flap type and angle for best takeoff performance

a. Lift drag ratio at $C_L = C_{Lx} / 1.44$

b. Flap angle for $C_L = C_{Lx} / 1.44$

landing is desirable as it makes possible a steep approach angle. Practical flying qualities limit the approach angle, however, especially with the larger high speed and high performance aircraft. As the speed is reduced the approach angle can be higher as long as adequate control power is available.

Although high drag may be desirable along with high levels of C_{Lx} during landing, it may be necessary to abort the landing in which case the lift drag ratio again must be high. For the aborted landing condition the problems of flap and wing designs are like the takeoff condition. That is, a certain minimum L/D is necessary to provide the rate of climb required see figure 24. In this case, however, the L/D needed is lower as the airplane is usually operating at a lower weight for landing and full power is generally allowed for this condition (19,b).

Full-Span Flaps. The maximum lift will, of course, be obtained with full-span flaps, provided that lateral (and other) control would still be sufficient. The maximum coefficient then depends upon the type of flap, its angle of deflection, the shape of the airfoil, forebody and the Reynolds number as discussed in Chapter IV. However, variation and combination of these parameters leads to hundreds of possibly "optimum" configurations. In order to hold down the number, we will consider the more practical shapes and we will correlate the maximum lift coefficients versus simple parameters such as the airfoil and thickness ratio. As far as the flow pattern at C_{Lx} is concerned, it may be correct to say that all types of flaps when used at larger angles of deflection exhibit separation. To say it in different words, the flap stalls first; lift may then continue to rise with the angle of attack; and the final stall may be expected to take place from somewhere along the upper surface of the airfoil and possibly at the leading edge of the airfoil. This is the reason for the development of leading edge devices for the prevention of separation as discussed in the next chapter.

(23) Experimental investigation of partial-span wing flaps:

- a) Wenzinger, Split Flaps, NACA TRpt 611 (1937).
- b) Silverstein-Katzoff-Hootman, Comparative Tunnel and Flight Investigation of Maximum Lift, NACA TRpt 618 (1937).
- c) House, Slotted Flaps on 23012 Wings, NACA TN 719 (1939); continuation of TN 472 (split flaps), TN 505 and TN 663 (split flaps) 1938.
- d) Neely, Tapered Wing With Fowler Flaps, NACA WRpt L-134 (1946).
- e) Johnson, Flaps on Straight Wing, NACA TN 2080 (1950).
- f) Schneider, Plain-Flap Ailerons, NACA TN 1738 (1948).
- g) Sherman, 18 Wing-Fuselage Combinations, NACA TN (1938).

CHAPTER VI — LEADING-EDGE HIGH-LIFT DEVICES

An important (or predominant) limitation of lift to be obtained in wings, is flow separation from the leading edge. Means of preventing or postponing such separation are, the use of leading-edge slots or slats, camber or the deflection of nose flaps, and boundary-layer control (blowing or by suction).

These devices are used to increase the maximum lift and/or to prevent stalling from the wing tips, thus preserving lateral (aileron) control. All types of leading-edge lift-increasing devices function by increasing the angle of attack where stall takes place. They thus control separation, while lift (circulation) is basically controlled by the position of the trailing edge (by angle of attack, with or without a flap).

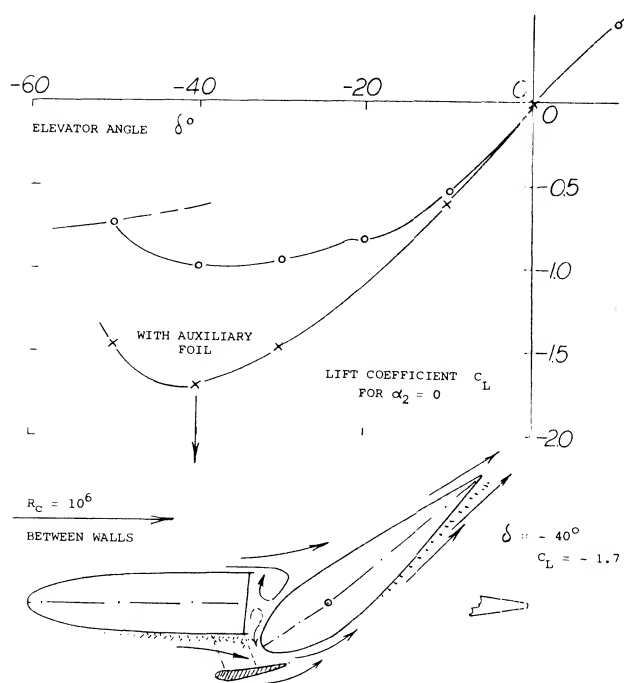


Figure 1. Horizontal-tail configuration tested (1) in a two-dimensional water tunnel; influence of a slot formed between elevator nose and fixed auxiliary airfoil on the negative lift in the landing condition of an airplane.

I. INFLUENCE OF SLOTS AND SLATS ON LIFT

Slots or slats are an effective means of preventing or postponing separation from the leading edge and they may help to postpone separation from the trailing edge. There are generally three types of leading edge devices:

- 1) fixed slots near the leading edge,
- 2) auxiliary airfoils ahead and above the leading edge,
- 3) extendable or automatically moving slats.

Principle. Boundary-layer control by means of a slot (such as in slotted trailing-edge flaps) is based on the concept of injecting momentum into a "tired" boundary layer. Near the leading edge of a wing the boundary layer is small however. In addition to the supply of momentum to the boundary layer the following mechanism seems to be important for the effectiveness of leading-edge slots or slats. Considering airfoil plus slat to be an entity, it is seen in figure 13, that the peak of the negative pressure distribution, is loaded onto the slat. Peak and subsequent positive pressure gradient on the "main" part of the airfoil, are thus appreciably reduced. Whatever boundary layer is formed along the upper side of the slat, is carried downstream as a thin sheet between the outer flow and the "jet" of fresh air exiting from the slot. In other words, the thickness of the boundary layer developing along the upper side of the airfoil, is reduced by the presence of a slot or slat. Still another important property of slots is demonstrated in Chapter V on "trailing-edge devices" (for all types of slotted flaps) or in figure 1 that is in a converging slot (as in a nozzle) an equalization of total pressure takes place, even though there may be a heavy boundary layer and/or separation at one side of their entrance. As a consequence, the efflux of momentum is comparatively uniform; and such slots are a suitable means of feeding momentum into the boundary layer at the upper side of flaps or airfoils. In the horizontal-tail configuration, as in figure 1 the maximum value of the negative lift coefficient is thus increased from 1.0 to 1.7.

- (1) Hoerner, Investigation of a Horizontal Tail Configuration, Fiesler Water Tunnel Rpt 14 (1939).

Fixed Slots. In the period of airplane development after 1930 efforts were undertaken to avoid or to reduce the structural complications of movable slats (see later). A fixed slot can be obtained simply by cutting a passage through the nose of an airfoil. With fixed slots such as shown in figure 2 the lift continues to increase above the angle of attack where the original plain wing stalls. Here as in the case of slats the lift at smaller angles of attack is somewhat lower than that of the plain airfoil. Similar results are reported in (2,b) for the more modern 23012 section. Leading-edge slots have been combined with other slots placed along the chord (2,c) eventually forming a cascade of vanes (2,c) and/or a combination with a trailing-edge slotted flap. Maximum lift coefficients up to the order of 4 have thus been obtained. However because of the lower structural design (strength) and performance at the low lift coefficients of high-speed flight such arrangements cannot be considered to be practical.

Drag. Assuming that a fixed slot would be effective by postponing separation and increasing lift its presence will increase the wing drag in the cruising and/or high-speed operation of an airplane. By rounding the leading edge of the main airfoil, the drag can be kept "low". For example, the coefficient of the shape as in figure 2, is increased by $\Delta C_{Ds} \approx 0.01$, in cruising condition, at $C_L = 0.3$ (and up to $C_L = 1.0$). When designing (around 1937) the Fieseler "Stork" (3) which would today be called a STOL aircraft, the principal requirements were low weight (aided by structural simplicity) combined with high lift. It was, therefore, decided to use a slat or slot of the conventional shape (3,a) and to leave it in extended position, accepting the added drag when flying at lower lift coefficients (such as at cruising speed). Water-tunnel tests reported on page 6-14 of "Fluid-Dynamic Drag" revealed, however, that there is a minimum of sectional drag associated with a fixed slot, provided that there is no flow through the slot (between slat and wing). The angle of attack where this flow pattern was obtained, could be controlled by slightly adjusting the trailing-edge wing flaps. As reported in (3,b), the section-drag coefficient of the wing was thus reduced from $C_{Ds} = 0.030$ to 0.018, at $C_L = 0.3$; and this magnitude was considered to be acceptable in a STOL-type airplane such as the "Stork". Even at the optimum lift coefficient (where the flow through the slot is smooth) slats produce some additional drag; the differential is in the order of $\Delta C_{Ds} = 0.01$.

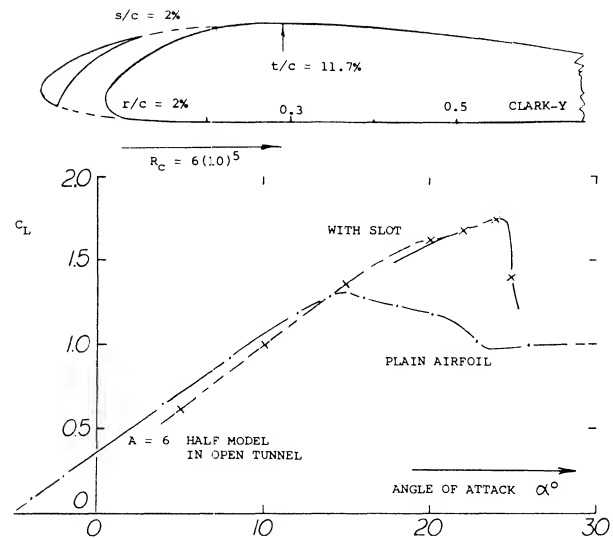


Figure 2. Example for a fixed slot cut into an airfoil (2,b).

Auxiliary Airfoils. Another way of avoiding the complications of slat mechanism is to place a low-drag auxiliary "vane" ahead and above the leading edge of an airfoil, in fixed position. For maximum lift, the position of such an auxiliary foil would be similar to that of slats forming a suitable converging nozzle "around" the nose of the main airfoil. Drag at low lift coefficients however is very high. Therefore, when selecting an "optimum" position, both the lift at high angles of attack, and the drag at lower lift coefficients must be considered. Full scale tests of a fixed auxiliary airfoil on a light twin aircraft are given in (4,c) another such compromise is shown in figure 3. Performance of various configurations is claimed in (4,a) to be as follows:

Configuration	C_{Dmin}	C_{Lx}	C_{Lx}/C_{Dmin}
Clark-Y plain wing	0.015 (0.015)	1.30 (1.30)	86
fixed slot (figure 2)	0.023 (0.022)	1.75 (1.65)	76
with auxiliary foil	0.019 (0.016)	1.95 (1.70)	104
with automatic slat	0.016 (0.014)	1.84 (1.63)	114

(2) Airfoils with fixed leading-edge slots:

- Handley Page in "Aeronautical Journal" 1921 p 270.
- Weick, Clark-Y Wing With Fixed Slots, NACA TRpt 407 (1932).
- Weick, Multiple-Slotted Clark-Y Airfoil, NACA TRpt 427 (1932).
- Bamber, 23012 With Several Forms of Slots, NACA TN 702 (1939).

(3) Fieseler "Stork" Fi-156, with fixed slat or slot:

- Krassilshchikoff, Optimum Configuration (used in the "Stork"), CAHI (Moscow) Rpts 105 (1931) 133 and 161 (1934); see Luschnau 1936 II (2) and (9).
- Petrikat, "Stork" Airfoil With Slat, Fieseler Water Tunnel Rpts 6 and 12 (1939); see Ybk D Lufo 1940 p I-248.
- Hoerner, Flight Testing the "Stork", Lilienthal Paper ZWB 099/006 (1938), see Luftwissen 1940 p 202; also Translation by Mississippi State College (1956).
- The 1500 "Storks" (1939/43) were preceded by one "Gugnunc" biplane (built by Handley Page in 1928) winner of the "Guggenheim Safe Aircraft Competition"; see report on that competition, New York (1930).
- The "Stork" has been imitated several times; see for example Pleines, Application of Slotted Wings, in (28,I). The last airplane of this type is the Dornier-27; with flaps, slats and propeller slipstream, $C_{Lx} = 5.3$.

The numbers in parentheses are based on combined "wing" area of airfoil plus slat or auxiliary foil, while the other numbers are on Clark-Y airfoil area. — There are two objections, however, to these experimental results:

- a) The Reynolds number of the auxiliary airfoil is only $9(10)^4$. Different optimum locations and larger lift increments may be expected at higher R'numbers.
- b) Arms are needed to support any slat or auxiliary foil. They must be expected to increase drag, and to reduce lift (including its maximum).

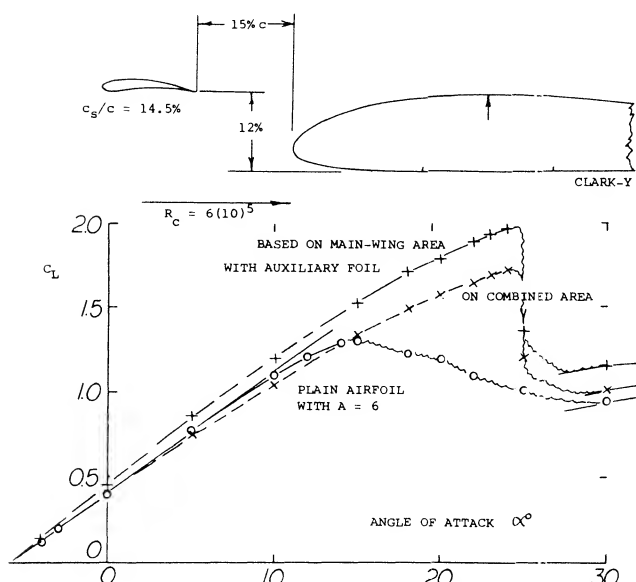


Figure 3. Optimum combination (providing maximum C_{Lx}/C_{Dmin}) of airfoil (4,a) with a fixed auxiliary foil, placed ahead and above the leading edge.

- (4) Investigation of airfoils with fixed auxiliary foils:
 - a) Weick, Clark-Y With Various Shapes, NACA TRpt 428 (1932).
 - b) Weick, With Various Chords and Shapes, NACA TRpt 472 (1933).
 - c) Fink, Fixed Auxiliary Airfoil or Slot on Light Twin Aircraft, Full Scale Test, NASA TN 7474.
- (5) Investigation of airfoils with slats:
 - a) Wenzinger, Clark-Y Wing With A = 6, NACA TRpt 400 (1931).
 - b) Jacobs, Airfoils Function of R'Number, NACA TRpt 586 (1937).
 - c) Weick, Fowler Flap and Slat, NACA TN 459 (1933).
 - d) Quinn, Combination With Flap and BL Control, NACA TN 1293 (1947).
 - e) Moss, Three Different Slat Chords, ARC RM 2705 (1952).
 - f) Axelsson, 64A010 Airfoil With Slat, NACA TN 3129 (1954).
 - g) Townend (NPL), Slots and BL Control, J RAS 1931 p 711.
 - h) Ormerod, Bristol Fighter, ARC RM 1351 (1930) and 1477 (1932).

When calculating the wing area, aspect ratio, lift-curve slope and induced drag, it does not matter whether the basic airfoil chord, or the combined area of airfoil plus auxiliary foil is used. The pitching moment of this configuration is like a tandem system with considerable interference. For the configuration as in figure 3, the center of pressure is constant at 20% of the Clark-Y chord, between $C_L = 0.7$ and C_{Lx} , while the CP of the plain airfoil is at and aft of 30% of the chord.

Maxwell Slat. A seemingly simple slat mechanism is shown in figure 4. The moving parts operate only by rotation, about fixed hinge axes. To close the slot, the slat is turned until it touches the upper side of the airfoil, and a plate is meant to cover the inlet at the lower side. The reference wing chord is the total (including the slat). Wind-tunnel tests (6) show this configuration to be effective in regard to lift, and efficient as far as drag at small lift coefficients is concerned. There are two reasons against this type of slot, however:

- 1) rotation alone does not provide any optimum location of the slat,
- 2) structurally, the system may be as complicated as really retracting the slat.

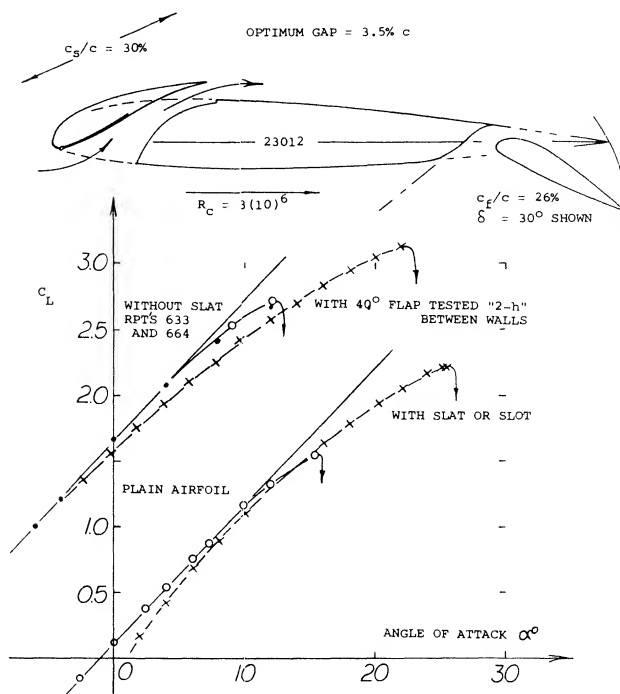


Figure 4. Example of a so-called Maxwell slat (6,b). The slot is obtained by moving two parts about a fixed axis.

- (6) Investigation of so-called Maxwell Slats:
 - a) Gauvain, Clark Y Maxwell Slat, NACA TN 598 (1937).
 - b) Lowry, 23012 Wing With 30% Slat, NACA WRpt L-693 (1941).
 - c) Gillis, 23012 With 18% Slat and Flaps, NACA WRpt L-574 (1941).
 - d) Turner, Flight Investigation, NACA WRpt A-88.

"Slats" are movable auxiliary airfoils or vanes, extended ahead of the leading edge of an airfoil to help the flow at higher lift coefficients, to get around that edge. At smaller lift coefficients (at higher flying speeds of an airplane) the slats are not needed. In fact, the drag of a far-extended and dipped slat would be prohibitive, see Chapter XVI, within the range of intermediate and low coefficients. As a consequence of separation from the lower side as shown in figure 5, drag coefficients as high as $C_{D_s} = 0.1$ are obtained which is in the order of 10 times that of the clean wing. Therefore, for good airplane performance slats are made retractable or automatic. Aerodynamic and kinematic development of such slats was first undertaken by Lachmann (7,d) and Handley Page, some time between 1920 and 1930. — The position of a slat in relation to the original airfoil, is defined by

- extension forward of the leading edge,
- downward droop or dip,
- size of the gap at the outlet of the slot,
- rotation or downward deflection.

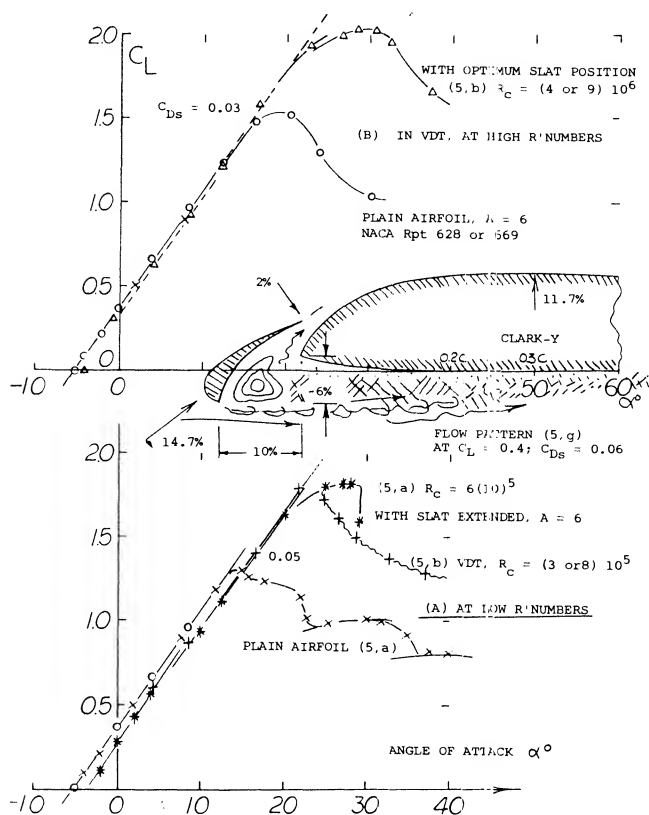


Figure 5. Lifting characteristics of a slatted airfoil at two very different Reynolds numbers.

- Airfoils with slats and trailing-edge flaps:
 - Seiferth, High-Lift Airfoils, Yearbk D Lufc 1939 p I-84.
 - Lyon, High-Lift Devices, ARC RM 2180 (1939).
 - Schuldenfrei, 23012 With Slat and Flaps, NACA WRpt L-261 (1942).

Reynolds Number. For a slat the Reynolds Number based on its chord is an order of magnitude lower than that of the wing section. So, for example, if the landing of an airplane takes place at $R_c = 10^7$, a wind-tunnel investigation may only be conducted at 10^6 , and the Reynolds number of the slat would possibly be as low as $R_s = 1.5 (10)^5$, which must be considered to be critical. Wind-tunnel results on slatted airfoils obtained below 10^6 , must therefore be accepted with reservation. Characteristics of a particular configuration are presented in figure 5, for two widely different R'numbers. Several discontinuities are evident for $R_c \approx 7(10)^5$; they stem from partial separations from slat and/or upper side of the airfoil. The variation of the maximum lift coefficient as a function of R_c as in figure 6, looks rather steady. There is a discontinuity, however, around $R_c = 10^6$, where a second maximum takes over. One set of points (between 10^6 and 10^7) also displays a "sudden" increase of C_{Lx} . Some slat configurations have sharp corners, both at the slat and the lower edge of the main airfoil nose. Whether intended or not, these corners might promote turbulent boundary-layer flow through the slot. It might also be tried to stimulate turbulence by trips (surface steps as in figures 8,b or 17,b, for example) or by distributed roughness (or turbulence generators; see later) placed near the outlet of the slot. Results of such tests do not seem to be available, however.

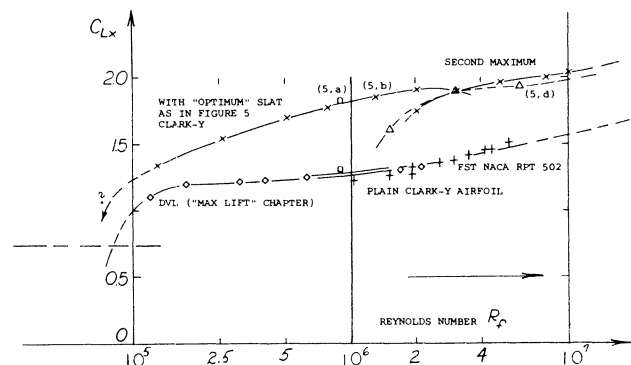


Figure 6. Maximum lift coefficients of airfoils with (and without) slats, as a function of the (effective) Reynolds number.

Slat Size. Maximum lift coefficients are plotted in figure 7 as a function of the chordlength ratio of the slat. For most of the airfoils tested, there is a sudden increase of C_{Lx} , at slat-chord ratios between $c_s/c = 0$, and $= 10\%$. This increment evidently indicates elimination of leading edge separation. It is not found in cambered sections with well-rounded noses, where such separation is not present

- For shapes of RAF sections (28, 38, 48, 34) see Relf, 6 Aerofoils in CAT, ARC RM 1706 (1936).

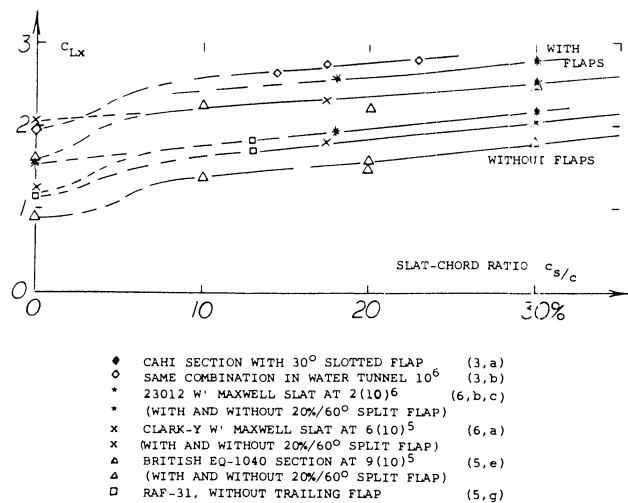


Figure 7. Maximum lift coefficients as a function of the slat-chord ratio.

Subsequently, all configurations tested, show a steady increment of C_{Lx} with the slat-chord ratio. It is suggested that lift grows simply because of the extension of airfoil chord. The average rate of growth is

$$\Delta C_{Lx} / C_{L*} \approx 1 + (c_s/c) \quad (2)$$

where $C_{L*} = C_{Lx}$ extrapolated to $c_s/c = \text{zero}$. The rate is higher than the average in otherwise plain airfoils; and it is lower in airfoils with trailing flaps deflected. In fact, the lines in figure 7 are essentially parallel to each other. They can be expressed by

$$\Delta C_{Lx} = (1.6 \text{ to } 2.0) c_s/c \quad (3)$$

The argument of extended airfoil chord does not apply to the Maxwell-type of slats. Nevertheless, they show the same rate of C_{Lx} growth as the conventional type of forward-extending slats. We may have some biplane effect here.

Design Rules. The basic rules for designing suitable slats given in (5,c) are

1. The slat chord should be at least 12% of airfoil chord.
2. The forward extension is at least 60% of slat chord.
3. The angle of the slat (below airfoil chord) should cover the stagnation point of the airfoil.
4. The slot gap should be around 3% of airfoil chord.
5. The slat thickness near leading edge = 2% of airfoil chord.

The angle of dip (rotation of the slat) is found in the same reference to be between 9 and 16° . For wings operating at high lift coefficients slot angles up to 60° are used. When comparing these dimensions with those of the selected configurations in figure 8, it must be realized that structural considerations are a reason for modest extension, while pitching moments (see below) call for small dip. Slats have been tested (5,e) with chord lengths and extensions up to 30% of the chord. They are not considered to be practical, however.

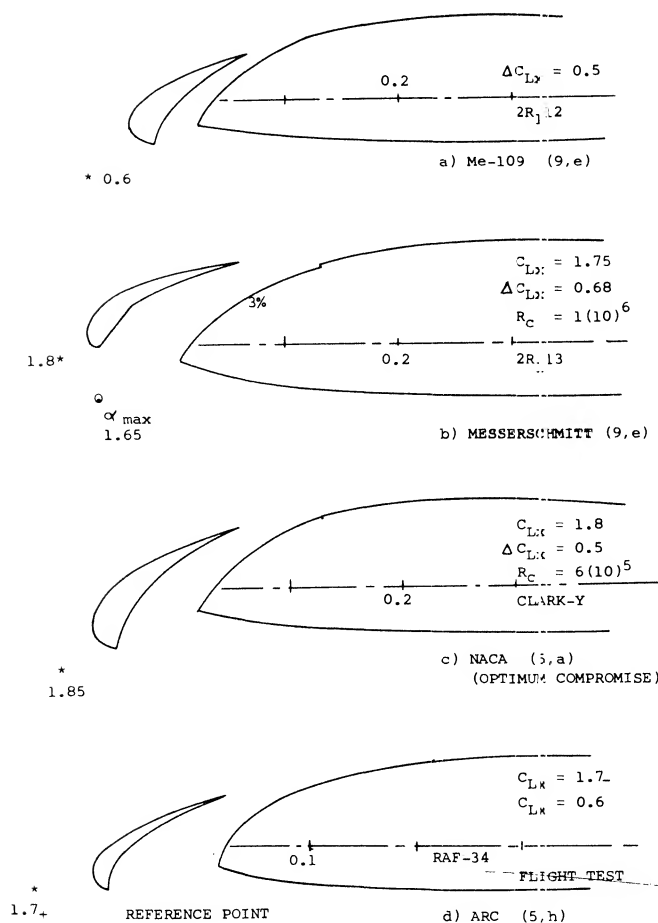


Figure 8. Shape and position of leading-edge slats, actually used or considered to be practical. (*) indicates location of reference point at which the maximum of C_{Lx} was obtained.

Loss of Lift. As seen in figures 2, 4, or 18, the lift coefficient drops somewhat when extending a slat, at constant angle of attack (such as at $\alpha = 10^\circ$). For a wing with automatic slats, this means that one wing tip might have 10% less lift than the other one, if there is a delay in the deployment of one of the slats. The loss of lift can be reduced by making the dip and/or slat gap smaller.

Pitching Moments. When extending a slat into the typical and most favorable position, two things happen: the effective wing chord is increased and when moving the slat down, the airfoil becomes cambered. As a consequence, the pitching moments are changed. As shown in figure 9, there is a positive increment of $dC_{m/4}/dC_L$, which means that the "aerodynamic center" moves forward. The forward extension of slats is usually less than their chord length. For an average $\Delta x/c_s = 2/3$, we tentatively obtain

$$\begin{aligned} (dC_{m/4}/dC_L) &= + (2/3) (c_s/c) 0.75 \\ &= 0.5 (c_s/c) \end{aligned} \quad (5)$$

where $0.75 = (1 - 0.25)$. This equation is confirmed by experimental results. As a tail-down moment, the derivative is destabilizing. The pitching moment due to camber (corresponding to droop or dip) as in part (b) of figure 9, is negative (nose-down). It thus aggravates the trim situation caused by trailing-edge flaps. It is shown in figure 30 of Chapter II, that the pitching moment of 230-type sections (similar in camber shape to that representing slats) increases with the camber location (x/c). A trend of $\Delta C_{mo} \sim (y/c)^2$ is seen, accordingly, in figure 9.

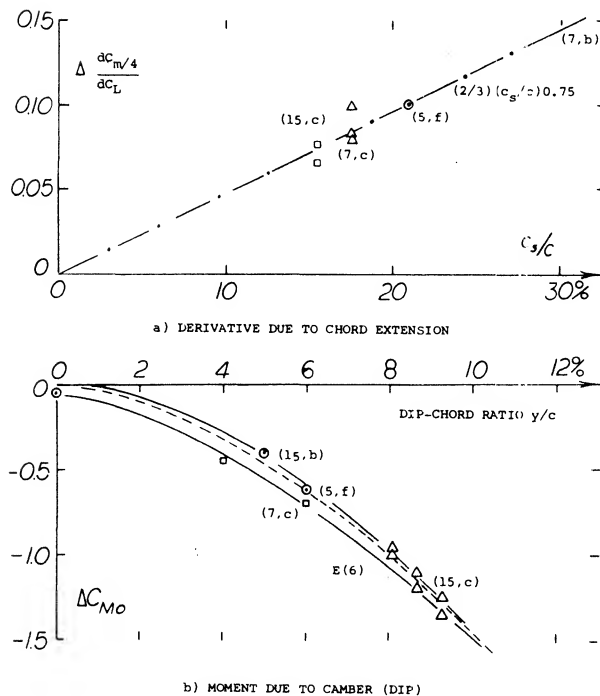


Figure 9. Pitching moments due to leading-edge slats.
a) Derivative due to chord extension
b) Moment due to camber (dip).

Combination With Trailing-Edge Flap. Basically, a leading-edge slat (or nose flap) increases the angle at which stalling takes place by a given increment. This increment may be the same when adding the leading-edge device to an airfoil equipped with a trailing-edge flap. The result can be expected to be a "very" high maximum lift coefficient. An example of such a configuration is presented in figure 10. There is a large hysteresis loop, reaching over some 25° of angle of attack (for $A = 4$). Without a slat, a 10° wide loop was found in the same test conditions. Such loops have also been found in airfoils without slats, evidently in the critical range of the Reynolds number where leading-edge separation disappears, see Chapter IV. If the hysteresis persists at larger full-scale Reynolds numbers, it can or has to be eliminated by means such as so-called double-slotted flaps (see Chapter V) or possibly by turbulence generators (on slats or ahead of trailing flaps). Another combination of slat and flap is illustrated in figure 11. Although the Reynolds number is appreciably higher than that in figure 10, the maximum lift obtained with a hardly extending flap is not higher.

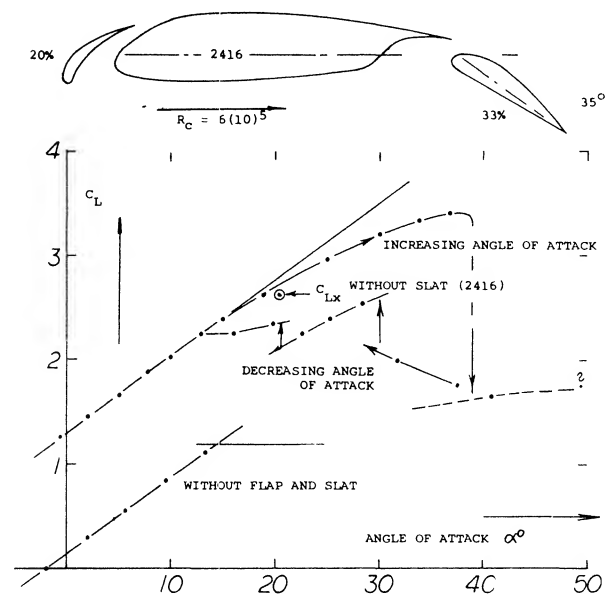


Figure 10. Example of a combination of slat with trailing-edge flap (7,a), tested on rectangular airfoil (with $A = 4$) in open wind tunnel.

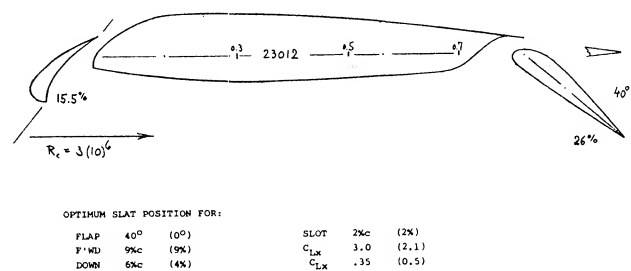


Figure 11. Lifting characteristics of an airfoil (7,c) with slat and trailing-edge flap.

Combined Pitching Moments. Trailing-edge flaps produce nose-down pitching moments of a considerable magnitude. As shown in part (b) of figure 9, the moment due to dip of a slat (added to that of a flap) makes trimming of an airplane difficult. Considering "optimum" slat position producing maximum C_{Lx} , a larger dip (larger by 1 or 2% of the airfoil chord) would be desirable, in combination with a flap. Some compensation by the positive derivative as in part (a) of figure 9, may help to trim an airplane; it reduces stability, however unless the flap contributes a negative component. With a Fowler flap as in (7,b) used in combination with a slat, the pitching moments are obtained at C_L between 2 and 4, are of the order of $C_{m/4} = -1$. As a matter of interest, the "viscous" section drag is in the order of $C_{DS} = 0.1$. Both these values are about 10 times what they are in an average plain airfoil section. It should also be considered that the negative lift in the horizontal tail, required to balance the pitching moment, reduces the lift gained by the lift device. This negative lift may correspond to a reduction of C_{Lx} of 0.1 or more.

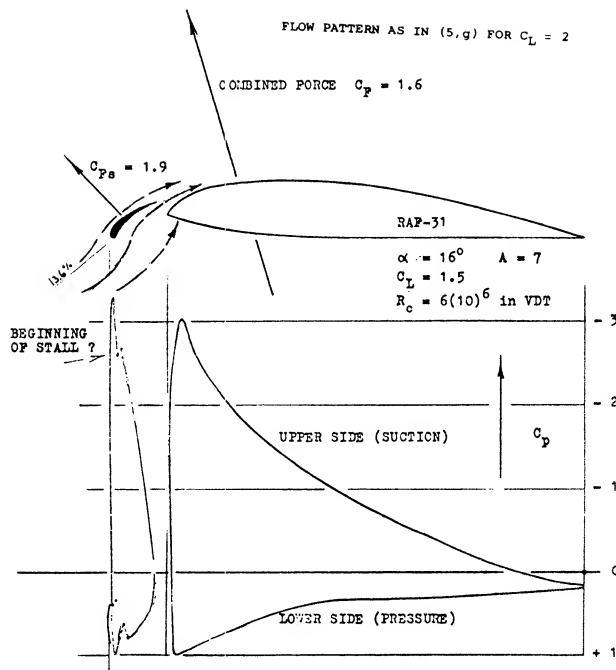


Figure 12. Pressure distribution around an airfoil section with a far-extended slat, tested (11,a) in the NACA's Variable Density Tunnel.

Pressure Distributions. In the beginning of this chapter, it was mentioned that "the peak of the distribution is loaded onto the slat". This is not quite the case as seen from the pressure distribution plot figure 12. We can argue, however, that the load is evenly distributed, between slat and main-foil nose. Therefore, the minimum pressure coefficient might be reduced from $C_P = -6$, for a similar plain airfoil at the same lift coefficient, to -3 , as tested for a combined $C_L = 1.5$. Distribution of load on the slat depend, however, upon shape and position (dip and inclination) of the slat. Figure 13 shows, for example, a peak value for the slat of $C_P = -8$, while that of the main airfoil is only -3 . In this case, the slat has really taken over the leading-edge load. In fact, when deflecting a trailing edge flap slotted, at 30 or 40° , for a $C_L \approx 2.8$ the slat-pressure peak is roughly doubled, while that on the main-foil nose is only modestly increased. Such considerations can be useful when designing slat configurations. Although at present the design of slots is a trial and error process good progress is being made in solving the problem with the use of high speed computers. This should give important improvements in the design.

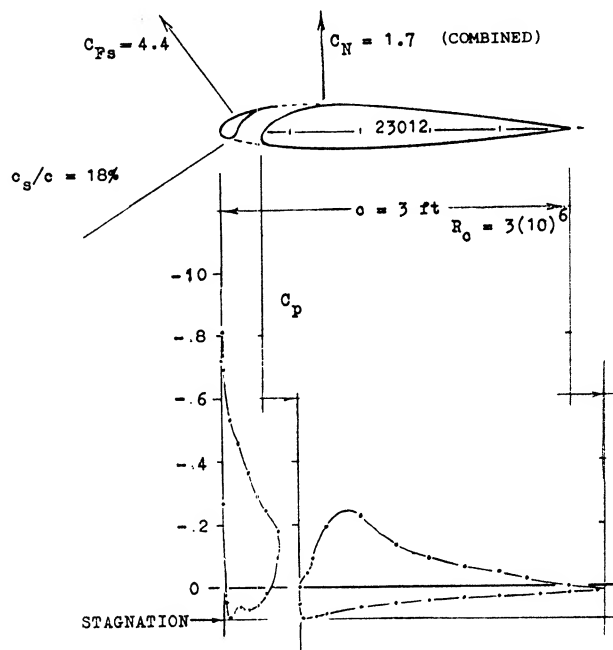


Figure 13. Pressure distribution around an airfoil section (11,c) with a well-rounded "slat" forming a fixed slot.

Slat Forces. As shown in figure 14, the forces (practically equal to those normal to the slat chord) might statistically be approximated by straight lines corresponding to

$$\Delta C_{Fs} \approx \Delta C_{Ns} \approx K (C_N \text{ or } C_L) \quad (10)$$

where "s" indicates forces referred to "inclined" slat area; and C_L the combined lift of the configuration referred to the basic airfoil chord or area. The factor K is between 3 and 4, for slats in extended position. Disregarding the fact that the flow separates (at lift coefficients say below 0.5, from the lower edge of a slat, provided that it remains extended) the lines in figure 14 are shifted laterally by certain values of ΔC_L ; that is, by airfoil-section camber, by dip and/or by trailing-flap deflection. Therefore, increased dip or deflection of a trailing flap, considerably reduces the slat load (for the same lift coefficient). The maximum loads are considerable, however with or without a flap and are in the order of $C_{Fs} = 4$ or 5.

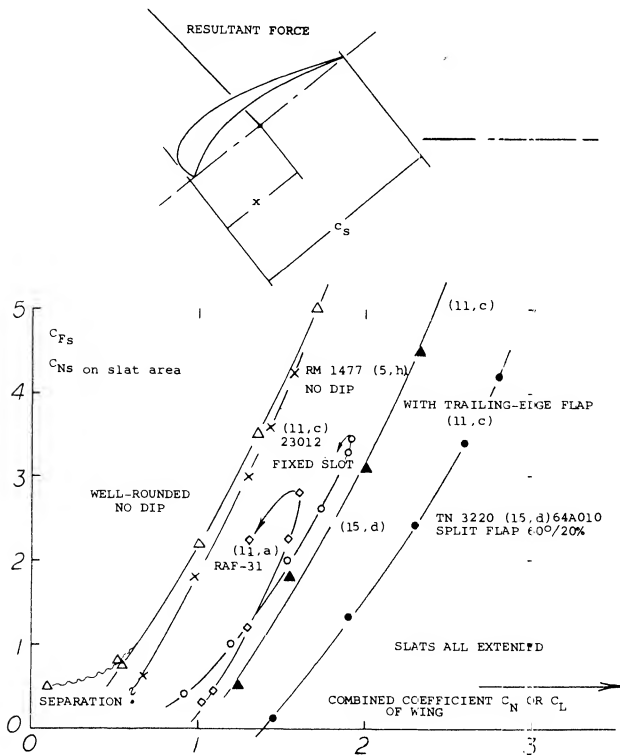


Figure 14. Slat normal forces (referred to slat-chord area) as a function of the combined lift coefficient.

Line of Force. To understand the nature of the slat force, it may be remembered that the tangential (chordwise) force of any airfoil section changes from positive (in the direction of drag) at smaller lift coefficients, to negative ("forward") at higher coefficients. To move an "automatic" slat out, a force is evidently required in the direction of its chord line, or of the motion as directed by its

kinematic system. Therefore, direction and location (center) of the slat force (rather than its magnitude) are responsible for its automatic transfer (out and in again). — As to the location (or center) of the slat force, along its subtangent chord line, the data in part (b) of figure 15, roughly indicate a comparatively constant value around $x/c_s = 40\%$; that is at higher lift coefficients.

Inclination. Regarding direction, figure 15 shows that $\alpha_s = 90^\circ$ may be reached at C_L between 0.2 and 0.4, in "conventional" airfoil sections. The slat force then tilts forward to between 70 and 60° , at C_L between 0.8 and 1.0. Upon opening (moving forward, above $C_L = 1.0$) the angle remains essentially the same. As the lift coefficient (or angle of attack) is increased, the force tilts forward more and more, thus causing the slat steadily to move forward.

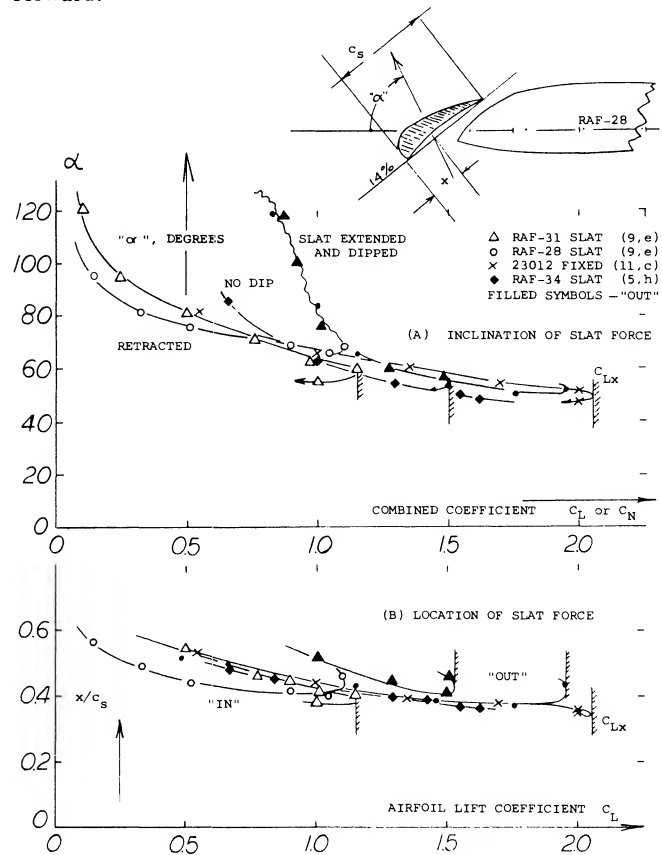


Figure 15. Direction (inclination) and location (center) of slat forces, as a function of the lift coefficient.

Kinematics. The mechanical mechanism permitting the slat to move, must be such that the extension takes place at higher lift coefficients (when needed) and in a smooth (continuous) manner. As illustrated in figure 17, there are two or three ways of doing this. As the angle of attack or the lift coefficient is increased, the slat forces eventually pull the slat out and move it forward. To design a smooth-working mechanism, center and direction of the slat force, as discussed above, have to be known (10).

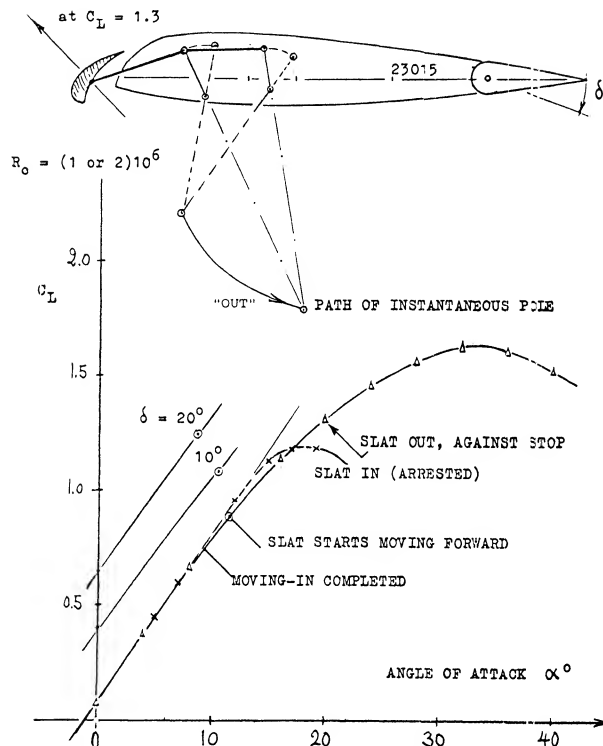


Figure 16. Performance of an automatically moving slat (9,c), tested between walls (with interference).

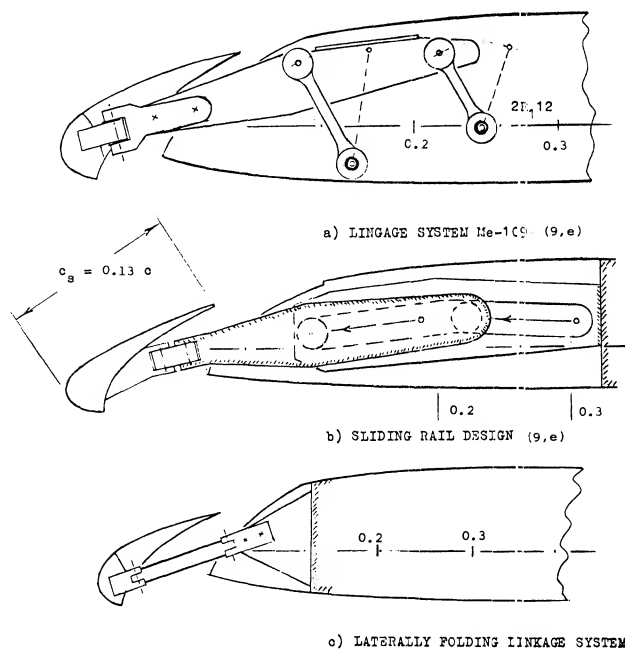


Figure 17. Three types of mechanical mechanisms, which can be used to extend a slat, or to let it move by itself.

- (9) Investigation of automatically moving slats:
- Bradfield, RAF Airfoil Wings, ARC RM 1190 and 1204 (1928); see also same type slats in RM 1192 and 1214.
 - Jennings, Flight Tests Linkage Variation, ARC RM 1677 (1932).
 - Petrikat, Slats in Water Tunnel, Ybk D Lufo 1940 p I-248; see (3,b).
 - Lachmann, Practical Information; ZFM 1923 Issues 9 & 10 p 71; ZFM 1924 Issue 10 p 109; ZFM 1930 Issue 16 and 17. See also his book (28).
 - Braun, Optimum Slats and Slat Kinematics; Messerschmitt Rpts TB 33 & 34, ZWB UM 7835 (1941) and 7836 (1942). Translation of TB-33 by North American Aviation CADO ATI-32590.

The linkage system as in figure 16 was developed (9,c) both analytically and by experiment. Assuming that the line along which the force is acting, remains constant, the motion of the slat will be steady and stable, as long as the instantaneous pole point (determined by the two lever lines) remains behind and/or above the force line. Forward extension and the size of the slot gap increase if the kinematic is arranged in such a manner that the pole point moves up, along the force line. Part (b) of figure 16 shows how the translation of the slat takes place:

at $C_L = 0.9$, the slat begins to move forward,
 at $C_L = 1.3$, it reaches a limiting stop,
 returning, the slat is fully retracted at $C_L = 0.8$.

When using a trailing-edge flap (or an aileron), start and termination of the slat motion take place at lift coefficients changed corresponding to flap deflection. Roughly, transfer (out or in) occurs at the same angle of attack.

Slot Pressure. The assumption that the slat force or at least its line of action remains constant, is not completely correct because of a certain variation of the pressure between slat and leading edge of the "main" airfoil. This pressure can become critical in the "closed" position of the slat. Average pressures corresponding to $C_p = -0.5$, and up to -1.2 are reported in (9,e) for example. Positive pressures are, on the other hand, found in (11,d) corresponding to $C_p = +0.1$, and $+0.2$, for a slat which has a small gap at the lower (pressure) side of the airfoil. A dangerous situation can arise when the trailing edge of the slat does not precisely fit onto the surface of the airfoil, thus leaving open a small gap at the upper side. The negative pressure thus developing is bound to keep the slat back up to a lift coefficient above that where it ordinarily would move forward. Subsequently, the slat will jump or pop out (suddenly) possibly banging against its stop.

Sliding Slats. In thin airfoil sections, a linkage system such as in figure 16, is structurally restricted by the wing thickness near the leading edge. The alternative solution as in part (c) of figure 17, has the disadvantage of moving the slat in spanwise direction. A more suitable design is shown in part (b) of the illustration. The slat, or a supporting pair of attachments, move along rails or tracks (by means of rollers).

- (10) Some of the modern airliners (as the Boeing 707 or 727, for example) have slats installed near the wing tips. It seems, however, that any automatic function is not considered to be practical or reliable. Instead, the slats are extended together with the trailing-edge flaps, by means of a hydraulic actuator. The slats are also out during takeoff.

Stall Control. The purpose of using leading edge slats (or slots) is twofold, to increase the maximum lift coefficient and/or to prevent wing-tip stalling. Since a large number of accidents are caused by wing stalling the use of slats can be an important safety device. When using slats to protect the wing tips, overall lift is usually not increased. Safety and controllability are increased, however, and the operational margin of lift below the maximum can safely be reduced. In a wing with part-span slats, two stalls take place, one at the angle of attack where the unslotted portion (in the center of the wing) loses lift, and the other one at a higher angle of attack where the flow over the wing tips (although protected by slats) also separates. The lift of such a wing is shown in figure 18. Note there definitely is a dip between the two maximum lift conditions. For satisfactory roll stability, the lift curve slope of the outboard parts of the wing panels should remain positive. Control by means of ailerons, may still be available, up to the "very" high angle of attack where the second maximum of the lift coefficient is found. Even beyond that maximum, there is increased lift due to the presence of the slats.

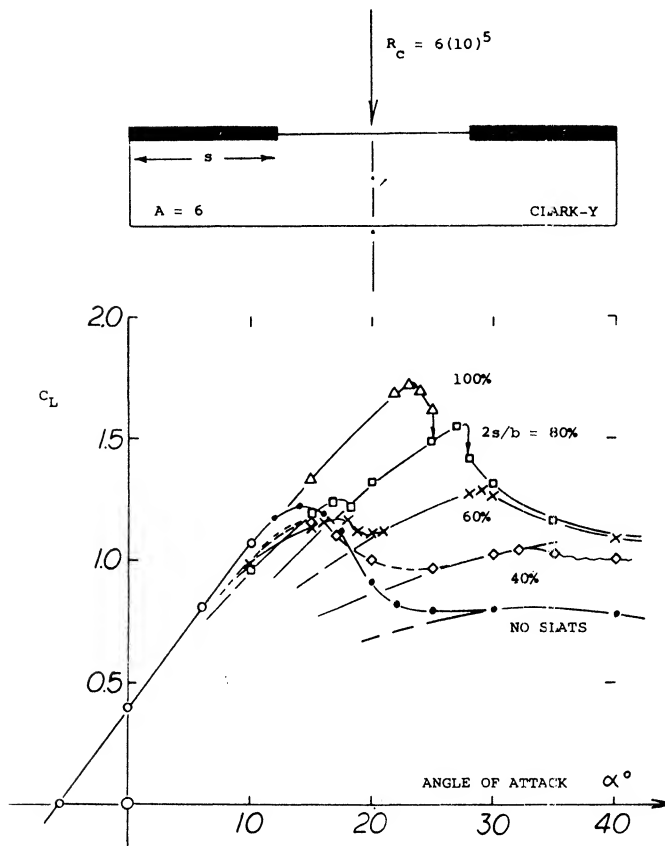


Figure 18. Lifting characteristics of a model wing (12,a) equipped with various lengths of outboard leading edge slats.

Span Ratio. The small high-wing airplane as in figure 19, was flight-tested (12,b) with various lengths of slat placed ahead of the leading edge, beginning from near the wing tips. At a constant angle of attack of 16° , total lift increases slightly with an increase in the slat length. For span ratios up to 0.6 or even 0.7, the maximum of lift reported, is evidently the first of the two mentioned above. For comparison, the maximum values of the wing in figure 18, have also been plotted in the graph. It then becomes apparent that under realistic conditions (including elevator effectiveness) the maximum lift is only really increased when extending the slats to the fuselage. A classical example of such an increment is the "Stork"; including the slipstream effect, lift coefficients were obtained (3,c) of $C_{LX} = 2.7$ without, and of 3.9 with 40° slotted wing flaps.

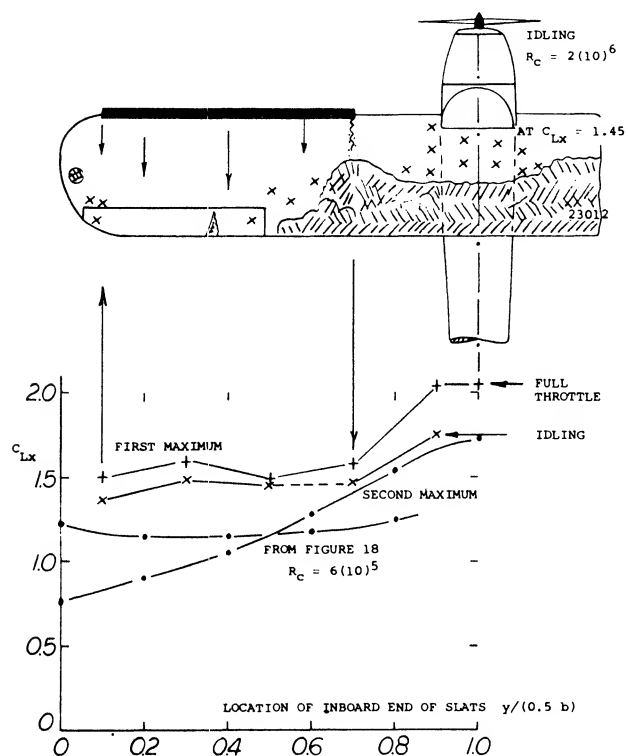


Figure 19. Flight-tested maximum lift of a high-wing airplane (12,b) as a function of the span ratio of outboard leading edge slats.

- (11) Pressure distributions around, and loads on slats:
 - a) Jacobs, Slotted RAF-31 in VDT, NACA TN 308 (1929).
 - b) Wenzinger, Loads on Slats and Flaps, NACA TN 690 (1939).
 - c) Harris, 23012 With Slot and Flap, NACA TRpt 732 (1942).
 - d) Arabian, On Swept Wing, NASA TN D-900 (1961).
- (12) Characteristics of part-span slots or slats:
 - a) Weick, Wing-Tip Slots, NACA TN 423 (1932); see also Lateral Control With Slots in TN 443 (1933).
 - b) Weick, Lateral Control in Flight, NACA TN 2948 (1953).
 - c) Hollingdale, Analysis Load Distribution on Tapered Wings With Part-Span Flaps and Slots, ARC RM 1774 (1937).

2. LEADING-EDGE OR NOSE FLAPS

The camber of a section, especially at the leading edge of an airfoil, improves the flow around the nose, especially from the stagnation point on the lower surface to the upper surface. Since the camber level needed to prevent separation at the higher lift coefficients is large and results in high drag at low cruise lift coefficients, other devices are used. Thus, instead of camber, leading edge devices similar to trailing edge flaps are used to improve the flow about the leading edge.

Nose Shape. In Chapter IV it was shown that in sections with little or no camber and a small radius, the flow separated at fairly low angles of attack near the leading edge causing the airfoil to stall. This is illustrated by the test data of (13,c) given on figure 32 for airfoils with various leading edge shapes.

Leading-Edge Camber. A well known airfoil shape is the NACA's 23012 section. Its mean line is straight over the rear 85% of the chord (to keep the pitching moment low, $C_{mo} = -0.015$) while the nose is pulled down, so to speak, to increase the maximum lift coefficient. A comparison of the maximum lift of the 23012 section with other 12% thick NACA sections as tested (13,d) in two dimensional flow at $R = 6(10)^6$ shows the advantage of camber at the leading edge:

Section NACA	Maximum Lift Coefficient
23012	1.72
2412	1.68
0012	1.57

So, there is some improvement over the straight section 0012; and the increment is at least as high as that due to 2% of conventional camber. Another airfoil section cambered according to the same principles as the 23012, is the modified 64AX10 as reported in (13,b). Considering the pulled-down 15% of the chord to be a flap, figure 22 suggests some increase of maximum lift; that is, from $C_{Lx} = 1.3$ to above 1.4, for 1.2% camber or $\sigma_o = - (4 \text{ or } 5)^\circ$.

(13) Airfoils with modified (drooped) leading edges:

- Kelly, 63-012 Airfoil with Nose Modifications, NACA TN 2228 (1950); see also figure 59 in the "maximum lift and stalling" chapter.
- Maki, 64A010 Nose Shape and C_{Lx} , NACA TN 3871 (1956).
- Butler, Leading-Edge Modifications, ARC CP-410 (1958).
- Abbott and Others, Summary of Airfoil Data, NACA TRpt 824 (1945).

Flap Theory. The improvement in C_{Lx} obtained by leading-edge camber are limited to an increase of less than 10%. A much more effective method is to deflect the airfoil-section nose in form of a movable "flap", as shown in figures 21 and 23, for example. An ingenious analysis encompassing both trailing- and leading-edge flaps, is presented in (14,b). Figure 20 shows the theoretical results of this study for lift variation due to nose-flap deflection, for the optimum or symmetrical lift coefficient and for the lift due to trailing-edge deflection. It is seen in the graph that lift due to deflection of nose flaps, is practically zero, for chord ratios, say up to 10%. To be sure, there is a decrease of lift (at constant angle of attack) particularly when using larger-size flaps.

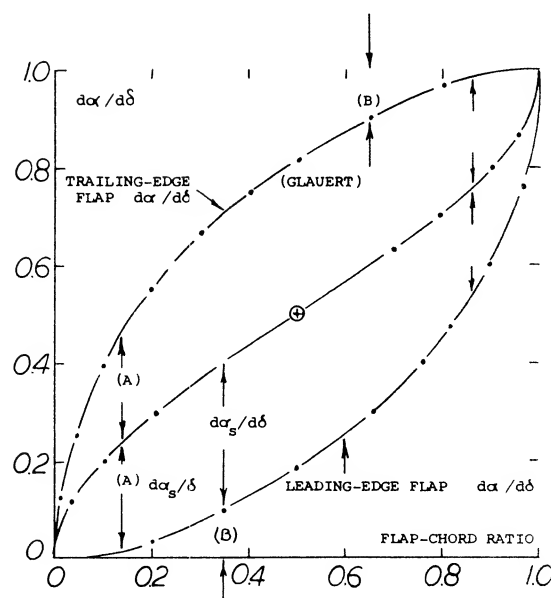


Figure 20. Theoretical predictions as to lift produced by leading and trailing edge flaps.

(14) Theoretical analysis of airfoil nose shape:

- Rettie, Velocity Distribution, ARC RM 3027 (1957).
- Roshko, Maximum Lift Due to Flaps, Douglas Rpt SM-23626 (1959).
- Glauert, Airfoil with Hinged Flap, ARC RM 1095 (1927).

Stalling Angle. As pointed out in (14,a) stalling from the nose of an airfoil section takes place when the stagnation point reaches a critical location "below" that nose. Denoting the angle of attack at which the flow comes onto the leading edge "smoothly", meeting it in a "symmetrical" manner thus placing the stagnation point right onto the nose, by the subscript "s", this angle approximately corresponds to

$$\frac{d\alpha_s}{d\delta_o} = - (2/\pi) \sqrt{c_o/c};$$

$$C_{Ls} = (dC_L/d\alpha)(2/\pi) \sin\delta_o \sqrt{c_o/c} \quad (12)$$

where δ_o = angle of nose-flap deflection, negative when pulling the flap down (so that α_s becomes positive). In other words, α_s is naturally increased when bending down the leading edge "into" the oncoming flow. For small flap-chord ratios, the "symmetrical" angle of attack is approximately

$$\alpha_s \sim \delta \sqrt{c_o/c} \quad (13)$$

Suction pressures "above" the nose vary as $(\alpha - \alpha_s)^2$. Assuming that there is a critical C_{pmin} (behind which stalling takes place) it may be expected that the maximum lift coefficient in two-dimensional flow, is

$$C_{Lx} = C_{Ls} + 2\pi(\alpha - \alpha_s) \quad (14)$$

where x indicates a maximum value, depending on parameters such as nose radius and Reynolds number. If this value is constant for a given airfoil, it can be concluded from equation (13) that

$$\Delta C_{Lx} = C_{Ls} \sim \delta \sqrt{c_o/c} \quad (16)$$

A more accurate, complete function for α_s , is included in figure 20. It should be noted that this graph is anti-symmetrical insofar as $A = A$, and $B = B$. The physical meaning of this symmetry is that in a trailing flap as well as for a correctly deflected leading flap, the stagnation "point" is at the leading edge.

Hinged Noses have been tested (15,a) as early as in 1920. Some more recent results are presented in figure 21. In combination with a standard 20% and 60° split flap, some deterioration of lift can be seen in the graph, growing as the deflection of the nose flap is increased from zero to -30 and -45°. Since the tests were conducted between wind-tunnel walls, it can be suspected that some boundary-layer interference is involved, in the "corners" between airfoil and walls. Some of the deterioration is also likely to be genuine, caused particularly by the negative pressure gradients around the bends of the flaps, followed by positive gradients.

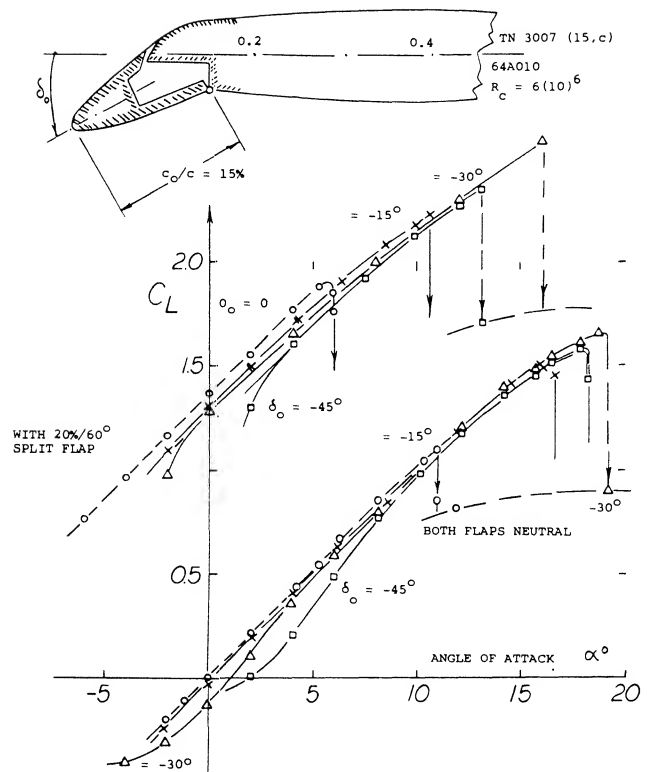


Figure 21. Hinged section nose; influence upon lift of airfoil section.

Optimum Flap Angle. In the particular configuration shown in figure 21, the maximum lift coefficient of the otherwise plain airfoil, is increased from $C_{Lx} = 1.1$ to a maximum of 1.66 for an optimum leading-edge deflection of $\delta_o = -30^\circ$. The same and other results are plotted in figure 22, as a function of the theoretical nose-flap parameter $\delta \sqrt{c_o/c}$ as in equation (16). It is seen, indeed, that $\Delta C_{Lx} \approx C_{Ls}$. Stalling takes place at higher lift coefficients, where the upper side of the airfoil is no longer able to support the flow against a strong pressure gradient.

(15) Experimental investigation of nose flaps:

- Harris, Biplane With Variable Camber, ARC RM 677 (1921).
- Lemme, With Hinged Slotted Nose, ZWB 1676 (1944); NACA TM 1108 and 1117.
- Kelly; 64A10 with Slat, Leading & Trailing Edge Flaps; NACA TN 3007 (1953).
- Kelly, Loads on Slat and L'Edge Flap as in (c), NACA TN 3220 (1954).
- Gambucci, 0006 With Leading and Trailing Edge Flaps, NACA TN 3797 (1956).
- Spence, On 40 Swept Airplane Model, ARC RM 2752 (1952).

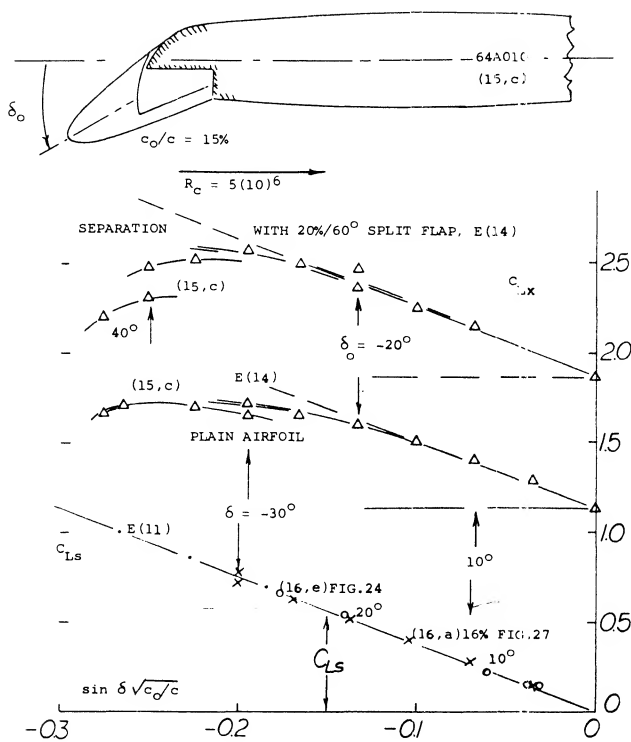


Figure 22. "Symmetrical" and maximum lift of (round-nosed) airfoil sections, as a function of the theoretical (14,b) leading-edge flap parameter.

Reynolds Number. In all leading-edge flaps, the boundary-layer flow is or can be laminar. Testing for example, an airfoil at $R_c = 10^6$, the R 'number of a 10% flap is only 10^5 . At a number $R_c = 10^6$, a 0009 section investigated in (15,b) only shows $C_{Lx} = 0.7$ for the plain airfoil, while with optimum nose flap, $C_{Lx} = 1.3$ is obtained. So, there is an appreciable increment. It still seems, however, that the flow remains laminar in this case, up to and beyond the bend above the leading-edge flap and may then separate because of the positive pressure gradient necessarily aft of the bend.

Leading and Trailing Edge Flaps. With the combination of leading and trailing edge flaps an increase in the maximum lift coefficient to a higher level is obtained. As seen in figure 22, the increment due to nose-flap deflection is approximately constant depending upon size, type and angle of the trailing-edge device. However, approaching $\sin \delta \sqrt{c_0/c} = -0.2$, which corresponds to $\delta_0 = -30^\circ$ for a 15% nose flap, separation and stalling takes place somewhere on the upper side of the airfoil. Another consideration regarding the use of flaps, are the pitching moments necessarily produced by their deflection. Increments $\Delta C_{m/4}$ (or values of ΔC_{m0}) taken at constant C_L , are plotted in figure 26. By comparison, the moment due to a 20% and 60° split flap corresponds to $C_{m0} \approx -0.20$. Deflection of a nose flap thus increases the already strong and undesirable pitching moments of flapped wings.

Sharp Leading Edges are as good (or possibly better than) rounded edges, as long as there is not much of a flow around them. As a consequence, deflection of such edges can lead to lift coefficients as high as those found in comparable round-nose configurations. This also means that the gain of the differential in maximum lift obtained by deflecting a sharp-edged nose flap, is greater than that for round-nosed sections. An example of a sharp-edged airfoil section is presented in figure 23. Due to separation the optimum nose-flap deflection of such sections can be expected to be more sensitive than round-nosed airfoil shapes (such as in figure 21, for example). In fact, their viscous drag plotted in figure 27, shows such pronounced minima, the best that C_{Lx} for any δ_0 can be determined. These values are included in figure 22. Looking closely (in figure 23), it is seen, however, that lift as a function of δ is not very sensitive as to variations of δ_0 , say by $+ \text{ or } - 10^\circ$ as against the optimum (giving minimum drag).

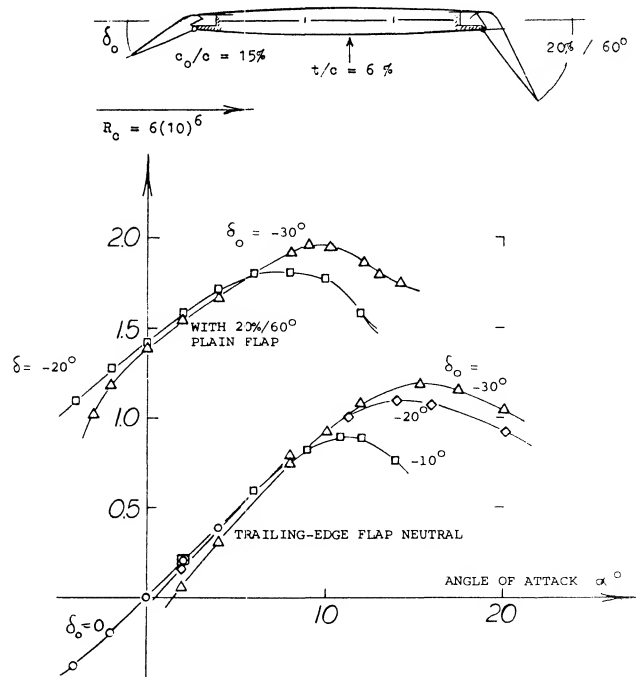


Figure 23. Example (16,e) for a sharp-edged nose flap deflected from a circular-arc airfoil section.

Maximum Lift. The mechanism of stalling in sharp-nosed airfoils is explained in Chapter IV and/or in (16,c). The maximum lift coefficient of sharp edge airfoils is given on figure 24. Laminar separation and turbulent reattachment of the flow over the upper side consumes some momentum. As a consequence, the C_{Lx} function of sections with sharp-edged nose flaps is no longer parallel to the C_{Lx} line (as in figure 22). It is also evident in figure 24 that in

combination with a trailing-edge flap, the increase of C_{Lx} with the nose-flap angle is still smaller. Although the differential in C_{Lx} due to the deflection of the leading edge flap is greater for a sharp edge airfoil, the actual C_{Lx} is lower than for a round nose section. $C_{Lx} = 2.0$ for the sharp nose as compared with 2.5 to 2.6 for the round nose section, figure 22.

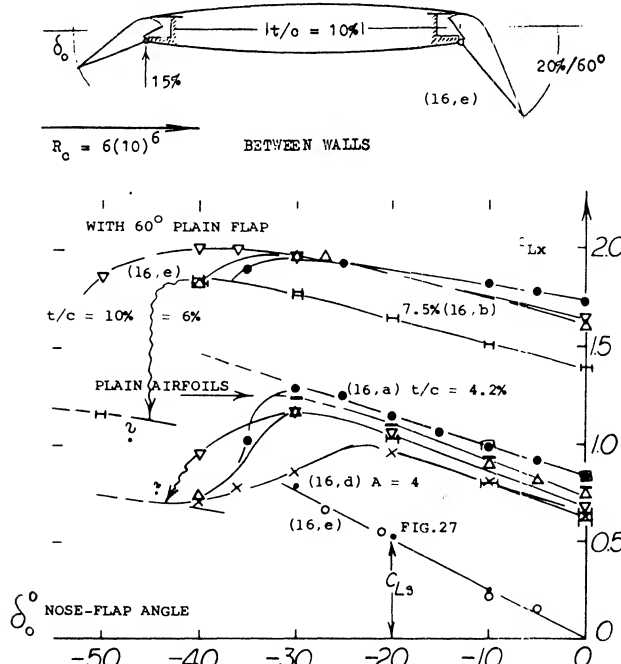


Figure 24. Sharp-edged airfoil sections; maximum-lift coefficients as a function of nose-flap deflection.

(16) Investigation of sharp-edged nose flaps:

- a) Rose, 4.3% Double-Wedge Airfoil with Flaps, NACA TN 1934 (1949).
- b) Marshall, Double Arc Section With 17% Flap, ARC RM 2365 (1950).
- c) Rose, Stalling of Sharp Airfoil With Nose Flap, NACA TN 2172 (1950). See also TN 1894 and 1923 (1949), and TN 2018 (1950) with various chord ratios.
- d) Lange, Wing with $A = 4$ and Circular Arc Sections, NACA TN 2823 (1952).
- e) Cahill, Summary Report on Forces of and Loads on Airfoils with Leading- and Trailing-Edge Flaps, NACA TRpt 1146 (1953).
- f) Croom, With Leading- and Trailing-Edge Flaps, NACA RM L1957J15 (also with BL control) and L1958B05 (also with spoiler).
- g) Powder, Biconvex Wing With Flaps, ARC RM 2157 (1946).

(17) Investigation of so-called Kruger flaps:

- a) Kruger, Laminar Wings with Nose Flaps, ZWB FM-1148 (1944);
- b) Kruger, Mustang Airfoil (including pressure distributions) ZWB UM-3153 (1944); see NACA TM 1177.
- c) Riegels, Russian Airfoil, ZWB UM-3067 (1944); see NACA TM 1127.
- d) Fullmer, 64-012 Airfoil With Kruger Flaps, NACA TN 1277 (1947).

Comparison With Slat. A sharp-edged (biconvex) airfoil was investigated (16, b) with leading- and trailing-edge devices. It is stated that "in view of the structural difficulties (of a slat) tests were also made using a simpler method", namely a same-size nose flap. Maximum lift coefficients obtained at $R_c \approx 10^6$ with a slotted flap at 46° , are as follows:

$C_{Lx} = 1.55$	for the airfoil with trailing-edge flap
$= 2.02$	with flap and optimum slat
$= 1.75$	with flap and 35° nose flap

The nose flap is roughly half as effective as the slat in this case.

Kruger Flap. The nose flaps presented so far, are simply portions of airfoil sections, suitably hinged so that they can be deflected. A different type is shown in figure 25, obtained by pulling out of the airfoil, or deflecting from its lower side, a comparatively thin extension of the chord. This flap is named after W. Kruger, who first investigated (17, a, b) various shapes at the AVA (Göttingen) in 1944. The Kruger flap is used in the inboard portions of some present-day swept wings (as in airliners). — Since this type of flap is extended forward of the basic airfoil chord, an increase of the lift-curve slope can be expected. This is seen to be true in figure 25, particularly when using the flap (a) on the otherwise plain airfoil. In combination with a trailing-edge split flap, lift coefficients (and pressure gradients) are evidently so high that interference (boundary-layer separation) takes place in the corners between suction side and the walls of the so-called two-dimensional wind tunnel used. Part of the deterioration can be genuine, however.

Nose Radius. As mentioned above, the gain in maximum lift obtained by the use of nose flaps, is particularly great for sharp-edged airfoil sections (where C_{Lx} is low, without any leading-edge device). The effectiveness of Kruger flaps is shown in (17, a) on various airfoil sections. Also considering the results as in figures 21, 22 and 23, the following statements can be made:

The effectiveness of nose flaps increases, as the leading-edge radius is reduced, particularly to below $r/c = 1\%$. Maximum values of $\Delta C_{Lx} = 0.6$ are obtained for supersonic-type sharp-edged airfoil sections (where $C_{Lx0} = 0.6$ or 0.7, only).

The increment in maximum lift can be expected to be small in round-nosed and well-cambered sections. For example, for a 12% thick airfoil with 4% reflexed camber, and $r/c = 1.6\%$, almost no increment at all was found (17, a).

These statements may also be correct for leading-edge slats.

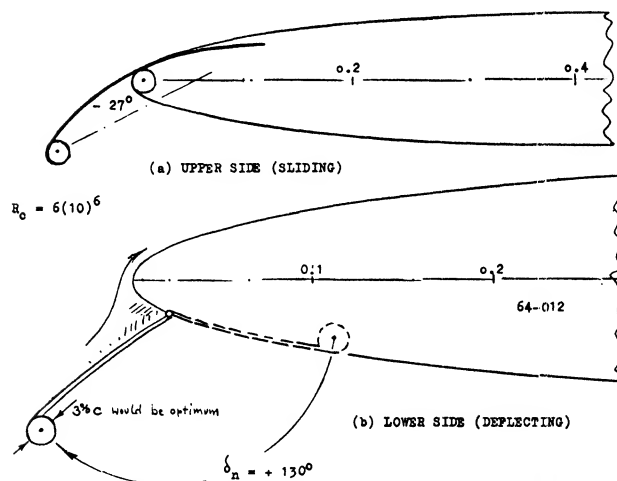
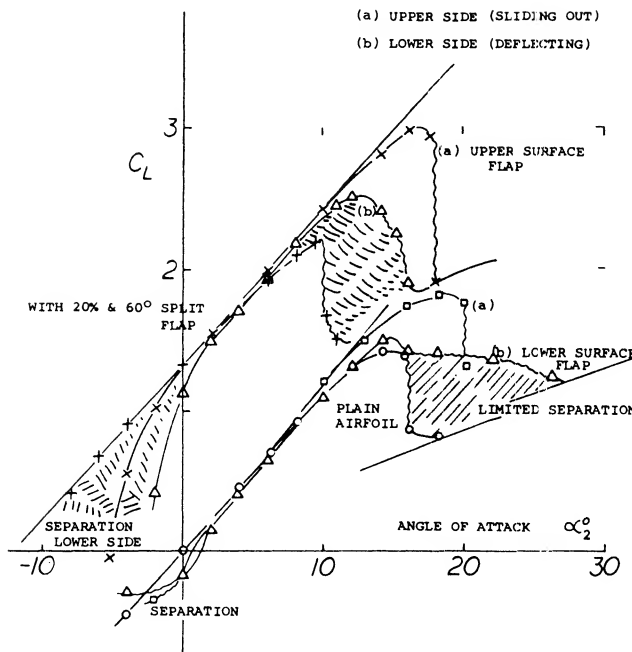


Figure 25. Lifting characteristics of Kruger-type Nose flaps.

a) Upper side (sliding out)
b) Lower side (deflecting).

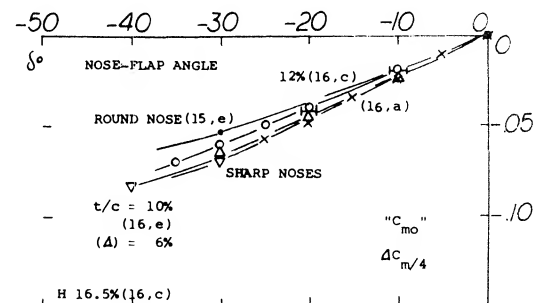
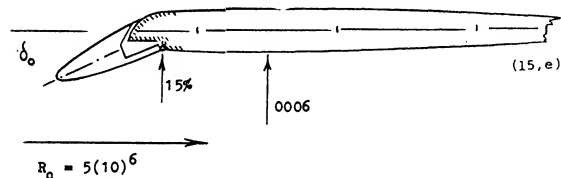
Stalling. Deflection of a leading-edge flap increases the angle of attack at which stalling takes place. For example, in figure 21, the increment is $\Delta \alpha$ between 8 and 10°. In combination with a split flap, stalling is quite sudden, however as seen on figure 25. In configuration (a) the lift coefficient drops from $C_{Lx} = 3.0$, to $C_{Lx} = 1.9$, at $\alpha_2 = 18^\circ$. Separation evidently "springs" from somewhere on or shortly aft of the nose flap. If the same flap would be used in combination with a cambered airfoil section, stalling might be more gentle (possibly beginning from the trailing edge). The (b) type Kruger flap in figure 25, can be deflected to any suitable angle. Maximum C_{Lx} is obtained for $\delta_n = + (110 \text{ or } 120)^\circ$, in the definition as in the illustration. We have plotted results for $\delta_n = + 130^\circ$, however. While the increment in maximum lift is not spectacular in this case, the quality of stalling is very

much improved. For the plain airfoil, a high lift coefficient is maintained up to $\alpha_2 = 25^\circ$, which is some 10° beyond that for C_{Lx} . It seems that laminar separation first takes place at the leading edge of the flap. Subsequently, the flow reattaches in turbulent form to the upper side of the airfoil. Final separation starts near the trailing edge, gradually progressing forward. In combination with the split flap, stalling develops over a range of some 4° of the angle of attack. Thus, the lower-side Kruger flap can be used to induce gentle stalling (18). Considering practical operation of an airplane, the "permissible" maximum lift, staying away from a sudden loss of lift would thus become satisfactory.

Pitching Moments. Nose flaps represent a forward extension of the wing chord, which adds a positive tail-down component to the pitching moment. In the configurations shown in figure 25, the variation corresponds to

$$\begin{aligned} dC_{m_4}/dC_L &= +0.06 && \text{for type (a)} \\ &= +0.05 && \text{for type (b)} \end{aligned}$$

Considering a flap extension in the order of 8% of the airfoil chord, a forward shift of the aerodynamic center could be expected, equal to $0.75 (0.08) = 0.06$, which comes close to the experimental results. Approximately the same shifts were found when using the nose flaps in combination with a standard split flap. All these derivatives are positive (destabilizing), in a manner similar to that of slats. Kruger flaps (if not extending too far down) might help, however, to reduce the large nose-down pitching moments caused by Fowler or similar flaps.

Figure 26. Pitching moments " C_{m0} " of $\approx 15\%$ chord leading-edge flaps.

(18) As pointed out in (10,e), damping by a positive $dC_L/d\alpha$ in the wing tips is considered to be at least as important to prevent rolling over, as the maintenance of high lift.

Camber. The pitching moment of airfoil sections consists of two components. That due to camber or deflection of a nose flap, is plotted in figure 26 in the form of " C_{m_0} " (defined for $C_L = 0$) or $\Delta C_{m/4}$ (taken for $C_L = \text{constant}$), as a function of the angle of deflection. Converting the angle (25°) of the configuration as shown, into a dip ratio ($y/c = (c_0/c) \sin \delta_0 = 6.3\%$) we find that the moment ($\Delta C_{m/4} = -0.05$) is of the same order of magnitude as that due to slats, in part (b) of figure 9. As mentioned in context with that illustration, the camber moment of nose flaps may also increase with their chord length.

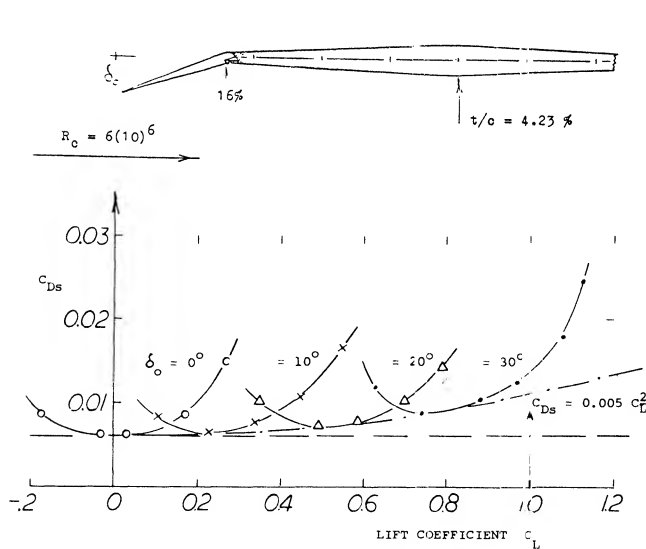
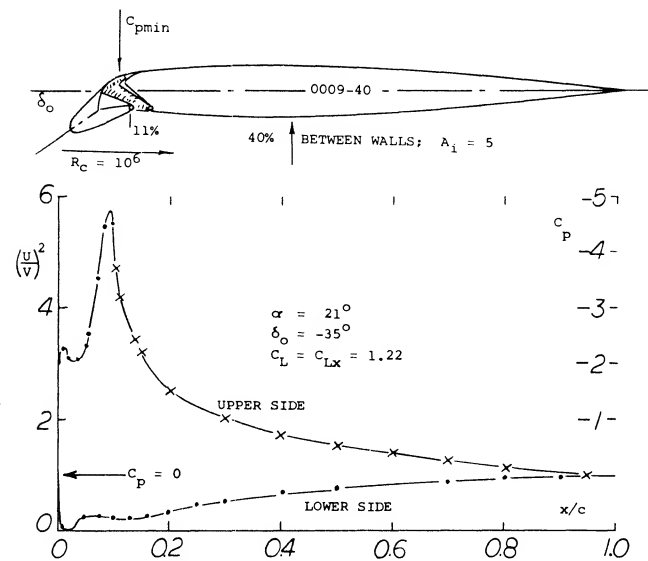


Figure 27. Viscous drag of a sharp-edged "supersonic" airfoil section (16,a) as a function of lift, for various angles of the nose flap as shown.

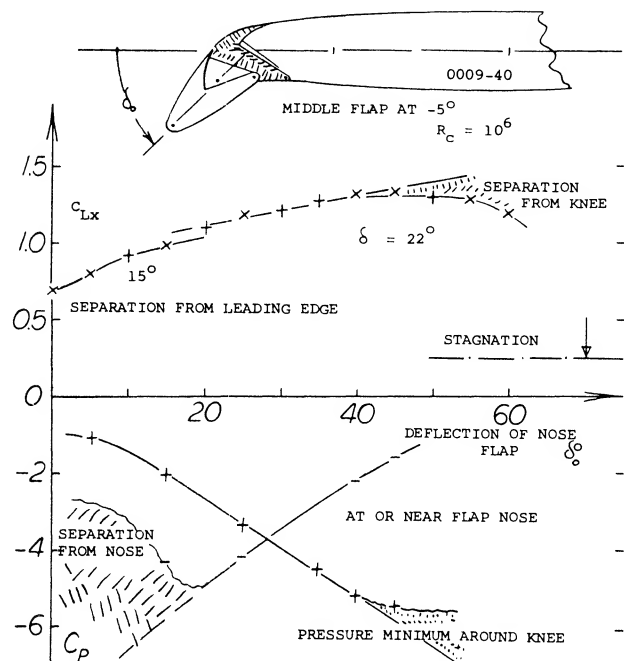
Drag. The increase in drag due to the deflection of a Kruger flap, can be found in (17,d). The increment of the "viscous" section drag for a flap similar to that as in figure 25(b), when in or near optimum deflection, corresponds to $\Delta C_{Ds} \approx 0.02$. Any round-nosed flap (such as in figure 21, for example) is likely to reduce the viscous drag increase with lift. As shown in figure 27, drag increases considerably, however, when deflecting a sharp-edged flap a few degrees above or below the "correct" position. In fact, the minimum of the section drag is so much pronounced that it permits plotting experimental values for C_{Ls} in figure 22. Equation (12) is well confirmed in this manner.

Pressure Distribution. A distribution typical for a round-nosed airfoil with a leading-edge flap deflected at one particular angle, is presented in figure 28. At or near C_{Lx} , such a distribution has two pressure peaks, one at the leading edge, and the other one at the bend or knee formed by deflection. The two peaks are plotted in part (B) of the illustration. At flap angles below -20° that is at $\delta_0 = -10^\circ$, for example some separation takes place from the leading edge. At angles above -40 or -50° , the

peak at the knee is too high, so that separation occurs from some place aft of that bend in the surface. The investigation (15,b) indicates that a peak of the maximum lift coefficient is obtained when the flap is deflected so far, that the first peak almost disappears. In the configuration considered, that condition is found at $\delta_0 = -45^\circ$, producing a $C_{Lx} = 1.33$. A little bit of flow around the nose of the flap from the lower to the upper side is desirable, however. It seems that such a flow promotes transition to turbulence, so that separation at the knee is prevented or postponed.



(A) Pressure distribution for one particular nose-flap angle, at maximum lift.



(B) Variation of the two negative pressure peaks as in (A) and of the maximum lift coefficient obtained, as a function of the nose-flap angle.

Figure 28. Pressure distribution around an airfoil (15,b) with round-nosed leading-edge flap:

Flap Forces. Integration of a pressure distribution yields both the resultant force in a nose flap, and its hinge moment. Using the peak-pressure values as in part (B) of figure 28, as an indication for the flap load, some exchange between the two peaks evidently takes place, as the flap angle, or the angle of attack and the lift coefficient are varied. The magnitude of the normal forces is shown in figure 29, indicated by a coefficient based on chord or area of the flap. The derivative is

$$(dC_{No}/dC_L) \text{ between } (2.8 \text{ and } 3.5) \quad (20)$$

with or without trailing-edge flap deflected and is also confirmed in (16,e) for the round-nosed flap as in figure 30. When deflecting the nose flap and/or when using a trailing-edge flap, the load is reducing, corresponding to a lateral shift of the straight lines in the graph, by certain values of ΔC_L . Empirically, the load is zero:

- when the lift coefficient C_L or ΔC_L is about half of that as in equation (12);
- when C_L or ΔC_L is about half of the (ΔC_L) due to trailing flap as in Chapter V.

Adding these two components, the lift coefficient in figure 29 is obtained.

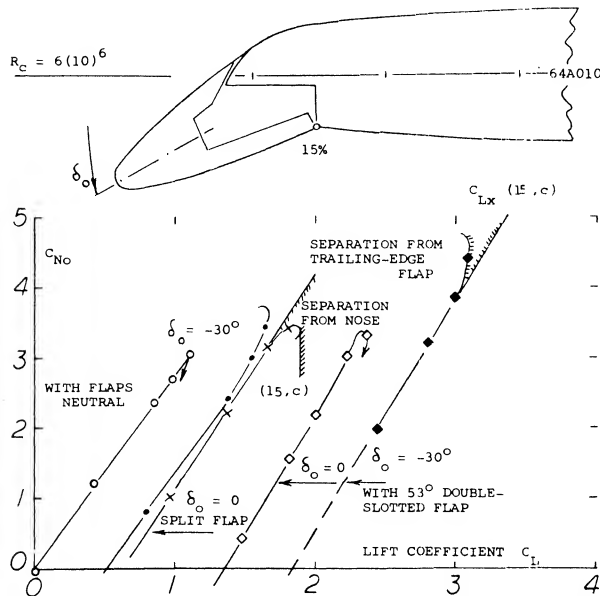


Figure 29. Load on a nose flap (15,d) indicated by the normal-force coefficient, as a function of the total lift coefficient produced.

- (19) Theoretical analysis of pressure and load distribution:
- Allen, Chordwise With Flaps, NACA TRpt 634 (1938); also TN 708 (1939).
 - Walz, Analysis for Nose and Trailing Flaps, ZWB FB 1170 (1940).
 - A demonstration of theoretical methods such as in (a) is included in (18,e).

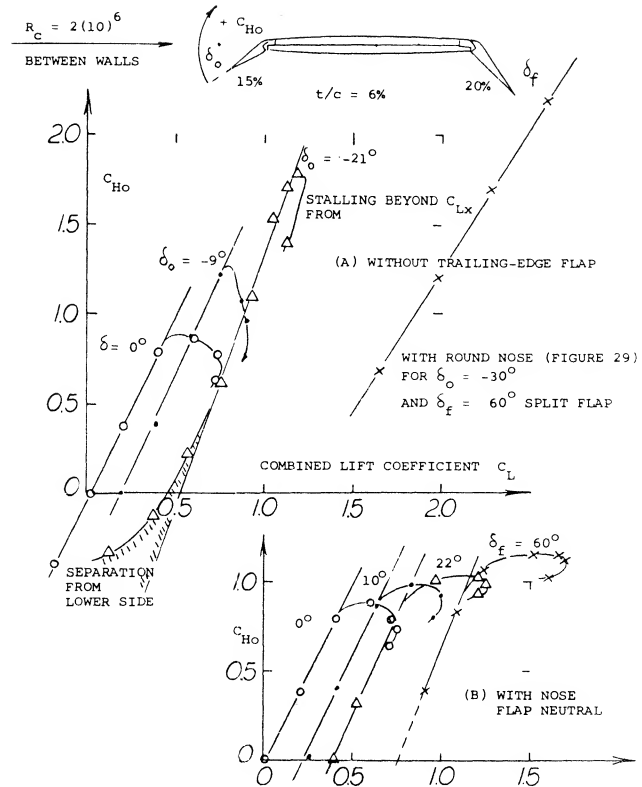


Figure 30. Hinge moments of a nose flap (16,e) as a function of the airfoil lift coefficient.

Hinge Moments of nose flaps consist of a component due to angle of attack and one due to deflection. For $\delta_o = 0$, the moment simply corresponds to a part of the airfoil lift or load. When deflecting a flap downward, the minimum pressure peak at or near the leading edge, reduces in magnitude, as shown in figure 28. Hinge moments "H" reduce accordingly. The coefficient

$$C_H = H/q c_o S_o = H/q c_o^2 b \quad (21)$$

(where "o" refers to the chord of the nose flap) is plotted in figure 30, as a function of the total lift coefficient. The derivative dC_H/dC_L is approximately:

- = 2.0 for the sharp-edged flap in the graph
- = 1.5 for the round-nosed flap as in figure 29.

The lateral shift in the lift coefficient is roughly:

$$\begin{aligned} \Delta C_L &= C_{L_s} \text{ equation (12) for sharp-nosed flaps,} \\ \Delta C_L &= 1/2 C_{L_s}, \text{ for round-nosed flaps,} \\ \Delta C_L &= (\Delta C_L) \text{ as for the normal force, above} \end{aligned}$$

The Kruger flaps deflected from the lower side (as in part (B) of figure 25) have loads and hinge moments different from those discussed above. As reported in (17,b) the normal-force coefficient varies between:

$$\begin{aligned} C_{No} &= -1.5 \quad (\text{down/back}) \quad \text{at low lift coefficients} \\ &= +3.7 \quad (\text{up/forward}) \quad \text{at high lift coefficients} \end{aligned}$$

3. BOUNDARY LAYER CONTROL NEAR THE LEADING EDGE

Elimination of the boundary layer by suction or restoration of its dynamic energy by blowing, are well-known means of keeping fluid flow attached. In Chapter V blowing over wing flaps is presented. The same type of control can also be used at or around the leading edge of lifting airfoils.

A. Control Through Turbulence or Vortex Generation

Any of the leading-edge devices discussed in this chapter may be used to guide the flow around the leading edge. Separation (stalling) will subsequently take place, however, when and if the boundary layer remains laminar. Consideration of transition turbulence, mixing and vortex generation is, therefore, important.

Laminar Separation takes place very soon after a still laminar boundary layer is directed to flow against an adverse positive pressure gradient. Strong gradients of this kind are encountered at higher lift coefficients on and behind every flap or slat placed at the leading edge of an airfoil. The fact that those devices are effective, can be explained by reasons as follows:

- The Reynolds number at the end of a flap or slat, is an order of magnitude larger than that "at" the not very round leading edge of a plain airfoil.
- The mechanism of laminar separation, followed by transition and re-attachment may also be active, preventing separation from behind flap or slat.
- Surface imperfections within a slot, or such as the gap near the hinge axis of a flap, may help or even be necessary to make these devices effective.

It is amazing that neither analysis (21,c), nor the numerous experiments with leading-edge devices, have really gone into the mechanism and/or into auxiliary means through which subsequent separation is prevented or postponed.

Transition. The optimum (out of 6) arrangements of a "leading-edge slat of rather unusual design" is presented in figure 31. It is debatable to call the "flap" a slat. Our explanation for the increase of lift from $C_{Lx} = 1.74$ to 2.02, due to the presence of the slot — is turbulence. The flow is likely to remain laminar to the end of the nose flap. It then separates, turns turbulent as it passes over the slot, and it meets the round nose of the main airfoil in this condition. In fact, a reduction of the maximum lift may be expected, if there were a flow through the slot.

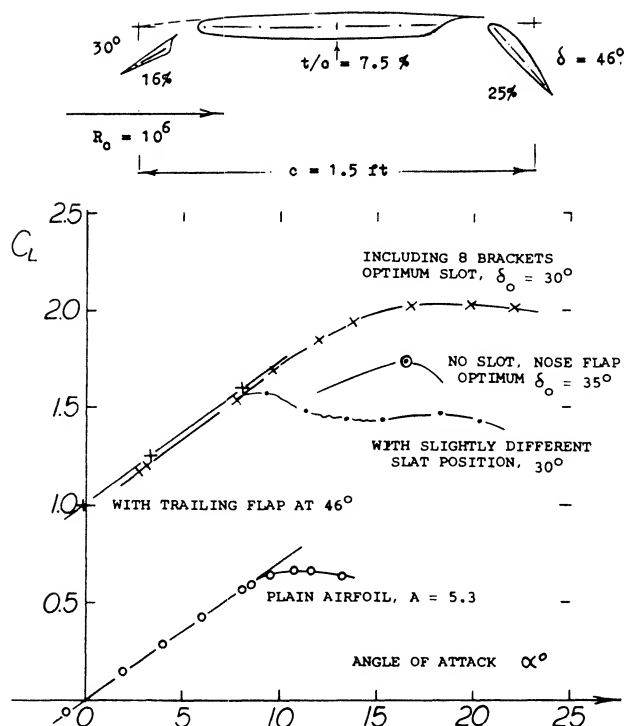


Figure 31. Lifting characteristics of an "Unusual Design" of a leading-edge slat or flap (16,b).

Vortex Generators have been investigated and are used on many aircraft primarily to improve the flow over trailing-edge flaps. The function of these devices is well described in (21,b). They are either ramps (or wedges) each forming a pair of trailing vortices like a little wing, or vanes (little half-span "wings" or plates) protruding from the wing surface at a lateral angle of attack thus producing each a tip vortex. When placing a number of such elements in a spanwise row within the boundary layer, a

- (20) Pressure distributions, loads and hinge moments of nose flaps:
 - Kelly, Leading-Edge Flaps, as in (17,d).
 - Kruger, With Kruger Flaps, as in (20,b).
 - Lemme, Round-Nose Flap, as in (17,b).
 - Cahill, Sharp-Edge Flap, as in (18,e).
- (21) Lachmann, "Boundary Layer and Flow Control", 2 Volumes, Pergamon Press (1961):
 - Summaries and Increase of Lift:
 - A major part of Volume I deals with trailing-edge blowing, and it is as such referenced in the "trailing-edge" chapter.
 - Williams, British Research (including nose suction).
 - Pleines, Slotted Wings (including Fieseler "Stork" and Dornier-27).
 - Basic considerations of separation control are presented in various places.
 - Wagner, Engineering Considerations of Suction and Blowing.
 - Primarily BL Control for Low Drag:
 - Most of Volume II deals with low drag, which is not part of this chapter.
 - Pearcey, Prevention of Separation by BL Control.

series of chordwise trailing vortices is formed. These helical vortices serve to exchange retarded particles of air near the surface of an airfoil with high-energy particles at the edge of the boundary layer. In short, momentum is transported toward the surface through mixing or turbulence. For vane-type generators placed on the upper side of an airfoil, in a single row the following dimensions are said (22,a) to be most effective:

h/c	=	1%	for the height ratio
y/h	=	6	for the lateral spacing
ℓ/h	=	2	for the chord length of the vane
β	=	15°	for the angle of yaw

The size, height, of vortex generators "should be related to the range of surface for which they are required to be effective — rather than to any local boundary-layer conditions". An example of the use of vortex generators is shown in figure 36, along the wing roots and ahead of the aileron.

Increasing Lift. It is reported (22,c) that the maximum lift of the NACA 23012 section was increased 30% by means of turbulence generators which postpone separation from the trailing edge. The influence of leading-edge separation of a 6% thick section (22,f) was very small, however; C_{Lx} was increased from 0.8, less than 10%. When placing "generators" ahead of the section nose, the beneficial effect is of a different nature. "Strakes" as shown in figure 32, do not really increase the maximum lift. They change stalling characteristics, however; increasing the angle of maximum lift by some 5° . The pattern shows how the flow reattaches itself "immediately", behind the protuberances as well as between them. — As far as nose flaps are concerned, it is suggested that the gap "around" the hinge axis, or the lip of the airfoil adjoining the flap, may produce transition and turbulence. In the case of slats, the

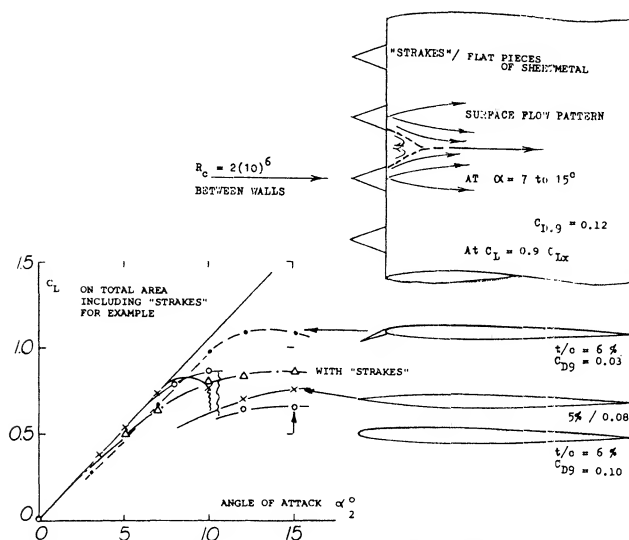


Figure 32. The influence of several leading-edge modifications (13,c) on the lift of a thin airfoil section.

converging (nozzle-like) slot formed when extending the slat, must be expected to stabilize laminar flow. It is, therefore, suggested that turbulence generators placed within the slot might improve the effectiveness of the slat. In fact, the Messerschmitt slat as in figure 8(b) shows a sheet-metal step (into which the slat is intended to fit, when retracted); and this step may very well act as a transition trip. See also figure 4.

B. Boundary-Layer Control by Suction

Around the leading edge of a conventional airfoil shape, the boundary layer is thin and laminar. Suction directly at the nose would, therefore, not make sense. There are some arrangements, however, whereby suction will guide the flow around the leading edge, subsequently preventing or postponing separation.

A Nose Shape, specially designed to be combined with boundary-layer control is shown in figure 33. Flow around the leading edge is accomplished by suction through a narrow slot as indicated. After most of the turning has been done, the flow is then directed against a comparatively modest pressure gradient along the upper side of the airfoil. As reported in (23,a): "unexpectedly, the increments in C_{Lx} correlated excellently in terms of the momentum sucked through the slot, not the Quantity" (25). The increase of maximum lift shown in the graph is impressive, however such nose shape would not be practical for high-speed flight.

(22) Mechanism of and experiments with vortex generators:

- Pearcey, Prevention of Separation, last contribution in (28,II).
- Bruynes (United Aircraft) Mixing Device, US Patent 2,558,816 (1951).
- There is a number of unpublished reports, listed in (a). Other such reports by United Aircraft Corporation (1947/1954) are mentioned in (e) & (f).
- Schubauer, Forced Mixing, J Fluid Mechs 8 (1960) Part I.
- Spangler, Influence on Skin Friction, NASA Contractor Rpt CR-145 (1964).
- Burnsall, Maximum Lift of 6% Section, NACA RM L1952G24.
- As reported by McFadden in NACA TN 3523 (1955), "vortex generators (at 35-percent chord) were found to be effective in both the wing-drooping and pitch-up problems" of the North American F-86 swept-wing airplane, at Mach numbers around 0.9.

(23) High lift through leading-edge slot suction:

- Williams, High-Lift Boundary-Layer Control, in Volume I of (28).
- Williams, Theoretical Investigations (RM 2693) and Tunnel Tests (RM 2876) of Nose-Slot Suction, ARC Rpts (1950/52); see also (28,I).
- McCullough, 63-012 Airfoil, NACA TN 1683 & 2041 (1948/50).

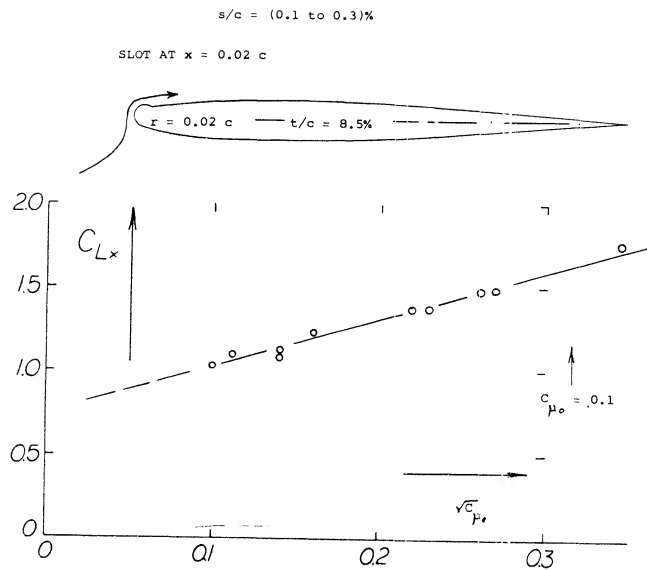


Figure 33. Boundary-layer control around the nose of a specially designed airfoil section (24,a,b) by suction through a narrow slot.

Leading-Edge Slot. The NACA 63-012 airfoil section was investigated (23,c) with various suction slots. Optimum dimensions (with or without a 40° plain trailing flap) were found to be as follows:

$$\begin{aligned} s/c &= 0.06\% && \text{for the width of the slot} \\ x/c &= 0.8\% && \text{for the chordwise location} \end{aligned}$$

The maximum lift coefficient was increased as shown in figure 34. Up to $C_q = 0.004$ (or somewhat higher) separation from the leading edge is evidently being eliminated, thus increasing lift by $\Delta C_{Lx} = 0.7$ for a plain airfoil, or $= 0.6$ (with trailing flap). Although "the abruptness of the stall was reduced" by suction, a margin of some 2 or 3 degrees in the two-dimensional angle of attack may not be considered to be satisfactory in the practical operation of an airplane. In the second phase of the investigation, another slot was added at 51% of the chord. Lift was further increased to $C_{Lx} = 2.4$, and $= 2.9$ (with trailing flap). Stalling returned to being really abrupt, however. The drop from $C_L = 2.4$, is estimated to be down to $C_L = 0.8$ (as in NACA Rpt 824, without flap and without suction). In conclusion, this type of suction boundary layer control to increase of maximum lift, does not seem to have a practical value. It should also be noted that without suction, the presence of the slot reduces the maximum lift noticeably.

Distributed Suction. A slot such as in figure 33, for example, also has a sink effect (thus also drawing some air from upstream). Since this effect is comparatively small, the location of a slot having a width between 0.1 and 0.6% of the chord, can be expected to be critical. As in suction applied to the nose of trailing edge flaps, see

figure 40 of Chapter V, suction distributed over a certain chordwise area, therefore, seems to be more practical. Tests (24,f) on a 0006 airfoil section, with suction through perforated sheet metal backed with felt, show the following near-optimum situation:

C_{Lx}	=	0.87	for the plain airfoil
C_{Lx}	=	0.69	with perforated nose
C_L	≈	1.30	with suction, at beginning stall
C_{Lx}	=	1.40	with tunnel-wall interference
x/c	=	1%	required area, from nose point
C_q	=	.001	required for up to $C_L = 1.3$

Because of severe tunnel-wall interference (3-dimensional flow pattern) stalling takes place over an interval of up to 8° of the angle of attack (whereby C_L increases from 1.3 to 1.4). This type of stall is not typical for boundary-layer control by suction.

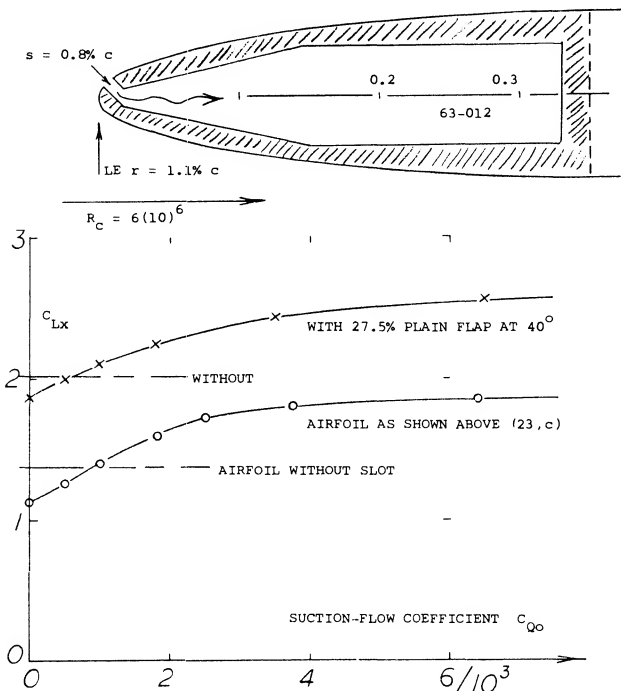


Figure 34. Maximum lift of the 63-012 airfoil section, as a function of suction (23,c) through a narrow slot near the leading edge.

(24) Area Suction around the airfoil nose:

- Gregory, 63A009 Section With Nose Suction, ARC RM 2900 (1952).
- Pankhurst, Stalling Properties, ARC RM 2666 (1953).
- Nuber, 64A212 Airfoil, NACA TN 1741 (1948).
- Dannenberg, 10.5% Section, NACA TN 2847 & 3093 (1952/53).
- Hunter, Flight Investigation, NACA TN 3062 (1954).
- Weiberg, 0006 Airfoil, NACA TN 3285 (1954).

Lift Increments. Two other airfoil sections with area suction near the nose, are shown in figure 35. The maximum lift coefficient increases with the chordwise extent of the porous area (indicated by the flow coefficient C_Q) in a manner similar to that due to slot suction, in figure 34. That is, leading-edge separation is more and more postponed, until at constant angle of attack (shown for $\alpha = 14^\circ$) a certain plateau of lift is reached. The fact that the maximum lift continues to increase as the suction flow increases, can be explained by a general improvement of the boundary-layer flow along the upper side of the airfoils tested. The behavior of the 10.5% airfoil is different, however. Separation from the leading edge (indicated by the area "S") is first eliminated. As above at constant angle of attack, a constant lift level is then reached, at $C_Q = 0.0015$. Further increased nose suction does not postpone further stalling then taking place from the trailing edge. — The "most economical" extent of nose suction in the 63A009 section, is around 3% of the upper surface. When using a trailing flap, the increments in figure 35 may be slightly smaller ($\Delta C_{Lx} = 0.4$ or 0.5) than those for the plain airfoils ($\Delta C_{Lx} = 0.5$). In other words, more suction is required to handle increased BL losses and pressure gradients.

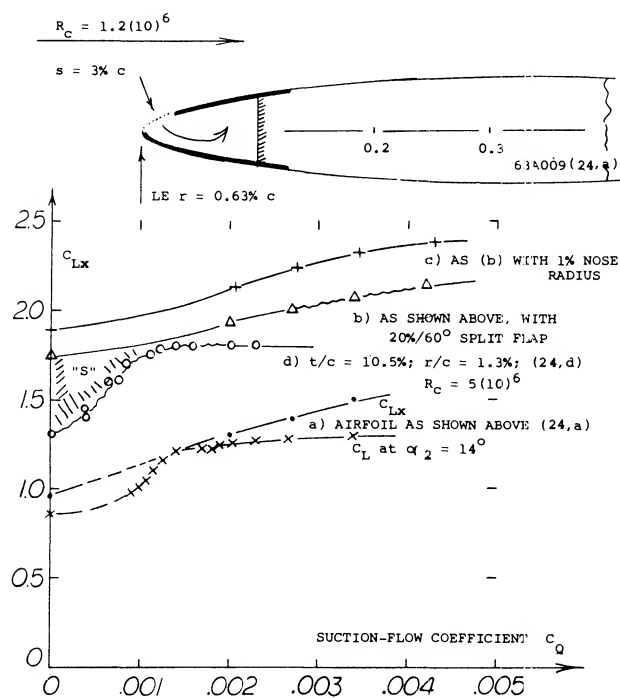


Figure 35. Maximum lift of symmetrical airfoil sections, as a function of the flow coefficient indicating boundary-layer control by suction through a porous area near the leading edge.

Porous Materials are needed to form the surface of an airfoil where boundary-layer control by suction is used. Various materials are listed (24,d) such as perforated sheet metal, paper, sintered metal, felt, wood, ceramic. Since the outside pressure is not constant in chordwise direction, suitable combinations (in layers) are selected in such a manner that any return flow across the porous area is

avoided, and the suction velocity is kept reasonably uniform. The permeability of any porous material is reduced when wetted. As reported in (24,b) sintered bronze becomes "saturated" in a rain fall of 1 inch/hour, within 3 minutes, so that the suction velocity (at constant pump power) reduces to 40%.

The Pressure Required to move air particles from outside, into the hollow nose of the airfoil, primarily corresponds to the local static pressure coefficient at the surface. It should be noted that theoretically the total pressure ($p + q$) is to be considered. Within the boundary layer, the dynamic pressure q is low, however. For the 0006 suction discussed above, at $C_{Lx} = 1.3$, the coefficient of the static pressure differential is between $C_p = -30$, directly at the nose point, and $C_p = -10$, at the end of the 1% suction area. With a standard (20% and 60°) split flap deflected from the trailing edge, the C_p values are -55 , and -20 , respectively. As mentioned above, there can thus be a "circulation" of flow in and out across the suction area. — When sucking through a slot, there is some loss (due to sharp edges). Across a porous material, the loss is likely to be appreciable. Approximately, the differential is $\Delta p \sim w$, where $w = Q/S_s$ = average velocity through the porous area. In the tests discussed (24,f), the suction velocity was in the order of $w = 0.1V$. For example, for $w = 10$ ft/sec, the pressure differential through the particular material used, is some 270 lb/ft². Considering this and a similar composition (of wire "cloth" and sheet metal) used in flight tests (24,e) a corresponding coefficient in the order of $\Delta C_p = 10$ may be assumed. Summing up, a static pressure differential corresponding to ΔC_p between 20 and 60, would thus be required to operate the 0006 suction system as needed. If including half of the potential dynamic pressure at the location of suction, we are left with a coefficient between 15 and 35. Static pressure coefficients of the 10.5% thick section in figure 35, are appreciably lower than those of the 0006 section. When approaching C_{Lx} , the minimum pressure peak reaches $C_p = -12$, reducing to about half of this value at the end (at 3.5% of the chord) of the most effective suction area.

Stalling. The quality of the stall of the airfoils in figure 35, is similar to that in typical tunnel-tested symmetrical sections, with little margin some 2° of the angle of attack and a drop, for example from $C_{Lx} = 1.8$ or 1.7 , probably down to 0.8 (as for the plain airfoil, in NACA Rpt 824). Although there is an improvement in stalling quality over the really abrupt type as in airfoils with slot suction, distributed suction (from near the leading edge) does not seem to be perfect either. Regarding other aspects of this subject, are covered in Chapter V.

- (25) For definitions of C_{Lx} and C_Q et cetera, see under "blowing" in the chapter on "trailing-edge high-lift devices". Including losses in a blowing slot, the flow coefficient C_Q obtained, may only be 50% of $(s/c) \sqrt{C_p}$.

In a Cambered Airfoil section, with a well-rounded upper side, separation (stalling) starts from the trailing edge. Boundary-layer control at or from near the leading edge is, therefore, not of very great value. as illustrated in (28,b), in comparison to blowing, the influence of suction is also more or less limited to the elimination of the boundary layer arriving at the slot. — The cambered section 64A212 was investigated (24,c) between wind-tunnel walls. A 2412 wing was flight-tested (24,e) on a small airplane. Principal results are as follows:

NACA 64A212 airfoil @ $C_q = 0.002$ C_{Lx} increased from 1.28 to 1.59
 NACA 2412 wing @ $C_q = 0.001$ C_{Lx} increased from 1.30 to 1.62

Other results of the flight tests are:

- With porous area, but without suction, $C_{Lx} = 1.2$ only.
- Suction power may have been too small.
- Some 60% inboard suction was as effective as full-span.
- With small wing flaps down, $C_{Lx} = 1.6$, increased to 1.8.
- With power and propeller on, there was hardly any increment.
- In heavy rain, the suction power is doubled.

A Nose Flap. With a nose similar in shape to those in figures 21 and 22 a large increase in C_{Lx} is obtained when the boundary-layer material is removed around the knee. As shown in figure 36, C_{Lx} is increased from around 1.4 to 2.2. In fact, this type of flap is only effective when used in combination with suction. It is possible that without suction (and with a sealed surface) laminar separation takes place at or behind the bend of the flap. With a deflection $\delta_o = -40^\circ$ rather than 20° the quality of stalling seems to be good, particularly in view of the 65-series foil section involved.

Trailing Flap. In combination with a part-span suction controlled trailing-edge flap, the lift coefficient of the airplane configuration as in figure 36, is increased from $C_{Lx} = 1.86$ without nose flap to 2.00 with $\delta = 30^\circ$ to 2.42 and with $\delta_o = 40^\circ$, $C_{qo} = 0.003$ to 2.65 (when adding vortex generators "VG" as shown). These values may not look as impressive as those likely to be found as the result of two-dimensional airfoil investigations. Including part-span effect and fuselage interference, they are close to reality, however.

(26) Boundary-layer control of nose flaps by suction:

- Holzhauser, Airplane With Flaps and BL Control, NACA RM A1957K01.
- Koenig, Wing Fuselage With Flaps and Suction, NACA RM A1956D23.
- There are many wind-tunnel results available, dealing with flaps and boundary-layer control on swept wings such as NACA RM A1953J26, A1955K29, A1956F01, A1957H21. Some information on such wings is presented in the "swept wing" chapter.
- Holzhauser, Tunnel and Flight Tests on a 35° Swept Wing With Leading-Edge Suction Flap, NACA TRpt 1276 (1956).

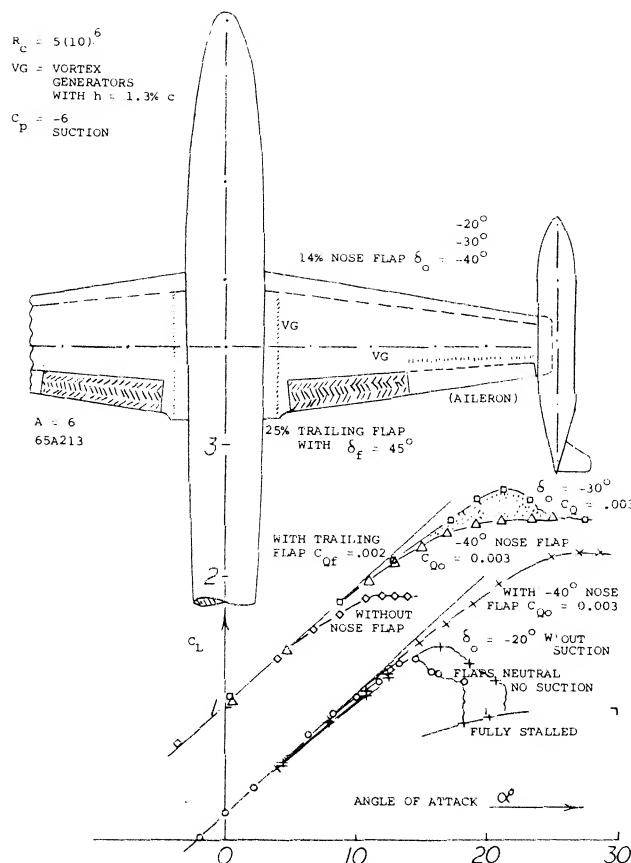


Figure 36. Lifting characteristics of an airplane configuration (26,a) equipped with flaps and boundary-layer control by suction.

Power Required. As stated under "pressure required", directly at the nose, the external pressure coefficients of the 10.5% thick airfoil (figure 35) are considerably lower in magnitude than those of the 0006 section. The chord-wise dimension of the suction area required, is threefold, however. Roughly, the same internal suction power may thus be needed. This power can be determined, using the methods as presented in Chapter V. In doing so, inlet and outlet pressures of pump or blower have to be considered. Near the leading edge, the dynamic pressure ($0.5 \rho U^2$) of the potential outside flow can be very high, say 20 times the ambient dynamic pressure. Since primarily boundary-layer material is sucked into the wing, only some fraction of that pressure is recovered. When considering the outlet pressure (against which the pump is working) there are two possibilities:

- discharge at some place, say into ambient pressure,
- blowing over a trailing-edge flap.

(27) Blowing from leading-edge flaps is found in:

- Schwieber, From Nose and Over Flap, ZWB FB 1658 (1942); NACA TM 1148.
- McLemore, Airplane Configuration With BL Control, NASA D-407 (1960).
- Weiberg, STOL Configuration With BL Control, NASA D-1032 (1961); also D-25 (same configuration) and NACA TN 4365 (with 2 instead of 4 propellers).

Since the static pressure is low around the bend of a deflected flap, such a combination would be comparatively efficient. — Disregarding dynamic pressure, and when blowing into ambient pressure, the equivalent drag coefficient for a boundary-layer control system at or near the leading edge, would be in the order of

$$\Delta C_D = C_Q C_P = 0.001 (20 \text{ to } 60) \approx 0.04 \quad (24)$$

where the numerical values are those of the 0006 section discussed above. Taking into account an internal efficiency of 50% (in ducts, blower, engine transmission) we may have a $\Delta C_D = 0.08$. This would be as much as the drag of an average airplane at $C_L \approx 1.1$, or 50% of that at $C_L \approx 1.6$.

Takeoff. Theoretically, all the engine power of an airplane would be available for boundary-layer control purposes, when landing. Takeoff might be equally important, however, and the estimate above implies that drag and engine power required during takeoff, would possibly by 50% increased when using leading-edge suction. One must also consider cost, weight and complexity of the system. After discussing and referencing these drawbacks, Wagner (21,e) therefore comes to the conclusion that suction in chordwise or spanwise combination with blowing (also using new principles of pumping and powering) would be a more acceptable proposition.

C. Boundary-Layer Control by Blowing

Blowing over trailing edge flaps and the "jet flap" are presented in Chapter V. Blowing can also be used at, or near, or around the leading edge of an airfoil, to prevent or postpone stalling (separation) at higher angles of attack.

"Round" Airfoil. Boundary-layer control was applied to a round-nosed and cambered section (28,b). As shown in figure 37, blowing is most effective from around $x = 0.4c$, as far as the magnitude of maximum lift is concerned. The experiments appear indicate that

$$\Delta C_L \sim \sqrt{s/c} \sim \sqrt{C_Q}; \quad \text{for } C_P = \text{constant}$$

Roughly, it may also be said that (25)

$$\Delta C_{Lx} \sim \sqrt{C_P} \sim C_Q; \quad \text{for } s/c = \text{constant}$$

where $C_P \sim C_Q^2$. The downstream-directed slot as in figure 37, was also used to try BL suction. In comparison,

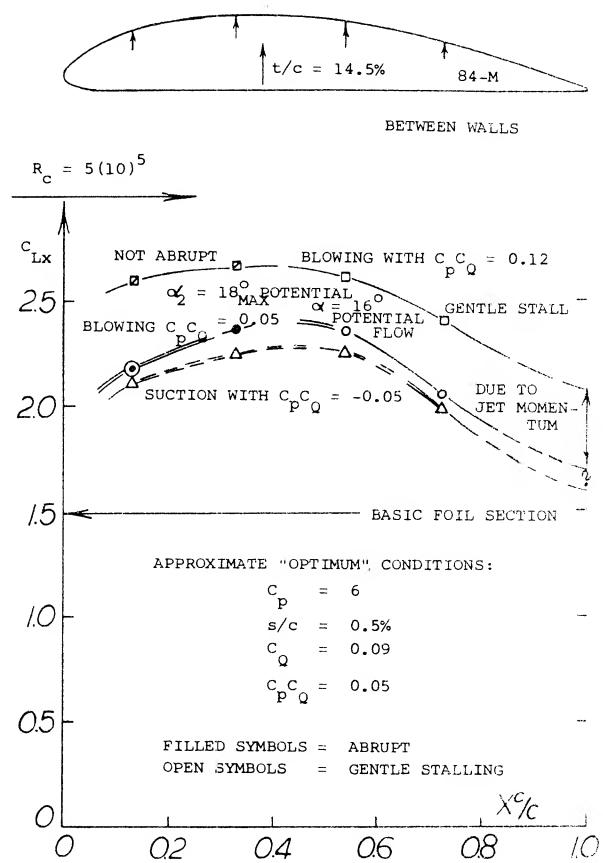


Figure 37. Boundary-layer control over a round-nosed and cambered airfoil section (28,b) by blowing (or suction) through a backward-opening slot; maximum lift as a function of slot position.

this type of control reaches a certain limit (after removing the boundary layer). By contrast, blowing downstream, not only restores full energy; as shown in the graph, for $C_P C_Q = 0.12$, it can also add momentum to the flow reaching to and beyond the trailing edge in a manner similar to that of a jet flap.

A Comparison of blowing and suction through two slots, is reported in (28,a). When discharging through forward slot, stalling of the RAF-31 section is comparatively gentle, between $\alpha = 14$ and 19° , for $A = 6$; maximum lift is increased from $C_{Lx} = 0.9$ to 1.6 . By comparison, when sucking (through rear slot) the drop in C_L is comparatively sharp, while the maximum lift obtained is only modest ($C_{Lx} = 1.2$). The result of suction is better, however, when using the forward slot ($C_{Lx} = 1.4$). Blowing is thus found to be superior as to lift as well as in regard to the quality of stalling. The low Reynolds number of this experimental investigation ($R_c = 2(10)^5$) should be noted, however.

Combined Blowing. The type of stall ("abrupt" or "gentle") is qualitatively indicated in figure 37. When blowing from near the leading edge, the loss of lift is likely to be abrupt. Stalling can be made more gentle in this case, by increased flow. Another way of improving the quality of stall, would be blowing from farther forward. This is done in the configuration as in figure 38, where blowing from the leading edge is combined with that over a 60° trailing-edge flap. For a given discharge at the flap, lift at constant angle of attack of a "wing" with $A_1 = 5$, increases along a straight line, as the momentum coefficient for the nose slot is increased. This increment represents increased circulation. It does not stem, however, from any improvement of the flow over the trailing flap. In fact, that flap stalls beyond a certain increment of lift, as the momentum coefficient of the flap discharge is no longer sufficient to keep the flow attached.

The Momentum Required to eliminate or to prevent separation, by blowing, can be estimated (28,c). We will assume an airfoil section with blowing from the nose, in round numbers:

α_2	= zero	angle of attack in 2-dimensional flow
δ_f	= 60	blowing trailing-edge flap, with $C_{\mu f} = 0.1$
C_L	= 3.0	maximum lift coefficient
s/c	= 0.2%	slot-width ratio, indicating outlet area
w/v	= 5	the blowing velocity ratio
C_{qo}	= 0.01	volume-flow coefficient of blowing
C_{po}	= 25	blowing pressure coefficient = $4 p/q$
$C_{\mu o}$	= 0.1	nose-slot momentum coefficient
x/c	= 0.7	indicating distance between slots

The procedure illustrated is as follows:

a) The loss of momentum between nose and flap corresponds to the BL thickness

$$\vartheta/c = (x/c)(U/V)^2 \quad 0.5 C_f \approx 0.005 \quad (27)$$

where U = average potential velocity along the upper side of the airfoil, assumed to be $= 2 V$; and $C_f = 0.003$.

b) The momentum discharged, has to be at least as great as the loss under (a):

$$C_{\mu} = (1.5\sqrt{\vartheta/c} + (U_s/V) \sqrt{2(s/c)})^2 \approx 0.08 \quad (28)$$

where U = potential velocity at the location of the slot, assumed to be $= 3V$.

In all these equations and values (25) compressibility has not been taken into account. Considering velocity ratios up to 5, and/or $C_P = 25$, a more accurate calculation as in (28,c,d) may be advisable. — For the airfoil in figure 38, the minimum moment coefficient computed above, is shown at the left edge of the graph.

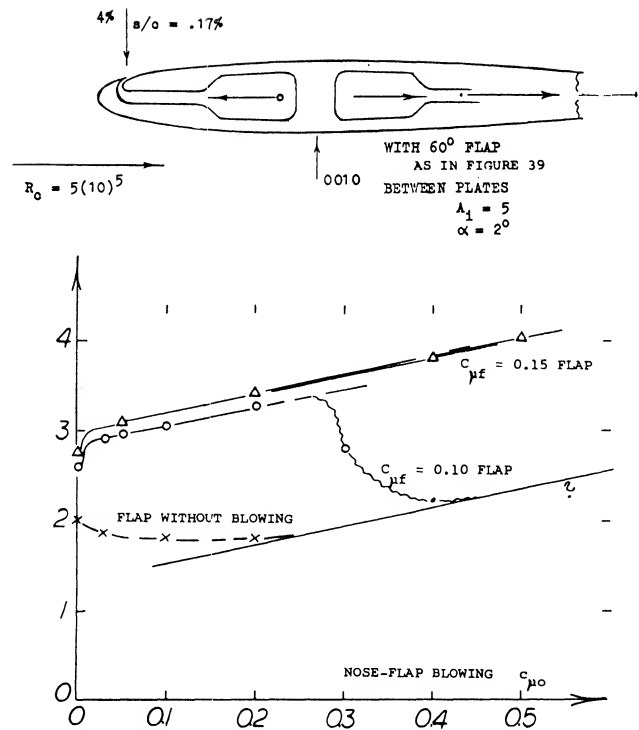


Figure 38. Lift of a "wing" (28,d) at constant angle of attack, as a function of the momentum coefficient indicating blowing from a leading-edge slot.

Ground Proximity. The configuration as in figure 38, was also tested (28,e) at higher Reynolds numbers (see figure 39) and in ground effect. A reduction of circulation is found near the ground, similar to that as shown in Chapter V for example from $C_L = 7$, down to half, at $h = 0.4c$. So, there is no incentive for designing high-lift airplanes in low-wing form. Assuming, $h = c$ to be a realistic height in a conventional airplane, the reduction is still from $C_L = 7$, for example, almost down to 5. The reduction is negligible, however, for a wing with $C_L = 4$.

Stalling. Blowing over the 60° flap of the configuration in figure 39 is so effective that a lift coefficient of almost $C_{Lx} = 8$ is obtained (30). Stalling takes place abruptly, however, within an interval of 1 or 2°, so that the use of such a wing would not be practical (would be dangerous). Separation (from the leading edge) could be prevented by means of a slat (or a nose flap). In the investigation quoted, blowing out of a slot located near the leading edge was used, however. With the help of this slot (and an

- (28) High lift through blowing along the upper side of airfoils:
- Perring (RAE), Withdrawing and Discharging, ARC RM 1100 (1927).
 - NACA: Knight TN 323 (1929) and Bamber Rpt 385 (1931); Blowing and Suction Through Backward-Opening Slot.
 - Thomas, a) Increasing Lift Through Flap Blowing, b) Calculation of Momentum Required, ZFW 1962 p 46.
 - Gersten, From Nose and Over Flap. Rpt DFL-189 (1962).
 - Lohr, Braunschweig Rpts DFL-0116 & -0188 (1961/63); also DLR-1964-02.

appreciable value of the momentum coefficient) a very gentle stall is obtained. This characteristic improves further when approaching the ground. Optimum conditions for the NACA 0010 airfoil configuration tested, including maximum lift, are then found when discharging half of a given value of momentum over the 60° flap, and the other half from the leading edge. An angle-of-attack range of 20° is thus obtained where the lift coefficient remains within plus/minus 5% of $C_L = 5$, for example. Of course, at lift coefficients of such magnitude, appreciable interference can be expected from the plates between which the airfoil was tested.

Pitching Moments. As reported in (28,e) blowing from the leading edge produces less negative (that is, more desirable) moments than when using trailing flaps producing the same lift increment. For example, at $C_L = 4$, using a total $C_{\mu} = 0.7$, the coefficient of the configuration as in figure 39, is in the order of:

$$\begin{aligned} C_{m/A} &= -0.6 && \text{when blowing over the flap} \\ &= -0.3 && \text{blowing } 1/2 \text{ nose and } 1/2 \text{ flap} \end{aligned}$$

However, the differential reduces when approaching maximum lift. At and beyond C_{Lx} , all pitching moments presented in (28,e) turn strongly negative. This tendency not confirmed in other references would make an airplane very stable, and stalling impossible. Regarding the configuration in figure 39, it must also be said that it is not "balanced". The angle of attack for C_{Lx} is around zero. The flap is too "strong". A smaller flap, a lower angle of deflection, or increased blowing from the nose flap at the leading edge would give a more desirable attitude at modestly positive angles of attack.

Blowing From the Knee of nose flaps is reported in several references. In (27,a) C_{Lx} is increased from 1.5 to $C_{Lx} = 3.0$, for a plain trailing-edge flap deflection of 30° , using a round-nose-flap angle δ_o between -5 and -25° , for $C_{qo} = 0.007$. For the airplane configuration as in figure 40, the following lift coefficients were obtained:

$$\begin{aligned} C_{Lx} &= 0.83 && \text{for the plain airfoil section} \\ &= 1.47 && \text{with } 37^\circ \text{ trailing, and } -30^\circ \text{ nose flap} \\ &= 1.92 && \text{with } \delta_f = 37^\circ, C_{\mu f} = 0.016; \text{ and } -40^\circ \text{ nose flap} \\ &= 2.10 && \text{with } \delta_f = 37^\circ; C_{\mu f} = 0.016; \delta_o = -50^\circ; C_{\mu o} = 0.010 \end{aligned}$$

In comparison to the very high moment coefficients with C_{μ} above unity as in figure 39 producing C_L higher than 7, the coefficients used or obtained in this configuration are modest; the combined C_{μ} is 0.026, and the highest

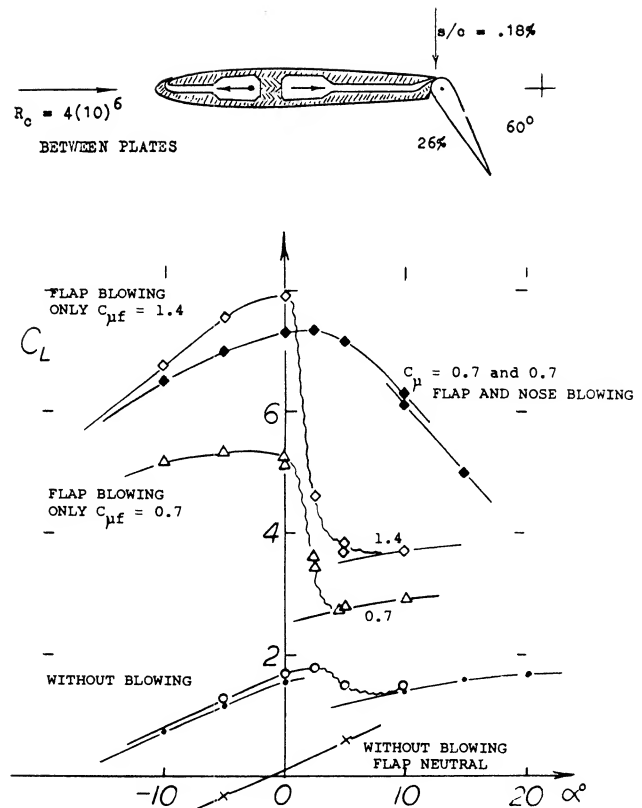


Figure 39. Lift characteristics of an airfoil (28,e) with trailing-edge flap and boundary-layer control by blowing.

C_{Lx} is 2.2. The larger lift increment comes from blowing over the trailing flaps. Deflection of, and blowing over the knees of the nose flaps makes these more effective, however, so that they can be deflected up to -50° . — Other advantages are:

- While $\delta_f = 47^\circ$ produces somewhat higher lift, the quality of stalling is better (more gentle) for $\delta_f = 37^\circ$.
- While $2/3$ span flaps provide about the same lift as full-span flaps, stalling is more gentle in the latter condition.
- No hysteresis was found in the $C_L(\alpha)$ function when using blowing flaps as indicated.
- For landing, "boundary-layer control results in a considerably reduced speed and reduced distance".
- When blowing over the ailerons (which are portions of the flaps) they were "very effective lateral control devices".

Tests on an actual North-American F-104 in a full scale tunnel using the same wing as in figure 40 with the same flaps, but with the ailerons neutral and a wider fuselage show only a $C_{Lx} = 1.57$.

Takeoff. In order to get some insight into performance, the characteristics of the airplane as in figure 40, are plotted in polar form. Takeoff (see analyses in (27,b,c)) is a more difficult operation than landing as engine power is limited. Not only high lift, but also drag and BL control power have to be considered. Besides the plain wing, the illustration shows two selected high-lift configurations, not necessarily optimum in performance, but with comparatively gentle stalling characteristics:

performance parameter	plain	without	with BLC	with "drag"
C_{Lx}	- 0.83	- 1.37	- 2.10	- 2.10
$(L/D)_x$	7.9 (0.3)	5.3 (0.8)	5.2 (1.1)	4.0 (1.3)
$(C_L^3/C_D^2)_x$	8 (0.8)	27 (1.1)	35 (1.5)	26 (1.7)
$(C_L^2/C_D)_x$	3.3 (0.7)	5.7 (1.2)	7.6 (1.9)	6.9 (2.0)
$\alpha_{.9x}$	- 12°	- 12°	- 14°	- 14°

C_{Lx} = maximum lift coefficient
 $(L/D)_x$ = maximum range ratio
 $(C_L^3/C_D^2)_x$ = maximum climb parameter
 $(C_L^2/C_D)_x$ = figure of merit (takeoff)
 $\alpha_{.9x}$ = angle of attack at $0.9 C_{Lx}$

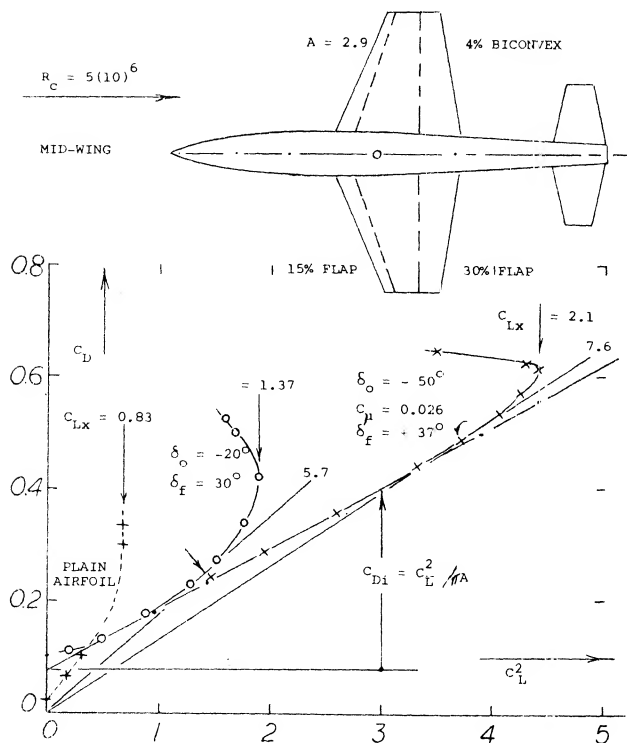


Figure 40. Drag-lift functions of a high-speed airplane configuration (27,b) with blowing from leading- and over trailing edge flaps. This configuration represents a model of the North American F-104, tests of which are reported in (NASA TN D-135).

The figure of merit discussed in Chapter V does not really indicate takeoff capability. It is easily obtained, however, in figure 40. The numbers in parentheses indicate the lift coefficients at which the maximum values of the respective parameters are found. — The tabulation shows first the BL-controlled configuration to be "better" when taking off and climbing. The drag equivalent to the power required to for blowing should be considered, however. Assuming an internal efficiency (in ducts and through the slots) of 50%, that drag may correspond to $\Delta C_D = 2 C_{\mu} = 0.05$, in the system considered. Performance parameters including the "drag" are listed in the last column above. They show the BL-controlled configuration to be inferior when climbing. However, takeoff is better than in the airplane with plain flaps no blowing and at any rate, the use of flaps (with or without BL control) increases takeoff and climb performance considerably over that of the plain wing that has a $t/c = 4\%$, is sharp-edged and a symmetrical section. The result of a more complex analysis in (27,b) shows that the distance to clear a 50-foot obstacle is reduced 25%, by the use boundary-layer control, under the following conditions:

- 1) most of ground run with flaps neutral, and without BL control;
- 2) conversion to high-lift configuration, shortly before lift-off;
- 3) using 8% of engine thrust for BL control (by air bleed).

A BL control system also has some structural weight. In the STOL aircraft as in (27,c) the weight fraction is stated to be between 1 and 2%. The pumping power required is said to be between 0.01 and 0.02 HP/lb, for a wing loading of 50 lb/ft².

Slot Design. In the practical construction of an airplane, it is simply not possible to provide spanwise slots for blowing (or suction) purposes, without any supporting interruption. In (27,b) testing was done to determine the consequences of partially blocking the slots at the leading and trailing-edge flaps. It is reported that "when one-quarter of the area of the slot(s) was blocked (by spacers 0.5% \bar{c} wide) and the value of C_{μ} was the same as that with the slot(s) fully open, no detrimental effect on the aerodynamic characteristics was noted".

(29) Description of the so-called Coanda effect:

- a) "Everybody" has seen a ball stably resting "on top" of a vertical jet of water. The principles of Bernoulli (1700 to 1782) or Venturi (1746 to 1822) are seen at work, in this spectacle, Coanda has tried to apply the fact that a jet of fluid clings to a curved surface, particularly in thrust augmentation nozzles.
- b) Metral, Coanda Effect, Pub Sci Tech Ministere de l'Air No. 218 (1948).
- c) Newman, Deflexion of Jet Sheets, Contribution in (28,I).
- d) Univ Toronto Inst Aerospace, Thrust Augmentation and Jet Sheet Deflection (1964); see DDC AD-610,525 and 611,759.

A *Horizontal Tail* (suitable for a “high-lift” transport aircraft) is investigated in (27,c). During landing of a conventional airplane, the stabilizer is producing positive lift, while the elevator is trying to reduce the lift of the tail, possibly to zero. When this is no longer feasible, the stabilizer or the whole horizontal tail has to be trimmed down to a negative angle against the fuselage. There are then two reasons why elevator and horizontal tail of a really high-lift airplane (STOL) may be inadequate in size and/or effectiveness:

- Deflection and/or extension of large and BL-controlled wing flaps necessarily produces large negative (nose-down) pitching moments.
- Corresponding to the high lift coefficients obtained (say, $C_{Lx} = 4$ or 5) the dynamic pressure at which the airplane is flying, is very low.

Of course, the wing flaps also produce increased downwash, thus helping the tail to provide the negative (tail-down) lift required to counterbalance the wing's pitching moment. Presence of, and interference by the fuselage is likely to reduce the average downwash, however. — In order to control a STOL-type airplane such as in (27,c) having a C_{Lx} above 6, and a C_{mH} in the order of 1.1, the tail surface as in figure 41, might be used. Including a nose flap with blowing around the “knee”, the maximum negative lift produced (in the presence of the fuselage) corresponds to $C_{LH} = -3$. Using a tail “volume” $V = (l/c)(S_H/S) = 3.8$ (0.28) = 1.06, the maximum pitching moment produced by the tail is indicated by

$$C_{mH} = \bar{V} C_{LH} = 1.06 (3) = 3.2 \quad (30)$$

Of course, to produce this value, the tail surface has to be trimmed to an angle of -14° , against the flow. Only 1/3 of the value is needed, however, in the airplane considered; and that much can be obtained by means of the BL-controlled elevator, at a lesser angle of tail setting, and possibly without any nose flap at all. However, deflecting the nose flap, and blowing around its “knee”, would prevent stalling of the tail surface.

Rotating Cylinder. In figure 38 of Chapter V, it is shown how rotation of a cylinder placed within, or replacing the trailing edge of an airfoil, is an effective means of getting the flow around that edge. A similar method of boundary-layer control (preventing separation) at the leading edge, is illustrated in figure 42. Considering the very low Reynolds number (below 10^5) the maximum lift obtained for $u/V = 3$, is impressive. All traces of laminar separation (including a hysteresis loop, in the lower part of the graph) have disappeared. At higher speeds of rotation, the cylinder can be considered to be a pump. It then accelerates the surface flow; and its effect may be similar to that of gentle blowing.

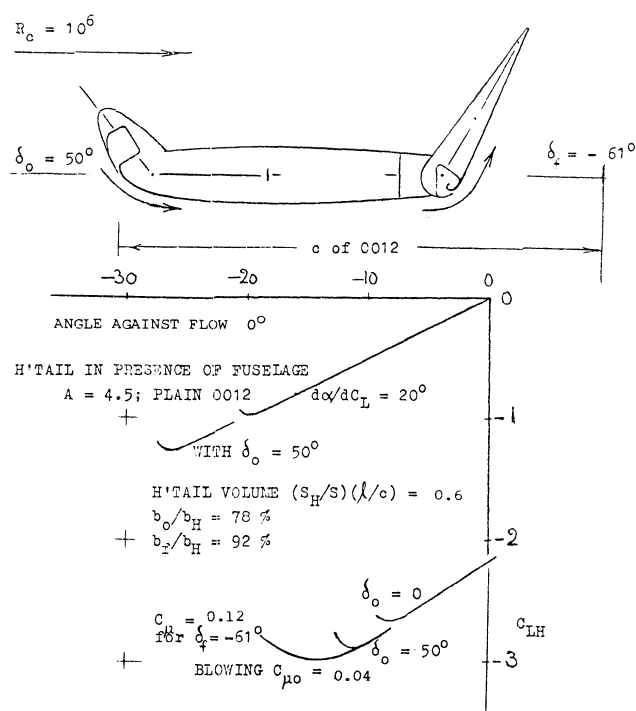


Figure 41. Negative lift produced in the horizontal tail of a STOL airplane configuration (27,c) evaluated from pitching-moment differentials.

High-Lift Combinations. A leading-edge slat was investigated (32) in combination with various other high-lift devices. As partly shown in figure 43, the following values were obtained:

$C_{Lx} = 1.30$ (gentle)	at $\alpha = 17^\circ$ for the plain airfoil
$= 2.05$ (sudden)	31° with leading-edge slat
$= 2.30$ (sudden)	16° with trailing-edge flap
$= 2.70$ (gentle)	24° with flap and slat
$= 2.00$ (sudden)	20° with upper-side blowing
$= 2.95$ (sudden)	34° with upper blowing and slat
$= 2.60$ (sudden)	21° with flap and upper blowing
$= 3.40$ (sudden)	31° with flap, upper blowing and slat

Similar lift values were found when replacing upper-side blowing by area suction. As far as the slat is concerned, its effect is largest when the trailing edge is either not “strained”, or protected (by blowing or suction). The quality of stalling indicated in parentheses above shows the slat does not help when it is operating at high load. A basic principle to be learned from these experiments is that leading edge devices are not only useful to increase maximum lift and are needed to prevent sudden leading-edge stalling, but also that they should also be balanced in size and design, against any trailing-edge devices, so that stalling starts from that edge, slowly proceeding forward.

Blowing Around Leading Edge. Suction from the leading edge (and possibly suction from any place on the upper side of an airfoil) is characterized by a more or less abrupt stall. As shown in several examples in this chapter, blowing (from suitable places on the upper side) produces, on the other hand, comparatively gentle stalling. However, the ultimate in harmless stall, and in maintaining lift beyond its maximum, may be expected by imitating the cylinder in figure 42, using the so-called Coanda effect (29); that is by blowing around the leading edge, from the lower to the upper side. In the experiments illustrated in figure 43, forward-facing slots were thus used located at 29 and 50%, respectively, of the chord. Dissipation of the jet sheet (primarily by mixing with the outside flow) was found to be so strong, however, that the maximum of its dynamic pressure is reduced to half, and its velocity to $1/4$, at a distance equal to some 10% of the chord. For the slots investigated, therefore, a real increment of maximum lift was not obtained. As demonstrated in the graph, the quality of stalling is definitely improved, however, from "abrupt" to "gentle". In other words, lift is appreciably increased (say doubled, under certain conditions) at angles of attack beyond that where the lift is maximum. In one configuration (involving upper-surface suction, but not shown in the illustration) a hysteresis loop with a width of 6° of the angle of attack, is eliminated by lower-surface blowing (although C_{Lx} is reduced). In the case of the plain airfoil, strong blowing (corresponding to $C_p = 15$) is required to obtain the beneficial effect of lower-surface blowing. At higher lift coefficients (with Zap flap deflected) the effect is only found in combination with a leading-edge slat (evidently guiding the discharged flow around that edge). It is expected, however, that this type of blowing would be more effective and efficient when using a slot further forward (say at or even ahead of 10% of the chord).

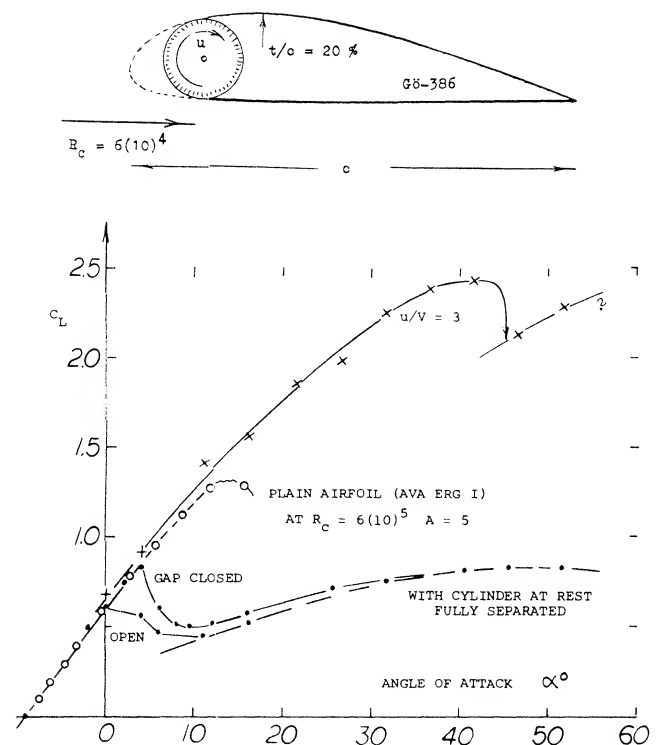


Figure 42. Boundary-layer control by means of a rotating cylinder replacing the leading edge of wing (31).

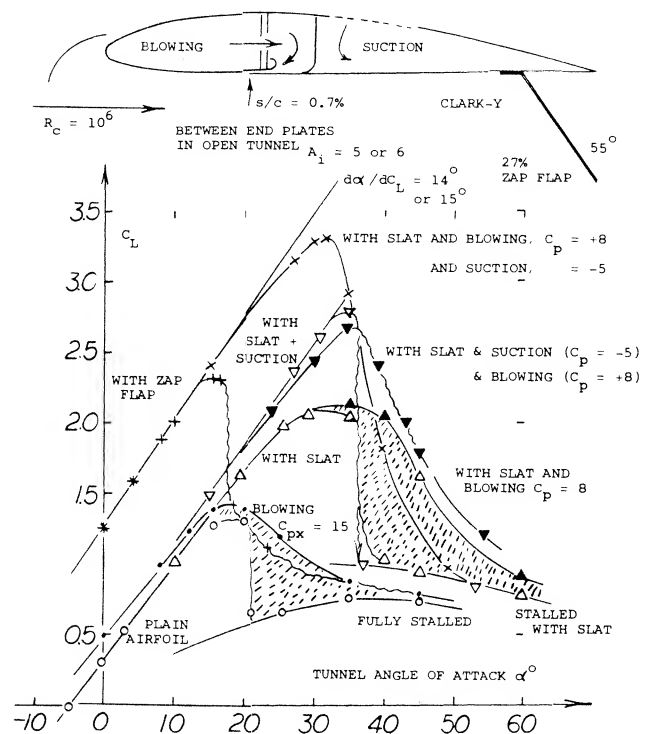


Figure 43. Lifting characteristics of an airfoil section (32) with high-lift devices, in combination with boundary-layer control by blowing (and suction).

(30) In figure 39, it should be noted that lift coefficients up to $C_{Lx} = 8$, are only obtained with extremely high momentum coefficients (up to $C_{\mu} = 1.4$). Such coefficients are typical of jet flaps as described in the "trailing edge" chapter. In effect, we have this type of flap in figures 38 and 39.

(31) Wolff, Rotating Cylinder in Leading Edge of Wing, Dutch Rpts RSL (Amsterdam); see translations NACA TM 307 & 354 (1926).

(32) Hoerner, Maximum Lift by Blowing, ZWB (DVL) FB-276/1&2 (1935).

CHAPTER VII — INFLUENCE OF COMPRESSIBILITY AT SUBSONIC SPEEDS

The compressibility of water is negligibly small for all speeds of vehicles (ships, boats, torpedos) even if they can go faster than 50 knots. Disregarding supersonic speeds, the compressibility of air (2) is so much greater that its influence upon aerodynamic characteristics must be taken into account at higher subsonic speeds.

1. PRINCIPLES OF COMPRESSIBLE FLUID FLOW

In a compressible fluid the propagation of pressure requires a finite amount of time to travel a given distance from the point of disturbance. This time is required as the disturbance travels at the local speed of sound relative to the body rather than instantaneously as assumed in incompressible flow. When the flight speed approaches the speed of sound the finite time element leads to changes in the flow pattern. This is illustrated in figure 1 showing the propagation of a disturbance moving at $M = 0$, $.5$ and 1.0 . It is interesting to note how the disturbances pile up in front of the body as the Mach number approaches 1.0 .

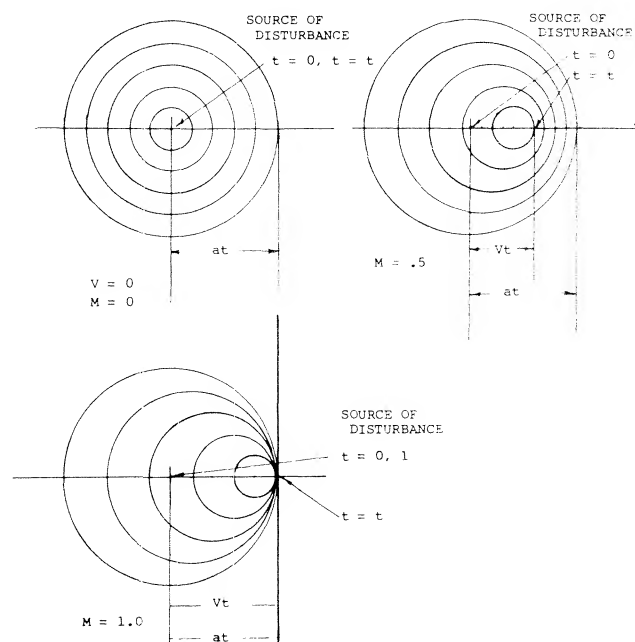
The Speed of Sound. The propagation of small disturbances of pressure, such as sound waves, occurs at the speed of sound which is given by

$$a^2 = 1/(\rho \, dp/d\rho) = (dp/d\rho) = \text{compressibility in (Nm}^2/\text{kg)} \quad (1)$$

Since in a perfect gas, $p \sim \rho^k$, where $k = 1.4$ in air, the speed of sound is

$$a = k p/\rho = k "R" T \approx 20 \, T(^{\circ}\text{K}) \quad (2)$$

where " R " = "gas constant" = energy ($\text{kg m}^2/\text{s}^2$) per kg and ($^{\circ}\text{K}$) = 29 in atmospheric air up to some 90 km of altitude. The speed thus increases with temperature. This means as well as others, that around a stagnation point, the speed (particularly in upstream direction) is increased, while in an area of reduced pressure (such as along the suction side of an airfoil) that speed is somewhat reduced.



- (1) Principles of compressible fluid flow:
 - a) Prandtl, "Essentials of Fluid-Dynamics", London 1952.
 - b) Liepmann and Roshko, "Elements of Gasdynamics", Wiley 1957.
 - c) Liepmann & Puckett, Aerodynamics of a Compressible Fluid, Wiley 1947.
- (2) Munk, Comments on Velocity of Sound, J.Aeror. Sci 1955 p 795.

Figure 1. Propagation of pressure disturbances in a compressible fluid in relationship to operating speed.

Impact Pressure. In considering the characteristics of compressible flow it is instructive to examine isentropic channel flow (1,c). If we consider a body at rest and the flow impinging on the body issuing from a reservoir, as illustrated in figure 2, it is possible to find relations in pressure, local speed of sound and density of use. At the ultimate limit of subsonic flow where the local Mach number is 1.0 the following ratios are obtained:

p_o/p	= 1.9	absolute pressure
T_o/T	= 1.20	absolute temperature
ρ_o/ρ	= 1.58	density ratio
a_o/a	= 1.10	speed of sound
q_o/q	= 1.28	impact pressure

The subscript o in the above indicates the conditions in the reservoir, which is also the condition on impact of a Pitot tube.

The local dynamic or impact pressure q is related to the local static pressure and Mach number by the equation

$$q = 1/2 \rho V^2 = \gamma p M^2/2 \quad (3)$$

The impact pressure can also be related to the difference between the reservoir pressure and the static pressure as a function of the Mach number

$$\begin{aligned} p_o - p/q &= 1 + (M^2/4) + (M^4/40) \\ &= 1.09 \text{ @ } M = .6 \\ &= 1.219 \text{ @ } M = .9 \end{aligned} \quad (4)$$

It should be noted that the dynamic pressure used in the coefficients such as C_L are still based upon the "dynamic" pressure q . This pressure

$$q = 0.5 \rho (M^2) a^2 = 0.5 \rho V^2 \quad (5)$$

(where all quantities are those in the ambient flow) is then a "potential" of the undisturbed flow, rather than a pressure differential which can directly be measured with the aid of a Pitot-static or Prandtl tube. In fact, there is some difficulty in wind-tunnel testing, in determining M -number, temperature and density.

As far as lift is concerned, the impact pressure as such is usually not considered, although it has consequences upon the pressure distribution of airfoil sections and wings (lifting or not lifting).

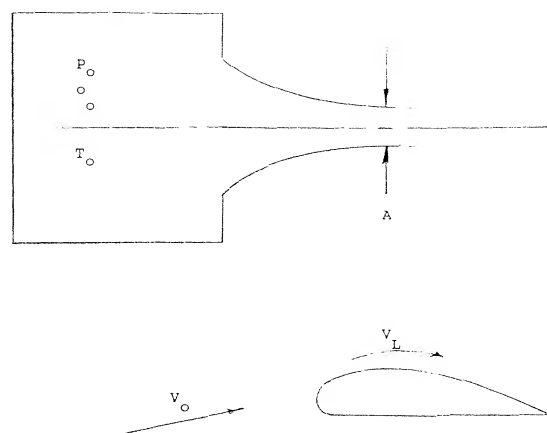


Figure 2. Compressible flow from a reservoir through a nozzle.

Prandtl-Glauert Rule (3). When approaching a wing, the air particles within a certain sheet of the stream slow down. They continue to be slowed down at the lower side of that wing, when it is lifting. As explained above, the pressure corresponding to reduced velocity is increased above that as expected according to Bernoulli's law of aerodynamic (or hydrodynamic) motion. What was said about the time required for pressure to propagate, also holds for negative pressure differentials as at the upper side of an airfoil (due to thickness as well as due to lift). To explain this phenomenon, it can also be said that the air particles do not have the proper time to be deflected around the convex upper surface of a lifting wing. As a consequence, the values of all pressure differentials and of the resulting normal or lift forces, increase as a function of the Mach number. As found by Prandtl (1,a), by Glauert (3,a) and probably by others, all differentials of the pressure and lift *coefficients* are approximately proportional to the Prandtl-Glauert factor.

$$1/\beta = 1/\sqrt{1 - M^2} \quad (6)$$

In reality, $1/\beta = \infty$ is never reached at $M = 1$, neither at the stagnation point (where $C_{p \max} = 1.28$) nor at the suction side of airfoils (where vacuum is the extreme limit, with $C_{p \min} = -1.43$, at $M = 1$).

Critical Velocity. We have considered static pressure above. For small variations along slender bodies or on airfoil sections at small lift coefficients the velocity differentials are approximately:

$$\Delta V/V = -0.5 C_p$$

However, at higher Mach numbers conditions are more complicated. In this text, maximum velocity around a body or wing is of particular interest as it may locally reach the speed of sound. This speed, in turn, is a function of the temperature at the point of maximum speed (or minimum pressure). The flow around the nose and past the suction side of a lifting airfoil is the same as that through a Laval nozzle (1,a,b). At the stagnation point we have the absolute "total" or reservoir pressure p_0 . From there, an expansion takes place. As in the smallest cross section of the nozzle, the speed of sound is reached at some point at the suction side, where p or C_p obtain their critical values, so that the local number $M_x = 1$. In air, conditions at that point (subscript x) are indicated by the following constant ratios:

p_x/p_0	= 0.528	absolute pressure
T_x/T_0	= 0.833	absolute temperature
a_x/a_0	= 0.913	local speed of sound
ρ_x/ρ_0	= 0.634	density ratio

where the subscript (•) refers to the reservoir condition (with $V = 0$) from where the flow originated (such as in the pressure tank of a wind tunnel, or in a stagnation point).

Critical Mach Number. The relations of the listed, to the "ambient" quantities in the undisturbed flow to which airfoil or body are exposed, may be found in texts such as (1,a,b). The critical Mach number is defined as that where C_p first reaches the critical negative value, that is where at a particular point of the surface the local speed of sound (corresponding to $M_x = V_x/a_x = 1$) is first attained. These values of critical pressure and ambient Mach number for M local equal to 1 may be found from the equations

$$\begin{aligned} p_x/q &= (0.75/M^2) (1 + 0.2 M^2)^{3.5} \\ C_{p_{\min}} &= (p_x/q) - (1.43/M^2) \end{aligned} \quad (7)$$

2. INFLUENCE OF COMPRESSIBILITY ON AIRFOIL SECTIONS

In two-dimensional flow patterns, there is basically less cross-sectional area available than around three-dimensional bodies, into which air particles and stream tubes can be deflected. As a consequence, airfoil sections are particularly sensitive to compressibility.

Prandtl-Glauert Factor. As explained in Chapter XV of "Fluid-Dynamic Drag", or in (1,a), the influence of compressibility upon the positive or negative static pressure differences along the sides of slender airfoil sections and upon the resulting load (lift) is essentially the same as that of an increase of the angle of attack. Therefore, in two-dimensional flow, pressure and lift coefficients increase (at least in good approximation) in proportion to the Prandtl-Glauert factor as in equation (2).

Pressure forces of lifting airfoil sections are plotted in figure 3. It is seen that lift coefficients, and the lift-curve slope grow in proportion to $1/\beta$. It can also be concluded from this graph, and equation 2, that at $M = 0.2$, the influence of compressibility is comparatively small; the factor is $1/\beta = 1.029$. For example, the number of an airplane taking off or landing at sea level at 100 knots, is $M = 0.15$. Compressibility can, therefore, be disregarded in many realistic conditions, as it is in most of the chapters of this text. However, at $M = 0.6$, lift and other coefficients are expected to be 25% increased. Such increments are not found, however, in airfoil sections with thickness ratios above some 14%. For example, the 0018 section as tested in (6,f) exhibits a derivative $(dC_L/d\alpha_0) = 0.083$, which remains constant up to $M = 0.6$. Increased and further increasing viscous losses in the flow over the upper side are evidently responsible for this result.

- (3) The Prandtl-Glauert rule is presented and improved:
- a) Glauert, presented in ARC RM 1135 (1927); see also (1,c).
 - b) von Karman, Compressibility in Aerodynamics, J.Aeron Sci 1941 p 337.
 - c) Kaplan, On Lifting Elliptical Cylinder, NACA Rpt 834 (1946).
 - d) Kaplan, Transonic Similarity Rules, NACA Rpt 894 (1948).
 - e) Mathews, Pressure Distribution on Bodies, NACA Rpt 1155 (1953).
 - f) Goethert, Modification for Bodies, Ybk D Lufo 1941 p 1-156; NACA TM 1105.

- (4) Characteristics of cambered airfoil sections:
- a) See 66-Series Airfoils in (5,a) and 10% Sections in (5,e).
 - b) Graham, 66-210 Airfoil Section, NACA TN 1396 (1947).
 - c) Stack, 4412 Airfoil Pressure and Forces, NACA Rpt 646 (1939).
 - d) Becker, 23012 Airfoil Section, NACA W'Rpt L-357 (1941).
 - f) Lindsey, 24 Airfoils 16-Series to $M = 0.8$, NACA TN 1546 (1948).
 - g) Summers, 64AX10 Series Airfoils, NACA TN 2096 (1950).
 - h) Van Dyke, 16 Six-Series Airfoil Sections, NACA TN 2670 (1952).

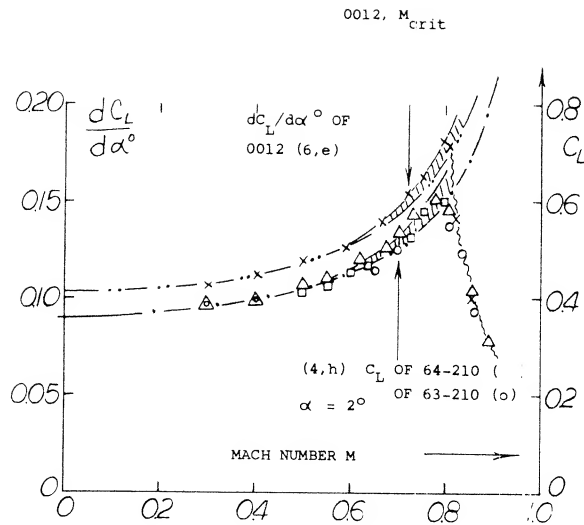


Figure 3. Examples for lift coefficient and lift-curve slope as a function of the Mach number, in two-dimensional flow.

Angle of Attack. When the lift-curve slope of an airfoil section is increased in proportion to $1/\beta$ then the "lift angle" should reduce in proportion to $\sqrt{1-M^2}$. In terms of the two-dimensional angle of attack, thus:

$$d\alpha_2/dC_L = 10^\circ \sqrt{1-M^2} \quad (8)$$

This function is essentially confirmed in figure 4. For example, at $M = 0.6$, the angle of attack required to produce a certain lift coefficient is 20% smaller than at $M \rightarrow 0$. In both graphs, the experimental points are seen diverging from the theoretical function, at about $M = 0.7$, or at $\sqrt{1-M^2} = 0.7$. The critical Mach number has been reached in this case (for example by the 0012 section, at $C_L = 0$) and the lift is higher, or the angle of attack lower, on account of a supersonic expansion along the upper side, when lifting.

The Minimum Pressure of a symmetrical airfoil section at zero lift in incompressible fluid (such as water, or in air at low speeds) is approximately

$$C_{pmin} = -2(t/2x) \quad (10)$$

where x = distance of the maximum thickness from the leading edge. Provided that the airfoil sections has proper camber, Chapter II, the negative pressure due to lift corresponds approximately to

$$C_{pmin} = -0.7 C_L \quad (11)$$

These empirical functions are taken from the "hydrodynamic" chapter of "Fluid-Dynamic Drag". In the case of foil sections with thickness location between 30 and

40% of the chord, minimum pressure due to lift at the upper, cambered side, might be assumed to coincide with that due to thickness. The two components may thus be added to each other. In incompressible fluid flow, the maximum velocity at a particular distance from the leading edge is then

$$V_x/V = \sqrt{1 - C_{pmin}} \quad (12)$$

For example, for $t/c = 10\%$, $x/c = 0.33$, $t/2x = 15\%$, and $C_L = 0.5$, a $C_{pmin} = -(0.31 + 0.40) = -0.71$ is obtained. More than half of this value is due to lift. The maximum speed on the upper side of this type of correctly cambered airfoil, in incompressible flow, is $V_x/V = \sqrt{1 + 0.71} = 1.3$. As explained before, the minimum pressure coefficient grows more negative, as the Mach number is increased, eventually reaching the critical condition. The drag- and lift divergence Mach numbers of a family of 4 airfoil sections are plotted in figure 5. Using equations (7) and (10) plus (11) a theoretical line is obtained. The experimental divergence points are up to 10% above this line, as the critical Mach number must be exceeded by a certain amount before a change can be recognized.

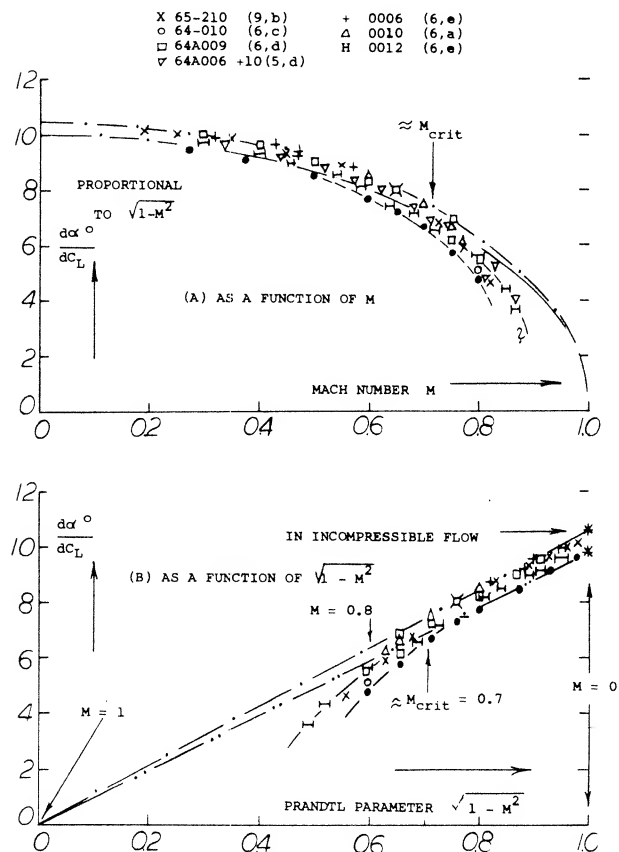


Figure 4. The "lift angle" of various airfoil sections, correlated with the Prandtl-Glauert Rule:

- (A) Lift angle as a function of the Prandtl parameter.
(B) Lift angle as a function of Mach number.

in symmetrical airfoil sections exposed to incompressible fluid flow. As explained in Chapter II, the nose radius is

$$r/c = (r/t)(t/c) = (rc/t^2)(t/c)^2 \quad (15)$$

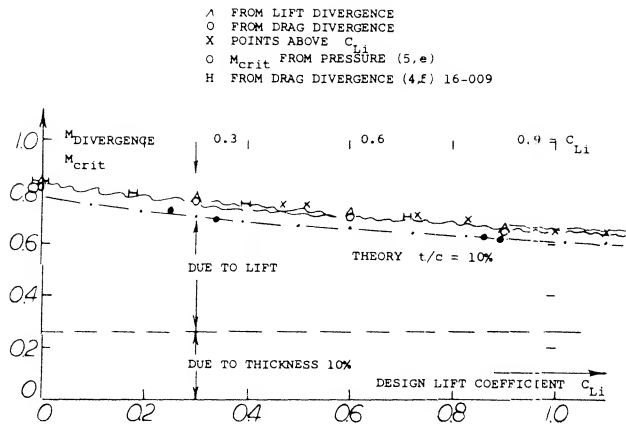


Figure 5. Experimental drag and lift divergence Mach numbers of a family of cambered 64AX10 airfoil sections (6,g) as a function of their design lift coefficients.

Leading Edge. The correct camber for $C_L = 0.5$ would theoretically (see the “airfoil section” chapter) be around 4% of the chord. Such a section would not be considered to be practical for high speed wings. Camber in the order of 2% was often used in airplanes, say around 1940. Even such modest camber is not very desirable in high-speed airplanes because of pitching and wing-twisting moments. Symmetrical sections may thus be preferred. When lifting, very high peaks of velocity and minimum pressure are developing around the nose of such sections. Regardless of section thickness (within conventional limits) these pressure peaks are theoretically a function of the nose radius r . As pointed out in (11) the peak is expected to correspond to

$$C_{pmin} \sim -C_L^2/(r/c) \quad (14)$$

where $(rc/t^2) = \text{constant}$ in a family of similar sections. For example, $(rc/t^2) = 1.1$ in the 4-digit series of airfoil sections, and ≈ 0.07 in NACA’s 64-series. Pressure distributions are reported, for example around the 64A010 section in (5,d). At lift coefficients somewhat above 0.2, this section develops a pressure minimum above the leading edge. At higher lift coefficients, this minimum grows into a very sharp peak. For example, at $C_L = 0.6$, the coefficient is $C_{pmin} \approx -2$. Various experimental results are plotted in figure 6, as a function of C_L . This part of the theoretical prediction as in equation (14) is thus confirmed. Because of viscous losses in the flow around less rounded edges, very high pressure coefficients (proportional to $1/r$, as in equation 14) do not come true, however. Rather, the minimum pressure coefficient is statistically found to be a function of $C_L^2/(t/c)$, as noted in (20).

Divergence. Below $C_L = 0.2$, the 64A010 section mentioned above, develops two pressure minima, one due to thickness and lift (near the location of maximum thickness) and one due to lift at or above the nose. The same two minima and the subsequent divergent Mach numbers (where drag and lift diverge from their steady variation, the drag rapidly increasing and the lift decreasing) are found in figure 7. The close-to-horizontal lines correspond to those in figure 5, while the two lateral branches represent the flow around the leading edges as in figure 6. The C_L level of the “bucket” corresponds to camber or design lift coefficient. The C_L size in terms of upper and lower limit is larger in thicker sections, and smaller in thinner ones.

- (5) Pressure distribution and lift of airfoils as a function of M-number:
- von Doenhoff, Cambered at Low Speed, NACA TN 1276 (1947).
 - Wall, Chordwise Distribution, NACA TN 1696 (1948).
 - Cooper, Testing the Same Wing as in (a), NACA TN 3162 (1954).
 - McCullough, 10% Sections Cambered at Low Speed, NACA TN 2177 (1950).
 - Graham, Five Airfoil Sections, NACA Rpt 832 (1945).
 - Goethert, 00XX Series, ZWB FB-1505 (1941); see Canadian Nat Res Laboratories Trans TT-25, 26, 27, 28, 29 (1947).
 - Nitzberg, Evaluation of (f) and (g), NACA TN 2825 (1952).
 - Tapered Wing, Original DVL Graphs Jf-712 (1944).

- (6) Airfoil Sections as a function of Mach number:
- Nitzberg, With 6 to 15% Thickness Ratio, NACA RM A1949G20.
 - Berggren, Leading-Edge Radius and Thickness, NACA TN 3172 (1954).
 - Wilson, 6 to 12% Sections 64-Series, NACA RM L1953C20.
 - Daley, Various Sections in Open Tunnel, NACA TN 3607 (1956).
 - Goethert, Airfoils in the DVL Tunnel, ZWB Rpt FB-1490 (1941); see Canadian Nat Res Laboratories Translation TT-31 (1947).
 - Goethert, In DVL Tunnel, Lilienthal Rpt 156 (1942); NACA TM 1240.
 - Goethert, Airfoils and Wings, Wright Field Lecture Notes 1948.
 - Loftin, 10% Thick Airfoil Sections, NACA TN 3244 (1954).

Pitching Moment. As explained in Chapter II, the longitudinal moment consists of two components, one due to camber and one due to lift. Both of them could be expected to grow according to the Prandtl-Glauert rule, that is in proportion to the pressure differentials and the lift arising in an airfoil section. As shown in (4.h) such variation of the moment due to camber (corresponding to $C_{L\alpha} = 0.2$) may actually take place. Other sources (4,d,f,g)(12,a) show essentially constant C_{m0} values, particularly for the 230 series (8), while airfoils tested between wind-tunnel walls (4,g)(6,b) exhibit rather irregular variations at higher lift coefficients and higher Mach numbers. If in doubt, the C_{m0} values grow somewhat in negative direction (nose-down) as the M 'number is increased. The growth is restricted, however, by increasing viscous losses.

Pitching Due to Lift. It is known (see figure 30, Chapter II) that contrary to theory, the longitudinal moment due to lift grows progressively more positive (or less negative) as the thickness ratio is increased. Because of viscosity (boundary layer) thicker sections lose lift on their upper side, and this loss is made up by increased suction around the leading edge. As seen in figure 8 the "one-sided thickening of the boundary layer" evidently increases, together with the Mach number. The static stability derivative (dC_m/dC_L) increases in positive direction (particularly in thicker sections), which means a reduction of static longitudinal stability (pitching up). As a consequence of section losses around the leading edge, really thin sections such as 0004 in (4,b) exhibit C_m values, hardly affected by the Mach number. Since C_L increases at the same time, their derivatives (dC_m/dC_L) reduces as the M 'number is increased.

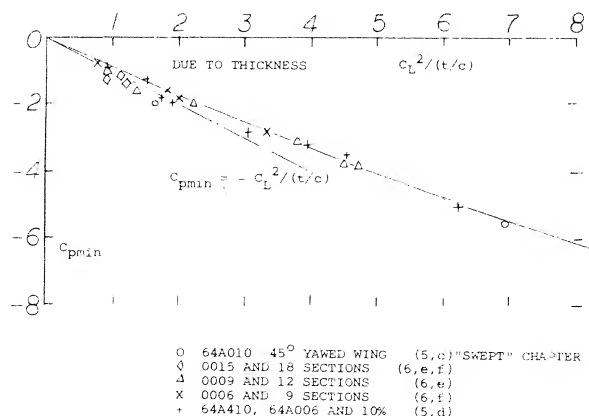


Figure 6. Evaluation of minimum pressure coefficients around the leading edge, primarily of symmetrical airfoil sections.

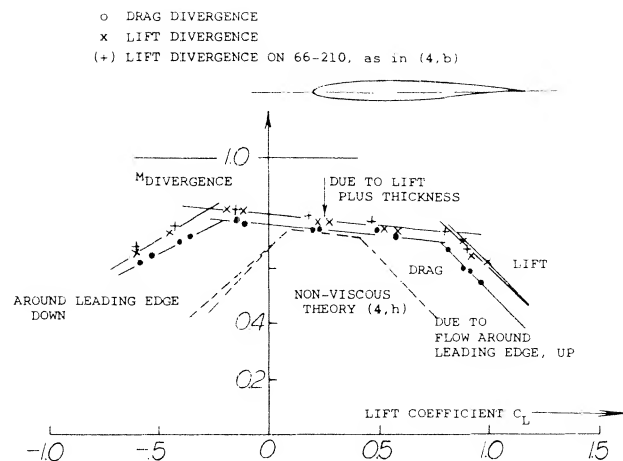


Figure 7. The critical and divergent Mach number of the 63-210 and 64-210 airfoil sections (6,h).

Sharp Leading Edges are used in airfoil sections intended to be flown at supersonic speeds. One and the same series of 6% thick symmetrical sections are investigated in (7,a) and (7,b). Around $\alpha = 0$, and $C_L = 0$, the lift-curve slope is highest in the 0006-63 section. However, as listed in figure 9, at $\alpha = 4^\circ$, the normal force coefficient is practically the same for all 4 sections shown. Also, the Mach number at which the maximum lift coefficient (near stalling) is obtained is essentially the same ($M = 0.8$) for all sections. Although $C_{L\alpha}$ is lower than for rounded edges, the flow manages to get around the sharp edges. In fact, at $M = 0.4$, the pressure distribution is basically the same in all 4 sections. At higher Mach numbers (say above 0.6) an area of supersonic flow develops, starting near the leading edge and eventually collapsing by way of a shock (sudden compression) at a location between 40 and 60% of the chord. The minimum pressure coefficients are in the order of $C_{pmin} = -1.7$ at M around 0.7, independent of the nose radius. The largest differences are found in the drag coefficient, which grows (at $\alpha = 4^\circ$) from 0.010 to 0.035, as the nose radius is made smaller and smaller (reduced from round to sharp). In conclusion, in the subsonic speeds range sharp-edged sections are not very efficient. They do develop lift, however; up to and above $M = 0.8$. The angle of attack for stalling separation from the upper side when approaching $C_{L\alpha}$ reduces from 9 or 10° at $M = 0.4$, to 7 or 8° at $M = 0.8$.

3. STRAIGHT WINGS AS USED IN HIGH-SPEED AIRPLANES

The influence of compressibility on the characteristics of wings, and considerations when using them in airplanes, are different to a degree from what is presented on airfoil sections.

Lift Angle. Applying the Prandtl-Glauert rule to the sectional component of the angle of attack (as in figure 4) the "lift angle" of wings with higher aspect ratios (say above 4) as presented in the "wing" chapter can be formulated as follows:

$$d\alpha/dC_L = 10\sqrt{1-M^2} + (K/A) \quad (16)$$

where $K = 20$ or somewhat larger, and $\sqrt{1-M^2} = 1/\text{"P"}$. Experimental results of wings with higher aspect ratios are plotted in figure 10, as a function of this parameter. A straight-line function is thus obtained for equation (16). For $A = 6$, agreement is found above $\sqrt{1-M^2} = 0.8$, that is at M numbers below 0.6. The experimental points for the wing with $A = 4$, can be matched by the equation when using the constant $K = 24$.

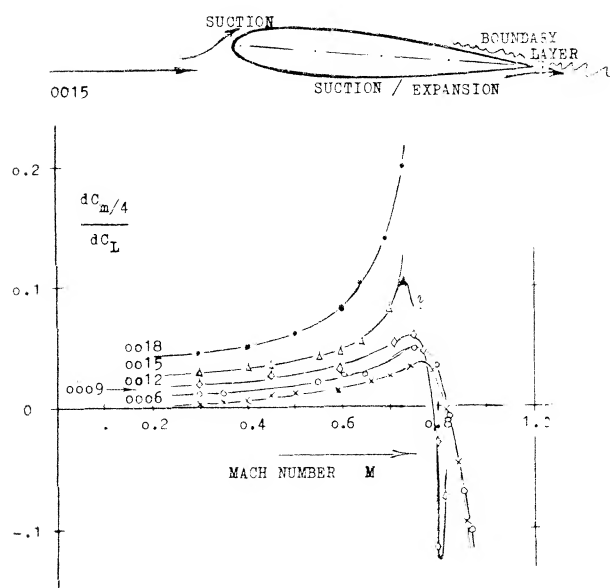


Figure 8. The influence of the nose radius (sharp leading edge) upon the characteristics of 6% thick airfoil sections (7,a,b).

Smaller Aspect Ratios. In order to include aspect ratios, say below $A = 4$, the formulation as in (10,a) is preferable. To take compressibility into account, the parameters to be plotted are

$$(10^\circ (dC_L/d\alpha)/\sqrt{1-M^2})$$

and

$$(\text{"F"} = A\sqrt{1-M^2}/0.9) \quad (17)$$

where $10^\circ = (2\pi/\alpha)(\pi/180)$. The function of the Prandtl factor "P" = $1/\sqrt{1-M^2}$ can be understood to be that of increasing the effectiveness $a = C_{L\alpha}/2\pi$. This ratio is increased from about 0.9 to (a "P"). In a formulation similar to that in (10,a):

$$(dC_L/d\alpha)/(0.1\sqrt{1-M^2}) = \text{"F"}/(2 + \sqrt{\text{"F"} + 4}) \quad (18)$$

where "F" as in equation (17) contains the Mach number. Available experimental results are plotted in figure 11 with the results at M numbers above the critical excluded. Since the value of the modified aspect ratio "F" is a function both of the geometric ratio and the Mach number, confirmation of the influence of compressibility is not directly evident. Examination of individual points seems to show that lift-curve slopes at higher Mach numbers tend to be slightly higher than expected. On the other hand, airfoil sections (5,h) such as 0015 and 0018, also lose lift as a consequence of an area of high-speed flow (suction as indicated in figure 8) developing not only on the upper, but also on the well-rounded lower side. Negative pressures of this kind are shown in (5,f & g), while at the same time boundary-layer losses are growing along the upper side (incipient separation from the trailing edge). Wings with such sections are not included in figure 11.

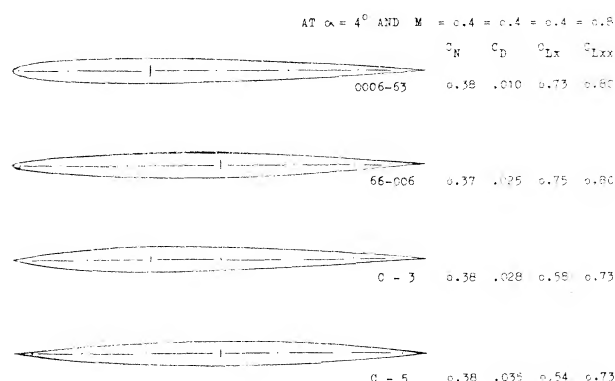


Figure 9. The variation of the stability derivatives (dC_n/dC_L) as a function of Mach number and thickness ratio (6,f).

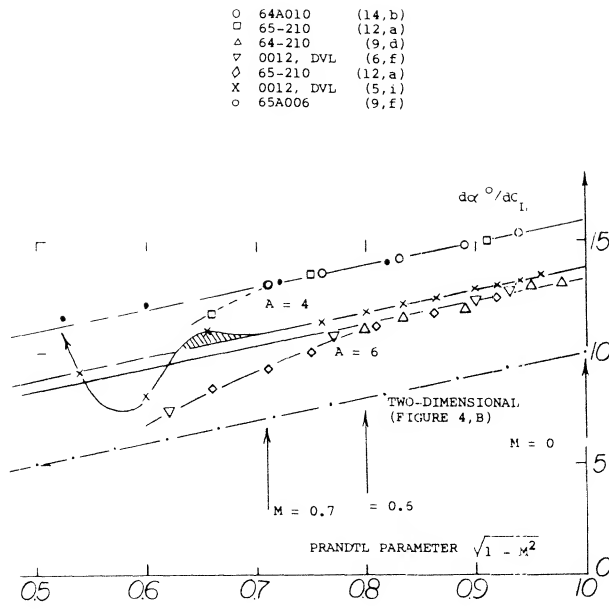


Figure 10. The lift angle of wings with aspect ratios $A = 4$, and $= 6$, as a function of the Prandtl parameter as in figure 4(A).

Lifting Bodies, such as cone-cylinder combinations or fuselages can be considered to be low-aspect ratio wings. Even though their lateral boundaries are well rounded, we can assume that at aspect ratios well below unity, their linear lift component corresponds to

$$(dC_L/d\alpha) \sim A \quad (19)$$

as in figure 11, without any influence of compressibility. However, it is not known yet how the second, non-linear component as presented in the "body" chapter may vary as a function of the Mach number. Since a slender wing is closer to a three-dimensional body than to a lifting line, it is suggested to use the modified Prandtl factor as derived from (3,f) in chapter XV of "Fluid-Dynamic Drag" in the simplified form of

$$P_3 = 1/\sqrt[4]{1-M^2} \quad (20)$$

The lift coefficient of a slender cone, at constant $\alpha = 12^\circ$, is plotted in figure 12 as a function of $\sqrt[4]{1-M^2}$. Here, as in the evaluation of other bodies (13) with aspect ratios between 0.3 and 0.6, it is found that the modified factor gives good results matching the experimental differentials of the lift coefficient. Of course, somewhere around $M = 0.9$, the factor (approaching infinity at $M = 1$) should no longer be expected to be applicable.

Tail Surfaces. Tail surfaces, horizontal or vertical, are basically "wings". Elevators and rudders are trailing-edge flaps. The lift-curve slope of tail surfaces is influenced by the fuselage (to which these surfaces are attached) and is accounted for as explained in the "control surface" chapter. It can be expected $(d\alpha/d\delta)$ their effectiveness may remain unaffected by compressibility. This means that the lift due to flap deflection increases with the Mach number at the same rate as $(dC_L/d\alpha)$. The lift angles of a particular surface are plotted in figure 13. The line through the $(d\delta/dC_L)$ data happens to have ordinates 1.5 times those through the $(d\alpha/dC_L)$ points. Therefore, $d\alpha/d\delta = 2/3$, a ratio which for a 30% flap is at the upper limit of what is shown on figure 2 of the "control" chapter.

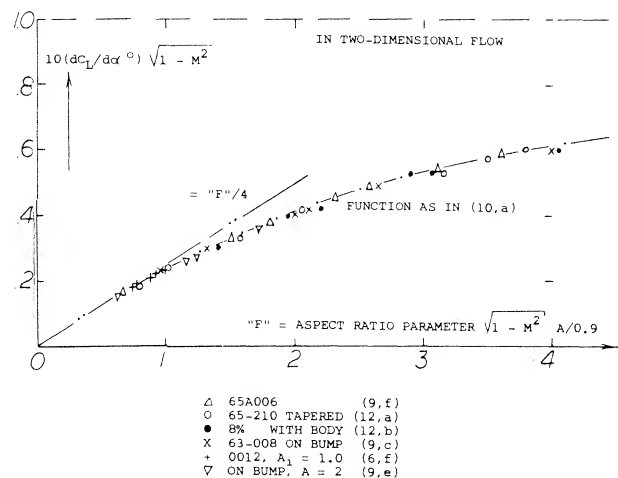


Figure 11. The lift-curve slope of wings as a function of their aspect-ratio parameter "F", as formulated in (10,a).

- (7) Characteristics of sharp-edged airfoil sections:
- Lindsey, 7 Different 6% Airfoils, NACA TN 1211 (1947).
 - Daley, 8 Different Airfoils as in (a), NACA TN 3424 (1955).
 - Henshall, Flow Pattern of Biconvex Section, ARC RM 3092 & 3093 (1957).
 - Circular-Arc Airfoils, NACA TN 2801 and NASA TN D-15.
 - NACA, Double-Wedge Airfoils, RM A1946G24 & L1949A12; also TN 3306.

- (8) Riegels, "Aerodynamische Profile", Oldenbourg Germany 1958. Experimental results as in (6,e,f) are listed in this book.

Control Flap. The pitching moment produced by a flap (keeping $C_L = \text{zero}$) is shown in figure 14. It varies in proportion to the Prandtl-Glauert factor (equation 6). The value extrapolated to "P" = 1, which means $M = 0$, agrees with those plotted in figure 4 of the "control" chapter. The hinge moment of the flap is also tested in (14,b). At deflections below $\delta = 7^\circ$, this moment is found to be independent of the Mach number. At δ above 8° , it seems to increase in proportion to "P". All moments considered continue to grow (or they remain constant, as the case may be) for some interval beyond the critical Mach number. Pressure distributions as in (14,b) show the peaks as suggested in figure 14. Depending upon lift coefficient and flap deflection, the critical Mach number can thus be encountered either at the leading edge, or in the vicinity of the maximum thickness, or around the hinge line of the flap.

Wing Flaps "always" cover only part of the span. Their characteristics can be considered in terms of two-dimensional flow, that is in reference to the airfoil section from which they are deflected. It is suggested to use the principle as demonstrated in figure 13, together with the part-span function as in figure 21 of Chapter V, to determine the lift-increasing effect of wing flaps. This procedure amounts to increasing lift and lift-curve slope in proportion to the Prandtl-Glauert factor. The spanwise lift or load distribution is particularly treated in (10,b).

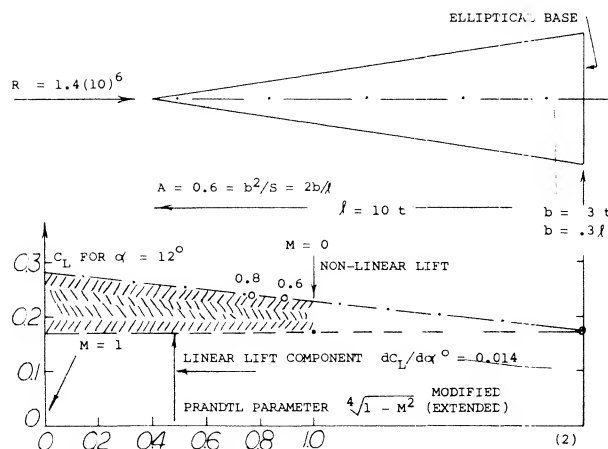


Figure 12. Lift analysis of an elliptical cone (13,b) tested at two Mach numbers, at constant $\alpha = 12^\circ$, as a function of the Prandtl parameter.

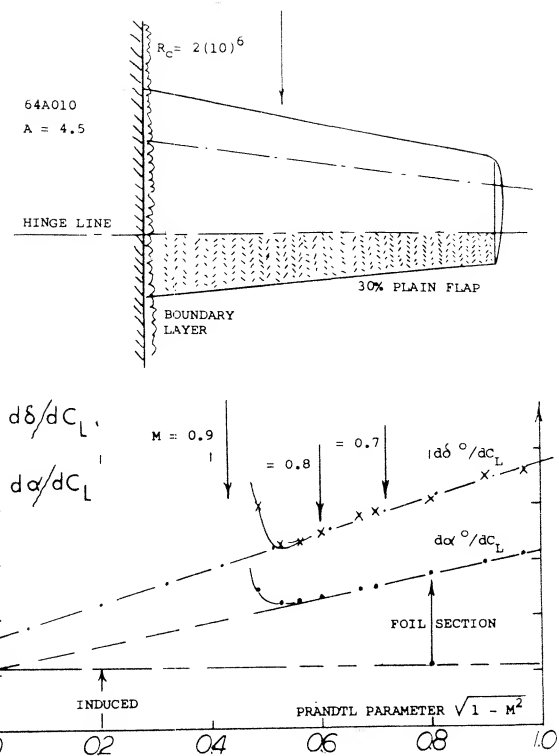


Figure 13. Effectiveness of a trailing-edge flap as a function of the Prandtl factor; tested (14,a) between tunnel walls.

Critical Lift. Airplanes flying at high speeds normally operate with reduced lift. Consider an airplane cruising at $M = 0.8$, at 9 km or 30,000 ft. At this altitude, the speed of sound is reduced to 0.9 of that at sea level. At the same time the atmospheric density is reduced to less than 40%, so that the lift coefficient required to support the craft may be between 0.3 and 0.4. Under these conditions, with a Prandtl factor "P" = $1/0.6 = 1.7$ or higher, the minimum pressure at the suction side may be between that as indicated by equations (10) and (11), say $C_{pmin} = -0.25 - 0.25 = -0.5$; and that as in figure 6, say $C_{pmin} = -1.0$. The critical Mach number is 0.7, accordingly, for a properly cambered section; or $M_{crit} = 0.6$ for a symmetrical section. In conclusion, the permissible M 'number can be below the 0.8 as assumed above. Of course, with 30° of sweep, the 0.8 is reduced to an effective value of $0.8 \cos 30^\circ = 0.7$; see the Chapter XV on swept wings.

- (9) Characteristics of wings as a function of Mach Number:
- Nelson, 36 Different Wings on Bump, NACA TN 3529 (1955).
 - Hamilton, 6 Wings 65-Series Airfoils, NACA Rpt 877 (1947).
 - Nelson, 22 Rectangular Wings on Bump, NACA TN 3501 (1955).
 - West, 64-210 Tapered Wing, NACA TN 1877 (1949).
 - Nelson, 38 Cambered Wings on Bump, NACA TN 3502 (1955).
 - Polhamus, 65A Series with $A = 2$ and $A = 4$, NACA TN 3469 (1955).

4. LIFT ABOVE THE CRITICAL MACH NUMBER

Deliberately, or in emergency situations, airplanes designed for subcritical conditions may be flown at, and get into, speeds appreciably higher than the "critical". Characteristics of straight wings up to $M = 1$ are therefore presented as follows.

Flow Around the Leading Edge. As pointed out, particularly in the first section of this chapter, upon exceeding the "critical" Mach number, forces and moments usually do not break down at once. In fact, in lifting symmetrical sections a strongly negative pressure gradient developing around the leading edge favors the boundary layer flow, leading it around the edge. To understand the flow pattern and the development of forces and moments, a selected number of chordwise pressure distributions is presented in figure 15. In what is called phase (1), the pressure distribution is essentially as in incompressible fluid flow, with a pressure peak and a continuous increase of the upperside pressure toward a slightly positive value at the trailing edge.

Supersonic Expansion. In figure 15, horizontal lines indicate the critical pressure level, as calculated using equation 7. It is evident that in phase (2) speeds are present appreciably above the local velocity of sound. An expansion takes place around the leading edge, similar to the Prandtl-Meyer type as in supersonic flow (1,a) extending to almost 50% of the chord. The average pressure coefficient is $C_p = -1.3$, in the example shown. It is this negative pressure obtained by expansion, rather than the Prandtl-Glauert mechanism, which produces the peak of the lift coefficient in figure 16. Recompression from $C_p = -1.3$, first to -0.3 , takes place through a mild shock. It must be noted that a further subsonic recompression develops in much the same manner as at lower Mach numbers, ending in a positive $C_p = 0.3$, at the trailing edge. As shown in Chapter XV of "Fluid-Dynamic Drag", divergence of the drag coefficient may be delayed over an interval of $\Delta M = +0.1$ or 0.2 . While such delays may at first be harmless, less desirable changes take place in the phases described next.

Shock Stall. Considering again the expanding flow in a Laval nozzle, that flow breaks down when the geometric expansion is too long or too steep. In the case of an airfoil at some angle of attack, this means that the boundary layer separates from the trailing edge and recompression takes place across a stronger shock (phase 3). When all of this happens suddenly, the drop in the lift coefficient is equally sudden. Such a drop is seen in figure 16(A) at $M = 0.8$. As reported in (6,g) shock and separation may also fluctuate back and forth; in other words, the flow pattern is not stable. In region (3), there is a discontinuity recognized in the variation of the longitudinal moment (to be discussed later).

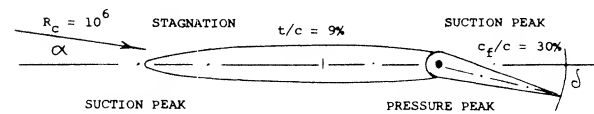
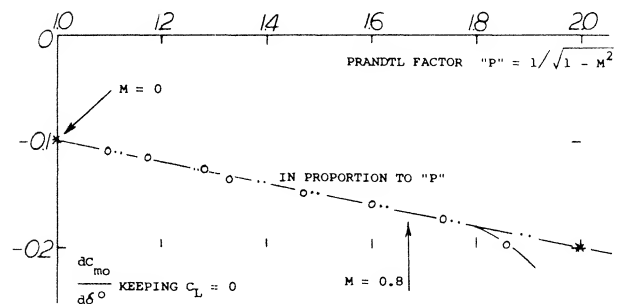


Figure 14. Pitching moment due to deflection of a control flap, tested (14,b) on the half-span model of a wing having an aspect ratio of 4.5.

- (10) Diederich (NACA), analysis of lift as a function of A'ratio and M'number:
- a) Correlation on the Basis of "F", TN 2335 (1951).
 - b) Spanwise Lift Distribution (Flaps), TN 2751 (1952).

- (11) Minimum pressure peaks on airfoil-section noses (theory):
- a) Kochanowsky, Pressure Distributions, Yearbk D Lufo 1940 p I-72.
 - b) Weber, Suction Peak on Sheared Wings, RAE TN Aero-2587 (1958).
- (12) Small aspect ratio wings as a function of M'number:
- a) Nelson, 65-210 Wings With A = 1 to 6, NACA RM A1949K18.
 - b) Allen, In Combination With Bodies, NACA RM A1953C19.
 - c) See references (9,a,e) with A'ratios of 0.5 to 6.
 - d) Smith, Delta Wing With Body, NACA RM 1950K20 & K21.
 - e) Squire, Ogee Wing With Body, RAE ARC C'Paper 585 (1959).

Minimum Lift. While on the upper side circulation is lost as a consequence of separation, a flow pattern similar to that on the upper side as in phase (2) develops along the lower side. An expansion takes place from the stagnation "point" toward the trailing edge. Negative pressure and negative lift grow considerably, thus reducing the resultant lift coefficient. The coefficient drops to less than half its peak value in this phase (4). In thicker sections (with well rounded lower side, not included in figure 16) the negative lift component can be such that the resultant lift is zero, at the constant angle of attack shown.

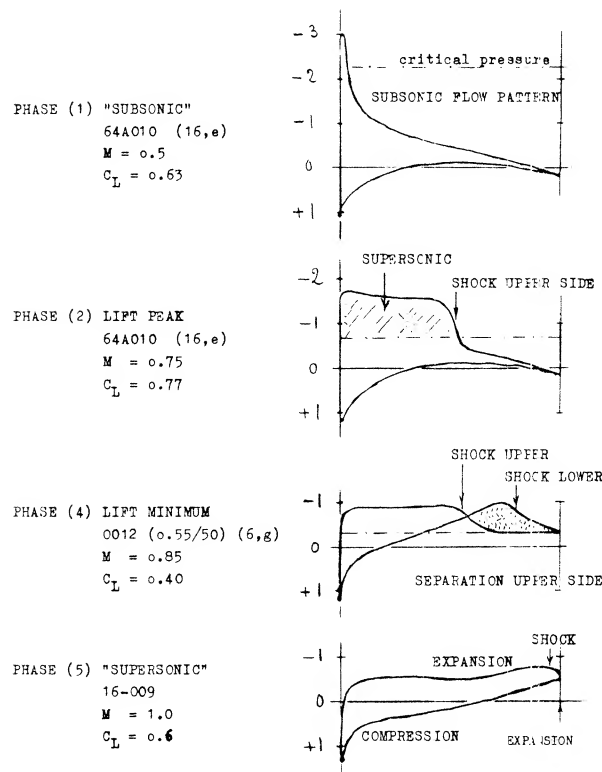


Figure 15. Typical examples of chordwise pressure distributions on airfoil sections, from subsonic through transonic Mach numbers, at $\alpha = 6^\circ$.

"Supersonic" Pattern (phase 5). As the Mach number is further increased, the shock at the upper side moves rapidly toward the trailing edge. The lift-reducing "loop" as in phase (4) of figure 15 disappears; and the lift recovers to some extent. At and above $M = 1$, a supersonic type of pressure distribution is obtained. As shown in figure 16, the lift coefficient approaches from there on, the function as indicated by supersonic theory. Expansion (on the upper side) and compression (on the lower side) also mean a considerable increase of the drag.

Center of Lift. The pitching moment can be presented in the form of the location $x =$ distance from the leading edge of the center of lift (or normal force):

$$x/c = 0.25 - (C_{m/4} / C_L) \quad (21)$$

Within the completely subsonic phase, nothing happens to the moment, excepting the increase of C_{m0} due to camber as stated in the second section of this chapter. Within the still "subsonic" phase (1) part (B) of figure 16 indicates a modest pitchup tendency. At a Mach number somewhat below that where the lift coefficient reaches its peak, the center of lift has moved forward from $x/c = 26\%$ to some 23%.

Pitching Down. In phase (2) as in figure 15, the center of lift is evidently farther back than in (1). Figure 16(B) shows that this movement continues into phase (3) where the center is at $x/c = 40\%$. The corresponding nose-down pitching moment could lead an airplane into a dive from where recovery is no longer possible.

Pitchup. The negative lift developing at the lower side, as in phase (4) of figure 15, evidently causes the far-forward locations, as indicated in figure 16(B), around $M = 0.95$. In an airplane with a straight wing, this change may mean not only pitching up, but also a dangerous loss of longitudinal stability (stalling). It is particularly in thicker sections (such as 0015, which is not shown in the graph) that negative pressures near the trailing edge of the lower side cause and/or aggravate the pitchup.

(13) Lifting characteristics of slender bodies:

- a) Taylor, Parabolic Blunt-Base Bodies, NASA TN D-14 (1959).
- b) Stivers, Various Elliptical Cones, NASA TN D-1149 (1961).

(14) Characteristics of flaps and control surfaces:

- a) Knappe, Heinkel Tunnel Tests, Yearbk D Lufo 1941 p I-96.
- b) Tinling, Horizontal Tail Surface, NACA RM A1949H11a.

(16) Airfoil characteristics at transonic Mach numbers:

- a) Ladson, Several 64-Series Airfoils, NACA RM L1957F05.
- b) Spreiter, Transonic Similarity Laws, NACA TN 2273 (1951).
- c) Ladson, 16-Series Pressure Distributions, NASA Memo 6-1-1959L.
- d) Crane, Wings With Aspect Ratio of 8, NACA RM L1951D24a.
- e) Stivers, Pressure & Forces 64A Series, NACA TN 3162 (1954).

Approaching $M = 1$, the flow pattern assumes a character similar to that at supersonic speeds. That is, expansion and attached flow are restored at the upper side, in this phase (5). As seen in figure 16(B), the center of pressure moves to the rear, ending up in a stable position slightly aft of $x/c = 40\%$.

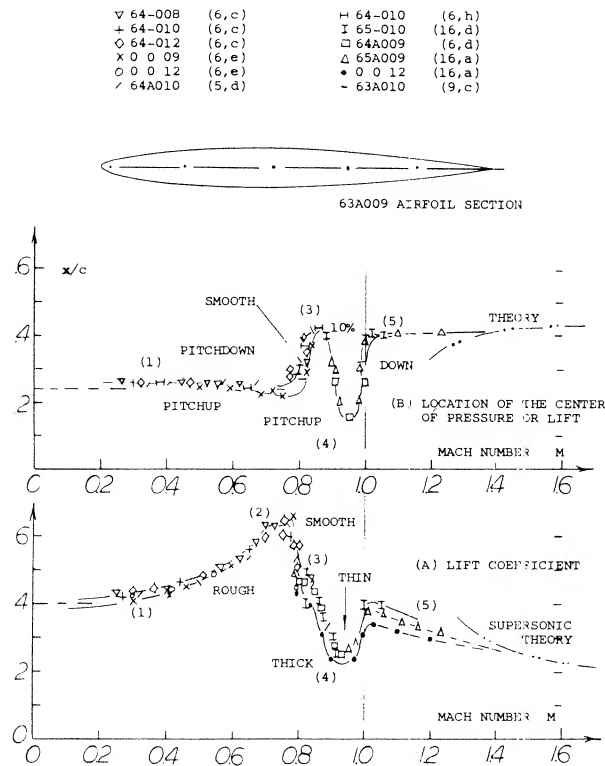


Figure 16. Lift and center of pressure of various symmetrical foil sections from subsonic through transonic M numbers, at constant angle of attack $\alpha = 4^\circ$.

Transonic Flight. The graphs in figure 16 were prepared for $\alpha = \text{constant} = 4^\circ$. In actual flight, the lift (in lb or newtons) would remain constant, when advancing in steady horizontal flight toward the sonic speed. The lift coefficient would thus vary roughly as $C_L \sim 1/M^2$. Qualitatively, however, the changes of lift and pitching moment would remain as described, including the up-down-up variations as in figure 16. These variations are undesirable and dangerous. The conclusion might thus be that conventional "subsonic" wing sections are not suitable at all to be used at transonic speeds. It is possible, however, to reduce the up-down-up variations through the use of

wings with small aspect ratios,

wing sweep in combination with area rule applied to the fuselage,

airfoil shape (thickness ratio, nose radius, trailing edge angle).

It is shown in (9,f) for example, how in small aspect ratios, the lift drop may reduce to nothing, as the thickness ratio is reduced from 12 to 4%. It is also shown, for example in (9,c,e), how a wing with $A = 4$ and $t/c = 6\%$, gets comparatively smoothly through the sonic speed range. There is one change, however, which cannot be avoided in ordinary wings; that is the transfer of the center of pressure or lift, from $x/c \approx 25\%$, at least to some 40% as at supersonic speeds. The planform most perfect in this respect (theoretically not exhibiting any difference at all) is the delta shape; see Chapter XVIII.

(18) Aereas of supersonic flow are investigated or stated:

- a) In Chapter XV of "Fluid-Dynamic Drag".
- b) By Goethert as in Reference (6,g).
- c) von Karman, Transonic Similarity Law, J. Math Phys 1947 p 182.
- d) The maximum local Mach number obtained, before the flow over the upper side breaks down (separates), is stated (b) to be in the order of 1.4 or 1.5.

(20) For small lift coefficients, interpretation of the experimental data in figure 6 seems to be suitable by

$$C_{Pmin} = -C_L^2 / (t/c)$$

The minimum pressure coefficient is not perfectly proportional to C_L at higher lift coefficients.

CHAPTER V III — HYDRODYNAMIC LIFT

Low-speed aerodynamics are often called hydrodynamics, simply meaning that compressibility of the fluid is negligibly small. As we will see, fluid-dynamic forces in water, are not necessarily similar to those in air, however, not even when disregarding cavitation.

A. FULLY SUBMERGED LIFTING

CHARACTERISTICS

All that has been said in previous chapters regarding boundary layer, Reynolds number, flow separation, lift or lateral forces of foils or control surfaces, also applies in liquids, such as water in particular. Although towing-tank tests are concentrating on "resistance" (of ships, boats) information is also available on fins, rudders, control surfaces and their forces; and of course, hydrofoils.

REYNOLDS NUMBER. Since everything in a towing tank is usually geared to water-surface effects (waves) and the proper Froude number, Reynolds numbers are so low that appendages are not tested at all in typical investigations. Considering, for example, a hull model 10 ft long, representing a 500 ft long ship designed for a speed of 20 knots (34 ft/sec or some 10 m/s), the maximum towing speed corresponds to

$$F_f = V/\sqrt{g\lambda} = 34/\sqrt{32(500)} = 0.27 \quad (1)$$

This is the "first" hollow of the wave resistance function, for which most ships are designed. The resulting model speed is $V = 1.5$ ft/sec, and the Reynolds number is

$$R_{\lambda} = V/\nu = 1.5(10)/10^{-5}/1.25 = 1.2(10)^6$$

However, the R -number of any rudder, stabilizing fin, or for the appendages of a submarine would only be in the order of 5% of that value, which is below 10^5 . Testing a rudder separately, and adding its forces to those of the ship, does not give realistic results either, because of the very considerable wake within which rudder (and propeller) are located. The problem of steering and stabilizing of ships is very often solved, relying heavily on statistics (past experience).

RUDDERS. To support the large forces originating in a rudder, its structural strength has to be adequate. Consider, for example, a destroyer (5,b) turning at full speed (say 35 knots = 60 ft/sec) and with full rudder (up to 35°). Conditions may then be as follows:

$S_R/lh =$	2 %	statistical rudder area (3)
$S_R =$	200 ft ²	total rudder area (1 or 2)
$q =$	3,600 lb/ft ²	dynamic pressure (no wake)
$C_N =$	1.0 — —	normal force coefficient
$N =$	700,000 lb	normal force in the rudder

The data are based on $l = 400$ ft and $l/b = 9$. Considering, however, the boundary layer (along a planing bottom) the rudder force may be reduced to some 60%. The force is then in the order of 5% of the ship's displacement weight (assumed to be 4000 long tons). However, when

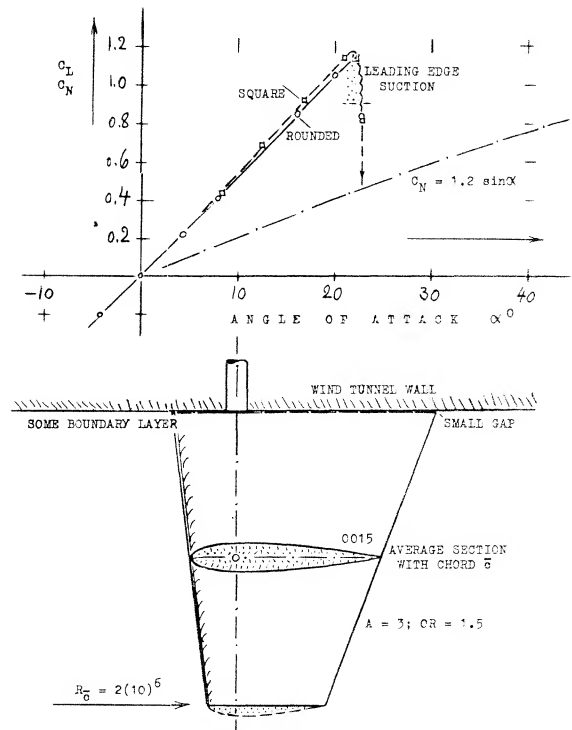


Figure 1. Lift of a plain control surface or rudder tested in a wind tunnel (1,b) in combination with an end plate (wall).

located within, or when flanking a propeller slipstream, the rudder force will be larger (5,b). The diameter of the rudder stock may be in the order of 1 or 2 ft, in any larger ship. In hydrodynamic terms, a thickness ratio of $t/c = 15\%$ is considered to be "modern". A number of such rudders (or control surfaces) have been tested (1)(6)(9) in wind tunnels. A convenient setup for doing such tests is to combine them with an endplate (or the wall of the test section), through which a rudderstock supports the model. Disregarding gap and boundary layer along the wall, the effective aspect ratio is then the "reflected" one, with a span b and an area twice the "exposed" dimensions. *Figure 1* shows a typical example. The lift-curve slope corresponds to what is said in the "wing" chapters. At $\alpha = 22^\circ$, the flow breaks down, evidently separating from the suction side. The maximum lift coefficient is almost $C_{Lx} = 1.2$. Considering the surface roughness usually found in ships, this value does not mean much, however. Lift due to leading edge suction is theoretically (7,a):

$$C_{Ls} \approx C_L [0.16 + (0.2/A^{3/2})] \quad (2)$$

Cutting off the peaks in figures 1 and 5 accordingly, we may tentatively account for surface roughness. The result is a lift function similar to that in part (A) of figure 3. Beyond the angle of maximum lift, the normal force will take over. As suggested in the "stalling" chapter, this force may correspond to

$$C_N = 1.2 \sin \alpha \quad (3)$$

where $1.2 = C_{D_s}$ = drag coefficient of a flat plate at $\alpha = 90^\circ$. For example, at $\alpha = 45^\circ$, the coefficient may be $C_N = 0.85$, and the lift component $C_L = 0.60$.

WALL GAP. Since the "wall" of a ship is usually curved, the structural gap may also open up as the fin is deflected. A "control surface" was tested (1,c) with gap ratios 'g's up to some 10%. It is shown in *figure 2*, how the angle of attack (or deflection) required to produce a certain lift coefficient, increases as the gap is widened. As already stated in chapter VII of "Fluid-Dynamic Drag", lifting-line theory is not confirmed at all. The flow through the gap is evidently restricted by separation. Eventually, the surface as in the illustration must be expected to assume a lift-curve slope corresponding to its exposed aspect ratio $A = 1$ (see the "wing" chapters).

ROLL-STABILIZING FINS have been introduced during the last decade to improve passenger comfort in a rolling sea (2). Such fins are half "wings" protruding from the hull in essentially lateral direction. Their angle of attack is automatically controlled by an electro-hydraulic system, sensing (and anticipating) angle and rate of the rolling motion. Some of the half "wings" tested (1) in wind tunnels, could be used as stabilizing fins. Lift-curve slopes and maximum lift correspond to what is said in the chapters dealing with "wings" and "stalling". Of course, there is a boundary layer (the "friction belt") around the hull of a ship. For example, at a position of 200 ft from the bow of a 500 ft long

ship, the total thickness of the BL is in the order of at least 1.5% of the 200 ft, which is 3 ft. As described in chapter II of "Fluid-Dynamic Drag", the corresponding displacement thickness is about 0.5 ft, and the momentum thickness is 0.3 ft (in comparison to a fin length of possibly 12 ft). Some fraction of these thicknesses, we might consider to be the equivalent of a gap. — When deflecting a pair of fins in the fashion of ailerons (one against the other) they interfere with each other, by producing a circulation, at least around the bottom of the hull. It is suggested that this interference be small.

SUBMARINES (8) have also horizontal fins called "planes", for control and stabilization (9) of longitudinal up and down motions. Because of some secrecy about design and characteristics of such vessels (in all nations concerned) specific experimental data do not seem to be available. However, any pair of "stabilizing" planes located near the stern, can be treated in the same way as the horizontal tail of an airplane; see the chapter on "longitudinal stability". In most submarines, a second pair of planes (8) was or still is installed near the bow. Its purpose is depth control (and faster diving). This is similar to that of a canard-type airplane (see in the "longitudinal" chapter). It must be assumed, however, that these forward planes made the boats unstable in pitch. Three men were required, accordingly, to maintain position and direction of motion, by means of manual control of planes and rudders. — For practical reasons, the forward planes had to be retractable. Beginning with the nuclear-powered "Skipjack", and also in the "Washington" class of United States submarines, the conning tower was moved forward somewhat, and a pair of "fairwater planes" attached to its sides. The tip to tip span of these planes does not exceed the beam of the hull.

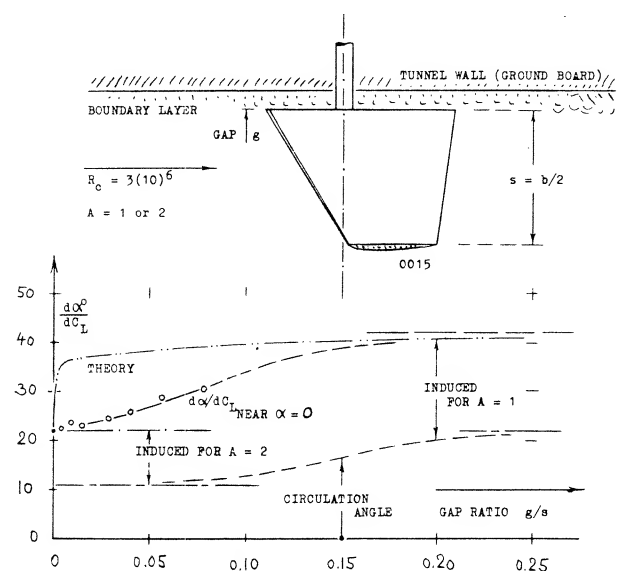
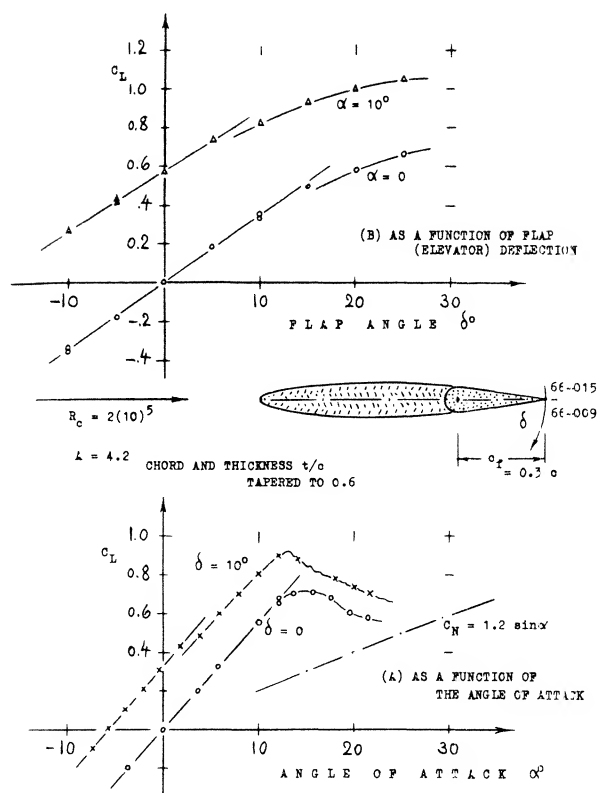


Figure 2. The influence of a "wall" gap upon the "lift angle" of a control surface (1,c).



CONTROL FLAPS. Any control surface or fin as described above, is bound to start cavitating, at higher lift coefficients in a rolling sea. The use of a trailing edge flap is therefore desirable, providing the foil section with camber. We might even use a fixed fin with a servo-controlled flap. Half of the horizontal tail surface of an airplane shown in figure 3, is a good example for marine application. The thickness ratio at the root is $t/c = 15\%$ (to withstand the large forces and bending moments in water) and the thickness is located at 47% of the chord (believed to be desirable to postpone cavitation). At the low Reynolds number $R_c = 2(10)^5$, the maximum coefficients are $C_{Lx} = 0.73$ for the plain surface at $\alpha = 15^\circ$, and 0.67 when deflecting the flap to 25° at $\alpha = 0$. Considering, however, the motion of the water against the fin, possibly at an angle of $\alpha = 12^\circ$, the maximum lift of the flapped surface corresponds to $C_{Lx} = 1.1$. Torque or hinge moments of the flap can be found in the "control" chapter.

Figure 3. Lifting characteristics of a horizontal tail surface (6,d) half of which could be used as a control surface (fin or plane) on the hull of a boat or submarine.

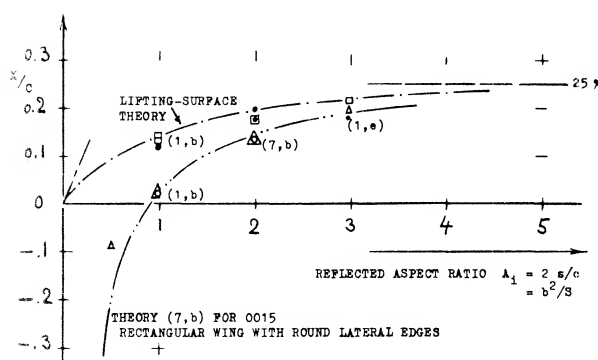


Figure 4. The center of pressure on the mean aerodynamic chord, of the linear component of lift of wings or control surfaces, as a function of the reflected aspect ratio.

- (1) Lift of half-span wings or control surfaces:
 - a) Windsor, 4 Surfaces, Md Tunnel Rpt 320 (1961).
 - b) Whicker, Family of Fins, DTMB Rpt 933 (1958).
 - c) Windsor, With Gap, Univ Md Tunnel Rpt 453
 - d) Chaplin, Edge Ahead, TMB Rpt 944 (1954).
 - e) Windsor, Collection of Data, Univ Md Rpt 1362-1.
- (2) Chadwick, Mechanics of Roll Stabilization Fins with 53 References, Trans SNAME 1955 p 237; also "Wanderer" Trials, Sperry Gyroscope Rpt 1956.
- (3) Saunders, Hydrodynamics in Ship Design (1957):
 - a) Volume I, Fluid Flow, Interactions, Hydrofoils.
 - b) Volume II, Fundamentals, Resistance, Design.
 - c) Volume III, Maneuvering and Wavegoing (1965).
 - d) Van Lammeren "Resistance-Propulsion-Steering" 1948.

RUDDER TORQUE. In wings, the pitching moment is primarily of interest for longitudinal stability and control. In rudders, this moment and/or the center of the normal forces represents the hinge moment or torque. As quoted, for example in (1,b), the center of pressure of the linear component of lift is at a distance from the leading edge (at the mean aerodynamic chord)

$$x/c = -(dC_{m\bullet}/dC_L) = 0.5 - (2 + \sqrt{A^2 + 4})/4(A + 2)$$

where the dot (\bullet) indicates that the moment is defined about the leading edge. This function is plotted in figure 4. For example, when placing the stock at $x/c = 0.15$ of a rudder with $A = 1$, the torque is expected to be near minimum. Of course, at higher angles of deflection, and in smaller aspect ratios, the non-linear component contributes to lift. Its center may be at $x/c = 0.7$ of the lateral or lower edge of surface or rudder. As a consequence, a turning-back component of moment will develop. Such a moment is definitely present at really high angles of attack or deflection, where the flow is separated (stalled). Since forces in this condition are not steady (they fluctuate considerably) they are usually not tested in tunnel investigations as in (1). Reference (1,b) suggests, however, that at angles around 30° , the center of pressure is around 50% of the chord, for a lift coefficient as estimated in figure 1. In conclusion, it is not possible to locate the stock of a rudder in such a manner that the torque would be near zero under all conditions of operation.

FAIRING. Rounding the lateral edge of a control surface, or the lower edge of a rudder, reduces slope and maximum of the lift. It should be noted that in figure 1, the lift coefficients are referred to one and the same area (without the fairing). Considering area and aspect ratio, the loss of lift due to round edge shape is as described in the "wing" chapter. When using half-round fairings, experiments and analysis as in (7,b) indicate that the effective span is approximately that of the trailing edge (b_t). Also, the center of pressure moves forward. As shown in figure 4, the CP of rectangular wings using the 0015 (or any similar section) is then "at" the leading edge, for an aspect ratio $b_t/c = 1$. In terms of $dC_m/dC_L = -x/c$, such wings become unstable. In terms of rudder torque, rounding the lower edge reduces its magnitude, or even renders the moment "negative." This is confirmed by experimental results in (1,b).

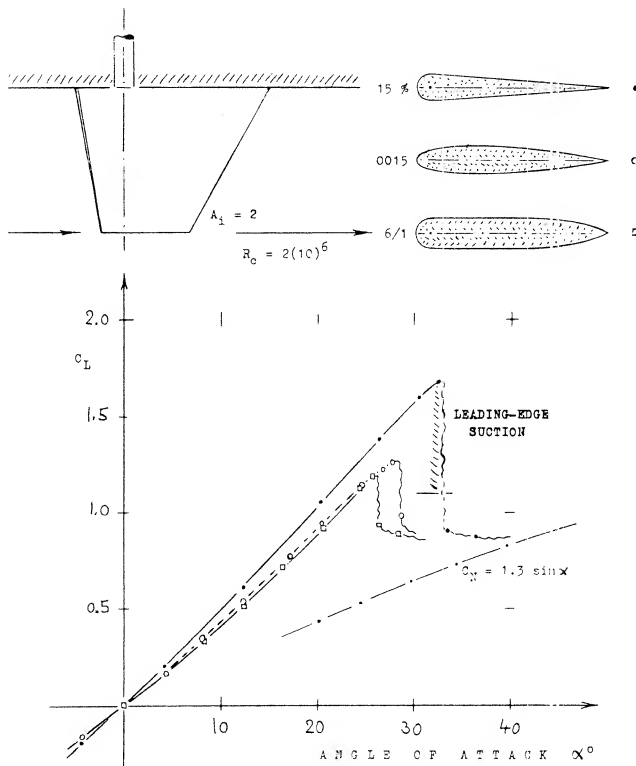


Figure 5. Lift of a control surface (rudder) for 3 different cross-section shapes (1,b).

FOIL SECTION. Three cross-section shapes are shown in figure 5. As found in the "control" chapter, a straight and thin trailing "wedge" produces the highest lift. Other experimental rudder section shapes are presented in figure 6. It is seen again that a thin and straight (or hollow) trailing end improves the maximum lift. It is also expected that simply giving the 0015 section a blunt trailing edge, will increase effectiveness.

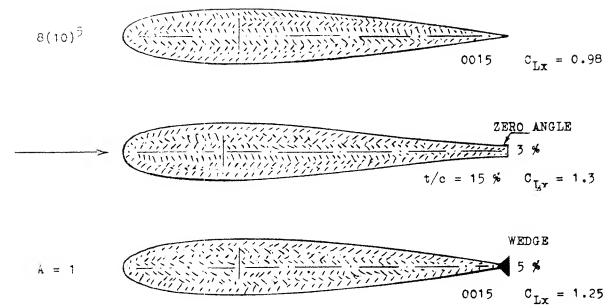


Figure 6. Effectiveness (maximum lift and normal-force coefficients) of three control or rudder section shapes, tested (4,c) in the form of rectangular "wings" with $A = 1$.

HULL WAKE. In conventional displacement ships, the whole rudder is functioning within the wide wake behind the hull. In propeller design, the reduced speed V_w is taken into account by means of the wake fraction

$$"w" = (V - V_w)/V \quad (4)$$

The fraction is quoted (3) to be between $"w" = 0.2$ and 0.4 in single-screw ships. So, for $"w" = 0.3$, we obtain an average $V_w/V = 0.7$ at the rudder, and an average $q_w/q \approx 0.5$. Considering, however, a ship in a steady turn (such as the airship in the "slender body" chapter) the rudder will, at least on the outside of the circle, be in or at the undisturbed flow.

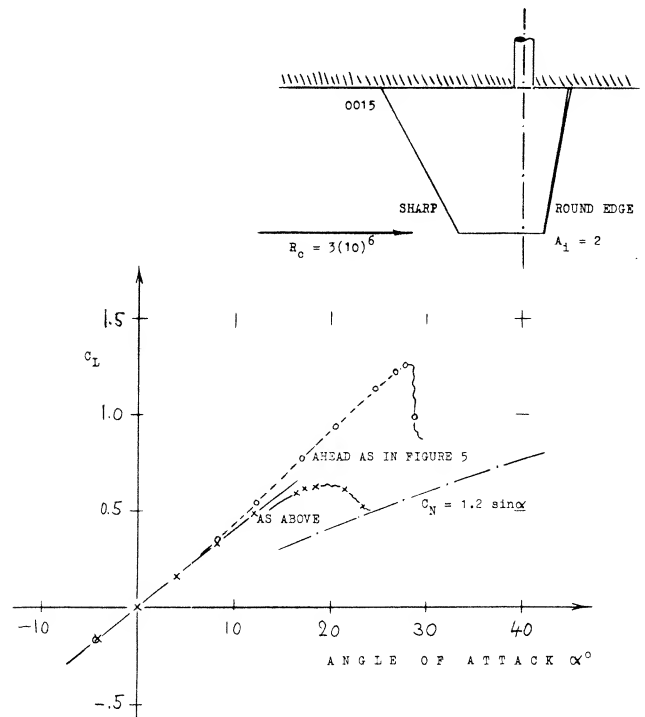


Figure 7. The "lift" of a rudder (or control surface) tested in astern direction (1,b).

ASTERN. Ships may also have to maneuver in the astern direction. The rudder is then exposed to full dynamic pressure (whatever there is at low speed). *Figure 7* shows that the maximum force coefficient may be reduced to half of that in the forward direction.

SLIPSTREAM. Maneuverability of ships is evidently not sufficient, using rudders of the 2% size mentioned above, under "rudders". Usually, therefore, the rudder is placed in the middle of the propeller slipstream. Deflection of this stream provides steering even at ship speeds close to zero. As reported in (4,b) the following rudder-force ratios were observed:

- 0.4 in the hull wake as against free flow
- 1.0 in wake, but with propeller, as against free flow
- 2.4 in slipstream as against without propeller
- 1.9 ditto, but in a steady turn

All these tests were made at a ship speed corresponding to F_h around 0.15. The 2.4 ratio is at the beginning of a turn, while in a steady turn (1.9) the angle of attack is naturally reduced (see the airship again). Statistical results are also listed in (5,c). The 180° turning "diameter" is in the order of " d "/ $l = 3$, for ships with the rudder in the propeller stream; and it is " d "/ $l = 4$ or larger, with a single rudder between twin screws.

- (4) Hydrodynamic characteristics of ship rudders:
 - a) Hagen, TMB Rpt C-398; also C-125 & 373 (1951).
 - b) Jaeger, Torque & Pressures, J. Shipb Progr 1955 p 243.
 - c) Thiemann, In Wind Tunnel, Schiff & Hafen 1962 p 42.
 - d) The 0015 section with various flaps (rudders) in NACA Wartime Rpts L-378, L-448, L-454 (1942).
- (5) Rudder forces and turning of ships:
 - a) Davidson, Turning & Steering, Trans SNAME 1944/46.
 - b) Becker & Brock, Trials, Trans SNAME 1958, p 310.
 - c) Mandel, Appendages, Trans SNAME 1953 p 464.
- (6) Control Surfaces with flaps, for ships or boats:
 - a) Windsor, 0015, Univ Md Tunnel Rpt 268 (1959).
 - b) Bowers, for submarine application, see (9,a).
 - c) White, Rudder in W Tunnel, TMB Rpt 1231 (1958).
 - d) Bates, Collection Tail Surfaces, NACA TN 1231.
- (7) Analysis of small aspect ratio wings:
 - a) Polhamus, Low A'Ratio Wings, NACA TN 3324.
 - b) Bartlett, Shape of Edges, J Sci 1955 p 517.
- (8) Information on modern submarines:
 - a) McKee, Design Practices, SNAME Paper 11, 1959.
 - b) Submarines & Destroyers, The Engineer Jan 1962.
 - c) Control, by McCandliss in IAS Paper 1961-45.
 - d) Malloy, Aircraft Techniques, IAS Paper 1961-42.
- (9) Control surfaces designed for submarines:
 - a) Bowers, on Simulated Hull, U Md Tunnel Rpt 259.
 - b) Harper, 0015 Hull, Georgia Inst Tech 1959.
 - c) Some "surfaces" under (1) for submarines?

COURSE STABILITY. Considering the hull of a ship to be the lower half of a streamline body, its destabilizing moment can be estimated on the basis of what is said in the "streamline body" chapter. The moment corresponds theoretically to

$$C_m = 'M'/q\nabla = k \sin(2\alpha) \approx 2k\alpha \approx 2\alpha \quad (5)$$

where k is in the order of 1.0, for more slender shapes. As such, the moment is proportional to the displacement volume ∇ or the displacement weight Δ . Consider, for example a freighter with

l	=	400 ft	overall length
V	=	9000 tons	displacement weight
∇	=	300,000 ft ³	displaced volume
S_R	=	200 ft ²	rudder area

The destabilizing moment may thus correspond to

$$'M'/q = 0.5 (2 \nabla \beta^2 \pi / 180) \approx 5,000 (\beta^2)$$

where β = angle of yaw, and 0.5 accounting for the heavy wake at the stern. The moment has to be balanced by that produced by devices such as fins, skegs, rudders at the stern of the hull. The stabilizing moment is proportional to rudder area (S_R) times moment arm (x) to the CG. For the freighter considered above, with the CG or CB assumed to be at 0.4 of its length, the stabilizing moment is tentatively

$$'M'/q = -(1 - "w")^2 S_R 0.5 l (dC_L/d\beta) \beta \quad (6)$$

For " w " = 0.3, and $(dC_L/d\beta) = 1/20^\circ$, we obtain $'M'/q = -1100 (\beta^2)$. This is far below the destabilizing value. We can assume, however, that the propeller provides stabilizing lateral forces. The hull itself (particularly when having a "V", rather than "U" shaped stern) may also contribute to stability. Finally, the assumption of a moment arm equal to 0.55 (to the CG) may not be correct in dynamic analysis. Rather the ship can be assumed to yaw about a point ahead of the CG, which means that the ship is also drifting (in lateral direction) or side-slipping, when yawing. The extreme of this combination is found in steady turns (5,a). The point about which the ship is yawing, is thus ahead of the CG. Assuming that the point might be near the bow, we arrive at a stabilizing moment which might be sufficiently large. Nevertheless, ships are known to go all across the Atlantic with their rudders correcting the course continuously by means of plus and minus up to 5° deflections. Airships are reported to have been unstable; and it should be noted that their Froude number was similar to that of ships, insofar as their density (in lb/ft³ of displacement) was equal to that of the surrounding fluid, just as in the case of ships.

B. CHARACTERISTICS OF LIFTING HYDROFOILS

Boats equipped with hydrofoils and thus "flying", with their hull out of the water, have been under development for more than 50 years. Characteristics of such foils have been analyzed and tested (in towing tanks).

SURFACE WAVES. Drag due to lift of fully submerged hydrofoils is explained at length in chapters X and XI of "Fluid-Dynamic Drag". As long as

$$d\alpha_i/dC_L = dC_{Di}/dC_L^2 \quad (7)$$

the angle due to lift can easily be derived from the drag functions. First of all, there is a surface wave. Water piles up above the hydrofoil moving below, thus starting a transverse wave train (with crest and trough lines essentially parallel to the foil). In two-dimensional flow, an angle similar to the induced angle (see the "wing" chapter) is caused by lift in the presence of a free water surface. Based upon submergence h and area ($b h$), indicated by subscript 'h', a universal function is obtained (see chapter XI of "Fluid-Dynamic Drag"). For froude numbers F_h above 5, we obtain approximately the angle due to the wave, but at the level of the foil:

$$d\alpha_w/dC_{Lh} = 0.5 F_h^2 = 0.5 g h/V^2 \quad (8)$$

where w indicates "wave". Considering $C_{Lh} = C_L (c/h)$, we find

$$\alpha_w^2 = K_w (0.5/F_h^2) (c/h) C_L (180/\pi) \quad (9)$$

The factor $K_w = f(b/h)$ (as in chapter XI of "Fluid-Dynamic Drag"), approximated by

$$K_w = (b/h)^{0.3}/4 \quad (10)$$

always smaller than unity, accounts for finite foil span. We can also write

$$d\alpha_w^0/dC_L = (K_w/F_c^2) (90/\pi) \quad (11)$$

where $F_c^2 = V^2/g c$. For a given hydrofoil craft (with constant weight, and foil dimensions b and c) it is then found that

$$\alpha_w \sim 1/V^4 h^{0.3} \quad (12)$$

or that

$$\alpha_w/\alpha_i \sim 1/V^6 h^{0.3} \quad (13)$$

For all practical purposes, therefore, this two-dimensional wave angle can be disregarded at the usually higher cruising speeds of hydrofoil boats. See

later under "takeoff", however. An important aspect of drag due to lift is also the fact that most towing-tank tests on hydrofoils are done above the critical or wave propagation speed

$$V_w = \sqrt{g H} \quad (14)$$

where H = depth of the water (to the bottom) of the tank (or possibly in a water tunnel). In short, "all" experimental results at higher speeds (and/or higher Reynolds numbers do not contain the two-dimensional type of wave angle and wave resistance (13)

INDUCED DRAG and the corresponding increment of the angle of attack are as in airplane wings, a function of the aspect ratio $A = b^2/S$. The surface of the water is deformed again by the presence of a lifting wing below. As shown in *figure 8*, a hollow appears on the center line of the wake, at $x = 1.4 b$. On the other hand, above the foil ends (wing tips), a pair of humps develops. Gravity distributes these humps in lateral directions, in form of 2 pairs of waves. Part of the "induced" drag can thus be called wave resistance. It can be said, however, that those waves are part of the trailing vortex system, partially transforming itself into trailing waves. At any rate, momentum is transferred from the moving hydrofoil onto the water; and it does not matter much, whether to name it "wave" or "induced".

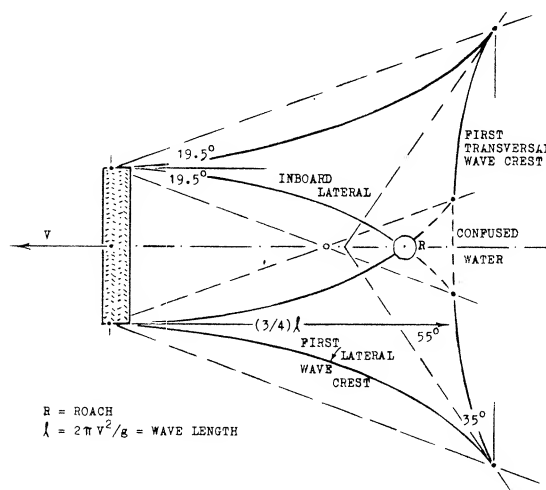


Figure 8. Theoretical wave pattern (11,b) caused by the motion of a fully submerged hydrofoil. The whole system moves to the left, with the viewer fixed to it. It must be understood that not the water as such moves together with the foil, but only its orbital wave motion. See also figure 19.

BIPLANE THEORY. Within the range of higher Froude numbers (as they are used in hydrofoil boats) the surface of the water follows more or less the stream of downwash going on below. Theoretically, therefore, the hydrofoil produces the same lift as the lower panel of a biplane configuration (see the "airplane" chapter). The

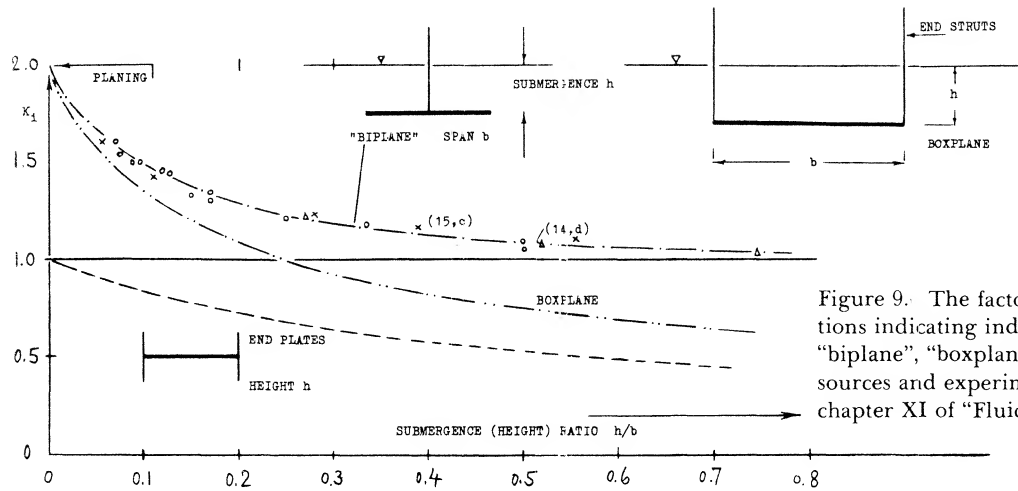


Figure 9. The factor K_i to be used in the equations indicating induced angle and drag, for "biplane", "boxplane" and end plates. Theoretical sources and experimental results are listed in chapter XI of "Fluid-Dynamic Drag".

vertical separation of this equivalent biplane is $(2h)$ where h = submergence of the foil. The induced angle is then

$$\alpha_i = K_i C_L / \pi A; \quad d\alpha_i / dC_L = 20 K_i / A \quad (15)$$

where 20 as in the "wing" chapter, while $K_i = 1$ for sufficiently large values of h/b , and $K_i = 2$ for the limiting case of the foil planing at the surface. This function is plotted in figure 9.

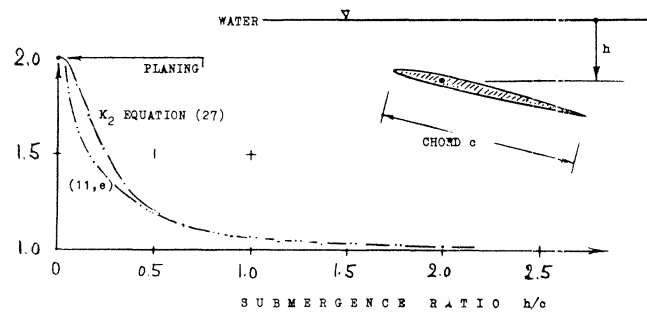


Figure 10. Factor K_2 (equation 27) indicating the increment of the two-dimensional angle of attack required for a submerged hydrofoil, to obtain a certain lift coefficient; equation (18).

- (10) Technical reports on hydrofoils and hydrofoil boats. A selection listed in (11) (14) (15). More than 300 sources (possibly half of them available to the public), between 1947 and 1961, are listed in "Bibliography and Literature Search" by Tech Info Center, North American Aviation Rpt S&ID 1961-157; AD-282,464.
- (11) Analysis of data on submerged hydrofoils:
- Wu, Finite Span, J Math & Phys 1954 p 207.
 - Breslin, Ship Theory for Hydrofoils, J. Ship Research Apr 1957, Mar 1960, Sept 1961.
 - Wadlin, Calculation, NACA TN 4168, NASA R-14.
 - Wadlin, Theor and Experiment, NACA Rpt 1232.
 - Schuster, Oscillating Foils, (1960); AD-257,305.
- (12) Lifting characteristics of biplane wings:
- Kuhn, Distribution Betw Panels, NACA Rpt 445.
 - Diehl, Relative Loading, NACA Rpt 458 (1933).

CIRCULATION. When approaching the free surface of the water, the lift of a two-dimensional hydrofoil reduces also. As pointed out in (11,e) the upper side of the foil loses lift, while the lower side remains unaffected by the proximity of the water surface. At or "in" the surface (planing) the circulation is reduced to half, for a given angle of attack. There are two analytical approaches to this effect:

- a) We will replace the upper panel of the imaginary biplane by a lifting line, tentatively with the same circulation as in the lower panel:

$$\Gamma = 0.5 C_L V c = w 2 r \pi \quad (16)$$

This means that at the radius $r = 2h$, there will be the circulation velocity

$$w/V = (C_L / 8 \pi) / (h/c) \quad (17)$$

This velocity w is a component directed against the oncoming V . This consideration leads to an increment of the angle of attack corresponding to

$$\Delta(d\alpha/dC_L^2) = (d\alpha/dC_L)(c/h)/4\pi = 0.08(d\alpha/dC_L)/(h/c)$$

where $d\alpha/dC_L$ = uncorrected biplane "lift angle" (equation 30). The formulation does no longer hold, say below $h/c = 0.4$; it does agree, however, with the more complete analysis in (12).

- b) According to (11,c) we have in two-dimensional flow, the factor

$$K_2 = [16(h/c)^2 + 2] / [16(h/c)^2 + 1] \quad (18)$$

This equation, also approximating three-dimensional conditions, is plotted in figure 10. The first term of the "lift angle" will then be

$$d\alpha_2^0 / dC_L = K_2 (10 + 10/A^2) \quad (19)$$

where $(10/A^2)$ taken from the "wing" chapter, accounts for the influence of the chord (lifting surface). A function for K_2 as indicated in (11,e) is also plotted in figure 10.

Experimental results proving (a) or (b) to be correct, are hard to find. It is suggested, however, to accept equations (18) and (19).

"LIFT ANGLE". Using the induced angle as in equation (20) the "lift angle" of a fully submerged hydrofoil (wing) is expected to be

$$d\alpha^{\circ}/dC_L = K_2[10 + (10/A^2)] + (K_i/20/A) \quad (20)$$

Experimental derivatives of hydrofoils are plotted in figure 11. Equation (30) serves well to explain the angles as tested.

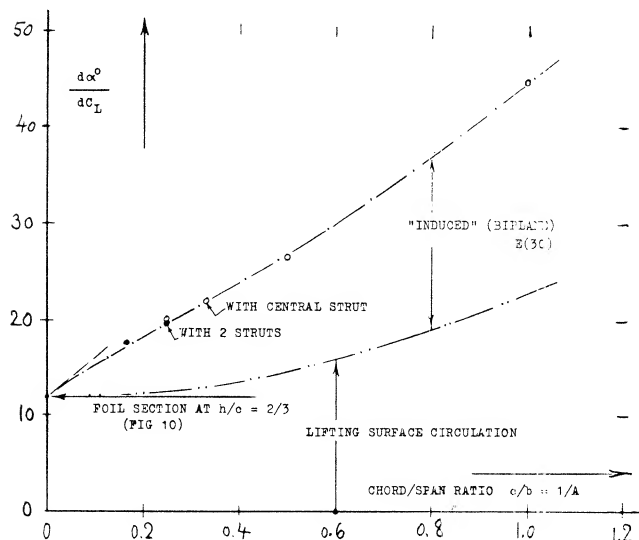


Figure 11. Lift angle of a family of hydrofoils (15,c) as a function of their chord/span ratio, at constant submergence $h = (2/3)c$; comparison with theory.

DRAG DUE TO LIFT. We see that the "induced" factor is involved in all terms of the lift equations. As stated in (11,c) this is partly empirical. When it comes to due-to-lift drag, it is necessary, however, to be specific. Regarding the linear component, the biplane concept indicates

$$C_{Di} = K_i C_L^2 / \pi A \quad (21)$$

It is suggested, however, to consider the increment of the angle of the lower panel as in equation (26) as a drag-increasing component. The non-linear component is a normal force. Its drag component is simply

$$\Delta C_D = \Delta C_N \sin \alpha \quad (22)$$

SMALL ASPECT RATIOS. Hydrofoils as considered so far, have higher aspect ratios (say at least $A = 3$). However, when using hydroskis, very small aspect ratios may also be of interest. Simplifying the formulation as in (11,c) we obtain for the linear term of the lift

$$dC_L/d\alpha = A 2 \pi / 3 K_i \approx A / 30^\circ K_i \quad (23)$$

Where K_i is taken from figure 9. Correlation of experimental points in figure 12, is not very good. Replacing the 30° by $360/\pi^2 = 36^\circ$, as in the "low aspect ratio" chapter, agreement is found with data from (16,c). The question then remains why lift reported in (16,a) is higher than expected by theory.

THE NON-LINEAR LIFT component of small-aspect-ratio hydrofoils can be important. Indicated by the normal-force coefficient, analysis in (11,c) predicts that for really small aspect ratios

$$\Delta C_N = 2(4/3) \sin^2 \alpha / K_i = 0.0008 (\alpha^\circ)^2 / K_i \quad (24)$$

where $4/3 =$ so-called cross-flow "drag" coefficient, and ' K_i ' taken from figure 9. In unrestricted flow (with $K_i = 1.0$) this formulation is well confirmed, particularly for cylindrical bodies, as in the "slender body" chapter with a factor of 1.1; and for sharp-edged plates (with $A \rightarrow 0$) in the "small A'ratio" chapter, with a factor of 2 or higher. In either case, the flow pattern is "separated". Experimental results are presented in figure 12, for plates with $A = 0.25$, at $\alpha = 10^\circ$. As found in (16,b) the presence of the strut supporting the plate increases the lift within the range of shallow submergences (at h/b below 0.2) up to 10%

HYDROSKIS (16,d) usually planing on the surface, may also (part of the time) be used in fully submerged condition. As shown in figure 12, their lift is less than that of flat plates. They seem to be less efficient on account of the bent-up leading edge (bow).

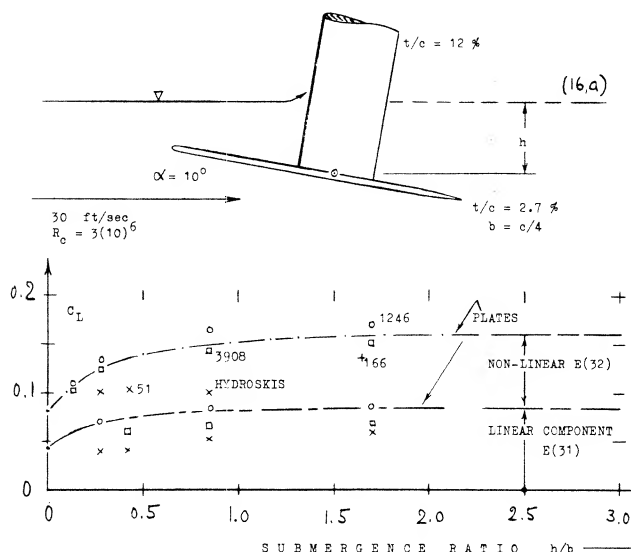


Figure 12. The lift of flat plates (16,a,c) and of profiled hydroskis (16,d), all having an aspect ratio of 0.25, as a function of their submergence ratio.

STRUTS are needed to support a hull above 2 or 3 hydrofoils. A larger main foil may have 2 struts, while a smaller control foil is usually connected with the hull by means of one central strut. As explained in chapter VIII of "Fluid-Dynamic Drag", any disturbance on the upper side of a wing is likely not just to reduce its lift,

but to increase its induced angle and induced drag. Results of wind-tunnel tests (15,e) on the assembly as in figure 13, are as follows:

configuration	$d\alpha/dC_L$	$d\alpha_i/dC_L$	$d\alpha_i/dC_L$	dC_D/dC_L^2	C_{Lx}
plain wing					
alone —	15.4°	3.9	0.068	0.077	1.05
wing with					
nacelle —	14.8°	4.3	0.075	0.078	0.86
wing-nacelle-					
strut —	15.2°	3.7	0.065	0.081	1.05
wing with					
strut —	16.0°	4.5	0.078	0.087	1.04

The two-dimensional "lift angle" is assumed to be 11.5° , for $A = 4$. There is no doubt that strut interference reduces the effective aspect ratio by some 10%. The nacelle acts, on the other hand, like a good fairing. Maximum lift ($C_{Lx} = 1.05$) was not affected by the strut.

ENDPLATES as described in the "wing" chapter can also be used in connection with hydrofoils. Regarding the factor K_i (figure 9) it is suggested to consider the foil as a lifting line or surface, with the same h/b as without plates, whose circulation and effective aspect ratio are increased. Experimental results (15,d) confirm this procedure, as long as the end plates do not touch the water surface.

- (13) An exception are the tests in (15,c).
- (14) NACA, Fully Submerged Hydrofoils Tested:
 - a) Benson & Land, Foils in T Tank, WRpt L-757 (1942).
 - b) Wadlin, Aspect Ratio 10, RM L9K14a (1950).
 - c) Wadlin-Ram-Vaug, Flat Plates, Rpt 1246 (1955).
 - d) Wadlin-Shuf-McGeh, Also Theory, Rpt 1232 (1955).
 - e) See references (15,d) and (17,a).
- (15) Fully-submerged hydrofoils (with struts):
 - a) Kaplan, With $A = 6$, Stevens ETT Letter Rpt 428.
 - b) Ripken, 16-509, Univ Minn SAF Lab Rpt 65 (1961).
 - c) Feldman, 6 Hydrofoils in Tank, DTMB Rpt 1801.
 - d) Wadlin, End Plates Struts, NACA RM L51B13; see (11,d).
 - e) Hoerner, Struts-Nacelles, G&C Rpt 14 (1953).
 - f) Jones, Various Foils, Convair Rpt ZH-146 (1950).
- (16) Characteristics of small-aspect-ratio hydrofoils:
 - a) Wadlin, Rectangular Flat Plates with $A = 0.125$, $= 0.25$, $= 1.0$; NACA Rpt 1246, TN 3079 & 3249 (1954).
 - b) Ramsen, Strut Interference, NACA TN 3420 (1955).
 - c) Vaughan, Plate to 80 ft/sec, NACA TN 3908 (1957).
 - d) Vaughan, Hydroskis, NASA TN D-51 & D-166 (1959).
- (17) Influence of control flaps upon hydrofoils:
 - a) Jones, 16-309 With Flaps in Towing Tank, Convair Rpt ZH-153 1961; AD-268,233.
 - b) Conolly, Review of Hydrofoils, J Aircr 1965 p 443.
 - c) Conolly, Flaps in Waves, Convair Rpt GDC-1953-032.

Figure 14. Lift angle required of a hydrofoil, tested (15,c) in two conditions, with a single central strut and with a pair of struts.

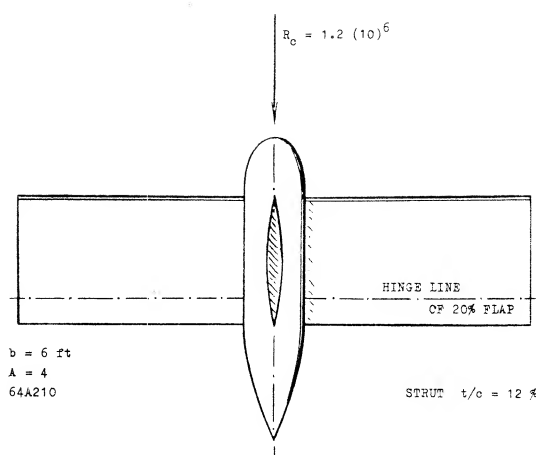
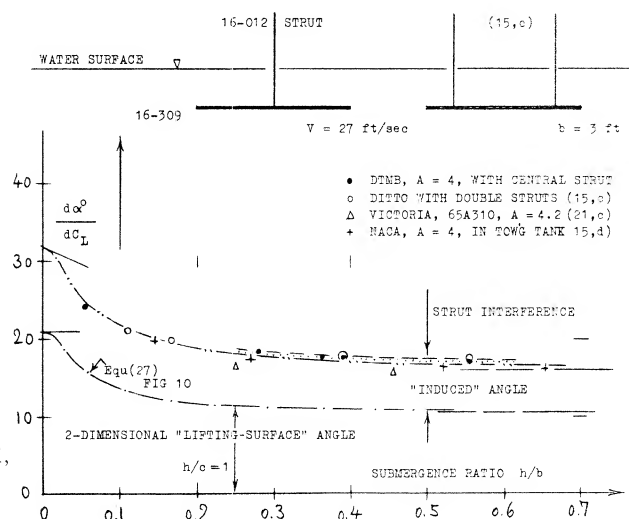


Figure 13. Wing-strut-nacelle configuration tested (15,e) in a wind tunnel.

END STRUTS. A pair of struts are often used to support a hydrofoil like a beam, that is with the struts located each, say at $1/4$ of the span from the lateral edges. In this manner, the struts have some end-plate effect. However, figure 14 does not confirm that $d\alpha/dC_L$ would be reduced, or lift increased, in comparison to a single central strut. When placing the struts at the very ends of a rectangular wing, a "boxplane" is obtained rather than the biplane discussed above. Theory indicates that the factor K_i as in figure 9, reduces from 2, at the surface, to zero for "very" deep submergence ratios. The connection between boxplane and biplane factor is approximately

$$K_{box} = K_i / (1 + h/b) \quad (25)$$

In reality, end struts are bound to disturb the flow at the upper side of the foil, as shown in (15,b), thus increasing induced angle and drag above that as indicated by theory.



CONTROL FLAPS are needed to balance and to stabilize a hydrofoil craft in roll and pitch. Their characteristics, including hinge moments, are available in the "control" chapter. Figure 15 presents experimental results obtained on the 16-309 section. On account of the comparatively large trailing "wedge" angle of this section, the control effectiveness breaks down at deflection angles beyond $+3^\circ$ and -5° , as a consequence of separation from the flap. Regarding control, this type of section (selected on the basis of higher non-cavitating speeds) cannot be considered to be desirable. With the minimum pressure intended to be located at 60% of the chord and a trailing wedge angle of 24° , early separation from the suction side of the flap must be expected. We have indicated in the graph what the lift due to flap deflection would be, if separation did not take place. On the basis of the experimental results presented in the control chapter, the effectiveness ratios $d\alpha/d\delta = (dC_L/d\delta)/(dC_L/d\alpha)$ should be as follows:

$$\begin{aligned} d\alpha/d\delta &= 0.8(0.48) = 0.38 & c_f/c &= 0.2, \text{ and } b_f/b = 0.8 \\ d\alpha/d\delta &= 0.6(0.60) = 0.36 & c_f/c &= 0.3, \text{ and } b_f/b = 0.6 \\ d\alpha/d\delta &= \text{average} = 0.38 & & \text{as tested (16,a) "1" and "4"} \end{aligned}$$

within the range of $\delta = -4^\circ$ to $+2^\circ$. However, outside this range, lift due to deflection is similar to that of split flaps, as indicated in the "flap" chapter. Drag is multiplied, for example tripled for a deflection of 10° . A different foil section and/or a flap shape modified as indicated in the "control" chapter, would certainly give a better performance, in regard to control, lift and drag. In fact, the plain flap in the configuration as in figure 13, provides a $d\alpha/d\delta = 0.46$, up to some 12° of deflection, on a 64A210 foil section; and that in figure 3, has a $d\alpha/d\delta = 0.63$, that is for a 30% flap.

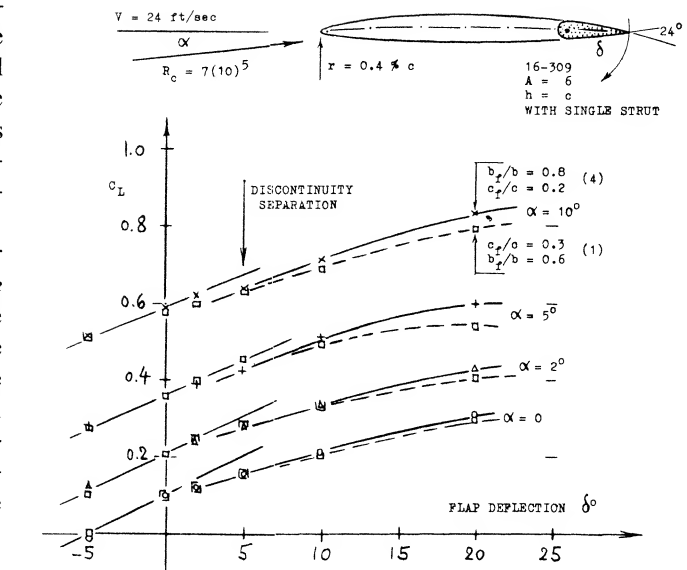
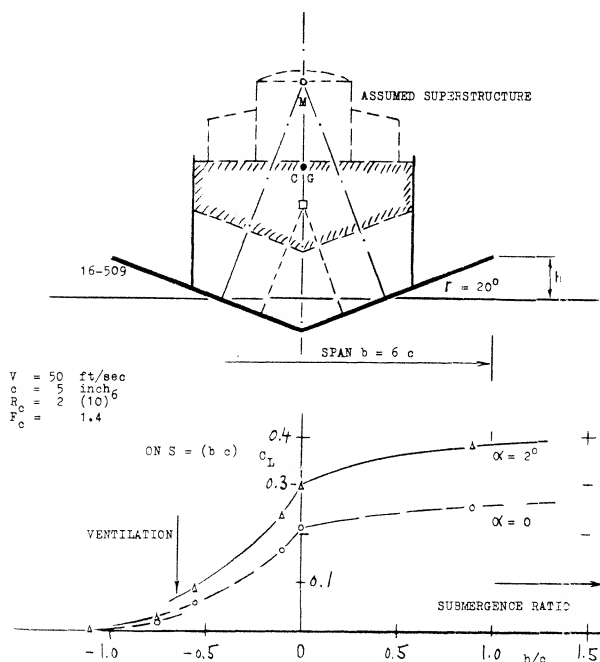


Figure 15. Lift of hydrofoil (17,a) produced by deflection of pairs of trailing-edge flaps.

SURFACE-PIERCING hydrofoils are intended to give height (heave), roll and pitching stability through their shape. In theory, their lift, induced angle, roll stability (metacentric height) and even the pitching characteristics of a tandem pair of such foils, is readily understood and susceptible to analysis. The lift of one such foil with a dihedral angle of 20° , is shown in figure 16, as a function of its submergence (but at constant speed and constant angle of attack). Referred to the geometrical total projected planform area, the coefficient reduces, as the foil emerges from the water. These towing-tank tests are performed in perfectly calm water and in steady forward motion. In reality, surface-piercing foils are very problematic because of ventilation irregularly creeping and/or breaking in, from the surface-piercing ends, particularly in sea waves. In the configuration as in figure 16, the struts serve as "fences". It is reported that at $h/b = -0.1$, "a more or less sudden breakdown of the flow over the upper surface occurs". This emergence ratio corresponds to the condition where the strut junctures are just out of the water. The average variation of lift with submergence (between $h/b = 0$, and -0.1) corresponds to $dC_L/d(h/b) = -2$. With this approximate derivative, all stability characteristics and motions of a craft can be estimated. The metacentric height is indicated in the illustration as the difference between point M and the CG. The apparently high roll stability also means that riding in sea waves will be rough.

Figure 16. Lift of a surface-piercing hydrofoil-strut configuration (18,a) as a function of its submergence.

THE “LIFT ANGLE” of surface-piercing fully-wetted dihedral hydrofoils as derived from (18,c) and from the formulations in this chapter and in the “wing” chapter, is expected to be

$$d\alpha/dC_L = (10 K_2/\cos\Gamma) + (10 K_2/A^2 \cos\Gamma) + (K_1 20/A)$$

Span, area and aspect ratio are based upon projected “wetted” dimensions. For the angle of the section (lifting surface) analysis as in (18,e) indicates a

$$K_2 = 2(1 - \Gamma/75) \quad (26)$$

where the angle of dihedral is in degrees. Adopting the average submergence (at 1/2 halfspan) as “the” submergence, it may be said that the equivalent of a “V” foil is a boxplane (figure 9) with a span equal to the distance between the surface-piercing points. Experimental results are plotted in figure 17 as a function of the projected wetted aspect ratio, that is of the ratio $c/b = 1/A$. The experimental points can be matched by equation (37) when reducing the aspect ratio by

$$\Delta A = \Delta b/c = 2(\Delta h/c)/\tan\Gamma = -0.2/\tan\Gamma \quad (27)$$

This means that for $\Gamma = 30^\circ$, the effective aspect ratio is $A_i = A - (1/3)$. In other words, the surface-piercing foil ends are not effective for a submergence $\Delta h = 0.1 c$, because of surface effects (disturbance and ventilation around the piercing points).

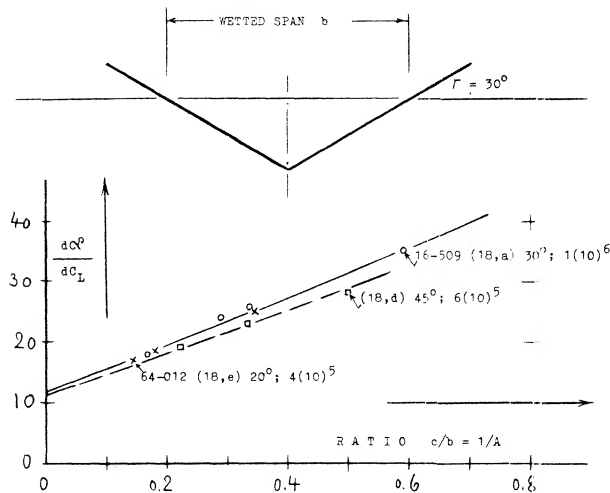


Figure 17. Lift angle of surface-piercing hydrofoils as a function of their wetted aspect ratio.

- (18) Characteristics of surface-piercing hydrofoils:
- Benson, With Struts, NACA W'Rpt L-758 (1942).
 - Sherman, Various Foil Sections, DTMB Rpt C-813.
 - Purser, "V" Tail Analysis, NACA Rpt 823 (1945).
 - Sottorf, In Hamburg T'Tank, ZWB FB 1319 (1940).
 - Bernicker, Flaps, Davidson Lab Rpt 964; AD-601,578

C. CHARACTERISTICS OF HYDROFOIL BOATS

Boats, supported by the dynamic lift of hydrofoils, thus “flying” above the water, have been developed over the past 50 or 60 years (19).

THE BENEFITS of lifting the hull out of the water are twofold; most of the impact of sea waves is avoided, and resistance (drag) at higher Froude numbers, is less than that of ordinary displacement and even planing boats. Disregarding cavitation, higher speeds can thus be obtained with acceptable power and a minimum of discomfort for crew and passengers. Not counting experimental boats, the highest *continuous* speeds reached are still below 40 knots, however, in comparison to some 32 knots as in the transatlantic “United States”, for example, or some 35 knots in any modern destroyer. There have been two types of boats developed, using either surface-piercing self-stabilizing foils, or fully-submerged and artificially stabilized systems. A few examples are listed in the table.

hydrofoil boat	foil system	Δ (tons)	l (ft)	BHP	V (kts)	$V_k/\Delta^{1/6}_t$
Supramar PT-20 (24)	surf'piercing	28	68	1350	37	20
"Sea Legs" (23,b)	submerged (o)	5	29	220	26	20
US Navy PCH (20)	submerged (o)	117	116	6000	40	18
"Raketa" (19,d)	submerged (●)	2	88	1000	35	21
"Victoria" (20,d)	submerged (o)	39	65	2000	37	19
Canada "400" (24,d)	surf'piercing	200	151	20000	50	21

(o) autopilot-controlled

(●) stabilized by planing plates forward

TABLE, listing a number of built and operating hydrofoil boats. The weight (in long tons) is fully loaded, the engine power is maximum continuous installed, the speed is continuous cruising.

SIZE AND SPEED have been discussed in the first chapter. It should be noticed that the sizes of the boats in the table above, are quite small, that is in comparison to ocean-going ships. An equivalent to the Froude number is $(V_k/\Delta^{1/6}_t)$. This number is for example:

ship or boat	Δ (tons)	V (kts)	$V_k/\Delta^{1/6}_t$	F_λ	l (ft)	$1/F_\lambda^2$
'United States'	54000	32	6	990	0.3	11
NW "Victoria"	37	36	20	65	1.4	5

We have also listed the Froude number in its usual definition. Both numbers show roughly the same ratio. Very instructive is the inverse of the square of the

Froude number, indicating that the loading (in pounds or tons) of the "United States" per square foot (or square meter), say of the plan form or bottom area of the hull, is roughly 20 times as high as that of the hydrofoil boat "Victoria". This means that for equal speed or dynamic pressure, the hydrofoil area required to lift a ship such as the "United States" out of the water, would be in the order of 2 times its bottom area, in comparison to say 10% of that area in the "Victoria". Since we need a certain aspect ratio for the foil (or foils) say in the order of $A = b^2/S = 5$, for efficiency, the combined span of the "Victoria's" pair of main foils is roughly equal to the beam, while that of the "United States" would have to be $\sqrt{20} = 4.5$ times the beam, which would be some 400 ft (or about 1/2 her length). In order to conform to the square-cube law about which this discussion goes, the speed of the "United States" would have to be increased to $V = \sqrt{20}$ (32 or 36) kts, which is in the order of 150 kts. This is, of course, impossible. In conclusion, and as explained in (23,c) hydrofoil-supported craft are thus limited to small sizes, where $V_k/\Delta_t^{1/6}$ may be in the order of 20; and we see in the table above, how remarkably constant this number is among the boats listed.

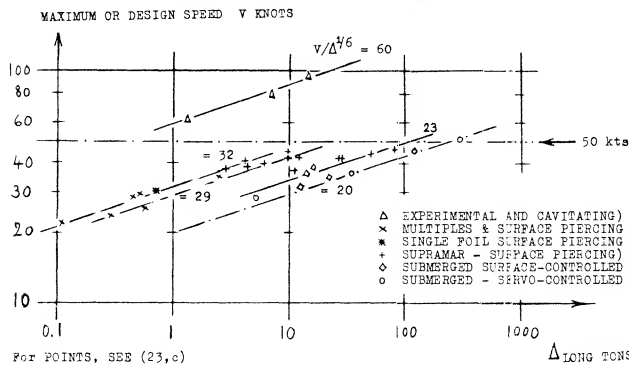


Figure 18. Statistical review of size (displacement weight in long tons) and maximum or design speed of operating or experimental hydrofoil boats (23,c).

If we assume that a number of 30 be the limit in the design of hydrofoil craft, their maximum feasible size would be in the order of 200 long tons for a maximum, hopefully cavitation-free speed of 50 kts. One way of increasing the size, is to increase the foil area S in relation to that of the hull ($l \cdot b$) or $(b')^2$ where $b' =$ beam of the hull. Assuming that the boats listed above, have a foil span $b = b'$ (restricted, so that the boats can come along a dock or pier), doubling their span would increase the supporting area, and the permissible ship size (in tons) fourfold. At the same time, the beam of the hull would increase to $2^{1/3} = 1.26$ times the original dimension, so that $b/b' = 2/1.26 = 1.6$. If this is considered acceptable from an operational point of view (24,f) the feasible size of subcavitating hydrofoil boats would be around 800 long tons. Such estimates and a statistical survey of existing or designed craft, are indicated in figure 18.

WAVE PATTERN. Regarding stability and control, the minimum number of foils required is two (as in airplanes), while the struts provide areas for lateral forces in turns and for directional stability and control. Considering the transverse wave system left behind a lifting foil (of larger aspect ratio and shallow submergence as in figure 8), it is theoretically possible to place the second foil at a distance downstream from the forward foil, where it rides so to speak, like a surfboard (but below the surface) somewhat ahead of the first wave crest. To say it in different words, the wave system produced by the second foil would possibly cancel the crests and troughs of the first one. The distance from the leading foil, at which the first crest is located, is 3/4 of the wave length

$$\lambda' = 2\pi V^2/g \quad (28)$$

and the distance x to the most favorable slope is 1/2 of this length. The corresponding Froude number is

$$F_x = 1/\sqrt{\pi} = 0.56 = \sqrt{g/x}$$

or equal to 0.5, in an average trochoidal wave (3,b). Locating now the second foil at 1/2 of the wave length behind the first foil, we obtain a distance

$$x = (\pi/g) V^2 \approx 0.1 V^2 \quad \text{in (ft)}$$

where V in (ft/sec). At this distance the second foil would theoretically be propelled forward with a thrust equal in magnitude to the drag due to lift of the first foil (complete recovery). Considering a boat cruising at 35 knots = 60 ft/sec, the separation required would be $x = 0.1 (60)^2 = 360$ ft. For comparison, the largest boat built to date (the AGH) has a length of 212 ft. Considering now a longer boat at 30 knots, we obtain tentatively $x = 265$ ft, hull length = 300 ft, but according to figure 18, a maximum displacement weight $\Delta \approx 100$ long tons. Traditionally, the weight of a 300 ft long ship would be around 2000 tons. In conclusion, wave-drag recovery is not feasible in any practical design. Could it be of interest, however, to study the feasibility of "flying" hydrofoil boats in formation?

DOWNWASH. Deeply submerged, a hydrofoil would produce downwash in the same manner as the wing of an airplane. As explained in the "longitudinal" chapter, downwash has two components. The one corresponding to the wing's circulation reduces quickly with distance from the lifting line at 1/4 of the chord. The other component is permanent; its maximum angle deep in the water (at the foil level) is

$$\varepsilon = 2\alpha_i = -2C_L/\pi A \approx -36^\circ C_L/A \quad (29)$$

For $A = 5$, for example, this angle would be $\varepsilon = -0.128 = -7.6^\circ$, for $C_L = 1$. In keeping with the biplane theory, this downwash might be expected to be increased when placing a hydrofoil near the free water surface, in proportion to K_i in figure 9. Analysis of towing-tank tests

with tandem pairs of foils (21) reveals a different mechanism, however. First, consider the downwash relative to the water surface. Assuming that this surface is a solid boundary (a ceiling) the theory of ground effect (see in the “airplane” chapter) suggests a downwash angle

$$d\epsilon^\circ/dC_L = -2K_g(180)/(\pi^2 A) = -36K_g/A \quad (30)$$

The ground factor (see chapter VII of “Fluid-Dynamic Drag”) can be approximated by

$$K_g = [30(h/b)^{3/2}] / [30(h/b)^{3/2} + 1] \quad (31)$$

According to this analysis, a hydrofoil produces a larger downwash angle when it is deeper in the water. This is experimentally confirmed (21,a) at the location below the first trough (where the wave angle as in figure 19, is zero).

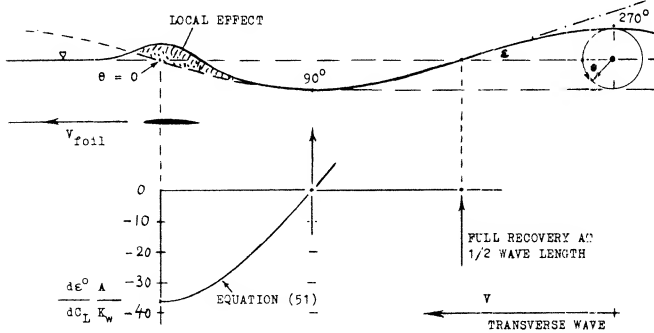


Figure 19. Wave pattern and downwash angle behind a submerged lifting hydrofoil. The wave amplitudes are shown in exaggerated size. See also figure 8.

WAVE ANGLE. Part of the induced angle as in equation (44) corresponds to a deformation of the water surface. On the basis of (11,a,b) it appears that at higher Froude numbers, the wave factor is

$$K_w = 2(K_i - 1) \quad (32)$$

This factor determines the amplitude of the undulating wave train, while

$$K_i = K_w + K_g \quad (33)$$

determines the “biplane” drag due to lift; and equation (45) the permanent downwash angle (under a ceiling as above a ground). Assuming that the transverse wave train be sinusoidal (only true for small amplitude), the wave angle (slope) corresponds to the cosine. In hydrofoil boats, or their foil systems, we are only interested in the first 1/4 wave length, beginning with a down slope at the forward foil, and ending with the first trough. This point is found (see figure 19) at the distance behind the first foil, equal to 1/4 wave length

$$x = 0.5 \pi V^2/g \approx 0.05 V^2 \quad (\text{ft}) \quad (34)$$

where V in ft/sec. The point is important insofar as there will be no down or upwash due to the wave motion, at that distance. For example, for a subcavitating cruising speed of 35 kts = 60 ft/sec, the distance is 180 ft. As such, it would just be possible to be reached by the second foil in the tandem system of a larger hydrofoil boat.

WAVE DOWNWASH. In all realistic hydrofoil boats, we will have to deal with the wave downwash in the first 1/4 of the wave length. As illustrated in figure 19, the downwash derivative between the lifting foil and the distance x as in equation (50) varies as the cosine of the angle Θ of the orbital wave motion, between zero and 90° . The maximum wave downwash angle (not including that due to the bound-vortex circulation) is expected to be

$$\epsilon^\circ = -36C_L K_w \cos \Theta / A \quad (35)$$

where K_w as in equation (15), and where $\cos \Theta$ and ϵ = zero, at the first trough (equation 50). For example, at $C_L = 1$, a hydrofoil with $A = 5$, flying at $h = c$, $h/b = 0.2$, with $K_i = 1.3$, $K_w = 0.6$, will produce a maximum wave angle $\epsilon = 4.3^\circ$. As a matter of interest, equation (49) is properly confirmed by $1.3 = 0.6 + 0.7$.

ROACH. Another interesting point in the “wake” of a hydrofoil is the intersection of the two inboard lines originating from the foil tips. Since their angle is theoretically constant (+ or -19.5°), the distance of the intersection is

$$x = b\sqrt{2} \quad (36)$$

where $\sqrt{2} = 0.5/\tan 19.5^\circ$. This does not mean that a pair of lateral waves would meet there, thus forming a roach. As pointed out before, in realistic hydrofoil boats, the first transverse wave crest is at least one hull length behind the stern. The roach will then be between that crest and the stern, see figure 8.

- (19) Reviews of hydrofoil boat development:
 - a) Oakley, State of Art, Aerospace Engg Dec 1962
 - b) Buermann & Hoerner, Naval Engrs J. 1964 p 191.
 - c) Buller, Status of Hy'foils, Interavia 1964 p 1692.
 - d) Soviet Hydrofoils, Interavia 1965 p 420; “Raketa”, Shipbuildg & Shipping Record of Sept 1958.
 - e) Hollenberg, Review, BuWeps 1960-53; AD-289,403.
 - f) Klante, USA Development, Schiff & Hafen 1964 p 347.
 - g) Yangos, Aeronautical Engineer on Hydrofoils, AGARD Rpt 473 (1963); AD-440,901.
 - h) Jane's “Surface Skimmer Systems”, McGraw Hill.
 - i) Periodical “Hovering Craft & Hydrofoil”, London.
- (20) Characteristics with fully submerged hydrofoils:
 - a) Miller, Hydrofoils, Nav Engrs J 1963 p 835.
 - b) Boeing, PC(H) Built for US Navy, Marine Engg Log Abstracts Feb 1964; AIAA Jc Aircraft 1966 p 79.
 - c) Hook, With Surface Feelers, The Syren & Shippg Jan 1959; Shipbdg & Shipping Record 1963 p 410.
 - d) Data NW Hydrofoil Lines & G&C (1966); see (22).
- (21) Pairs of hydrofoils in tandem:
 - a) Kaplan and Sutherland, Stevens ETT Rpts 407, 410, 417, 428, 429 (1951).
 - b) Wetzel, Interference, Univ Minn SAF Lab Rpt 61 (1962) & Paper 50(B) 1965.
 - c) Van Dyck, 3-Foil Combination, Stevens Davidson Lab Rpt 975 (1963).

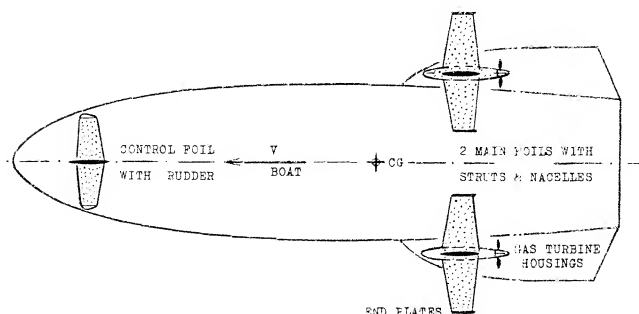
A TYPICAL HYDROFOIL BOAT might be the "Victoria" (20,d). Characteristics are as follows:

Δ	=	39	1-tons	maximum loaded weight
W	=	83,000	lb	ditto, weight in pounds
l	=	65	ft	overall length
b	=	16	ft	beam of the hull
S	=	92	ft ²	combined area of 3 foils
c	=	3	ft	average chord of main foils
b	=	12	ft	span of each of 2 main foils
A	=	4.0	—	aspect ratio of main foils
A_i	=	4.7	—	ditto, considering end plates
h	=	5.5	ft	foil submergence when flying
V	=	35	knots	cruising speed
V	=	60	ft/sec	ditto, in ft/sec
C	=	8	0.25	— design lift coefficient (cruising)
P	=	3,000	BHP	maximum continuous combined of 2
D	=	0.1	W	when cruising (calm water)
V_t	=	18	knots	speed when taking off
C_L	=	0.9	—	at takeoff (just flying)
n	=	75	—	number of passengers

THREE FOILS. A combination of three foils as in the "Victoria", each supported by a single central strut, has advantages as follows.

- The foils can readily be retracted by swinging them sideways, and lengthwise respectively, particularly in the "airplane" type configuration where the single rear foil may swing around the transom.
- In the canard configuration (as in figure 20) the forward foil controls the height (altitude), while flaps in the pair of main foils make corrective motions.
- Speaking summarily, the induced and/or wave drag of one of the 3 foils might be recovered.

Towing tank tests were undertaken (21,c) on the 3-foil configuration of the "Victoria", as in figure 20. The two main foils are hopefully located within the upwash areas outside the span of the control foil forward. Indeed, while the induced "lift angle" of one main foil tested alone, is 5.1° , there is some reduction due to upwash, that is down to 3.9° . Another test yields a differential of 1.0° ; the average is 1.1° . It should be realized, however, that the angles discussed are those of the whole system pitching in unison. When considering the control action of one of the 3 foils alone, its lift-curve slope will essentially be that of an isolated foil (with $d\alpha/dC_L = 15.6^\circ$, or $dC_L/d\alpha^\circ = 0.064$, or $d\alpha/d\delta = 0.55$, in each of the main foils, for example).



MAIN FOIL. Since the transverse wave system is a function of the Froude number, the above results only apply to the number based on longitudinal distance x , between canard and main foils

$$F = V/\sqrt{gx} = 17/\sqrt{32(3.8)} = 54/\sqrt{32(38)} = 1.54$$

where the first set of values applies to the 1/10 scale model, while the second set represents full scale conditions at $V = 54/1.7 = 32$ kts. In terms of V^2 , the distance is $x = 0.013 V^2$ (in ft). In figure 19, we are thus at $x/0.25l = 0.013/0.05 = 0.26$, where the wave downwash angle is comparatively large. For a full-scale submergence of 5.5 ft (to the foil level) and an aspect ratio of the forward foil $A_i = 4.7$, the downwash angle (in the vicinity of the center line) is estimated to amount to $d\epsilon/dC_L = -6.0^\circ$. Considering now a continuous main foil, obtained by joining the two main foils together at the centerline, their induced drag would tentatively correspond to an average downwash angle of $d\epsilon^\circ/dC_L = (1.0 + 1.0 - 6.0)/3 = -1.3^\circ$. For an aspect ratio $A = 2(4.3) = 8.6$, with a submergence ratio $h/b = 0.23$, the induced drag of the main foil (pitching together with the canard foil) would be

$$\begin{aligned} dC_{Di}/dC_L^2 &= (K_i/\pi A) - (d\epsilon/dC_L) \\ &= (1.25/27) + (1.3\pi/180) = 0.069 \end{aligned}$$

For comparison, the pair of split main foils alone, has 0.078; and the whole foil system together would have 0.072, instead of 0.065 as for the 3-foil configuration. The increment is $(0.072/0.065) - 1 = 11\%$. When cruising at $C_L = 0.25$, the increment would be in the order of 3% of the total drag. In conclusion, the advantage of a split main foil lies in its convenient retractability as well as in reduced drag.

TAKEOFF. A situation where lift and drag due to lift are strongly involved, is takeoff. A hydrofoil boat is a more or less constant-angle-of-attack type of a vehicle. So far, trailing-edge flaps have not seriously been used to increase maximum lift. In automatically controlled systems, the flaps (or possibly the whole foil) are deflected, however, particularly at lower speeds and during takeoff. Maximum lift coefficients obtained in this manner, are up to $C_L = 1$, at the moment where the keel leaves the water. Taking the "Victoria" as an example, the induced or due-to-lift angles of attack required, will then be as follows:

- The biplane-type angle (equation 20) with a K_i value (fig 9) for twice the submergence h as in cruising condition. For $K_i = 1.03$, and $A_i = 4.7$, the result is $\alpha_i = 4.2^\circ$, instead of 4.1° (as for an unlimited field of flow), and $C_{Di} = 4.2\pi/180 = 0.073$, instead of 0.071, for an assumed $C_L = 1$.

Figure 20. The 3-foil system of the "Victoria" (20,d) seen from below, tested in a towing tank (21,c)

- b) The transverse-wave angle as in equation (14). Considering that at takeoff (subscript t), $V_t = 0.5 V$, while $h_t = 2 h$ (where parameters without a subscript indicate design or cruising condition) the Froude number at takeoff $F_h = V_t / \sqrt{g h_t}$ may only be 36% of that when cruising. In case of the "Victoria", this number is $F_h = 36(1.7) / \sqrt{32(5.5)} = 4.6$; and at takeoff, $F_h = 1.6$. For such a small number, equation (14) is no longer applicable. Figure 30 in chapter XI of "Fluid-Dynamic Drag" indicates a $\Delta\alpha = 0.09 K_w (c/h) (180/\pi) = 0.35^\circ$, where $K_w = 0.25$, ---- and $c/h = 3/11$. The corresponding maximum increment of drag due to lift corresponds to $\Delta C_D = (0.25) 0.09 (c/h) = 0.006$.
- c) The additional angle required to make up for the reduced dynamic pressure at the lower panel of the "biplane" (equation 26). For $C_L = 1$, this angle amounts to $\Delta\alpha = (5/\pi)/3.7 = 0.43^\circ$; the drag increment is indicated by $\Delta C_D = 0.43 (\pi/180) = 0.007$.
- d) Regarding the angle of attack required to reach $C_L = 1$, equation (29) still has to be taken into account. The circulation-type increment of the angle is in the order of 0.6° . All the four increments are of the same order of magnitude. The combined value is $\Delta\alpha = 1.5^\circ$, in addition to the "aerodynamic" $\alpha_i = 4.1^\circ$, for $C_L = 1$.

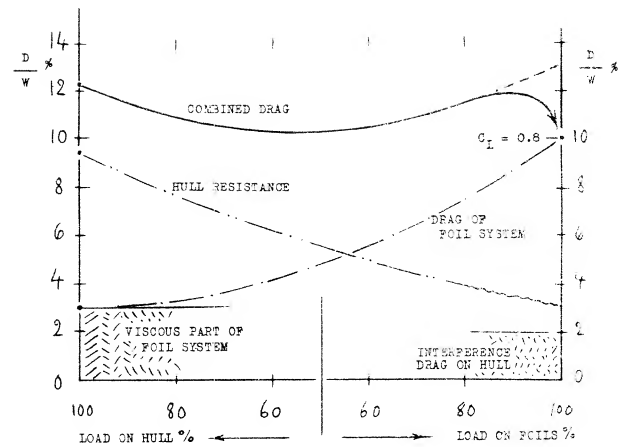


Figure 21. Drag of a hydrofoil boat similar to the "Victoria" (20,d) at takeoff speed, estimated on the basis of foil tests (figure 20) and towing-tank investigations of the hull as in (21,c).

SIZE-SPEED-SUBMERGENCE. Drag due to lift (which amounts to some 80% in the takeoff condition considered) may be more important than the angle of attack. This drag is increased to $(0.094/0.079) = 1.19$ times the biplane value, as in (a) above. Total drag at takeoff is increased some 14%. — Considering now takeoff conditions in more general terms (but still at $C_L = 1$), it follows from equations (14)(15) that

$$\Delta C_D / C_{Di} = \Delta\alpha / \alpha_i \sim (c/V_t^2) A^{1.3}; \quad \Delta\alpha \sim c A^{0.3} / V_t^2$$

and from equation (26) that

$$\Delta C_D / C_{Di} = \Delta\alpha / \alpha_i \sim b/h; \quad \text{but } \Delta\alpha \sim c/h$$

We summarize these trends by saying that at takeoff, $\Delta C_D \sim \Delta\alpha$ is primarily:

$$\begin{aligned} \Delta C_D &\sim c && \text{which means size of foils and craft,} \\ \Delta C_D &\sim 1/V_t^2 && \text{which means low design speed,} \\ \Delta C_D &\sim 1/h && \text{means submergence and sea waves.} \end{aligned}$$

- (22) The "Victoria", designed by Gibbs & Cox (New York City) for Northwest Hydrofoil Lines (W.I. Niedermair, Seattle, Wash.) built by Maryland Shipbuilding & Drydock Co (Baltimore) is operating between Seattle (Washington) and British Columbia (Canada).
- (23) Performance characteristics of hydrofoil craft:
- Hoerner, Takeoff, G&C TRpt 6 for ONR (1952).
 - Hoerner, Tests of "Sea Legs", G&C Rpt (1958).
 - Hoerner, Size-Speed-Power of Hydrofoil Craft, (26,b).
- (24) Hydrofoil boats of the surface-piercing type:
- Von Schertel, Transportation (German & Supramar) SNAME Paper 1958; Am Soc Nav Engrs J 1959 p 603.
 - Büller, Hydrofoil Boats, Ybk STG 1952 p 119.
 - Harbaugh, Development, SNAME Paper 2-h (1965).
 - Canadian FHE-400, Shippg World Shipb Aug 1964.
 - Lewis, For Canadian Navy, SNAME Paper 2-1 (1965).
 - The boat (d,e) has a foil-span/beam ratio of 3, so that it resembles an airplane in planform.
- (25) Consideration of size & speed of hydrofoil boats:
- See under "size and speed" in the first chapter.
 - Hoerner, S-S-P, Naval Engrs Journal 1963 p 915.

HULL LIFT. The lift coefficient $C_L = 1$, mentioned above for takeoff, is not necessarily the optimum (giving least drag). Rather, it is usually preferable to let a planing hull carry some of the weight, to get over the hump in the drag/speed function. The optimum distribution of load depends very much upon the resistance characteristics of the hull. Depending upon the Froude number at takeoff speed, a suitable hull may be selected, tentatively with a length/beam ratio of 4. It is shown in figure 21, how hull resistance and hydrofoil drag vary as a function of speed. The resistance is taken from towing-tank tests on a hard-chine hull with characteristics similar to those of the "Victoria". An amount of $\Delta D/W = 2\%$ is added to account for interference with the struts attached to the bottom. Starting point for the foil system is $\Delta D/W = 3\%$ representing the fully (11 ft) submerged struts plus nacelles. The foil system's

drag due to lift corresponds to $dC_D/dC_L^2 = 0.065 + 0.010$, where the second component accounts for the increase of the viscous drag (including interference). As in other configurations, minimum combined drag is obtained roughly with 50% load (weight W) each on the hull bottom and on the hydrofoils. To get from the minimum ($D/W = 10.5\%$) to the takeoff point (where the keel leaves the water, with 100% of the load on the foils) it is necessary, first to go to some 12% of drag. This is done by deflecting the control flaps of the main foils and the angle of the canard foil. The latter one can also be used to maintain the optimum angle of trim during the takeoff run (which is around 3° , keel against water-line). It can also be understood, that lift-increasing devices (special flaps) are not needed in hydrofoil boats. The induced drag would increase the hump drag ($D/W = 12\%$). Of course, acceleration both in longitudinal and in vertical direction, require some additional thrust, not thinking of sea waves against which the boat may have to take off. In fact, the full-throttle thrust of the "Victoria" at 19 knots, is some 17,000 lb, which is almost $T/W = 20\%$. With a margin above the hump of some 6000 lb, the 87,000 lb of fully loaded weight can be accelerated by

$$\Delta T/W/g = 6000(32)/87,000 = 2.2 \text{ ft/sec}^2$$

The control system can then be used (by way of an altimeter) to make the boat "jump" up to the cruising level, corresponding to a foil submergence of 5.5 ft. As pointed out in chapter XI of "Fluid-Dynamic Drag", resistance then reduces; and the minimum obtained in the "Victoria" is $D/W = 9\%$, at 26 or 27 knots. At the maximum continuous speed of 36 kts, the drag ratio is $D/W = 10\%$. A speed of 39 kts can be obtained (in calm water) by reducing submergence to 3 ft.

Figure 22. Geometry and forces during the steady-state turn of a hydrofoil craft.

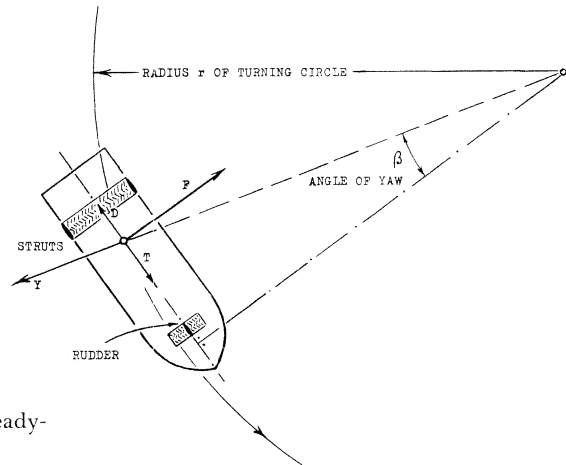
TURNING. When turning, any vehicle needs a centripetal force Y to resist or balance the centrifugal force

$$Y = 'M'V^2/r = 2WV^2/gd \quad (37)$$

where $'M' = W/g = \text{mass}$, and $d = 2r = \text{diameter of the turning circle}$; see figure 22. In airplanes...this force is provided by a component of the wing's "lift", obtained by banking properly. In displacement ships as in airships, the lateral force is the lateral "lift" (or "resistance") of the hull (including stem, rudder, vertical fins) as described in the "slender body" chapter. In hydrofoil craft, banking is theoretically possible. Indeed, the surface-piercing type is supposed to bank in a manner similar to that of certain more or less planing motorboats (having a suitably dihedral bottom). Most of the boats with fully submerged hydrofoils are turning "flat", however, thus avoiding broaching of the outside foil tips (particularly in sea waves). In this case, the struts have to provide the lateral lift force Y . Solving equation (60) for the turning diameter:

$$d = 2r = 2'M'V^2/Y = 2V^2/a = (2/g)V^2/(a/g) \quad (38)$$

where the hydrodynamic force $Y = 'M' a$, and $a = \text{lateral acceleration}$.



SURFACE-PIERCING hydrofoil boats, particularly of the Schertel-Supramar type (24,a,c) are at this time operating in larger numbers, in passenger-carrying services, primarily in sheltered waters. Considering, however, military applications in open, or at least in coastal waters, there is only a limited advantage in such boats, over conventional patrol or motor-torpedo boats, in regard to speed, stability and riding comfort in a sea-way. To point out the importance of seakeeping in these and other hydrofoil boats, it may be mentioned that the world-speed record in so-called hydroplanes (gliding, riding or flying on 3 points over perfectly calm water) is around 200 mph (some 170 knots), while seaplanes are available, or could be built again, with minimum speeds, say around 100 kts. In other words, the problem is to go continuously fast in water which is not calm, but may have waves up to 6 ft in height (crest to trough, as in sea state 4).

LATERAL FOIL FORCES are essentially proportional to the angle of yaw or sideslipping (which is a necessity in any turn). The required forces can be produced by struts, by dihedral of the foils, and/or by end plates attached to the foils. For the latter, see the "wing" chapter. Lateral forces of "V" shaped foils can be found in the chapter on "directional stability", under "V" tails. Regarding surface-piercing dihedral hydrofoils, a metacenter (the lift center) different from the one responsible for roll stability must be considered. This is indicated by dashed lines in figure 16. It is seen that in the particular emergence depicted, the craft is not balanced (it will heel outward). This type of boat has to slow down before making a turn, so that a larger wetted span is obtained. The lift center can also be raised by replacing the apex of the "V" shape by a horizontal piece of foil.

STRUT FORCES. Boats with fully submerged hydrofoils need vertical struts (with lateral area) for turning (and stability). As a tolerable level of acceleration in equation (61), $a = 0.2 g$ may be assumed. Disregarding ventilation, a surface-piercing strut is a "lifting wing", with the hydrofoil below acting as a large end plate. A pair of struts could also be considered to be not only a biplane, but even a "boxplane". As an example, we will assume a single-strut configuration (similar to those of the "Victoria") with dimensions as follows.

$$\begin{aligned} A &= 4.5 = \text{aspect ratio of hydro foil} \\ c &= c = \text{chord of foil and strut} \\ h/b &= 1/3 = \text{foil submergence ratio} \\ h/c &= 1.5 = \text{wetted aspect ratio of strut} \end{aligned}$$

The surface flow pattern past a yawed, lateral-lift producing strut is a function of the Froude number $F_c = V/\sqrt{g c}$. Within the range of high numbers (as we have them in hydrofoil struts) the theory of antisymmetrically twisted wings (28,d) predicts an effective aspect ratio of the strut equal to that of the submerged part. Considering the foil to be an end plate with (h/b) (strut) $= (b/h)$ (foil) $= 3$, the effective ratio is theoretically doubled; thus $A_i = 2(1.5) = 3$. The flow pattern at the water surface shows some water piled up at the pressure side, and a depression (hollow) forming along the suction side. — Experimental lift coefficients of a strut are plotted in figure 23. Evaluation of these and other data (on surface-piercing foils) leads to the conclusion that a piece of the strut "at" the water surface equal to at least Δh or $\Delta b = 0.10 c$, is not producing lift (on account of spray?). This means that the effective area is reduced as well as the effective aspect ratio. According to the "wing" chapter, the lateral angle required, corresponds to

$$d\beta^\circ/dC_{lat} = 11 + (11/A_i^2) + (26/A_i) \quad (39)$$

In a similar manner, for aspect ratios below unity (as in the "small aspect ratio" chapter):

$$dC_{lat}/d\beta^\circ = 0.8(\pi^2/360)A_i = 0.022 A_i \quad (40)$$

for the forces of the strut. As seen in figure 23, the two equations describe very well the tested forces. Regarding the non-linear component of lift, it is reasoned that it cannot develop at the piercing point of the strut. This component might then be approximated by

$$\Delta C_L = \sin^2 \beta / A \quad (41)$$

Figure 24. Lateral forces of surface-piercing struts (around zero angle of yaw) as a function of their submerged aspect ratio.

(28) Lateral forces of hydrofoil boats when turning:

- Schwanecke, Surf-Piercing, Schiffstechnik 1957.
- Dingee, Skids Strut, Stevens ETT Rpt 472 (1952).
- Hoerner, Turning Analysis, included in (23,b).
- Chey & Kowalski, Testing of Strut & Strut-Foil Interference, Stevens Davidson Lab Rpt 936 (1963).

LIMITATIONS. It is seen in figure 23, that the lift (lateral force) of one of the two struts breaks down at $\beta = 14^\circ$, from $C_{lat} = 0.3$. This breakdown due to ventilation, is discussed in the next section. Other limitations as to turning, are the rolling moment to be balanced by "aileron" deflection in the hydrofoils, the effectiveness of the rudder(s) (attached to, or part of one or more struts), and the power required to overcome the increased drag (due to lateral-force-producing struts, aileron deflection, and foil-strut interference,

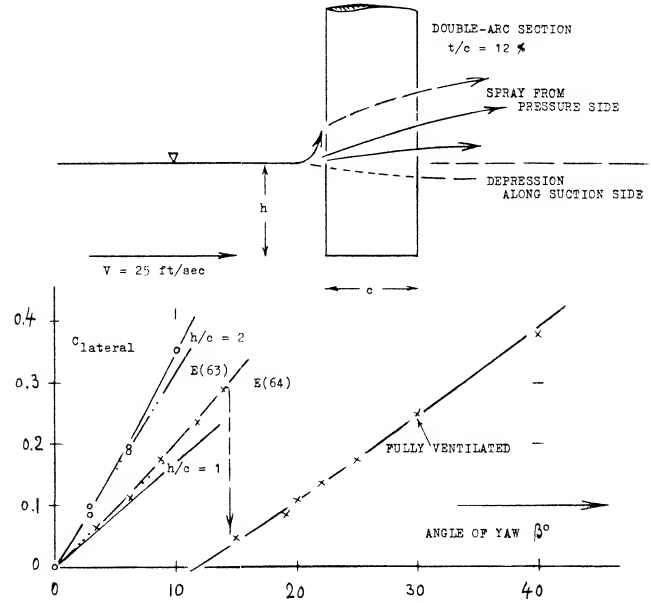
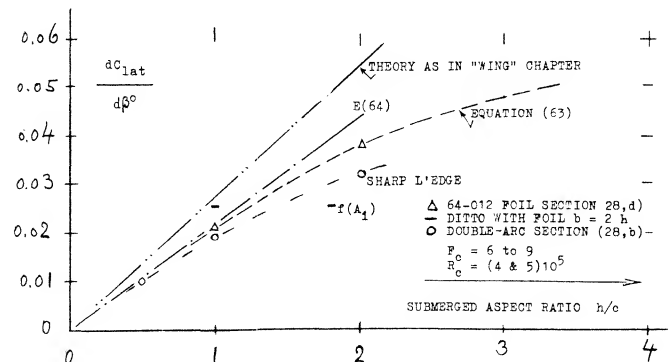


Figure 23. Lateral forces originating in a surface-piercing strut, tested (28,b) at $F_c = 9$, and $R_c = 4(10)^5$, in a towing tank.

INTERFERENCE. The lateral-force derivatives (around $\beta = 0$) of struts from two different sources, are plotted in figure 24, as a function of their submerged aspect ratio. The theoretical functions (equations 63 and 64) agree well with the tests on an airfoil-type section. A sharp-edged section evidently loses some suction lift. Considering a hydrofoil attached to the lower end of the strut to be an end plate, the K_i factor as in figure 9 could be used to increase the *effective* aspect ratio. As shown by the pair of single points (—) in figure 24, there are considerable interference losses, however, at the strut-foil juncture, thus reducing the force slope



4. LIFT-CAVITATION-VENTILATION

The basic principles of cavitation are given in Chapter I and in "Fluid-Dynamic Drag". As the speed is increased, cavitation will be encountered and the lift of the foil will be reduced. Thus, lift will be obtained on an airfoil in spite of cavitation. At speeds lower than cavitation would be expected, it can be shown that with proper ventilation a finite cavitation number can be simulated.

Incipient Cavitation. The critical cavitation number is that where at a particular point on the surface of a body or wing the local static pressure reduces to that of vaporization. This means that

$$p_{min} - p_v = q C_{pmin} + p_a - p_v = 0 \quad (42)$$

or:

$$C_{pmin} = -(p_a - p_v) / q = -\sigma_a \approx -195/(V, m/s) \quad (43)$$

Vice versa, the incipient cavitation number is

$$\sigma_i = -C_{pmin} \approx 195/(V, m/s) \quad (44)$$

and the critical speed is

$$\begin{aligned} V_{crit} &= \sqrt{195/\sigma_a} \text{ in (m/s)} \\ V_{crit} &= 26/\sqrt{\sigma_a} \text{ in knots} \end{aligned} \quad (45)$$

Minimum Pressure. The minimum pressure coefficients are known for body shapes such as foil sections in particular, and thus the critical speed where cavitation can be expected can be found in equations 44 and 45. In "Fluid-Dynamic Drag", C_{pmin} for zero lift, as well as for optimum camber, are given as a function of the lift coefficient. Both of these functions are quoted in the "compressibility" chapter.

$$C_{pmin} = -2.1 (t/2x) @ C_L = 0 \quad (46)$$

where x = location of the maximum thickness (for example at 40% of the chord). Also for properly cambered sections:

$$\Delta C_{pmin} = -K C_{Lopt} \quad (47)$$

where K between 0.75 (for thickness locations near 30% of the chord) and 0.85 (for locations around 50% of the chord). Adding the two components the minimum

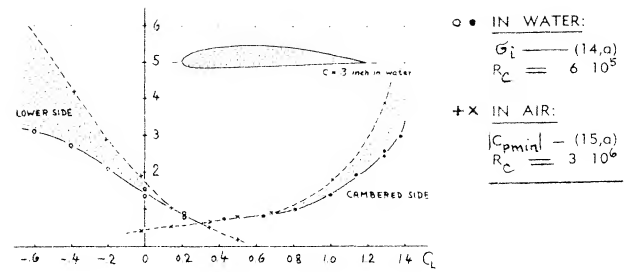


Figure 25. Comparison of σ_i and C_{pmin} for 4412 section, tested in water and wind tunnel, respectively.

pressure at the upper side of foil sections or hydrofoils is obtained at and around their design lift coefficient. As an example, the 4412 section is shown in figure 25, both tested for pressure distribution in a wind tunnel (29,a) and for incipient cavitation in a water tunnel (30,d). At lift coefficients, at least between 0.2 and 0.6, complete agreement is found. This means that cavitation readily starts when the minimum pressure reduces to the level of the vapor pressure. In a water tunnel cavitation is achieved either by increasing the speed (the q in C_{pmin}) or by reducing the pressure within the tunnel as a whole (the p_a in σ).

Pressure Peaks. There is a mathematical relationship not only between the minimum pressure coefficient of any foil section, but also between the critical Mach number (in air) and the critical cavitation number and/or the critical speed (in water). Both these critical speeds can be exceeded, however, without any loss of lift, when the minimum pressure appears only in a more or less narrow peak. Since the reasons and extent of these transgressions are different, it is not possible in the presence of peaks to make correct predictions in regard to cavitation, neither on a theoretical basis nor from experimental evidence in air. As shown in "Fluid-Dynamic Drag" the delay as found around the leading edges of foil sections seems to correspond to

$$\Delta \sigma_i = -0.08 C_{pmin}^2 \quad (48)$$

An example is shown in figure 26. Within a "bucket" similar to that as found in laminar-type airfoil sections, the cavitation number (indicating the onset of cavitation) agrees with the minimum pressure coefficient found as the sum of equations 46 and 47. Outside the bucket the cavitation number increases at a rather high rate. This means that cavitation starts at a much lower speed. If, for example, $\sigma_i = 2$ (at the upper side of a foil section, at $C_L = 0.9$) instead of $\sigma_i = 0.5$ (at C_L around 0.4) then the critical speed in open water will be reduced in accordance with equation 45 roughly from 40 to $\sqrt{0.5/2} \cdot 40 = 20$ knots.

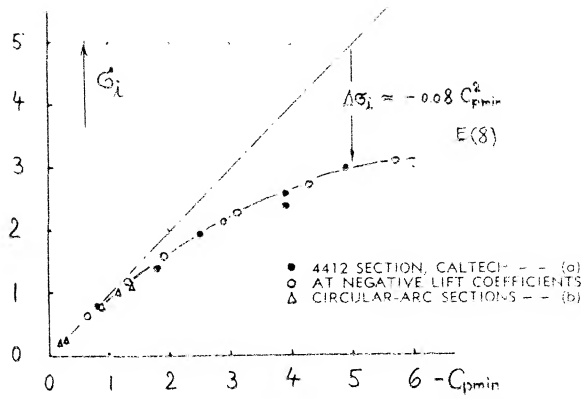


Figure 26. Statistical analysis of the "delay of cavitation in peaked pressure distributions (14).

Delay of Cavitation. Even a sharp-edged circular-arc section shows a "bucket", figure 17, Chapter X of "Fluid-Dynamic Drag", between $C_L = 0.4$ and 0.6 . To explain the delay of incipient cavitation it can first be said that the theoretically expected extremely high pressure peaks around a sharp edge do not really develop. However, as indicated by equation 48 there is definitely a delay even when the pressure is reduced to below the level where the water is supposed to start boiling. To understand this statement, it may be remembered that water tunnels are usually pressurized in a manner similar to the fluid-dynamic conditions of a submarine. To explain the delay, it is suggested that heat transfer is necessary. Another explanation is simply that any vapor bubble needs time to grow around a microscopic nucleus. At any rate, time is short for a particle of water being exposed to the low pressure within a peak of the distribution. Since that time is proportional to (x/v) , where x is a small fraction of the chord, the delay of cavitation as in equation 48 may also depend upon size and speed of a hydrofoil. If this is true, we may be able to correlate experimental results on the basis of a Froude number $F_c^2 = (V^2/gc)$. As illustrated by the theory (32,d) and figure 27, considering the time element it can be expected that a full-scale hydrofoil would cavitate more readily than a model in a towing tank. Considering a pressurized water tunnel, the difference would be even more pronounced.

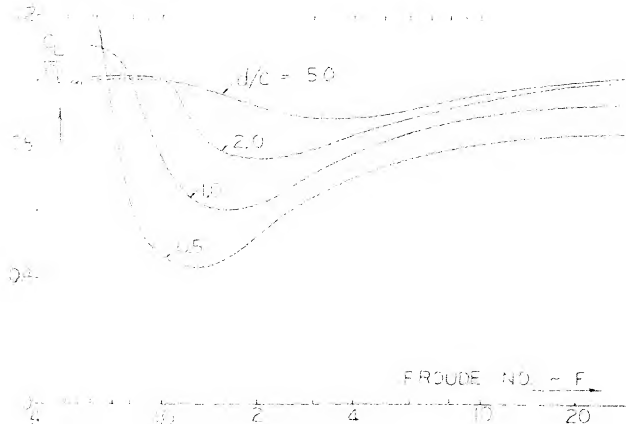


Figure 27. Froude number and depth chord ratio effect on the lift ratio of a submerged flat plate (32,d).

Flat Plate. As shown in (32,a) and "Fluid-Dynamic Drag" and in conjunction with equation 15, the basic lift slope of a two dimensional flat plate is different depending on the operating condition. For instance, if the plate is fully wetted

$$dC_L/d\alpha = 2\pi \quad (49)$$

However, if the foil is planning

$$dC_L/d\alpha = \pi \quad (50)$$

On figure 27 a factor K is given showing the change of lift slope as a function of distance to the surface. A foil that is operating at $\sigma = 0$, supercavitating, has a lift slope $1/4$ that of the fully wetted foil or

$$dC_L/d\alpha = \pi/2 \quad (51)$$

Equations 49 to 51 apply only at $\sigma = 0$ as they are based on linear theory.

Aspect Ratio Effect. The effect of aspect ratio can be determined from the equation

$$K = C_{L3D}/C_{L\infty} \quad (52)$$

In (32,b) it was shown that K is only weakly dependent on the cavitation number.

Based on wing theory

$$dC_{L3D}/d\alpha = a_0 A/(A + 1 + (a_0/\pi))$$

Using equations 49 to 52 the lift curve slope becomes for wings with a finite aspect ratio

$$a) \text{ fully wetted foils } a_{3D} = 2\pi A/(A + 3) \quad (53)$$

$$b) \text{ planning foils } a_{3D} = \pi A/(A + 2) \quad (54)$$

$$c) \text{ supercavitating foils } a_{3D} = \pi A/(2A + 3) \quad (55)$$

Test data for a flat plate with $A = 3.25$ from (33,a) is given on figure 28. At very low angles of attack and cavitation number σ approaching zero, the lift curve slope is nearly the same as the noncavitating case. However, as soon as the cavitating bubble begins to form the lift slope is reduced. This occurs at angles of attack above $\alpha = 6^\circ$ for wings with an aspect ratio of 2 to 3. At angles above 6° the lift slope is described with good accuracy by equation 55, figure 29, as under these conditions the flow is nearly fully cavitating.

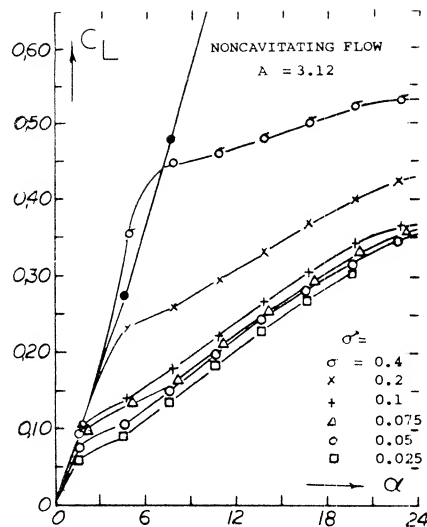


Figure 26. Flat plate of aspect ratio of 3.12 tested in a water tunnel (33,a).

Cavitation Number Effect. At cavitation numbers above zero it was shown (32,e) that the normal force coefficient is increased by $\Delta C_N = \sigma$. Evaluation of the data of (33,a) indicates that

$$C_L = .8 \sigma \quad (56)$$

Based on this analysis it would appear as in the case of small aspect ratio wing, Chapter XVII, that the flow about the edges is of importance.

Supercavitation. Since cavitation is no longer avoidable in conventional foil sections at the higher speeds, the idea was conceived to accept cavitation at the upper side and to make the best of it by forming the lower side properly. Figure 30 presents one such supercavitation section. Increased drag, a shortcoming of such sections is the fact that in a hydrofoil boat, for example, the flow pattern has necessarily to go through a transition from fully attached or fully separated to fully cavitated. Another disadvantage is found in the fact that drag can take place within certain boundaries of the lift coefficient. Even in marine propellers where cavitation is a well-known plaque, no supercavitating designs seem to be in practical operation some ten years after their invention.

- (30) Conventional foil sections with incipient cavitation:
- (a) Johnson (BuShips), Hydrofoil-Strut Arrays, Paper SNAME (Southern California) 1964; see Marine Technology 1964.
 - (b) King, Influence of Sweepback, NACA RM L 52J10.
 - (c) Kermeen; 4412, Walchner and 66-012, CalTech Hydro Rpts 47-5 and 7 (1956).
 - (d) Daily, 4412 Cavitating, ASME Transactions 1949 p 269.
 - (e) Hoerner, Inception on Foil Systems, G&C TRpt 8 for ONR (1952).

FLUID DYNAMIC LIFT

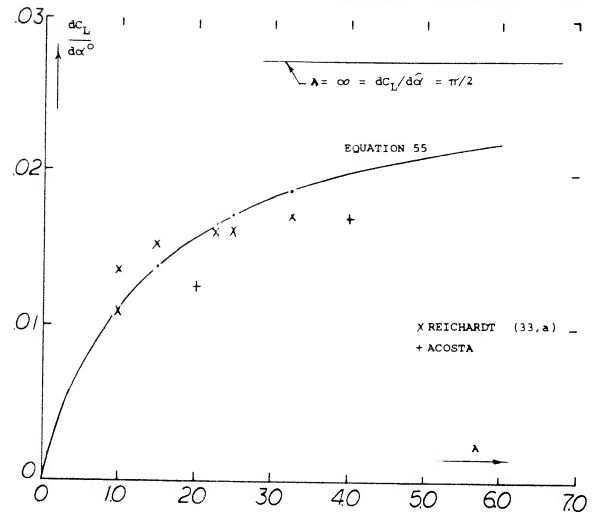


Figure 29. Lift curve slope for cavitating rectangular flat plate wings as a function of aspect ratio.

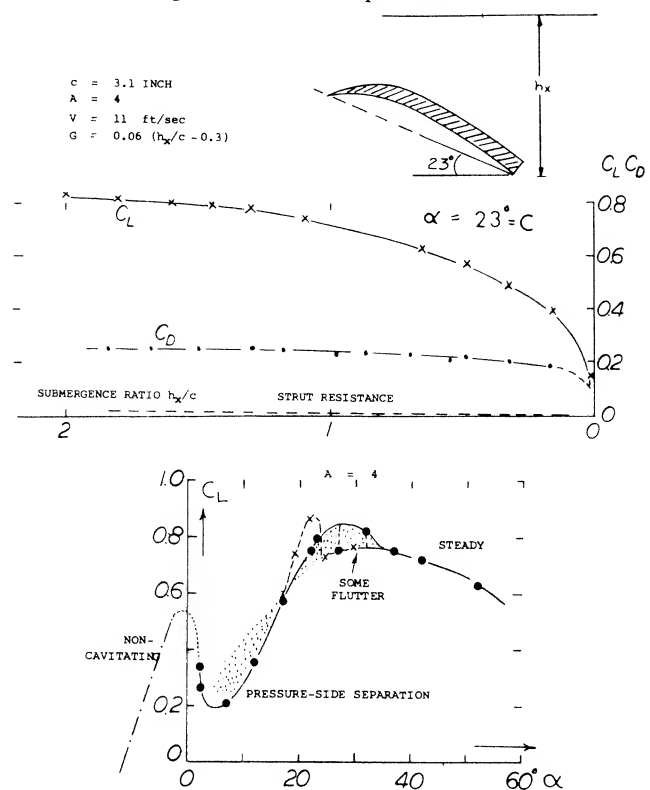


Figure 30. Lift characteristics of a supercavitating foil including effects of submergence.

- (31) Structure and rudder sections with incipient cavitation:
- (a) Macovsky, prediction for $c/t = 6$ Sections, DTMB Rpt 879 (1948).
- (32) Supercavitating Hydrofoils Theory:
- (a) Acosta, Three-Dimensional Supercavitating Hydrofoils, Ca. Inst of Technology to ONR 1974.
 - (b) Nishujama, Theory Hydrofoils Finite Span, ZAMM Vol 50, 1970.
 - (c) Acosta, Hydrofoils and Hydrofoil Craft Annual Review Fluid Mechanics, Vol 5 1973.
 - (d) Hough, J. Ship Res. 13:53-60 (1969)
 - (e) Betz, Influence of Cavitation Upon Ship Propellers, Proc. 3rd International Congress, Mechanics Stockholm 1930 Vol. 1 page 411.
- (33) Finite Hydrofoil Wings
- (a) Reichardt, Rectangular Wings with Cavitation, Max-Planck-Institute for Stomungsforschung Gutlingen 1967.

CHAPTER IX — CHARACTERISTICS OF AIRPLANE CONTROL SURFACES

To control motion and position of an airplane within the air space, forces applied at will, and at suitable locations, are obviously required. Such forces could be lifting or dragging; but usually they are of the lift-producing or normal-force type. This means that the forces in the wing panels or of the horizontal and vertical tail surfaces are changed by means of suitable devices so as to obtain and to control desired motions and positions of the aircraft. The almost exclusive control device is the “flap”. Aerodynamic characteristics of control flaps are thus the subject in the following text. Ailerons (and spoilers) are described and discussed in the chapter on “roll control”, however.

I. GEOMETRY OF CONTROL FLAPS

DEFINITIONS. A control flap is a portion of the foil section (or of the control surface) near the trailing edge, hinged to the “fixed” portion forward, so that it can be deflected up and down (or right and left, respectively) thus changing normal force and/or lift. It is useful to realize in this respect, that trailing-edge wing flaps (used when landing an airplane), ailerons, elevators, rudders, are basically one and the same device, controlling circulation of wing or tail surface, respectively. It is, therefore, suitable to give these various parts of an airplane a common name; that name is “flap”. We may also speak of “control flaps”; and it is then obvious that we primarily think of those three devices with which all conventional airplanes are “controlled”, the elevator, the rudder and a pair of ailerons.

- (1) As explained in the chapter on “straight wings”.
- (2) -- Theoretical characteristics of hinged systems:
 - a) Glauert, Relationships, ARC RM 1095 (1927).
 - b) Perring, Multiple Flaps, ARC RM 1171 (1928).
 - c) Keune, Basic, Lufo 1936 p 85 & 1937 p 585.
 - d) Flügge-Lotz, Hinge Gaps, ZWB FB 847 & 954.
 - e) Ames, Flaps and Tabs, NACA T Rpt 721 (1941).
 - f) Swanson, Aspect Ratio, NACA T Rpt 911 (1943).
 - g) Lyons, Lift of Tail Surfaces, ARC RM 2308 (1950).
 - h) Bryant, Correlation, ARC RM 2730 (1955).
- (3) Most of the analysis in this chapter deals with the linear portions of the various functions.

FLAP CHORD. The “useful” chord of a flap measures aft of its hinge axis, and is usually defined by the chord ratio c_{flap}/c , where “f” is from “flap”. Foil-section forces (produced by flap deflection) are always referred to total chord and “wing” area. In configurations where the flap chord (or the chord ratio c_{flap}/c) is not constant across the span, the area ratio S_{flap}/S might be substituted for the chord ratio. Since aerodynamic characteristics are usually not a linear function of flap chord, such substitution can only be an approximation, however.

2. LIFTING CHARACTERISTICS OF FLAPS

HORIZONTAL TAIL SURFACE. Experimental results of a horizontal tail surface are presented in *figure 1*. As a function of the angle of attack, the lift varies corresponding to a lift-curve slope dictated by the aspect ratio (1). Deflection of the elevator by plus or minus 8° , simply shifts the $C_L(\alpha)$ function up or down, respectively, by a certain differential. Of course, at higher angles of attack, separation takes place: (a) from the suction side in general (see figure 1-a, at $\alpha \approx 15^\circ$) as in other foil sections; (b) from the suction side of the elevator as in figure 1-a, at $\delta = 8^\circ$ and $\alpha \approx 6^\circ$, or in figure 1-b, at $\delta > 14^\circ$. As a function of elevator deflection, as in figure 1-b, lift increases (within the range of small and moderate angles) in linear proportion to the elevator angle. For angles of attack different from zero, the lift function is shifted up and down, respectively, in a manner similar to that described above. At deflection angles exceeding 12° or 15° , flow separation takes place from the suction side of the elevator. It is evident, however, that the lift coefficient continues to increase (at a lesser rate) after passing through a more or less pronounced “dip” (3).

CONTROL EFFECTIVENESS. Through comparison of the results in parts (a) and (b) of figure 1, it is found that deflection of the elevator produces a certain lift differential per degree, equal to 71% of that due to angle of attack. In other words, the "effectiveness" of that particular elevator, i.e., the lift produced by the flap in comparison to that of the surface as a whole, is

$$(dC_L/d\delta)/(dC_L/d\alpha) = 0.037/0.052 = 0.71 \quad (1)$$

In practical operation (when used as part of an airplane) the elevator is usually not expected to produce lift. Rather, its *basic function is to cancel the lift* produced by changes in the angle of attack (during maneuvers or when trimming the airplane to a different speed). It is, therefore, suitable to consider results such as in figure 1, at $C_L = \text{constant}$. Plotting, for example for $C_L = \text{zero}$, the elevator angle " δ ", required to *compensate* for the angle of attack " α ", as in figure 1-c, a slope

$$d\alpha/d\delta = 0.71 = -(dC_L/d\delta)/(dC_L/d\alpha) \quad (2)$$

is obtained. This slope is identical to the effectiveness ratio in equation (1), except for the sign. In this text, $d\alpha/d\delta$ is usually considered to be the effectiveness ratio, and thus used with a positive sign.

THEORY (2). Below $\delta = 15^\circ$, figure 1 (and the later figure 17) show linear variations of the parameters plotted. It is within such limited regions of δ and α , that theory can make useful predictions as to forces and motions produced by flaps (3). The lift of a foil section is controlled by the angle of attack and by direction or location of the trailing edge (Kutta-Joukowski principle). That location can be changed by camber or by deflection of some portion of the section adjoining the trailing edge. Therefore, when deflecting the elevator as in figure 1, or the flap as in figure 3, at constant angle of attack of the forward portion of wing or tail surface, an increment of lift or normal force is produced. In the absence of skin friction, boundary layer and separation, the lift force increases in proportion to the angle of deflection " δ " (or possibly in proportion to the sine of that angle). The deflection angle is thus the equivalent of a certain variation of the angle of attack, as indicated above by the ratio $(d\alpha/d\delta)$. This ratio is a function of the chord ratio c_f/c . The complete theoretical function (but not the experimental function) can be approximated by

$$d\alpha/d\delta = \sqrt{c_f/c} \cdot 4/\pi \quad (4)$$

CHORD RATIO. Because of the presence of the boundary layer, particularly near the trailing edge, $d\alpha/d\delta$ ratios evaluated from experiments, are always less than indicated by theory. Experimental results (at small and/or moderate angles, of deflection and/or attack) were collected from various sources; they are plotted in figure 2. Practical results are as follows:

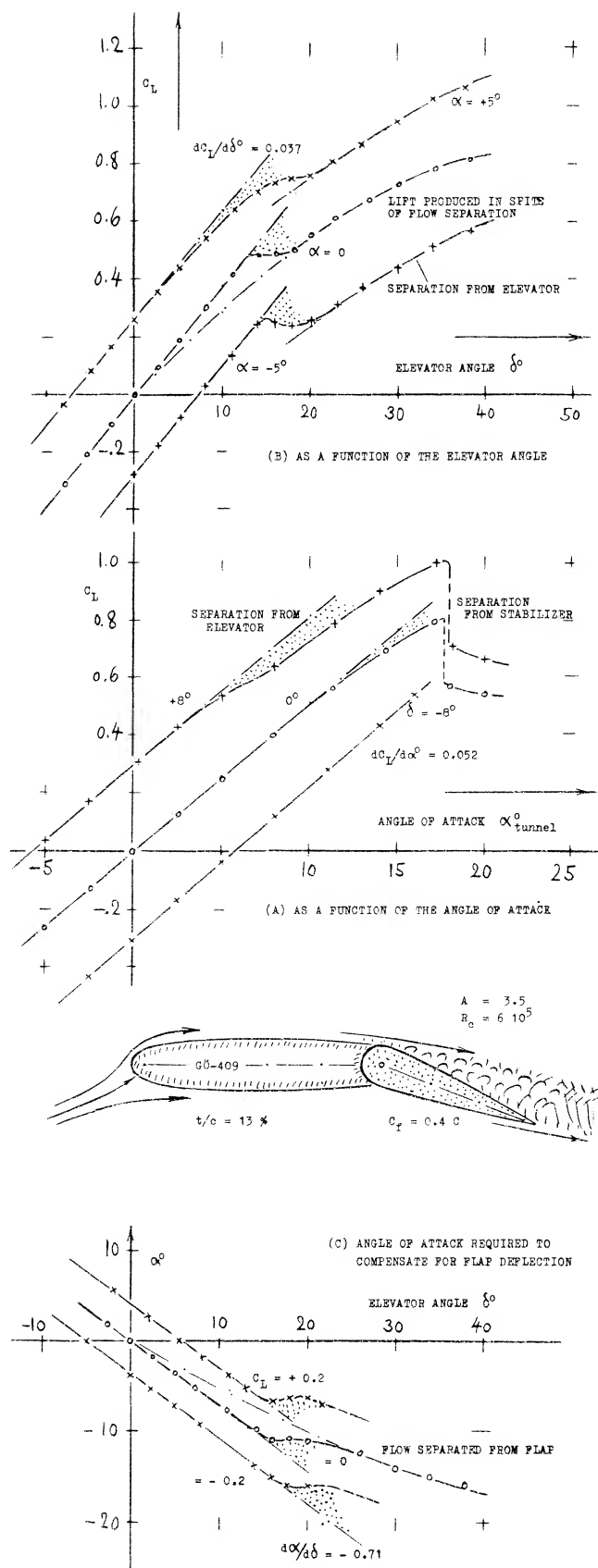


Figure 1. Lifting characteristics of an isolated rectangular horizontal tail surface tested (4,c,d) in open wind tunnel.

- The loss of effectiveness (in comparison to the theoretical function) increases as the size of the deflected part of the chord reduces, in relation to the boundary-layer thickness.
- At $c_f/c \rightarrow$ zero, the experimental function apparently joins with that corresponding to fully separated flap flow.
- Theory presents an upper limit to the values of $d\alpha/d\delta$; there is no simple function to express the experimental results as plotted.
- The simplest configuration, suitable to obtain high $d\alpha/d\delta$ ratios, is that of plain flaps (without, or with minimum gaps).
- Control effectiveness is reduced by section thickness and particularly by the trailing-edge "wedge" angle.
- When tested in presence of a fuselage, elevators do not necessarily have reduced $d\alpha/d\delta$ ratios (5), although the lift-curve slopes, $dC_L/d\alpha$ as well as $dC_L/d\delta$, are usually reduced.
- Overhanging-nose balance usually *increases* the effectiveness ratio.
- Hinge or control gaps (ahead of the flap) usually reduce effectiveness.

Most of these parameters (and others) will be discussed further under corresponding headings.

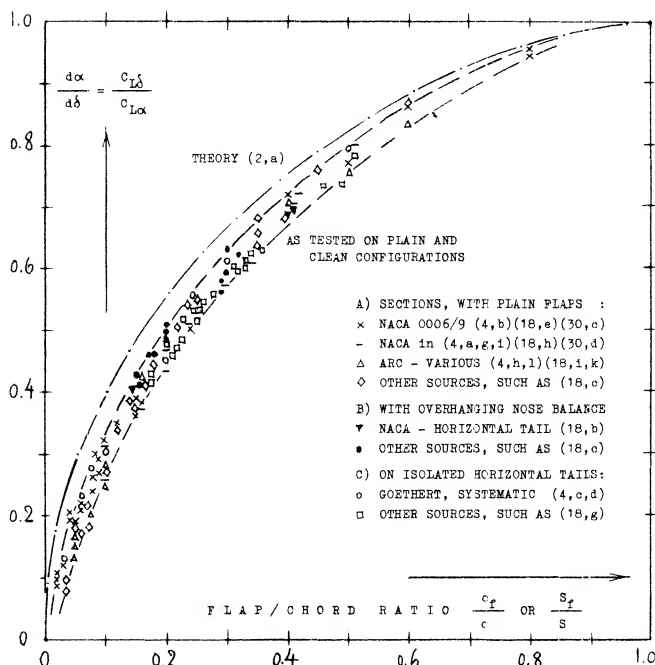


Figure 2. Effectiveness ratio of various types of trailing-edge control flaps (elevators, rudders, ailerons) as a function of their chord ratio.

Lower ratios correspond to higher thickness ratios, wider control gaps, surface roughness and lesser R 'numbers, while higher ratios are the consequence of slender sections, sealed gaps and thinner boundary layers.

ASPECT RATIO. The lift-curve slope of a tail surface, such as that in figure 1, is obviously a function of its aspect ratio. Corresponding to the presence of a certain hinge gap ahead of the flap, of balancing devices and of brackets, levers and rods necessary to support and to operate the flap, that lift-curve slope is usually several % smaller than that of the plain and smooth airfoil. It is then expected and assumed that the slope of the lift due to flap deflection $dC_L/d\delta$ changes with the A 'ratio in the same manner as $dC_L/d\alpha$. This assumption is sufficiently accurate, for practical purposes. Conditions at small A 'ratios where the principle no longer holds, are discussed later.

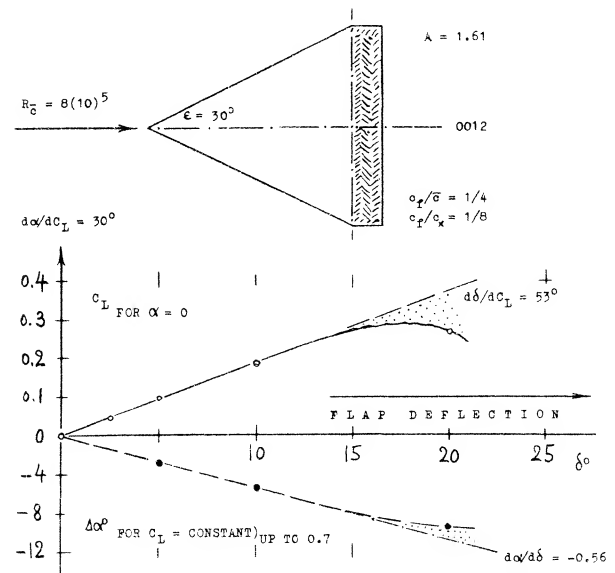


Figure 3. Lift due to, and angle of compensation of a rectangular flap attached to the trailing edge of a delta wing (6).

WING SHAPE. Generally, it makes little difference, in regard to the lifting characteristics of control flaps, whether the shape of the fixed part of a tail surface is rectangular, tapered or elliptical. As an extreme extreme example, a delta wing is presented in figure 3, equipped with a constant-chord trailing-edge flap. The lift-due-to-flap derivative is constant up to $\delta = 12^\circ$ or 13° . The effectiveness ratio $d\alpha/d\delta = 0.54$, found constant between $C_L = 0$ and 0.7 , agrees with the average in figure 2, at $S_f/S = 0.25$. Very nearly the same ratio was also found for a delta wing with $A = 3.95$; see the two points in figure 10.a. Since the lift-curve slope of such wings, with the two tips cut off (as in figure 3) can be as high as that of same-aspect-ratio rectangular or tapered wings, such highly tapered shapes, *with straight trailing edges*, seem to be promising when used as tail surfaces.

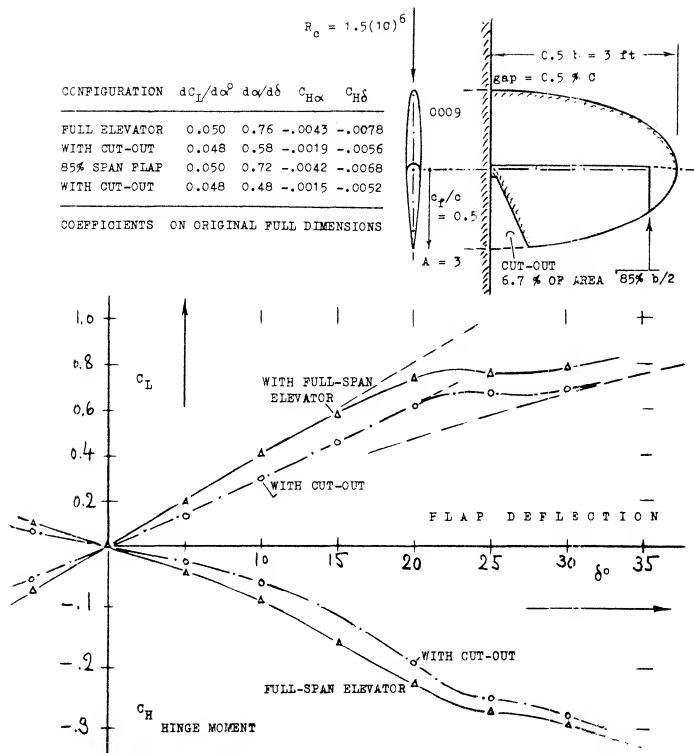


Figure 3/4. Experimental investigation (4,n) of half-span horizontal tail surface with cut-out and part-span elevator.

FLAP-SPAN RATIO. Control flaps do not always have a constant chord (or chord ratio) across the span, and they may not always be full-span. When averaging the flap-chord ratio, the simplest procedure is to substitute the area ratio S_f/S . It must be kept in mind, however, that lift properties (such as $d\alpha/d\delta$) are roughly proportional to $\sqrt{C_f}$, while hinge moments roughly correspond to $(c_f)^2$. Using S_f/S can thus yield misleading results, particularly in configurations where the flap span is less than the overall span of the control surface. Control flaps may be cut off or "inset" at the outer ends, or they may be cut out elsewhere (such as the elevator in figure (3/4), for example). In part-span condition, it will be best (if still approximate) to determine derivatives on the basis of a suitable average chord ratio, and to multiply the result (lift, longitudinal moment, hinge moment) with the span ratio b_f/b . Analysis in (2,g) suggests that, for example, a flap on one half span only, is expected to have 0.5 lift effectiveness. A flap over half the span in the center of the "wing" may result in 0.6 effectiveness, while a pair of outboard flaps, covering together half of the span, will only produce 0.4 times the effectiveness of a full-span flap. In other words, a cut-out in the center of a horizontal tail takes away more control effectiveness than same-size cut-offs at the lateral ends. It appears, however, that the rear lateral corners of any lifting surface have an importance for the magnitude of lift produced, which is not recognized by theory. Therefore, any deviation from rectangular flap shape, by cutting off or rounding the rear corners, is found (4,c) to reduce lift, pitching and hinge moments.

3. PITCHING MOMENTS DUE TO FLAPS.

Flap/Chord Ratio. Deflection of a trailing-edge flap produces an additional longitudinal moment identical in character to the zero-lift coefficient C_{m0} of foil sections. In other words, this moment is independent of lift and reference axis. Figure 4 shows the slope of the coefficient, plotted against the chord ratio. The theoretical moment displays a maximum at $c_f/c \approx 0.26$. The experimental values are all smaller than predicted, because of presence and growth of the boundary-layer. Pressure losses encountered near the trailing edge have to be made up by increased lift forces near the leading edge. In the vicinity of $c_f/c = 0.3$, tested moments are thus between 75 and 80% of the theoretical values.

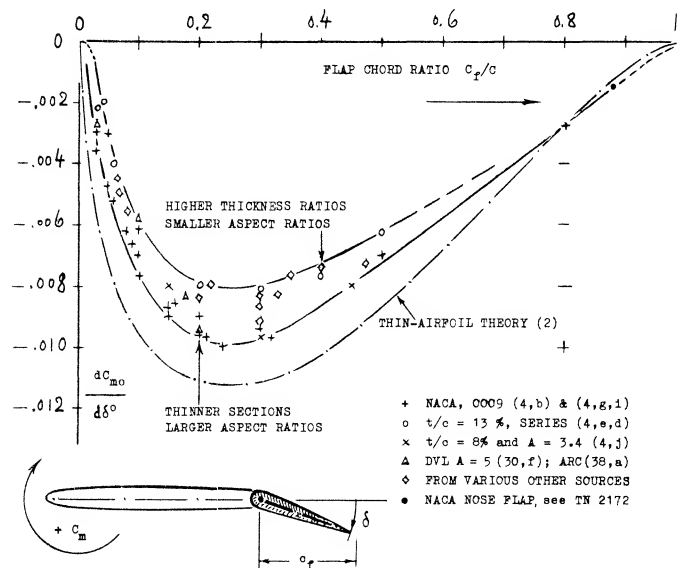


Figure 4. Pitching moment due to trailing-edge flap deflection as a function of chord ratio.

COMPARISON WITH CAMBER. Deflection of a flap represents a variation of section shape similar to camber. Considering position and direction of the trailing edge, 1 degree deflection of a flap hinged at 0.5 of the foil-section chord, represents geometrically $0.25/57.3 \equiv 0.43\%$ camber. The corresponding value of C_{m0} (as found for $x/c = 0.5$, in the "foil section" chapter) is $0.025 (0.43) \approx 0.010$, while figure 4 indicates a slope of 0.007. The difference is due to the different type of curvature of the camber line; the tangent angle of that line at the trailing edge, is usually larger in a cambered foil section.

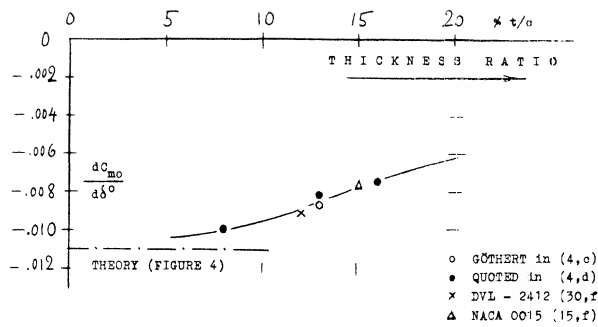


Figure 5. Pitching moment due to flap deflection as a function of section thickness ratio, for chord ratios c_f/c between 0.2 and 0.3.

THICKNESS RATIO. Both pressure distribution and boundary-layer growth are a function of foil-section thickness ratio. Consequently, the pitching moment due to flap deflection varies with that thickness ratio. The value of the derivative $dC_m/d\delta$, as plotted in figure 5, decreases as the thickness ratio is increased, thus explaining some or most of the spread in figure 4. A parameter better suited than thickness ratio, to correlate pitching moment derivatives, would probably be the trailing-edge "wedge" angle (as in the later figure 13).

MOMENT DUE TO LIFT. As in plain airfoil sections, the aerodynamic center of a flapped section might be expected not to be exactly at the quarter-chord point. Statistical evaluation in (4,d) shows that the A' center of "conventional" flapped sections is approximately at $x/c = 22\%$, which is 1 or 2% ahead of the usual location in such sections. The total of the pitching moment of a symmetrical, but flapped foil section, taken about the leading edge (with a "dot" to indicate this definition) thus corresponds to

$$C_{m\cdot} \approx (dC_{m\cdot}/d\delta)\delta - (x/c)C_L \quad (6)$$

where $(dC_{m\cdot}/d\delta)$ as in figures 4 and 5, and where x/c = location of the aerodynamic center.

- (4) Experimental characteristics of hinged flaps:
 - a) Silverstein, Horizontal Tail Surfaces, NACA T Rpt 688 (1940); also J Aeron Sci 1939 p 361.
 - b) Ames and Others, 0009 Pressure Distributions, NACA TN 734, 759, 761 (1939/40), see (2,e).
 - c) Göthert, Systematic Investigations, ZWB FB 552 & 553 (1938/40); Yearbk D Lufo 1940 p 1-542.
 - d) Göthert, Horizontal-Tail Characteristics, Ringbuch Luftfahrt Technik (Chap I-A-13, 1940).
 - e) Ergebnisse AVA Gött, Vol. III (1926) p 102.
 - f) Dods, A' Ratio and Sweep, NACA TN 3497 (1955).
 - g) Wenzinger, Wing Flaps, NACA TR 554 (1936).
 - h) Irving, Elevators, ARC RM 679 (1920).
 - i) Jacobs, Pressure Distrib., NACA T Rpt 360 (1930).
 - j) Polish Results, see (4,d) also NACA TR 688.
 - k) NACA, Report/Memorandum L1948D09.
 - l) Glauert, ARC RM 761 (1921) & RM 1095 (1927).
 - m) Abbott-Doenhoff-Stivers, NACA TR 824 (1945).
 - n) Swanson, Tail Surface, NACA TN 1275 (1947).
 - o) Spearman, With 25 & 50% Flaps, NACA TN 1517.
- (5) The span ratio b_f/b is taken into account in these cases. In presence of a fuselage, "b" of a horizontal tail is to be measured from tip to tip, while the span of the elevator is usually reduced either by a cut-out or corresponding to the width of the fuselage.
- (6) Truckenbrodt, Flapped Delta Wing, ZFW 1956 p 235.

CENTER OF PRESSURE. The "point" where the resultant of the chordwise lift distribution is located, is at

$$x/c = -dC_{m\cdot}/dC_L \quad (7)$$

The lift of a symmetrical but flapped foil section can be considered in two components. The first, corresponding to angle of attack, is at or near (or ahead) of 0.25 of the chord. The second component is the differential added through flap deflection, at constant angle of attack. Its location in two-dimensional flow

$$x_{\Delta}/c = (\Delta C_{m\cdot}/\Delta C_L) \quad (10)$$

– is theoretically expected to be at 0.5 of the chord for flap-chord ratios c_f/c approaching zero. Figure 6 shows how the " Δ " location reduces from there as the chord ratio is increased. In three-dimensional flow (corresponding to finite aspect ratios) the " Δ " location is further aft, however. Thus considering a tail surface, for example at $\alpha =$ zero, the lift produced by flap deflection corresponds to

$$\Delta C_L = (dC_L/d\delta)\delta = (dC_L/d\alpha)\delta(d\alpha/d\delta) \quad (12)$$

The moment due to this lift coefficient corresponds to

$$\Delta C_{m\cdot} = (dC_{m\cdot}/d\delta)\delta + (dC_{m\cdot}/dC_L)(\Delta C_L) \quad (13)$$

The center of pressure of ΔC_L is then found to be at

$$x_{\Delta}/c = -(dC_{m\cdot}/d\delta)/(dC_L/d\delta) - (dC_{m\cdot}/dC_L) \quad (14)$$

It is obvious that $(dC_L/d\alpha)$ and $(dC_L/d\delta)$ are functions of the aspect ratio. Using average tested values for all the derivatives involved, we have computed " Δ " locations for two different "lift angles" and aspect ratios. They are plotted in figure 6 together with some experimental results. It then becomes evident that the " Δ " location for c_f/c between 0.1 and 0.2 and for A between 4 and 10, is in the vicinity of 50% of the chord; and this location is as that in equation (10).

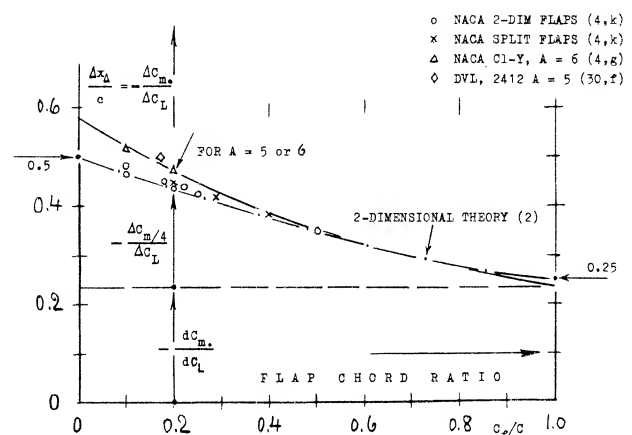


Figure 6. Center of pressure location of the lift produced by flap deflection.

4. HINGE MOMENTS OF PLAIN CONTROL FLAPS

DEFINITIONS. The hinge moments "H" of flaps, ailerons, elevators and rudders are conveniently presented in the form of the coefficient based on chordwise length, and area of the "flap" portion (measured aft of the hinge line):

$$C_H = H / (q S_f c_f); \text{ where: } S_f c_f = b(c_f)^2 \quad (18)$$

In configurations where c_f is not constant, the mean of $(c_f)^2$ is the best reference length to be used for the hinge moment. There is a basic convention in the field of aeronautics to designate longitudinal (pitching) motions and moments as positive when their direction is "nose-up" (and "tail-down"). Positive deflection of a control surface thus produces a "negative" moment. When discussing "large" or "small" hinge moments, the *magnitude* of the torque, usually resisting positive flap deflection, is meant in the following.

DERIVATIVES. Theory (2) considers a flat plate (with zero thickness) with a portion of the chord near the trailing edge, deflected by the angle " δ ", in two-dimensional flow. When deflecting this "flap", a hinge moment originates, corresponding to coefficients and derivatives as follows:

(a) At constant deflection angle the hinge moment varies corresponding to

$$C_H = (dC_H / dC_L) C_L \quad (19)$$

This case applies when changing the angle of attack; and the derivative is (for most practical purposes) independent of the aspect ratio.

(b) At constant lift coefficient (id est, when compensating flap deflection in one direction, by a change of the angle of attack in the other direction) the moment corresponds to

$$C_H = (dC_H / d\delta) \delta \quad (20)$$

Note that for $C_L = \text{constant}$, the induced angle of attack is constant. The function of $dC_H / d\delta$ as in figure 8, can thus also be considered to be independent of the aspect ratio. The two derivatives (a) and (b) appear to be the most perfect form to present hinge moments. The NACA has been using, in practically all publications, different forms, however:

(c) At constant angle of deflection, the moment varies corresponding to

$$C_H = C_{H\alpha} \alpha; \text{ where } C_{H\alpha} = (dC_H / dC_L)(dC_L / d\alpha)$$

Since $dC_L / d\alpha$ is a function of the aspect ratio, the derivative $C_{H\alpha}$ grows in magnitude as the aspect ratio is increased.

(d) At constant angle of attack, the hinge moment varies as a consequence of flap deflection as

$$C_H = C_{H\delta} \delta \quad (22)$$

where $C_{H\delta}$ = combined derivative, due to δ plus due to C_L produced by δ . This derivative is thus

$$C_{H\delta} = dC_H / d\delta + (dC_H / dC_L)(dC_L / d\delta) \quad (23)$$

which is again a function of aspect ratio.

The derivatives (c) and (d) have two advantages. They are conveniently determined in wind-tunnel experiments; and they present the two variations of hinge moment in such a manner that their relative magnitude is obvious.

HINGE MOMENT DUE TO LIFT. Experimental results are plotted in figure 7 together with the theoretical prediction. Conclusions are as follows:

- Experimental moments are always smaller than those indicated by theory. Presence and growth of the boundary layer are responsible for the difference. Reynolds number, surface roughness and size or shape of the control gap affect the magnitude of the derivative.
- The moment is sensitive to section thickness and trailing-wedge angle.

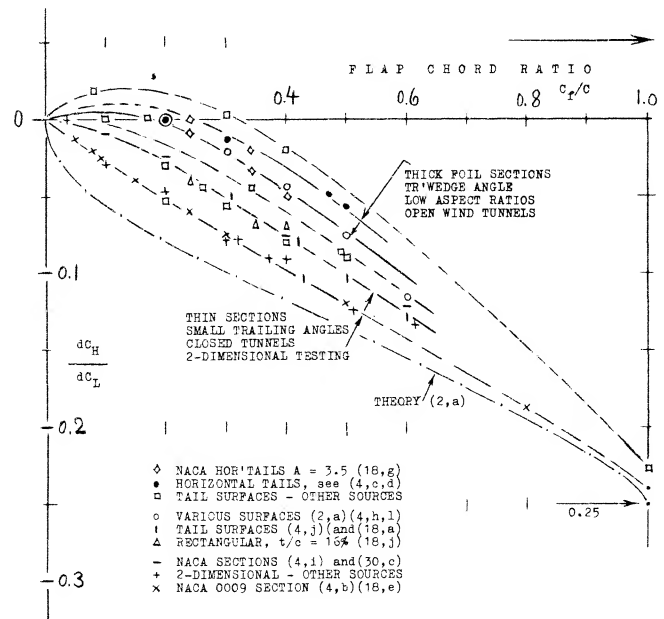


Figure 7. Hinge moment of trailing-edge flaps due to lift, for $\delta = \text{constant}$.

- (c) The moment reduces with the aspect ratio of the control surface.
- (d) It is suspected that test conditions (open-jet as against closed-type wind tunnel) have an effect similar to that of the aspect ratio.
- (e) Approaching zero chord ratio, the hinge moment due to lift can become very small. A combination of small A'ratio and large trailing-wedge angle reverses the direction of the moment altogether.

Details of the various effects listed will be presented later.

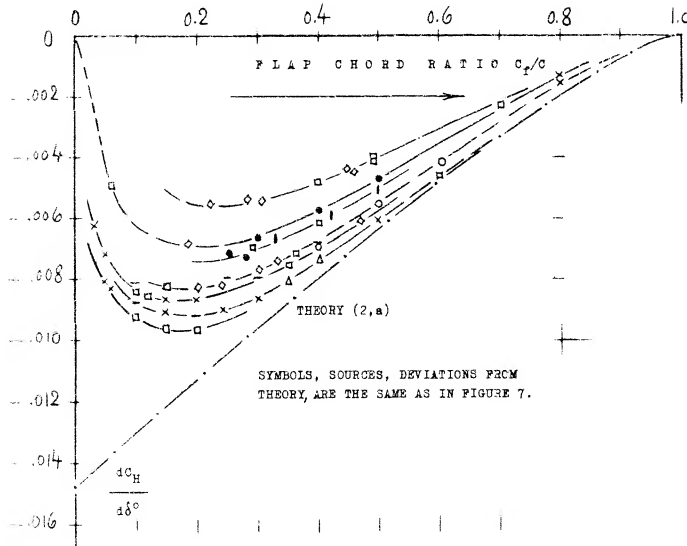


Figure 8. Hinge moment of trailing-edge flaps due to deflection, for $C_L = \text{constant}$.

THE HINGE MOMENT DUE TO FLAP deflection (at constant lift coefficient) corresponds to derivative plotted in figure 8. Again because of viscosity and the effects listed above, the moment is less than predicted by theory. The scatter of the experimental points is considerable, if not as wide percentage-wise as in figure 7. In comparison to the component due to lift, the moment corresponding to $dC_H/d\delta$ is usually larger in realistic control configurations. Also, as mentioned before, tail surfaces predominantly operate at constant lift coefficient. For small and moderate chord ratios, figure 8, therefore, gives most of the information needed in the estimation of the hinge moments of plain elevators and rudders.

- (8) It is general practice in tunnel testing to correct the angle of attack for boundary effects of the wind stream. A corresponding correction (likely in proportion to $d\alpha/d\delta$) should be applied to the flap angle. We have, wherever possible, used uncorrected tunnel-tested values for the angle of attack.

HINGE MOMENTS OF LANDING FLAPS. Trailing-edge flaps, used to increase the lift coefficient of wings (see the special chapter on this subject), are a case that might suitably be considered at constant angle of attack. The hinge moment of a flap extending over the entire span of the wing, is then:

$$C_H = C_{H_0} + (dC_H/d\delta)\delta + (dC_H/dC_L)\Delta C_L \quad (24)$$

where C_{H_0} represents a certain basic moment due to shape (camber) of the foil section involved and corresponding to the original lift coefficient. The last term in the equation can be written as a function of the deflection angle:

$$\Delta C_H = (dC_H/dC_L)(dC_L/d\alpha)(d\alpha/d\delta)\delta \quad (25)$$

The lift-curve slope in this equation corresponds to the wing's aspect ratio; see the chapter on "wings". The $d\alpha/d\delta$ ratio is indicated in figure 2. As mentioned above, the combined derivative $C_H\delta$ (equation 23) is also frequently reported in connection with control surfaces.

EXAMPLE. We will assume a tail surface at constant angle of attack, having a lift angle $d\alpha/dC_L = 16^\circ$. The chord ratio of elevator or rudder, respectively, may be $c_f/c = 0.33$. We then find from the various graphs:

$$(dC_H/dC_L) = -0.03; \quad (dC_H/d\delta^\circ) = -0.007$$

For $\alpha = 0$, the component of the hinge moment due to lift is then found through the use of equation (25):

$$\Delta(dC_H/d\delta^\circ) = -0.03(0.58)/16 = -0.001$$

The total moment (at constant angle of attack) corresponds to

$$C_H\delta^\circ = -0.007 - 0.001 = -0.008$$

As mentioned before, the component due to lift is but small in comparison to that due to flap deflection. It should be noted, however, that the values in figure 7 increase with the chord ratio, while those in figure 8 reduce, at chord ratios above 0.2 (eventually to zero). The derivative dC_H/dC_L could therefore not be disregarded in flaps with unusually high chord ratios.

STICK-FREE CONDITION. We will consider an airplane with a control system which is completely mass-balanced and free of mechanical friction. When the control stick of that system is left free, the elevator (and/or the rudder) will assume a certain deflection angle at which the aerodynamic hinge moment is zero.

That angle corresponds to

$$d\delta/dC_L = -(dC_H/dC_L)/(dC_H/d\delta) \quad (27)$$

Points evaluated from experiments, through the use of this equation, are plotted in part (A) of figure 9. The divergence of these points from the theoretical function is similar to that in figures 7 and 8. Below $c_f/c = 0.2$, $d\delta/dC_L$ becomes very small. Depending upon aspect ratio and trailing wedge angle, to be discussed later, the derivative $d\delta/dC_L$ can also change direction, which means that the control flap would tend to move *against* the oncoming flow.

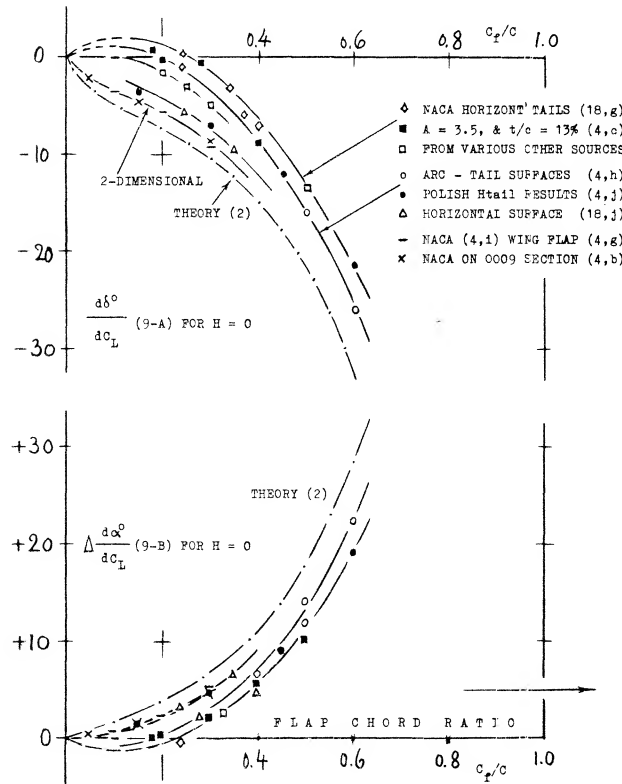


Figure 9. Stick-free characteristics of control surfaces as a function of their flap-chord ratio.

STICK-FREE STABILITY. Considering a horizontal tail surface, its stabilizing effect $dC_L/d\alpha$ is usually reduced when leaving the control stick free. In a plain flap, the increment of the angle of attack, required to maintain a certain lift coefficient, is

$$\Delta(d\alpha/dC_L) = -(d\delta/dC_L)(d\alpha/d\delta) \quad (28)$$

where $(d\delta/dC_L)$ as in equation (27). Experimental results of this increment of the "lift angle" are plotted in part (B) of figure 9. Usually, the increment is positive; and any such increment means a reduction of the lift-curve slope. This destabilizing effect of a stick-free control surface increases as the flap-chord ratio is increased. The fact that below $c_f/c = 0.3$ or 0.2 , a free elevator or rudder can be stabilizing, will be discussed later.

5. INFLUENCE OF ASPECT RATIO AND FORM

As pointed out before, the derivatives of control-flap forces and moments can be taken in such a manner that they are theoretically independent of the aspect ratio of wing or tail surface. Actually, a flow pattern similar to two-dimensional cannot be expected to exist at and near the lateral edges. Other deviations must be expected on account of plan-form shapes different from rectangular and straight, such as sweepback in particular.

INFLUENCE OF ASPECT RATIO. Lifting surfaces have tips, ends or lateral edges where the pressure distribution is no longer similar to two-dimensional. The influence of finite span upon the control characteristics is conveniently considered in terms of the aspect ratio. A systematic investigation into forces and moments of plain horizontal tail surfaces as a function of the A' ratio is specifically reported in (4,c,d). Figure 10 presents the influence in terms of the derivatives explained in the first part of this chapter. Results for chord ratios between 0.2 and 0.4 are as follows:

- (a) The effectiveness ratio $d\alpha/d\delta$ hardly varies, down to $A = 2$. While a number of experimental values reported in (4,d,c) but not reproduced in figure 10-A,

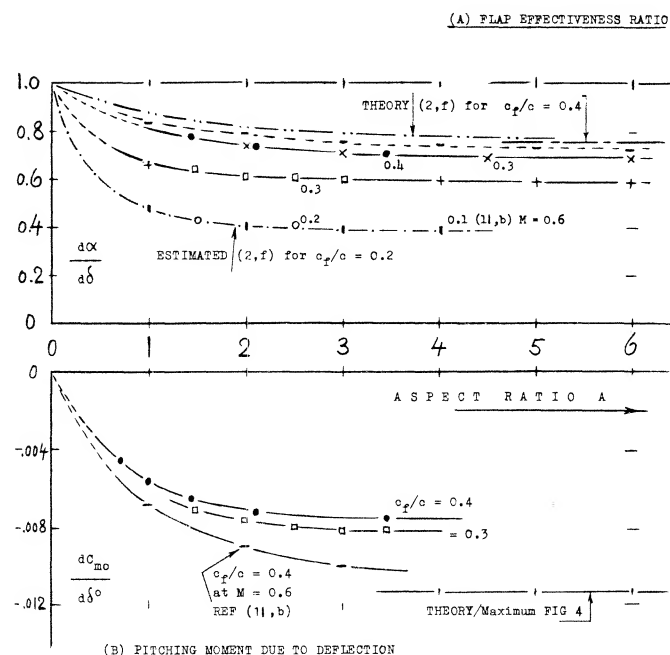


Figure 10 (A & B)

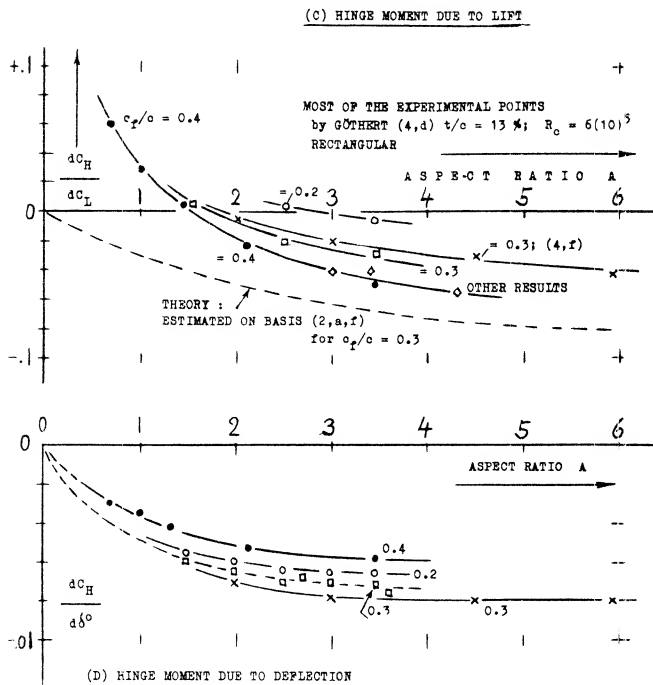
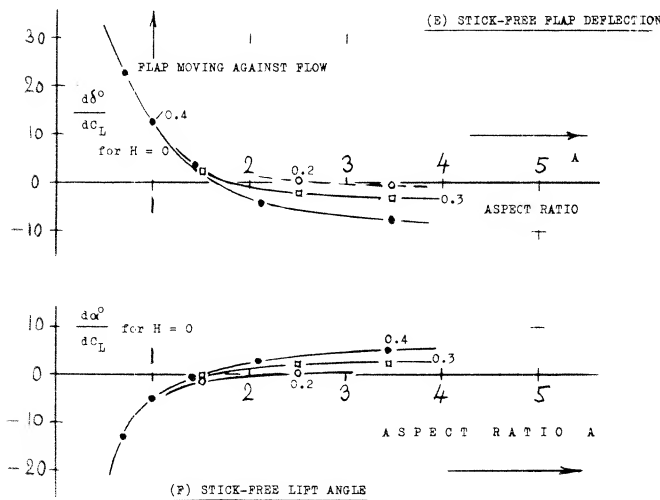


Figure 10. Influence of the aspect ratio upon the various characteristics of trailing-edge flaps.



- (11) Influence of aspect ratio on control flaps:
- See aspect ratio in reference (4,e,d).
 - Lowry, Influence of A'ratio, NACA RM L56E18.
 - For aspect-ratio theory see reference (2,f).
 - Dods, Horizontal Tails, NACA TN 3497 (1955).

indicates a decrease of the effectiveness ratio below $A = 2$ or 1 , lifting-surface theory (2,f) predicts an increase to unity, as the A'ratio approaches zero.

- The pitching moment $dC_m/d\delta$ reduces as the A'ratio is reduced. The change is similar to that of dC_m/dC_L (due to the linear lift component) as explained in the chapter on "straight wings".
- The derivative dC_H/dC_L reduces as the A'ratio is reduced; and it changes direction or sign, roughly between $A = 3$ and 1 . The influence is still noticeable at least up to $A = 5$.
- The hinge moment due to flap deflection (at $C_L = \text{constant}$) reduces in a manner similar to the pitching moment under (b). Values which can, for practical purposes, be accepted as constant, may be expected above $A \approx 3$.
- The deflection of a stick-free elevator or rudder (at zero hinge moment) not only reduces as the A'ratio is reduced, it can also change sign (at A between 2.5 and 1.5 as in the graph). The variation corresponds to that under (c).
- The increment of $d\alpha/dC_L$ due to stick-free control flap, corresponds to the variation of the deflection angle under (e). At and below $A = 2.5$ or 1.5 , the flaps of the tested configurations tend to move against the oncoming flow.

INDUCED ANGLE. As explained in the chapter on "small aspect ratios", the mechanism of circulation reaches a certain limiting condition, roughly at an aspect ratio equal to unity. Below $A = 1$, and disregarding any "cross-flow" lift component (as at higher angles of attack), lift is produced "near" the leading edge, while the trailing edge contributes "nothing", because of "complete" downwash. Lift and pitching moment produced by, and hinge moments of control flaps can thus be expected to decrease as the A'ratio is reduced. The variations as in parts (B) and (D) of figure 10 are thus explained. It must be noted, however, that in small aspect ratios, both the control surface as such, as the flap (when deflected) produce an additional non-linear lift component.

REVERSAL OF HINGE MOMENTS. Finite aspect-ratio (lifting-surface) theory in (2,f) confirms the reasoning in the preceding paragraph. Evaluated in the form as in this text, the theory yields a hinge-moment derivative due to lift, reducing toward nothing, as the A'ratio approaches zero. Part of the trend as in part (C) of figure 10, is thus explained. However, experimental results, if not below $A = 2.5$, then below $A = 1.5$, clearly demonstrate a reversal of the moment, corresponding to a positive sign. This reversal is similar to that as found later (see figure 14) resulting from larger trailing-edge angles. It appears that the trailing-wedge effect is enlarged by the type of flow pattern past the afterbody of small-aspect-ratio wings.

SWEEPBACK. As a function of the angle of sweep, the lift curve slope ($dC_L/d\alpha$) of a series of wings having one and the same finite aspect ratio, reduces approximately or not quite, in proportion to the cosine of the angle of sweep " Λ "; see the "swept wing" chapter. The angle of sweepback in tapered wings or control surfaces, measured in each half span at the flap hinge line, is somewhat smaller than the angle of sweep conventionally defined for the quarter-chord line. It seems that the hinge-line sweep is applicable to the forces and moments of and due to flap deflection. We have, therefore, used this type of angle when plotting the experimental points in figure 11, wherever " δ " is involved. The deflection angle of a control flap (such as an elevator) measured in the direction of flow or flight, is only $(\cos\Lambda)$ times the angle δ measured about the hinge axis. Tentatively, therefore, the lift-curve slope due to deflection (at constant angle of attack) may vary as

$$dC_L/d\delta \sim \cos^2\Lambda \quad (30)$$

This variation is reasonably well confirmed in (12,f). As a consequence, the flap effectiveness ratio can be expected to vary as

$$d\alpha/d\delta \sim \cos\Lambda \quad (31)$$

Confirmation by experiments as in part (A) of figure 11, is acceptable. It is suggested, however, that the flow pattern is too much 3-dimensional for the lifting-line approximation above.

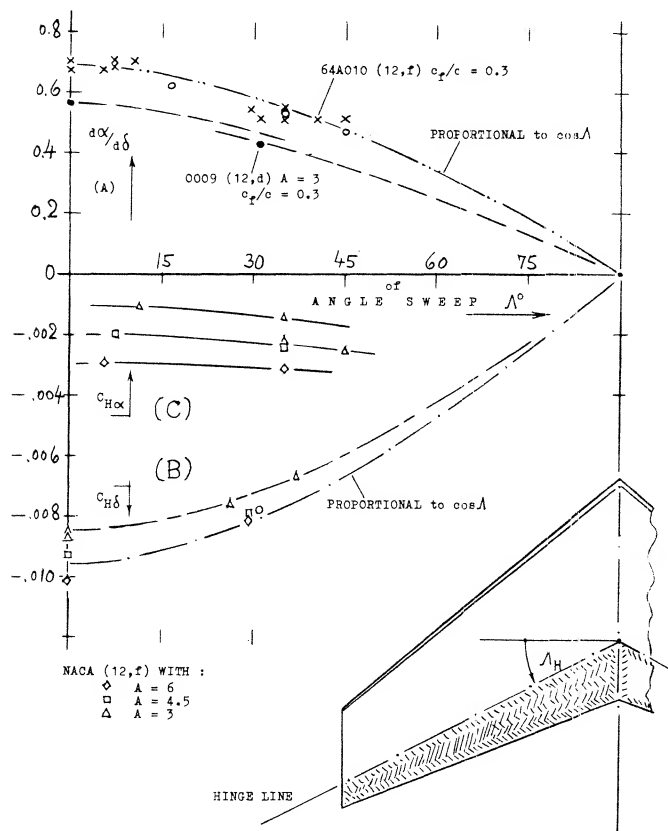


Figure 11. Flap characteristics as a function of the angle of sweep of wing or control surface.

HINGE MOMENTS (of plain flaps) may be expected to be proportional to the lift produced by their deflection. Therefore: $dH/d\delta \sim \cos^2\Lambda$. Considering, however, the moment arm of any swept flap normal to its hinge axis, to reduce in proportion to $\cos\Lambda$, we obtain

$$C_{H\delta} \sim \cos\Lambda \quad (32)$$

Confirmation is found in part (B) of figure 11. As far as the hinge moment due to lift or angle of attack is concerned, theory (12,g) predicts a modest increase as a function of sweepback. The results plotted in part (C) of the graph, confirm this prediction. The derivative, which is small in the first place, might also be considered to be independent of the angle of sweep.

PLAN-FORM SHAPE. It is explained in the chapter dealing with "straight wings", that the lateral edges and the rear plan-form corners of a wing are important in regard to lift, and lift-curve slope. Examination of experimental results shows that edges and corners also have an effect on forces and moments of and due to flaps. In particular:

The derivatives $dC_L/d\delta$ and $d\alpha/d\delta$ of a control surface having an elliptical plan form, are noticeably reduced as against those obtained for a comparable rectangular surface.

The magnitude of hinge-moment derivatives is reduced; particularly dC_H/dC_L , thus providing increased ($dC_L/d\alpha$) in stick-free condition.

6. INFLUENCE OF FLAP-SECTION SHAPE

As explained before, foil section *thickness* has an influence upon control-flap characteristics. It has been discovered, however, that the angle at the trailing edge, included by upper and lower flap side, and other variations of flap-section shape are more directly responsible for such effects than the foil thickness ratio. Various shape parameters are discussed in this section.

SECTION THICKNESS. The control derivatives of a flapped and tabbed 0015 foil section are presented in figure 12. In comparison to other sections with thickness ratios between 9 and 12%, the following conclusions can be drawn:

- The lift-curve slope is reduced, corresponding to section thickness ratio. The influence of a 0.5% hinge gap on $dC_L/d\alpha$ is noticeable.

- (b) In sealed condition, the effectiveness ratios $d\alpha/d\delta$, both of flap and tab, are "normal". The influence of a hinge gap is considerable.
- (c) The $dC_m/d\delta$ derivative fits into the pattern as in figure 4.
- (d) The value of dC_H/dC_L is low (see figure 7). This is evidently a true thickness and/or trailing-wedge effect.
- (e) The values of $dC_H/d\delta$, for flap and for the tab, are average (see figure 8). With open hinge gap, the flap moment is noticeably reduced.
- (f) The value of the stick-free lift-curve slope is comparatively high, evidently because of the derivative as under (d).

All in all, characteristics of this 15% thick section are thus not too much different from those of sections with smaller thickness ratios, although flow pattern, forces and moments are evidently somewhat more sensitive as to hinge-gap interference.

TRAILING-WEDGE ANGLE. Modern laminar-type and high-speed foil sections have (if with "true" 6-Series contour) a hollow (cusped) afterbody shape. Their trailing-wedge angles are, as a consequence, smaller than those of other, more conventional sections. One and the same trailing-wedge angle can thus be connected either with a bulging or a hollow flap shape. *Figure 13* shows three different ways of changing the shape of a control flap together with that of the foil section:

- (12) Flaps on swept-back wings:
 - d) Harper, NACA TN 2495 (1951); (18,d) (22,c).
 - e) Letko, Swept-Back Wings, NACA TN 1046 (1946).
 - f) Dods, Horizontal Tails, NACA TN 3497 (1955).
 - g) Dods, Swept-Wing Theory, NACA TN 2288 (1951).
- (13) In the discussion of flap characteristics as a function of aspect ratio, derivatives considered are those at and around zero lift. At aspect ratios approaching zero, a non-linear, "second" term of lift originates as a function of the angle of attack or when deflecting a trailing-edge flap.
- (15) Influence of foil section shape:
 - a) Lockwood, Beveled, NACA W Rpt L-666 (1944).
 - b) Jones, Beveled Trailing Edge, NACA WR L-464.
 - c) See Harper (18,d), Various Foil Sections.
 - d) Batson, 0015 Modified, ARC RM 2698 (1943).
 - e) Halliday, Rudder Moments, ARC RM 2184 (1941).
 - f) Sears, Flap and Tab, NACA WR L-454 (1942).
 - g) Toll, Surface Distortion, NACA TN 1296 (1947).
 - h) Toll, Lateral Control, NACA T Rpt 868 (1947).
 - i) Crane, Modifications, NACA T Rpt 803 (1944).
 - j) Hemenover, T'Edge Angle, NACA TN 3174 (1954).
 - k) Halliday, Boundary Layer, ARC RM 2730 (1955).
 - l) ARC, Flaps, RM 1996, 2008, 2256, 2506 (1942/45).

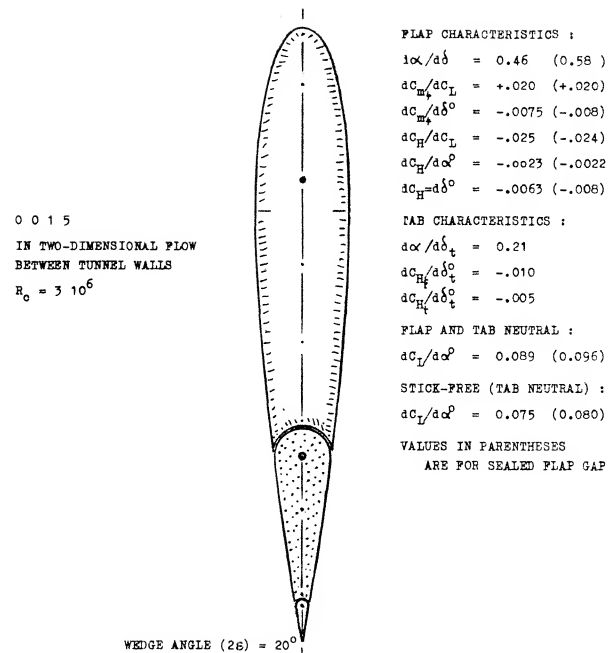


Figure 12. Control characteristics of a configuration based on 0015 foil section, tested (15,f) in two-dimensional flow.

- (a) When changing the section thickness ratio, the flap shape (thickness) varies accordingly.
- (b) A similar variation is obtained when shifting the position of maximum section thickness along the foil chord, back or forth.
- (c) As mentioned above, certain foil sections have a cusped (hollow or concave) shape in that portion of the chord where flaps might be installed. For example, a 63-010 section (in its original and true form) will thus result in a flap shape considerably different from that in a 0010 section.

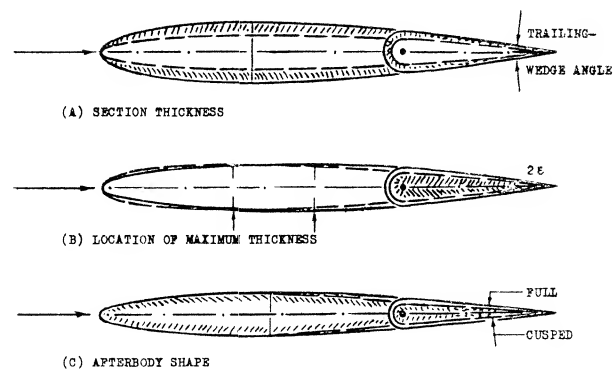


Figure 13. Variation of flap thickness ratio and of flap shape as a function of section parameters.

Of course, the flap shape can also be modified by willful deviation from the true section contour (as in figure 14 for example). In all these cases, the included angle (2ϵ) at the trailing edge, which we may call *trailing "wedge" angle*, can statistically be used as a measure for thickness (at the hinge line) and/or curvature (at the sides) of the flap. — Experimental derivatives from various sources are plotted in figure 14 as a function of the trailing-wedge angle. The lift-curve slope (for $\delta = \text{constant} = \text{zero}$) reduces as the wedge angle is increased. The flap-effectiveness ratio (see part 'B' of the graph) reduces also. For example, when increasing the wedge angle from 10 to 20°, the flap's lift-curve slope $dC_L/d\delta$ reduces, possibly to $0.95(0.94) \approx 90\%$.

HINGE MOMENTS. Parts (D) and (E) of figure 14 show that the magnitude of flap-hinge moments decreases considerably (and progressively) as the trailing-wedge angle is increased. In fact the due-to-lift derivative is reduced to zero at wedge angles between 15 and 25°; and it crosses over into the "positive" region above these angles. The magnitude of the due-to-deflection derivative (in part 'E' of the graph) reduces also appreciably, although it may not necessarily reach the zero line. When comparing the hinge moment ratios as in figure 13 with those in figures 7 and 8, it can be concluded that all variations can readily be explained on the basis of what the trailing-wedge angle stands for. The conclusion for the practical designer is that thick and convex foil-sections and "bulging" flap shapes result in low hinge-moment derivatives, while thin and hollow (cusped) foil and flap shapes, i.e. with thin trailing wedges, can be expected to produce hinge moments approaching the theoretical functions.

STICK-FREE CHARACTERISTICS are a consequence of the hinge-moment derivatives. Part (C) of figure 14 shows that the stick-free (zero-moment) lift-curve slope increases slowly, as the trailing-wedge angle is increased. In other words, the stick-free stabilizing effect of a (mechanically balanced) tail surface can be increased by increasing the wedge angle. It is to be noted that the lift-curve slope is equal to that in stick-fixed condition, at the wedge angle for which $dC_H/dC_L = \text{zero}$. Beyond that angle, the slope increases further, which means that the flap moves by itself against the oncoming flow, upon increasing the angle of attack.

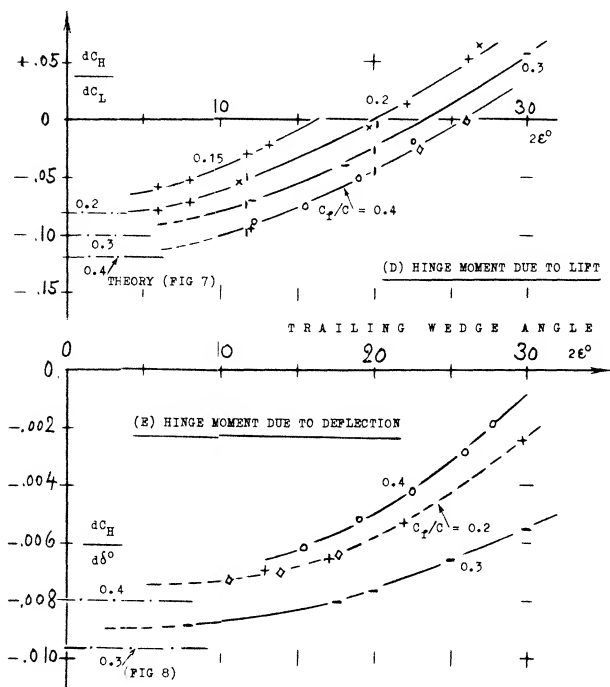
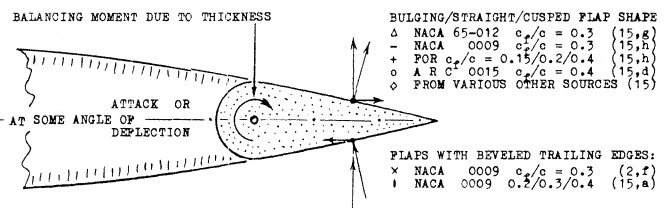
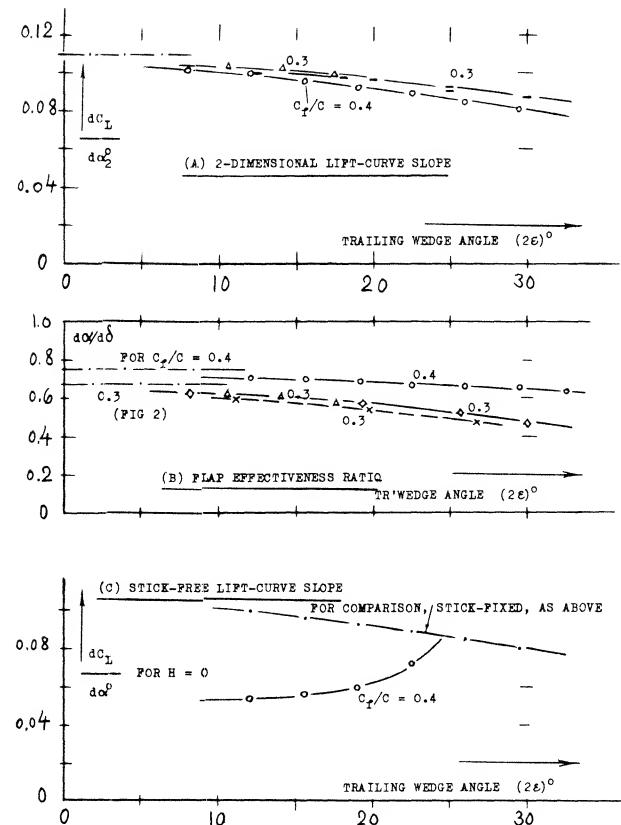


Figure 14. Influence of flap thickness and shape, as measured by the trailing-wedge angle, upon the characteristics of plain flaps.

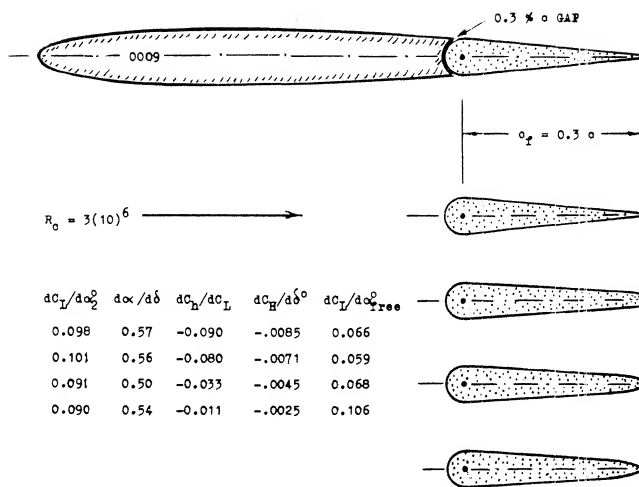


Figure 15. Influence of various modifications of shape upon the characteristics of a control flap, tested (15,b) under two-dimensional conditions.

BEVELED TRAILING EDGES. Since flap shape, as described above, considerably affects hinge moments, suitable variations may be used to change the level of these moments. It can be convenient, for example, in a finished airplane, to exchange an elevator or rudder with a somewhat differently shaped design. Figure 15 illustrates several possible modifications of a flap; consequences are tabulated. We can see that neither thickening the trailing edge, nor rounding of that edge (with a comparatively *small* radius) has much of an effect upon hinge moments (although the parasitic drag is increased). However, curvature in form of an elliptical contour, or beveling of the thickened trailing edge (to an enclosed angle of 20 or 30°) reduces the hinge-moment derivatives considerably. This type of beveling (necessarily combined with increased flap thickness) is obviously a form similar to convex (bulging) flap shape, id est with the location of curvature far aft.

PRESSURE DISTRIBUTION. Hinge moments are the result of pressure distributions; and those distributions evidently change appreciably, not just in size but also in character, as thickness ratio, trailing-wedge angle or flap curvature are varied. Explanation of reduced and reversed hinge moments is possible by considering two components:

- Pressure forces on the 1/2 cylindrical forward edge of the flap cannot produce any hinge moment; and those along the flanks could not either in a really thin flap (id est a flat plate). However, in a flap with
- As a function of the angle of attack, the consequence of separation from a trailing wedge can be such that a reversal of the lift-curve slope takes place; see the chapter on "airfoil sections".
- Within a limited range of the angles involved, the pressure distribution varies in linear proportion to them. The pressure coefficients can thus be presented in form of derivatives, as in figure 16.

sufficient thickness ratio, the *tangential* components of the pressure forces do produce a hinge-moment component. Positive pressure forces on the pressure side, and negative ones on the suction side, form together a force couple, the direction of which is such that it *tends* to move the flap *against* the on-coming flow.

- Tested pressure-distributions due to angle of attack and due to flap deflection (17), are plotted in figure 16 for a beveled flap shape. The two derivatives show practically identical loops near the trailing edge; and these loops, representing "negative" hinge-moment components, are obviously responsible for much or most of the reduction (and possibly reversal) of the hinge moments evident in figure 13.

THE FLOW PATTERN connected with any pressure-distribution loop of the type as in figure 15, is most likely as follows:

- On the suction side of convex (bulging) or beveled flaps, boundary layer material tends to accumulate "at" the trailing edge. With or without local separation of the flow, the pressure, therefore, discontinues to rise to a positive value at the trailing edge.
- On the pressure side, the pressure gradient is essentially negative. Boundary layer growth (and separation) are thus prevented; and the flow follows the curvature of the flap surface. Negative pressures (suction) may thus develop as shown.

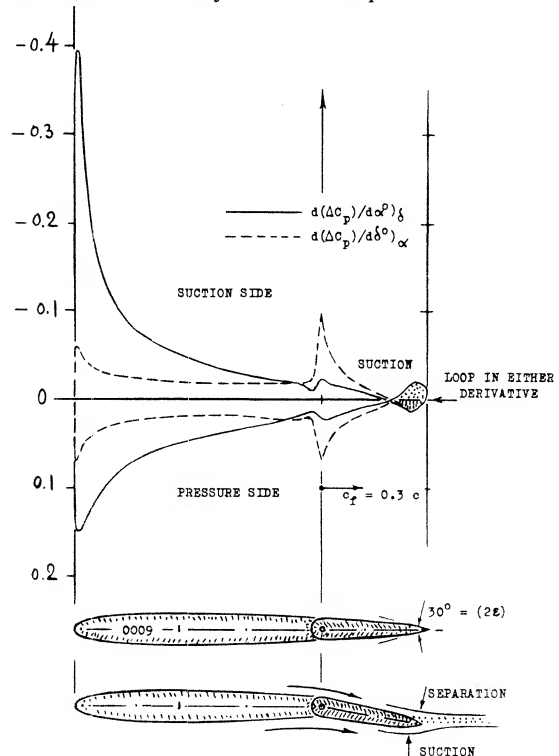


Figure 16. Pressure-distribution derivatives for a 0009 foil section with a beveled control flap.

The flow from the upper and that from the lower side of the flap, join each other at or beyond the trailing edge at one and the same pressure level (near zero). A loop is formed in the pressure distribution, accordingly. It can also be said that the flow pattern described is similar to an imaginary one in which the rear stagnation point is shifted around the trailing edge, onto the suction side.

FLAP CAMBER (a one-sided curvature in the flanks of a flap) is usually found only in ailerons, and is as such discussed in the chapter on this subject. Camber in the magnitude of 1% of the flap chord, produces a differential $\Delta C_H \approx 0.024$, in the direction to the convex side. Here as in all other cases of flap-section curvature the convex side is obviously subjected to a component of suction, while a hollow flap side encounters increased pressure.

"S" TYPE MOMENTS. Beveling of thickened flaps is described above and presented in figure 15, for example, as a means of reducing hinge moments. Figure 17 demonstrates, however, that such reduction has limitations. The low hinge-moment derivative $C_{H\delta} = -0.0025$ is restricted (in that particular example) to a narrow "c" range of less than plus or minus 5° . The amounts of suction which the lower side of the beveled portion of the flap can gain, and which the upper side can lose, are evidently reducing as the flap angle is increased. Beyond plus and minus 20° , the hinge moment approaches values corresponding to $C_{H\delta} = -0.0090$ which is about the level for a plain flap (see figure 8). Beveling of the type as in figure 16, obviously reduces hinge moments where they are small; and it does not materially reduce them where they are large. The "S" shape of the hinge-moment function is not desirable.

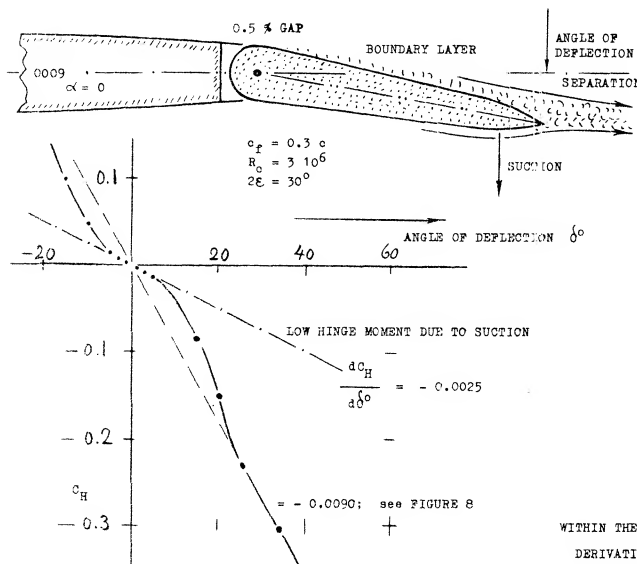


Figure 17. Characteristics of a control flap with beveled trailing edge, tested (15,a) under two-dimensional conditions.

7. OVERHANGING-NOSE BALANCE

All hinge moments presented so far, are those of "plain" flaps. Elevators, rudders and ailerons of this type can be used in small and low-speed airplanes, where hinge moments or forces do not exceed a magnitude which the pilot can apply with his hands to the control stick. In larger sizes (and at higher speeds) some type of aerodynamic balance designed into the control flaps is desirable or necessary: to reduce the pilot's efforts and to prevent fatigue, to make the airplane more maneuverable, to reduce structural strain in flaps and control linkages. The most frequently used type of balance is by means of an overhanging nose (leading edge) added to the control flap.

DEFINITIONS. When deflecting a control flap, static pressure increases on one side, and a certain negative pressure arises on the other side. Upon adding an overhanging "nose" to the control flap (or by moving the hinge axis back) some aerodynamic balance of forces normal to the flap chord can thus be expected. Since the control effect depends upon the chord " c_f ". The length of the flap nose (c_b , with "b" from balance) is defined forward from the hinge axis. This length may be expressed as a fraction, either of the total flap chord or of the chord " c_f ". We have selected to use the latter definition.

EXAMPLE. Experimental characteristics of a control surface configuration balanced by an overhanging nose, are presented in figure 18. The variation of lift as a function of flap deflection and of angle of attack, is of the same type as described in connection with figure 1. Part (C) of figure 18 shows, however, that lift is reduced on account of nose balance, at higher angles of attack (such as 20°) and at larger deflections (above 30° under the conditions as tested). As far as flap effectiveness is concerned, the ratio $d\alpha/d\delta$ corresponds to the statistical function as in figure 2. Comparison with other data (see later) indicates that the hinge moment as in part (D) of the illustration, is appreciably reduced as against that

WITHIN THE RANGE OF LINEAR VARIATION,

DERIVATIVES ARE AS FOLLOWS :

$$dC_L/d\alpha^\circ)_\delta = 0.089 \quad (0.090)$$

$$d\alpha/d\delta)_C = 0.50 \quad (0.53)$$

$$dC_L/d\alpha^\circ_{free} = 0.144 \quad (0.144)$$

$$dC_m/dC_L)_\delta = +0.049 \quad (+0.049)$$

$$dC_m/d\delta^\circ)_C = -0.0040 \quad (-0.0044)$$

$$dC_H/d\delta^\circ)_\alpha = -0.0025 \quad (-0.0044)$$

$$dC_H/d\delta^\circ)_C = -0.0047 \quad (-0.0050)$$

$$dC_H/d\alpha^\circ)_\delta = +0.0036 \quad (-0.0010)$$

IN PARENTHESES FOR SEALED HINGE GAP.

$$dC_H/dC_L)_\delta = +0.040 \quad (+0.011)$$

of the same flap with only a nose corresponding to the radius around the hinge axis. The same graph also demonstrates:

- that the constant portion of hinge moment slope $C_H \delta$ is practically the same for the angles of attack tested (between -10° and $+20^\circ$.)
- that the range of deflection angles within which the slope $C_H \delta$ is really constant, is limited (between plus and minus 10 or possibly 20° , under the conditions as tested).

It should be kept in mind that the hinge-moment derivatives as presented in the following paragraphs and illustrations, are only those corresponding to the linear variation as noted in part (D) of figure 18. For hinge moments at higher angles of deflection and/or attack, see the next section.

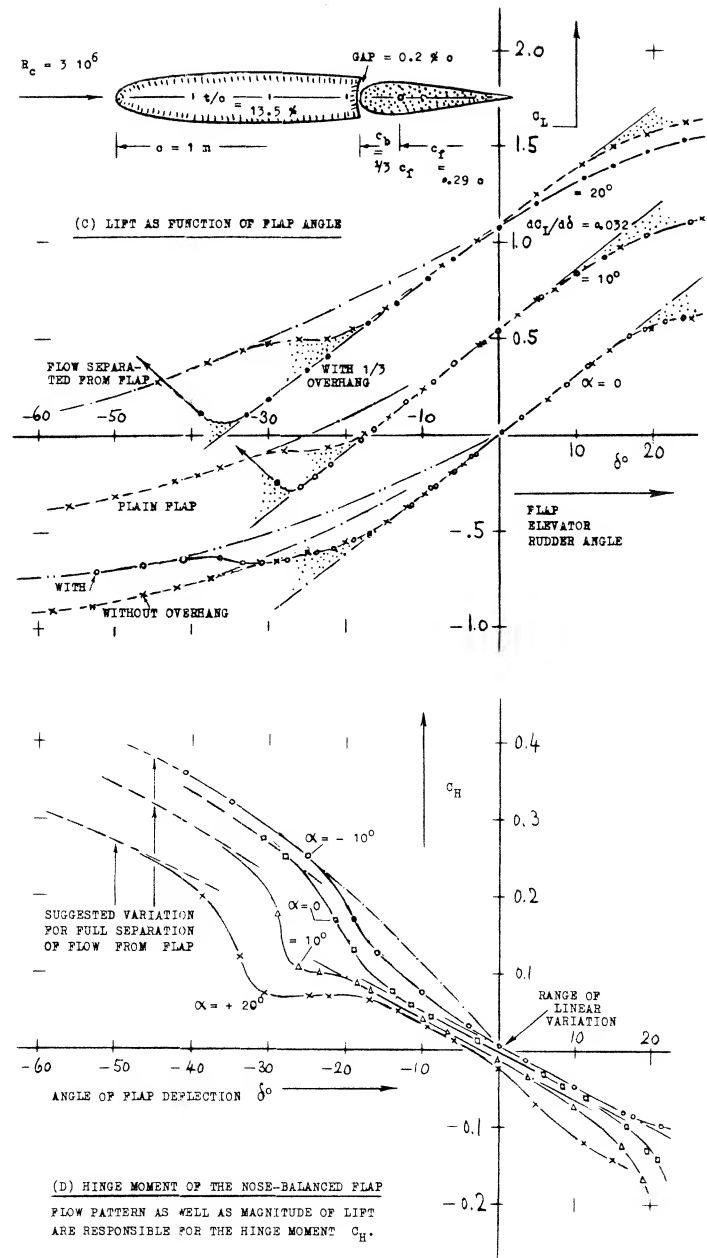
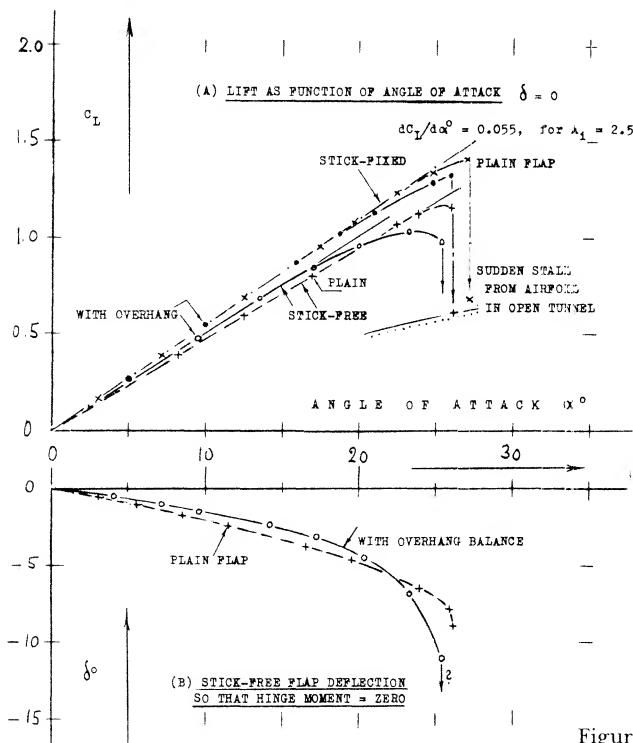


Figure 18. Characteristics of a control-flap configuration balanced by overhanging nose, as tested (18,c) between end plates in open jet wind tunnel.

- (18) Investigation of overhanging-nose balances:
 - Gorski, CAHI (Moscow) (1930); see (4,a).
 - Goett, Elevator Shape, NACA T Rpt 675 (1939).
 - Junkers W-Tunnel Results D-7182/91 (1942).
 - Harper, Aerodynamic Balance, NACA TN 2495.
 - Sears, Control Surfaces, NACA WR L-663 (1943).
 - Purser, Correlation, NACA W Rpt L-665 (1944).
 - Bates, Tail Surfaces, NACA TN 1291 (1947).
 - Smith, Elevators, NACA T Rpt 278 (1927).
 - Bradfield, Controls, ARC RM 1420 (1931).
 - Dirksen, Tails, ZWB 359 (1935); see (4,d).
 - Adamson, Nose and Gap, ARC RM 2326 (1940).
 - Riebe, 0009 Various, NACA WR L-196 (1945).
 - Tamburello, Tail, NACA W Rpt L-41 (1946).
 - Hoggard, Flaps, NACA TN 1248 (1947).
- (19) Kirste, Trav Cercle Etudes Aerot Vol 7 (1932).

OVERHANG LENGTH. Considering the effective length of the overhanging flap nose, finite thickness of foil section and flap have to be taken into account. A "plain" flap has usually a half-round nose corresponding to foil-section thickness at the hinge axis. All pressure forces on this half-circular shape are directed toward the hinge axis. As mentioned before, they can thus not contribute to balance; the corresponding nose length is ineffective. Depending upon section thickness (at the location of the hinge) and flap chord, this length can be between 5 and 20% of the chord c_f . Upon increasing the nose length beyond this lower limit, the magnitude of the hinge-moment derivatives reduces steadily, such as illustrated in figure 19.

LIFTING CHARACTERISTICS. The results tabulated in figure 19, show that the lift-curve slope $dC_L/d\alpha$ is reduced when adding an overhanging nose, evidently because of the surface discontinuity (gap) necessitated. The flap effectiveness ratio $d\alpha/d\delta$ is, on the other hand, increased so that the lift curve slope due to flap deflection $dC_L/d\delta$ is seen to be increased, a few percent. In other words, within the range of small and moderate angles of deflection, a well-rounded flap nose usually improves the flow past the suction side, around the bend produced by flap deflection.

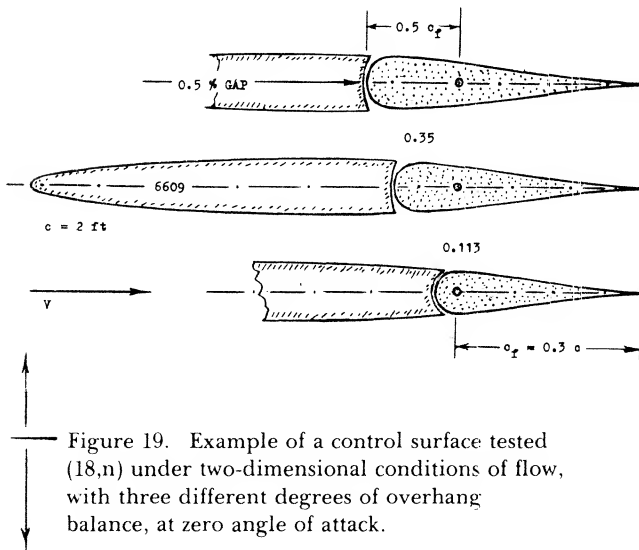
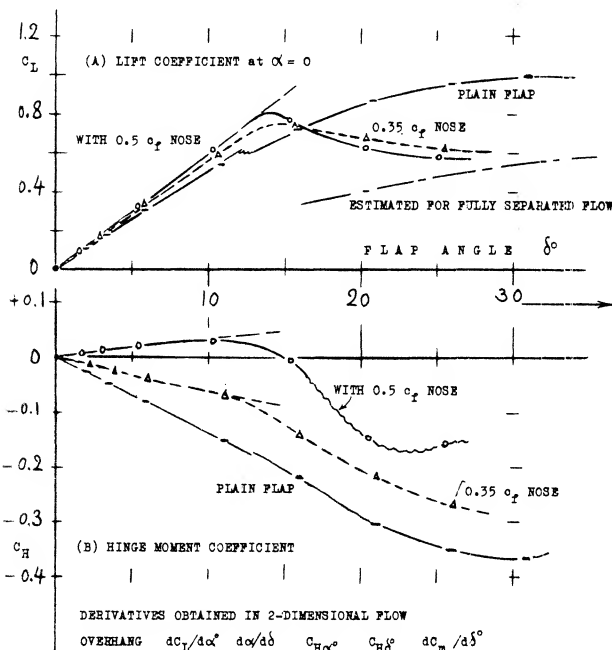


Figure 19. Example of a control surface tested (18,n) under two-dimensional conditions of flow, with three different degrees of overhang balance, at zero angle of attack.



(B) HINGE MOMENT COEFFICIENT

DERIVATIVES OBTAINED IN 2-DIMENSIONAL FLOW

OVERHANG	$dC_L/d\alpha$	$d\alpha/d\delta$	$C_{H\alpha}$	$C_{H\delta}$	$dC_{H\delta}/d\delta$
0.11 c_f	0.095	0.55	-0.008	-0.013	-0.0094
0.35 c_f	0.087	0.62	-0.007	-0.007	-0.0086
0.50 c_f	0.081	0.66	-0.001	-0.003	-0.0096

HINGE MOMENTS. Three different hinge-moment derivatives are plotted in figure 20 as a function of the nose-balance length ratio c_b/c_f . The derivative due to angle of attack (i.e., due to lift) as in part (A) reduces, slowly at first, with the nose length ratio; and it reaches zero at length ratios between 40 and 50%. The moment due to deflection is usually more important than that due to lift. Part (C) of the graph demonstrates how $dC_H/d\delta$ reduces as the length of the balancing elevator or rudder nose is increased. Assuming that the pressure or normal-force distribution along the flap chord be triangular (reducing to zero at the trailing edge) we may qualitatively compute the hinge moment and its variation due to adding a nose portion. This was done, taking into account that the first piece of overhang, assumed to be 12.5% of the aft-of-hinge-axis flap chord, would be ineffective (see above). The semi-theoretical function, included in graph (C), confirms the general character of the experimental lines.

CHARACTERISTICS AT $\alpha = \text{ZERO}$. So far, all control-flap characteristics have been considered within the non-dimensional system of partial derivatives. Normal forces and hinge moments at constant angle of attack can directly be of interest, however: (a) in the beginning on an airplane maneuver, when suddenly deflecting a control flap, (b) in wind-tunnel testing, where investigation at zero angle of attack is comparatively simple. — For $\alpha = \text{zero}$, the *complete* hinge-moment derivative is

$$C_{H\delta} = (dC_H/d\delta)_{\alpha} + (dC_H/dC_L)_{\delta} (dC_L/d\alpha) (d\alpha/d\delta)$$

Because of the slope $dC_L/d\alpha$, the aspect ratio and other conditions affecting lift (such as those of a wind tunnel) have considerable influence upon the derivative; see (8).

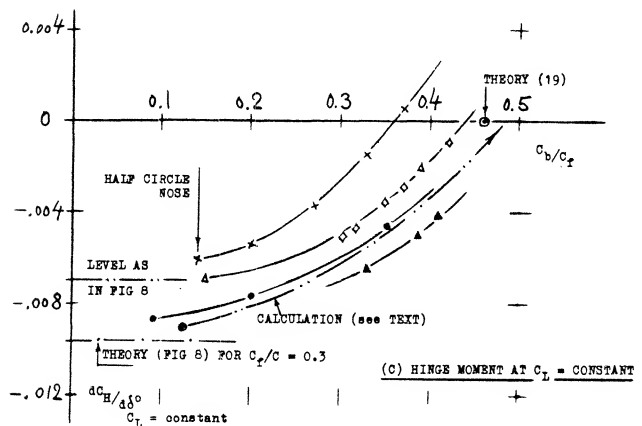


Figure 20. Hinge-moment derivatives of horizontal tail surfaces with $A \approx 3$ to 4, as a function of overhanging-nose balance

NOSE SHAPE. Results of systematic flap or nose-shape investigations are plotted in *figure 21*. Principle results are as follows:

- Considering hinge moment as a function of deflection, the partial derivative dC_H/dC_L (as in part 'A' of figure 20) is of lesser importance. The complete derivative $C_H\delta$, id est at $\alpha = 0$, therefore, provides quick *comparison* between different shapes, types of balance, and flap-chord ratios — provided that aspect ratio and test conditions are kept constant.
- As far as lift is concerned, it can be stated that the slope $dC_L/d\delta$ is on the *average* not affected by overhanging-nose balance. Depending upon nose *shape*, the flow around the bend at the suction side, toward the flap, may be somewhat improved or somewhat obstructed, however, in comparison to that past a plain flap. As a consequence $C_L(\delta)$ is not always a straight line.
- The maximum lifting effect (C_{Lmx} at $\alpha = 0$) is also a function of nose shape.

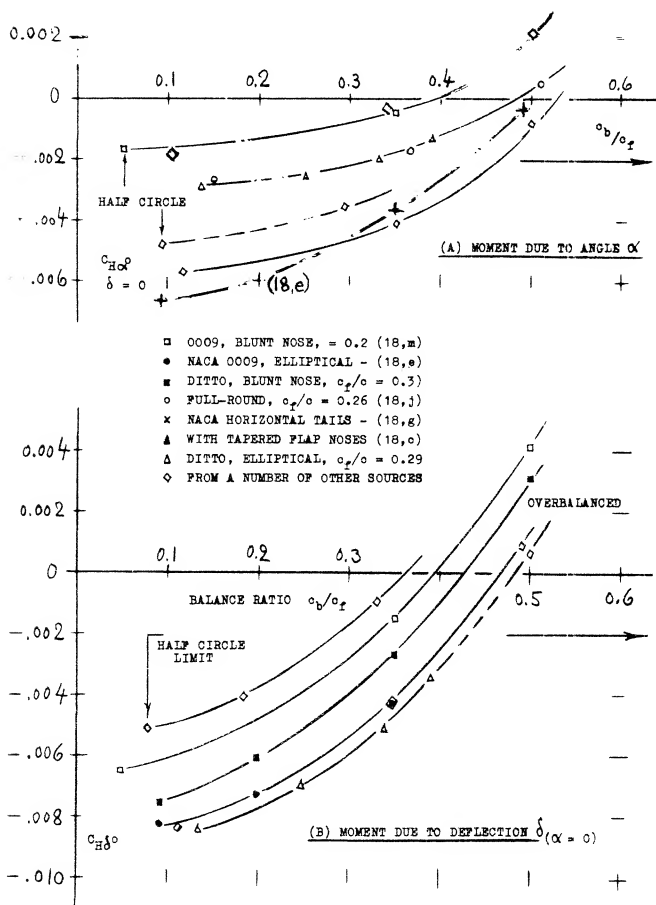


Figure 20. Hinge-moment derivatives of horizontal tail surfaces with $A = 3$ to 4, as a function of overhanging-nose balance ratio.

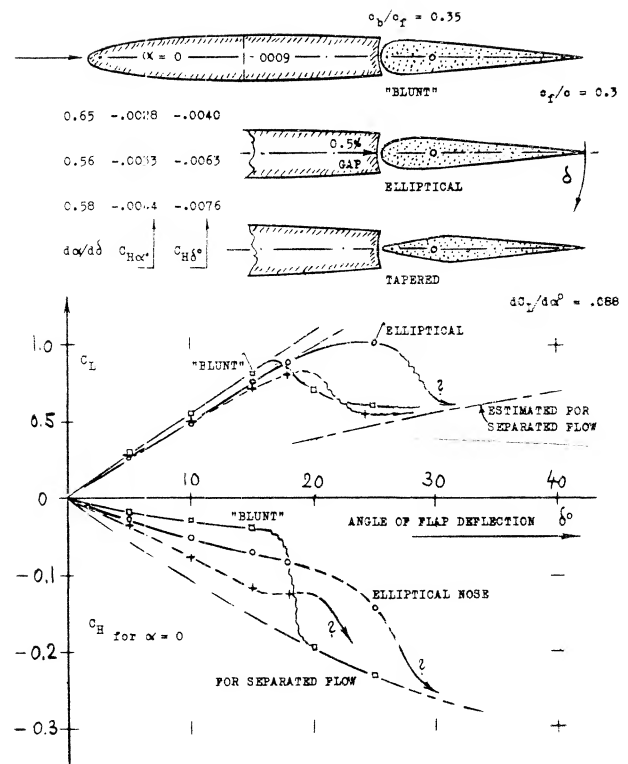


Figure 21. Lift and hinge moment characteristics of a control surface, at zero angle of attack, balanced by means of an overhanging nose.

- Tapered nose shapes (giving the flap a more or less sharp leading edge) do not readily come in contact with the outside flow. Their balancing effect corresponds to the local pressure differential between upper and lower side of wing or tail surface.
- Well rounded and "full" nose shapes "emerge" on one side from the contour of the foil section. Strong suction forces develop, as a consequence, reducing the hinge moment appreciably.

The suction forces arising on the emerging side of an overhanging nose provide an important fraction of the balancing effect; and it is this influence which causes much of the wide spread in the results as plotted in part (B) of figure 20. Depending upon shape, length, and deflection, the flap nose can also facilitate the flow past the bend in the suction side, so that $dC_L/d\delta$ slopes and maximum lift coefficients may be obtained which are higher than those due to same-size plain flaps. This applies to roughly 1/2 elliptical nose shapes. On the other hand, conditions around the bend can also be such that flow separation takes place *suddenly*, accompanied by a drop of the lift coefficient to a comparatively low level. Such termination of effectiveness is seen, for example in figure 21, beyond the deflection angle where the highly tapered nose comes out of the suction-side contour.

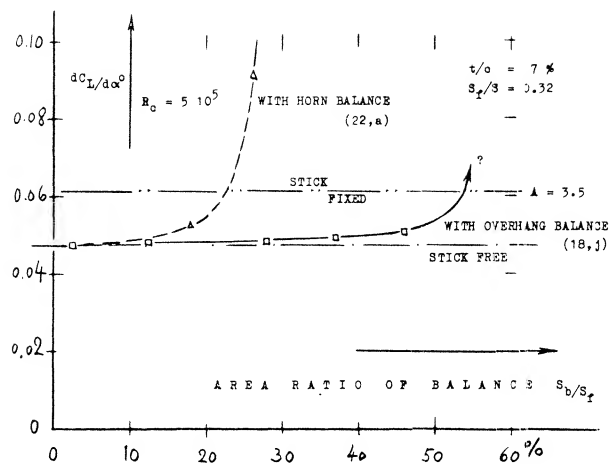


Figure 22. Stick-free stabilizing effect of tail surfaces equipped with overhanging balance, as a function of the nose length ratio.

STICK-FREE CHARACTERISTICS. At the nose-length ratio, where in part (A) of figure 20 the due-to-lift (or due-to-angle-of-attack) derivative crosses the zero axis, the stick-free lift-curve slope of a control surface is evidently equal to that with fixed stick. Stick-free characteristics (as in figure 9) can readily be determined from the derivatives in figure 20. Some results in the form of $dC_L/d\alpha$, are plotted in figure 22. The stabilizing effect increases with the nose-length ratio, at first very slowly. Beyond the ratio where dC_H/dC_L crosses the zero line, the stick-free flap motion can only be stable as long as the $dC_H/d\delta$ derivative is still "negative".

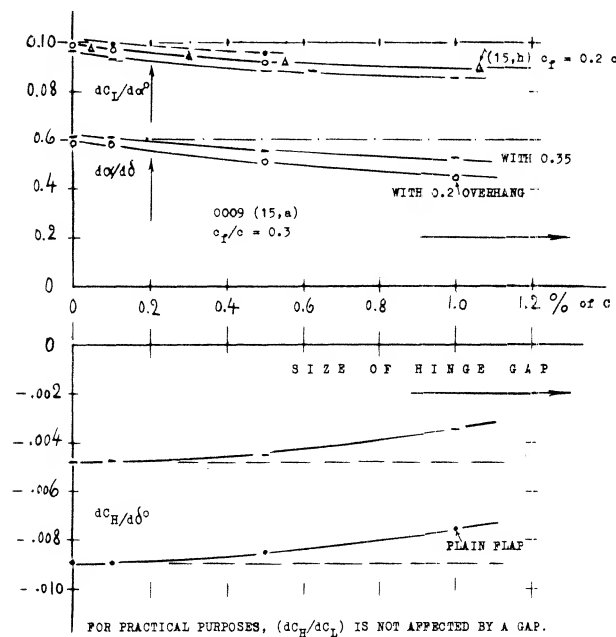


Figure 23. Experimental results indicating the influence of gaps upon tail surface lift and hinge moments.

HINGE GAPS. Every control flap requires some clearance to permit motion free of mechanical friction. We will assume that the width of the gap between flap nose and the fixed part of wing or tail surface of an airplane, may be in the order of 1/4 inch, or 1 cm. Measured as a fraction of total full-scale chord, the gap may then have a width "s" between 0.3 and 0.6% of that chord. Aerodynamic consequences of hinge gaps are:

- a reduction of lift-curve slope,
- a reduction of flap effectiveness,
- an influence upon hinge moments.

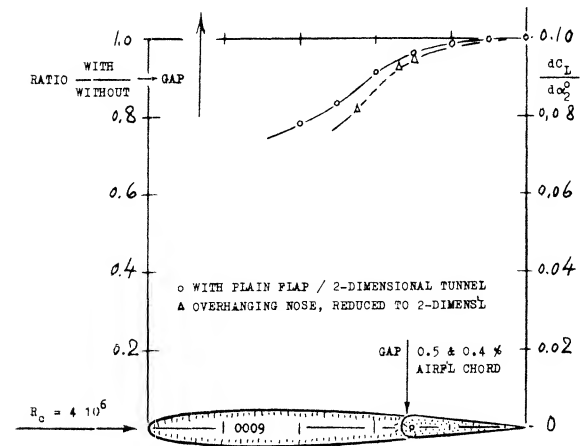


Figure 24. Lift-curve slope as affected by the location of a hinge gap. Data from (18,g).

THE INFLUENCE UPON LIFT is twofold. Figure 23 shows that $(dC_L/d\alpha)$ as well as flap effectiveness $d\alpha/d\delta$ decreases steadily when opening up the hinge gap. This means that the lifting effect $dC_L/d\delta$ may be reduced between 17 and 32% for the rather extreme gap size of 1% of foil chord. The influence upon lift of the comparatively large openings (voids) connected with overhanging-nose balance, can also be found in the tabulation in figure 19. The lift-curve slope decreases uniformly with the size of an open overhang balance. A certain interaction must be expected between nose size and/or shape and the size of the control gap. Figure 24 demonstrates that the influence of a plain control gap upon the lift-curve slope is also a function of location or of flap-chord ratio.

Figure 26. Example of a covered internal overhanging nose balance, as tested (18,d) on the half model of a horizontal tail surface.

COVERED BALANCE. Figure 23 shows a small influence of presence and size of gaps upon the hinge moment due to lift. The openings (gaps) necessarily connected with the open overhanging-nose type of balance, increase the parasitic drag of a tail surface, possibly by 10%. One has, therefore, tried to cover the openings, for example as in the last configuration in figure 26. It is readily understood that lifting, drag-, and pitching-moment characteristics of such configurations will be essentially the same as those of and due to plain flaps. Of course, the effectiveness (lift) of such "internal" balances is necessarily limited (for example, by a maximum deflection angle of 16° , instead of 25 or 30°); see figure 25.

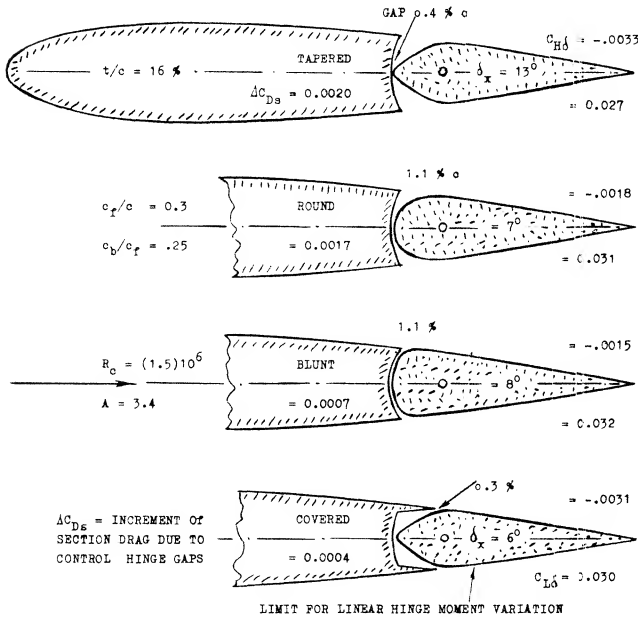
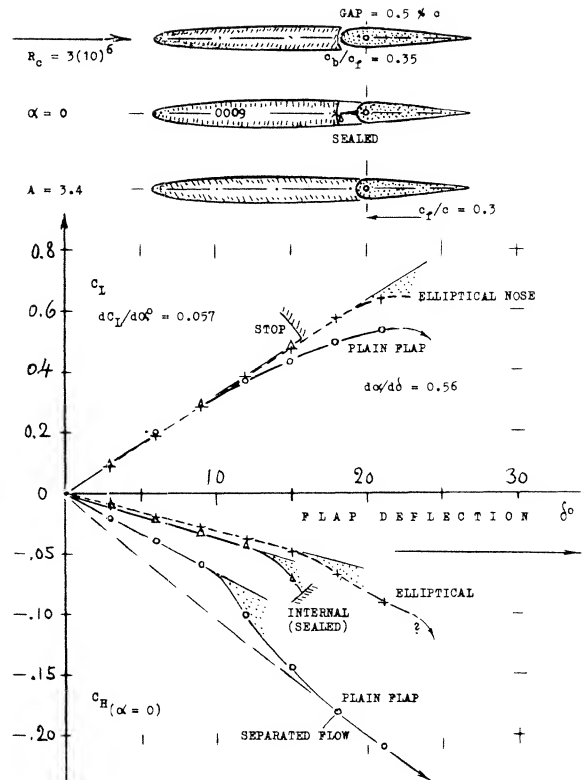


Figure 25. Characteristics of an elevator flap, tested (18,k) with 4 different shapes of a 25% overhanging nose balance.

Figure 27. Influence of internal gap size upon the hinge moment of a flapped foil section balanced by a covered overhanging nose, tested (19,e).

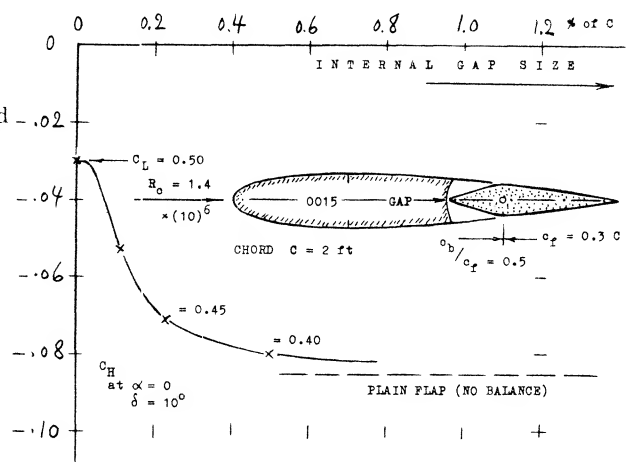
- (20) Characteristics of internal balance:
- See references (18,d) (18,e) (18,k).
 - Braslow, Internal, NACA TN 1048 (1946).
 - Pressure distribution derivatives see (18,m).
 - Denaci, Internal, NACA W Rpt L-432 (1943).
- (21) The internal balancing nose plate can also be displaced to one side, thus permitting deflection, for example, between $+10$ and -20° .



PRESSURE DIFFERENTIAL. Balancing forces correspond to the pressure differential between upper and lower section side, in the small gaps at the ends of the cover plates. As derived from basic foil-section and flap theory, this differential is roughly expected to be of the form:

$$\Delta C_p = k_1 (dC_L/d\alpha)\alpha + k_2 (dC_L/d\delta)\delta \quad (38)$$

where $dC_L/d\delta = (dC_L/d\alpha)(d\alpha/d\delta)$ and where k_1 and k_2 are constants depending upon section shape and the location of the gaps, approximately defined by c_f/c . Evaluation of tested values (20.b) indicates, for example, that for $c_f/c = 0.2$, the constants are in the order of $k_1 = 0.40$ and k_2 between 0.10 and 0.15. Figure 27 demonstrates, however, that the pressure differential between the covered sides of the nose decreases rapidly, when introducing the gap required to permit free motion of the flap. Leakage across the nose gap may be prevented by means of a suitable seal, such as in figure 26.



COVER PLATES. As described in (20,d) characteristics of an internal-type balance can also be influenced by bending the cover plates:

- when bending them out of the true section contour, the magnitude of the moments due to deflection reduce within limits.
- by bending the plates to within the section contour, the value of the moment due to deflection increases somewhat.
- in either case, the hinge moment due to lift (or angle of attack) changes in the direction opposite to that of the moment above.

The local pressure at and directly aft of the edge of each plate is evidently responsible for these effects.

INTERNAL EFFICIENCY. Figure 26 proves that internal balance can reduce hinge moments. Of course, the balancing effect also corresponds to the length of the plate ahead of the flap; and that length is restricted through the geometry within the covered space (21). Even disregarding this restriction, the graph demonstrates that an internal balance is somewhat less efficient than a comparable well-shaped open overhanging-nose. balance. The advantage of the internal type of balance is thus found in the reduction of drag as stated above.

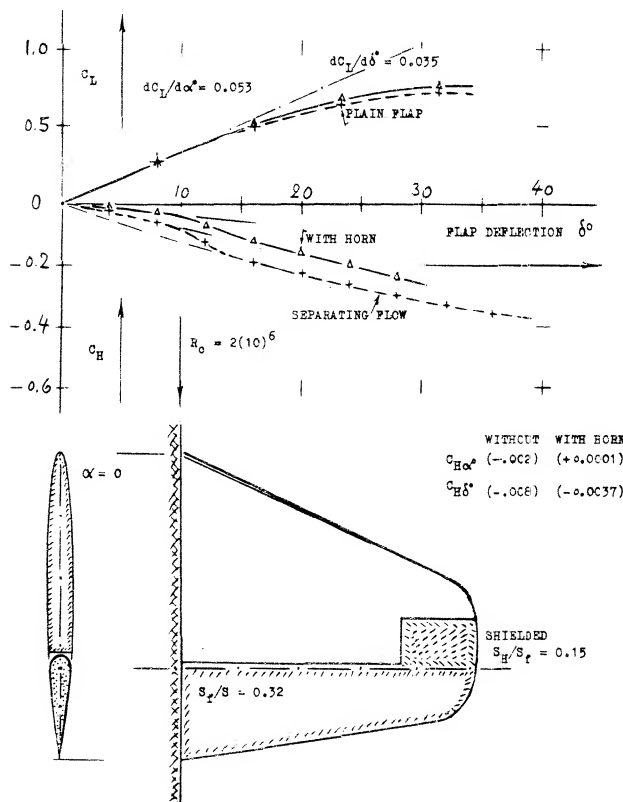


Figure 28. Lift and hinge moment of vertical (or 1/2 horizontal) tail surface tested (22,b) with and without horn balance.

THE HORN-TYPE BALANCE, as for example in figure 28, could be considered to be a part-span overhanging-nose type. Such horns are located at the outer ends of tail surfaces. Lift and hinge moment show the familiar behavior, first a linear range of variation, as a function of flap deflection, and then a transition to a higher slope, due to flow separation from the suction side of the flap. The balancing effect is, of course, a function of chord-wise and spanwise dimensions of the horn. The simplest method of defining horn size, is the area ratio S_H/S where S_H = area of the horn, measured ahead of the hinge axis, thus including a part of the radius-type nose which every plain flap usually has.

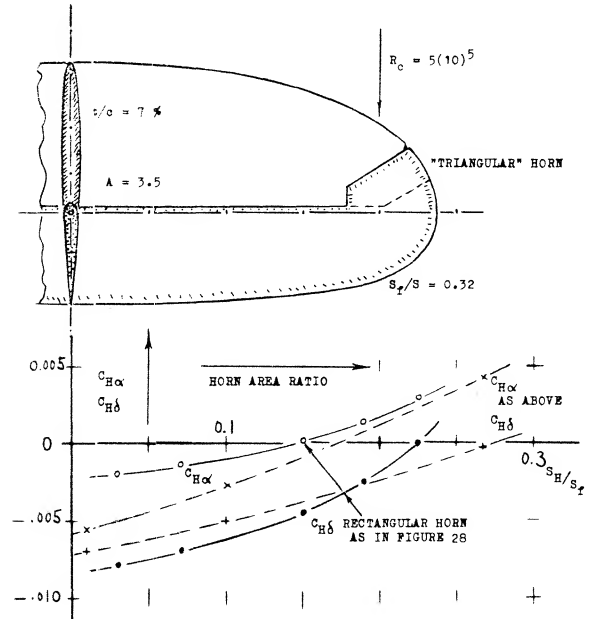


Figure 29. Influence of horn-balance size upon the hinge-moment derivatives of horizontal (or vertical) tail surfaces.

THE HINGE-MOMENT derivative $C_{H\alpha}$ and the total derivative $C_{H\delta}$ of two horn-balanced tail surfaces are plotted in figure 29, as a function of the horn-area ratio. $C_{H\alpha}$ reaches first and crosses the zero line, in a manner similar to that of the overhanging-nose type balance in figure 20. There are some differences, according to shape and arrangement of horns:

- The two configurations, tested with "shielded" horns (figure 28 and 29) show approximately the same slope of balance versus area ratio.
- Exposed horns (as in figure 30) evidently have the strongest effect of reducing hinge moments, particularly in regard to $C_{H\alpha}$.
- Depending upon shape and location of the horn, $C_{H\delta}$ can be made zero by an area ratio between 18 and 28%.

If in view of maneuverability, a positive (stabilizing) $C_{H\alpha}$ derivative is undesirable, A shielded horn type may therefore, be used to advantage.

GUARDS. When deflecting a horn-balanced flap, the flow over horn and adjoining surface becomes disturbed and separated. As reported in (22,2) a "guard", in form of an end plate, was placed within the gap of a configuration similar to that in figure 30. As a result: (a) Lift-curve slope increased some 6%. (b) The derivative $dC_L/d\delta$ increased some 5%. (c) Hinge moment due to deflection reduced some 10%. — The guard evidently improves the flow pattern over the horn and along the gap as it opens up.

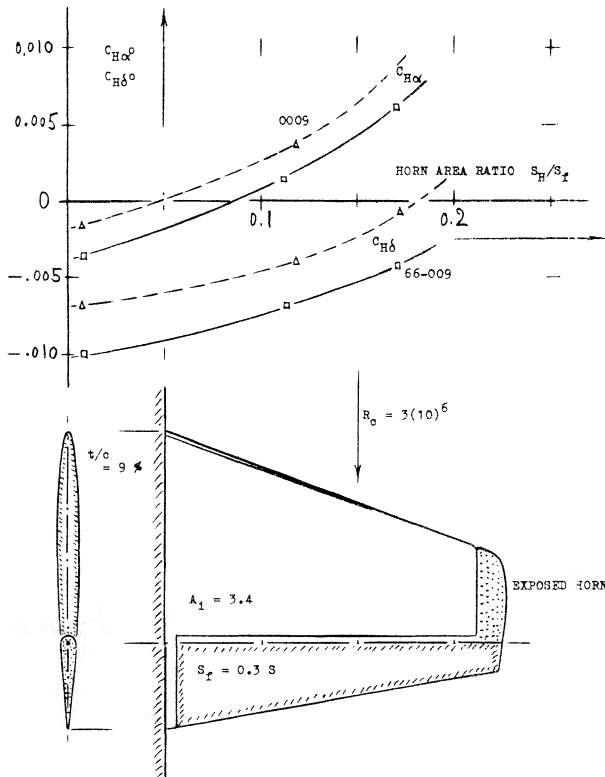


Figure 30. Exposed horns as tested by NACA (22.c) on two different foil-section shapes.

Figure 31. Critical flap angle and critical lift coefficient indicating when flow separates from flap so that lift diverges from linear variation.

- (22) Characteristics of horn-type balance:
 - a) Aachen, Horizontal Tail, ZWB FB-359.
 - b) Lowry, Vertical Tail, NACA W Rpt L-516 (1944).
 - c) Harper, Control Characteristics (Section and Balance Shape, Sweepback), NACA TN 2495 (1951).
 - d) Sears, as in reference (18,e).
 - e) Liddell, Guards, NACA W Rpt L-60 (1944).
- (23) — The sine function is not a perfect interpretation. The order of magnitude of forces and moments in separated flow, is correctly indicated, however.
- (24) Hoerner, Tail for "Storch", Fieseler Rpt 1939.
- (25) Stone, Spinning Attitudes, NACA TN 1400 (1947).
- (26) NACA, Split Flaps, TR 668 & 679 (1940/41).

8. CONTROL-FLAP CHARACTERISTICS AT HIGHER DEFLECTION ANGLES

At an angle of deflection, say between 10 and 20°, the flow usually separates from the suction side of trailing-edge flaps. On the other hand, all control flaps used in conventional airplanes, are usually designed so that they may be deflected to angles, say between 25 and possibly above 30°. Characteristics at such high angles are as described in the following section.

THE CRITICAL FLAP ANGLE, where the lift produced by deflection starts to deviate from the linear variation, as for example in figure 1 or 18, is a function of section shape, type of balance, angle of attack, aspect ratio, of other geometrical parameters as well as of the viscous conditions of the fluid flow. Figure 31 presents critical flap angles, for zero angle of attack, as a function of the flap-chord ratio: The critical angle and the corresponding lift coefficient increase with the chord ratio; and they reduce to nothing as the flap chord is decreased to zero. The angle reaches a maximum (indicating optimum section camber due to flap deflection) at c_f/c somewhat above 0.5. — The critical lift coefficient is comparatively independent of the aspect ratio. Depending upon section shape, maximum lift coefficients obtained through flap deflection, at zero angle of attack, are between 0.8 and 1.2.

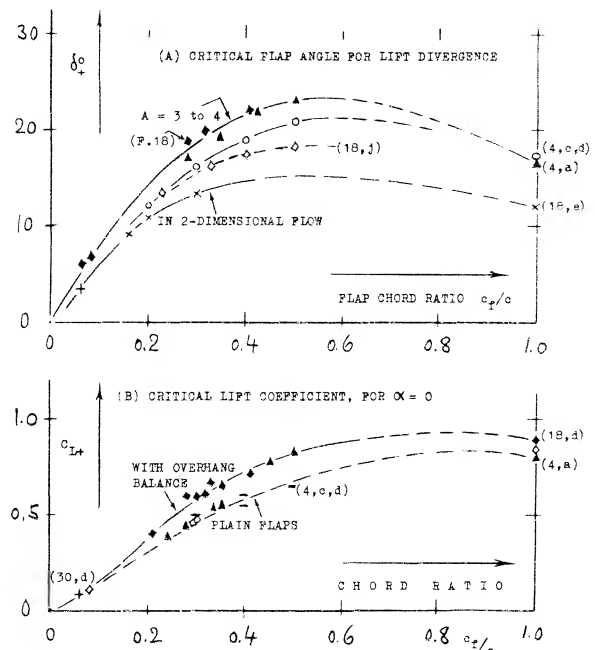
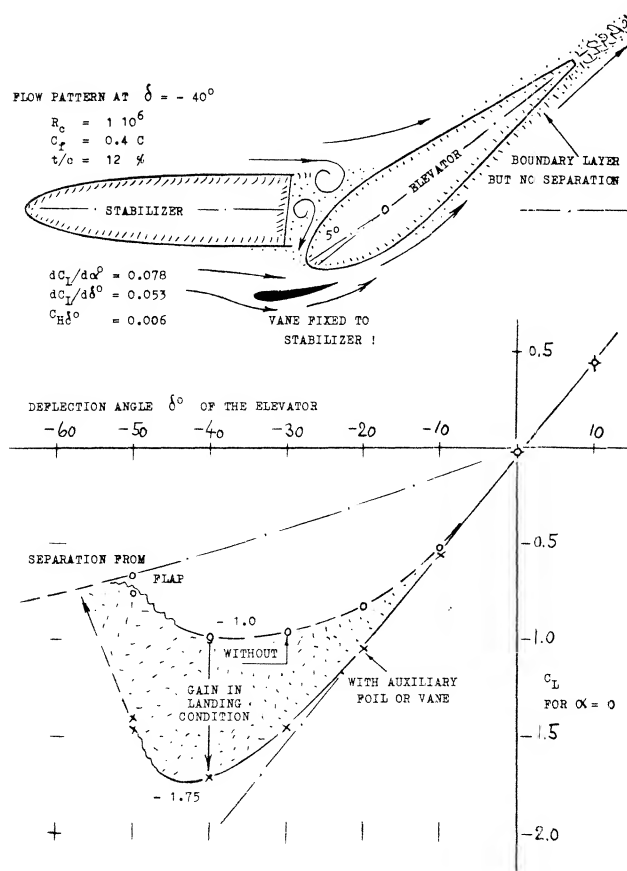


Figure 32. Influence of an auxiliary foil or vane (fixed to the stabilizer) upon the lift produced by the elevator at high angle of deflection. The horizontal tail section was tested (24) flow pattern was observed in a water tunnel.



AUXILIARY FOIL. During the landing of an airplane, the task of the elevator is to reduce or to compensate for the lift corresponding to the positive angle of attack of the horizontal tail surface. It is, therefore, suitable to design surface or elevator in an unsymmetrical manner. The maximum values of lift of the elevator in figure 32, were then found to be $C_L = -1.0$, as against $+0.9$ in the other direction. To avoid separation at angles above 15° , an auxiliary foil was then attached (a vane, fixed to the stabilizer). As shown in the illustration, the flow was successfully kept attached up to angles around $\delta = -40^\circ$. The magnitude of lift was thus increased to $C_L = -1.75$, an increment of 75% at zero angle of attack. Considering a typical landing condition, at $\alpha = +10^\circ$, the value of the minimum lift coefficient (obtained by deflection $\delta = -40^\circ$) was increased from -0.6 to -1.4 , that is more than doubled (24).

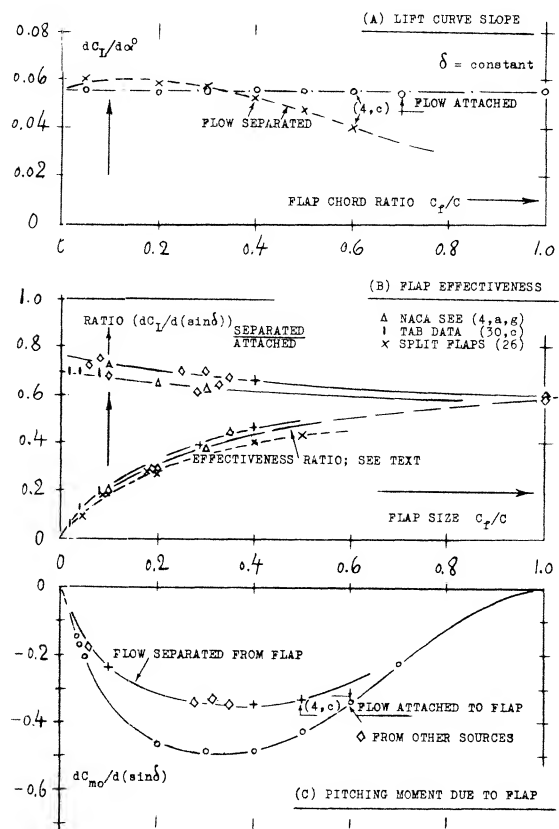
Figure 33. Characteristics of flapped configurations, such as horizontal tail surfaces in particular, at higher angles of deflection where the flow is separated from the suction side.

LIFT-CURVE SLOPE. At flap deflections exceeding the critical angle, a control surface still has a defined lift-curve slope, as long as the flow remains attached to the forward part of the foil section. Figure 33(A) shows that the slope is somewhat higher than that of the surface with fully attached flow, within the range of chord ratios below 0.3. It seems that the flap has in this case, an effect similar to that of a blunt trailing edge which is known to improve lift-curve slope as well as maximum lift. At chord ratios above 0.3, the slope decreases considerably.

FLAP EFFECTIVENESS. As demonstrated in figures 1 and 18, the lift of a flap continues to increase, after passing through a more or less pronounced dip, as the deflection is increased above the critical angle. The same graphs also suggest that the lift produced by a flap, under conditions where the flow is separated from its suction side, that this lift increases very roughly in proportion to the sine of the flap angle (23). It is thus possible to approximate statistically and for practical purposes, the effectiveness of a flap above its critical angle, by the ratio

$$[dC_L/d(\sin\delta)]/[dC_L/d(\sin\alpha)] = d(\sin\alpha)/d(\sin\delta) \quad (39)$$

where $dC_L/d(\sin\alpha)$ = lift-curve slope of the lifting surface in plain fully-attached flow. Evaluation of experimental results, as in figure 33(B), shows that this ratio is related to the effectiveness as in figure 2. The ratio of the two ratios, also plotted in the graph, is between 0.6 and 0.7. At chord ratios approaching zero (as in tabs) the effectiveness ratio in figure 33(B) coincides with that in figure 2.



THE PITCHING MOMENT due to deflection of flaps with separated suction-side flow, may also be interpolated by means of a sine function. Approximate results of this type are plotted in *figure 33(C)*. In comparison to those in *figure 4*, pitching moments due to separated-flow flaps, are only 1/2 or possibly 2/3 of those in attached-flow condition. The moment obviously corresponds with the effectiveness ratio.

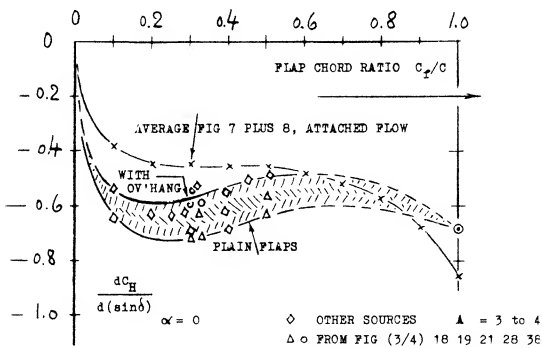


Figure 34. Rough indication for the hinge moment derivative of horizontal or vertical tails, at higher angles of deflection where the flow is separated from the suction side of elevator or rudder.

HINGE MOMENTS at very high angles of attack, as they are encountered during spinning (25) are much higher than those represented by dC_H/dC_L in *figure 7*. Disregarding some discontinuity directly within the range of stalling (separation), the moment roughly varies as

$$-C_H \sim \sin^2 \alpha \quad (39)$$

approaching the order of -0.5 at $\alpha = 90^\circ$. As a function of flap deflection (with the flow past the forward part of the foil section still attached) hinge moments at higher angles as indicated in various graphs may be approximated by $C_H \sim -\sin \delta$. Results (for zero angle of attack) as plotted in *figure 34*, vary as a function of the flap chord ratio, in a manner similar to an average curve derived for attached flow condition. Within the range of practical chord ratios, the derivative (on δ in degrees) is in the order of $C_{H\delta} = -0.012$, depending on parameters as discussed in connection with *figures 7* and *8*. In separated condition, hinge moments are 20 to 60% higher than in fully attached flow. As seen, for example in *figure 21*, the balancing effect of an overhanging nose is greatly reduced. The derivative of such flaps is around $C_{H\delta} = -0.010$.

9. CHARACTERISTICS OF CONTROL TABS

“Tabs” are small-size auxiliary flaps attached to, or part of the trailing edge of control flaps. Hinge moments can efficiently be changed by tabs.

MECHANICS OF TRAILING EDGE TABS are basically the same as those of control flaps. We thus find:

their effectiveness or influence upon lift in *figure 2*,

upon longitudinal or pitching moment in *figure 4*,

their own hinge moments in *figures 7* and *8*.

As illustrated in *figure 35*, trailing-edge tabs can be used in 5 different ways, to modify the characteristics of control surfaces.

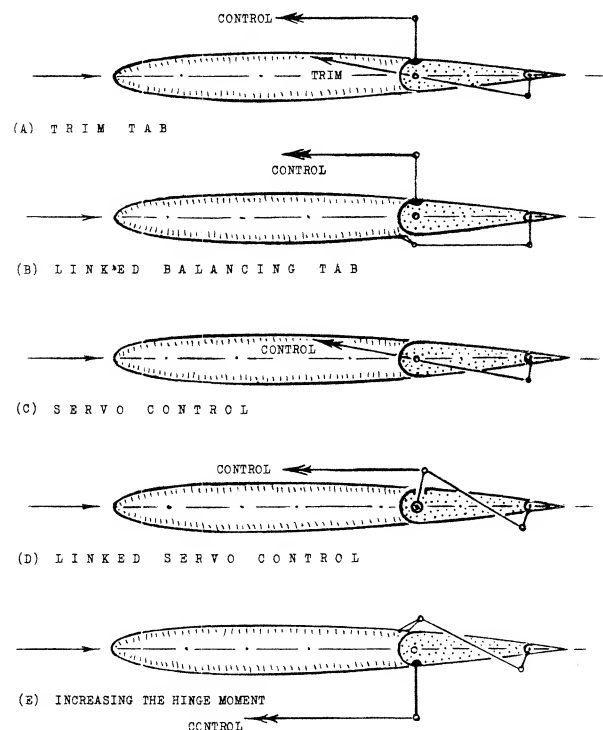
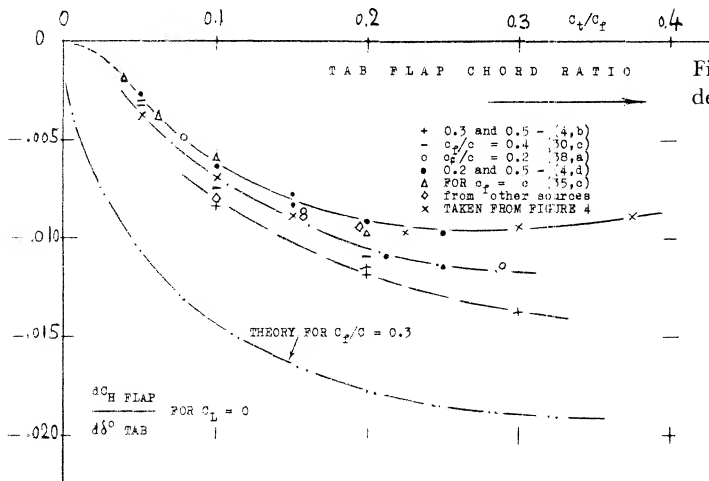


Figure 35. Sketch showing various basic uses of trailing-edge tabs.

THE HINGE MOMENT of the tab proper will be discussed later. The influence of the tab upon the hinge moment of the control flap to which it is attached, is theoretically (30) a function of the flap-chord ratio. The influence of viscosity in combination with foil-section and flap shape, evidently obscures that of the flap-chord ratio. Results for ratios between 0.2 and 0.5 are plotted in figure 36, as a function of the tab-chord ratio. Deviation from theory is largest within the range of tab-chord ratios below 0.1. Realistic results might be approximated by

$$(dC_H/d\delta_t^{\circ})_{\delta C_L} = -k (c_t/c_f) \quad (40)$$

where $k = 0.05$ or $= 0.06$ applies to smaller flap-chord ratios (in the order of 0.2) and to heavier boundary layers, and $k = 0.07$ or $= 0.08$ to larger flap-chord ratios (in the order of 0.4) and to smooth configurations at higher Reynolds numbers. For tab-chord ratios in the order of 0.2, the variation of the flap-hinge moments due to tab deflection, is thus roughly proportional (a) to the tab angle, and (b) to the tab-chord ratio (32). Since a flap with a chord equal to that of the foil section, is simply a plain "wing" surface, the pitching moment as in figure 4, is realized to be the equivalent of a hinge-moment. Points included in figure 36, approximately agree with those obtained for conventional flap-chord ratios.



TRIM TABS. The most widely used application of tabs is as in figure 35(A) where the zero-hinge-moment deflection of elevator, rudder or possibly aileron, is changed by suitable deflection of a tab, by means of a lever near the pilot's seat. Consider as an example, a horizontal tail with $c_t/c_f = 0.1$, and $dC_H/d\delta^{\circ} = -0.007$. Assuming now that the control-flap deflection is to be changed by $+5^{\circ}$, keeping $C_L \approx$ constant, the required tab deflection is obtained through the use of equation (40); thus:

$$\delta_t^{\circ} = \Delta C_H / (k c_t/c_f) = (dC_H/d\delta^{\circ}) \delta^{\circ} / (k c_t/c_f) \quad (42)$$

which yields in the example above, a tab deflection of minus 5 or 6° .

EFFECTIVENESS. To be sure, deflection of a balancing tab (in the direction opposite to that of the control flap) somewhat reduces effectiveness. When, for example, using a tab with $c_t = 0.1 c_f$, geared so that $\delta_t = -\delta$, the reduction of $d\alpha/d\delta$ can readily be found from figure 2. Assuming that $d\alpha/d\delta \sim (c_f \text{ or } c_t)/c$, as it is roughly true within the range of small chord ratios, the effectiveness $d\alpha/d\delta$, and lift per degree of deflection produced by the control flap, are reduced by $\approx 10\%$. Therefore, in the example above, both tab angle and flap deflection should be made some 10% larger, in order to keep $C_L =$ constant.

LINKED-TAB BALANCE. When gearing or coupling the tab in the manner as illustrated in figure 35(B) it automatically deflects (from the control-flap chord) when moving the flap, in a direction opposite to this motion. Hinge moments produced by the tab then tend to balance those of the flap. For example, for $c_f/c = 0.3$, the hinge moment corresponds to $dC_H/d\delta \approx -0.008$ (see figure 8). It can then be found in figure 36 that, for a coupling ratio of $\delta_t/\delta = -1$, a full-span tab with $c_t = 0.13 c_f$, will fully cancel the flap's hinge moment. Or, when selecting a tab chord $c_t = 0.1 c_f$ for example, or reducing the tab span to $0.10/0.13 = 0.77$ times the flap span, or by reducing the coupling ratio from 1.0 to 0.77, the hinge moment will be reduced to $(100 - 77) = 23\%$, in the example considered.

Figure 36. The trimming or balancing effect of tab deflection upon the hinge moment of control flaps.

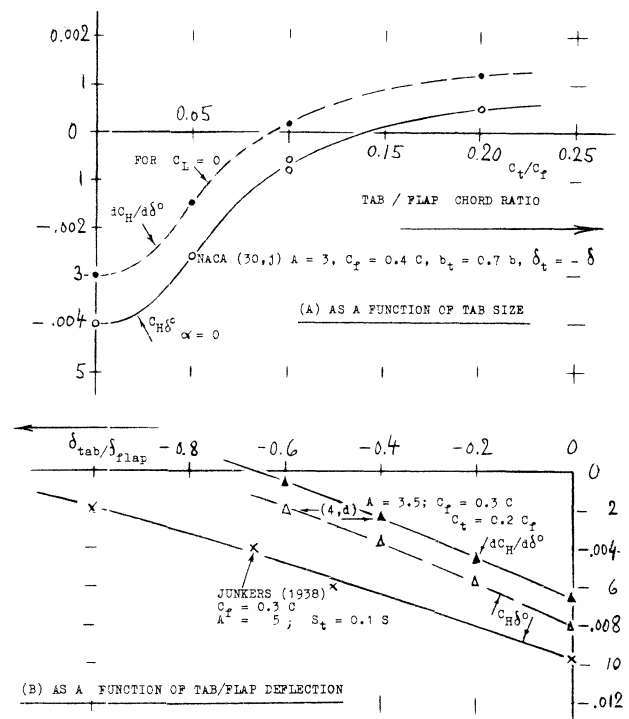


Figure 37. Hinge moment of two tail surfaces as reduced by linked deflection of tabs.

REDUCTION OF HINGE MOMENTS. Figure 37 shows hinge moments of two horizontal tail surfaces as a function of: (a) size (chord) of the linked tab; (b) deflection ratio of the linked tab. — Moments can be reduced "easily", for example by means of a tab with $c_t/c_f = 0.1$ and a deflection ratio between 0.5 and 1.0. Figure 38 demonstrates that linked-tab balance is effective, not only in the case of a plain flap, but also in combination with an internal balance. Hinge moments can thus be reduced down to a few percent of the original function.

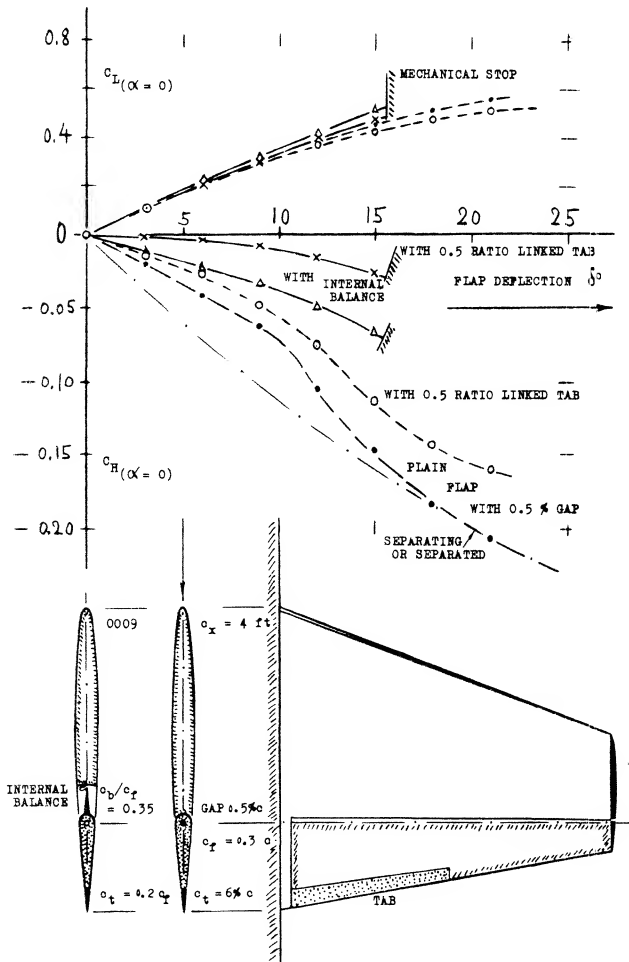


Figure 38. Influence of a linked trailing-edge tab upon the lift and hinge-moment characteristics of a tail surface.

- (30) Characteristics of flap-plus-tab systems:
- For theory, see references (2,b) and (2,e).
 - For results, see references (4,b) and (4,d).
 - Harris, Moments due to Tabs, NACA T Rpt 528.
 - Wenzinger, Pressure Distrib., NACA T Rpt 574.
 - Bausch, Wing, Yearbk D. Lufo 1940 p.I-182.
 - Crandall, Correlation, NACA TN 1049 (1946).
 - Brewer, Balanced Tabs, NACA TN 1403 (1947).
 - 0015 with Flap and Tab, ARC RM 2314 (1943).
- (32) For tab-chord ratios exceeding 0.2, interpolation by $dC_H/d\delta_t \sim \sqrt{c_t/c_f}$ would be better.
- (33) Note that the hinge moment due to lift (at fixed flap angle) is not affected by a tab.

BOOSTING HINGE MOMENTS. Full cancellation of the control moment is hardly ever desirable. In fact, there have been small and low-speed airplanes (and there seem to be some sailplanes) where stick forces in the longitudinal direction are *increased* by adding a tab to the elevator, geared in such a manner that it deflects in the same direction as the elevator; see part (E) of figure 35. Three things are accomplished in this way: (a) hinge moments are suitably increased (whenever this is desirable); (b) control effectiveness is somewhat increased; (c) longitudinal stability of the airplane is improved.

LEADING TAB. An interesting application of a linked trailing-edge tab is shown in figure 39. The elevator is basically overbalanced by means of a 50% overhanging nose. However, the tab is linked in such a manner that it deflects in the same direction as the elevator flap. The derivative $C_{H\delta}$ is then made negative (stable): (a) by the leading deflection of the tab, thus counterbalancing the overhang; b) to a degree by the reaction in the elevator to the tab's hinge moment. The linkage ratio δ_t/δ as recommended in the conclusion of (37) is 0.5. The mechanism described also has the advantage of providing increased effectiveness, so that a lesser deflection will be sufficient to obtain a certain lift coefficient. It can also be noted that $C_{H\alpha}$ is positive. This means that longitudinal stability of the airplane is not reduced, but slightly improved, when leaving the control stick free.

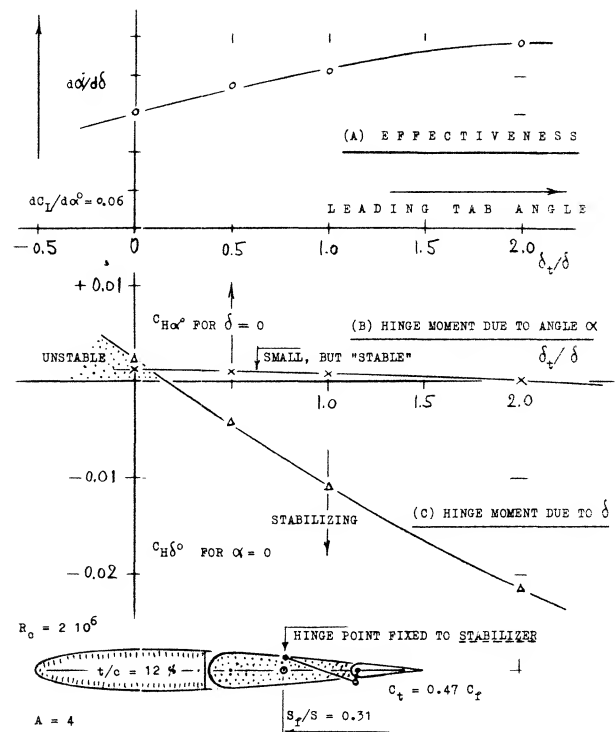


Figure 39. Effectiveness and hinge moments of a horizontal (or vertical) tail surface as described in the text, loaded by a leading tab (37).

STICK-FREE CONDITION. In a tabbed configuration where the hinge moment is reduced to nothing, the control flap will simply move to a certain limiting position (to a mechanical stop or to a point where the flow separates from the flap's suction side). Quantitatively, combination of equations (27) and (28) indicates that

$$\Delta(d\alpha/dC_L) = +(d\alpha/d\delta)(dC_H/dC_L)/(dC_H/d\delta) \quad (44)$$

The influence of the tab upon $(dC_H/d\delta)$ corresponds to

$$\Delta(dC_H/d\delta) = (\delta_t/\delta)(dC_H/d\delta_t) \quad (49)$$

where (δ_t/δ) = coupling ratio (negative) and $(dC_H/d\delta_t)$ as in figure 36 or in equation (40). Using that equation, the reduction of the hinge moment is found to correspond to

$$\Delta(dC_H/d\delta) = k(\delta_t/\delta)(c_t/c_f) \quad (50)$$

To simplify discussion, we may also assume that the coupling ratio be $\delta_t/\delta = -1$, so that the chord ratio (c_t/c_f) becomes the measure for the tab effect. To arrive at quantitative results, we will consider two different control-flap configurations:

(a) an aileron (or horizontal-tail) installation with:

$$c_f/c = 0.2; d\alpha/d\delta = 0.45; d\alpha/dC_L = 15^\circ$$

(b) a horizontal (or vertical) tail surface with:

$$c_f/c = 0.4; d\alpha/d\delta = 0.70; d\alpha/dC_L = 20^\circ$$

where $(d\alpha/dC_L)$ is meant to be for fixed-control condition. Using equations (49) and (50) in conjunction with values taken from the various graphs, stick-free lift curve slopes have been computed for the two cases. Figure 40 presents these values as a function of the tab size. The loss of stabilization can be considerable, particularly in the tail surface considered.

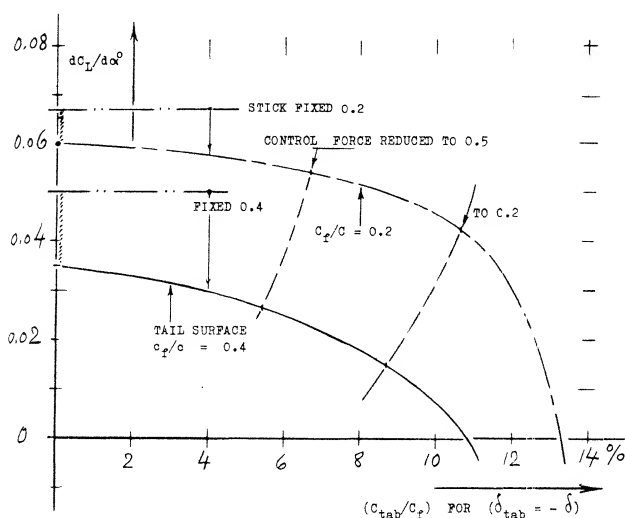


Figure 40. The stick-free stabilizing effect of
(a) an "aileron" section with $c_f/c = 0.2$
(b) a tail surface with $c_f/c = 0.4$
computed as explained in the text.

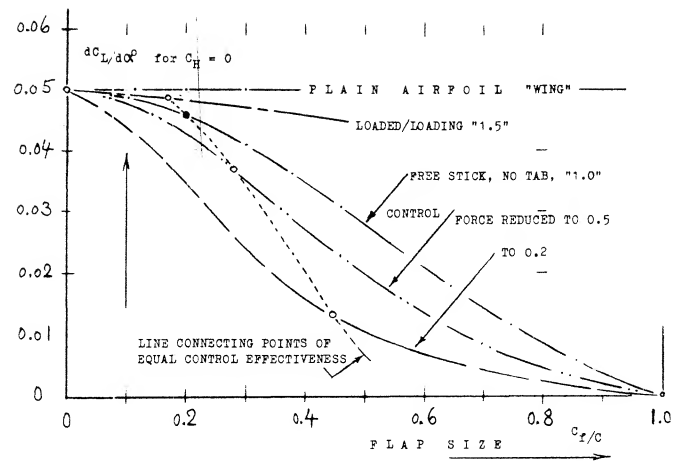


Figure 41. The stick-free stabilizing effect of tab-balanced control surfaces as a function of the flap-chord ratio.

FLAP SIZE. The most important parameter affecting stabilization is the chord ratio of the control flap. Using the same functions as above, we have computed the stick-free lift-curve slope of a horizontal (or vertical) tail surface similar to that in case (b) above, but with varying flap-chord ratio. Figure 41 shows the lift-curve slope, as a function of the chord ratio, with balancing trailing-edge tab, geared at a ratio so that the hinge moments are reduced to 1/2 and to 1/5, respectively. The loss of stick-free stabilization is again seen to be very considerable. Of course, small flaps may not be sufficient in regard to the maximum lifting or compensating effect they are expected or required to produce. Unfortunately, the stabilizing effect of tabbed tail surfaces reduces more and more as the flap-chord ratio is increased. In addition, it should be realized that reduction of "hinge moments" to 1/2 or to 1/5 as assumed, is not really proper. These moments grow in proportion to the square of the flap chord. Accordingly, a small flap might not need any balance at all, while it might be desirable or necessary to reduce the torque of a larger flap, not just to 1/5, but possibly to 1/10. A line connecting points of equal hinge moments (equal in foot-pounds) is shown in figure 41, thus demonstrating the fact that the stabilizing effect of geared-tab control surfaces reduces very strongly, after exceeding a certain range of small flap-chord ratios.

SERVO CONTROL. Deflection of a tab (rather than of the flap itself) by means of some small control force as in figure 35(C) can be utilized to move larger-size control flaps (elevators, rudders, ailerons). This type of servo system has been tried on ship rudders, in an effort to reduce the heavy steering machinery usually required (39). In airplanes, the servo-tab system has been used in a number of larger airplanes (40) to operate the rudder. The straight-forward system has a number of drawbacks, however: (a) it will not work at higher deflection angles because of flow separation; (b) it may

fail at low speeds where mechanical friction will interfere; (c) it will reduce stick-free stabilization considerably (36); (d) the doubly-linked system can invite flutter trouble (44); (e) there is a time lag involved in the operation (41,b). — Regarding the last point, dynamic behavior (45) is as follows. After sudden deflection of the tab, the flap assumes the proper position almost aperiodically, but after a delay in the order of 1 second (as tested on a larger than full-scale model). The delay is proportional to $\sqrt{I/q}$, where I = mass moment of inertia and q = dynamic pressure. When suddenly releasing tab and flap, both components oscillate several times, before coming to rest in the balanced position. — Nevertheless, the aerodynamic mechanism of servo-tab control deserves to be presented.

REDUCTION OF TORQUE. A servo-tab system can be considered to be a type of fluid-dynamic balance. The tab deflection required to move a control flap (within the linear range of their characteristics, and at $C_L = \text{constant} \approx \text{zero}$) is found from equating their hinge moments:

$$(dC_H/d\delta)\delta = -(dC_H/d\delta_t)\delta_t \quad (52)$$

For assumed chord ratios of $c_f/c = 0.4$ and $c_t/c_f = 0.2$, for example, the deflection-angle ratio would be

$$\delta_t/\delta = -(dC_H/d\delta)/(dC_H/d\delta_t) \approx -0.5 \quad (53)$$

where the moment due to tab deflection is obtained from equation (40) for $c_t/c = 0.2$ (0.4) = 0.8. The control moment (at the stick) required to deflect the tab, in comparison to that of the control flap without any balance, approximately corresponds to

$$(\text{servo tab})/(\text{plain flap}) = -(\delta_t/\delta)(c_t/c_f)^2 \quad (54)$$

which is equal to 2% in the example considered. Theoretical possibilities of this system thus appear to be great (41).

- (35) Characteristics of linked-tab balance:
 - a) Harper, Tail Surfaces, NACA TN 2495 (1951).
 - b) Dunn, DC-6 Airplane Control Surfaces, Proc Internat Aeron Conf IAS/RAS, New York 1949.
 - c) Balancing Tabs, ARC RM 2510 (1941).
- (36) Stiess, Influence of Linked-Tab Upon Stability and Control, Yearbk D. Lufo 1941 p.I-252.
- (37) McKee, H-Tail Leading Tab, NACA WR L-702 (1943).
- (38) Characteristics of servo-tab control:
 - a) ARC, Rudders, RM 1105 & 1514 (1927/32).
 - b) Reid, Servo Control, J Aeron Sci 1934 p. 155.
 - c) Wright, Servo-Control, ARC RM 1186 (1928).
 - d) ARC, Servo Ailerons, RM 1262 (1929).
- (39) Steering machinery including accessories of an ocean liner may weightwise be in the order of 20 tons. This much may only be 0.1% of the vessel's displacement weight, however.
- (40) Reid (38,b) reports that between 1921 and 1925 some 25 sea-going ships were equipped with servo-tab rudders. He also reports that between 1926 and 1934 a number of larger British airplanes were using servo rudders.

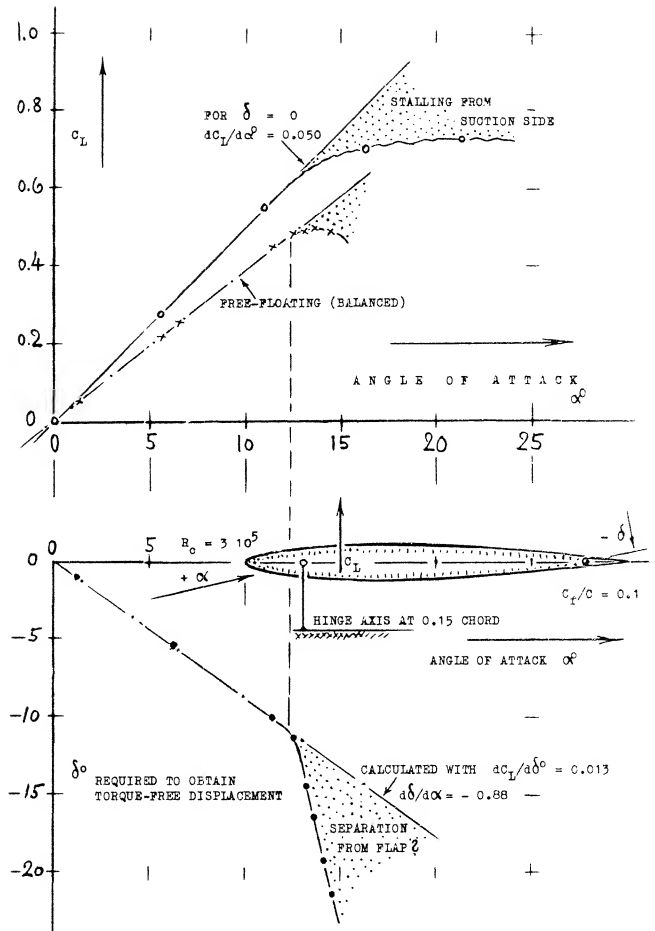


Figure 42. Example of an all-movable servo-flap controlled tail surface, as tested (38,c), and as calculated (see text).

FULLY-MOVABLE TAIL. Figure 42 shows characteristics of a *fully* movable servo-tab operated tail surface. We want to determine the control forces required. Since there is no fixed part (fin or stabilizer) we can consider the hinge moment of the surface either as that of a flapped section with $c_f/c = 1.0$, or as longitudinal (pitching) moment of that section. To keep the notation as in control flaps, use of figures 7 and 8, at $c_f/c = 1$ is recommended. A simplified analysis is possible, however, through consideration of the location along the chord: (a) of the lift due to angle of attack; (b) of the additional (negative) lift due to deflection of flap or tab (whatever name we want to give in this case). — The component under (a) was experimentally (38,c) found to be at ≈ 0.225 of the chord. For the hinge location at $0.15c$ (see subscript "x") the moment arm of (a) is then $0.225 - 0.15 = 0.075$; and the hinge moment of the plain foil corresponds to $dC_{mx}/dC_{L0} = -0.075$. When using the servo flap (or tab) to deflect the surface as a whole, the longitudinal moment due to lift must obviously be cancelled by that due to deflection of the flap. In order to obtain the same lift coefficient, α has to

be somewhat larger, however, than in the plain foil; the ratio of the angle is

$$(\alpha + \Delta\alpha)/\alpha = 1 - (d\alpha/d\delta)(\delta/\alpha)$$

which is 1.26 for the configuration considered. In a simplified analysis, we will assume that the lift differential produced by the flap has its center of pressure at 0.5 chord (as explained in connection with figure 6). The moment arm of the due-to-flap force is then $\Delta x/c = \Delta C_m/\Delta C_L = 0.50 - 0.15 = 0.35$, in the case considered. Since $\Delta C_L/C_L = (1/1.26) - 1 = -0.21$, the hinge moment due to flap- or tab deflection is

$$dC_{mx}/dC_L = dC_H/dC_L = +0.35 \cdot 0.21 = +0.074 \quad (56)$$

This value is sufficiently close to that as tested. The results in figure 42 have thus been checked by analysis.

TAB-HINGE MOMENTS (at the tab's hinge line) are usually very small; see figures 7 and 8 at c_f/c below 5% and consider moment proportional to c_t^2 . Considering the servo-control flap as in figure 42, its torque can be determined through the use of equation (40). As a function of C_L , the flap's or tab's resultant hinge moment corresponds to

$$(dC_H/dC_L)_t = (dC_H/dC_L) + (dC_H/d\delta)_t / (dC_L/d\delta)_t$$

where $(dC_L/d\delta)_t$ to be computed, or equal to 0.013 as tested for the configuration in figure 42. Using values picked from figures 7 and 8, the variation of the tab hinge moment is found to be

$$(dC_H/dC_L) \approx 0 + 0.008/0.013 = 0.6 \quad (58)$$

This derivative is based upon flap or tab chord. In order to make a comparison with the hinge moment of the plain foil, the result must be multiplied with $(c_f/c)^2 = 1/100$. The tab-moment derivative, referred to total foil chord, is thus 0.006, which is some 8% of that of the plain foil balanced at 0.15 of its chord. Considering the tab deflection required, corresponding to $\delta_t/\delta = -0.87$, the control moment (in the steering column) required for servo-tab operation, will only be $0.87(0.08) \approx 7\%$ of that required to move the unbalanced control surface to the same lift coefficient.

BALANCE OF TAB TORQUE. Boundary layer thickness reduces the tab effectiveness. Gaps around the tab's hinge axis are also undesirable. As far as hinge moments (around the same axis) are concerned, reference (30,h) demonstrates that an overhanging-nose type of balance can be very effective, in a manner and to a degree similar to what is explained in a previous section on this subject.

LINKED SERVO SYSTEM. As stated in the beginning, simple servo-tab control has serious operational disadvantages. In fact, this system is no longer used. Control characteristics were substantially improved, however, by suitable mechanical coupling between flap and tab. One such system is illustrated in figure 35(D). Because of the lever linking (but not connecting) the actuating rod with the flap's hinge point, a certain moment can be transferred to the flap and not only to the tab. The mechanism can be understood by considering limiting conditions: (a) when keeping the flap fixed, the control rod causes a deflection of the tab; (b) when keeping the tab fixed (against the flap), the control rod causes directly a deflection of the flap. — The control force of the linked servo system corresponds to the total derivative

$$\frac{dC_H}{d\delta} = \frac{(dC_H/d\delta)_L + (dC_L/d\delta)(dC_H/dC_L)_0}{1 - [K(c_f/c_t)^2(b/b_t)(dC_H/d\delta_t)/(dC_H/d\delta)_t]}$$

where b_t/b = tab-span ratio (which might be less than unity and K mechanical coupling ratio between tab and flap in stick-fixed condition. This ratio $K = d\delta/d\delta_t$ is negative, $K \approx -0.5$ in the configuration as in figure 35(D). Selecting average values for the derivatives to be used in the equation, that configuration is expected to operate at a control force which is only 1% of that of the same flap without balance

SPRING-TAB CONTROL. The servo-tab system in figure 35(C), is based upon aerodynamic forces and thus dependent upon dynamic pressure and flying speed. Replacing the actuating element in that system by a mechanical spring and providing suitable stops, servo operation begins after exceeding a minimum hinge moment (in feet-pounds) and it terminates upon reaching a certain control force (in pounds) corresponding to loading and elastic constant of the spring element used. Such a system is as in figure 35(D). When moving the control stick, the tab is deflected first (compressing the spring element), thus causing the desired deflection of the flap in a manner similar to that of a simple servo-tab system. Upon reaching a certain limiting torque, either because of high dynamic pressure or at larger angles of deflection (when flying at lower speeds), the control lever goes against a stop; and the flap is then directly controlled by rod and stick. The theory of this system has been worked out (49); considerable experimentation is reported (50). Advantages are as follows: (a) Stick-free stability is not affected, particularly when the spring-tab system is preloaded. (b) Time lag and "sloppy" performance are eliminated. (c) Overcontrolling (due to small control forces) is prevented. (d) In high-speed pull-out maneuvers, stick force is (or can be made) proportional to acceleration. (e) Whenever necessary, the control flap can be moved to high angles of deflection (such as during the landing maneuver).

CONTROL FORCES. As far as control moments are concerned, it may be assumed that tab torque $\sim (dC_H/d\delta)_L$, while disregarding the influence of α or C_L and δ . The contribution from the direct displacement of the flap against the spring element, is proportional to the spring constant. For an extremely weak spring, we obtain the small control forces as discussed above for the "linked" servo system. For an extremely stiff spring, the control moment is equal to that of the flap without tab assistance. With the control lever against one of the stops and the tab in the corresponding end position, the hinge moment is that of the flap without balance, minus a differential corresponding to the final tab deflection. Various modifications of the system are possible. Examples for stick forces obtained through such arrangements are presented near the end of the "aileron" chapter.

10. COMPRESSIBILITY EFFECTS ON CONTROL SURFACES

As discussed in Chapter VII the effect of compressibility in the subsonic range is to cause an increase of the slope of the lift curve below the critical Mach number and a sharp change in both lift and drag above the critical Mach number. Since it is desirable to have no sudden changes in the control characteristics of the airplane with changes of speed, compressibility effects are important considerations in the design of control surfaces.

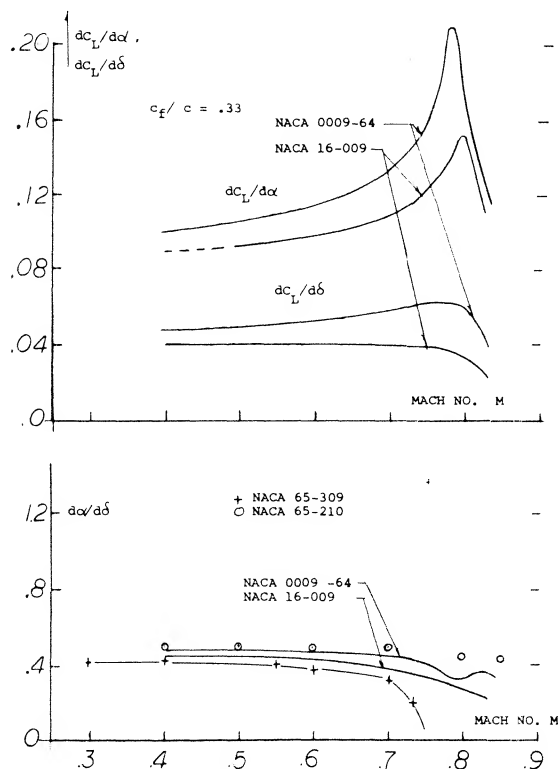


Figure 43. Flap effectiveness of two dimensional sections as a function of Mach number.

Flap Effectiveness Ratio. As shown on page 9-2, effectiveness ratio of flaps is determined by the ratio of $dC_L/d\delta$ to $dC_L/d\alpha$ or $d\alpha/d\delta$. For a flapped airfoil two dimensional operating below the critical Mach number tests (51,a) show that both lift curve slopes will increase with the Prandtl-Glauert factor $1/\sqrt{1-M^2}$. The effectiveness ratio then should not change below the critical Mach number at least for flaps mounted on a two dimensional airfoil. This is illustrated on figure 43 for symmetrical airfoils with a 33% chord flap. The increase of $dC_L/d\alpha$ as the critical Mach number is approached is sharper than $dC_L/d\delta$ as illustrated, so that below M_{cr} the effectiveness decreases slightly. The important decrease in flap effectiveness ratio illustrated on figure 43 occurs at a Mach number above the critical, and is dependent on the load distribution and where on the airfoil the local shock wave is first formed. Although the lift curve slopes shown on figure 43 apply at angles up to 5° , it can be expected that non-linearities will be encountered at the higher angles.

- (41) Characteristics of Flettner-type flaps:
 - a) The servo-tab mechanism was originally patented to Anton Flettner, whose name was occasionally applied to tabs in general.
 - b) Operation of the simple Flettner-type servo-tab system has been called "sluggish".
- (45) Stauffer, Motions of Servo-Tab Control Flap as Function of Time, Ybk D Lufo 1942, I-308.
- (49) Analysis of spring-tab control systems:
 - a) Brown, Tab Controls, ARC RM 1979 (1941).
 - b) Imlay, Aileron, NACA W Rpt L-318 (1944).
- (50) Experimentation with spring-tab control systems:
 - a) Zeller, Flap Tab, Ybk D Lufo 1941 p. I-33.
 - b) Crandall, Hinge Moments, NACA TN 1049 (1946).
 - c) Harris, Reduction, NACA T Rpt 528 (1935).
 - d) Phillips, Elevator, NACA T Rpt 797 (1944).
 - e) Morgan, Spitfire Tests, ARC RM 2029 (1942).
 - f) Nivision, Tab Elevator, ARC RM 2268 (1946).
 - g) ARC, Spring-Tab Ailerons, RM 2059 (1944).
- (51) Influence of compressibility upon flap characteristics:
 - (a) Stevenson, NACA 0009-64 Airfoil with 33.4% Chord Flap, NACA TN 1417.
 - (b) Stevenson, 9% Foil Sections, NACA TN 1406 & 1417 (1947).
 - (c) Lindsey, 9% Foil with 30% Flap, NACA RM L56L11.
 - (d) Lowry, Rectangular Wings, NACA RM L56E18.
 - (e) Whitcomb, Transonic on Swept Wing, NASA TN D-620 (1961).
 - (f) MacLeod, Bump Tests, NACA RM L50G03.
 - (g) Tirling, Horizontal Tail A = 4.5, NACA RM A9H11a.
- (52) Theory finite A wings:
 - (a) Kuchemann, Transonic Drag Sweptback Wings, J. Roy Aero Soc. 61, 37 (1957).
- (53) Transonic flaps on pointed wings:
 - (a) Boyd, Triangular, NACA RM A1952D01c & L04.
 - (b) Guy, Swept Wing, NACA RM L54G12a & L56F11.
 - (c) NACA, Delta Wings, RM L53I04 & L54B08.

Aspect Ratio. Horizontal and vertical surfaces with or without flaps will have their lift curve slope influenced by compressibility as shown in Chapter VII. In the case of a tail surface with sweep, the lift slope is corrected for compressibility effects below the critical by the equation from (55)

$$dC_L/d\alpha = (A + 2 \cos \Lambda) / (A \delta_2 + 2 \cos \Lambda) (dC_L/d\alpha)_{M=0} \quad (55)$$

where $\delta_2 = \sqrt{1 - M^2 \cos^2 \Lambda}$ and Λ is the angle of sweep. At aspect ratios larger than 3 and below the critical Mach number, equation 55 shows good agreement with test results as illustrated on figure 55 for the variation of $dC_L/d\alpha$ with M . When flaps are installed on such surfaces, these characteristics with Mach number of $dC_L/d\delta$ can also be found with equation 55 by using $dC_L/d\delta$ instead of $dC_L/d\alpha$. As shown on figure 44, good agreement is also obtained with test and theory for the effects of compressibility on flap deflection. Since $d\alpha/dC_L$ and $d\delta/dC_L$ are dependent on the same factor as a function of M , the variation of the ratio of $d\alpha/d\delta$ with Mach number is essentially flat up to the critical, as illustrated on figure 44. Above M_{cr} the flap effectiveness ratio decreases in the same manner as for the two dimensional case.

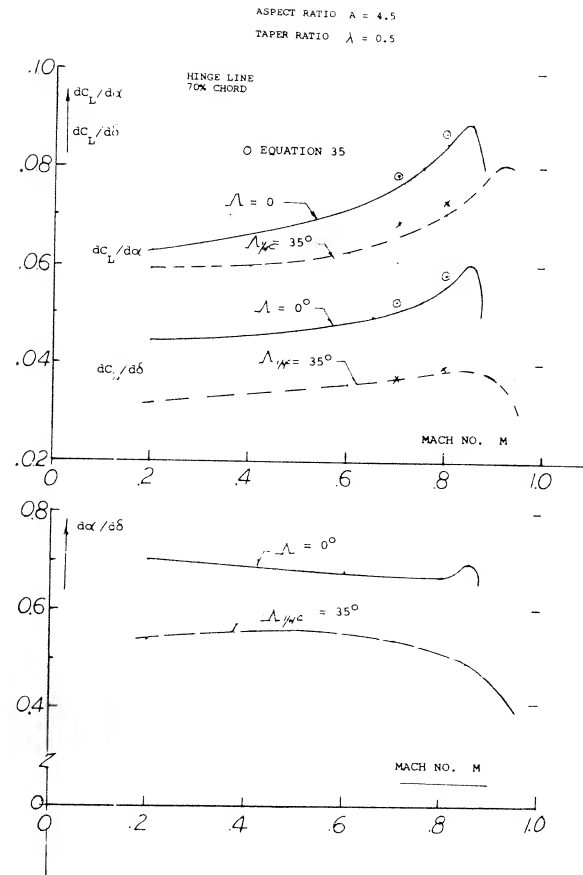


Figure 44. Effects of compressibility on flap effectiveness for straight and swept wings.

Hinge Moment - Mach Number. The flap hinge moment coefficient variation with Mach number is given on figure 45 for a sealed flap configuration (51.g). At $\alpha = 0$ and low deflection angles the hinge moment coefficient is nearly constant up to Mach numbers just below the critical. At flap angles above 10° , C_{he} increases with Mach number approximately as would be calculated using the Prandtl-Glauert correction. It would appear that up to the critical Mach number the section hinge moment derivative C_{he} for control devices should then be corrected in accordance with the P-G rule, thus

$$(C_{he})_M = (C_{he})_{M=0} / \sqrt{1 - M^2} \quad (56)$$

The above equation should hold up to the critical Mach number of the section, which will be a function of the section type and deflection angle.

Critical Mach Number. The critical Mach number of the control surface determines where the flap effectiveness becomes non-linear, as illustrated on figure 45. Thus to obtain the desired characteristics, the control surface is designed with a critical Mach number. This is done by choosing the proper sections and planforms to give the necessary high critical Mach number characteristics. As shown in Chapter VII, section camber and thickness ratio should be low for high levels of M_{cr} . Whereas in Chapters XV and XVII a high sweep angle and a low aspect ratio are needed to obtain a high critical Mach number.

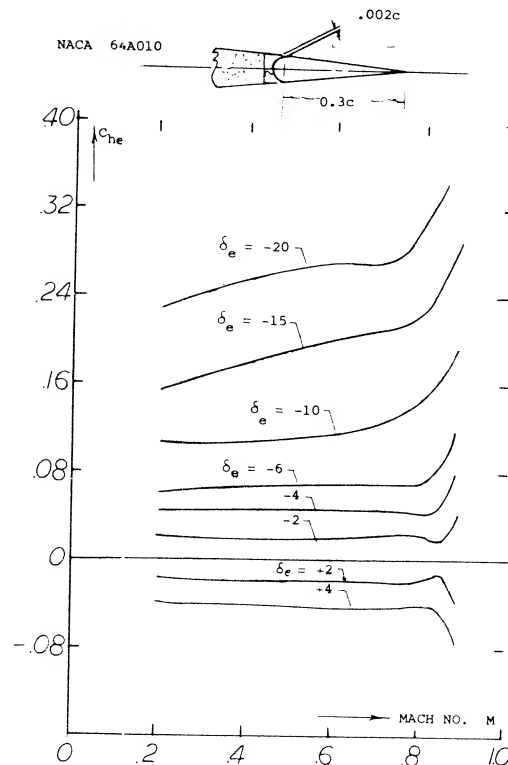


Figure 45. Flap hinge moment characteristics as a function of Mach number.

CHAPTER X — ROLL CONTROL OF AIRPLANES

Roll control of aircraft has been and continues to be a major design problem as it is necessary to maintain or change the attitude of the aircraft throughout the operating speed range. The control of the airplane in roll is especially important during approach and landing to provide the pilot with the ability to counter and/or hold lateral displacements in the event of gusts and engine failure. Effective lateral control during landing is also needed for proper alignment with, and touchdown on the runway. With the development of STOL aircraft the lateral control effectiveness as a function of stalling speed is an important factor in determining the landing distance, as its design directly influences the $C_{L\alpha}$ of the wing. If the required $C_{L\alpha}$ is not compatible with the lateral control system the only alternative is a direct reaction type of control, which can lead to considerable difficulties. The problem of providing a roll control system for STOL aircraft is compounded by the need to use full span flaps to provide peak values of $C_{L\alpha}$.

During flight maneuvers control in roll is needed in combination with yaw control and is especially important for fighter type aircraft. The need to develop high rates of roll for fighter airplanes has led to considerable research and development and consideration of many different types of systems.

DEFINITION. An aileron is a flap type device located at the wing trailing edge and capable of inducing a rolling moment through a differential deflection. The deflection angle of one aileron is defined by the angle δ_1 and the total angle deflection is $\delta_{\Sigma} = \delta_1 + \delta_2$. Rolling moments are also obtained by the use of spoilers of various types. The deflection of the spoiler reduces the wing lift and thus provides the necessary moment.

1. CHARACTERISTICS IN ROLL.

A wing symmetrical about the longitudinal axis of an airplane, no control deflections, will maintain its attitude unless disturbed by a change in velocity or angle, for instance due to a gust. A stable type wing will tend to return to the original undisturbed position but a means of control must be provided to allow the pilot to make the necessary corrections. The original method provided by the Wright Brothers was "Wing warping" but they also referred to flaps and other means in their patent (1). Since the original invention of a means for lateral control there have been hundreds of different types of devices used and investigated for controlling the airplane in roll. Some of the more important devices developed are illustrated in figure 1. The objective of the devices used for roll control is to provide a moment, thus it is necessary to produce either an increase or a decrease of lift on opposite wing panels. The rolling moment developed is defined in coefficient form by the equation

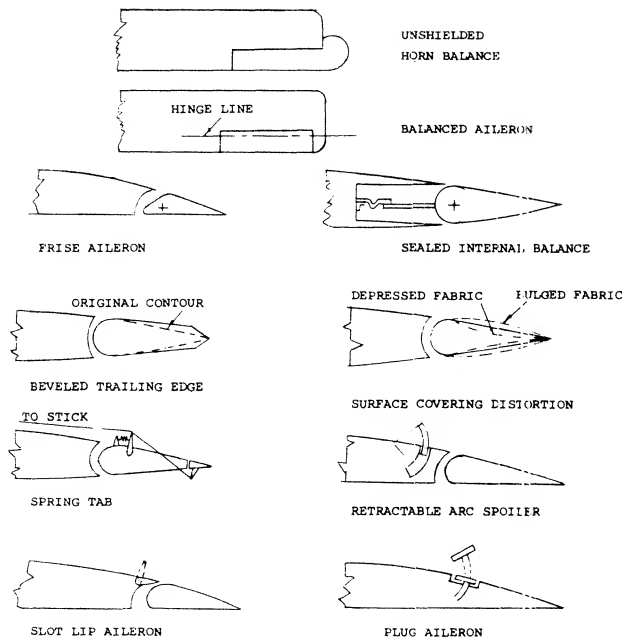
$$C_{\ell} = M_{\ell}/qbS \quad (1)$$

where "b" represents the moment arm and C_{ℓ} is the non-dimensional coefficient. Since the aileron changes the geometry of the wing to develop a moment it becomes like a propeller or twisted helicopter rotor. With the initial deflection of the aileron the largest moments and roll accelerations are produced. As the rate of roll is increased the moment and acceleration are reduced due to the rolling velocity until the rate stabilizes. This is known as roll damping and is measured by $C_{\ell p}$ the damping in roll coefficient

$$C_{\ell p} = \delta C_{\ell}/\delta (pb/2V) \quad (2)$$

where "p" is the roll rate and "V" is the free stream velocity. The rate of roll achieved by a given system depends on the aileron effectiveness, the wing initial operating lift coefficient, the planform and its flexibility.

(1) United States Patent Office Patent No. 821,393 "Flying Machine" dated May 22, 1906.



SEE ALSO FIGURES 8, 21, and 22.

Figure 1. Various types of lateral control devices.

The aileron effectiveness ratio is measured by $d\alpha/d\delta$ which as noted in Chapter IX corresponds to the lift change due to the flap deflection compared to the lift change due to a change in section angle of attack. This measure is a function of the flap chord ratio and thickness ratio of the flapped section, figure 2, Chapter IX.

An aileron to be effective must of course operate on the wing section below the stall angle. Thus as a result of an aileron deflection lift will continue to increase. This is an important consideration, especially in the design of lateral control devices for vehicles which must land at low speeds such as STOL and general aviation aircraft.

The deflection of an aileron can result in high twisting moments in the wing structure which reduces the moment generated. As the speed is increased this adverse twist increases until the loads become high enough to cause a reversal where the airplane will roll in the opposite direction to the control deflection produced at low speed. This speed is known as the aileron "reversal speed".

(2) Lateral Control Specification:

- (a) Perkins, Airplane Performance Stability & Control, J Wiley & Sons, Inc., 1949.
- (b) Toll et al, Summary of Lateral-Control Research, NACA TR 868.
- (c) Gillruth Control Requirements, NACA TR 755.
- (d) Stability and Control Requirements, AAF Spec. No.R-1815.
- (e) Creer, B.Y. and all Lateral Control Requirements, NASA Memo 1-29-59A.

Design Requirements. Many specifications have been published relating to the design requirements for roll control and the associated lateral control devices (2). The older specifications for lateral control generally related the requirement to the parameter $pb/2V$ the helix angle described by the wing tip (see later section Helix Angle). For large cargo and bombardment type aircraft the minimum value of $pb/2V$ was considered to be .07 for full aileron deflection and .09 for fighter types. The use of the parameter $pb/2V$ is somewhat arbitrary for specifying lateral control devices and, therefore, better means have been developed. For instance, some specifications require the achievement of a certain bank angle after one second where other specifications require that the airplane be capable of making a 20° banked turn with or against a failed engine. It appears, however, that a better specification would include the effects of roll damping and aileron control power in terms of roll acceleration (2,e). Since lateral control specifications change periodically the current requirement must be established for design use.

In addition to providing the required roll effectiveness the lateral control system should also provide a linear roll response to a control motion without adverse coupling into yaw or pitch. Generally the yaw coupling is the most important and it is desired to develop the roll without retarding the forward movement of the up going wing. Spoilers have a favorable yaw characteristic in this sense.

Flap Type Ailerons. Conventional ailerons are basically "flaps". However, their characteristics differ from those of elevators and rudders, as follows:

- a) They are practically always part-span
- b) The control forces are a combination between left and right
- c) Their lift coefficient, on the average, are higher than that of tail surfaces
- d) yawing (side-slipping) effects the characteristics of ailerons.

Figure 2 shows lifting characteristics of three sizes of plain flaps which could be used as ailerons as tested on an airfoil having an aspect ratio of 6. For example, as shown on figure 2,a, at a positive angle of deflection of 10° , the lift is shifted to higher levels, the level depending on the flap-chord ratio. Within the range of moderate flap deflection angles, the lift coefficient varies along straight lines, the slope being a function of the chord ratio corresponding to principles explained in connection with figure 2, Chapter IX. As in other control flaps, separation takes place (a) from the flap, above a limiting deflection between 15 and 20° ; (b) from the suction side of the airfoil and flap, as a function of the angle of attack (at lift coefficients roughly above 1.0). As with landing flaps, the maximum lift coefficient is increased corresponding to flap chord and angle of deflection. In separated condition,

the lift still increases (at a lesser rate) as a function of the angle of deflection, particularly as long as the flow is still attached to the forward part of the wing section. At $\alpha = \text{constant} = 0$, the coefficient reaches a maximum in the vicinity of $\delta = 70^\circ$, figure 2,b. As in tail surfaces, theoretical analysis is restricted to the linear portions of the lift forces (and the associated moments). The statistical results, for example as in figures 2, 4, 7, 8 of Chapter IX, readily apply to wing sections using plain aileron flaps.

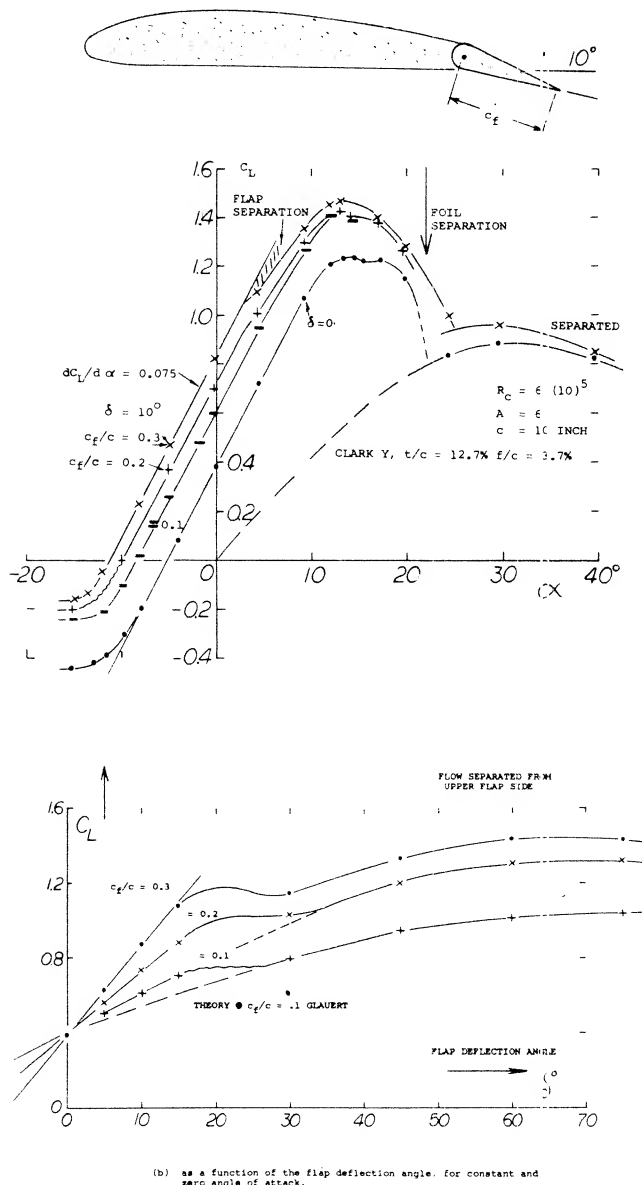


Figure 2. Lifting characteristics of a rectangular airfoil (3,i) fitted with three sizes of plain trailing-edge flaps.

- As a function of the angle of attack, for constant flap deflection.
- As a function of the flap deflection angle, for constant and zero angle of attack.

Part-Span Flaps. Since ailerons practically never extend over all of the full wing span, the characteristics of part-span flaps are of interest. Experimental evidence is meager in this respect. Results of one investigation are illustrated, however, in figure 3, where the lift-curve slopes of the wing due to flap deflection is given as a function of the flap-span ratio for the cases

- when increasing the flap span from the center line (case of a pair of wing landing flaps)
- for a pair of outboard flaps, representing ailerons.

The lift produced increases with the span ratio as indicated on figure 3 and inboard flaps are more effective (as to lift, not as to rolling moment) than outboard flaps. Estimated slopes of the lift coefficient based upon the wing portions "covered" by the flaps, are also plotted in figure 3. The slope is highest in the wider vicinity of the wing center, and it drops off around the wing tips.

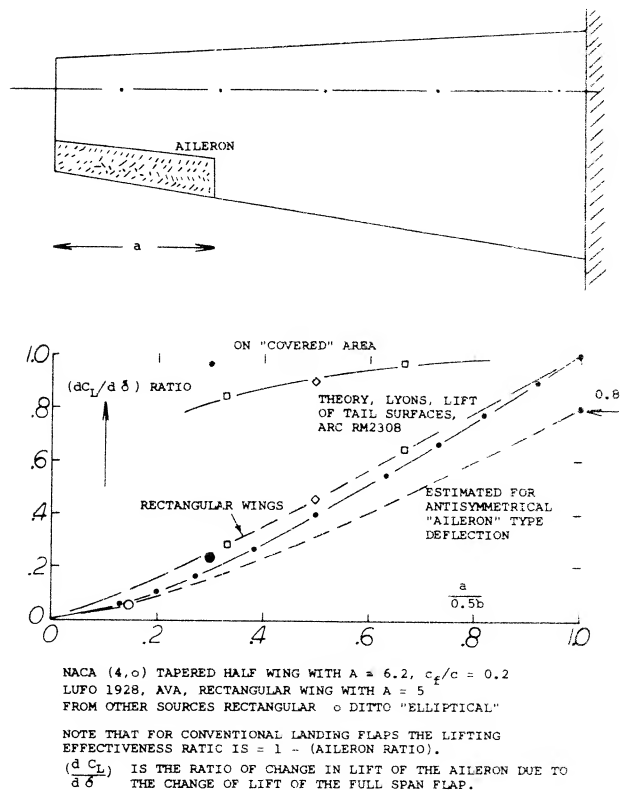


Figure 3. Theoretical and experimental results, indicating the lifting effectiveness of part-span ailerons.

- Experimental characteristics of ailerons:
 - Anon, Properties of Ailerons, ARC RM 550,615,651.
 - Heald, Chord and Span, NACA T Rpt 298 (1928) & 343 (1930).
 - Weick, At High Angles of Attack, NACA T Rpt 419 (1931).
 - Weick, Resume and Analysis, NACA T Rpt 605 (1937).
 - Crane, Modifications, NACA T Rpt 803 (1944).
 - Wenzinger, On Tapered Wing, NACA T Rpt 611 (1937).
 - Wenzinger, Ailerons and Split Flaps, NACA TN 661 (1938).
 - Rogallo, Collection of Data, NACA W Rpt L-419 (1944).
 - Wenzinger, Plain and Split Flaps, NACA T Rpt 554 (1936).

The lift-curve slope of the wing portions "covered" by ailerons, due to their angle of deflection, corresponds to the $d\alpha/d\delta$ ratio as in figure 2, Chapter IX. The $dC_L/d\alpha$ to be used, is not that of the wing, however, (a) because the ailerons occupy only part of the wing span, (b) because the deflection of conventional ailerons is antisymmetric (up on one side, and down at the other). Theory predicts that for the lift differentials plus and minus ΔC_L of a pair of full-span ailerons, the effective aspect ratio is half of that of the wing. If, for example, $A = 6$ the flap angle required to produce a certain lift differential must be based upon the induced angle of attack

$$d\alpha_{\text{eff}}/dC_L = 1/(\pi \cdot 0.5 A) = 57.3/(\pi \cdot 3) \approx 6^\circ \quad (3)$$

where $57.3 = 180/\pi$. Each wing panel's effective lift angle (Chapter III) is then

$$d\alpha/dC_L \approx 10 + 6 = 16^\circ, \\ \text{instead of } 10 + 3 = 13^\circ$$

and the effective lift-curve slope for ΔC_L is $1/16^\circ = 0.062$ instead of 0.077 as for the wing as a whole. Conventional ailerons are only part-span, however. Considering, for example, an aileron flap adjoining the lateral edge of a rectangular wing, with the extremely small span ratio $a/b = 0.1$ only, we may expect the effective aspect ratio (as far as lift due to aileron deflection is concerned) to be between 1.0 (geometrical) and 2.0 (when assuming that the rest of the wing acts as an end- or reflection plate).

Rolling Moment Due to Aileron Deflection. When initiating or reversing a roll, motion is caused by a rolling moment. This moment can easily be measured statically using wind tunnel models of wings or airplanes. The angle of attack in the wing panels is uniform and constant in this case. The rolling moment " M_L " (5) is the consequence of lift differentials produced by antisymmetric aileron deflection. Theoretical methods are available (6) for predicting rolling moments due to aileron deflection. Considering a part-span aileron, the initial moment produced corresponds to:

- the wing area "covered" by the aileron
- the chord ratio of the aileron flap
- the deflection angle of the aileron
- the moment arm (aileron to center line)
- the wing twist due to aileron loads.

Assuming that equation (3) may still hold for aileron-span ratios in the vicinity of 0.5, the lift differential produced by a pair of antisymmetrically deflected ailerons of a given chord ratio is

$$\Delta C_L \approx (dC_L/d\alpha)_2 (S_a/S)(d\alpha/d\alpha)\delta \quad (4)$$

where "2" indicates that the lift-curve slope corresponds to $1/2$ the actual aspect ratio, or to 2 times the wing's induced angle of attack. In the case of rectangular wings, the ratio of the effective area covered by one of the two ailerons, is:

$$S_a/S = a/b \quad (5)$$

where "a" = spanwise length of *one* aileron flap. The moment arm "y" of the lift differentials (about the center line of wing or airplane) may be assumed to be that of the geometric center of S_a . The rolling-moment coefficient $C_L = M_L/qSb$, of a pair of ailerons corresponding to a given area and chord ratio is then:

$$dC_L/d(\Delta\delta) = \Delta C_L y/0.5 b \quad (6)$$

where $\Delta\delta$ = deflection-angle differential between one side and the other. In aileron systems where up and down deflections are equal, the differential is $\Delta\delta = 2/\delta$.

Part-Span Ailerons. Rolling moments due to aileron deflection are plotted in figure 4 against the span ratio. The slope of the lines in the graph is a measure for the rolling-moment effectiveness of ailerons as a function of

- (4) Ailerons and lateral airplane control:
 - Toll, Summary, NACA T Rpt 868 (1947).
 - Weick, Airplane Motions, NACA T Rpt 570 (1936).
 - Weick, Lateral Control Research, NACA T Rpt 605 (1937).
 - Weick, Ordinary Ailerons, NACA TN 449 (1933).
 - Weick, Skewed Ailerons, NACA T Rpts 444 & 445 (1932).
 - Weick, On Wing with Slat, NACA TN 451 (1933).
 - Heald, Chord and Span of Ailerons, NACA T Rpt 343 (1930).
 - Gilruth, Lateral Control Required, NACA T Rpt 715 (1941).
 - Weick and Wenzinger, Ordinary Ailerons, NACA T Rpt 419 (1932).
 - Johnson, Various Ailerons, NACA TN 2199 (1950).
 - Naeseth, Influence of Aspect Ratio, NACA TN 2348 (1951).
 - Fischel, At High Speed, NACA TN 1473 (1947).
 - Fischel, Aspect Ratio, NACA T Rpt 1091 (1952).
 - Higgins, Flap and Aileron, NACA T Rpt 260 (1927).
 - Schneider, Span and TE Angle, NACA TN 1738 (1948).
- (5) The " L " indicates the longitudinal axis about which the motion takes place.

their span ratio. That slope is maximum in the vicinity of 0.7 of the half span; and it is minimum at and near the wing center line. Ailerons are usually part-span, located in the outboard part of each half span. The need for large landing flaps, in almost all modern airplanes, is a strong reason for making the ailerons as short as permissible. In order to obtain one and the same rolling moment (or rate of roll) part-span ailerons have to be larger in chord ratio than full-span ailerons. Since hinge moments are predominantly dictated by chord, stick forces of part-span ailerons are necessarily higher than those of comparable full-span installations. For example, a $\frac{1}{2}$ half-span aileron has to be approximately 1.5 times as long in chord as a full-span aileron; and it will then have roughly 2 times the hinge moment (per degree of deflection).

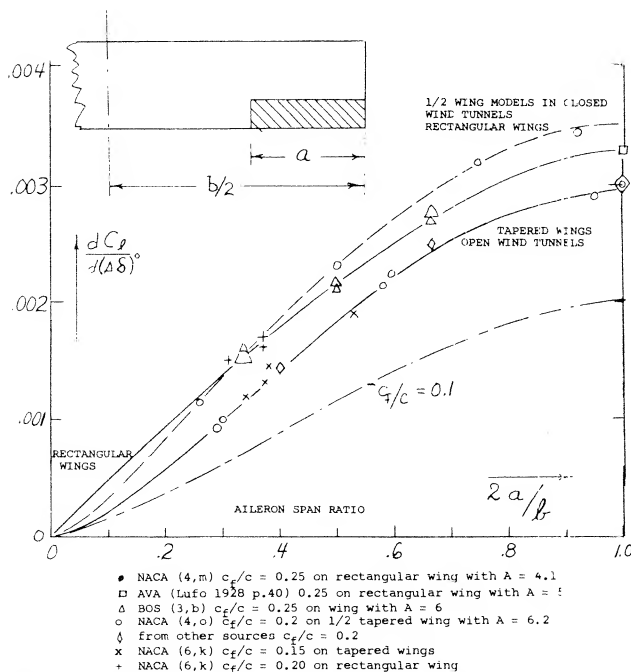


Figure 4. Wing rolling moment, presented in the form of a derivative, produced by deflection of ailerons as a function of their span ratio.

(6) Theoretical Analysis of rolling moments due to ailerons:

- Pearson, Loading Due to Ailerons, NACA TN 589 (1937).
- Pearson, Stability and Control, NACA T Rpt 635 (1938).
- Heald, Moments Due to Ailerons, NACA TN's 441 & 448 (1933).
- Munk, Rolling Moments, NACA TN 187 (1924).
- Wieselsberger, Aileron Effects, NACA TM 510 (1929).
- DeYoung, Antisymmetric Span Loading, NACA T Rpts 1056 & 1071.
- Martina, Rolling and Yawing Moments, NACA T Rpt 1167 (1954).
- DeYoung, Span Loading, NACA TN's 2011 & 2140 (1950).
- Theory of Wing With Ailerons, ARC RM 1259 (1929).

Aspect Ratio. Available wind-tunnel results on rolling-moment effectiveness of half-span ailerons are plotted in figure 5 as a function of the wing's aspect ratio. Note that in the form as in equation (6) the derivative also applies to only one aileron, for which $\Delta\delta = \delta$. Both moments obtained from a pair of ailerons and from single ailerons can thus be plotted in one and the same graph. Using equation (4), it is assumed that $d\alpha/d\delta = 0.5$ and $S_a/S = 0.5$. The lift-curve slope is taken for $\frac{1}{2}$ of the aspect ratio, as a function of that ratio as presented in Chapter III for rectangular plan form and for a foil-section efficiency $a = 0.9$. The moment arm as in equation (6) is assumed to be $y/(0.5b) = 0.75$. The function thus obtained, plotted in figure 5, agrees qualitatively well with experimental results. The type of lines in figure 5 also agrees with more elaborate theoretical predictions (7). The most important result is the fact that the rolling moment increases with the aspect ratio. Roughly interpolating the function in the graph by $C_H \approx \sqrt{A}$, we find that the rolling moment (in foot-pounds) of an airplane flying at a certain speed, is

$$M_L \sim b^2 \quad (7)$$

One "b" represents the moment arm of the ailerons, while the other "b" indicates the influence of the lift curve slope of the wing.

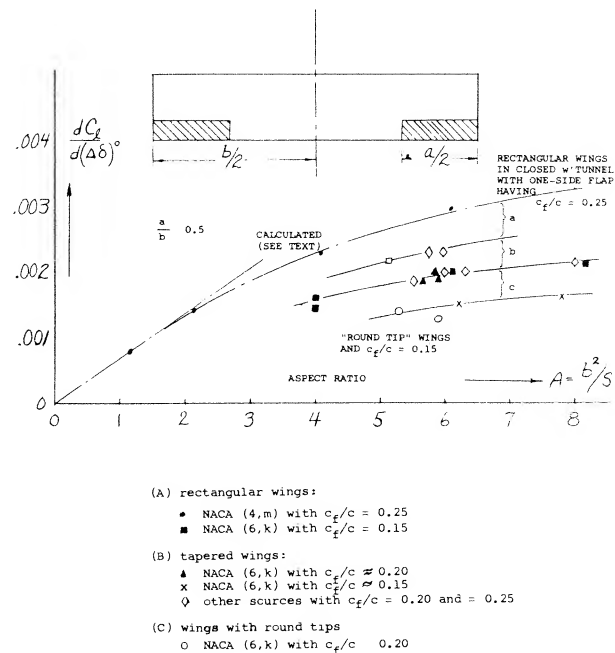


Figure 5. The rolling-moment derivative of approximately half-span ailerons as a function of wing aspect ratio.

- rectangular wings
- tapered wings
- wings with round tips.

Tunnel Testing. Conditions of antisymmetrical aileron deflection are not always simulated in wind-tunnel tests. This is particularly true when half-span models are used (3) in closed test sections (8). Differentials as indicated in figure 5 are due to:

- a) tapered as against rectangular wing shape $c_f/c = 0.20$ as against $= 0.25$ and wind-tunnel interference
- b) wings in open as against closed-type wind tunnels full — as against half-span wing models
- c) "round" wing as against rectangular $c_f/c = 0.15$ as against $= 0.25$

In conclusion, rolling moments available for tapered wings under realistic conditions are less than those obtained when testing wind tunnel models with rectangular wings.

Aileron Effectiveness. The static rolling moment produced by aileron deflection may be approximated as being proportional to $(\sqrt{A}(2a/b)\sqrt{c_f/c})$. For aircraft where the hinge moment is a limiting factor $M_h \sim C_h$ and thus the hinge moment per degree of aileron deflection is a design condition. Evaluation of the data plotted in figures 4 and 5 leads to

$$dC_h/d(\delta^\circ) \approx k(\sqrt{A}(2a/b)\sqrt{c_f/c}) \quad (8)$$

where after elimination of closed-tunnel and half-wing model results, the factor is

$$\begin{aligned} k &\approx 0.0035 \text{ for "round" wings} \\ &\approx 0.0040 \text{ for tapered wings} \\ &\approx 0.0045 \text{ for rectangular wings} \end{aligned}$$

"Round" means shapes which are rounded off at the wing tips, thus cutting away from the outer end of the aileron flaps.

Rolling Velocity. The static rolling moment produced by aileron deflection, discussed so far, can only be present at the beginning of a roll. The moment is, therefore, a measure for the rotational acceleration of an airplane when going into a rolling motion as previously noted. Another measure for aileron effectiveness is the terminal rolling velocity obtained in a steady roll. This rotational speed is usually given in the non-dimensional form of the speed ratio

$$u/V = pb/2V \quad (9)$$

where the circumferential speed of the wing tips

$$u = p(0.5b)$$

and p = angular velocity about the longitudinal airplane axis (in radians per second).

Helix Angle. Note that u/V is the angle against the normal plane of the helix line along which the wing tips move during the motion. Typical maximum helix angles of World War II fighter airplanes as listed in (4,a) are

$$u/V = pb/2V = \text{between } 0.06 \text{ and } 0.12 \quad (10)$$

measured in radians. The values obtainable at higher speeds (where stick forces are the limiting element, are only half of those stated. The rolling velocity of these airplanes are roughly between 50 and 130 degrees per second. As a function of their size it can be said that there is a tendency toward constant up or down wing-tip speed u . For example, at a lift coefficient of ≈ 0.8 (after take-off or when approaching the landing field) a fighter with a span of 35 ft and an airliner with 120 ft, might both be able to move their wing tips, up or down, at a maximum speed in the order of 20 ft/sec.

Rolling Effectiveness. The effectiveness of a lateral control can be described by the ratio of the wing helix angle $pb/2V$ to the aileron deflection angle. The helix angle described by the wing tip is ω , eq (9). Using constant units, radians or degrees we obtain the non-dimensional derivatives

$$d\omega/d\delta = 180 d(u/V)/\pi \delta^\circ \quad (11)$$

In terms of the wing damping ratio eq (11) becomes

$$d\omega/d\delta = dC_L/C_{Lp} d\delta \quad (12)$$

Thus the effectiveness in roll is measured by the ratio of the rolling moment per degree to roll damping. This effectiveness parameter is a function of size of the aileron as well as the aspect ratio of the wing, and for practical purposes is

$$d\omega/d\delta \sim (2a/b)c_f/c/\sqrt{A} \quad (13)$$

(7) Unconventional types of ailerons:

- (a) Weick, Floating-Tip Ailerons, NACA T Rpt 424 (1932).
- (b) Weick, Floating-Tip Ailerons, NACA TN 458 (1933).
- (c) Weick, Short-Wide Ailerons, NACA T Rpt 494 (1934).
- (d) Sawyer, On TE of Wing flap, NACA T Rpt 883 (1947).
- (e) Ashkenas, With Large-Span Flaps, NACA TN 1015 (1946).
- (f) Dearborn, Zap Ailerons, NACA TN 596 (1937).
- (g) Reed, External-Airfoil Flaps, NACA TN 604 (1937).
- (h) Weick, External Ailerons, NACA T Rpt 510 (1935).
- (i) Soule, Flight Tests Full-Span Flaps, NACA T Rpt 517.
- (j) Platt, External Airfoil Flaps, NACA T Rpt 603 (1937).
- (k) Fishel, Collection of Data, NACA TN 1404 (1948).

- (8) The aileron angle should be corrected in the same direction as the angle of attack, with $d\alpha/d\delta$ applied as factor of proportionality.

A wing with a large aileron and a small aspect ratio would therefore have a higher rolling effectiveness per degree deflection than the same aileron on a long wing. From the statistical values derived from test data, figure 6, we see that for example at $(2a/b)c_f/c/A$ equal to 0.1 that w/δ equals .5. Thus, the rolling velocity of an airplane can be calculated as a function of the aileron dimensions used and the aspect ratio. For the case of two ailerons deflected a total increment of δ , the equation for rolling effectiveness is from figure 6 approximately

$$w/\delta = 2.5(2a/b) \sqrt{c_f/c} / \sqrt{A} = u/V \delta \quad (14)$$

so that the wing tip speed ratio is

$$u/V = \pi/180 \delta^\circ (w/\delta)$$

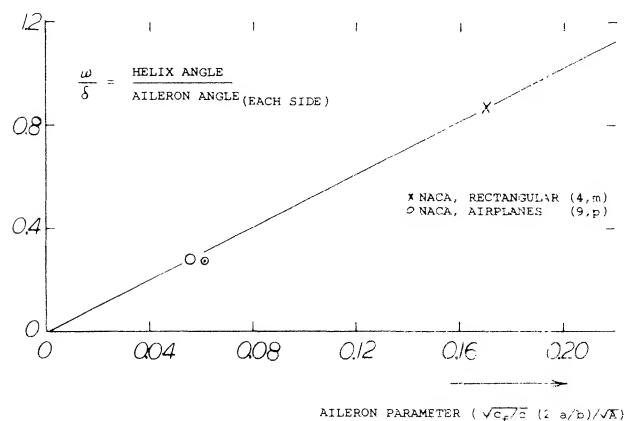


Figure 6. Helix-angle derivative of airplane wings; statistical evaluation of wind-tunnel and flight tests as a function of a parameter indicating the aileron size.

- (9) Investigation of spoiler-type devices by the NACA:
- (a) Weick, Rolling Moments Obtained, NACA IN 415 (1932).
 - (b) Weick, Ailerons and Spoilers, NACA T Rpt 494 (1934).
 - (c) Weick, Slots and Spoilers, NACA TN 443 (1933).
 - (d) Shortal, Location and Effects, NACA TN 499 (1934).
 - (e) Shortal, Slot-Lip Ailerons, NACA T Rpt 602 (1937).
 - (f) Soule, Flight Investigation, NACA T Rpt 517 (1935).
 - (g) Wetmore, Retractable Ailerons, NACA TN 714 (1939).
 - (h) Wenzinger, NACA TN 801 and T Rpt 706 (1941).
 - (i) Rogallo, Plug-Type Aileron, NACA W Rpt L-376 & 420 (1941).
 - (j) Spahr, Flight Investigation, NACA W Rpt A-28 (1943).
 - (k) Spahr, Flight Investigation, NACA TN 1123 (1947).
 - (l) Fishel, Location of Spoiler, NACA TN 1294 (1947).
 - (m) Deters, With Full-Span Flaps, NACA TN 1409 (1947).
 - (n) Schneider, On Swept Wing, NACA TN 1646 (1948).
 - (o) Fishel, Retractable Ailerons, NACA T Rpt 1091 (1952).
 - (p) Fishel, Collection of Data, TN 1404 (1948).
 - (q) Wenzinger, Lateral Devices, NACA TN 659 (1958).
 - (r) NACA, T Notes 1015, 1245, 1409, 3705, 4057.

Sweepback. It is explained in Chapter IX how control flap characteristics change with the angle of sweep. As a consequence, aileron effectiveness reduces basically in proportion to $\cos^2 \Lambda$, when keeping the aspect ratio constant. Experimental results from a series of swept wings are plotted in figure 7, showing good agreement with the theoretical prediction even though the aspect ratio is not kept constant in this investigation.

Internal Force. In contrast to elevators or rudders, flap type ailerons are always provided in pairs. They move antisymmetrically against each other and they are interconnected by means of a linkage system. In neutral position the hinge moments of the aileron flaps are usually somewhat “up”, on account of positive wing lift. The structural element (rod or possibly cable) connecting the two sides, therefore, takes up the corresponding “internal” force, for example in the form of tension.

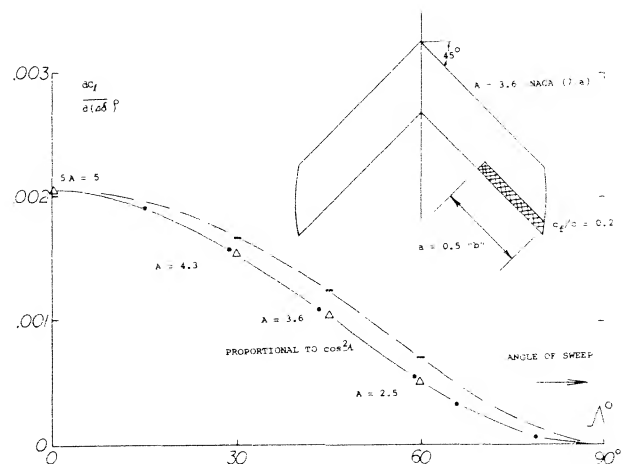


Figure 7. The effectiveness of an aileron flap as a function of the wing sweep-back angle.

Stick Force. The control moment (stick force) is the sum of or the difference between (depending on the sign definition) the right and the left aileron. Primarily, therefore, the lateral stick force corresponds to the flap hinge moment derivative $dC_H/d\delta$. In fact, in a steady roll (with deflection, rate of roll and lift coefficient \approx constant) the hinge moments of plain ailerons can correctly be determined on the basis of figure 8, Chapter IX. On the other hand, stick forces for sudden aileron deflection (when initiating or reversing a roll) correspond to the total derivative as in equation (24) of Chapter IX, where C_L represents the plus-minus ΔC_L produced by the ailerons.

Differential Linkage. The wing's lift and the flap hinge moment corresponding to that lift can be utilized to reduce lateral stick forces, when desirable. As mentioned above, each aileron flap usually has an up-floating tendency. By designing the linkage system connecting the two ailerons with the control stick (or wheel) in such a manner that the up-going flap has a somewhat larger deflection than of the corresponding down-going flap, it is realized that the mean deflection of the two flaps of $0.5(\delta_1 + \delta_2)$ is somewhat up. The lift or normal force supported on the surface of the pair of flaps operating at opposite angles, ailerons, helps reduce the hinge moments produced by their deflection. For practical results see (10).

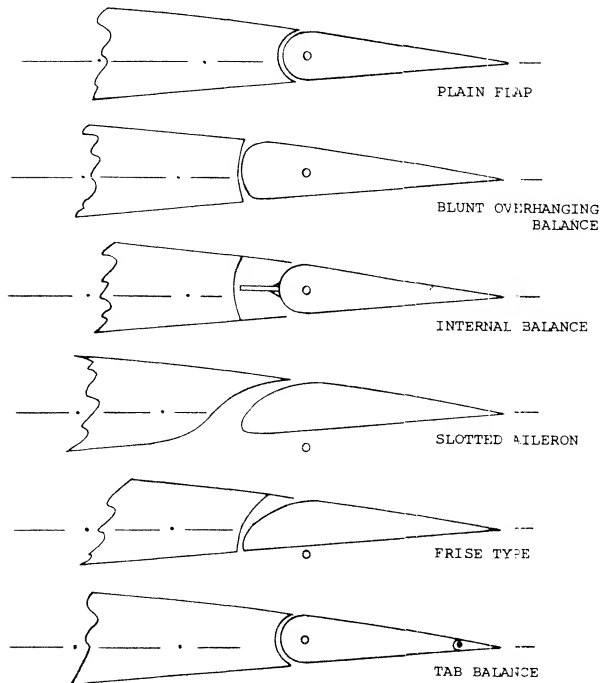


Figure 8. Various flap shapes and types of balance suitable to be used as ailerons.

Nose Balance. To reduce the hinge moments of aileron flaps some type of overhanging nose can be used as described in Chapter IX and shown on figure 26. In fact, symmetrical (and comparatively blunt) open noses have occasionally been used. The external-horn balance was at one time found to be convenient and sufficient to balance the ailerons of smaller and low-speed aircraft, such as certain Fokker airplanes. Another possibility of balancing aileron flaps is the internal type, see figure 8.

(10) Differential-linkage balancing of ailerons:

- (a) Weick, Rigged-Up Ailerons, NACA T Rpt 423 (1932).
- (b) Differential Linkages, NACA TN's 586 & 653 (1936/38).
- (c) Differential Gearing, ARC RM 2526 (1940).

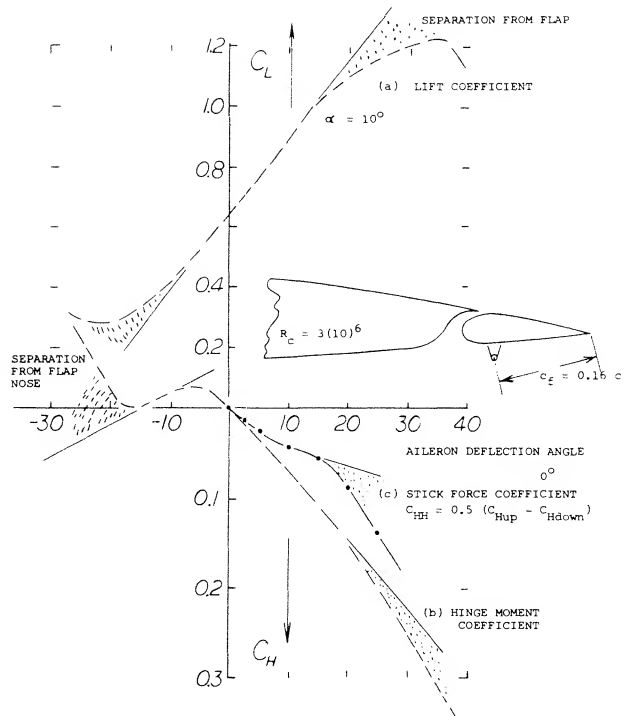


Figure 9. Slotted aileron flap tested (11,k) on rectangular airfoil with $A = 2.4$ in open wind tunnel.

Slotted Ailerons. Because of the "always" positive lift of the wing to which ailerons are attached, flap-section shapes favoring suction-side flow are desirable. One such type is the slotted aileron, evidently fashioned after (or developed during the same period of time as) the slotted type of landing flap described in Chapter V. Figure 9 shows that such ailerons have unsymmetrical hinge-moment characteristics. The flap nose is comparatively inefficient at positive angles of deflection, while in the range of negative deflection suction forces of appreciable magnitude develop past the lower side of the nose as it emerges from the contour of the foil section. When combining hinge moments of one side up with the other side down, fairly straight control (stick) moments can be obtained, however, as illustrated later. Figure 10 presents hinge-moment derivatives for positive and negative deflection.

(11) Investigation of slotted and Frise-type aileron flaps:

- (a) Weick, Slotted Ailerons, NACA T Rpt 422 (1932).
- (b) Hartshorn, Frise-Type, ARC RM 1587 (1934).
- (c) Kaul, Slot Shape, Yearbk D.Lufo 1941 p.1-315.
- (d) Ehrhardt, Me-109 Ailerons, Messerschmitt WKB 2 (1943).
- (e) Purser, Analysis of Data, NACA W Rpt L-665 (1944).
- (f) Batson, Surface Curvature, ARC RM 2506 (1953).
- (g) Aileron Flap Camber, ARC RM 2495 (1947).
- (h) Letko, Frise-Type Aileron, NACA W Rpt L-325 (1943).
- (i) Hoerner, Ju-228 Aileron Tested on Full-Scale Wing, Junker Rpt Kobu-Ew 895 (1941).
- (j) Toll, Hinge Moment Parameters, NACA TN 1711 (1948).
- (k) Junkers Wind-Tunnel Results Strote Graphs D-6761 (1941).

Yawing Moment. When turning an airplane, both the ailerons and the rudder are deflected in proper direction. Most or all of the rudder displacement is required, however, not to make the turn, but simply to compensate for the adverse or “negative” yawing moment produced in the wing panels by deflection of conventional ailerons. Aileron flaps change lift; lift is increased in one side and decreased in the other side of the wing. With the change in lift, induced drag (equal to local lift times induced angle) is increased in the outside wing panel, and it is decreased in the other panel. Considering a pair of symmetrically deflected ailerons, the induced-drag differential in each wing panel corresponds to

$$\Delta C_{Di} = \Delta C_L (\alpha_i) = \frac{(\Delta C_L) 2C_{Lo}}{(\pi A)} \quad (15)$$

where the function for (α_i) is in equation (3). Since ΔC_L is positive on one side of the wing and negative in the other, a yawing moment is thus obtained corresponding to $2(\Delta C_{Di})y$, where y = moment arm to wing center line. The coefficient of the moment (11) of a pair of ailerons is then:

$$C_n = M_n / (q S b) = \frac{4(y/b)(\Delta C_L) C_{Lo}}{(\pi A)} \quad (16)$$

where ΔC_L is in equation (4). The ratio of yawing to rolling moment is

$$\frac{C_n}{C_l} = - \frac{\Delta C_{Di}}{\Delta C_L} = - \frac{4 C_{Lo}}{(\pi A)} = - 1.28 C_{Lo} / A \quad (17)$$

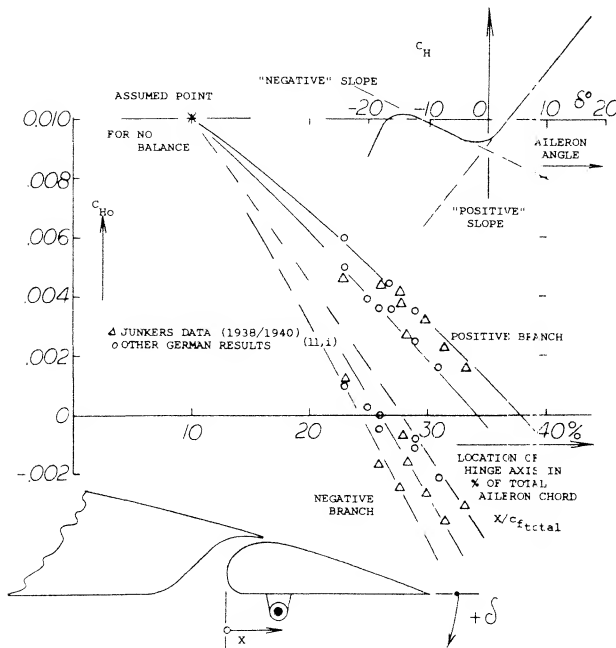


Figure 10. Statistical evaluation of the hinge moments of slotted aileron flaps.

where the minus sign signifies that the yawing moment is adverse to the turning maneuver of the airplane. Such yawing moments coupled with roll control complicate handling of the airplane. “Negative” moments also reduce the magnitude of the rolling-moment and the resultant rate of roll, unless the pilot fully compensates by means of the rudder.

The “Frise” Aileron. This type aileron, figure 8, was invented (11) to reduce or to compensate for the unfavorable “negative” yawing moments associated with flap-type lateral control devices. It was expected that flow separation would soon take place after the sharp lower edge of the aileron nose moved out into the flow. Parasitic drag corresponding to such separation was to counteract the undesirable variation of the induced drag as described above. The disadvantages of this design are:

- flow separation is bound to reduce effectiveness.
- separation is likely to be accompanied by fluctuations and vibrations.

Figure 11 shows shape and characteristics of a typical Frise-type aileron flap. When deflecting this flap downward, lift increases steadily, and it continues to do so in the presence of flow separation developing along the suction side of the flap. This separation is evident from, and/or it results in a progressively increasing hinge moment. When deflecting the flap upward, strong suction forces develop at first around its lower leading edge as it emerges from the foil-section contour. Depending upon the sharpness of the edge, separation along the lower side of the flap starts at negative deflection angles between 7 and 15°. As a consequence, effectiveness reduces considerably while the hinge moment increases rapidly, from approximately zero to a level as indicated by a line connecting the two extremes of the hinge-moment function, figure 11.

Stick-Force Coefficient. Average derivatives as found, respectively, in the positive and negative branches of the hinge-moment function of slotted and/or Frise-type aileron flaps, are plotted in figure 10. When adding the values of the hinge-moment contribution from one side (down, for example) to that of the other side (up) we obtain a number representing the lateral stick force required to deflect a pair of ailerons. Dividing the combined value by 2, we obtain the stick force coefficient, properly referred to the sum of the aileron areas:

$$C_{HH} = 0.5(C_{HUP} - C_{Hdown}) \quad (18)$$

- (12) The subscript n as in equation (16) indicates the vertical or normal axis of the airplane, about which the yawing moment is defined.

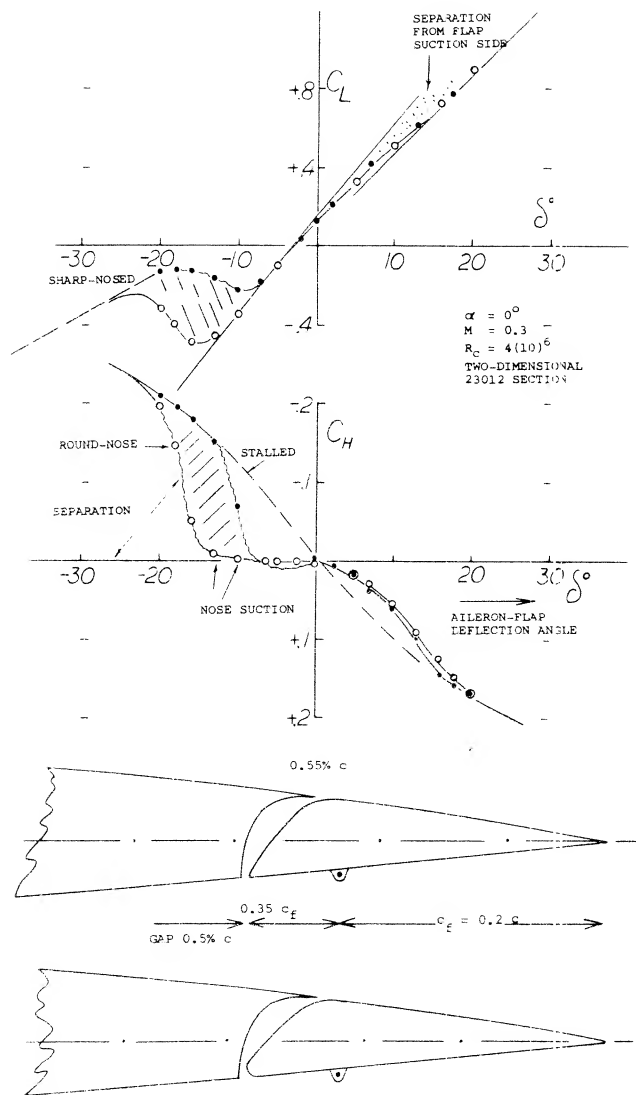


Figure 11. Characteristics of a Frise-type aileron flap tested in a two-dimensional wind-tunnel set-up (11,h), for two different leading-edge radii.

Examples for the stick-force characteristics of two aileron flaps are presented in figure 12. Practical results are as follows:

- Comparatively irregular $C_H(\delta)$ functions of the single aileron can result in a surprisingly smooth stick-force variation. Truly, one side compensates for the other.
- In case of the Frise-type aileron, the more or less sudden separation from the lower side of the flap nose produces a more or less steep increase of the stick-force coefficient.
- A reduction of the hinge moments to half, to a third or possibly to a quarter seems to be feasible or to be the practical limit for this type of overhanging-nose balance.
- Note that the effectiveness of the Frise-type aileron flap discontinues as separation from the nose takes place.

Stick-Force Slope. Considering the Frise-type aileron as in figure 11, it can be realized that when putting together the right-or-up with the left-or-down flap, the resultant stick force has a slope around the neutral position at $\delta = 0$, practically equal to zero. A control system with such a characteristic is not desirable. To increase the stick-force slope, the flap deflection at which the slope of the hinge moment is zero, should be somewhat negative (such as in figure 9 and 12, for example). Means of shifting that angle are as follows:

- Adjusting the neutral position of the two aileron flaps to a somewhat positive angle.
- Displacing the flap nose sufficiently up so that it emerges from the foil-section contour at a somewhat more negative angle of deflection.
- Combination of (a) with the use of a trailing-edge tab, compensating for the change of lift coefficient and pitching moment (C_{m0}) resulting from (a).

Taking into consideration that the hinge-moment and stick-force characteristics are also a function of angle of attack or lift coefficient, it will be appreciated that the type of overhang-balanced ailerons described above can be very cumbersome when attempting to reduce the hinge moment substantially.

Rigging-Up. The slotted type as well as the Frise form of ailerons are characterized by hinge moments:

- increasing strongly within the range of positive flap deflection
- roughly equal to zero (or somewhat unstable) for upward deflection.

As a consequence, the resultant control-stick moment essentially corresponds to the positive hinge-moment slope of down-going aileron flap. As mentioned above (under a), the relative contribution of the two sides can be changed, however, by changing the neutral position of the flaps. Pulling down both ailerons will thus increase the stick force required, while rigging up as described in (13,a,b) may appreciably reduce that force. Here again, the use of tabs (as mentioned in c above) may be desirable.

(13) Rigged-up aileron characteristics:

- Weick, Rigged-Up Ailerons, NACA T Rpt 423 (1932).
- Murray, Rigged-Up Ailerons, NACA W Rpt L-289 (1944).

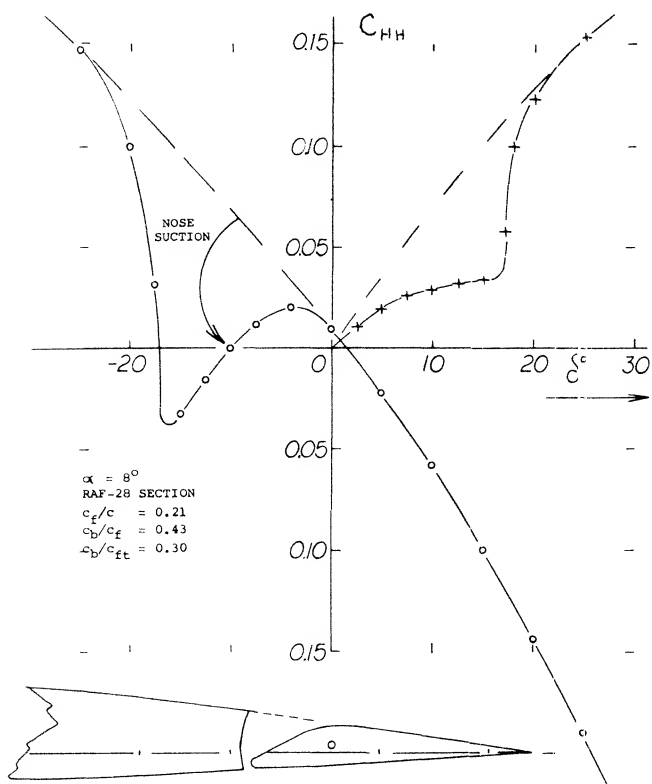
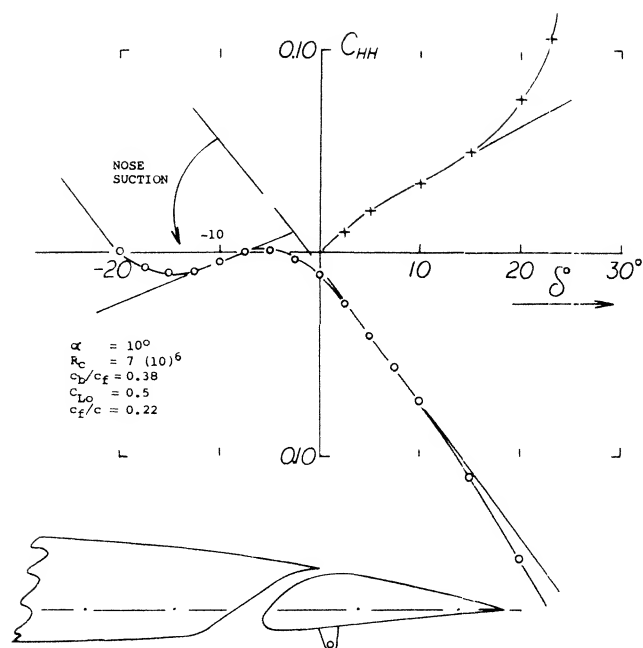


Figure 12. Slotted and Frise-type aileron hinge-moment and stick-force characteristics.

- Slotted aileron (11,h) tested on full-scale wing.
- Frise-type aileron (11,b) tested on $A = 6$ rectangular wing model.

Tab Balancing. The various types of tabs described in Chapter IX can be and have been applied to ailerons. The linked or geared tab is particularly effective in reducing hinge moments and lateral stick forces to a fraction of what they are for plain aileron flaps. However, due to the reduction of the stick-free lift-curve slope in linked-tab configurations, possibly to zero for higher flap-chord-ratios, such arrangements may not be permissible in larger airplanes. Thus for the case of a rolling motion, the ends of the wing covered by aileron flaps may be deficient in damping qualities, caused by a reduced lift curve slope for the case of the stick or control wheel free. As a consequence, the airplane would continue to roll once this motion has started, and the airplane would not be stable about its longitudinal axis for the "stick-free" case.

Spring-Tab Ailerons. Stability can be restored or maintained by restricting tab operation in such a manner that for zero hinge moment (corresponding to stick-free condition) and a suitable range of lower hinge moments, operation is just as that of an unbalanced plain pair of aileron flaps. This is done by means of the arrangement as in figure 13 where there are two levers "leading into" each aileron flap. One of these driving the tab is directly connected with the control stick, while the other one, rigidly attached to the flap, is linked to the main lever by means of a spring element. This element as shown in figure 13 has the following characteristics:

- As long as the flap's hinge moment is small, the element acts as a rigid link. This is obtained by preloading the spring. Control characteristics are then those of a plain flap.
- When the flap hinge moment is large, the spring compresses corresponding to its mechanical constant. As a consequence, any lateral displacement of the control stick directly deflects the tab, which provides the moment necessary to drive the aileron flap in the opposite direction. This system thus behaves like a servo-tab type control.
- Under conditions between the two extremes under (a) and (b) the torque deflecting the aileron flap is the sum of that due to tab deflection plus that corresponding to the force transmitted through the spring.

Effectiveness. The flap or control angle at which the spring starts to be compressed and the tab to be deflected depends upon the preload provided and the dynamic pressure at which the system is tested or used. In the case as in figure 13, the "critical" angle happens to be $\delta = 9^\circ$. Above this angle, the tab deflects corresponding to $d(\delta_t)/d\delta \approx -0.8$, while the loss of flap deflection due to spring compression is $d(\Delta\delta)/d\delta \approx -0.3$. The resultant loss of effectiveness is

$$\Delta(dC_L/d\delta) = (dC_L/d\delta)_0 ((d(\Delta\delta)/d\delta) + (d\delta/d\delta_\epsilon)) / (d\delta_\epsilon/d\delta) \quad (19)$$

where $(dC_L/d\delta)_0 = 0.033$ as tested and $(d\delta/d\delta_\epsilon) = (d\alpha/d\delta_\epsilon)/(d\alpha/d\delta) = 0.2/0.6 = 1/3$, as found in figure 2, Chapter IX. The numerical result is

$$(dC_L/d\delta) = -0.033 (0.3 + (1/3) 0.8) = -0.019$$

As a consequence, the lift continues increasing above $\delta = 9^\circ$ at the rate of $dC_L/d\delta = 0.033 - 0.019 = 0.014$. The reduction of effectiveness is appreciable in the case considered, where, $c_F/c = 0.31$.

Control Moment. The hinge moment of the plain aileron flap investigated, corresponds to $C_H \delta \approx 0.008$. Disregarding the loss of flap deflection as stated above, the balancing moment provided by the tab can be expected to be as indicated in figure 36, Chapter IX where we tentatively find $dC_H/d\delta_\epsilon = -0.01$. Consequently:

$$\Delta(dC_H/d\delta) = (dC_H/d\delta_\epsilon) (d\delta_\epsilon/d\delta) = -0.01 (0.8) = -0.008$$

which is sufficiently close to the differential as tested between $\delta = 10$ and 20° . The average reduction at higher flap angles is roughly 50% under the conditions as tested. Upon reducing the spring's preload, reduction of the control moment down to 25% could easily be obtained, while still retaining a range of no tab deflection in the order of plus and minus 5° .

Full-Span Wing Flaps. All modern airplanes are equipped with wing flaps in order to reduce landing and, to a lesser degree, take-off speed. Such flaps are, of course, most effective when extended over the entire span of the wing. Lateral (roll) control by means of ordinary ailerons, is then complicated by reasons as follows:

- the ailerons interfere with the outboard part of the wing flaps, so that the rolling-moment coefficients obtained are somehow reduced.
- the rolling moments in foot-pounds, being proportional to $1/C_L$, are appreciably reduced when increasing C_L by means of wing flaps.
- the adverse yawing moments connected with flap-type ailerons grow with the lift coefficient, while those obtainable from rudder deflection (needed to balance the aileron-induced moments) reduce as $1/C_L$.

(14) Analysis of spring-tab control systems:

- Brown, Spring-Tab Controls, ARC RM 979 (1941).
- Imlay, Spring-Tab Aileron Tests, NACA W Rpt L-318 (1944).

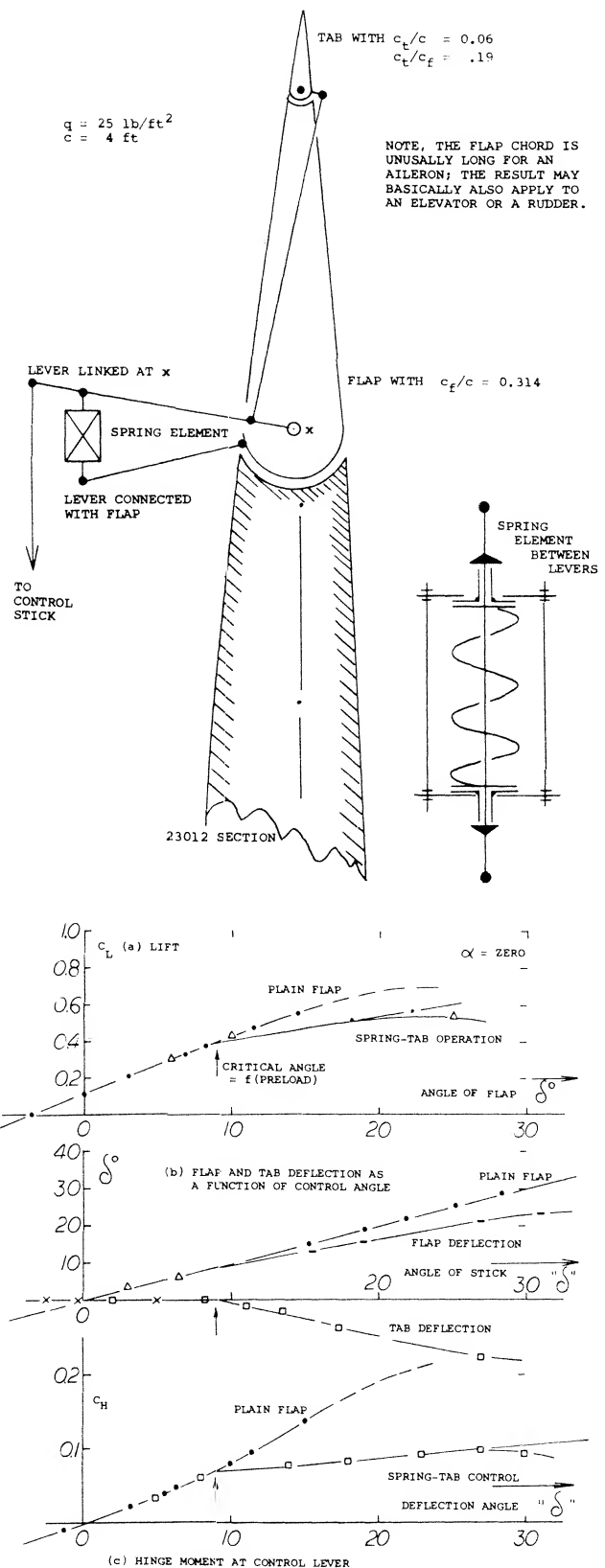


Figure 13. Example for spring-tab configuration on a 23012 airfoil section tested (14,b) between tunnel walls but with "aileron" flap only covering one half of the span.

The last complication can indeed come to the point where adverse yawing and side-slipping produce an adverse rolling moment large enough to move the airplane against the ailerons. To overcome the difficulties listed, improved and/or new types of lateral control devices have been developed. There are basically two types of such devices:

- trailing-edge flaps similar to, or modifications of, ordinary ailerons
- several types of spoiling devices at the upper wing side.

Trailing-Edge Deflection. An obvious method of roll control in flapped wings is by means of certain outboard portions of the wing (lift) flaps themselves. Figure 2 demonstrates, however, that not much effectiveness may be expected beyond a flap deflection in the order of 20° . The only means of improving the effectiveness is, in this case, differentiation of the aileron motion in such a manner that the upward displacement is larger than downward. In the end all that this control system amounts to is a pair of ordinary or possibly slotted ailerons, pulled down somewhat (say by 20°) together with some type of inboard wing flaps. All of the disadvantages listed above apply to the system.

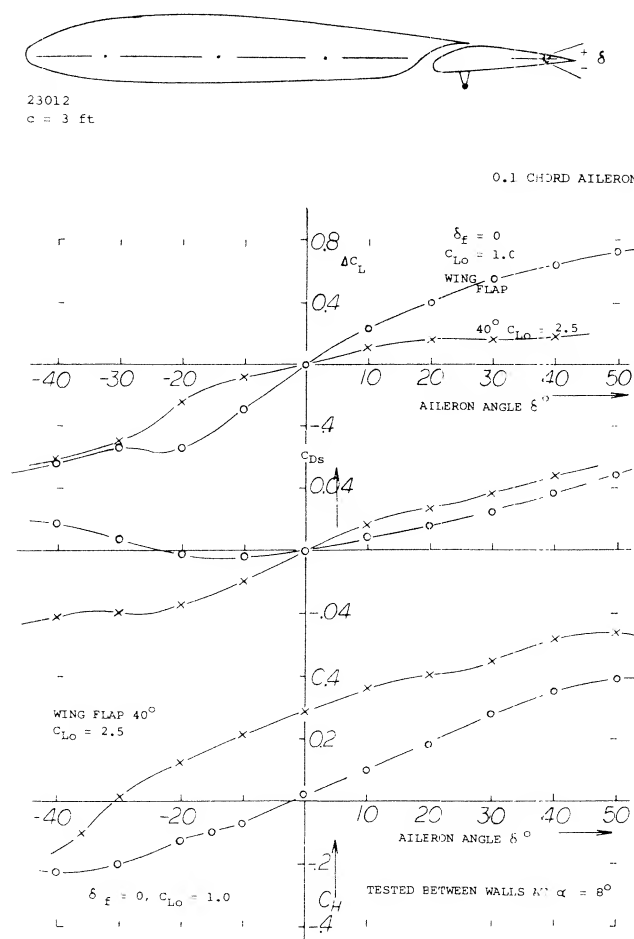


Figure 14. Combination of a plain trailing-edge aileron flap with a slotted lift flap, tested (7,k) between tunnel walls.

Duplex Flap. Figure 14 shows characteristics of a plain aileron flap attached to or located at the trailing edge of a slotted lift flap. Results of the two-dimensional investigation are:

- The aileron effectiveness at 40° lift-flap deflection is but $\approx 30\%$ of that at zero deflection.
- Effectiveness at negative aileron angles is generally slowly increasing, while that at positive angles is decreasing.
- The wing-flap position has little influence on the variation of the hinge moments $C_H \delta$.
- Because of $(dC_H/d\alpha)$ the aileron is loaded in its neutral position.

On the basis of (b) aileron linkage could be arranged in such a manner that upward deflection is larger than downward. The “up-floating” hinge moment as under (d) would then reduce stick forces, but it would at the same time reduce the stability of the roll-control system. In conclusion, aileron effectiveness is not provided by duplex flaps where it is needed most, namely at higher lift coefficients (and at associated lower flying speeds).

Split-Flap Aileron. Split flaps are ordinarily not used for control purposes. Their lift-producing characteristics are similar to, if less effective than, those of conventional control flaps. Figure 15 shows the combination of two such flaps. Although both flaps could be deflected in the same direction as ailerons, only the upper one was used for control purposes during wind-tunnel tests. Results of the investigation are as follows:

- Aileron effectiveness for a split-flap deflection of 60° is slightly higher than for neutral position.
- Hinge moments for 60° lift-flap deflection correspond to the effectiveness as in (a).
- Both effectiveness and hinge moment have a tendency, near the neutral position of the aileron flap, of lagging. It appears that the flap has to penetrate “through” the boundary layer before it can become effective.
- The “viscous” or parasitic component of drag increases as a function of the aileron deflection angle. This increase (connected with the upward, lift-reducing deflection of the flap) is very desirable in turning maneuvers of airplanes.

Regarding (d) it should be noted that the differential of the section drag coefficient is positive for negative (up) deflection of the aileron flap, while that in figure 14 is negative. In conclusion, it may be said that among the flap-type ailerons tested the split-flap type appears to be the most effective design to be used in combination with full-span wing flaps. In regard to high-speed drag (when the wing flaps are in neutral position) it seems to be necessary to deflect an outboard position of the lift flap together with the upper-side aileron flap for roll control.

2. CHARACTERISTICS OF SPOILERS.

Definition. A spoiler is basically a device that "spoils" the flow about a wing section (or possibly about a tail-surface) in such a manner that a lift differential is produced. Under certain conditions (when placed at the pressure side) such devices also produce lift, however, and their characteristics then resemble those of ordinary aileron flaps. The distinction between the two types of control thus seems to depend upon the fact whether or not spoiling of the flow pattern is an intended and primary or necessary effect of the device (12).

Mechanism. It is explained in Chapter II how circulation around an airfoil is reduced by friction and boundary-layer displacement. When enlarging the B'layer thickness at the suction side or when replacing that layer by a "wake" behind some obstruction such as a spoiler, lift is further reduced. It follows from this mechanism:

- that spoilers can most efficiently be applied at the suction (upper) side
- that effectiveness is highest when placing the spoiler at or near the point of maximum local velocity or minimum pressure
- that the spoiler effectiveness increases with the lift coefficient.

As a consequence, the spoiler can be the most effective means of lateral airplane control at higher lift coefficients (i.e. at low flying speeds) where conventional ailerons have the tendency to fail (a) because of separation from their suction side, (b) because of rolling moment (in foot-pounds) being proportional to V^2 , where V = speed of the airplane.

Thin Foil Sections. As explained in Chapters II and IV there are two basic types of foil sections:

- essentially straight and thin sections with leading-edge stalling
- round-nose and more or less cambered sections with trailing-edge stalling.

Figure 16 presents the lift effectiveness of a "spoiler" flap (simulated by a triangular ridge) extended from the upper side of a thin and straight foil section. The lift differential produced is:

- comparatively small
- nearly independent of the angle of attack
- comparatively independent of location along chord.

The effectiveness increases approximately in proportion to the height of the spoiler flap. The lift differential produced in thin ($t/c = 4$ or 6%) and straight foil sections is in the order of

$$-\Delta C_L = (3 \text{ or } 4) h/c \quad (20)$$

It may thus seem to be possible to use a spoiler, for example, in a horizontal tail surface, and they have indeed been used (or proposed to be used) in the control surfaces of missiles (possibly for reasons other than aerodynamic). We will see, however, that spoilers can be used more profitably in combination with round-nosed (15) and cambered foil sections that exhibit trailing edge stalling as in wings, and they are then used for lateral control.

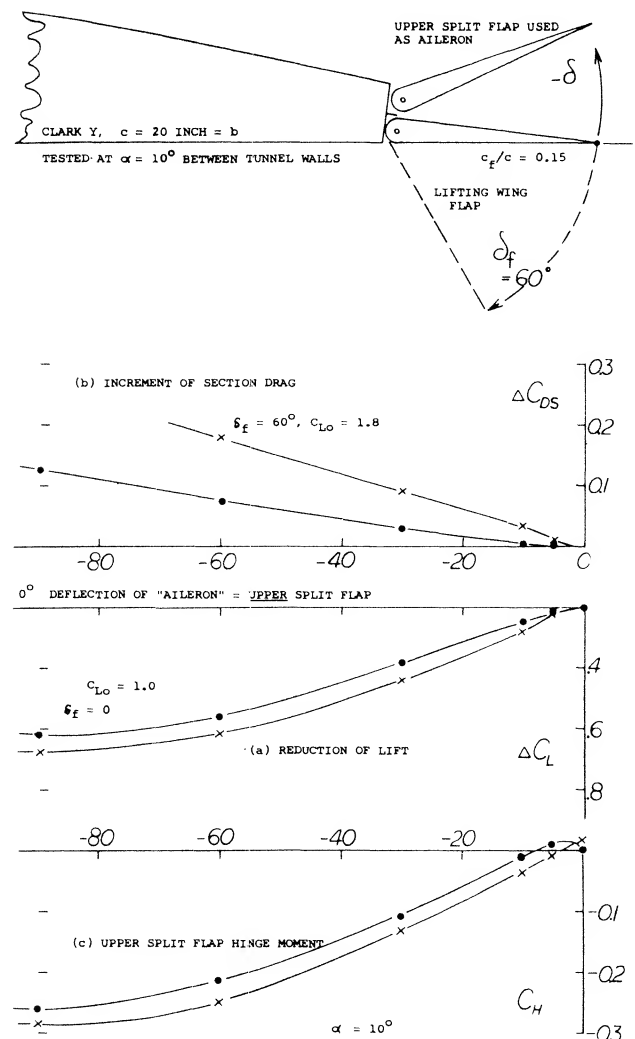


Figure 15. Double split flap arrangement, combining a lifting flap with an upper-side lateral control flap, tested (7,k) between tunnel walls.

(15) Spoilers used in thin and straight foil sections:

- Hammond, On 4 and 6% Foils, NACA RM L56F20.
- Croom, Pressure Distributions, NACA RM L58B05.

Solid Spoiler Flaps. The simplest design of a spoiler is a split-type flap, deflected from the upper side of a wing. Solid flaps of this kind have several shortcomings, however:

- their influence upon lift as a function of deflection, develops in a continuous manner.
- they are likely to cause vibration and buffeting.
- they have hinge moments of appreciable, if not considerable, magnitude.
- their effectiveness is subjected to a timewise delay between their deflection and the reduction of the lift.

For practical purposes all of these shortcomings can be eliminated by using non-solid spoilers (such as grids, or preferably rake-like devices) and by extending them in the direction normal to the upper surface, from within, usually along a certain arc, provided by a lever suitably hinged to the wing structure. An example of a realistic, if experimental, full-scale installation of this type is illustrated in figure 22,c.

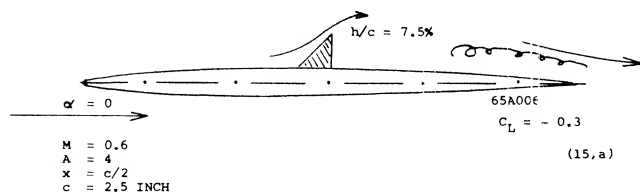


Figure 16. Example of a spoiler flap on the upper side of a thin and straight foil section tested (15) on a rectangular wing having an aspect ratio of 4.

(16) Spoilers tested on swept and delta wings:

- Schneider, Swept Wings, NACA RM L47F19 and L49D06; TN 1646 (1948).
- Wiley, On 60° Delta Wing, NACA RM L52J13.
- Croom, On 60° Delta Wing, NACA RM L52J24.
- Lovell, Plug Type, NACA TN 2089 & 2247 (1950).

(17) Experimentation with suction-side spoilers:

- ARC, Slots and Interceptors, RM's 1292 & 1442 (1930/32).
- Kramer and Zobel, Spoilers in Wind Tunnel and in Flight, ZWB FB Rpts 583,964,1304 (1936/40); NACA RM 1307.
- Hoerner, Rake-Type Spoiler, Fieseler Water-Tunnel Rpts 7 and 13 (1939); also Dr.-Ing. Thesis, TH Berlin 1941.
- v.Doepp, Spoiler Investigations for Ju-288, Junkers Wind-Tunnel Rpts S.260,S.325,S.387 (1940/41).
- Jones, Evaluation, IAS Preprint No.510 (1955).
- Jodlbauer, Spoiler for BFW-M-27, ZWB, Rpt FB 329 (1935).

Time Lag is very important if undesirable characteristic of spoilers. The change of circulation through trailing-edge displacement by means of a flap takes place without any noticeable (although yet measurable) time lag between deflection and the result in form of a lift differential. The change in flow pattern after projecting a spoiler, however, can take so much time that the reaction of the airplane is delayed objectionably. As an example, the tunnel-tested history of two particular spoilers is presented in figure 17. Fluid-dynamic time (z) is conveniently measured by the number of chord lengths traveled. That number is the non-dimensional ratio

$$X/c = z V/c \quad (21)$$

where $X = z V =$ distance traveled within the time z . In the case of the solid spoiler flap in figure 17,a, sudden projection (which takes $X/c = 1.5$ as indicated by a first arrow) even causes the lift at first to increase slightly. The flow does not separate immediately. Rather, it climbs over the obstacle which thus exhibits a camber effect remotely similar to that expected in non-viscous fluid flow. It then takes 4 chord lengths before the lift starts dropping below the original undisturbed level, and some 12 lengths before it finally reaches the terminal lower level. The airplane response time to a lateral control force will be added to the time lag of the spoiler, thus causing a considerable delay to the desired control correction. Such a delay will also be an irritation to the pilot through the lack of tightness in the control system. As a consequence, the danger of overcontrolling is very great by too much control-stick or -wheel deflection after the original deflection did not produce any direct effect.

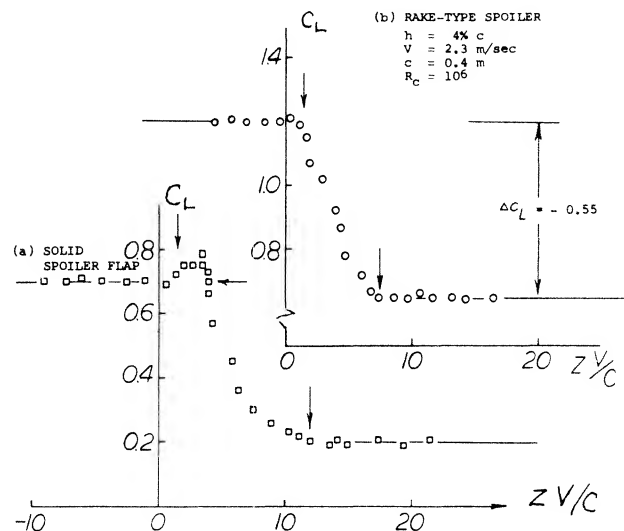


Figure 17. Time lag as tested in a water tunnel (23) for two different types of spoilers. The parameter $z V/c$ indicates the number of wing chords traveled.

Rake-Type Spoiler. Measured time-lag data from a number of sources have been assembled in figure 18. Conventional ailerons are included for comparison. It is seen that the delays A and B, as defined in the tabulation, are roughly as follows:

in conventional ailerons	A = 0	B = 5
for solid spoiler plates	A = 7	B = 20
for rake-type spoilers	A = 2	B = 7

The improvement due to ventilation of the space behind the spoiler, as in the rake-type, is very considerable.

The pressure distribution around a foil section (in the center of a low-aspect-ratio rectangular wing model) is presented in figure 19 without, and in the presence of, a rake-type spoiler at the location as shown. The lift differential produced ($\Delta C_L = -0.5$) corresponds primarily to a reduction of the negative amount (suction) of the pressure coefficient at the suction side, ahead of the spoiler, in the order of $\Delta C_p = 1$. In the presence of the spoiler, circulation is evidently appreciably reduced. A considerably enlarged boundary layer springs from the spoiler. Disregarding the trailing-edge flap (to be discussed later), the suction-side flow is *not* separated, however.

Chordwise Location. Figure 20 presents effectiveness as well as time lag of spoilers as a function of their chordwise location. As mentioned before, effectiveness (measured in the form of lift reduction ΔC_L from $C_{L0} = 1$, produced by full spoiler extension) increases as the spoiling device is moved forward along the foil chord. Maximum effect is obtained between $X/c = 0.2$ and 0.3 , and that effect can be appreciably higher than that of an aileron at the trailing edge. The time lag (as in the upper part of figure 20) also increases as the spoiler is moved forward. Time lag can be said to be approximately proportional to effectiveness. Disregarding a lesser influence of the magnitude of the original lift coefficient (at which the spoiler is used), the total delays as listed in figure 18 and as tested elsewhere, may be approximated by

$$X/c = k \Delta C_L \quad (22)$$

where $k = (x/c)/\Delta C_L$ has roughly values as follows:

k = 24	for solid-plate spoilers
= 8	for rake-type spoilers
= 6	for conventional ailerons.

The final delay can thus considerably be reduced by ventilation across the spoiler element.

TYPE OF SPOILER		A	B	z (sec)
solid, flight test	(9,b)	6	26	0.3
solid, wind tunnel	(17,b)	10	19	0.5
solid, flight test	(17,f)	7	14	0.3
solid, wind tunnel	(17,b)	7	17	0.3
screen, wind tunnel	(17,b)	3	12	0.1
saw-tooth, flight test	(9,b)	3	18	0.1
perforated, wind tunnel	(17,b)	5	12	0.2
ditto, ventilated	(17,b)	2	8	0.1
solid in water tunnel	(17,c)	4	12	0.3
ditto, but rake type	(17,c)	1.5	7	0.1
slot-lip aileron	(9,e)	1	11	-
conventional aileron	(17,b)	0	5	0
ditto (in wind tunnel)	(17,b)	0.6	8	-
ditto, flight test	(17,f)	0	5	0
ditto, flight test	(9,e)	0	4	0
ditto, flight test	(9,b)	0	5	0

A and B indicate chord lengths traveled, before lift reduction begins (A) and before the terminal reduced level of lift is reached (B). The time "z" represents the delay corresponding to A, under assumed landing conditions where $V \approx 140$ ft/sec (≈ 80 kts) and for $c \approx 7$ ft; hence "z" = $(7/140) A = A/20$.

Figure 18. Tabulation of data from various sources, indicating the lag of time between projection of a spoiler and the reduction of lift eventually caused by the spoiler.

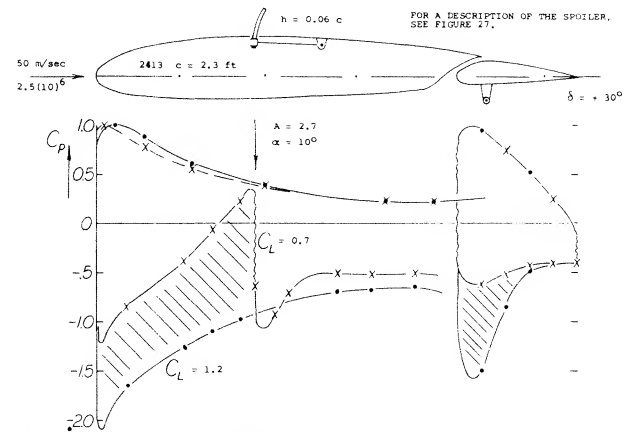


Figure 19. Pressure distribution around the mid-span section of a high lift rectangular wing model without and with a "rake" type spoiler extended from the upper side. (17,c).

Slot-Lip Aileron. Ventilation can also be obtained by opening some kind of duct leading from the wing's pressure side to behind the spoiler. In the so-called plug aileron, see figure 24, a ventilating slot is opened when the plug-shaped spoiler plate is projected from the upper surface. Another way of opening a slot is as in the original slot-lip aileron, an example of which is shown in figure 21,a. Effectiveness of this configuration is high; the time lag (see in figure 18) is considerably reduced. However, the duct leading through the wing is not very desirable and the drag added by the opening in the lower side (if left uncovered) reduces the efficiency of the wing. In an advanced form, as in part b of the illustration, the space ahead of a slotted wing flap is conveniently utilized. Results of slot-lip tests are as follows (see figure 21,c):

- At very small deflection angles the slot lip has characteristics similar to, but poorer than those of, an ordinary aileron, as there may be a 5 or 10° dead range of deflection.
- Upon exceeding a comparatively small upward deflection the slot lip causes the flow to break away from the upper side of the landing flap (if deflected), and the slot lip has the functions and characteristics as a true spoiler.
- Separation as under (b) must be expected to take place suddenly, say at $\delta = -5^\circ$.
- Effectiveness is much higher for 60° flap deflection than for neutral position.
- Hinge moments are irregular, particularly for neutral wing-flap position because of the separation as under (c).
- Drag increases with upward slot-lip deflection in a manner similar to that of the split-flap aileron described in a preceding section, thus providing a desirable positive component of yawing moment, see part (d) of figure 21.

In conclusion, this type of slot-lip aileron (as other spoiler types located near the trailing edge) is found to be sufficiently effective in combination with a deflected wing flap. It seems to be unsatisfactory, however, without such deflection.

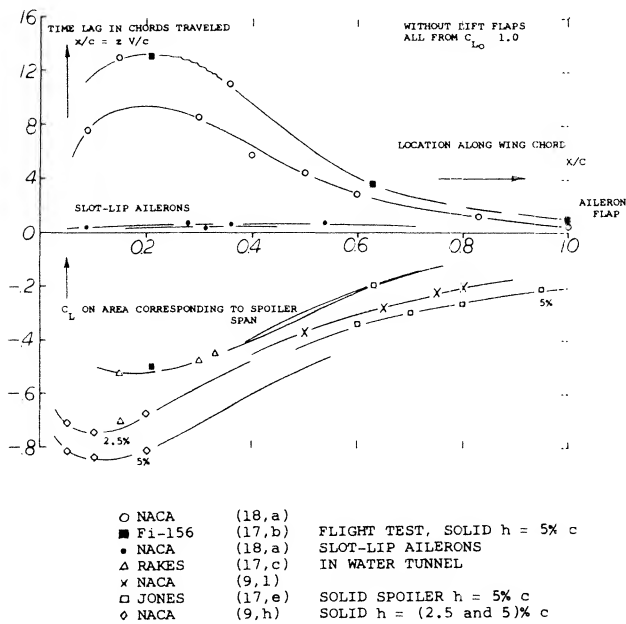


Figure 20. Characteristics of suction-side spoilers as a function of their location along the foil-section chord.

- Time lag measured to the point where the reduced lift level is reached.
- Effectiveness obtained for an original undisturbed lift coefficient $C_{L0} = 1.0$.

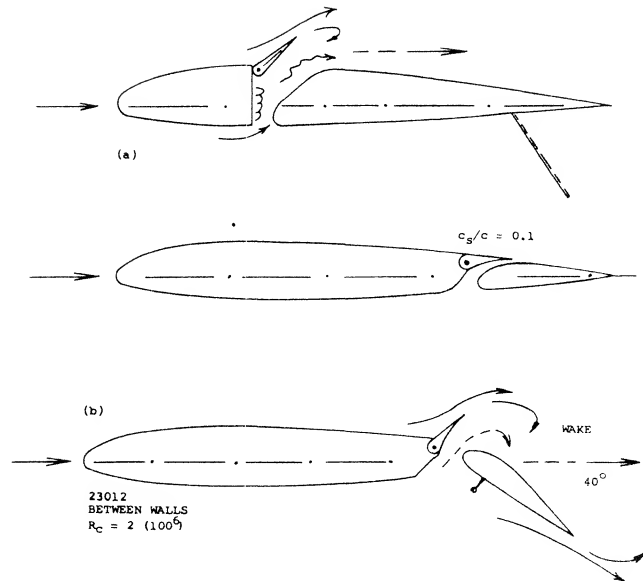


Figure 21. Two versions of the slot-lip spoiler (9).

- Original slot-lip configuration (9,e,h).
- Combination with slotted wing flap.
- Lift coefficient of (b) as a function of slot-lip deflection.
- Section drag coefficient associated with slot-lip deflection.

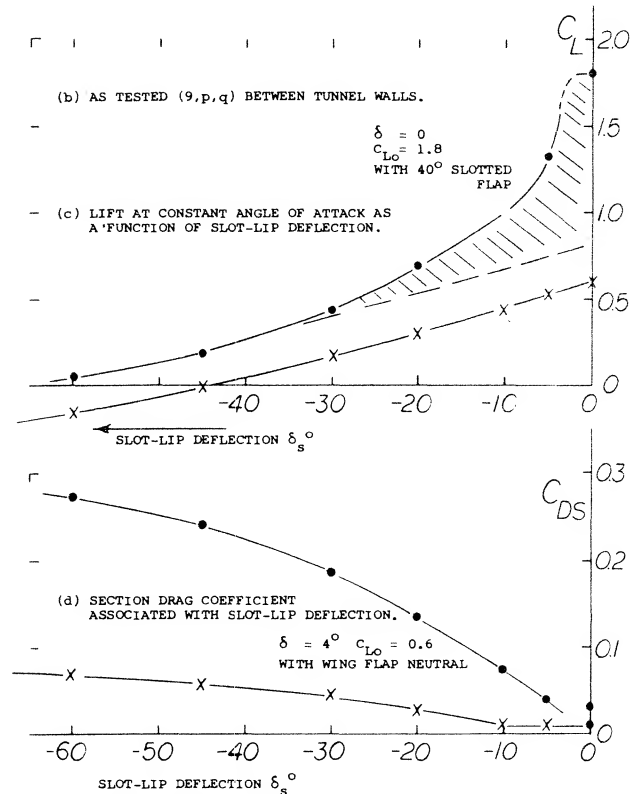


Figure 21. Lift and drag of the slot-lip configuration.

Effectiveness as a Function of Lift. The lift coefficient of a foil section is presented in figure 22 without and with a rake-type spoiler projected from the upper side. It is seen that the differential of the lift coefficient increases with the original (undisturbed) value of that coefficient. It is also evident that for constant spoiler projection, the lift curve slope is appreciably reduced. Lift differentials are plotted in figure 23 as a function of the original lift coefficient. At $C_{L0} = 0$, there is evidently some negative lift caused by the projection of spoilers from the upper side of the wings or foil sections tested. This is thus an example where the spoiler produces lift, rather than destroying lift. As the lift coefficient is increased the differentials grow along straight lines. It should also be noted that the spoiler effectiveness does not discontinue at or beyond the maximum lift coefficient. The effectiveness reduces, however, and it reaches zero at an angle of attack where the flow is really separated from the suction side.

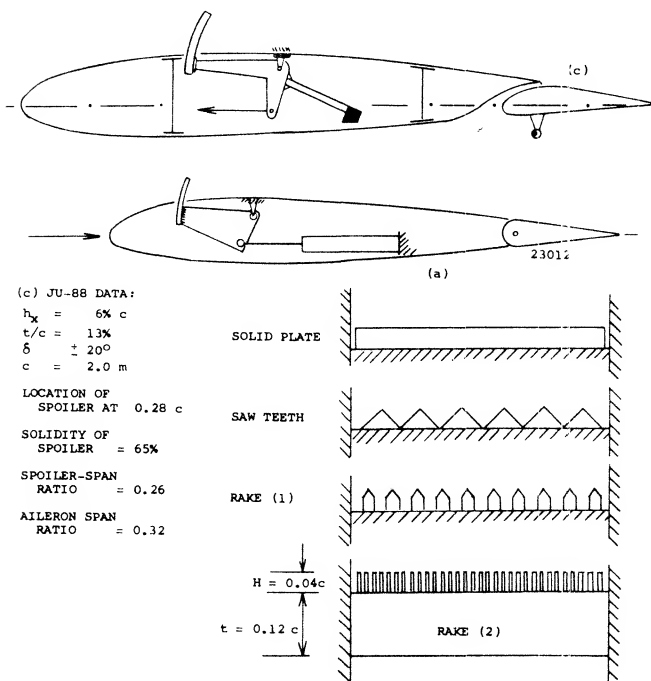


Figure 22. Rake-type Spoiler.

- a) Configuration and spoiler shapes as tested in a water tunnel (17,c).
 b) Lift as a function of the angle of attack.
 c) Experimental full-scale installation (17,c) in Ju-88, tested for Ju-288 (19).

(18) Characteristics of slot-lip ailerons & plug-type spoilers:

- (a) Weick, Tunnel Tests, NACA TN 547 (1935).
 (b) Shortall, Flight Tests, NACA T Rpt 602.
 (c) See NACA Tech Reports 443 and 605; and (7,k).
 (d) NACA TN 547 and 1079.
 (e) Ragallo, With Full-Span Flaps, J.A.Sci. 1950 p.
 (f) Fischel, Plug Spoiler Brake, NACA T Rpt 1034 (1951; also T Notes 1473,1663,1802,1872 (1948/49).

(19) The Ju-288 was a high-speed bomber during World War II:

- (a) Jane's All the World's Aircraft.
 (b) Hoerner, Spoiler Control System, Dr.-Ing. habil. Thesis, 1941.

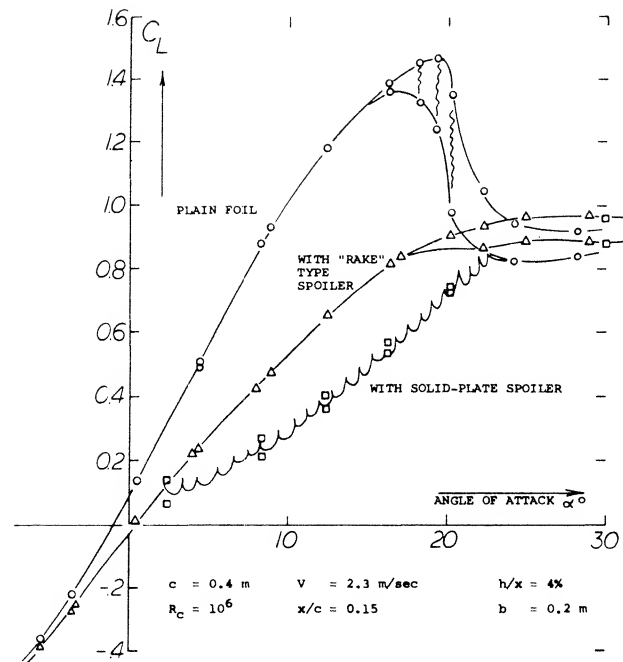


Figure 22. (b) Lift as a function of the angle of attack as tested between walls, with and without the rake type spoiler.

Helix Angle. When projecting and keeping projected a spoiler device, a steady-state cork-screw motion is obtained similar to that described for flap-type ailerons, see equation 10. As an example, here are results quoted from (20,c) on the performance of an experimental airplane (Fairchild-22):

tapered wing with	$A = 10 -$
wing span	$b = 34$ ft
spoiler span	$a = .33 b/2$
spoiler location at	$x \approx .72 c$
height of spoiler	$h = .10 c$
per second rolling at 100 mph	$p = 0.6$ rad

The helix angle at 100 mph = 147 ft/sec, is:

$$u/V = p b/2V = 0.6 (34)/(2 \cdot 147) \approx 0.07 = 4^\circ$$

This value is near the lower boundary of the range as indicated in equation 103. Results reported in (4,a) show in a similar manner rolling performance of a P-61 airplane, as follows:

wing span	$b = 66$ ft
spoiler span	$a = .34 b/2$
spoiler location	$x = .73 c$
height of spoiler	$h = 7\% c$

At a speed of 334 mph = 490 ft/sec the rolling velocity obtained was

34 degrees/sec for spoiler alone
50 degrees/sec for spoiler plus aileron.

The small guide ailerons used (at the wing tips) were deflected to plus/minus 15°, where the stick force reached 80 or 85 lb. The helix angle corresponding to the rolling velocities listed are 0.04 and 0.06, respectively.

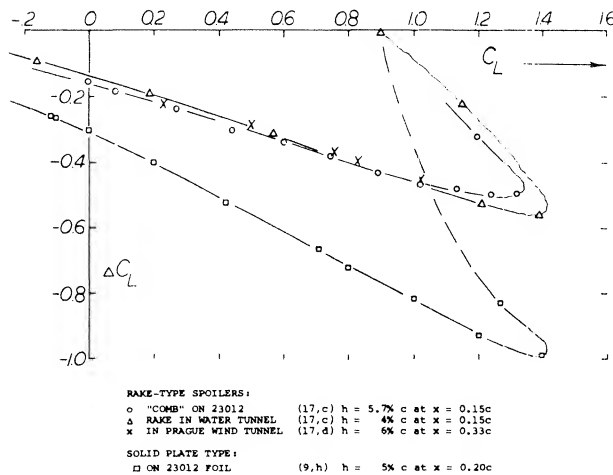


Figure 23. Effectiveness of spoiler control as a function of the lift coefficient at which the spoiler is used.

Spoilers in Presence of Wing Flaps. In regard to effectiveness we have seen that:

- spoilers will be most effective when used in combination with a more or less round-nosed, cambered, high-lift foil section.
- the effectiveness grows with the lift coefficient at which the spoiler is used.

When projecting a spoiler from the upper side of a wing, the flow will also be disturbed where it passes the wing or aileron flap (if there is one), and the spoiler will make the flow break away from a deflected trailing edge wing flap (provided that the flow was still attached). This is particularly true in the case of a slotted flap as demonstrated in figure 21,e, where the shaded area is due to separation from the flap, while the function C_L (δ_s) with the flap in neutral position, represents the ordinary spoiler effect.

(20) Lateral control wing spoilers, flight-tested:

- Weick, Rolling Moments, NACA T Rpt 494 (1934).
- Soule, With Full-Span Flaps, NACA T Rpt 517 (1935).
- Wetmore, Retractable Ailerons, NACA TN 714 (1939).
- Shortal, Slot-Lip Spoiler, NACA T Rpt 602 (1937).
- Fikes, Plug on Swept Wing, NACA RM L52A03 (1934).
- Gilruth, Lateral Requirements, NACA T Rpt 715 (1941).
- Sphor, Spoiler Arrangements, NACA TN 1123 (1947).

Flap Flow. An arrangement similar to the slot-lip spoiler is the plug type, mentioned before in connection with time lag and ventilation. Figure 24 presents shape and the principle characteristics of a configuration of this type. We see in particular:

- that the rolling moment increases with the lift coefficient, at which the spoiler is used.
- that the effectiveness is higher with, and it grows with, the deflection angle of a slotted lift flap.
- that effectiveness reaches a maximum at a flap angle in the order of 40°.

The type of flap flow, whether attached or separated, is of basic importance. Any plug-type of slot-lip spoiler cannot destroy much lift produced at and due to the wing flap, unless the flow is attached to its upper or suction side. It must be concluded, accordingly, that any spoiler, when used in combination with a trailing-edge split flap (behind which the flow is always separated), will only have an

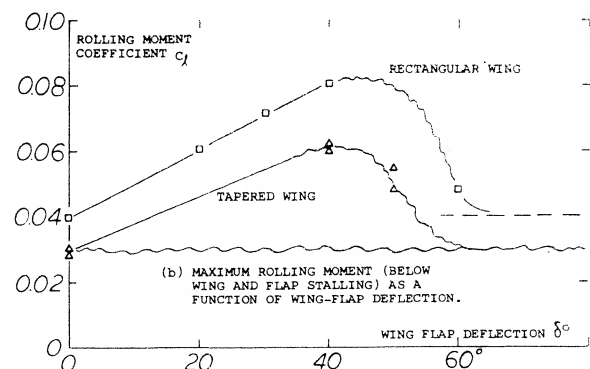
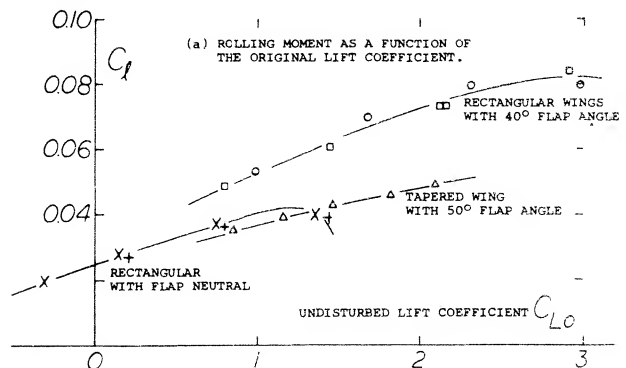
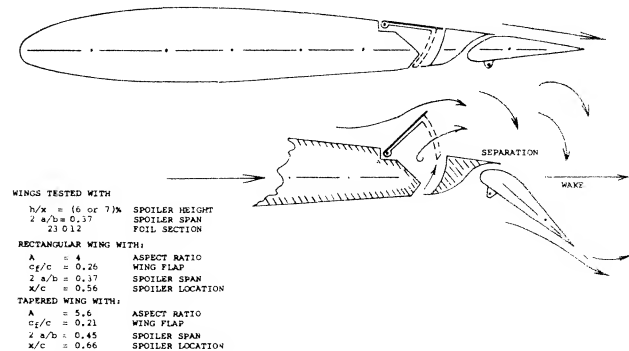


Figure 24. Characteristics of a plug-type spoiler flap (9,p) in combination with a full-span slotted wing (lift, landing) flap.

effectiveness somehow equal to that with the wing flap in neutral position. For illustration, see the effectiveness of the plug-type spoiler in figure 24 in presence of a wing flap deflected to 50° (where the flow must be assumed to be separated from the suction side of the flap). The high values of the lift reducing effect as in figure 21,c up to $\Delta C_L = -1.7$ can also partly be attributed to a reduction of the foil-section circulation because of the slot opened up ahead of the lift flap. Including flow separation from a slotted flap deflected between 20 and 40° , the slot lip as in figure 21,b has an effectiveness, measured in the form of (ΔC_L) , between -1.5 and -1.8 at undisturbed lift coefficients C_{L0} between 1.1 and 2.7 . Such values are roughly 2 times those of the solid-plate and some 3 times the maximum of those of the rake-type spoilers as in figure 23. Thus destroying practically all of the lift produced by the foil section as well as by flap deflection, the slot-lip spoiler appears to be extremely effective at higher lift coefficients.

Induced Yawing Moments. When changing the lift coefficient in the part of the wing span covered by an aileron flap or a spoiler, by a certain ΔC_L , the induced drag for that part is calculated using equation 15. As mentioned before (in connection with the Frise-type aileron), the significance of this differential rests in the fact that it causes a yawing moment the direction of which is opposed to the motion of an airplane when making a turn. Since the rolling moment is the result of the lift differential ΔC_L , and the yawing moment is proportional to ΔC_{D_L} , we obtain the moment ratio as in equation 17. We have evaluated that equation for an aspect ratio $A = 4$. Experimental results plotted in figure 25 confirm the analysis well, when considering a small positive and constant component evidently reflecting the variation of the viscous foil section drag as a function of flap deflection.

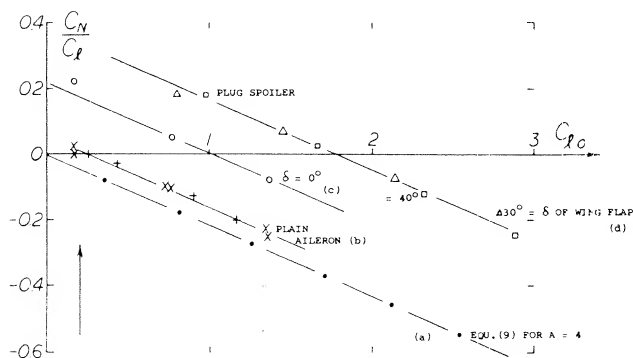


Figure 25. The variation of the yawing moment of rectangular aspect-ratio-4 wings, presented in the form of the moment ratio C_N/C_L as a function of the lift coefficient at which lateral control is applied:

- as indicated by theory (see text)
- due to plain aileron deflection
- due to a "plug" spoiler while $\delta = 0$
- due to a spoiler in presence of a slotted wing flap deflected to 30 and 40° .

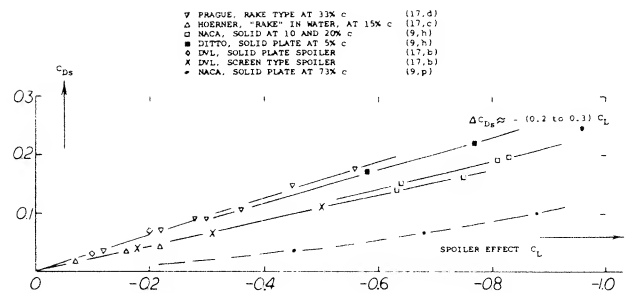


Figure 26. Parasitic drag associated with the lift differential produced by various suction-side spoiler devices.

Parasite Drag. When deflecting a spoiler, the flow past the suction side of the airfoil section separates. As a result of this separation there is an increase of parasite drag. Drag coefficients tested on rectangular wing models equipped with full-span suction-side spoilers are plotted in figure 26. The section drag increases in proportion to the lift differential caused by the various types of spoilers tested. Therefore:

$$\Delta C_{D_S} = -k (\Delta C_L) \quad (23)$$

where k is between 0.2 and 0.3 for forward spoiler locations between 0.1 and 0.3 or 0.4 of the chord. There is one example in the graph, representing a plug-type or slot-lip spoiler, at a location $x = 0.73$ c. The factor k is only 0.1 in this case. The increase in parasite drag due to spoiler deflection results in an increase in the yaw to roll moment coefficients (into the more or less desirable positive range) by an amount of ≈ 0.2 , on account of a plug-type spoiler located at $x = 0.56$ of the chord, figure 25. Note that the moment ratio is equivalent to the factor k in the last equation. When using spoilers in combination with slotted wing flaps (at deflection angles such as 30 or 40° where the flow is still attached to their suction side) the parasite drag due to spoiler projection is almost doubled. The factor equal to the moment ratio is between 0.3 and 0.4 . In conclusion, spoilers present a usually desirable positive contribution to the yawing moment when turning an airplane. It is conceivable, however, that the positive due-to-spoiler yawing moment might be too large at smaller lift coefficients, particularly when diving an airplane at or close to $C_L = \text{zero}$.

(21) Lift control by means of jet sheets:

- Childress, Princeton Aero Engg Rpts 365,391,422 (1956/58).
- Lowry, Jet Spoiler, NACA RM L53109a.
- Schult, Spoilers and Jet Controls, NACA RM L56H29.

Combination With Aileron Flap. We have seen that spoilers have comparatively high effectiveness at higher lift coefficients, particularly when used in combination with a lifting (slotted) wing flap. Spoilers may also reduce the yawing caused by the rolling moment produced in the wing to zero. Combination of a spoiler with a pair of possibly small-span ailerons promises advantages as follows:

- The ailerons will eliminate or sufficiently cover the time lag associated with plain spoiler operation.
- The ailerons will also cover the dead range of their projection (such as found in figures 21,c and 27,a).
- Ailerons will provide a desirable amount of hinge and control moment, which retractable arc-type spoilers do not have.
- In regard to yawing moments, a suitable combination of spoiler and aileron flaps may provide the most desirable or most acceptable solution.
- While ailerons do not function well in combination with full-span flaps, spoilers will work particularly well when placed in front of wing flaps.

An example of a lateral control system in which a short aileron is combined with a spoiler is presented in figure 28.

Spoiler and Plain Flap. The experimental results in figure 27 confirm the fact that (without presence of a deflected lift flap) a spoiler may not have sufficient effectiveness. Roughly, the rolling moment produced by a spoiler (projected on the upper side of the foil section) is equal to that due to deflection of an aileron flap on one side of the wing. Consequently, when using a pair of aileron flaps, their combined power will be twice that of the spoiler. Using now the spoiler together with an aileron flap located behind, in the same part of the wing span, figure 27 shows that their combined effectiveness is somewhat less than the sum of their individual powers.

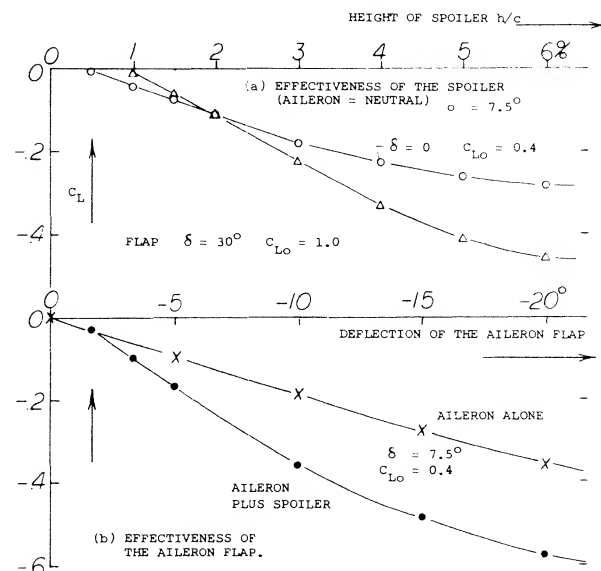
Spoiler Span. The model of a large 6-engine airplane was investigated as to lateral control (9m). When increasing in steps the spanwise length of a screen-type spoiler, at 0.65 chord, the rolling moment produced increases as shown in figure 28,a. For comparison, results for another series of spoilers are also plotted in the graph, beginning in the center of the wing. The function obtained is very similar to that in figure 4. Regarding yawing moments, figure 28,b shows a positive value corresponding to an increment of the section drag coefficient by $\Delta C_{D3} \approx 0.06$. The moment due to control by means of the short-span aileron flap is, on the other hand, negative (see equations 16 and 17). Figure 28,b also illustrates the fact that a spoiler produces a rolling moment roughly equal to that of a one-side aileron flap.

Flight Testing. Wind and water tunnel investigations of the comb or rake type suction-side spoilers (as in figures 22 or 27) show among others:

- that effectiveness is high in comparison to more down-stream locations.
- that time lag (delay) is small, but still twice that of a conventional aileron.

A combination of rake type spoiler with a slotted wing flap and with an independent short-span aileron was subsequently flight-tested, in 1941, on the Ju-88 airplane. In comparison to the original condition of the airplane, the span of the ailerons was reduced to half (the wing flaps were extended, accordingly). Results are as follows:

- At higher lift coefficients, lateral control effectiveness is higher than that of the original configuration.
- At higher speeds (i.e. at lesser lift coefficients) control effectiveness is lower than in the original condition; effectiveness is fully satisfactory, however.
- The spoiler's positive yawing-moment component increases the control effectiveness, by avoiding yawing in the wrong direction.
- Positive yawing moments also improve handling qualities in turns, when maneuvering only one of two engines, and during blind flying (on instruments).



The foil, flap and spoiler configuration tested is as in figure 19. There are 30 prongs in a piece of span equal to the chord. The clearance between the prongs is 0.4 of their spacing, so that the spoiler solidity is 60%.

Figure 27. Effectiveness of spoiler and aileron flap as tested (17,c,d) full-span on a rectangular wing model with $A = 2.6$.

Jet Spoiler. Another method of spoiling the suction-side flow of an airfoil is by means of a jet discharging at a suitable location. Devices of this type are described in (21). The spoiling effect of the jet sheet is expected to be a function of the momentum coefficient

$$C_{\mu} = (w/v)^2 (s/c) (b_s/b) \quad (24)$$

where w = jet velocity, s = width of the slot from which the jet issues, and b_s = spanwise length of that slot. It is said in the second of two reports (21,a), however, that "aerodynamic time lag may not be any less than for mechanical spoilers". It is obvious that a jet sheet could as well be issued from the trailing edge of a wing thus forming a jet flap aileron, presumably with characteristics similar to those of mechanical flaps.

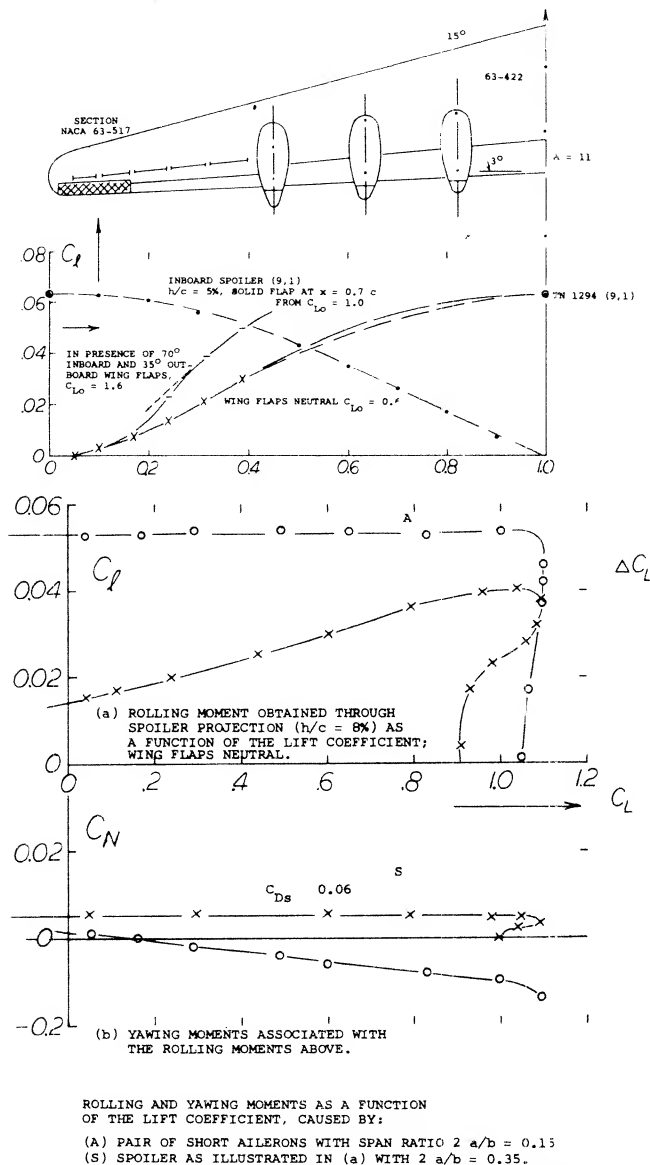


Figure 28. (a) Configuration tested (9,m) at $R_c = 9(10)^6$; and rolling moment caused by spoiler projection ($h/c = 8\%$) as a function of the span ratio $2 a/b$. For comparison one-side aileron with full outboard span $2 a/b = 0.41$.

(b) Rolling moment coefficient of a 6-engine pusher-type airplane model (9,m).

3. INFLUENCE OF COMPRESSIBILITY UPON LATERAL CONTROL.

After dealing with all the details of control effectiveness and hinge moments, there is one influence left to be discussed, namely compressibility and/or Mach number.

Prandtl Glauert Factor. The lift-curve slope of foil sections (not that of wings having finite aspect ratios) grows in proportion to the Prandtl Glauert factor

$$PG = 1/\sqrt{1 - M^2} \quad (25)$$

Experimental evidence as in (22) proves that due-to-flap lift-curve slopes $dC_L/d\alpha$, also tend to increase in proportion to PG, although the boundary layer can have an influence reducing this effect.

Hinge Moments. Usually, hinge moments due to flap deflection are proportional to $dC_L/d\delta$. Hinge moments may, therefore, be expected also to grow in proportion to or possibly at a lesser rate than PG.

Spoilers. The effectiveness of suction-side spoiler devices usually increases with the lift coefficient. As a consequence, effectiveness may be expected to grow in proportion to PG. Experimental results listed in (9,p) confirm the prediction, although tunnel blocking (choking) seems to exaggerate the influence.

Critical Mach Number. The Prandtl-Glauert rule cited above ceases to apply as soon as at any point of the foil-and-flap section the velocity of sound is first reached. The maximum local velocities are a function of thickness ratio, lift coefficient and section shape. Considering a deflected and lifting control flap, a critical point is found at the suction side of the flap near its nose where the contour makes a bend. Particularly critical conditions (high local velocities) must be expected at the exposed side of an overhanging nose balance. The balancing qualities of such noses may thus be limited by compressibility, and the flap effectiveness may be expected to be reduced at the same time.

- (22) Influence of compressibility upon flap characteristics:
- (a) Stevenson, 9% Foil Sections, NACA TN 1406 & 1417 (1947).
 - (b) Hammond, Flaps and Spoilers, NACA RM L53D29a; also RM L56F20.
 - (c) Lindsey, 9% Foil with 30% Flap, NACA RM L56L11.
 - (d) Lowry, Rectangular Wings, NACA RM L56E18.
 - (e) Whitcomb, Transonic on Swept Wing, NASA TN D-620 (1961).
 - (f) MacLeod, Bump Tests, NACA RM L50G03.
 - (g) Using free-flight rockets, NACA RM L48A07 & L48I23.
- (23) In a low-speed water tunnel, the time scale is considerably larger than in a wind tunnel (at one and the same Reynolds number).

CHAPTER XI — LONGITUDINAL STABILITY

CHARACTERISTICS OF AIRPLANES

Stability is the built-in tendency of a vehicle to return by itself to a certain state of equilibrium. For example, a railroad vehicle is extremely stable in regard to pitching (and rolling) motions. Ships have considerable stability (based on buoyancy). By comparison, the stability of all types of aircraft is much more sensitive and complex, resting upon the interaction by means of the flow of air between half a dozen component parts, such as wing, fuselage, propulsion system and tail surfaces in particular.

In this and Chapters XII, XIII and XIV the general characteristics of aircraft stability will be discussed. In particular, the stability will be covered in terms of the fundamental parameters for the longitudinal, directional and lateral modes (1). Included in the treatment will be the basis for determining the stability derivatives of the wing, fuselage, tail and propulsion systems. We will also consider static and dynamic stability of simple and plain aircraft configurations.

FOR MANY PRACTICAL PURPOSES THE NORMAL FORCES AS SHOWN, APPROXIMATELY EQUAL TO LIFT, CAN BE USED IN STATIC STABILITY.

- a - TO AERODYNAMIC CENTER OF WING (o)
- n - TO NEUTRAL POINT OF CONFIGURATION
- q - TO CENTER OF GRAVITY (-)

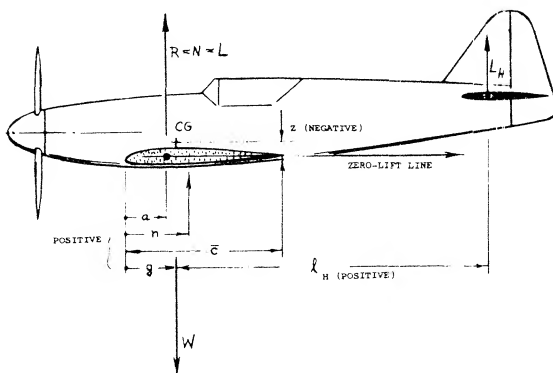


Figure 1. Geometry of airplane configuration showing the static balance of weight and aerodynamic forces.

- (1) It seems that airplanes were flown for years, before their stability was first formulated by Bryan, "Stability in Aviation", London 1911.

1. FUNDAMENTALS OF LONGITUDINAL STABILITY

Longitudinal motions of an airplane, the motions in a vertical plane, can tentatively be analyzed without reference to motions in other directions, on the simple assumption that the craft is kept on course and that rolling is prevented by proper control.

Parameters Involved. The aerodynamic forces and moments of an airplane are function of shape, arrangement and interference of the component parts. Their magnitude and possibly their character, may change as a function of speed (Mach number) and altitude (Reynolds number). The resultant stability may also be affected by structural elasticity of the components and/or the configuration. The operational necessity of control by means of the elevator (hinge moments, weight and strain in the system) will also have an effect upon stability. Longitudinal characteristics may be altogether different during the landing maneuver (flaps, landing gear, ground effect). Propulsion by jet engines, propellers, or ducted fans cause dynamic interaction problems which have a very considerable influence upon stability. The stability of aircraft motions also involves mass- aerodynamic forces and aeroelasticity arising as a consequence of such motions. Many or some of the parameters mentioned, may or will, therefore, be affected during the motions of which they are the cause and/or integral part. As a consequence, when including all variations of shape, interaction and operation, the number of parameters possibly to be considered, may reach the order of 100. Stability analysis may thus appear to be an unsurmountably difficult problem, particularly in view of the fact that a longitudinal shift of the center of gravity by plus or minus a very few percent of the wing chord, can be the difference between a stable or unstable airplane. Fortunately, most of those parameters are of secondary importance; many of them have not even been analyzed and/or tested. Some of them are, on the other hand, are of predominant importance such as downwash and possibly thrust in particular. Indeed, consideration of "a dozen" selected parameters will and has to be sufficient in the practical analysis of stability.

Notation. As described in the Chapter I, there is a basic convention regarding positive and negative directions of dimensions, forces and moments. The following symbols and conventions will apply. For an airplane as in figure 1, in the longitudinal plane of symmetry, about and in reference to its center of gravity CG there are the geometric factors:

- x = longitudinal distance parallel to the zero-lift line of the mean wing section.
- z = distance between the wing's aerodynamic center and the CG, in normal (vertical) direction.
- \bar{c} = mean aerodynamic chord "mac", replacing the wing aerodynamically.
- ℓ_H = distance of horizontal tail quarter-chord point from CG.
- H = subscript indicating the horizontal tail.
- $M = C_m q S \bar{c}$ = pitching moment, usually about the CG.
- CP = center of pressure or lift forces.
- AC = aerodynamic center of wing ($C_m = \text{constant}$)

There is also a "neutral" point, representing the aerodynamic center of the wing plus tail configuration.

The Signs The following sign convention will be used in this text:

lift and drag	=	positive
"up" direction	=	positive
nose-up moment	=	positive
wind direction	=	positive
downwash velocity	=	negative

In particular, a positive pitching moment tends to increase the angle of attack, thus leading to stalling. A positive value of the derivative $dC_m/d\alpha$ or dC_m/dC_L , means a lack of stability. Therefore, to be stable, every airplane should have a negative pitching moment derivative. The definition of moment arms is more difficult. As far as geometry is concerned, we will consider the distance of any point on the chord of a wings (or on the axis of a fuselage body) aft of the leading edge (or the nose, respectively) to be positive. However, when it comes to pitching moments due to positive lift forces, usually about the CG, the moment arm of the horizontal tail must evidently be counted as negative, while that of the wing (assuming that the CP is ahead of the CG) has a positive value.

Static Stability. The oscillatory motions of an airplane in longitudinal direction (pitching, heaving, variation of speed) can properly be described by a set of equations. Assuming, however, that the motions may be sufficiently slow (thus eliminating all derivatives against time), the

dynamic forces and moments (due to inertia and/or acceleration) may tentatively be disregarded. By neglecting these contributions, the stability of an airplane becomes the favorable interaction between gravity (weight) and aerodynamic (lifting) forces and moments. This type of stability can easily be determined in a wind tunnel by hinging an airplane model about the lateral axis through the point representing the center of gravity. The slope or strength of the restoring moment $dM/d\alpha$ is then called "static stability". Such investigations provide indispensable information regarding aerodynamic forces and moments contributed by wing, fuselage, propulsion system tail surface etc. and give an insight into the downwash and wake effects. The investigations lead to practical measures of changes necessary for improving stability. Disregarding extreme conditions (such as particularly in more or less "ballistic" missiles) static stability is the most important component of dynamic stability; and as far as airplanes are concerned, static stability can be said to be a prerequisite of dynamic stability.

Balance. In airplanes, usually one of the less important parameters contributing to stability is drag. To simplify the consideration of balance and stability, we will thus assume the basic system of forces and moments as in figure 1. Specifically, the lifting or resultant forces are assumed to be normal to the wing section's zero lift line, through its aerodynamic center AC (which means approximately through the trailing edge). All dimensions are measured in directions parallel or normal to that line. For $C_m = 0$, longitudinal characteristics of the "airframe" are then described by a pair of simple equations, the first of them indicating balance:

$$L(\Delta x) + L_H \ell_H = \text{zero}; \quad L(\Delta x) = L/\ell_H \quad (1)$$

where the first term represents the pitching moment of the wing and the second term that of the horizontal tail. For forces and positions as illustrated in figure 1, the moment arm $\Delta x = g - a$, has a positive value, while that of the tail ℓ_H must be counted to be negative. In the form of non-dimensional coefficients (based on wing dimensions) balance is defined by

$$C_L (\Delta x/c) = C_{LH} (S_H/S) (\ell_H/c) \quad (2)$$

where $(S_H/S) (\ell_H/c) = \bar{v}_H$ = horizontal-tail "volume" (because it has the dimension of ft^3).

Basic Stability Equation. A second equation describes the variations of forces and moments, as the airframe is slowly rotated (at constant tunnel speed V) about the transverse axis through the CG. For a vertical distance (see figure 1) $z = 0$, the airplane is then stable, provided that

$$(dL_H/d\alpha) |l_H/c| > (dI/d\alpha)(\Delta x/c) \quad (3)$$

where $\Delta x/c$ as above, $= g - a$. Replacing the lift by its coefficient " C_{LH} " and L_H by $C_{LH} q(S_H/S)$, stability is indicated by

$$(dC_{LH}/d\alpha) V_H > (dC_L/d\alpha)(\Delta x/c) \quad (4)$$

where V_H as above. On the basis of these equations, any type of combination of two "wings" might be made "stable", including tandem and canard configurations. The reasons for preferring one particular type, larger wing plus comparatively small horizontal tail aft for airplanes are:

- 1) concentration of lift in one large-span wing is most efficient,
- 2) a "small" horizontal surface is sufficient for stabilization,
- 3) location at the tail promises longitudinal control up to and beyond C_{Lx} ,
- 4) location within the propeller slipstream provides improved control at low speeds, such as on the ground.

Equation (4) also means that for longitudinal stability, the sum of the two sides, equal to the derivative of the complete system (for example, with fixed elevator) must be negative; thus:

$$(dC_m/dC_L) = (dC_m/d\alpha)(d\alpha/dC_L) < 0 \quad (5)$$

Free Moment. Provided that the wing section is cambered (or owing to the deflection of wing flaps) there is usually a free moment indicated by $C_{mo} = M_o/qSc$ (independent of lift, and thus also at zero lift). Including this component, equation (2) reads in non-dimensional form:

$$C_{mg} = C_{mo} + ((g - a)/c) C_L + C_{mH} = 0 \quad (6)$$

where g = longitudinal location of the CG, while a = location of the aerodynamic center (including the influence of the fuselage, etc.). The free moment is thus balanced by the horizontal tail. In a conventional airplane configuration, C_{mH} is adjusted by suitable deflection of the elevator so that balance is obtained for a particular lift coefficient, corresponding to speed or dynamic pressure when flying. It should be noted, however, that as a con-

stant if not changed by slipstream effects, C_{mo} does not affect stability. This is the distinction between balance and stability.

Although the equations presented above for the static stability case are simple, determination of the longitudinal stability of an airplane is complex because

- (a) various interference effects that cannot be disregarded,
- (b) the wing downwash has a large effect on the resultant lift curve slope of the horizontal tail surface,
- (c) forces of, and interference by the propeller (or the propelling jet) are needed in the operation of powered airplanes.

Only the simplest type of configuration without wing flaps and without propulsion effects will be considered in the following sections of this chapter. The influence of the propulsion system on longitudinal stability is covered in Chapter XII.

DYNAMIC LONGITUDINAL STABILITY. After an aircraft is disturbed from its flight path two basic motions are obtained: 1) a long-period or phugoid oscillation and 2) a short-period oscillation. These oscillations may be developed even though the static longitudinal stability of the aircraft is satisfactory. The long-period phugoid oscillation may involve several seconds depending on the particular airplane. This motion is normally hardly noticed by the experienced pilot who automatically damps it out with the stick or power changes. The short-period oscillation, however, must be adequately damped in the basic airplane system for satisfactory dynamic longitudinal stability. If the airplane has an undamped short period oscillation, attempts to correct the difficulty can lead to pilot induced oscillations, PIO'S, which accent the unstable condition.

The analysis of the dynamic stability problem requires the use of the basic equations of motion and the identification of many stability derivatives. With the stability derivatives involving velocity, angle of attack, q , elevator angle, compressibility, moments, etc. the dynamics of the airplane are analyzed for at least the stick fixed and stick free cases. The development of the basic equations of motion and their analysis in terms of dynamic stability are covered in many available sources, for instance (2,h,g) and, therefore, will not be repeated here. Rather a basic understanding of the static longitudinal problem is considered. From the material presented, the derivatives needed for the dynamic analysis can be determined with a greater degree of accuracy.

2. LONGITUDINAL CHARACTERISTICS OF WING-FUSELAGE COMBINATIONS

The basic components of an airplane are wing and fuselage. Their longitudinal characteristics influencing stability are presented here.

Stream Curvature. The longitudinal moment of airfoil sections are treated in the Chapter II as a function of the type and operating conditions. When using their characteristics, it must be realized that airplane wings, always having a finite span, impart a permanent downward deflection upon a certain stream of air. Since the deflection takes place within the chord of the wing, the effective camber of its section is reduced. The corresponding reduction of the usually negative free or zero-lift pitching moment coefficient is approximately:

$$\Delta C_{mo} = + 0.044/A \quad (7)$$

which means that for $A = 4.4$, for example, the aerodynamic center is shifted forward 1% of the wing chord. Since most of the C_{mo} values presented for airfoil sections in Chapter II, stem from tests on wings with $A = 6$, the difference as per equation (7) is usually unimportant in the analysis of wings having conventional aspect ratios.

Aerodynamic Chord (3). Airplane wings are usually not rectangular accordingly their chord length varies along the span. A mean chord, to which pitching moments can be referred, should account for the distribution of lift (load) across the span. If possible, the mean chord should represent the aerodynamic characteristics of the wing as to magnitude and location. This can be done for "straight" and untwisted elliptical plan forms:

$$\bar{c} = (2/s) \int_0^s (c^2 dy) = (S/3\pi) c_x = 0.85 c_x \quad (8)$$

where $s = b/s =$ half span, and $c_x =$ maximum chord (in the center). The location of the "mac" chord (equation 8) is at

$$y/s = (2/sS) \int_0^s (cy/dy) = (4/3\pi) s = 0.42 s \quad (9)$$

(2) General treatment of longitudinal stability:

- Braun, Rpt IB6 Ringbuch Luft Tech, 1940; also Lecture at AF Inst Tech, WP AF Base, Ohio, 1948.
- Diehl, Engineering Aerodynamics, 1928 & 1936, Ronald Press.
- Zimmerman, Analysis, NACA T Rpt 521 (1935).
- Gilruth, Prediction, NACA T Rpt 711 (1941).
- Gates, Longitudinal Stability, ARC RM 1118 (1927).
- Perkins-Hage, Performance Stability Control, New York 1950.
- Babister, Aircraft Stability and Control, Pergamon Press, Vol. 1 1961

Length and location of the chord indicated by these two equations, represents that of an imaginary equivalent "rectangular" wing. Therefore, when giving the wing some angle of dihedral, the (0.42 s) station can be expected to indicate the vertical location of the center of lift. However, wings are rarely elliptical; and if they are, they may be twisted, they will be combined with a fuselage, and they may carry partial-span flaps or engine nacelles. In short, their lift distribution will not really be elliptical. Assuming, on the other hand, that the load distribution of a plain rectangular wing be elliptical, its mean aerodynamic chord (equal to the geometric chord) would then be located at $y = 0.42 s$, while it actually is in the vicinity of 0.46 s.

Tapered Wings. The pitching moment characteristics of tapered wings as derived from their theoretical lift distribution, are tabulated in (3,c) as a function of taper and aspect ratio. The use of these results is not very practical, however, and is not always realistic. A better definition of length and location of the mean aerodynamic chord, reflecting and approximating the findings in that report, and the result of equations (13) and (14) as well, is shown in figure 2. The lateral location of the "mac" varies between $y = (1/3)(b/2)$ for zero taper ratio (as in doubly triangular or "diamond" wings) and $y = 0.5$ for rectangular plan forms. The chord length increases from $c = (S/b)$ as for rectangular plan forms to $(4/3)(S/b)$ for zero taper ratio.

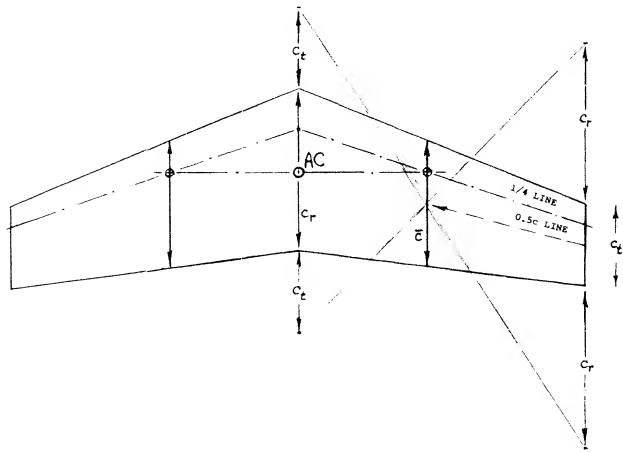


Figure 2. Graphical determination of the mean aerodynamic chord and the aerodynamic axis of a tapered wing.

(3) Determination of aerodynamic chord and center:

- Crean, A'Center, The Aircraft-Engineer, April 1936.
- Diehl, Mean Aerodynamic Chord, NACA T Rpt 751 (1942).
- Anderson, Tapered Wings, NACA T Rpt 572 (1936).
- Lachmann, Tapered-Wing Characteristics, Flight, Oct. 1936.
- Blenk, Stream Curvature, ZaMM 1925 p 36.

This “mac” definition, is generally used in all but the “old” reports of the NACA. However, in a wing with 0.5 taper ratio (as in the illustration) the mean aerodynamic chord is 1.02 S/b, and its location is at $y = 0.45$ s. The mean chord S/b at the position of 0.42 s (as in equation 9) might, therefore, as well be used in many practical wing shapes. The wing’s aerodynamic axis, connecting the aerodynamic centers (or the quarter points) on the mean chords, moves up together with the two wing panels, when they are given dihedral.

Wing Moment. In conventional mid-wing and low-wing configurations (as in figure 1, for example), the CG is essentially at the level of the wing. In a typical high-wing or even “parasol” type arrangements, the wing can be at an appreciable distance above the CG. In such a case, the longitudinal force (primarily the tangential component of the lift) of the wing has to be included in the analysis. In reference to the CG, (the hinge axis about which the airplane is pitching) the wing forces produce the moment (marked by the subscript “g”):

$$C_{mg} = C_{m0} + (\Delta x/c)C_L + (z/c)C_{DS} - (z/c)(d\alpha/dC_L)C_L^2 \quad (10)$$

where $x = g - a$ — longitudinal distance between CG and the wing’s aerodynamic center (measured parallel to the zero lift line, positive when the AC is forward of the CG) and where z = vertical distance (positive when the AC is above the CG). As suggested before, the term containing the section drag coefficient may usually be disregarded. The “lift angle” in the last term is that in two-dimensional flow thus independent of the aspect ratio, theoretically equal to $0.5/\pi$ and actually $\approx 10^\circ$ ($\pi/180$) ≈ 0.17 (in radians). This term represents the tangential, forward-directed and thus “negative” component of lift. Using (4) the lesser value 0.15, differentiation of the equation yields the stability contribution of the wing

$$dC_m/dC_L = (\Delta x/c) - 0.3 (z/c) C_L ; d\Delta C_m/dC_L^2 = 0.3 (z/c) \quad (11)$$

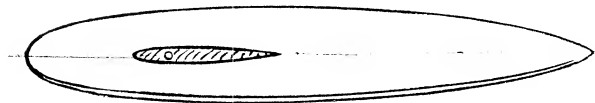
where $0.3 = 2(0.15)$. Thus with the airplane’s CG not at the level of the wing’s AC, dC_m/dC_L can no longer be expected to be constant as a function of lift coefficient or flying speed. In case of a low-wing configuration (provided that the CG is really above the mean aerodynamic chord of the wing) the wing’s dC_m/dC_L may grow less negative (less stable) as C_L is increased, while in a high-wing airplane, the opposite is true.

(4) Compensation for C_{DS} , — Diehl (1,b) recommends a value of 0.15. The corresponding factor in equation 12 is 0.30.

Lift Due to Fuselage. The lift of conventional low wing plus fuselage configurations is generally higher by some essentially constant amount than a high wing combination. Depending upon fuselage shape and size the lift-curve slope of the combination tends to be somewhat increased, particularly for mid-wing configurations. An example of such interaction is presented in figure 3. Principle results are as follows:

- The lift-curve slope of a wing and fuselage together is some 5% higher than that of the wing alone.
- When changing the angle of attach of the wing against the fuselage body (kept at zero angle of attack, the lift-curve slope is some 5% lower than that of the wing alone.

WING 0012 RECTANGULAR $A = b/c = 6$
FUSELAGE ROUND WITH $1/b = 2/3$; $1/d = 6$



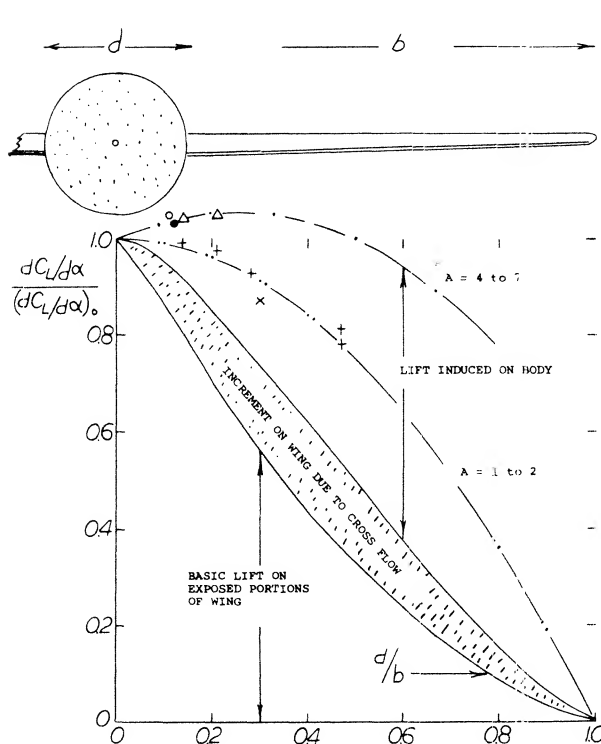
a) WING ALONE (NO FUSELAGE)	$dC_L/d\alpha$	= 0.077
b) WING PITCHED AGAINST FUSELAGE (KEPT AT $\alpha = 0$)		= 0.073
c) WING PLUS FUSELAGE TOGETHER		= 0.080
d) A TAPERED WING (7,c) YIELDS	0.077; 0.074; 0.080	

Figure 3. Influence of a fuselage upon the lift of a wing as tested (7,b) in NACA VDTunnell at $R_L = 3(10)^6$ or $R_F = 8(10)^6$.

Regarding (b) it must be mentioned that in the design of airplanes, the wing is usually set at a certain positive angle of a few or several degrees, against the fuselage. It must be noted that such an angle of incidence (denoted by i) produces a certain lift differential (negative in comparison to the lift of the wing alone). However, the lift-curve slope of the wing plus fuselage combination is basically not affected by that angle.

Cross Flow. The fuselage does not fully replace the lift of the portion of the wing “covered”. However, as explained in the Chapter XIX, a cross or “ 2α ” flow (5) develops around the sides of every cylindrical or streamline or “round” fuselage body when inclined at an angle of attack against the wind. As a consequence of this cross flow which is increased by the upwash ahead of the wing the angle of attack at, and lift on the wing roots are also increased. However, when rotating the wing against the fuselage operating at zero angle of attack as in figure 3

(test b) the cross flow does not develop and in this case $dC_L/d\alpha$ is reduced below the value for the wing alone. In airplanes (where wing and fuselage are rigidly attached to each other) the cross flow effect is so strong that the lift of wing-fuselage combinations grows at first with the d/b ratio, as illustrated in figure 4. After reaching a maximum ratio of ≈ 1.06 , in the vicinity of $d/b = 0.15$, the combined lift reduces, however, tending toward zero as the fuselage diameter would ultimately approach the size of the span.



- Δ JUNKER, RECTANG LOW WING $A = 6$, SEE (6,e)
 \circ NACA, RECTANGULAR MID WING $A = 6$ (7,b)
 $+$ OTHER LARGER ASPECT RATIO COMBINATIONS
 \times JUNKERS, HIGH OR LOW WING, SEE (6,e)
 \times DVL, TRIANGULAR WINGS, $A = 1.3$ & 2 , SEE (6,e)
 \circ NACA, $A = 3$ TAPERED, WING COMPONENT (6,g)

AS DERIVED IN (6,e) THE COMPONENTS OF LIFT IN LARGER ASPECT RATIOS ARE APPROXIMATELY AS FOLLOWS:

- a) EXPOSED PORTIONS OF WING: $L/L_0 = (1 - (d/b))^{5/3}$
 b) DUE TO CROSS FLOW (UPWASH): $L/L_0 = (d/b)(1 - (d/b))^{5/3}$
 c) INDUCED ON BODY BY WING: $L/L_0 = (d/b)(1 + (d/b))(1 - (d/b))^{2/3}$

A SIMILAR SET OF EQUATIONS LEADS TO THE FUNCTION AS PLOTTED FOR SMALL ASPECT RATIOS.

Figure 4. The lift curve slope of wing-fuselage combinations as a function of the diameter (or width) ratio d/b .

- (5) "Cross flow" and "upwash" are covered in connection with Chapter IX on the "horizontal tail", Chapter XII on "engine nacelles", and Chapter XIX on "streamline bodies".

Moment Due to Fuselage. As explained in the Chapter XIX the fluid-dynamic moment originating in slender fuselages, consists of two components:

- 1) From a positive lift on the forebody due to potential flow
- 2) From the negative lift on the afterbody as a result of the vortex flow.

In conventional wing-fuselage combinations, the angle of attack of the fuselage's tail within the wing's field of downwash, is comparatively small. For the purpose of longitudinal stability analysis it will therefore assume that the "second" (stabilizing) component of moment is zero. This is the moment produced by boundary-layer accumulation and "viscous" lift originating at the upper (suction) side of the fuselage, near its trailing end. The longitudinal moment of fuselages in combination with a wing, can then be expected, essentially to be a "free" moment (with no resultant lift force). Also from Chapter XIX the destabilizing free moment of round fuselage-type bodies in free flow, is approximately

$$M_F / (q S_o \ell) = \tilde{\alpha} ;$$

$$\text{or } C_{mF} = M_F / (q (d')^2 \ell) = \alpha^\circ / 720 = \alpha^\circ / 73 \quad (12)$$

where 'd' = maximum width, equal to the maximum diameter of the affected volume of air, $\tilde{\alpha}$ is the angle of attack in radians $S_o = (d')^2 \pi / 4$, and ℓ = length of the body. Referred to the dimensions of an airplane:

$$\Delta (dC_m / d\tilde{\alpha}) = (S_o / S) (\ell / \bar{c})$$

$$\Delta (dC_m / dC_L) = (S_o / S) (\ell / \bar{c}) (d\tilde{\alpha} / dC_L) \quad (13)$$

where $(S_o / S) (\ell / \bar{c})$ should not be confused with the tail "volume" of airplane configurations.

- (6) Lift of wing-fuselage combinations:

- a) Vandrey, Theoretical Analysis, Lufo 1937 p 347.
- b) Multhopp, Fuselages, Lufo 1941 p 52 (NACA TM 1036).
- c) See results in references under (7), such as b) & c).
- d) Liess, Lift and Downwash Analysis; see (14,a).
- e) Hoerner, T Rpt F-TR-1187-ND Wright Patterson AF Base (1948).
- f) Lange, Small A' Ratios, ZWB Doct UM 1023/1 to 5.
- g) Mayer-Gillis, Load Distribution Among Wing Fuselage Tail, L50J13, L51E14a, L53E08.
- h) Analysis is found in NACA RM A51G24, L51J19 & L52J27a.

Wing Interference. The magnitude of the free fuselage moment is increased along the forebody by the upwash induced by the wing. Moment differentials obtained from wing models tested (7) with and without fuselage (essentially in mid-wing locations) have been evaluated. Figure 5 shows how those differentials vary as a function of the longitudinal location of the wing. The moment reduces to approximately zero as the wing moves toward the nose of the fuselage and reaches and crosses the theoretical level for a wing position approximately at half the fuselage length. A particular example for tail-fuselage interaction is shown in figure 6. The pitching moment derivatives given are referred to airframe dimensions. The moment ratio $0.0028/0.0068 = 0.41$ using theory, equation 12 fits reasonably well into figure 5, while the ratio $0.0028/0.0051 = 0.55$ from tests of fuselage alone would not. It seems that the body shape alone exhibits a stabilizing "viscous" component $\Delta(dC_m/d\alpha) \approx -0.002$ (on account of its rather bluff rear end) so that $dC_m/d\alpha = 0.0051$ as tested, instead of 0.0068 as predicted by theory.

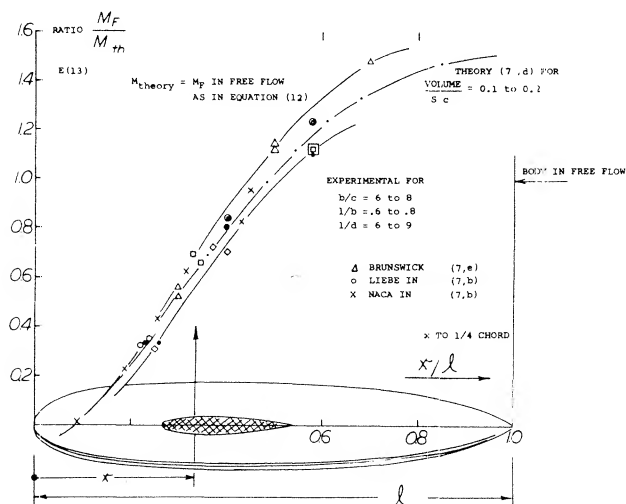


Figure 5. The free (zero-lift) moment of fuselages and/or similar bodies, as affected by the presence of the wing.

Upwash/Downwash. At $x/l \rightarrow 1.0$, as in the combination of a horizontal tail surface and fuselage (where most of the body length is ahead of the wing the moment differentials plotted in figure 5, surpass the value as in undisturbed free flow). There is some upwash ahead of the wing, which accounts for this increment of the destabilizing body moment. The downwash behind the wing can,

- (7) Contribution of fuselage to longitudinal moment:
- Vandrey, Analysis, Yearbk D Lufo 1940 p I-367.
 - Jacobs, 209 Combinations, NACA T Rpt 540 (1935).
 - Sherman, Interference of Wing-Fuselage Combinations, NACA T Rpt 575 (1936); and TN 1272 (1937); see also TN 641 & 642 (1938) for special junctures.
 - Liebe, Theoretical Analysis, Ybk D Lufo 1942 p I-280.
 - Moller, Ybk D Lufo 1942 p I-336; also ZFW 1953 p 2.
 - Yates, Flying Boat Hulls, NACA TN 1305 (1947).

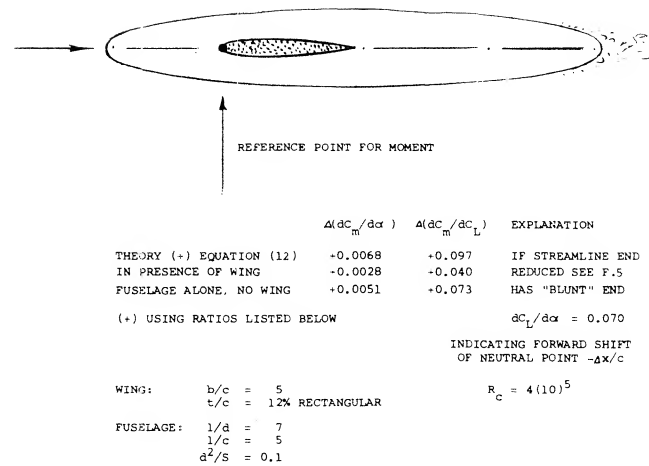
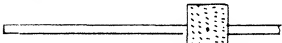
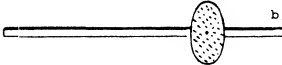
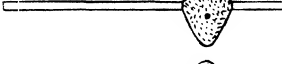
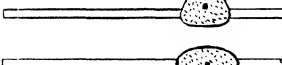
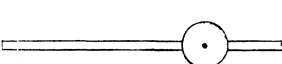
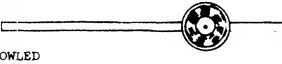


Figure 6. Example (17,a) for the contribution of a fuselage body to the pitching moment of an airplane configuration.

on the other hand, be used to explain the moment change due to the vertical position of the wing. For a longitudinal position $x/l = 0.25$, tests reported in (7,b) shows moments of the fuselage body as in figure 3, as follows:

wing arrangement	M_F/M_{th}	explanation
low wing	0.15	fuselage seems to be in maximum downwash
mid wing	0.40	similar to configuration as in figure 6
high wing	0.75	afterbody seems to be in reduced downwash

Fuselage Shape. The longitudinal fuselage edges, such as a rectangular (instead of a round) cross-section shape, increase stability slightly when applied aft of the wing and particularly near the tail end and reduce stability when used ahead of the wing. Characteristics of wing-body combinations as affected by the fuselage's cross-sectional shape, are listed in figure 7. Both the rectangular and the upright elliptical fuselage shape, present pitching moments which are less positive (less unstable) than the round shape. In the elliptical shape, it seems that the forebody causes less cross flow, while the afterbody of the "square" shape seems to be more stable on account of its lateral edges. When adding a radial-type engine in the nose of the fuselage, stability of the combination (without tail) is little affected. All of the configurations shown in figure 7 have fuselage moment ratios below unity. Figure 5 demonstrates, however, how much that ratio depends upon the longitudinal position of the wing along the fuselage.

CONFIGURATION	$dc_{L_b}/d\alpha$	$C_{L_b}^a$	(AC)% ^c	C_{Dmin}
0012 RECTANGULAR $A = 6$	0.077	1.54	24.0	0.0080
	0.081 (.081)	1.44 (1.52)	22.7 (22.6)	0.0122 (.0121)
	0.079 (.080)	1.53 (1.55)	22.6 (23.0)	0.0123 (.0117)
	0.080 (.081)	1.27 (1.30)	21.0 (22.0)	0.0117 (.0117)
	0.081 (.082)	1.25 (1.34)	21.3 (21.9)	0.0117 (.0117)
	0.082 (.084)	1.29 (1.37)	21.6 (22.2)	0.0118 (.0118)
	0.080 (.081)	1.21 (1.23)	21.0 (22.0)	0.0115 (.0115)
ROUND	0.080 (.081)	1.47 (1.50)	20.9 (21.1)	0.0141 (.0138)
COWLED	0.079 (.080)	1.19 (1.20)	20.9 (21.5)	0.0258 (.0256)
RADIAL ENGINE				

ALL VALUES IN PARENTHESES ARE FOR CONFIGURATIONS WITH WING-ROOT FILLETS.
a) AT $R_c = 3(10)^6$ IN VARIABLE DENSITY TUNNEL; $R_f = 8(10)^6$.
b) WITH 0018/09 TAPERED WING HAVING CHARACTERISTICS SIMILAR TO THE 0012.
c) BREAK-AWAY OF LIFT AT $C_L = 1.0$; ALL OTHERS BREAK CLOSE TO C_{Lb} .
FUSELAGES WITH $l/b = 2/3$ OF $l = 4$ c; ROUND SHAPE AS IN FIGURE 3.
WHEN TESTED ALONE, THE RECTANGULAR FUSELAGE SHAPE PRODUCES $\Delta(dc_{L_b}/d\alpha) = +.03$
(BASED ON WING DIMENSIONS, AROUND THE $l/4$ AXIS). THE ROUND FUSELAGE
PRODUCES $\Delta(dc_{L_b}/d\alpha) = + 0.05$.

Figure 7. Lift and longitudinal characteristics of a wing in combination with various fuselage shapes, as tested (7,b,c) in NACA VDT.

The Flying Boat Hull, shown in figure 8 produces, in presence of the wing, positive (bow up) pitching moments which are larger than predicted by equation (12). We may assume that the hard-chined bottom of the forebody (ahead of the CG at ≈ 0.4 of the length) may produce some lift, in the same manner as a small aspect ratio wing. Using the corresponding function given in Chapter III the forebody lift, based on the square of the hull beam, corresponds to

$$dC_{L_b}/d\alpha = \pi^2/360 = 0.027$$

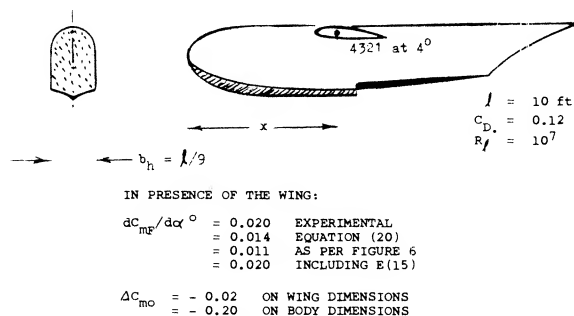


Figure 8. Pitching moment characteristics of or due to the hull of a flying boat (7,f). The definition of the coefficient is $C_{m\gamma} = M/(q b l)$.

For a moment arm of this lift, equal to 0.85 times forebody length, an additional moment is then found in the order of

$$\Delta(dC_{MB}/d\alpha) = 0.027 (0.85) 0.4 = 0.009 \quad (14)$$

The afterbody is assumed to be without such lift, within the downwash of the wing.

Fillets usually reduce the viscous losses of momentum along the wing roots. In this manner, they thus tend to increase the non-viscous interaction between wing and fuselage. The results in figure 7 obtained with fillets (tabulated in parentheses) generally show:

- 1) somewhat increased lift curve slopes,
- 2) somewhat increased maximum lift coefficients,
- 3) in "round" body shapes, a $\Delta(AC) \approx - 0.5\%$ c.

When applied to the fuselage with rectangular cross-section shape, fillets do not have much of an effect.

Fuselage Ducts. The principle stated above, whereby fuselage moments are proportional to the volume of air affected by them (equation 12) also applies to various other bodies (such as to external stores, for example) and to the addition of such bodies to wing or fuselage. Figure 9 shows as an example, the influence of inlet ducts for jet engines, simulated by adding solid half bodies to the sides of the fuselage. Moments of the configurations referred to the volume parameter ($l d^2$) of the basic fuselage body, are plotted in the graph versus the "span" ratio 'd'/d show,

(a) Lateral ducts with constant length, when exposed to an angle of attack, cause the unstable moment derivative of the configuration, approximately to grow in proportion to the "span" ratio, as postulated by equation (12).

(b) In configurations with the ducts on top of or below the fuselage, the pitching moment essentially remains unaffected. Again, the moment derivative corresponds to the dimension 'd' measured normal to the direction of angular displacement.

(8) Characteristics of ducts, stores, et cetera:

- a) Jaquet, Airplane With Ducts, NACA TN 3481 (1955).
- b) Wilson, Twin-Engine Nacelles, NACA W Rpt L-428 (1940).
- c) Crigler, Propeller in Pitch & Yaw, NACA TN 2585 (1952); also Comparison with Experiments, W Rpt L-362.
- d) Silvers, Influence of Missiles, NACA RM L54D20.

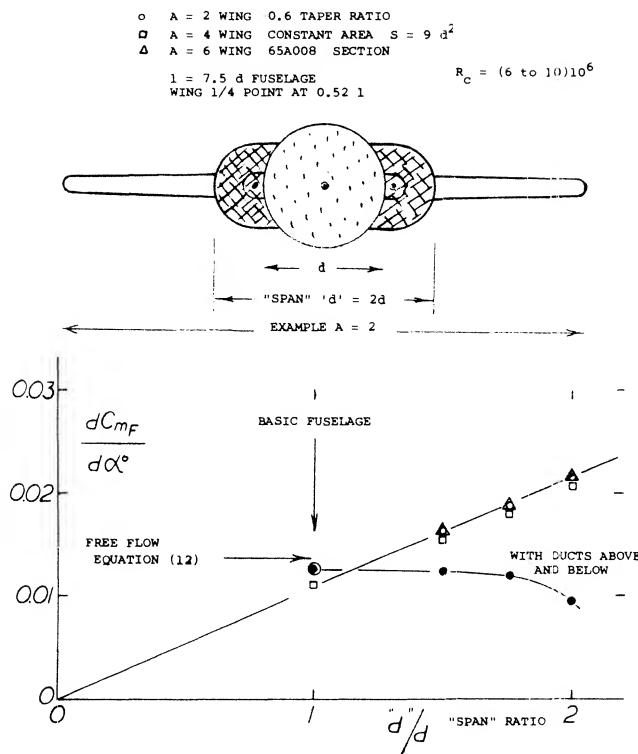


Figure 9. Free (zero-lift) pitching moment contribution of duct bodies added to a wing-fuselage configuration (8,a).

Stalling. The above discussion regarding wing-fuselage interference, primarily applies at small and moderately high lift coefficients. At the higher lift coefficients, stalling in straight wings is likely to begin at the roots, where the flow is strained the most. The pitching moment changes, accordingly, in negative (stabilizing) direction. For example, in the wing-fuselage combinations tested in (7,b,c) values of ΔC_{m_4} in the order of -0.1 or even -0.2 , can be observed when stalling. The corresponding shift in the center of lift is between 8 and 16% of the wing chord (to the rear). Longitudinal stability is improved as a result of stalling (returning the airplane to lower angles of attack) a) because of the shift in the center of lift and b) from the reduced downwash in the center of the wing (along the fuselage). Fillets, designed to postpone wing-root stalling, will be discussed later, in connection with downwash.

3. HORIZONTAL TAIL CHARACTERISTICS

The horizontal tail surface is a lifting device, similar to the wing and is appreciably affected by the fuselage to which it is usually attached.

Cross Flow. Fuselage interference upon the horizontal surface located in the conventional location “at” the tail is twofold. There is first the cross-flow effect mentioned above in connection with wing plus fuselage combinations. Figure 5 suggests, when placing a wing or a tail surface at or near the end of a fuselage, that the destabilizing (positive) fuselage moment will be increased above its value in free flow (without the tail surface present). This is evidently a consequence of the “ 2α ” type upwash (5) ahead of the leading edge of the horizontal surface. If the fuselage’s destabilizing moment is increased, the stabilizing effect of the body-tail combination is reduced, accordingly. For an average conventional configuration, the maximum increment $\Delta M/M_{th} \approx 0.5$, as at $x/\ell \rightarrow 1$, in figure 5, can be found to be equivalent to a reduction of the stabilizing moment of the wings (larger than tail surfaces) represented in that graph and in the order of several percent.

Fuselage Interference. As pointed out in “Fluid-Dynamic Drag” (9) when adding a fuselage to the horizontal surface, its lift distribution is usually disturbed (possibly interrupted) by the boundary layer of viscous wake developing along the fuselage. To demonstrate this effect, we present first the situation as in figure 10, where a wing (or tail surface) is placed in a wind-tunnel stream, in the center of which the velocity distribution is “dented” (in the direction normal to the span of the wing). After integrating the dynamic pressure across the span of the lifting surface, we obtain an average $\Delta \bar{q}/q$ which may also be considered to be a gap in the stream (normal to the surface) having a width $b_g/b_H = \Delta \bar{q}/q$. The lift and/or the lift-curve slope of the wing is reduced on account of this gap in its center, not just in proportion to the average dynamic pressure, but at a rate increasing with the size of the gap. Qualitatively, the result in figure 10 can be explained:

- when reducing the lift in proportion to the average dynamic pressure, thus accounting for a reduction of effective area corresponding to the “gap”;
- when reducing the effective aspect ratio as a function of $\Delta \bar{q}/q$ in the manner as described in “Fluid-Dynamic Drag” (9).

(9) See “Fluid-Dynamic Drag”, Chapter VIII, under “induced interference drag”.

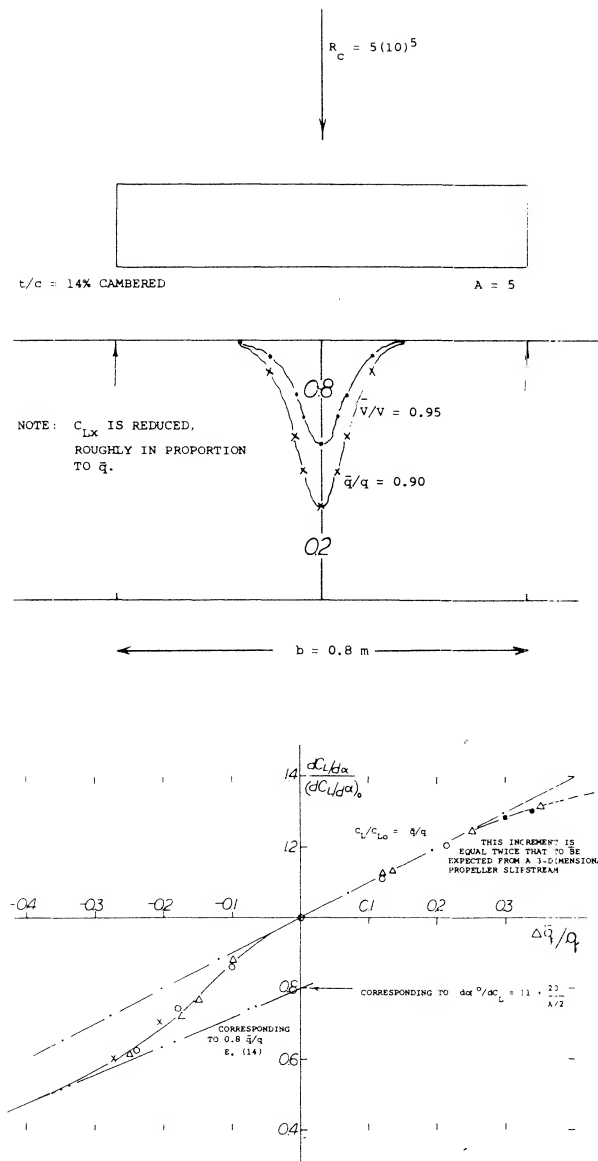


Figure 10. Influence of a dent or gap in the velocity and/or dynamic pressure distribution, upon the lift of a wing or a horizontal tail surface (14,c). The dent is two-dimensional, up and down, and not limited as a fuselage wake (or a slipstream) would be.

The lower limit indicated in the graph, corresponds to $A_i/A = 0.5$ (\bar{q}/q), used in the equation (taken from the Chapter III)

$$d\alpha/dC_L = 11 + (20/A_i) \quad (15)$$

The experimental points drop from the upper line (corresponding to (a) above) to that lower limit. The reductions of tail efficiency thus obtained, are greater than those derived above under "cross flow". A horizontal tail is basically smaller than the wings in figure 5; and the viscous type of fuselage interference is predominant, accordingly.

The Load Distribution across the span of the horizontal tail surface of a "typical" fighter airplane was measured in flight (10,h). Considering the cut-out for the rudder, it may not be surprising that the distribution shown in figure 11 has a considerable dent (deficiency) when suddenly pulling up (thus producing a negative load). However, the same type of dent is obtained after 2 seconds, when the airplane has reached a certain angle of attack, giving it \approx constant acceleration (and constant lift) corresponding to a total of 3.6 "g". For an elevator angle now near neutral, the tested lift coefficient $C_{LH} = +0.5$ is essentially due to angle of attack, thus including the cross-flow assistance by the fuselage (if there is any). The distribution obtained can be analyzed in two different ways:

a) We can assume that the airplane's fuselage (including canopy, wing roots, engine parts, radiators, shanks of the idling propeller, and various spots of roughness) may have a drag corresponding to $\Delta C_D = 0.01$ (on wing area). Based on horizontal area $S_H = 0.2$ S, a coefficient $C_{DH} = 0.01/0.2 = 0.05$ is then obtained. According to the evaluation in Chapter VIII of "Fluid-Dynamic Drag", a ratio of $A_i/A = 0.6$ is then found.

b) If completing the lift distribution in figure 11, across the span in elliptical form, a load can be estimated as follows:

$$L = 250 (\pi/4) 12.8 = 2500 \text{ lb}$$

where 250 = maximum lb/ft in the center, and 12.8 = b_H . This load is 1.25 times as high as tested. To account for the difference, we will first assume a reduction of effective area by 10%. Using the basic equation for the "lift angle" (see Chapter III)

$$d\alpha/dC_L = (11^\circ/0.9) + 20^\circ/(0.9 (A_i/A) 3.4) = 12 + 6.5/(A_i/A)$$

where 3.4 = A_H = geometrical aspect ratio including the part covered by the fuselage. Solving this equation twice (once for $A_i/A = 1.0$, and once for an estimated ratio in the vicinity of 0.6, as in (a) above) a ratio of $A_i/A = 0.59$ is found for the lift angle ratio of 1.25 estimated above. This result agrees with that in (a).

(10) Characteristics of horizontal tail surfaces:

- Letko, Fuselage with Tail (23,c), NACA TN 3857 (1956).
- Lyons, Lift of Control Surfaces, ARC RM 2308 (1950).
- Greenberg, Free Control Analysis, NACA T Rpt 791 (1944).
- Plate Interference, NACA TN 408 & W Rpt L-660.
- For Airship Fins, see NACA T Rpts 394 and 604.
- Engelhardt, Interference of Fuselage Upon Horizontal Tail, Aerody Lab TH Munchen Rpts 1 and 3/1943.
- Gillis, Fuselage Plus Tail, NACA W Rpt L-391 (1942).
- Garvin, Load Distribution in Flight, NACA TN 1483 (1947).
- Polhamus, Stability with "V" Tail, NACA TN 1478 (1947).

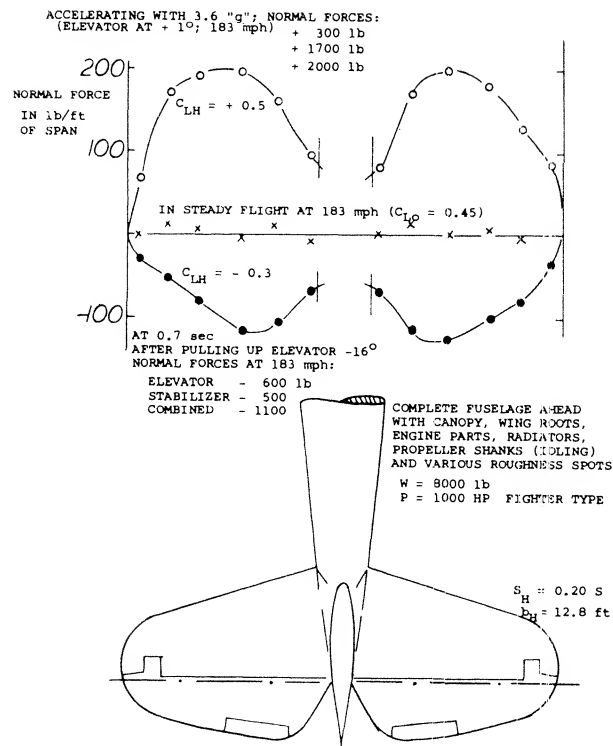


Figure 11. Load distribution across the span of a horizontal tail flight-tested (10,h) while gliding (power-off) at 183 mph, where $C_L = 0.45$, in sudden pull-up maneuver, to 3.6 "g" total.

Surface Roughness. To prove that the viscous wake of the fuselage has considerable influence upon the horizontal-tail effectiveness, some basic tests were made (10,f). The stabilizing tail moment was determined both on a smooth and on a rather rough fuselage body. At angles of attack between 6 and 8°, differentials $\Delta C_{mH}/\Delta\alpha$, taken from figure 12, are as follows:

	smooth	ratio	rough	ratio
tail plus fuselage	- 0.046	0.70	- 0.037	0.56
tail differential	- 0.054	0.82	- 0.042	0.64
for H'tail surface alone $\Delta C_{mH}/\Delta\alpha =$			- 0.066	1.00

The tail differential effectiveness is reduced 18% in presence of the smooth fuselage (having a basic drag corresponding to $C_D = 0.05$, or $C_{DH} = 0.02$) and 36% for the rough fuselage (with $C_D = 0.20$, or $C_{DH} = 0.08$). Obviously, the effectiveness reduces as a function of the fuselage drag, as explained in (9). If defining the coefficient

$C_{mHH} = M_H/qS_H l_H$, where M_H = pitching-moment differential due to horizontal tail, this coefficient should theoretically be equal to C_{LH} . However the moments as tested (10,f) were some 5% less, which means that the effective tail arm is 5% shorter than the geometrical arm. This reduction, indicated in figure 12, is discussed later, under "effective tail length".

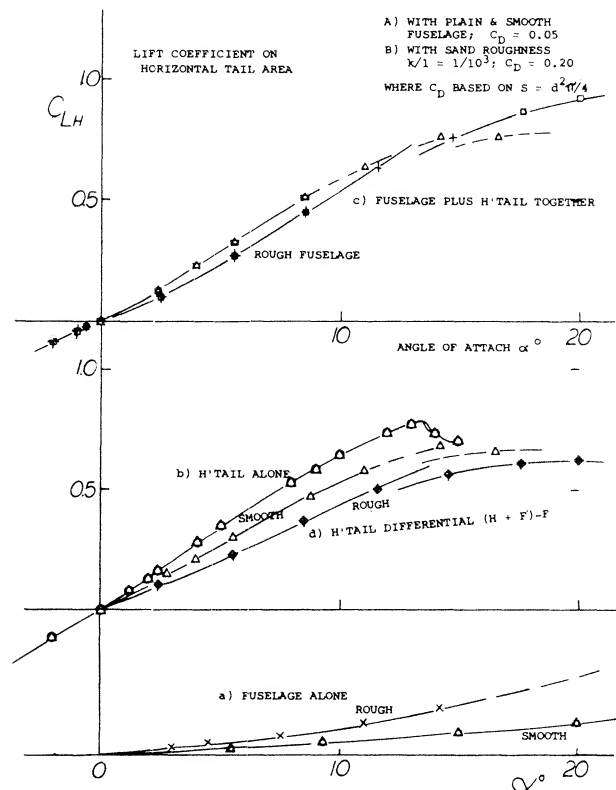
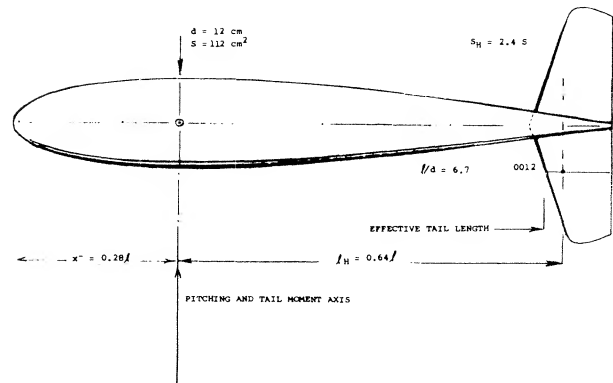


Figure 12. Example for the interference of a fuselage body upon the effectiveness of a horizontal tail surface as tested (10,f) $R_H = 4(10)^5$.

A) with plain and smooth fuselage; $C_D = 0.05$
B) with sand roughness $k/1 = 1/10^3$; $C_D = 0.20$ where C_D based on $S = d^2/4$.

Statistical Evaluation. In a typical (but smooth) configuration, the fuselage-tail interference may be such that the effective aspect ratio is reduced to $A_{\mu i} \approx 0.7 A_{\mu}$. The corresponding reduction of a conventional tail's lift-curve slope can be expected to be in the order of $(1 - 0.7)/3 = 10\%$. Note that in this formulation, the viscous influence of the fuselage (usually expressed in form of a reduction of the dynamic pressure at the tail) is "fully" accounted for. In other words, we do not assume that the average dynamic pressure across the span of the horizontal tail, would be reduced in the order of 10%, simply because there is a wing ahead the wake sheet of which may not, or should not impinge upon the tail surface. Statistically, wetted surface and drag of the fuselage is proportional to $(\ell \text{ or } d \text{ or } a)^2$, where ℓ = length, d = maximum diameter, and a as indicated in figure 13. At least for small a/b ratios and/or for smaller aspect ratios, it can then be shown that the reduction $\Delta(dC_L/d\alpha)$ is proportional to $(a/b_{\mu})^2$. The corresponding theoretical function presents an upper limit to the experimental ratios on figure 13. Even the fins of airships (in the vicinity of $(a/b_{\mu}) = 0.6$ —fit into the statistical pattern. Tentatively, for "smooth" fuselages, the ratio of lifting effectiveness, in comparison to that of the horizontal tail alone (without interference) is

$$T\text{-ratio} = (0.94 \pm 0.02) (1 - (a/b_{\mu})^2)$$

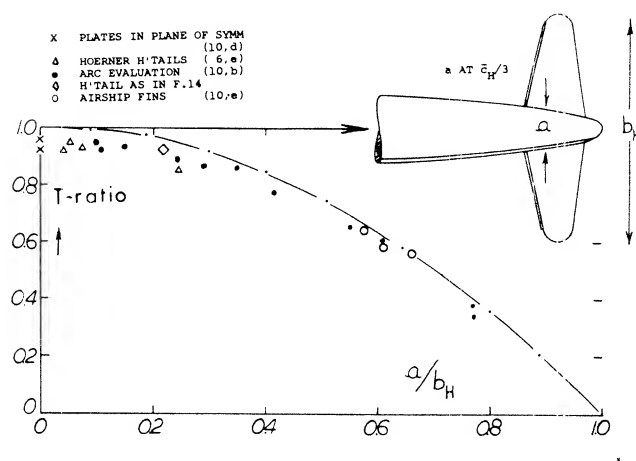
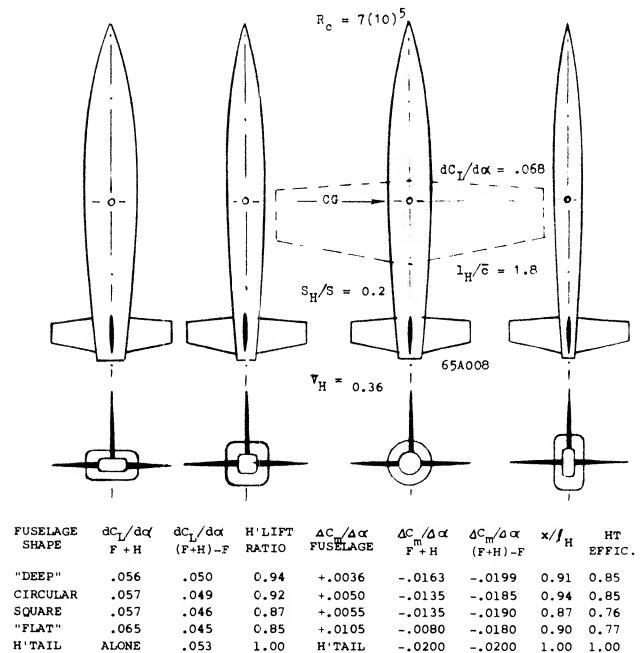


Figure 13. Statistical evaluation of the interference effect of the fuselage upon the stabilizing effect of horizontal tail surfaces.

Fuselage Shape. Results of a wind-tunnel investigation (10, a) of a horizontal tail tested at the end of four fuselage bodies, differing in cross-section shape, are presented in figure 14. Differentials taken between $\alpha = 0$ and 8° , based on horizontal tail area are listed in the illustration. The loss of lift in the presence of the fuselage (corresponding to the horizontal lift ratio") is between 6 and 15%, caused by interference of plain and smooth fuselage bodies as described above. When added to the

fuselage, the horizontal tail appears has the least interference of lift and moment in combination with the "deep" and/or the circular shape. By comparison, the square shape seems to cause some disturbance at the roots of the horizontal tail, while the flat shape although having the highest combined lift-curve slope, may suffer somewhat from too much cross flow at the tail roots thus resulting in a differential ratio of only 0.85.



C_m IS BASED ON THE DIMENSIONS OF THE WING FOR WHICH THE FUSELAGE AND TAIL ARE INTENDED TO BE USED, CORRESPONDING TO $V_H = 0.36$. FOR EXAMPLE, IN THE FIRST LINE: $0.05(.36) = 0.018$; $0.018/0.0199 = 0.91$; $0.91(.94) = 0.85$.

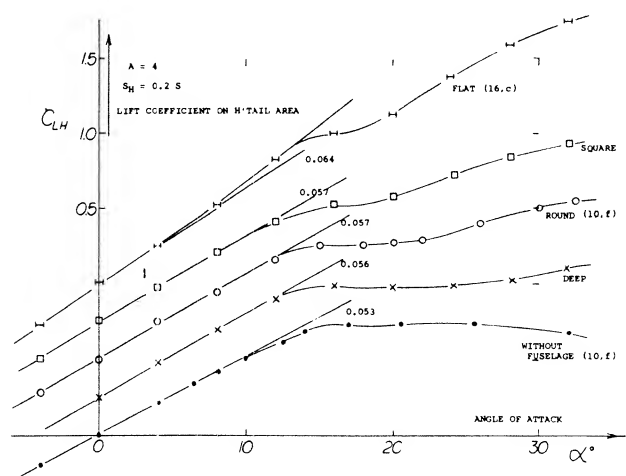


Figure 14. Influence of fuselage shape, and interaction with the horizontal tail surface, in regard to longitudinal stability (10, a).

Effective Tail Length. The stability, does not depend the lift produced by the horizontal tail surface, but rather on the pitching moment obtained from the equation.

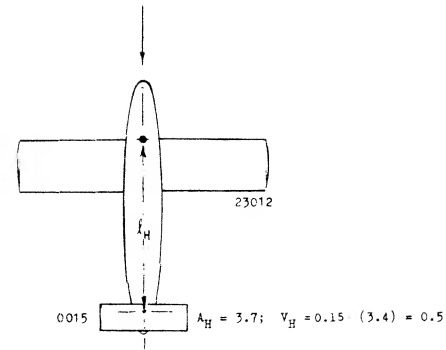
$$dC_{m_{1/4}}/dC_L = (dC_{L_H}/d\alpha) (S_H/S) (\ell/\bar{c}) \quad (16)$$

In other words, the moment arm of the tail is important and that arm is not necessarily equal to the geometrical dimension measured to the 1/4 chord point. For example, in the first line of the tabulation in figure 14, the effective arm "x" corresponds to $x/\ell_H = 0.050 (0.36)/0.0199 = 0.91$, where $0.36 = \text{tail volume } V_H = (S_H/S) (\ell_H/c)$. The horizontal tail as tested on three of the fuselage shapes, produces moments corresponding to arms which are between 6 and 13% shorter than the geometrical distances measured to the CG location of the airplane configuration for which the tests were undertaken. There is probably some mutual interaction, upwash (as explained under "cross flow" above) and viscous-type lift of the fuselage "at" the trailing end (see context to figure 7). Considering net stabilizing effect of *tail plus fuselage* ($F + H$) the "deep" shape in figure 14, is seen to be the most effective one (with $\Delta C_m/\Delta\alpha^\circ = -0.0163$). This cannot be a general conclusion, however. It seems that the arrangements as tested, with 53% of the fuselage length forward of the CG, is not typical. If, for example, selecting the 1/4 point of the fuselage length as reference or CG point, the flat fuselage configuration emerges as the most stable, with $\Delta C_m/\Delta\alpha \approx -0.050$ for ($F + H$), in comparison to -0.040 as for the square shape, and ≈ -0.035 for the two other forms. Thus, to improve stability, it would be profitable to make the forebody "deep" or round (and short), while a flat or square (and long) afterbody can be expected further to contribute to longitudinal stability.

Horizontal Tail Contribution. Longitudinal characteristics of a simple airplane configuration are presented in figure 15. Evaluation of tail effectiveness leads to results as follows:

- The loss of effectiveness of the horizontal tail due to fuselage interferences is 9%. The effectiveness ratio is 0.91, accordingly.
- When adding the fuselage to the wing plus tail arrangement (as tested without fuselage), an effectiveness ratio of $0.023/0.0265 = 0.87$ is obtained.

The fact that the tail moment under (b) is somewhat less than under (a) can be explained by way of increased downwash (to be discussed later).



a) PERFORMANCE OF HORIZONTAL TAIL SURFACE:

CONFIGURATION TESTED	$(dC_{m_{1/4}}/d\alpha)$	$(dC_{m_{1/4}}/dC_L)$	RATIO	EXPLANATION
HORIZONTAL TAIL ALONE	-0.023	-0.33	1.00	ON WING DIMENSIONS
MOUNTED ON FUSELAGE	-0.021	-0.30	0.91	FUSELAGE INTERFERENCE
BEHIND WING (NO FUSELAGE)	-0.011	-0.15	0.45	IN WING DOWNWASH
IN COMPLETE CONFIGURATION	-0.009	-0.13	0.39	DOWNWASH & FUSELAGE

NOTE THAT $0.39/0.45 = 0.87$ IS LESS THAN 0.91; FUSELAGE -- INCREASED DOWNWASH

b) CHARACTERISTICS OF CONFIGURATION:

COMBINATION TESTED	$dC_L/d\alpha$	$dC_m/d\alpha$	$(n/c)\%$	EXPLANATION
WING ALONE	0.068	-0.0166	24.4	BASIC CONDITION
WING WITH FUSELAGE	0.070	-0.0140	20.0	FUSELAGE EFFECT
WING PLUS H-TAIL (+)	0.070	-0.0265	38.0	TAIL STABILIZATION
WING + FUSELAGE + TAIL	0.072	-0.0230	32.0	COMPLETE AIRPLANE

(+) NO FUSELAGE PRESENT

Figure 15. Longitudinal characteristics of a simple airplane configuration

wing: $b/c = 5$; 23012 section; $R_c = 4(10)^5$; ref. (16,a)
 fuselage: $1/d = 7$; $1/b = 1.0$; see also figure 6.

Free Elevator. In wind-tunnel investigations, longitudinal and/or other stabilities are usually tested with the control flaps (elevator) fixed. As explained in the Chapter IV, the lift-curve slope usually reduces in the "stick-free" condition. Since it is desirable that an airplane remains stable for the stick free case the design and/or CG location should be such that a correspondingly reduced tail contribution can be tolerated. The reduction to be expected for an average conventional tail surface due to the stick free case may be in the order of 15%. However, tab-balanced control flaps can reduce tail effectiveness much more, while a large overhanging-nose type of balance may not reduce stability at all.

General Method. To obtain the stabilizing moment of the horizontal surface the following procedure is used:

- Find in Chapters III & IX the lift-curve slope of the isolated tail as a function of aspect ratio, including such effects as roughness and control or balance gaps.
- Determine the effective aspect ratio, reduced as a consequence of viscous fuselage interference, as explained above (9), or use directly the effectiveness ratio as in figure 13.

- c) Use in the determination of the pitching moment, an arm which is somewhat shorter than the geometrical arm, either by 10%, or by a differential equal to 1/2 the maximum fuselage diameter.

For conventional (more or less "round") and completely smooth fuselage shapes, it may also be said that the horizontal tail together with the fuselage may produce almost the same lift as the tail surface alone. This seems to be true in a smooth-fuselage-tail configuration reported in (10,g). A similar result is found for the configuration as in figure 14, with the round fuselage shape. Then using an arm reduced, say by 10%, the right order of magnitude of the stabilizing moment may be obtained. Less horizontal tail contributions may apply in full-scale conditions, however, as explained in connection with figure 11.

"V" Tail. To reduce drag and weight the vertical and horizontal surfaces have been combined in form as shown in figure 16. As pointed out in Chapter III, the panels of such a "V" tail retain their normal force derivative $dC_N/d\alpha_n$ where α_n = angle of attack measured in the direction normal to each panel's axis. Since $L = \cos^2\Gamma$, and $\alpha_n = \alpha \cos\Gamma$, the lift curve slope of a "V" tail (when used in longitudinal direction) can be expected to be

$$(dC_L/d\alpha)_H = (dC_N/d\alpha_n) \cos^2\Gamma \quad (17)$$

where Γ = angle of dihedral, and the coefficients are based on combined panel area. For $dC_N/d\alpha_n$ the value of the same tail at $\Gamma = 0$, is to be used, including fuselage interference. The plain configuration investigated in (10,i) exhibits essentially straight $C_m(C_L)$ functions within the range of lift coefficients below $C_L = 0.8$, with $C_{LX} = 1.0$. The corresponding derivatives are plotted in figure 16. The results are as follows:

- a) To make an airplane stable, the folded-down "V" tail area has to be larger than that of a straight horizontal surface. On the basis of a conventional $S_H/S = 20\%$, a "V" tail area

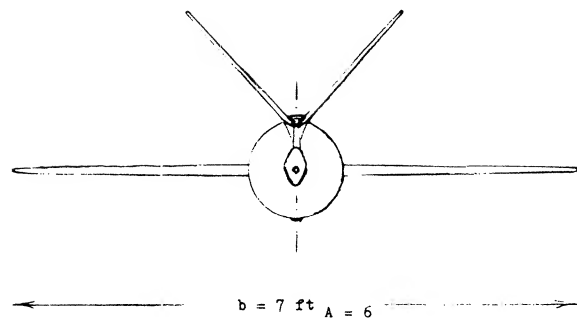
$$S_V/S = 0.2 \cos^2\Gamma \quad (18)$$

may thus be needed. In the design as in (10,i) a 41% tail surface ratio was used.

- b) When varying the dihedral angle of the "V" surface, the derivative dC_m/di (where i = angle against fuselage) changes corresponding to equation (17).

- c) The axes about which the elevator flaps are deflected, have directions different from that of the angle of incidence. Therefore, as derived from "V" geometry, and as shown in figure 16, the derivative varies as

$$dC_m/d\delta \sim \cos\Gamma \quad (19)$$



AIRPLANE MODEL SEEN FROM BEHIND, TESTED AT $R_c = 2(10)^6$

$s_v = 0.29 b$ EACH "V" TAIL PANEL
 $S_v = 0.41 S$ COMBINED AREA "V" TAIL
 $S_f = 0.18 S_v$ "ELEVATOR" FLAP AREA
 $l_H = 2.9 \bar{c}$ MOMENT ARM OF TAIL
 $V_v = 1.2$ TOTAL TAIL "VOLUME"
 0.085 = LIFT-CURVE SLOPE AT $M = 0.3$

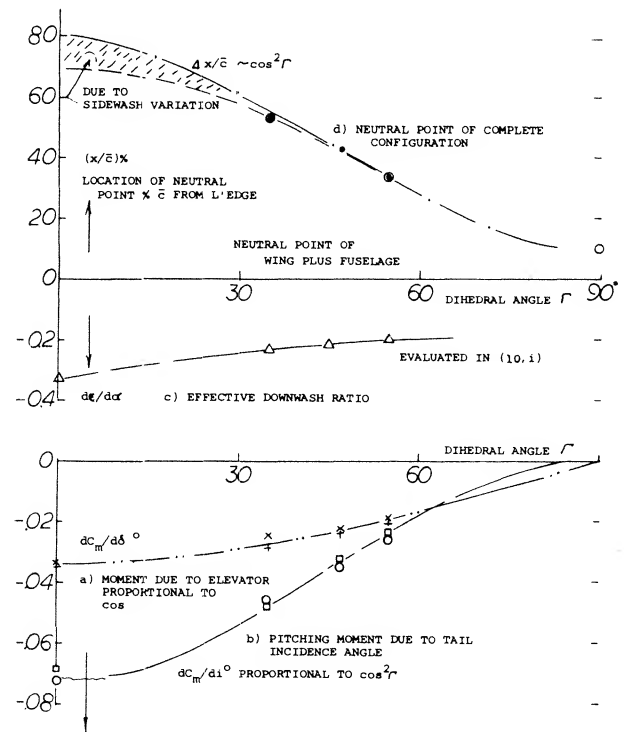


Figure 16. Shape and characteristics of a "V" type combined tail-surface assembly, tested (10,i) on a plain mid-wing wind-tunnel configuration.

Sidewash. As explained in (10,i), a "V" tail surface is subjected, not only to downwash (in vertical or normal direction) but also to some sidewash induced by the wing's lateral tip vortices. With the tail located *above* the vortex sheet, each panel of the tail in figure 16 receives sidewash in a direction toward the vertical plane of symmetry. As a consequence, their aerodynamic angle of attack (normal to their axis or edges) is increased. The

effective downwash angle (derived from the pitching moment contribution) is reduced accordingly. As plotted in part (c) of figure 16, a reduction from $d\epsilon/d\alpha = -0.33$ to -0.21 (id est by $\approx 1/3$) is thus possible. The stability of the airplane model tested, basically varies corresponding to the neutral-point location

$$\Delta x/c \approx dC_{mH}/dC_L / \sim \cos^2 \Gamma \quad (20)$$

After modifying this function with $(1 + d\epsilon/d\alpha)$ the variation as in part (d) of the illustration is correctly obtained.

Tail Size. Of course, when folded down to $\Gamma = 0$, a tail surface with $S_V/S = 41\%$ (as in figure 16) is no longer suitable, and the location of the neutral point at $70\% c$ would not make an efficient design. About $1/2$ the area can be expected to be sufficient, while a vertical surface (in a size corresponding to $S_V/S \approx 10\%$) will be needed. In conclusion, when using a combination “V” tail, it does not seem to be certain that any wetted area and skin-friction drag would be saved. There are other advantages, however, to a “V” tail. Therefore this type of tail will be discussed further, in connection with “multiple-engine” airplanes as well as in the Chapter XII dealing with “lateral stability”.

4. CHARACTERISTICS OF WING DOWNWASH

In its conventional location, the horizontal tail of an airplane is obviously exposed to the downwash produced by the wing. Realistic prediction of downwash is somewhat complex, although the flow pattern can readily be understood.

Mechanism of Downwash. Considerable effort has been put into the analysis of downwash (11) as a function of:

- wing plan-form shape and aspect ratio,
- roll-up situation and longitudinal tail location,
- vertical location of the tail, in relation to the downwash sheet.

None of the solutions are complete, let alone simple enough to be used in practical design work and the agreement with experimental results is conditional. The mechanism of downwash can physically be explained, however. Consider the point (o) in figure 17, each of the lateral vortices emanating from the wing tips, induces a downwash velocity at that point. The “bound” vortex (the lifting line) also induces a downwash component and this component directly representing the circulation around the wing sections, reduces as the point (o) considered is moved downstream.

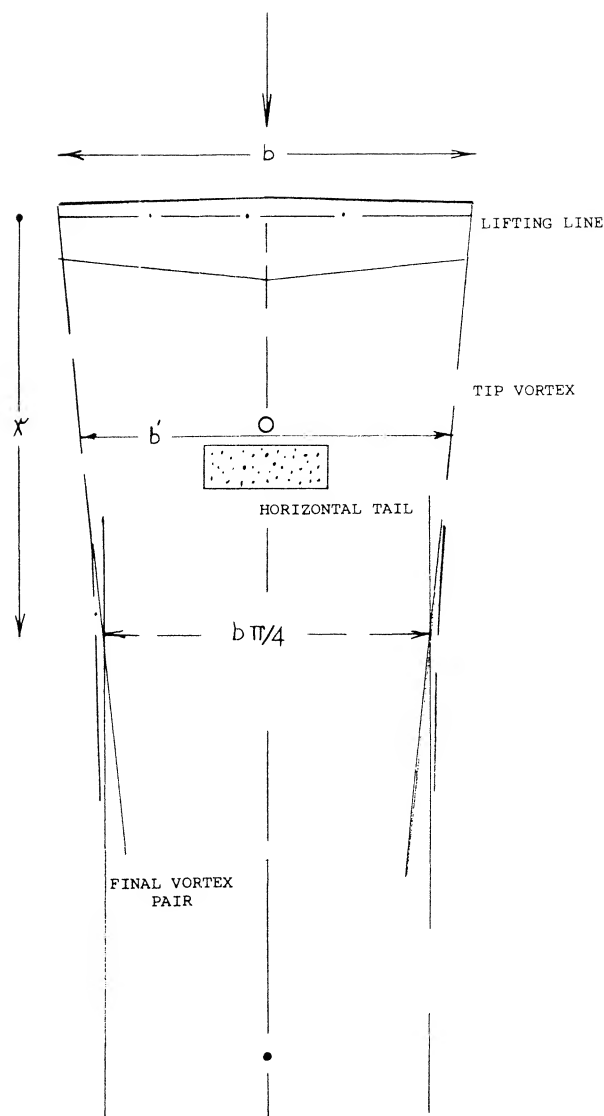


Figure 17. Horizontal plan, showing the geometry of vortex sheet and tip-vortex pair.

(11) Analysis of wing downwash:

- Flugge-Lotz, Report on Downwash w/out and with Slipstream, Ybk D Lufo 1938 p I-172; also Lufo 1938 p 552 & 1940 p 161.
- There are over 100 other references listed in (a).
- Kaden, Rolling-Up Process, Ing Archiv 1931 p 141.
- Silverstein, Downwash & Wake, NACA T Rpt 648 (1939).
- Diederich, Calculation of Downwash, NACA TN 2353 (1951).
- Spreiter, Trailing Vortex Sheet, J Aeron Sci 1951 p 21.
- Helmhold, Downwash Analysis, ZFM 1925 p 291 & 1927 p 11.
- Multhopp, Downwash Analysis, Lufo 1938 p 463.

Trailing System. Figure 18 shows a lateral view (a) of the central part of the vortex sheet, originating from the trailing edge, and (b) of the pair of trailing vortices developing from the wing tips. The vortex sheet leaves the trailing edge in a direction corresponding to the aerodynamic angle of attack (measured against the zero lift line of the section). The maximum downwash angle is $\xi_x = -\alpha_c$, accordingly. Behind a wing with elliptical distribution, the downward velocity of the tip-vortex cores is

$$w = -(C_L/A) V 4/\pi^3; \text{ or } w/V = \alpha_c 4/\pi^2 \approx 0.4 \alpha_c \quad (21)$$

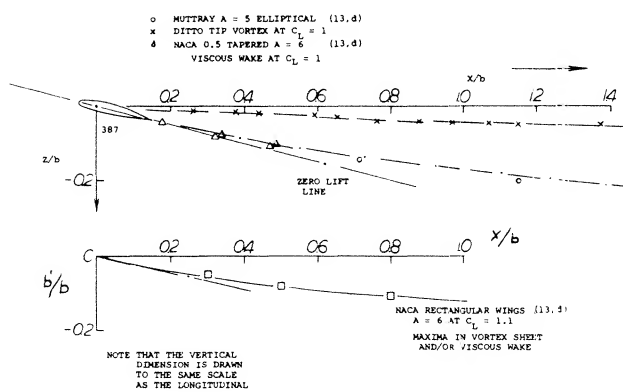
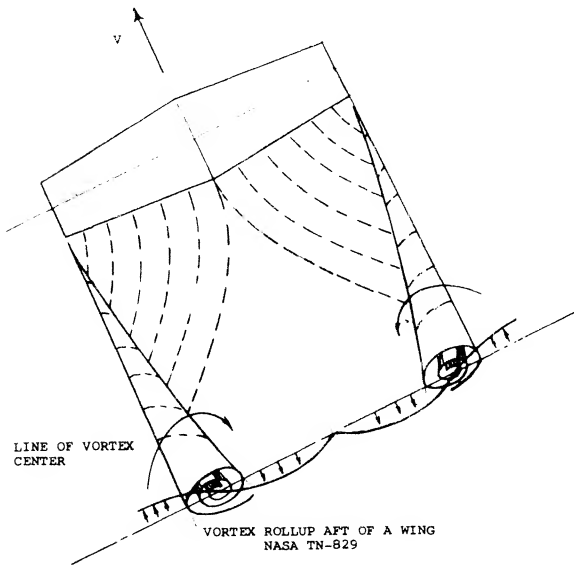


Figure 18. Vortex sheet (in the plane of symmetry) and tip-vortex location as seen in the vertical plane.

where w and α_c , both are negative quantities. The final velocity in the plane of symmetry is

$$w = -(C_L/A) V (4/\pi^3); \text{ or } w/V = (16/\pi^2) \alpha_c \approx 1.6 \alpha_c = \xi$$

The cores thus move down at 1/4 of the final downwash velocity in the plane of symmetry.

Downwash Due to Circulation. The component of downwash representing the circulation around the bound vortex (lifting line) is not "permanent". It affects the horizontal tail surface, nevertheless. For elliptical lift distribution (along the wing span) the angle (in radians) due to circulation velocity "v" is basically

$$\xi_c = -v/V \approx -(0.25/\pi) C_L (c/x) \quad (22)$$

where x = downstream distance from the lifting line at the quarter chord point, in the center of the wing. In terms of the induced angle of attack $\alpha_c = -C_L/\pi A$,

$$\xi_c/\alpha_c = 0.25 (x/b) \quad (23)$$

This function, plotted in the lower part of figure 19, reduces rapidly as the distance x (= tail length) is increased. It is, therefore, desirable to locate the horizontal tail as far aft as possible in order to obtain good stability.

Rolling Up. Upon leaving the trailing edge of the wing, the vortex sheet immediately starts rolling up (11,c) at the lateral edges into a pair of tip vortices. Using terminology as in figure 17, the distance (12) behind the wing's lifting line for roll up is for a wing with elliptical loading:

$$x/b = 0.28 A/C \quad (24)$$

For example, at $C_L = 1$ and for $A = 5$ (as in figure 18) the distance is $x = 1.4 b$. Thus, at the usual location of a horizontal tail, rolling up is not yet completed. After completion, the "sheet" has disappeared. In its place we have then a downwash "field" between the pair of trailing vortices.

Final Downwash. The magnitude of the downwash component resulting from the trailing vortices reduces as the roll-up process goes on. In particular, the angle ratio behind elliptical wings theoretically assumes the final value.

$$\xi/\alpha_c = (4/\pi^2) = 1.62 \approx 1.6 \quad (25)$$

(12) Influence of wing shape on downwash:

- a) Crowe, Tapered Wings, Aircr Engg March 1937 p 59.
- b) Muttray, Cut-Out, Lufo 1935 p 28 (NACA TM 787).
- c) Schulz, Plan-Form Analysis, Lufo 1942 p 367.

Along the center line of the wing, theory (11) indicates maximum values (found "in" the vortex sheet) in the form of a constant multiple of the induced angle of attack α_i of the wing, approximately as follows:

plan form	A	ϵ/α_i vortex sheet	ϵ/α_i rolled-up
tapered to zero	10	3.5	2.5
tapered ratio = 1/3	7	2.2	1.8
elliptical	any	2.0	1.6
taper ratio ≈ 0.7	6	1.7	1.4
rectangular	6	1.4	1.3
rectangular	10	1.3	1.2

In highly tapered (triangular) wings, lift and downwash are concentrated around the plane of symmetry. For wings with a rectangular plan form the downwash is relatively small in the plane of symmetry. Using equation (24) the downstream distance beyond which the "rolled-up" values ϵ/α_i are to be used is estimated using equation 24. No simple formulation for the transition from the "sheet" values to the final rolled-up levels are available however. Experiments confirm the influences of the lift coefficient, corresponding to the distance within which transition takes place. Results for a tapered wing (13,c) plotted in figure 19, are on the line roughly indicating an upper limit, for $C_L = 0.6$ and coincide with a lower-limit line at $C_L = 1.5$. Theoretically, this transition is a stabilizing component in the mechanism of longitudinal stability of airplanes. It can be estimated to increase the tail-moment contribution by a few %.

Combined Downwash. We have combined the downwash component due to circulation with the final values listed in the table above which is not strictly correct. However, agreement with experimental results plotted in figure 19 is encouraging while agreement with available analytical predictions (11) is not satisfactory. Our formulation can at least be used to interpolate and extrapolate experimental results. In the range of smaller lift coefficients, the upper lines should be used, while at coefficients above unity, the lower lines should indicate angle ratios closer to reality. As stated before, the downwash angle at the trailing edge is simply $\epsilon = -\alpha$. Neither the functions presented above, nor the usual theoretical solutions (11) necessarily connect to that boundary condition.

(13) Downwash behind wings, experimental:

- Piercy, In Rear of Aerofoil, ARC RM 578 (1919).
- Muttray, Behind Rectangular and Elliptical Wing, Lufo 1935 p 28 (see NACA TM 787); also Lufo 1938 p 109 (TM 876).
- Wallace, Behind Split Flaps, NACA T Rpt 539 (1935).
- Silverstein, General Investigation, NACA T Rpt 651 (1939).
- Silverstein, Wind Tunnel Interference, NACA T Rpt 609 (1937).
- Parsons, Tapered Wing, NACA TN 521 (1935).
- Hirst, Tail Behind Wing, ARC RM 1478 (1932).

Variation in Vertical Plane. Figure 19 is meant to show maximum values of the downwash angle as they are found at the level of the vortex sheet coming from the trailing edge of the wing. The vertical position of that sheet (see figure 18) is approximately given by an angle measured from the wing's quarter chord point and against its zero lift axis. The value of this angle is always larger than that of the final downwash angle. For a rectangular wing of aspect ratio 6, at a distance $x/b = 0.5$, the angle is, for example, $\approx 2\alpha$. It is an empirical observation, however, that maximum downwash angles are found in a "layer" located somewhat above the viscous wake sheet. Above and below the "maximum" sheet, the angle reduces in the manner as shown in figure 20. No simple theoretical formulation of the reduction is available. The experimental results in the graph may be approximated, however, by

$$d(\Delta\epsilon/\epsilon_x)/dz/b \approx -1.5 \quad (26)$$

where z = distance above or below the sheet. It can be stated that by placing the horizontal tail below the vortex sheet, longitudinal stability can be improved, particularly on account of the downwash gradient along the path through which the tail of an airplane moves when changing the angle of attack.

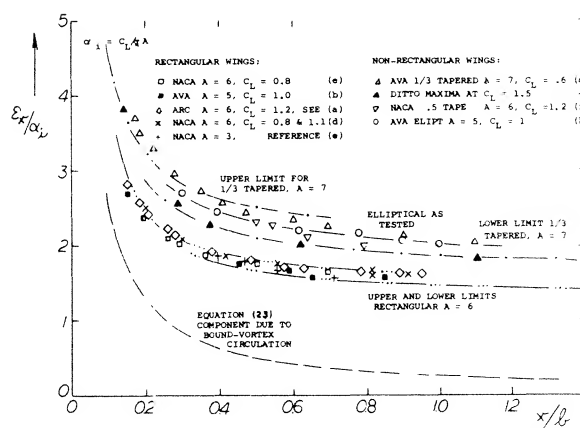


Figure 19. Maximum downwash angle ratio "in" the vortex sheet, in the wing plane of symmetry, as a function of downstream distance x (13).

(14) Influence of fuselage upon downwash:

- Liess-Riegels, Analysis, Ybk D Lufo 1942 p I-366.
- White, Fuselage Interference, NACA T Rpt 482 (1934).
- Schlichting, Wing in Interrupted Flow, Ybk D Lufo 1940 p 81.

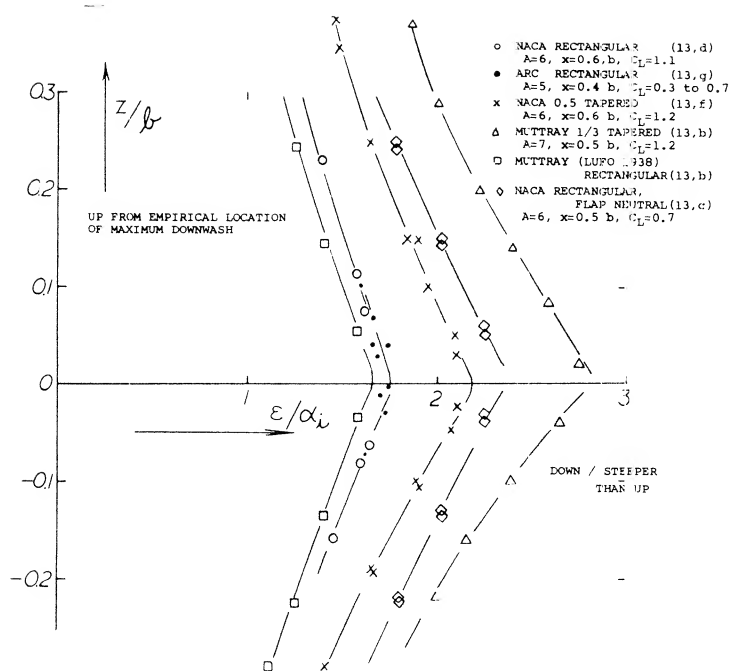


Figure 20. Downwash distribution in vertical plane of symmetry, behind plain wings as tested (13).

Fuselage Downwash Interference. All downwash considerations so far, apply to isolated wings. With the addition the fuselage in the form of a slender body the lift distribution changes across the span of the wing and thus a change of the average downwash at the tail is obtainable since

- As explained in context with figure 4, lift (and lift-curve slope) can be assumed to be increased at and near the wing roots with a corresponding increase of downwash (14,a).
- Viscous interference and/or flow separation along the wing roots may, on the other hand, reduce the downwash.
- The fuselage leaves behind a viscous wake; downwash may be affected by this wake.
- As a consequence of cross or "2 α " flow, downwash can be expected to be reduced at the horizontal-tail roots.

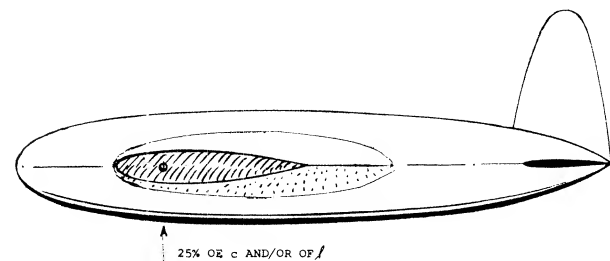
The net result of fuselage interference thus depends upon shape and on quality of the wing-fuselage combination. For example, in figure 15, the tail effectiveness ratio ($1 + d\varepsilon/d\alpha$) is reduced from 0.45 to $(0.87/0.91)0.45 = 0.43$, when adding fuselage plus tail in comparison to tail without fuselage. It can thus be concluded that the downwash ratio is increased from $d\varepsilon/d\alpha = (1 - 0.45) = 0.55$, to $(1 - 0.43) = 0.57$ or 4%, as a result of fuselage interference.

Since this is small a practical assumption might be that with conventional smooth wind-tunnel models the influence of the fuselage upon the variation of downwash ($d\varepsilon/d\alpha$) might be disregarded, at least within the range of low and moderately high lift coefficients. There are, on the other hand, many examples, showing a reduction of downwash on account of viscous fuselage interference as discussed in following paragraph.

Wing Roots. Hardly any airplane design is as plain and smooth as, for example, the wind-tunnel model in figure 21. For instance, the real (if obsolete) airplane depicted in figure 22 (built before 1933) has a fuselage with rectangular cross-section. The lower edges of this shape lead into the leading edges of the wing roots. Ahead of each root, there is also an attachment supporting a pair of struts belonging to the landing gear. As a consequence, the flow along the wing roots is disturbed, if not separated at lift coefficients above 0.6. This disturbance causes:

- an increase, of the drag due to lift by $\approx 30\%$, or 12% based on the total drag at $C_L = 0.7$ (climbing).
- a reduction of horizontal tail effectiveness by 7% (viscous wake effect);
- a reduction of downwash (as shown qualitatively in the illustration) from an estimated ratio of $d\varepsilon/d\alpha = -0.50$ to -0.26 .

While (b) is slightly destabilizing, the reduction of downwash to $\approx 1/2$, is stabilizing. Corresponding to $\Delta(dC_m/dC_L) = -0.20$ due to tail, the stabilized length is 20% of the chord, in the original rough condition of the airplane (with $d\varepsilon/d\alpha = -0.26$).



WING: 0018/09 TAPERED $A = 6$, $R_C = 3(10)^6$ VDT (23,d), $\varepsilon/1 = 1/4$
 FUSELAGE: $l/d = 5.9$, HINGED AT $1/4$ OF THE LENGTH
 HORIZONTAL TAIL SURFACE: $S_H/S = 0.14$; $H/C = 2.6$; $V_H = 0.36$; $A_H = 4.5$

LOCATION OF AERODYNAMIC CENTER AND NEUTRAL STABILITY POINT, % CHORD

	AC W'OUT TAIL	NP WITH TAIL	$d(NP)$ H'TAIL
a) WING ALONE	23.0%	---	---
b) NO FILLETS	21.6%	36.0%	14.4%
c) WITH FILLETS	22.4%	35.2%	12.8%

Figure 21. Influence of wing-root fillets on stability characteristics of a simple airplane configuration (23,d). NP = neutral point.

Wing-Root Fillets. To prevent separation at higher angles of attack, particularly along the upper (suction) side of low-wing airplanes wing root fillets are used. With suitable fillets, the maximum lift is increased, buffeting in wing and tail assembly is avoided and climb performance is improved. However, when first introducing wing-root fillets (possibly around or before 1930) it was soon discovered that they tend to increase downwash and thus to reduce longitudinal stability. In the airplane, as in figure 22, addition of large fillets extending downstream 1.7 c, and to 0.25 c above the trailing edge, and 0.3 c in spanwise direction (at the trailing edge), produced the following results:

- (a) $C_{L\alpha}$ (without power) increased from 1.2 to 1.3,
- (b) downwash increased from $d\epsilon/d\alpha = -0.26$ to -0.55 ,
- (c) stabilized length reduced from (0.20 to 0.13)c.

Derivatives of a simple, clean and smooth airplane configuration are listed in figure 21. The stabilizing effect of the tail, in the configuration without fillets, is 15% of the chord, and that of the tail without downwash is 32%. It follows that without fillets, $d\alpha_H/d\alpha = (1 + d\epsilon/d\alpha) = 0.15/0.32 = 0.47$ and $d\epsilon/d\alpha = -0.53$. When adding fillets, the aerodynamic center of the wing plus fuselage combination is shifted to the rear, approximately 1% of the chord. Against the new AC point, the stabilizing effect of the horizontal tail is reduced corresponding to 2% of the chord. The influence of the fillets corresponding to this 2%, leads to $(1 + d\epsilon/d\alpha) = 0.41$ and to $d\epsilon/d\alpha = -0.59$. The downwash increase with fillets is 12%. And while this increment is not comparable to that in the extremely disturbed airplane in figure 22, the influence of wing-root fillets upon stability should not be disregarded.

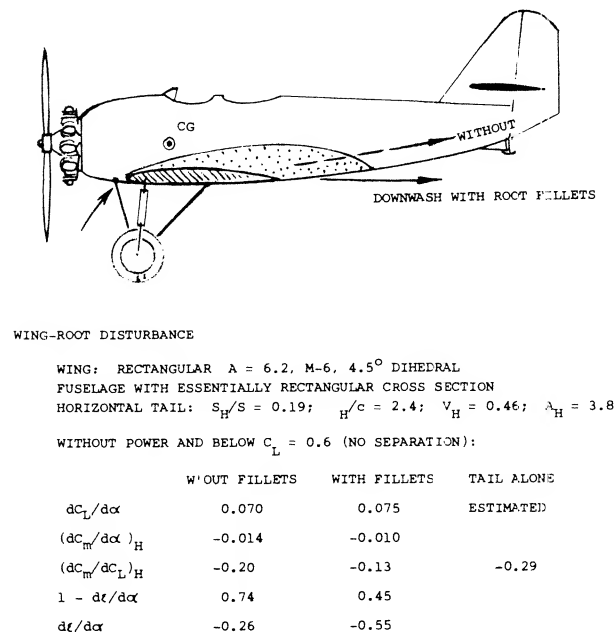


Figure 22. Longitudinal stability characteristics of a full-scale airplane tested in a wind tunnel (14,b); in original form (no fillets) and with large wing-root fillets.

Cut-Outs. Downwash can be reduced by pulling the rear ends of the fillets up. While this produces a distortion of the vortex sheet, it does basically not mean that the derivative of the average downwash angle $d\epsilon/d\alpha$ would be reduced. An efficient reduction of the derivative, can "only" be obtained by reducing the lift-curve slope in the center of the wing. This can, and has been done, by disturbing the flow past the wing roots on purpose, by means of roughness or obstacles such as spanwise strips of material placed near the leading edge. Another method is to reduce the wing chord by cutting away from the trailing edge at the roots. An example of such a cut-out is presented in figure 23. Downwash at the location of the tail is locally reduced from $d\epsilon/dC_L \approx -7$ to a minimum of -2 . For an assumed span of the horizontal tail equal to $1/3$ of that of the wing, the average downwash angle is reduced to $d\epsilon/dC_L \approx -5$, which is 70% of that of the wing without cut-outs (and without fuselage). On the basis of the lift angle of the configuration $d\alpha/dC_L \approx 13$, the downwash reduction obtained, means an increase of the tail effectiveness corresponding to $(1 + d\epsilon/d\alpha)$ from 0.46 to 0.62. Since cut-outs might cause increased induced drag, stability is seen to interfere with performance particularly during climb.

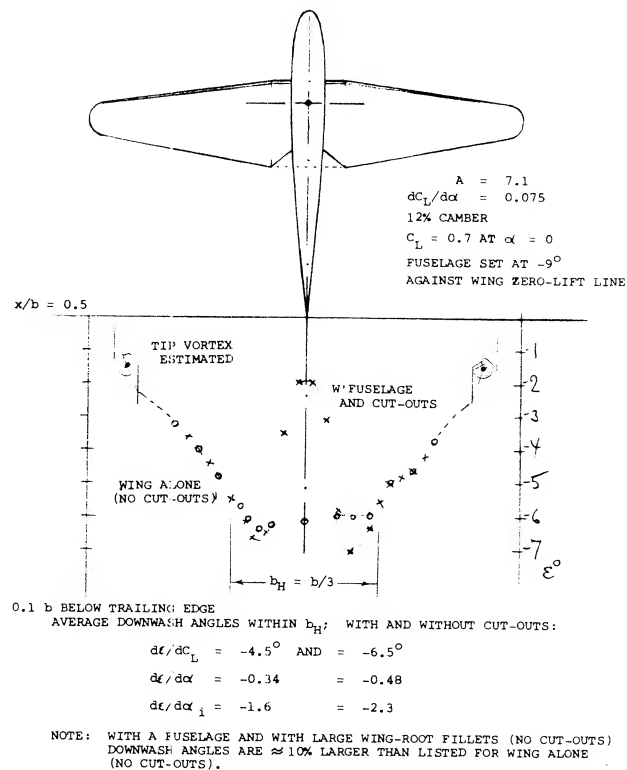


Figure 23. Example (13,c) for the influence of wing-root cut-outs upon the downwash at the location of the tail.

5. SIMPLE AIRPLANE CONFIGURATIONS

Using the various components of longitudinal moment together with the downwash mechanism, it is now possible to evaluate or to predict the static stability of plain wing-fuselage-tail configurations.

Moment Due to Tail. Figure 15 presents characteristics of a simple airplane configuration. The stabilizing moment derivative (dC_m/dC_L) of the horizontal tail is found from the difference of the tests with tail on and tail off. The tail's moment is theoretically

$$dC_{m_H}/dC_L = -(dC_L/d\alpha)_H (S_H/S) (\ell_H/c) (1 + d\varepsilon/d\alpha) (d\alpha/dC_L) \quad (27)$$

In the example as in the illustration, the known terms in this equation are $dC_L/d\alpha = 0.07$, $S_H/S = 0.15$, $\ell_H/\bar{c} = 3.4$, so that $V_H = 0.5$. By comparison of the stabilizing moments, with and without the wing, we find $(1 + (d\varepsilon/d\alpha)) = 0.45$, so that $d\varepsilon/d\alpha = -0.55$. The rest is as tested.

Neutral Point. When moving the CG of an airplane aft stability reduces to zero when reaching the neutral point (neutral stability). For a given configuration, with a pitching moment as in equation (27), this point is indicated by

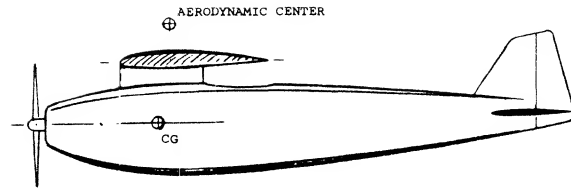
$$(a/c) - (n/c) = dC_{m_H}/dC_L \quad (28)$$

To be stable, n must be longer than a (see figure 1). Since ℓ_H changes little when changing g and n , if the variation of the combined C_L due to a change in C_{LH} is small, the absolute value of the combined dC_m/dC_L (about the leading edge) is equal to n/c . The location " n " of the neutral point is thus aft of the leading edge. Usually, the fuselage contributes a positive $\Delta(dC_m/dC_L)$, resulting in a forward shift of the AC while the horizontal tail provides the stabilizing dC_{m_H}/dC_L , usually between -0.1 and -0.2 , thus extending the neutral point, say to 30 or possibly 35% of the chord. All these variations are indicated by

$$\Delta x/c = -\Delta(dC_m/dC_L) \quad (29)$$

High Wing. Figure 24 gives an example for the neutral point of a "parasol" configuration. Between $C_L = 0$ and 0.9, the neutral point moves from $x/c = 0.34$ to above 0.6. This variation is primarily caused by the stabilizing action of the wing's lift at its AC in reference to the CG. In a manner similar to that in airfoil sections and/or in wings, an aerodynamic center can also be determined for an airplane configuration; the neutral point. This can approximately be considering

$$\Delta C_m = -(z/c)(d\alpha/dC_L) C_L^2 \quad (30)$$



AVION W
WING: $A = b/c = 6$ RECTANGULAR AND STRAIGHT, $dC_L/d\alpha = 0.078; 4(10)^5$
HORIZONTAL TAIL: $S_H/S = 0.14; \ell_H/c = 2.3; V_H = 0.32$; WITH CUT-OUT
AERODYNAMIC CENTER AT $x/c = 0.34$, and $z/c = 0.25$, AS AGAINST WING LE
CENTER OF GRAVITY ASSUMED AT $x/c = 0.25$, AND $z/c = -0.40$
REFERENCE (17,e) TESTED AT $R_c = 4(10)^5$

IN THE GRAPH INDICATING:

- A - $\Delta C_m = -0.09 C_L$ DUE TO CG 9% AHEAD OF AC
- B - $\Delta C_m = -0.09 C_L^2$ DUE TO CG 0.4 c BELOW AC
- C - $\Delta C_m \sim C_L^2$ DUE TO VARIATION OF DOWNWASH $d\varepsilon/d\alpha$

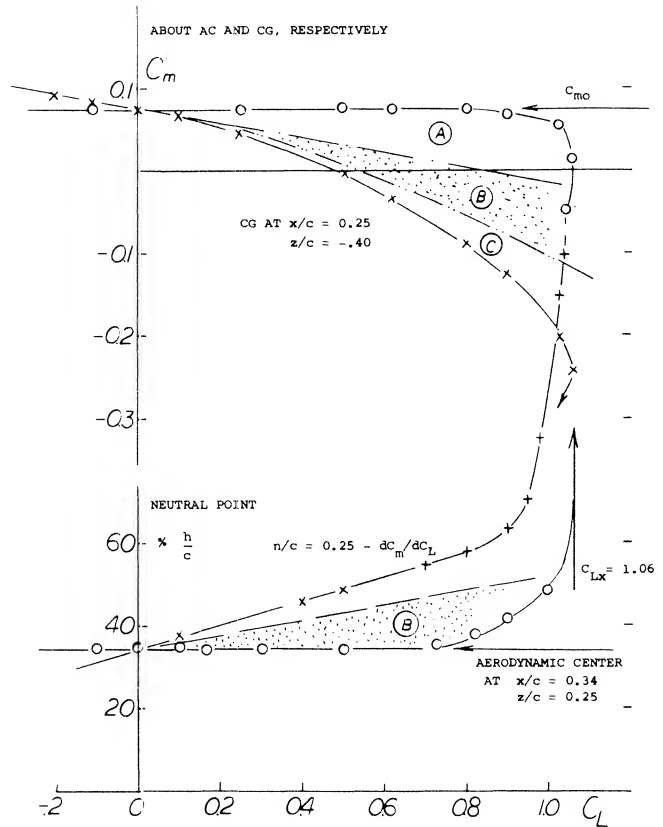


Figure 24. Longitudinal characteristics of a "parasol" type airplane configuration. Aerodynamic center and neutral points, all including the horizontal tail, set at -4.5 against wing zero lift line.

In the graph indicating:

- A - $C_m = -0.09 C_L$ due to CG 9% ahead of AC
- B - $C_m = -0.09 C_L^2$ due to CG 0.4 c below AC
- C - $C_m C_L^2$ due to variation of downwash $d\varepsilon/d\alpha$

where z = positive in a high-wing arrangement. Note that the influence of vertical displacement corresponds to that of a mechanical pendulum, the CG is suspended below the wing's center of lift. It should also be noted that $d(\Delta C_m)/dC_L^2 = \text{constant}$ for a certain displacement "z" of the wing against the CG or vice versa. In the case of figure 24, it was found by trial and error, that the $C_m(C_L)$ function can be made into a line practically straight between $C_L = 0.2$ and $+0.8$, when raising the reference point to the level of $z = 0.24 c$, above the wing's zero lift line. The neutral point NP (aerodynamic center of the configuration, including the horizontal tail) is thus found to be at

$$x = 0.34 c; \quad \text{and} \quad z = 0.24 c$$

measured from wing leading edge and above its zero lift line (which corresponds to $\alpha_o = -0.7^\circ$). The explanation for the comparatively high location of the NP (in figure 24) may be found:

- in lift (and drag) originating and/or increasing in the rear end of the low aspect ratio "square" fuselage, as the angle of attack is increased;
- possibly of some progressive viscous interference of the fuselage with the wing's downwash;
- in the low position of the horizontal tail in relation to the wing and its downwash sheet (see later under "low horizontal tail").

It is thus seen that the downwash and its variation, as the tail moves up or down as a function of C_L , contribute to the position of the "aerodynamic center." In view of the reduction of stability due to propeller and slipstream action (discussed later) an increase of dC_m/dC_L as indicated in equation 30 may be desirable to a degree. On the other hand, strong stability at high lift coefficients, makes control of the airplane during a landing maneuver difficult, particularly when the airplane is designed for tail-down and tail-first type of contact with the ground.

Wing Wake. As shown in (15,d) the turbulent viscous wake emanating from the trailing edge of an average plain wing section, has the following characteristics at a conventional location of the horizontal tail:

- $x = 2 c$, measured from trailing edge of wing
- $\theta/c = 0.5 C_{DS} \approx 0.005$ = momentum thickness ratio
- $\delta \Delta \approx 1.10$ = displacement thickness of wake
- $V_{\min} \approx 0.94 V$ = minimum speed, in center of wake
- $\delta \approx 0.1_+ c$ = total thickness of wake

- (15) Interference of wing wake upon horizontal tail:
 - Ruden, Study, Ybk D Lufo 1939 p 1,98 & 1940 p 1,204.
 - Watter, Interference, J Aeron Sci 1938 p 300.
 - White, Wing-Fuselage Interference, NACA T Rpt 482 (1934).
 - Lieblein, Wake Characteristics, NACA TN 3711 (1956).
 - Spence, Wake Behind Foil, ARC CP 125 (1952).
 - See Silverstein in NACA T Rpt 651 (17,d).

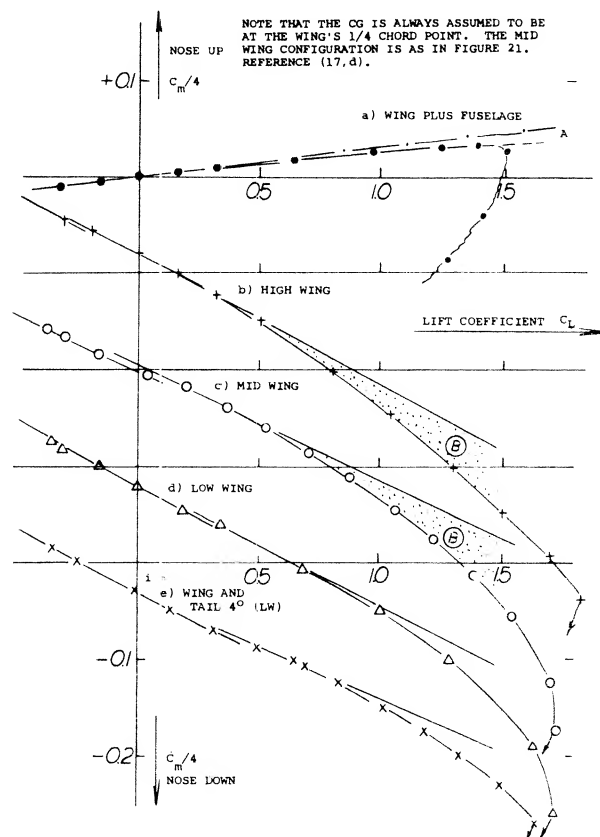
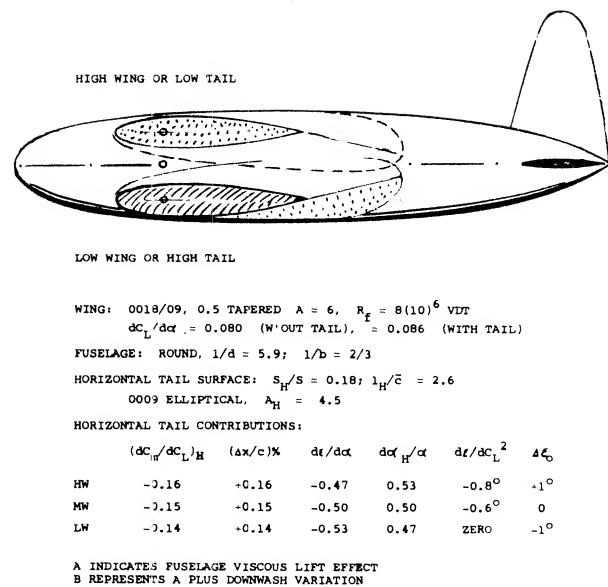


Figure 25. Influence of vertical location of the horizontal tail surface as against wing and vortex sheet. Note that the CG is always assumed to be at the wing's 1/4 chord point. The Mid Wing configuration is as in figure 21. Reference (17,d).

Depending upon the geometrical arrangement, the wake sheet may meet the horizontal tail surface, at a certain angle of attack or lift coefficient. A theoretical and experimental study (15,a) indicates that in this event, the lift of the tail surface basically corresponds to the reduced dynamic pressure within the wake. However, within a field of flow with a velocity gradient in the direction normal to its span, an airfoil becomes attracted toward

the side of increasing velocity. The result can be a certain irregularity in the forces or moments supplied by the horizontal tail surface. Pitching moment coefficients of a simple airplane configuration are plotted in figure 25:

- (a) for wing plus fuselage, mid-wing configuration,
- (b) with wing and CG in high position
- (c) for a symmetrical mid-wing combination,
- (d) for a wing and CG in lowered position,
- (e) for a wing and tail setting of $+4^\circ$ against the fuselage.

By reasons of symmetry, configuration (b) must have an inflection around C_L and/or $\alpha = \text{zero}$. There are evidently "dents" in the $C_m(C_L)$ functions of (d) and (e), at $C_L \approx 0.3$ and 0.4 , respectively. At these critical lift coefficients, the slope dC_m/dC_L is locally reduced. Of course, in the operation of an airplane, the "mixing" action of the propeller (if any) or variations of wing shape causing a distortion of the vortex sheet (such as dihedral, cut-outs, flaps) may render the dent in the $C_m(C_L)$ function insignificant.

Low Horizontal Tail. From the data on the mid-wing configuration in figure 25, it is seen that the $C_m(C_L)$ function is curved in such a manner that the value of dC_m/dC_L increases with lift coefficient. The reason for this is the wing plus fuselage alone function of C_m vs C_L , figure 25, and evidently the fact that the tail (when below the vortex sheet) moves into the field of reducing downwash shown in figure 20. At a conventional tail location $x/b \approx 0.6$, the variation may be approximated by equation (26). For the mid wing in figure 25, the angular displacement of the horizontal tail away from the vortex sheet is $\approx -0.25 \alpha$, so that $\Delta z/b = -0.25 (d\alpha/dC_L) C_L \approx -0.06 C_L$, at $x/b = 0.6$. The resultant increment of the angle of attack at the tail corresponds to

$$\Delta(d\epsilon/d\alpha) \approx -(\Delta z/b) d\epsilon_x/d\alpha = -1.5 (0.06) C_L 0.5$$

$$-0.045 C_L \quad (31)$$

where $d\epsilon_x/d\alpha$ is assumed to be -0.5 . The change of the angle at the tail is thus proportional to $\alpha_0 C_L \sim \alpha_0^2$; or C_L^2 , where the dot indicates that the angle is measured from the zero lift line. For an assumed aerodynamic angle of attack at the tail $\alpha_{\mu_0} = (1 - 0.5) \alpha = 0.5 \alpha$, the increment of this angle reaches the magnitude of 9% (in the example considered) at $C_L = 1$. Differentiation then yields an increment of the tail contribution to longitudinal stability of 18% at $C_L = 1$, which may mean an extension of the neutral point by $\Delta x/c = -4(dC_m/dC_L)$ in the order of 4%, in a conventional airplane.

Vertical Position of Tail. There is considerable evidence indicating that an improvement of stability does take place, as the horizontal tail moves below the vortex and wake sheet. For example, the midwing configuration in figure 25 shows an increment of the tail-moment contribution at $C_L = 1$, in the order of 8% (not counting the increment due to fuselage). The high wing or low-tail arrangement in the same graph has a tail moment of 12%.

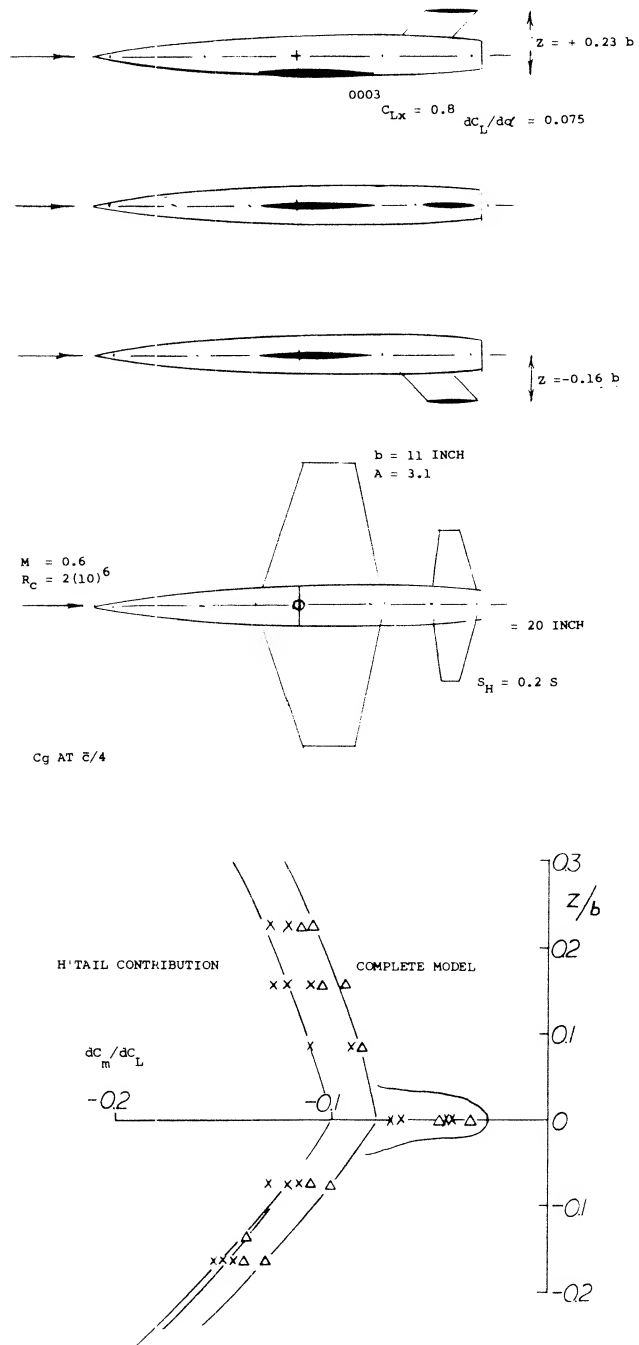


Figure 26. Longitudinal static stability characteristics of a plain configuration as a function of the vertical position of the horizontal tail surface (20,a).

Another advantage of the latter configuration (with the CG at the wing's quarter point) is the fact that the horizontal tail is always below the vortex sheet where (as in figure 20) the downwash is less than the maximum. As a consequence, the *low-tail configuration* exhibits a $dC_m/dC_L = 0.18$ (at $C_L = 0.8$), while the mid-wing type has only -0.16 . Results of a systematic investigation (20,a) are plotted in figure 26 and indicate:

- With the horizontal tail either above or below the vortex sheet, the stabilizing contribution of the tail is increased in comparison to that on fuselage center line.
- The improvement is greater below than above the wing chord. The derivative $d\epsilon/dz$ is evidently favorable below, and unfavorable above the vortex sheet.
- Directly on the fuselage (at its center line) the tail contribution is extremely low. It must be assumed that viscous interference (described in the "horizontal tail" section) is maximum here.

"T" Tail. An extreme measure to avoid interference with the downwash sheet as well as with any wake, is to place the horizontal tail as high as possible. An example of a very high location of the horizontal tail surface, on top of the vertical surface (thus forming a "T" tail) is shown in figure 27. The tested pitching-moment derivatives (at lift coefficients below ≈ 0.5) are as follows:

	dC_m/dC_L	dC_{mH}/dC_L
for wing plus fuselage	$+0.13$	zero
with H'tail on fuselage CL	$+0.05$	0.08
with "T" tail ($h = 0.6\ell_H$)	-0.12	-0.25

where the members in the last column indicate the stabilizing differentials of the horizontal tail. The $+0.13$ is essentially due to the fuselage, hinged at 0.54 of its length (a point not typical in conventional airplanes). With the horizontal tail located on the fuselage center line, the configuration is not stable. Analysis using equations 22 and 23 suggests that the downwash angle is

$$d\epsilon/dC_L \approx -9.2 - 2.3 = -11.5^\circ$$

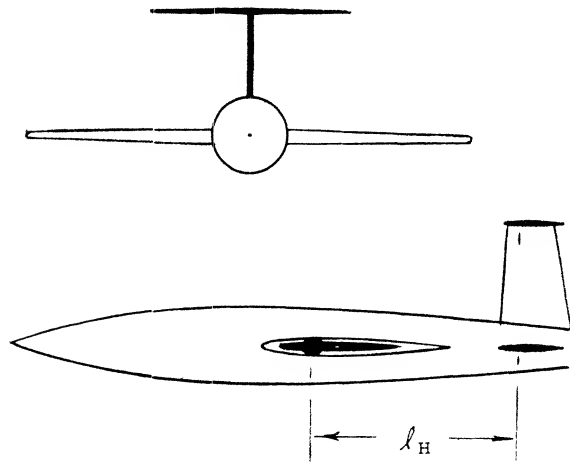
which is 2.5 times the induced angle of attack. The influence of the fuselage upon the effective aspect ratio is estimated to result in $A_L = 0.7(4) = 2.8$. Using the corresponding lift angle of

$$(d\alpha/dC_L)_H = 10.5 + 6.5 = 17^\circ$$

the contribution of the horizontal tail then is calculated to be

$$dC_{mH}/dC_L = -(d\alpha_H/d\alpha)(S_H/S)(\ell_H/\bar{c})(d\alpha/dC_L)/(d\alpha/dC_L)_H \quad (32)$$

where $d\alpha_H/d\alpha = (15 - 11.5)/15 = 0.23$ only. Using the ratios as indicated in the illustration, and the lift angle of the wing $d\alpha/dC_L = 15^\circ$ as tested, the value $dC_{mH}/dC_L \approx -0.085$ is obtained. This compares with the test value of -0.08 shown on figure 27. Considering now the horizontal



WING: 0.6 TAPERED $A = 4$, 65A008
 H'TAIL: $S_H/S = 0.2$; $\ell_H/\bar{c} = 1.8$
 $h/H = 0.6$ FOR "T" TAIL

HORIZONTAL TAIL CONTRIBUTION:

	dC_{mH}/dC_L	$\Delta x/\bar{c}$
ON FUSELAGE CL	-0.08	$+8\%$
"T" TAIL POSITION	-0.25	$+25\%$

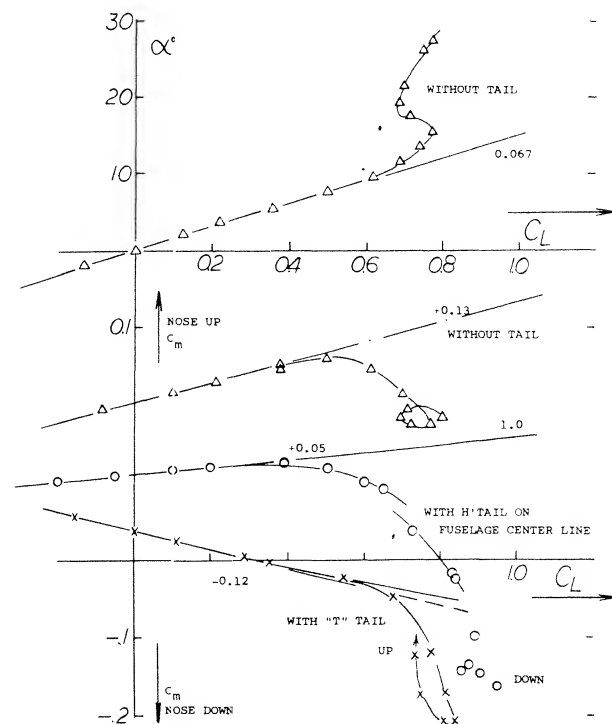


Figure 27. Influence of vertical position of the horizontal tail surface (20,d) on longitudinal stability. $R_c = 8(10)^5$.

surface raised to the top of the vertical tail, we may expect that the downwash is reduced to 0.6 of that assumed above (see figure 20). Fuselage interference is assumed to be zero; in fact, the upper side of the horizontal surface is completely undisturbed. Since $A_H = 4 = A$ as in the wing, we obtain $d\alpha_H/d\alpha = (15 - 7)/15 = 0.53$, which is more than twice the 0.23 ratio for $d\alpha_H/d\alpha$ above. Consequently:

$$dC_{mH}/dC_L = -0.53(0.2)2.1 = -0.22$$

while -0.25 was obtained from test (see figure 27). The "T" tail configuration thus does two things:

it avoids the downwash maximum near the vortex sheet,
it avoids viscosity-induced fuselage (wake) interference.

"T" Tail at High Angles: While the "T" tail, as in figure 27, is safely placed outside (above) the wing wake, the variation of downwash as in figure 20, should be expected to reduce stability, in the range of higher lift coefficients corresponding to what is explained above under "low horizontal tail". Indeed, comparison of the $C_m(C_L)$ functions in figure 27, without tail and with "T" tail, reveals a reduction of the stabilizing tail moment between $C_L = 0.3$ and 0.6, similar in absolute magnitude to the stabilizing amount of $|0.45| C_L^2$, derived above for a low-tail configuration. Therefore, the advantage of the "T" tail arrangement rests primarily in the elimination of fuselage interference. Disregarding structural considerations, a really high location of the horizontal tail has another disadvantage. At very high angles of attack, the horizontal surface is bound to get into the wake from the *stalled* wing. As seen in figure 27, the pitching moment then turns unstable (into the positive direction) thus presenting a situation which is likely to get into the "deep stall condition, Chapter XVI.

Aspect Ratio. A given tail plus fuselage assembly was tested (17,f) in combination with 3 wings having the same area, but differing in aspect ratio, between 2 and 6. The lift of the horizontal tail is found as the differential between the complete configuration and wing plus fuselage (tested without tail). Including for $A = \infty$, or $1/A = 0$, the slope $(dC_L/d\alpha)_H$ of tail plus fuselage tested alone, figure 28 demonstrates how the lift of the tail is reduced with a reduction of aspect ratio on account of increased downwash. It follows that

$$d\alpha_H/d\alpha = (dC_{LH}/d\alpha)/(dC_L/d\alpha) \quad (33)$$

and $d\epsilon/d\alpha = d\alpha_H/d\alpha - 1$, so that

$$d\epsilon/dC_L = (d\alpha_H/d\alpha)(d\alpha/dC_L) - d\alpha/dC_L$$

where $d\alpha/dC_L$ = lift angle of the respective wings as tested (plotted at the top of the graph). It is thus seen

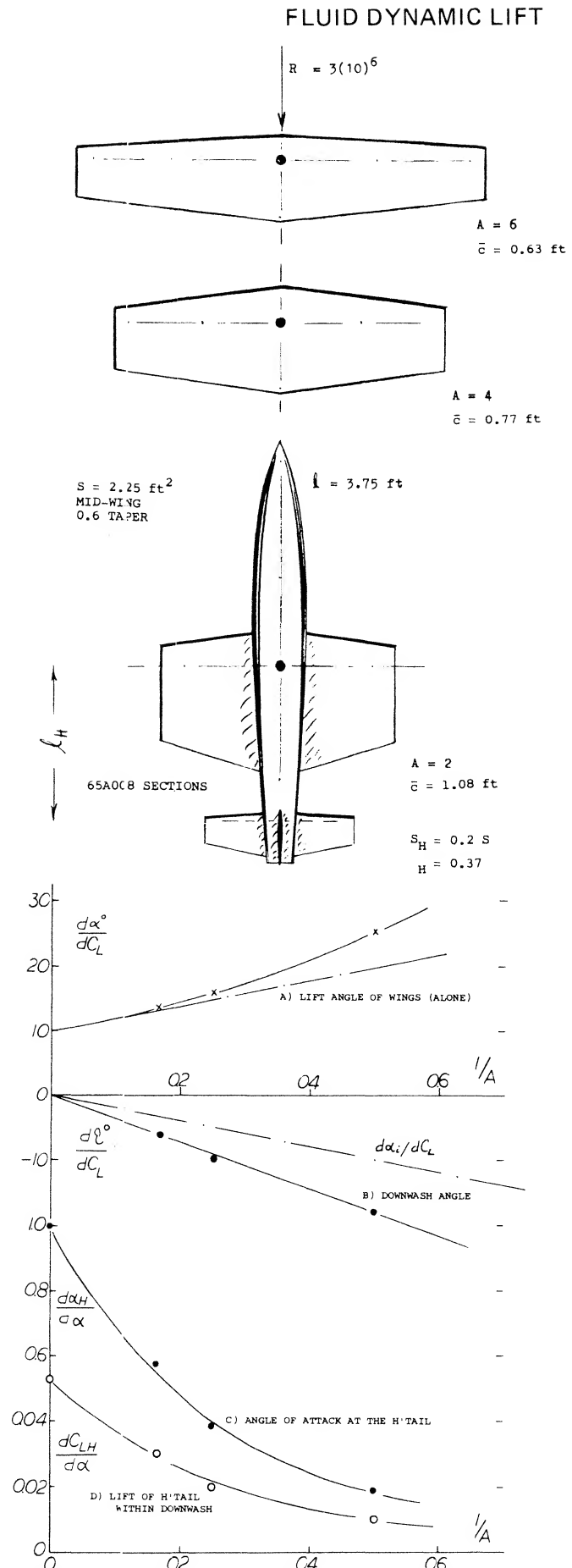


Figure 28. Longitudinal characteristics of a basic airplane configuration (16,f) particularly of the horizontal tail, as a function of the wing's aspect ratio.

that downwash increases and the stabilizing contribution of the tail reduces as the aspect ratio of the wing is reduced. For example, at $A = 2$, where $l_H/\bar{c} = 0.37 \ell/1.08 = 1.3$ and $V = 1.3 (0.2) = 0.26$, the tail contribution is $dC_{mH}/dC_L = - (dC_{LH}/d\alpha) V_H (d\alpha/dC_L) = - 0.01 (0.26) 25 = - 6.5\%$, which is only $\approx 1/3$ of what it is in average conventional airplane configurations.

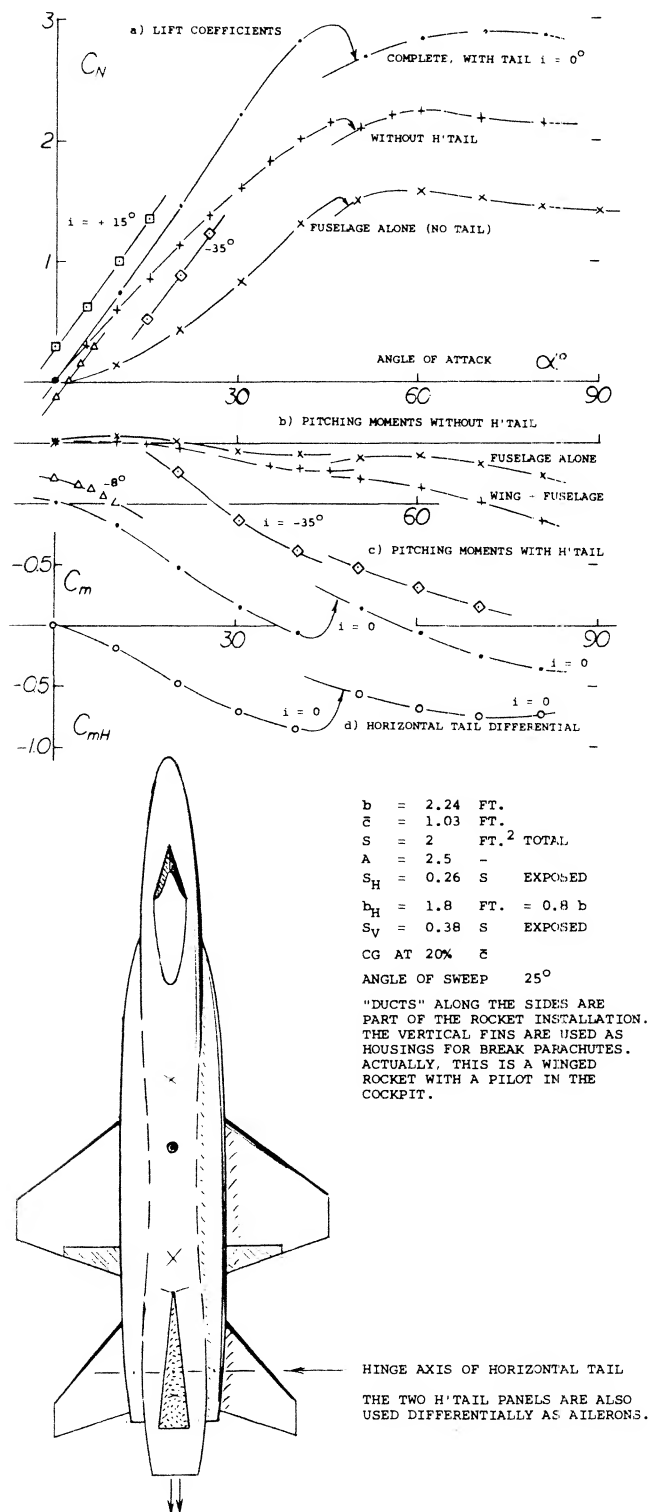


Figure 29. Longitudinal characteristics of a model (22,b) similar to the NASA and North American "X-15", tunnel-tested at low speeds ($R_c = 2(10)^6$).

Big Fuselages. Small aspect ratios are used on winged missiles (21), where not only downwash is a problem but also the size of the body in comparison to wing and tail is critical. Another example involving small wings and a large fuselage, is the high-altitude research craft X-15. Characteristics of a model similar to this airplane are presented in figure 29. The maximum width of the body is $0.34 b$; its plan-form area is ≈ 1.4 times total wing area. Analysis of these data show:

- The lift curve slope (without horizontal tail) within the range of small angles of attack, $dC_L/d\alpha = 0.055$, corresponds to $A = 2.5$.
- The maximum lift coefficient (without tail) is $C_{L\max} \approx 0.7 C_N = 1.5$, at $\alpha = 45^\circ$.
- When adding the horizontal tail, its contributions to lift and pitching moment are not linear.
- There is a critical angle of attack near 50° , where forces and moments exhibit discontinuities.

The non-linearities (c) and the discontinuities seem to be a consequence of the fuselage flow pattern (separation). It must be noted, however, that the wing eliminates most of the fuselage lift, by way of downwash, so that the lift-curve slope as in (a), is fairly constant.

Tail Contributions. The interaction between fuselage and horizontal tail in the configuration as in figure 29, is complex. A qualitative analysis is as follows:

- By comparison of $dC_m/di = - 0.026$ with $dC_L/di = 0.020$, a tail length $l_H = (0.027/0.020)c = 1.35 c$ is found.
 - Based on exposed area of $S_H = 0.26 S$, the lift-curve slope of the tail is $dC_{LH}/di = 0.020/0.26 = 0.077$, which seems to be proper for an "exposed" aspect ratio of $A = b_H^2/S_H = 6.3$.
- Simple airplane configurations in wind tunnels:
 - Schlichting, Interference, Ybk D Lufo 1943, Rpt IA028; see (10,e).
 - Gruenling, Investigation of Me-109 Model, ZWB UM 7857 (1944).
 - Sherman, 17 Combinations, NACA T Rpt 678 (1939).
 - Service Technique Aeronautique (Belgium), Bull 15, Feb 1935.
 - f) Stivers, NACA TN 4238 (1958) and NASA D-13 (1959).
 - g) Fournier, Three-Body Configuration, NASA TN D-217 (1960).
 - Influence of vertical CG location:
 - Andrews, Flight (Aircraft Eng) 1937 No. 1474 & 1479.
 - Francis, Notes on Stability, ARC RM 1833 (1938).
 - Bryant, "Puss Moth" High Wing, ARC RM 1687 (1935).

- Further variants of the configurations as in figures 25,26,27, references (17,f)(18,d)(20,d), are reported in NACA RM A52D23/E01/L15a, in TN 3551,3857, and in NASA D-13; between 1952 and 1959.

- (c) At $\alpha = 20^\circ$, the tail moment differential is $\Delta C_{mH}/\Delta \alpha = -0.022$, in presence of the wing. This is less than the $dC_m/dj = -0.026$ above.
- (d) Again at $\alpha = 20^\circ$, the lift differential due to tail is $\Delta C_L/\Delta \alpha = 0.016$. Combining this value with the derivative in (c), a tail moment arm $l_H = (0.022/0.016)c = 1.38c$ is obtained.

The difference between the derivatives as against j and α , is due to downwash as well as to a more or less unknown contribution of the fuselage. On the basis of S_H (total) = $2.1 S_H$ (exposed) = $0.55 S$, a $(\Delta C_L/\Delta \alpha)_H = 0.016/0.55 = 0.029$ is obtained. Comparison with 0.077 as in (b) leads to $d\alpha_H/d\alpha = 0.029/0.077 = 0.38$ and $d\varepsilon/d\alpha = -0.62$. These values seem to be reasonable. More accurate predictions cannot be made, however, for a configuration:

where the fuselage is long and wide,
where the tail length is no longer than \approx wing chord.

To show the problematic character of the analysis, the downwash as derived above, is only 1.4 times the induced angle, which seems low.

X-15. The model in figure 29, is evidently one representing the NASA-North American research airplane "X-15". Flight-test reports (22,c) reveal that the airplane is flown approximately:

at $\alpha = 10^\circ$	and with $i = -12^\circ$	launching
at $\alpha = 5^\circ$	and with $i = -9^\circ$	climbing
at $\alpha = 15^\circ$	and with $i = -20^\circ$	recovering

This means that operation is at C_L between 0.2 and 0.8. This range is small in comparison to that in figure 29. Other data and expected performance (22) of this airplane are:

$b = 22$ ft	$T_x = 60,000$ lb	$W = 31,000$ lb with fuel
$M = 6$	$V_x = 3,500$ kts	$W = 13,000$ lb burnt-out
$l = 50$ ft	$S = 200$ ft ²	max altitude $\approx 250,000$ ft

- (20) Influence of vertical location of the H'tail:
- Stivers, Vertical Location of Tail, NACA RM A57110.
 - Multhopp, "T" Tails, Aero Digest, May 1955.
 - Interaction with V'tail, see NACA TN 1050 & 2907.
 - Letko, in connection with (17,c), NACA TN 3431 (1955).
- (21) Nielsen, Wing Body Tail Combinations, NACA T Rpt 1307 (1957).
- (22) Aerodynamic characteristics of the X-15 research airplane:
- Clark, Space Flight, Aero Space Engg, April 1959 p 43.
 - Bowman, Tunnel-Tested Characteristics, NASA TN D-403 (1960).
 - Flight Test Analyses, NASA TN D-615,623,723,1057,1059,1060,1159 (1960/62).
 - Weil, Review of Operation, NASA TN D-1278 (1962).
 - For data, see Jane's All the World's Aircraft 1961/62 p 292.

Long Fuselage. The configuration in figure 30 serves first as another illustration for a long fuselage (forward). Assuming that the body in the middle may have a weight equal to $1/4$ of the total, its addition moves forward the combined CG more than 20% of the "mac"; thus $\Delta (dC_m/dC_L) \approx -0.20$, on account of fuselage weight. Its aerodynamic contribution is, on the other hand, $\Delta (dC_m/dC_L) = +0.07$. A long fuselage forward thus more than cancels its destabilizing effect; and we have an explanation, how long-nosed configurations such as that in figure 29, for example, can be stable in longitudinal direction.

Zero-Lift Moment. Theoretically the fuselage does not develop lift. Its free moment (+ 0.07) has to be compensated, however, by a positive lift force in the horizontal tail. At higher lift coefficients, say at $C_L = 1.0$, therefore, $\Delta C_{mH} = -0.07$, which means in the configuration considered a $\Delta C_{LH} = +0.07/0.66 \approx 0.1$ and a total $C_{LH} \approx 0.2$. This would not be a problem; in fact, in an airplane using wing flaps, the fuselage moment would tend to overcome the negative (nose-down) moment produced by those flaps. On the other hand for a range of small lift coefficients (at high speeds) near $C_L = 0$, the differential depends entirely upon the angle "i" at which the wing is set against the fuselage. In a convention design, i (measured at the wing's zero-lift line) is in the order of

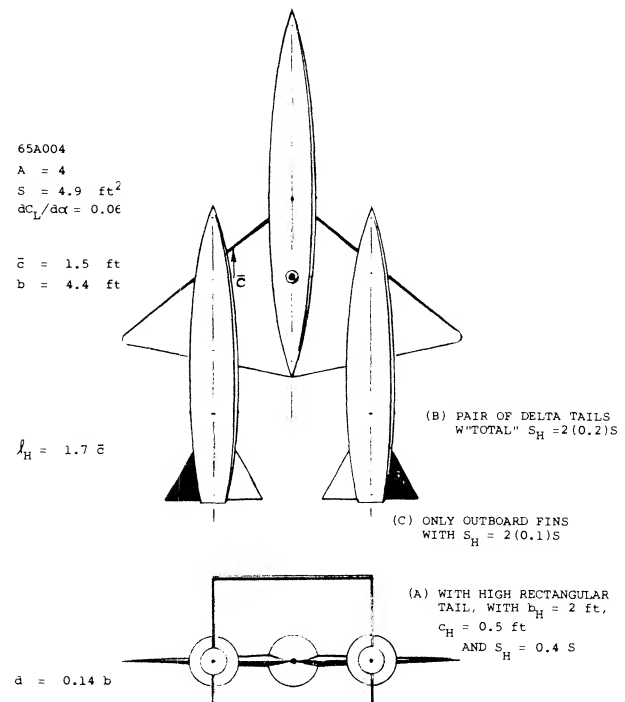


Figure 30. Three-body airplane configuration tested (17,g) at $M = 0.2$ and $R_c = 2(10)^6$. See text for principle results.

several degrees, so that the fuselage may be in horizontal position when cruising. Thus $i = 0.3/0.06 = 5$, for example, for an assumed $dC_L/d\alpha = 0.06$. To balance the fuselage moment at $C_L = 0$, for instance high speed dive, a negative (down) load in the horizontal tail is required. In the example considered, that load would be in the order of 50% of the airplane's weight (estimated on the basis of conventional values for tail volume et cetera), assuming a terminal speed two times the cruising speed and disregarding any changes due to compressibility.

Taper Ratio. It is explained in the "downwash" section, that rectangular wings have less, and tapered plan forms more downwash in their center plane. Using a final (rolled-up) ratio $\epsilon/\alpha_L = 2.6$ and an increment of at least 0.1 (as derived from equation 23),

$$d\epsilon/d\alpha = -(\epsilon/\alpha_L)(d\alpha_L/d\alpha) = -2.7(5/17) = 0.8$$

or even higher, can be estimated for the doubly-triangular wing shape in figure 30. Analysis of the wide and large tail surface ($S_H/S = 0.4$) stretched out between the two nacelles (with $A_H = 4$, plus end-plate effect supplied by the vertical fins) leads to an average effective ratio α_H/α somewhat below 0.2. The configuration shown, or any similar, highly tapered wing, is thus rather inefficient in regard to longitudinal stability.

Across the Span. The magnitude of downwash is primarily considered in or near the plane of symmetry. The distribution across the wing span depends on the lift coefficient. In rectangular wings, downwash increases slightly on either side of the plane of symmetry. In tapered plan forms, it decreases on the other hand; and it does so to a considerable degree in highly tapered wings such as that in figure 30. As a consequence, the stabilizing effectiveness of the horizontal tail, is a function of its lateral location. Results when using a pair of surfaces attached to the nacelles, as in part (B) of the illustration, are as follows:

tail configuration	dC_{mH}/dC_L	$d\alpha_H/d\alpha$	$d\epsilon/d\alpha$
pair of delta tails	0.13	0.4	- 0.6
outboard pair of tails	0.10	0.6	- 0.4
estimated for inboard pair	0.03	0.2	- 0.8

In short, the inboard panels are very inefficient by comparison, on account of a high downwash ratio.

6. CHARACTERISTICS OF CANARD CONFIGURATIONS

The basic equations of longitudinal balance and stability suggest that "any" type of combination of two "wings" may be used in designing an airplane. One unconventional arrangement is the canard type configuration, flying tail-first, so-to-speak.

Canard Principles. Many pages of this and of the next chapter, are devoted to the description of all the interaction and interference effects to which a horizontal tail surface are subjected. From time to time, the possibility has, therefore, been investigated of placing the "stabilizer" ahead of the wing, where "no" disturbance may have to be expected. Another argument in favor of this arrangement is the fact that the canard surface will reach its maximum lift at a lesser airplane angle of attack (and/or wing lift-coefficient) than a tail surface (located in the wing's downwash). It has been stated accordingly, that the wing of the canard-type airplane would be stall-safe. While this can certainly be true, stalling of the canard surface must be expected to have consequences. As the history of airplane design demonstrates, therefore, canard configurations have only been built and tried (23,a,b) for experimental purposes. There are specific applications, however, particularly in winged missiles, where operation at higher lift coefficients may not be required. There can also be other inducements in the areas of drag and arrangement VTOL types (23,f) in favor of a canard system, such as in large supersonic airplanes (24), for example.

(23) Characteristics of canard-type airplanes:

- a) Focke-Wulf "Ente", see NACA Rpts AC59 (1927) & 132 (1931).
- b) Hubner, Focke-Wulf F-19 "Ente", ZFM 1933 p 223.
- c) Kiel, Stability of "Ente" Airplanes, NACA TM 612 (1931).
- d) Flying Model of Curtiss P-55, tested in Full-Scale Tunnel, NACA W Rpts L-627, 630, 650 (1943/45).
- e) Sandahl, Body Wing Canard, NACA TN 1295 (1947).
- f) Borst, High Speed VTOL Aircraft Aerospace Eng. Aug 1962

- (24) Hibbard, Supersonic Transport Airplanes (Aero Space Engg, July 1959 p 32) with V = 1500 kts, are proposed with Canard Control. Drag penalty associated with trim at $M = 3$ is so great, that canard configuration is selected.

Tandem Configuration. We will first consider the tandem system as in part (a) of figure 31. The separation distance between the two wings may be $\ell = b$. The upwash at the place of the forward wing is assumed to be zero, while the downwash at the second wing may correspond to $d\epsilon/d\alpha = -0.5$. Using equation (2) balance requires

$$C_{m1} = C_{L1} (S_1/S)(\ell_1/\ell) = |C_{m2}| \\ = C_{L2} (S_2/S)(|\ell_2/\ell|) \quad (34)$$

where $S = S_1 + S_2$, and $\ell = \ell_1 + (\ell_2) =$ separation distance = reference length. In terms of the angle of attack

$$(dC_L/d\alpha)\alpha(S_1/S)(\ell_1/\ell) = (dC_L/d\alpha)(\alpha_{u1} + i)(S_2/S)\ell_2/\ell \quad (35)$$

where $\alpha_{u1} = (1 - 0.5)\alpha$, and $i =$ angle at which the second wing is set against the first one. One and the same slope $dC_L/d\alpha$ shall be assumed to apply to either wing (when flying alone). Therefore:

$$\alpha S_1 \ell_1 = (0.5\alpha + i) S_2 (\ell_2) \quad (36)$$

where the absolute value is used for the arm ℓ_2 . In a tandem system (where $S_1 = S_2 = 0.5 S$):

$$\alpha \ell_1 = (0.5\alpha + i/\alpha) |\ell_2| ; \text{ or } \ell_2 = (0.5 + i/\alpha) |\ell_2| \quad (37)$$

where the 0.5 reflects the influence of the downwash.

Stability. Using next equation (5) static stability requires that

$$|dC_{m2}/d\alpha| > dC_{m1}/d\alpha \\ 0.5(dC_L/d\alpha)(S_2/S)|\ell_2/\ell| > (dC_L/d\alpha)(S_1/S)(\ell_1/\ell) \quad (38)$$

Note that ℓ_1 is considered to be positive, and ℓ_2 to be negative. For neutral stability, thus:

$$0.5 S_2 |\ell_2| = S_1 \ell_1 \quad (39)$$

and in a tandem system (where $S_2 = S_1 = 0.5 S$)

$$0.25|\ell_2| = 0.5 \ell_1 ; \text{ or } \ell_1 = 0.5 |\ell_2| \quad (40)$$

In fact, to be stable, ℓ_1 must be somewhat shorter than $0.5 \ell_2$. Introducing now the maximum permissible ℓ_1 into equation (37)

$$\ell_1 = 0.5 |\ell_2| = (0.5 + i/\alpha) |\ell_2| \quad (41)$$

we correctly obtain $i = 0$. We will now specify a stability corresponding to $dC_m/dC_L = (dC_m/d\alpha)(d\alpha/dC_L)$, for example $= -0.01$, which means a stabilized length of $\Delta x/\ell = 1\%$ of the separation distance ' ℓ '. For an assumed $dC_L/d\alpha = 0.06$, we then obtain

$$dC_m/d\alpha^0 = -0.06 (\Delta x/\ell) = dC_{m1}/d\alpha + dC_{m2}/d\alpha \\ = 0.06 (0.5) (\ell_1/\ell) - 0.5 (0.06) 0.5 |\ell_2/\ell| \\ = 0.03 (\ell_1/\ell) - 0.015 |\ell_2/\ell|$$

Since $|\ell_2| = \ell - \ell_1$, we obtain

$$dC_m/d\alpha^0 = 0.03 (\ell_1/\ell) - 0.015 (1 - \ell_1/\ell) - 0.06 (\Delta x/\ell)$$

and the moment arm of the first wing:

$$\ell_1/\ell = (1/3) - (4/3) \Delta x/\ell \quad (42)$$

For neutral stability ($\Delta x/\ell =$ zero), this equation correctly yields $\ell_1 = \ell/3$.

Control. Combining equations (37) and (42)

$$\ell_1/\ell = (0.5 + i/\alpha) \ell_2/\ell = (1/3) - (4/3)(\Delta x/\ell) \quad (43)$$

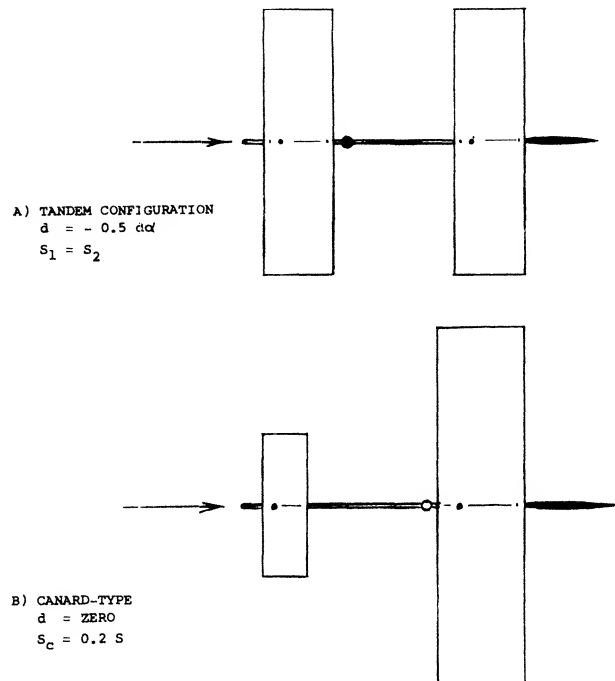


Figure 31. Basic geometry of tandem and canard-type configurations.

After replacing ℓ_2 again, we eventually obtain the approximation

$$i/\alpha = -6(\Delta x/\ell) + 8(\Delta x/\ell)^2 \approx -6(\Delta x/\ell) \quad (44)$$

Thus, the tandem system considered can be expected to be stable when and if the CG is ahead of the 1/3 point of the separation distance. The configuration can be controlled or trimmed by reducing the angle of attack of the rear wing, roughly at the ratio of $\Delta i/\Delta \alpha = -6\%$ for each stabilized percent of the separation distance.

Canard Analysis. Assume that the forward wing reduces in area, say to 25% the rear wing, or to 20% of the combined area. In a rough analysis, we may assume no interference between the two “wings” (no downwash). The neutral location of the CG is then found to be at

$$\ell_1 = |\ell_2|(S/S_c) = 5|\ell_2| = (5/6)\ell \quad (45)$$

where S_c = area of the canard surface. To be stable, the CG must be placed 1% of the reference length ahead of the neutral point, for each increment equal to 0.01, of the stability derivative dC_m/dC_L . This is as in conventional airplane configurations, but only when the wing is not affected by downwash or upwash, respectively of the smaller, stabilizing surface (located either ahead or aft).

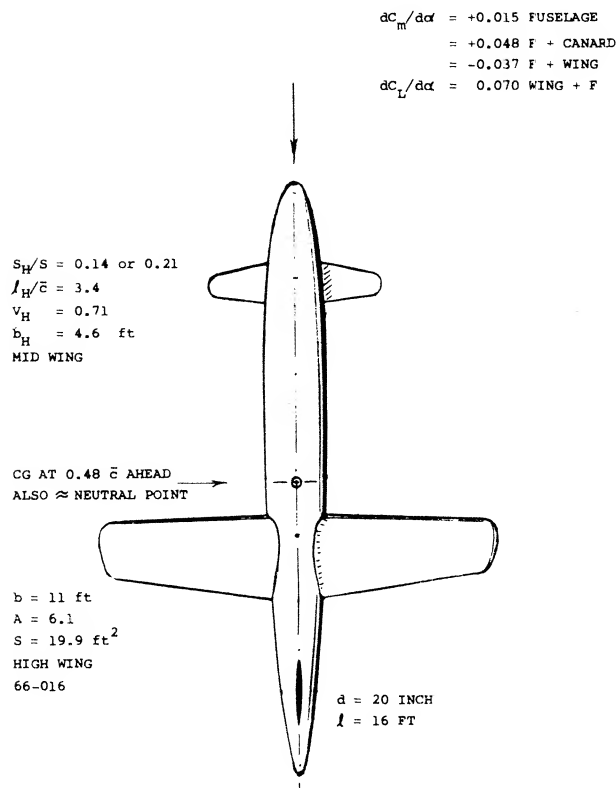


Figure 32. Large-scale canard model as tested in the Propeller-Research Tunnel (23,e). $R_c = 1.5(10)^6$.

Basic Configuration. The large-scale model of a canard configuration is shown in figure 32, consisting of a plain body of revolution, a straight wing in high position, and a stabilizing surface mounted mid-wing near the nose of the fuselage. Pressure-distribution tests indicate that the load distributions across the span, both of the wing and canard surface, display considerable dents in the center. The one in the wing, seems to be responsible for an induced drag at least 10% higher than expected. The effectiveness of the canard surface can be understood when assuming that the part of the fuselage “covered”, only produced 1/2 of the lift as it would, without the fuselage present.

Canard Effectiveness. Investigation of the canard surface of light weight Curtiss P-55, figure 33 airplane in the NACA's Full-Scale Tunnel (23,d) reveals:

- (a) When rotating the canard surface against the fuselage, its force varies corresponding to $dC_{NH}/di = 0.042$.
- (b) When rotating the surface together with the fuselage, the differential corresponds to $dC_{NH}/d\alpha = 0.057$.

The load distribution, plotted in figure 34, shows a deep dent or gap in the center of the canard-surface span. The pressure distribution induced upon the fuselage, does not fill up the gap. Evidently, there is not much body left ahead of the leading edge, where a cross flow could develop. In fact, the gap is so big that we may consider 15% of the canard surface to be cut out and to be ineffective. Using the function explained in the Chapter III the “lift angle” may thus be expected to be

$$d\alpha/dC_{LH} = (10.5 + 19/A_H)/0.85 = 14.9/0.85 = 17.4^\circ \quad (46)$$

where $A_H = 4.4$, including the part covered by the fuselage. The result as under (b) above is $1/0.057 = 17.6^\circ$. Note that we did not reduce the effective aspect ratio since the boundary layer and/or wake at the nose of the fuselage are very small. Note also that area and aspect ratio and lift curve slope of the canard surface used in the following tests, are larger than those of the surface used in figure 34.

Stability Contributions. The pitching moment characteristics of the P-55, as tested with the CG located at 12% of the “mac” (id est, behind its leading “edge”) are plotted in part (a) of figure 33. Without the stabilizer, the configuration is stable, $dC_m/d\alpha = -0.0063$ or $dC_m/dC_L = -0.0063/0.07 = -0.09$, where $0.07 = dC_L/d\alpha$, as tested. To balance this moment at a certain lift coefficient the canard surface has to provide a positive (destabilizing) moment. Stabilization in any canard configuration can thus only be obtained from the wing and that contribution is not adequate in the condition as tested, with the CG at 12% “mac”. Positive stability can be obtained, for

example, by moving the CG forward to the leading edge of the "mac". Part (b) of the illustration shows the corresponding pitching moment characteristics. To trim the airplane, say to $C_L = 0.5$ where $\alpha = 7^\circ$, a stabilizer angle i of at least $+7^\circ$ is required. The aerodynamic angle is then $\alpha_H = \alpha + i = 7 + 7 = 14^\circ$, and the lift or normal-force coefficient of the canard surface is between 0.8 and 0.9. In other words, this coefficient grows faster than that of the wing.

$W = 8000 \text{ lb}$	EXPERIMENTAL: 4000 lb
$b = 41 \text{ ft}$	$S = 210 \text{ ft}^2$
$\bar{c} = 5.6 \text{ ft}$	$S_H = 10\% S$, "LARGE" CANARD
$A = 8$	$S_V = 13\% S$, IN 3 FINS
$t/c = 15\%$	$C_{Lx} = 1.1$ WITHOUT FLAPS
$dc_L/d\alpha = 0.07$	$C_{Dmin} = 0.021$
28° ANGLE OF SWEEP	ALL MOVABLE CANARD SURFACE

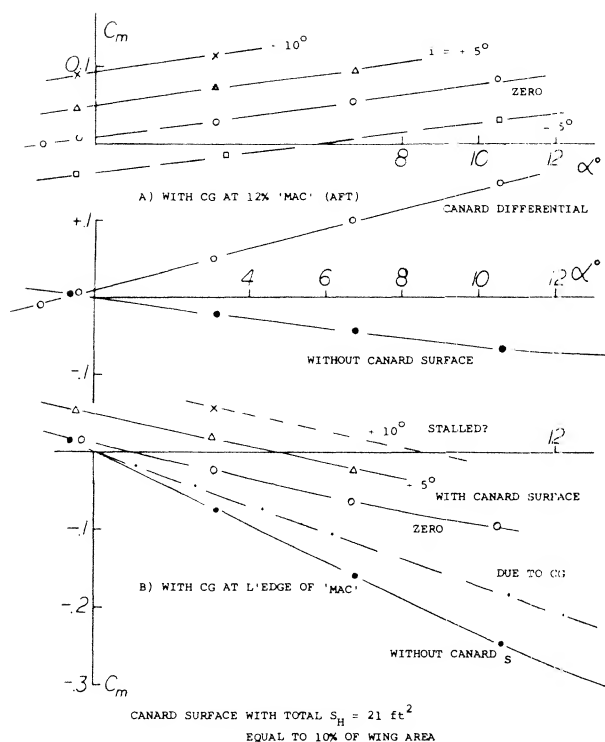
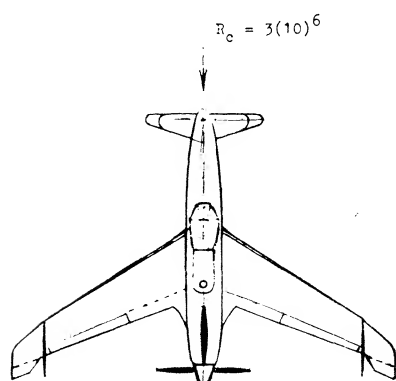


Figure 33. Longitudinal characteristics of Curtiss P-55 airplane, as tested (23,b) in the Full-Scale Tunnel. Data of full-scale craft listed.

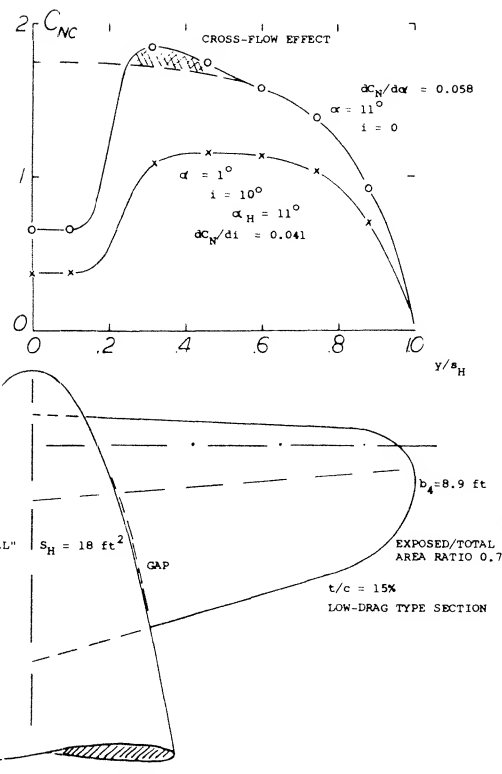


Figure 34. Lift or load distribution of the "small" (23,b) canard surface of the Airplane as in figure 33. P-55.

Stalling of the canard surface takes place at $\alpha \approx 15^\circ$, where $C_{LH} \approx 1.0$. Stability is still preserved at the corresponding lift coefficient of the wing ($C_L \approx 0.6$). In fact, stability increases on account of stalling. It is completely *impossible*, however, to trim the airplane above this limiting coefficient. Since negative lift in the canard surface will "never" be of any practical interest, the airfoil section used should preferably be cambered, thus providing higher maximum lift. To avoid sudden stalling (which might prove to be "fatal" for the airplane) the section shape should be such that stalling starts gently (from the trailing edge). One way of extending the range of effectiveness of the canard surface, is to make its surface larger. Roughly, to double the maximum lift coefficient at which the P-55 could be flown (from $C_L = 0.6$ to 1.2) it would be necessary to double the size of the stabilizer area (from 10% to 20% of the wing area).

Aspect Ratio. It is basically desirable that the canard foil produces comparatively large positive lift-forces — with a lift-curve slope as low as practicable. Therefore, the canard surface should have a small aspect ratio. For example, the "larger" surface ($S_H = 10\% S$) used in the configuration in figure 33, has a geometrical $A = 6.8$. Upon reducing this ratio, say to 1/3, its lift curve slope can be expected to be reduced to 70%. As a consequence, stability would be increased by $\Delta (dC_m/dC_L) = -0.06$. After relocating the CG, accordingly, control (trim) might then be obtained up to $C_L \approx 0.8$ (instead of 0.5 as with the large-aspect-ratio canard surface).

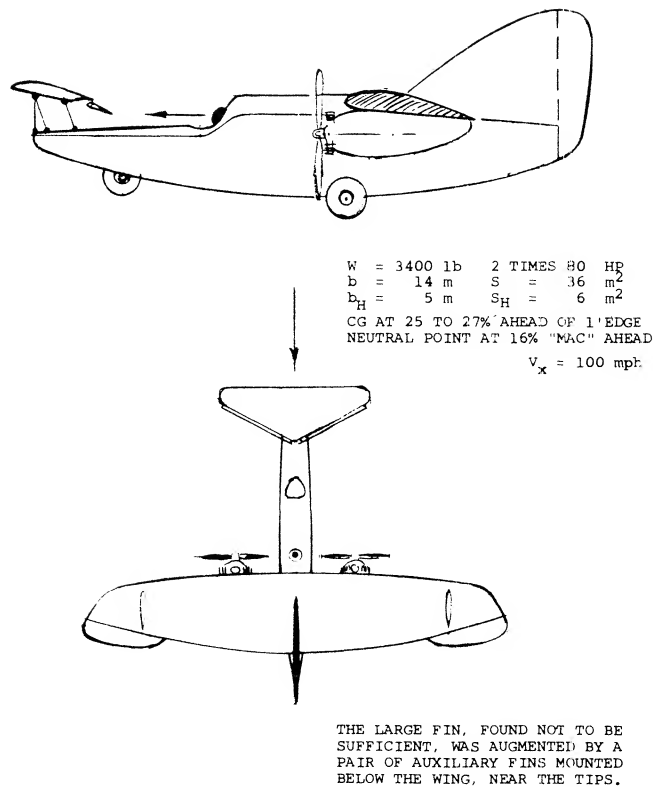


Figure 35. Focke-Wulf F-19 "Ente" research airplane, built and flight-tested (23,a,b) between 1927 and in 1936.

Full Scale Experience. One of the few canard-type airplanes built and flight-tested is the Focke-Wulf "Ente" (first 1927, and then 1936), shown in figure 35. Reports by its designer and the principal research pilot (23,a,b) reveal practical results as follows:

A) Advantages:

- (a) It is true that the wing of a canard-type airplane cannot be stalled.
- (b) The canard type does not have any slipstream interference.
- (c) Lateral (aileron) control is fully available, at all times.
- (d) Even when and if the airplane could be controlled to angles of attack above stalling (as tested to $\alpha = 45^\circ$, in a wind tunnel) spinning is "safe"; the CG located "ahead" of the wing prevents flat spins.
- (e) The configuration lends itself to the use of a nose-wheel tricycle landing gear.

B) Disadvantages:

- (a) When the canard surface stalls, the airplane recovers by way of a certain dive. This is dangerous when it happens near the ground and in particular during the landing approach.

- (b) The fuselage (extending far forward) is destabilizing about the vertical or normal axis. As a consequence, unusually large vertical "tail" surfaces are required.
- (c) Longitudinal control is sluggish by comparison, particularly during take-off where the slipstream does not help.
- (d) In regard to speed performance, the canard configuration is said to be potentially inefficient.

In view of the positive load to be carried by the canard surface, the 1936 "Ente" had an area ratio $S_H/S = 17\%$, a well-cambered section, set at an angle of $i = +10^\circ$, and it is equipped with full-span trailing-edge flaps, used as elevators. At a usual CG position 26% "mac" ahead of the wing's l'edge, the stability corresponds to $dC_m/dC_L = -0.10$. When taking off at $C_L = 1.2$ (total on wing surface), the lift coefficient in the canard surface must have been C_{LH} between 1 and 2.

High-Speed Configurations. While the canard configuration does not seem to be profitable when used in otherwise conventional airplanes, there may be other applications where stabilization by means of a surface ahead of the wing will be desirable:

- (a) in winged and guided missiles, where higher lift coefficients (as in airplanes when landing) may not be required.
- (b) in supersonic and low-aspect ratio airplanes, where the canard arrangement is said to present less drag.
- (c) in configurations where the engines and their weight are located aft, a comparatively long portion of the fuselage is ahead of the wing. The fuselage can, therefore, conveniently be utilized as a "boom" supporting the horizontal control surface.

Supersonic Airplane. Figure 36 presents the pitching moments of a straight-wing configuration, tested at $M = 0.7$. As explained elsewhere, lifting and longitudinal characteristics at this M -number, are essentially or qualitatively as in incompressible fluid flow. From figure 36 it is noted that:

- (a) Because of the low aspect ratios of 3.0 and 3.1, the $C_L(\alpha)$ functions of wing and control surface are slightly non-linear.
- (b) The wing pitching moment non-linearity is increased by the swept-back position of the sharp lateral edges, in reference to the CG.
- (c) After including a certain non-linear component due to the fuselage, the $C_m(C_L)$ function of wing plus fuselage, is distinctly non-linear. This is to say, the value of the negative C_m grows with C_L at an increasing rate.

- (d) After adding the positive moment due to the canard surface, stability is reduced to zero at C_L near zero, for a position of the CG at 3% of the "mac". The pitching moment coefficient increases roughly as $C_m = -0.2 C_L^2$.
- (e) The canard foil stalls at $\alpha_H = 10^\circ$, where its lift coefficient is somewhat above 0.5 and the moment contribution C_{mH} between 0.07 and 0.08.

To Improve the longitudinal characteristics, the nonlinearities characteristics of the wing (not the canard surface) should be eliminated, the maximum lift of the canard surface should be increased and its lift-curve slope be reduced. Steps as follows would be suitable:

- 1) reduce the canard A'ratio, and increase its area at the same time,
- 2) increase the canard moment arm, thus assisting area,
- 3) reduce sweepback (making leading edge straight),
- 4) reduce the fuselage diameter, if possible.

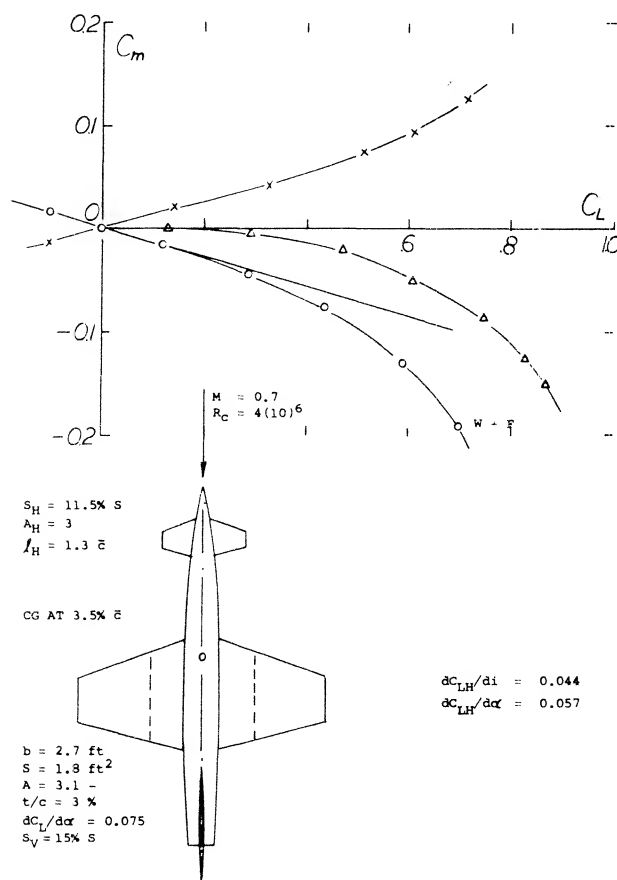


Figure 36. Pitching moment characteristics of a high-speed airplane configuration, with canard control (25,a).

(25) Characteristics of high-speed canard designs:

- a) Peterson, With Straight-Wing, NACA RM A57K27.
- b) Boyd, Delta Configurations, RM A57J15 and A57K14.
- c) Peterson, Delta at High Speeds, RM A57K26.
- d) For comparison see same wing-body combinations as in (a),(b),(c), with horizontal tail aft in (19).

LONG: $l_H = 1.8 \bar{c}$
 $v_H = 0.23$
 $S_H = 7\% S$ EXPOSED
 $= 13\% S$ TOTAL

SHORT: $l_H = 1.2 \bar{c}$
 $v_H = 0.15$

$b = 2.2 \text{ ft}$
 $A = 2$
 0003-63
 $\Delta C_{LH}/\Delta\alpha = 0.05$
 $S = b^2/2$ (TOTAL)

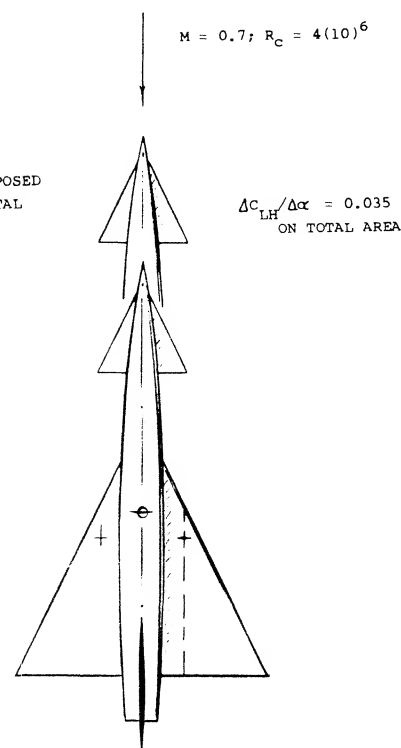


Figure 37. Longitudinal characteristics of a high-speed delta-wing canard configuration, tested (25,b) at $M = 0.7$, with two different lengths of fuselage and canard moment arm.

Fuselage Length. Comparative tests on the delta-wing configuration as in figure 37, show the influence of the length of fuselage and canard moment arm:

- (a) The lift in the exposed panels of the canard surface is independent of fuselage length; $\Delta C_N/\Delta\alpha = 0.063$, based on exposed area (equal to 6.9% of that of the wing).
- (b) The canard moment arms are $l_H = 1.2 \bar{c}$ for the short, and $1.8 \bar{c}$ for the long fuselage; the ratio is ≈ 1.5 . By comparison, the moment differentials due to the surface correspond to a ratio of 1.8.
- (c) The longer fuselage causes an increment $\Delta(dC_m/dC_L)$ between + 0.03 and + 0.04.
- (d) The canard surface stalls at an angle of attack ($\alpha + i$) $\approx 25^\circ$, where its lift or normal-force coefficient is in the order of 1.4. The corresponding maximum canard contribution is analytically:

$$C_{mH} = + 1.4 (0.069) 1.2 \approx + 0.12 \text{ for the short fuselage}$$

$$= + 1.4 (0.069) 1.8 \approx + 0.18 \text{ for the long fuselage}$$

As discussed in the next paragraph, the "long" moment is even larger than this. The longer fuselage thus permits either to trim to at least 1.5 times the wing lift coefficient, or to compensate for at least 1.5 times in terms of $\Delta(dC_m/dC_L)$ of the configuration.

Interference. The canard surface leaves behind a certain downwash — and a pair of tip vortices. The possible interference of this system with the wing is mentioned in several reports (25). In the case where the canard surface is large the downwash is highly destabilizing. However if the distance is large and the front surface small the consequences of such interference are of minor importance. Theory predicts that the two lifting surfaces have the same induced characteristics as a wing to whose load distribution the lift of the canard surface is added. In reality, the wing load is expected to be reduced in the center, and to be increased outside the canard span. Again, this may not be important in a small straight wing. However, in the example of a delta wing as in figure 37, a relocation of lift from the center outboard, can be expected to make the wing's pitching moment more negative (nose-down and stabilizing). There is some indication of possible interference in (b) above, where the canard moment grows to "1.8", while the moment arm ratio is only 1.5. It can be speculated that the short-fuselage design exhibits a differential due to interference in the order of $\Delta(dC_m/dC_L) = -0.02$. This differential can readily be explained, as above. The fact that the long configuration does *not* experience a similar differential, may be associated with the much longer distance that the downwash field has to proceed, before it reaches the wing. It is also likely that the canard downwash reduces the positive moment of the fuselage. Finally, $d\epsilon/d\alpha$ at the location of the wing, must be expected to reduce, as the angle of attack is increased.

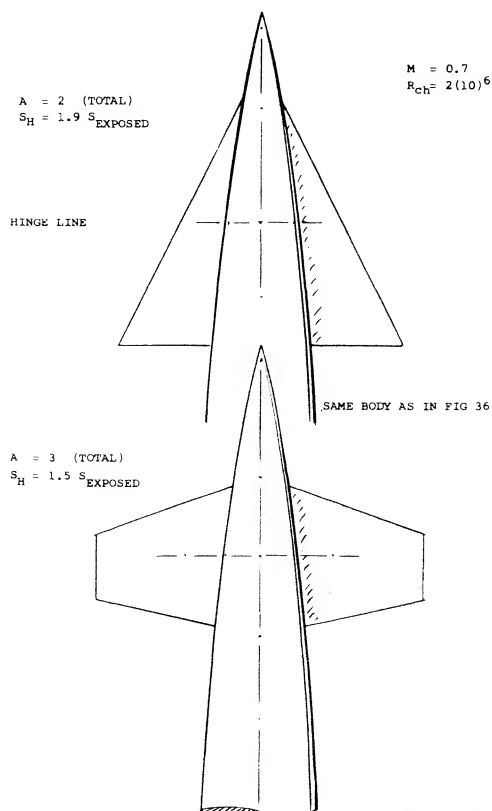


Figure 38. Lifting characteristics of two canard surfaces differing in shape and aspect ratio as tested (25,b,c) on one and the same fuselage body.

Delta Canard While above, the moment arm of the canard surface is found to be of value in postponing stalling, the fact remains that this surface *always contributes a destabilizing moment*. Using equations (38) and (44), the location of the neutral point behind the canard surface is found to be

$$l_i/l = (S/S_c)/(1 + S/S_c)(dC_L/d\alpha)/(dC_L/d\alpha) \quad (47)$$

Stability can thus be increased by reducing the lift-curve slope of the canard, in comparison to that of the wing. In view of

$$d\alpha/dC_L \approx 11 + 20/A$$

(Chapter III) this can be done by reducing the aspect ratio of the canard surface. When, for example, a wing with $A = 6$ is combined with a canard surface having $A_H = 6$, equation (44) indicates $l_i/l = 5/6$. Reducing A_H , say to 2, we obtain the ratio

$$(dC_L/d\alpha)/(dC_L/d\alpha)_H =$$

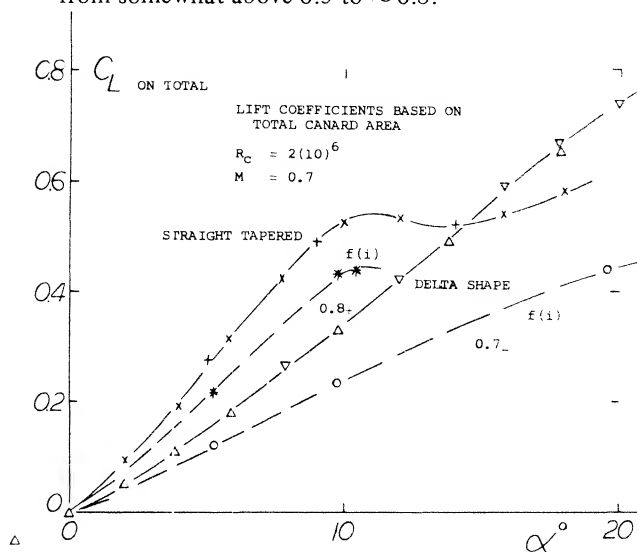
$$(d\alpha/dC_L)_H/(d\alpha/dC_L) \approx 1.5$$

and a neutral point at

$$l_i/l = 7.5/8.5 = 0.88$$

instead of $5/6 = 0.83$. The difference is 0.05. — A particular version of an aspect-ratio-2 canard surface, is the delta shape in figure 38. In comparison to a straight surface (with $A = 3$) it is seen:

- that the lift-curve slope $\Delta C_L/\Delta\alpha$, at $\alpha = 8^\circ$, is reduced from 0.055 to 0.033.
- that the stalling angle is increased from 10° to above 20° , and the maximum useable canard lift coefficient from somewhat above 0.5 to ≈ 0.8 .



7. CHARACTERISTICS OF TAILLESS CONFIGURATIONS

Considering performance (drag), tail surfaces are basically an operational necessity, usually not contributing to lift. Also, to support them in their conventional place, the fuselage must be made longer than it would have to be, just to house payload and equipment. During some 40 years of aviation history, therefore, the idea has been advanced, discussed (27), investigated and partly converted into hardware, of flying without a tail in a wing-only airplane.

Stability of Airfoil (26). The pitching moment of an airfoil section, about an assumed CG (on chord line) is

$$C_{m_g} = C_{m_0} + (\Delta x/c) C_L \quad (48)$$

where $x = g - a$ = distance between CG and AC (which may be at $\sim 24\%$ c). The stability derivative

$$dC_{m_g}/dC_L = -\Delta x/c \quad (49)$$

is negative = stable, as long as the CG is located ahead of the AC, ie, forward of $\approx 24\%$ of the chord. In order to obtain balance, it is now necessary to keep

$$\begin{aligned} C_{m_0} + (\Delta x/c) C_L &= \text{zero}; \\ \text{or } C_{m_0} &= -(\Delta x/c) C_L \end{aligned} \quad (50)$$

This can be done by changing camber such as deflecting a trailing edge flap. For positive lift coefficients, an airfoil section with reflexed camber line promises to be most efficient. Such a section (with $C_{m_0} = 0$) can then be trimmed to a desired positive lift coefficient by pulling the flap up. Theoretically, stable and balanced flight can thus be obtained in a simple wing. For example, for a CG location at 22% c, the static stability derivative may be $0.22 - 0.24 = 0.02$. Using derivatives as found in the Chapter IX, the required deflection of a 20% flap, would be $\delta \approx -4 C_L$. For each additional $\%$ of the chord through which the CG is moved forward, another $\Delta(\delta/dC_L) = -2^\circ$ will be required.

Wing Sweep. A tailless airplane, simply relying on the qualities of a straight wing, is likely to be very sensitive. The wing would provide too little damping (about the lateral axis). A swept wing (having a longer length, between apex and rear end of the lateral edges) would, therefore, be more suitable, using the wing tips for stabilization and control. Considering the areas near the tips to be a pair of horizontal tail surfaces, we then have a configuration which is basically similar to the conventional wing plus tail arrangement. The wing tips can and have also been used to carry a pair of vertical fins, to provide directional stability and control. One of the first such airplanes built and flown was by Dunne in 1910. This airplane was propelled by a pusher propeller, conveniently located “in” the center of the configuration. An early British development was the “Pterodactyl” (28,a,b). Several similar airplanes (most of them gliders) were designed and built by Lippisch (28,c).

Wing Flaps in or near the center of the wing, could “never” be balanced in a straight-wing tailless airplane. However, as explained in the “wing” chapter, the center of the lift produced by trailing-edge flaps, is (at least theoretically) at or slightly ahead of 50% of the chord. Therefore, in a sufficiently swept wing, inboard flaps can produce lift at a location ahead of the wing’s aerodynamic axis. As proposed in (28,b) such flaps could then also be used for pitch control; and their $d(\Delta C_L)/dC_L$ would be positive rather than negative (as explained above for elevons), when using them as “elevators”.

Swept-Forward Another solution to control a tailless airplane, is to sweep the wing forward, as for example, in the design in figure 39. The configuration can be trimmed by pulling up the inboard flaps. Using the average tested value $dC_m/d\delta^\circ = 0.005$, a flap deflection $\delta^\circ = 8^\circ$ is needed, for example, to balance the moment at $C_L = 1.0$. It seems however, that conditions (and shortcomings) basically remain as they are in a swept-back wing configuration.

(28) Consideration of tailless airplanes:

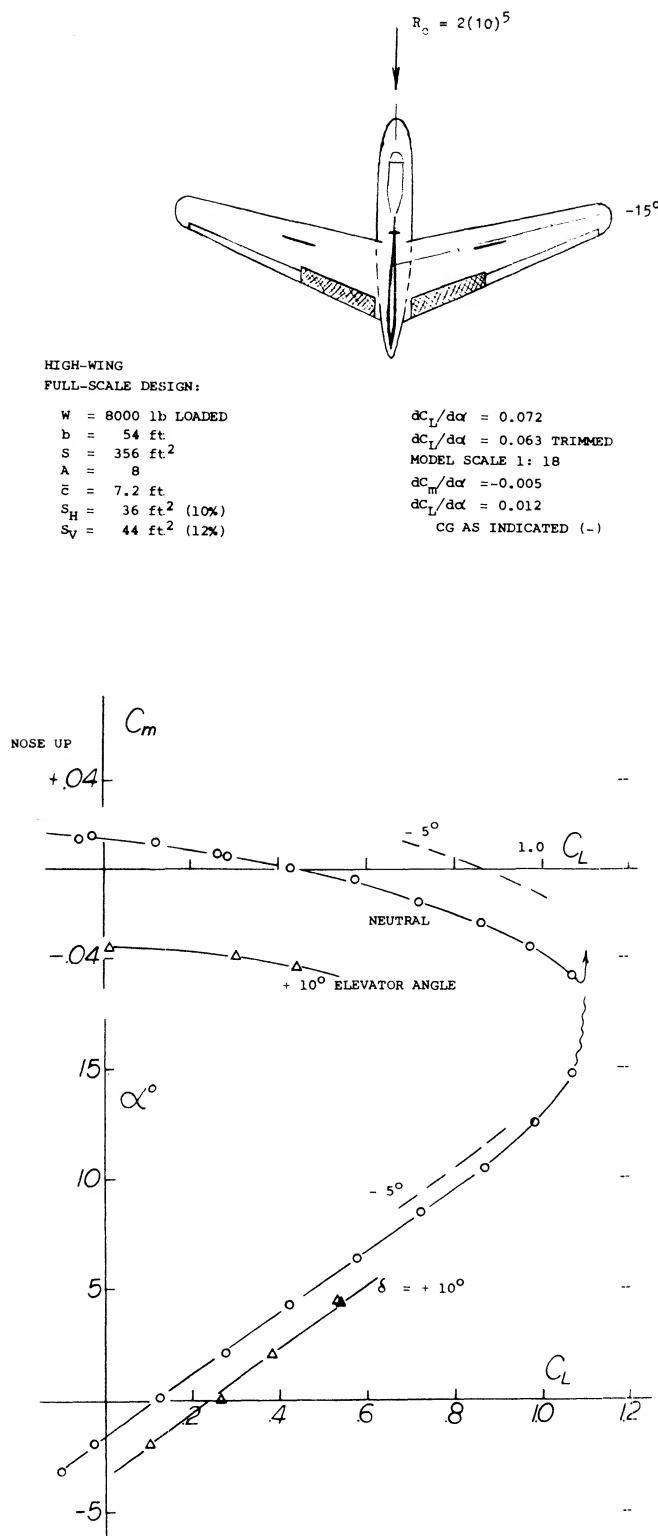
- a) Hill, Tailless Airplane, J RAS 1926 p 519.
- b) Jones, Stability & Control, NACA TN 837 (1941).
- c) Lippisch, “Storch” Glider, L’Aerophile Feb 1930 p 35 (NACA TM 564); also “Dreieck I”, NACA AC-159 (1932).
- d) Donlan, Stability & Control, NACA T Rpt 796 (1944).

(29) Characteristics of tailless airplanes, tested:

- a) Weick, Swept Wing, NACA TN 463 (1933).
- b) Lippisch, “Storch” Type, Ybk D Lufo 1937 p I-300.
- c) Gates, “Pterodactyl” Design, ARC RM 1423 (1932).
- d) Stone, Cornelius Glider, NACA W Rpt L-738 (1946).
- e) Brewer, Northrup in F-Scale Tunnel, W Rpt L-628 (1944).
- f) Tailless Airplane, see NACA W Rpts L-42 and L-50.

(26) Wurster, Analysis and Experimental Investigation of Stable (swept and twisted) Wings, Ybk D Lufo 1937 p I-115.

(27) Ankenbruck, Comparison of Performance, Conventional/-Tailless/Tail-Boom, NACA TN 1477 (1947).



Delta Wings. Aircraft using a delta wing lends itself naturally to be without horizontal tail. Tunnel results on a model similar to the original Convair F-102, are shown in figure 40. Below the stall (at an untrimmed lift coefficient $C_L \approx 1.3$) the neutral point is at $\approx 35\%$ "mac". To trim the airplane, an elevon deflection

$$d\delta/dC_L = -(dC_m/dC_L)/(dC_m/d\delta) = -0.04/0.005 = -8^\circ$$

is necessary for the CG location as during the tests. In other words, to trim the airplane to $C_L = 1.0$, an elevon angle $\delta = -8^\circ$ is required. At the same time, the airplane loses some lift corresponding to

$$\Delta C_L/C_L = (dC_L/d\delta)(d\delta/dC_L) = -0.013(8) \approx -10\%$$

The maximum lift coefficient is reduced, corresponding to an elevon deflection $\delta = -30^\circ$ required to trim.

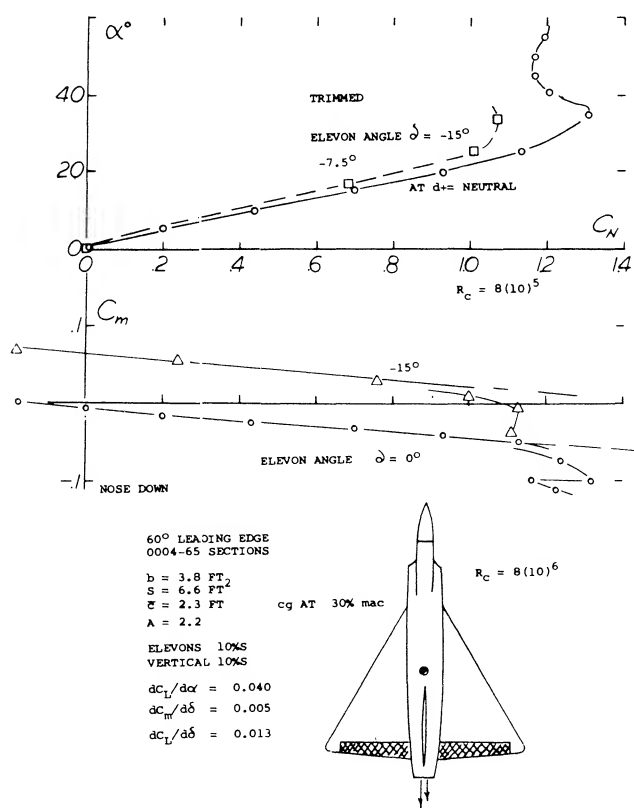


Figure 40. Delta-wing configuration similar to Convair F-102, tested at $M = 0.7$ (30,a).

Figure 39. Characteristics of a tailless, swept-forward fuel-glider design. Tested at $R_C = 2(10)^5$.

- (30) High-speed tailless delta airplanes:
- Hewes, 60 Delta Configuration, NACA RM L54G22a.
 - White, Flight-Tested, NASA Memo 4-15-59A, Douglas F4D-1. Other characteristics of same airplane, see RM A52E23/J30/J31.
- (31) "Tailless" rocket-powered interceptor airplane Me-163, see Chapter XIV of "Fluid-Dynamic Drag".

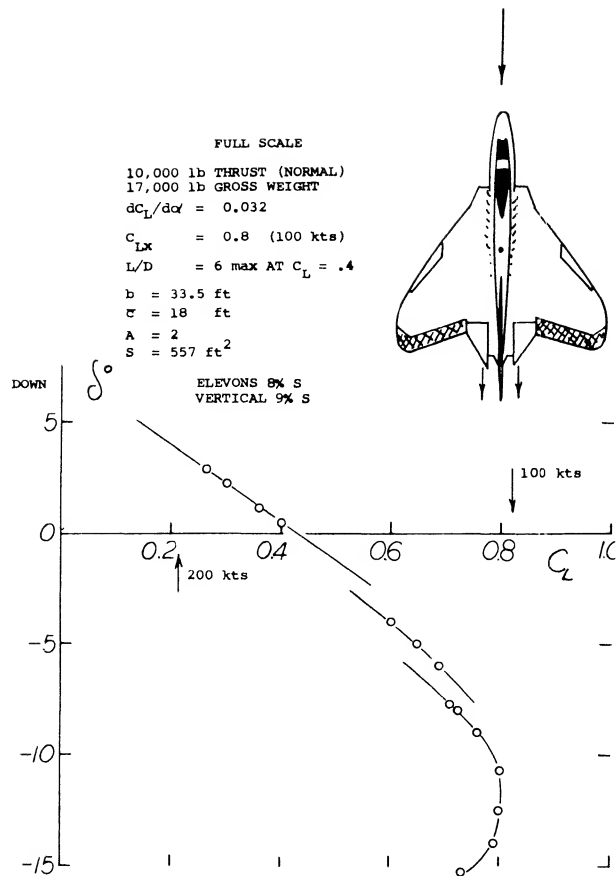


Figure 41. Elevon angle required of Douglas F 40-1 carrier-based airplane (30,b).

Trim Required. Results of flight tests on a full-scale carrier-based jet airplane are reported in figure 41. The discontinuities in the elevon deflection are confirmed by corresponding jumps in the stick force. They seem to be a consequence of the automatic leading-edge slats as shown in the illustration. For the CG location as tested, the elevon angle corresponds to $d\delta/dC_L = -14^\circ$. Assuming that other derivatives might be similar in magnitude to those of the model in figure 40, the static stability may be

$$dC_m/dC_L = -(dC_m/d\delta)(d\delta/dC_L) = -0.005(14) = -0.07$$

in the condition as tested. The neutral point of the airplane would then be at $24.4 + 7.0 = 31.4\%$ of the "mac". The trimmed maximum lift coefficient ($C_{L\alpha} = 0.8$) is obtained with the help of $\delta = -11$ or -12° . It seems that the slats make the elevons more effective at higher angles of attack, although they do not help to increase the maximum operationally obtainable lift.

Interceptor. The research efforts reported in (28,c) and (29,b) eventually led to the first rocket-powered and "tailless", operational airplane (31). Here as in many other configurations designed without a special horizontal control surface, one can argue whether a vertical surface is a tail or not. Apart from delta designs, one of the very few operational tailless airplanes is or was the U.S. Navy's F7U-1 "Cutlass" fighter (33). To provide directional stability, this airplane carries a pair of fins (above the wing), each approximately at $\frac{1}{2}$ span. Principles of tailless airplanes and some results of model tests are presented in (32).

Conclusion. After reviewing various aspects of tailless airplanes, it may seem that the original idea of saving wetted area (by combining, at least the horizontal tail with the wing) will not necessarily reduce drag. A larger wing area will most likely result, and larger vertical fins. It has also been explained in (27) that size and speed of the airplane are to be considered together with the problem of the tail. In particular, modern high-speed airplanes have fuselages which are large in comparison to the wings. As a consequence:

- (a) The original idea of stowing away everything within the wing, can no longer be realized.
- (b) The fuselage is available anyhow as a "boom" to carry both the vertical and the horizontal tail surfaces.

However, there can always be reasons apart from performance, to make a tailless airplane desirable. One such type of configuration is delta-wing fighter airplanes. See Chapter XVIII.

(32) Donlan, Longitudinal and Lateral Characteristics of Tailless Airplanes, NACA T Rpt 796 (1944).

(33) U. S. Navy "Cutlass" F7U-1, by Chance Vought, "fastest Navy fighter in production"; see Jane's All the World's Aircraft 1952, or "Aero Digest" Annual Directory 1951 p 37.
 $b \approx 40$ ft $W \approx 27,000$ lb
 $V_x \approx 600$ kts $T_x \approx 10,000$ lb

CHAPTER XII — PROPULSION LIFT AND STABILITY

The lift force by the propulsion system may range from zero to over one hundred percent of the weight of the aircraft as in the case of helicopters. The propulsion system of STOL airplanes may generate lift directly or may induce increased levels of lift from the increased velocity of the slipstream passing over the wings and fuselage. The addition of lift with boundary layer control either by blowing or sucking is a form of propulsion lift, as power must be directly expended. In this context all types of lift could be thought of as powered lift; however, we shall define propulsion lift as that generated by the device normally used only for overcoming the drag of the airplane. The effects of the wash or slipstream on the wing lift produced by the propulsion devices will also be included in this chapter. The lift increment from boundary layer control through the use of power by internal blowing or sucking is discussed in Chapters V and IV.

Because the lift force produced by the propulsion device can be large it has an important effect on the stability of the airplane. This will be considered in terms of the lift, moments and interaction developed by the propulsion device.

1. LIFT OF PROPULSION SYSTEMS

All types of propulsion systems will generate lift as well as thrust; the level depending on the operating angle of attack of the system, the flight condition and the type. Propulsion systems generate thrust by imparting an increase of velocity to the mass of fluid handled. If the fluid is deflected downward as illustrated in figure 1, then a lift force is produced as well as thrust force. The levels of lift produced will depend on the mass of fluid handled and velocity imparted in the downward direction, figure 1. Thrust systems are classed in terms of disk loading, the thrust per unit disk area, as illustrated in the table:

THRUST DEVICE	RANGE OF DISK LOADING — T/S-psf
Helicopter Rotor	5 to 15
VTOL Propeller	15 to 50
STOL Propeller	30 to 70
Conventional Propeller	40 to 90
Ducted Fan	100 to 150
Lift Engine	500 to 700
Turbo Fan	1200 to 1500
Jet Engine	~ 1700

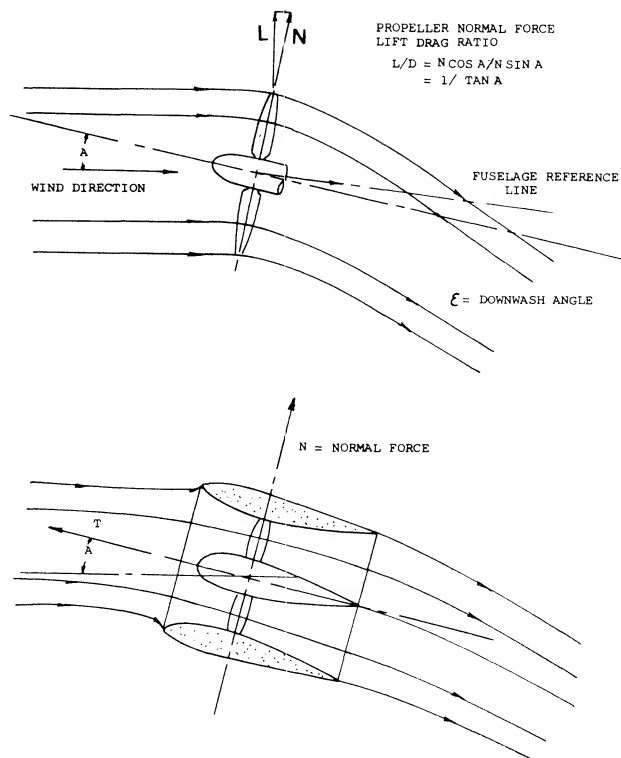


Figure 1. Flow and forces of propellers and ducted fans operating at an angle of attack.

The thrust or the lift to power ratio of the engine types given in the above table operating at the static condition is given on figure 2. The large thrust to power ratio shown at low disk loadings is the reason for the use of these loadings on helicopter rotors. The propulsion devices given in the above table are also listed in the order of the mass flow handled. The largest devices handle the greatest mass flow and give the fluid the smallest increase in velocity since the mass flow,

$$m = \rho A \Delta V$$

$$T = m \Delta V$$

where V is the velocity through the disk area A and ΔV is the increment of velocity imparted to the air.

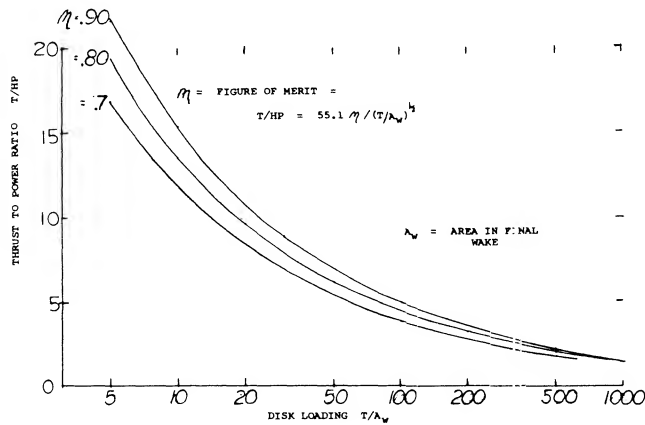


Figure 2. Thrust to power variation of helicopter rotors, propellers, ducted fans and turbofan engines as function of disk loading.

LIFT - Thrust Characteristics, Rotors and Propellers. The lift and thrust produced by rotors and propellers are generated in basically the same manner and depends to a large extent on the operating condition and shaft angle of attack. When the rotor is operating at an angle of 90° all the thrust produced equals lift, figure 2, whereas at a shaft angle equal to zero the lift is zero. At a condition where the rotor shaft is at an angle of attack with respect to the free stream a force in the plane of the disk is produced known as the normal force. Thus, in addition to the lift produced by the component of thrust in the vertical plane, lift is also produced from the normal force vector resolved in the vertical plane. This normal force is shown in comparison to that produced by a wing on figure 3.

The propeller or rotor produces a normal force only when the shaft is operating at an angle of attack with respect to the wind direction. The manner in which this force is developed is discussed in (1) and is illustrated as follows:

Consider a propeller operating at an angle of attack as shown in figure 4. Assume the propeller has four blades and that two of the blades are at the horizontal position. From figure 4 it will be noted that when the blades are at the horizontal position an increase in lift on the blade advancing down and a decrease in lift on the blade coming up are obtained. This is the result of the increase and decrease of section angle of attack and speed on the blades going down and up, respectively. It will be seen that these forces resolve themselves into a normal force in the axis of rotation and that the forces also result in a turning or yawing moment about the shaft.

The equations for calculating the normal force and moment have been derived from blade element theory in a manner such as given in (1) as follows:

$$F_N = \frac{B}{2} q \left(\frac{1}{2} \sin 2A \right) \int_0^R \times \left(\frac{a \sin \phi}{1 + \frac{\tan A \sin 2\phi}{2}} + 2C_L \cos \gamma \right) b dr \quad (2)$$

$$M = \frac{B}{2} q \left(\frac{1}{2} \sin 2A \right) \int_0^R \times \left(\frac{a \cos \phi}{1 + \frac{\tan A \sin 2\phi}{2}} + 2C_L \cos \gamma \right) b r dr \quad (3)$$

where

F_N = normal force

M = shaft moment

B = blade number

q = dynamic pressure = $\frac{1}{2} \rho V^2$

a = slope of lift curve

ϕ = relative wind angle

$\gamma = \tan^{-1} \frac{V \cos A}{x \pi n D + V \sin A}$

b = blade chord

R = propeller radius

- (1) Normal force theory -- isolated propellers:
 - a) Flachsbar, experiments, ZFM 1929 p 606 (NACA TM 562).
 - b) Lesley, Propeller in Yaw, NACA T Rpt (1937).
 - c) Ribner, Propellers in Yaw, NACA T Rpts 819 & 820 (1945).
 - d) Crigler, Calculation of Forces, NACA TN 2585 (1952); see also Correlation in W Rpt L-362 (1944).
 - e) Demele, Normal Forces, NACA RM A54D22.

For a right-hand rotating propeller with positive lift normal force, the moment results in yaw couple to the left; the opposite being true for a left-hand propeller.

It can be shown for small values of A equations 2 and 3 can be reduced to

$$F_N = K' BAqAFD^2 \sin \beta_{0.7} (a_{0.7} + 2C_{L0.7} \cot \beta_{0.7}) / K_i \quad (4)$$

$$M = K' BAqAFD^2 \cos \beta_{0.7} (a_{0.7} + 2C_{L0.7} \cot \beta_{0.7}) / K_i \quad (5)$$

where

$$K' = 1.1$$

$$AF = \text{activity factor}$$

$$D = \text{propeller diameter}$$

$$\beta_{0.7} = \text{blade angle measured at the 0.7 blade radius}$$

$$C_L = \text{operating lift coefficient}$$

$$K_i = 450,000$$

Equations 4 and 5 give a good first approximation of the normal force and moment at angles up to $\sim 15^\circ$.

The calculation of the propeller normal force above is based on the assumption that the slope of the lift curve slope for two dimensional flow applies and is not affected by the cyclic variation of the lift force ΔL , figure 4. This is a reasonable assumption up to a shaft angle of 45° as the variation of lift causes a change in the strength of the shed vortices which cancels at the blade, allowing the use of equation 3 for calculating the in plane normal force.

- (2) Normal Force Test Data – isolated propellers:
- McLemore, Angle of Attack to 180° , NACA TN 3228 (1954).
 - v.Doepp, Junkers Results, ZWB Tech Berichte 1941 p 61.
 - Yaggy, 3 Propellers to $\alpha = 85^\circ$, NASA TN D-318 (1960).
 - Weil, Two Propellers, NACA T Rpt 941 (1949).

- (3) Upwash ahead of straight wings:
- Roberts, Twin-Engine Airplane, NACA TN 2192 (1950).
 - Yaggy, Survey (TN 2192) and Prediction (TN 2528), NACA.
 - Rogallo, Analysis, NACA T Rpt 1295 (1956); also for swept wings in TN 2795, 2894, 2957 (1952/53).

Comparisons of the test (2,c) and calculated values of normal force based on equations 3 and 4 show generally good agreement up to shaft angles of 45° , figure 5. At shaft angles above 60° the correlation is poor and more refined methods based on helicopter theories must be used.

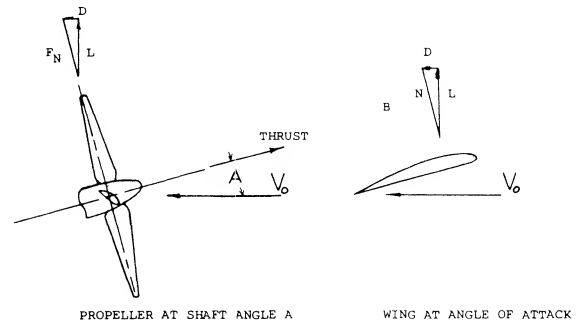


Figure 3. Comparison of normal force produced by wings and propellers.

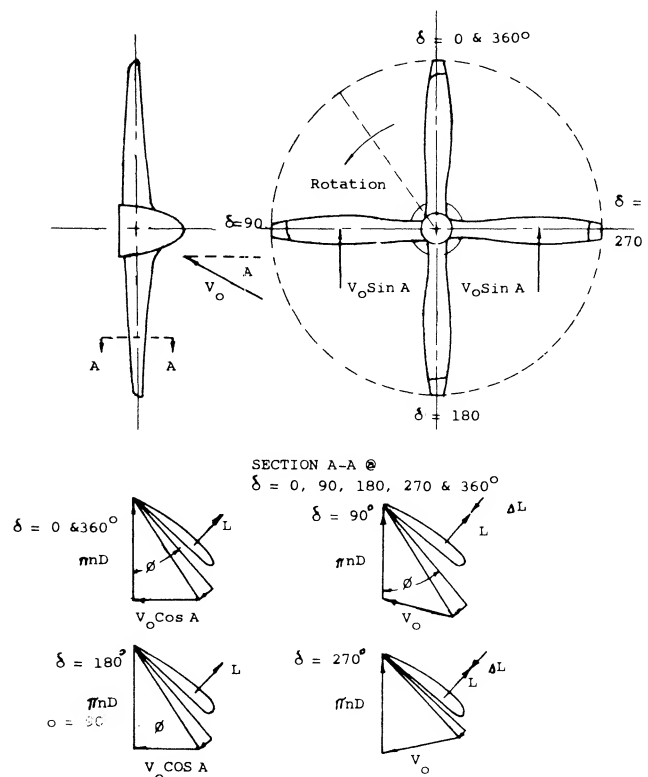


Figure 4. Force and velocity diagram of a propeller at angle of Attack A.

- (4) Normal Force V/STOL Aircraft:
- Borst, The High-Speed VTOL X-100 and M200 Aircraft, Aerospace Engineering, August 1962.
 - Borst, The X-19 VTOL Aircraft, NYAS, Vol 107, 1963.
 - Kuchemann and Weber, Aerodynamics of Propulsion, McGraw-Hill Book Co., New York 1953.

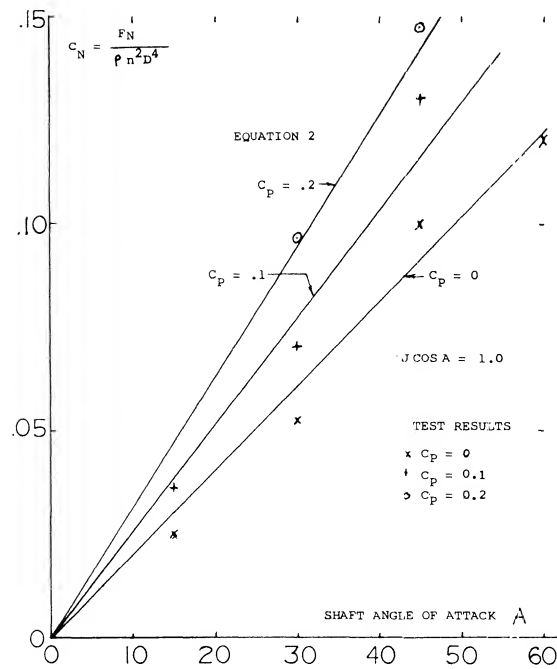


Figure 5. Comparison of test and calculated normal force for an isolated propeller (2,c).

Induced Flow – Upwash. As shown in equations 3 and 4 as well as in figure 5, the flow angle into the disk of the propeller directly influences the normal force. Since propellers are usually installed in front of wing where an upwash is encountered, the inflow angle into the disk is changed from free stream thus influencing the normal force. These changes are large and may be estimated based on the test data of (3) where detailed measurements of the inflow velocity have been made. Computer programs based on theory are also available for estimating the inflow angle at the disk, taking into account the effects of the wing upwash and the variation of the flow about the wing and nacelle. From these methods the inflow angle A should be determined and used in equations 3 and 4 for calculating the propeller forces and moments.

The wing upwash as illustrated on figure 6 generally results in a high inflow angle at the propeller at the climb condition when the aircraft is operating at low speeds and high coefficients. This increases the normal lift force of the propeller.

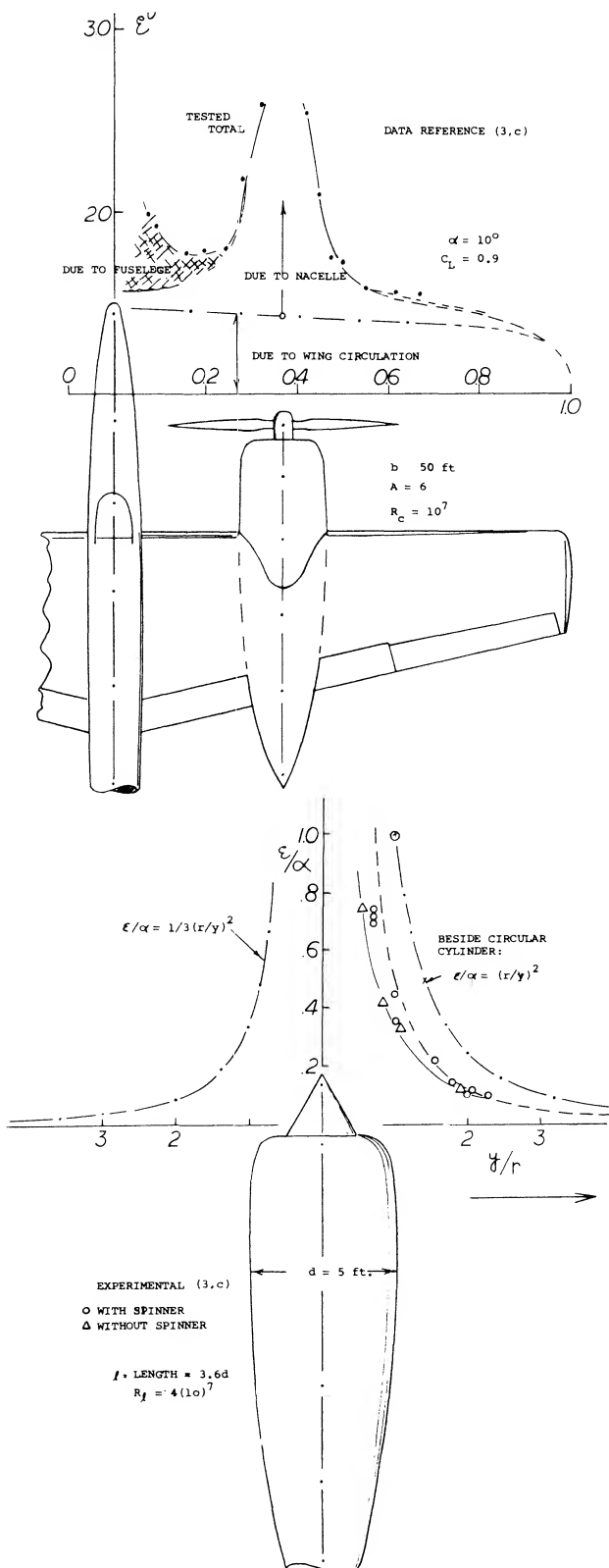


Figure 6. Flow upwash of wing-fuselage-nacelle combination in the plane of the propeller disk.

(5) Ducted Fan Lift:

- Mort, K., 7-Foot Diameter Duct Prop Test, NASA TN D-4142.
- Goodson, Tilting-Shrouded-Propeller VTOL Model, NASA TN D-987.
- V/STOL Conf. 1966.
- Grunwald, Shrouded-Propeller Configurations, NASA D-995.
- Koenig, Wingless VTOL Aircraft, TN D-1335.

Propeller Lift and Thrust. The thrust and normal force measured normal to, and in the plane of the disk can be resolved into components in the direction of flight and in the lift direction as shown on figure 3. Resolved in this manner, the lift becomes a straight line function up to very high angles of attack, figure 7. The coefficients C_L and C_X are based on the free stream dynamic pressure and the disk area S_p , thus

$$C_{LP} = (T \sin A + N \cos A) q S_p \quad (6)$$

$$C_{XP} = (T \cos A - N \sin A) q S_p \quad (7)$$

The lift and axial force coefficients C_{LP} and C_{XP} are a function of advance ratio as noted in figure 7 and depend on the detailed characteristics of the propeller as indicated in equations 4 and 5. Note the straight line characteristic of the lift curve. Unlike a wing there is no sudden stall such as shown in Chapter IV. This characteristic is desirable for V/STOL aircraft that must operate through a large variation of angle of attack.

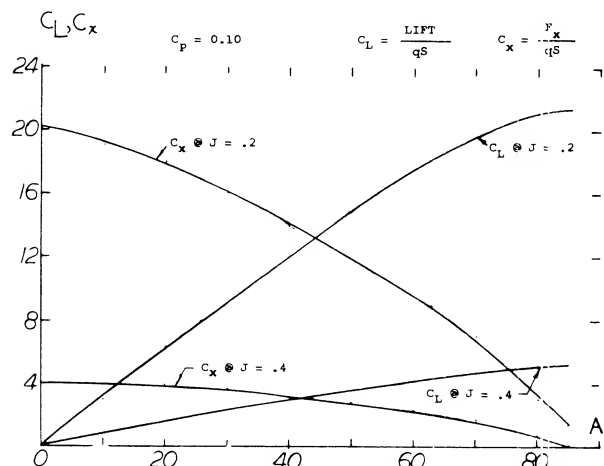


Figure 7. Total axial and vertical force variation of propellers operating at an angle of attack.

Propeller and Rotor Moments. In addition to the thrust and normal force, a rotor or propeller operating at an angle of attack will produce yawing and pitching moments that become large, especially at high angles of attack. The yawing moment developed may be determined based on equations 3 or 5 or from wind tunnel test data, such as (2,c). The pitching moment becomes especially important at high shaft angle for V/STOL aircraft as it becomes a major factor in the design of the longitudinal control power.

For conventional airplanes the yawing moment produced by the propellers is destabilizing for tractor installations if all propellers are rotating in the same direction. This destabilizing moment is usually referred to as the fin effect (1,c) and is a function of the diameter and blade area as noted in equation 5. Since the yawing moment of a propeller at an angle of attack is dependent on the

direction of rotation it can be eliminated on a multi-propeller aircraft with the use of opposite rotation.

Normal Force V/STOL Aircraft. A propeller is a good device for developing high lift power ratios at hover, figure 2, and can produce thrust as well as lift at forward velocity. For this reason it can be used on V/STOL aircraft performing a dual function of providing thrust and lift at all flight conditions. To do this it is necessary to use opposite rotating propellers operating in pairs so the large yawing moments associated with the development of large values of normal force can be cancelled.

With such a system a linear lift force is obtained with angle of attack and it is possible to obtain lift forces of sufficient magnitude to fly an airplane without wings (4). This principle was demonstrated with a full scale airplane, figure 8, where the propellers provided approximately 70% of the lift force at a forward speed of 175 MPH.

In nature, the dragon fly is another example of the use of propulsive lift to fly without fixed wings, figures 9 from (4) illustrates this principle. Although nature does not provide for complete rotation of the wings the rapid oscillation of the wings does simulate the action of a dual rotation propeller, thus providing thrust and lift from the same unit.

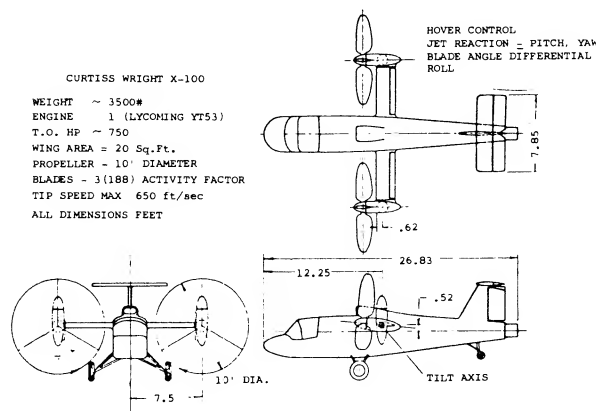


Figure 8. The Curtiss V/STOL X-100 airplane for demonstrating propeller lift with normal force.

As noted in equation 2, the propulsive lift of a rigid propeller is dependent on the shaft angle of attack, the propeller diameter, the total solidity, as well as the operating condition. If the blade angle is varied cyclically the lift force can be further increased. This must be done by increasing the blade angle of the down going blade while decreasing the blade angle of the up going blade. The same mechanism used for increasing the propulsion lift could be used for control at hover and low speeds, as in the case of a helicopter.

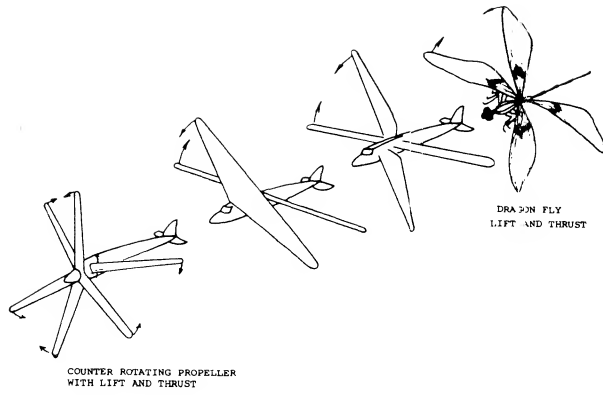


Figure 9. Lift and normal force in nature as shown by the flight of the dragon fly.

The use of the propulsion system to generate lift requires that the shaft angle be low to obtain high values of L/D . From figure 2 it will be noted that

$$L/D = 1/\tan A \quad (8)$$

Thus, to obtain high values of lift drag the shaft angle, A , must be low. This requires that the q as shown in equation 4 be high so that the required lift is obtained at the low A angles.

Ducted Fan-Propellers. The ducted fan or propeller is effective for the production of lift as well as thrust when operating at an angle of attack above zero. The ducted fan has been therefore used and proposed for a number of V/STOL aircraft including a VTOL airplane without wings (5,e). Also because of its high thrust to power and lift ratio, the ducted fan has been applied for the power lift, control and thrust of airships. In the application of ducted fans for producing lift and thrust the duct can be operated at an angle of attack or the exit flow can be deflected with vanes to obtain lift.

The ducted fan is an efficient device especially at low speeds as the interaction between the fan and the duct is mutually advantageous. The induction of flow through the duct by the fan produces a pressure reduction on the leading edge of the duct that gives a duct thrust force which adds to that thrust produced by the fan. The duct controls the flow at the fan and eliminates the radial flow and the tip losses that are associated with conventional open propellers. The elimination of the radial flow at the disk of the ducted fan is only accomplished if the duct is designed to produce the thrust level equal to that needed to obtain the ratio given on figure 9.a. This rotor thrust to the total thrust ratio, T_R/T_T , is dependent on the power level of the rotor and the advance ratio, J . When the duct develops the required thrust ratio the duct flow controls the conditions at the disk and so prevents radial flow, assuming the rotor duct clearance is zero. When designing the duct to achieve the required thrust level a procedure must be used that accounts for the thrust produced

by the rotor and its advance ratio. This procedure is also used for determining the velocity at the rotor as induced by the duct so that the performance of the rotor can be calculated using a procedure such as is given in Chapter II.

The thrust developed by the ducted fan is dependent on the blade to duct tip clearance. These losses are large unless steps are taken to seal the tip or reduce the clearance to a minimum. The efficiency of the fan corrected for the tip loss can be calculated from the equation

$$\eta_c = \eta (1.00002 - 2.654 R_c/R - 158.35 (R_c/R)^2 + 163 (R_c/R)^3) \quad (9)$$

where η_c = the corrected duct fan efficiency
 η = efficiency with zero tip clearance
 R_c = clearance between the rotor tip and duct wall
 R = rotor radius

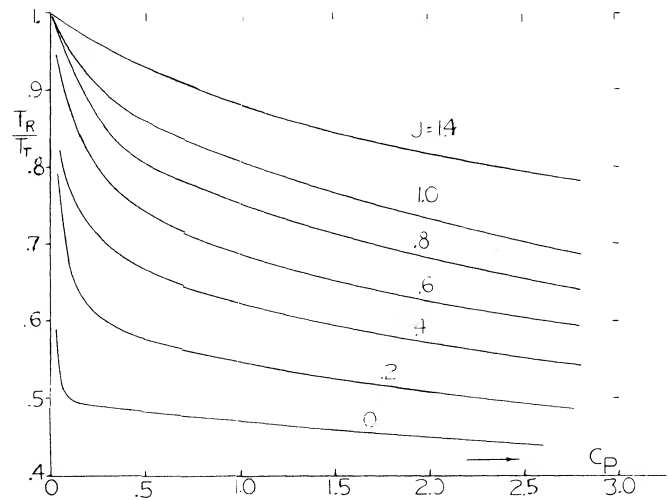


Figure 9a. Rotor thrust to total thrust ratio for ducted fan required to control radial flow.

The ducted fan can be considered to be a ring wing with the fan inducing air through it, figure 10. As such the ducted propeller produces lift when operating at an angle of attack. The lift produced, $(5,a)$ is a function of the advance ratio, the thrust coefficient and the angle of attack as shown on figure 10. The lift, drag, thrust and moment coefficients given on figure 10 are based on q and the projected area of the duct S . Thus

$$\begin{aligned} T_c &= T_o / q S & C_L &= L / q S \\ C_D &= D / q S & C_m &= m / q S \end{aligned} \quad (9)$$

where $S = cde$, de is the exit diameter, and c the duct length.

The values of C_L and C_D , T_C and moment coefficient C_m are high on figure 10 as the tests were conducted at low values of q and advance ratio. At the conditions tested the force in the drag direction is negative and so is a thrust force.

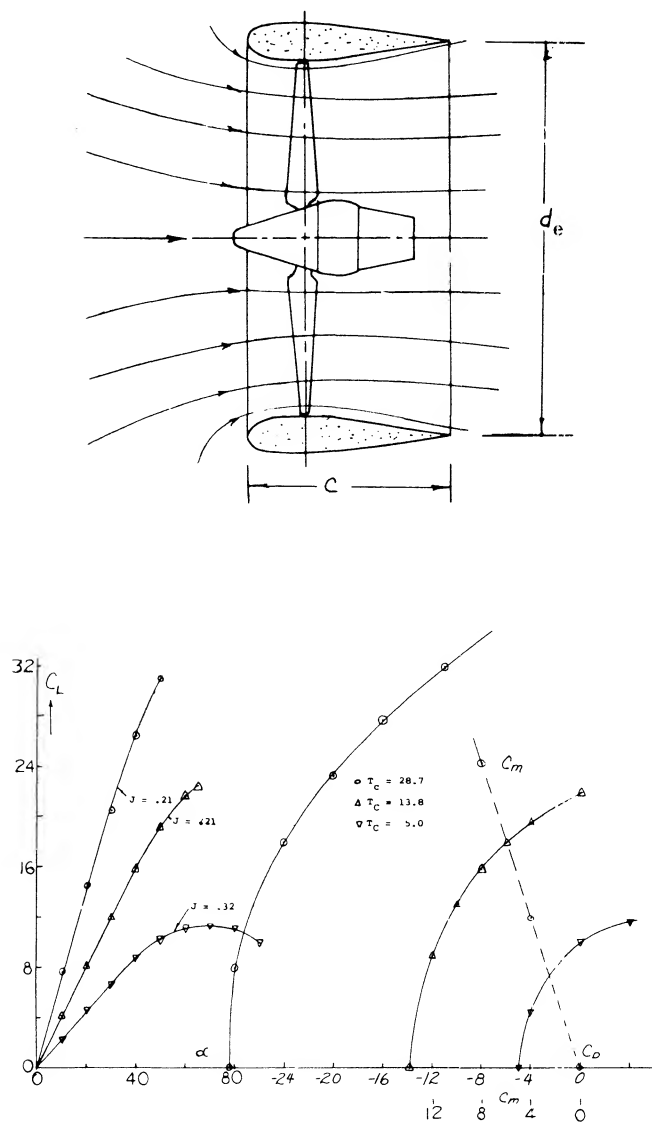


Figure 10. Lift variation of a large ducted propeller over a high angle of attack range.

Lip Stall Ducted Fans. A ducted fan will tend to stall with an increase of the shaft angle of attack. Like a wing, stall takes place in the form of separation of the leading lip of the duct as illustrated in figure 11. The conditions where separation are encountered are a function of the shaft angle of attack, Reynolds number, inlet radius and the thrust coefficient T_C . Not only does the stall cause a loss of lift but it also causes a large increase in the noise level of the system and a decrease of thrust and efficiency. Because of the separation of the inner lip the propeller will encounter unsymmetrical flow which reduces the thrust and increases the blade stresses.

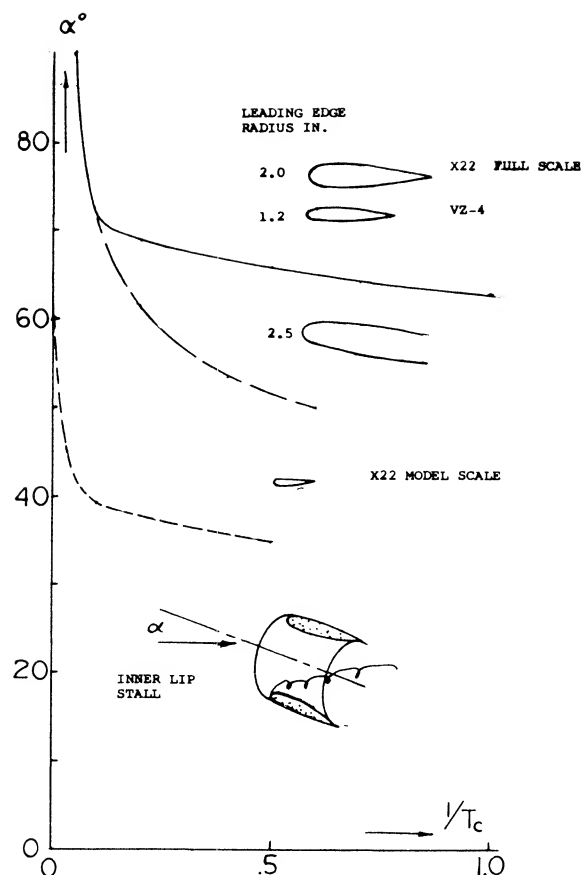


Figure 11. Inner lip duct lip stall as a function of angle of attack for ducted propellers.

The angle of attack where separation can be expected on the upstream lip as a function of the thrust coefficient is illustrated on figure 11, based on tests of 4 and 7 foot diameter ducted fans and models. It should be noted that model tests of ducted fans indicate a much lower angle for stall even with large modifications of the lip radius (5,b). This illustrates the importance of q , Reynolds number and shows that model test results should be used with caution for predicting results especially where separation is involved.

Tests (5,c) also have shown that separation will occur on the outside of the duct as illustrated in figure 12. This separation is also a function of the lip radius, Reynolds number and thrust coefficient. Upper lip separation is not as serious a problem as the separation on the leading lip, although an increase in drag is encountered. When separation takes place on the upper lip only a minor reduction in the slope of the lift curve is encountered.

Separation leading to duct stall can also be observed from plots of $1/T_C$ as a function of angle of attack as illustrated on figure 12 from (5,d). This curve shows that the separation considerably reduces the thrust produced by the duct.

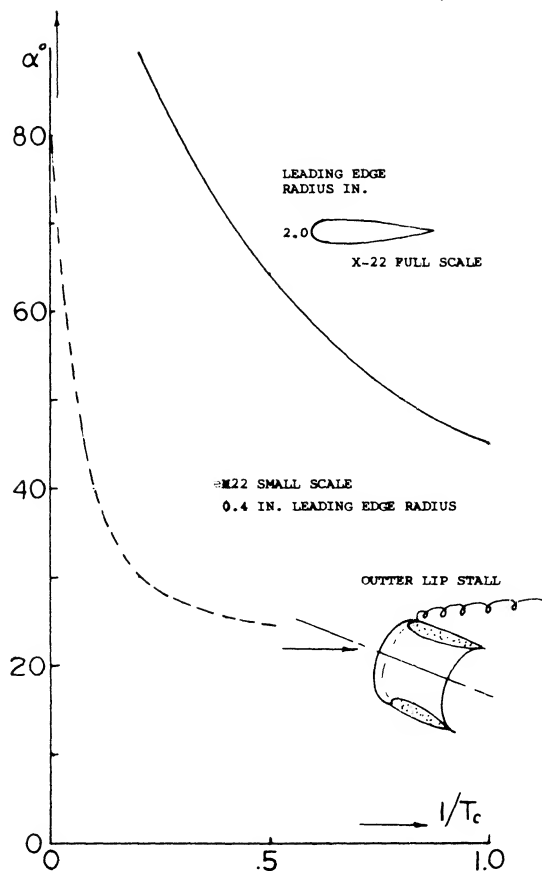


Figure 12. Outer lip duct lip stall as a function angle of attack for ducted propellers.

Duct Moments. Ducted propellers develop a pitching moment which increases with angle of attack as shown on figure 10. This pitching moment appears to be mainly a function of the lift coefficient and is mainly independent of the thrust coefficient and the advance ratio.

Unlike a propeller the yawing moment appears to be low for ducted fans with increases in angle of attack at least to an angle of 30 degrees, (5,a). It would appear that the length of duct in this case is sufficient to produce a symmetrical axial flow through the duct. Thus, it would be expected that the propeller or fan in the duct has very little effect on the overall lift as the normal force is essentially zero. When the flow separates on the forward lip this may no longer be the case.

Lift Engines. Light weight engines have been developed for direct lift applications. The lift produced by the engines is dependent on their placement on the aircraft. As shown in (5,c) the lift can be increased up to three times that of the static thrust of the engine depending on the configuration.

Engine Lift Turbofans, Turbojets. The lift produced by isolated turbofan or turbojet engines would be smaller per unit thrust developed than either propeller or ducted fans. This would be expected as the lift is developed based on the projected area of the engine nacelle, which would be

smaller per unit power than the ducted propeller. The lift produced by turbofan engines is small in comparison to that of the complete airplane and is usually only important for interference and stability effects.

Because of the higher thrust coefficients of turbofan and turbojet engines the lip stall problem is delayed to higher angles of attack than shown for ducted fans. If operation is encountered at the higher angles the intake should be treated in much the same manner as the ducted fans discussed in the last section.

2. INFLUENCE OF PROPELLER SLIPSTREAM ON WINGS

Because the propulsion system must react on the air to produce thrust, the velocity in the slipstream is higher than in the free stream the magnitude is directly proportional to the disk loading. With a high disk loading the area of the slipstream is smaller than with light loadings for a given level of thrust. Thus, thrust systems such as propellers will have a large slipstream area with a relatively small increase in velocity. For this reason the propeller slipstream of tractor type airplanes will impinge on large portions of the airplane, the area of the wing and fuselage effected depending on the configuration. Airplanes have been designed to minimize slipstream effects by using pusher propellers. A notable example is the six engine pusher propeller B-36 airplane. Many other pusher propeller installations have been built but usually they never reached production. In the case of the B-36 the pusher configuration was selected as it was desired to eliminate the propeller slipstream effects on the wing and to maintain laminar flow.

With tractor installation it is possible to have an airplane configuration using ducted fans, turbofan engine or jet engines where the slipstream does not impinge on the airplane structure. Because the effects of the slipstream can be desirable as well as harmful, it may not be an advantage to eliminate all slipstream effects on the airplane. This, of course, will depend on the particular airplane and its performance goals.

(6) Slipstream Effects - Propellers:

- a) Theodorsen, Static Propellers & Helicopter Rotors, AHS 25th Forum, 1969.
- b) Jameson, A., Propeller-Wing Flow Interaction, NASA SP-228; also NASA CR-1632.
- c) Smelt & Davis, Lift Due to Slipstream, ARC RM 1788 (1937).
- d) Stuper, Evaluation, Lufo 1935 p 267; 1938 p 181.
- f) Bradfield, Airscrew and Wing, ARC RM 1212 (1929).
- g) Kuhn, Wing-Propeller Combination, NACA T Rpt 1263 (1956); also Continuation, NASA D-17 (1959).
- h) Kuhn, Propeller & Wing & Flap, NASA Memo 1-16-1959, L.
- i) AVA Gottingen, Wing in Slipstream, Erg I (1920) p 112.

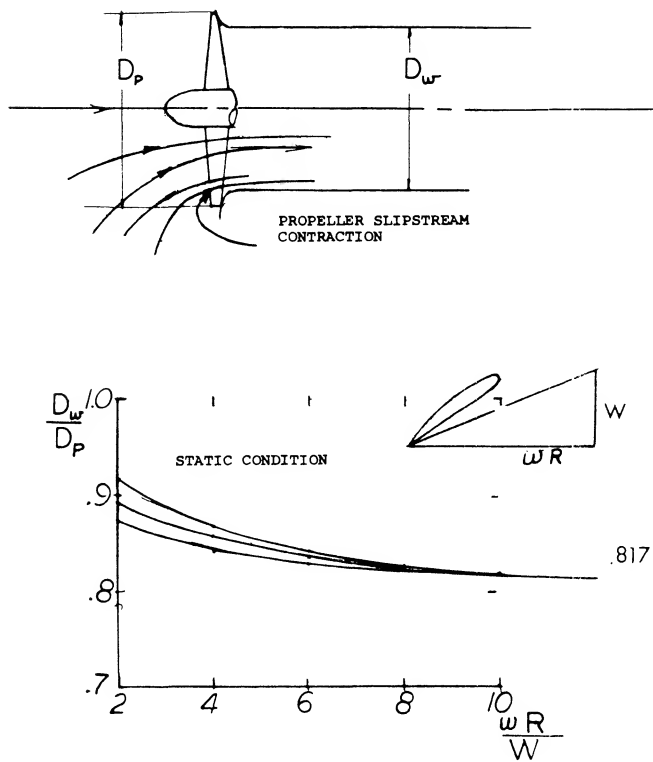


Figure 13. Slipstream contraction ratio for propellers operating at the static condition.

Slipstream Characteristics – Propellers. The flow characteristics in the propeller slipstream are complex because there is no duct to control the flow. The general characteristics are as follows:

- 1) The axial free stream velocity is increased; one half the increase taking place in the propeller disk, the other one half in the final wake.
- 2) The diameter of the slipstream is approximately equal to that of the propeller, especially at the normal forward flight conditions.
- 3) At zero velocity and low forward speeds the slipstream contracts between .816 and .92 depending on the loading and the forward velocity, figure 13, (6,a).
- 4) The slipstream contraction takes place very close to the propeller disk as illustrated on figure 13.
- 5) Because of the rapid contraction of the propeller slipstream the average axial velocity in the final wake is used for determining wake effects using equation

$$v = T/m = T/S_p \rho V'$$

where S_p is the propeller disk area and V' is the axial velocity through the disk.

6) At several propeller diameters aft of the disk, the wake expands with a 15 degree included angle like that of most streams.

7) The actual velocity imparted to the slipstream by the propeller consists of axial, radial and tangential components of velocity, which are periodic in nature. Immediately downstream of each blade the velocity increment is a maximum. In between the blades the velocity increment is a minimum, but is still more than 50% of the peak. Except at zero and low speeds the radial velocity is small and can be neglected. The tangential component of velocity in the slipstream is in the same direction as the propeller rotation.

8) The increase of the axial velocity is not uniform across the disk but varies as the thrust and torque loading, as is illustrated in figure 14.

9) When the propeller is operating at an angle of attack the down going blade produces a higher level of thrust than that of the up going blade. This results in an increase of the slipstream velocity aft of the blade with the higher level of thrust.

10) Due to mixing and damping the flow irregularity found immediately aft of the propeller is expected to become more or less steady.

11) As a result of the lift produced by a propeller when operating at an angle of attack the slipstream is deflected downward, thus reducing the horizontal tail effectiveness.

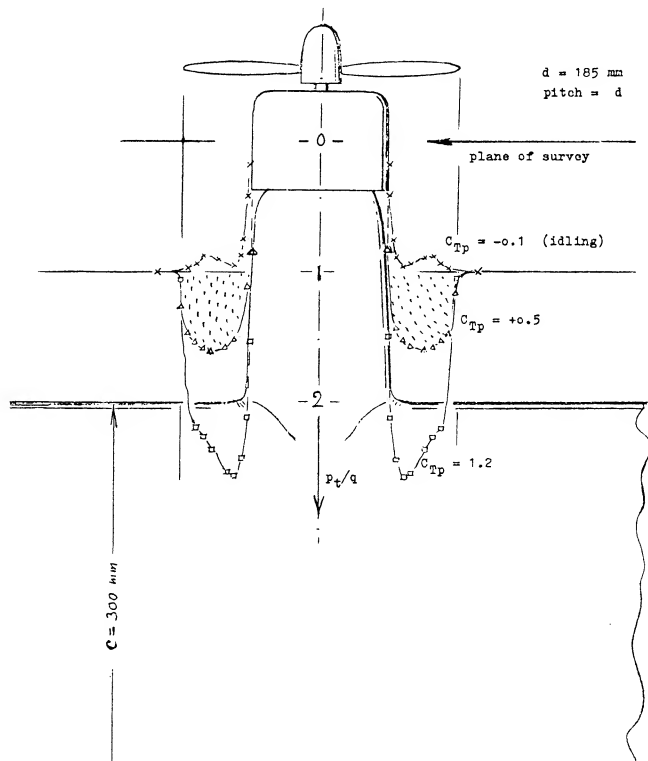


Figure 14. Variation of dynamic pressure in the slipstream of a propeller at $T_c = -0.1$ to 1.2. (Abring, Pressure Distribution, ZWB FD 1908 (1942). ZWB

Propeller Slipstream – Thrust Effects. Although the actual characteristics of the propeller slipstream are complex it is generally permissible to assume a uniform increase in the dynamic pressure for finding its effects on the air-plane. Thus the dynamic pressure in the slipstream q'' is

$$q'' = q + T/S_p \quad (10)$$

where S_p is the area of the propeller disk $= D^2/4$.

For evaluating the propeller wing combination non-dimensional thrust coefficients based on the stream dynamic pressure are preferred. These coefficients are based on conditions in the free stream and in the slipstream. Thus

$$T_c = T/q S_p \quad (11)$$

$$T'_c = T/q'' S_p \quad (12)$$

Where T_c is the propeller thrust coefficient based on the free stream dynamic pressure and the primes indicate the coefficient based on the dynamic pressure q'' in the propeller slipstream. In the test and analysis of propeller V/STOL aircraft the thrust coefficient T'_c based on the total forces of all propellers, wing area and q is used. Thus

$$T'_c = T'/qS = \frac{T'_c}{1 - T'_c} \frac{K S_p}{S} \quad (13)$$

where K is the number of propellers and T' = total thrust force.

Lift Due to Slipstream. When wing is immersed in the propeller slipstream an increase lift will be obtained due to the increased q . If the angle of attack is well below that for stall and the effect of the rotational velocity change is small, the lift coefficient can be described in terms of the thrust coefficient and section data by the equation

$$C_L = C_L'' / (1 - T'_c) \quad (14)$$

Thus, the actual lift coefficient based on free stream conditions is increased over the section data.

For the analysis of V/STOL airplanes it is more convenient to use the total wing area and number of propellers in developing the overall performance characteristics.

$$C_L = C_L'' (1 + T_c S/K S_p) \quad (15)$$

where K is the number of propellers.

Propeller Wing Lift. The combined lift of a tractor propeller wing combination is higher than the sum of each component alone. The wing lift is increased by the increment of slipstream velocity of the propeller, equation 10, while the lift component of the propeller normal force is increased due to the increase of upwash angle of the wing. In addition to increasing the dynamic pressure at the wing the propeller alters the angle of attack and decreases the lift slope (6,b). An example of the combined lift of the propeller wing combination is given on figure 15 as a function of $K T_c$. Here, K is the number of the propellers on the wing and T_c is equal to $T/q S_p$. Note the slope of the lift curve increases due to the direct lift effect and the velocity increase of the slipstream. The maximum lift of the combination depends only on $K T_c$.

On figure 15 the normal force coefficient and its slope are given for the propeller alone without the nacelle used with the wing. Note the relatively straight line variation of C_{Np} with angle of attack for this case.

Propeller Jet Effect on Wing Lift. When the wing is operating in the propeller slipstream the effective angle of attack is changed along with the lift curve slope. Thus, to calculate the combined lift of the propeller wing combination it is necessary to determine the effect of the propeller jet on the wing, in addition to the propeller normal force and the increase dynamic pressure (6,b).

If only one propeller is operating in front of a wing panel the effective jet aspect ratio is one. However, if two or more propellers are used, the jet aspect ratio is found from the equation 16 assuming the spacing is close enough so that the jet is continuous

$$A_j = B/H \quad (16)$$

where B and H are the height and width of the jet.

From the detailed calculations of (6,b) the slope of the lift curve can be found for the wing operating in the wake of the propellers from equation 17 and 18

$$C_{L\alpha o} = C_{L\alpha 1} (A + 2) / [A + A_j + (2.5/1 + A)] \quad (17)$$

$$C_{L\alpha \mu} = \frac{C_{L\alpha 1} / 1 + [(C_{L\alpha 1} / C_{L\alpha o}) - 1] [(1 - \mu) / (1 + A_j \mu)]}{(18)}$$

where $\mu = V/V_j$ the ratio of the free stream velocity to the jet velocity or the velocity in the slipstream aft of the propeller. The subscript 1 represents the case where the

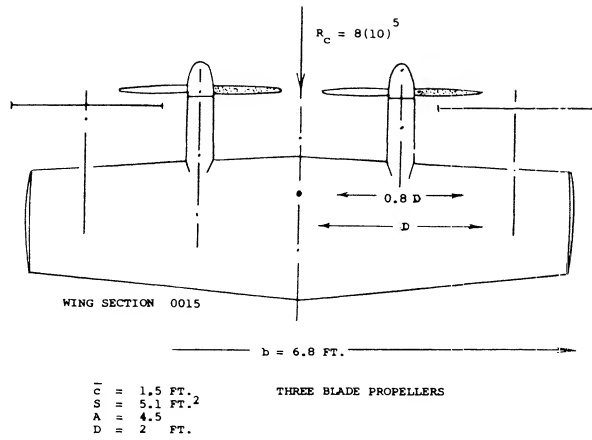
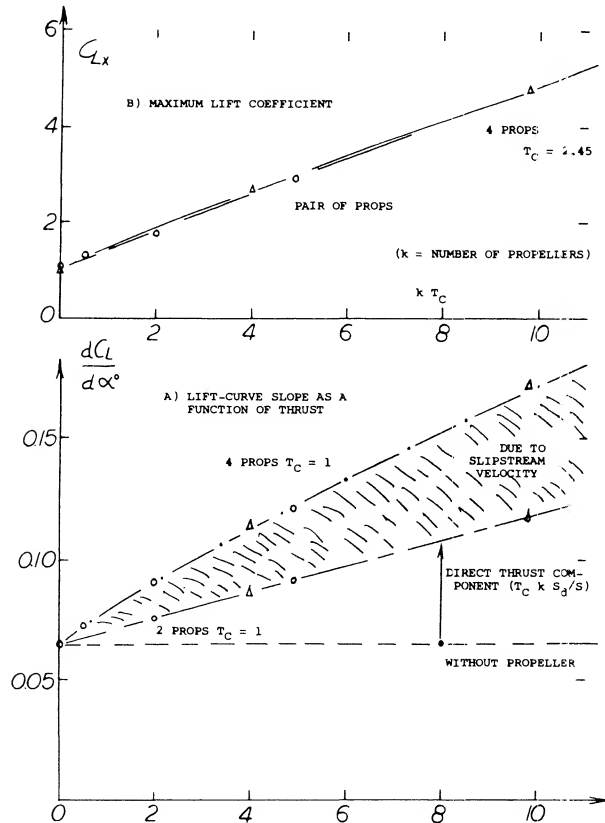


Figure 15. The lift of a STOL propeller-wing combination (6,g) as a function of the thrust coefficient.



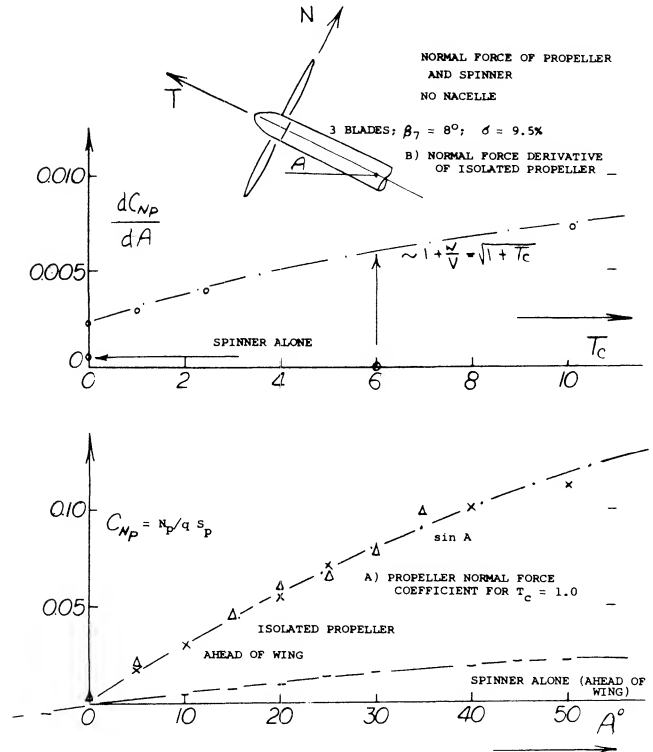
velocity over the wing is the jet velocity and o is the free stream velocity. Thus, equation 18 gives the lift curve slope for the free stream velocity case in terms of the slope when the free stream velocity equals the jet velocity. To find the lift curve slope at μ , equation 18 must be used. Note all the values of the slope are based on q in the jet. Based on this the slope decreases as the external flow is reduced.

The drag is also effected by the jet flow on the wing. If $r = C_D/C_L^2$ then

$$r_o = r_i .76(A_j + e^A j) + .53 \quad (19)$$

$$r_u = r_i [(r_o/r_i) + [1 + A_j - (r_o/r_i)]\mu^2 / (1 - A_j\mu^2)] \quad (20)$$

The above equations are valid for the range of $A > \frac{1}{2}A_j$.



Turning Effectiveness. The ability of a wing to turn the flow is a measure of the lift that can be produced. From the data of (6,b) the turning effectiveness of a wing operating in the wake of a jet flow is presented on figure 16. For the wing operating at zero forward speed the effectiveness is increased by an increase of the jet aspect ratio and a decrease in wing aspect ratio. Thus the lift of the wing will increase as the jet becomes narrower. This shows the advantage of several small propellers washing the wing rather than one large prop.

Total Wing Propeller Lift. The total wing propeller lift is thus calculated by finding the propeller normal force operating in the upwash produced by the wing, adding the change in the wing lift due to the jet effect of the propeller and its associated slipstream velocity. Good correlation with experimental data have been obtained using this procedure for unflapped wings with the propeller thrust axis nearly parallel to the wing chord line. When flaps are used the accuracy correlation is reduced but a good first approximation is obtained.

3. SLIPSTREAM EFFECTS OF DUCTED PROPELLER AND FAN ENGINE ON WINGS

The reduced temperature of the efflux produced by ducted propellers and turbo fan engines has made it possible to direct their flow over the wing to increase lift. The lift increase produced by the wing due to slipstream effects is a function of the conditions in the slipstream, which depends on the thrust loading of the engine. The data for combinations of fan engines is generally presented in terms of conditions in the slipstream which are different from those used for propellers and are given as follows:

Turbine Engine Definitions. The conditions in the slipstream of a turbo fan engine are described by the gross thrust which is

$$\text{Gross Thrust} = F_g = m_j V_j \quad (21)$$

where m_j is the mass flow at the engine nozzle exit and V_j is the jet exit velocity. Gross thrust is equal to the net thrust F when the engine is at zero velocity. Thus, at $V = 0$

$$F_g = F_n \quad (22)$$

Net thrust is the actual thrust of the engine and is equal to the change in momentum of the fluid passing through the engine. It is thus equal to the gross thrust minus the drag caused by accelerating the air being swallowed by the engine to the forward velocity of the engine. Thus, if the efflux of the engine were deflected, say 90° , to produce only lift, the mass of air handled times the free stream velocity would be drag. The net thrust F_n is the flight direction and is then

$$F_n = F_g \cos \varepsilon - m_c V_o \quad (23)$$

where ε is the turning angle of the flow and m_c is the mass flow handled by the compressor.

In some NASA reports F_A is used to define the axial force, the force along the x axis of the body, figure 1. This is taken to be the total force on the system, including the net force F_n and the drag force D .

Since the gross describes conditions in the slipstream of the engine the other characteristics of the engine wing combination may be defined in terms of the coefficient C

$$C_{\mu} = F_g / q S = T / q S \quad (24)$$

where T = the static thrust of the engine and S the wing area, sometimes used as the semi span area. The dynamic pressure q is based in the free stream.

In comparing the effectiveness of the turning of various systems, the static-thrust recovery efficiency is used. This efficiency is defined by

$$\eta = \sqrt{F_A^2 + F_N^2} / T \quad (25)$$

Ducted Propeller Wing Lift. A ducted propeller mounted in front of a wing arranged so that its efflux washes the upper and lower surfaces will also increase lift. Like an open propeller, the lift is increased due to the higher slipstream velocity and the increment is a function of the turning angle of the flow. Based on (6,b), ducted propellers can be expected to provide high lift augmentation as the increase improves with increasing jet aspect ratio and a corresponding decrease in the slipstream net thickness, figure 16. Thus it is desirable to use several small diameter jets, such as ducted fans, in front of a wing to produce the greatest lift augmentation for a given total thrust.

To obtain the required thrust at small diameters ducted propellers are needed for good propulsive efficiency. With ducted propellers the total wing can be immersed in the jet wake and flaps can be used to further augment the turning of the flow (7,a). As shown on figure 17, the basic wing lift is increased by the turning of the jet and an increase of circulation lift. A measure of the effectiveness of turning with the flaps set at 90° is given on figure 18. From this plot it appears that the best split of the wake occurs for $1/4$ above the wing. Here the greatest turning is obtained, along with the highest lift to thrust ratio.

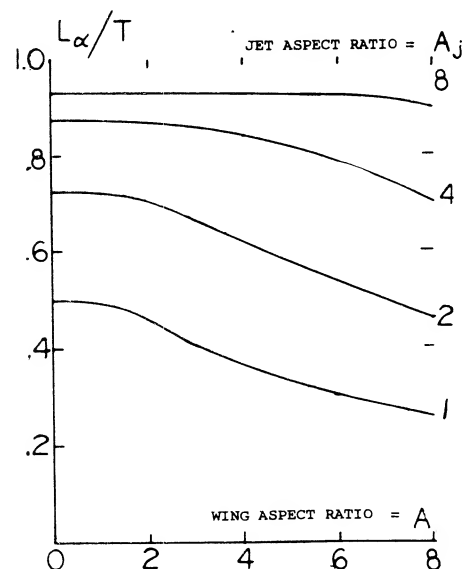
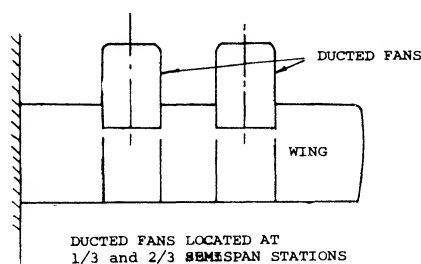
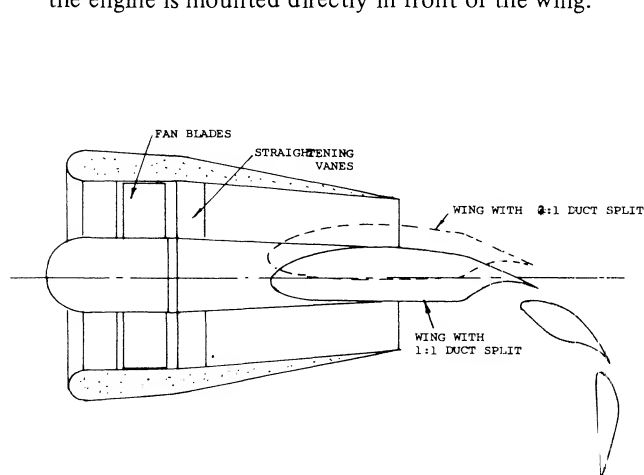


Figure 16. Turning effectiveness of rectangular wings in static jets, $\mu = 0$.

Wing Lift with Turbo Jet Engines. Like propellers and ducted fans, turbo jet engines can augment the lift of a wing to make possible reduced takeoff and landings with effective lift coefficients much higher than is possible with flaps. Since the size of the turbo jet engine is much smaller than the ducted fan and propeller, there are many more configurations that can be used to increase the wing lift. Possible configurations that have been considered are illustrated on figure 19 and include basically underslung engines with various flaps and engines mounted over the wing. Also included is the possible configuration where the engine is mounted directly in front of the wing.



1 : 2 DUCT SPLIT FIGURE 18

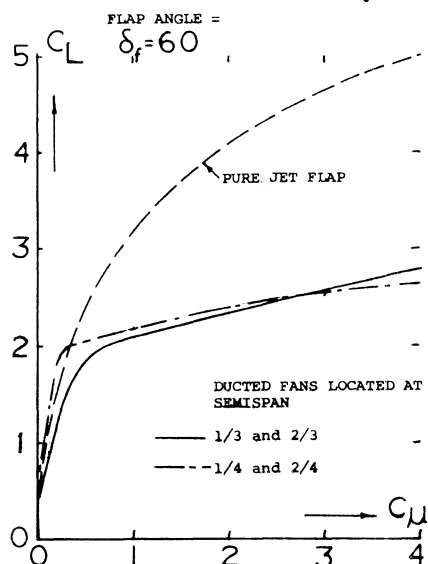


Figure 17. Lift augmentation due to flaps for wing ducted fan configuration (7,a).

The configuration chosen will depend on the performance improvement possible, safety considerations, weight and the noise produced. With the underslung configuration the flap deflection will increase the noise level, figure 20. Since noise is an important consideration, especially with STOL aircraft, the choice of configuration will probably hinge on the level of noise produced.

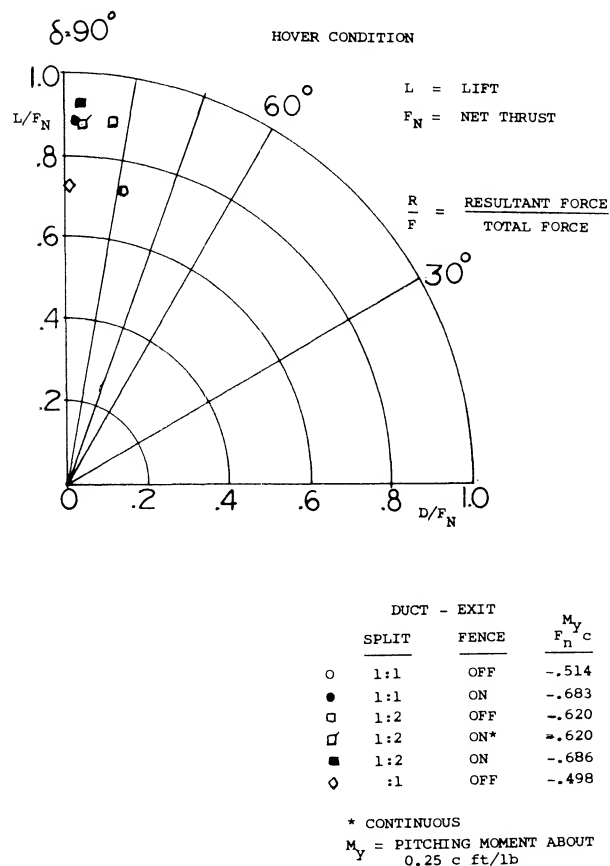


Figure 18. Turning effectiveness of flaps on wing with a ducted fan.

- (7) Ducted Fan Wing Interaction:
 - a) Newsome, W., Deflected-Slipstream Cruise-Fan Wing, NASA TN D-4262.
 - b) McKinney, Fan-Powered V/STOL Aircraft, NASA SP-116.
- (8) Underslung Engines – Wing Augmentation:
 - a) Parlett, Wind-Tunnel Test Jet Transport with External-Flow Jet Flap, NASA TN D-6058.
 - b) Powers, Experimental STOL Configuration with Externally Blown Flap Wing or Augmentor Wing, NASA TN D-7454.
 - c) Patterson, High-Bypass Engine Wing-Nacelle Interference Drag, NASA TN D-4693.
 - d) Parlett, STOL Model with Externally Blown Jet Flap, NASA TN D-7411.
 - e) Zabinsky, STOL Designs for NASA Short Haul Transport Study, NASA SP-116, P-339.

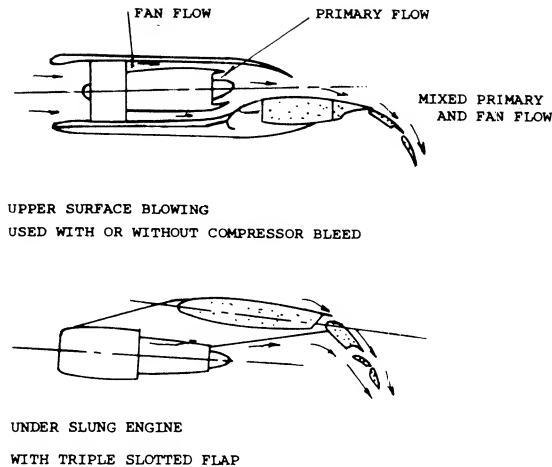


Figure 19. Types of wing lift augmentation systems for use with turbojet and turbofan engines.

Lift with Underslung Engines. By deflecting flaps directly in the efflux of a turbo fan engine very high operating lift coefficients (8,a) and Chapter 5 are obtained. As shown on figure 21, a maximum lift coefficient as high as 8 is possible with a C_{μ} of 3.5 and the use of a wing equipped with double slotted trail edge flaps and a leading edge flap. Associated with the high lift coefficient is a large diving moment so that the trimmed lift is lower, however. Because of the large lift coefficient the downwash at the tail becomes very large, requiring careful placement of the horizontal tail.

Typical operation of a wing with externally blown flaps is given in figure 22 from (8,e). In this case the wing is operated at lift coefficients considerably below the maximum to allow for an engine failure. This is a major problem in the design of augmented lift systems, as lateral moment also becomes very large due to the lift loss in area of the failed engine (8,d).

Although large values of C_L are possible with underslung nacelle wing combinations, the practical aspects of safety, noise and trim reduces the lift advantages so that other configurations become more desirable.

Propulsion Lift Engines Over Wing. The need for noise reduction of STOL aircraft plus the indication that a wing could be very effective in turning the efflux of engines led to consideration of exhausting the flow over the wing upper surface. This system with low jet velocities can lead to a low noise configuration (9,c). A possible arrangement of such a system, figure 20,b, indicates that high turning efficiencies can be obtained along with large improvements of the total lift (9,a,b).

The turning efficiency for flap settings of 20 to 60° nozzles of various aspect ratios are given on figure 23. Based on tests at the static condition the higher levels of turning efficiency appear to be for those cases where the flow spreads out on the wing forming a high energy jet that follows the wing contour. For instance, (9,b) when flap guide vanes were used on the aspect ratio 2 nozzle turning equivalent to a nozzle of aspect ratio 4 were obtained. Typical untrimmed lift drag and moment characteristics are given on figure 23 for the aspect ratio 4 nozzle and the flaps set at 60°. As with the underslung engines, the full potential of lift augmentation cannot be realized due to trim and engine out considerations. However, with further development this method of improving lift is expected to be highly competitive.

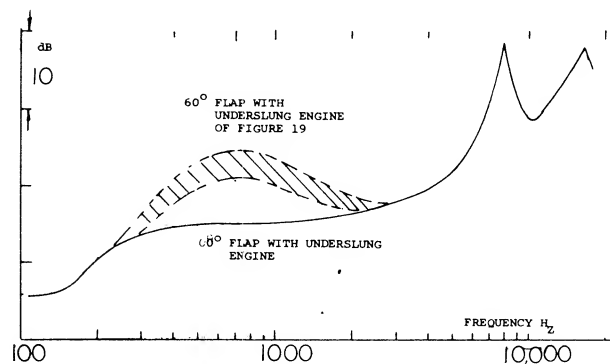


Figure 20. Effect of flap deflection on noise level for external blown underslung flaps.

- (9) Upper Surface Blown Jet-Flap:
 - a) Phelps, A., Wind-Tunnel Investigation, NASA TN D-7399.
 - b) Smith, C.C., Large-Scale Semispan Unswept Wind-Tunnel Test, NASA TN D-7526.
 - c) Reshotko, Engine Over the Wing Nose, J of Aircraft April 1974.
- (10) Effects of Jet Flow on Wings:
 - a) Putnam, Jet Flow on Wings, $M = .4$ to $.95$, TN D-7367.

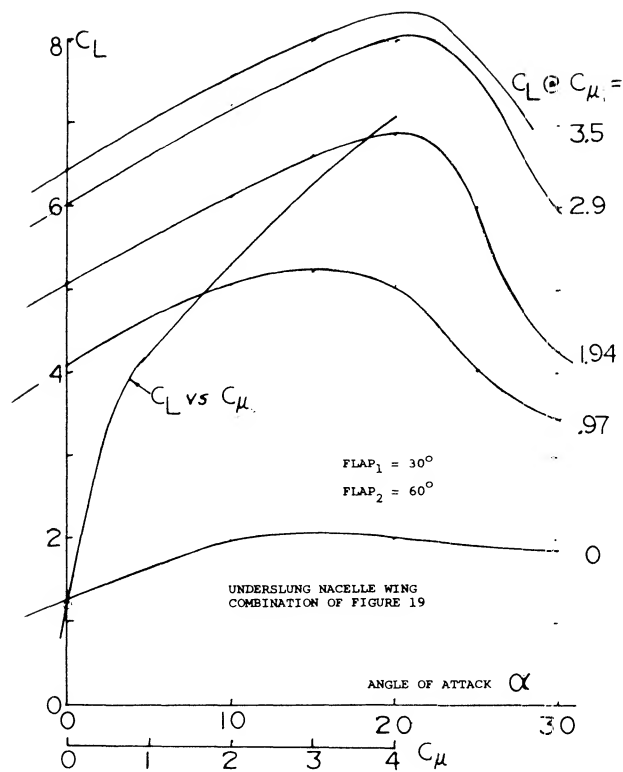


Figure 21. Lift augmentation with underslung turbofan engines with wings using double slotted flaps.

4. SLIPSTREAM EFFECTS ON TAIL SURFACES

In the design and stability analysis of the tail surfaces it is necessary to determine the flow conditions with regard to velocity and direction. The flow at the tail surfaces is effected by the wings and fuselage as discussed in Chapters XIII and XIV and can be influenced by the slipstream wash of the propulsive system. This is especially true with propeller driven airplanes as the slipstream cross section is large with respect to the airplane. This makes it nearly impossible to locate the tail surface outside the slipstream at all the flight conditions. In the case of tractor single engine propeller airplanes, the tail surface is influenced by the propeller wash at all conditions. This can be a beneficial effect, except when the airplane is operating at a large yaw angle for instance where the tail goes outside the slipstream.

Because of the higher velocities of the efflux of the ducted propeller and turbo fan engines, it is possible to locate the power plants in positions where the exhaust flow will not directly impinge on the tail surfaces. Because of the higher velocity of the engines, their body shape and induced effects their location becomes important in the design of the tail.

In this section the influence of propulsive lift on the design and analysis of the tail surfaces will be considered.

Wing Lift Interaction with External Jet. When a wing operates in the wake of jet engines a large increase in both the lift and drag coefficients would be expected due to the increased dynamic pressure in the jets. Considering only the forces on the wing the data of (10,a) indicates a nearly constant increment of C_L with changes in angle of attack, figure 24. The increment changes with Mach number up $M = 0.9$ and increases with the engine pressure ratio. Since the jet remains fixed in relation to the wing the flow from the jet will be essentially the same relative to the wing at all angles. Thus, when the angle of attack changes, the efflux of the engine does not change relative to the wing, explaining why the increment in lift remains constant with angle.

At the lower angles of attack, the drag is increased by the efflux of the engine. When the operating C_L is greater than .2 the jet exhaust on the wing causes a drag reduction due to a reduction of the induced effects. The pitching moment was not changed due to jet exhaust over the wing.

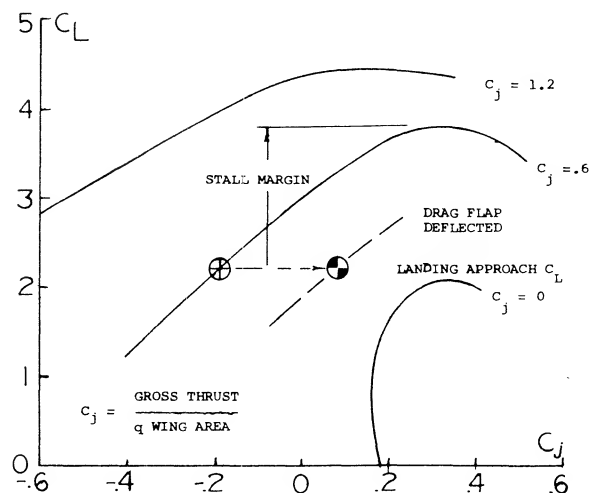


Figure 22. External blown flap system operating characteristics during landing.

Slipstream Flow Field. The flow field at the location of the tail as affected by the slipstream of a propeller has repeatedly been mapped (11), (12) showing the distribution of direction (downwash) as well as that of the dynamic pressure. Such surveys can be extremely irregular and their study is likely to suggest that tail surfaces may never work to satisfaction within the slipstream of a propeller. As an example, one such distribution is shown schematically in figure 25. The slipstream is distorted. Behind the usual single-rotation type of propeller (in the airplane tested, turning counter-clockwise) the two sides are not symmetrical. The slipstream rotation (corresponding to torque) modified by the directing effect of the wing is displayed, both in the downwash and in the dynamic pressure concentration in certain spots. As a consequence, the average downwash is increased in the left and reduced in the right tail-surface panel of the airplane tested.

Tail Load Distribution. The tail load distribution of the P-40 airplane (tested in the NACA's Full-Scale Tunnel) is shown in figure 26:

1) Without the propeller and at zero angle of yaw we can expect the loading to be symmetric. The dynamic pressure ratio (outside the fuselage) is essentially $q_H/q = 1.0$. At $C_L = 0.8$ in the wing, the average downwash angle at the tail is $\varepsilon = -6.5^\circ$ so that $\alpha_H = 10 - 6.5 = 3.5^\circ$.

2) The resultant average tail force corresponds to $C_{NH} = 0.14$, so that $(dC_N/d\alpha)_H = 0.04$. This small lift curve slope reflects the strong interference of the fuselage, practically interrupting the lift in the center of the tail surface.

3) With propeller and power on, with a thrust coefficient $T_C = 0.7$, everything is strongly asymmetric. In particular, corresponding to a downwash angle increased to the level of $\varepsilon = -13^\circ$ the lift on the right side of the horizontal surface is rendered somewhat negative. The average tail force is about half of that with the propeller off. In fact, the tail effectiveness in the power-on condition as shown would be better when taking the right side panel off completely, see (13,h).

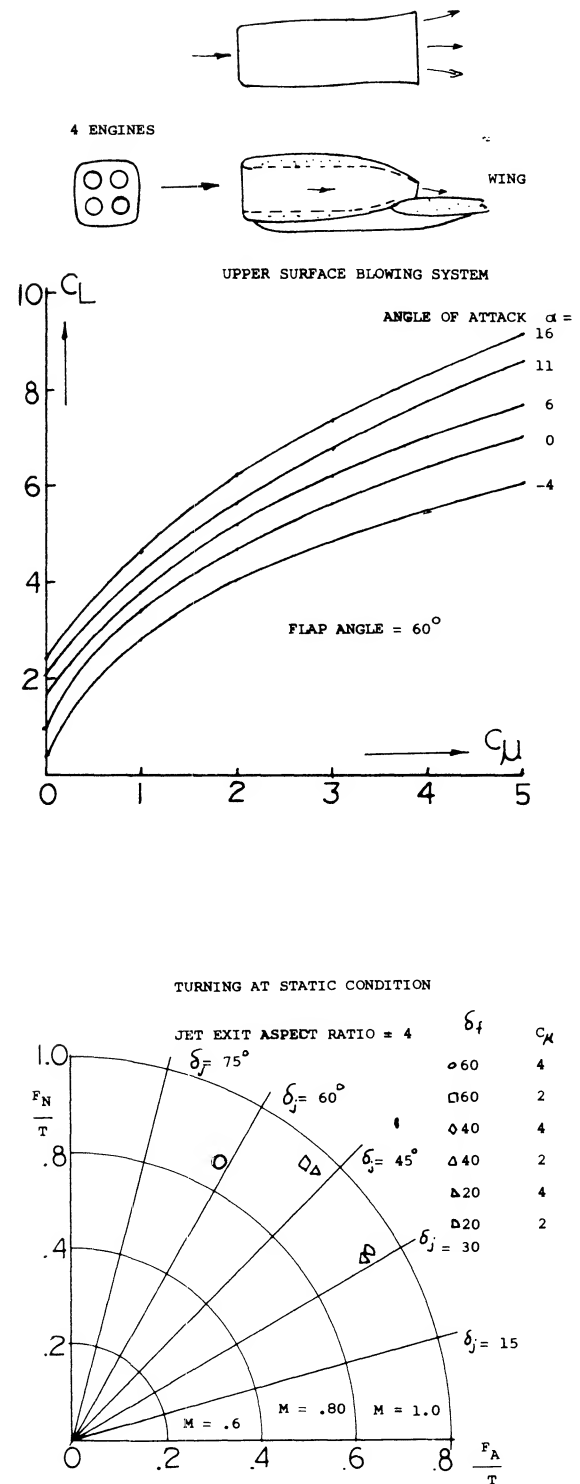


Figure 23. Turning efficiency of various nozzle configurations for wings with upper surface blowing.

(11) Influence of propeller slipstream on downwash:

- Stuper, Slipstream on Tail, Lufo 1938 p 181 (NACA TM 874).
- ARC, Downwash in Slipstream, RM 882 (1924).
- Katzoff, Slipstream Effects, NACA T Rpt 690 (1940).
- Helmhold, Airplane Model, Lufo 1938 p 3.
- Muttray, Distribution, Lufo 1938 p 109 (NACA TM 876).
- In biplane configuration, ARC RM 1488.
- Goett, Pitching Moments, NACA W'Rpt L-761.

(12) Downwash behind isolated propellers:

- Glauret, ARC RM 882; see Durant IV p 357.
- Turin, Experimental, J Roy A Soc 1936 p 388.

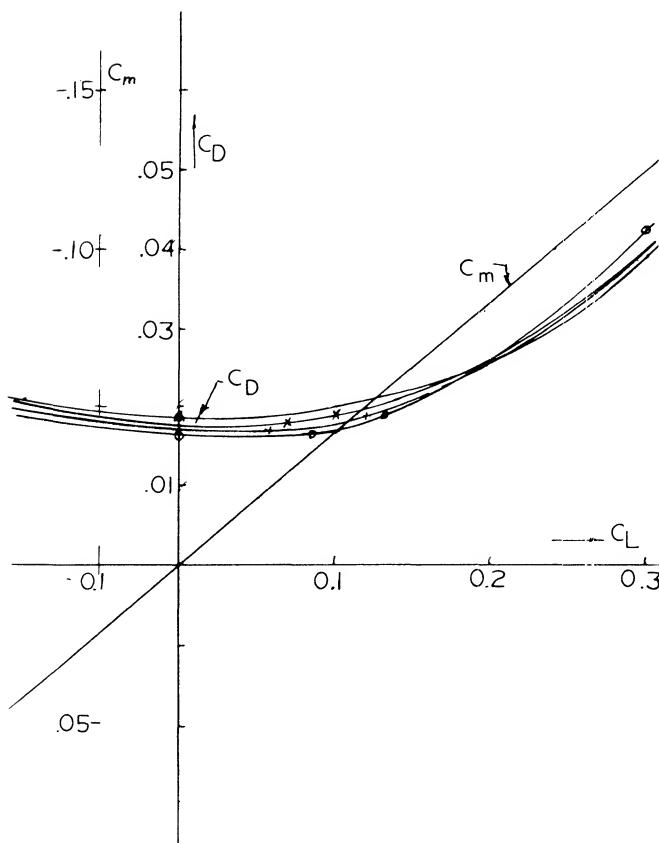
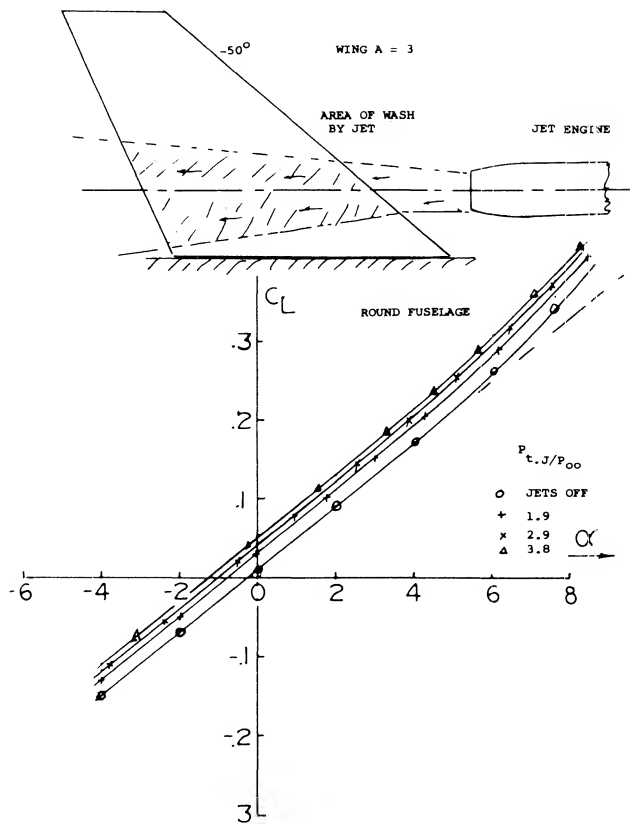


Figure 24. External jet effect on the performance of a 50° swept leading-edge aspect ratio 3 wing with a taper ratio of 0.3.

4) When at positive angle of yaw (nose to right, tail to left) the basic wing downwash tends to be increased at the right side. However, power and slipstream of the right-turning propeller have an opposite tendency. The most severe asymmetric loading (in pounds) must be expected at high speeds (low lift coefficients) when sideslipping to the left (left wing forward). A corresponding yawing to the right usually takes place in pull-up maneuvers, caused by the gyroscopic moment of the right-turning propeller.

However irregular the distribution may be, horizontal surfaces pick up comparatively continuous normal forces, and they are not necessarily very sensitive as to local dynamic pressure variations. We will, therefore, disregard distributions at first, and we shall evaluate, consider and use the consequences of slipstream as they are integrated by the horizontal surface.

Dynamic Pressure at the Tail. The dynamic pressure within the slipstream of a propeller at the horizontal tail is theoretically

$$q_H = q(1 + T_c); \quad q_H/q = 1 + T_c \quad (26)$$

where $q = 0.5 \rho V^2$ = dynamic pressure corresponding to the airplane's speed "V". In other words, the added pressure ratio is

$$\Delta q/q = T_c \quad (27)$$

Considering a horizontal tail surface completely located within the slipstream, its reactions to variations in the angle of attack or the elevator angle would then tentatively be proportional to the ratio to q_H/q . Under realistic conditions, the influence upon the tail surface is smaller however:

- 1) Depending on what you call thrust (at the propeller or "net effective") the slipstream loses some of its Δq through friction along the fuselage, et cetera.
- 2) The slipstream mixes with the surrounding flow so that the differential indicated by equation 27 is reduced.
- 3) The horizontal surface may not entirely be covered by the slipstream (or by those of two or more propellers, according to configuration).
- 4) The distribution of the dynamic pressure across the span of the tail surface is non-uniform, as mentioned above.

5) The slipstream is limited in size. The lift in the H'tail, therefore, cannot be expected to increase "fully" in proportion to $(1 + T_c)$ as in equation 26.

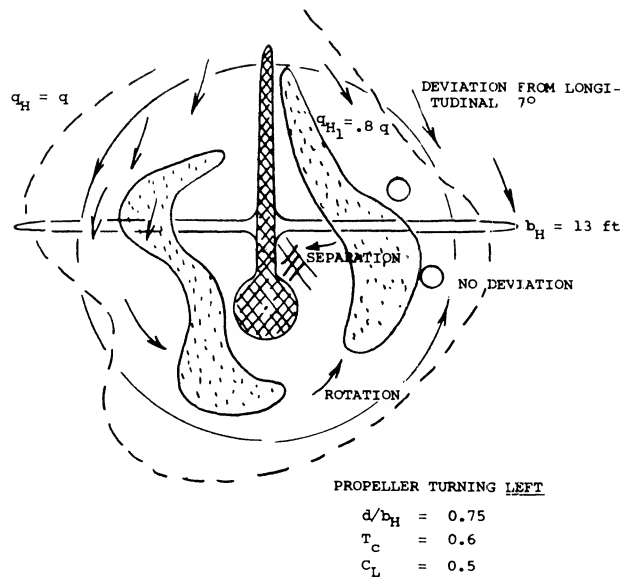


Figure 25. Example for the distribution of dynamic pressure and downwash in the vicinity of the horizontal tail of a single-engine airplane.

Horizontal Tail Span. The effective dynamic pressure effects at the horizontal tail have been determined from available experimental results. In cases where the pressure was directly tested, an average value was taken from the distribution across the horizontal-tail span. In some cases the effective pressure was determined from the C_m variation caused by changing the angle of incidence of the tail surface against the fuselage. The dynamic pressure ratios thus obtained are plotted in figure 27. The average ratio reduces as the horizontal span is increased beyond the diameter of the single-propeller slipstream. For example, at $b_H = d$ corresponding to $d/b_H = 1$ the graph indicates a q_H/q between $(0.6 \text{ and } 0.7)T_C$ so that $q_H/q \approx 1 + (2/3)T_C$. At $d > (1.0 \text{ or } 1.2) b_H$ the added pressure ratio may reach a certain plateau, between $(0.7 \text{ and } 0.8) T_C$. As a rough approximation, one might assume

$$q_H/q \approx 1 + 0.5 T_C \quad (28)$$

for "conventional" tractor-propeller-driven airplanes.

Dynamic Pressure Effects. Considering an airplane in powered flight we will assume that it performs pitching oscillations, at constant speed, with the thrust, thrust coefficient and dynamic pressure constant at the tail. The contribution of the horizontal tail is then proportional to the angle of attack, times

$$(1 + d\varepsilon/d\alpha)(q_H/q) = (1 + d\varepsilon/d\alpha)(1 + k T_C)$$

where $k = .5$ as possibly as in equation (28). For example, at $C_{L\alpha} = 1$, $T_C = 1$ for $k = 0.5$ and $d\varepsilon/d\alpha = -0.4$, we may expect to have a tail effectiveness, corresponding to $0.6(1.5) = 0.09 = \text{constant}$. However, the airplane is likely to change speed during its pitching motions. Neither q_H/q nor downwash and a number of forces and moments depending upon the thrust coefficient are, therefore, constant when considering the "static" derivative dC_m/dC_L .

Vertical Variation. The evaluation above is based upon the condition that the horizontal tail is really "in" the slipstream, as far as vertical location is concerned. Dynamic pressure ratios are plotted in figure 28 versus the vertical displacement z , above or below the "center" of the slipstream at the location of the tail. The function found might be expressed by

$$q_H/q = \cos^n \psi^\circ; \text{ where } \psi^\circ = k(z/r)^m$$

where k , m and n are suitable constants. In the form as interpreted, a maximum value of

$$d(q_H/q)/d(z/r) = -2 \quad (29)$$

might be encountered when "leaving" the slipstream area due to the loading distribution on the propeller blade.

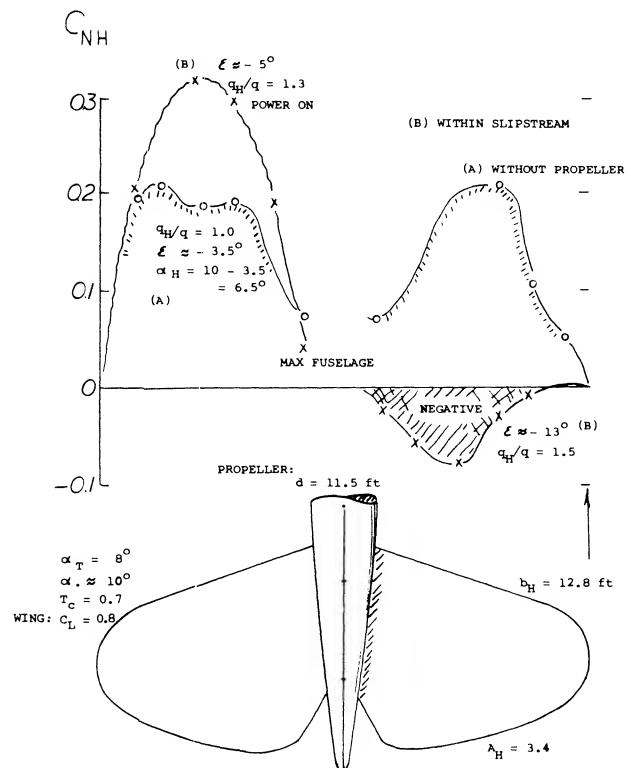


Figure 26. Load distribution on a horizontal tail surface as tested (14):
A) without propeller, B) within slipstream.

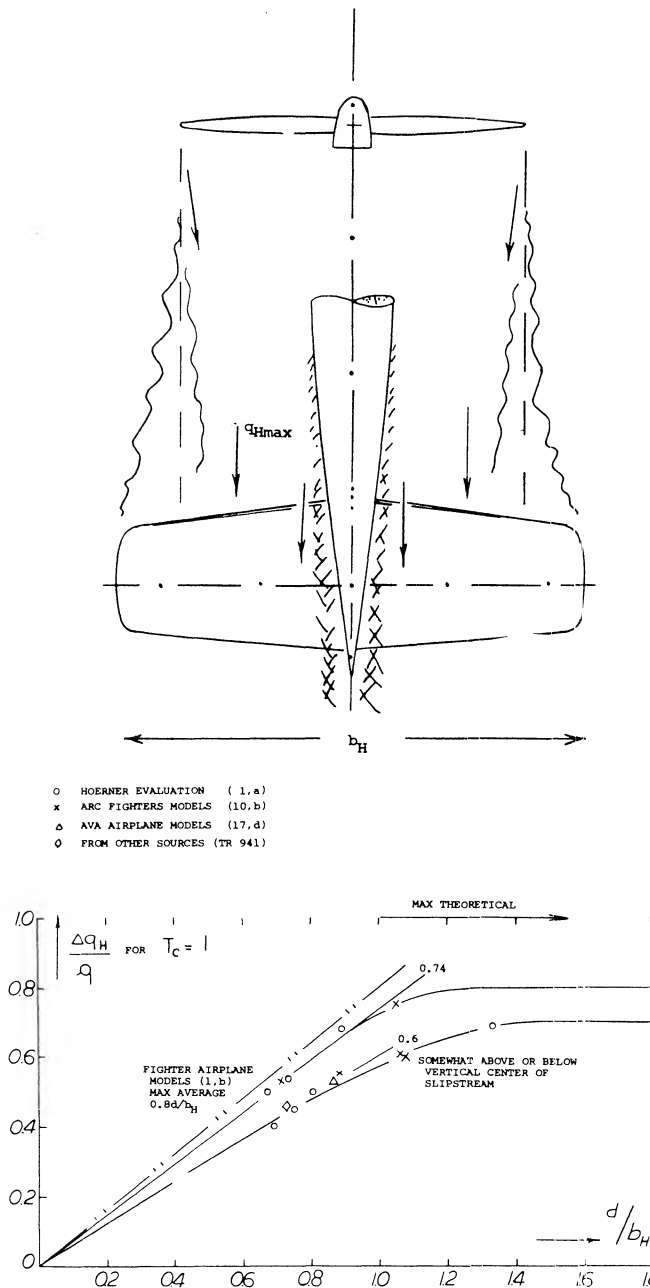


Figure 27. Mean dynamic pressure ratio at the horizontal tail located across the slipstream of single-engine airplane configurations.

Downwash Angle. The downwash angle is generally $\varepsilon = w/V$, where w = downward velocity imparted by the wing. After adding propeller and slipstream both the downwash velocity (w) and the longitudinal velocity (V) are increased, so that

$$\varepsilon = (w + \Delta w)/(V + v) \quad (30)$$

where w and ε = negative, and v = increment of V . Directly behind the trailing edge of a wing the downwash angle can be expected to be the same as without the slipstream ($\varepsilon \approx -\alpha$). Subsequently, the slipstream tends

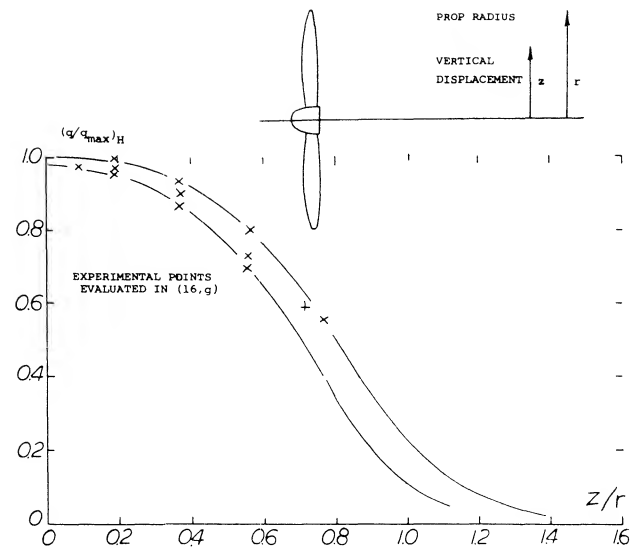


Figure 28. Variation of the average dynamic pressure across the slipstream, at the location of the horizontal tail, as a function of vertical displacement from the "center".

to keep that direction, so that its angle is not reduced as much as the downwash sheet. In fact, the slipstream may be expected to be directed downward at least as much as that of an isolated slipstream or jet. As illustrated in figure 29, the downwash at "some" distance behind such a propeller, is theoretically $w = -v\alpha$, so that the angle corresponds to

$$\begin{aligned} \varepsilon/\alpha &= -v/(V + v) \\ &= -(\sqrt{1 + T_c} - 1)/\sqrt{1 + T_c} \\ &= -(1 - (1/\sqrt{1 + T_c})) \end{aligned} \quad (31)$$

The fuselage of an airplane was tested (15,g) with operating propeller in front, but without the wing. As plotted in figure 30, the resultant average downwash angle in the slipstream at the location of the tail can be expressed by

$$\varepsilon = -0.21 \propto T_c^{3/4} \quad (32)$$

where the $3/4$ power produces a function similar in character to that in equation (31). For example, at $T_c = 1$, that equation yields $\varepsilon/\alpha = -0.29$. Momentum is evidently lost in the slipstream through dissipation and by way of friction along the fuselage. A similar investigation of a fuselage plus propeller, but no wing, in (16,c) shows downwash angles around 80% of the theoretical expectation.

Fuselage + Wing + Propeller. When adding a propeller operating at zero thrust to a fuselage-wing combination, it is quite often found that C_L as in figure 31 and $\Delta\epsilon$ as in figure 32 are both higher (by a few%) than without the propeller. It is also possible that the downwash angle increases at a rate higher than indicated by equation (33) over a small range of the thrust coefficient. The flow pattern along the wing roots (or along the engine nacelles) becomes evidently improved by the slipstream (mixing, turbulence, energy). It seems to be necessary, however, that there is a flow separation first, before the slipstream can have this effect. — Average downwash angles, evaluated from distributions at the location of the horizontal surface or as integrated by the tail, are plotted in figure 32. For an average value of $d\epsilon_o = -0.5 d\alpha$ (as in wings with A in the order of 6, at the usual location of the horizontal tail) equation (31) changes into

$$\Delta\epsilon/\epsilon_o = 2 - 2/\sqrt{1+T_c} \quad (33)$$

The experimental points plotted in this form are between 0.5 and 0.8 of the theoretical expectation. Again, there are evidently losses in the slipstream this time also along the wing roots. One reason for the spread in the graph is the wing plan form. In comparison to a tapered wing, a rectangular wing has only some 75% of the downwash in its center plane. When adding the propeller slipstream, therefore, the ratio ϵ/ϵ_o must be expected to be higher in the rectangular and smaller in highly tapered wings.

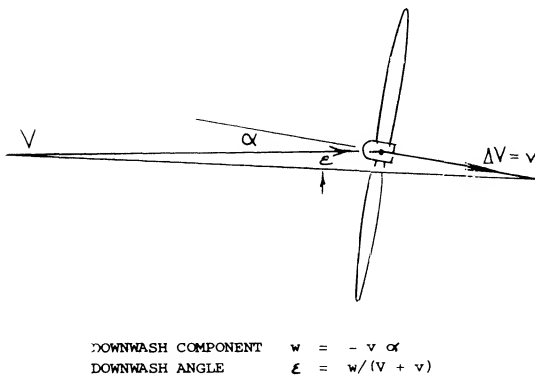


Figure 29. Downwash produced by a propeller; see (15,b). Example for $\alpha = 10^\circ$, $T_c = 1$ and $v/V = 0.4$. The resulting downwash angle is theoretically $\epsilon = -2.9^\circ$.

- (13) Influence of single propeller on stability, experimental:
- Goett, Tilted-Engine Axis, NACA T Rpt 774 (1944).
 - Priestley, Fighter Airplanes, ARC RM 2732 (1953).
 - Recant, Pursuit Model, NACA W Rpt L-710 (1942).
 - Weil, Curtiss BTC-2, NACA W Rpt L-667 (1944).
 - J Aeron Sci, High Wing, 1936 p 73; Low Wing, 1937 p 411.
 - Wallace, Influence on Low Wing, NACA TN 1239 (1947).
 - Purser, Unsymmetrical Horizontal Tail, NACA TN 1474 (1947).

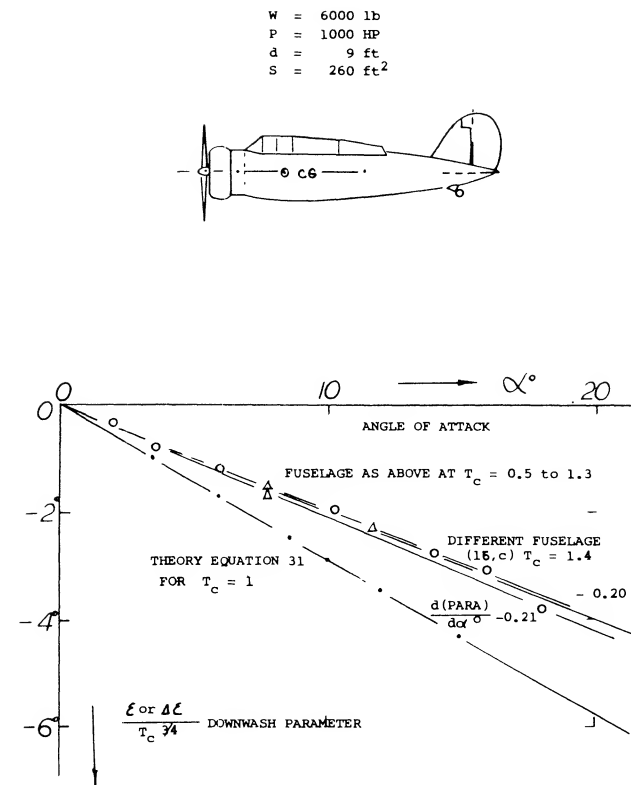


Figure 30. Fuselage with running propeller of Navy SBA-1 airplane. Downwash due to the slipstream.

Wing Roots. It is explained in the preceding chapter how most fillets increase, and that cut-outs reduce the downwash derivative at the location of the tail. Downwash angles tested behind the cut-out configuration as in figure 33 of the first chapter on "longitudinal stability" are included (\square) in figure 32. It is seen that the downwash is reduced to 70% of that of the original complete wing (denoted by ϵ_o). When adding the propeller slipstream it seems that the 70% ratio is maintained (70% of the increasing function). Cut-outs should, therefore, be very effective in regard to stability. Since the propeller more than replaces the lift that is likely to be lost on account of the cut-away wing chord, not much of a deterioration of performance may be expected. On the other hand, wing-root fillets leading to increased downwash derivatives must be considered to be detrimental to longitudinal stability, particularly when in the slipstream.

- (14) Sweberg, Horizontal Tail Load Distribution, NACA W Rpt L-227 (1944).
- (15) Flow field behind twin-engine nacelles:
- Stiess, Do-17 in Flight, Ybk D Lufo 1938 p I-206.
 - Schmidt, Do-17 in Flight, Ybk D Lufo 1941 p I-443.
 - In 2- and 4-engine pusher configurations, see (11,c).

Jet Propulsion. Jets originating from engines mounted in the wing can also be expected to have some effect upon the flow conditions at the horizontal tail. In the example of a twin-engine airplane as in figure 34, each jet produces some 1500 lbs of thrust through an outlet (nozzle) area of not more than 1.2 ft². In climb condition, the corresponding thrust coefficient (on outlet area) is in the order of $T_c = 30$, which is more than 30 times what a conventional propeller would have in the same flight condition.

a) WING-NACELLE COMBINATIONS

- ▲ AVA HS-124 TWIN ENGINES $2 S_d/S = 0.35$ (21,b)
- NACA MW NACELLE WITH $S_d/S = 0.17$ (20,a)
- NACA TWIN ENGINES MID-WING (22,f)
- NACA TWIN ENGINES $2 S_d/S = 0.33$ (20,b)
- x NACA B-28 TWIN ENGINES (22,c)
- γ ARC MID-WING NACELLE (6,c)
- ι NACA NACELLE MID-WING (20,a)
- NACA 4-UNDERSLUNG NACELLES (23,h)
- AVA WING PLUS MW PROPELLER, 0.21 (16,a)

b) LOW-WING CONFIGURATIONS:

- ▲ NACA PURSUIT W' $S_d/S = 0.38$ (1,b)
- ▽ NACA No. 12/13 FIGHTER, $z/c = 0.1$ (1,b) (13,d)
- + ARC "SPITEFUL" WITH $S_d/S = 0.48$ (13,b)
- ▲ He-70 AND Me-109 AIRPLANES (19,b)
- ι NACA PURSUIT AIRPLANE $R_c = 5(10)^5$ (13,c)

c) MID-WING CONFIGURATIONS:

- δ ARC WITH PROPELLERS $3 S_d/S = 0.74$ (6,d)
- h ARC $A = 6$, $d/c = 1.34$, $C_{L0} = 0.6$ (6,a)
- = NACA WITHOUT TAIL, $S_d/S = 0.35$ (13,a)

d) HIGH-WING AIRPLANES:

- ι ARC "PUSS MOTH" AIRPLANE (18,f)
- v AVA DORNIER 10 AIRPLANE (19,a)
- ι LOCKHEED "VEGA" AIRPLANE HW (18,b)

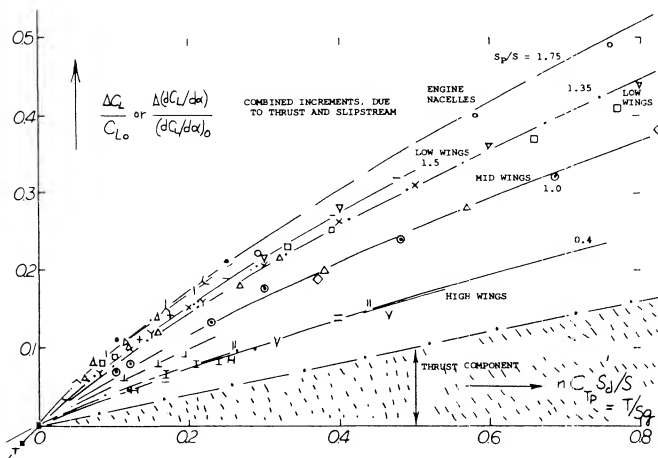


Figure 31. Experimental results indicated the lift increment of tractor-propeller-wing configurations resulting from thrust and slipstream.

(16) Jet Engine Effects on Tail Surfaces:

- a) Ray, Configuration Variables on Subsonic Longitudinal Stability.
- b) Brewer, Bell P-59 Bomber in FST, NASA W Rpt L-626 (1945).
- c) Blackaby, Jet Outlet Direction, NACA TN 2379 (1951).
- d)
- e) Duguet, Aerodynamics of Jet Nacelles on the Real Fuselage, 2nd European Aero Congress, Holland.
- f) Patterson, Tip Mounted Fan-jet Engine on the Lift-induced Vortex, TN D-5729.

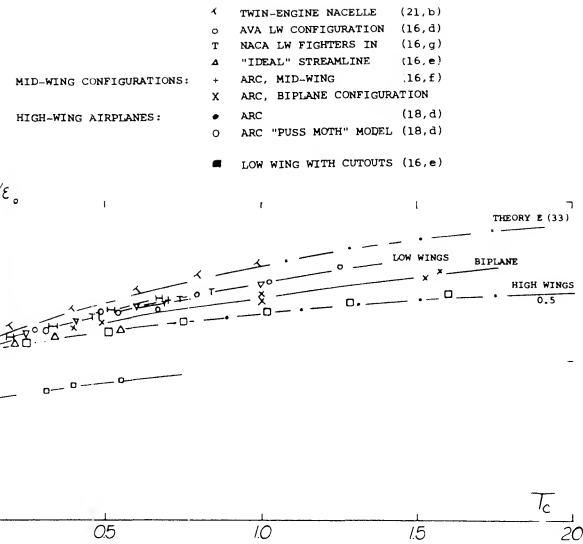


Figure 32. Magnification of downwash behind wings and wing-fuselage configurations as a function of the propeller thrust coefficient.

Downwash Due to Jet. Strong jets as described above may have a downwash practically equal to their angle of attack, $\epsilon = -\alpha$. In comparison to the slipstream of a propeller, the size (diameter) of a jet is small, however. The combined cross-sectional area (2.4 ft²) of the two jets in figure 34 is not more than 3.5% of the horizontal tail area (69 ft²). By comparison of the pitching moments with and without tail and thrust, respectively, it is found in the graph that the downwash angle variation $d\epsilon/dC_L$ or $d\epsilon/d\alpha$ is increased by jet action between 30 and 40%. Qualitatively this result may be explained by spreading the downwash momentum of the jets over a cross-section area equal to that of the horizontal tail. For $C_L = 0.6$, where $T_c = 30$, we may then obtain, for $2 S_d/S = 0.035$.

$$\Delta \epsilon / \epsilon = 0.4 (30) 0.035 \approx 40\%$$

where "0.4" is assumed to be the $\Delta (d\epsilon/d\alpha)$ in the original jet as against the downwash ratio behind the wing at zero thrust. This analysis should be refined by introducing $T_c \sim C_L$, and $\Delta \epsilon = f(T_c)$. A physical explanation for the influence of the jets upon downwash at the level of the horizontal tail is their dissipation, the transfer of momentum through mixing, upon the surrounding flow.

(17) High-wing, low-propeller airplane configurations:

- a) See several German airplane designs in (18,a).
- b) Millikan, Lockheed "Vega", J A Sci 3 (1936) p 79.
- c) Hagerman, Single Engine, NACA TN 1339 (1947); for lateral characteristics of same configuration, see TN 1379.
- d) Bryant-Williams, "Puss Moth", ARC RM 1687 (1936).
- e) Avion "W", Serv Tech Aeronautique (Brussels) Bull 15 (1935).

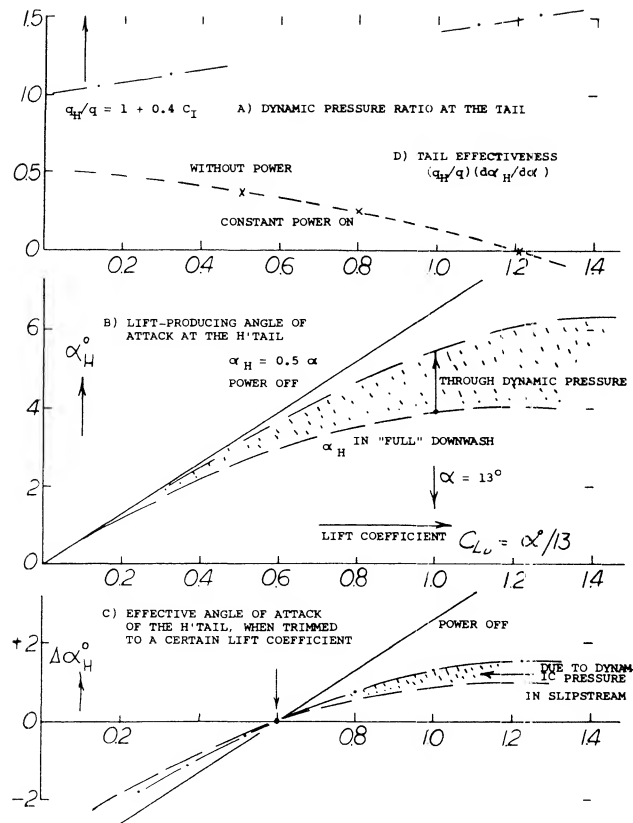


Figure 33. Result of a basic analysis regarding the contribution to stability of the horizontal tail, as affected by downwash and propulsion (slipstream).

Jet Engine Effects on Tail Surfaces. Although the efflux produced by jet engines does not impinge directly on the horizontal and vertical tail surfaces, their location influences the flow at these surfaces (16,a). The level of interference produced by the engines depends on their location, thrust, wing lift augmentation and flight speed. The engine location and orientation with respect to the aircraft cg influences the directional and longitudinal stability due to the thrust moment arms. For instance, the engine out yawing moment of tail mounted engines is generally less than for aircraft with wing mounted engines due to the reduced moment arm. This is especially true for typical four engine transport aircraft as compared with aft mounted two engine aircraft.

(18) Airplane models with running propeller:

- Stuper, Collection of Data, Ringb Luftf Technik IA12 (1939).
- He-70 and AR-196, tested at AVA, are included in (a).
- Hoerner, "Fi-157" in DVL Tunnel, Fieseler Rpt April 1937.
- Weil, 29 Configurations, NACA TN 1722 (1948); T Rpt 941.

Aft Mounted Engine Tail Interference. Rear mounted engines will influence the longitudinal stability of aircraft due to the flow induced on the tail surfaces by the lift of the engines and their supporting structure, by their thrust line orientation with respect to the cg and by interference effects. The aft location of the engine can also be important with regard to the flow interference of the wing on the intake air of the engine. This is illustrated on figure 35 for typical aircraft with aft mounted engines as a function of angle of attack and yaw angle for a range of the flow coefficients (16,e).

The lifting forces of aft mounted jet engines, including induced and interference effects, will effect the aircraft stability and the tail design. This is illustrated in (16,a) where the placement of aft mounted engines on a transport type airplane is investigated. As might be expected, the nacelles located furthest aft generally have the most favorable effect on longitudinal stability, especially at the higher angles of attack, figure 36. This result is expected on the basis of the lift produced by the engine nacelles and their interference effects on the horizontal tail. When the engines are mounted forward on the airplane, it will be noted from figure 36 that a destabilizing moment is produced when the angle of attack is above 20 degrees. At this condition the wake of the flow across the engine nacelles is spoiling the lift of the horizontal tail, thus reducing the stability.

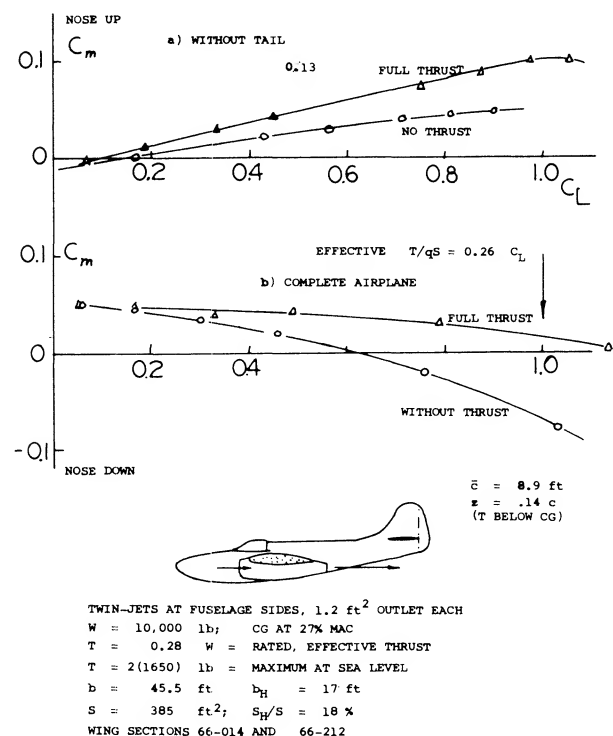


Figure 34. Bell P-59 first U.S. jet-propelled fighter (around 1943) as tested (16,b) in the Full-Scale Tunnel.

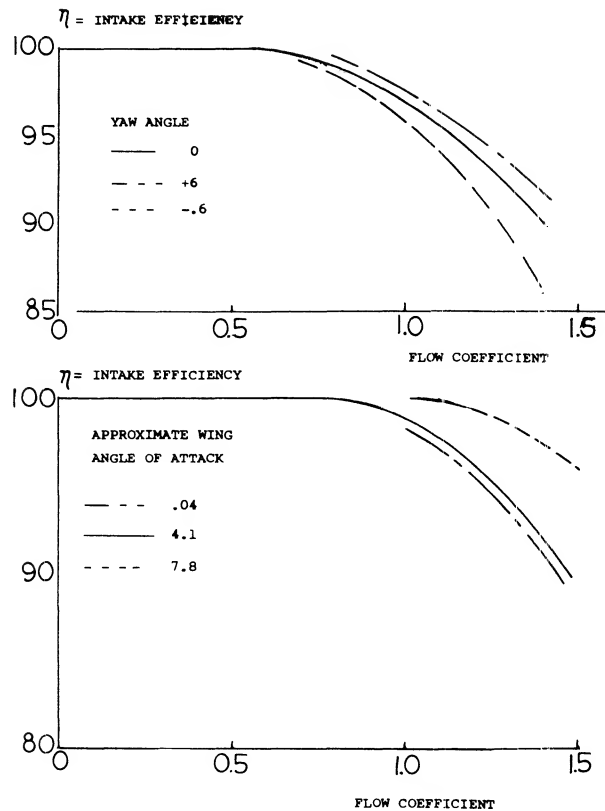


Figure 35. Intake efficiency of aft mounted nacelles as a function of angle of yaw and wing angle of attack.

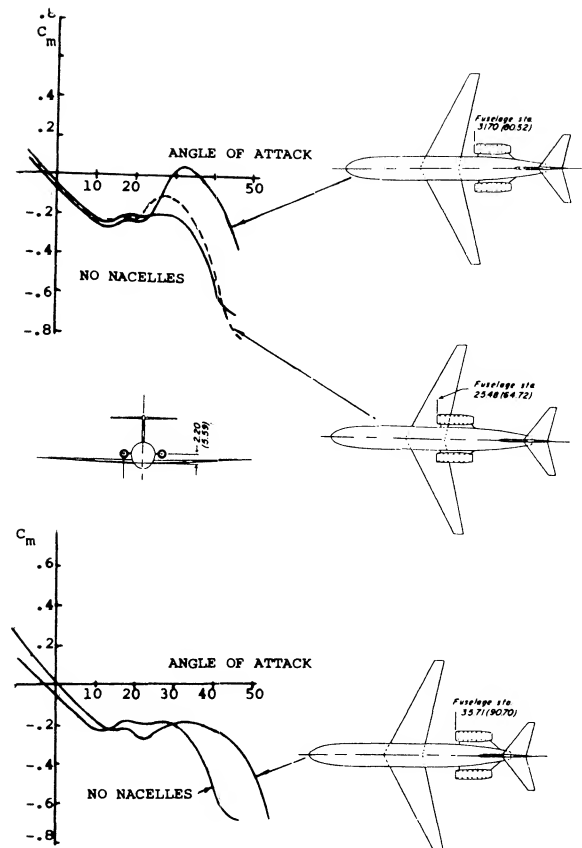


Figure 36. Effect of aft mounted nacelles on longitudinal stability.

Engine-Nacelle-Fuselage Integration. The fuselage nacelle combination can be designed to eliminate interference effects and prevent separation on the cowl by using a coke bottle type contour. Test (23) indicates the axial force can be reduced to just the added skin friction of the engine cowl skin friction. This is accomplished with a thin NACA-1 series cowl which gives a favorable interference effect that more than cancelled out the nacelle pressure drag. Very high drag Mach numbers (0.97) are achieved with such a design.

(19) Engine nacelles with propellers:

- a) Wood, Combinations, NACA T Rpts 415, 436, 462 (1932/33).
- b) Kuhn, Wing-Propeller Combination, NACA T Rpt 1263 (1956).

(20) Contra-rotation in twin-engine airplanes:

- a) Engines or propellers rotating in opposite directions are undesirable with respect to fabrication and number of spare parts to be kept available.
- b) Seiferth, In Wind Tunnel, Ybk D Lufo 1938 p I-220.
- c) Stiess, Do-17 in Flight, Ybk D Lufo 1938 p I-206.

(21) Investigation of twin-engine airplanes:

- a) Hoerner, Longitudinal Stability of Ju-288 Bomber in the DVL Wind Tunnel, Junkers Rpt Kobu-EW, 18 March 1941.
- b) Rogallo, NA B-28 Stability, NACA W Rpt L-295 (1943).
- c) Johnson, Lockheed "Electra", J A Sci 1935/36 p 1.
- d) Weiberg, Transport Airplane, NACA TN 4365 (1958).
- e) Sweberg, Twin Engine, NACA W Rpt L-425 (1942).
- f) Bryant, Longitudinal Stability, ARC RM 2310 (1940).
- g) Morris, Analysis of Flight Tests, ARC RM 2701 (1953).

(22) Investigation of 4-engine airplanes:

- a) Mathews, Boeing B-29, NACA TN 2238, T Rpt 1076 (1952).
- b) Weiberg, Transport Airplane, NASA TN D-25 (1959).
- c) Cowley, Armstrong-Whitworth 4 Engines, ARC RM 1624 (1933).
- d) Edwards, 4-Engine Swept Wing, NACA TN 3789 (1953/6).

(23) Blaka, Aft Engine Nacelles for $M=0.6$ to 1.0 , NASA TMX-3178.

Slipstream Effects of Wing Mounted Engines. As with aft mounted engines, the induced and interference effects of wing mounted engines will influence the flow at the tail surfaces and thus the stability. This is illustrated on figure 37, which shows the destabilizing moment curve of wing mounted nacelles when operating at angles above 20°.

With wing mounted nacelles arranged to produce high levels of lift augmentation, the size and location of the horizontal tail becomes critical as is discussed in (8,a). The high lift augmentation of the wing by the engine will result in high downwash angles at the normal horizontal tail location, which reduces the longitudinal stability. By moving the horizontal forward to a region outside the wake, the stability problem can be overcome.

An investigation was made of the effects of the engine located at the wing tip (16,f). In this case the engine is used to counter the tip vortex of the wing and thus improve the drag in a manner similar to tip tanks. The interference drag of other engine locations are covered for the larger fan jet engines, such as (16,g.).

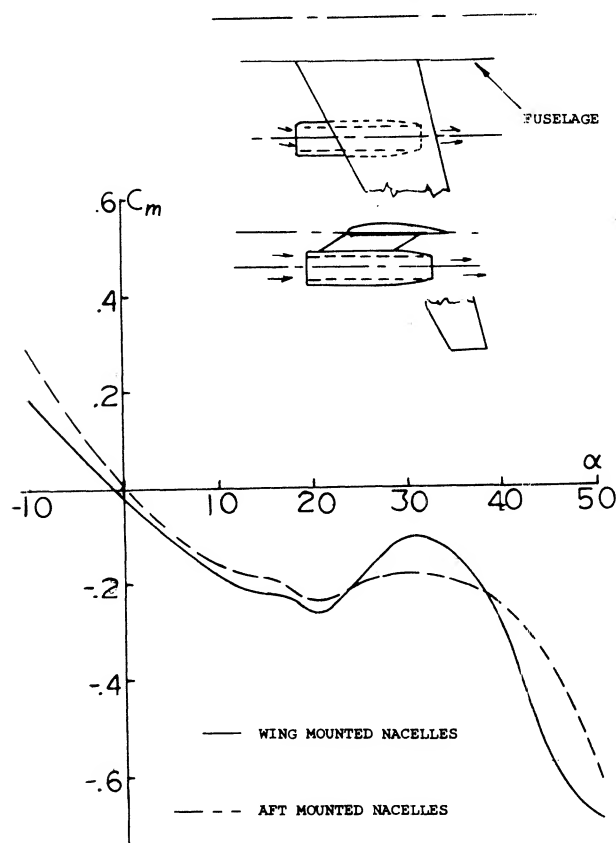


Figure 37. Influence of wing mounted nacelles on longitudinal stability.

(24) Section lift as influenced by rotation

- Hemmelskamp, Tests of sections on a propeller, Göttingen, Rep. No. 2, 1950.
- Baskin et al, Theory of the lifting airscrew, NASA TT F-823
- Schlichting, Boundary layer theory, McGraw Hill 1979
- Stepniewski, Rotary Wing Aerodynamics, NASA CR 3082

FLUID DYNAMIC LIFT

SECTION LIFT AS INFLUENCED BY ROTATION

Blade Section Lift: The thrust or lift produced by helicopter rotors, propellers and fans depends on the blade section lift characteristics. The lift of the blade sections is influenced by the three dimensional boundary layer developed on the blade due to the effects of rotation. Tests on various sections of a rotating propeller (24,a) have shown that both the lift curve slope and the maximum lift coefficient of a section will increase when installed on a rotating blade. These data (figure 38) show the increases are greater on the inboard sections. On the outboard sections of the propeller the section lift characteristics approach that of the two dimensional airfoil. These data confirm the pressure distribution data given in (24,b) and the operating characteristics of propellers which show much higher blade angles for stall than would be expected based on two dimensional airfoil data. This is illustrated by a $C_{L\alpha}$ of 3.2 for the section near the hub, $r/R = .4$, compared with the two dimensional value of $C_{L\alpha}$ of 1.4 as shown on figure 38.

The increase in $C_{L\alpha}$ on the inboard sections is caused by a delay of separation due to the action of centrifugal force causing an outward displacement of the boundary layer and a corresponding reduction of its thickness. This boundary layer displacement sets up Coriolis forces (24,c) which accelerate the boundary layer in the direction of the flow. Thus a favorable gradient is set up which prevents separation and thus leads to the improved lift curve slope and the $C_{L\alpha}$ observed on the inboard sections of the propeller.

Based on the above it is apparent that when applying two dimensional airfoil data in the analysis of helicopter rotors, propellers and fans that the effects of rotation on the characteristics of the airfoil data must be considered. The effects of rotational speed, blade radius, airfoil type and basic operational lift will influence the magnitude of the change that can be expected.

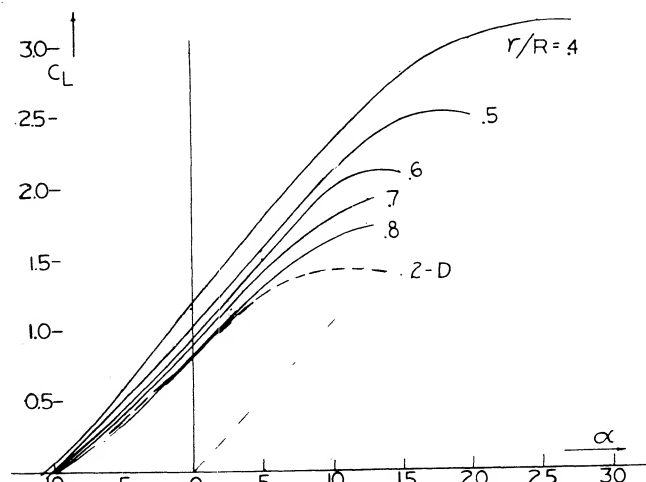


Figure 38. Section lift coefficients as measured on a rotating propeller as a function of blade radius.

CHAPTER XIII — DIRECTIONAL CHARACTERISTICS OF AIRPLANES

In considering the directional characteristics of airplanes it is assumed that the wings are kept horizontal by a suitable deflection of the ailerons. Thus, the vertical axis may be isolated from those in the other two directions. The static stability of such motions is then of the same type as that of a weather vane ("weather cock"). Subjects discussed in this chapter are: yaw moments due to fuselage and engine nacelles, stabilizing and control characteristics of the vertical tail and the influence of the propulsion system on yaw moments. Yaw moments arising in the wing (in connection with roll moments) are presented in Chapter XIV on lateral stability.

I. GENERAL

Reference. The system of axes used in this chapter is illustrated in figure 1. The angle of yaw " ψ " and/or of sideslipping " β ", due to yaw or when sideslipping, are defined about the vertical or lift axis, while the "lateral" force is normal to the fuselage axis. There is a convention whereby forces and moments are designated to be positive when their direction coincides with "positive" displacement of the airplane, that is a motion to the right is positive as seen by the pilot. It must be noted, however, that the angles β and ψ have opposite signs. A stabilizing yaw moment ("N") produced by a vertical tail-surface would thus be represented by a positive value of the derivative $d"N"/d\beta$, or a negative value of $d"N"/d\psi$, while the derivative of the lateral force in the tail responsible for the moment would have the opposite sign in either case. To avoid any misunderstanding, it is recommended to think in terms of "stabilizing" or "destabilizing", regardless of the direction (right or left) into which the airplane may turn.

"Yawing" is meant to indicate *rotation* about the normal (or vertical axis). The angle of yaw " ψ ", indicates the angular displacement about that axis, of the airplane in relation to the wind. In contradistinction, *sideslipping* means a lateral displacement of an airplane, without rotation, as in figure 1. However, to get into a sideslip, the pilot has to yaw his airplane first. As far as the usual wind tunnel tests are concerned, the models are not "yawing" at all. The term "yawing" moment thus seems to be misleading. Actually, static forces and moments are measured at an angle of yaw, or in sideslipping condition. It thus seems to be better to call this type of moment "yaw moment". In a dynamic analysis of motions about the normal axis, there is also a damping moment due to yawing. This moment will be discussed in the dynamic part of Chapter XIV dealing with "lateral stability".

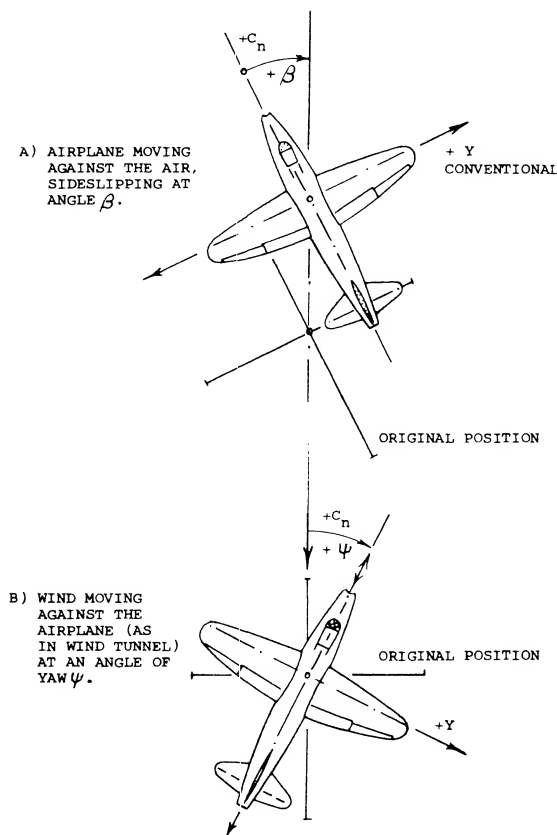


Figure 1. System of axes used in analysis and presentation of directional characteristics of airplanes.

(1) Regarding systems of reference for forces and moments, see NACA Rpt 474 (1933), or Perkins & Hage "Performance Stability Control".

Yaw Moments arising in conventional airplane configurations, are as follows:

- due to fuselage and nacelles, usually destabilizing;
- stabilizing moment provided by the vertical tail surface;
- a destabilizing contribution due to propeller normal force. (see figure 3 chapter XII)

The yaw moment derivative of the wing can theoretically be zero. In reality, a stabilizing component is associated with the roll moment which every airplane requires for lateral stability, chapter XIV. In the discussion of directional stability in this chapter, it is assumed that any roll moment be eliminated (balanced) by aileron deflection. In short, the wing is assumed not to contribute to the yaw moment of the airplane.

Notation. The notation specifically applying to directional characteristics is as follows:

Y = lateral force; "N" = yaw moment

where "N" (indicating the "normal" axis about which the moment is defined) should not be confused with N, denoting "normal force". Non-dimensional coefficients are

$$C_Y = Y/qS; \quad \text{and} \quad C_N = "N"/qSb \quad (1)$$

where S = wing area and b = wing span of the airplane considered. Usually, and at least within the range of lift coefficients below stalling, the lateral force as well as the yaw moment vary in proportion to the angle of sideslipping. The most convenient way to describe this variation is by means of the derivatives

$$C_{Y\beta} = dC_Y/d\beta; \quad \text{and} \quad C_{N\beta} = dC_N/d\beta \quad (2)$$

where β = angle of sideslipping, in degrees. In airplanes, the axis about which the yaw moment is taken, is usually the vertical (or the normal) through the CG.

Static Stability. Like the longitudinal case an airplane will have or will be statically stable when it has the tendency to return to its direction of flight after being disturbed. Although there is always an interacting roll effect it is possible to assume proper compensation so that the yaw stability is treated separately. Thus if the airplane has static stability in yaw a moment must be generated from the displacement that will tend to return it to a zero sideslip. Thus in the stability axis of notation $dC_N/d\beta$ must be positive, figure 1, if the airplane is to be statically stable in yaw.

II. YAW MOMENTS OF FUSELAGES

The longitudinal moments of slender bodies are presented in Chapter XIX dealing with these bodies. The yaw moment characteristics of airplane fuselages are as follows.

Basic Moments. Theoretically (without viscosity, boundary layer, etc.) any elongated body such as a circular cylinder for example, in longitudinal (axial) flow, develops a destabilizing moment. This moment tends to turn the cylinder or any streamline body into the stable position at or near α or $\beta = 90^\circ$. Also, under ideal conditions, there is neither drag nor lift. Accordingly, the ideal moment is "free", it is independent of the point of reference. In reality, every "slender" body develops a type of lift normal or lateral force, similar to that as found in slender wings.

Contrary to conditions in such wings (where the linear lift component is concentrated near the leading edge), this force originates by way of viscous boundary layer momentum losses, primarily in the rear half of the body length. Thus with conventional fuselages the yaw moment resulting from such lateral forces, is stabilizing.

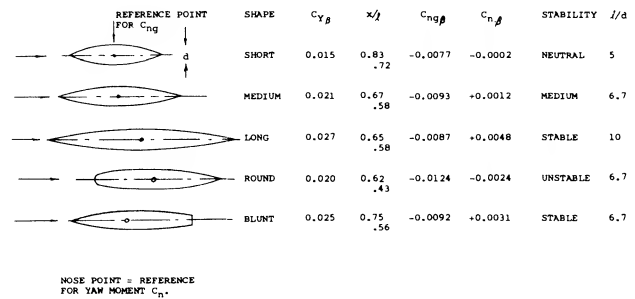


Figure 2. Directional characteristics of a series of *streamline bodies* or fuselages.

Fineness Ratio. A series of three streamline bodies is shown in figure 2, varying in length/diameter ratio between 5 and 10. The yaw moment of these bodies is presented in form of the coefficient

$$C_N = "N"/q\ell d^2 \quad (3)$$

To facilitate analysis, the moment is also referenced to the nose of the bodies, in form of the derivative

$$C_{N\beta} = C_{N\beta} + 0.5 C_{Y\beta} \quad (4)$$

where $0.5 = \Delta x/\ell$ = distance between the nose point and the original reference axis at 0.5ℓ . Any moment about the nose point is the sum of two components:

- the destabilizing theoretical or the moment based on ideal flow.
- the stabilizing moment due to the lateral force.

As explained in Chapter XIX on “slender bodies”, the maximum moment based on ideal flow approximately corresponds to

$$C_{\eta\beta} = -0.015 \text{ (destabilizing)} \quad (5)$$

In comparison to this equation, the theoretical moment decreases if the fullness of the body shape and/or the length ratio is reduced. The theoretical derivative is approximately:

$$C_{\eta\beta} = \begin{aligned} &= -0.015 \text{ for high length to diameter ratios} \\ &= -0.012 \text{ for length} = 6 \text{ (diameter)} \\ &= -0.009 \text{ for length} = 4 \text{ (diameter)} \end{aligned}$$

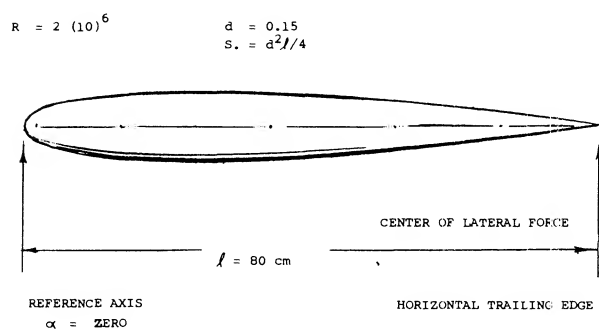
Lateral Force. As noted in figure 2 the lateral force coefficient of the bodies is referred to the square of their diameter

$$C_{Yd} = Y/q d^2 \quad (6)$$

the derivative of this coefficient increases approximately in proportion to the length ratio. This means that the lateral force grows in proportion to wetted area, skin friction and drag. If referring the coefficient to the “area” ($d\ell$) the roughly constant force derivative

$$dC_Y/d\beta = (d\ell) dC_{Yd}/d\beta = 0.003 \quad (7)$$

is obtained. This value must be expected to vary in proportion to the body’s drag coefficient (shape, surface roughness, appendages, interference).



DERIVATIVES AROUND $\beta = 0$:			
$C_{lat} = Y/zS$	$C_{Y\beta}$	SMOOTH	ROUGH
$C_{n.} = "N"/qS\ell$	$C_{n\beta}$	0.0080	0.0170
$C_{D.} = D_{min}/qS$	$C_{D\beta}$	-0.0098	-0.0046
		0.051	0.202
			MINIMUM DRAG

Roughness. The streamline body in figure 3, was tested (2,j) in smooth condition as well as with sand-type roughness applied to the surface. Using a grain size k of 0.9 mm, so that $k/\ell \approx 0.001$, the minimum drag coefficient was increased fourfold and the lateral force was doubled. In non-viscous fluid flow, the longitudinal of yaw moment would correspond to equation 5. Considering skin friction and when adding roughness, two things are to be expected:

- 1) the theoretical destabilizing moment will be reduced
- 2) part of that moment will be replaced by lateral force.

Since the force is likely to develop or to be centered in the rear half of the body length, the corresponding moment about the fuselage’s or airplane’s CG, is usually stabilizing.

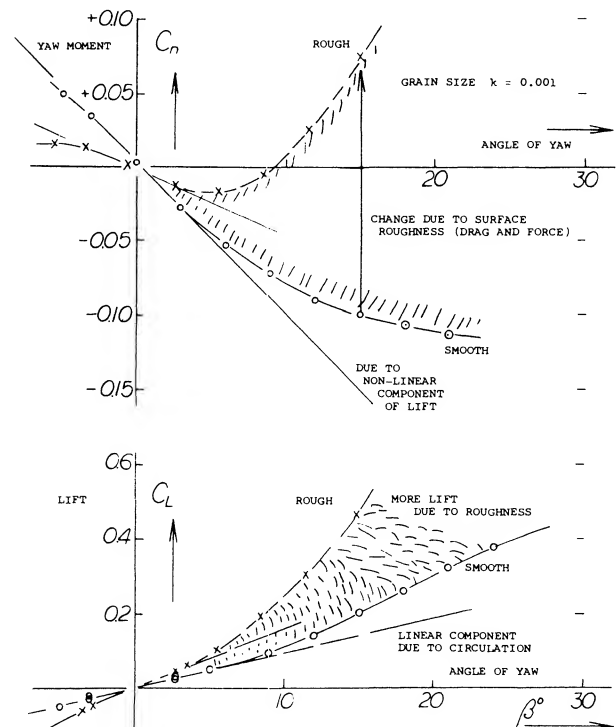


Figure 3. Directional characteristics of a simple fuselage body, tested (2,j):

- a) in smooth condition,
- b) with sand-type roughness added.

- (2) Directional characteristics of fuselage bodies:
 - a) See references in the chapter on “slender bodies”.
 - b) Allen, Influence of Viscosity, NACA Rpt 1048 (1951).
 - c) Queijo, Tail Size and Length, NACA Rpt 1049 (1951).
 - d) Lichtenstein, Tail Length, NACA Rpt 1096 (1952).
 - e) Bates, Flat Fuselage Shapes, NACA TN 3429 (1955).
 - f) Letko, Cross Section Shape, NACA TN 3551 (1955).
 - h) Letko, Cross-Section Shapes, NACA TN 3857 (1956).
 - i) Pass, Directional Stability Information, NACA TN 775 (1940).
 - j) Engelhardt & Hoerner, Influence of Surface Roughness, Rpt Aerodynamic Laboratory TH Munich 1/1943.

Location of Force. In the sand-covered body in figure 3, the experimental results can be obtained analytically when reducing the ideal moment equation 5 by 20%, and assuming that the lateral force be centered around 0.6 of the body length. The three lengths in figure 2 have been evaluated, using tested values and equation 5 with a constant of -0.012 as well as -0.011 . Using equation 7 the stabilizing component due to lateral force, is estimated to be

$$C_{n\beta} = + (x/\ell) 0.003 (\ell/d) \quad (8)$$

It then seems that the center of the viscous force is at x between 0.6 and 0.8 of the body length.

Shape. It is evident in figure 2, that the body with the round and full forebody has a larger destabilizing moment. On the other hand, the last shape, with a heavier afterbody (and a blunt base) is seen to be more stable. The family of plain fuselage bodies shown in figure 4 was tested (2,f,g,h) with the same length and volume, but differing in cross-sectional shape. At angles of yaw up to 8° for one shape and to 15° for another the lateral forces and yaw moments vary in linear proportion to the lateral angle, so that the corresponding derivatives are constant. In terms of fuselage length ℓ and the diameter d of the "round" type, results are presented in form of the coefficients defined above. The moment derivative is listed as tested (about the half-length axis) as well as about the nose point. In terms of lateral force the rectangular shapes behave in a manner similar to "wings". The "flat" body produces the smallest, and the upright rectangular shape the largest lateral force.

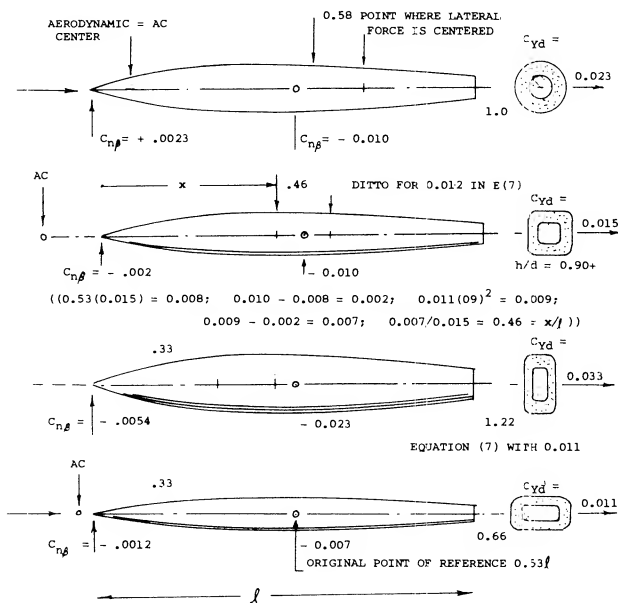


Figure 4. Lateral and directional characteristics of a family of four basic fuselage shapes, analyzed as explained in the text.

Analysis. All body shapes in figure 4, except the round one, are slightly unstable (about the nose point). This means, considering the fuselages to be wind vanes, they would assume a small angle of yaw (either positive or negative). The lateral curvature of the rectangular shapes evidently produces destabilizing suction forces. Using slender-body theory as presented in Chapter XIX, the basic destabilizing moment corresponds to the derivative as in equation 5 using the maximum height (h) instead of (d), and with a constant of 0.011. Referring the moments of all shapes tested, to the diameter (d) of the circular cross section, their theoretical derivatives are

$$dC_{nd}/d = 0.011 (h/d)^2 = C_{nd\beta} \quad (9)$$

After subtracting this ideal from the experimental total values, derivatives $C_{ny\beta}$ are obtained, tentatively representing the moments due to the tested lateral forces. The center of these forces is then found to be at

$$x/\ell = C_{ny\beta} / C_{yd\beta} \quad (10)$$

In the rectangular shapes, the center is between 0.3 and 0.5 of the length. The round shape shows, on the other hand, a location between 0.6 and 0.7 of the length. It seems that the flow goes smoothly *around* the forward end of this fuselage, and a lateral force only develops on the leeward side of the rear half of the length.

"Ducts". Figure 5 presents the directional characteristics of a fuselage to which a pair of "ducts" (solid bodies, without internal flow) were added. When exposed to an angle of yaw, the destabilizing moment is increased due to the ducts located on top and below the fuselage. Roughly, the ideal moment might be expected to grow with the square of the combined height "h", as indicated by equation 5 used with a constant of 0.012. In reality, the lateral area of the fuselage plus duct combination increases at a lesser rate than h . Also, the lateral force, the derivative of which is plotted in the lower part of the graph, is likely to contribute a stabilizing component to the yaw moment. Assuming, for example, a location of the force's center, 0.3ℓ behind the yaw axis, approximately $2/3$ of the differential indicated, can be explained. For the rest, it can be argued that the constant of equation 5 must reduce, as lateral forces replace the ideal moment.

Lateral Ducts. The vertical inlets shown in figure 5, were also tested when attached to the sides of the fuselage as wing root ducts. The graph shows that the value of the unstable yaw-moment derivative slowly reduces with a reduction of combined width of fuselage plus the pair of ducts. Important is the fact that the moment does not grow with the volume added to the fuselage. Rather, height and lateral projection are responsible for the magnitude of the destabilizing yaw moment. The reduction as

tested, might be explained by viscosity. It should also be noted that the pitching moments of the "ducts" as shown in figure 5, are presented in Chapter XI.

When applying ducts to the side of the fuselage it is generally desirable to install a boundary layer bleed system or allow the duct area to project above the boundary layer. This is necessary so as to provide the engine with air at high levels of ram efficiency. Also, if the inlet ducts supply a single plenum chamber it is possible to encounter a directional instability. Such an instability was encountered on the original F-80 airplane. In this case the airplane tended to yaw to an angle where one side duct had clean air without boundary layer flow, the opposite side being effectively stalled. The stabilizing yaw moment corrected the yaw angle causing the other duct to operate in clean air. This alternate filling of the opposite duct resulted in a yaw oscillation that was unsatisfactory. The addition of boundary layer bleed ducts in the system corrected the problem.

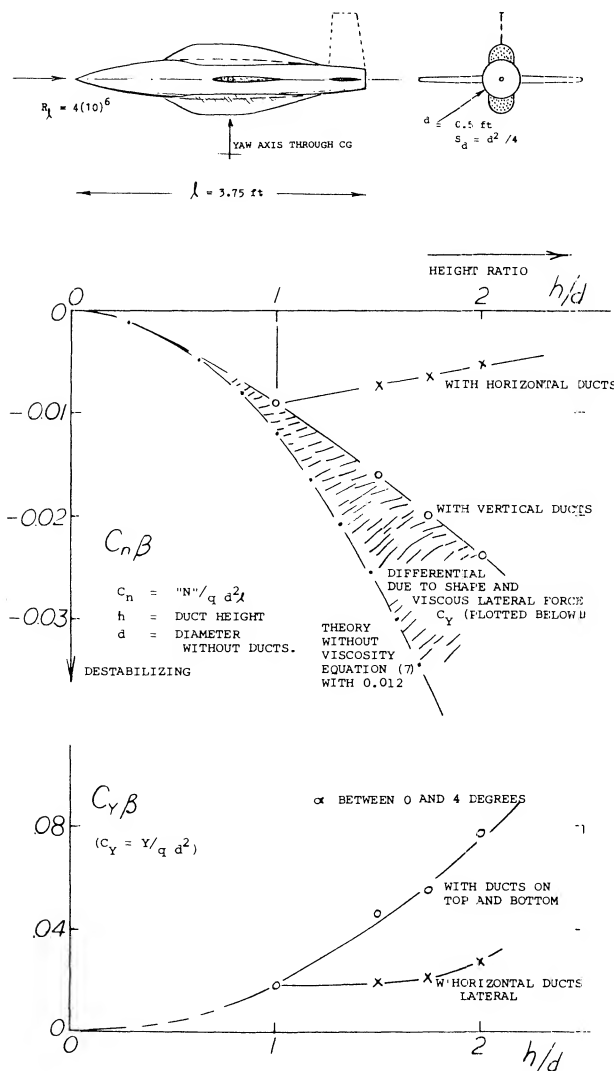


Figure 5. Directional characteristics of a fuselage (TN 3481) with a pair of "ducts" added on top and bottom.

Fuselage Forward. Directional characteristics of a wing-body combinations are presented in figure 6. The "fuselage" in the center might be found in a configuration where the tail surfaces are supported by a pair of booms within a tailless airplane. Dividing the fuselage contributions (based upon wing dimensions):

$$\Delta C_{n\beta} / \Delta C_{Y\beta} = -0.0012 / 0.0010 = -1.2 = \Delta x / b \quad (11)$$

we find that the neutral point in regard to the moment about the vertical axis, is located at $(1.2 b)$ forward of the CG of the airplane. The yaw moment caused by viscosity and lateral force evidently combines with the ideal moment to make the configuration very unstable. Assuming that this ideal moment may correspond to

$$C_{n\beta} = (l/b)(d^2/S) 0.013 = 0.99 (0.077) 0.013 = -0.0010 \quad (12)$$

the remaining component is $-(0.0012 - 0.0010) = -0.0002$. Dividing by the derivative of the lateral force coefficient $\Delta C_{Y\beta} = 0.0010$, yields $\Delta x/b = -0.0002/0.0010 = 0.20$. In other words, the center of the lateral force is estimated to be $(0.20 b)$ ahead of the CG at $x/l = 0.55$, as shown in the illustration.

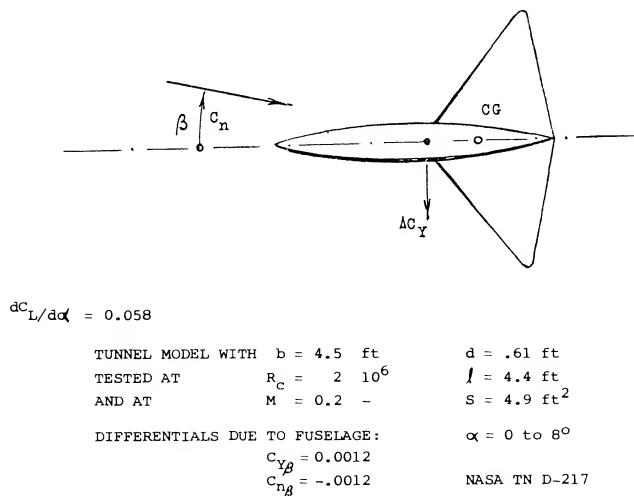
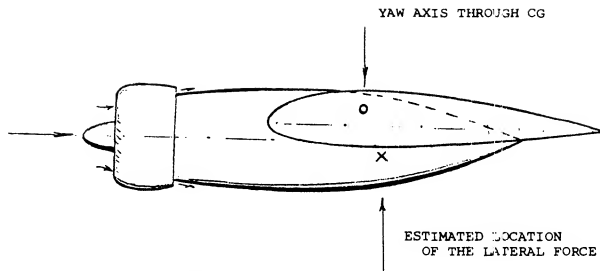


Figure 6. The yaw moment contribution of a forward located fuselage.

Engine Nacelles. The "fuselage" in figure 6 resembles a plain and smooth engine nacelle. Analysis as above, suggests that the stabilizing yaw moment due to lateral force about the CG of a conventional airplane configuration may be small. Equation 7 might thus be adequate to predict the yaw moment due to ordinary engine nacelles. Engine nacelles, installed in the wing, also differ from fuselages as to their length. The ratio l/d is smaller and the nacelle body generally blends into the wing. A model-tested example of a typical nacelle is presented in figure 7.



FULL-SCALE AIRPLANE DATA:

FOCKE-WULF FW-200
LONG RANGE (ATLANTIC)
OPERATIONAL ABOUT 1940

b = 33 m
S = 121 m²
V_x = 360 km/h
4 x 720 HP
C_D = 0.02 min

ENGINE NACELLE TESTED AS ONE OF 4,
ON A 1 TO 25 SCALE MODEL AT
R_C = 4(10)⁶ FULL-SCALE NACELLE
DIAMETER = 1.4 m

ENGINE NACELLE TESTED AS ONE OF 4,
ON A 1 TO 25 SCALE MODEL AT R_C = 4(10)⁶
FULL-SCALE NACELLE DIAMETER = 1.4 m

Figure 7. Directional characteristics of an engine nacelle (3,b) tested as part of the wind tunnel model of a 4-engine military airplane.

Splitting the body into two halves, the upper one may roughly have an effective length ratio $\ell/d = 2$, and the lower one = 4. As explained above, the yaw moment coefficient, equation 5, reduces with the length ratio. The reduction factor is about 0.6 for $\ell/d = 4$ and 0.4 for $\ell/d = 2$; the average is 0.5. Since the length is different in the two halves of the nacelle considered, we will refer the moment as tested to (d^3); thus:

$$C_{nd^3} = "N"/q d^3 = C_{nd}(\ell/d) \quad (13)$$

Using the factor as above and the average "exposed" length ratio = 3, we obtain from equation 7:

$$(C_{nd^3})_\beta = -0.5 (0.013) 3 = -0.020$$

This result is slightly higher than the tested value (0.019). Using the experimental lateral force differential due to the nacelle, $(C_{yd})_\beta = 0.005$, a stabilizing component

$$(C_{nd^3})_\beta = (C_{yd})_\beta (\Delta x/d) = 0.005 (\Delta x/d)$$

can be found. To explain the difference as above $(0.020 - 0.019) = 0.001$, the center of C_{yd} must be assumed to be $(0.001/0.005) = 0.2$ nacelle diameters aft of the yaw axis through the CG (as indicated in the illustration). However, the cowling (ring) at the front end of the nacelle would increase the destabilizing moment above the value of -0.020 as computed above.

- (3) Directional characteristics of engine nacelles:
a) Fournier, "Exotic" Configuration, NASA D-217 (1960).
b) Pabst, FW-200 Airplane, Focke Wulf Wind-Tunnel Rpt 41 (1938).

Airplane Configurations. The fuselage and engine nacelles of typical airplane configurations without a vertical tail attached and propellers have destabilizing yaw moments about as follows:

single engine in fuselage	$C_{n\beta} = -0.0001$
typical twin-engine	$= -0.0002$
four-nacelle configuration	$= -0.0003$

These moments are small by comparison with typical vertical tail surface which contributes a stabilizing derivative between 0.0005 and 0.0010.

III. VERTICAL TAIL CHARACTERISTICS

The purpose of the vertical tail surface is to provide directional stability and control moments. Analysis of the yaw moments developed is complicated by the structural connection between tail, fuselage and horizontal surface.

1. FUSELAGE INTERACTION

In all airplanes with a central vertical fin, the fuselage has a considerable influence upon the lateral forces produced on and by the vertical surface.

Aspect Ratio. Modern airplanes usually have vertical tail surfaces with an exposed geometric aspect ratio larger than unity. The lateral or normal forces originating in them, may thus be proportional to the angle of yaw or sideslip. The lateral force characteristics of vertical tails can be from the data such as (5,a) or that of Chapter XVIII. In the statistical evaluation of tested lateral forces (subscript "lat") we will use equation (12) of Chapter XVIII, for indicating the yaw angle required to produce a certain force in the vertical tail. This equation is:

$$d\beta/dC_{lat} = 10^\circ + (10^\circ/A_{\chi}^2) + 19^\circ/A_{\chi} \quad (14)$$

Because of physical continuity between fuselage and tail, it is difficult to determine the effective ratio A_{χ} ; and the magnitude of the effective lateral area due to the appreciable amount of fuselage interference upon the vertical surface.

- (4) Yaw moments due to other appendages:
a) Jaquet, Fuselage with Ducts, NACA TN 3481 (1955).
b) MacLachlan, Influence of Canopies, NACA TN 1052 (1946).
c) External stores or tanks.
- (5) Lateral Force on tails
a) Dods, Nine Related Horizontal Tails NACA TN 3497.

Cylindrical Fuselage. In configurations where the fuselage is a body of revolution, a simple geometric definition for finding the span, area and aspect ratio of the vertical tail surface is to use the distance from the tip to the body's center line. Lateral force characteristics are shown in figure 9 of a rectangular fin attached to a cylindrical "fuselage". This configuration is basically similar to the combination of a wing with a tip tank. A theory of the interaction is presented in (7); and tip-tank results are evaluated in the Chapter III.

Roughly, the cylinder will have a lift-increasing effect similar to an end plate. The effective aspect ratio is theoretically increased by a maximum of

$$\Delta A = A_V(d/b); \quad A_{\chi} = A_V(1 + d/b) \quad (15)$$

Considering the results in figure 8, the "force angle" of the vertical surfaces tested without the presence of a horizontal surface can be explained by combining equations (14) and (15). For example, for the geometrical aspect ratio $A_V = 1.33$ (measured to the center line of the fuselage) we obtain a sectional angle $d\beta/dC_{lat} = 15.7^\circ$, and an included component of $19/1.33 = 14.3^\circ$. The combined angle is 30° , and the force derivative is thus $dC_{lat}/d\beta = 0.033$. This is much smaller than the tested value (0.043). To account for the end plate effect of the fuselage ($d/h = 2/3$), the function in figure 15 of the Chapter III can be used. The effective aspect ratio is then found to be $A_{\chi} \approx 1.33(1.5) = 2$; and the derivative of the lateral angle required, is expected to be $d\beta/dC_{lat} = 10 + 2.5 + 9.5 = 22^\circ$. The corresponding slope of the lateral force is $dC_{lat}/d\beta = 0.045$ which is close to the tested value of 0.043. Part (b) of the illustration shows that a tapering afterbody results in somewhat reduced tail effectiveness.

Fuselage Force. In case (c) of figure 9, another vertical tail surface is attached, not to the end of the fuselage, but somewhere near half of its length. The lateral force due to the tail surface (having an aspect ratio of 2.2) is so high that it cannot adequately be explained in the manner as above. Load distribution tests (6,c) carried out on the last (swept) fin in the illustration, reveal that the combined lateral force, on the fin and induced upon the fuselage by the fin, is about 50% larger than that in the exposed vertical area. It thus seems that presence of the fin converts that part of the fuselage into a piece of "wing". The vertical tail effectiveness can be explained or predicted, using equations (14) and (15) considering an area producing lateral forces to be effective within the fuselage, equal in magnitude to (d c) as indicated in figure 8. In practical designs it does not seem likely, however, that a tail surface would not be located near the very end of the fuselage (where the moment arm is longest).

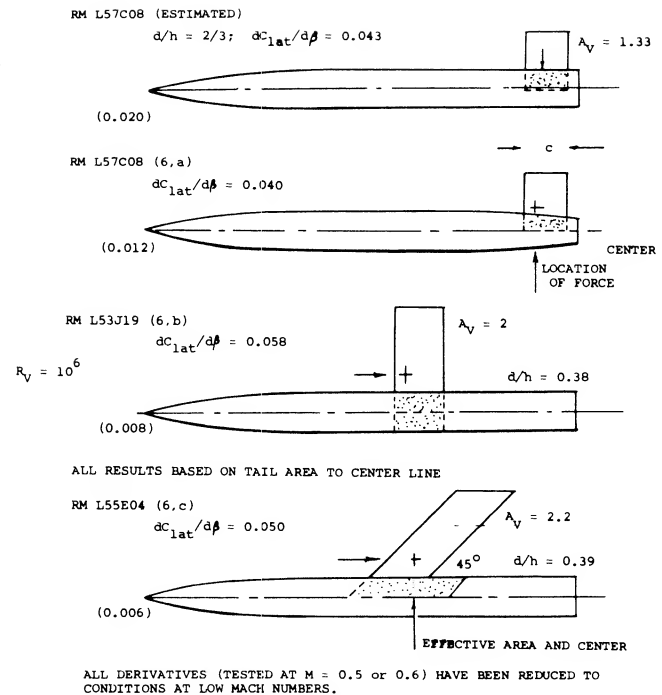


Figure 8. Lateral force derivatives of vertical fins when attached to cylindrical fuselages.

Fuselage Diameter. The type of fuselage as in figure 9, may be used in aircraft exhausting the propelling jet through the blunt base. Airplanes with propeller propulsion, generally have fuselages with a more or less tapering tail end. Experimental investigation of several "families" of vertical fins (9) (10) (11) (12) permits evaluation of their effectiveness as a function of the size of the fuselage to which they are added. In one of those (8) the vertical tail aspect ratio varies between 0.5 and 4.0, and its area S_V between 0.6 and 6.0 of the fuselage's frontal area S . Results have been transformed to our method of defining vertical dimensions from fuselage center line. Figure 9 demonstrates for the nominal aspect ratio $A_V = 2$, how the lateral force angle derivative $d\beta/dC_{lat} = 1/(dC_{lat}/d\beta)$ varies as a function of the tail size ratio h_V/d_V , where d_V = diameter of the fuselage at the quarter-chord location of the vertical tail attached to it.

- (6) Vertical tails on cylindrical fuselages:
 - a) Sleeman, Various Configurations, NACA RM L57C08.
 - b) Wiley, Fin on Cylinder, NACA RM L53J19.
 - c) Wiley, Swept Fin & Horizontal Tail, NACA RM L55E04.
 - d) Few, Tails on Boat-Tailed Body, RM L57D22.
- (7) Theoretical analysis of fuselage interaction:
 - a) Hartley, Wings with Tip Tanks, ARC CP 147 (1954).
 - b) Weber, Wings with Cylinder, ARC RM 2889 (1957).
- (8) Michael, V-Tail Fuselage Interference, NACA TN 3135 (1954).

The results can be interpolated by

$$d\beta/dC_{lat} = 12^\circ + 18/A_{\lambda}$$

where A_{λ} = effective aspect ratio of the tail surface, including the end-plate effect of the fuselage:

$$A_{\lambda} = 2(1 + 2(d_V/h_f)) \quad (16)$$

Assuming that the maximum diameter of the fuselage might statistically be $d = 2 d_V$, we readily obtain equation (15). The fuselage's end-plate effect is thus the reason why the functions in figures 10 and 20 are or should not be straight lines.

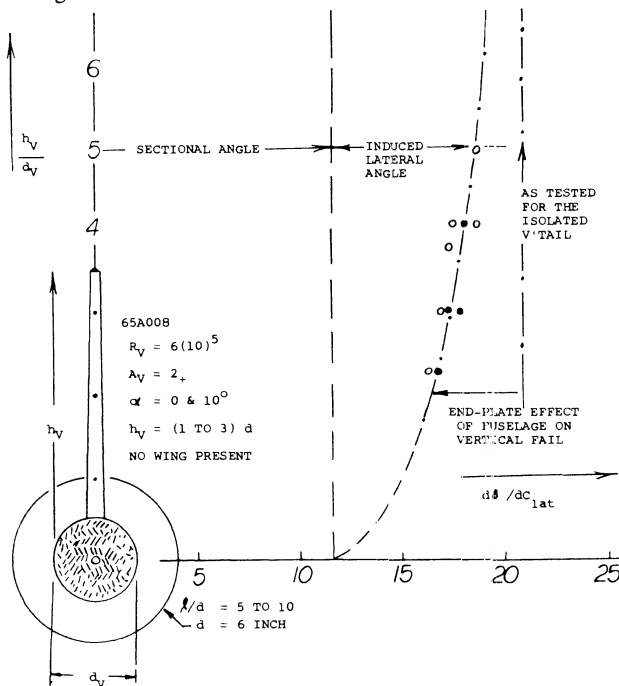


Figure 9. Evaluation (8) showing the end-plate effect of the fuselage upon the vertical tail surface.

Fuselage Length has an effect different from diameter. In figure 11, we have plotted the lateral force slopes of several series of vertical tail surfaces against the size ratio h/ℓ . The tail effectiveness increased by the end-plate effect of the fuselage is reduced because of presence and growth of the boundary layer along the fuselage. Since the "volume" of the viscous wake at the end of the fuselage is proportional to its length " ℓ ", the favorable interaction with the vertical surface (fin) is reduced as a function of ℓ/h , or increasing with h/ℓ . Of course, when increasing the size of the vertical surface indefinitely, the force derivative should come down again, ending up at the level as for the isolated tail.

(9) Influence of horizontal on vertical tail:

- Katzoff, End-Plate Effect, NACA TN 797 (1941).
- Murray, End-Plate Effect, NACA TN 1050 (1946).
- Brewer, Swept Tail Surfaces, NACA TN 2010 (1950).
- Rotta, Aerodynamic Characteristics of Wing with End Plate at One Tip, Ingenieur Archiv 1942 p. 119.
- Root, Empennage Design, J. Aero. Sci. 1939 p. 353.
- MacLachlan, Directional Stability, NACA TN 1052 (1946).
- Marino, Load Distribution, NACA TN 2488 (1952).

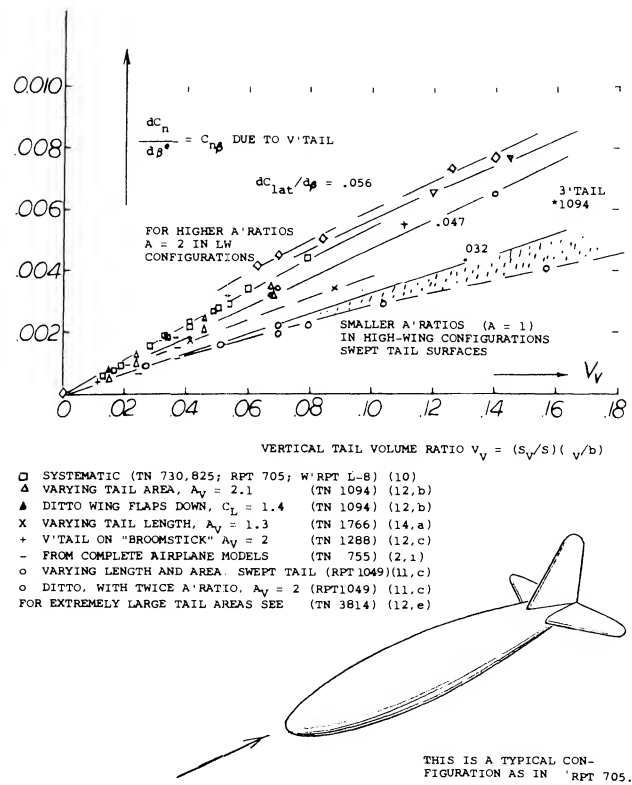


Figure 10. Yaw-moment contribution of vertical tail surfaces as a function of their "volume" ratio.

WRPTS L-8, 12, 17 (10)
0009 TAIL SECTION
d = 5.5 INCH
l = 32
l = 37
l = 42 INCH
h = 7
l = 9
l = 10 INCH
h_H = 16 INCH
A_V = 2.2
R = 4 10^6
- WITHOUT WING
(ALL OTHER TESTS WITH
WING, AT α = 0
ALSO WITH HORIZONTAL
TAIL ON)

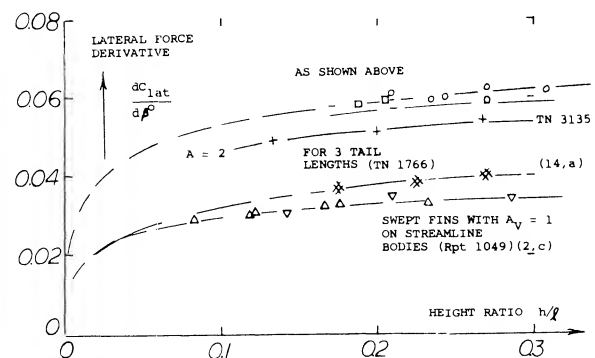
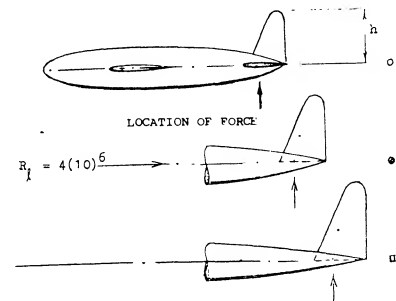


Figure 11. The effectiveness (lateral force derivative) of vertical tail surfaces when attached to the end of the fuselage.

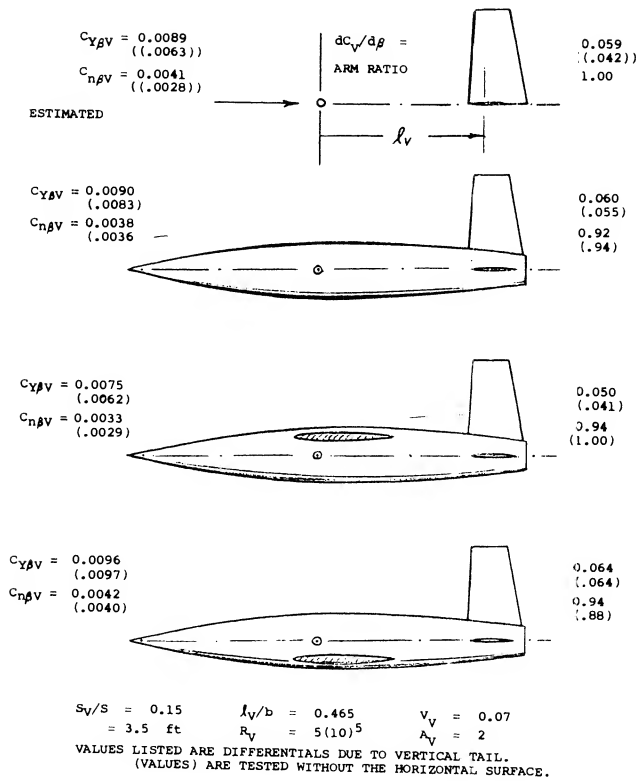


Figure 12. Interference of wing and fuselage upon the lateral force and the yaw moment produced by the vertical tail surface.

- (10) Lateral investigation of one and the same basic wing-fuselage-tail configuration in NACA wind tunnels:
- Bamber, I — Several 23012 Wings, TN 703 (1939).
 - Bamber, II — Lateral Characteristics, TN 730 (1939).
 - Recant, III — Component Characteristics, TN 825 (1941).
 - Recant, Side Flow at Tail, TN 804 (1941).
 - Jacobs, 209 Combinations Pitching, Rpt 540 (1935).
 - House, 4 Wings, 2 Fuselages, 2 Fins, Rpt 705 (1941).
- (10) g) Fehlnner, I — 5 V'Areas, 3 Fuselage Lengths, W'Rpt L-12(1944).
- h) Hollingworth, II & III — Same as in (g), W'Rpt L-8 & 17 (1945).
- i) Recant, IV — Wedge-Shaped Fuselage, W'Rpt L-520 (1942).
- j) Wallace, V — Tapered Wing, W'Rpt L-459 (1943).
- (11) Related wing, fuselage, swept tail model family:
- Brewer, Lateral Characteristics, TN 2010 (1950).
 - Letko, V'tail Stability Contribution, TN 2175 (1950).
 - Queijo, Size & Length of V'Tail, Rpt 1049 (1951).
 - Lichtenstein, Tail Length and H'Tail, Rpt 1096 (1952).
 - Yawing characteristics of same family, see NACA TN 2358.
 - Longitudinal characteristics, see NACA TN 2381 & 2382.
 - Wolhart, Three Aspect Ratios, TN 3649 (1956).
 - Also references (2,f,h) and (4,a) and (13,f).

- (12) Lateral stability and control characteristics:
- Schlichting, Interaction Between Wing Fuselage and Tail Surfaces, Ybk D Lufo 1943 Rpt IA028.
 - McKinney, Lateral Stability, NACA TN 1094 (1946).
 - Maggin, Swept Model Flight Tests, NACA TN 1288 (1946).
 - Michael, Fuselage V'Tail Interaction, TN 3135 (1954).

2. INFLUENCE OF WING AND HORIZONTAL STABILIZER ON VERTICAL TAIL

In conventional airplane design, the horizontal tail surface is more or less closely combined with the vertical surface. The interaction between them, and influence of the wing upon the vertical tail are covered in this section.

Sidewash. Consider the configuration at the bottom of figure 13, where the wing is located at the lower side of the fuselage. The flow around the lower side when operating at an angle of yaw is reduced, while flow over the upper side is increased. A rotation, or circulation of the flow, is thus produced, about the longitudinal axis of the fuselage. At the vertical tail surface location above the fuselage the flow over the top represents a certain side-wash and it combines with the lateral velocity component due to sideslipping. In the case of a low-wing configuration, this type of sidewash is stabilizing. Sidewash angles (σ) at the location of the vertical tail surface, where directly measured (10,d) for the "shortest" among the configurations are illustrated in figure 11. Without a horizontal surface present, average angles were found to be as follows:

configuration	$d\delta$	$d\delta/d\beta$ ($d\delta/d\beta$)	type of flow	dC_{lat}	$d\beta$ ratio
high wing	- 0.040	- 0.40	reduced side flow	0.030	0.64
no wing	+ 0.360	0	basic cross flow	0.047	1.00
low wing	+ 0.640	+ 0.28	increased flow	0.057	1.21

HIGH WING WITH $x = 0.20$ C_x

- a) WINDMILLING:
 $C_{YBV} = 0.0080 - 0.0040 = 0.0040$
 $C_{nBV} = 0.0010 + 0.0008 = 0.0018$
- b) WITH POWER:
 $C_{YBV} = 0.0100 - 0.0050 = 0.0050$
 $C_{nBV} = 0.0010 + 0.0010 = 0.0020$

1/5 SCALE MODEL, WITH:

$S = 9.4 \text{ ft}^2$
 $b = 7.5 \text{ ft}$
 $d_p = 2 \text{ ft}$
 $c = 1.35 \text{ ft}$
 $C_x = 4/3 \text{ } \bar{c}$
 $S_v = 13\% S$
 (EXPOSED FIN + RUDDER)
 $l_v = 0.44 b$
 $R_c = 10^6$
 POWER, SO THAT:
 $T = 0.18 W$
 $C_{Tp} = 0.54 -$

LOW WING WITH $x = -0.16$ C_x

- a) WIND MILLING:
 $C_{YBV} = 0.0100 - 0.0050 = 0.0050$
 $C_{nBV} = 0.0017 + 0.0008 = 0.0025$
- b) WITH POWER ON:
 $C_{YBV} = 0.0140 - 0.0055 = 0.0085$
 $C_{nBV} = 0.0021 + 0.0009 = 0.0030$

RATIOS OF VERTICAL TAIL CONTRIBUTION ARE: HW/LW = 0.7, or
 LW/HW = 1.4

NOTE: FIRST VALUES ARE WITH TAIL. SECOND VALUES WITHOUT.
 LOW WING IS MUCH MORE STABLE THAN HIGH WING.
 POWER INCREASES SIDEWASH AND STABILITY IN LOW WING.

Figure 13. One and the same type of airplane configuration tested (21,g,h) in low-wing as well as in high-wing arrangement.

For example in the LW configuration, the local angle of sideslip is $(1 + 0.64)\beta$; and the ratio is $1.64/1.36 = 1.2$. The force derivatives vary roughly in proportion to those of the flow angle $(\beta + \epsilon)$. In form of an equation, therefore, the lateral force in the vertical tail corresponds to

$$dC_{lat}/d\beta = (1 + \Delta(d\delta/d\beta))(dC_{lat}/d\beta)_o \quad (17)$$

where (o) indicates the force derivative of the tail on fuselage, but in the absence of a wing. The difference between LW and HW is appreciable.

Horizontal Tail Interference. Results of a wind-tunnel investigation (13,f,g) on the interference of horizontal tails are presented in figure 12. In comparison to the lateral tail-force derivative without the wing, ratios are as follows:

configuration	w'out H'tail	ratio	with H'tail	ratio
high wing	0.75 (0.65)	0.70	0.83 (0.82)	0.82
mid wing	1.00 (1.00)	1.00	0.98 (0.99)	1.00
low wing	1.16 (1.15)	1.16	1.07 (1.06)	1.07

The ratios found are confirmed by results listed in parentheses as quoted from (12,d). In comparison to low-wing conditions explained above, all high-wing configurations are lower in directional stability. In the presence of the horizontal tail, the variations due to wing position are generally less than without that surface. The rotation or circulation of the flow field discussed above, is evidently reduced when adding a pair of horizontal "fins" to the fuselage.

Influence of Canopy. The experimental results discussed so far, regarding cross flow and sidewash at the vertical tail, apply to perfectly smooth and plain wind tunnel models. Test results for the complete airplane configuration shown in figure 13, tested with the wing in low as well as in high position show:

- Without the vertical tail, lateral forces and yaw moments are essentially the same for both wing positions.
- With the tail on, its contribution to both force and moment is larger for the low-wing configuration.

The ratios of the due to tail derivatives, LW/HW ≈ 1.4 , or HW/LW ≈ 0.7 , are in the same order of magnitude as those which can be obtained above.

(13) Sidewash induced by wing and fuselage:

- Bamber, Wing + Fuselage + Fin, NACA TN 730 (1939).
- House, Wings Fuselages Fins, NACA Rpt 705 (1941).
- Recant, Side Flow at V'Tail, NACA TN 804 & 825 (1941).
- Schlichting, Wing & Fuselage, Ybk D Lufo 1941 p. I-300.
- Sweberg, Load on V'Tail, NACA W'Rpt L-426 (1944).
- Goodman, Wing and H'Tail, NACA TN 2504 (1951).

End-Plate Effect. A horizontal tail surface added to a vertical fin, would be expected to have the same effect as an end plate attached to a wing tip. For an average horizontal tail which may have a span twice the height of the vertical tail surface the effective aspect ratio of the surface is theoretically increased to $A_v = 1.8 A$ as indicated in Chapter III. Based on equation (14) the lateral force derivative $dC_{lat}/d\beta$ of the tail assembly would then be increased from 0.026 to 0.042 for $A_v = 1$, or from 0.045 to 0.063 for $A_v = 2$, for example ratio's of 1.6 and 1.4 respectively.

Fuselage Wake. Experimental values for $dC_{lat}/d\beta$, showing the influence of the horizontal upon the vertical tail, are as follows:

Figure No.	A	fuselage type	$dC_{lat}/d\beta$		ratio
			Without Hor. Tail	With Hor. Tail	
16	2.2	cylindrical	0.056	0.062	1.10
12	2.0	tapering	0.055	0.060	1.09
11	2.2	streamline	0.048	0.058	1.21
14	1.4	airplane	0.028	0.031	1.10
19	2.3	tapering	0.040	0.042	1.05

It is evident from these statistics that the large improvement indicated by theory, resulting in a ratio around 1.5 (as discussed above) are not obtained in configurations where the horizontal tail is attached to the fuselage. It must be assumed that the wake (boundary layer) developing along the fuselage disrupts the lifting line or the trailing vortex sheet originating from the tail assembly eliminating the predicted and plate effect.

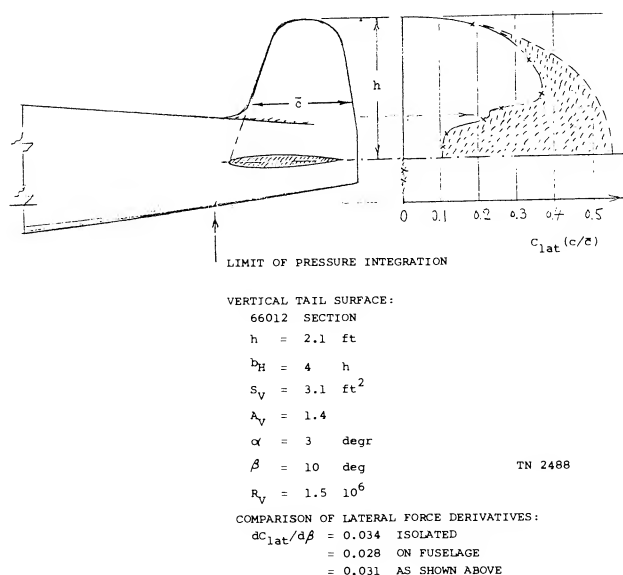


Figure 14. Distribution of lateral or normal force (load) in vertical surface and fuselage tail end of a fighter-type airplane configuration (9,g).

The Load Distribution over the vertical surface of a conventional airplane configuration, is plotted in figure 14. While the load in the tail end of the fuselage is practically zero without surfaces attached, a small lateral force is induced when adding the vertical fin. The force in the tail of the fuselage is further increased when adding the horizontal surface (preferably in the lowest possible position). However, the lateral force in the vertical surface is very much reduced as against the theoretically expected load. In fact, when attached to the fuselage, the force derivative of the fin in figure 14 is smaller than in free flow.

$$\begin{aligned} dC_{lat}/d\beta &= 0.039 && \text{in free flow (estimated)} \\ &= 0.023 && \text{when attached to fuselage} \\ &= 0.027 && \text{with horizontal tail as shown} \end{aligned}$$

To explain this result obtained at a reasonably large Reynolds number the original report (9,g) stated "large losses in dynamic pressure resulting from the wakes of the canopy and wing-fuselage juncture, were found to occur in the vicinity of the vertical tail".

It can also be said that the vertical tail, having an exposed area ratio S_v/S between 5 and 6% only, is too small and not high enough.

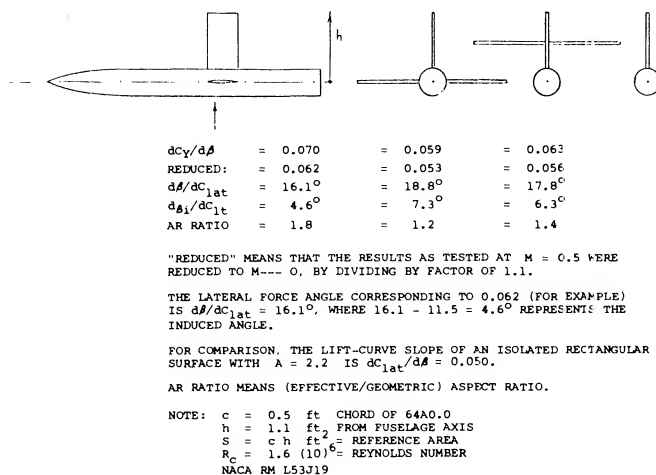


Figure 15. Effectiveness of a vertical tail surface (fin) tested (6,b) on a cylindrical "fuselage".

Horizontal Tail Position. In all examples listed above, the horizontal tail increases the effectiveness of the vertical surface by approximately 10%. From the available experimental results plotted in figure 16 the vertical position of the horizontal surface on the vertical fin changes the lateral force derivative as follows:

- The horizontal surface at 1/2 the height of the vertical tail reduces the effectiveness.
- maximum derivatives are obtained with the horizontal on top of the vertical tail

- (14) NACA fighter-type airplane model with 3 tail lengths:
- Johnson, Longitudinal & Lateral, TN 1766 (1948).
 - Purser, Slipstream Rotation, TN 1146 (1946).
 - Purser, Unsymmetrical H-Tails, TN 1474 (1947).

"T" Tail. In uppermost position, the horizontal surface forms a "T" together with the vertical fin. As explained in (15,e), advantages of the "T" tail are as follows:

- the stabilizing effectiveness of the vertical tail is increased.
- the horizontal tail is removed from the field of maximum downwash and the irregularities of the propeller slipstream (if there is one).
- lateral tail effectiveness is preserved to highest angles of attack.

A "T" tail is also included in figure 17. Another "bold" configuration is shown in figure 18. In all examples tested, the experimental values obtained, remain somewhat below the theoretically expected lateral force derivatives.

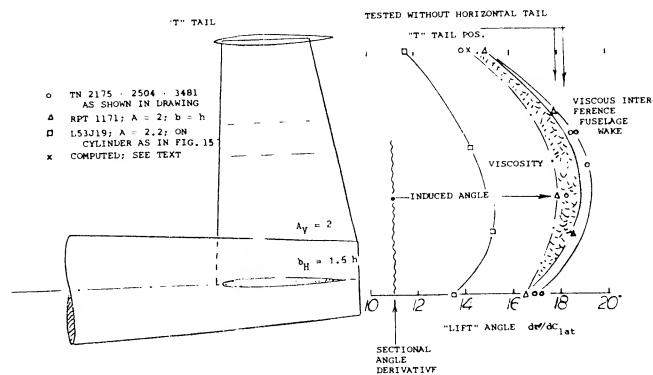


Figure 16. Effectiveness of vertical tail surfaces, as a function of the vertical position at which the horizontal surface is attached.

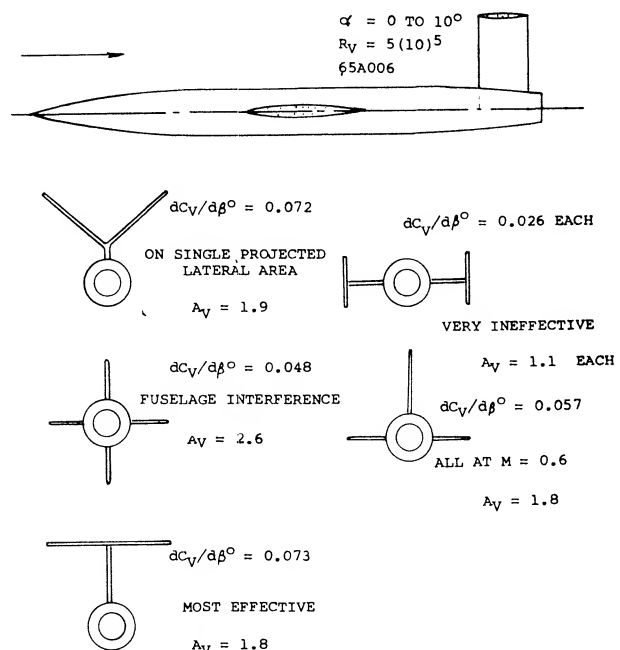


Figure 17. Lateral force derivative developing in the tail configuration shown (6,a).

(15) Characteristics of "T" tails:

- Sleeman, Auxiliary Surfaces, NASA D-804 (1961).
- Goodson, "T" Tail and Double Tail, NASA D-950 (1961).
- Multhopp, "T" Tails, Aero Digest May 1955.

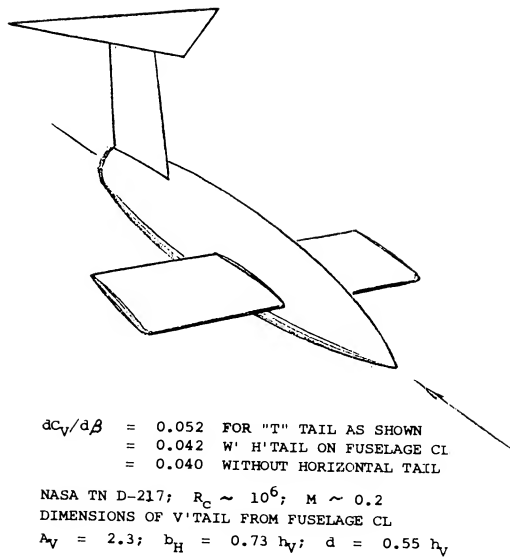


Figure 18. Lateral force characteristics of a vertical tail surface (16,b) for three different arrangements of the horizontal surface, including that of a "T" tail.

"V" Tail. The lifting characteristics of dihedral wings are presented in Chapter III. The neutral force in each panel of a combined horizontal plus vertical tail assembly as in figure 19, approximately corresponds to

$$dC_N/d\alpha_n = (dC_L/d\alpha)_o$$

where "o" indicates the lift curve slope for the dihedral angle $\Gamma = 0$. When exposing the "V" tail to an angle of yaw, the angle of attack normal to the panels changes as

$$\alpha_n \sim \sin \beta \sin \Gamma$$

The lateral component of the neutral forces ($F_y = N \sin \Gamma$) thus corresponds to

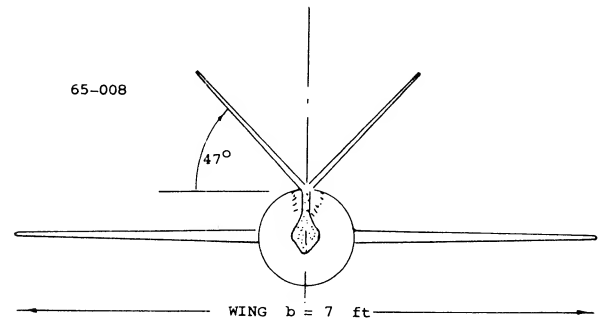
$$dC_{lat}/d\beta = (dC_L/d\alpha)_o \sin^2 \Gamma$$

This mechanism is easily understood for zero lift (where the angle of attack is zero). When at an angle of yaw, one side (one panel) then assumes a positive and the other one a negative normal force. Disregarding a rolling moment, the resultant is the lateral force indicated in the last equation.

"V" Derivatives. Experimental results of a "V" tail tested alone (without a fuselage) are presented in Chapter XI. Lateral and longitudinal characteristics of a single-engine airplane model using a variable "V" tail are reported in (17,c). Figure 19 shows configuration and derivatives as tested. It should be noted in particular:

- 1) that interference and flow separation starts above $\Gamma = 45^\circ$,
- 2) that the tail panels move up and into reduced downwash, as the dihedral angle is increased,
- 3) that a roll moment due to yaw is obtained, similar to that in a dihedral wing.

The particular "V" tail tested, is mounted on top of a dorsal "trunk". The apex point of the tail is thus raised above the fuselage wake. The dorsal part also adds to lateral surface area. As a result, the lateral force derivative is some 30% larger than according to basic "V" tail theory (see Chapter III).



TUNNEL MODEL OF A HIGH SPEED AIRPLANE CONFIGURATION:

$$S = 8.1 \text{ ft}^2 \quad A' \text{ RATIO OF TAIL} = 5, \text{ FOLDED DOWN}$$

$$\bar{e} = 1.2 \text{ ft}$$

$$S_t = .41 S \quad \text{TO HINGE LINE OF "ELERUDDER"}$$

$$l_t = .53 b, \quad \text{SHOULD BE } 0.47 b, \text{ EFFECTIVE}$$

$$\text{NACA TN 1478 (18,c)}$$

$$\text{DERIVATIVES IN THE GRAPHS REPRESENT THE TAIL CONTRIBUTIONS}$$

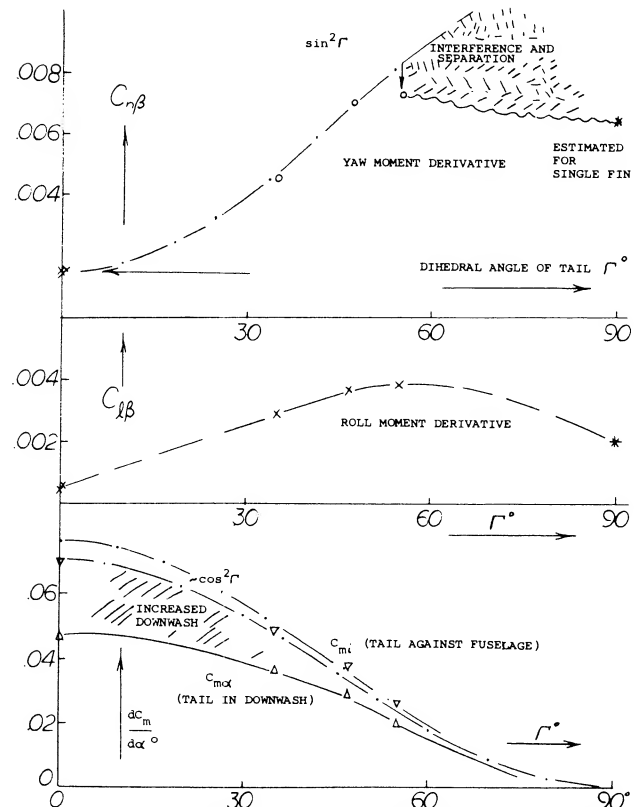


Figure 19. Characteristics of a "V" tail, tested (17,c) as part of an airplane configuration.

Area Required. A dihedral angle of 30° provides a ratio between vertical and horizontal tail performance that is comparable to conventional tail assemblies. The linear dimensions (chord end projected horizontal span) of the "V" tail should then be $1/\cos 30^\circ = 1.16$ times those of the equivalent conventional horizontal tail. The total surface area required, is roughly the same. Therefore, if drag is to be reduced by using a "V" tail, this can only be expected on the basis of reduced interference (only 2 panels joining the fuselage, instead of the conventional 3). It must also be taken into consideration that the combination of two different control surfaces in one unit, may pose some problems in design, construction and operation.

"Y" Tail. To avoid any fuselage interference of the "viscous" type described above, the "V" tail can be moved up in the manner as shown in figure 20, thus forming a "Y", together with the added vertical stub (19). Since in the tail family tested, the horizontal span b_H is kept constant, we have referred all coefficients to the area (cb_H). Of course, the stub must be expected to contribute some lateral force of its own.

Graph (A) indicates how the derivative $dC_{lat}/d\beta$ increases with the height ratio of the vertical part of the configuration. As the tail surfaces are raised more and more, something similar to a "T" tail is obtained; and the "Y" tail is thus realized to be a crossbreed between "V" and "T". When increasing the dihedral angle of the tail in figure 20, keeping the span b_H constant, the lateral force derivative increases in the manner as shown in Graph (B).

Pitching Moment. Consideration of "V" or "Y" tails is not complete without some account of their longitudinal contribution. Pitching moments of the tail configurations in figure 20, were measured behind a wing with the same aspect ratio and twice the linear dimensions of the horizontal tail projection. Using the tail volume $V_H = 0.25/0.6 = 0.42$, the derivatives $dC_{LH}/d\alpha$ were obtained as plotted in the graphs. The lifting or pitching effectiveness of the tail:

increases when raising the tail assembly out of fuselage wake and wing downwash,
increases slightly when making the dihedral angle larger, while keeping b_H constant.

- (16) Characteristics of unusual tail configurations:
- Sleeman, Tail Configurations, NACA RM L57C08.
 - Fournier, "Exotic" Configurations, NASA D-217 (1960).
 - See "V" tails in (18) and "T" tails in (16).
 - Sleeman (see a), "Y" Tails, NACA RM L56A06a.
- (17) Characteristics of "V" tail surfaces:
- Purser, Simple Vee-Tail Theory, NACA T Rpt 823 (1945).
 - Schade, Isolated Vee-Tail Surfaces, NACA TN 1369 (1947).
 - Polhamus, Airplane with Vee Tail, NACA TN 1478 (1947).

For comparison, we have also put a pair of points into the two graphs, representing a "T" tail having the same height and span as the "Y" tail in figure 21. The lateral and longitudinal effectiveness of the "T" tail is equal to the best "Y" tails. In final analysis, the roll moments due to vertical tails when at an angle of yaw also must be considered, Chapter XIII.

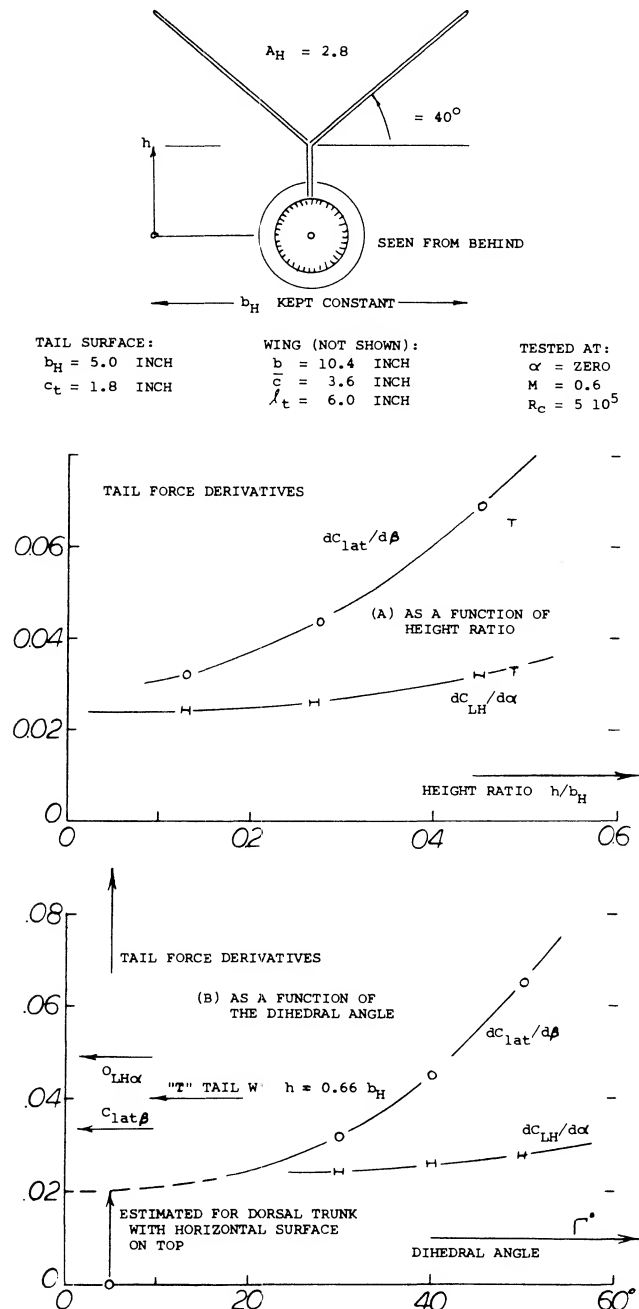


Figure 20. Stability characteristics of a "Y" shaped tail assembly (16,d):

(A) as a function of vertical location (length of dorsal piece),
(B) as a function of the angle of dihedral.

(18) In the configuration as in figure 21, there is little "viscous" fuselage interference. When used in connection with the tail end of a conventional fuselage, wake interference would be similar to that in figures 13 and 14.

(19) Ribner, Propellers in Yaw, NACA Rpt 819 & 820 (1945).

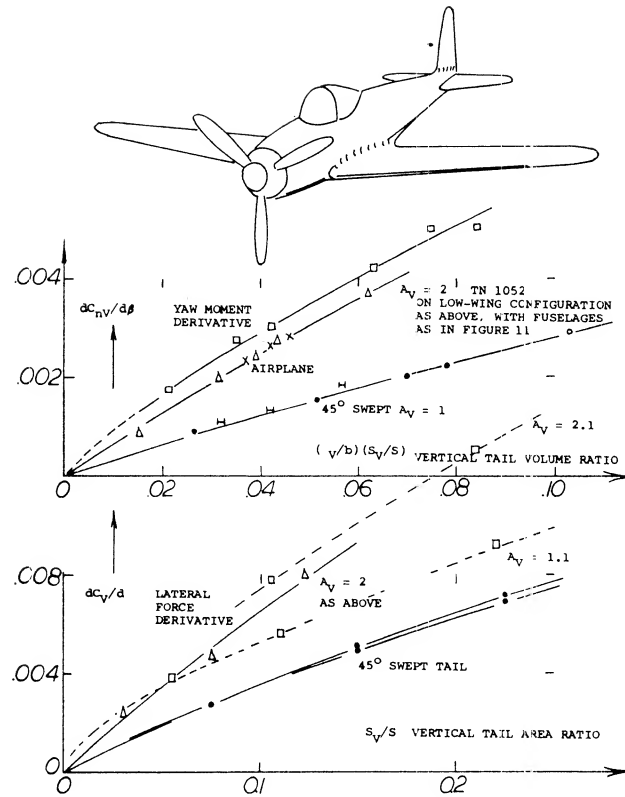


Figure 21. Contributions to the directional stability derivatives, of and due to vertical tail surfaces, as a function of their size and moment arm ratios.

3. YAW MOMENT ARMS

So far, only the development of lateral forces have been presented. Ultimately, a vertical tail surface is expected to contribute a stabilizing yaw moment, however. The arms providing such moments are discussed in the following, together with other means (fins) supplementing directional stability.

Vertical Tail Volume. The yaw moment produced by the vertical tail surface, can be expected to grow in proportion to both, area and arm (tail length). In coefficient form therefore,

$$dC_{nV}/d\beta = (dC_{lat}/d\beta)(S_V/S)(\ell_V/b) \quad (18)$$

where the value of $(dC_{lat}/d\beta)$ primarily depends upon the shape (aspect ratio) of the tail surface. The term $(S_V \ell_V)$ has the dimensions of a volume. The vertical tail volume ratio

$$V_V = (S_V/S)(\ell_V/b) \quad (19)$$

is thus a fixed characteristic of the airplane configuration.

Yaw Moment. A lateral force originating in the vertical surface, is expected to produce a yaw moment ("N" about the "normal" axis of the airplane) corresponding to

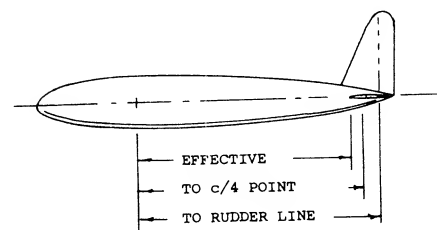
$$C_N = "N"/qSb = C_{lat}(\ell_V/b)(S_V/S) = C_{lat}V_V \quad (20)$$

When sideslipping, the derivative is expected to be

$$C_{N\beta} = dC_N/d\beta = (dC_{lat}/d\beta)V_V \quad (21)$$

Within reason, both the lateral tail force and the yaw moment derivatives are independent of angle of attack and/or wing-lift coefficient of the configuration. Test data for yaw-moment contributions of vertical tail surfaces are given in figure 21. They increase essentially in proportion to the volume ratio provided by tail size and length. There is a difference, however, between the influence of length and vertical area. As explained in connection with figure 11, the lateral force derivative reduces somewhat as the length of the fuselage is increased. This influence is evident in figure 21, and it is marked accordingly.

Moment Arm. One particular fuselage plus tail configuration is shown in figure 22. Dividing the derivative $C_{N\beta V}$ by that of the lateral force $C_{Y\beta V}$ the effective moment arm ℓ_V is obtained, in the form of ℓ_V/b . This arm is, of course, shorter than that measured to the rudder hinge line. However, the effective arm is also shorter (94%) than the distance of the quarter-chord point of the vertical tail surface from the reference axis (through the CG of the airplane for which the tests are undertaken). It thus seems that some lift is induced in the fuselage, somewhat ahead of the vertical tail's root chord. This result is confirmed in figures 11, 12, 23, where the effective moment arms are between 3 and 8% shorter than the geometrical tail length (to the aerodynamic center point of the vertical surface). In terms of fuselage maximum diameter or tail root chord, the reductions listed are between 10 and 25%.



EVALUATION FROM L-17 (10,h)
MEDIUM-LONG FUSELAGE
WITH 9.7% S VERTICAL TAIL
TESTED WITHOUT A WING, BUT
BASED ON WING DIMENSIONS;
TAIL CONTRIBUTIONS ARE:

C_{nV}	=	0.0032
C_{YV}	=	0.0071
ℓ_V/b	=	0.0032/0.0071
	=	0.45 EFFECTIVE ARM RATIO
	=	0.48 TO c/4 POINT OF TAIL
	=	0.52 TO RUDDER HINGE LINE

Figure 22. Moment arms of the vertical tail of an airplane configuration derived from wind-tunnel tests (10,h).

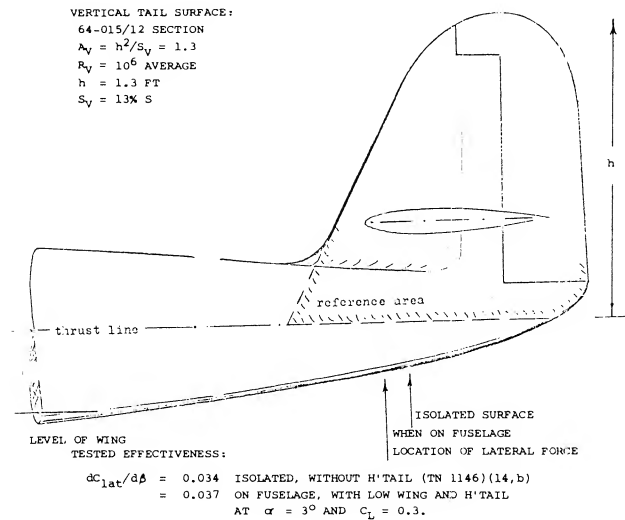


Figure 23. Lateral force provided by the vertical tail surface of a fighter-type airplane (14,a).

Fuselage Shape. The influence of the cross-sectional shape of the fuselage upon the directional characteristics is discussed in connection with the results in figure 4. The same series of bodies are shown in figure 24 combined with tail surfaces. The contribution of the vertical tail to the lateral force is essentially the same for the three fuselage shapes. The effective moment arms differ only slightly; they are all shorter than the geometrical distances to the quarter-chord line of the tail.

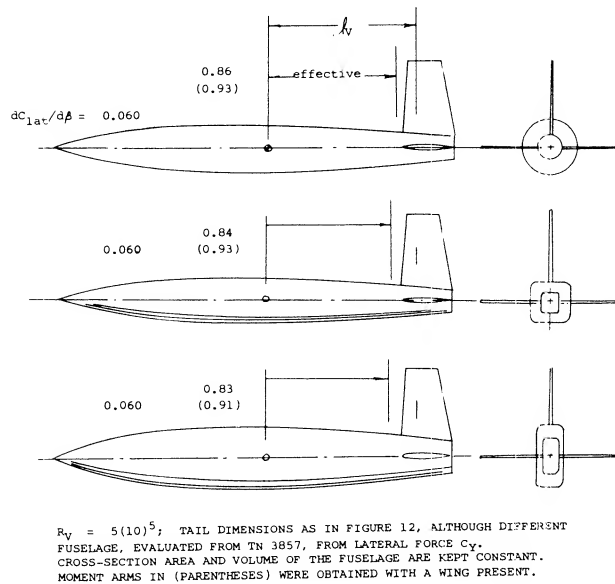


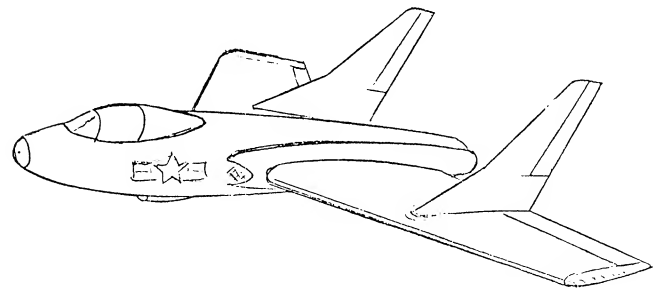
Figure 24. Influence of fuselage cross-section shape upon the lateral force and the moment arm of the vertical tail surface.

(20) As explained in the Chapter XI it is more correctly the speed in the slipstream increasing the tail force. It is customary, however, to speak of "dynamic pressure", which should be understood to mean an effective pressure.

Fins on Top of the Wing. In tailless airplane configurations, some kind of vertical fin are required for directional stability. In swept-back configurations, a convenient place to attach such fins, is on top of the wing. Each fin of the airplane shown in figure 25 has an area equal to 9% of that of the wing. The geometric aspect ratio is $A_V = h^2/S_V = 1.5$. There are two effects to be considered:

- The wing can be considered to be a very large one-side end plate. The effective aspect ratio of the fins may thus be $A_{\chi} = 1.9 A_V = 2.8$.
- The pair of fins may interact with each other. For a lateral distance $y = 1.9 h$, or $(y/h)(A_V/A_{\chi}) = 1.0$, figure 23 in the Chapter III (set up in terms of biplane interference) leads to the result that the effective aspect ratio is reduced from 2.8 to $A_{\chi} = 0.9 (2.8) = 2.5$.

Using equation (14) the derivative of the lateral fin forces can be determined. It can be expected, however, that interference with the suction side of the wing will reduce the effectiveness of the fins somewhat (possibly by 10%). The moment arm (to the CG) available in the "Cutlass" configuration, is only $\approx 1/4$ of the wing span. To obtain the required stability, the combined fin area has to be larger than in a conventional configuration; it is 18% of the wing area in figure 25.



CHANCE-VOUGHT, SINCE 1951
F7U-3 "CUTLASS" $A = 3$
CARRIER-BASED FIGHTER

$b = 40$ ft
 $w = 27,000$ lb
 $V_x = 580$ kts
PAIR OF JET ENGINES, EACH:
 $T = 5,000$ lb

VERTICAL SURFACES WITH:

$S_V = 0.09 S$

$l_V = 0.27 b$

VERTICAL TAIL VOLUME 0.05

30 to 40 DEGREES SWEEP

Figure 25. View of Chance-Vought F7U-3 "Cutlass" tailless airplane (25,c).

- Influence of propeller power in fighter-type airplanes:
 - Recant, Curtiss XP-62 Model, W'Rpt L-779 (1943).
 - Goodson, Fleetwings XBTK-1, W'Rpt L-786 (1945).
 - Sweberg, Grumman XF6F-4 Directional, W'Rpt L-109 (1945).
 - Sweberg, Load Distribution in Tail, W'Rpt L-426 (1944).
 - Purser, Rotation LW Airplane Model, NACA TN 1146 (1946).
 - Johnson, V-Tail Modifications in Slipstream, NACA Rpt 973 (1950).

(22) Characteristics with dual-rotation propellers:

- Neely, With Single and Dual Propeller, W'Rpt L-83 (1944).
- Recant, Curtiss XP-62 Model, as in ref (22,b).
- Wallace, Curtiss, XBTC-2 Model, W'Rpt L-787 (1944).

Twin Tails. Another type of fins is sometimes used in twin-engine airplanes. To facilitate handling on the ground, by keeping the rudders within the propeller slipstream, twin vertical surfaces can be attached to the ends of the horizontal tail, in the form of "end plates". An example of this type of design is the Lockheed L1049, 749 "Constellation" airplanes. Results of a systematic wind-tunnel investigation on twin vertical surfaces, are presented in figure 46 which indicates that:

- 1) the effectiveness $dC_N/d\beta$ increases with the aspect ratio,
- 2) shape "4" (straight trailing edge) is better than "3" (for the same aspect ratio),
- 3) there are discontinuities in two of the shapes investigated,
- 4) the type of surfaces tested, is effective up to $\beta = 30$ and possibly 40 .

The discontinuities mentioned seem to be caused by flow separation on one side where the horizontal tail interferes with the suction side of the vertical surface. The high angles permissible, are simply a consequence of the low aspect ratios used.

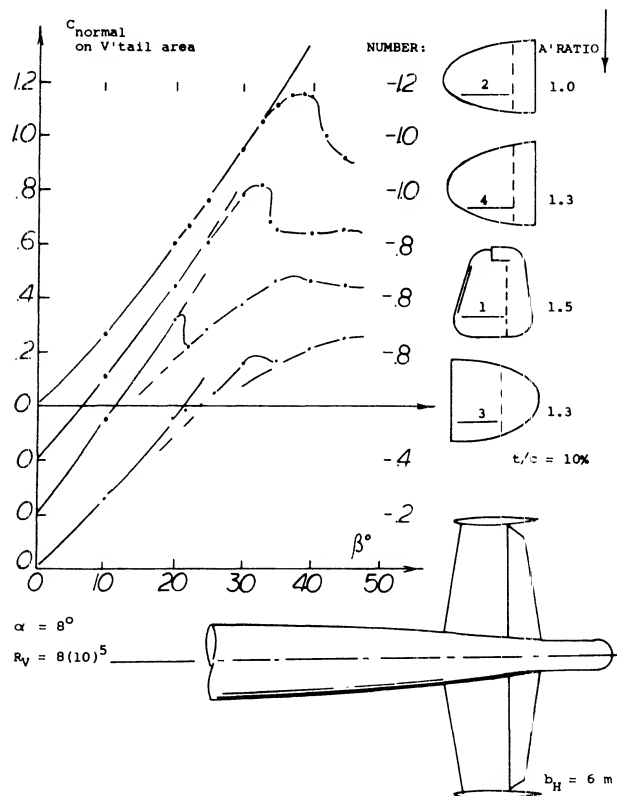
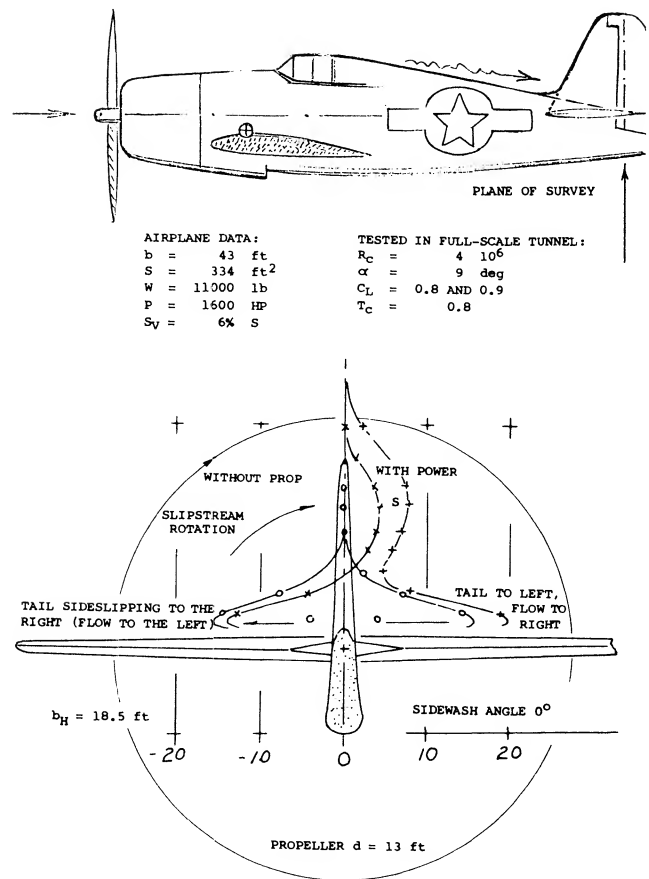


Figure 26. Several shapes of twin vertical tail surfaces tested (30) on a model of the Do-217 airplane.

FLUID DYNAMIC LIFT



TAIL AND DISTRIBUTION AS SEEN FROM BEHIND
(C) DUE TO FLOW ACROSS THE FUSELAGE
(S) DUE TO SLIPSTREAM ROTATION ($T_c = 0.8$)
TESTED AT PLUS AND MINUS 10° ANGLE OF YAW
OVER MOST OF THE VERTICAL TAIL AREA, THE
DYNAMIC PRESSURE RATIO IS
 $q/q_0 = 1.0$ WITHOUT PROPELLER
UP TO 2.0 WITH POWER ON
NEAR THE UPPER EDGE OF THE FUSELAGE, THE
DYNAMIC PRESSURE RATIO DROPS TO
0.4 AND 0.8, RESPECTIVELY

Figure 27. Results of wind-tunnel tests (21,e) on the Grumman F6F fighter-type airplane, showing the distribution of sideward flow at the location of the vertical tail.

- (23) Lateral characteristics of high-wing airplanes:
 - a) Hagerman, HW Airplane w'Power & Flaps, NACA TN 1379 (1947).
 - b) Same model in low wing arrangement, see Tamburello, NACA TN 1327.
 - c) Longitudinal characteristics of same models, TN 1239 and 1339.
 - d) McMillan, "Puss Moth", ARC RM 1794 (1937); also Batson, RM 1631 (1935).
 - e) Paulson, Fighter in Inverted Flight, NACA W'Rpt L-15 (1945).
- (24) Lateral directional characteristics of jet-propelled airplanes:
 - a) Brewer, Bell P-59 in Full Scale Tunnel, W'Rpt L-626 (1945).
 - b) NACA (Douglas) X-3 research airplane: Flight-test results, Bellman, NACA RM H54117. Wind-tunnel tests on very similar model, NASA Memo 1-22-59L.
 - c) A single tail-jet and a twin jet (in the wing) airplane are reported by Davis, Effect of Jet on Stability, NACA W'Rpt A-31 (1944). The "changes in directional stability and trim are negligible".

IV. INFLUENCE OF PROPULSION

The influence of propulsion system on the directional characteristics of an airplane is dependent on the forces and moments produced when operating at an angle relative to the flow. In addition the slipstream and the induced effects of the propulsion system can produce important interaction effects that will influence the results. Propeller driven airplanes produce large forces and moments when operating at an angle of attack and have a large slipstream which often infringes on the aerodynamic surfaces of the airplane as discussed in Chapter XII. Although few new propeller aircraft are being designed and built the influence of propellers are covered as this will serve as a basis for the systems using jet propulsion, especially with the trend toward much higher by-pass ratio. This is desirable as considerably more data is available on the subject of propellers than for jet systems.

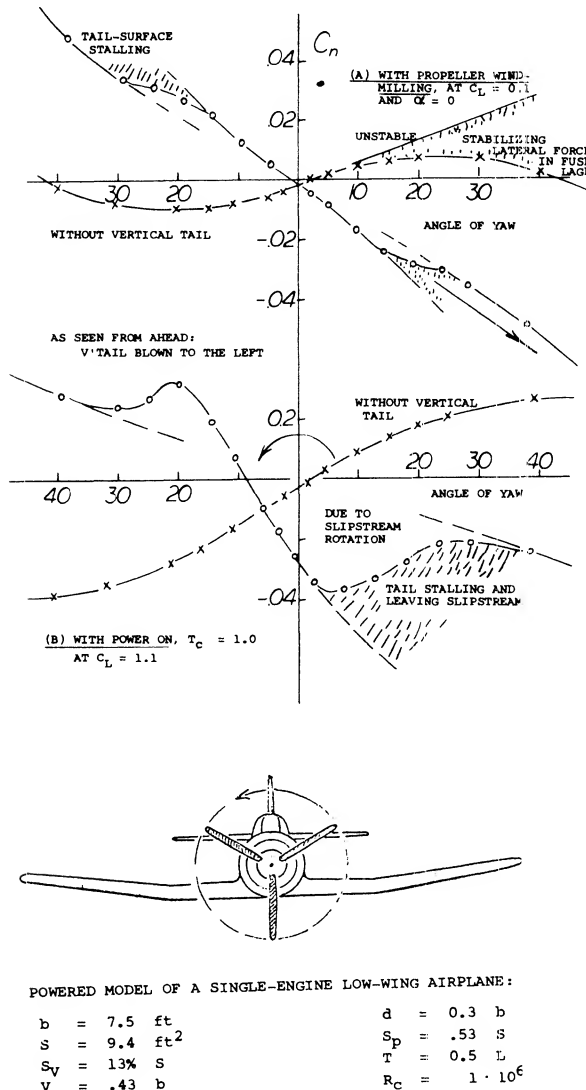


Figure 28. Yaw moments of a low wing airplane configuration (14,a) in cruising condition:
(A) with propeller windmilling
(B) with full power on $T_c = 1.0$.

1. MOMENT DUE TO FORCES IN THE PROPELLER

The normal forces originating in propellers when at an angle of attack are explained in the Chapter XII. The same type forces are also obtained when sideslipping due to the angularity of flow into the disk.

Tractor Propeller. The propeller of single-engine airplanes (such as the fighters, for example, in figures 27 and 28) may have:

- a solidity ratio $S_B/S_P = 10\%$
- a "0.7" blade angle " β " = 30
- a disk area $d^2\pi/4$ $S_P = S/3$
- a moment arm to CG = $b/4$

Using the derivative $dC_{N\beta}/d\beta = 0.035$, as found in Chapter XII the lateral force may correspond to

$$C_{Y\beta P} = (dC_{N\beta}/d\beta) (S_B/S_P) (S_P/S) = 0.035 (0.3)/3 = 0.0012 \quad (31)$$

and the yaw moment due to the normal force of the propeller may correspond to

$$C_{N\beta P} = -dC_{Y\beta P} (\ell_P/b) = -0.0012/4 = -0.0003(32)$$

For comparison, the derivative due to the fuselage may be in the order of -0.0001 , and that due to vertical tail up to $+0.0010$. So, the propeller-force moment is usually the most destabilizing single component of any powerful (tractor-type) single-engine airplane configuration, such as fighters in particular.

Pusher Propeller. Directional characteristics of a "tailless" airplane configuration are shown in figure 29. While a pusher propeller at the end of a fuselage is an unusual arrangement, the results promise to shed light on the interaction between this type of propeller and the wing or a vertical tail located ahead.

The yaw moment of the wing fuselage combination displays the usual destabilizing moment due to the fuselage.

The addition of a vertical tail ("double", above and below the fuselage) stabilizes the yaw moment.

When adding the windmilling propeller (no thrust) the normal forces originating in the propeller blades increase directional stability, propeller fin effect (19).

Finally, when adding power to the configuration, a maximum of directional stability is obtained.

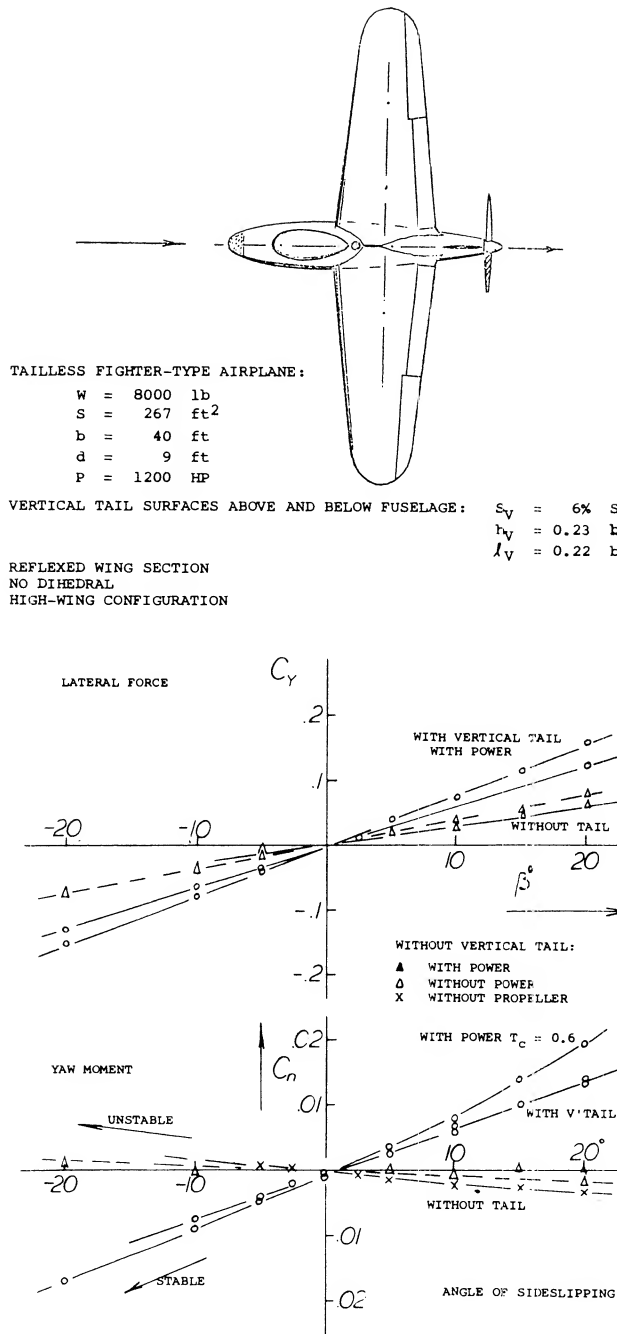


Figure 29. Directional characteristics of a tailless and *pusher-propeller* fighter-type airplane tested (25,b) on a 1/10 scale tunnel model.

The propeller slipstream is the consequence of a pressure increment $\Delta C_P = T_C$, across the propeller disk. The average increment (v) of the speed "in" the disk is theoretically

$$v/V = 0.5 \sqrt{1 + T_C} \quad (22)$$

Where T_C = the propeller thrust coefficient = T/qSp . Full speed, corresponding to twice this increment, is theoretically reached at some distance (say beyond one diameter) behind the propeller. As far as the flow ahead of the propeller is concerned, the disk represents a "sink", into which air is attached from "all" sides. Only a small influence can be expected, accordingly, of the propeller upon the vertical tail surface located ahead of it. Equation (22) suggests, on the other hand, that normal force in the, and yaw moment contribution of the propeller proper, be increased, for example by 40% for $T_C = 1$. Results plotted in figure 29 show an effect somewhat stronger than according to this reasoning. The added increment must be due to the influence of the propeller (suction) upon the tail surface.

2. INFLUENCE OF THE SLIPSTREAM UPON THE VERTICAL TAIL

The slipstream of the propulsion system has two particular characteristics. It has an increased dynamic pressure; and it changes to a degree, the direction of flow when sideslipping.

Sidewash. In propeller-driven airplanes, the vertical tail surface is usually located within the slipstream. The tail is thus exposed to a certain destabilizing sidewash and to a stabilizing increase of dynamic pressure. For example, at $T_C = 1$, the added velocity is $v \approx 0.4 V$. As demonstrated in figure 30, the sidewash component of v , corresponds to

$$w/v = -\beta$$

where β = angle of sideslip in radians. The maximum possible reduction of the sidewash angle against the axis of an isolated propeller, will then be

$$\sigma = w/(V + v) = -\beta(v)/(V + v); \quad (23)$$

$$d\sigma/d\beta = -1/(1 + (V/v)) = (1/\sqrt{1 + T_C}) - 1$$

(25) Stability and control of tailless airplanes:

- Donlan, Review & Summary, NACA Rpt 796 (1944).
- Seacord, Tailless Pusher-Propeller Fighter, W'Rpt L-199 (1946).
- Chance-Vought F7U "Cutlass", see Green "Jet Aircraft of the World", Hannover House 1955.
- Brewer, Kaiser Tailless Model, W'Rpt L-531 (1946).

(26) Influence of dorsal and similar fins:

- Recant, Curtiss XP-62 Model, W'Rpt L-779 (1943).
- Wallace, Curtiss XBTC-2, NACA W'Rpt L-787 (1944).
- Ventral fins (at low R'number), see (33,d).
- Hoggard, Fuselage with Dorsal Fins, NACA TN 785 (1940).
- Queijo, Damping Fins, NACA TN 3814 (1956).

For very small values of thrust, the sidewash derivative is simply $d\sigma/d\beta = -0.5 T_C$. For $T_C = 1$, as mentioned above, theory expects:

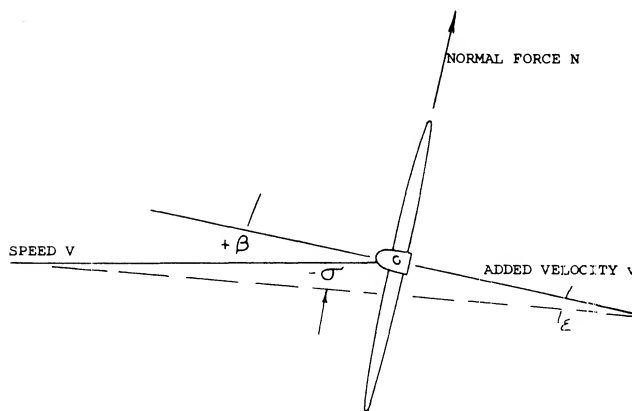
$$d\sigma/d\beta = -1/(1 + 2.5) = -0.28$$

so that the effective angle at the vertical tail might be reduced (in this particular case) to $(1 - 0.28) = 0.72$. A survey of the flow at the location of the vertical tail surface of a low-wing airplane is shown in figure 27:

- Without power (with dynamic pressure at the tail, essentially $q_v = q$) the previously discussed type of cross flow is seen taking place over the upper edge of the fuselage. The maximum sidewash angle is about 1.5 times the angle of sideslip; and it is symmetrical to the two sides of sideslip.
- In power-on condition (thrust coefficient $T_C = 0.8$) it is evident how slipstream rotation adds a component to the right, in the direction where the blades sweep through the upper half of the propeller circle.
- As a consequence of (a) plus (b) there is a strong sidewash to the right, when sideslipping to the left, amounting to between 5 and 20°, or 0.5 and 2.0 times the angle of sideslip.

The reduction of the sidewash angle due to slipstream (tested, but not directly evident in figure 27) is in the order of $d\sigma/d\beta = -0.11$ for $T_C = 0.8$, and at $C_L = 0.9$. This decrement is in the order of 1/2 of what is predicted in equation (23). It appears that the slipstream does not retain its original direction (if it ever reaches the sidewash angle as expected theoretically). Tentatively, we may thus write:

$$d\sigma/d\beta = -0.5 (1/1 + T_C) - 1 \quad (24)$$



SIDEWASH COMPONENT DUE TO SLIPSTREAM

SIDEWASH ANGLE $\sigma = w/(V + v)$

ANGLE AT V-TAIL $\epsilon = \beta + \sigma$

$$w = -v$$

$$\sigma = w/(V + v)$$

$$\epsilon = \beta + \sigma$$

Figure 30. Velocities and *sidewash* within the propeller slipstream.

Dynamic Pressure. The lateral force produced in the vertical tail should correspond to

$$dC_{lat}/d\beta = (dC_{lat}/d\beta)_o (1 + d\sigma/d\beta) (q_v/q) \quad (25)$$

where $(dC_{lat}/d\beta)$ is meant to be the lateral force derivative of the vertical tail without slipstream, but while attached to the fuselage. For the dynamic pressure (20) at the vertical tail:

$$q_v/q = 1 + T_C \quad (26)$$

An average value for k is 0.5 when considering horizontal tail surfaces. According to the tests in (21,e) it seems, however, that the vertical surface of an airplane such as in figure 27, is located in that part of the upper half of the slipstream where its velocity is higher. Therefore, a constant $k = 0.8$ may be used in the equation. For example for a set of parameters

$$T_C = 1.0; \quad d\sigma/d\beta = -0.15; \quad q_v/q = 1.8$$

the lateral force in the tail and/or the yaw moment contribution by the vertical surface, can be expected to be increased by the factor

$$(1 + d\sigma/d\beta)(q_v/q) = (1 - 0.15) 1.8 = 1.5 \quad (27)$$

Factors of this type have been evaluated in (22,e). They seem to agree with equations (24) (26) (27). The analysis also agrees fairly well with what is reported in (22) on airplane models using dual-rotating propellers (where the slipstream is symmetrical, without rotation). For example, directional stability of the fighter airplane as in figure 31, is doubled on account of slipstream, in climb condition (full power with $T_C = 1.4$, at $C_L = 1.3$). This statement should not be misunderstood, however. Stable yaw-moment derivatives of that airplane are as follows:

$$\begin{aligned} dC_{\eta}/d\beta &= 0.0018 \quad \text{without the propeller (figure 32)} \\ &= 0.0011 \quad \text{with propeller, idling} \\ &= 0.0024 \quad \text{with full power (figure 32)} \end{aligned}$$

(27) Propeller power in twin-engine airplanes:

- Jones, Sideslipping Multi-Engine Airplane, ARC RM 1455 (1932).
- Hartman, One One Engine, NACA TN 646 (1938).
- Rogallo, B-28 Direction of Rotation, W'Rpt L-295 (1943).
- Pitkin, B-28 with One Propeller, W'Rpt L-191 (1945).
- Goodson, Asymmetric Thrust, NACA TN 2979 (1953).
- Pitkin, Rotation and Tail Size, NACA W'Rpt L-354 (1943).

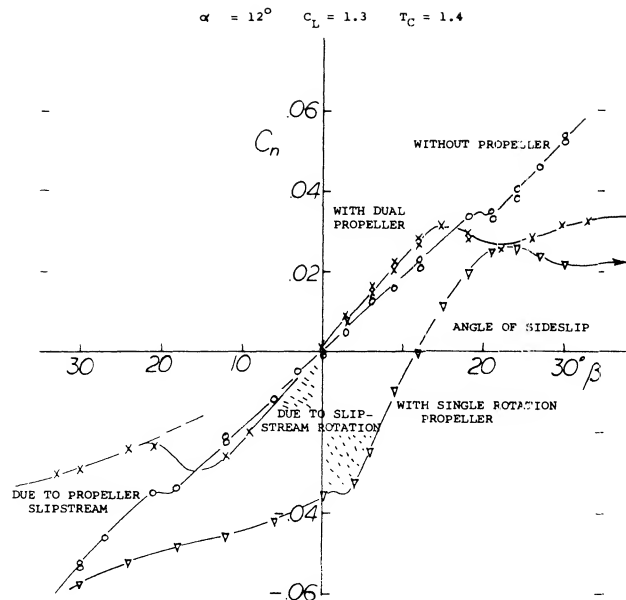


Figure 31. Yaw moments of the single-engine airplane as in figure 3, with single and dual rotation propeller (22,a).

Wing Flaps. Flow conditions at the tail are also a function of the airplane's angle of attack. Because of the wake developing along the back of the fuselage, and behind the canopy, the effective dynamic pressure and the stabilizing contribution of the vertical tail can be expected to reduce, as the lift coefficient is increased. In wind-tunnel models, at low Reynolds numbers, such as in part (A) of figure 32 for example (where $R_C = 6(10)^5$) the loss in tail effectiveness can amount to 50%. This weakness within a few degrees around zero angle of yaw, disappears however, when deflecting the wing flaps. The angle of attack of the fuselage is evidently reduced in this case. A beneficial effect of flaps is also found in the airplane configuration discussed above (as in figures 31 and 32). With flaps down, the yaw-moment derivatives are some 20% higher. It seems that the flaps make a low-wing configuration even more "low", and a high-wing arrangement less "high". It is thus assumed that the favorable sidewash at the location of the vertical tail (above the fuselage) is increased when deflecting the flaps. This conclusion is confirmed in the upper part of figure 34 where the stability derivative is seen increasing as a function of the thrust coefficient. In the condition with wing flaps down, the differential due to vertical tail is about 1/3 larger than in cruising condition (where the flaps are in neutral position). As a further example, stable yaw-moment derivatives are quoted for the two airplanes, as in figure 13:

(28) The same B-28 airplane as in figure 39, is discussed in the second "longitudinal" chapter.

(29) Stauer, Twin Vertical Tail Forces, Ybk D Lufo 1940 p. I,383. For the horizontal tail of Do-217, see Ybk 1942 p. I,208.

condition, with flaps neutral flaps deflected

a) low wing	$dC_n/d\beta$	$dC_n/d\beta$
windmilling	0.0018	0.0028
constant power on	0.0019	0.0053
with T_C	= 0.15	= 0.90
b) high wing		
windmilling	0.0011	0.0012
constant power on	0.0011	0.0030
with T_C	= 0.15	= 0.90

Directional stability of the low wing configuration is always higher than that in high wing arrangement.

CURTISS XBTC-2
 $b = 50$ ft
 $S = 406$ ft²
 $W = 16000$ lb
 $P = 3000$ HP
 $d = 14$ ft
 $S_y = 0.1$ S
 2 x 3 BLADED DUAL ROTATION PROPELLER
 50° FULL-SPAN SLOTTED WING FLAPS
 23° BLADE ANGLE AT TAKE-OFF
 30° BLADE ANGLE WHEN CRUISING
 1/8 SCALE MODEL TESTED, AT
 $R_C = 7(10)^5$ W'RPT L-787

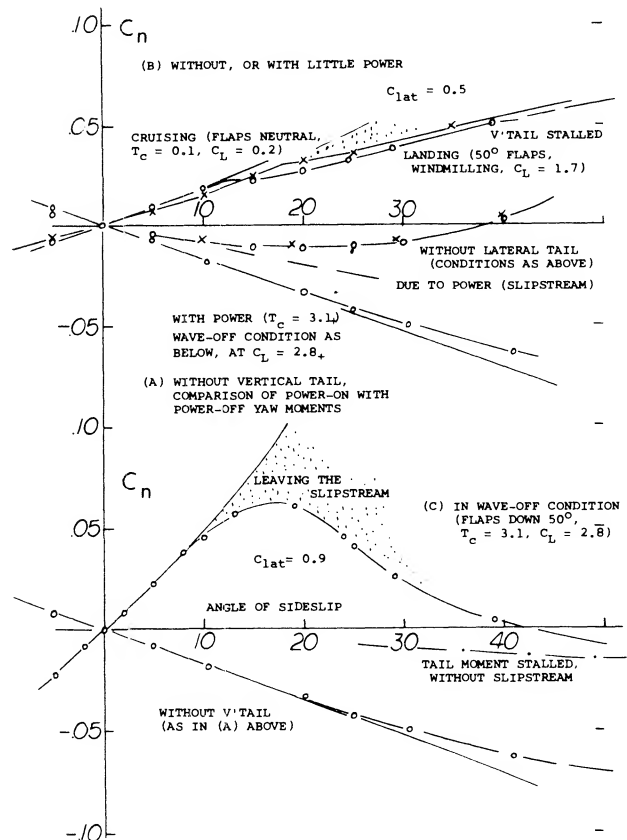
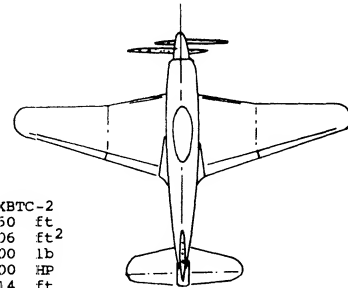


Figure 32. Yaw moments of the powered model of the Curtiss XBTC-2 fighter

(A) in cruising condition,

(B) with flaps down and take-off power.

Inverted Flight. Another consequence of flap deflection is the fact that the asymmetric type of yaw moment function as in figures 29 and 31, is reduced considerably. It seems not only the wing plus flaps take out part of the slipstream rotation; the slipstream also may be deflected down so far that the vertical tail is no longer affected very much. This conclusion is borne out by tests (31) on a low-wing airplane when flying upside down. In this inverted attitude (at $\alpha = -10^\circ$ for $C_L = 0.7$, for example), the vertical tail surface is below and essentially out of the slipstream. Directional stability is about the same, accordingly, as in power-off (windmilling) condition.

0.32 SCALE MODEL OF
2300 HP FIGHTER TYPE

TEST CONDITIONS:

$b = 15$ ft
 $S = 38$ ft²
 $d = 4$ ft
 $O = 0$ -
 $C_L = .15$ -
 $C_{Tp} = .08$ -
 $R_C = 4 \cdot 10^6$
 $23^\circ =$ BLADE ANGLE
 $27\% =$ SOLIDITY
 $S_p = .33$ S

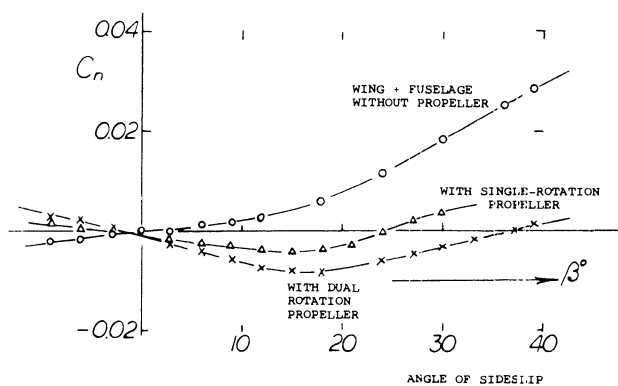
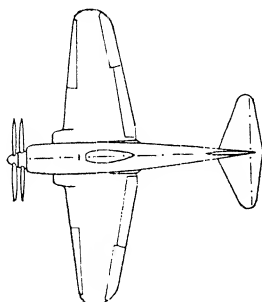


Figure 33. Yaw moments of a fighter airplane tested (22,a) with single and dual rotation propeller.

- (30) Twin-engine airplanes on one propeller:
- Douglas, After Engine Failure, J. Aeron. Sci. 1935 p. 132.
 - Hartman, One One Engine, NACA TN 646 (1938).
 - Schmidt, Multiple-Engine Control, Ybk D Lufo 1943, Rpt IA-030.
 - Pitkin, B-28 on One Engine, NACA W'Rpt L-191 (1945).
 - Goodson, Influence of Thrust Reversal, TN 2979 (1953).
- (31) Characteristics of fighter-type airplanes, flight-tested:
- Goranson, Qualities of F-47 Airplane, NACA TN 2675 (1952).
 - Johnson, Rudder and Sideslipping Curtiss P-40, W'Rpt L-547 (1942).
 - White, North American P-51 "Mustang", W'Rpt L-566 (1943).
 - Johnson, Flying Qualities Bell P-39, W'Rpt L-602 (1943).
- (32) Ray Effects of Large sideslip angles on stability of "T" tail configurations NASA TM X-1665

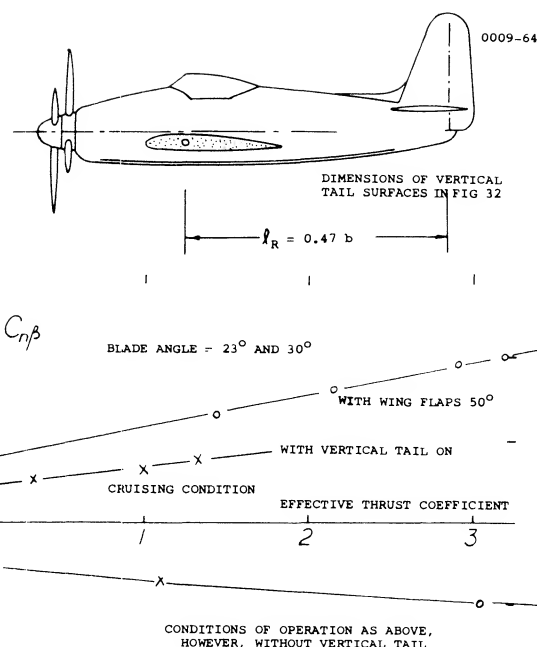


Figure 34. Yaw moments of the Curtiss XBCT-2 airplane (22,d) as a function of the propeller thrust coefficient.

Jet Propulsion. The use of jet engines for propulsion has eliminated many of the directional stability problems encountered with propeller driven airplanes. For instance there is no direct slipstream effects on the tail as the engines are located so that the tail surfaces are not washed by the hot efflux of the engines. The location of the engines of the airplane do influence the flow at the tail surface however and thus effects the directional stability derivative, $C_{n\beta}$. For instance the fore aft location of the engines relative to the vertical tail changes $C_{n\beta}$ as a function of the angle of attack (32). This variation is caused by the cross flow over the fuselage and engine nacelles and is illustrated on figure 35.

As found in the arrangement as in figure 36, there can be certain interference effects, however. When at an angle of yaw, the air passing through the engines gets deflected laterally. The consequence is a lateral force ΔY which can be calculated on the basis of the engine mass flow. Depending upon the longitudinal position of the engine ducts (in relation to the airplane's CG) the resulting yaw moment can be "positive" or "negative". For the airplane as in figure 36, the moment should be expected to be destabilizing. The experimental result is a small stabilizing increment, however. Analysis suggests that a stabilizing force is induced in the particular configuration considered, in the vertical tail. It seems that the presence of the pair of jets makes the configuration more "low wing", thus inducing some stabilizing sidewash at the location of the vertical tail.

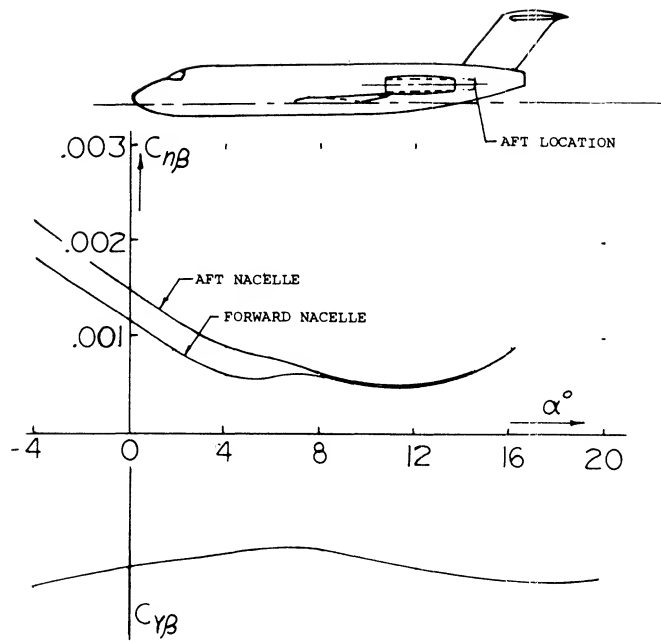
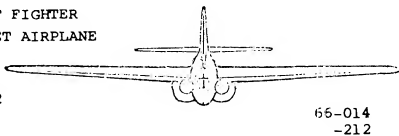


Figure 35. Engine nacelle effect on the effective yawing moment and side force derivatives.

Flow Separation. The only problem regarding the directional characteristics of the jet-propelled airplane in figure 36, is a strong reduction of the derivative $dC_{\eta}/d\beta$ from 0.008 to 0.003, in landing condition (wing flaps down 45° , engines "inoperative" as in the wind tunnel). It seems that there are a pair of separated spaces behind the two engines attached to the sides of the fuselage, thus reducing the dynamic pressure at the vertical (and horizontal) tail surfaces.

BELL P-59 TWIN-JET FIGHTER
US FIRST (1942) JET AIRPLANE
SEEN FROM BEHIND

b = 45.5 ft
S = 386 ft²
W = 12000 lb
T = 2 2000 lb
V_x = 360 kts
S_V = 8% S
l_V = 0.43 b



AS TESTED IN FULL SCALE TUNNEL:

$dC_Y/d\beta = 0.0050$ IN ALL CONDITIONS
 $dC_{\eta}/d\beta = 0.0008$ IN CRUISING CONDITION
= 0.0003 WITH FLAPS 45° AND
ENGINES INOPERATIVE

W'RPT L-626

Figure 36. Directional stability derivatives of Bell P-59, first U.S. jet airplane as tested (24,a) in the Full Scale Tunnel.

V. CHARACTERISTICS AT HIGHER ANGLES OF YAW

So far, primarily yaw-moment and other derivatives have been presented and discussed as they are found at and around zero angle of sideslip, say within plus-minus 10° . When going beyond such limits, two changes take place:

- 1) the vertical tail surface may stall,
- 2) the tail may "drop" out of the propeller slipstream.

These events and their influence upon stability and control are as follows.

Fuselage. Shown in the Chapter XIX a "second" non-linear component of lift, cross-wind or normal force develops on streamline bodies at the longer angles. Since the location of this lift component is somewhere in the after-body, the corresponding yaw moment about the CG of a typical airplane (located, say at $1/3$ of the fuselage length) is stabilizing. The directional characteristics of propeller driven fighter-type airplane are presented in figure 28. Without power, and without vertical tail, the yaw moment derivative $dC_{\eta}/d\beta$ of the configuration reduces from the original value of -0.0007 or -0.0008 , to zero at $\beta =$ plus or minus 20° ; and it then turns stable reaching comparatively large slopes around and beyond $\beta =$ plus or minus 40° . There may be some component of yaw moment included in the tested function, caused by the roll moment in the wing, due to yaw. Neglecting this component, the non-linear differentials tentatively lead to a moment arm of the normal forces in the fuselage

$$l_N/b = \Delta C_{\eta}/\Delta C_Y = 0.30 \text{ or } 0.35$$

This distance from the CG of the airplane ahead of the tail surface, in the middle of the dorsal fin, would appear to be reasonable for the non-linear component of the fuselage's lateral or normal force.

(33) Twin-engine airplanes, flight-tested:

- a) Sjöberg, Douglas A-26, W'Rpts L-606, 607, 608 (1945).
- b) Crane, DeHavilland "Mosquito", W'Rpt L-593 (1945).

Displacement. In Chapter XII it was shown how the propeller slipstream is cut in two parts are displaced in lateral direction, as a consequence of torque and rotation, the upper "half" to one side and the lower one to the other side. If looking at the airplane in figure 29, *from ahead*, the propeller is turning counter clockwise, a right hand prop. Since the configuration is that of a low wing (with most of the propeller disk above the wing) the slipstream is displaced to the side into which the tail moves at negative angles, left on the graph. On this side, therefore, the slope of the yawing moment contribution of the vertical surface $C_{\eta_{BV}}$ has a large increase. On the other hand, when sideslipping to the other side (to the right in the graph) the derivative is reducing to and below zero. When trimming the airplane by deflecting the rudder so that $C_{\eta} = 0$, the airplane is still stable directionally, at and near $\psi = 0$. However, at and beyond $\psi = +6^\circ$, as in part (B) of figure 28, that is when sideslipping to the left as seen by the pilot the airplane becomes unstable. The same type of slipstream displacement is also responsible for the asymmetry of the sidewash distribution in figure 27, in power-on condition.

Slipstream. As noted above slipstream rotation causes the unfavorable asymmetric condition shown on figure 28. This is eliminated on normal jet propelled airplanes as the design is set up so the slipstream does not impinge on the tail. Slipstream rotation is also eliminated by the use of dual rotation propellers or with the use of ducted fans designed for peak performance using vanes to eliminate the rotational losses.

Tail Stalling. Vertical surfaces do stall, at higher angles of yaw however, together with the aft end of the fuselage high stabilizing are still obtained. The reasons why an airplane as in figure 32 turns highly unstable at yaw angles beyond plus/minus 20° , are other than stalling:

- the vertical tail moves out of the propeller slipstream laterally,
- the destabilizing normal forces in the propeller is high,
- there is a considerable destabilizing interference between slipstream and fuselage.

When leaving the rudder alone (not shown in figure 32) a definitely unstable condition is obtained, at $\beta =$ plus or minus 10° . In the case of tiem (c) it appears that the slipstream reduces considerably the stabilizing non-linear lateral-force component of the fuselage. This interaction will be discussed after explaining the mechanism of dorsal fins.

Dorsal Fins. While sideslip angles up to plus-minus 20° seem to be sufficient in any normal operation of the airplane, the loss of restoring forces and moments at larger angles might be dangerous when spinning the airplane. A device expected to improve the directional characteristics, are dorsal and/or ventral fins. Fins of the type as in figure 37, do not have any effect on the yaw moment of the fuselage body, within the range of plus-minus 3° angle of yaw.

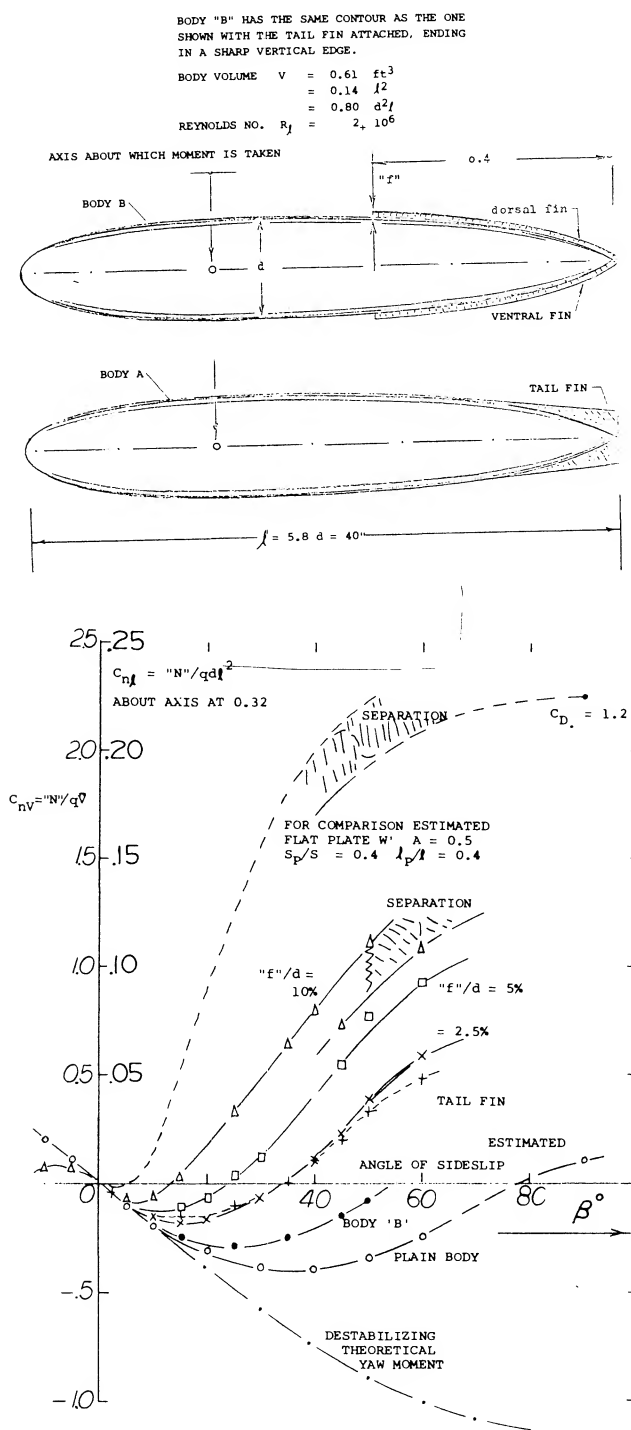


Figure 37. Yaw moments of a plain fuselage body with and without *dorsal and ventral fins* (28,a).

Between $\beta = 10$ and 50 or 60° , the stabilizing influence of the fins in figure 37 is considerable. The principle by which they work, is to increase the fuselage's "natural" non-linear normal or lateral-force component. This cross-flow component explained in Chapters III and XXI, is basically of the type

$$C_N \sim \sin^2 \alpha; \text{ or } C_Y \sim \sin^2 \beta \quad (28)$$

In the extreme, the rear end of the fuselage may be thought of being converted by the addition of dorsal and ventral fins, into a "flat plate". We have estimated the yaw moment of the body in figure 37, assuming that a lateral area aft equal to 0.4 of the body's area be a plate, with an aspect ratio of 0.5 and an average moment arm to the yaw axis at 0.32ℓ , equal to 0.4 of the body length ℓ . Using normal forces as in the Chapter III, the uppermost curve in the graph is thus obtained. Evaluating the experimental results in (26,a) with the aid of equation (28), it is found that the "ridges" change flow pattern and cross-flow drag coefficient of the sections of the fuselage to which they are attached. Considering in figure 37, a single point, at $\beta = 30^\circ$, where $\sin^2 \beta = 0.25$, the lateral force can be expected to correspond to the coefficient based on projected lateral area

$$C_{N_D} = 0.35 = C_{D_D} \sin^2 \beta = C_{D_D} 0.25$$

The resultant cross-flow drag coefficient of the part of the fuselage "covered" by the fins is $C_{D_D} = 1.4$. After subtracting some value for the plain fuselage, the component attributable to the presence of the fins may be $\Delta C_{D_D} = 1.0$. The height of these fins in figure 37, is 5% each of the maximum body diameter. Their combined lateral area S_D is about 13% of the portion of the fuselage "covered" by them S_F . We will assume that C_{D_D} be proportional to that area ratio. Thus

$$\Delta C_{D_D} = 8 (S_D/S_F) \quad (29)$$

Dividing $\Delta C_N/\Delta C_Y$, the center of the lateral force produced in figure 37, is found roughly to coincide with that of the fins.

Airplane Configuration. Dorsal fins have been tested as a means of improving the characteristics of several airplanes (26). As an extreme example, yaw moment characteristics are shown in part (B) of figure 38 of an airplane for the cases of a high powered dual-rotation propeller, and with the rudder free to move.

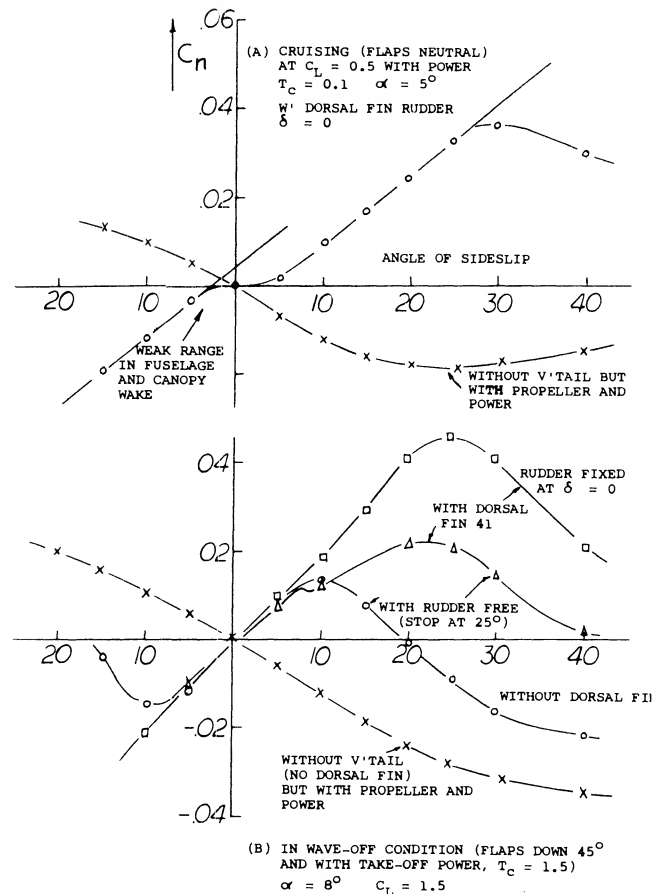
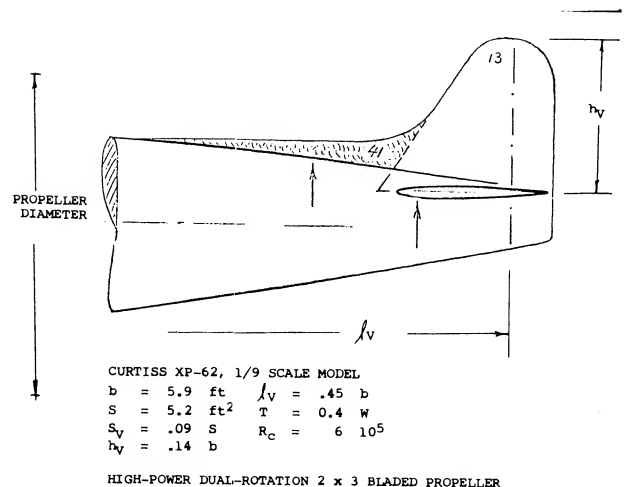


Figure 38. Influence of a dorsal fin on yaw moment of a fighter-type airplane (27,b).

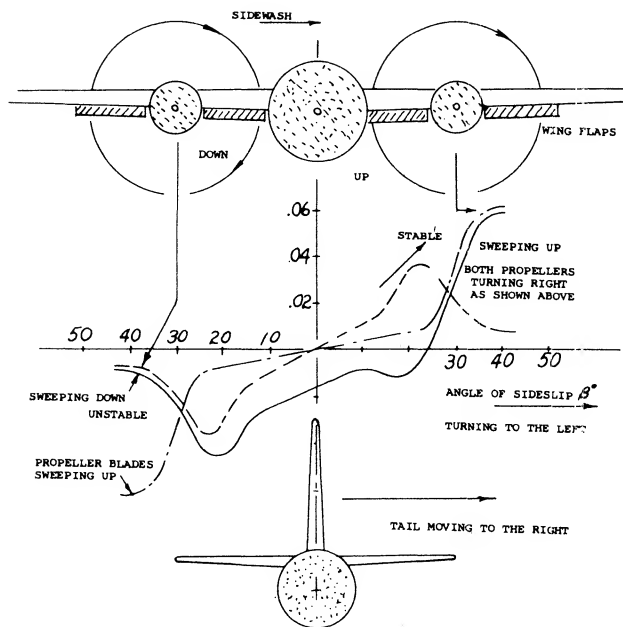


Figure 39. Yaw-moment functions of the B-28 twin-engine bomber, in wave-off condition (flaps down, full power on) for three modes of propeller operation.

Directional stability starts to deteriorate at plus or minus 10° angle of yaw. If left alone, the airplane would seek a point of balance beyond 40°. As stated before, the contribution by dorsal fins to directional stability in more or less straight flight around $\beta = 0$ is negligibly small. In fact, by disturbing the cross flow around the leading edge of the vertical tail surface, the derivative, $C_{n\beta}$, can even be reduced when adding a dorsal fin, although a ventral fin (at the lower side of the fuselage) would probably be somewhat beneficial. The fin as shown in the illustration can be analyzed, using equation (29). In doing so, it must be taken into account however that:

1. the low wing increases the cross flow (some 30%),
2. the slipstream reduces that flow (some 20%),
3. the dynamic pressure along the fuselage is increased (equation 26).

For the yaw-moment differential $\Delta C_Y = 0.085$, as at $\beta = 40^\circ$, a lateral drag coefficient $\Delta C_{D\beta}$ is thus obtained, which is similar in magnitude to that as found above for the fin in figure 37. Assuming this coefficient, the lateral force contribution of the dorsal fin is figure 38, can be estimated to be

$$\Delta C_Y = (S_D/S)(\sin^2 \beta)(q_\infty/q) \Delta C_{D\beta} \quad (30)$$

where β_e = effective lateral angle = $\beta(1 + d\sigma/d\beta)$. The moment arm of this force $l_n = 0.28 b$, corresponding to $l_D/b = \Delta C_n/\Delta C_Y$ is indicated in the drawing.

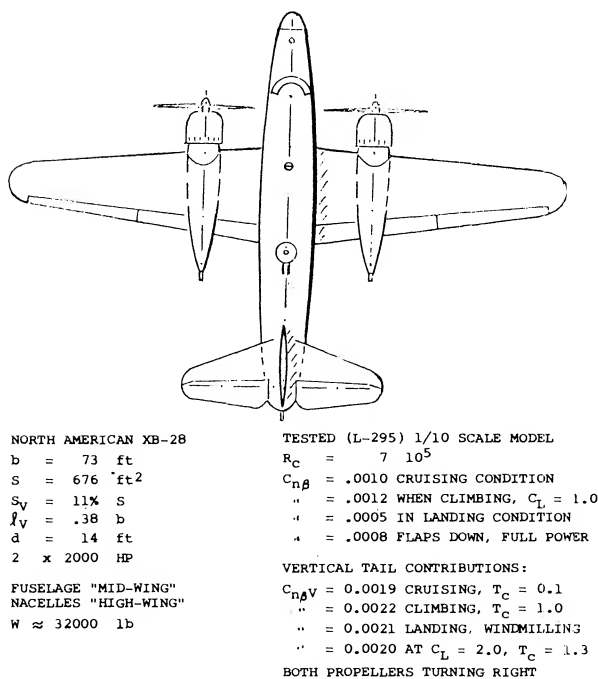


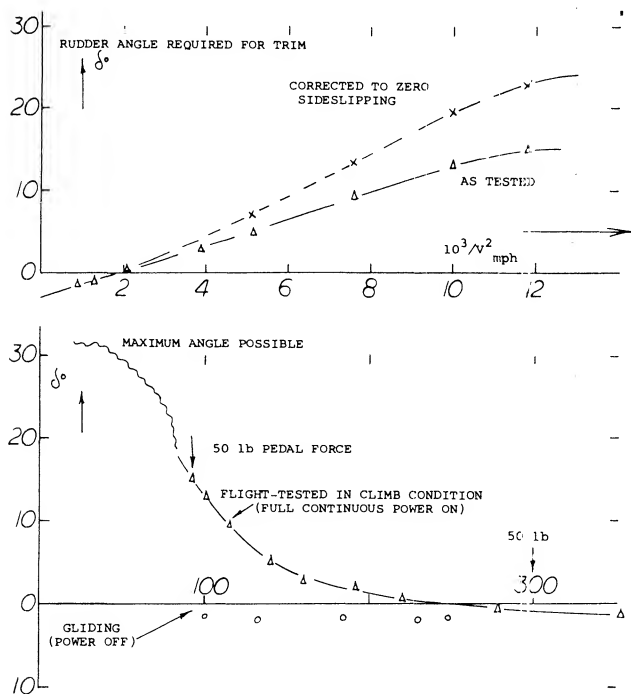
Figure 39. Yaw moment characteristics of the twin-propeller B-28, tested (27,c) in a powered wind-tunnel model.

Propeller Moment. It was found above, in part (A) of figure 32, that the destabilizing contribution by a powered propeller grows with the angle of yaw at a rate higher than linear. The explanation is contained in equation (30) where the lateral force due to dorsal fins (or that originating in the tail end of the fuselage body) is seen to be proportional to the square of β . $\beta = \beta(1 + d\sigma/d\beta)$. In other words, since $d\sigma/d\beta$ due to slipstream is negative, the stabilizing contribution of the fuselage can easily be reduced. For $T_C = 3.1$, as in figure 32, equation (23) yields a $d\sigma/d\beta = -0.5$. At $\beta = 30^\circ$, thus $\beta_e = 15^\circ$, so that the stabilizing component of the fuselage is reduced to 1/4. It can be concluded that single-propeller airplanes reach a practical limit as to their power, say corresponding to $T_C = 2$ or 3, beyond which they may no longer be "manageable" when sideslipping.

Twin Propellers. Directional characteristics of the twin engine aircraft are tabulated in figure 38. Within the range of $\beta = \text{plus-minus } 10^\circ$, results can be generalized as follows:

- the normal force of the propellers (with power, corresponding to $T_c = 1.3$, but not shown in the illustration) is almost as large as that of the tail surface,
- power does not have a noticeable influence upon the fuselage contributions,
- power does not seem to have an effect upon the contributions by the vertical tail surface,
- deflection of the wing flaps considerably increases (not shown in figure 39) the lateral force in the fuselage (presumably next to the wing roots).

The vertical tail is evidently located between the two slipstreams. In the cruising condition (flaps neutral) the $C_{\eta}(\beta)$ function is fairly regular between plus and minus 20° .



NORTH AMERICAN P-51 "MUSTANG"
POSSIBLY THE FIRST OPERATIONAL
AIRPLANE USING A LAMINAR-TYPE
FOIL SECTION, PRESUMABLY OF THE
64 SERIES WITH 16 TO 11% THICK-
NESS AND 1.2% CAMBER DEVELOPED
AROUND 1942

b = 37 ft 0.5 TAPERED
S = 236 ft² A = 5.8
d = 10.5 ft 3-BLADED
S_v = 8.5% S RUDDER 52%
W = 8000 lb LOW WING

Figure 40. Rudder angles required to trim P-51 "Mustang", flight-tested by NACA (31,c).

Pair of Slipstreams. The direction of propeller rotation in twin-engine airplanes will influence the flow pattern at, and stabilizing effect of the horizontal tail surface (28) and Chapter XII. The effect of the propellers on the directional stability of a B-28 for the case of both propellers turning right are given on figure 40. The results for the flaps done case $T_c = 1.3$, $C_L = 2.0$ are:

- At $\beta = 0$ no tail, a moment is obtained corresponding to $C_{\eta} = -0.01$, turning the airplane to the left. The left slipstream seems to blow slightly across the fuselage.
- The moment under (a) is doubled when adding the tail surfaces. A sidewash to the right, is evidently produced at the location of the vertical tail by propeller blades and slipstream turning in this direction.
- As in figure 28, the $C_{\eta}(\beta)$ function is asymmetric. The stable range is wider when yawing to the right (to $\beta = -20^\circ$) and limited (to $\beta = +10^\circ$) when turning to the left (as seen by the pilot).
- It seems, when turning to the left, the vertical tail begins to "lean" against the right-side slipstream at angles above $\beta = +20^\circ$. The slope increases to a maximum in the order of $dC_{\eta}/d\beta = +0.03$.
- When turning to the right, the tail surface seems to stall at an angle $\beta = -20$ or -25° . The slope reverses to maximum values of $dC_{\eta}/d\beta$ between -0.03 and -0.04 .

Opposite-Rotation (28). When arranging engines or propellers, turning in opposite directions, flow pattern and directional characteristics evidently become symmetrical. Characteristics in figure 39 are as follows:

- When yawing to the right, stalling takes place as in (e) above, in the case where both engines turn so that the blades sweep down at the inboard sides of the nacelles. Note that the left propeller turns clockwise (as in (e) above).
- When yawing to the left, the same stabilizing interference as in (d) above is obtained, in the case where the propellers turn sweeping up at the inboard sides. Note that the right propeller turns as in (d) above.
- It is apparent that none of the three modes of twin-propeller rotation will remedy all of the irregularities in the yaw moment function. For displacement up to plus-minus 20° , contra-rotation as in (a) seems to be best, while at angles up to plus-minus 40° , the opposite mode of operation (blades up) is superior (at least in the B-28 configuration).

Shape, dimensions, arrangement, power used and other parameters may affect the directional characteristics of any specific airplane. However, the evaluation presented above, displays the type of interference to be expected between the vertical tail and the pair of slipstreams in twin-engine airplane configurations.

VI. DIRECTIONAL CONTROL OF AIRCRAFT

The deflection of the rudder will cause the development of a lift or lateral force that will generate a yawing moment, causing the airplane to seek a new sideslip angle heading. The change in the sideslip angle heading is generally directly influenced by the rudder angle deflection. The center of the lateral force on the rudder can be well above the CG of the airplane which will induce a rolling moment that requires crossed controls if a steady sideslip is required.

Design Requirements. The design requirements for the rudder depend on the type of airplane. For light single engine the rudder design will be based on the sideslipping needed for control of the glide path and alignment of the runway during landing. Thus when operating in a cross wind it is necessary to have a sideslip angle so to touch down the rudder is reversed to allow the aircraft to be aligned to the runway.

The most critical requirement for the rudder is the counteracting of the yawing effect of a failed engine on multi-engine aircraft. This is especially true with aircraft having the engines well outboard on the wing so that large moment arms are involved. With some of the early large turboprop aircraft it was necessary to consider not only the loss of thrust due to the failed engine, but also the possibility of negative thrust due to the propeller developing reverse thrust. In the case of the latter condition the rudder design problem became impossible, thus requiring other solutions.

The conditions for the rudder design are determined by the civil air regulations which define a minimum control speed parameter, V_{MC} , where with the most critical engine out it must be possible to maintain straight flight with zero yaw. The minimum control speed is usually tied in with the stall speed with power and the most aft CG location. Thus, the rudder must be designed to provide sufficient lateral force so that the yaw moment exceeds that exerted by the engine out conditions.

Rudder Control. Basically, the effectiveness of the rudder depends upon the flap chord ratio c_f/c . As described in the Chapter IX, effectiveness may statistically be indicated by the parameter $d\beta/d\delta \approx 0.5$. This value means that deflection of the rudder by $\delta = 1^\circ$, changes the lateral force as much as it would be changed by a differential of the sideslip angle $\Delta\beta = 2^\circ$. Single-propeller airplanes, such as the fighter in figure 40 for example, have a directional trim or rudder problem. Because of slipstream rotation, the vertical tail is blown to one side. For a right hand propeller, therefore, the airplane tends to turn to the left. The rudder angle required to prevent turning and/or sideslipping, is plotted on figure 41 as a function of the indicated airspeed. To reduce rudder deflection and force required, the fin is usually built onto the fuselage at a small lateral angle, such as $i_v = 2^\circ$ in the P-51, for example. Around $V = 240$ mph, where the rudder angle is zero, the average sidewash angle due to full-power slipstream is evidently equal to that of the tail setting. The rudder angle required for trim grows considerably as the airspeed is reduced.

Analysis. We will assume that power and torque Q of the engine be constant. The average speed w representing slipstream rotation is roughly

$$w \sim Q/S_p V$$

where $S_p V$ = approximation for the rate of volume (and mass) flow through the propeller disk. The sidewash angle is then

$$w/V \sim 1/V^2 \quad (31)$$

We have plotted in part (B) of figure 40, the rudder angles required for trim, versus $1/V^2$. The function obtained is essentially linear. There are certain secondary effects to be considered, however:

- For maximum rudder pedal forces of plus-minus 50 lb, some elastic deficiency can be assumed in the rudder angle as recorded.
- At 90 mph, where the pedal force is 50 lb, the pilot is evidently tired to do more. The airplane is sideslipping at $\beta = 10^\circ$.
- In the analysis above, the slipstream velocity v (added in downstream direction) is disregarded. The sidewash angle is actually $w / (V + v)$.

Sideslipping as in (b) can theoretically be eliminated by deflecting the rudder further, corresponding to

$$\Delta \delta = \beta (d\delta/d\beta)$$

where the derivative has the value of 0.8, as tested for the same condition of flight. Considering elasticity as in (b) above and on account of (c) above, the upper line in graph (B) must be expected to level off. The value required at $V = 0$, at the start of the take-off run of the airplane, might be the maximum possible rudder angle, which is 32° for the P-51. If the vertical tail were not be within the slipstream, it could be difficult to handle the P-51 or any other single-propeller airplane while taxiing on the ground, particularly in lateral wind.

Sideslipping To increase the drag control the rate of descent and align the airplane with the runway sideslipping is used. To prevent the airplane from sideslipping, the ailerons have to be deflected thus providing an angle of bank. In steady-state and straight sideslipping motion, conditions are as follows:

- the rudder balances the yaw moment, also producing some lateral force,
- the ailerons balance the roll moment, keeping the airplane banked,
- a component of the airplane's weight counteracts the lateral force.

Sideslipping is also a convenient method of testing in flight, stability, control effectiveness, and forces necessary to deflect the control elements.

Flight Testing. In an airplane flying in any steady-state equilibrium, there are no "free" moments. Besides speed, all there is to be measured are angles. For one of the many airplanes investigated (31)(33) typical flight-test results are presented in figure 41. The graph shows

- the rudder deflection required
- the aileron angle required
- the angle of bank required

all as a function of the angle of sideslip, gliding at one particular speed of the resulting straight motion, and at the constant lift coefficient $C_L = 0.6$. The aileron deflection neutralizes the roll moment primarily originating in the wing as a consequence of dihedral. From the frontal view of the airplane tested, it is evident that there will not be much of interference between the slipstreams and the

central vertical tail. Therefore, results in cruising (power-on) condition are not very much different from those shown in gliding (power-off) condition, for that particular airplane.

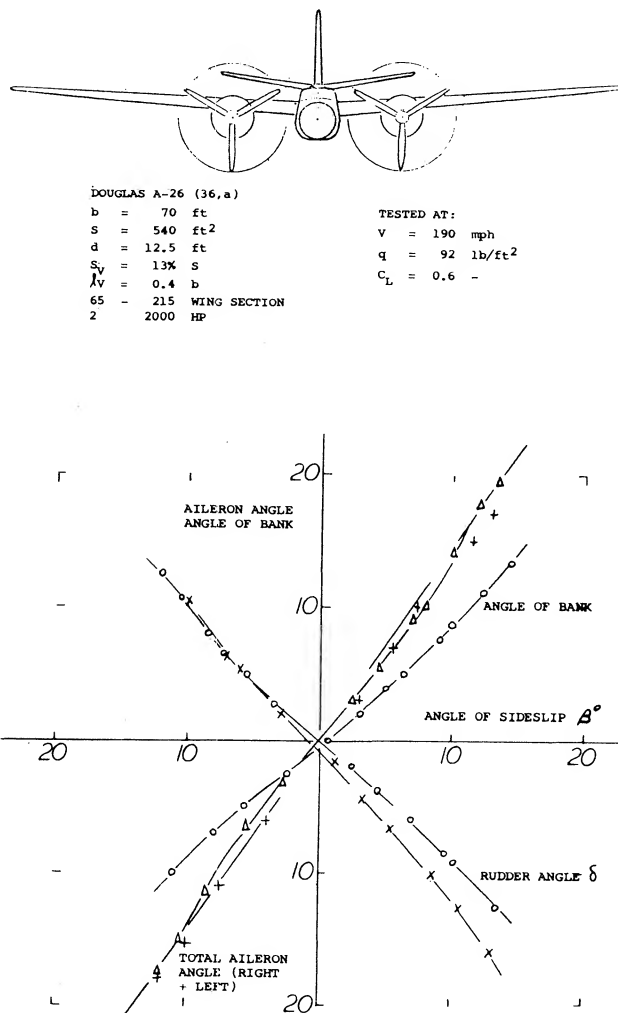


Figure 41. Characteristics of a twin-engine airplane in steady sideslipping motion (33,a).

Lateral Force. In banked condition, the component of the airplane's weight in lateral direction is $Y = W \sin \varphi$, where φ = angle of bank. The lateral force derivative is thus found to be

$$dC_Y/d\beta = (\pi/180)(d\varphi/d\beta)(W/qS) \quad (32)$$

where $q = 0.5 \rho V^2$. Assuming that the force derivative be independent of the angle of attack (lift coefficient), the angle of bank required to balance a certain angle of sideslip, can be expected to vary in proportion to the

dynamic pressure. Flight-test results of several airplanes are plotted in figure 42. For $W = 12,000$ lb, wing area $S = 300$ ft², the loading of the F-47 is $W/S = 40$ lb/ft². The lateral derivative is then

$$dC_Y/d\beta = (W/S)(d\gamma/d\beta)/q \approx 0.010$$

where $d\gamma/d\beta = 0.014$ as in the graph. This derivative is not the same as in a wind-tunnel model, however. Rather, it represents the lateral force of the airplane in trimmed condition, id est for $C_n = \text{zero}$.

Yaw Moment. The significance of the flight tests described is found in the fact that the control deflections measured can be used to determine the static stability of the airplane. The yaw moment corresponds to

$$dC_n/d\beta = (d\delta/d\beta)(d\beta/d\delta)(dC_{lat}/d\beta)V_V \quad (33)$$

where $d\beta/d\delta =$ rudder effectiveness ratio, and $dC_{lat}/d\beta =$ lateral force slope of the vertical tail surface used. For example, in figure 41, the derivative $d\delta/d\beta = (d\delta/d\gamma)/(d\beta/d\gamma) = 0.8$. A large value of the flight-tested $d\delta/d\beta$ can indicate two things:

1. that the rudder effectiveness ($d\beta/d\delta$) is small,
2. that directional stability (resulting from the last half of the equation) is large. The effectiveness can be estimated (see $d\alpha/d\delta$ in Chapter IX) or it may be assumed to have an average value, say of 0.6 for rudders. For a conventional type rudder, therefore, the flight-tested derivative $d\delta/d\beta$ is considered to be a measure for the directional stability

$$dC_n/d\beta \sim (d\delta/d\beta) \quad (34)$$

Using the tail volume ratio $V_V = 0.054$ and the statistical value of $dC_{lat}/d\beta = 0.04$, the directional stability derivative of the airplane in figure 41, may thus be

$$dC_n/d\beta = 0.8 (0.6) 0.04 (0.054) \approx 0.001$$

Inopporative Engine. Multi-engine aircraft are designed so that the airplane can continue to fly after one or more engines fail. When an engine fails a yawing moment is encountered due to the asymmetrical thrust developed by the operating engines and the drag of the dead engine as illustrated on figure 44. This yaw moment may be very large if the propeller on the dead engine is windmilling and the failed engine is capable of absorbing a large amount of torque. For this case the negative thrust produced by the windmilling propeller can be as large as the positive thrust on the operating engines. Thus the yaw moment produced by the vertical tail must be very large to balance that moment produced by the failed engine. In many cases the moment required is larger than is possible with a practical design. As stated in (30,b) the most suitable method of flying on one engine, is to balance the yaw moment by rudder deflection, and to prevent sideslipping by banking the airplane toward the side of the operating engine. The result is a lateral force primarily in the vertical tail surface, supporting a smaller part of the airplane's weight, in a manner similar to that as explained in connection with figure 42. An example for this mode of operation is shown in figure 43. To be able to maneuver, the make turns and to climb after a landing approach may have failed, it is desirable that full power of the operating engine be used. As stated in (30,d) "the asymmetric power condition, to a large extent dictates the design of the vertical tail surface".

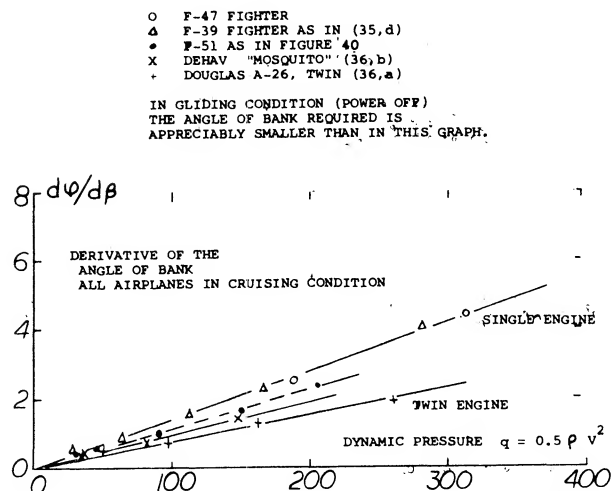
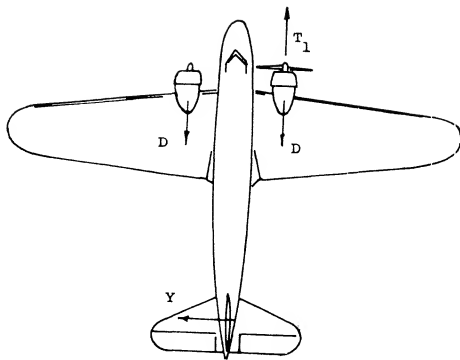


Figure 42. Derivative of the angle of bank in steady sideslipping motion, as a function of the dynamic pressure at which the airplane is flying.



1/5 SCALE MODEL OF TRANSPORT AIRPLANE
(AROUND 1934) WITH:

b =	76 ft	R _C =	1 10 ⁶ AS TESTED
S =	850 ft ²	V _x =	200 mph MAXIMUM SPEED
d =	10 ft	S _v =	8% S
W =	13500 lb	S _R =	0.6 S _v
P =	700 HP	IN ONE ENGINE	

RESULT OF INVESTIGATION:

C _L =	1.2	LIFT COEFFICIENT AT WHICH TESTED
C _n =	0.02	YAW MOMENT DUE TO ONE ENGINE
δ =	20°	RUDDER ANGLE TO COMPENSATE C _n
β =	8°	RESULTANT ANGLE OF SIDESLIP
φ =	2°	ANGLE IN BANKED MODE
β =	11°	RUDDER ANGLE IN THIS MODE

Figure 43. Example (30,b) for the operation of an airplane with one of two engines inoperative.

Yaw Moment. In the design of the vertical tail surface for the engine out case the low speed take-off condition is critical. Here the dynamic pressure is low so that the deflection and area required to produce the necessary lateral force is very high.

As an example of a somewhat more powerful configuration, the one-engine operation of the B-28 (as in figure 39) may be analyzed. As indicated in (27,c) maximum-power thrust in one propeller is approximately $T = 0.1 \cdot W$. The corresponding moment is "N" = 0.1 (32,000) 11 = 36,000 (ft-lb) where the moment arm to the CG is 11 ft. To balance (trim) this moment, the vertical tail surface has to provide a lateral force $Y = 36,000/28 = 1300$ lb, for its moment arm $l_V = 28$ ft. Based on a tail area $S_V = 75$ ft², the corresponding lateral force coefficient is

$$C_{lat} = 1300 / (75 \cdot 0.5 \rho V^2)$$

As found in the "control" chapter, the maximum coefficient producible by 25° rudder deflection, at zero angle of sideslip, is in the order of 0.6. For comparison, the coefficient obtained in (30,e) for 30° rudder deflection, is 0.63. Solving now the last equation, a minimum permissible speed of 106 mph is obtained. The corresponding lift coefficient of the airplane is $C_L = 1.6$. This may be close to the maximum lift coefficient of this airplane in power-off (landing) condition. Disregarding rudder pedal forces, therefore, the B-28 appears to have satisfactory qualities in one-engine operation.

CHAPTER XIV — LATERAL STABILITY CHARACTERISTICS OF AIRPLANES

Lateral stability is a function of the yawing and rolling moments, the lateral force and their associated cross coupling. The stability of the airplane from these forces and moments must be determined by a dynamic analysis as the motion is time dependent. However, the most important contribution to such a dynamic stability analysis comes from so-called “static” stability derivatives, i.e. from the derivatives of forces and moments with angles of roll, yaw and pitch. Static stability is, therefore, considered first while principles, derivatives, theory and practical results of dynamic lateral stability are presented in the last part of this chapter.

Static Stability. Evaluation of theoretical and experimental derivatives of wings as a function of the angle of yaw is broken down into:

- (a) characteristics of straight wings
- (b) derivatives of dihedral wings
- (c) analysis of swept wings.

Under each of these headings we will consider the variation of lateral forces, the rolling moment (about the longitudinal axis) and yawing moments (about the vertical or normal axis).

Components. When rotating an airplane about the two axes considered in this chapter, the three basic parts — wing, fuselage (also engine nacelles if any) and vertical tail surface — each contributes components of aerodynamic forces and/or moments. We will consider these components separately:

- (aa) characteristics of the wing as listed above
- (bb) moments and/or influence of the “fuselage”
- (cc) forces and moments due to the vertical tail.

We will also have to include mutual interactions between those airplane parts. In fact, the fuselage usually does not contribute any rolling moment of its own, however, it may change those moments of the wing.

Nomenclature. Besides the basic symbols listed in the first chapter, we will specifically use the following in the treatment of lateral characteristics:

Y = lateral force
“L” = rolling moment
N = yawing moment.

The symbol “L” (from “longitudinal”, indicating the axis about which the moment is defined) should not be confused with L, denoting lift. Lateral characteristics are presented in the form of non-dimensional coefficients:

$$C_Y = Y/qS; C_L = “L”/qSb; C_N = N/qSb \quad (1)$$

Note that the moments are referred to the span (and not to the half span as found in some of the sources referred to). In the discussion of lateral characteristics, the following terms should also be understood:

- 1) “Yaw” indicates an angular displacement (by the angle β) about the normal axis x axis of the airframe.
- 2) “Yawing” indicates an angular rate of motion about the same axis.
- 3) “Sideslipping” indicates a lateral velocity in the direction of the wing span.

Derivative Notation. The notation developed in dealing with the equations of motion and the analysis of aircraft stability greatly simplifies the task and helps in the overall understanding. This system is generally used in the industry and the research agency and is adopted for this chapter. The important derivatives used are per radian unless otherwise noted and are:

$$C_{L\beta} = \partial C_L / \partial \beta$$

Effective dihedral, rate of change of rolling moment coefficient with angle of sideslip.

$$C_{N\beta} = \partial C_N / \partial \beta$$

Directional-stability derivative, rate of change of yawing-moment coefficient with angle of sideslip.

$$C_{Y\beta} = \partial C_Y / \partial \beta$$

Lateral-force derivative, rate of change of lateral-force coefficient with angle of sideslip.

$$C_{n_T} = \partial C_N / \partial (rb/2V)$$

Damping-in-yaw derivative, rate of change of yawing-moment coefficient with yawing-angular-velocity factor.

$$C_{n_p} = C_N / \partial (pb/2V)$$

Rate of change of yawing-moment coefficient with rolling-angular-velocity factor.

$$C_{l_p} = C_l / \delta (pb/2V)$$

Damping-in-roll derivative, rate of change of rolling-moment coefficient with rolling-angular-velocity factor.

$$C_{l_r} = \partial C_l / \delta (rb/2V)$$

Rate of change of rolling-moment coefficient with yawing-angular-velocity factor.

$$C_{Y_p} = \partial C_Y / \delta (pb/2V)$$

Rate of change of lateral-force coefficient with rolling-angular-velocity factor.

$$C_{Y_r} = \partial C_Y / \delta (rb/2V)$$

Rate of change of lateral-force coefficient with yawing-angular-velocity factor.

Systems of Reference. The rolling moment is basically taken about the longitudinal axis of the airplane (air-frame); and the yawing moment is about the axis *normal* to both the longitudinal axis and the wing span. This system of reference which we may call the *air-frame system* is the one in which a pilot senses position and motion of his airplane. There is also the "*wind system*", however; as we may have it, for example, in such wind tunnels where the balance is fixed to the tunnel, while the wing or airplane model is rotated in reference to the balance to produce the angle of yaw. As far as rolling is concerned, the difference between the moment measured about the longitudinal airplane axis and that about the direction of flow or flight is usually very small; it corresponds to the cosine of the angle of yaw (1). Accordingly, when considering derivatives taken at small angles of attack and about the neutral position (at $\beta = 0$), there is no difference between the two systems as far as *moments* are concerned. As we will see later, considerable differences can arise, however, in the lateral force *Y* depending on the direction, either along the wing span or normal to the direction of flow or flight in which it is measured or defined.

Stability Axis. The axis system most universally used is stability axis, figure 1, and is used in this chapter unless otherwise stated. In this system the Z-axis is in the plane of symmetry and perpendicular to the relative wind, the X-axis is in the plane of symmetry of the airplane and is perpendicular to the Z-axis, and the Y-axis is perpendicular to the plane of symmetry. The sign convention used with the stability axis is shown on figure 1. In this sign convention:

- (1) That difference can be important, however, when considering larger angles of attack, such as in stalled and/or spinning conditions.

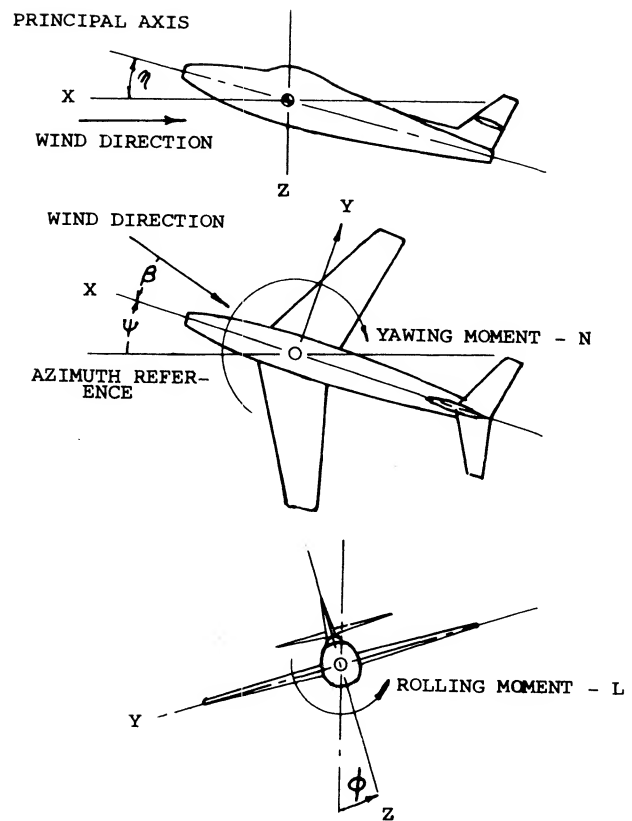


Figure 1. Stability axis system, positive direction indicated for forces, moments and displacement.

- a) The rolling moment derivative $dC_l/d\beta$ is considered to be negative when the advancing wing tip (or wing panel) is *lifted* by the moment.
- b) The derivative of the yawing moment is defined as positive when the moment tends to *return* the airplane to the neutral, $\beta = 0$ position.
- c) The lateral force derivative is defined as positive when the force causes the airplane to move to the right.

1. FORCES AND MOMENTS OF STRAIGHT WINGS.

Wing moments are usually the consequence of changes in the *lift* distribution. Rolling and yawing moments are thus coupled with each other and they may be a function of lift, i.e. of the wing's lift coefficient. (2)

Lift of Sideslipping Wings. According to the cross-flow principle, Chapter XV, the lift of a two-dimensional airfoil kept at a certain angle of attack (measured in the direction of the airfoil chord) varies as

$$L \sim \cos^2 \beta \quad (1)$$

Under the three-dimensional conditions of a wing with a finite aspect ratio that principle is no longer suitable to explain the variation of lift, the reduction of lift is much more complicated. For example, the lift of a disk (circular plate) reduces as

$$L \sim \cos^2 \beta \quad (2)$$

when keeping the angle of attack constant in the direction of the longitudinal “wing” axis. As demonstrated in figure 2, equation (1) serves well enough, however, to predict the lift of sideslipping wings having aspect ratios between 5 and 6. When the airplane is operating at low angles of attack the reduction of lift due to sideslipping may not be important. In this case constant lift is maintained simply by a small displacement of the elevator by the pilot. However, when operating near stall the lift reduction due to sideslipping could lead to stall problems, especially during landing.

Lateral Forces. The lateral forces of straight wings operating at an angle of yaw at zero bank angle are developed from viscous (friction plus some form drag) and a component of drag due to lift. The fractional component is simply

$$C_{Yf} \approx -C_{Ds} \sin \beta \approx -C_{Ds} \beta^\circ \pi / 180 \quad (3)$$

With a section-drag coefficient $C_{Ds} = 0.02$ the average lateral force derivatives of wing models in reference to the stability axis system (in the direction perpendicular to the X axis) is given on figure 3 in comparison with test data. Based on the test data the force seems to increase somewhat with the lift coefficient. Note that in a smooth full-scale wing $C_{Ds} = 0.01$ or less would be closer to reality.

Consequently:

$$dC_{Yf}/d\beta^\circ \approx -0.0001 \text{ to } 0.0002 \quad (4)$$

which is extremely small in comparison to components due to dihedral, fuselage and vertical tail of an airplane (3).

- (2) Tunnel-tested characteristics of straight wings:
- Bamber, Plan Forms, NACA TN 703 & 730 (1939).
 - British ARC, Reports RM 394, 1059, 1203, 2019.
 - Blenk, Dihedral Sweep Twist, Lufo 1929 p 27.
 - Zimmerman, Small Aspect Ratios, NACA TRpt 431 (1932).
 - Shortal, Shape and Dihedral, NACA TR 548 (1935).
 - Doetsch, 6-Component, Yearbk D Lufo 1940 p I-62.
 - AVA Gottingen, results quoted by Seifirth (5,d).
 - Moller, Rectangular Wings, Lufo 1941 p 243.
 - Results from AVA Gottingen, see (5,d).
 - Hansen, Elliptical Wings, Ybk D Lufo 1942 p I-160.
- (3) The smallness of the lateral forces is also the reason for the scatter of the experimental points in figure 3.

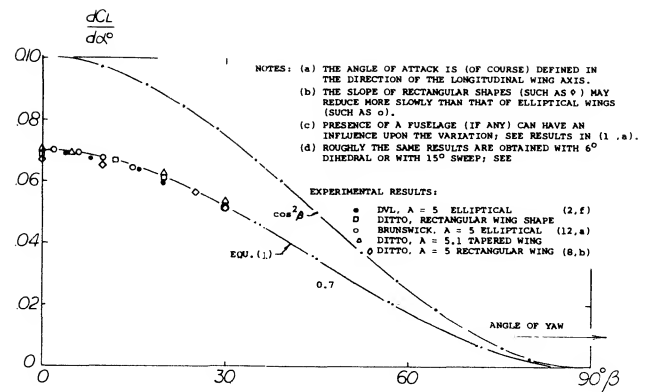


Figure 2. Lift-curve slope of various wings with aspect ratios in the order of 5 and 6, as a function of the angle of yaw.

Component of Lift. Assuming that the lift or total-pressure-force vector of a sideslipping wing may still be in a plane normal to the X Y axis, figure 1, the induced drag must be expected to present a lateral component normal to the direction of flow or flight, as indicated in the sketch in figure 4. That component is

$$\begin{aligned} C_{Y_L} &= -C_{Di} \sin \beta \\ dC_{Y_L}/d\beta &= -C_L^2 / \pi A \\ dC_{Y_L}/d\beta^\circ &= -C_L^2 / 180 A \end{aligned} \quad (5)$$

This equation, plotted in the lower part of figure 3, for $A = 3$ and 6 , is sufficiently well confirmed by experimental results. Note that in the direction transverse to that of flow or flight, the stability axis, both the positive (frictional) and the negative (due-to-lift) lateral forces are existing, while in the airframe system only the frictional component is obtained. Equation (6) was also evaluated as a function of the aspect ratio. Figure 5 suggests that the lateral force due to lift (in the direction transverse to that

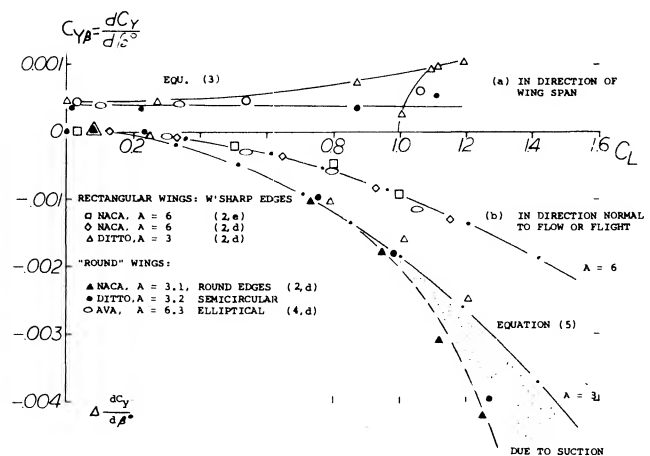


Figure 3. Lateral force derivative of plane and straight wings as a function of their lift coefficient.

of flow or flight) may be of appreciable magnitude at higher lift coefficients and/or in smaller A ratios. "Round" wings (in this case, meaning to have round lateral edges) evidently develop suction forces around the advancing wing tip thus leading to increased *negative* lateral forces, while sharp-edged rectangular wings (as used frequently in wind-tunnel experimentation) show evidence of a positive lateral component presumably originating at the lateral areas of the wing tips.

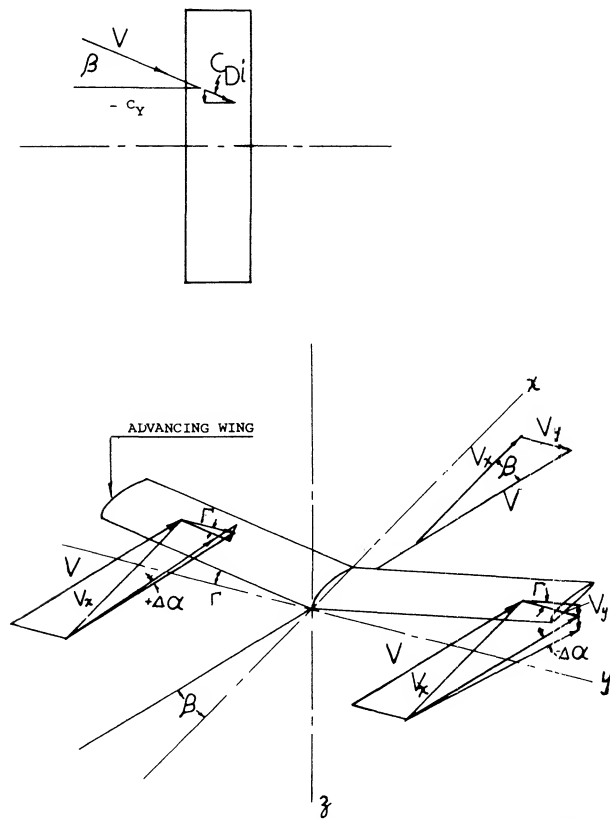


Figure 4. Wing at zero angle of attack with a positive *dihedral* angle Γ showing positive change in angle of attack of advancing wing.

Rolling Moments. Rolling moments are, of course, a consequence of lifting forces; and, within the usual range of the angle of attack where separation does not take place, the rolling moments are found to be proportional to the lift. We can thus conveniently use the derivative dC_L/dC_L . Early analysis (4,a) predicted, on the basis of lifting-line type of induced angle (downwash) distribution, a "negative" rolling moment derivative, meaning that the wing is expected to roll down into the oncoming wind. This type of moment would not be desirable in the operation of airplanes. Experimental results (for the conventional range of wing aspect ratio), however, do not confirm the prediction. A more advanced theory (4,c) based on lifting surface principles (5) correctly yields "positive" moments due to sideslip, i.e. forces tending to lift up the advancing wing panel.

FLUID DYNAMIC LIFT

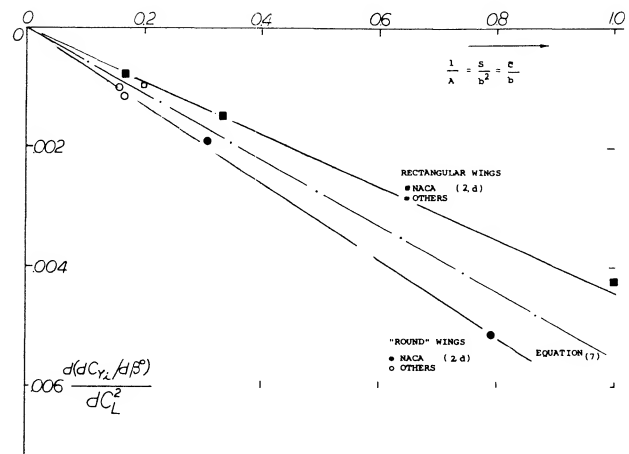


Figure 5. Lateral force derivative of *straight* wings as a function of their chord/span ratio.

Aspect Ratio. The derivative dC_L/dC_L is found to be proportional to the angle of yaw, up to plus or minus some 30° , which should cover the full range of sideslipping angles encountered in flight maneuvers. It is, therefore, justifiable to evaluate and to use the derivative

$$d(\partial C_L / \partial \beta^\circ) / dC_L = dC_{L\beta^\circ} / dC_L \quad (6)$$

Experimental results plotted in figure 6 as a function of the wing's chord/span ratio $\bar{c}/b = 1/A = S/b^2$ agree qualitatively with the complex theoretical functions (not shown in the graph). At very large aspect ratios, below $1/A = 0.1$, figure 6, there is evidence of the theoretical result mentioned above whereby the rolling moment to be expected is "negative". Rectangular wings (as used in wind-tunnel work) have considerably higher positive rolling moments than wings with round tips. Tapered wings (the type most widely used in modern airplanes) have characteristics similar to those of round type wings (where round, this time, is meant to indicate also elliptical or somehow rounded planforms). In conclusion, the rolling moment due to sideslip of straight wings is found to be a function of the aspect ratio and shape of the wing tips or lateral edges.

- (4) Analysis of lateral wing characteristics:
 - (a) Weinig, Sideslipping and Swept Wings, Lufo 1937 p 45.
 - (b) Hoerner, Characteristics of Wings in Yaw, Lufo 1939 p 178.
 - (c) Weissinger, Wing in Sideslip, Ybk D Lufo 1940 p I-138. and I-145, also 1943 Part IA; see NACA T Memo 1120.
 - (d) Seiferth, Review, Ringbuch Lu-Technik IA 14 (1940).
- (5) A finite-aspect-ratio wing at an angle of yaw must be considered as a lifting surface (rather than a "line"). In such a surface the lateral edges tend to become leading and trailing edges, respectively, when increasing the angle of yaw.

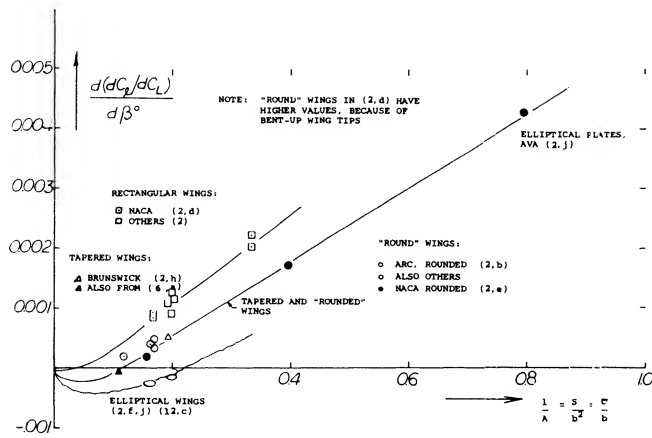


Figure 6. Derivative of the rolling moment due to sideslip of plan and straight wings.

Yawing Moment. The advancing wing panel, producing increased lift, also exhibits increased drag due to lift, which is essentially induced drag; and the drag differential between the two wing panels thus produces a “positive” yawing moment, i.e. a moment tending to return the wing to its original position. For angles of yaw between plus and minus 25° , the wing moment is found to be proportional to that angle. Since induced drag is proportional to the square of the lift coefficient, the yawing moment due to lift is also found to be proportional to that square. We have, therefore, plotted in figure 7 the quantity

$$d(dC_n/d\beta^\circ)/dC_L^2 = dC_{n\beta}/dC_L^2 \quad (7)$$

Interpolation of the experimental points does not show any negative moments corresponding to those in figure 6 below $1/A = 0.1$. It is suggested that viscous effects, not taken into account by theory, are responsible for negative values shown.

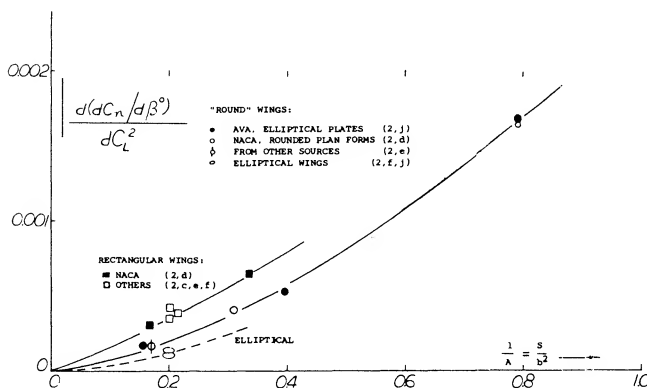


Figure 7. Yawing-moment derivative of plan and straight wings as a function of their chord/span ratio.

2. LATERAL CHARACTERISTICS DUE TO DIHEDRAL

Dihedral of “V” shape has a considerable influence upon forces and moments of sideslipping wings.

Lift Differentials. When placing a dihedral or “V” shaped wing at an angle of yaw, the angle of attack (against the flow) of the forward panel is geometrically increased; and that of the trailing panel is reduced figure 4. The differential of the angle of attack is

$$\Delta\alpha = \pm\beta\Gamma \quad (8)$$

where Γ = angle of dihedral. The differential of the lift coefficient in each panel, corresponding to that of the angle of attack, is

$$\Delta C_L = \pm\beta\Gamma dC_L/d\alpha \quad (9)$$

When considering a wing with an antisymmetrical variation of the angle of attack, the lift-curve slope to be used in equation (9) corresponds to *half* the aspect ratio of the wing. Following procedures as given in Chapter III, the “lift angle” to be used in equation (9) is then:

$$d\alpha^\circ/dC_L \approx 10 + (19/0.5 A) \quad (10)$$

Lateral Force. The lateral force due to dihedral is simply the sum of the spanwise components of the lift differentials in the two wing panels:

$$C_{Yd} = +\beta\Gamma^2 dC_L/d\alpha \quad (11)$$

For example, for $A = 5$ the “lift angle” is $d\alpha/dC_L = 17$. Measuring all angles in degrees, the lateral force derivative for dihedral wings with $A = 5$ is thus expected to be

$$dC_{Yd}/d\beta^\circ = +(\pi/180)^2 \Gamma^2 / 17 = +1.8 \Gamma^2 / 10^5 \quad (12)$$

Experimental results for model wings with $A = 5$ and 6, as plotted in figure 8, confirm the equation.

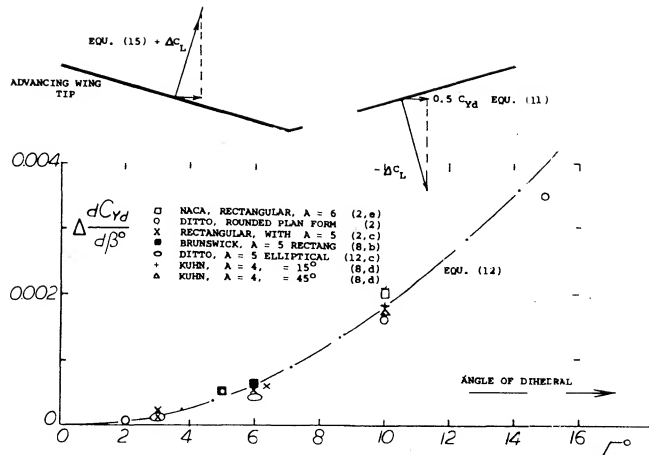


Figure 8. Lateral force derivative of various wings having aspect ratios in the order of 5 and 6, as a function of the *dihedral* angle.

Small Aspect Ratios. As shown in Chapter XVII the lift of small aspect ratio wings approximately corresponds to $dC_L/d\alpha = 0.5\pi A$. Using again the half-aspect ratio principle, the lift-curve slope to be used for the differentials in the wing panels is accordingly:

$$dC_{Lat}/d\beta = 0.25\pi A \quad (13)$$

where β = angle of yaw, in radians. Using this function, and expressing all angles in degrees, equation 11 transforms into

$$d(dC_Y/d\beta^2)/d(\beta^2) = (\pi/180)^2 0.25\pi A = 0.41 A/10^6 \quad (14)$$

This equation is the straight line as in figure 9. We have also solved and plotted in that graph equation 11 using for the "lift-curve" slope the inverted equation 10, which applies to higher aspect ratios. Experimental results should be bounded by the two theoretical functions. While experimental confirmation is limited to aspect ratios between 5 and 6, the lateral force coefficient due to dihedral must be expected to increase with the aspect ratio.

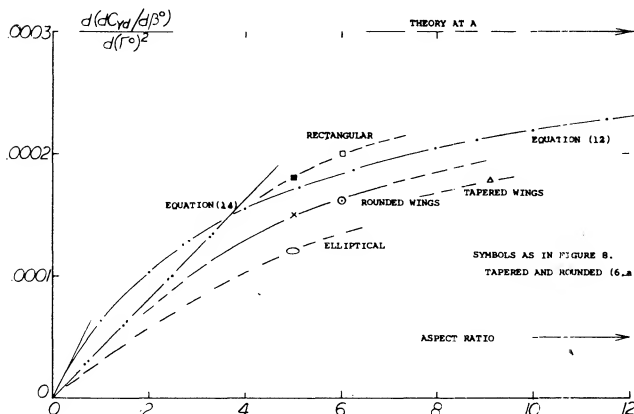


Figure 9. Lateral-force derivative of *dihedral* wings as a function of their A' ratio.

Rolling Moment. Another consequence of the lift differentials as in equation 9 is a rolling moment of the character as plotted in figure 10 for $A = 5$ and 6. When assuming that the moment arm ($b/2$) of each wing panel be 0.4, the rolling moment due to dihedral tentatively corresponds to

$$C_{ld} = 0.5 \cdot 0.4\beta \Gamma dC_L/d\alpha \quad (15)$$

Expressing the lift-curve slope corresponding to equation (10) and measuring all the angles in degrees, we obtain the derivative for the range of higher aspect ratios as plotted in figure 11. For small aspect ratios, we obtain through combination of equations (13) and (14):

$$d(dC_{ld}/d\beta^2)/d\beta^2 = 0.5 (\pi/180)^2 0.1\pi A \approx 5 A/10^5 \quad (16)$$

representing in figure 11 the straight line through the origin. As in the lateral force (figure 10) experimental evidence is limited; results are expected to be bounded by the theoretical lines as indicated.

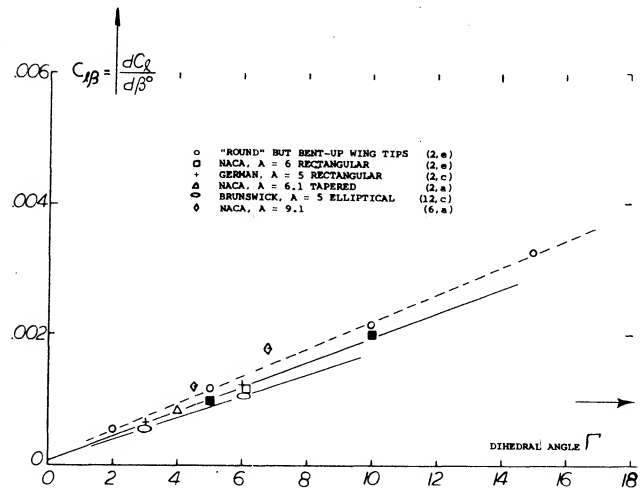


Figure 10. Rolling-moment derivative of various wings having aspect ratios in the order of 5 and 6, as a function of the *dihedral* angle.

Yawing Moment. When analyzing the moment of a wing with dihedral one could first expect, on the basis of drag, that the advancing wing panel (having higher lift than the trailing panel) must have the higher induced drag, and that a "positive" yawing moment (tending to return the airframe to neutral position) would thus result. Actually, "negative" moment derivatives are found when testing such wings. The lift differentials ΔC_L (as in equation 9) are considerably larger than the induced-drag differentials, and yawing moments corresponding to them are, therefore, predominant. To understand this type of moment,

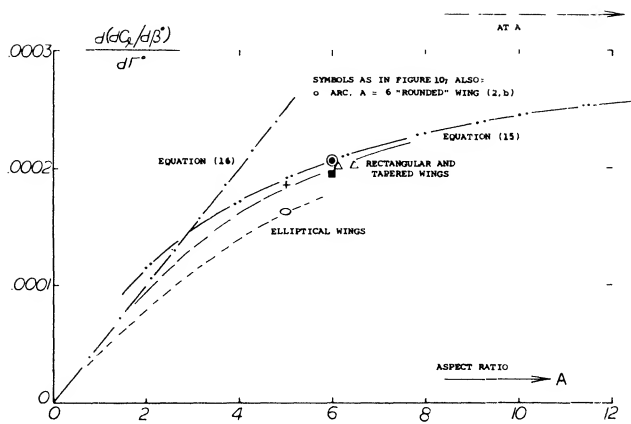


Figure 11. Rolling-moment derivative of *dihedral* wings as a function of their aspect ratio.

consider the wing as in figure 12. In the flow-fixed system of reference, it is necessary to apply lifting-surface (rather than lifting-line) principles. In other words, suction must be expected at and around the advancing lateral edge (or "tip") of the wing, and the induced drag must be expected to be in the direction of the oncoming air flow (rather than in the direction of the chord). Accordingly, the lift in the advancing wing panel is normal to both the induced drag and to the axis or the spar (beam) of the panel. In this manner, the lift of the leading panel is then found to be inclined *forward* in reference to the panel axis (as shown in the sketch), and that of the trailing panel to be turned back, accordingly. The result is a "negative" moment due to lift, i.e. an "unstable" moment, tending to increase the angle of yaw.

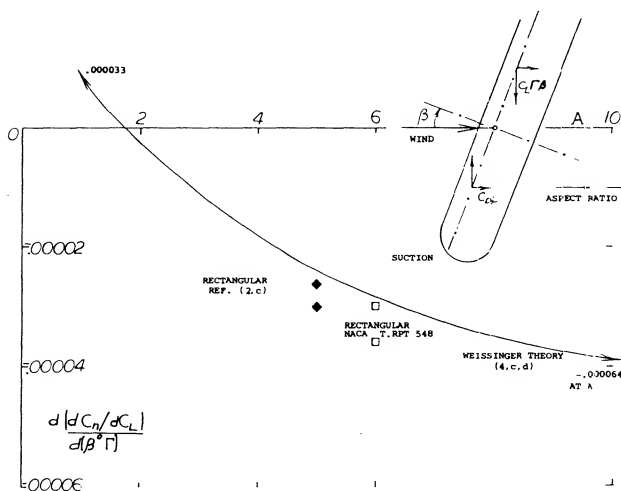


Figure 12. Yawing-moment derivative due to *dihedral* as a function of wing aspect ratio.

(6) Characteristics due to dihedral:

- Purser, Simplified "V" Theory, NACA TR 823 (1945).
- Moller, Dihedral & Sweep, Lufo 1941 p 243.
- Richter, Inboard Dihedral, Lufo 1939 p 112.

Numerical Results. The yawing moment of wings with dihedral is plotted in figure 12. Analysis as in (4,c,d) in a simplified form is as follows: The yawing moment due to dihedral of an elliptical wing corresponds to

$$C_{nd} = (2/3\pi) C_L \beta \Gamma ((A - 1.9)/(A + 3.8)) \quad (17)$$

where the aspect ratio factor is the same as in (4,c,d). For angles in degrees, the derivative is

$$\frac{d(C_N/d\beta^\circ)}{d(\beta^\circ \Gamma^\circ)} = - (6.45/10^4) ((A - 1.9)/(A + 3.8)) \quad (18)$$

This function, plotted in figure 12, shows primarily negative yawing moments, increasing in magnitude with the aspect ratio. At aspect ratios below 2, the moment turns positive. Obviously, the induced drag (as in the sketch shown with the graph) grows comparatively large there, so that the lift in the advancing panel is no longer turned forward and that in the trailing panel no longer tilted back in reference to the spanwise direction, as explained in the preceding paragraph.

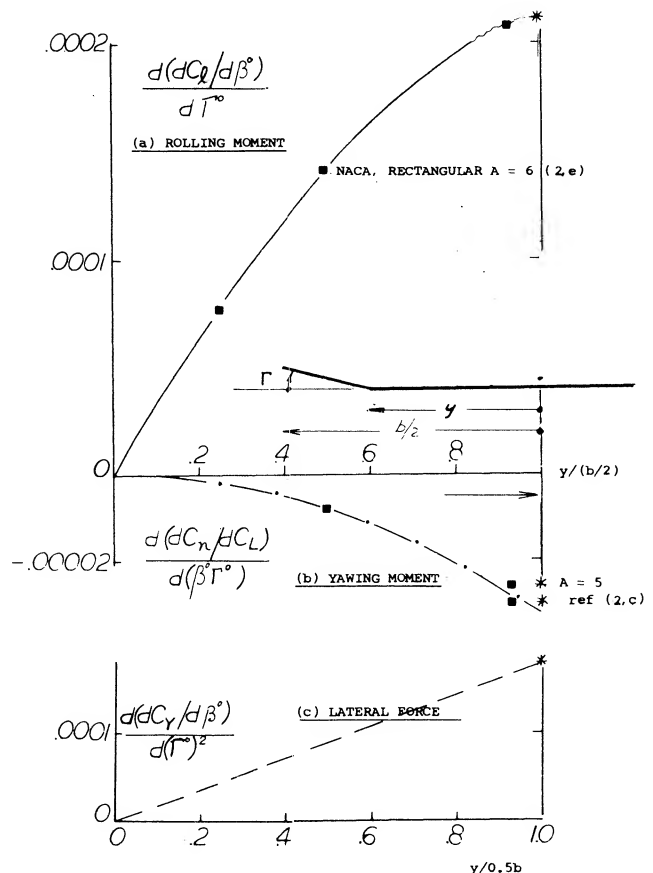


Figure 13. Lateral characteristics of a wing due to part-span *dihedral*.

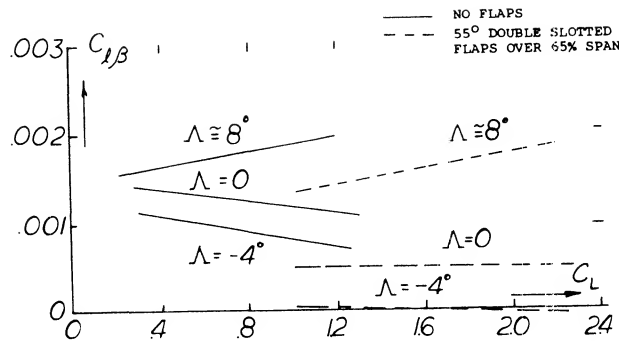


Figure 14. Effect of flaps on the effective *dihedral* derivative $C_{L\beta}$ as a function of operating C_L .

Part-Span Dihedral. In wing shapes where only part of the span is dihedralized, i.e. where only the wing tips are bent up, moments and forces are, of course, less than those derived above for full-span "V" shape. Figure 13 represents characteristics of a particular wing, having $A = 6$, as a function of the dihedralized outboard span fraction. It is also possible, however, to design a wing in such a manner that only certain inboard fractions of the two panels are dihedralized; see (6,c). Because of the comparatively short moment arm of the dihedralized portions, the resulting moments are small in this type of wing.

Influence of Wing Flaps. Conventional landing flaps are of the part-span and inboard type. They may also be used (at a moderate angle of deflection) during take-off and while climbing. Their influence upon the characteristics of wings is basically similar to that of tapered plan form and/or wing twist. The variation of $C_{L\beta}$ for flaps deflected (7) indicates a loss of effective dihedral for straight tapered wings, figure 14. The effective dihedral loss appears in this case to be independent of length of the span flaps deflected.

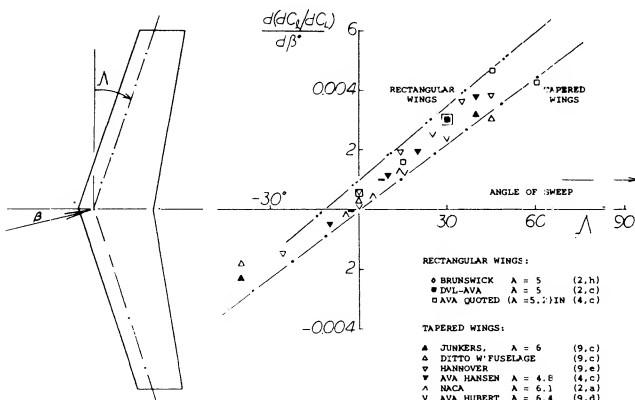


Figure 15. Rolling-moment derivative due to yaw of wings having aspect ratios in the order of 5 and 6, as a function of their angle of sweep.

3. LATERAL CHARACTERISTICS OF SWEEP WING

Sweep, primarily meant to indicate swept-back wing shape, causes rolling moments and corresponding yawing moments of an appreciable magnitude.

Lift Differential. To understand the character of the rolling moment arising in a swept wing when sideslipping, we will first consider the two panels as though they were separated from each other. Corresponding to the cross-flow principle as discussed in Chapter XV the lift in each panel is then approximately proportional to $\cos^2(\Lambda + \beta)$ where Λ = angle of sweep as in figure 14. It is explained, however, in (4,c) that in a swept wing (where the two panels are connected with each other) the reduction of lift is only proportional to $\cos(\Lambda + \beta)$. The local lift coefficient in each panel is thus:

$$C_{Ls} = C_L \cos(\Lambda + \beta) = C_L (\cos \beta \cos \Lambda \pm \sin \beta \sin \Lambda) \quad (19)$$

where "s" indicates "sweep" and where C_L = original combined lift coefficient of the wing. The differential between the two panels (based on total wing area) is then

$$\Delta C_L = C_L \sin \beta \sin \Lambda \quad (20)$$

In a wing of finite aspect ratio, the distribution of the induced angle of attack varies in such a manner that the lift in the advancing panel is somewhat increased above that as in equation (19) while the lift in the trailing panel is somewhat reduced. As a consequence, (4,c) indicates

$$\Delta C_L = C_L \sin \beta (\tan \Lambda + 2 \sin \Lambda / (A + 4)) \quad (21)$$

Rolling Moment. The effect of sweep on the rolling moment follows from the last equation by assuming a moment arm for each panel equal to $0.45 b/2$; thus $C_{Ls} = 0.225 \Delta C_L$. Measuring β in degrees the derivative is then:

$$\begin{aligned} d(C_{Ls}/d\beta)/dC_L &= 0.225 (\tan \Lambda + 2 \sin \Lambda / (A + 4)) \pi / 180 \\ &\approx .00007^\circ (1 + 2/(A + 4)) \end{aligned} \quad (22)$$

We have plotted this equation in figure 15 for $A = 5$. While theory leads to an infinite value at $\Lambda = 90^\circ$, because of $\tan \Lambda$, tests at higher angles of sweep do not seem to confirm this. Agreement with other experimental points can be improved by shifting the function up by an amount up to 0.001, thus accounting for the moment at zero angle of sweep as in figure 6. Round tip and tapered

- (7) Influence of wing flaps on lateral characteristics:
(a) Teplitz, Configuration w'Flaps, NACA TR 800 (1944).

wings may be expected to have lesser moments due to sweep than rectangular (wind-tunnel model) wings. We have labeled the two theoretical lines in figure 15 as “rectangular” and “round” accordingly. As a function of the aspect ratio, figure 16 presents equation (22) for a moment arm equal to $0.45 b/2$. Experimental confirmation is limited to aspect ratios between 5 and 6. The interpretation and extrapolation on the basis of the principles as in (4,c) are considered to be correct, however.

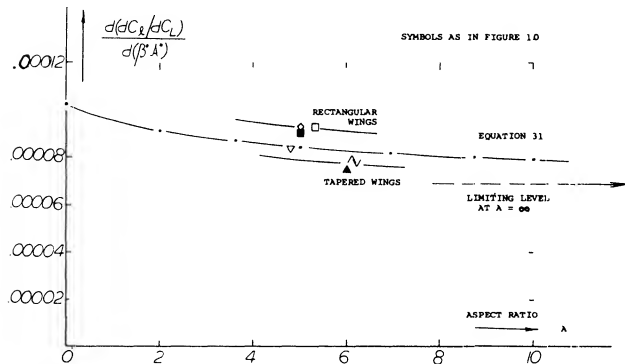


Figure 16. Rolling-moment derivative of swept wings as a function of their aspect ratio.

As shown in (8,a) the effective dihedral of swept back wings increases rapidly with C_L relative to straight wings, figure 17. At the higher lift coefficients there is a sharp reduction of $-C_{l\beta}$ with an associated drop in the effectiveness of the dihedral angle Γ . The sharp break in the variation of $C_{l\beta}$ with lift is caused by the stalling of the tips of the advancing wing, Chapter XVI, which reduces the corrective moment. When operating at low angles the $C_{l\beta}$ of swept forward wings have little variation with C_L . However, as noted in (10) there is a sharp increase of effective dihedral at lift coefficients above .5.

Yawing Moment. For swept wings the differential variation of drag in the two wing panels determines the yawing moment. Considering viscous section drag, the moment arm of this component in each wing panel varies as $\cos(\Lambda + \beta)$. Using the drag coefficient C_{Ds} and a moment arm equal to $0.45 b/2$, the component of yawing moment caused by viscosity $C_{\eta_{sv}}$ is then

$$C_{\eta_{sv}} = 0.45 C_{Ds} \sin \beta \sin \Lambda \quad (23)$$

For $C_{Ds} = 0.01$ (as roughly in an airplane wing) we obtain the derivative of the yawing moment due to sweep C_{η_s}

$$dC_{\eta_s}/d(\beta^\circ \Lambda^\circ) = 1.4/10^6 \quad (24)$$

which is comparatively small but “positive”.

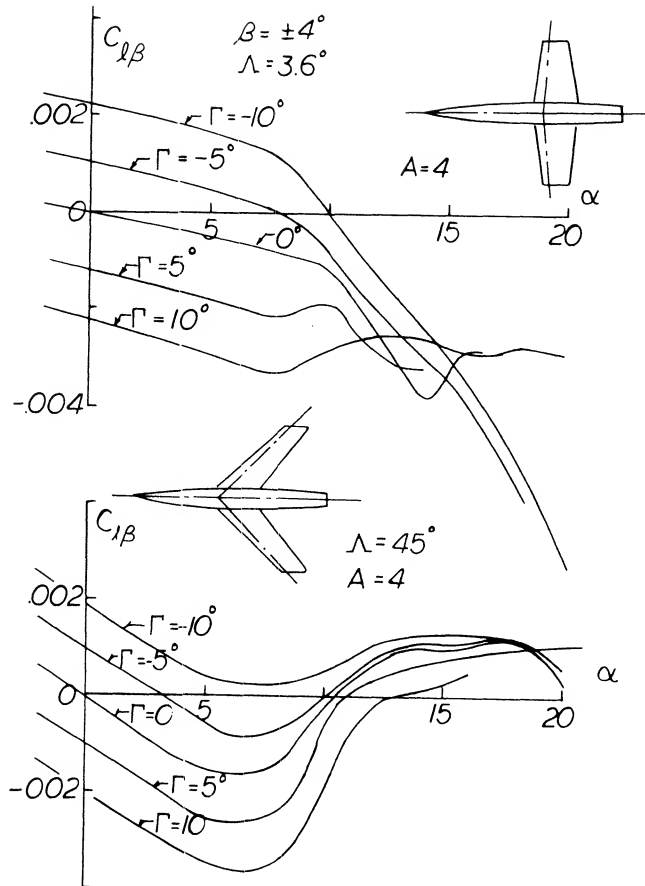


Figure 17. Variation of effective dihedral $C_{l\beta}$ as a function of angle of attack for sweep angles $\Lambda = 3.6^\circ$ and 45° , $A = 4$.

Component Due to Lift. As a result of the production of lift, and drag due to lift in the wing panels, a “positive” yawing moment is to be expected. Evaluation of analysis in (4,c) yields for an elliptical lift distribution:

$$dC_{\eta_{sl}}/d\beta \approx (C_L/5)(dC_L/d\beta) \approx C_L^2 \tan \Lambda / 20 \quad (25)$$

This component is stable, as well as the viscous moment above and varies in proportion to the square of the lift coefficient. Measuring the angles in degrees:

$$dC_{\eta_{sl}}/d\beta^\circ \approx 1.5 C_L^2 \Lambda^\circ 10^{-5} \quad (26)$$

- (8) Dihedral effects of swept wings:
 - (a) Kuhn, Straight and 45° Swept Wings, NACA RML53F09.
- (9) Lateral characteristics of swept wings:
 - (a) Toll, Derivatives of Swept Wing, NACA TN 1581 (1948).
 - (b) Goodman, A'ratio and Sweep Rolling, NACA TR 968 (1950).
 - (c) v.Doepp, Ju-287 swept back and forward wing models, Junkers Wind Tunnel Results S-1943, 1 & 2, 46, 69, 72 and 1944/2.
 - (d) Hubert, Swept Wings, Yearbk D Lufo 1937 p I-129.
 - (e) Luetgebrune, Swept Wings, ZWB Rpt FB-1458 (1941).
 - (f) Letko, Stability of Swept Wings, NACA TN 1046 (1946).
- (10) Campbell, Factors Affecting Lateral Stability, NACA Univ Conference 1948.

In a wing of conventional shape, the relative magnitude of the "induced" component and that as derived in this paragraph is such that at small lift coefficients the viscous moment predominates. At lift coefficients in the vicinity of $C_L = 1$, the induced component is larger than the viscous-type moment for angles of sweep exceeding some 10° , and is very much larger at angles in the order of $\Lambda = 30^\circ$. Since separation of the two components is not readily possible, we have subtracted from tested yawing-moment values the value at or near $C_L = 0$, or sometimes an estimated value (see equation 24); and we have then plotted the remaining values in figure 18. The results are higher than indicated by equation (26). As shown in (4,c) there is a small influence of the aspect ratio in the order of 5% (good for A between 4 and 20). Using also the tangent instead of the angle of sweep sufficient agreement can be obtained. As usual, the rectangular wings have larger moments than tapered ones.

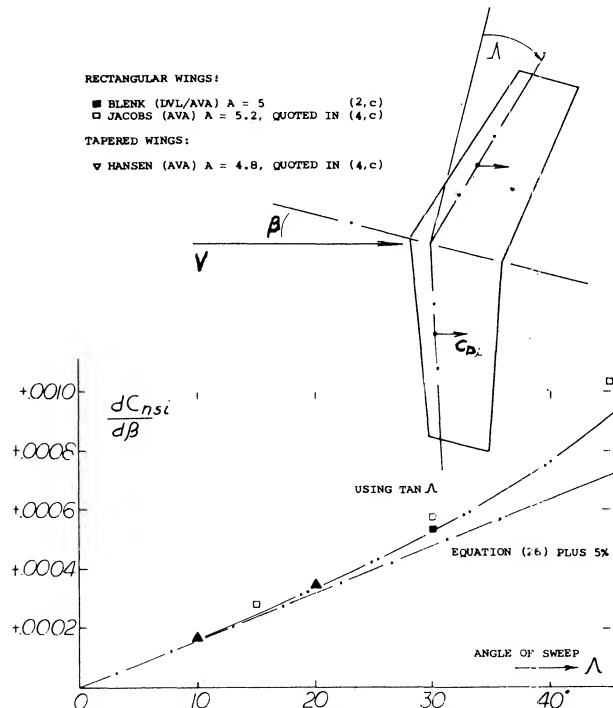


Figure 18. Derivative of the yawing moment due to lift as a function of the angle of sweep.

4. INFLUENCE OF FUSELAGE ON ROLLING MOMENT

Although conventional fuselage shapes do not produce a significant rolling moment, their interference effects upon the wing moments are large and cannot be disregarded. Such effects are particularly evident in regard to the rolling moment when sideslipping.

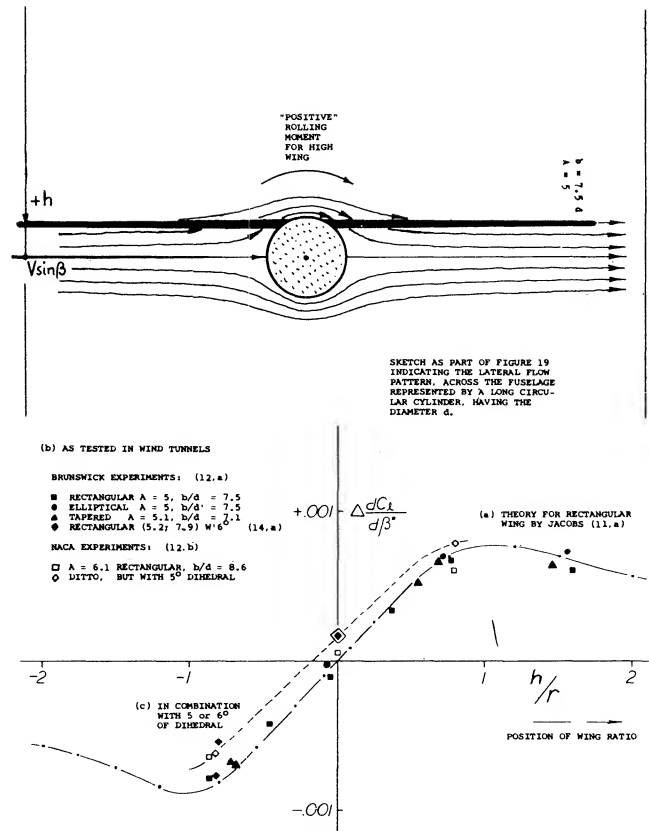


Figure 19. Derivative of the rolling moment induced by the fuselage, as a function of vertical wing position.

Flow Pattern. Figure 19 presents the basic flow pattern across a fuselage body operating at an angle of yaw. When adding a straight wing in a position which is high in relation to the fuselage, the aerodynamic or effective angle of attack is obviously increased on the windward side and it is reduced on the leeward side. This results in a "positive" rolling moment tending to raise the leading wing panel. This moment is of the same character as that caused by dihedral. Of course, in the case of a low-wing combination, the direction of the resulting rolling moment is opposite to that of the high wing as shown in the illustration. Therefore, presence of the fuselage is the equivalent of a certain amount of

- positive wing dihedral for the high-wing
- negative wing dihedral for the low-wing configuration.

(11) Analysis of rolling moments due to fuselage:

- Jacobs, Analysis, Yearbk D Lufo 1941 p I-165.
- Braun, Rotational Body, Ybk D Lufo 1942 p I-246.
- Maruhn, Rectangular Shapes, Ybk D Lufo 1942 p I-263.

Analysis. Evaluation of the two-dimensional cross-flow field as in (11,a) of a fuselage with an equivalent infinitely long cylinder then yields a flow-angle distribution along the lateral axis (beam) and a corresponding lift distribution. The resultant rolling moment is essentially independent of the wing's lift coefficient and is a function of the geometry of the wing-fuselage combination. As an example, numerical results for a specific configuration taken from (12,a) are given in figure 19. Experimental results confirm the theoretical prediction with reasonable accuracy. In the two extreme positions, at $h/r = \text{plus and minus } 1.0$, the rolling moment derivative produced by the fuselage is the equivalent of plus/minus 3.5° dihedral, i.e. for the configurations as tested having b/d in the order of 8.

Fuselage/Wing Size. The influence of the fuselage described above was analytically studied (11,a) for a number of configurations with the following results:

- 1) The effect of a body with $l/d = 7$ is up to 10% smaller than that of a long cylinder.
- 2) The influence of wing shape (rectangular or elliptical) is small.
- 3) The rolling moment is for practical purposes independent of the wing's aspect ratio, meaning that the increment of the coefficient $\Delta C_l \sim 1/\sqrt{A}$ for constant wing area.
- 4) The increment of the rolling-moment coefficient derivative is proportional to $(d/b)^2$ and it reduces in proportion to $1/b^2$ for a given fuselage. The moment is proportional to $(d^2 \bar{c})$ where \bar{c} = average wing chord; therefore, $"L"/(q d^2 \bar{c}) = \text{constant}$ for a given body shape.

Shape of Fuselage. Various cross-sectional shapes (circular, elliptical, square, rectangular) have analytically been investigated (11). For practical purposes, it can be deduced from the results:

- a) A square fuselage shape (with rounded edges) has approximately the same effect as a circular shape (as in figure 19) provided that the fuselage volume (rather than the d/b ratio) is kept constant.
- b) In the case of fuselages with elliptical or rectangular cross-section shapes the rolling moment induced by them increases approximately in proportion to the height/width ratio, again provided that volume or cross-sectional area is kept constant.

(12) Lateral characteristics of wing-fuselage configurations:

- (a) Moller, 6-Component Results, Ybk D Lufo 1942 p I-336.
- (b) Bamber, Wing, Fuselage & Fin, NACA TN 730 (1940).
- (c) Schlichting, Review of Subject, Ybk D Lufo 1940 p I-113.

Dihedral. As noted above, the effect of the fuselage upon rolling moment is the equivalent of a certain wing dihedral. It is also stated that the derivative of the coefficient (indicating rolling moment in relation to wing lift) varies in proportion to (d/b) . Any small-span (small-aspect ratio) and high-wing airplane configuration is therefore liable to have too much rolling moment due to yaw. An example of such a configuration is the Lockheed F-104 high-speed fighter airplane. Rolling moments are reduced by giving the wing a few degrees of *negative* dihedral. All low-wing airplanes have, on the other hand, appreciable amounts of positive dihedral (between 5 and 10°), (a) to counter-act the "negative" effect of their fuselage and (b) to provide the magnitude of rolling moment desirable for optimum handling and for lateral stability.

Influence of Wing Flaps. Conventional landing flaps are of the part-span and inboard type. They may also be used (at a moderate angle of deflection) during take-off and while climbing. Their influence upon the characteristics of wings is basically similar to that of tapered plan form and/or wing twist.

5. THEORY – DYNAMIC LATERAL STABILITY

The theory for determining the dynamic stability characteristics of airplanes is relatively complex and lengthy, especially with all six equations of motion. The complete development of these equations and their analysis has been done by several authors (13,a,c,d) specializing on the subject of stability and control, and will not be repeated here. We will provide sufficient information for developing a basic understanding of the problem and show the important relationship of some of the stability derivatives. In the following section variations of the forces and moments leading to the stability dynamic derivatives will then be covered.

Basic Equations. In developing the equations of motion for an airplane certain simplifying assumptions are usually made. These are:

- a) Second order terms are neglected – the disturbances are small.
- b) The motion is steady about the symmetrical plane. The six equations of motion can be broken up into the longitudinal and lateral modes.
- c) The changes in lift and moments due to changes in motion are instantaneous.
- d) The controls are fixed.

The effects of free controls, stick free case, are covered in (13,a,c) and involve many more degrees of freedom including the hinge moment variations of the control surface. From (13,b) the equations of motion based on these assumptions are as follows — referred to the airplane stability axis:

Roll

$$2 \mu_b (K_x^2 D_b^2 \phi + K_{xz} D_b^2 \psi) = C_{\dot{\phi}} \phi + 1/2 C_{\dot{\phi}} D_b \phi + 1/2 C_{\dot{\phi}} D_b \psi \quad (27)$$

Yaw

$$2 \mu_b (K_z^2 D_b^2 \psi + K_{xz} D_b^2 \phi) = C_{\dot{\psi}} \psi + 1/2 C_{\dot{\psi}} D_b \psi + 1/2 C_{\dot{\psi}} D_b \phi \quad (28)$$

Sideslip

$$2 \mu_b (D_b \beta + D_b \psi) = C_{\dot{\beta}} \beta + 1/2 C_{\dot{\beta}} D_b \beta + C_L \phi + 1/2 C_{\dot{\beta}} D_b \psi + (C_L \tan \gamma) \psi \quad (29)$$

Where $\mu_b =$ airplane relative density factor = $(m/P S b)$ some authors use b' for the wing semi span instead of b .
 $K_x =$ nondimensional radius of gyration in roll about longitudinal axis.
 $K_z =$ nondimensional radius of gyration in yaw about the vertical stability axis.
 $D_b =$ differential operator (d/d_{sb})

On the right hand side of the above equation the aerodynamic characteristics of the airplane are given while the moment of inertia, product of inertia and acceleration are given on the left side.

Rolling Derivatives. In equations 27, 28 and 29 C_{np} , C_{lp} and C_{yp} the derivatives due to the rolling velocity are encountered. These rolling derivatives are taken with respect to the effective helix angle of the wing and thus depend on both the forward and rolling velocity. The yawing moment due to roll C_{np} is mainly determined by

the wing and tail geometry, the lift and the drag. The contribution of the wing can be estimated from the equation (30) and figure 20 taken from (13,d).

$$C_{np} = \frac{(\Delta C_{np})_1}{C_L} C_L + \frac{(\Delta C_{np})_2}{(\Delta C_{Do}) \alpha} C_{Do} \alpha \quad (30)$$

The vertical tail configuration to C_{np} is found from the equation

$$C_{npt} = -(2l/b)(z/b) C_{y\beta t} \quad (31)$$

where $C_{y\beta t}$ is determined considering the sidewash and effective tail length data of Chapter XIII.

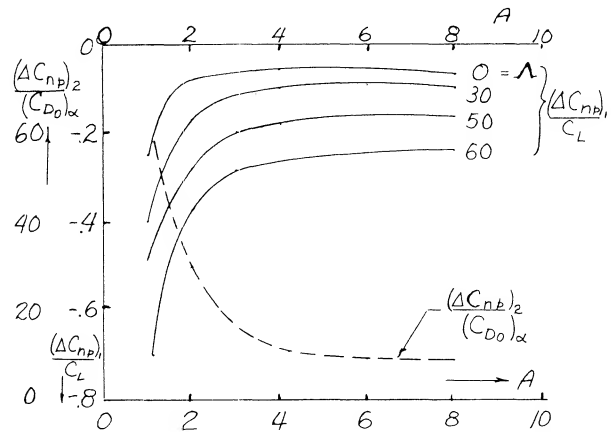


Figure 20. Variation with aspect ratio and sweep angle of components required to find C_{np} with equation 30, from (13,d).

Damping in Roll. The rolling moment due to rolling, C_{lp} , is mainly a function of the wing, sweep angle, taper ratio, and operating C_L . Based on the method and data given in (13,d) which appears to be accurate and well accepted the C_{lp} can be calculated from equation 32 using the data of figure 21 to find C_{lp} at $C_L = 0$. Equation 32 is then used to find the value of C_{lp} at the operating lift coefficient C_L

$$C_{lp} = (C_{lp})_{C_L=0} \frac{(C_{L\alpha}) C_L}{(C_{L\alpha})} - \frac{C_L^2}{8 A \cos \Lambda} \left(1 + 2 \sin \Lambda \frac{A + 2 \cos \Lambda}{A + 4 \cos \Lambda} \right) - .125 (C_D - C_L^2 \pi A) \quad (32)$$

The slope of the lift curve for the wing $C_{L\alpha}$ at $C_L = 0$ and the operating C_L is found using the data given in Chapters II and III. The effect of high lift flaps on the damping in roll of the wing are accounted for by using the proper slope of the lift curve corresponding for these devices as determined from the data of Chapters V and VI. If the wing has tip tanks, corrections as presented in (13,d) must be applied to the calculated value of C_{lp} .

(13) Lateral Stability Theory:

- Babister, A.W., Aircraft Stability and Control, Pergamon Press 1961.
- Stemfield, L., Dynamic Stability, NACA University Conf 1948.
- Perkins & Hage, Airplane Performance Stability and Control, John Wiley & Sons, 1949.
- Campbell & McKinney, Calculating Methods Dynamic Lateral Stability, NACA TR 1098.

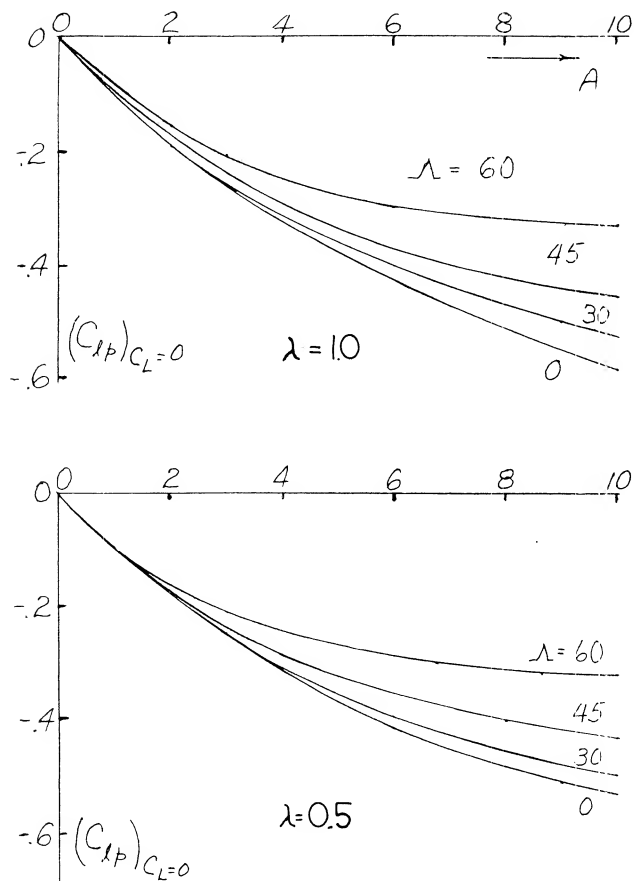


Figure 21. Wing rolling moment derivatives for $C_L = 0$, $a_0 = 2\pi$ equation 32 (13,d).

The contribution of the horizontal and vertical tail to C_{lp} can be estimated in a similar manner to the wing, however, the value is usually small and is neglected.

Lateral Force Due to Rolling. For a wing operating at conditions where the drag due to separation is low the derivative C_{yp} , lateral force due to rolling, can be determined from equation 33.

$$C_{yp} = C_L [(A + \cos \Lambda)/(A + 4 \cos \Lambda)] \tan \Lambda + 1/A \quad (33)$$

The value of C_{yp} at high lift coefficients from test data is lower than would be calculated from equation (33). At these conditions test data should be used if possible to find the lateral force derivative due to rolling. The lateral force derivative due to the vertical tail can also be estimated using equation (34). The side force derivative C_y for the tail used in equation 34 is obtained from the data of Chapter XIII.

$$C_{yp \text{ tail}} = 2 (Z/b) C_{y \text{ tail}} \quad (34)$$

The procedures for estimating the rolling derivatives given above apply only in the subsonic speed range.

Yawing Derivatives. The derivatives of the yaw and rolling moments and the side force with the yawing motion, C_{nr} , C_{lr} and C_{yr} also appear in the equations of motion (27, 28 and 29). The damping in yaw derivative, C_{nr} is not greatly affected by the fuselage and wing as the velocity change due to yaw is relatively low. The vertical tail has a larger effect as it presents its flat surface to the motion. At moderate angles of attack the value of C_{nr} due to the vertical tail may be found from the equation

$$C_{nr \text{ tail}} = 2(\ell/b)^2 C_{y\beta \text{ tail}} \quad (35)$$

The side force derivative $C_{y\beta}$ is obtained from the data of Chapter XIII.

The rolling moment due to yaw, C_{lr} , is mainly effected by the wing and vertical tail. This occurs due to the angular velocity of the wings which cause an increase in lift on the advancing wing and a corresponding lift decrease on the retreating wing. These changes in lift result in a rolling moment which can be estimated for straight wings from equation (36) developed from the data of (13,d).

$$C_{lrw} = C_L (.04A + .24) \quad (36)$$

The effect of the vertical tail is estimated from the equation

$$C_{lrx} = -2 (\ell/b) C_{l\beta \text{ tail}} \quad (37)$$

In the case of the side force derivative due to yaw the theory appears to be inadequate so that experimental data should be used. The effect of the vertical tail however can be found from equation

$$C_{yrx} = -2 \ell/b C_{y\beta \text{ tail}} \quad (38)$$

Dynamic Stability. The linear differential equations (27, 28 and 29) with constant coefficients are solved in the usual manner for these types, assuming that the following substitutions can be made:

$$\delta_0 e^{n\tau} = \delta, \quad \psi e^{n\tau} = \psi, \quad \beta_0 e^{n\tau} = \beta$$

With these substitutions a characteristic equation for is obtained.

$$A \lambda^4 + B \lambda^3 + C \lambda^2 + D \lambda + E = 0 \quad (39)$$

Where A, B, C, D and E are functions of the aerodynamic and mass properties of the airplane which in turn depend on the steady state flight conditions. It is shown in (13,a) there are four different types of motion depending on the roots of the characteristic equation (39).

- 1) When λ is real and positive the motion increases steadily with time and the aircraft is unstable.
- 2) If λ is real and negative the airplane is dynamically stable.
- 3) With complex root containing a negative real part, the motion is a damped oscillation tending toward zero.
- 4) When λ is complex with a real part positive an increasing oscillation motion is obtained tending toward infinity, unstable.

Also when λ is zero the motion persists undamped and if it is complex with a zero real part, simple harmonic motion is obtained.

Based on the analysis of equation (39) to determine the characteristics of its roots presented in (13,b,d) stability boundary conditions can be set up for any airplane and operating conditions.

These stability boundary are useful for evaluating the stability of an airplane configuration and are illustrated on figure 22 in terms of $C_{L\beta}$ vs $C_{n\beta}$. When the airplane passes through the upper boundary, one of the real roots becomes positive indicating the airplane is unstable. This is known as spiral instability.

Spiral Stability. An airplane disturbed from its flight path with say a control input or a gust can start to fly in a spiral path, figure 23. This is caused by a yaw and a bank and a sideslip motion, which increases in magnitude. This will be dynamically unstable if the airplane is operating from characteristics which fall in the unstable region, indicated on figure 22. In this case, the spiral flight path of the airplane becomes increasingly steep unless corrective controls are applied by the pilot. Usually, when the aircraft encounters spiral instability the time period is long, exceeding a minute so that pilot can easily apply the corrective controls. An aircraft will generally be stable in the spiral mode when it has high effective dihedral in comparison with its directional stability, figure 22. If the directional stability is high in comparison with dihedral, spiral instability can be expected.

Lateral Oscillation. As shown in (13,b) the motion becomes unstable when the airplane is below the lower curve on $C_{L\beta}$ vs $C_{n\beta}$ plot, figure 22. This stability boundary is for the case of zero damping and operating below the line means the airplane motion becomes divergent with time. As the effective directional stability is increased, the lateral oscillation time to damp to half amplitude is decreased and the period is also decreased as is illustrated on figure 22.

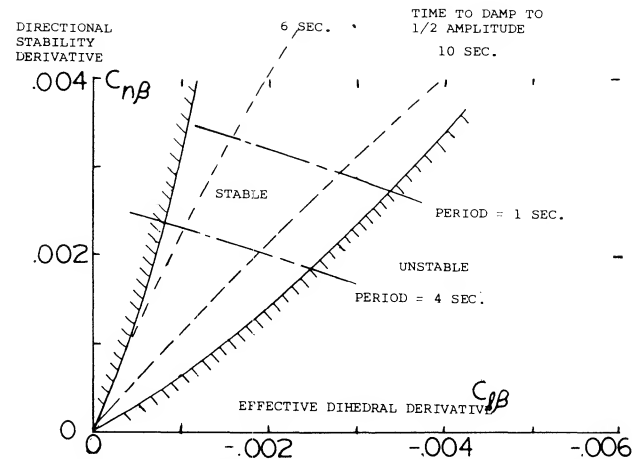


Figure 22. Lateral-stability boundaries for hypothetical high speed aircraft.

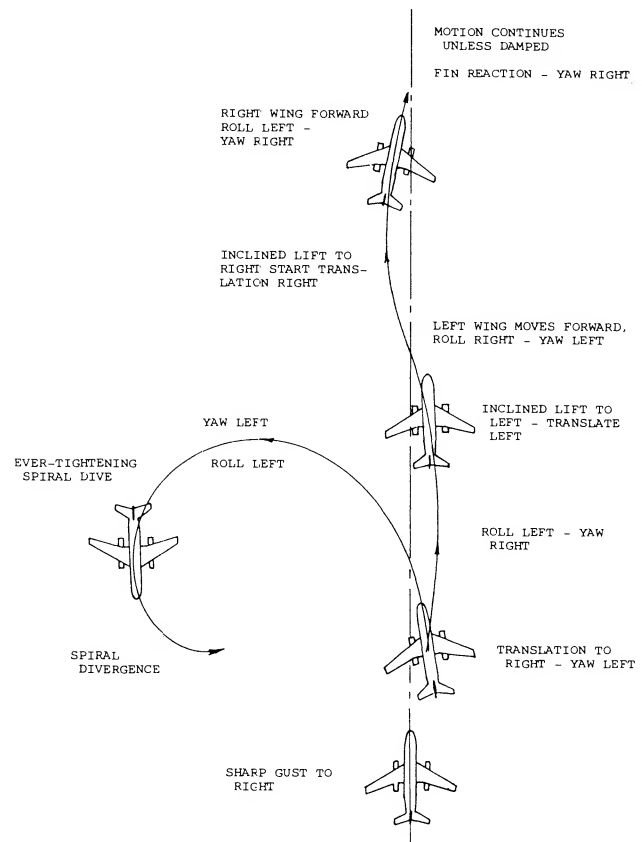


Figure 23. Aircraft motion during spiral instability and Dutch roll.

- (14) Flying Qualities - Specifications:
- (a) MIL-F-8785 (ASG) Amendment 4, 12 Nov 1957.
 - (b) USAF Spec. No. 1815-B, 1 June 1947.
 - (c) Navaer SR-119B, 1 June 1948.

Some of the earlier specifications (14,b,c) relating to the desired flying qualities of an airplane used a criteria for time to damp to half amplitude as a function of the period of oscillation. This criteria, illustrated on figure 24, has been found to be unsuitable for elevating high performance aircraft as it does not adequately consider the pilots requirements. It has been found necessary to rely on pilots opinion to establish the proper damping ratio because of the complex inter-relationship between the airplane dynamics and the control function. Also, when operating with positive damping the lateral oscillation couples with a yaw oscillation and a sideslip, which gives a motion after a disturbance known as “Dutch” roll.

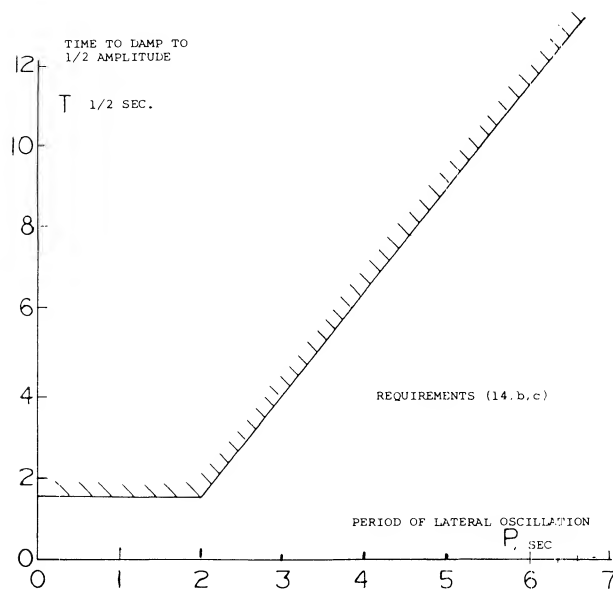


Figure 24. Desired damping characteristics as a function of period of lateral oscillation (14,b,c).

“Dutch” Roll. The “Dutch” roll characteristic of an airplane has become an important design consideration, especially with high performance and STOL aircraft. The “Dutch” roll is characterized by a rolling, sideslipping and yawing motion where the frequency about both axis is of the same order of magnitude but they are slightly out of phase. Thus, if we have a rolling motion as in figure 23, say to the right, with a corresponding sideslipping right yaw followed with a left roll and yaw where the yaw motion follows the roll, the airplane is in the “Dutch” roll mode. The frequency of the motion is much higher than for the spiral stability case. When the effective dihedral is very high in comparison to the directional stability the lateral-directional oscillation may actually become dynamically unstable and increase in amplitude.

Thus, in comparing the requirement for good “Dutch” roll characteristics with spiral stability a variance is noted between the need for high effective dihedral and directional stability.

Lateral Directional Stability – High Angles. Due to the stalling characteristics of swept wings, fuselage flow interaction on the tail, there have been many problems with lateral-directional stability when operating at high angles of attack. An example of the unfavorable characteristics of a jet fighter type airplane at high angles is given in (15,a). This airplane, figure 25, encountered directional divergence brought about by a simultaneous loss of directional stability and effective dihedral when operating at high angles of attack. This loss of directional and lateral stability is a part of one cycle of a highly unstable “Dutch” roll oscillation. The loss of the stability is caused by stalling of the leading wing panel at high angles and the adverse sidewash as illustrated in figure 25.

The “Dutch” roll instability time to damp to half amplitude, $t_{1/2}$, and the period of oscillation, P , can be predicted based on theoretical methods (15,a) from the equations

$$P = 2 / d \text{ (b/v)} \quad (40)$$

$$T = -.693/c \text{ (b/v)} \quad (41)$$

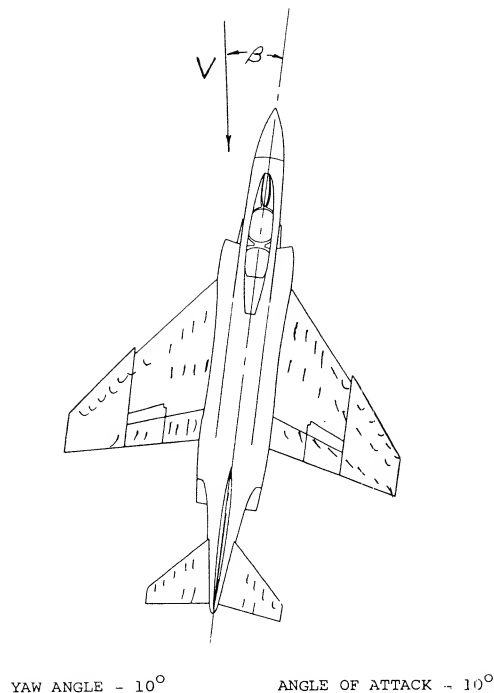
Where c and d are the real and the imaginary parts of the root of the characteristic equation. When the quantity $1/t_{1/2}$ becomes negative the airplane becomes dynamically unstable as illustrated in figure 24. To accurately find the roots of the characteristic equation and thus find the resultant instability it is necessary to find the many derivatives of the airplane as a function of angle of attack. At high angles of attack where separation of the flow is encountered it is necessary to use wind tunnel test data to find the derivatives and thus evaluate the stability. And here Re and M and roughness are subject to scale effects.

(15) Complete Airplanes:

- (a) Chambers and Anglin, Lateral-Directional Stability of a Fighter Airplane, NASA TN D-5361.
- (b) Heinle, Lateral Oscillation Several Aircraft, NACA RM A52J06.
- (c) Campbell & McKinney, Aircraft with Satisfactory Dutch Roll Oscillation, NACA TR 1199.
- (d) Ray, Large Sideslip Angles – T-Tail Transport, NASA TM X-1665.

(16) Lateral-Directional Handling Qualities:

- (a) Ashkenas & McRuer, Handling Qualities from Pilot-Vehicle Considerations, Aerospace Engineering, Feb. 1962.
- (b) Ashkenas, Lateral-Directional Handling Qualities, US AFFDL-TR-65-138, Part II, Nov. 1965.
- (c) Miller & Franklin, Lateral-Directional Flying Qualities for Power Approach, J. Aircraft Vol 5. No. 2 1968.
- (d) Vomaske, Sadoff and Drinkwater, Lateral-Directional Couplings – Fixed-Base Simulator, NASA TN D-1141.
- (e) Teper, Lateral-Directional Handling Qualities, J. Aircraft May, June 1966.



STALL TAKES PLACE ON LEADING WING PANEL AND CAUSES A LOSS OF EFFECTIVE DIHEDRAL. BEHIND STALL, FLOW IS REVERSED CAUSING A LOSS OF TAIL EFFECTIVENESS AT HIGH ANGLES OF ATTACK.

Figure 25. High performance fighter aircraft at a high angle of attack and yaw angle.

6. LATERAL DIRECTIONAL FLYING QUALITIES

The basic flying qualities of an airplane must be satisfactory throughout the operating range especially with high performance STOL and fighter type airplanes. Operating problems at the low speed landing condition and at high altitudes are caused by low damping conditions when operating at high lift coefficients. In cruising flight problems are encountered due to low damping which are a direct function of the geometric characteristics of the airplane. These problems have often led to the use of artificial mechanical stability augmentation systems (SAS). Although it is desirable to design the airplane to have the desired basic stability this is not always possible, so that SAS systems become a requirement. In fact, most modern high performance swept wing aircraft use SAS systems to obtain the desired level of stability and so reduce the work load of the pilot.

(17) Simulator Pilot Ratings:

- (a) Cooper, Understanding and Interpreting Pilot Opinion, Aero.Eng. Review, Vol 16, March 1957.
- (b) Phillips, Flying Qualities, NACA TR 927.
- (c) Taylor, Lateral-Directional Handling, NASA P TN D-5358.

Pilot Ratings. Because of the opposite requirements of the levels required of effective dihedral, $C_{l\beta}$, and directional stability, $C_{n\beta}$, it is necessary to use pilot ratings to establish the best configuration and the gains needed in the SAS system. Pilot ratings based on the Cooper ten point rating system (17,a) are very effective and consistent for evaluating a configuration. As noted on table 1, the Cooper rating system judges a configuration in terms of the ease of flying the airplane. A rating of 1 is the best and 10 the worst. Cooper ratings are obtained by the operation of flight simulators, variable stability test airplanes or the actual airplane being evaluated (17). The degree of correlation of the ratings between the various methods depends on the level of simulation used and are usually quite consistent in trend. To provide the data for evaluating new designs the pilot ratings must be related to the aerodynamic characteristics of the airplane as discussed in (16,b).

Aircraft Handling Qualities. Investigations have been made to determine the characteristics of the control system and the inherent stability to obtain high pilot ratings. These investigations (16) have been made to determine the specific parameters best suited, such as roll damping and roll acceleration for correlation with pilot ratings. Such correlations are incorporated into aircraft design specifications that the designer must meet. If the constraints of the configuration or its operation are limiting in achieving the desired stability it may be necessary to obtain the needed characteristics with a SAS system. SAS systems have been used on many high performance aircraft, including most STOL and VTOL types. Any information available which relates Cooper rating to period, $t_{1/2}$, or stability derivative combination would be very useful.

TABLE 1. PILOT-OPINION RATING SYSTEM

OPERATING CONDITIONS	ADJECTIVE RATING	NUMERICAL RATING	DESCRIPTION	PRIMARY MISSION ACCOMPLISHED	CAN BE LANDED
NORMAL OPERATION	SATISFACTORY	1	EXCELLENT, INCLUDES OPTIMUM	YES	YES
		2	GOOD, PLEASANT TO FLY	YES	YES
		3	SATISFACTORY, BUT WITH SOME MILDLY UNPLEASANT CHARACTERISTICS	YES	YES
		4	ACCEPTABLE, BUT WITH UNPLEASANT CHARACTERISTICS	YES	YES
EMERGENCY OPERATION	UNSATISFACTORY	5	UNACCEPTABLE FOR NORMAL OPERATION	DOUBTFUL	YES
		6	ACCEPTABLE FOR EMERGENCY CONDITION ONLY ¹	DOUBTFUL	YES
		7	UNACCEPTABLE EVEN FOR EMERGENCY CONDITION ¹	NO	DOUBTFUL
NO OPERATION	UNACCEPTABLE	8	UNACCEPTABLE - DANGEROUS	NO	NO
		9	UNACCEPTABLE - UNCONTROLLABLE	NO	NO
	CATASTROPHIC	10	MOTIONS POSSIBLY VIOLENT ENOUGH TO PREVENT PILOT ESCAPE	NO	NO

¹FAILURE OF A STABILITY AUGMENTER.

(18) Stability Augmentation System:

- (a) Montgomery, Differential Synthesis to Design, J of Aircraft, July, Aug 1969.

CHAPTER XV — LIFT OF SWEEPED WINGS

Possibly the most dramatic single development in the aerodynamic design of aircraft is the invention, the exploration and the practical application of the swept wing, first in high-speed-combat (1947) and then in commercial transport airplanes (1952). In this first chapter dealing with sweep, characteristics of wings are presented as follows: principles of swept wings, the lift of swept wings, influence of compressibility on lift. Some of the characteristics of wings already discussed in other chapters are found to be more complicated for swept wings.

1. PRINCIPLES OF SWEEP-WING FLOW

Swept wings have specifically been developed to increase the critical Mach number. Thus, higher cruise speeds are possible without encountering a high drag rise due to high operating Mach numbers. Further, since the critical Mach number decreases with increasing section thickness ratio and camber the effects of increasing these parameters, say for structural reasons, can be compensated for with an increase of the sweep angle.

GEOMETRY. The elements of swept wings are the wing panels. As shown in figure 1 the simplest way of “producing” a swept wing is by sweeping (yawing) the two panels (as in variable-sweep airplanes). The wing sections are thus kept constant constant normal to each panel axis. The span and aspect ratio of such wings are reduced in the process:

$$b = b_o \cos \Lambda; \quad A = A_o \cos \Lambda \quad (1)$$

where the subscript “o” refers to the unswept wing.

The tips of a “yawed” swept wing are usually modified to a “sheared” form, as shown in figure 1,b. In reports such as (1) or (26,c,h) a leading edge curving back near the wing tips has been developed in England, evidently accommodating the trailing vortices which cannot very well be suppressed; see figure 1,b. The angle of sweep Λ is

usually defined as that of the quarter-chord line. As we will see later, this is one of the fallacies of theoretical aerodynamics, however. In figure 1, we have used the $\frac{1}{2}$ chord line for the definition of sweep. It is interesting to note that when looking at a swept plan form, particularly as in part (c) of the illustration, one tends to overestimate its aspect ratio. The eye evidently sees the elongation of the two panels, and the “aspect ratio” of the panels is obviously what the structural engineer has to cope with.

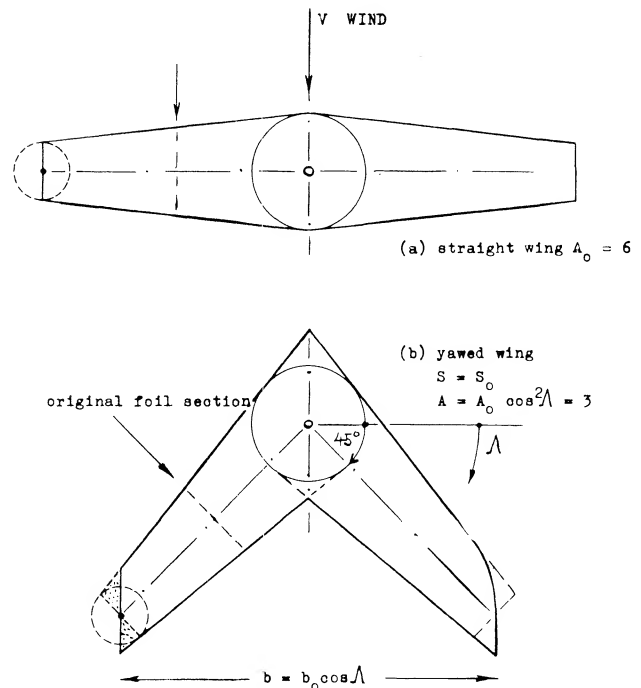


Figure 1. Geometry of swept wings; example of a tapered wing with $A_{c/4} = 6$, swept to $\Lambda_{c/4} = 45^\circ$.

- (1) Bagley, “Aerodynamic Principles of Swept Wings”, Vol 3 “Progress in Aeron Sciences”, Pergamon 1962.

SHEARED WING. A sheared wing is produced by moving (on paper) the wing sections parallel to one another in flow or flight direction until the desired angle of sweep is obtained. Since span and aspect ratio remain constant in this case, and the wing tips retain their lateral edges (as they are usually designed for airplanes) this definition seems to be preferable in analysis and discussion. It should be indicated, however, whether the foil sections are defined in the direction of flow (sheared) or normal to edges or axes of the wing panels (yawed). The thickness ratio is:

$$(t/c)_V = (t/c)_n \cos \Lambda \quad (2)$$

where V indicates the direction of flow or flight, and "n" that of the component w , that is "normal" to the edges or axes of the wing panels.

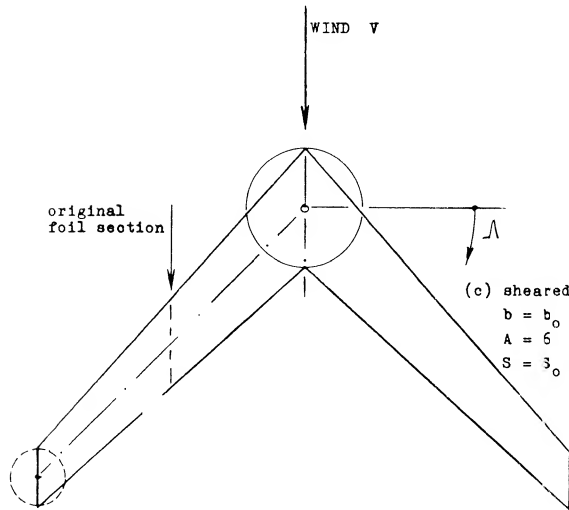


Figure 1a. Geometry of swept wings: cont.

CROSS-FLOW PRINCIPLE. To understand the aerodynamic mechanism of sweep, we will consider a long and narrow piece of wing, similar to that in figure 2, moving across a stream of air ejected from the nozzle of an open-type wind tunnel. Evidently, the wing is subjected to the velocity w . However, since the wing itself is moving sideways with the velocity u , the resultant speed of air against the wing is the geometrical sum

$$V = \sqrt{w^2 + u^2} \quad (3)$$

To say it in different words, the speed "V" (of a swept-wing airplane) can be split up into the components

$$(w = V \cos \Lambda) \quad \text{and} \quad (u = V \sin \Lambda) \quad (4)$$

As long as skin friction is of little or no importance, (2,d) the u component does not have an influence upon the pressure forces (drag, lift, pitching moment, wing-flaps, compressibility) produced by the component w . In other words, we could calculate and/or measure for example lift:

$$L = C_{L\alpha} \alpha_n S (0.5 \rho w^2) \quad (5)$$

where $C_{L\alpha}$ = lift-curve slope in two-dimensional flow would be a constant characteristic of the airfoil section, such as $(0.9 \cdot 2\pi) - 0.01$, and α_n defined in the direction of w that is normal to the edges of the wing. Referring this result to direction and magnitude of the "total" speed V , the dynamic pressure has to be modified corresponding to

$$(0.5 \rho w^2)/q = (w/V)^2 = \cos^2 \Lambda \quad (6)$$

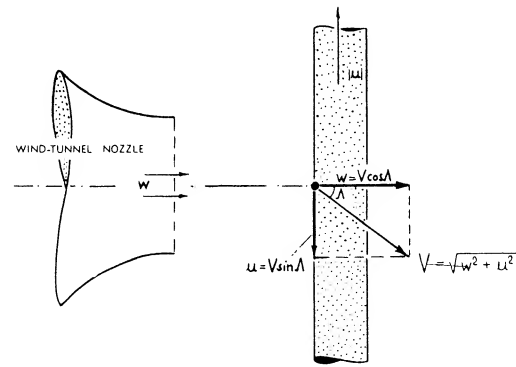


Figure 2. Experiment explaining the "cross-flow" or "cosine" principle in the panels of swept wings.

In the new system, which corresponds to a straight wing flying at an angle of yaw (sideslipping), the angle of attack measured in the direction of V is reduced to

$$\alpha = \alpha_n \cos \Lambda \quad (7)$$

In two-dimensional flow the lift is then

$$L = C_{L\alpha} S (\alpha_n / \alpha) [(0.5 \rho w^2)/q] q \quad (8)$$

and the coefficient, with subscript "2", is for condition in the direction of flight

- (2) Lift of airfoil sections in oblique flow:
- a) Lippisch, Pressures in Oblique Flow, ZWB FB 1669 (1942), NACA TM 1115; also Koch ZWB UM 3006.
 - b) Dannenberg, Pressure Distribution, NACA TN 2160.
 - c) Watkins, Streamline Pattern, NACA TN 1231 (1947).
 - d) Cross-flow principle, III & XV of "Fluid Dyn Drag".

$$C_{L2} = C_{L\alpha} (\alpha_2 / \cos \Lambda) \cos^2 \Lambda = C_{L\alpha} \alpha_2 \cos \Lambda \quad (9)$$

In other words, the lift-curve slope is $(dC_L / d\alpha)_2 = (C_{L\alpha} \cos \Lambda)$; and the lift is $L \sim \cos \Lambda$, for $\alpha = \text{constant}$ in the direction of flow or flight.

YAWED AIRFOIL. Experimental results of a wing obliquely spanning the closed test section of a wind tunnel at an angle of 45 degrees are presented in figure 3.

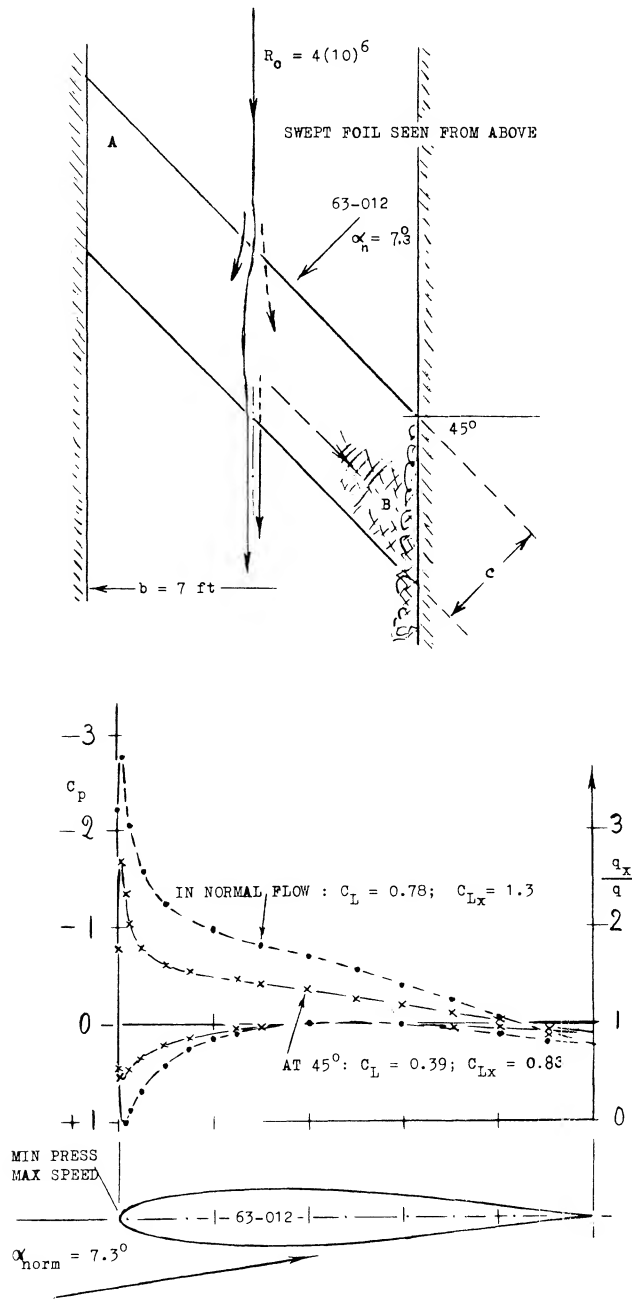


Figure 3. Flow pattern and pressure distribution of an airfoil, tested (2,c) between tunnel walls, at an angle of yaw or sweep $\Delta c/4 = 45^\circ$. The angle of attack is defined in the direction normal to the geometric span (axis) of the wings tested.

Note that the panel is of the “yawed” type, and that $c = \text{constant}$ (measured in the direction normal to the edges). The flow is essentially two-dimensional. As tested at half-span, pressure and lift coefficients are reduced in comparison to the same airfoil at $\Lambda = 0$, in proportion to $\cos^2 \Lambda = 0.5$; thus for a normal flow lift coefficient of 0.78 the effective value is: $C_L = 0.5 (0.78) = 0.39$. It should be noted that the dashed line on figure 3 is drawn to $\frac{1}{2}$ scale of the solid line, yet meeting most of the test points. However, if the angle of attack has been kept constant in the direction of flow (parallel to the tunnel walls) the lift and $dC_L / d\alpha$ will be proportional to $\cos \Lambda = 0.71$, thus confirming equation (9). Based on the data presented in figure 3 the following observations are made:

a) Because of the presence of the tunnel walls the cross flow is not correct at both ends of the airfoil.
b) The forward end of the foil evidently pushes down some volume of air. A corresponding upwash (circulation across the stream) is thus induced ahead of the downstream area of the wing. As a consequence, lift in this end is some 10% higher, and in the upstream end 10% lower than in the center.

c) The boundary layer flows (at the higher lift coefficients) from the upstream end of the wing, picking up on its way roughly parallel to the trailing edge, finally arriving at the downstream end of the airfoil.

d) As a consequence of (b) and (c) stalling (separation) takes place first at the sweptback on downstream end. Maximum lift in the center sections of the two airfoils is reached approximately at the same angle α , defined in tunnel direction. The coefficient is reduced, however, from $C_{Lx} = 1.30$, as in the airfoil at $\Lambda = 0$, to 0.83. This value of C_{Lx} is some 10% less than $C_{Lx} \cos \Lambda = (1.3) .71 = .923$ which is the theoretical expectation.

e) If the downwind end of the wing fully produced the lift corresponding to the upwash stated under (b), the flow would be two-dimensional. Because of the boundary layer transport under (c), lift is deficient on the downwind side thus leading to part-stalling as under (d). As a consequence, the streamtube splitting “at” the leading edge does not recombine past the trailing edge. This means that a certain rotation and/or circulation (a vortex) is left behind in the tunnel stream. This transfer of momentum results in an induced drag loss.

f) At $C_L = 0$ the wake-measured minimum drag coefficient is $C_D = 0.0041$ for either of the two laminar-type airfoils tested. The C_L size of the laminar “bucket” is reduced, however, by sweep, possibly in proportion to $\cos \Lambda$. At $\alpha = 6^\circ$ (in the direction of tunnel flow) $C_D = 0.0007$ for either of the two angles of yaw tested; the lift coefficients are different, however.

Qualitatively, all components of the flow pattern properties discussed above are found in real swept wings!

DIRECTION OF FLOW. In spite of the cosine principle of "cross" flow, the average direction of the flow of air past the upper and lower sides of any swept wing is essentially that of the undisturbed outside flow. As a consequence, the Reynolds number (basically responsible for the development of the boundary layer) is properly defined using the average wing chord measured in that direction and the undisturbed velocity of flow or flight (3). It should also be noted that wing attachments such as engines, pylons supporting them, all kinds of fairings and the rails (tracks) supporting Fowler-type or multiple-slotted wing flaps, and finally fences (see later) are usually arranged in the same direction.

SIDESLIPPING. At an angle of yaw β , or when sideslipping, the lift of a straight wing changes in proportion to the effective dynamic pressure as in equation (6), and its sectional "lift angle" measured normal to the wing edges, increases accordingly. The induced angle is based on the wing span which is reduced in the direction of flow or flight in proportion to $\cos \beta$. Consequently, $(d\alpha_i/dC_L) \sim 1/\cos^2 \beta$ (where α_i is defined in the direction of flight), or $(d\alpha_{n_i}/dC_L) \sim 1/\cos^2 \beta$. Using the formulation as in Chapter II, the total angle (normal to the wing edges) is then approximately:

$$d\alpha_n/dC_L = (10/\cos^2 \beta) + (20/A \cos^3 \beta) \quad (10)$$

The angle of flow or flight is

$$d\alpha/dC_L = (10/\cos^2 \beta) + (20/A \cos^2 \beta) \quad (11)$$

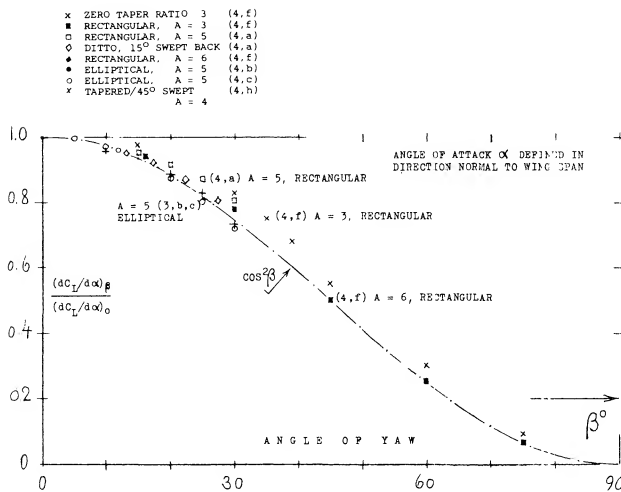


Figure 4. Lift-curve slope of straight wings when sideslipping at an angle of yaw.

- (3) The boundary layer on yawed or swept wings:
- Kuethe, Velocities in the BL, NACA TN 1946 (1949).
 - Wild, BL on Yawed Wings, J Aeron Sci 1949 p 41.
 - Ashkenas, Turbulent B'Layer, NACA TN 3383 (1955).
 - Haines, Flow Pattern 40/60° Sweep, ARC RM 3192.
 - Bolts, BL Stability for Sweep, NASA TN D-338.

The fact that experimental results plotted in figure 4 more or less follow a simple $\cos^2 \beta$ function suggests that the first term in the equation deteriorates as a consequence of the boundary layer flow as stated under (c) above. It is seen, however, that an elliptical wing and one with zero taper ratio follow equation (10). In the case of a rectangular wing there is a secondary effect involved. When turning such a wing into an oblique flow, the span (measured between diagonally opposed corners) increases to a certain limit, particularly in small aspect ratios. As a consequence, the induced component of their lift angle may not increase within some range of the angle of yaw, such as 19° , for example, for $A = 3$. Our interest is, however, not in plain wings flying at an angle of yaw, and this may not be the best way of considering swept wings.

2. LIFT OF SWEEPED WINGS.

When analyzing swept wings, the angle of attack of swept wing is defined as that in the plane of symmetry, the dynamic pressure in the direction of flow or flight, and the wing span the straight distance between the wing tips or lateral edges.

WING CENTER. Cross flow is not possible along the center line of the wing (nor really along the wing roots of an airplane). Pressure distributions for a typical swept back wing are shown in figure 5. The character of those, say in the vicinity of $\frac{1}{2}$ the half-span, is the same as found in conventional airfoil sections. The flow pattern around the apex of the swept wing is three-dimensional, however, and the pressure distribution is flat, by comparison. The cross-flow principle has nevertheless been found to give satisfactory information as to the total or average lift of swept wings, particularly at higher aspect ratios.

LIFT DISTRIBUTION. Induced angle of attack and induced drag of swept wings would be the same as for elliptical, or properly tapered straight wings, provided that the distribution of lift across the span would still be elliptical, or at least nearly so. As previously noted, the lift tends to be shifted, however, from the upstream to the downstream areas of these wings. Load distributions are shown in figure 6 for three different wings. While the

- (4) The lift of straight wings when sideslipping:
- Moller, Rectangular, Luft'forschung 1941 p 243.
 - Doetsch, Rect & Elliptical, Ybk D Lufo 1940, I-62.
 - Schlichting, Survey, Yearbk D Lufo 1940 p I-113.
 - Purser, Various Wing Shapes, NACA TN 2445, (1951).
 - Hansen, 5 Elliptical, Yearbk D. Lufo 1942 p I-160.
 - Goodson, Swept Sideslipping, NACA RM L1955 L20.
- (5) Chordwise distributions measured on swept wings:
- Thiel, Straight/Swept, ZWB UM 1293, NACA TM 1126.
 - See results in references (2,a) (7,a) (7,b) (12,e).
 - Whitcomb, Isobares, NACA RM L1950K27, K28, L07.

distribution across the straight wing is roughly elliptical, the swept-back shape exhibits a deficiency in the center and overloaded outboard parts. On the other hand, the swept-forward wing shows comparatively small loads on the forward ends and an overloaded center. These load distributions have severe consequences in regard to stalling, maximum lift, longitudinal stability (pitching up) and control (downwash and wake at the horizontal tail); and in the swept-back shape also upon roll stability and control. All of these aspects are discussed later in this and Chapter XVI.

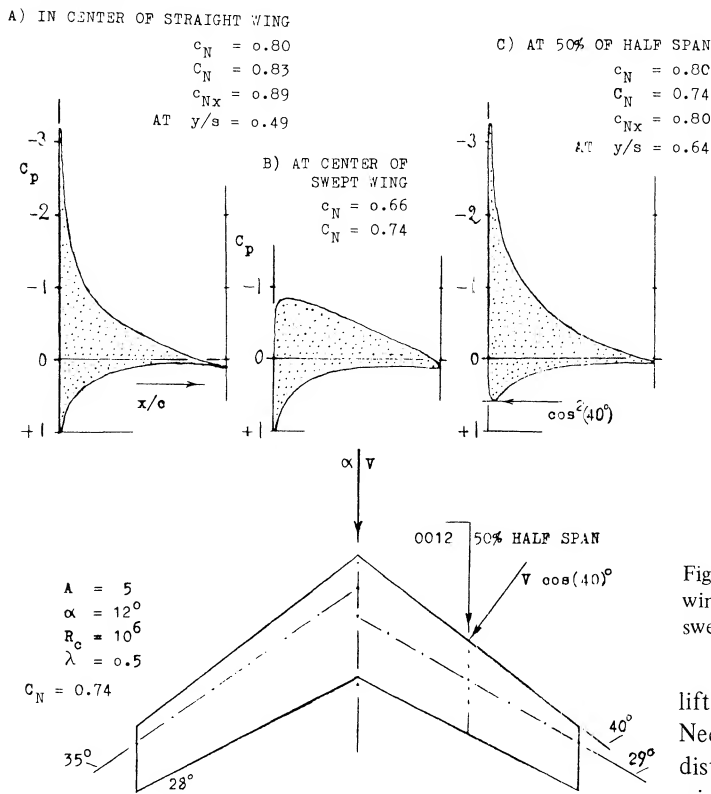


Figure 5. Chordwise pressure distributions tested (5,a) at several stations along the span of a straight and a swept wing.

TAPER RATIO. As pointed out above, and as seen in figure 6, the load distribution of swept wings can be considerably different from elliptical. To make these distributions nearly elliptical, theory (6,f) indicates the required taper ratios as plotted in figure 7. For a wing swept back to $\Lambda = 30^\circ$, for example, a taper ratio of $\lambda = 0.15$ would thus be needed. The idea is to give the wing more

- (6) Predicting spanwise loading of swept wings:
- Weissinger, Original Method (1940), NACA TM 1120.
 - Multhopp, Lifting-Surface, Brit RAE Rpt Aero 2353.
 - Schneider, Comparison/Experiments, NACA Rpt 1208.
 - Kuchemann, Calculated Distribution, ARC RM 2935.
 - Toll, Stability Derivatives, NACA TN 1581.
 - DeYoung, For Arbitrary Plan Form, NACA Rpt 921.
 - Van Dorn, Comparison of Methods, NACA TN 1476.
 - Falkner, On 3 Wings $A = 6$, ARC RM 2596 (1952).

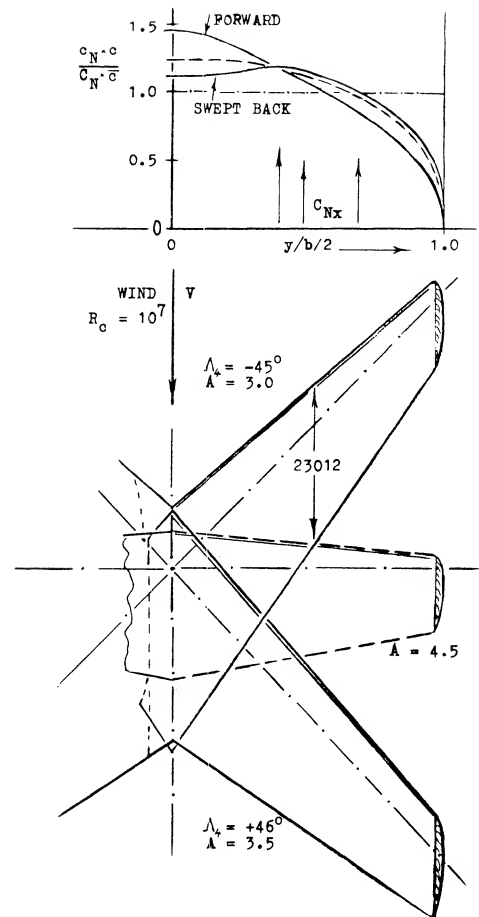


Figure 6. Load distribution across the span of three different wings (7,a) showing the variation as a function of the angle of sweep.

lift in the center and to reduce the loads on the wing tips. Necessarily this would mean higher lift coefficients (as distinct from loads (L/q) per ft or meter of span) on the wing tips. In a practical wing design, the result would be a very undesirable type of tip stalling. Aside from such considerations, references (8,a) indicates that (in the combination of a 45° swept wing with a fuselage) a taper ratio of 1.0 (rectangular panels) is as efficient in producing lift as 0.6 (tapered); and either one of these is better than a taper ratio of 0.3. Another method of making the lift distribution nearly elliptical is indicated in (1). The center of the wing might be given an increased angle of attack $\Delta \alpha = A/6$.

- (7) Spanwise load distribution, experimental:
- Jacobs, 4 Wings, ZWB UM 2052 NACA TM 1164.
 - Loving, Including Fuselage, NACA RM L54B09.
 - Mendelsohn, Forward & Back, NACA TN 1351; also same model with flaps, Letko TN 1352.
- (8) Experimental characteristics of swept wings:
- King, Wing-Fuselage Combinations, NACA TN 3867.
 - German ZWB Reports FB 1411 and 1458.
 - Tolhurst, Vortex Sheet 63° Swept, NACA TN 3175.
 - Cahill, Tapered $A = 4$, NACA RM L9J20/L50F16.
 - Kuchemann, 45° Swept Wings, ARC RM 2882.
 - Hopkins, With $-40^\circ/+45^\circ$ Sweep, NACA TN 2284.
 - Goodman, Various Wings in NACA TN 1835 & 1924.

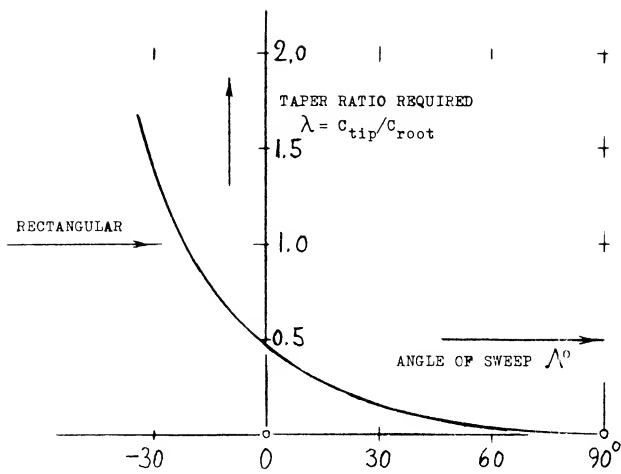


Figure 7. Taper ratios, theoretically required to make or to keep the lift distribution of swept wings as "good" as elliptical (6,f).

FORWARD SWEEP. If there are any over-all merits of swept-forward wings they are found in the "never" stalling wing tips (discussed in Chapter XVI). For finding lift the simple theory expects the cosine principle to apply in the same manner as in swept-back wings. As shown in figure 6, their spanwise load distribution is different, however. Lift and drag characteristics of a swept-forward, in comparison to a swept-back wing (having roughly the same aspect ratio), are presented in figure 8. Flow separation in the center of the swept-forward wing begins around $\alpha = 10^\circ$, where $C_L \approx 0.7$. This is particularly evident in part (b) of figure 8. Loss of lift and growth of drag are considerable. Stalling in the swept-back wing seems to be "creeping" between $C_L = 0.7$ and 1.05. As far as the magnitude of lift is concerned, this does not have too much of an influence, however.

INDUCED ANGLE. As stated in Chapter III, the induced angle is a minimum for the optimum distribution of lift across the span of any straight wing. To account for the influence of sweep, there does not seem to be any simple method available. It follows, however, from what is presented in Chapter VII of "Fluid Dynamic Drag" that the increment of the induced drag corresponds to

$$\Delta \alpha_i / \alpha_i = (k/A)A \quad (12)$$

where (k/A) is a function only of the taper ratio. Using the approximation as in figure 5 of Chapter III, we find for the induced angle (rather than drag):

$$\Delta (d\alpha_L / dC_L) \approx (K/A)^{1/3} \quad (13)$$

In straight wings realistic values of K , that is for tapered wings with λ between 0.4 and 1.0, may be in the order of 0.05. Equation (13) thus leads to values well below 0.1° . Considering an increment of 1% in the induced drag to be negligibly small, the possible influence of lift distribution may be disregarded (that is, in comparison to the various other uncertainties in any airplane configuration).

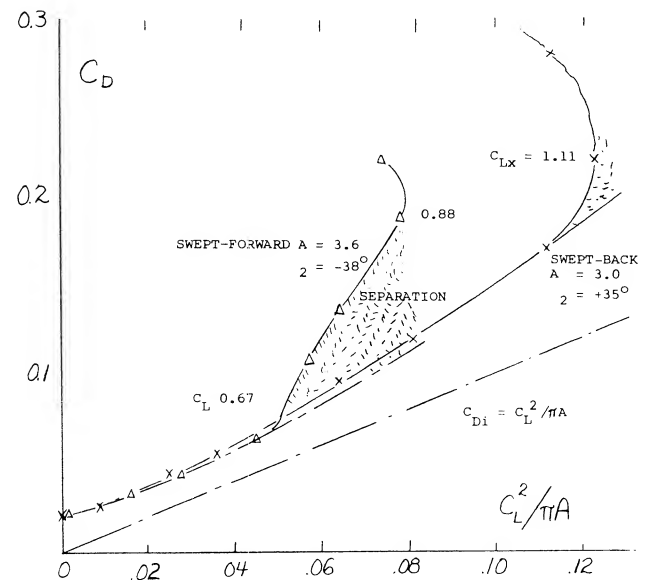
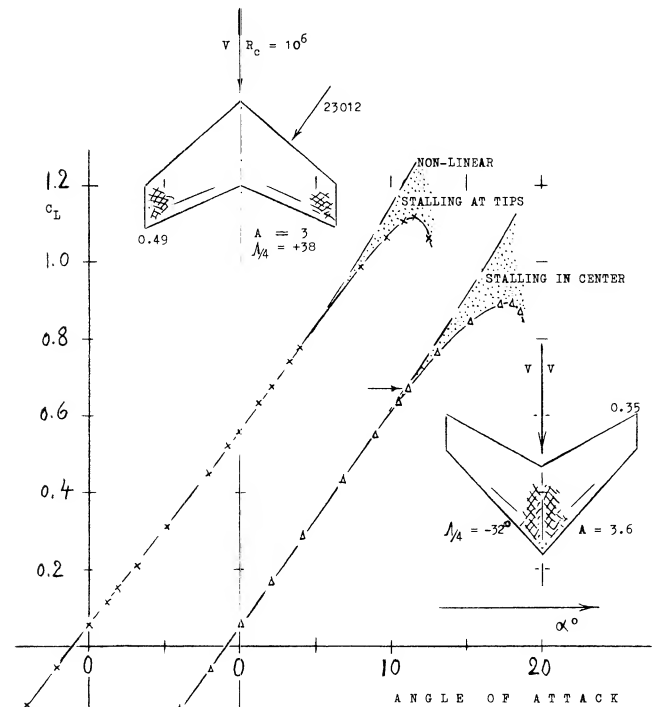


Figure 8. Lift and drag data of a swept-forward in comparison to that of a swept-back wing (9,f).

DRAG DUE TO LIFT. To determine the drag due to lift as a function of angle of attack as in the set-up in figure 2, the panels should be rotated (twisted as a whole) against the center axis of the swept wing. This is done in most airplanes, at least by some 3° , to keep fuselage and passengers on a level floor when cruising. Aerodynamic rotation is also obtained when deflecting trailing edge flaps and/or ailerons. In all wind-tunnel tests, the whole wing is pitched, however, rather than rotating the wing panels relative to the center body, a perfectly plane wing, such as a swept-back flat plate, the tips drop below the level of the center. A negative angle of dihedral thus develops. The influence of dihedral as such is comparatively small (see Chapter III). In swept wings, the lifting forces are tilted sideways, however, in addition to being tilted back by the induced angle. As found empirically (in Chapter VII of "Fluid Dynamic Drag") the drag due to lift increases accordingly, corresponding to

$$dC_D / dC_L^2 \sim 1/\cos \Lambda \quad (14)$$

It is believed that this increment (of induced and/or separation drag) is due to viscosity (boundary layer accumulation at the ends of the swept-back wing panels).

LIFT ANGLE. The angle-due-to-lift involved in equation (14) would lead to the following modification of the "lift angle" presented at length in Chapter III thus, if all the drag in equation 14 were considered to be induced

$$d\alpha_i / dC_L = dC_D / dC_L^2 = 20 / A \cos \Lambda \quad (15)$$

and the total angle of wings with larger aspect ratio

$$d\alpha^0 / dC_L = (10 / \cos \Lambda) + [20 / (A \cos \Lambda)] \quad (16)$$

Writing this equation in the form of

$$dC_L / d\alpha = \cos \Lambda / [10 + (20/A)] \quad (17)$$

a qualified confirmation is obtained by the results in figure 9. Assuming, however, that the induced drag of a swept wing be the same as that of a straight planform, the angle of attack of wings with not too small aspect ratios should be expected to be

$$(d\alpha^0 / dC_L) = (10 / \cos \Lambda_+) + (20/A) \quad (18)$$

For $\Lambda_+ = 25^\circ$, figure 11 confirms this function sufficiently well. However, the lift angles for $\Lambda = 50^\circ$ are definitely higher than expected by equation 18. For the $\Lambda = 50^\circ$ wing using equation (16) the right order of magnitude of $d\alpha^0 / dC_L$ is obtained. The mechanism of highly swept wings is thus believed to be different than that expected by the simple swept theory. The accumulation of boundary layer mentioned above can also be expected to be larger in higher aspect ratios (in long wing panels), while in smaller aspect ratios the distinction between swept and straight wings generally disappears; thus the boundary layer effects of swept wings must be considered.

The lift angle increment believed to be attributed to viscosity based on experimental results is given in figure 10. This increment appears to be a function of $1/\cos^2 \Lambda$.

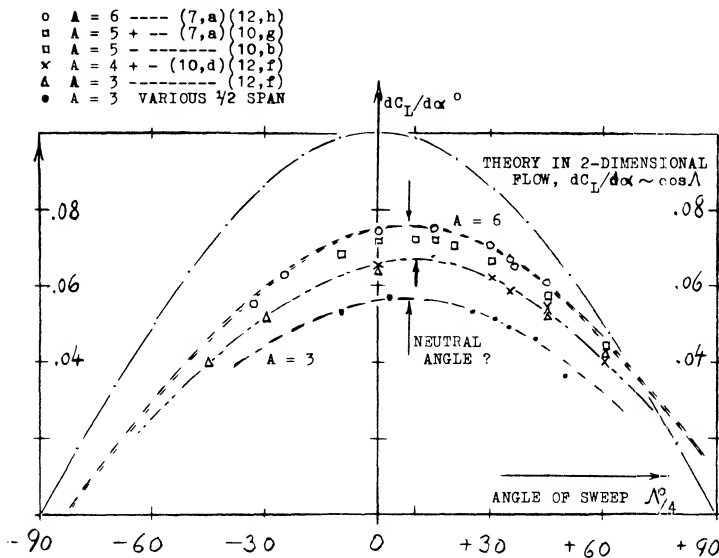


Figure 9. Lift-curve slopes of wings having aspect ratios between 3 and 6, as a function of their angle of sweep.

(9) Families of swept wings, at low speeds:

- a) Wolhart, $A = 2$ to 6 , 60° Sweep, NACA TN 4397.
- b) Thomas, $A = 2$ to 6 , 45° , NACA TN 4077.
- c) Thomas, $A = 2$ and 3 , 60° Sweep, NACA RM L55L30.
- d) Foster, 45° with $A = 3$ & 5 , NACA RM L1955H04.
- e) Purser, -45° to $+60^\circ$ Sweep, NACA TN 2445.
- f) Lowry, Half-Span, $A = 1$ to 2.5 , NACA TN 1284.
- g) NACA, Tapered 0 to 30° Sweep, NACA Rpts 572 & 627.
- h) Letko, With 0 to 60° Sweep, NACA TN 1046.
- i) Bennett, 3 Related Wings, NACA TN 1278.

(10) Influence of fuselage on lift of swept wings:

- a) Pressure & Load Distributions, (7,b,c)(9,b).
- b) West, Fuselage Location, NACA RM L1953B02 (21,e).
- c) Johnson, Wing With Bodies, NACA RM L1953J09a.
- d) Schlichting, Influence, ARC RM 2582.
- 11) Diederich (NACA), analysis of lift $f(A)$ and $f(\Lambda)$:
 - a) Correlation on the Basis of "F", TN 2335.
 - b) Spanwise Lift Distribution (Flaps), TN 2751.
- (12) Wings with negative (forward) angles of sweep:
 - a) Hopkins, Half Wings $A = 3$ to 7 , NACA TN 2284.
 - b) German ZWB Rpts FB 1411 and 1458 (1940)(8,b).
 - c) Junkers Ju-287, Jane's A W Aircraft 1945/45; or Aircraft Fighting Powers, Vol 7 Harborough 1946.
 - d) McCormack, Stalling Swept-Forward, NACA TN 1797.
 - e) Whitcomb, at $M = 0.6$, NACA RM L1950K28 (5,d).
 - f) Purser, $A = 3$ With $-45^\circ/+60^\circ$ Sweep, NACA (9,e).

Thus, one way of describing the lift of highly swept wings is to add a constant increment in figure 11, which might be of the form

$$\Delta(d\alpha^\circ/dC_L) = 1/\cos^2\Lambda \quad (19)$$

For $\Lambda_+ = 50^\circ$ the corresponding line in the graph averages the experimental points.

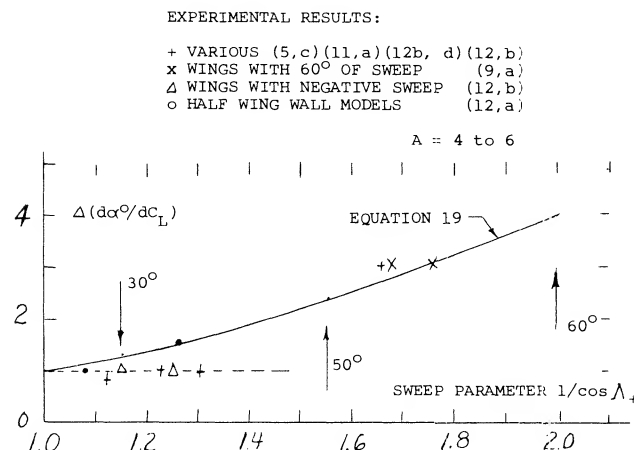


Figure 10. Increment of the lift angle caused by viscosity, as a function of the sweep parameter ($1/\cos\Lambda_+$).

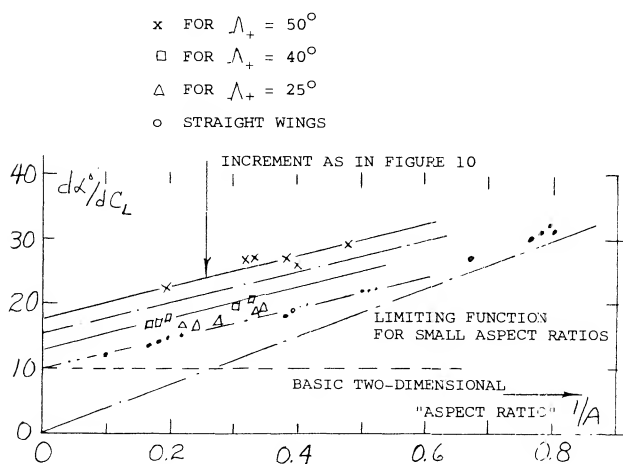


Figure 11. The lift angle of swept wings (with larger aspect ratios) as a function of ($1/A$).

NEUTRAL ANGLE OF SWEEP. It is seen in figure 9 that the "zero" angle of sweep (where $dC_L/d\alpha$ is highest) is shifted to $\Lambda/4$ around $+5^\circ$ for $A = 6$. A corresponding shift by 5° is observed in Chapter VII of "Fluid Dynamic Drag" for the minimum of dC_D/dC_L^2 . This is an empirical fact. It can be said, however, that there is no cross flow at the center line of swept wings. The cosine principle applies in the outboard parts, say in the outboard two-thirds of the half spans. Shown for example in (26,c) and (26,h) the aerodynamic center of lift of the sections is around $x/c = 40\%$ in the center of a typical swept-back

wing, and at $x/c \approx 24\%$ over most of the outboard two-thirds of the half span. In the words of (25,b) the "pressure peak line" determines the effective angle of sweep. The effective reduction of positive angles of sweep as in equations (20) and (35) is thus explained. To approximate the neutral angle as in figure 9 the line connecting the $1/2$ chord point of the root chord with the $1/4$ point at the lateral wing edges is suggested to indicate the effective angle of sweep. This angle is illustrated in figure 5, where it happens to be 29° instead of 35° . In tapered wings, the difference as against the usual $1/4$ chord definition is then found to correspond to

$$(\Delta\Lambda) = -(1/A)\tan(1/1 + \lambda) \quad (20)$$

For an assumed taper ratio $\lambda = 0.5$, the differential is $\Delta\Lambda = -34^\circ/A$. For example, for $A = 5$, a $\Delta\Lambda \approx 7^\circ$ is indicated, which is not too much in comparison to what is evident in figure 9. We will identify the effective angle of sweep by the subscript (+), thus $\Lambda_+ = \Delta\Lambda + \Lambda/4$, and use this angle in equations (16) and (17). Thus equation 17 becomes

$$(d\alpha^\circ/dC_L) = (10/\cos\Lambda_+) + (20/A \cos\Lambda_+) \quad (21)$$

INFLUENCE OF FUSELAGE. A convenient wind-tunnel technique is to attach half of the wing span (a half wing) to a wall or an end plate. Results are as follows:

- a) As stated above, the lift-curve slope is reduced because of the boundary layer present and/or developing along the "wall".
- b) The flow pattern past the roots of swept-forward wings (as sketched in figure 8) seems to be improved, at least in comparison to that of swept-back wings, where the roots are rather disturbed.

Since fuselages do have a boundary layer, "wall" interference could reduce the lift-curve slope of swept-back wings. However, lift is generally increased and the "lift angle" decreased when testing in combination with a fuselage body. Shown in (7,c) the lift (in units of force per unit of span) carried by the fuselage is roughly the same as in the inboard $1/2$ of the half-span of the 45° swept-back wing. This means that the dip of load as in figure 6, for example, is not present. In fact, there is possibly a pair of peaks induced by the fuselage on the wing roots (by way of the two-alpha principle, as explained in Chapter III). Thus, the lift on and by the fuselage is larger than it would be in the center of the wing when tested alone. As a consequence, the total lift of the wing-body configuration is increased over that as indicated in the various illustrations.

The influence of the body upon lift depends upon its size. As a function of the diameter ratio d/b , figure 12 shows how the combined lift L_{WB} varies, resulting approximately in

$$L_{WB}/L_W = 1 + 0.5 (d/b) \quad (22)$$

valid up to $d/b = 0.4$. References such as (9,b) confirm that lift is increased by the presence of a body in mid-wing position. As an interesting byproduct, the maximum lift coefficient (based on original wing area) is increased from $C_{Lx} = 0.9$ to 1.8 when adding a fuselage with $d/b = 0.4$. Considering the high lift at $d/b = 1$, that is of the body alone, it should be realized that there would be in that graph a body with a length equal to 5 or 7 times the span of the original wing.

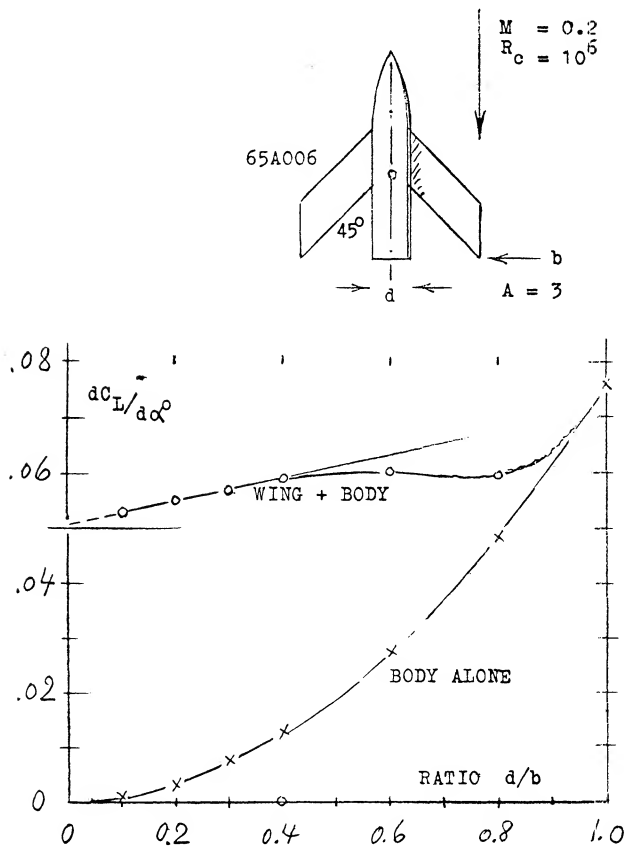


Figure 12. The lift-curve slope (up to $C_L = 0.8$) of wing-body combinations (10,c) as a function of the diameter/span ratio.

- (13) Characteristics of "M" and "W" swept wings:
- See Reference (4,f).
 - Henderson, Variable Sweep "M", NASA TN D-3025 (1965).
 - Diederich, Loading of M & W, NACA RM L51E29.
 - McKee, M-W-Swept Comparison, NACA RM L1953J02a.
 - Brebner, Analysis Cranked Wings, ARC RM 2947 (1955).
 - Ray, Variable Sweep M Wing, NASA TND-3025 (1965).
 - Campbell, Small Scale Test "M" & "W" Wings, NASA RM 50H25a.

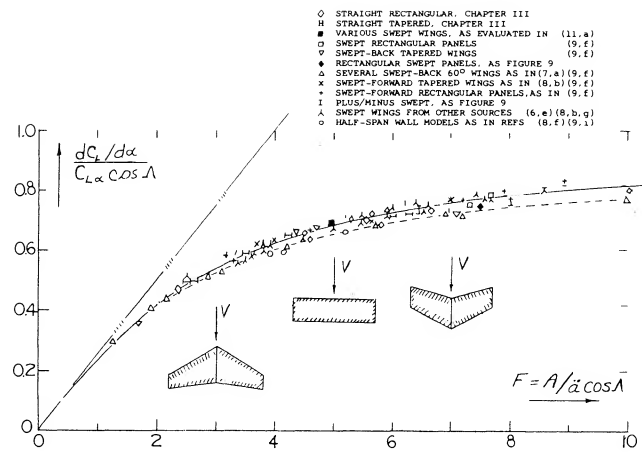


Figure 13. Generalized presentation (11,a) of the lift curve slope of swept (and of straight) wings, as a function of their aspect ratio parameter "F". The angles of sweep were "corrected" as per equation (15/20) when evaluating the experimental points.

ASPECT RATIO. The function such as in equation (21) is no longer correct within the range of aspect ratios, say below 4. A very useful method describing the lift-curve slope of swept wings down to aspect ratios below unity is presented in (11,a). Defining the modified aspect ratio

$$F = A/a \cos \Lambda, \quad (23)$$

the lift-curve slope of swept and/or straight wings is indicated by the ratio

$$(dC_L/d\alpha)/(C_{L\alpha_2} \cos \Lambda_+) = F/(2 + \sqrt{F^2 + 4}) \quad (24)$$

For conventional airfoil sections we can assume $a = 0.9$ and $C_{L\alpha} = (dC_L/d\alpha_2) = 0.1$. Available experimental results have been evaluated on this basis and plotted in figure 13 in the form of

$$(dC_L/d\alpha)/(0.1 \cos \Lambda_+) = F/(2 + \sqrt{F^2 + 4}) \quad (25)$$

Aspect ratios between zero and infinity are covered by this equation. The assumptions made in (11,a) permit presentation of a broad field of aspect ratios and sweep angles in one graph. Below $F = 0.8$ a limiting linear function is found. Combining equations (23) and (25) we obtain

$$dC_L/d\alpha^\circ = A/36 \quad (26)$$

for "A" well below unity and for not too large angles of sweep. This equation is essentially the same function as that in the chapter dealing with "low-aspect-ratio wings". The interesting result is that *the influence of the angle of sweep simply disappears.*

"CRANKED" WINGS - M & W. Wings with a planform shape of an "M" or "W" are also called "cranked" wings (13,b). The idea for the use of these shapes was to delay or eliminate the pitch up moment encountered with swept wings, see Chapter XVI, and thus allow the use of higher values of sweep. Also, the same degree of sweep can be obtained with "M" or "W" without the need of extending the tips so far back. This was thought to have structural and aero-elastic advantages.

Tests did show an advantage with the pitch up moment at angle near stall (13,f). The performance of the "M" and "W" planform wings was expected to be below that of the plane sweptback wing because of poor flow at the bends of the wing. The data of (12,b) does not confirm this as shown on figure 14. In fact, the performance of the "W" wing is slightly better than the equivalent 60° swept back wing, except near maximum lift. Although there appear to be advantages in the use of "M" or "W" wings, the practical design and construction problems have apparently eliminated their use.

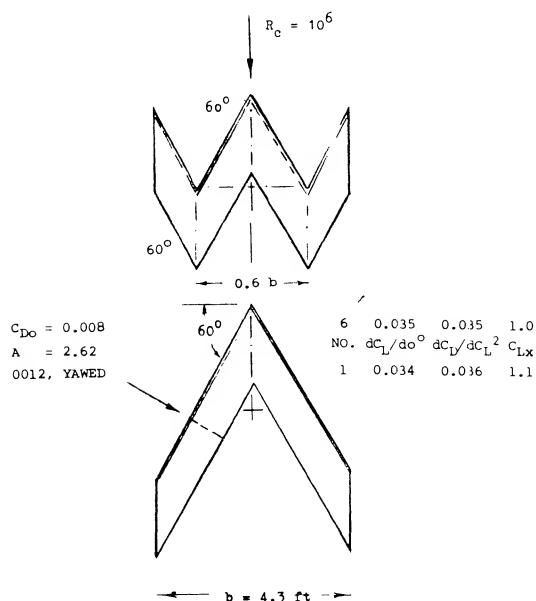


Figure 14. Characteristics of a 60° "cranked" or "W" wing in comparison to those of a plain swept wing (29,f).

- (14) End plates or tip tanks on swept wings:
- Salter, End Plates & Tanks, ARC C'Paper 196.
 - RAE, Tanks on Swept Wing, ARC RM 2951.
 - Kuchemann, End Plates, ARC C'Paper 104.
 - Riebe, End Plates 45° Swept, NACA TN 2229.
 - Hubert, With End Plates, Ybk D Lufo 1937 p I-129.
 - Schuldenfrei, $A = 2.5$, 40° Sweep, NACA TN 2482.
 - Williams, Straight & 30° Swept, ARC RM 2151.
 - Goodman, Lateral With Fins, NACA TN 2534.
 - Henderson, Sweptback Wing-Body End Plates M'Numbers 0.40 to 0.93, NASA TN D-389.

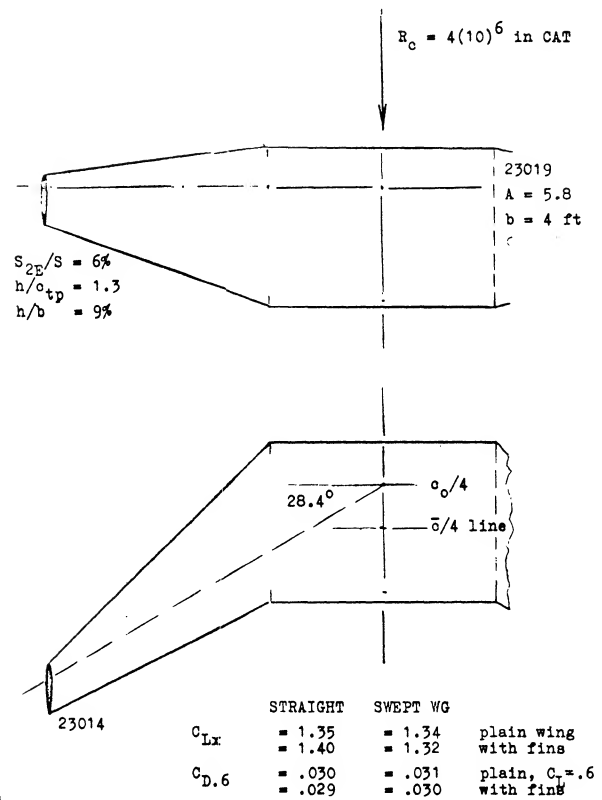


Figure 15. The influence of end plates (fins) on upper side, upon the characteristics of a straight and a swept wing (14,g); comparison of the two wings with each other.

END PLATES. As presented in Chapter III any addition of end plates increases the lift-curve slope of straight wings. The maximum of (L/D) of swept wings is reduced, however, as shown in (14,g). The flow over the wing tips (prone to stall) is evidently made more difficult by the presence of end plates, after exceeding small lift coefficients. Some drag and lift results are presented in figure 15. At $C_L = 0.6$, total drag is somewhat reduced when adding the upper-surface fins. For a height ratio of $h/b = 9\%$ the reduction could be expected (see Chapter VII of "Fluid Dynamic Drag") to be in the order of $\Delta C_D = -.003$, which is 10% of the total at $C_D = 0.6$. Interference (not only in the swept, but in the straight wing as well) increases the viscous drag more than 30%. The maximum lift of either the straight or swept wings is only slightly effected by the use of end plates on the upper side. In (14,g) the end plates (on upper side) were also kanted, by 7.5° in and out, respectively. When kanted-in (toed-out, we would say) the flow pattern within the corner between wing surface and plates was slightly improved. When kanted outward, drag was increased. It thus shows that the weak flow over the wing tips cannot be improved appreciably.

VERTICAL FINS. Vertical fins on top and/or below the wing can be used in tailless airplanes (using sweep-back) and will provide directional stability, Chapter XII. In the configuration as in figure 16, there is a small increase of

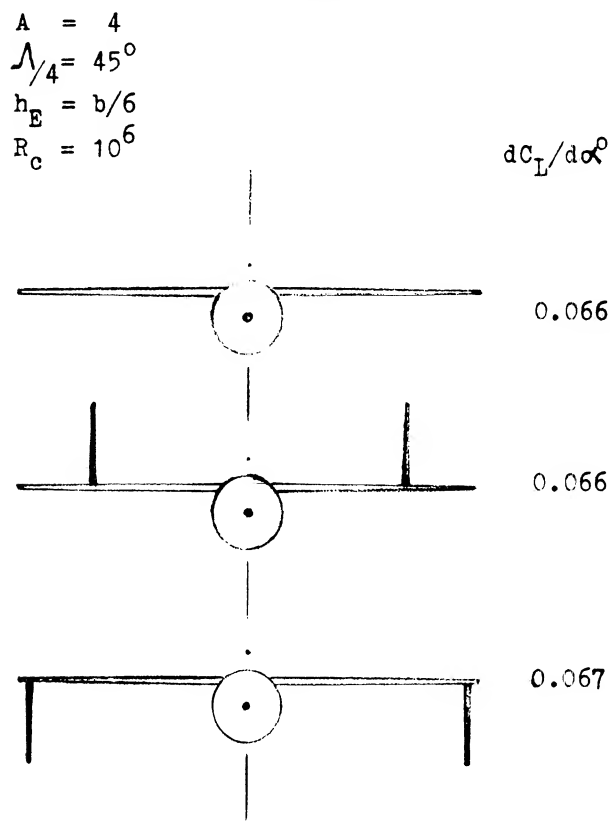


Figure 16. The influence of vertical fins added to a wing-body configuration (14,h) upon its lift.

lift for end plates placed below the wing tips. From Chapter III the induced angle can be expected to be $d\alpha_i/dC_L = [20/A(1 + 2/6)] = 3.3^\circ$, instead of 5.0° . For an angle of sweep $\Lambda = 37^\circ$, the increment in the lift-curve slope should thus have been in the order of 9%. However, with the fins placed on top of the wing, there is no increment at all. Again, the tips of swept-back wings are found to be inefficient, and not susceptible to improvement of the flow pattern.

ENGINE NACELLES. The pylons (struts) supporting jet engines below the wing (15) are in aerodynamic respect similar to end plates, moved inboard (say to $\frac{1}{2}$ half span). They might thus be expected somewhat to increase the lift-curve slope. Even engines without pylons, but underslung (16), have an effect of this kind. As shown in figure 17, the lift-curve slope increases slightly when moving the nacelles toward the wing tips. The lift/drag ratio is, of course, higher with the nacelles in midwing position than when located inboard (less frontal area). Also, the maximum of that ratio (at $C_L \approx 0.3$) increases noticeably when moving the nacelles outboard.

- (15) NACA, external stores on Douglas D-558-II:
 a) Silvers, Various Shapes Subsonic, RM L1955D11.
 b) Kelly, In 2 Spanwise Locations, RM L1955107.
 c) Smith, Characteristics at $M = 2$, RM L1954F02.
- (16) Engine nacelles on swept wings:
 a) Pressure Distribution, ZWB UM 3176, NACA TM 1226.
 b) Boltz, Pressures and Forces, NACA RM A1950E09.
 c) Silvers, Spanwise Position, NACA RM L1753H17.
 d) Pearson, At Transonic Speeds, NACA RM L1957G17.
 e) Hieser, Sweep and Fences, NACA TN 1709.

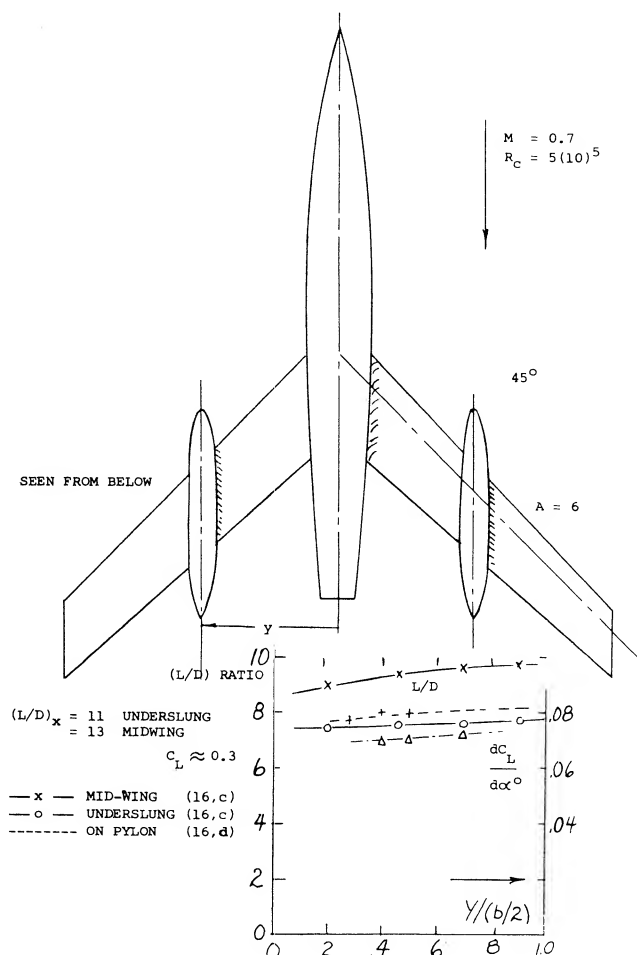


Figure 17. Influence of engine nacelles (16,c) upon the lifting characteristics of a swept wing.

TIP TANKS — SWEEPED WINGS. Wing tip tanks are used on swept wings for the same reasons as were discussed for straight wings in Chapter III. Also, the general flow and interference characteristics encountered are similar. The relative performance (17,c) of a swept wing with and without tip tanks is shown on figures 18 and 19 and includes data with end plates of a comparative height. As shown on figure 18, the lift curve slope increases from .054 for the wing with square tips to .063 with tip tanks. This increase is even larger than for the wing with end plates of a similar height. The data plotted on figure 18 is all referred to coefficients based on the original wing area. However, if the lift angle and slope are adjusted for the change in area and aspect ratio, the end plate effect of tip tanks agrees with corresponding data for end plates.

In comparing the drag as measured in (17,c) the use of tip tanks does not show any improvement over the original sharp tip wing, figure 18. This result cannot be generalized, however. In the configuration as tested, there was a

gap left between tanks and lateral edges of the wing, at each end (in the order of 10% of the tank diameter, by reasons unknown). As a consequence, an appreciable amount of interference drag must be expected due to separation; and this drag component evidently grows with the lift coefficient (flow through the gaps) so that the reduction of the induced angle, which is evident in the lift-curve slope, is completely wiped out. To account for possibly similar imperfections when fitting tanks to real airplanes, it is suggested in Chapter VII of "Fluid Dynamic Drag" that the endplate effect of the tip tanks may correspond to only half of their diameter, so that $\Delta A/A = -d/b$ should be used when estimating the drag due to lift.

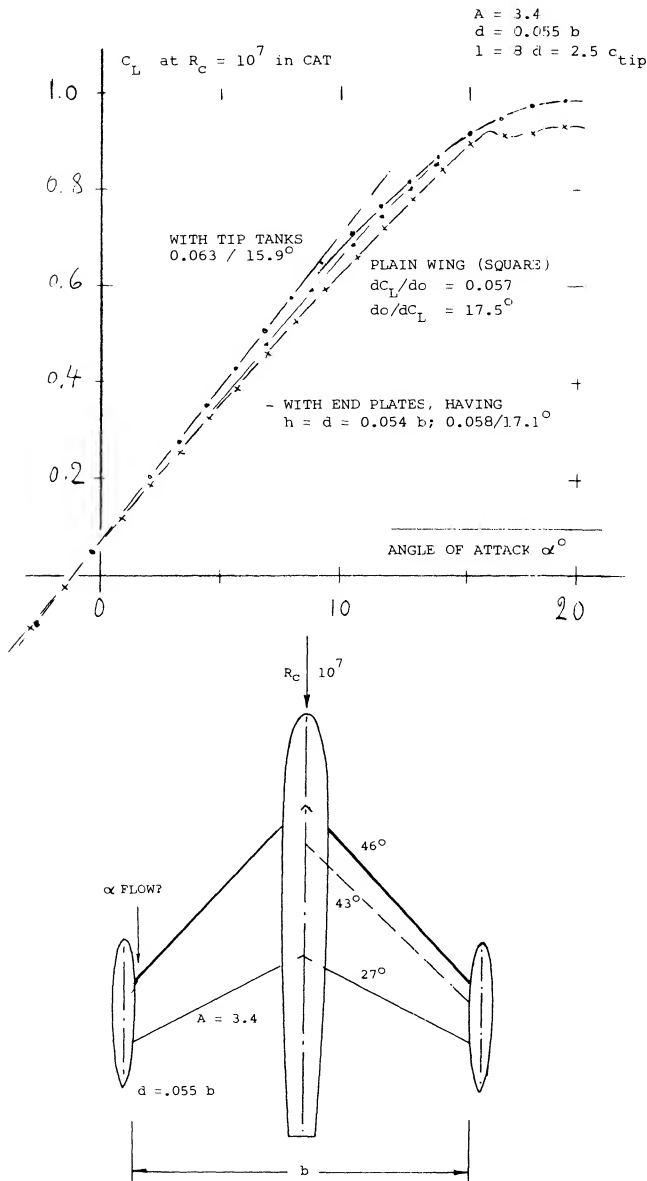


Figure 18. Lift characteristics (17,c) of a swept wing with and without tip tanks. All coefficients based on original wing area.

(17) Tip Tanks - Swept Wings:

- a) Robinson Wing-Tip-Tank Combination NACA RM L53B18.
- b) NACA Wind-Tunnel Investigation RM A5F02 & L8J04.

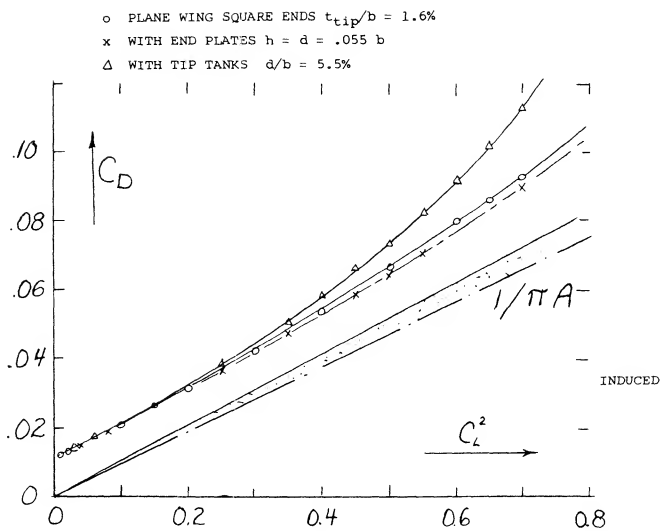


Figure 19. Drag characteristics (17,c) of a swept wing with and without tip tanks. All coefficients based on original wing area.

CONTROL FLAPS. Control flaps, such as elevators or rudders are thoroughly treated in Chapters IX and X. Their effectiveness is indicated by

$$d\alpha / d\delta = (dC_L / d\alpha) / (dC_L / d\delta) \quad (27)$$

When used in swept wings or tail surfaces (18,a), the hinge line is also swept. It must be realized that the two angles α and δ are measured in different directions. Considering the cross-flow principle in the panels of a swept lifting surface, the ratio as in equation (27) can then be expected to decrease as

$$d\alpha / d\delta \sim \cos \Lambda \quad (28)$$

The scattering results in figure 20 seem to confirm this reduction. An inspection of the effectiveness of outboard ailerons (19) shows that their roll moments reduce at a rate even stronger than in proportion to $\cos \Lambda$. The same deterioration is also found in swept-forward wings (19,a).

- (17) c) Salter and Jones (NPL), Swept Wing with End Plates in CAT, ARC Current Paper 196(1954).
- d) Hartlet, Tip-Tank analysis, ARC CP 147.
- e) RAE, On Swept-Back Wing, ARC RM 2951.
- f) Weber, Analysis Wing & Body, ARC RM 2889.
- g) NACA Tunnel Tests, RM A5FO2, A5GO2, L9JO4.
- (18) Effectiveness of Swept trailing-edge flaps:
 - a) Dods, Horizontal Tails, NACA TN 3497.
 - b) Harper, Tail Surfaces, NACA TN 2495.
 - c) Small Chord Ratios, NACA TN 2169 and RM L8H20.
 - d) Young, Wing Flaps, ARC RM 2622.
- (19) Effectiveness of ailerons on swept wings:
 - a) Luoma, Ailerons on Wings, NACA L1947I15.
 - b) Bennett, Roll Moments Swept Wings, NACA TN 1278.

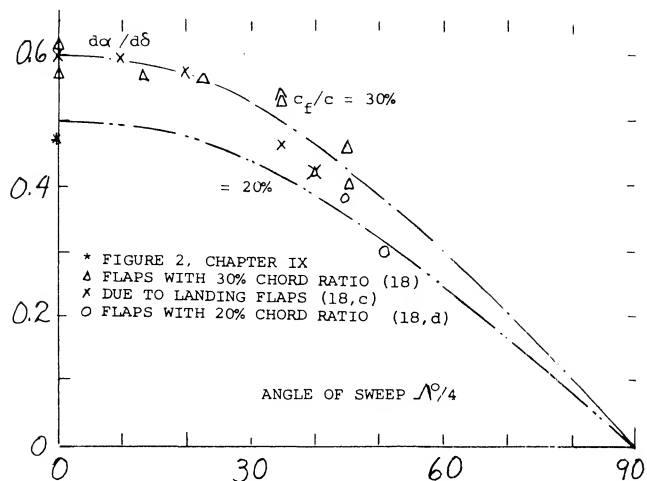


Figure 20. Lifting effectiveness of full-span wing- and/or control-surface flaps, as a function of their angle of sweep.

GROUND EFFECT: Ground effect, that is the influence of ground proximity when taking off or landing, upon the lift of straight wings, is presented in Chapter XX. In the case of swept wings, it can be visualized that the tips of a wing with 60° sweep, for example, would eventually touch the ground, while the apex is still high in the air. Lift and drag of a 40° swept wing are plotted in figure 21. Around zero lift the induced angle ratio (for $C_L = \text{constant}$) is approximately ($d\alpha_i^3/d\alpha_{\infty}$)

$$= 0.54 \text{ evaluated from lift}$$

$$= 0.63 \text{ corresponding to drag.}$$

These values are smaller than those in figure 28 of Chapter III, for $h/b = 0.18$, measured to $3/4$ of the mean chord. As discussed in that chapter, reasonable agreement can be found when defining the ground distance to the $3/4$ point of the mean chord. This would also straighten out the $C_L(\alpha)$ function. However, above $C_L = 0.7$ a deficiency of lift is seen to exist in the presence of the ground. The cause is stated in (20,b) to be "intermittent stalling" along the trailing edges (outboard). — The ground effect is, of course, of particular interest when landing an airplane; and that is usually done with the wing flaps extended. Deflected flaps are aerodynamically equivalent to an increase of the angle of attack. As found in (20,b) the same reduction of the induced angle is obtained as in figure 21. Stalling begins, however, at the same lift coefficient as without flaps. Subsequently, the drag due to lift increases progressively with the lift coefficient. The flapped center portion of the wing eventually stalls, resulting in a maximum lift coefficient reduced from 1.41 (in free flow) to 1.24 (near the ground).

(20) Influence of ground on lifting swept wings:

- Thomas, Theory/Experiment, Ybk WGL 1958 p 53.
- Furlong, Experimental, NACA TN 2487 or Rpt 1218.
- Hafer, Z Flugwissenschaften 1958 p 20.
- Wyatt, On "M" Wing, ARC C'Paper 541.
- Wood, Effect on "Swift Model, ARC C'Paper 458.

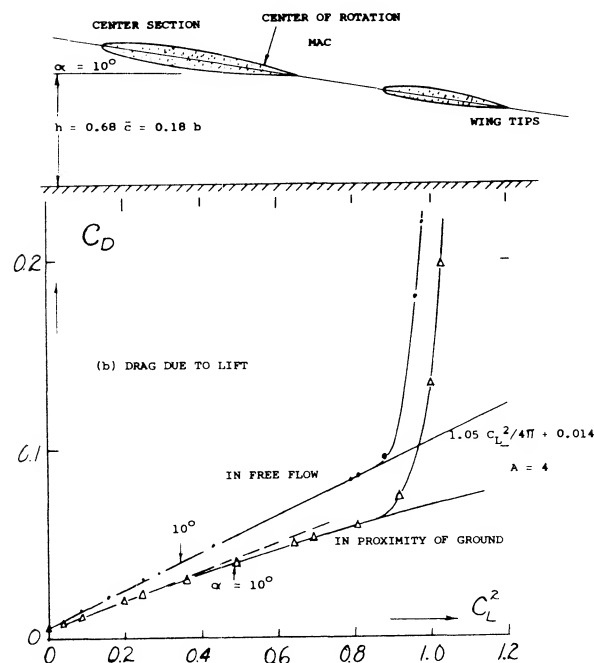
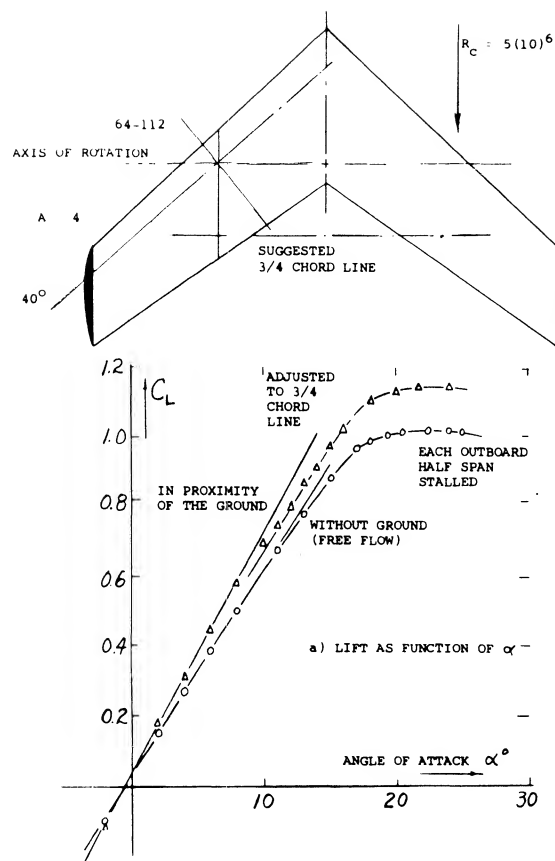


Figure 21. Influence of ground proximity upon the induced characteristics of a swept wing (28,b).

3. INFLUENCE OF COMPRESSIBILITY ON SWEEP WINGS.

When used in subsonic airplanes, the critical Mach number of swept wings is of primary interest. However, as in other wings, compressibility also affects the aerodynamic forces at speeds below the critical.

ANGLE OF SWEEP. As in incompressible flow, the lift of a swept wing is approximated by that of the two panels, say at $\frac{1}{2}$ of their span, exposed to the components of the air speed each normal to their quarter-chord or equal-pressure axes; that is to $(V \cos \Lambda)$ as in figure 2. However, as pointed out in (21,b,c) the Prandtl-Glauert rule (see Chapter VII) can also be formulated as saying that any wing in compressible fluid flow produces the same lift as a wing whose dimensions in the direction of flow have been increased in proportion to the Prandtl factor $P = 1/\sqrt{1-M^2}$. This means that not only the chord, but also the angle of sweep of that reference wing are increased. Accordingly, the effective angle (subscript e) corresponds to

$$\tan \Lambda_e = \tan \Lambda_+ / \sqrt{1-M^2} \quad (29)$$

It then follows that

$$\cos \Lambda_e \sqrt{1-(M \cos \Lambda_+)^2} = \cos \Lambda_+ \sqrt{1-M^2} \quad (30)$$

where $\sqrt{1-M^2}$ as in Chapter VII.

LIFT ANGLE. Based upon the foregoing and equation (21) the lift-curve slope of a swept wing with infinite aspect ratio, in a compressible fluid flow, is expected to be

$$\begin{aligned} dC_L / d\alpha_2^0 &= 0.1 \cos \Lambda_e / \sqrt{1-M^2} \\ dC_L / d\alpha_2^0 &= 0.1 \cos \Lambda_+ / \sqrt{1-(M \cos \Lambda_+)^2} \end{aligned} \quad (31)$$

where $0.1 = (dC_L / d\alpha_2^0)_2$ of a straight wing, with subscript 2 indicating two-dimensional conditions of flow. The lift angle is accordingly:

$$d\alpha / dC_L = 10 \sqrt{1-M^2} / \cos \Lambda_e = 10 \sqrt{1-(M \cos \Lambda_+)^2} / \cos \Lambda_+ \quad (32)$$

- (21) Principles and rules for compressible flow:
 a) Liepmann, "Elements Gasdynamics", Wiley 1957.
 b) Diederich, Correlation, NACA TN 2335, as (11,a).
 c) Goethert, Bodies, Ybk D Lu 1941; NACA TM 1105
 d) Kuchemann, Bodies of Revolution, J Aeron Sci;

$$C_P / C_{P_{inc}} = \Lambda V / V = \sqrt{P} = 1 / (1 - M^2)^{1/4}$$

The second version has the advantage that the effective angle of sweep (equation 29) does not have to be computed.

Assuming now that the induced drag and the angle due to lift ($20/A$) are no larger than in straight wings, the lift angle of swept wings with higher aspect ratios (say above $A = 4$) is

$$d\alpha^0 / dC_L = (10 \sqrt{1-(M \cos \Lambda_+)^2} / \cos \Lambda_+) + (20/A) \quad (33)$$

where $(M \cos \Lambda_+)$ can be considered to be an effective Mach number, for which the root in the equation can be taken from figure 1 in Chapter VII. Available experimental data are plotted in figure 22. While evaluating the many sources as in (22), it was found that on the average, wings tested in combination with a fuselage have $d\alpha / dC_L$ values larger by 1° , and half-span wing models (mounted on the wind-tunnel wall) have values lower by 1° , than plain 45° swept wings. However, results obtained on half wings, placed on so-called bumps in wind tunnels or on the wings of flying airplanes as in (22,c,h) for example are not affected by the thin boundary layer developing over those bumps. To obtain one single line, $20/A = 5^\circ$ plus/minus 1° was subtracted from the reported lift angles; and the parameter of the section, expected to be

$$(d\alpha^0 / dC_L) \cos \Lambda_+ = 10^\circ \sqrt{1-(M \cos \Lambda_+)^2} \quad (34)$$

was plotted accordingly, figure 22, with promising results.

- 65A006 W' BODY (22,a)
- ! W' BODY ON STING (22,b)
- + 1/2 SPAN ON BUMP (22,c)
- $R_C = 3(10)^\circ$, BODY (22,d)
- x 65A006 W' BODY (22,e)
- ◇ W' TRIMMED H' TAIL (22,f)
- ▽ DITTO, $\cos \Lambda_+ = 0.8$ (22,g)
- HALF-SPAN MODEL (22,d)
- HALF WING (BUMP) (22,h)

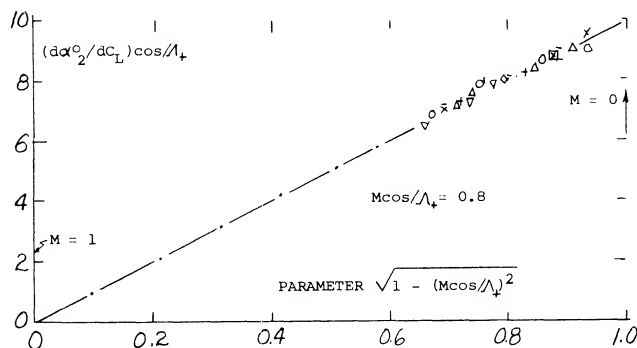


Figure 22. Sectional component of the "lift angle" of 45° swept wings, with $A = 4$, as a function of the Mach number parameter.

- (22) 45° swept wings as a function of Mach number:
 a) Polhamus, Directional Stability, NACA TN 3896.
 b) Donlan, Testing Techniques, NACA RM L1950H02.
 c) Polhamus, Wings on Bump, NACA RM L51C26.

It must be noted, however, that because of wind-tunnel interference, values higher or lower than indicated can be found in various references. For practical purposes, equation (33) is suggested to be sufficiently accurate. It shows that the sectional lift angle is as indicated by equation (31). For example, for $M = 0.9$, and $\Lambda/4 = 35^\circ$ as in the F-86 fighter airplane (24) the two-dimensional part of the lift angle is reduced, as against conditions in incompressible fluid flow, by some 3° . In spite of the angle of sweep (increasing the lift angle by almost 2°) the lift-curve slope is increased in this example. The reduction of the angle due to compressibility amounts to some 5° , from that of the same wing (with $A = 4.8$) in incompressible fluid flow, in the order of $d\alpha/dC_L = 14^\circ$; the result is $d\alpha/dC_L = 11^\circ$, or $= 10^\circ$, when considering the influence of the fuselage. This result agrees with flight-test and full-scale wind-tunnel data reported in (24).

LARGER ANGLES OF SWEEP. Evaluations similar to that in figure 22 can be made for different aspect ratios and angles of sweep. On the basis of equation (21) it can be expected that the lift angle may be increased by a component proportional to $1/\cos^2 \Lambda$. Figure 23 exhibits a single point for $\Lambda = 52^\circ$ and $M = 0.8$, showing about 60% of the increment as given by the equation. It is suggested again that viscosity (boundary layer accumulation on the wing tips) is responsible for the deterioration of the few experimental points at angles of sweep between 50 and 60° (see also figure 24). In fact, at $\Lambda = 60^\circ$, where $\cos \Lambda = 0.5$, the effective thickness ratio of the wing sections (in the direction normal to the panel edges or axes) is twice that of a straight wing. The boundary layer is also increased in thickness by the velocity component ($V \sin \Lambda$) along the panels. The type of flow pattern thus developing will be further discussed in Chapter XVI.

ASPECT RATIO. Disregarding the possible influence of viscosity (creeping flow separation in larger angles of sweep, as above) the most suitable lift formulation, for swept wings with aspect ratios between zero and infinity, is as in (11,a) similar to that in figure 12. Experimental

results in figure 24 do not readily confirm the theoretically expected lift-curve slopes. The spread is up to $+10\%$ and -5% . Examination of the experimental conditions leads to the following statements:

- In combination with fuselages, lift is markedly increased. Using equation (22) a body diameter $d = 0.2 b$ would explain a 10% increment.
- There are several inconsistencies in the data plotted. It can be assumed that wind-tunnel blockage or other test conditions are responsible.
- The points evaluated from tests in (25,a) show good correlation between a 47Λ swept and an essentially straight wing.
- As in figures 12 and 20, half-span wings have low lift coefficients. However, when tested on a bump, their lift is on the average as high as expected by theory.
- Reference (25,b) although affected by tunnel blockage, gives a comparison between wings swept to plus and minus 35 and 45° . Correlation as shown in the graph was only obtained, however, after changing the consequence of equation (20) into

$$\Delta \Lambda^\circ = -25/\Lambda \quad (35)$$

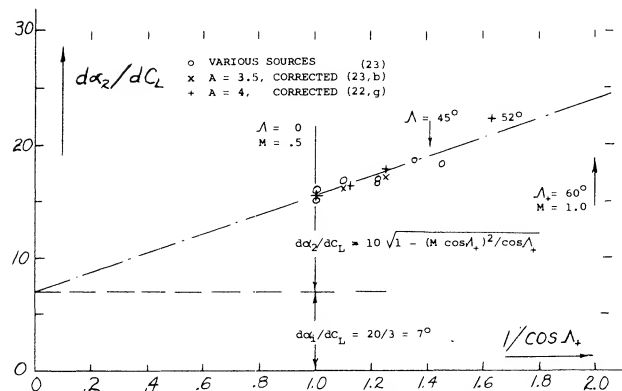


Figure 23. The lift angle of swept-wing-fuselage combinations with $A = 3$, and $M \cos \Lambda_\pm = 0.5$.

- (22) d) Goodson, With Edge Extensions, NACA RM L52K21.
e) West, With Extensions, RM L1953B02(10,b)
f) Faber, Using Free-Fall Method, NACA RM L1953D10.
g) Goodson, With Fuselage, NASA Memo 10-10-1958L.
h) Polhamus, Bump Test Results, NACA RM L1951H30.
- (23) Swept Wings with $A = 3$, function of Mach number:
a) Murray, Methods of Predicting, NACA TN 1739.
b) Bielat, 11/35/47° Sweep, NACA RM L1952B08.
c) Wetzel, NACA RM A1954A04, A1954J20, A1955H04a.
d) Knechtel, 19/45/53° Sweep, NACA RM A1955A03.
e) Knechtel, Highly Swept Wings, NACA RM A57F06b.
f) Bielat, With $t/c = 4$ to 12%, NACA RM L1951I04a.
- (24) Characteristics of North American F-86 airplane:
a) Triplett, Dynamic Flight Tests, NACA Rpt 1250.
b) Anderson, Pitch-Up High-Speed, NACA Rpt 1237.
c) McFadden, Vortex Generators, NACA TN 3523.
d) Tollhurst, Blowing Over Flaps, NACA TN 4283.

CRITICAL MACH NUMBER. As discussed in Chapter VII, the critical Mach number is theoretically that at which at some point, usually at the upper surface of a lifting wing, the local velocity is equal to the sonic speed. Upon exceeding the critical Mach number, forces and moments are likely to show variations different from

- (25) Subsonic characteristics of various swept wings:
a) Silvers, Wings With Missiles, NACA RM L54D20.
b) Whitcomb, Wing Plus/Minus 45° , NACA RM 46J01a.
c) Sutton, With Body Contouring, NACA RM A1956J08.
d) Goethert, Lil'thal Rpt 156 (1943); NACA TM 1102.

those at lower speeds. According to the cross-flow principle of swept wings, the sonic speed first to be encountered in their panels corresponds to $M = 1/\cos \Lambda$, where Λ may be equal to Λ_+ , determined as per equation (20) or (35). Considering, however, a reduction of the critical speed due to thickness (say $t/c = 9\%$) at some small lift coefficient (say $C_L = 0.1$) the corresponding Mach number would be in the order of

$$M_{CRIT} = 0.77/\cos \Lambda_+ \quad (36)$$

It is seen in figure 23, how this upper number can grow into the supersonic range. At $\Lambda_+ = 40^\circ$, the critical number in the wing panels is $M = 1$, in the example considered.

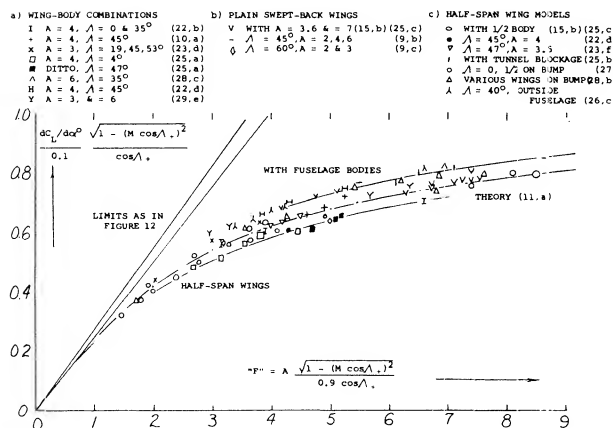


Figure 24. The lift-curve slope of swept wings at Mach numbers between 0.4 and 0.9, as a function (16,a) of the aspect-ratio parameter "F".

(26) Pressure distribution across the span of wings:

- Neumark, Critical M'Number, ARC RM 2821. Transonic similarity as in this report also in Chapter XV of "Fluid Dynamic Drag". See also ARC RM 2713 & 2717.
- Kuchemann, With W'out Body, ARC RM 2908 & 2935.
- Holmes, 40° With 10% Sections, ARC RM 2930.
- Weber (RAE/ARC), Symmetrical Sections (RM 2918), Cambered Sections (RM 3026), Centre Part of Wing (RM 3098); also J/RAS 1959 p 476.
- Cook, Comparison at High Speeds, ARC RM 3194.
- Runckel, 45° 65A004 Transonic, NASA TN D-712.
- See also the chordwise distributions under (5).
- Bagley, Calculated, ARC C'Paper 675.

CENTER OF A SWEEPED WING. In the center of a swept wing there cannot be a cross flow. As explained in (26,b) the superevelocities along the center line of a swept-back wing are usually lower than in the wing panels, when considering conditions at zero lift. The low-speed minimum pressure coefficient in the wing center is plotted in figure 25, particularly for 12% thick RAE sheared foil sections (26,b) as a function of the angle of sweep. The flow around and over the *apex* of a swept-back wing is more or less three-dimensional. However, as a consequence of the flow components converging onto the center line, from the swept-back wing panels, quasi-two-dimensional conditions are obtained along most of the way toward the trailing edge of the center part of the wing. In other words, we have to deal with the full speed V . Taking up the example again as in connection with equation (32), figure 22 indicates for $\Lambda_+ = 40^\circ$, at low speeds, an average $C_{pmin} = -2.1 (t/c) = -0.19$. Using figure 2 of Chapter VII, the critical Mach number in the center of the wing is then $M = 0.83$. This value is appreciably higher than that of a straight wing having the same airfoil section; $M_{crit} = 0.77$. The two critical M'numbers are shown in figure 26 as a function of the angle of sweep. Points derived from pressure distribution data (26,b) agree with transonic similarity theory (26,a) after taking into account the difference between "sheared" and "yawed" thickness ratio. It must be remembered, however, that reaching the critical M'number does not yet mean a divergence of forces. Drag-divergence Mach numbers of swept-back wings for zero (or sufficiently small) lift coefficients are plotted in figure 27, using the correlation as in (28,b). These numbers can be some 5% higher than the critical values. The graph suggests that the delay of divergence (but not the divergence Mach number as such) increases with the thickness ratio t/c .

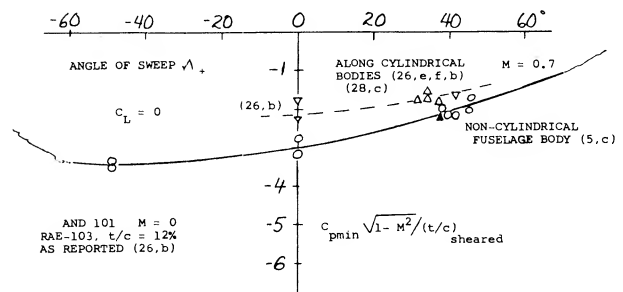


Figure 25. Minimum pressure coefficient on center line (or on panel roots) of wings, as a function of their angle of sweep, for $C_L = 0$ or below 0.2. At $\Lambda = \text{plus and minus } 90^\circ$, theory expects the pressure differential to end up at zero. For fore and aft symmetrical (circular arc) sections, theory (26,a) predicts a minimum pressure function similar as above, but symmetrical about the zero Λ axis.

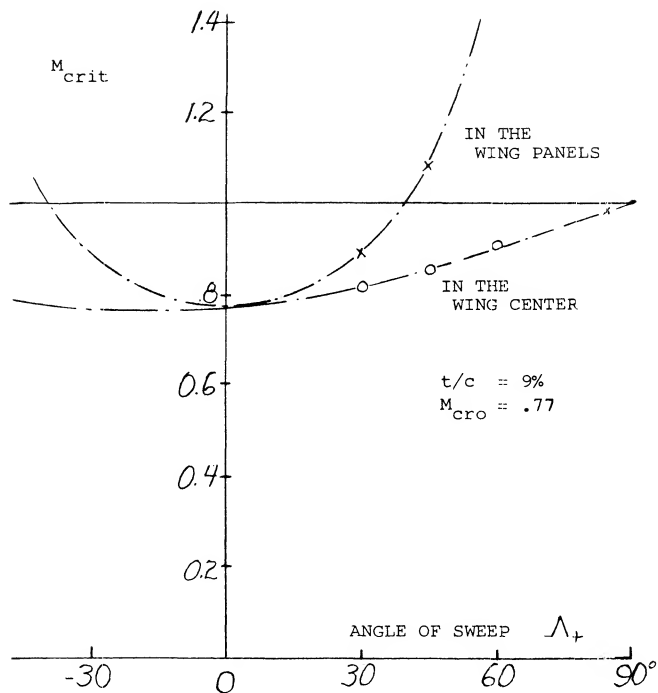


Figure 26. Example for the critical Mach numbers of wings, due to their thickness, at lift coefficients below 0.1, as a function of their angle of sweep.

a) WITH FUSELAGE, WING ROOTS

- (10,a) (22,e) (25,a) (28,a)
- (23,d,e)
- (23,f)
- △ (22,b)
- △ OTHERS

b) HALF SPAN ON BUMP

- (25,b)
- x (28,b)

c) HALF SPAN ON WALL

- + (25,b)

t/c "SHEARED"
(PARALLEL TO CENTER LINE)

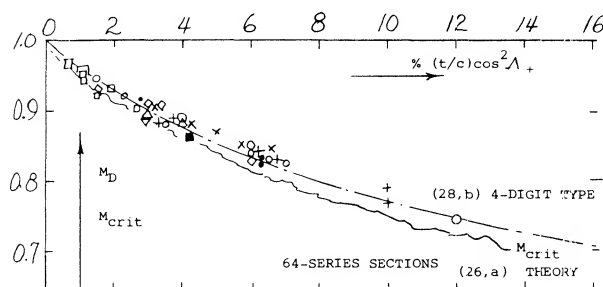
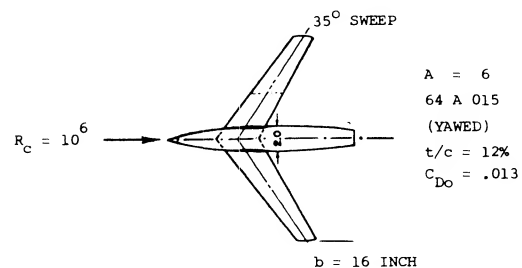


Figure 27. Critical Mach number of swept-back wings due to thickness (on center line) indicated by the divergence of drag, for lift coefficients below 0.1.

WING ROOTS. Considering conventional airplane configurations, there is necessarily a fuselage covering the center area of a swept wing. As demonstrated in "Fluid Dynamic Drag", whatever is done to the shape of slender bodies their critical speed is below $M = 1$, say at $M = 0.95$. Subsequently, they are exposed to supersonic velocities along their surface, and recompression becomes deficient. Regarding the interference with the two panels of a swept wing, theoretical and experimental results reported in (26) indicate that the panel roots adjoining a more or less cylindrical fuselage body, exhibit at zero lift, approximately the same pressures and distributions as described above for the center line of a wing alone. A few wing-root points are included in figure 25. In fact, in a particular configuration (23,f) the wing root thickness can be increased to critical or divergence Mach number (at zero lift). This result will change, however, at positive lift coefficients (say above 0.2) where the wing roots are bound to become more critical in the two-alpha flow induced by the fuselage. Also, considering the super-velocities along curved fuselage shapes, pressures along the wing roots must be expected to be lower than in the panels.



WITH BASIC BODY	W' CONTOURED BODY	
$M_{DD} = 0.85$	$= 0.89$	DRAW DIVERGENCE
$M_{LD} = 0.84$	$= 0.86$	LIFT DIVERGENCE
$M_{D.3} = 0.82$	$= 0.84$	DRAW AT $C_L = .3$

Figure 28. Example (28,c) of fuselage contouring, intended to increase the critical or force-divergence Mach number of swept wings. The indentation is shown along the wing roots as a pair of heavy lines.

CONTOURING (29). Figure 28 shows how suitable contouring of the fuselage walls (similar to that according to the transonic area rule) makes room for the typical panel cross flow to develop. The critical Mach number of the wing roots may thus be increased, from the lower boundary as in figure 26 possibly to the supersonic values as in (27) Nelson, Straight Wings on Bump, NACA TN 3501, 3502.

sufficiently swept panels. The fuselage retains its critical subsonic Mach number, however. Critical flow conditions of any swept wing, or wing-fuselage combination, are thus always reached below $M = 1$. By suitable contouring or shaping according to the transonic area rule not a subject of this text, but see (1) for example expansion, recompression and shock formation along the body may be kept harmless. As an example (26,b) pressure coefficients on the roots of a wing with $t/c = 12\%$, at $C_L = \text{zero}$, and at low speeds, are quoted as follows:

C_{pmin}	$= -0.31$	straight wing with cylindrical fuselage
	$= -0.25$	same wing with contoured fuselage
	$= -0.23$	in panels of 45° sheared wing
	$= -0.19$	roots of 45° wing with cylindrical body
	$= -0.22$	roots in presence of contoured fuselage.

In case of a lifting wing (to be discussed below) contouring can be applied above the wing roots (2,c) thus making room for the converging streamlines at the upper side. As shown in (29,d) a similar effect is obtained when placing the wing panels on top of the fuselage (high-wing).

FUSELAGE INTERFERENCE. At an angle of attack, the roots of any wing (straight or swept) are considerably affected by the fuselage. As explained in Chapter VIII of "Fluid Dynamic Drag and Chapter XX, any cylindrical body produces a two-alpha flow, resulting in upwash at the wing roots. As a consequence, pressure distributions as in (26,f) and (29,a,b) exhibit peaks near the leading edge of the panel roots beginning at $C_L = 0.2$ in a symmetrical, and at $C_L = 0.4$ in a 5% cambered section (5,c). Aided by the spanwise boundary-layer flow (described in Chapter XVI of this text) lift coefficients on the wing roots can thus be very high, say twice as high as in the remainder of the panels. In thin and symmetrical wing sections, these pressure peaks are cut down considerably by laminar separation. As shown in (26,f) and (29,b) the load distribution, as in figure 6, is nevertheless filled up to an essentially elliptical shape; and this fuselage effect is the reason for increased lift-curve slopes mentioned in connection with figures 13 and 24. Wing-root pressure distributions (29) vary corresponding to section thickness between 3 and 9%, and camber between 0 and 5% of the chord. Minimum pressure coefficients differ considerably, and it is impossible to find any reasonable correlation. It can be argued, however, that local supersonic "spots" developing on the wing roots at higher subsonic Mach numbers will not have any noticeable influence upon flow pattern and lift of swept-back wing-fuselage combinations. Disregarding, therefore, these peaks the minimum pressure coefficients found around 40% of the root chords of swept-back wings, may be said to be in the order of

$$C_{pmin} = -2(t/c) \cos^2 \Lambda - K C_L \quad (36)$$

where C_L = average wing coefficient, and K in the order of 0.4 for symmetrical sections with $t/c = 4\%$; about twice that high for $t/c = 7\%$; and up to 1.2 for properly cambered root sections. Thin and sharp leading edges thus lead to more or less local separation, while rounded and cambered sections permit the two-alpha flow to produce high lift with extended low-pressure areas developing on the wing roots.

CRITICAL LIFT. As suggested in (26,a,b) the full speed V , and the Prandtl factor as in figure 1 of Chapter VII, have to be considered in the center or on the roots of a swept wing. Therefore:

$$C_{pmin} = C_{pminc} / \sqrt{1 - M^2} \quad (37)$$

where C_{pminc} = incompressible coefficient, for example as in equation (36). It should be noted that the pressure coefficient on the wing roots grows as a function of Mach number, at a higher rate than any coefficient in the swept panels (as in equation 36, or as shown implicitly in figure 26). For statistical purposes (as in figure 29) it is suggested to use $K = 1$, in the last equation. As explained before, a subsonic flow pattern can be maintained in the panels of swept wings, say between 0.3 and 0.9 of the half span, at lift coefficients below 0.1 or 0.2, up to Mach numbers in the order of $(0.8 \cos \Lambda)$. For example, it is demonstrated in (28,e) that the cosine principle still holds at a Mach number of 1.2, in the outboard 75% of the half span of a sufficiently swept-back wing, at or near zero lift. However, when really lifting, a negative pressure ridge appears in the wing panels, near their leading edges, when using essentially symmetrical wing sections. As shown in figure 6 of Chapter VII, it is statistically and approximately (for low lift coefficients, and at low speeds):

$$C_{pmin} = -C_L^2 / (t/c) \quad (38)$$

In the panels of a swept wing, we have to substitute, corresponding to the cosine principle: $(C_{pmin} / \cos^2 \Lambda)$ for (C_{pmin}) ; $(C_L / \cos^2 \Lambda)$ for (C_L) ; $(t/c) / \cos \Lambda$ for (t/c) ; $(M \cos \Lambda)$ for (M) . Equation (38) thus reads, for a sheared wing:

$$C_{pmin} / \cos^2 \Lambda = (C_L / \cos^2 \Lambda)^2 \cos \Lambda / (t/c) \quad (39)$$

(28) Flow and forces above critical M-number:

- Whitcomb, 65A006 / $A = 4 / 45^\circ$, NACA RM L1952D01.
- Polhamus, Transonic Bump Results, NACA TN 3469.
- VonKarman, Similarity, J Math Phys 1947 p 182.
- Ackeret, Swept High Speeds, NACA TM 1320.
- Bagley, Shape and Drag, ARC C'Paper 512.

Using the Prandtl factor corresponding to $\sqrt{1 - (M \cos \Lambda)^2}$ (see figure 1 of Chapter VII) the critical Mach number ($M \cos \Lambda$) is then found in figure 2 of the same chapter for $(C_{p \min} / \cos^2 \Lambda)$. Confirming the procedure, a set of experimental points obtained on a 45° swept wing, was reduced to $\Lambda = 0$, and included in figure 6 of Chapter VII. The result is of the same type as the upper boundary in figure 26. This means that the critical number $M_{crit} = (M \cos \Lambda) / \cos \Lambda$, can still be supersonic. As an example, a wing with $t/c = 9\%$, and $\Lambda = 40^\circ$, was evaluated regarding critical Mach number. As shown in figure 29, the critical number in the wing panels is highest at lift coefficients below 0.25. In fact, the permissible speeds remain supersonic up to C_L slightly above 0.15. Within the range of smaller lift coefficients, force divergence is first caused by high speeds (low pressures) on the wing roots. We have plotted a line using $K = 1$ in equation (36). In conclusion, the cosine principle (being the foundation of swept-wing design) does not necessarily prevent supersonic velocities and their consequences (drag, shocks, buffeting) along the wing roots. However, contouring of the fuselage body as described above can possibly produce a flow pattern over the upper side of the wing roots, similar to that in the wing panels. Even then, the body itself is bound to retain a subsonic critical Mach number (say $M = 0.95$); and the body will pay a penalty (say at $M = 1$, by supersonic expansion, recompression through a shock, and drag) for letting the wing remain subcritical.

FORWARD SWEEP. The most interesting fact to be noted in figure 25 and 26 is the sensitivity of the center of swept-forward wings. As shown in (12,e), the minimum pressure on center line (at zero lift) is approximately:

$$\begin{aligned} C_{p \min} &= -0.25, \quad \text{at } x/c = 0.37, \quad \text{in center } 45^\circ \text{ swept-back} \\ &= -0.27, \quad \text{at } x/c = 0.25, \quad \text{average in wing panels} \\ &= -0.60, \quad \text{at } x/c = 0.03, \quad \text{center } 45^\circ \text{ swept-forward} \end{aligned}$$

It is thus seen how the swept-forward panels induce considerable supersonic velocity near the leading "edge" of the wing center. This situation becomes even more pronounced when lifting. As shown in figure 6, lift and lift coefficient are concentrated in the center of a swept-forward wing. Experimental results reported in (12,e) indicate peaked minimum pressure coefficients near the leading edge of the center of a 30° swept wing, roughly as follows:

$$\begin{aligned} C_{p \min} &= \quad -0.3, \quad \text{for swept-back panels} \\ &\quad -0.6, \quad \text{for the straight wing} \\ &\quad -1.2, \quad \text{swept-forward panels.} \end{aligned}$$

Conditions of the tunnel tests were as follows:

wing yawed 30° from	$A = 9$, to $A = 7.5$
yawed airfoil section	65 — 210
lift coefficient approximately	$C_L = .35$
Mach number of testing	$M = 0.6$

Although the result cannot be generalized, the value of $C_{p \min}$ in the center when swept-back is in the order of half of that for the straight wing and twice that high in the swept-forward condition. The corresponding critical Mach numbers at the center (or on the wing roots) are in the order of

$$\begin{aligned} M_{crit} &= 0.8, \quad \text{for yawed-back panels} \\ &= 0.7, \quad \text{for the straight wing} \\ &= 0.6, \quad \text{for yawed-forward panels.} \end{aligned}$$

In conclusion, the swept-forward type of wing is not promising in regard to critical speed. It must be said again, however, that forces do not necessarily diverge at the critical Mach number. The drag coefficient in the roots of the wing just quoted is only $C_D = 0.015$, at $M = 0.8$, in comparison to 0.008 in the panels. It is also interesting to note that the center of a 45° swept-forward wing tested (12,g) at low speed, stalls at $C_L = 0.5$, while the lift-curve slope continues to $C_L = 0.7$, and the maximum is $C_{Lx} = 1.0$. Similar conditions are seen in figure 8. Local drag coefficients at the wing roots can then (12,e) be up to 10 times as high as in the panels.

ENGINE NACELLES. When the engine nacelles is built into the panels, the interference effect upon swept wings is similar to that of a fuselage. In fact, in a swept-back wing the inboard junctures (corners) have a flow pattern similar to that in the center of a swept-forward wing. Low pressures are concentrated in a peak near the leading edge. This condition is aggravated at any lift coefficient different from zero or "symmetrical" (see Chapter II). Even without the help of compressibility, flow separation (as in part (b) of figure 8) is easily encountered. As an example, pressure distributions around an engine nacelle (16,a) installed in a 35° swept-back wing, with 12% sheared sections, show at $C_L = 0.3$, peaked minima at the inboard side, more than twice as high as in the outboard corner.

(29) Pressures along roots of swept wings:

- Mugler, Wing + Body, NASA Memo 10-20-1958L.
- Cassetini 53° Swept Transonic, NASA TN D-971.
- McDevitt, Body Contouring, NACA RM A1955B21.
- Dickson, Wing-Fuselage Height, NACA RM A55C30.
- McDevitt, Investigation of Fuselage Contouring on Wing-Body Combinations, NACA RM A1957A02.
- Contouring first tried at DVL (4)(25,d)(26,b).

By comparison, the critical Mach number in the particular configuration tested would be $M_{crit} = 0.6$ outboard, but below 0.5 inboard. Another example (21,c) with 45 sweep, using 65A006 sections, shows at $C_L = 0.3$ a drag divergence number $M_D = 0.96$ without nacelles, and $M = 0.92$ with nacelles. Some creeping divergence is evident, however, beginning at $M = 0.8$.

HIGH-SPEED PERFORMANCE. From what is said in this section regarding critical Mach number it can be concluded that the gain in maximum cruising speed of airplanes through the use of swept wings is limited, see figures 26 and 29. Modern airliners may, on the average, be operating as follows:

having an aspect ratio $A = 7$,
with some 30° of sweepback,
cruising at coefficient $C_L = 0.3$,
at an altitude of 9 km, 30,000 ft.
critical Mach number below 0.8,
maximum M number, approaching 0.9.

If their speed is up to 1000 km/h (some 600 mph, or above 500 knots) that must be compared with some 700 km/h (or less than 400 knots in the previous generation of (straight-wing and propeller-driven) transport airplanes. Upon inspecting figure 26, it can then be concluded that the increase of cruising speed was brought about not just by sweepback, but also by jet propulsion. In aerodynamic respect, consideration of range (as in Chapter I) would call for a cruising lift coefficient in the order of 0.35. As indicated in figure 29, the critical Mach number for this coefficient might only be between 0.6 and 0.7. On the basis of experimental results such as in (26,c) for example, the permissible coefficient for $M = 0.8$ may be noticeably higher than indicated by M_{crit} , say at least $C_L = 0.3$. A weak and evidently harmless shock front can be seen across the wing panels (under favorable conditions of sunlight) by airline passengers prepared for the phenomenon.

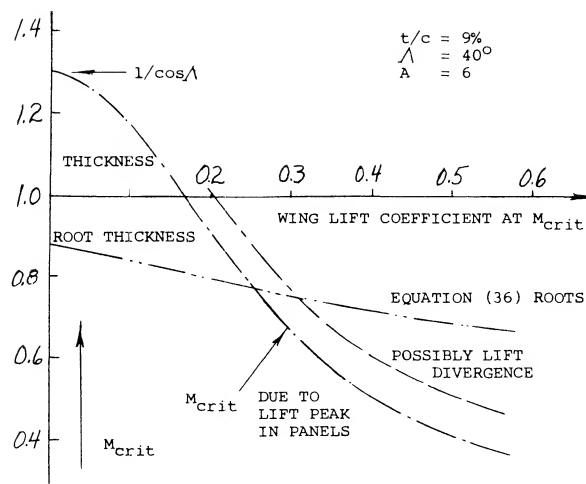


Figure 29. Critical Mach numbers of a particular swept wing, as a function of its lift coefficient.

CHAPTER XVI – STALLING OF SWEEPED WINGS (PITCHING, ROLLING AND YAWING)

The stalling characteristics of airfoil sections and straight wings along with the maximum lift coefficients are discussed in Chapter IV for single element airfoils. The effects on C_{LX} by the use of trailing edge flaps, leading edge slats and other high lift devices are covered in Chapters V and VI. These chapters provide the necessary basis for the study of the stall characteristics of swept wings which are very different from those of straight wings, especially when operating at high angles of attack. The stall, maximum lift, moment and drag characteristics of swept wings are generally very unfavorable and thus special attention is required in the design to achieve satisfactory flying qualities. The unfavorable high angle and stall characteristics of swept wings are accepted because of their good high speed performance and associated higher Mach number prior to the drag rise qualities discussed in Chapter XV and in the book “Fluid Dynamic Drag”.

The variation of the pitching moment with angle of attack when operating at or near maximum lift is one of the major problems of swept wings. This problem is caused by an unstable pitch up moment of the wing at both high and low Mach numbers which leads to unsatisfactory aircraft flying qualities. For this reason, when considering the maximum lift and stalling characteristics of swept wings the variation of the pitching moment becomes of major importance.

The flow characteristics effecting the stall properties of swept wings are influenced by the aspect ratio, sweep angle, load distribution, planform and operating condition. The wing design modifications used to obtain satisfactory operation are covered. These design modifications will include the use of planform changes, flaps, slats, camber, wash out, spoilers and fences. Where possible the data will be given for estimating the effects of these aero-dynamic devices on the stalling characteristics of swept wings.

Definitions: Aspect ratio, taper ratio and sweep angle are defined as in Chapter XV. A simple or plain swept wing is considered to be an untwisted wing of straight tapered planform with no spanwise variation of airfoil section. Such simple straight wings are also considered to have low camber airfoil sections.

1. CHARACTERISTICS AT HIGH ANGLES OF SIMPLE SWEEPED WINGS.

Typical characteristics of simple swept wings (1) with $\Lambda = 35$ and 45° as a function of angle of attack are given on figure 1. Although the change of lift as stall is approached and exceeded is generally gradual, the drag rise is very steep and the pitching moment curve becomes positive. These moment and drag characteristics tend to increase the wing angle of attack which is destabilizing and, of course, undesirable. Thus, modifications are required to eliminate or reduce the pitch up moment developed by swept wings. The stall characteristics discussed above are caused by the loss of lift at the wing tips which are located aft of the aerodynamic center. This lift loss causes a pitch up moment and is aggravated by a vortex formed on the leading edge of the wing that flows spanwise inboard from the tip. With increasing angle of attack this vortex is shed further inboard from the tip causing an effective loss of aspect ratio with a sharp increase in drag as shown on figure 1. Thus it is also noted that at the stall angle the drag increases sharply reflecting the increase in separation and the decrease of effective aspect ratio.

- (1) Stall characteristics of plain swept wings:
 - a) Hunton Section Characteristics $\Lambda = 45^\circ$, $A = 6$, NACA TN 3008.
 - b) Goodman & Brewer, Low Speed, Aspect Ratio & Sweep Characteristics. NACA TN 1669.
 - c) Turner, Effects of Sweep on C_{LX} , $A = 4$, NACA TN 3468
 - d) Platt and Brooks, Effects of $\Lambda = 0, 35$ and 45 at Transonic Speeds, NACA RM L54L31b
 - e) Hopkins, Effects of Sweep Forward and Back, $\Lambda = -40$ to $+45^\circ$, $A = 2.8$ to 6.8 , NACA TN 2284.
 - f) Kuhn and Wiggins, 45° Swept Wing at $A = 2, 4$ & 6 with fuselage, NACA RM L52A29.
 - g) Pursen, Swept & Yawed Wings of Various Planforms, NACA TN 2445.
 - h) Haines, Tests of 50° Swept Wings, ARC R&M 3043.

Although the variation of the lift coefficient curve with angle is gradual after the stall is encountered, the usable value of lift coefficient is much lower than C_{LX} because of the pitch up moment. This problem increases with speed as high speed buffet is encountered. Thus a relatively low useful value of lift are obtained at the higher operating Mach numbers. For these reasons when considering swept wing aircraft the stall characteristics encountered at both ends of the flight range are critical.

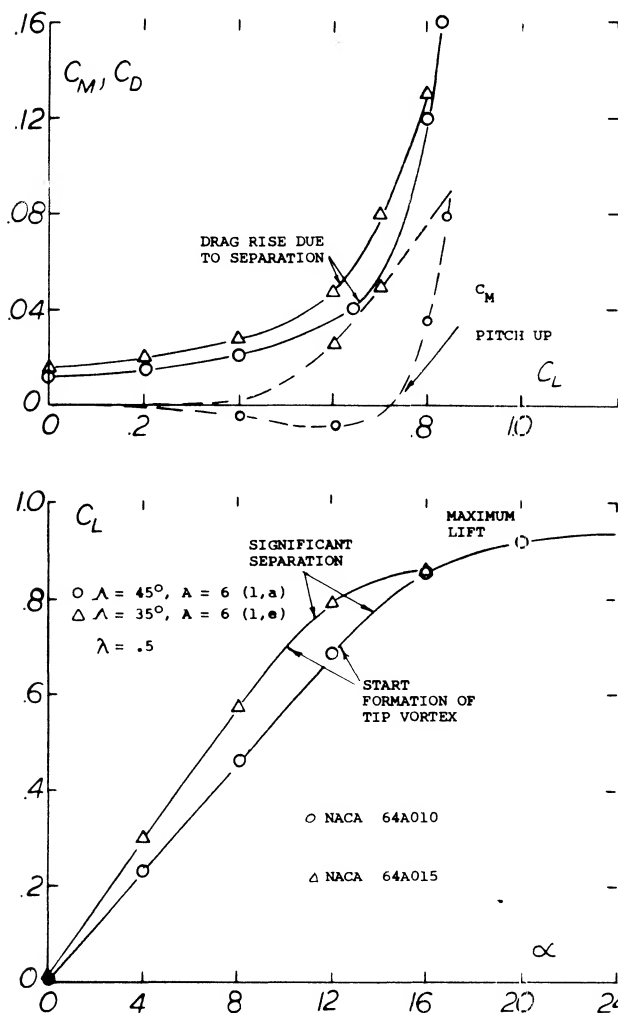


Figure 1. Typical characteristics of swept wing operating at high angles of attack.

MAXIMUM LIFT - SWEEPED WINGS. As discussed in the last chapter the characteristics of airfoils installed on a swept wing, in accordance with the simple sweep theory, depend on the flow velocity normal to the effective wing chord line. The section ordinates normal to this chord line determine the pressure distribution on the airfoil. Figure 3 in Chapter XV shows that the pressure distribution on the airfoil is independent of the sweep angle, provided the velocity chosen is parallel to the chord line. Thus for a swept wing

$$C_P = C_{Ps} \cos^2 \Lambda \quad (1)$$

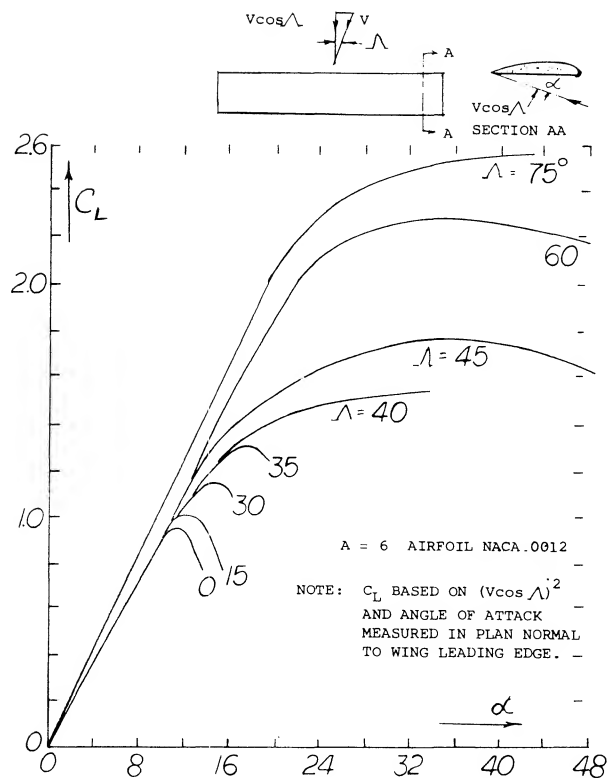


Figure 2. Based on tests (1,g) of a yawed wing, effect of yaw angle on section lift coefficient. Velocity measured normal to chord line.

where C_{Ps} is the pressure coefficient of a two dimensional section. Since the shape of the pressure distribution curve of an airfoil determines the maximum lift coefficient we can, therefore, expect that

$$C_{LX} = C_{LXS} \cos^2 \Lambda \quad (2)$$

where C_{LXS} is the maximum lift coefficient of the section in two dimensional flow. Thus for a 45° swept wing, the maximum lift would be expected to be half that of an equivalent straight wing.

Tests (1,g) of a rectangular wing of $A = 6$ at yaw angles of 0 to 75° show, in figure 2 that C_{LXS} actually increases with sweep or yaw angle rather than remaining constant as would be indicated by equation 2. At an equivalent sweep angle of 45° the level of C_{LXS} shown is nearly twice that expected by equation 2.

Further experimental confirmation of the maximum lift characteristics of swept wings (1) tested as complete wings and on a reflection plane shows an increase of C_{LX} with Λ . These data, figure 3, show that both angle of sweep and aspect ratio are important in determining the level of maximum lift.

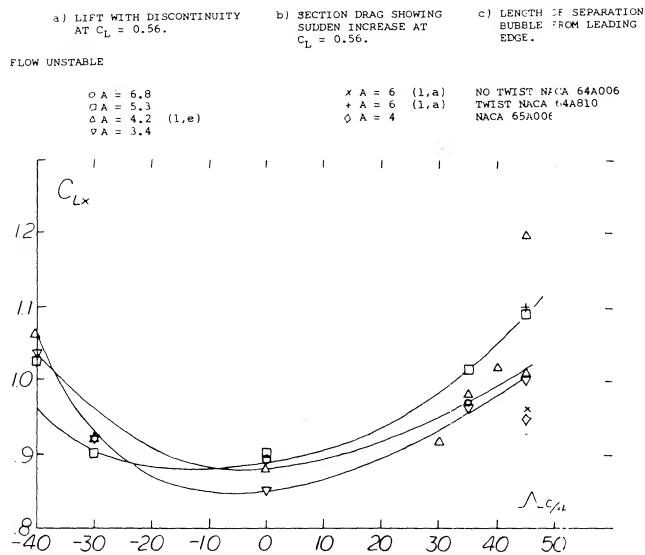


Figure 3. Sweep angle and aspect ratio effects on C_{Lx} for simple swept wings.

WING TIP FLOW. In a manner similar to that of straight wings, a flow of air (including some boundary-layer material) around the lateral edge, is caused by the pressure difference between the lower and upper side of the wing. At the same time the boundary-layer material as in figure 4 moves along the upper side toward the wing tip. As illustrated in figure 4, the two streams meet and combine, thus forming a strong trailing vortex. It should be noted that at (A) there is a weak stagnation point (causing a small secondary vortex), while at (B) a pressure minimum is obtained, thus indicating location and path of the vortex as in figure 4. Another weak vortex is formed at C.

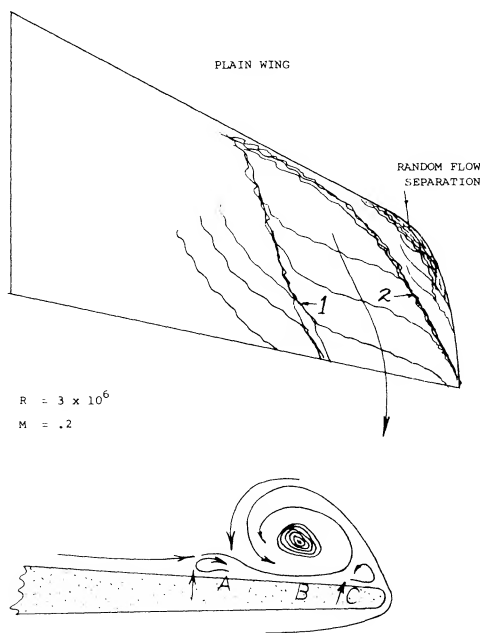


Figure 4. Surface flow pattern at the stalled tip of a plain stalled wing (1,h).

With increasing angle of attack, the main vortex grows in diameter (if that word can be used) and it moves farther inboard, as far as one tip chord, for example, at $\alpha = 15^\circ$ for the wing as in figure 4. The lines (1) and (2) in the illustration roughly indicate the boundaries of the main vortex. Since the flow is a fully separated area at (3), the forward corner of the wing may just as well be cut off as shown.

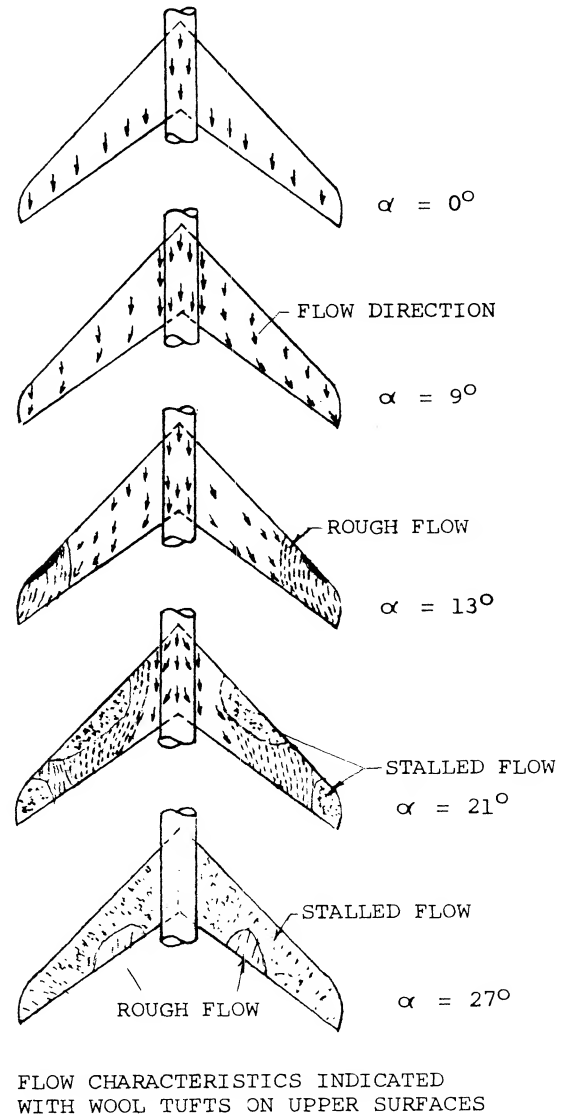


Figure 5. Stalling characteristics of a 45° A = 6 swept wing without flaps. $R = 4.5 \times 16$

BOUNDARY LAYER FLOW. The increase of C_{Lx} of swept wings above that expected by the simple sweep theory is caused by the flow of the boundary layer from root to tip, especially near the trailing edge of the wing. Thus the boundary layer flow acts in a manner similar to the use of suction for preventing separation, and allows the wing section to develop a higher lift coefficient than would be measured in two dimensional flow. The reason for the boundary layer flow is illustrated on figure 5 and is caused by the span and chordwise pressure distribution

on the wing. Consider for instance the pressure distribution of sections AA and BB shown on figure 6. At point (a) on section AA it is noted that the negative pressure remains lower in the chordwise direction than spanwise until point (b) is reached. Thus, the flow will move along the chord as shown. However, when point (b) is reached the pressure is lower outboard at (c) on section BB than at (c'). This causes the flow to move in the spanwise direction.

Since the spanwise flow of the boundary layer prevents separation on the inboard sections of the wing unstable flow first starts at the tip of the wing and is a function of the airfoil section type, leading edge radius and Reynolds number. This tip separation spreads to the leading edge at the tip and continues to move inboard with increasing angle of attack as shown on figure 5. With a further increase of angle the vortex separates from the leading edge inboard of the tip and flows chordwise. This leaves the tip of the wing completely stalled. The span station where the separation takes place continues to move inboard with increasing angle of attack.

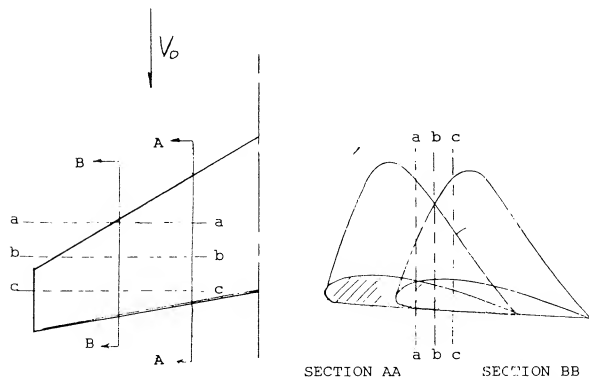


Figure 6. Section pressure distribution for swept back wings as influencing boundary layer flow.

The actual flow pattern in the boundary layer and, therefore, the degree of improvement of section C_{LX} depends on the geometry of the wing including aspect ratio, sweep angle, taper ratio, wash out and section type. The data given on figure 7 illustrates the variation of the local sectional lift coefficient as a function of span location. The variation of the corresponding two dimensional section data corrected for sweep according to the cosine principle is shown for comparison.

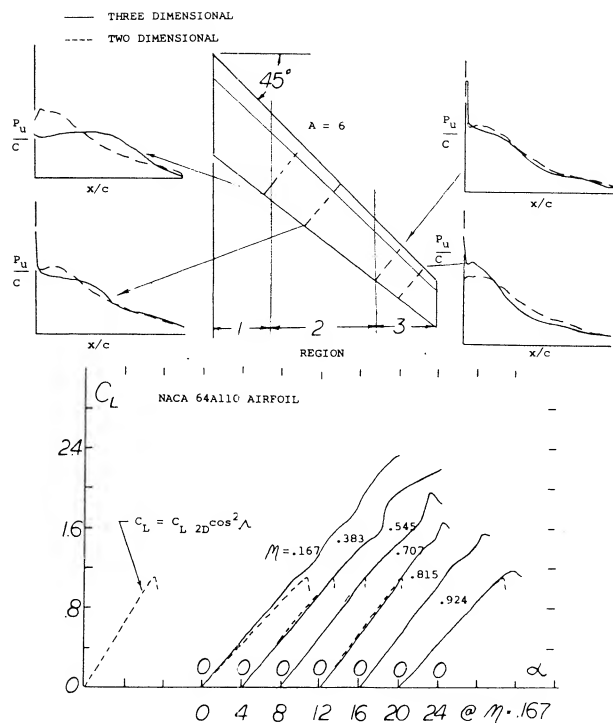


Figure 7. Lift and pressure distributions for $\Lambda c/4, a = 6$ plain swept wing (1,a).

The data (1,a) given in figure 7 shows that the local variation of C_L with α has the same slope in the middle of the wing semi-span as would be predicted based on airfoil section tests. The lift, however, continues to increase with angle to much higher values than predicted due to the boundary layer transport. The increase of C_{LX} compared to the two dimensional data is much higher inboard than near the tip. At the tip C_{LX} nearly equals the two dimensional value corrected according to equation (2). This illustrates that without the boundary layer transport effect the maximum lift would be lower than that of straight wings.

(2) Theoretical Methods:

- a) Anderson, Determination of the Characteristics of Tapered Wings, NACA TR 572.
- b) Kuchemann, Loading Straight & Swept Wings, ARC 15633, R&M 2935.
- c) Lamar, Multihrops Approach for Predicting Lifting Pressures Subsonic Flow, NASA TN D-4427.
- d) DeYoung, Span Loading Arbitrary Planforms Subsonic, NACA TR 921.
- e) Blackwell, Load Distributions Swept Wings with Pylon Plates, Subsonic, NASA TN D-5335.
- f) Van Dorm, Companion of Theoretical Methods Swept Wings, NACA TN 1476.
- g) Papas, Leading-Edge Swept Wings at Low Speeds, JAS Vol. 21, 10 '54

INFLUENCE OF SECTION STALL. In Chapter IV it was shown that the chordwise location of the flap separation has an important influence on the type and magnitude of stall. For instance, the flow can separate at the leading edge as a short or long bubble or separation can start at the trailing edge and increase in intensity until it covers the entire airfoil. The variation of lift with angle of attack and the type of stall are shown to be dependent on where separation takes place on the airfoil. In the case of swept wings, the stall is also effected by the chordwise location of separation.

In the case of swept wing the spanwise boundary layer transport does not influence the type of stall on the outboard sections of the wings from that expected in two dimensional flow corrected according to the cosine principle, figure 7. However, on the inboard sections the effects of the boundary layer improve conditions at the trailing edge sufficiently so the stall generally starts by leading edge separation. This is illustrated in figure 7. Outboard on the wing the suction in boundary layer also protects the trailing edge from separation, thus stall takes place first at the leading edge. A vortex is formed at the leading edge starting outboard on the wing in a manner similar to the vortex formed in conjunction with sharp leading edge stall discussed in Chapter IV. In spite of the leading edge separation where a sharp stall is expected the stall of the swept wing remains gradual with increasing angle of attack.

It has been shown (2,b) that a swept wing can be considered into three regions as shown on figure 7. In the center section panel region the chordwise loading due to incidence can be represented

$$C_D \approx [(1 - X)/x]^n \quad (3)$$

where x is the chordwise station being considered and $n = 1/2$ as in two dimensional flow. In this region the local slope of the lift curve is

$$dC_L / d\alpha = 2\pi \cos \Lambda \quad (4)$$

At the region toward the fuselage the chordwise loading varies according to equation with n equal to $1/2$ at the edge of region two to

$$n = 2(1 - 2\Lambda/\pi) \text{ (at root)}$$

at the wing root. The flow on the wing near the root is thus equivalent to section operating in a negatively cambered airflow. This leads to a new slope of the lift curve

$$dC_L / d\alpha = 2\pi(1 - 2\Lambda/\pi) \quad (5)$$

On the other hand in the region toward the tip the chordwise loading n varies from $1/2$ at the edge of region two to

$$n = 2(1 + 2\Lambda/\pi) \text{ (at tip)}$$

The above value of n lead to the equation

$$dC_L / d\alpha = 2\pi(1 + 2\Lambda/\pi) \text{ (at the tip)} \quad (6)$$

Thus, in contrast to the root the tip sections operate in a positively cambered flow. This effectively reduces the camber of the section and tends to lower the C_{Lmax} .

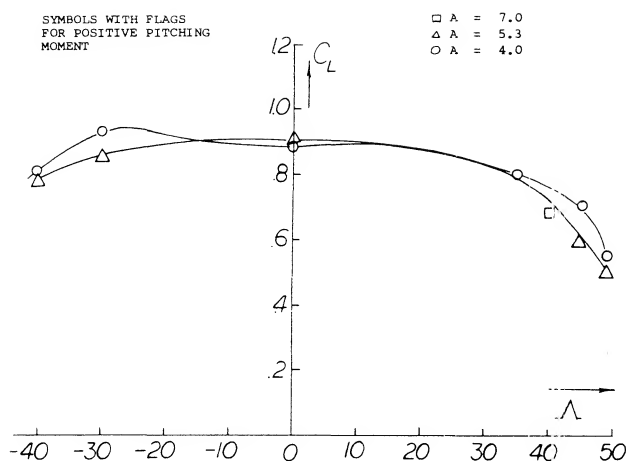
Unfortunately, the effect of the boundary layer flow is much stronger than the flow curvature induced at the root and tip of the wing in modifying the section maximum lift characteristics. In the middle sections of the wing panel however, the characteristics of two dimensional sections are a useful guide to determining the lower value of the section C_{LX} especially when leading edge stalling is to be encountered, Chapter IV.

ASPECT RATIO. The effect of the longer panels of high aspect ratio wings is to increase the flow of the boundary layer material in the outboard direction. This increased flow improves the effective boundary layer control at the inboard sections of the wing with a higher section maximum lift coefficient. As a consequence, the higher aspect ratio wings have an increased level of C_{LX} as shown on figure 3.

Although an increase in C_{LX} is obtained with higher aspect ratio swept wings, tip stalling can take place at a lower angle of attack or operating C_L . Thus, the effective or usable maximum lift of higher aspect ratio plane wings is lower. The operating C_L of the wing where stalling takes place can be identified by the sharp increase in drag or where C_D exceeds the value (figure 1)

$$C_D = C_L^2 / \pi AR e \quad (7)$$

A second way, other than actually measuring the individual section pressure distribution, of finding the onset of tip stalling is a break in the moment curve in the positive direction as shown on figure 1. Based on remaining below an operating C_L where stall takes place, simple swept wings have a lower usable value of C_L with increasing aspect ratio and also sweep angle. This is shown from the limited data given on figure 8.

Figure 8. Usable operating C_L for simple swept wings.

CRITICAL ANGLE OF SWEEP. In considering the usable operating C_L of swept wing, tip stalling is generally the major factor as this leads to the unstable pitch up moment. The combination of aspect ratio and angle of sweep influence the stall and thus the moment.

Thus, for any aspect ratio an angle of sweep can be identified above which a pitch up moment will be encountered. Based on experimental data (3) the range of aspect ratio and sweep angle for a stable pitching moment curve was established, figure 9.

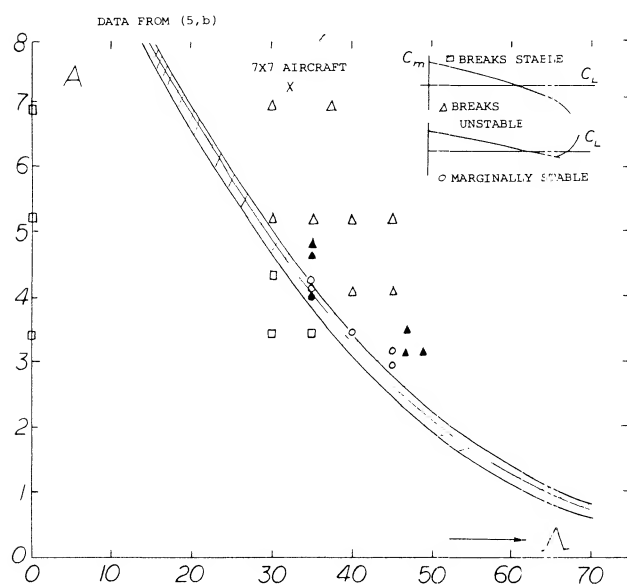


Figure 9. Critical angle of sweep for swept wings.

(3) Aspect Ratio Effects:

- a) Turner, Sweep and Aspect Ratio Effects on $C_{L\alpha}$, NACA TN 3468.
- b) Also (1,a) (1,e) (1,g).

For a given wing aspect ratio the critical angle of sweep can thus be determined from the data of figure 9. The curve of critical angle of sweep shows that smaller angles must be used with the higher aspect ratio wings. This is caused by the increase of boundary layer flow which increases the section $C_{L\alpha}$ in a greater proportion inboard than at the tip. Typical swept wing airliners have aspect ratios in the range of 7 to 8. Based on this aspect ratio the permissible angle of sweep given on figure 9 would be around 20° . Since an angle of yaw must be considered of at least 10° , say during a sharp turn, we are therefore left with a permissible sweep angle of only 10° . Modern airliners, for instance the 7X7 series, DC-X types, and fighter aircraft have sweep angles from 25 to 40 plus degrees. Thus, the simple swept wing must be modified for satisfactory operation.

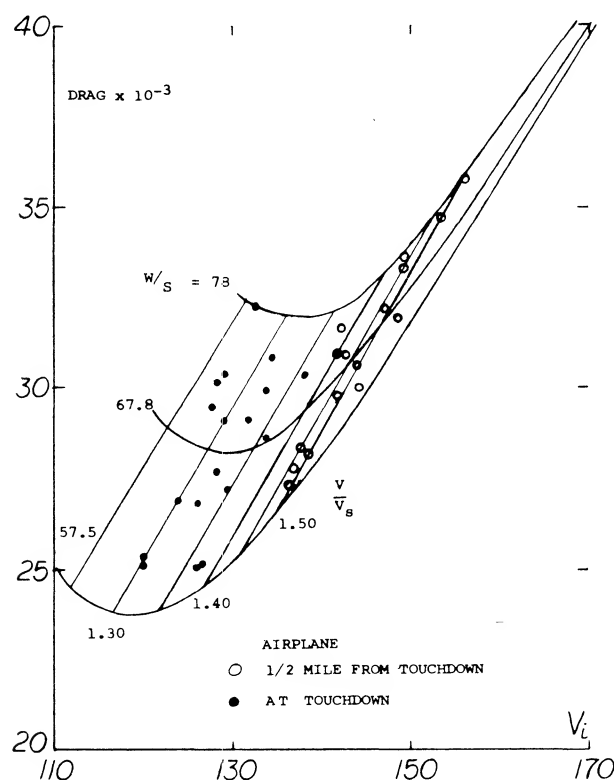


Figure 10. Drag characteristics of a typical jet transport airplane as a function of speed, wing loading and stall ratio (4).

DRAG AT MAXIMUM LIFT. For a typical swept wing airplane as the ratio of flight speed to the stall decreases, the drag also decreases (4) reaching a minimum at $V_0/V_S = 1.3$, figure 10. With a further decrease of speed, the drag then increases due to the increase of separation as stall is approached. This increase in drag with decreasing speed causes a speed instability condition that results in a loss of speed and lift unless corrective measures are used, such as a rapid increase of power. When landing in poor weather, the pitch up moment in combination with a smooth gradual stall and drag increase can produce a disaster, especially if the engine response time is low.

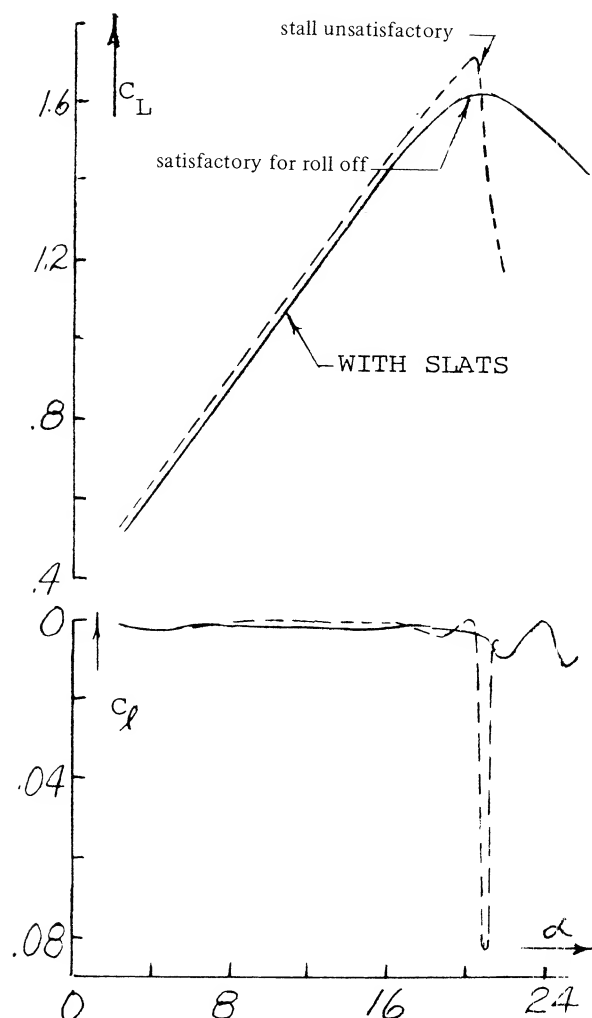


Figure 11. Stall characteristics of a swept wing airplane for acceptable and unacceptable roll.

LONGITUDINAL STABILITY. The pitch up moment due to stalling at the tip of a swept wing will result in an unstable aircraft. Thus, as noted in Chapter XI, instead of returning to a lower angle of attack due to a disturbance as with a stable configuration, the angle will become larger increasing the stall. For airplanes operating in the take off and landing range the wing designer has the choice of many different combinations of high lift devices to develop a stable configuration as noted in the section "Design for High C_{LX} ". To develop a wing with a negative pitching moment in those combinations of A and Λ exceeding the critical angle of sweep, figure 9, the load distribution must be changed so the inboard sections stall first. As noted later in this chapter and (5), the shifting in load to the inboard sections is impossible with some very high sweep angles and aspect ratio combinations. However, improvements of usable operating lift coefficients of swept wings can still be achieved. This can be done with leading edge extensions, slots and in some cases fences.

(4) Fischel, Low Speed Operation of Jet Transports, NASA M 3-1-59H.

LATERAL STABILITY. Separation at the wing tips and the associated stall is especially undesirable from lateral stability considerations. For instance, if the stall is especially sharp a small change in angle of attack on either wing of an aircraft can cause stall with an associate sharp roll off (6,a). This, as in straight taper wing aircraft, results in unsatisfactory flying qualities. Shown in figure 11 is the variation of lift for a wing with $\Lambda = 35^\circ$ that in unsatisfactory flying qualities. By using leading edge modification fences the shape of the curve was made more rounded and satisfactory lateral stability characteristics were obtained. Separation at the wing tip also causes the ailerons to become ineffective. In fact, it is noted that several transport aircraft have two pairs of ailerons, one at about 1/2 span, figure 35.

STALL OF SWEEPED FORWARD WINGS. As shown in Chapter XV, figure 8 swept forward wings stall near their center sections first, (1,g). This characteristic is desirable from control considerations as the outboard sections are free from separation and the lateral control devices remain effective. Thus, it can be expected that lateral stability and control will be retained with aircraft equipped with swept forward wings. It can also be hoped that the early flow separation, such as is shown on figure 12, will give the pilot a clear warning and provide a pitch down moment by the way of reduced downwash at the horizontal tail surface.

Although the stall of swept forward wing occurs first on the inboard station the unstable pitch up moment is still encountered after the wing sweep angle and aspect ratio exceeds the critical value shown on figure 9. A comparison of the moment curves for swept forward wing with $\Lambda = 46.6^\circ$ and 60° given on figure 12 confirms this. The separated flow encountered inboard with swept forward wings will also lead to buffet problems, especially at high speeds. The loading about the wings elastic axis also can possibly lead to structural problems, as the wing will tend to twist up in angles which could lead to aeroelastic problems.

- (5) Elimination of Pitch-Up Swept Wings:
 - a) Weil, Design Studies, NACA RM L53123c.
 - b) Furlong Summary of the Low-Speed Longitudinal Characteristics of Swept Wings, NACA TR 1339.
- (6) Lateral Characteristics of Sweep Wings near Stall:
 - a) Anderson, Roll-off in Low-speed Stalls on a 35° Swept Wing, also fences, NACA RM A53G22.
 - b) Goodson, Ailerons on Variation of Swept Wings, NACA RM L55L20.

FUSELAGE INTERFERENCE. Due to the increased wing loading of high speed swept wing airplanes the fuselage is often much larger in relation to the wing than some of the slower aircraft. Therefore, the fuselage interaction with the wings becomes an important factor in its effect on load distribution, C_{LX} , flow separation and buffet. At low Mach numbers, (7,a), during takeoff and landing the body adds to the lift in terms of the lift produced by itself and that induced on the wing. The induced lift disappears at C_{LX} but the body lift can increase the maximum by as much as 15% for the zero flapped condition, figure 13. The actual value of ΔC_{LX} will depend on the body size and the sweep angle, since the sweep angle will determine the angle at stall and the body lift will increase with an increase of angle of attack. At the low speed condition the body has only a small effect on the wing load distribution, especially near stall (7,a).

The overall effects of the fuselage on the lift coefficient where the pitch up moment becomes positive are small (7,b) even with large changes in shape and wing location. Also, changes in fuselage shape and wing location appeared to have little effect on the variation of pitch up moment as the stall is approached. The main influence of such changes on the stability of the aircraft was in yaw as discussed in Chapter XII.

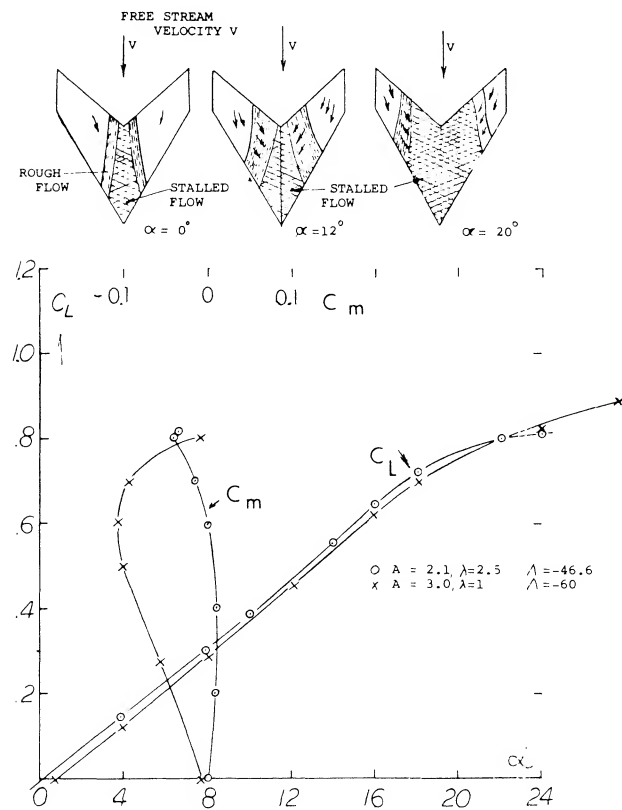


Figure 12. Swept forward wing lift, moment and stalling characteristics (1,g).

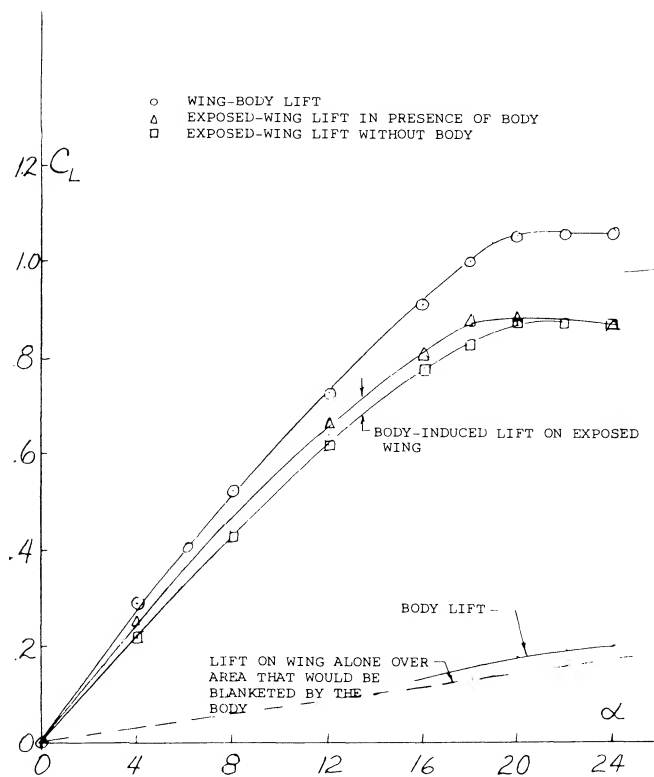
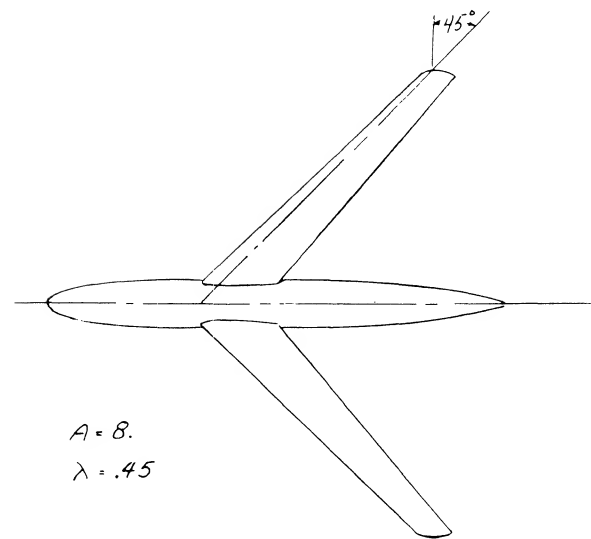


Figure 13. Division of wing and body lift.

The fuselage shape and contour at the wing junction has a large influence on the level of usable lift coefficients of a swept wing operating at high Mach numbers. Tests have indicated that with proper modification of the wing junction, using the methods of (7,c,d) important improvements in pitching moment characteristics, drag and slope of the lift curve can be obtained at high speeds. The largest effects of the change in contour occur at Mach numbers above the critical.

DYNAMIC STALL. In Chapter IV it was shown that the maximum lift of straight wings is influenced by the rate of change of the angle of attack. Tests (8) indicate that the rate of change of angle of attack also increases C_{LX} for swept wings. For $\Lambda = 35^\circ$ the increase of C_{LX} is larger than for a corresponding straight wing, figure 14. The hysteresis loop developed by straight wings, figure 28, Chapter IV, would also apply for swept wing.

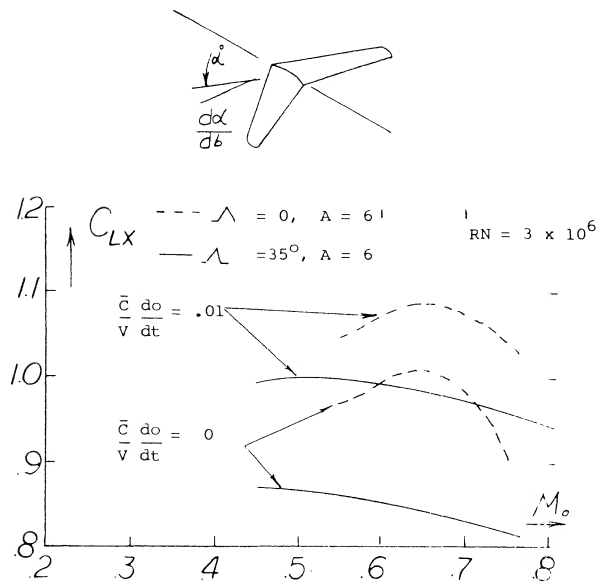


Figure 14. Dynamic stall effects for swept wings.

PREDICTION OF SWEEP WING STALL. In the design and analysis of swept back wings it is necessary to predict the wing operating C_L at which stall takes place. Such procedures are needed to find the conditions where wing section stall may induce a pitch up moment and the effects of wing modification used to delay stall. There are several methods of analysis (2,a,c,d,e) that have been developed for finding the load distribution of wings as a function of planform, twist, section camber and operating conditions. These theoretical methods are based on span loading and lifting surface theories and predict the results with good accuracy at conditions below C_{LX} . Thus, for instance (1,d) can be used to calculate the load distribution variation as a function of operating C_L for any swept back wing. If many calculations are required high speed computing machines are used with (1,c) or (1,e).

In Chapter XV it was shown that the pressure distribution could be accurately predicted on a swept wing section from two dimensional airfoil data. This is done based on the simple sweep theory which shows that a wing section normal to the quarter chord line has the same characteristics of a two dimensional wing if the conditions are based on a component of free stream velocity normal to the quarter chord line. This simple sweep theory appears to apply with good accuracy when operating below the stall angle. However, as noted in figure 7, the three dimensional flow improves C_{LX} to values much above those predicted used in two dimensional airfoil data. This is especially true on the inboard sections of the wing. Thus, if the procedure (9,a) for finding first occurrence of stall is based on the calculated load distribution of (1,c) and two dimensional data, the predicted value of C_{LX} will be much lower than measured. Since the improvement of C_{LX} of section data due to sweep cannot be predicted by theory it will be necessary to use the two dimensional data as given in Chapter IV to estimate where stalling first takes place. The section stall data should be for the Reynolds and Mach numbers based on the velocity component normal to the quarter chord line of the wing. Also, in accordance with the simple sweep theory the airfoil section is that normal to the wing quarter chord line.

An example of the load distribution for a swept wing is given on figure 15. Based on simple sweep theory the corresponding section stall is also shown. Based on these two plots the wing would be estimated to first stall at the semi span station $M = .68$. The boundary layer flow increases the C_{LX} as shown so that the actual first stall is located at $M = .79$.

The calculated lift coefficient where section stall is first encountered on a swept wing is lower than measured by approximately .01 as indicated in (9,a) or about 20%. The trend with changes in sweep angle and aspect ratio appears to be good so that the effects of changes can be expected to be determined with reasonable accuracy.

(7) Fuselage Interference:

- a) Martina, Body Effects on Spanwise Load, NACA TN 3730.
- b) King, Effects of Cross-Section Shape and Wing Height, NACA RM L55J25.
- c) Kudemann, Design of Wing Function for Swept Wing at High Mach Numbers, RAE 2219.
- d) Weber, Design of Wing Function, cont., Addendum RAE 2219.
- e) McDevitt, Body-contouring at Root Sweptback Wings, NACA TN 3672.

(8) Dynamic Stall:

- a) Conner, Effect of Angle of Attack Rate on Max. Lift, NASA CR 321.
- b) Rainey, Stall-Flutter Thin Wings, NACA TN 3622.

(9) Review Reports:

- a) Harper, Stall Characteristics Swept Wings, NASA TN D2373.
- b) Toll, Longitudinal Characteristics of Wings, NACA RM L53121b.

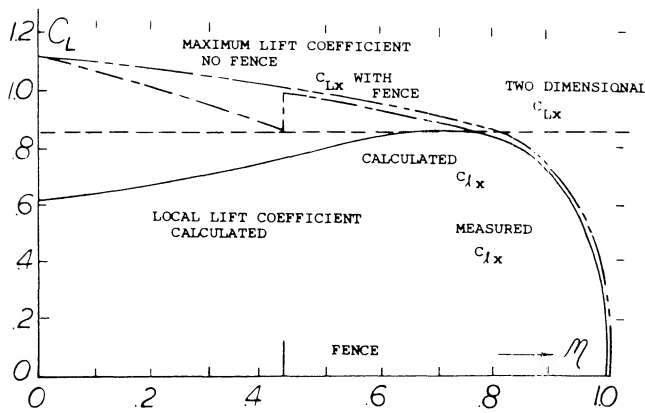


Figure 15. Comparison of calculated lift distribution for location on onset of stall and the effects of a fence.

Although the method given above is a good approximation for finding the station where stall first occurs it does not give satisfactory results for estimating the spanwise load distribution at high angles. This is due to the large increase of lift coefficient, especially on the inboard sections as shown on figure 7. For wings with $\Lambda = 45^\circ$ analysis of (10,b) indicates the load distribution at high angles can be approximated by the equation

$$C_n = C_n(\eta = .5) \sqrt{\frac{15 - (50 - \alpha)\eta'}{15 + (50 - \alpha)\eta'}} \quad (8)$$

where C_n = The airfoil normal force coefficient.
 α = Wing angle of attack.
 η' = Semi span distance from mid span = .5, η' is minus inboard of $\eta = .5$ and plus outboard.

With the equation 8 and the distribution function shown on figure 16 an approximation of the load distribution on the wing operating at high angles of attack can be found for a known value of C_n . The distribution function of

figure 16 was set up for $\Lambda = 45^\circ$ and strictly applies only for wings with this angle; however, it is believed that it will be suitable for wings with sweep angles of 35 to 50 degrees.

2. SWEEP WING MODIFICATIONS FOR STALL.

From the previous discussion of the characteristics of simple swept wings operating at high angles of attack, it is apparent that changes are needed to prevent tip stall and the positive pitching moment prior to and after the development of C_{Lx} . The modification should not lead to an increase in drag near stall nor should decrease the lift drag ratio of the design condition or spoil the other desirable qualities of the wing.

Modifications to improve stall and pitching moment are needed for swept wings operating at the take off and landing condition and at high speeds. At take off and landing the effects of flaps, slats and other leading edge devices must be considered. During high speed operation the drag of such devices is high so only clean wings with low drag characteristics are used.

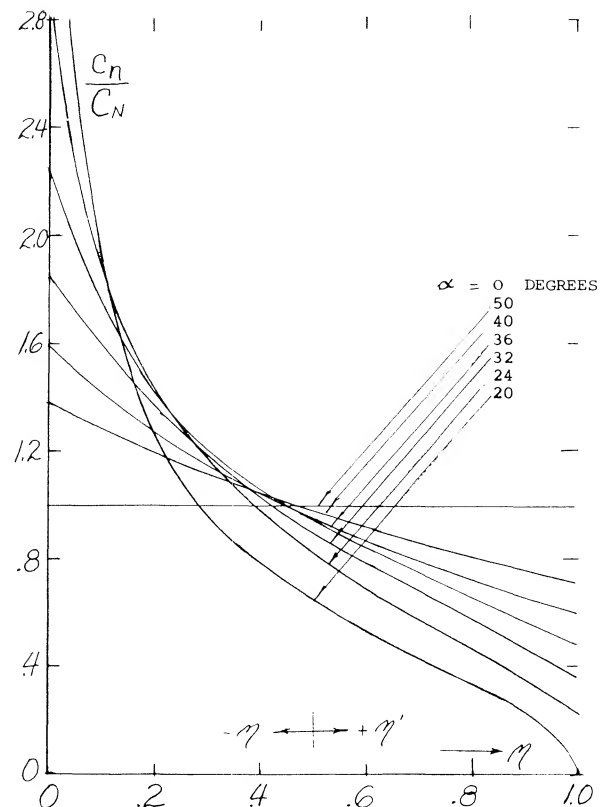


Figure 16. Swept wing distribution function $\Lambda = 45^\circ$.

- (10) Spanwise Load and Section Lift Swept Wings:
- Hunton, Section Characteristics of Two 45° Swept Wings, A = 6, NACA TN 3008.
 - Axelson and Haacker, A 45° Swept Wing with Body Combinations, NASA Memo 1-18-59A.
 - Graham, Low-speed Tests 45° Swept Wing, A = 3, R to 4.8 x 10, NACA RM L51H13, also TR 1208.
 - Hunton and James, Use of Two Dimensional Data in Predicting Loading with Flaps, etc., NACA TN 3040.
 - Woodward, Swept Back Wing With Constant C_{Lx} , $\Lambda = 35^\circ$, RAE TR 71050.

TWIST AND CAMBER MODIFICATION. In the case of straight tapered wings it was shown in Chapter IV that the undesirable tip stalling could be eliminated by changing the load distribution on the wing. This change was made with tapered wings by reducing the angle of attack at the tip, "wash out". A similar change could have been made to make the wing stall inboard by increasing the section camber or the wing chord on the outboard stations. In the case of straight wings a relatively simple change in load distribution will correct the tip stalling problem.

With swept wings, especially those with high aspect ratio and sweep angle, such corrections in load distribution do not necessarily eliminate tip stalling and the corresponding positive pitching moment. For instance in the case of a 45° swept aspect ratio 6 wing with a $\Lambda = .5$, an increase of camber to $C_{L\alpha} = .8$ and 10 degrees of wash out did not eliminate tip stalling (10,a). As shown on figure 17, this highly modified wing still has the undesirable positive pitching moment at stall.

The large increase in $C_{L\alpha}$ on the inboard stations due to the boundary layer flow makes it extremely difficult to correct tip stalling with the application of twist and camber. As noted on figure 7, $C_{L\alpha}$ is 50% above the value based on section data at the .545 wing station. At the tip stations however, the $C_{L\alpha}$ is nearly equal to the value expected from section data. To make the wing stall inboard first, large changes in the spanwise distribution

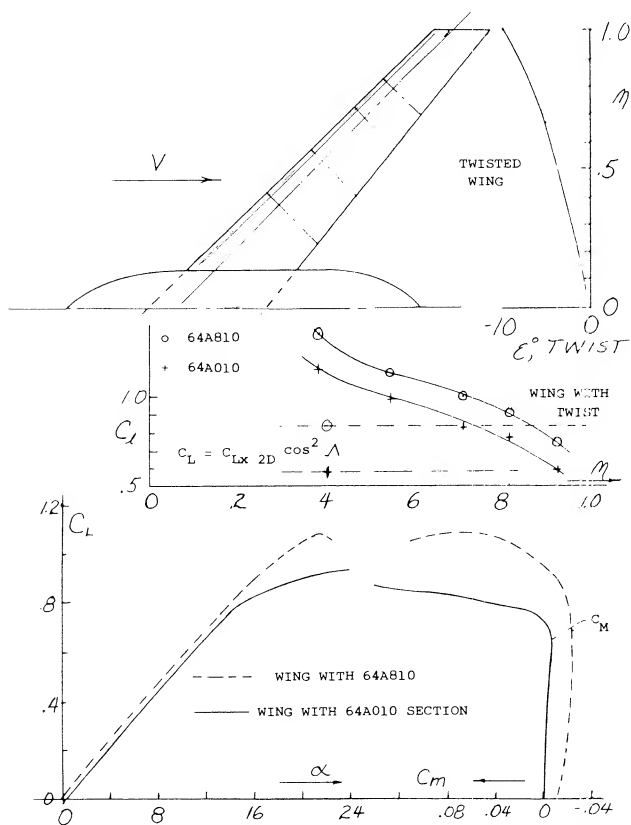


Figure 17. Camber and washout changes to improve usable operating lift coefficient (1,a).

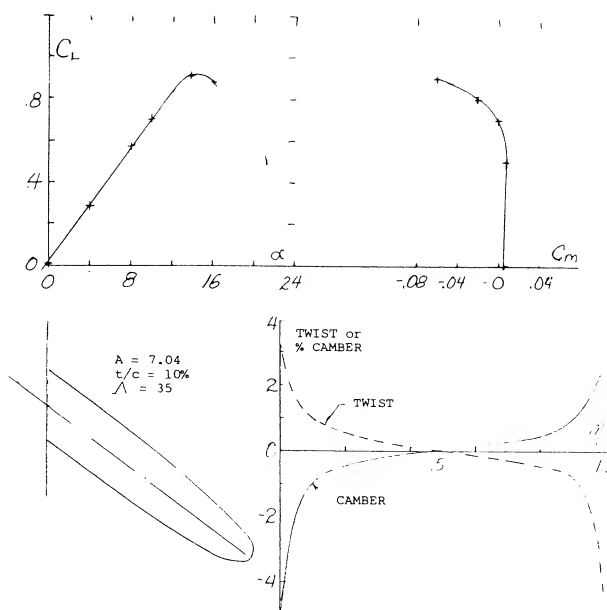


Figure 18. Lift and pitching moment characteristics of a 35° swept wing designed for constant $C_L = .8$ without auxiliary devices (10,e).

angle or camber are required and the changes necessary will increase with aspect ratio and sweep angle. The large increase in camber and angle outboard will be undesirable from drag consideration, thus it may be desirable to increase the taper and so reduce the tip chord to obtain the desired loading.

A design study and experimental program (10,e) to investigate the performance of a wing with a constant spanwise pressure near $C_{L\alpha}$ was conducted to determine if the local stall could be made to occur inboard. The wing investigated had a sweep angle, $\Lambda = 35^\circ$, $A = 7.04$ and $t/c = 10\%$. The twist and camber distribution used to obtain a constant C_L near maximum lift is shown on figure 18. It should be noted that the wing has an extensive twist and camber change from root to tip, including the use of negative camber inboard.

The tests did indicate that the operating C_L was constant across the span near the stall angle taking into account Reynolds number and local flow problems at the wing root. The test data, figure 18, however, indicated that as the wing stalls a strong pitch up moment is encountered. Although the pitch up moment would be expected for a similar simple swept wing, the modification of camber, chord and twist should have been sufficient to give the desired negative pitching moment. The boundary layer flow and detailed vortex distribution of the swept wing must change the detailed section pressure distribution to develop the positive pitching moment. Since large variations of twist, camber and chord appear to only partially improve the characteristics of a swept wing, other devices must be employed to achieve the desired results.

BOUNDARY LAYER FENCES. In the earliest days of propeller-driven airplanes the engine nacelles usually in mid-wing position (and in the slipstreams) may have prevented any spanwise boundary layer transport. In single-engine airplanes and in all modern configurations where the jet engines are mounted, whether below the wing or behind the wing at the sides of the fuselage, the boundary layer transport described previously can be reduced by fences (thin plates) placed on the upper wing surface. The fences may be used across the entire wing chord or may cover only the leading or trailing edges. The use of wing fences is to effectively dam the boundary layer air and to direct it back on the wing in the direction of flow so that the effect of the inboard section is not felt by the outboard section.

The use of fences for control of the boundary layer on wings has been investigated for many different combinations of sweep and aspect ratio. For instance, on a wing with 40° sweep and $A = 7$ (11,a) full chord streamwise fences were tested along with various other configurations. In general the usable operating C_L was increased before an unstable moment was encountered, but even with the largest number of fences the pitch up moment was not eliminated, figure 19. The fences tended to increase the wing L/D at the higher lift coefficients but as might be expected reduced the L/D at low C_L . A reduction in size and number appeared to reduce the usable operating C_L (11,c). The lack of success of fences for eliminating the adverse pitching moment can be attributed to their localized action. For instance, consider the variation of spanwise loading and section maximum lift coefficient as illustrated in figure 15. The section C_{Lx} decreases toward the tip because of the spanwise flow of boundary layer. With the addition of a fence, as shown, the action of the spanwise flow is decreased locally with the result that locally the value of C_{Lx} is equal to the two dimensional value. However the boundary layer action again develops outboard of the fence in this case, it has little effect on the overall value of C_{Lx} for the wing. For this reason, except in a few specialized cases, the use of fences will have limited success.

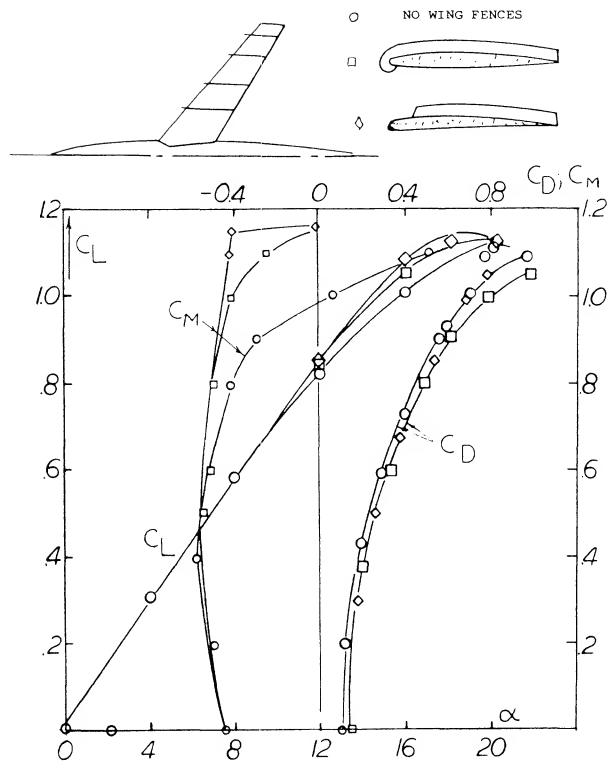


Figure 19. Effect of wing fences on the longitudinal stability of a 40° swept wing fuselage combination.

INVERSE TAPER. A radical attempt at preventing wing-tip stalling is shown in figure 20. The chord increasing toward the wing tips is expected to prevent stalling simply by reducing the lift coefficient near the tips. In comparison to a conventional (tapered) wing comparable in aspect ratio and angle of sweep, it is seen that the lift curve slope is reduced. Assuming that the influence of the increased-length lateral edges may be cancelled by their rounded shape, we may conclude that the influence of lift distribution (loaded near the wing tips) is responsible for an increased average induced lift angle. As a matter of fact, when extrapolating the functions in figure 9 of Chapter III into the field of taper ratios above unity, we obtain for $\lambda = 1.6$, a correction ΔA in the order of -0.5 . Notwithstanding the considerable differences in aspect ratio and the angle of sweep, a similar value is found when evaluating the experimental slope in figure 20 within the range of small lift coefficients. As to stalling, that begins at $C_L = 0.4$ or 0.5 (as reported in (12,a) on the wing tips. This type of flow separation is also evident in the drag which increases rapidly to a level some 100% above that of the conventional swept wing, figure 8, Chapter XV. Note also, that the maximum lift coefficient (although for a different unidentified foil section) is appreciably reduced. In conclusion, increasing the chord outboard does not really help improve the characteristics of swept back wings.

(11) Effect of Wing Fences on Swept Wings:

- Dickson, Swept Airplanes With Fences, NACA RM A55C30a.
- Sutton, Sweptback Wing with Four-Digit Sections to $M = 0.92$, NACA RM A54L08.
- Bray, Fences on Longitudinal Stability, NACA RM A53F23.
- Sutton, Fuselage-Tail Combinations $\Lambda = 40, 45, 50$, NACA RM A57F06a.
- Hieser, Swept Wing with Nacelles, NACA TN 1709

(12) Taper Effects:

- Purser, Various Swept Shapes, NACA TN 2445.
- Polhamus, Airplane Configuration Effects on Static Stability, NACA RM L56A09a.

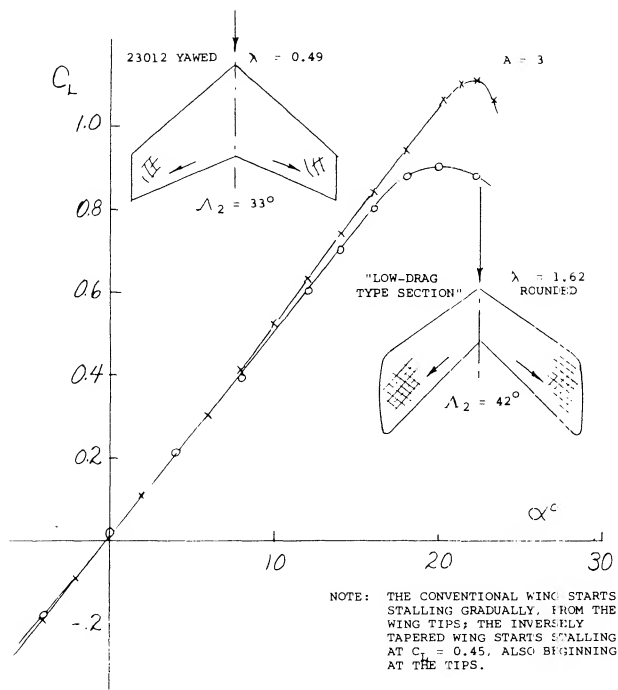


Figure 20. Lift of an inversely tapered swept wing, (12,a), in comparison to that of a conventional wing.

POSITIVE WING TAPER. In the previous section it was shown that the use of inverse taper to prevent tip stalling and thus reduce the pitch up moment is not too effective. Tests (12,b) on swept wings of $\Lambda = 45^\circ$ and $A = 4$ indicate that highly tapered wings are effective in delaying the operating C_L for pitch up even though the configuration of the wing is above the critical value given in figure 9. This is illustrated in figure 21, which shows that a taper ratio of 6 will delay the pitch up to an operating C_L of 0.6 compared with approximately 0.2 for an untapered wing. Figure 21 also indicates that with a low tail configuration the aircraft will have satisfactory longitudinal stability up to operating lift coefficients of 0.6 or slightly better.

LEADING EDGE EXTENSIONS. As previously discussed, wing design modifications to eliminate the tip stall and the associated pitch up moment by changing the load distribution have not been effective. To eliminate the pitch up moment and tip stalling, especially at higher speeds, requires modifications at the wing tip to delay the stall to values of C_{LX} over that occurring inboard. Since the sections generally used with swept wings have a low thickness ratio outboard separation and stalling first take place at the leading edge. To protect the leading edge from separation and stall, many different types of fixed leading extensions were designed and investigated (13) on swept wings. The modifications to the wing leading edge consisted of extensions of various span length, chord length, droop angle and leading edge radius.

A typical example of leading edge wing extension is shown on figure 22 for $\Lambda = 45^\circ$ and $A = 6$. As noted on figure 9, the wing would be expected to have a strong pitch up moment at high operating lift coefficients. By adding a 15% leading edge extension at the .55 semi span station, the pitch up moment was delayed to a $C_L = .95$ as compared to .6 for the basic wing. The use of larger extensions spanwise appeared to improve the pitching moment characteristic; however, if too much of the wing is covered by a leading edge extension, (15,a) the inboard sections of the wing again become too effective with the result that the tip will stall first. The correct length of the leading edge extension must be selected for each combination of sweep angle and aspect ratio.

In addition to improving the flow around the airfoil the leading edge extension will develop a vortex at its inboard end. This vortex, as shown in figure 23, is shed and flows chordwise effectively blocking the spanwise flow of the air in the boundary layer. This allows the outboard section to develop a higher C_{LX} in relation to the inboard sections and improves the effectiveness of the leading edge extension. Tests (13) have been made of slots in the wing to duplicate this vortex with limited success in improving the C_L where the pitching moment breaks in the stable direction.

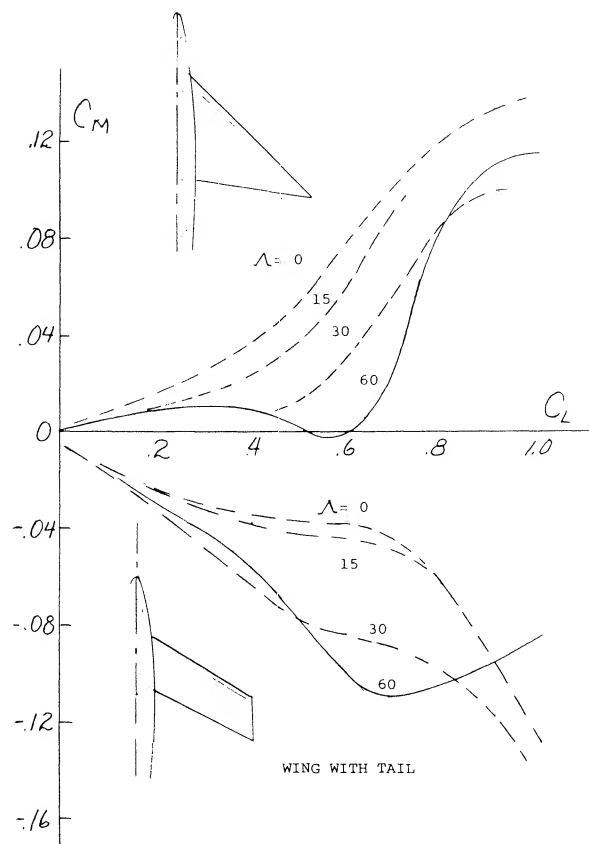


Figure 21. Taper ratio effect on wing pitching moment (12,b).

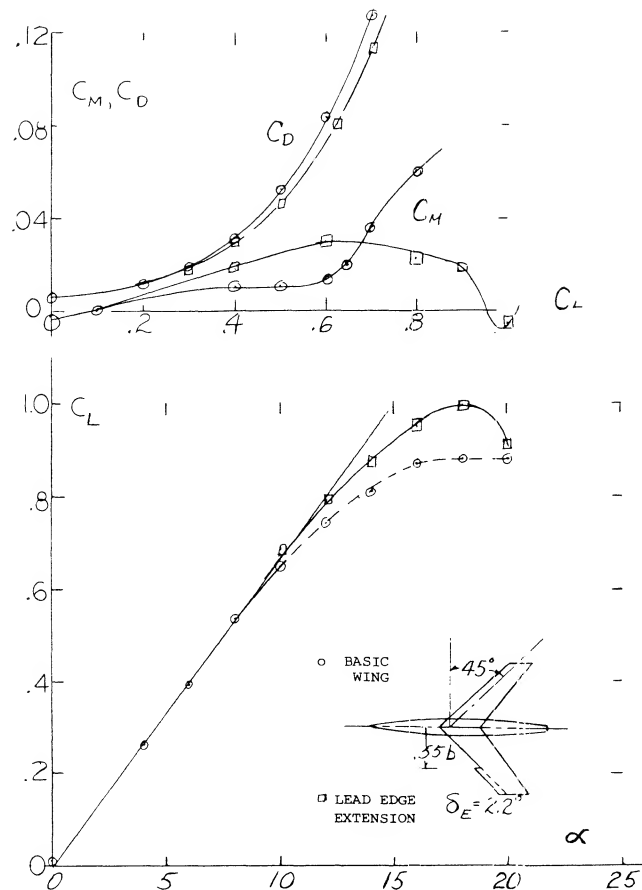


Figure 22. Delay of adverse pitching moment due to use of 15% leading edge extensions set at $E = 2.2$.

(13) Leading Edge Extensions Swept Wings:

- Kelley, H.N., Low Speed Tests $\Lambda = 45^\circ$, $A = 5$, NACA RM L55H19.
- Goodson and Few, Extension & Fence Tests, $\Lambda = 45^\circ$, $A = 4$, NACA RM L52K21.
- Whitcomb & Norton, Extension, Notches & Droop $\Lambda = 45^\circ$, NASA TN D834.
- Sutton, Extensions for $\Lambda = 40^\circ$, $A = 7$, NACA RM 55129.
- Liner, Martz, Three Extensions, 55, 65, 70%, $\Lambda = 45^\circ$, $A = 5$, NACA RM L53B02.
- Lowry & Schneiter, Slots and Extensions & A Variations, $\Lambda = 60^\circ$, NACA TN 1284.
- Demele, Inverse Taper Leading Edge Flap, $\Lambda = 45^\circ$, NASA TN D138.
- Weil & Morrison, Notches, Extension and Fences and Fences, $\Lambda = 45^\circ$, $A = 4$, NACA RM L53J27Ja.
- Goodson, Leading Edge Chord Extensions, $A = 4$, $\Lambda = 40^\circ$, NACA RM L52118.
- Spreeman, Chord Extensions, Flaps & Fences, $M = .4$ to $.9$, $A = 4$, $\Lambda = 45^\circ$, NACA TN 3845.
- West, Chord Extension, Fences, $M = .4$ to 1.03 , $A = 4$, $\Lambda = 45^\circ$, NACA RM L53B02.
- Furlong, A Summary Low Speed Longitudinal Characteristics - Swept Wing, NACA TR 1339.
- TN 3040.

As a result of the use of slats and leading edge extensions the critical angle of sweep is improved as a function of aspect ratio, as illustrated on figure 24. Thus based on the available test data stable pitching moments can be obtained at higher angles of sweep or aspect ratios with the proper choice of leading edge devices. Two dimensional airfoil characteristics and the methods described previously can be used to find the size of the extensions needed. In general, the size becomes critical with increasing sweep angles.

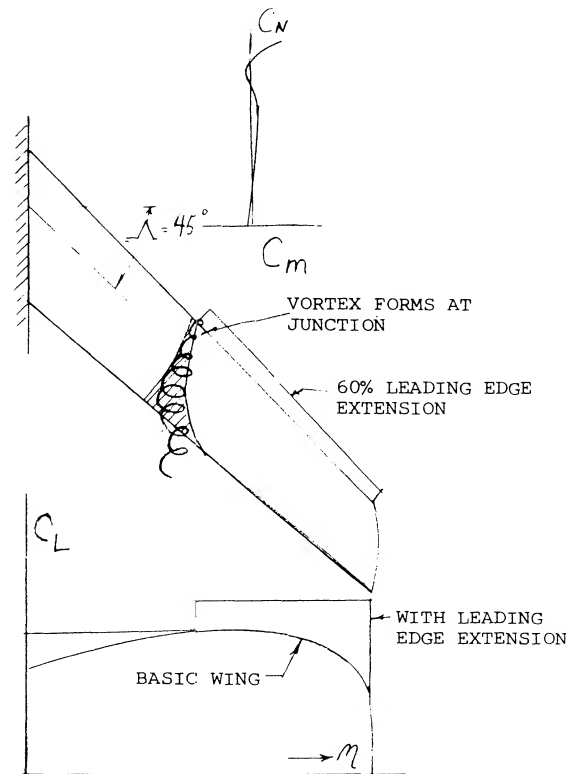


Figure 23. Formation of vortex at leading edge extension junction blocking boundary layer (9,a).

(14) Compressibility Effects on Maximum Lift:

- Hall, Swept Wing Flow Pattern, $M = .6$ to 1.6 , ARC R&M 3271.
- Mayers, Transonic Buffet 60° Swept Wing AIAA Paper 69-793.
- Sutton, Buffet Investigation of an Airplane Configuration, NACA RM A57F06a.
- Ray, Buffet Characteristics Swept Wings, NASA TN D5805.
- Turner, Lift, Drag and Pitching for Swept Wing in Transonic Range, NACA Transonic Conference 1949.
- Whitcomb, Bodies added on a wing for high speed. NACA TN 4293

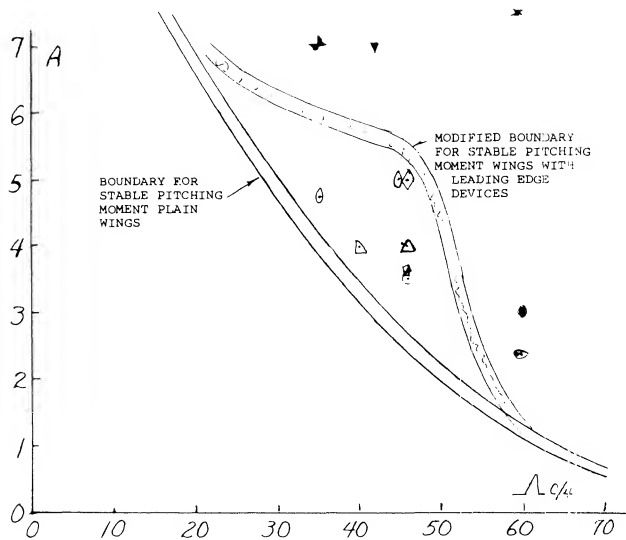


Figure 24. Critical angle of sweep as modified by leading edge devices.

3. COMPRESSIBILITY EFFECTS.

As the operating Mach number increases and exceeds the critical, the influence of compressibility becomes of major importance in the design and operation of swept wings. In addition to having a large influence on the drag, the effects of compressibility effect the usable operating C_L prior to buffet, maximum lift, the longitudinal pitching moment and stability. The variation of the maximum lift coefficient with Mach number on figure 25 illustrates compressibility effects for a range of sweep angles of plain wings with an aspect ratio of 4. The effects of compressibility are also influenced by the nose radius, taper ratio, aspect ratio and load distribution. These parameters influence the location of shock waves and the corresponding areas of separation as a function of operating Mach number (14,e).

Flow at high Mach number. To illustrate the flow associated with swept wings at high Mach numbers as a function of the operating condition, the variation of the location of the vortices and the various shock waves formed on the wing are shown on figure 26. In the Mach number range below .85 it will be noted that with increasing angle of attack vortices are formed on the lead edge of the wing and tend to move inboard, leaving the tip stalled with separated flow at the high angles. At a Mach number of .95 a standing shock wave is first formed near the tip of the wing due to the local velocity exceeding $M = 1$. At this Mach number, the standing shock moves inboard with increasing angle of attack and again the leading edge vortex is formed. It behaves in the same manner as the vortex at the lower Mach numbers. At even higher Mach numbers in the neighborhood of 1.4, the standing shock wave is first formed near the trailing edge of the wing at

zero angle of attack. With increasing angles a shock is formed toward the lead edge of the wing. The lead edge vortex is formed aft this shock. With further increases in angle of attack the tip of the wing becomes highly ineffective, especially at the higher Mach numbers. The highly complex flow pattern discussed above from (14,a) is typical and influences the conditions where buffet takes place. The various regions of flow for a 53.5° swept wing of $A = 2.8$ and $\lambda = .333$ are given on figure 27.

BUFFETING. As a result of the shock waves and vortex flow separation, buffeting is encountered on swept wings in the transonic flow region. This unsteady flow limits the operating C_L to a so-called buffet limit. The limiting C_L is influenced by the aerodynamic parameters of the wing, sweep angle, section type, taper ratio, aspect ratio and load distribution. Light buffet generally coincides with the drag divergent Mach number where the first shock wave is formed. The critical pitch up lift coefficient is generally at C_L 's higher than those for the buffet boundary. This means that the pilot may be warned by structural vibrations prior to pitch up. As noted in (14,b) there are four different regions of the wing that must be considered for buffet effects:

- 1) The upper leading edge
- 2) The tip region
- 3) Downstream area influenced by leading edge vorticity
- 4) The trailing edge location.

These regions are identified on figure 27 as a function of angle of attack and Mach number. As a result of the combined effects in the above region of vortex formation and bursting along with the intersection of shock waves the C_L for buffet, C_{L_B} , can be severely reduced, especially with wings where $\Lambda > 50^\circ$.

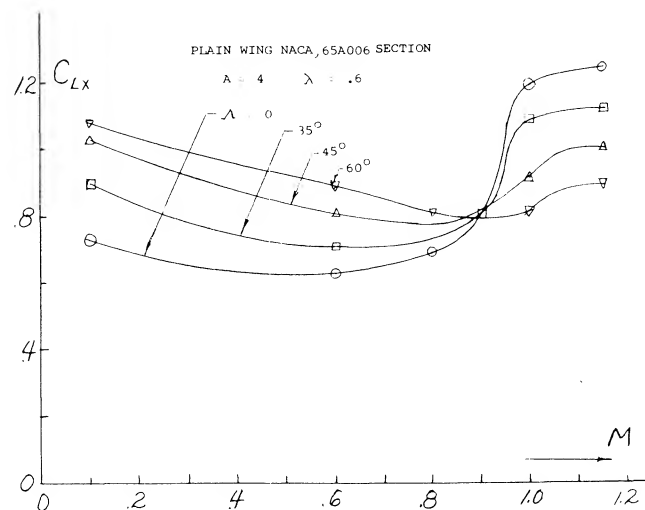


Figure 25. Maximum lift characteristics of plain aspect ratio for swept wings as influenced by compressibility (14,e).

The results of tests conducted to $M = .93$ indicated that for wings in the sweep range of 25 to 45° and aspect ratio 4 to 6 the highest buffet lift coefficient is obtained with the wing with the best aerodynamic efficiency. This is illustrated in figure 28.

When operating at transonic Mach numbers with swept wings of high aspect ratio the separation and associated buffet can be delayed to a higher speed with the addition of bodies on the upper surface of the wing (14,f). These bodies cause an actual reduction of drag as well as an improvement of the pitching moment characteristics of the configuration, figure 29. The bodies reduce the separation by eliminating the extensive cross flow in a manner similar to fences. Such bodies have been used on commercial transport aircraft with a reported improvement in cruising speed.

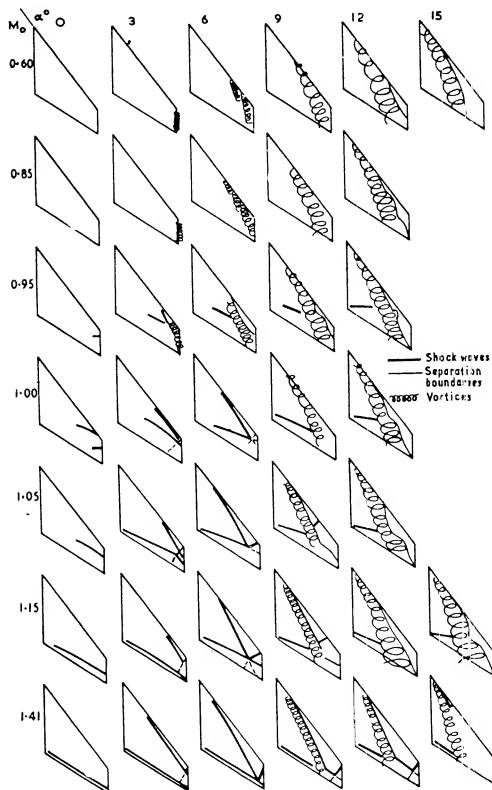


Figure 26. Variation of lead edge vortex separation shock waves and separated boundaries as a function of Mach number. Aspect Ratio = 2.8, Sweep Angle = 53.5° .

(15) Leading Edge Slats:

- Huntton, Slats and Flaps on a Swept Wing, Section Characteristics, NACA TN 3040.
- Naeseth, Double Slotted Flaps with a Leading Edge Slat $\Lambda = 35^\circ$, NASA D103.
- Adcock, Leading Edge Slots to Aircraft With Swept Wings, Vol. 1, Boundary Layer & Flow Control, Pergamon Press 1961.
- Olason, Design Philosophy Boeing 737 J of A. Nov-Dec 1966

NUMBERS INDICATE REGIONS OF:

- (1) ATTACHED FLOW, NO SHOCK WAVES.
- (2) SEPARATION AT THE LEADING EDGE FORMING A VORTEX.
- (3) FORWARD SHOCK WAVE ONLY, NO SEPARATION.
- (4) FORWARD SHOCK WAVE ONLY, SEPARATION AT THE SHOCK FORMING A VORTEX.
- (5) INITIAL TIP SHOCK WAVE, WITH OR WITHOUT A REAR SHOCK.
- (6) FORWARD AND REAR SHOCK WAVES PRESENT, NO SEPARATION.
- (7) FORWARD AND REAR SHOCK WAVES PRESENT, SEPARATION BEHIND THE FORWARD SHOCK FORMING A VORTEX.
- (8) REAR SHOCK WAVE ONLY, LEADING-EDGE SEPARATION FORMING A VORTEX.
- (9) FORWARD AND REAR SHOCK WAVES INTERSECTING ON THE WING WITH A STRONG OUTBOARD SHOCK WAVE CAUSING SEPARATION.
- (10) FORWARD AND REAR SHOCK WAVES INTERSECTING AT THE TRAILING EDGE.
- (11) REAR SHOCK WAVE ONLY, NO SEPARATION.

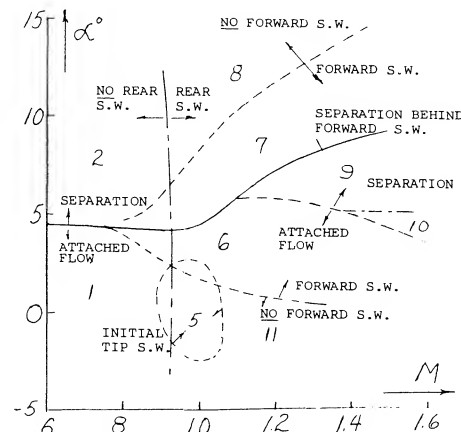


Figure 27. Regions in which shock and/or separation occur on a complete wing. Aspect Ratio = 2.8, Sweep Angle = 53.5° .

4. HIGH LIFT DEVICES FOR SWEEPED WINGS.

The use of swept wings on transport aircraft has led to the development and application of highly sophisticated devices to increase the lift and reduce the adverse pitching moment at the takeoff and landing conditions. With the first generation of swept wing jet airplanes the devices to increase lift were relatively simple. The need to increase the payload while maintaining the same airport restrictions resulted in the use of more advanced high lift devices. The STOL transport with field length requirements of 3,000 feet or less force the use of even more advanced devices for increasing lift of swept wing aircraft.

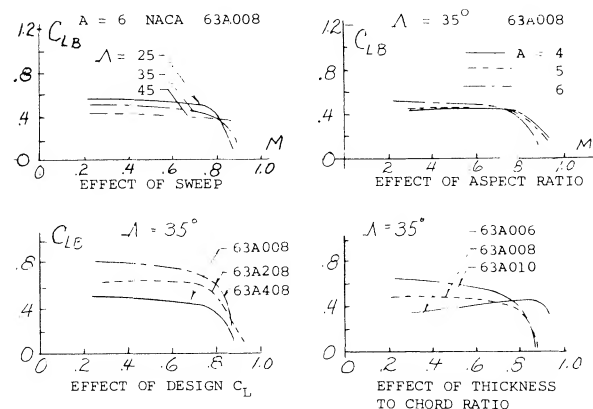


Figure 28. Effect of wing parameters on operating lift coefficient for buffet, C_{LB} .

WING LOADING. The need for high lift devices on swept wing is apparent when the wing loading is examined. Fighter airplanes typical of World War II could be pulled out of a dive (at well below the speed of sound) with 10 “g’s” (if needed) without stalling. Their wing loading was in the order of 40 lb/ft² (below 200 kg/m²). By comparison, a modern transport airplane may have wing loadings of 100 lb/ft² (more than 400 kg/m²). For the same landing speed, the airliner should thus have a maximum lift coefficient, 100/40 = 2.5, or at least two times as high as that of the assumed fighter. This means that C_{LX} should be in the neighborhood of 2.7 to 3. When operating at these high lifts the induced drag coefficient may then be four times as high, and the total D/L at C_{LX} possibly three times as high. This means roughly a sinking speed also three times as high as that during the landing approach of the fighter some 20 years earlier.

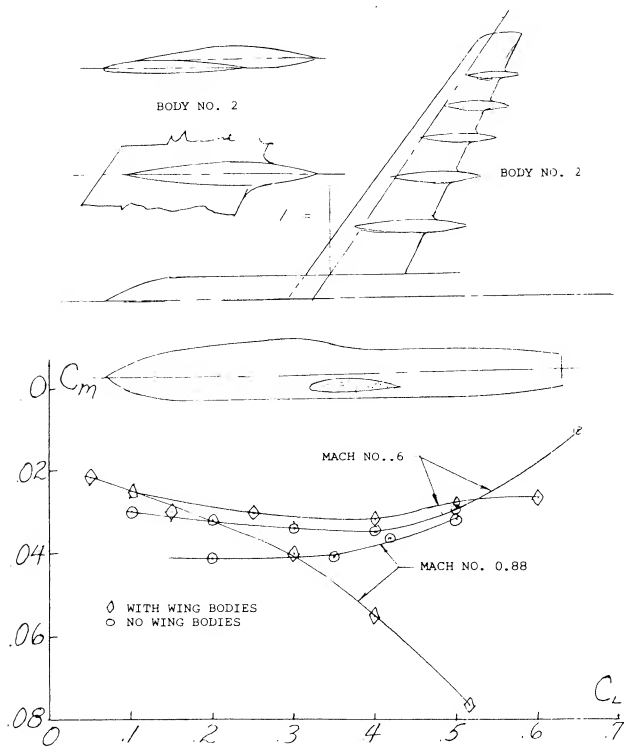


Figure 29. Use of special bodies on a wing to improve lift moment characteristics at high subsonic speeds.

DESIGN FOR HIGH C_{LX} . Due to the high wing loading the design of auxiliary devices for high lift on swept wing requires consideration of the drag and pitching moments characteristics as well as the overall complication of the mechanism. Because the flap and slat systems become more complex as the requirement for C_{LX} is increased it becomes a major design problem to develop the simplest and most effective total system. This is apparent when one observes the wing during the take off and landing conditions when it appears to come apart in all directions as a result of deploying the various high lift flaps and slats. The choice and location of the high lift devices is dependent on the geometry of the wing which is determined based on the high speed cruising requirements.

To determine the best configuration of the multi-element airfoils, the lift requirements are established spanwise on the wing so that at each station two dimensional data can be applied. The data on the high lift characteristics of leading and trailing edge devices are given in Chapters V and VI. The combination of slats, leading and trailing edge flaps for a swept wing should be selected so that the stall first occurs inboard to provide a stable moment curve, a negative pitching moment, through the stall. The high lift devices should also be selected so that the drag is compatible with the engine thrust during take off and emergency landing conditions.

In addition to developing a wing with high lift and good pitching moment characteristics it is necessary to maintain minimum drag so that peak take off and landing performance can be obtained. This is necessary as the drag must be compatible with the engine thrust, especially during emergency conditions. To determine the best performance that can be obtained the lift drag ratio of the wing is found based on the drag coefficient from the equation

$$C_D = C_{D0} + C_L^2 / e \pi A \quad (9)$$

Where e is the span efficiency and C_{D0} is the drag coefficient at zero lift. Thus, for any wing the ideal or best lift drag ratio can be established as a function of C_L . The actual performance can then be compared to the ideal to determine where improvements are needed.

On figure 30 the ideal lift drag ratio for $A = 7$ compared with test data (17,a) of various combinations of flaps and leading edge devices. From such a study the best combinations of high lift devices can be found for the wing at any lift coefficient.

- (16) Leading Edge Flaps:
 - a) Griner, Lateral and Longitudinal Stability $\mathcal{A} = 47.7^\circ$, $A = 6$, NACA RM L53G09.
- (17) Trailing Edge Flaps:
 - a) Naeseth, Double Slotted Flaps – Swept Wing Transport, NASA TN D103.
 - b) Capone, Longitudinal Characteristics Subsonic Transport, NASA TN D5971.

Because of the boundary layer transport as influencing maximum lift, especially inboard, high lift devices must be very effective, especially with those used outboard. For instance as was shown on figure 7, the sectional lift coefficient is twice as high as the corrected two dimensional at the .383 station for a swept wing with $\Lambda = 45^\circ$ and $A = 6$, while at the tip maximum lift coefficients are nearly equal. Thus, to obtain the required characteristics of C_L and C_M large increases in C_{LX} are needed for the outboard sections if the entire wing is stalled at the same angle.

In (9,a) it was shown that leading edge devices covering as much as the outer 75% of a 35° swept wing would provide sufficient protection from stall to obtain a stable pitching moment. With $\Lambda = 45^\circ$ only one combination tested gave the required stable pitching moment while at $\Lambda = 60$ the moment remained unstable.

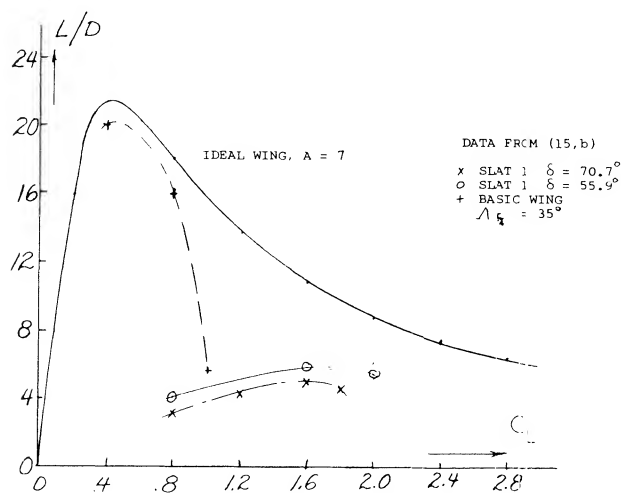


Figure 30. Maximum lift drag ratio for wings of a fixed aspect ratio in comparison with actual wings with high lift devices.

I

LEADING EDGE SLAT. The slat, figure 1, Chapter V, is used on many swept wing airplanes to prevent stall on the leading edge. Generally, the slats cover approximately 50% of the span and are installed in segments so their angle can be varied to get the desired stall protection. The slats increase C_{LX} of the airfoil with or without trailing edge flaps. The design and performance improvement of the slat as used on two dimensional sections is covered in Chapter VI. In the application of slats to a swept back wing to prevent the unstable pitch up moment while obtaining maximum lift, it is necessary to use as large a surface as possible (15,c). The tip chord of the slat should be as large as practical with 30% of the wing chord being considered a maximum. The slat should extend inboard as far as possible without causing the unfavorable pitch up moment as stall approaches. The slat should also be extended as far outboard as possible. However, it is not necessary to extend it outboard of the point shown on figure 31. The ends of the slats are generally cut off on a plane normal to the quarter chord point, also shown on

figure 31. Further details on the design of slats are given in Chapter VI, including load and moment data. In the selection of the slat maximum operating angle it is necessary to use a deflection that will cover the stagnation point. This requires a much larger angle than is normally covered in the literature, especially for wings with very high values of C_{LX} .

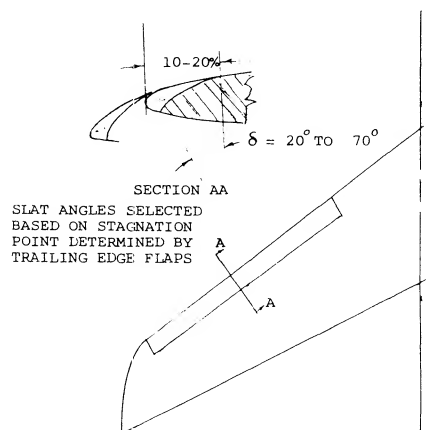


Figure 31. Slat geometry as installed on a swept wing to protect tip stall (15,c).

The choice of the slat position is a function of the position of the trailing edge flaps and is determined by the lift drag ratio of the system (15,d). Shown on figure 32 is the lift drag ratio as a function of operating C_L for the slats retracted at take off position and at landing for a typical transport airplane. The triple slotted trailing edge flaps are at the best angle for peak performance. It should be noted that with the flap set for the take off the slat is operating at approximately 45° with no slot, or in the sealed position. This is done to achieve peak performance, maximum L/D and C_{LX} .

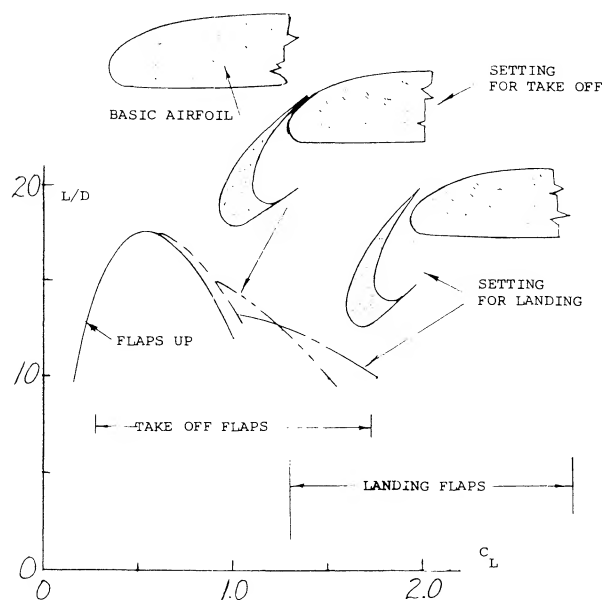


Figure 32. Effect of leading edge slat setting on take off and landing performance (15,d).

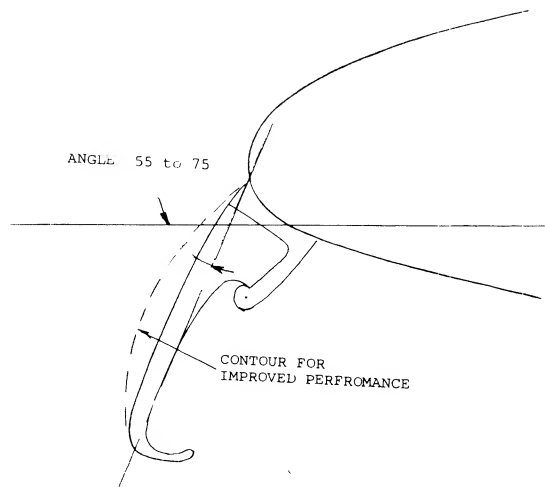


Figure 33. Leading edge flap geometry.

LEADING EDGE FLAPS. The leading edge flap is also used to prevent separation on the wing and increase C_{LX} . The device known as a Kruger flap may either swing out from the lower surface of the wing or may be part of the wing leading edge, sliding out as illustrated in figure 25 of Chapter VI. The performance improvement gained with the use of leading edge flaps is similar to that measured with slats (15) and is achieved by the effective increase of camber at the wing leading edge. The maximum lift and its corresponding angle of a swept wing is influenced by the length of the flap, its deflection angle and leading edge radius. Although the leading edge flap is generally flat, as shown in figure 33, improvements have been found with the use of curvature as is used on the 747 airplane. The performance characteristics of Kruger flaps can be estimated using the data of figure 26 Chapter VI.

As tested on a 47.5° swept (13,1) leading edge flaps have little effect on the C_{LX} when operating without trailing edge flap, the improvement in $C_L = .07$ maximum for the best combination of angle and area, figure 34. The largest improvement in performance is the lift drag ratio at C_{LX} which is important from take off and landing consideration. Although the increment of maximum lift due to the deployment of leading edge flaps is small when operating on a clean wing, large improvements in C_{LX} can be expected when it is operating in conjunction with trailing edge devices as shown in Chapter VI.

TRAILING EDGE FLAPS. The maximum lift of swept wings with leading slats and flaps is determined by the type and effective area of the trailing edge flap. Most sweep wing transport aircraft use either a double or triple slotted flap system which achieves levels of C_{LX} in two dimensional flow of approximately 3.3 or better while maintaining relatively low levels of angle of attack, which

is desirable at takeoff and landing. These levels transform into C_{LX} for the complete swept wing of 2.9 to 3.1. The details of the design of trailing edge flaps are given in Chapter V and include concepts of blowing to further increase maximum lift.

In the application of trailing edge flaps to swept wings the spanwise coverage is set up to provide as much area as possible within the constriction of nacelles and lateral control devices. After the type of flap has been chosen the deployment angles must be established for the takeoff and landing conditions. These angles are established based on the lift drag ratio (15,d) as illustrated on figure 32. Note that the trail edge flap angle is linked to the leading edge slat to control its angle. Since the lift drag ratio controls the takeoff and climb performance, the level of drag developed by the high lift devices is as important as C_{LX} .

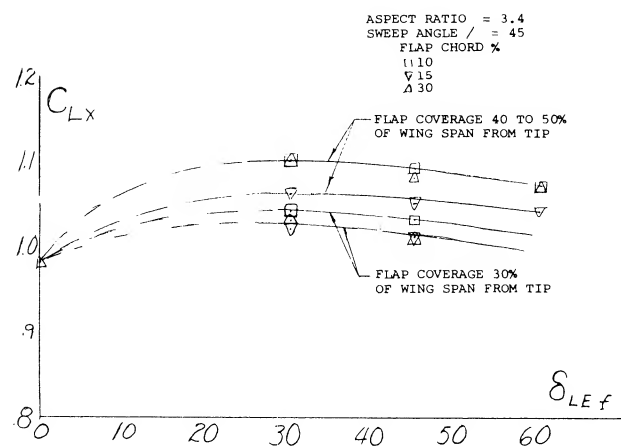


Figure 34. Effect of leading edge flaps on the maximum lift coefficient of swept wings.

TYPICAL HIGH LIFT DEVICES — SWEEPED WINGS. As indicated in the previous sections swept wings are designed using a series of leading edge slats, leading edge flaps and trailing edge devices. An example of how these are installed on a typical swept wing transport airplane is shown on figure 35. It will be noted that leading edge slats cover approximately 60% of the wing span and these are located outboard. The angle of the leading edge slats varies as a function of the percent deployment of the flap system. This is done to maintain the minimum drag necessary for best takeoff, climb, descent and landing performances. The leading edge slats are arranged in four segments with the maximum deployment angle on the outboard sections. This effectively gives the maximum lift increase outboard where it is needed. Leading edge flaps, which swing out from the under surface of the wing, are employed inboard to increase maximum lift during the final stage of the landing. The Kruger flaps are used on the inboard sections of the wing because of the large leading edge radius of the thicker sections of the wing.

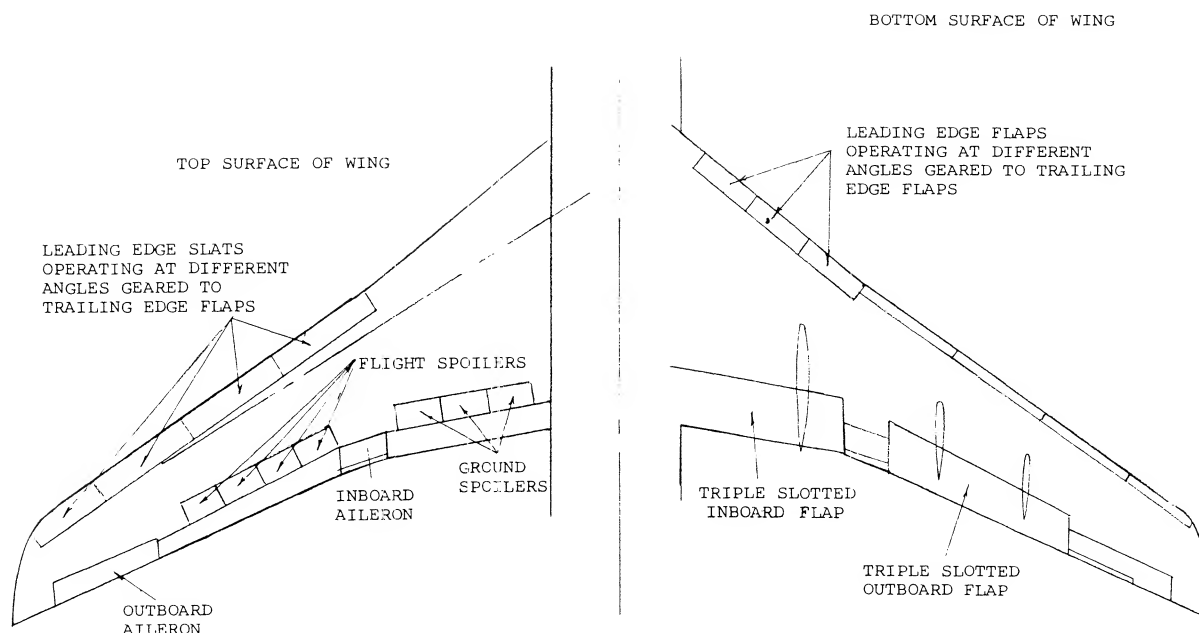


Figure 35. Typical transport aircraft wing configuration including slat and flap locations.

As shown on figure 35, the wing incorporates triple slotted flaps located inboard and outboard. Between the flaps an inboard aileron for lateral control, and on the outboard section another aileron is used. The triple slotted flaps operate at angles varying from 5° to 40° depending on the flight mode. The highest flap angle is useful just before touchdown. Also employed on the wings are flight and ground spoilers. The flight spoilers are used to increase the drag during descent to limit air speed and are located just about the outboard flaps. The ground spoilers, located above the inboard trailing edge flap, are used to kill the lift on touchdown to provide improved braking forces.

The wing described is typical for that found on aircraft introduced in the 1960's. Later transport aircraft use even more complicated devices, as the maximum lift during both take off and landing is extremely important with regard to the economics of swept wing aircraft. For instance, the Kruger flap is curved during its deployment as shown on figure 33. With the introduction of STOL aircraft the devices will become even more complicated and extensive and will incorporate all the concepts discussed in Chapters V and VI.

5. DEEP STALL.

The advent of the swept wing transport aircraft with aft "T-TAILS" and aft mounted nacelles has led to a number of fatalities that stem from the aircraft entering a region known as "deep stall". The first major accident from deep stall occurred during a test flight of a twin engine swept wing T-TAIL airplane while determining its stall characteristics.

Basic Cause. The basic cause of deep stall is the unstable pitching moment generated by the wing when operating at high lift coefficients, (18). This moment tends to drive the airplane to high angles of attack unless corrective action is undertaken. Since swept wing aircraft stall at very high angles of attack, it is possible for the airplane to be at a very high angle. In this condition the separated flow from the wing and nacelles, (18,a), blanket the horizontal tail with low energy air making it an ineffective control, as illustrated on figure 36. The separated wing flow reduces the maximum available nose-down pitching moment, figure 37, so that once the airplane exceeds an angle of attack of 40° the airplane is locked in a deep stall condition. When in this condition the drag is very high, due to the separated flow, making it impossible to add enough thrust to fly the airplane out of this condition. Lateral controls are also ineffective due to stalling at the wing tips.

Deep Stall Prevention. Since an airplane can always enter a stall in the event of bad weather or other emergencies, the design must be changed to eliminate the problems discussed above.

There are several ways in which this can be accomplished and these have been discussed in previous sections of this chapter. Basically, the wing and wing flap systems must be designed to eliminate nacelles which leads to the use of T-TAILS, the strategic location of wing fences can be used with moderately swept wings, such as the early DC-9s. These fences induce a vortex over the horizontal tail which energizes the flow and maintains effective controls (18,f). Other methods of eliminating the blanketing of the horizontal tail is by the strategic location of the nacelles with respect to the fuselage.

Since the down wash produced by the center section of the wing can impinge on a high T-TAIL at the deep stall condition, some aircraft have been designed with a low horizontal tail of conventional types which remains effective at high angles of attack. Thus, effectiveness is obtained because the lower tail operates in air that is not affected by the wing wake. The low tail requires that the engines be placed elsewhere on the aircraft, which can also lead to other problems.

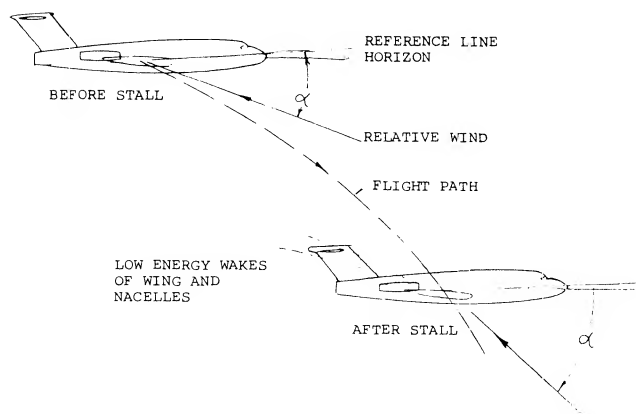


Figure 36. Aircraft entering deep stall condition.

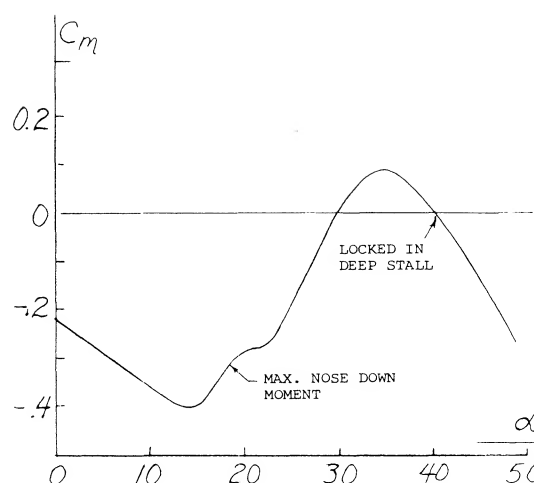


Figure 37. Typical variation of pitching moment before and after deep stall condition.

Mechanical Warning Devices. Since the stalling of swept wing aircraft can lead to extremely dangerous conditions, many mechanical devices have been investigated to warn the pilot of impending stall. These devices include both stick shakers and stick pushers. The stick shaker is arranged so that as stall is approaching the pilot is given warning by artificial shaking. With smaller aircraft, buffeting usually provides the necessary warning by shaking the stick, but with heavier aircraft with more advanced control systems, an artificial means is required. Another means of preventing the pilot from entering a stall is to effectively take the airplane out of his hands with a “stick pusher”. Such a device is used on several T-Tail swept wing transport aircraft as discussed in (18,e). There are, of course, many pros and cons with regard to the stick pusher configuration, but it has been selected as an effective safety device as the deep stall condition is such a disastrous maneuver.

(18) Deep Stall:

- a) Polhamus, Deep-Stall of T-Tail Aircraft Space and Aeronautics May 1966
- b) Powers, Deep-Stall Pitch-Up T-Tail Aircraft NASA TN D-3370
- c) Thomas, Longitudinal Behaviour Near-Stall AGARD Proc. No. 17
- d) Taylor, Stability of T-Tail Transports, J. Aircraft July 1966
- e) Davies, Deep Stalling, Flight International 18 March 1965
- f) Shevell, Design Features of the DC-9, J. Aircraft, Nov. 1966.

CHAPTER XVII

CHARACTERISTICS OF SMALL ASPECT RATIO WINGS

The flow around the tips of a low aspect ratio wing has a greater influence on the operating characteristics than for wings with $A = 5$ and above. Thus for low aspect ratio wings, the procedures and data given in Chapters III and XV do not apply. In this chapter low aspect ratio wings with rectangular, tapered and round planforms will be considered. Included will be wings with swept leading and trailing edges. Those classes of wings with delta type planforms will be considered in the next chapter. Small or low aspect ratio wings are defined as those with $A < 3$. Between $A = 3$ and 4 the aspect ratio is defined as the intermediate type.

The lift curve slope of low aspect ratio wings increases with angle of attack up to the stall angle rather than remaining linear as in the case of conventional wings. The increase in slope is a secondary effect that takes place over and above the basic circulation lift slope. In the treatment of low A wings, first the basic slope characteristics will be covered and then the secondary non linear effects.

1. BASIC LIFT CURVE SLOPE

When considering the theory for determining the performance of small aspect ratio wings the conventional lifting line concept can no longer be used because of the long chord to span ratio. Thus, the lift cannot be assumed to act on a line and must be spread out over the surface of the airfoil. Also, the influence of the lateral edges (a minor effect in larger aspect ratios) becomes more and more predominant as the aspect ratio approaches zero. As in the "straight wing" chapter, small aspect ratios rectangular lifting surfaces with sharp lateral edges are found to be very effective.

FLOW MECHANISM. The lifting-line theory given in Chapter III represents very well wings with aspect ratios above $A = 5$. In the case of a wing having a chord which is long in comparison to, or let's say longer than the span, wings with small aspect ratios, the trailing edge of the wing is exposed to a flow which has been deflected by the leading edge. In this manner the airfoil sections of any finite-span wing are placed within a field of streamlines which are curved in proportion to the permanent deflection (downwash) produced by their own lift. In other words, the chord and curvature are large so that the ratio of the chord in the radius of the stream curvature is also large. As a consequence, the airfoil sections lose lift, their sectional lift-curve slope is less than in two-dimensional flow and the lift angle of the average section is increased. Of course, the induced angle is also increased corresponding to C_L / A as in larger aspect ratios.

Lifting Surface. Several attempts (1) have been made to extend the lifting-line theory into the range of small aspect ratios or to replace it by so-called lifting-surface theory which accounts for the effect of the wing chord upon the lifting characteristics. One such theory is presented as follows: According to (1,a) the sections of rectangular low- A -ratio wings are aerodynamically in the same position as those in a two-dimensional cascade of airfoils. This analogy amounts to replacing the wing surface by a large number of lifting lines. Disregarding those near the leading edge, an individual airfoil or vane in that cascade develops less lift per unit of angle of attack than in free flow (that is, less than one airfoil alone) because of the downwash already produced by the other vanes located ahead. The average two-dimensional lift-curve slope is reduced accordingly to:

$$dC_L / d\alpha_2 = 2 \pi k a \quad (1)$$

where the subscript '2' indicates the two-dimensional sectional angle of attack required and the correction factor k is

$$k = (A/2a)\tanh(2a/a) \quad (2)$$

as plotted in figure 1.

SLENDER WINGS. Below $A = 1$ the factor as in figure 1 is simply

$$k = 0.5 A/a = 0.5 "A" \quad (3)$$

The resulting sectional "lift angle" in this range from equations 1 and 3 is

$$d\alpha_2/dC_L = 1/(\pi A) \quad (4)$$

This is also equal to the induced lift angle as in Chapter III. The geometric angle required is the combination of the induced and two-dimensional angle, and is

$$d\alpha/dC_L = 2/\pi(A) \text{ or } dC_L/d\alpha = 0.5\pi A \quad (5)$$

in radians

As shown in figure 2, the equations 4 and 5 indicate that below $A \approx 1$ with $k = 0.5 "A"$, $d\alpha_i/d\alpha = 0.5$ and/or $\alpha = 2\alpha_i$. The physical meaning of this result is that the final downwash angle $\epsilon = 2\alpha_i$ is reached before the trailing edge of such wings. Cutting off some piece from this edge does not, therefore, reduce the lift for a given span (considering only small values of the lift coefficient). This conclusion can be formulated by referring the lift coefficient to the "span area" b , rather

than to the conventional wing area. For $C_{Lb} = L/qb^2$ we thus obtain $dC_{Lb}/d\alpha = \pi/2 = \text{constant}$, which shows that the linear lift of such wings (with A between 0 and a maximum of 1, and at "small" lift coefficients) is independent of their chord. This fact is also the reason that the factor 'a', the slope of the lift curve, no longer appears in equation (5). If there are any viscous (boundary-layer) losses, there are many airfoils farther downstream in the cascade which can make up for those losses.

Another theoretical treatment (1,i) of low aspect ratio wings takes into account the flow about the lateral edges. This is done by considering the flow of the airfoil of the low aspect ratio wing as two dimensional when viewed in cross section perpendicular to the longitudinal axis. This flow superposed on the original stream leads to the same result as given in equation 5. The analysis was done by first considering pointed wings and showing that no lift is developed downstream of the section with the longest span. This is a necessary condition to satisfy the Kutta condition. Thus only the flow ahead of the section influences the lift at any station and not the flow downstream as in high aspect ratio wing theory. This concept also leads to the equation for the induced drag coefficient

$$C_{Di} = C_L \alpha / 2 \quad \text{in radians} \quad (6)$$

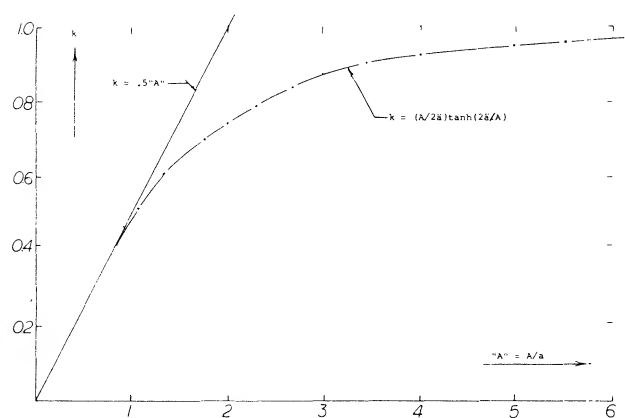


Figure 1. Weinig's theoretical function (1,a) indicating a correction to the section lift or the sectional angle of attack of the linear lift component of small aspect ratio wings. The approximation noted in the lower part of this illustration is perfect, down to $A = 1.5$.

- (1) Small-aspect-ratio linear wing theory:
 - (a) Weinig, Small Span, Lufo 1936, 405; NACA TM 1151.
 - (b) Weissinger, Yearbk D Lufo 1940 p I-145; ZWB Rpt FB 1553 (1942), see NACA TM 1553; Tech Berichte ZWB 1943; ZWB Rpt UM 1392 (1944); Math Nachrichten 1949 p 46; ZFW 1956 p 225; see NACA TM 1120 and TN 3476.
 - (c) Falkner, ARC RM 1910 (1943) and 2596 (1948).
 - (d) Jones, Correction for Chord, NACA TN 817 (1941).
 - (e) Lawrence, Journal Aeron Sciences 1951 p 683.
 - (f) Kuchemann, Straight & Swept, ARC RM 2935 (1956).
 - (g) Pistolesi, 3/4 Chord Principle, Conf Lil'thal Ges Lufo 1937 p 214; applied by Weissinger (1,b).
 - (h) Taylor, Lifting Surface, ARC RM 3051 (1957).
 - (i) Jones, Properties of Low-Aspect-Ratio Pointed Wings, NACA TR 835.

- (2) The function for sharp rectangular wings as described in the text, corresponds to $a = 0.9$ and $\Delta b/c = 0$; while that for "round" wings is obtained for $a = 0.9$, $(\Delta b/c) = -0.2$, and $\Delta b/c = -0.2/\sqrt[3]{1 + 2/A^2}$, while $\Delta b/b = (\Delta b/c)/A$ and $k = f("A")$ as in figure 1, where $A_i = A + \Delta b/c$. Note that the latter line ends below $A = 1$ in a constant lift ratio of 0.8 as against that of the sharp-rectangular wings.

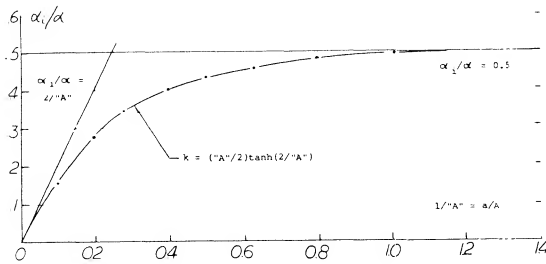


Figure 2. Ratio of induced angle of attack to geometric value, based on equations 4 and 5.

Lift-Curve Slope. Writing the angle in degrees equation (5) reads:

$$dC_L/d\alpha^\circ = \pi^2 A/360 = 0.0274 A. \quad (7)$$

This function is well confirmed in figure 3 by experimental results on thin rectangular plates. The presented points have carefully been determined as tangents of the lift-curve slopes in the vicinity of $C_L = 0$. In some cases (not plotted) these tangents are not readily available; the theory then serves to understand such experimental data. Up to about $A = 2.5$ lifting characteristics of sharp-edged rectangular wings can be approximated in form of their lift angle

$$d\alpha/dC_L = (36.5/A) + 2 \text{ A @ } A = 2.5 \quad (8)$$

Effective Span. We have explained in Chapter III how rounded lateral edges and "round" planforms reduce the effective aspect ratio of wings. In the range of low A 'ratios, this influence takes on the character of $A_i/A = \text{constant}$, for a given shape of the edges and/or the planform. Assuming that the effective span of a rectangular wing be reduced by $\Delta b/b$, the effective area is reduced to $S_e/S = (1 + \Delta b/b)$ and the effective aspect ratio A_i/A also to $(1 + \Delta b/b)$, where Δb has a negative value. Keeping the lift coefficient based upon the original area, we then find that the lift-curve slope of wings with aspect ratios below unity is reduced in proportion to $(1 + \Delta b/b)$, thus:

$$dC_L/d\alpha^\circ = (1 + \Delta b/b)^2 0.0274 A \quad (9)$$

Thus based on equation 8, half of the reduction is due to area and the other half due to aspect ratio. The experimental points in figure 3 indicate span reductions as follows:

- (3) Experimental characteristics in small aspect ratios:
 - (a) Voepel, AVA Rpt 1946, RAE Translation No. 276.
 - (b) Kuchemann, Collection Experimental Results from Various Sources in "Method for Load Distribution", ARC RM 2935 (1956); "complete" bibliography included.
 - (c) Gottingen, Rectangular, Erg AVA I (1921) & III (1927).
 - (d) Scholz, Forces and Pressures, Forschung Ing'Wesen 1949/50 p 85.
 - (e) Whicker, Control Surfaces, TMB Rpt 933 (1958).
 - (f) Weinstein, Planing Plate, NACA TN 2981 (1953).

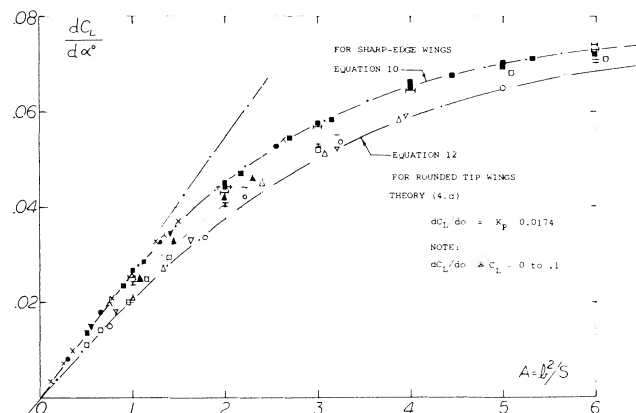
Plan form	Lateral Edges	$\Delta b/b$	$(1 + \Delta b/b)^2$
Rectangular	Sharp	zero	1.00
Elliptical	Sharp	-0.04	0.92
Rectangular	Round	-0.09	0.83
Rounded	Round	-0.12	0.78
Delta wing	Round	-0.12	0.78

A value of $(1 + \Delta b/b)^2 \approx (1 + 2 \Delta b/b) \approx 0.8$ has been used in figure 3 to obtain the lift-curve slope of "round" wings from experimental data below $A = 1$.

HIGHER ASPECT RATIOS. The hyperbolic tangent as in equation (2) is tabulated in mathematical or engineering handbooks. Up to an argument " x " = 6° , or = 0.1, $\tanh "x" = \sin "x"$. The hyperbolic tanh function reaches unity at " x " = 360° , or more precisely at " x " = ∞ . As the factor k varies between (0.5 " A ") at A below unity, and 1.0 at $A \rightarrow \infty$ the angle ratio (α_i/α) varies between 0.5 and $(2/\sqrt{A})$. Within the range between $A > 1$, and = 5 or 10, a transition takes place from the low A 'ratio to the lifting-line function. Using $a = 0.9$, and the induced angle $(20/A)$, we can use for sharp-edged rectangular wings the same equation as in Chapter III:

$$d\alpha'/dC_L = 10 + (8/A^2) + (20/A) \quad (10)$$

Experimental points, plotted in figure 3, in the form of the lift-curve slope, confirm this function very well.



CODE TO FIGURE 3

- * SHARP RECTANGULAR PLATES (5, a, c)
- PROFILED RECTANG, SQUARE ENDS (3, c, d) (5, b)
- ▲ PROFILED DELTA WINGS (5, d, e)
- 0012 DELTA WINGS, BRUNSWICK (5, h)
- PROFILED RECTANG, ROUNDED EDGES (5, a, b)
- ROUNDED AND ROUNDED WINGS (3, d) (5, b)
- TAPERED WINGS, SQUARE ENDS (6, a, c, d)
- TAPERED AND ROUNDED (6, b)
- SHARP ELLIPTICAL PLATES AVA (5, h)
- + RECTANGULAR W' ROUNDED EDGES (5, h)
- A RECTANGULAR PLATES D-1374

Figure 3. Linear lift-curve slope (at small lift coefficients) of wings (and plates) as a function of their aspect ratio.

Round Tip Wings. We have found that Δb values for round and rounded tip wings are constant in the form of $(\Delta b/b)$ for small A'ratios, equation 8 and in the form of $(\Delta b/c)$ for larger aspect ratios. In between these extremes there must be a transition. Mathematically this transition can be accomplished by putting

$$(\Delta b/c) = (\Delta b/c) / \sqrt{1 + 2/A^n} \quad (11)$$

where (.) indicates the value as in small A'ratios. Note that at $A=0$, there will be $(\Delta b/b) = (\Delta b/c) / \sqrt{1 + 2/A^n} = \text{constant}$. — We have empirically found that $n = 3$ is suitable; and that above $A = 2$, constant values $(\Delta b/c)$ can be used, as for example those listed in various illustrations in Chapter III, without further correction. As in that chapter, the lift angle of typical round tip type wings, is

$$d\alpha / dC_L = 10 + (10/A^2) + (26/A) \quad (12)$$

as plotted in figure 3. A "corection" to lifting-line theory, for round planforms, is proposed in (1,d). Using again $a = 0.9$, this formulation gives results between those for the sharp-rectangular and the "round" wings as in figure 3. We prefer equations 10 and 12, giving us a distinction between two extreme shapes of otherwise straight wings.

- (4) Theoretical Analysis non-linear lift small A'ratios:
 - (a) Bollay, At Zero Aspect Ratio, Zts Ang Math Mech 1939 p 21; also in J Aeron Sci 1936/37 p 294.
 - (b) Empirical, see NACA TN 2044 & 3430, T Memo 1151.
 - (c) Theoretical considerations (J Aeron Sci 1953 p 430, 1954 p 134 & 690) indicate a term $C_L \sim \sqrt{A}$. Such a trend may account for the type of increase as in figure 7 between $A = 0$ and 0.5.
 - (d) Attempts at analyzing mechanism and lift due to the lateral-edge vortices of delta wings are also found in J Aeron Sci 1954 p 212 & 649; see also Weissinger, ZFW 1956 p 225 and Mangler, R Soc London Proc Ser A 1959 p 200.
 - (e) Brown, Delta Wings, NACA TN 3430 (1955).
 - (f) Gersten, Non-Linear Theory, ZFW 1957 p 276 and Ybk WGL 1958 p 25.
 - (g) Lamar Leading-Edge-Suction Analogy around side edges NASA TR R-428.
- (5) Experimental investigation of rectangular wings:
 - (a) Winter, Plates and Wings of Short Span, Forschung 1935 p 40 & 67; Translation NACA T Memo 798.
 - (b) Zimmerman, Clark-Y Airfoils, NACA T Rpt 431 (1932); see also J Aeron Sci 1935 p 156.
 - (c) Wadlin, Hydrodynamic Rectangular Plates, NACA TN 2790, TN 3079 & 3249 or T Rpt 1246 (1955).
 - (d) AVA Gottingen, Ergebnisse I & III (1921/27).
 - (e) Scholz, Forschung Ing'Wesen 1949/50 p 85.
 - (f) Bartlett, Edge Shape, J Aeron Sci 1955 p 517.
 - (g) Weinstein, Planing Plate, NACA TN 2981 (1953).
 - (h) Brebner, Series of Wings, RAE (1965); AD-480253.
 - (i) Campbell, Small A'ratios, ARC RM 3142 (1960).

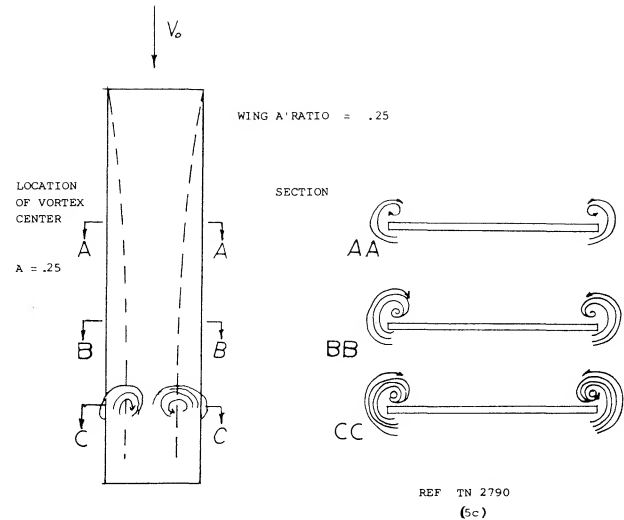


Figure 4. Development and location of tip vortices on low aspect ratio wings.

2. NON-LINEAR LIFT COMPONENT

The lift curve slope of low A'ratio wings increases with angle of attack over the basic slope determined from equations 10 and 12 on figure 3. This non-linear increase of the lift curve slope is a function of the wing aspect ratio, its lateral edges and the component of velocity normal to the wing. The lift component above the circulation lift has been the subject of many investigations (4) and is a function of the flow about the lateral edges of the wing. In some ways it appears that the non-linear component of lift is caused by the drag based on the normal velocity component. Although the vortices at the lateral edges are on the upper surface of the wing they appear to be stable, thus giving some doubt to the drag concept where the Karman vortex street might be expected.

- (6) Lifting characteristics of tapered wings:
 - (a) Anderson, 22 Tapered Wings, NACA T Rpt 572 & 627 (1936/38); also Analysis in Rpt 665 (1939).
 - (b) Whicker, Control Fins, TMB Rpt 933 (1958).
 - (c) Wolhart, With $A = 2$ to 6, NACA TN 3649 (1956).
 - (d) Allen, 3 Taper Ratios on Fuselage, NACA RM A1953C19.
 - (e) King, Taper-Ratio Series, NACA TN 3867 (1956).
- (7) It has been observed on a circular cylinder that the vortex street ceases to exist below a certain angle of attack.
- (8) (a) Anderson, Systematic Investigation of 22 Tapered Wings, NACA T Reports 572, 627, 665. (b) Larger aspect ratios, NACA TR 669. Larger A'ratios, NACA T Rpts 669 & 824, ARC RM 1708.

Basic Flow. The flow pattern of slender wings can best be understood by considering the extreme case of $A \rightarrow 0$. Physically, this condition can be produced by placing a long strip of material in a wind stream, at a longitudinal angle of attack. Since there is "no" leading or trailing edge, there cannot be any circulation as explained in Chapter II. Lift is still produced, however, by downward deflection of, and by imparting momentum onto a certain cross section or "slot" of, the air flow. This is accomplished by a pair of vortex sheets curling around the lateral edges, as shown in figure 4. This type of flow was observed from test of a flat plate with an aspect ratio of .25 (5,c) where tuft studies and flow measurements were taken. As shown in the illustration, the streamlines are spreading outboard on the lower side of such wings. The flow separates from the upper side and a strong vortex forms along each edge. It cannot be said, however, that all of the flow is separated. The inboard sides of the vortices impinge upon the wing, and they are the mechanism through which some fluid is transported from the lower to the upper surface. Eventually, the flow leaves the trailing edge in a manner similar to that of any conventional wing. We may consider the vortex system to be fully rolled up, however, essentially consisting of a pair of contrarotating vortices.

Cross Flow. The manner in which the non-linear component of lift of slender wings is often explained is by stating it is equal to the force developed in the lift direction by drag, based on the velocity normal to the wing. If the component of velocity normal to the wing is $V \sin \alpha$ then the force normal to the wing is

$$N = C_D 0.5 \rho (V_0 \sin \alpha)^2 \quad (13)$$

as explained in Chapter XV and in the book "Fluid Dynamic Drag". Resolving N in the lift direction

$$\Delta L_N = N \cos \alpha = C_D 0.5 \rho (V_0 \sin \alpha)^2 \cos \alpha \quad (14)$$

where ΔL_N is equal to the non-linear component of the lift. If the corresponding part of the total lift coefficient is ΔC_{L_N} then

$$\Delta C_{L_N} = C_D \sin^2 \alpha \cos \alpha \quad (15)$$

Since there is some doubt that the non-linear component of lift is the same as that represented by the drag coefficient in normal flow we will substitute the factor k' for C_D in the above equation, thus:

$$\Delta C_{L_N} = k' \sin^2 \alpha \cos \alpha \quad (16)$$

The question on the use of C_D in equation 15 is because of the apparent lack of a vortex street (7). Such a street can be understood to be produced by separation with alternately forming vortices. It is possible that the main component of flow $V \cos \alpha$ tends to stabilize the vortices so that they form continuously and are carried away down stream. Thus, the vortices do not build up in size and separate as with a flat plate normal to the wing. When suppressing the lateral motion (by a "splitter" plate placed in its plane of symmetry) ordinary more or less symmetrical and steady separation takes place. As shown in Chapter III of "Fluid Dynamic Drag", the coefficient is then reduced to $C_D = 1.6$. The magnitude of the factor k' in equation 16 is thus doubtful, if really identifying it with drag.

Theory. Many attempts have been made to find a solution for the seemingly simple flow pattern of slender wings (4). For $A = 0$, which means the case of a very long straight strip of material exposed to a flow at a certain angle of attack, the lift function is

$$\Delta C_L = k' \sin^2 \alpha \cos \alpha \quad (17)$$

For the wing with $A = 0$ the potential lift slope, $dC_L/d\alpha$ is zero at $\alpha = 0$, figure 5. Thus the total lift coefficient of the zero A wing is that of equation 17. According to (4 a) $k' = 2$. The close agreement with the drag coefficient in two dimensional flow in this case is only coincidental however.

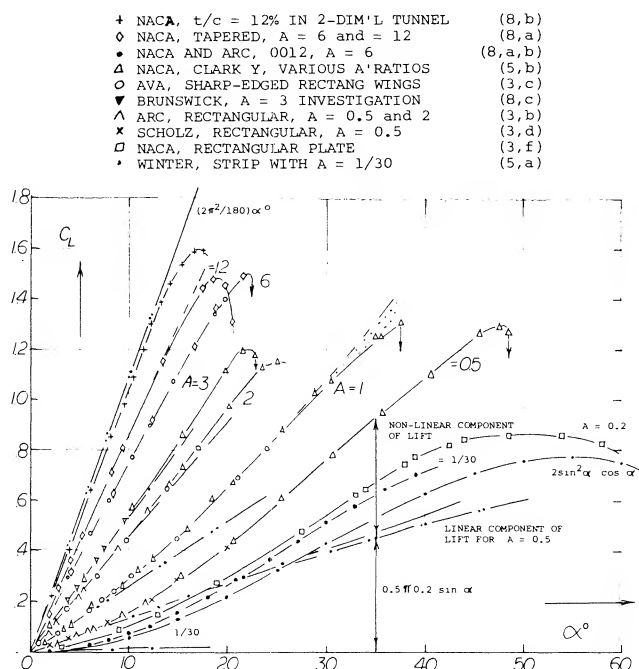


Figure 5. Lift coefficient of profiled, sharp-edged rectangular (and of some other) wings, as a function of angle of attack (adjusted for zero lift where necessary) for various aspect ratios.

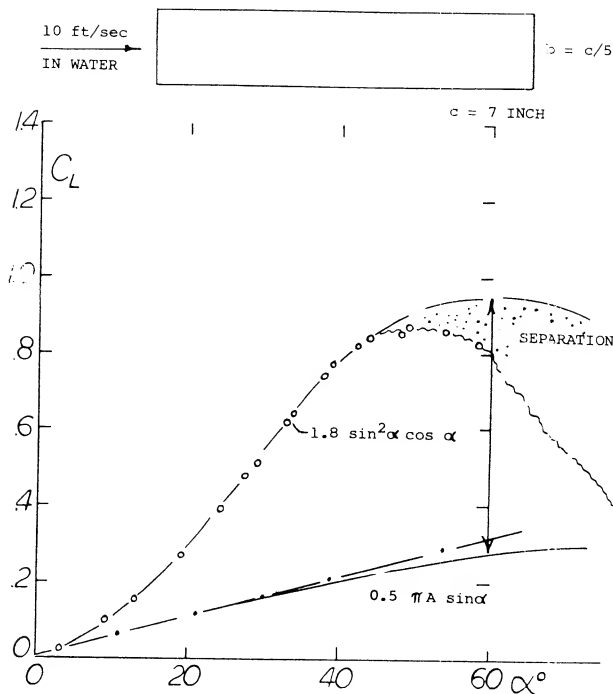


Figure 6. Lift characteristics of a thin flat plate having an aspect ratio of $A = 0.2$, tested fully submerged in a towing tank (3,f).

Two Components of Lift. Wings never have a ratio $A = 0$. There are always edges which can be considered either to be trailing (thus causing some circulation) or leading (permitting some circulating flow to get around). A number of experimental lift functions are plotted in figure 5 for aspect ratios between 0. and 12. It is generally assumed that the lift of such wings is made up of two components, a linear one (due to circulation) equations 5 and 6, and a non-linear or quadratic term (due to the lateral-edge vortex flow). As an example, experimental results of a plate having an A -ratio of 0.2 are presented in figure 6. After subtracting a linear component found by equation 5, it is found that equation 17 agrees well with the experimental points when using $k' = 1.8$.

End Plate Effect. According to (9,a) a vortex sheet (rather than a "round" vortex) originates along each of the lateral edges. These sheets combine with the sheet coming from the trailing edge so that a U-shaped vortex wake is formed. One can then say that the long-chord wing leaves behind a vortex pattern very similar to that of a (short-chord) wing fitted with end plates. In rectangular wings, the height 'h' of the imaginary end plates is assumed to be equal to the vertical distance between vortex core and trailing edge. At A -ratios below unity, this height corresponds to $\alpha_i = 0.5 \alpha$; hence:

$$h \approx \alpha_i c = 0.5 \alpha c \quad (18)$$

As derived from theory and from experiments, the increase of the effective aspect ratio through addition of end plates, is approximately $\Delta A / A = 2 h / b$ (see equation 11). Substituting the suggested height (equation 18) we obtain

$$\Delta A \approx 2 A \alpha_i c / b = 2 \alpha_i \quad (19)$$

Consequently, for wings with $A < 1$, and $2 \alpha_i = \alpha$, the increment in effective aspect ratio is found to be $\Delta A \approx \alpha$. The effective aspect ratio $A_i = A + \Delta A$ of such wings, therefore, increases with the angle of attack; and the lift increases at a rate higher than linear (9,c). Combining equations 5 and 19, replacing α by the more correct term of $\sin \alpha$, and after introducing $\cos \alpha$ (to indicate the difference between the vertical lift and the inclined normal force), the lift coefficient of wings with aspect ratios below unity may tentatively be

$$C_L = 0.5 \pi \sin \alpha \cos \alpha (A + \alpha) \quad (20)$$

The "second" component of lift in this equation is

$$\Delta C_L = 0.5 \pi \sin^2 \alpha \cos \alpha \approx 0.5 \pi \alpha \quad (21)$$

This time, the factor k is almost = 1.6. The end-plate formulation gives a qualitative explanation for the existence of two different components of lift in aspect ratios below unity. However, quantitative questions such as to the shape of wing planform and lateral edges remain unanswered.

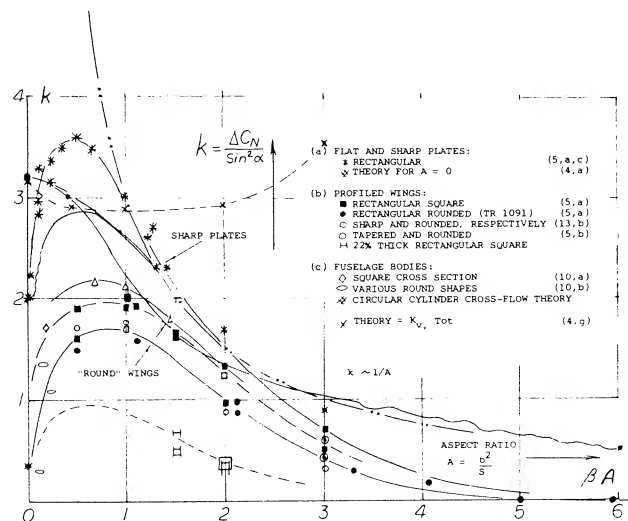


Figure 7. Second, non-linear component of lift, of plates and profiled lifting devices (wings) as a function of their aspect ratio.

Non-Linear Component. Using equations 10 and 12 or the functions plotted in figure 3, the linear circulation-type lift, potential flow lift, can be determined from experimental results such as in figure 5, for example. The non-linear "second" lift component of wings can thus be isolated from total values of lift or normal force. Such statistical data are plotted in figure 7 in the form of

$$(\Delta C_L / \sin^2 \alpha) \text{ or } (\Delta C_N / \sin^2 \alpha) \quad (22)$$

This type of evaluation is somewhat uncertain insofar as the value of the linear component depends upon planform and lateral-edge shape of each wing tested. There cannot be much doubt, however, about the following conclusions:

- The value of 'k' to be used in equations 16 and 17 in order to obtain the second component of lift varies between zero and a maximum of 3.6.
- Sharp-edged plates show the highest values of 'k'. They seem to meet the theoretical value of 2 as in (3,a) at $A = 0$.
- Wings with rounded lateral edges show 'k' factors which are considerably reduced, together with the effective span of such wings.
- Lift-producing efficiency is also affected by "round" planform. Wings with full-span and straight trailing edges are, on the other hand, most efficient as to the magnitude of the non-linear lift component.

Leading-Edge-Suction. Using an extension of the leading-edge suction analogy presented in (5,a,a) of chapter XVIII a theoretical method of finding the characteristics of low A wings with various planforms has been developed. This theoretical approach (4,g) finds the potential flow and non-linear lift terms for various wing planforms. For rectangular planform wings the theoretical potential flow lift agrees closely with that given on figure 5. The lift due to the vortices developed on the top wing surface as shown in figure 4 are given in terms of k as a function of A on figure 7. In the low aspect ratio range from $A = 0.3$ to 1.5 the theoretical leading-edge-suction analogy method appears to agree with the statistical data. This is especially true considering that the theory applies for wings with sharp edges.

(9) End-plate principle and non-linear lift:

- Mangler, in Yearbook D Lufo 1939 p I-139.
- Expansion of the principle in (1,f).
- The principle is but a way of explaining that the volume (mass) of air onto which a downward momentum is imparted by the wing increases in proportion to the angle of attack and to the chord. That the principle is not perfect becomes apparent when considering drag due to lift of such small-A-ratio wings; see "Fluid Dynamic Drag". The solution as in (4,f) assumes not only "end plates", but a complete "box" of streamlines.

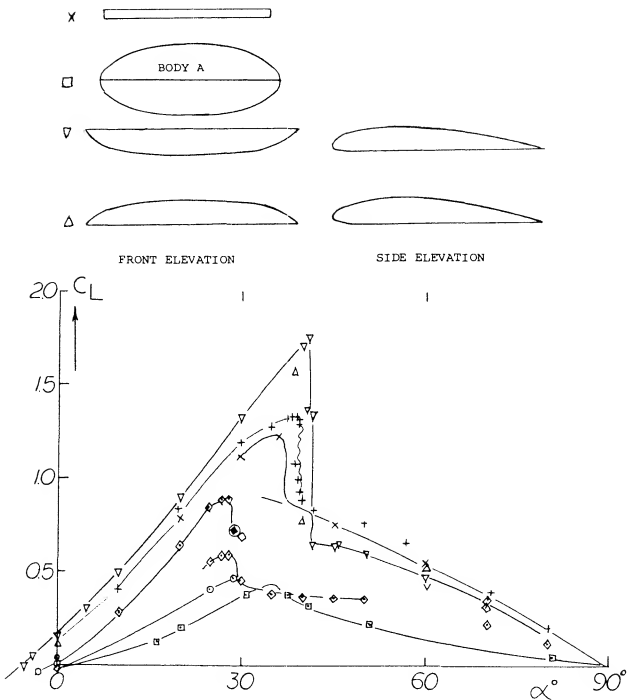


Figure 8. Characteristics of small aspect ratio wings with circular planforms and dihedral. Clark-Y Sections.

In the absence of any solution really indicating the magnitude of the second lift term, the statistical results in figure 7 will permit to estimate that component in practical applications. Regarding the magnitude of k' around $A = 0.5$, it is suspected that theories advanced so far (6) are not based upon the right mechanism. It is suggested that each lateral vortex not only produces lift by itself, but that it also increases the circulation over the rest of the wing area. Any end-plate effect (as in equation 18) may thus lead to the exponential increase as in figure 7, between $A = 6$ and 1. On the other hand, at $A = 0$, there is no circulation which could be increased. According to these speculations, we end up with two non-linear components of lift; and it might not be a coincidence that $k' = 2$ (as per equation 17) plus 1.6 (as per equation 21) equals 3.6 (as seen to be the maximum in figure 7).

(10) Lift characteristics of streamline bodies:

- AVA Gottingen, Fuselages, Ergebnisse II (1923); see also Muttray in Lufo 1928/29 p 37.
 - Bates, Various Fuselage Bodies, NACA TN 3429 (1949).
 - NASA D-1374.
- (11)
- AVA Gottingen, Flat Disk, Ergebnisse IV (1932).
 - Zimmerman, 3 Clark-Y Wings, NACA TN 539 (1935).
 - Mugler, Lenticular Shape, NASA TM X-423 (1960).
 - Ware, Stability and Control, NASA TM X-431 (1960).
 - Demele, With Fins and Flaps, TN D-788 and TM X-566.

3. CHARACTERISTIC DATA

Some of the detailed test data on low aspect ratio wings confirm the concepts discussed in the previous section. However, because of the many variables involved it is difficult to determine that portion of the non-linear lift curve, yaw effects, maximum lift and compressibility effects of low aspect ratio wings. Thus, some of the available experimental data relating to these problems are presented in addition to the data given on figure 5.

Circular Planform. Disks and circular "wings" are an extreme of round planform. Available experimental data are plotted in figure 8. Sharp-edged plates have a linear lift-curve slope as high as indicated by the upper line in figure 3. The Clark-Y profile wings (11,b) are at least in the forward 50% of their lateral edges rounded; and their lift is reduced accordingly, to the lower limit as in figure 3, at $A = 4/\pi = 1.27$. If the cross section shape is viewed based on drag it appears the wings with the flat tops should have the highest lift. This is generally true as noted in figure 8.

Ellipsoid. When increasing the thickness ratio of a disc, we may arrive at bodies similar to those in body (A) of figure 8. Such shapes have been wind-tunnel tested in (11,c,d,e) with stabilizing flaps and fins attached, for possible use as re-entry vehicles (from outer space). To us, the ellipsoid in the graph, is the perfect example for the life-reducing effect of rounded trailing and lateral edges of any wing. As a matter of interest, the maximum (L/D) ratio of the shape shown is 10, at $C_L = 0.2$. Effectiveness can greatly be improved by horizontal tail flaps (11,d,c) which are necessary anyhow to stabilize and to control the body when really used as a vehicle.

The Discus. Disregarding any dreams of "flying saucers", the athletic implement called discus seems to be the only practical application of a circular planform. The ballistics and aerodynamics of the discus have been investigated by Ganslen (12,b). Figure 9 presents the aerodynamic forces. The lift shows clearly an initial linear slope and a non-linear movement. Stalling takes place at $\alpha = 29^\circ$. The normal force resumes growing above 40° , reading at 90° the drag coefficient $C_D = 1.06$. The pitching moment (not reported) is certainly "up". The longest distances, some 60 meters, throwing a discus are obtained when launching at some 35° (against the horizontal) but at an angle of attack (against air) slightly below zero. The rotation imparted when properly throwing (some 6 revolutions per second) stabilized the discus, thus minimizing the pitchup (against the horizontal). The ballistic trajectory necessarily ends, however, at an angle of attack above 35° , that is in stalled condition. At least part of its way, the discus is, nevertheless, gliding at an (L/d) ratio reaching a maximum of 3, at $\alpha = 10^\circ$ (against the air).

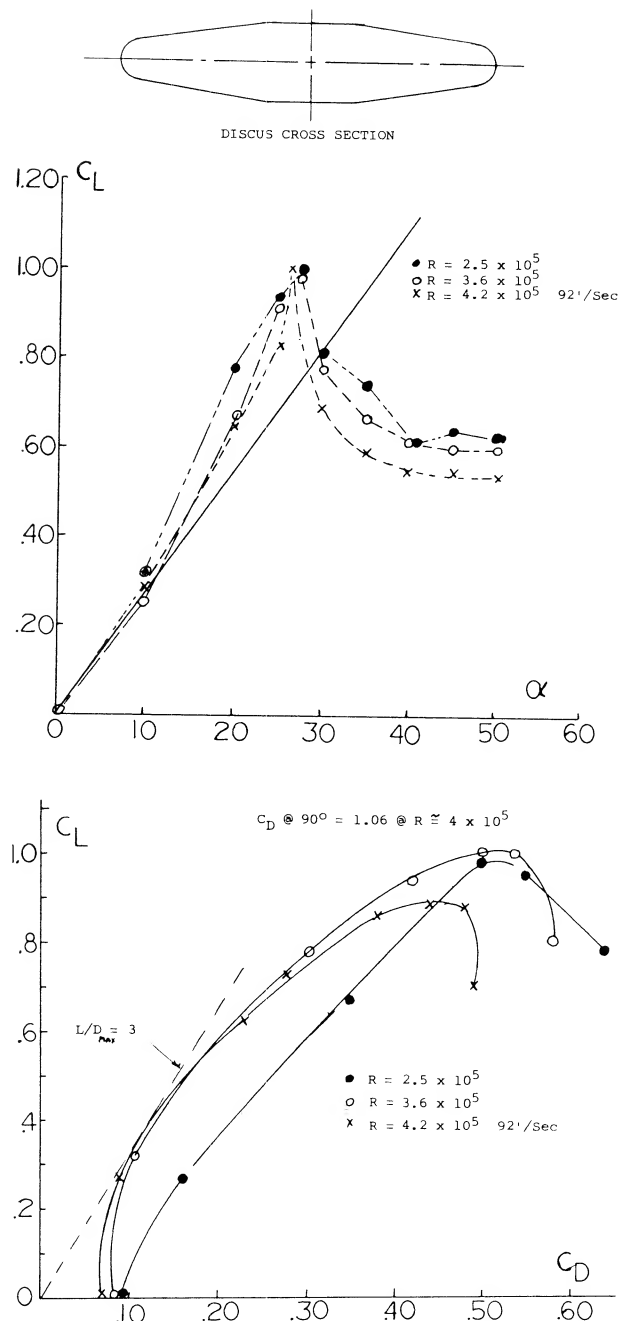


Figure 9. Lift and drag characteristics of discus.

Streamline Body. The flat body as in figure 10 may be a streamline body. As such it should be discussed in the chapter on this subject. However, we can also claim this body to be a low-aspect-ratio wing with rounded lateral edges. Doing so, it must be noted that there is a straight and blunt trailing edge. The non-linear component is only $(\Delta C_L / \sin^2 \alpha) = 0.15$, for $A = 0.16$. As seen in figure 10, this is the lowest point near $A = \text{zero}$.

The well-rounded shape in combination with a high Reynolds number is evidently responsible for this result. The flow simply gets around the lateral edges. By comparison, a sharp-edged flat plate having approximately the same aspect ratio exhibits twice as much non-linear lift as the round body. The linear lift component is also low for the flat body, around $\frac{1}{2}$ the theoretical value as in figure 3. It is suggested that the blunt (and sharp) trailing edge of the body prevents this component from being still lower.

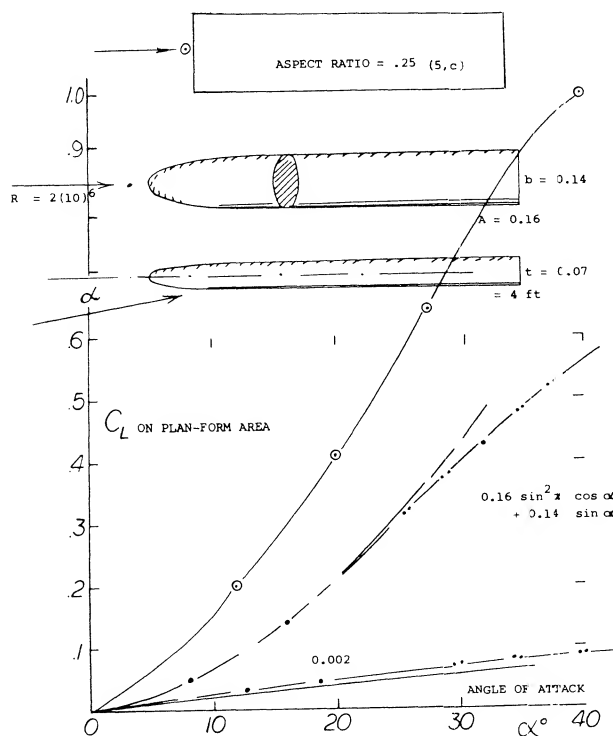


Figure 10. Lift and drag characteristics of a flat streamline body (10,b).

Flap Characteristics. As previously noted the area of a small A'ratio wing aft of its maximum effective width does not produce lift. This occurs as explained in (1,i) because the downwash produced by the sections in front of the maximum effective width will operate in a flow field equal to the angle of attack of the section. Thus, the flow becomes parallel to these sections. The ratio of the lift to the total, C_{Lc} / C_{LT} , as measured in (5,c) is given on figure 11 as a function of chord length. For the flat plate rectangular wing, operating at $\alpha = 10^\circ$, 95% of the lift is generated on 60% of the wing chord. Thus, the effectiveness of the area where flaps would be used is reduced and we would expect that flap effectiveness would also be less.

Tests of flaps on rectangular wings with $A = 1.25$ from (13,a) figure 12 show that below a flap to wing chord ratio $C_f / C = .25$ the lift slope is not linear. This tends to confirm the data of figure 11 and also shows the importance of the trail edge shape or angle on flap effectiveness.

The characteristics of flaps as a function of aspect ratio is given on figure 13. For the 30% chord flaps tested in (13,b) the effectiveness is reduced with both A'ratio and sweep angle. With a reduction of A'ratio below 2 it is expected that 30% flaps will be even less effective than the trend illustrated on figure 13.

Horizontal Tail Surfaces. Low and moderate aspect ratio wings are used as horizontal tail surfaces. Available experimental results for such surfaces are given on figure 14. In some applications gaps are found for the rudder and the planform is rounded. The use of a correction factor a of .85 for the surfaces without gaps and .75 with gaps results in good correlation of the experimental data. Further discussions of the characteristics of tail surfaces are given in Chapter IX.

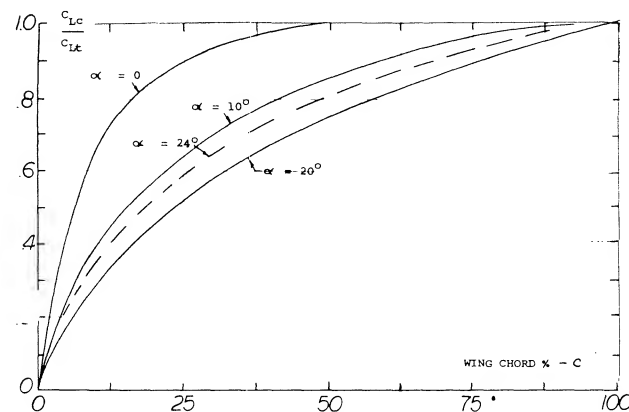


Figure 11. Ratio of C_{Lc} , lift to a given chord station to the total lift coefficient C_{LT} , for a rectangular wing of $A = .25$.

- (12) Dr. R. V. Ganslen, Physiologist at McDonnell, St. Louis:
 - (a) The Javelin, see "streamline body" chapter.
 - (b) Aerodynamics of the Discus, Athletic Journal, Apr. 1964.
- (13) Flap characteristics on small aspect ratio wings:
 - (a) Campbell, Rectangular Wings of Small Aspect Ratio, ARC R&M 3142.
 - (b) Dods, Nine Horizontal Tails, NACA TN 3497.

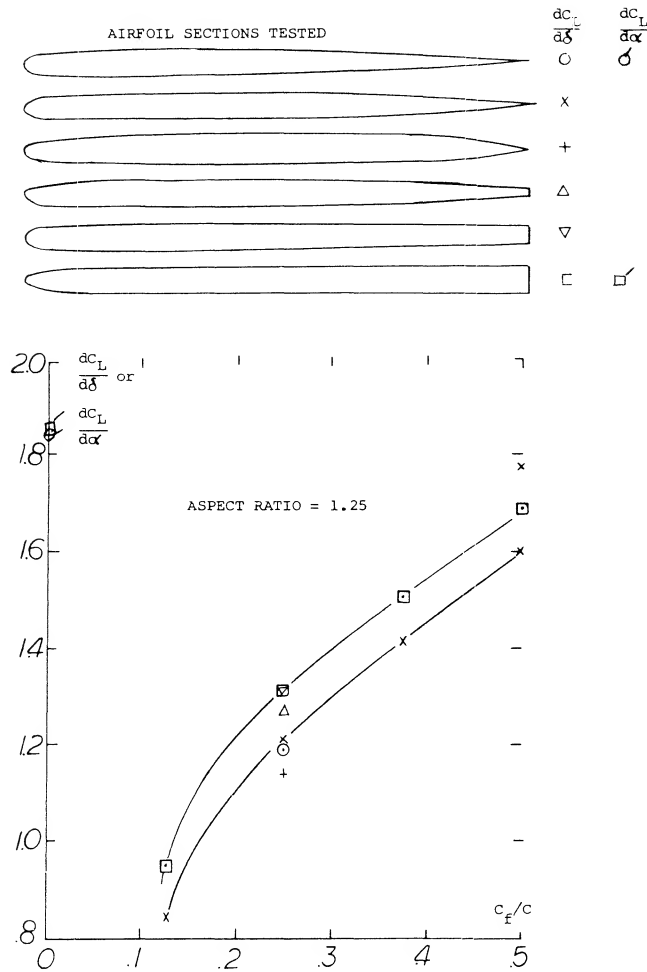


Figure 12. Flap effectiveness as a function of flap chord ratio for a rectangular wing with A'ratio = 1.25.

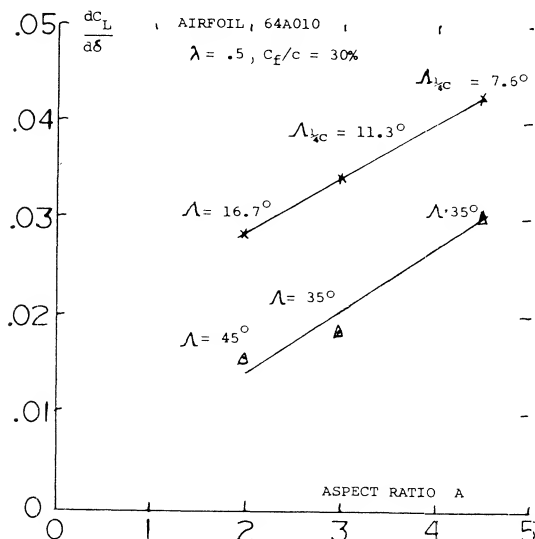


Figure 13. Flap effectiveness on low A'ratio wings with and without sweep.

Ring Wings. As far as low A'ratios are concerned, we can, for example, consider the cowling of a jet engine or a ducted propeller to be a ring airfoil. Such an airfoil, in the outside shape of a barrel, was also placed around a jet engine (with the pilot on top) thus providing a "wing" (to be used in high-speed flight) for an extreme version of a VTOL aircraft, figure 15. In connection with that project, theoretical and experimental work on small A'ratio wings was undertaken. As pointed out in (14,c) the lift then corresponds to the coefficient based upon the square of the diameter

$$C_{Ld} = \pi \sin \alpha \quad (23)$$

Note that this lift component is twice that of a plain wing as in equation 5. Before proceeding any further, it may be pointed out that corresponding to their roundness (no lateral edges) ring wings do not display any non-linear type of lift. This is clearly brought out by tests on a series of such airfoils with ratios d/c between $1/3$ and 3 as reported in (14,e). If there is a second component, we may find it in figure 16 at angles of attack between 50° and 90° where the flow pattern is fully separated. At small angles equation (23) represents all of the lift of small-aspect ratio ring wings.

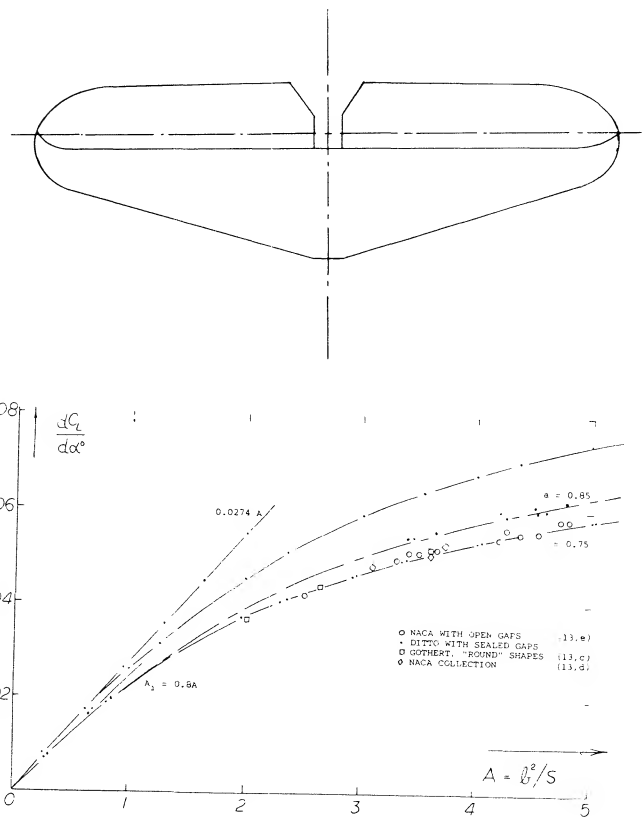


Figure 14. The lift-curve slope of horizontal tail surfaces tested alone (without fuselage) as a function of their aspect ratio.

Aspect Ratio. Referred to the area $S = d c$

$$C_L = \pi(d/c) \sin \alpha ; dC_L / d\alpha = \quad (24)$$

$$\left(\pi^2 / 180 \right) (d/c) = 0.055 (d/c)$$

Experimental results in figure 17 confirm the equation (24) very well. Regarding the airfoils as in figure 17, the effective diameter is questionable in connection with the highly cambered Clark Y foil section. We have assumed a $d/c = 0.1$ to account for some of the airfoil thickness corresponding alternate points are included in figure 17. Agreement with the "sharp" rectangular wings in figure 3 is obtained at small aspect ratios, when referring C_L to the area $(2 d c)$. This result means physically that the volume of air affected (deflected) by the ring wing corresponds to a stream cylinder with a cross-section area two times that of the opening area of the ring.

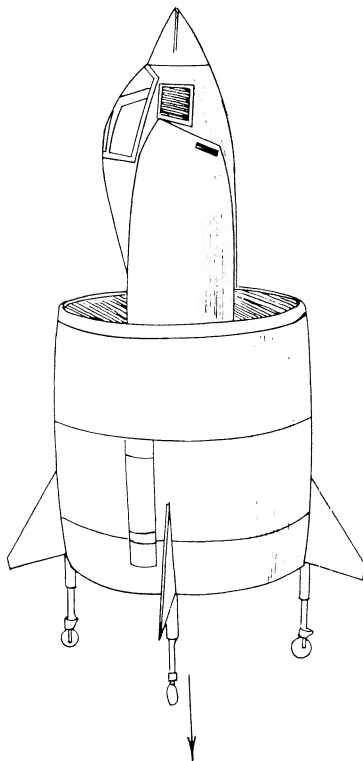


Figure 15. Jet-powered French VTOL aircraft SNECMA "Coleopter", as shown on the cover of Newsweek 5 Oct. 1959.

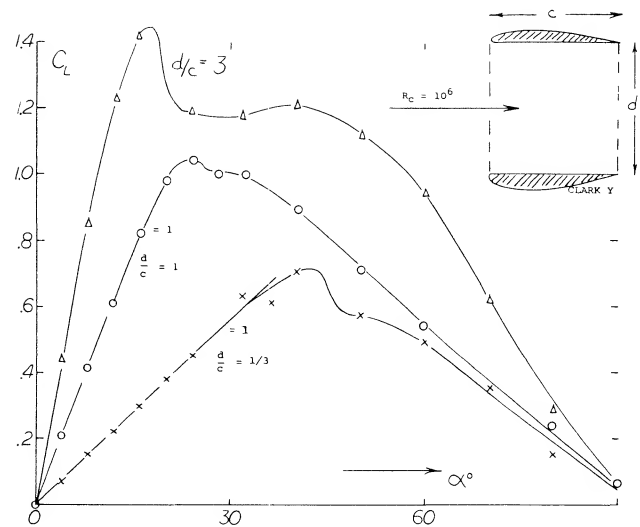


Figure 16. Lift of a series of ring wings (14,e).

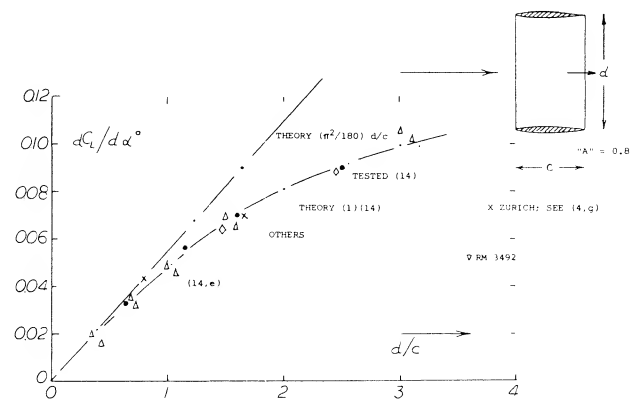


Figure 17. Lift-curve slope of ring-shaped wings as a function of their aspect ratio (14).

- (14) Characteristics of small aspect ratio ring wings:
- (a) Weissinger, Ring-Wing Theory; Rpts 2,39,42 (1955/57) of DFL; and ZFW 1956 p 141; also USAF OSR TN 1958-224.
 - (b) Richter, Ring Aerodynamics, Yearbk WGL 1955.
 - (c) Fletcher, 5 Annular Foils, NACA TN 4117 (1957).
 - (d) As developed in France, see Seibold, Ring Plus Machinery, Yearbk WGL 1954 p 116.
 - (e) Weissinger, Ring Plus Body, AFOSR TN 60-343 (1960).

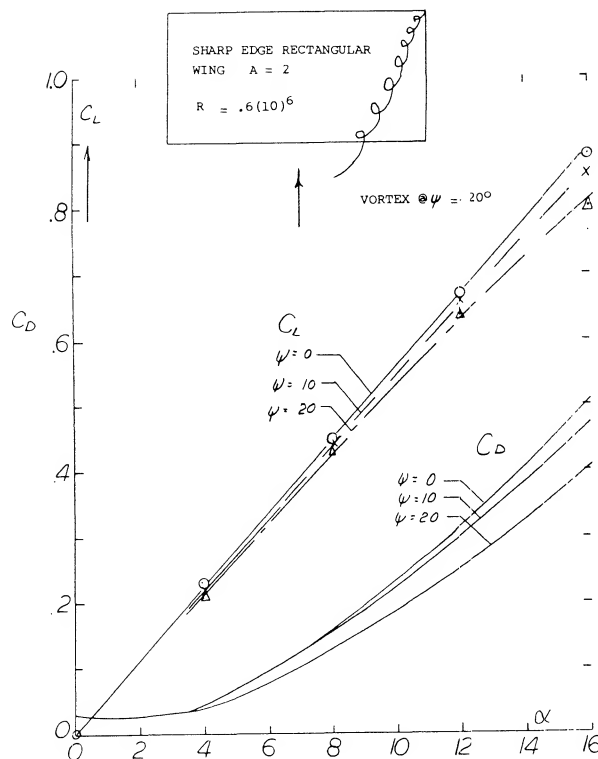


Figure 18. Lift and drag characteristics of a low aspect ratio wing operating at yaw angles.

EFFECTS OF YAW. The influence of the wing tip on the characteristic of low aspect ratio wings operating in yaw can be large. For instance, a rectangular wing with an aspect ratio of one becomes a double delta or diamond shaped wing with the one tip becoming the leading edge. Thus, if the wing were operating at a yaw angle of 45° the tip shape would have the same influence as the original leading edge. When operating at a yaw angle the vortices at the tip become influenced by the tip sweep angle.

Smoke surveys (15,a) on a rectangular wing of $A = 2$ indicated that position of the tip vortices are influenced by the yaw angle as well as the angle of attack. Typical results are given on figure 18. Note that with increasing lift the vortices move inward from the tip but the movement is less as yaw angle is increased. The upstream vortex height decreases with angle of attack, while the vortex from the downstream decreases in height. From figure 18 it will be noted that both the lift and drag decrease with increasing yaw angle. If the effective aspect ratio or span is considered it would be expected that the lift would increase with yaw angle as indicated by equation 7.

4. COMPRESSIBILITY

Low aspect ratio wings are used for high speed aircraft because of the delay of the drag rise and improved performance at Mach number above 1.0. The change in the Mach number for the drag rise and the drag at high speed of low aspect ratio wing is given in the book "Fluid Dynamic Drag".

LIFT AT $M < 1$. Compressibility encountered at higher subsonic speeds affects the sectional lift angle, that is, in large-aspect-ratio wings, see Chapter VII. For slender wings (say, below $A = 1$) the formulation (1,i) predicts that compressibility does not have any influence upon the linear, circulation-type lift component. According to the Prandtl-Glauert rule, any wing reacts as though its chord would be lengthened in proportion to the Prandtl factor

$$''P'' = 1 / \sqrt{1 - M^2} = 1/\beta \quad (25)$$

This means that the effective area is increased and the aspect ratio decreased. According to Equation 5, the lift-curve slope is not affected by these variations.

In aspect ratios above $A = 1$, there is a transition between the two extreme ranges considered above. It may be instructive, however, to use equation 23 with a modified Prandtl function reducing the sectional angle of attack for low lift coefficients

$$d\alpha / dC_L = (10 + 8/A^2)(1 - M^2)^n + 20/A \quad (26)$$

- (15) Effect of yaw on low aspect ratio wings:
(a) Schock, Low A'ratio Wings with Sharp Leading Edges, Princeton Aero Eng Report No. 574.
- (16) Compressibility effects:
(a) Ferri, Elements of Aerodynamics of Supersonic Flows, Macmillan Co. 1949.

The exponent varies between zero at A well below unity, and $n = 0.5$ for higher aspect ratios. We have evaluated available experimental results (16). After excluding various points which simply cannot be right, the most likely function of n is as in figure 19.

Non-Linear Lift. The effects of compressibility on the non-linear component of lift is not described by any available theory. If the increase is due to drag based on the flow normal to the wing it would be expected that the component would not change at Mach numbers below 1. However, if the component also depends on the cross sectional area and this is effectively increased by compressibility, the non-linear component 1 should increase with Mach number. Thus the k determined from figure 7 would be modified for compressibility by the equation

$$k = P \Delta C_L / \sin^2 \alpha \quad (27)$$

where $P = 1/(1 - M^2)^n$ and n is the Prandtl-Glauert factor modified by A 'ratio given on figure 19. More study and experimental data is required to confirm equation 27.

Transonic Range. Above the critical Mach number the lift curve slope of low aspect ratio wings is reduced by the formation of shock waves on the upper surface. These shock waves effect the lift in the same manner as for a two dimensional wing, Chapter VII. The result of this is a sharp reduction of lift after the critical is reached with a recovery at approximately $M = 1$, as illustrated on figure 20. The Mach number at which the lift slope break occurs is a function of the aspect ratio and the angle of sweep.

For straight wings this Mach number can be estimated using figure 21. The minimum lift slope will be obtained at

$$M_{L_m} = (1 + M_{L_B})^{1/2} \quad (28)$$

(17) Low aspect ratio wing tests including C_{L_α} :

- (a) Nelson, Wings on Transonic Bump, NACA TN 3501.
- (b) Nelson, 38 Cambered Wings, NACA TN 3502 (1955).
- (c) Nelson, 36 Symmetrical on Bump, NACA TN 3529.
- (d) Nelson, 65-210 Wings with $A = 1$ to 6, NACA RM A 9K18.
- (e) Allen, Plan-Form Body Taper Effects and Mach No. Effects $A = 2, 3$ and 4, NACA A53C19.
- (f) Jones, Low Speed Tests Rectangular Planform $A = 1, 2$ and 3 Wings, NACA RM L52G18.
- (g) Dods, Test of Nine Related Horizontal Tails $A = 2$ to 6, NACA TN 3497.
- (h) Graham, Large Triangular Wings, NACA RM A50A04a.
- (i) Zimmerman, Clark Y Airfoils of Small A 'ratio, NACA TR 431.

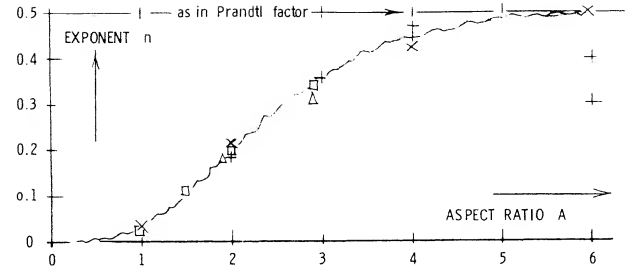


Figure 19. Correction to Prandtl-Glauert compressibility equation for aspect ratio.

Where M_{L_B} is the Mach number where the force break occurs and M_{L_m} is the Mach number at the minimum lift slope. The reduction in slope at M_{L_m} is a function of thickness and aspect ratio and can be estimated using figure 22. It is noted that when the thickness ratio of the wing is below 5% low aspect ratio wings do not exhibit a reduction in lift slope.

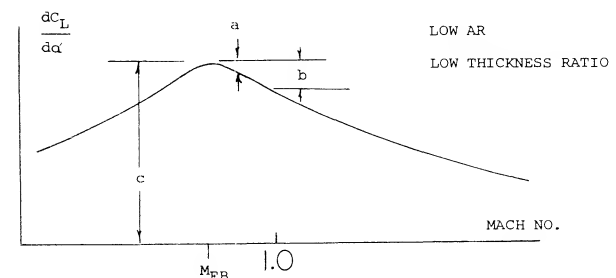
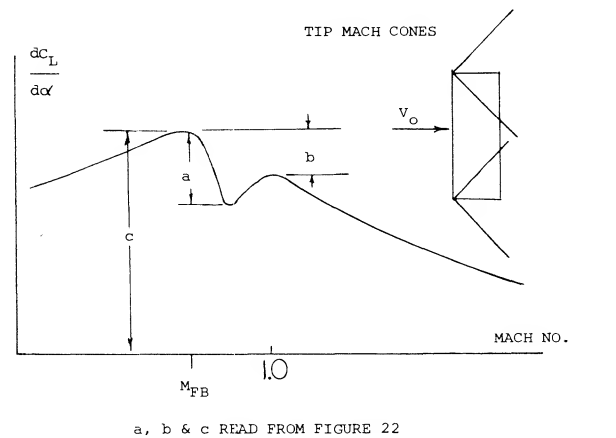


Figure 20. Typical variation of lift curve slope in the transonic range with associated shock waves.

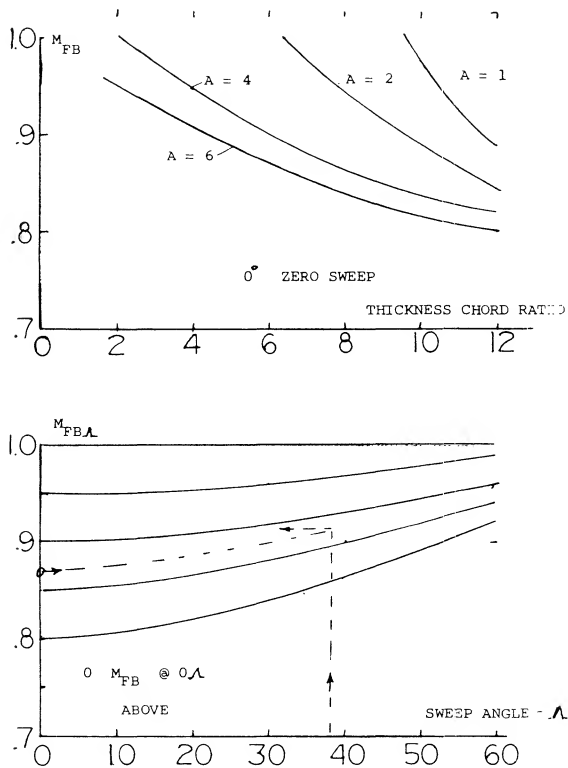


Figure 21. Charts for calculating force break Mach number of straight and swept wings.

SUPERSONIC RANGE. At Mach numbers above those where the shock waves are attached to the wing, theory (16,a) provides a good insight into the performance of wings. At low lift coefficients the linearized theory gives for the lift curve slope the equation

$$\frac{dC_L}{d\alpha^\circ} = \frac{\pi}{45 \sqrt{M_\infty^2 - 1}} \left(1 - \frac{1}{2A \sqrt{M_\infty^2 - 1}} \right) \quad (29)$$

This applies to rectangular wings where the center portion of the wing is operating in two dimensional flow and the tips are within the Mach cone as illustrated in figure 23.

It is expected that as in the subsonic range a non-linear component of lift will be generated that will add to that of equation 29.

5. MAXIMUM LIFT

The maximum lift characteristics of straight and swept wings with a high aspect ratio are given in Chapters IV and XVI. Because of the greater influence of the tips, the planform shape of low aspect ratio wings is the dominant factor influencing the C_{LX} and angle of attack at which it occurs. The actual airfoil section used is of secondary importance in determining C_{LX} , especially with very low aspect ratio wing, $A < 1$.

Theoretical Maximum. The theoretical maximum lift of two dimensional wings was shown in Chapter IV to be 4π but could not exceed the value described by

$$C_{LX} = 1.94 A \quad (30)$$

Equation 30 gives the maximum lift that could be expected by flow circulation. For very low A ratio wings the actual C_{LX} exceeds that of equation 30 because of the secondary lift term. This is illustrated on figures 6 and 22 for a rectangular wing with $A = 0.2$ where C_{LX} is .95 compared to the expected maximum value from equation 30 of .388. Near C_{LX} the secondary lift term caused by the flow normal to the wing was larger than the circulation lift term and results in a $C_{LX} = .562$.

The maximum lift and stalling characteristics of low aspect ratio wings vary widely as shown on figures 5, 6 and 8. Since the stalling process is due to separation and is influenced by the secondary lift of the wing, theoretical solutions are lacking.

Variation of C_{LX} With Aspect Ratio. In figure 23 the C_{LX} is given as a function of aspect ratio from the test data of (17). In the range of $A \approx 3$ comparison of the data with that presented in Chapter IV indicates that to estimate C_{LX} in this range the more extensive empirical data given in the chapter on stalling should be used. Below an aspect ratio of 2 C_{LX} appears to increase with decreasing A ratio until the theoretical maximum is obtained and then starts to decrease. The data on figure 23 again illustrates further examples of C_{LX} exceeding the theoretical maximum. In the lower aspect ratio range $A < 1$, C_{LX} appears to be nearly insensitive to the section configuration, although the tip configuration appears to be important. Wings with rounded tip tend to have higher values of C_{LX} than square tip wings.

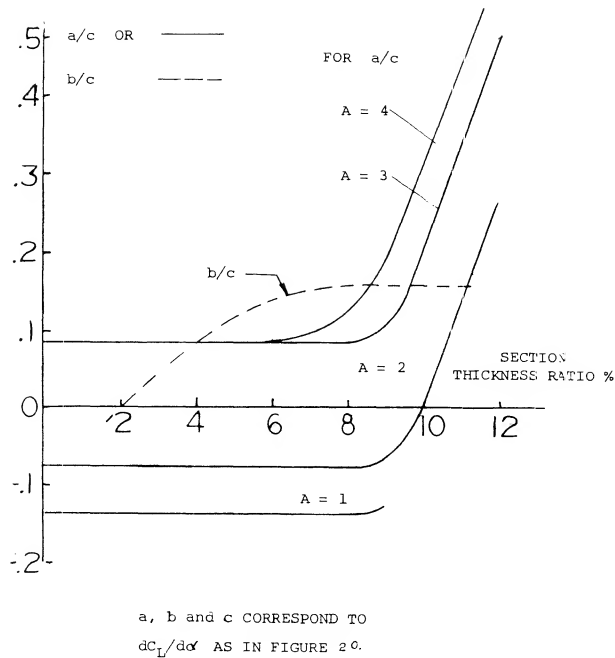


Figure 22. Data for estimating critical points of lift curve slope in transonic range.

At A above 1.5 there is a large variation of C_{LX} which depends on cross section, taper ratio and leading edge sweep angle. Tip shape also appears as an important parameter influencing C_{LX} . The condition of the leading edge and, therefore, Reynolds number effects C_{LX} , the change being similar to that noted in Chapter IV where airfoils tested in the smooth condition show a ΔC_{LX} 0.3 to 0.4 above the value tested in the rough condition. Except for those points noted the data given in figure 22 should be assumed to correspond to the rough leading edge condition.

Type of Stall. The test data given on figures 5, 6 and 8 show that the stall can either be very sudden or rounded. At $A > 3$ the type of stall appears to depend on the leading edge radius as discussed previously. When the wing has an A 'ratio below 2 the shape of the leading edge has little influence and both sharp and well rounded types of stall are observed. It does appear that when the C_{LX} exceeds that expected based on the two dimensional section, the stall will be very sharp. This is illustrated for the wings using Clark Y sections.

FLAT PLATE	$\Lambda = 0, \lambda = 1.0$	RN .45 to $1.8(10)^6$	(17,h)
NACA 63A004	$\Lambda = 0, \lambda = 1.0$	RN=1.25 - $1.70(10)^6$	
NACA 63A006	$\Lambda = 0, \lambda = 1.0$		
63A010	$\Lambda = 16.7$ to $7.6, \lambda = .5$	$3(10)^6$	(17,g)
63A010	$\Lambda = 35^\circ$ to 45°		(17,g)
NACA 0012	LE = ROUGH		(17,f)
NACA 0012	LE = SMOOTH		
CLARK Y	SQUARE TIPS		(17,i)
CLARK Y	ROUND TIPS		(11,b)
CLARK Y	ROUND TIPS		(11,b)
FLAT PLATE IN WATER, FIGURE 6.			

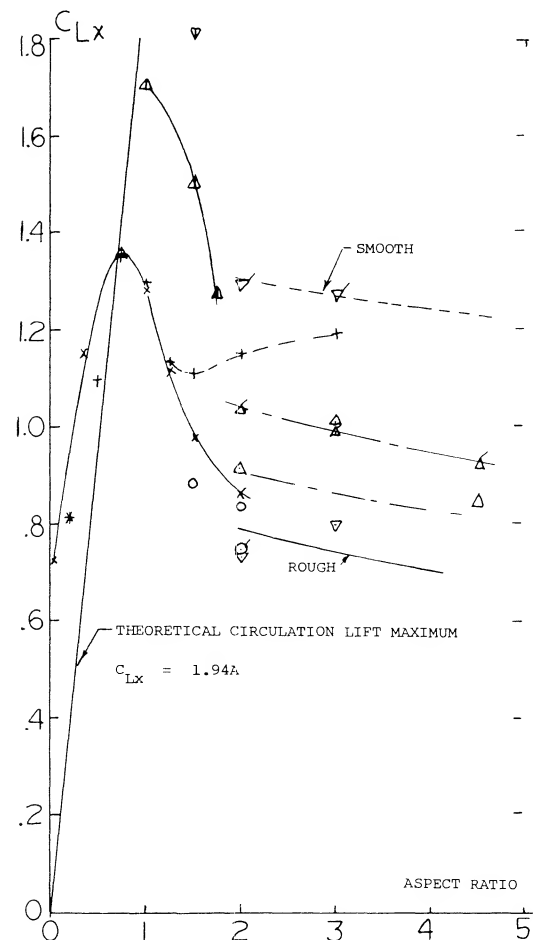


Figure 23. Maximum lift of small aspect ratio wings including theoretical maximum for circulation lift.

CHAPTER XVIII

CHARACTERISTICS OF DELTA WINGS

Triangular wings with a straight trailing edge (point flying first) are called delta wings, according to their resemblance with the Greek letter Δ . At least in larger aspect ratios they can be considered to be wings with zero taper ratio (pointed wing tips) and with a swept-back $\frac{1}{4}$ chord line. Such wings would be impractical, however, because of wing-tip stalling and low lift drag ratios at subsonic speeds. Rather, delta wings are primarily designed for supersonic speeds. Their leading edges are highly swept so that the aspect ratio is usually small. Thus, the lift drag ratio at subsonic speeds is low. The leading edges of delta wings are also lateral edges. Circulation around such edges is obviously different from what was originally meant by that word in two-dimensional flow past airfoil sections; and the flow pattern is essentially different from that of straight wings, within the range of aspect ratios as used in airplanes.

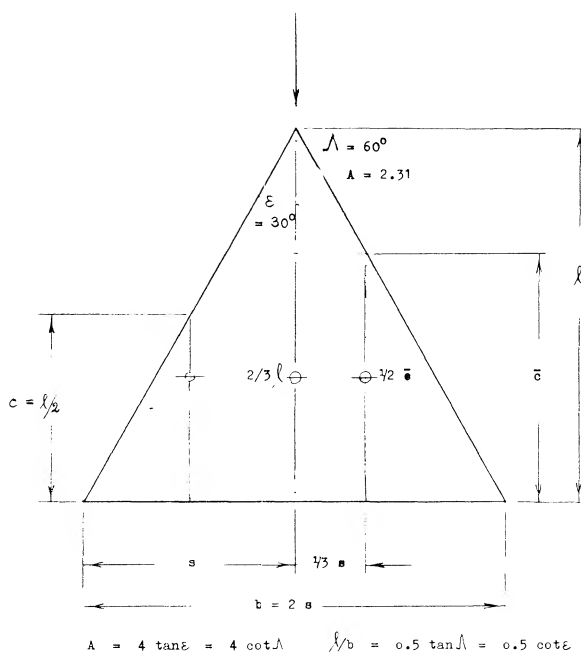


Figure 1. Geometry of delta wings, illustrated by the example of an equilateral triangle.

1. CHARACTERISTICS OF DELTA WINGS

In the range of low aspect ratio wings the delta shape is of particular interest. It is used in high speed aircraft, and there is analysis available explaining and predicting at least part of the lift.

Geometry. Wings in the shape of a delta (with a straight trailing edge) are obtained by combination of sweep and taper. As shown in figure 1, this type of wing is defined by the following parameters:

Λ = leading edge angle of sweep

$\epsilon = 90 - \Lambda$ = half vertex angle

$A = 2b/l$ = aspect ratio = b^2/S

= $4/\tan \Lambda$ for delta wings.

If defining a mean aerodynamic chord in the manner as

shown for tapered wings in Chapter III, that chord measures $c = (2/3)l$. However, since the load distribution of slender delta wings is different from that in conventional planforms, there is no reason to use this type of mean chord. In straight delta wings the length " l " would be a natural dimension to define a length ratio. However, to accommodate shapes differing in contour (such as parabolic or "gothic" planforms) the mean geometric chord $c = S/b = l/2$ shall be used.

When the trailing edge of delta wings is modified from a straight line the planform is changed to an arrow or a diamond shape as is illustrated on figure 2. For an arrow wing, the wing notch ratio a/l is positive while for the diamond shape a/l is negative. The notch parameter is used to determine the coefficients for finding the vortex and potential flow lift.

2. FLOW CHARACTERISTICS

The flow characteristics around a delta wing are influenced by the leading edge angle, cross section shape and angle of attack. These characteristics determine the position and strength of a pair of vortices that start at the apex of the wing. The vortices formed are described as leading-edge vortices and are located on the top surface of the wings, the core proceeding downstream to the trailing-edge at an angle slightly greater than the leading-edge angle of sweep. Aft of the trailing-edge the vortices continue downstream in the direction of flow at a downwash angle proportional to the lift. These vortices exert a large influence on the lift characteristics of the delta wing, especially at the higher angles of attack.

Leading-Edge Vortices. The leading-edge vortices of delta wings have been observed and measured by several investigators (1). Many techniques including tuft surveys, oil film studies, condensation trail photographs and water tunnel studies have been used. Based on these observations the vortex flow pattern for a typical wing is illustrated in figure 3. Vortex sheets are shed off the leading-edges and blow back over the upper surface rolling up to form a pair of stable vortices. These vortices appear on top of the wing and increase in intensity downstream from the apex. By the time the vortex sheet reaches the wing trailing-edge it is fully developed. The pressure differential between the upper and lower surfaces causes the flow velocity and the formation of the leading-edge vortices. As would be expected the pressure difference increases with angle of attack with a resultant increase in the strength of the vortices. As the apex angle of the delta wing decreases, a reduction of aspect ratio, the tip vortices on either side will interfere. The tip vortices on the upper surface of the wing proceed downstream at a downwash angle corresponding to the lift of the wing until they break up.

Flow Pattern. Details of the flow pattern around the edge of a slender delta wing operating at a 15° angle of attack were determined from (1,a) and are given in figure 4. The pressure survey at the 42% root chord show a strong flow around the edge of the wing due to the pressure difference between the upper and lower surface. The vortex sheet originating from the edge rolls up in a large single vortex core. This is basically the same type flow encountered with any other wing. The difference is due to the fact that the lateral edges are long in comparison to the span of the slender shape wings considered.

With the rolling-up process there is a strong lateral flow toward the edges as indicated in figure 3. A secondary separation and the formation of another small vortex is developed from this flow. The direction of rotation of this vortex is opposite to the main leading-edge vortex, figure 3. In the main leading-edge vortex there is a progressive reduction of the total pressure and increasing intensity of the edge vortex sheets with increasing angle of attack.

The pressure distribution across the span is shown in part (B) of figure 4. Most of the normal force is produced in the outer 1/2 or 2/3 of the semispan on the upper surface. This type of pressure distribution is influenced by the tip vortices as well as the normal circulation flow on the wing.

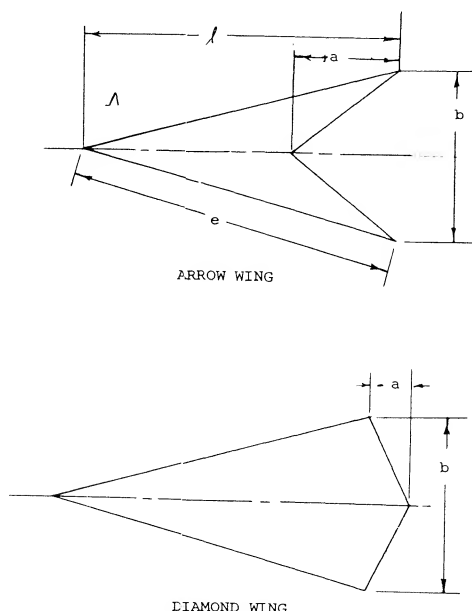


Figure 2. Characteristics of arrow and diamond shape delta wing modifications.

- (1) The flow pattern of slender delta wings:
 - a) Fink, Experiments on Vortex Separation, R&M 3489.
 - b) Lee, Delta Wing Flow, ARC RM 3077 (1958).
 - c) Bird, Flow Visualization, NACA TN 2674 (1952) & TN D-5045.
 - d) Earnshaw, Structure of a Leading-edge Vortex, R&M 3281.
 - e) Peckham, Series of Uncambered Pointed Wings, R&M 3186.
 - f) Poisson-Quinton, Water Tunnel Visualization Vortex Flow, A.A. June 1967.

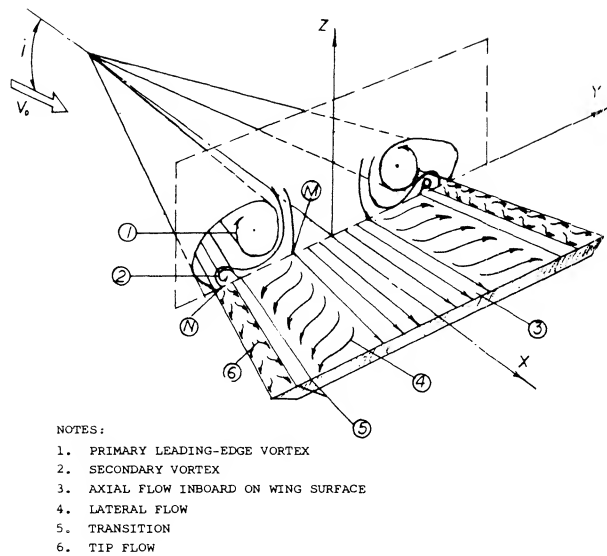


Figure 3. Flow distribution of a sharp-edge delta wing showing primary and secondary leading-edge vortices.

Vortex Pair. The pair of leading-edge vortices are located with respect to the wing as shown on figure 5. The height of the core above the wing increases with angle of attack, but the spanwise position decreases. Aft of the wing the core of the vortices achieves a downwash angle equal to approximately 0.5α . Theory does not predict the location of these vortices with any accuracy (2).

Vortex Breakdown. The leading-edge vortex remains stable along the wing surface and proceeds downstream until bursting takes place (3). At bursting the vortex becomes irregular and influences the flow pattern. With a further increase of angle of attack, the vortex bursting takes place on the wing starting at the trailing edge. As the

angle of attack increases further, the bursting point moves toward the apex. Although the vortex core breakdown represents an abrupt increase of the core diameter with increased dissipation, it does not lead to a complete absence of vortex type flow. However, when the vortex bursting takes place at the wing trailing-edge, it can be expected that the vortex lift increment will decrease with further increases of the angle of incidence.

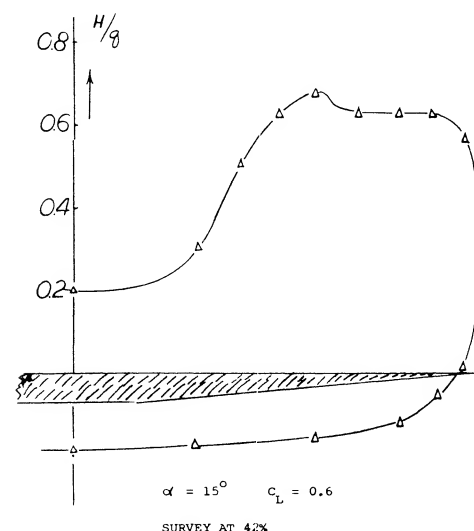
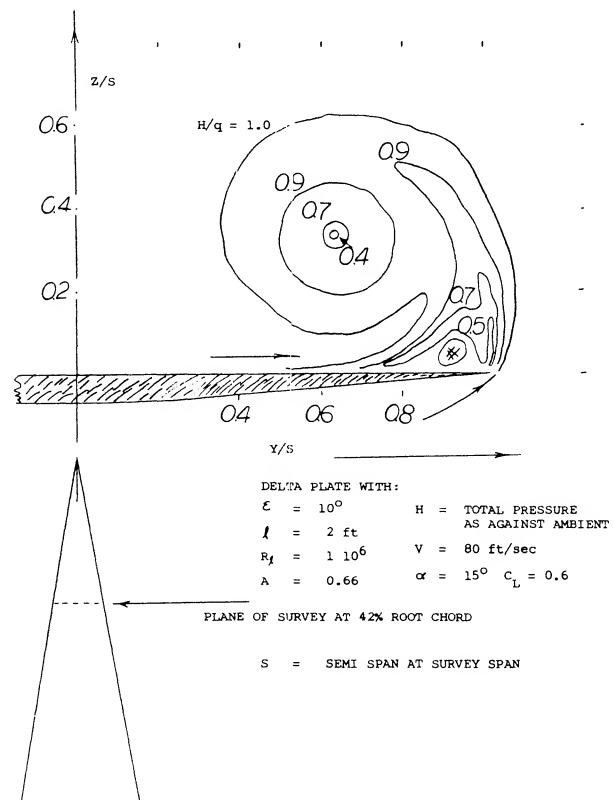


Figure 4. Pressure survey of flow pattern in the vicinity of the tip of a delta wing, including spanwise load survey.

- (2) Analysis considering delta wing vortex formation:
 - a) Legendre, Recherche Aeronautique No. 30, 31, 35 (1952/53).
 - b) Brown, "Separation", NACA TN 3430 and J Aeron Sci 1954 p 690.
 - c) Chang, Non-linear Lift, J Aeron Sci 1954 p 212.
 - d) Jones, NACA T Rpt 835 (1946); also J Aeron Sci 1951 p 685.
 - e) British Efforts, ARC RM 1910, 2596, 2819, 3116.
 - f) NACA, Wing Theory, T Rpts 921 & 962 (1948/50)
 - g) Lomax, Slender Wing Theory, NACA T Rpt 1105 (1952).

Lift Variation. The typical experiment results (4,h) of the variation of the lift and moment of a slender, sharp edge, flat delta wing is given on figure 6. As a result of the potential flow and vortex lift created by the vortices described above, the lift curve is non-linear as is illustrated. The slope of the lift curve increases with angle of attack until vortex bursting takes place, after which a stall takes place with a corresponding reduction of lift. The angle and chordwise location for the vortex bursting is also given on figure 6. The vortex bursting was determined from flow observations. The slope of the moment curve is negative and linear up to the stall angle.

The initial slope of the lift curve at zero angle of incidence represents the linear portion of the lift curve and is equal to the potential or circulation lift of the wing. This portion of the lift curve is the same as was observed in the case of low aspect ratio wings and can only be estimated at zero angle of attack from the experimental data. Above this angle the potential flow lift follows a $\sin \cos^2 \alpha$ function indicated by theory as discussed in the next section.

The experimental lift curve shown in figure 6 also contains the component or lift which is produced by the leading-edge vortices. This lift component is referred to as vortex lift and follows an angle function corresponding to $\sin^2 \alpha \cos \alpha$ until there is an apparent limit due to vortex breakdown. The vortex lift increment is illustrated on figure 6 and can be calculated for sharp-edged flat wings as shown in the next section.

60° Delta Wings. The characteristics of a larger aspect ratio delta wing are given on figure 7. This wing is a flat plate with rounded leading-edges with zero camber and $A = 2.31$. The results shown in terms of the normal force coefficient indicate a maximum lift at $\alpha = 33^\circ$ dropping to a value of .88 at $\alpha = 45^\circ$.

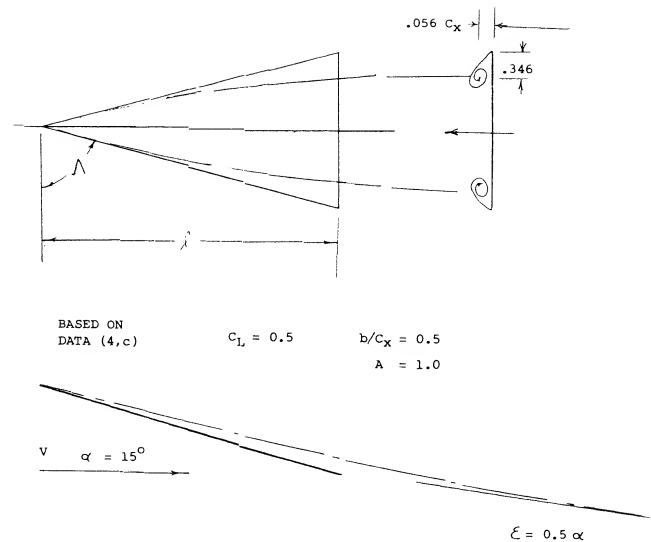


Figure 5. Location of leading-edge vortices with respect to a delta wing of $A = 1.0$.

Lift to $\alpha = 90^\circ$. The lift coefficients as in figure 7 sooner or later reach maximum values beyond which the flow separates from the suction side. However, as shown, after an appreciable drop there is still lift at angles of attack between 20 and 40° corresponding to lift coefficients between 0.7 and 0.8 . Lift at still larger angles, to 90° , is the result of pressure at the lower side of negative pressure within the separated space at the upper side and as a consequence of some circulation. This type of flow pattern in larger A 'ratios at larger angles of attack, characterized by an alternating vortex street, is different from the cross-flow type described above. Basically, we may consider lift at angles near 90° to be a component of pressure drag. To estimate the variation of lift and normal force to $\alpha = 90^\circ$ we assumed, therefore, that $C_N = C_D = 1.2$ (for a flat plate) and reduces as the function $1.2 \sin^2 \alpha$. The normal force variation for the entire wing is given for the range based on this variation. At intermediate angles (between 30 and 60°) there is evidently some additional component of lift, other than that due to drag, due to circulation and to deflection of the flow field including the viscous wake.

The history of lift (or normal force) is reflected in the center of pressure point, shown in the upper part of the graph. The center of pressure is first located at $x/l = 0.56$ or 0.57 . On account of the non-linear component, the point moves forward as far as to 0.54 of the chord. At $\alpha = 90^\circ$, the center of pressure will necessarily be at the geometric center of the delta plate, at $2/3$ of the length. As the "wing" stalls (between 30 and 40°) the pressure point moves aft, roughly 10% of the length of the plate.

- (3) Vortex bursting on delta wings:
 - a) Wentz, Vortex Breakdown on Slender Sharp-edge Wings, AIAA No. 69-778.
 - b) Earnshaw, Vortex Breakdown Position Sharp-edge Wings, RAE C.P. 828.
 - c) Lambourne, Breakdown of Certain Types of Vortex, NPL Report 1166.

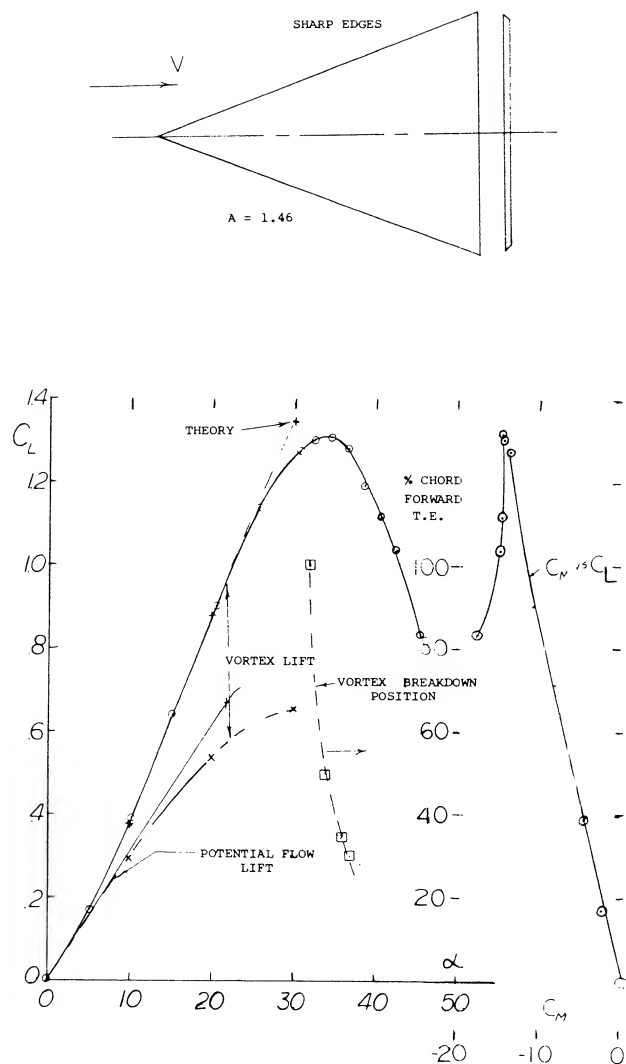


Figure 6. Typical variation of lift and moment coefficients of a sharp-edge delta wing, including vortex bursting location.

- (4) Experimental characteristics of delta wings:
- Jones and Miles, Plates, ARC RM 2518 (1952).
 - Peckham, Pointed Wings, RAE ARC RM 3186 (1961).
 - Jones, Modified in CAT, ARC RM 2871 (1954).
 - Lange-Wacke, ZWB UM 1023/5 (NACA T Memo 1176).
 - Lee, Delta Wing Flow, ARC RM 3077 (1958).
 - Tosti, Derivatives, NACA TN 1468, see T Rpt 1105.
 - Truckenbrodt, 0012 Deltas, ZFW 1956 p 236; also Swept and Deltas, ZFW 1954 p 185; also Stalling in Rpt 1957/11a Inst Fluid Mechanics TH Brunswick; also Feindt, same subject Rpt 1956/36.
 - Lawford, Low Speed Sharp-edge Delta Wing, R&M 3338.
 - Letko, Lateral Stability, NACA RM L57A30
 - Jorgensen, Cones with Plates, NACA Rpt 1376
 - Tosti, Low Aspect Ratios, NACA TN 1468

3. ANALYTICAL ANALYSIS

The theory for calculating the lift characteristics of delta wings has received considerable attention (2) without the development of an exact solution. The difficulty appears to be the determination of the location of the leading edge vortices. Further, problems due to separation such as might be developed about a round edge, further complicates finding an exact solution. A procedure has been developed, however, for calculating the potential flow and vortex lift components for sharp edge flat plate delta wings. This procedure (5,a,b,c,d) is based on a leading edge suction analogy and is very effective for finding the lift components. Although it is limited to sharp edge type wings this procedure will be used as a basis for determining the lift of delta type wings. The effects of changes due to planform shape, edge radius, flaps, control devices and bodies not considered by the leading-edge suction analogy are then determined based on experimental data.

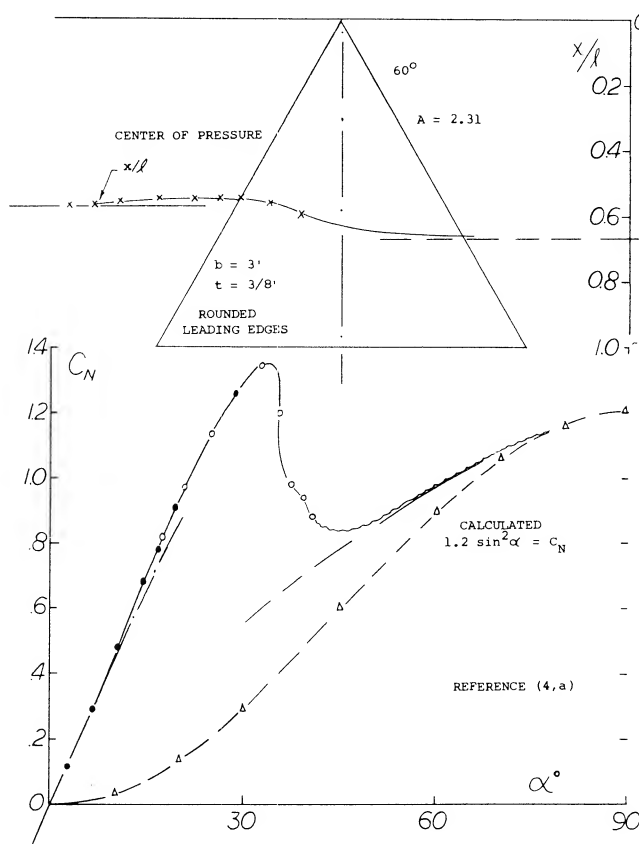


Figure 7. Characteristics of a larger aspect ratio delta wing to high angles of attack.

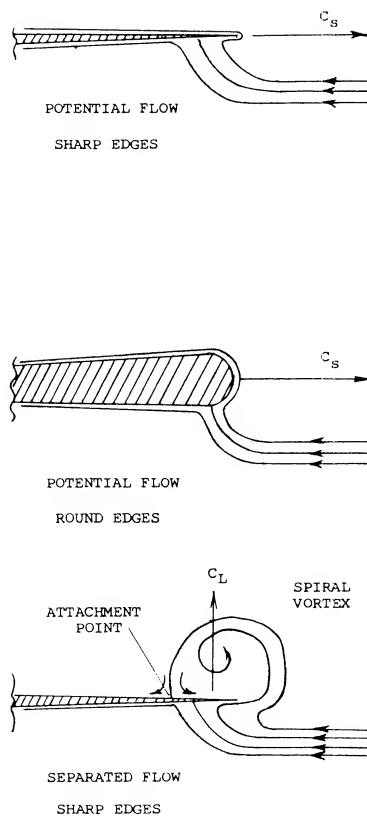


Figure 8. Leading-edge flow conditions comparing theoretical and actual conditions.

Potential Flow Lift. The potential flow lift component of sharp edge wings is determined assuming no leading edge suction can be developed, since a Kutta type condition is assumed to exist (5,a), figure 8. It is further assumed that the flow reattaches downstream of the leading edge vortex. Although the potential flow lift is reduced by the assumed loss of leading-edge suction, which should be changed to the vortex lift term, it is retained for convenience. Without leading-edge suction the resultant force for plain wings is the potential flow wing normal force which depends on the strength of the circulation. The strength of the circulation about the lifting surface requires the velocity normal to the wing induced by the complete vortex system to be equal to $V \sin \alpha$. The velocity of the flow is thus parallel to the wings satisfying the Kutta condition at the trailing edge. By this method a coefficient K_p is determined which is related to the potential flow lift coefficient C_{LP} by

$$C_L = K_p \sin \alpha \cos \alpha \quad (1)$$

Equation 1 becomes for small angles

$$C_L = K_p \alpha; \quad dC_L/d\alpha = .0174 K_p \quad (2)$$

Since K_p is dependent on the planform it has been found by a suitable lifting-surface theory (5,3) as a function of aspect ratio for delta, arrow and diamond shape wings and is given on figure 9. The lift coefficient due to potential flow is then calculated using equation 1 and a value of K_p from figure 9, which depends on the planform of the wing.

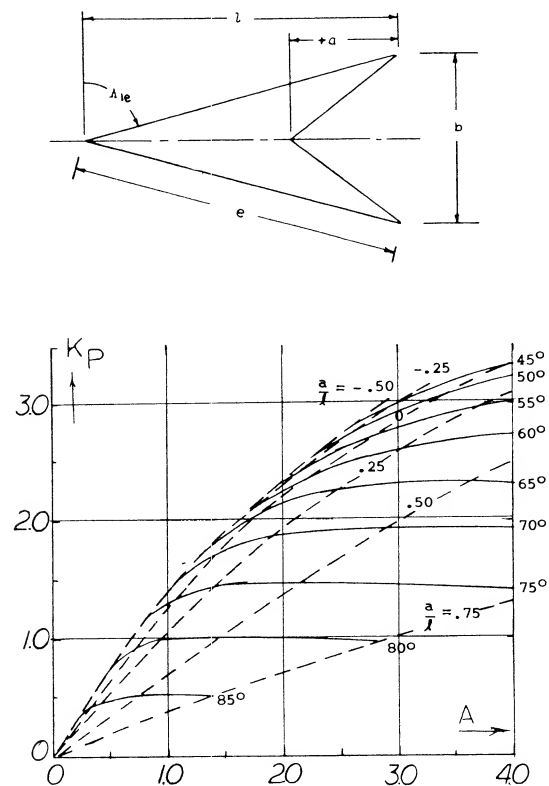


Figure 9. Potential flow lift constant as a function of planform parameters

- (5) Theoretical Analysis:
 - a) Polhamus, Vortex Lift Based on Leading-edge Suction Analogy, NASA TN D-3767.
 - b) Polhamus, Application of Leading-edge Suction Analogy for Delta Wings, NASA TN D-4739.
 - c) Polhamus, Charts for Predicting Characteristics of Delta Wings, NASA TN D-4739.
 - d) Polhamus, Predictions of Vortex-Lift by Leading-edge Suction Analogy, J of Aircraft, April 1971.
- (6) Experimental investigation of "parabolic" planforms:
 - a) Peckham, Series of Pointed Wings, ARC R&M 3186.
 - b) Spencer, Series of Planforms, NASA TN D-1374 (1962).
 - c) Kirby, "Thin Slender Wings", Letter report to Hoerner.

Vortex Lift. The flow developed by the leading-edge vortices on the top surface of the wings results in the development of the vortex lift component of lift. This lift component is generated by the downward momentum produced by the flow over the wing leading-edge from the pair of counter-rotational vortices above the wing, as is illustrated on figure 3. The suction peaks associated with the leading edge vortices give an increase in the lift curve slope with incidence and so causes the characteristic non-linear lift curve of slender delta type wings.

Theory. There have been many attempts to develop a theory for calculating the position of the leading-edge vortices on a wing and their effect on lift (2). These efforts have generally failed so that correlation with test data is poor. As in the case of low aspect ratio wings, the non-linear lift has been analyzed on basis of a drag based on the flow normal to the wing. This concept results in a lift increment equal to

$$C_L = C_D \sin^2 \alpha \cos \alpha \quad (3)$$

where C_D is the drag coefficient of the wing operating at an angle of attack equal to 90° . Fairly good correlation of test data is obtained with this procedure as indicated in conjunction with figure 7, Chapter XVII. However, at the lower angles of attack it appears that this is not the correct concept for calculating the change in lift due to the vortex flow of delta wings.

Leading-edge Suction Analogy. With the assumption of the leading-edge analogy (5,a,b,c,d) a procedure was developed that can be used to calculate the vortex lift increment. This method was developed for sharp edge delta type wings. The leading-edge suction analogy depends on the assumption that the thrust due to suction produced by the vortex in front of the wing is the same as that produced by the vortices on top of the wing. Thus, the vortices needed in the theoretical solution are not real in the sense of their location, since the experimental results show they are located on top of the wing, figure 3. By assuming that the thrust or suction force produced by the vortices is the same as produced by the actual vortices on the wing, lift increment is calculated by the equation

$$C_L = K_V \sin^2 \alpha \cos \alpha \quad (4)$$

The value of K_V was developed in (5,a) for delta type, arrow and diamond planform wings with sharp edges and zero camber and is given in figure 10.

The value of K_V for plain delta wings is approximately equal to π . This is considerably above any drag coefficient that might be expected for a delta wing operating at an angle of attack of 90° . It would, therefore, appear that the concept of drag is not valid for predicting the non-linear lift term of delta wings.

The calculated vortex and potential flow lift using equations 2 and 4 agree closely with measured values up to 20° as illustrated in figure 6. This correlation is typical for slender type flat delta wings with sharp edges which the theory assumes. Because of this excellent correlation a base is available for evaluating changes due to leading-edge radius, camber, flaps, control devices and bodies.

Vortex Lift to Total Lift. The vortex lift becomes the primary component as the sweep angle or slenderness of the wing is increased. This is illustrated by the data of figure 11 that shows the lift ratio as a function of aspect ratio.

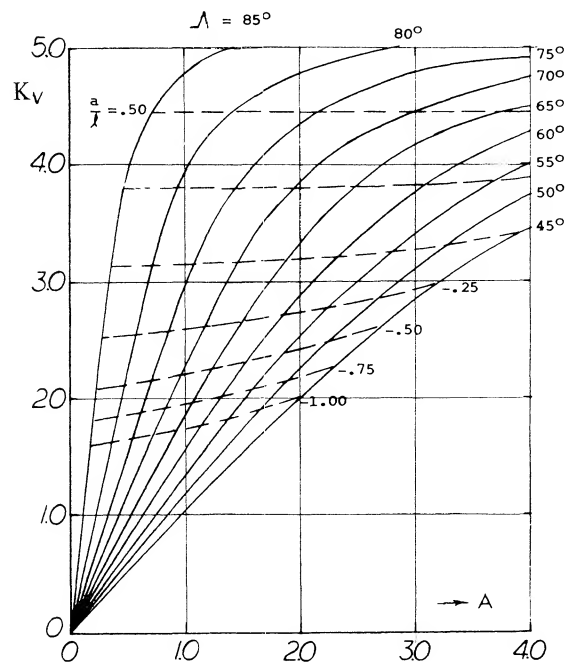


Figure 10. K_V plot vortex-lift constant as a function of planform parameters.

$$\alpha = 12^\circ$$

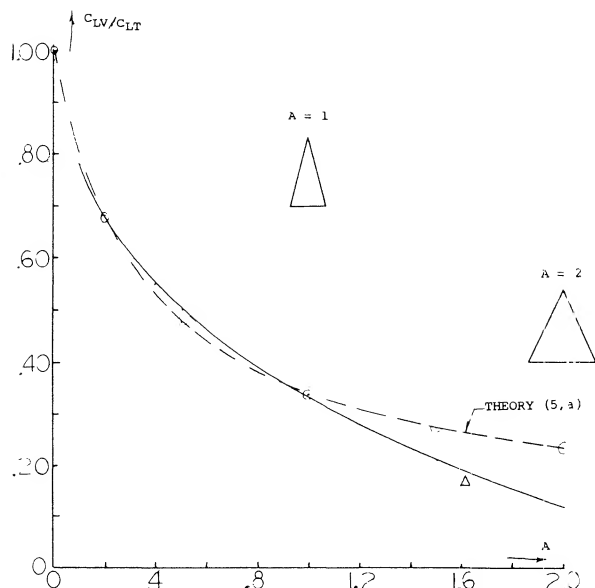


Figure 11. Comparison of vortex lift to total for delta wings $A = 0$ to 2.0.

Delta-Low Aspect Ratio Wing Analysis. The large difference shown in the value of K_V in comparison to C_D was not obtained with low aspect ratio wings, Chapter XVII. This could be due to the change in the potential lift curve between delta and low aspect ratio wings. The potential lift term determined for low aspect ratio wings is much higher than that for delta wings. Thus, the component due to the vortex flow is lower as determined from the experimental data for low aspect ratio wings. Since the potential flow can only be estimated from the test data, the question cannot be resolved. For this reason it is necessary to separate the analysis of the two types of wings until a more unified theory is developed.

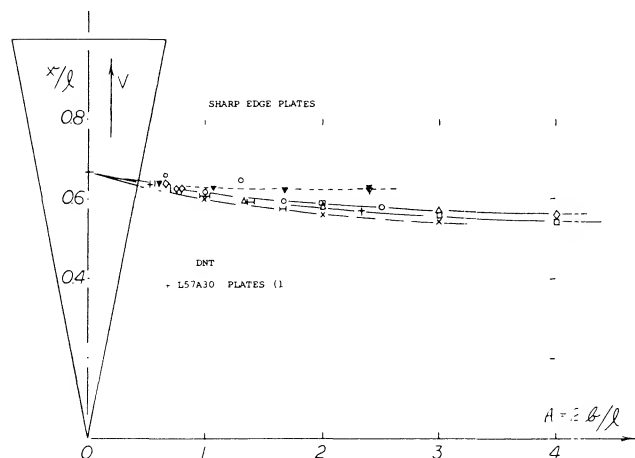


Figure 12. Aerodynamic center of delta wings derived from experimental results.

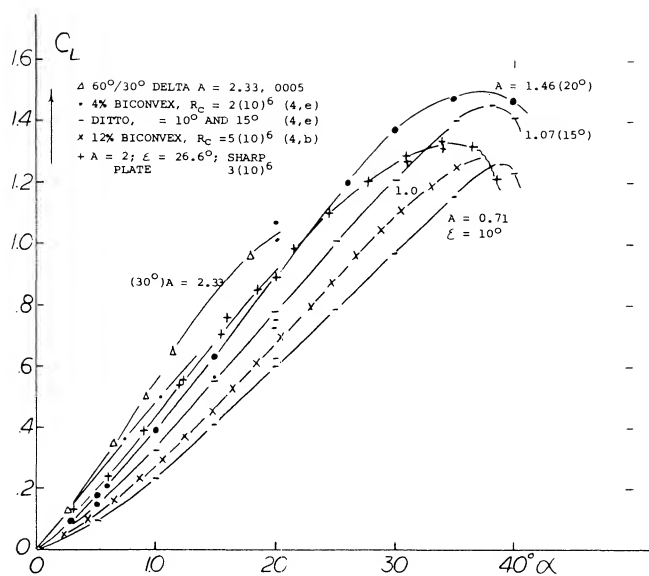


Figure 13. Lift characteristics of delta wings having sharp-edge (biconvex) airfoil sections tested by ARC (4) at low speeds.

The Aerodynamic Center. The chordwise position where the coefficient of the pitch moment is constant, aerodynamic center, is theoretically:

at $x/c = 0.25$, in foil sections or straight wings

at $x/l = 2/3$, in slender delta wings.

Considering a delta wing to be a swept and highly tapered shape, a mean aerodynamic chord can be found using figure 2 of the first "longitudinal" chapter. As mentioned in connection with figure 1, this chord would be $c = (2/3)l$. In aspect ratios approaching zero, in very slender delta wings, the theoretical position of the aerodynamic center at $x = (2/3)l$, corresponds to $0.5c$, rather than to $0.25c$ as in large A' ratios. However, we will refer the position of the center to the length l of the delta wings considered. Experimental results evaluated from dC_m/dC_L slopes at small angles of attack (around zero lift) are plotted in figure 12. Assuming that the position, say at $A = 10$, would be close to $x/l = 0.5$, it is seen moving toward the trailing edge as the A' ratio is reduced. All of the series of wings and plates investigated seem to approach the $2/3$ position as their aspect ratio approaches zero. The limit up to which delta wings would

actually be used may be $A = 2$ (where $l/b = 1$). In this planform shape, profiled (and round-edged) wings show positions $x/l = 0.59$. By comparison, flat plates have a more forward position, namely at 56% of the length (at $A = 2$).

4. CONFIGURATION VARIABLES

Changes in the lifting characteristics of delta type wings due to changes of geometry from the simple shapes considered in the previous section can only be determined by test. Considerable test data is available so that these effects including changes in planform shape, leading-edge radius, camber and control devices can be found and compared with the lift characteristics of the simple wing found by the modified theory.

Aspect Ratio. The effect of changes in aspect ratio sharp-edge delta wings based on low speed wing tunnel tests is given on figure 13. Since the potential flow lift term can only be estimated by determining the slope at $C_L = 0$ and in accordance with equation 1 it varies as $\sin \alpha \cos^2 \alpha$, comparison with the calculated values are made based on the total lift. The agreement between the calculated total lift based on equations 1 and 3 and test data is good for the entire range to $A = 2.3$, and for angles of attack below where vortex bursting might be expected. The increase of the slope of the lift curve with aspect ratio and angle of attack predicted by the modified theory (5,a) and test data is thus confirmed.

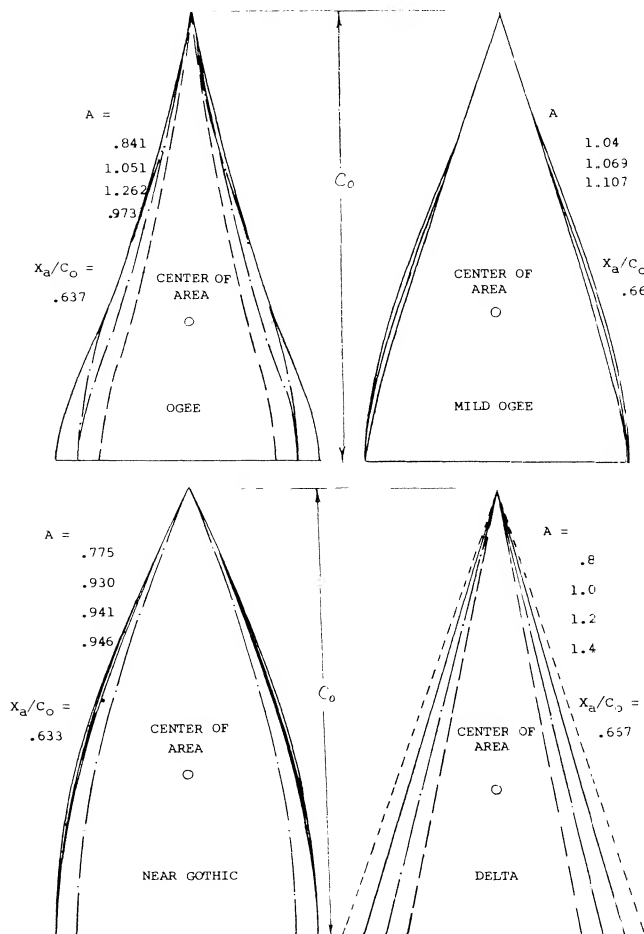


Figure 14. Planform shapes of slender delta wing tested, including ogee, gothic and delta types.

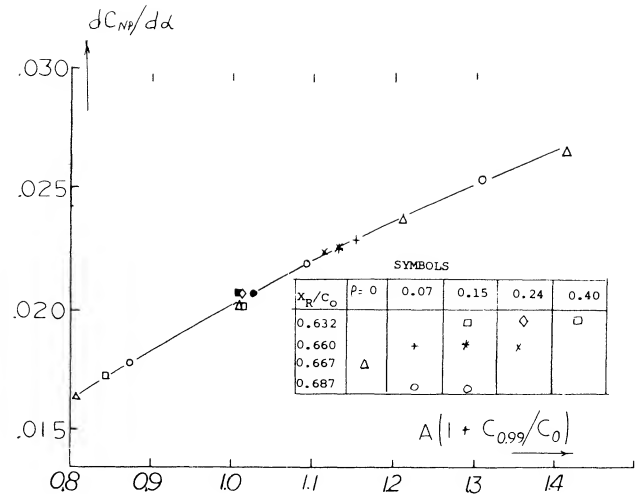


Figure 15. Potential flow lift of ogee, gothic and delta wings collapsed to a single line.

Planform Shape. The effects of changes of planform shape from the simple delta wing on the potential flow and vortex lift coefficients has been found for a series of sharp leading-edge delta type wings for A from .75 to 1.25 (6). The shapes evaluated include ogee, gothic and delta wings, figure 14. The test data for these wings were collapsed into a single line (7) for both the potential flow and vortex lift components.

Potential Flow Lift. A single line for the potential flow lift curve slope of the series of wings was obtained, figure 15, plotting $dC/d\alpha$ as a function of the factor $A(1 + C_{0.99}/C_0)$. By modifying the aspect ratio by the above factor the planform shape effects are normalized more in line with theory. Since the potential flow lift curve slope can only be estimated from test data at zero C_L the data given on figure 15 applies strictly for low angles of attack. To find the slope due to changes in angle of attack the data should be modified by the factor $\sin \alpha \cos^2 \alpha$. The corresponding theoretical line for the potential flow lift calculated from equation 1 and figure 9 is also shown on figure 15. This curve indicates a loss of lift in comparison to the theoretical which increases with aspect ratio.

- (7) Delta wings experimental characteristics:
- Fink, Zeit Flug Wissenschaft 1956 p 247.
 - British ARC, RM 2518 & 3077.
 - NACA, Tech Note 1650.
 - Hall, Wing-Body Configurations, NACA RM A53A30.
 - See also (6).
 - McKay, Reversing Triangular Wing Body, NACA 51H23.
 - Lange, 0012 Wings, 'ZWB Rpt UM 1023/5; NACA TM 1176.

Vortex Lift. The vortex lift element of delta type slender wings can be correlated into a single line, as shown on figure 16, by modifying the normal force slope using a factor which depends on the span at a semispan from the trailing-edge. This factor

$$f(S) = b'/b \quad (5)$$

where $b' =$ the span at a distance $b/2$ from the trailing edge. For the range of aspect ratios considered good correlation is obtained when the corrected slope is plotted as a function of α°/A , figure 16. At α_i/A above 20 the correlated data is below that calculated by theory equation 3, figure 10, indicating the vortices have started to break down in lift effectiveness.

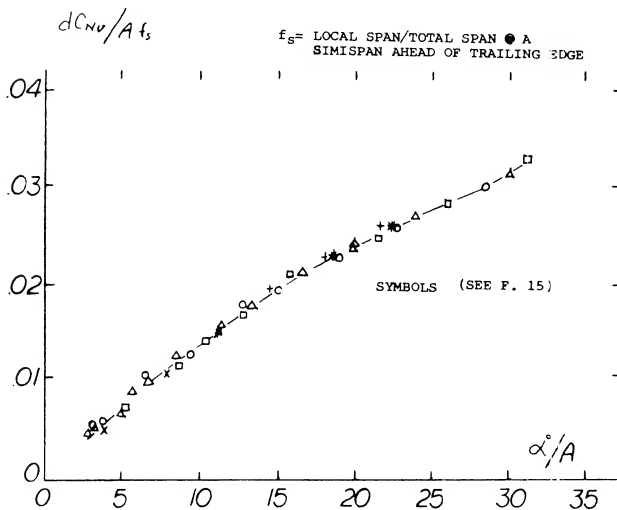


Figure 16. Vortex lift element of delta type wings correlated into a single line.

Leading-Edge Shape. The leading-edge shape, which can also be considered to be the tip shape of delta wings, has a large effect on the lift produced by the wings. It appears that the proper formation of the vortex in conjunction with the spanwise flow is essential to the production of lift. As previously noted, the formation of the vortex and estimation of its lift is based on the assumption of sharp edges as illustrated in figure 8. Any deviation in shape from the assumed sharp edge can be expected to produce a reduction in the lift. From the flow patterns observed (8) it appears that the effect of leading-edge shape mainly effects the vortex lift. This is difficult to confirm as the vortex and circulation lift components are not measured separately.

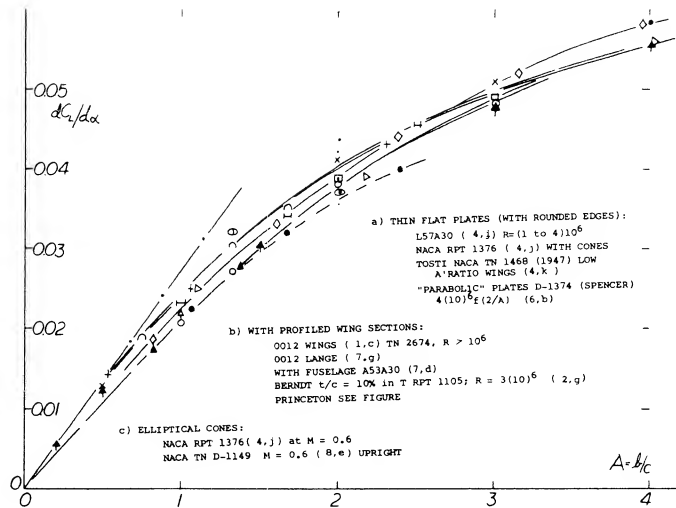


Figure 17. Lift curve slope of a series of delta wings showing effect of leading edge condition and comparison with calculated values.

Circulation Lift - Leading-Edge Shape. The potential flow or lift produced by circulation can be estimated from test data of the complete wing by finding the slope of the lift curve at zero angle of attack. Although this can only be done at low angles of attack, it is possible to find the effects of leading-edge radius at least in this range. Shown in figure 17 is the lift curve slope as a function of aspect ratio for different types of leading-edge radius. Also given is the theoretical variation based on the leading-edge suction analogy. In the aspect ratio range up to 1.5 the test data splits the estimated value. While at the higher values of A the experimental slope is above that calculated. Wings with sharp leading edges appear to have higher lift coefficients than wings with round leading edges. It appears, therefore, that part of the lift loss due to tip shape may be associated with circulation lift. We tend to discount this, however, due to the general inaccuracies in the data and slope estimation.

Vortex Lift - Leading-Edge Shape. Because of the non-linear shape of the lift curve of delta wings, C_L is examined at two different angles of attack, 10 and 20 degrees, as a function of aspect ratio, figure 18. The test data is divided up into that for sharp or round leading wings and is compared with the lift calculated by equations 1 and 3. The available data on sharp leading-edge wings shows good agreement with the calculated values at both angles. The wings with round leading edges have a marked reduction in lift with increasing aspect ratio. This is especially true at the higher angles and aspect ratios above 2.0 where the lift drops off with increasing A . For instance at A above four the lift curve slope begins to decrease when taken at $\alpha = 10^\circ$, figure 18. This is due to vortex breakdown as discussed in the next section.

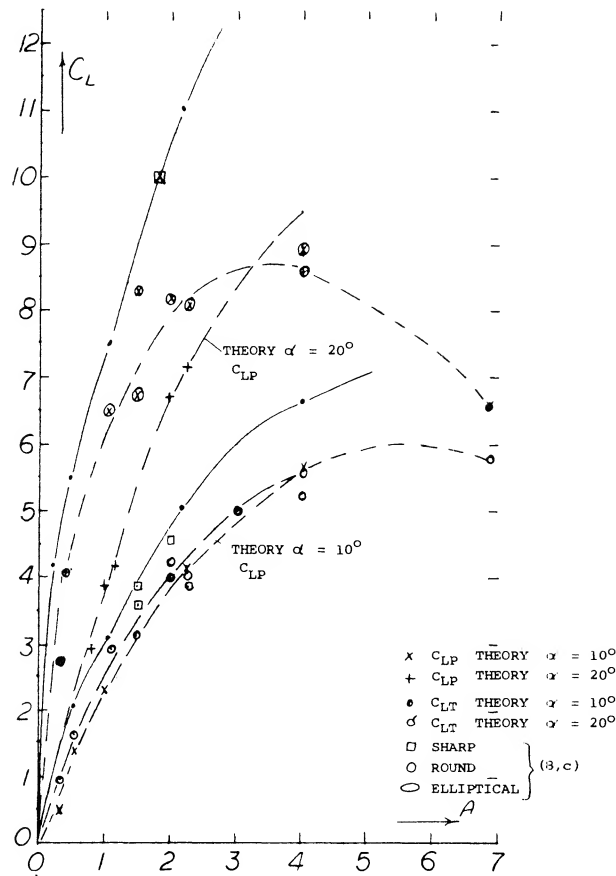


Figure 18. Effect of edge shape on the lift of delta wings at angles of attack of 10° and 20° .

Camber. To obtain the desired characteristics of delta wings at the high speed flight condition camber may be used, (9,a,b). In this case camber was used to obtain design lift coefficients as high as .075 with the achieved value being 85 to over 100% of the design value. The lift characteristic of the wing with camber appears to follow the uncamber wing with an increment equal to the design value. For wings with an ogee planform the use of camber increased the lift drag ratio (9,b) and has a large influence on the position of center of pressure, depending on the chordwise distribution.

In (9,c) a series of wings of varying camber with an aspect ratio equal to 1.0 were tested to determine the non-linear effects, figure 19. The C_L at $\alpha = 0$, 10° and 20° show that the local angle at the leading edge has a large effect, especially over 40 degrees. The inverse

dihedral angle plus an angle at the leading edge of 17 degrees appears to be the most effective way of improving lift.

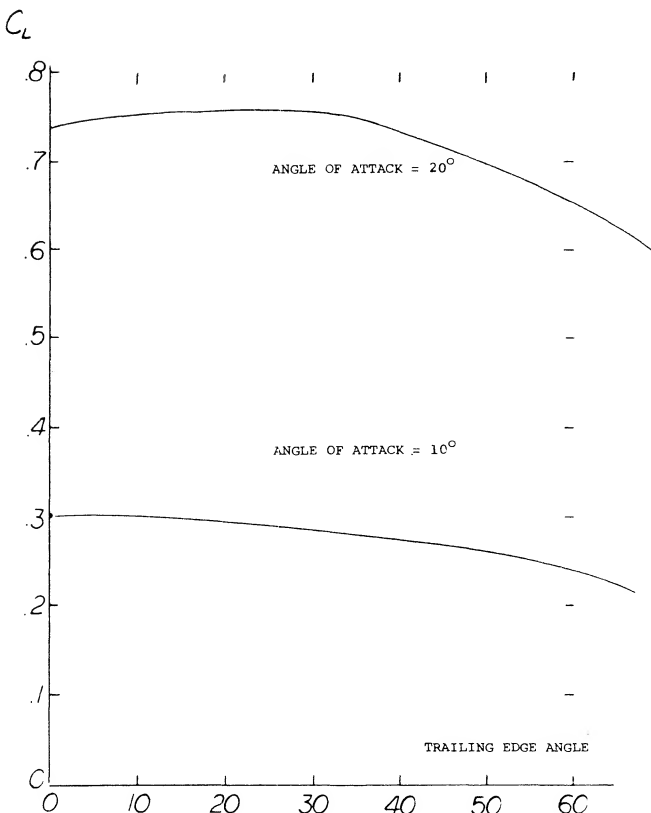
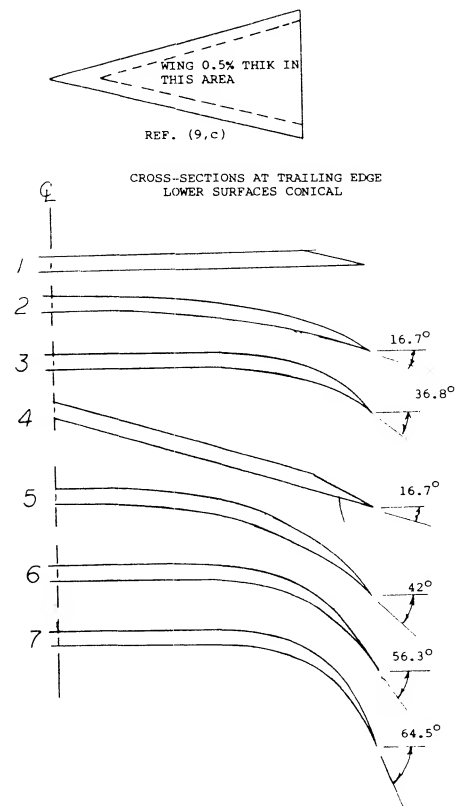
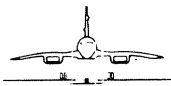
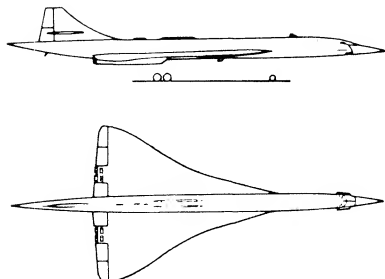


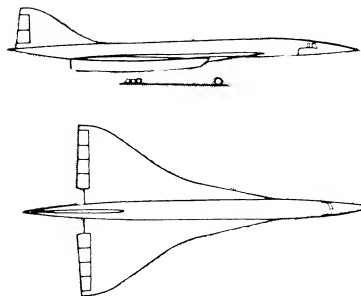
Figure 19. Variation of lift at $\alpha = 10^\circ$ and 20° as a function of camber.

- (8) Characteristics of sharp-edged arrowhead wings:
- Buell, Flat-top Configuration, NASA Memo 3-5-59A.
 - Treon, Hypersonic Configuration, NASA TM X-364
 - Bartlett, Edge Shape, J Aeron Sci 19-55 p. 517.
 - Shanks, Six Plates, NASA TN D-1822 (1963).
 - Jorgensen, Cones with Plates, NACA Rpt 1378

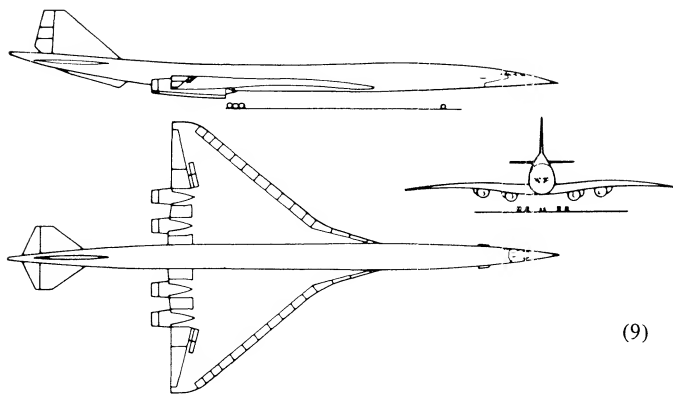
BRITISH/FRENCH CONCORDE



RUSSIAN TU-144



UNITED STATES SST



Double Delta Wings. The double delta wing is used for high speed airplanes for reducing the large rearward aerodynamic-center shift that occurs between subsonic to supersonic flight. Examples of double delta wing configurations are shown on figure 20 for supersonic transport type airplanes (10,d). This shift is obtained because of the change in aerodynamic loading from the rear delta at high speeds. Even with the use of the double delta configuration it may be necessary to shift fuel longitudinally to maintain the desired stability.

The effect of the use of a double delta wing planform on lift characteristics can be determined based on the leading-edge suction analogy (5,c). For the case where a glove or second delta is added to the basic wing the factors in the lift equation K_P and K_V are given as a function of the sweep angle of the leading edge, figure 21. For this case the vortex lift will increase with an increase of the first wing delta angle while the potential flow lift decreases. This is probably due to the increase in length of the leading-edge vortex and the effective decrease in aspect ratio due to the leading delta. The net result of this is a decrease of total lift compared to the basic wing, figure 22.

The experimental data (10,e) given on figure 22 shows that nearly the same lift is obtained with the double delta wings as the basic wing. Although the level is below the theoretical values, the improvement is probably due to the delay of the vortex lift breakdown to higher angles. Thus, the addition of the glove does not appear to reduce the wing lift. The choice of the combination of double delta wings will thus depend on the center of pressure shift needed in the design and the lift drag ratio, see figure 31.

Figure 20. Supersonic transport aircraft using double delta planform wings.

- (9) Camber effects of delta type wings:
- Dobson, Cambered Wing of Slender Ogee Planform, ARC C.P. 778.
 - Earnshaw, Low Speed Tests Series of Cambered Ogee Wings, ARC C.P. 775.
 - Squire, Non-linear Lift of Slender Wings, ARC C.P. 924.
 - Smith, Conical Camber to Produce Flow Attachment-Theory, R&M 3289.
 - Dollyhigh, Aft Tail Fighter with Cambered, Uncambered Wings & Uncambered Fuselage, NASA TM X-3078.

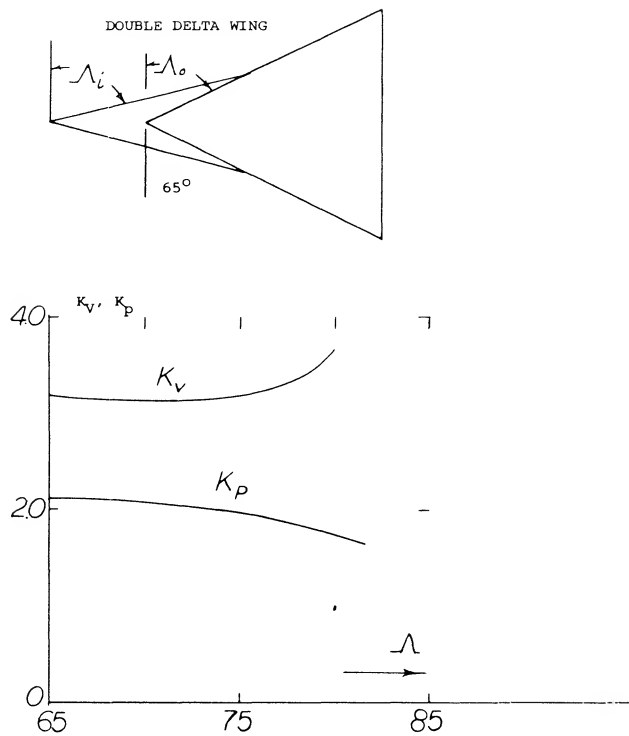


Figure 21. Potential flow and vortex lift factors, K_p and K_v for 65° basic delta wing with glove.

Wing + Bodies. As shown in Chapter XIX on the lift characteristics of streamline bodies, vortices are formed that are similar in nature to those produced with delta wings. These vortices lead to the 2α flow on the body and in the vicinity of the wing root with the result that a strong interaction is encountered. Thus, in determining the characteristics of the wing and fuselage it is necessary to consider:

- effect of the wing vortices on the wing
- interference of the wing vortices on the fuselage
- effect of the fuselage vortices on the fuselage
- interference of the fuselage vortices on the wing.

The influence of the fuselage on the lift curve slope of delta wings is given on figure 23 for $A = 1$ and 2 . The 2α cross flow of the body reduces the lift on the wing body combination. This is further confirmed by the two dimensional data of (11,b) which shows the effect of wing position. As the wing moves forward the lift increases as shown approaching the theoretical value for the wing alone. This would be expected as the body vortices influence a smaller portion of the wing as it moves forward. In (11) a theoretical procedure for calculating the lift of the combination is given which includes consideration of the fuselage vortices and gives good agreement with the experimental data. In this theory the wing is replaced by a continuous vortex distribution. The trailing vortices are then located in sheets inclined at an angle of α_∞ with respect to the wing plane. Non-linear lifting surface theory is then used to solve for the effects of these vortices on the wing (11,a).

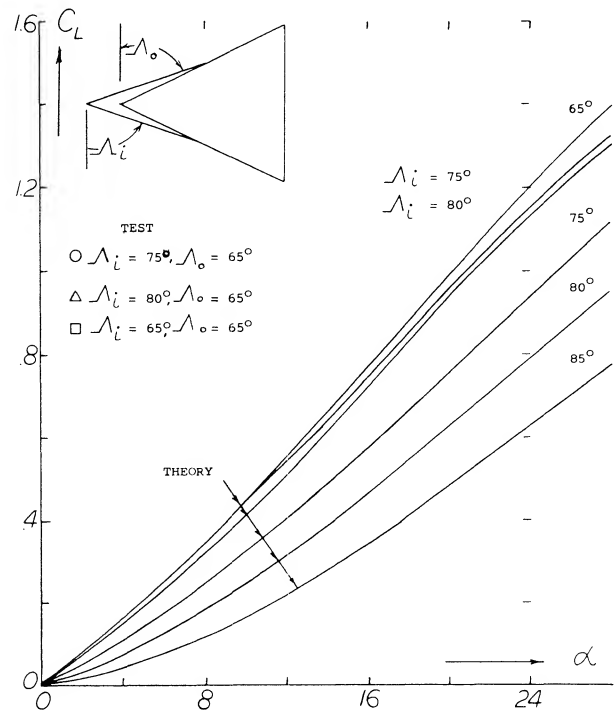


Figure 22. Lift coefficient for wings with and without double delta planforms.

(10) Double Delta wings:

- Freeman, Low Speed Flight and Force Investigations NASA TN-4179.
- Hopkins, Cranked Leading-edge Wing-Body Combinations $M = .4$ to 2.94 , NASA TN D-4211.
- Corsiglia, Aircraft Model Double-Delta Wing Longitudinal and Lateral Characteristics, NASA TN-5102.
- Boeing Document 1971.
- Wentz, Sharp-edged Slender Wings, AIAA Paper 69-778.

(11) Wing-body combinations:

- Otto, Non-linear Lift and Pitching Moment Coefficients, J of A/C, Aug 1974.
- Hall, Lift, Drag and Pitching Moment of Low-aspect-ratio Wing and Bodies, NACA RMA53A30.

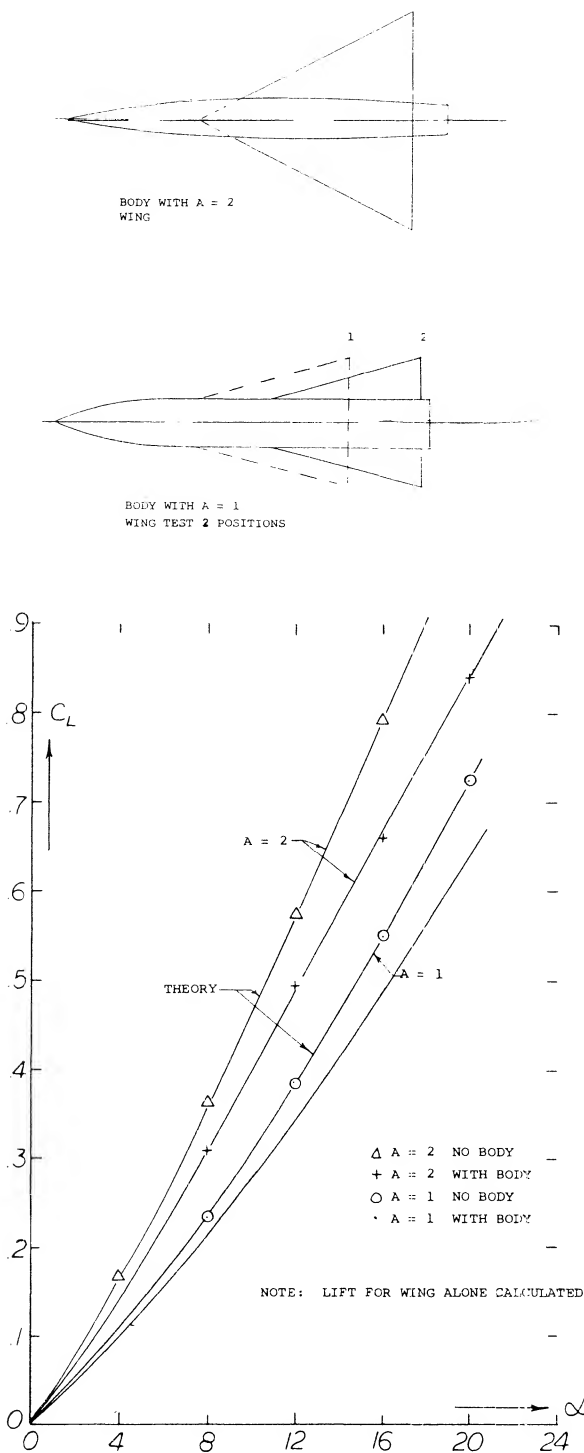


Figure 23. Wing body combinations for delta wings of A = 1 and 2.

Delta - Point Flying Last. Delta wings are usually thought of and designed as flying with their vortex point first. Results of such a shape tested in the point-last direction are presented in figure 24. It is very interesting to see that the point-last plate has the smallest linear lift-curve slope, although it presents a "perfect" leading edge to the stream. In other words, the trailing edge is at

least as important in the aspect ratios tested for producing lift as the leading edge. It should be noted, however, that the simple conclusion as in (8,d), whereby a wing with zero trailing-edge span may be expected not to produce any circulation, does not appear to be correct. Regarding the second non-linear component of lift, the point-last delta shape is again seen to be the least effective. This result seems to be a confirmation of the end-plate principle presented above. In the shape considered, the lateral vortex sheets are canted in a direction reducing their effectiveness.

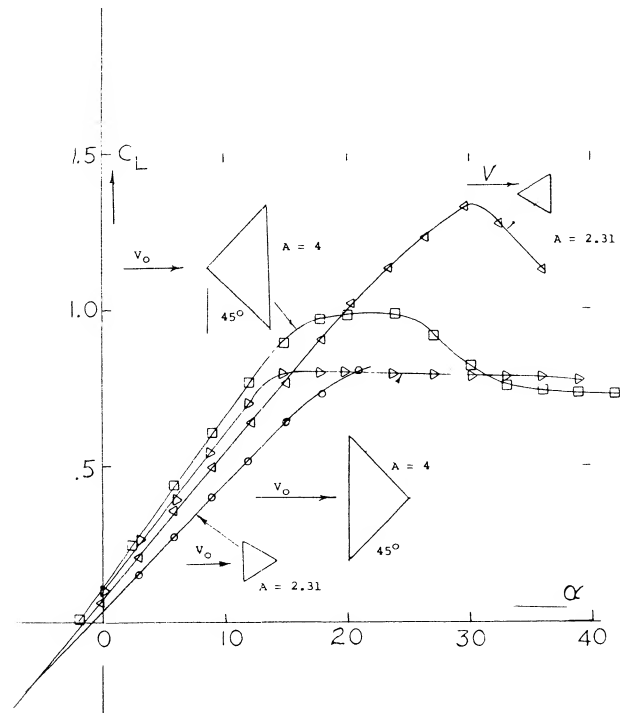


Figure 24. Comparison of lift of delta wings and wings with point flying last.

(12) Vortex breakdown on delta wings:

- Wentz, Vortex Breakdown on Sharp-edge Wings, AIAA Paper No. 69-778 and NASA CR-714.
- Earnshaw, Vortex-breakdown Position-Sharp-edge, ARC, C.P. No. 828.
- Lambourne, Breakdown of Certain Types of Vortex, NPC Report 1165.
- Polhamus, Vortex-lift by L.E. Suction Analogy, J of Aircraft, April 1971.
- Snyder, Theory of the Delta Wing, Wichita State U., AR66-4.
- Lawford, Sharp-edge Delta Wing-Position L.E. Vortex Breakdown, RM 3338.

5. VORTEX BREAKDOWN — WING STALL

The Leading-edge vortex formed by a delta wing proceeds downstream as a tightly rolled tube illustrated in figure 3, until it becomes unstable and experiences an abrupt expansion, vortex bursting. At the lower angles of attack the abrupt expansions occur downstream from the trailing edge. As the angle of attack and/or aspect ratio of the wing is increased the vortex bursting moves upstream and intersects the wing trailing edge. With further increases of A and/or α the breakdown moves forward, ending at the vortex of the wing. Although there are two types of vortex breakdown (12,a) no attempt is made here to find differences on the wing lift.

Effect on Lift. When the vortex breakdown occurs aft of the wing trailing edge, the vortex lift predicted by equations 1 and 3 continues to increase with angle of attack. This occurs because the vortex reattaches as required by the leading-edge suction analogy. As the vortex bursting position approaches the wing trailing edge reattachment fails and the lift is reduced. This lift reduction occurs when the vortex is slightly aft of the trailing edge of delta type wings as the vortex producing the lift is helical in nature, requiring area for full recovery of lift (12,f). The reduction of lift occurs as shown on figure 25 as the vortex breakdown moves forward on the wing preventing reattachment until the bursting at the vortex of the wing. At this point the vortex lift is zero. At this point it should be noted that tests (12,g) show blowing near the wing leading edge tends to prevent vortex breakdown. This allows the lift to follow that predicted by the suction analogy (5,a).

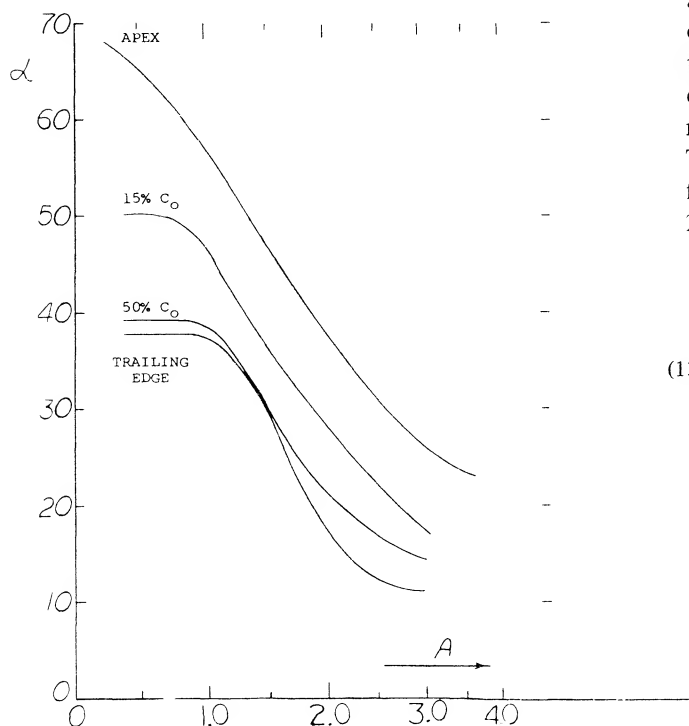


Figure 25. Leading edge vortex breakdown position for sharp edge delta wings.

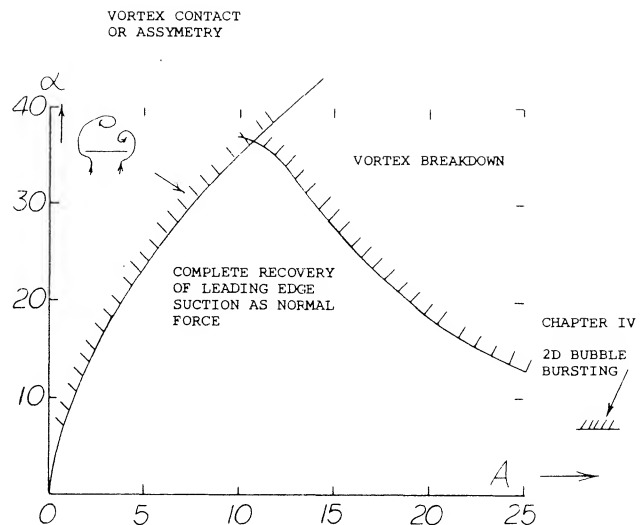


Figure 26. Limits of angle of attack for vortex breakdown or intersection.

Vortex Breakdown Position. The angle of attack and wing aspect ratio influence the location of the vortex breakdown position as shown on figure 26. The position for the vortex bursting has been obtained from flow visualization techniques, such as smoke (12,a) and is a good indication where the reduction in vortex lift will occur, and the extent.

Slender Wings. In the case of very slender wings, low aspect ratio, the vortices on either side will make contact or have an asymmetry before vortex breakdown occurs. In this case the height of the vortices above the wing are different producing a difference in lift that causes a strong rolling moment. This results in another limitation in lift. The conditions for the contact have been determined from rolling moment data (12,d) and are given on figure 26.

- (13) Flaps on delta wings:
- Corsiglia, Large-scale Test Low A Delta Wing, TN D-3621.
 - Holford, Split Flaps on 48° Delta Wings, $A = 3.03$, ARC R&M 2996.
 - Hawes, Constant-chord Ailavator on a Triangular Wing, NACA RM L51A26.
 - Brown, $A = 1.85$ Delta Wing with Double Slotted Flaps, NACA RM L56D03.
 - Croom, Thin 60° Delta Wing with Double Slotted Flap, NACA RM L54L03a.
 - Spencer, Longitudinal Control Delta Wings with Nose Deflection and Trailing-edge Flaps, NASA TN D-1482.
 - Thomas, Wing-tip Controls on Delta Wings, ARC R&M No. 3086.
 - Koenig, Delta-wing with Mid Chord Flaps, NACA TN D-2552.

6. HIGH LIFT AND CONTROL DEVICES

The application of flaps to obtain high lift and control for delta wings requires consideration of the differences in flow produced as a result of the leading-edge vortex. As discussed earlier in this chapter, the leading-edge vortex increases the lift which is non-linear with respect to the angle of attack. Further, the flow produced as a result of the vortex changes the pressure distribution on the wing, so that it might be expected that the effect on lift of a flap deflected into the vortex would be different than if deflected away from the vortex. Since the vortex is influenced by the shape of the leading edge, the effectiveness of flaps will be different for wings with different types of cross sections.

There are many different types of flaps that can be installed on delta wings, such as plain, split and slotted types. Because of the limited span it is generally necessary to use these flaps to obtain high lift and control in pitch and roll. Such flaps are called elevons.

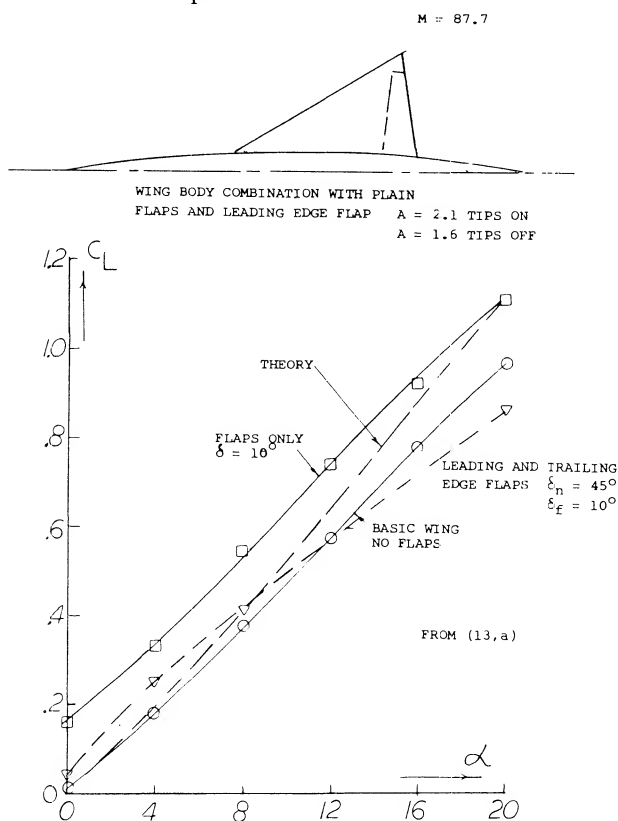


Figure 27. Delta wing body combination with plain flaps.

Plain Flaps. The characteristics of plain rectangular flaps attached to the trailing edge of a round leading-edge delta wing are shown on figure 3, Chapter IX. On the basis of flap area to total wing area, the effectiveness of the flaps would be predicted from figure 2 of Chapter IX which was developed from test of flaps on straight wings. The use of flap area to wing area to predict the effectiveness is

further confirmed by tests of a large model delta wing in the 40 x 80 foot wind tunnel (13,a). A delta wing with sharp leading edges and a plain type of flap and a fuselage was tested, figure 27.

$$\text{Flap Effectiveness} = (dC_L/d\alpha) / (dC_L/d\delta) \quad (6)$$

is close to that predicted for this type of flap on figure 2 of Chapter IX. Although the wing tested has sharp leading edges, a comparison of the lift with the theoretical prediction indicated the slope of the lift curve is low. The low lift curve slope does not appear to change the flap effectiveness and is probably caused by the central body.

Split Flaps. Tests of 60° split flaps on a delta wing with an aspect ratio of 3.03 are given on figure 28. These tests (13,b) were done in conjunction with spoiler flaps of the same size to be used together as dive breaks or separately for increasing lift. The flaps were tested at various chordwise locations on the wing for different length spans and flap chords. The split flaps were also tested in the vented and non-vented configurations as indicated on figure 28.

Based on equation 1 of Chapter V the flap effectiveness can be measured in terms of $(C_f/C)^n$ for flaps on rectangular wings. For such wings with the same type of section test in conjunction with the above data, the data of (13,b) indicates n would be 1.03. As above, the flap effectiveness ratio is found in terms of the area ratio. This indicates for delta wings with split flaps the effectiveness is

$$d\delta/d\alpha = (S_f/S)^{.93} \quad (7)$$

The test data of (13,b) also indicated that if the flap is vented the n would increase. Further, the inboard flaps are more effective than those outboard when located toward the trailing edge of the wing.

The effect of deflecting split flaps located on the upper surface of the wing is given on figure 27. The effectiveness for decreasing lift is the same order of magnitude as for increasing lift with the flaps located on the lower surfaces of the wing, speed breaks are obtained without changing the basic lift slope of the wing.

Double Slotted Flaps. Because of the high angle of attack needed for landing with delta wing aircraft and the low span, double slotted flaps have been investigated (13,d,e). Typical results are presented on figure 29 for a wing body configuration with double slotted flaps extending to the .666 spanwise station. The flaps were investigated with a large and a small intermediate foil. Up to flap angles of 45° both configurations had nearly the same performance at zero angle of attack. This performance improves

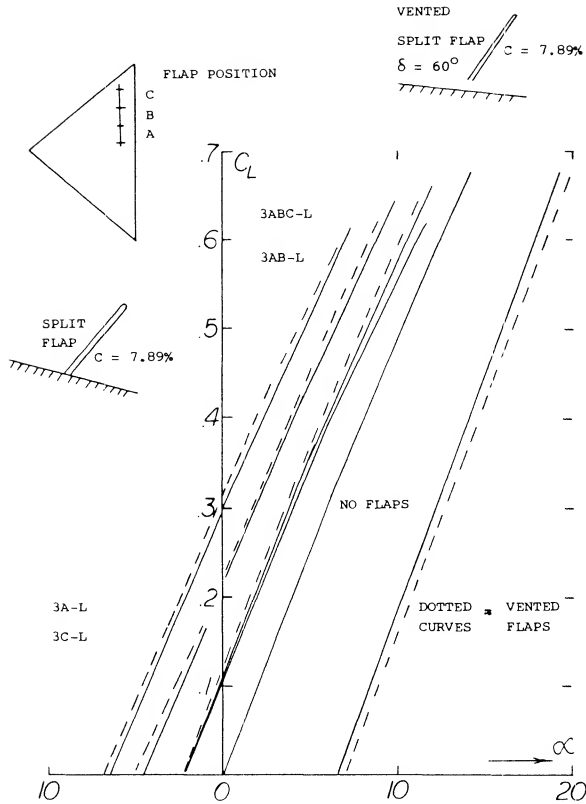


Figure 28. Upper or lower split flaps on a delta wing.

with flap angle for the configuration with the larger foil for $\Delta\alpha \cong 6^\circ$. Above this angle the payoff in ΔC_L is reduced with flap angle until at $C_{L\alpha}$ the $\delta_f = 45^\circ$ is best. It is observed that the wing with $\delta_f = 45^\circ$ has the same lift curve as the basic configuration up to the stall angle.

For the wing with the double slotted flap with an adequate intermediate foil the flap effectiveness can be predicted based on the flap type, area ratio and the deflection angle, using data such as given in Chapter V. It therefore appears that the performance of flaps on delta wings can be predicted with good accuracy based on the characteristics of the flaps determined on straight wings.

Part Span Flaps. Tests (13,c) were of part span flaps on one side of a delta wing, figure 30, to find the effectiveness as a function of spanwise location. From the data given it can be concluded that the effect of the location of the flap spanwise is of secondary importance and the lifting effectiveness is proportional to the span fraction. Regardless of flap-span fraction, use the value of b/c as the aspect ratio responsible for the flap lift curve slope. For the configuration in figure 30 that ratio is $A_f = b/c_f = 9$, and the "lift angle" is

$$d\alpha / dC_L = 11 + 20/9 = 13.2^\circ \quad (8)$$

so that $dC_L / d\alpha = 0.076$. The fraction of the "half" span flap is actually $0.9/2 = 0.45$. The lift due to flap deflection may thus be

$$dC_{L_b} / d\delta = 0.076(S_f / b^2) = 0.076(0.45)/A \quad (9)$$

The result of 0.0038 is somewhat larger than the tested value ($0.0081/2.31 = 0.0035$).

Aileron. The half and/or part-span trailing-edge flaps of the delta wing in figure 31 can conveniently be used as ailerons. Of course, in regard to their moment about the longitudinal axis, there is a difference between outboard and inboard flaps. The roll-moment contributions listed in the illustration yield arms "y" as follows: outboard and inboard flaps. The roll-moment contributions listed in the illustration yield arms "y" as follows:

$$\begin{aligned} y/b &= 0.0004/0.0045 = 0.1; (0.12) \\ &= 0.0012/0.0040 = 0.3; (0.33) \\ &= 0.0016/0.0081 = 0.2; (0.25) \end{aligned}$$

For comparison, the purely geometrical ratios are added in parentheses. Tentatively, therefore, the moment arms may be considered to be between 0.8 and 0.9 of the geometrical ones.

In examining the rolling moments as determined from test, the difference between positive and negative aileron deflection is small at the lower angles of attack. Further, no significant changes are noted between wings with round or sharp leading edges. This indicates that the leading-edge vortex does not influence the results in this range.

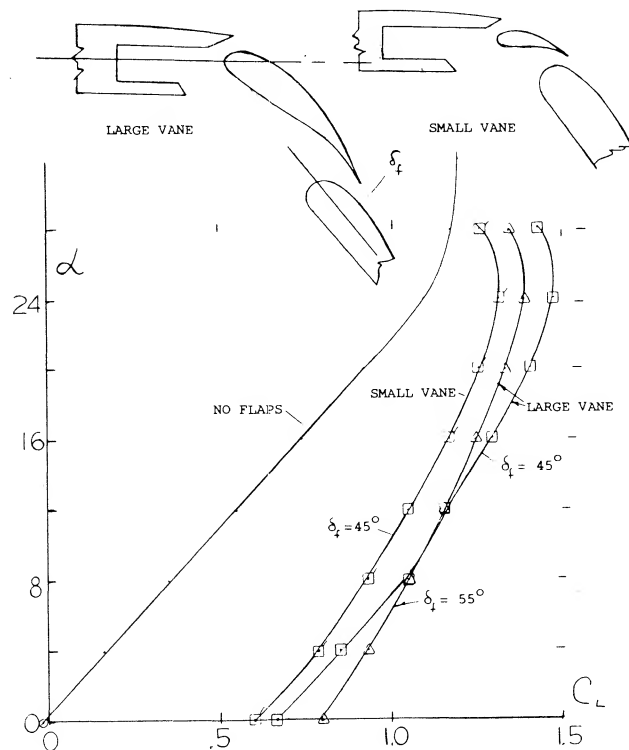


Figure 29. Double slotted flaps on delta wing airplane.

Antisymmetric Deflection. In a conventional, more or less straight wing (with higher aspect ratio) the anti-symmetric deflection of the ailerons produces lift differentials in each wing panel corresponding to a lift curve slope based upon $\frac{1}{2}$ the wing's aspect ratio. Based on the results of (13.c) the use of up and down ailerons will double the rolling moment shown on figure 30, determined for one side of the wing. At the lower angles of attack the yawing moment is negative with up or down flap deflection switching at angles above 10 degrees. This change will effect the flying qualities of the aircraft thus requiring special design consideration.

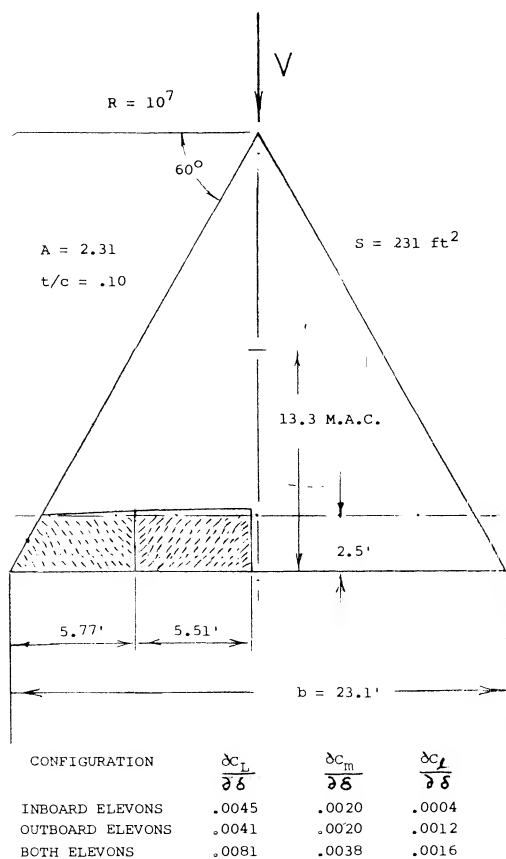


Figure 30. Part span flaps on a large delta wing.

- (14) Parawings:
- Rogallo, Flexible Wings for Transportation.
 - Sleeman, Parawing Aerodynamics, A&A Engineering, June 1963.
 - Mendenhall, Aero Characteristics of Two-lobed Parawings, NASA CR-1166 and J of A/C, Nov, Dec 1968.
 - Polhamus, Experimental and Theoretical Studies of Parawings A = 3 and 6, NASA TND-972.

FLUID DYNAMIC LIFT

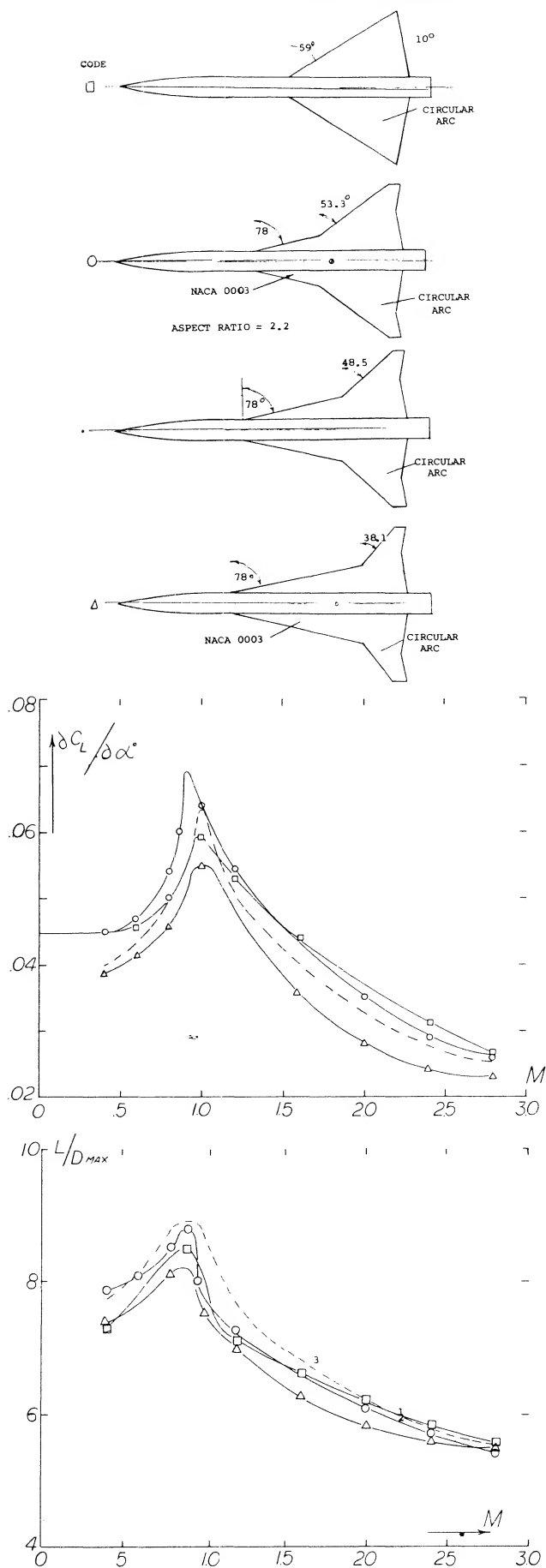


Figure 31. Lift curve slope and lift-drag ratio as a function of Mach number for delta and double delta wing airplanes.

7. COMPRESSIBILITY EFFECTS — DELTA WINGS

As previously noted delta wings are primarily used on aircraft operating at Mach numbers above 1.0. At these conditions their performance is superior to other configurations with the result of their selection for many high speed aircraft, including the supersonic transport types. The variable swept wing can be thought of as a delta type when in the fully swept configuration and thus can be included as the one best type for operation at $M = 1$.

Subsonic Compressibility Effects. The performance of delta wings given previously in this chapter is for conditions where compressibility effects are zero, $M = 0$. The effect of increased Mach number is shown in figure 31 and shows an increase in both the slope of the lift curve and lift drag ratio, which peaks at $M = 1$. The variation of the lift curve slope with M is due to compressibility and can be accounted by the Prandtl Glauert transformation such as described in Chapter VII. With this correction the potential lift represented by K_P is increased by compressibility to a greater extent than the vortex lift correction K_V . To find K_P , K_V the aspect ratio is corrected by the equation

$$A' = A \sqrt{1 - M^2} \quad (10)$$

where A' is the aspect ratio used to read K_P and K_V on figures 9 and 10, and M is the free stream Mach number. The K factors must also be corrected thus

$$K_{Pc} = K_P / \sqrt{1 - M^2} \quad (11)$$

$$K_{Vc} = K_V f_M \quad (12)$$

$$f_M = \sqrt{1 + \tan^2 \Lambda / \beta + \tan^2 \Lambda} \quad (13)$$

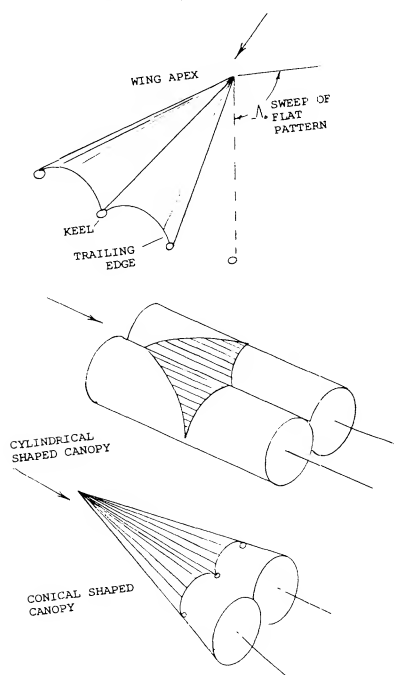


Figure 32. Geometry characteristics of parawings.

Comparison of the variation of the lift curve slope calculated with equations (11) and (12) with that measured in figure 31 indicates good agreement.

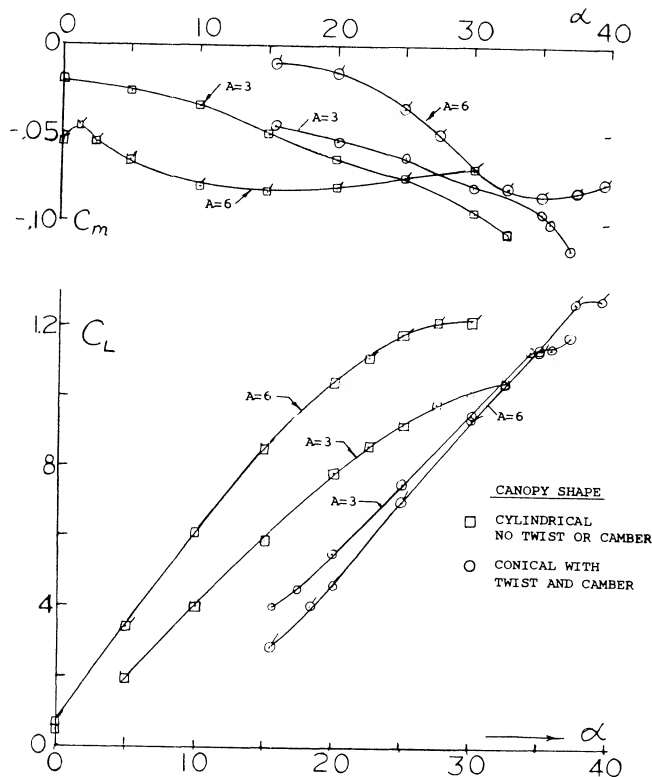


Figure 33. Lifting and moment characteristics of two-lobed parawings, $A = 3$ and 6 .

Lift at Supersonic Speeds. To determine the lift of delta wings at $M > 1$ the leading-edge suction analogy is also used. Here the constants of K_P and K_V can be determined based on a linearized theory (12,d) with the result that

$$K_P = \pi A / 2E \quad (14)$$

and

$$K_V = \pi [(16 - (A\beta)^2)(A^2 + 16)]^{1/2} / 16E^2 \quad (15)$$

where E = elliptic integral of the second kind where modules = $[1 - (\cot \Lambda_{LE})^2]^{1/2}$. In this case $\beta = \sqrt{M^2 - 1}$.

In (12,d) comparisons of the calculated results of equations (14) and (15) with test data indicate good agreement.

8. PARAWINGS

Parawings are a form of delta wings in the sense that their planform has the delta slope; however, these lifting surfaces with a parachutelike tension structure are completely different. In this case the wing surface slope is maintained by the balance of forces between the airload on the surfaces and the tension in the supporting structure. These wings have been considered for use for a large variety of tasks from hang type gliders to wings for the recovery of space vehicles (14,a). The flexibility of the structure and its capability of being folded broaden the potential uses of parawings so that a brief discussion of their characteristics is desirable.

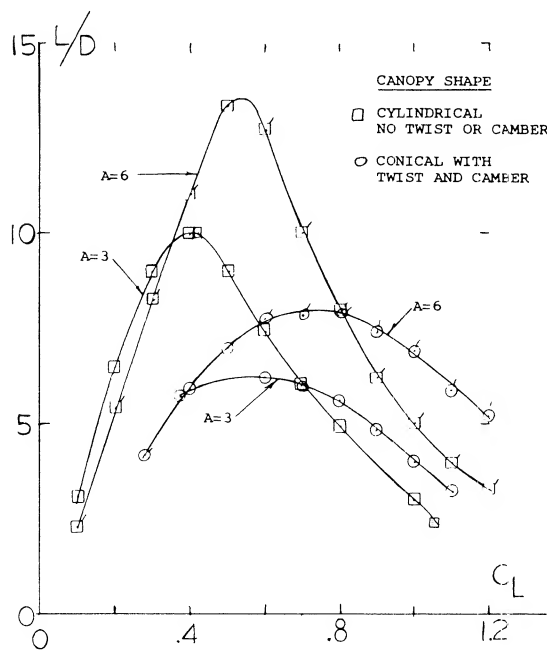


Figure 34. Lift-drag characteristics of two-lobed parawings.

Geometric Characteristics. The parawing can be designed in many forms as discussed in (14,b), however, only the two-lobed type illustrated in figure 32 will be considered here. As noted in the figure, the wing has a central keel with two straight or curved booms to form the leading edges. The canopies are generally formed as a conical or cylindrical shape as illustrated, and the booms are spread by a bar that also serves to support the load. The shape of the trailing edge will be determined by the sweep of the flat pattern angle Λ_0 and the actual sweep angle of the boom. Although rigid members are considered for the booms and keel, a tension structure can be used to improve the storage characteristics. In this case a balance must be made of the forces to obtain the shape needed for flight and control.

Lift Characteristics. The lifting characteristics of parawings depend on the type of canopy used and the aspect ratio. Typical test results (14,d) are given on figure 33 for wings with both types of canopies. The lift coefficient is based on the area of the flat wing pattern. The most striking difference between the two types of wings is the angle of attack for a given lift coefficient. Much larger angles are needed for the same lift coefficient with the conical wing. In the case of the $A = 6$ wings, $C_{L\alpha}$ are nearly the same. At $A = 3$ the $C_{L\alpha}$ of the conical wing is slightly better than the cylindrical wing. At the lower values of angle of attack the conical wing is limited by flutter at the trailing edges. This occurs at lift coefficients below .4 as indicated.

The effective shape of the conical wing results in a large variation of twist between the inboard and outboard sections so that the wing tip is operating at a negative lift at moderate lift coefficients. The twist or washout can be eliminated in the case of the cylindrical wing, which leads to tip stalling as $C_{L\alpha}$ is approached. The difference in the local angle of attack in the case of the two types of canopies determines the difference in the stalling characteristics and the lift drag ratio.

Longitudinal Moment. The variation of the pitching moment is given on figure 33. These data indicate that the wings will have a negative pitching moment at zero angle of attack so that for typical parawing applications the center of gravity must be located well below the wing to achieve trim and stability. In the normal operating range with such an arrangement good positive stability is obtained. However, at both the low and high lift coefficient negative stability is obtained which can lead to an end over end tumbling motion (14,b).

Lift-Drag Characteristics. At a given aspect ratio the canopy shape is the major factor influencing the lift-drag ratio that can be obtained with parawings, as illustrated on figure 34. For wings with the same aspect ratio the cylindrical shape gives a large improvement in the lift-drag ratio over that obtained with the conical shape. This is due to the improved load distribution resulting from the zero wing twist distribution. The improvement in load distribution almost doubles the lift-drag ratio of the wing, figure 34. With the use of a small degree of washout further improvements in L/D_{max} can be obtained along with $C_{L\alpha}$.

CHAPTER XIX

LIFTING CHARACTERISTICS OF STREAMLINE BODIES

Streamline bodies and similar elongated shapes are used wherever the drag must be kept to a minimum. These bodies are, therefore, used for all types of missiles, aircraft fuselages, engine nacelles, airships, fairings and any other object that should have minimum drag. In addition to the drag force streamline bodies produce a lift force and longitudinal or yaw moments which are covered in this chapter.

Geometry. When considering aerodynamic characteristics of streamline bodies as such, their coefficients are to be based on the dimensions:

d = diameter (if circular as in a body of revolution)

b = width (span) or height, normal to angle against flow

ℓ = overall length of body

x = distance from nose, along axis.

The most important dimensions are b and ℓ ; and we will preferably use the coefficients

$$C_{Nb} = N/q b^2 \quad \text{for lift or normal force}$$

$$C_{m\ell} = M/q \ell b^2 \quad \text{for longitudinal moment}$$

It should be noted that in an isolated body of revolution, there is no difference between the derivatives of pitch moment ($dC_m/d\alpha$) and of yaw moment ($dC_n/d\beta$). The maximum cross-section or frontal area of rotationally symmetric bodies is $S_o = d^2\pi/4$. The projected lateral or plan-form area S_+ (if used as the equivalent of "wing" area) is approximately:

$$S_+ = (0.8) \ell d \quad \text{in ellipsoids (or airships)}$$

$$= (2/3) \ell d \quad \text{in pointed streamline bodies}$$

where $0.8 \approx \pi/4$. This area is indicative of the non-linear cross-flow forces, at higher angles. In the case of airships and flying-boat hulls, their volume denoted by \bar{V} is significant for performance (buoyancy). Therefore, coefficients are very often based on the length $\bar{V}^{1/3}$, the area $\bar{V}^{2/3}$; and the moments are referred to the volume \bar{V} . The ratios of volume in streamline bodies of revolution are roughly as follows:

$$\bar{V} = 0.6 \ell d^2 \quad \text{in ellipsoids (airship bodies)}$$

$$\bar{V} = 0.5 \ell d^2 \quad \text{in pointed streamline shapes}$$

In naval architecture, in regard to the displacement of ships, this type of ratio is called the block coefficient, "B." Thus for bodies of revolution

$$\text{"B"} = \bar{V}/\ell d^2 = .5 \text{ to } .6$$

1. LIFT DUE TO CIRCULATION

A streamline body operating at an angle of attack develops a lifting or normal force similar to that of a low aspect ratio wing. As explained in Chapter XVIII this force consists of two different components, due to circulation and cross-flow.

Theory as presented in (1,a) predicts that in a slender body of revolution, lift develops corresponding to local cross forces per unit length:

$$dF/dz = q(dS_o/dx) \sin(2\alpha) \quad (1)$$

where dS_o/dx = rate of change of cross-section area. When integrating this equation over the length of a complete ("closed") streamline body, positive lift is found in the forebody and a negative contribution in the afterbody; the resultant lift is always zero. Considering, however, a circular cone with finite length and a blunt base, its lift coefficient based on base or frontal area S_o , is found to be

$$C_{Lo} = \sin(2\alpha) = 2 \sin\alpha \cos\alpha \approx 2\alpha \quad (2)$$

This type of lift is due to longitudinal circulation as in wings and/or airfoil sections.

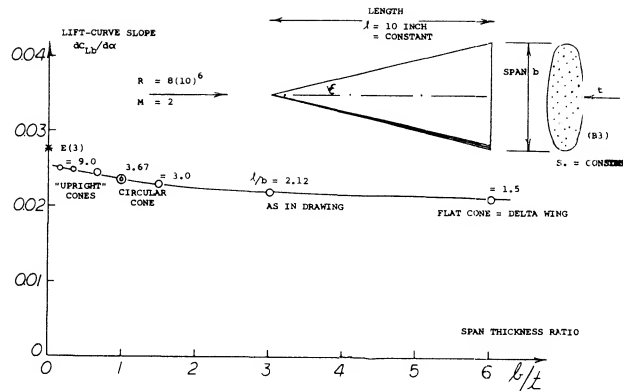


Figure 1. Lift-curve slope of a family of elliptical cones, tested (3,a) at $M = 2$.

Elliptical Cones. The forces discussed do not correspond to the volume of the body, but to that of the air affected by the body. The cylinder of air deflected by a conical body corresponds to its "span" b (see figures 1 or 2). Therefore, to accommodate cones with cross-section shapes other than circular, it is best to refer their lift to the area $S_b = b^2$. The lift-curve slope of elliptical cones from equations 1 and 2.

$$dC_{Lb}/d\alpha (\pi/2)(\pi/180) = \pi^2/360 = 0.0274 \quad (3)$$

Where C_{Lb} is the lift coefficient based on b^2 .

Experimental results on a "family" of cones with elliptical cross section shape varying in span/thickness ratio, are plotted in figure 1. Although their lift is between 10 and 20% below the theoretical level, the graph demonstrates the fact that equation 3 applies to "all" types of cones, from slender "upright" elliptical shapes (with t considerably larger than b) to slender delta wings (with t zero).

Delta Wings. The derivative of the linear (circulation-type) component of lift as in equation (3) is the same as that for small aspect ratio wings, Chapter XVII. In fact, the cone in figure 1, with $b = 6t$, can very well be considered to be a delta wing. Experimental results of another family of elliptical cones (with $b = 3t = \text{constant}$) is plotted in figure 2. At larger values of the length ratio, the same average level is obtained as in figure 1. At the other end of the scale, the aspect ratio increases toward infinity. For example, at $\ell/b = 1$, the ratio is $A = 2b^2/b\ell = 2(b/\ell) = 2$, which is no longer slender. Modifying equation 6 in Chapter III to $(12 + (10/A^2) + (20/A))$; and replacing A by $2b/\ell$, we can write

$$d\alpha/dC_{Lb} = (24b/\ell) + (5\ell/b) + 1.7 \quad (4)$$

This function, resulting in $dC_{Lb}/d\alpha = \text{zero}$ at $\ell/b = \text{zero}$, is verified by test on various slender delta wings. Equation 4 also extrapolates with good results the test results on cones toward $\ell/b = \text{zero}$.

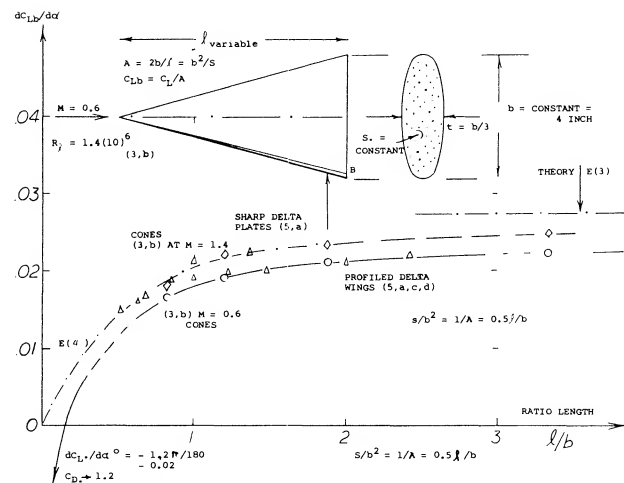


Figure 2. The lifting characteristics of a family of elliptical cones as a function of their length ratio.

(1) Theoretical analysis of slender bodies:

- Munk, Airship Theory, NACA T Rpt 184 & 191 (1923/24); also in Vols I & VI of Durand's "Aerodynamic Theory".
- Vandrey, Pitching Moment, Yearbk D'Lufo 1940 p I-367.
- Lighthill, Supersonic Body Flow, ARC RM 2003 (1945).
- Tobak, Derivatives of Cones, NACA TN 3788 (1956).
- Kaplan, Potential Flow, NACA T Rpt 516 (1935).
- Sacks, Forces and Derivatives, NACA TN 3283 (1954).
- Spreiter, Wing-Body Configurations, NACA T Rpt 962.
- Young, Family of Bodies, ARC RM 2204 (1945).
- Upton, Airship Analysis, NACA T Rpt 405 (1932).

(2) Characteristics of pyramidal bodies:

- Flatau, Chem RD Labs, Spec Pub 1-31 (1961); Astia 270250.
- Paulson, Delta Vehicle, NASA TN D-913 (1961).
- Ware, Reentry Configuration, NASA TN D-646 (1961).
- Olstad, Same as (c) at $M = 0.6$ to 1.2, NASA TN D-655 (1961).

(3) Lifting characteristics of conical bodies:

- Jorgensen, Elliptical Cones, NACA T Rpt 1376 (1958).
- Stivers, Family of Cones, NASA TN D-1149 (1961).
- Flatau, Army Chem RD Labs Spec Pub 1-32 (1961); Astia 270838.

Mach Number. The cones as in figure 1, were tested at a supersonic speed, corresponding to $M = 2$. The cross-flow velocity on which the lift of a slender cone depends, is $w = V \sin \alpha$. At the sides of circular cones, this component will be doubled corresponding to the “2 alpha” principle. The perturbation velocity due to the displacement by the cone is approximately $(V \sin \epsilon)$, where ϵ = half-vertex angle. For example, for α and ϵ , each equal to 0.1 (corresponding to 5 or 6 degrees) the maximum cross-flow velocity may then be $w = 0.3 V$. Therefore, the effective Mach number for the experiments as in figure 1, is only a fraction of the number at which the wind tunnel was operating. Ultimately there will be a critical condition, however, where the Mach cone coincides with that placed around the longer axis of the elliptical cross section. For $M = 2$, the corresponding critical cone shape corresponds to $l/b = 3.5$ which is obtained above $b/t = 6$ in the graph. Results on the other family of cones (in figure 2) are shown both for $M = 0.6$ and $= 1.4$. The fact that there is a difference (in the order of 10%) in the lift coefficient between subsonic and supersonic speed, may partly be accidental. Within the limitations of theory (really slender cones at small angles of attack) there would not be any difference. The other fact, that none of the values tested comes closer than to 90% of the theoretical level, equation 3, is easily explained on the basis of “round” lateral edges. Evidence presented in Chapter III confirms that 80 or 90% will be a reasonable value to be used in combination with equation 3.

Lateral Forces. The type of cone as in figure 1 was tested for $b/t = 6$ as well as for $t/b = 6$. Considering the cone with $b/t = 6$, to be a delta wing, the point at $b/t = 1/6$, represents the lateral force derivative (based on the square of the span $b = 6 t$)

$$dC_{Yb} / d\beta = (t/b)^2 dC_{Lb} / d\alpha = 0.025/6^2 = 0.0007 \quad (5)$$

for that particular wing.

- (4) Analysis of slender (delta) wings:
 - a) Jones, Delta-Wing Lift, NACA T Rpt 835 (1946); also J Aeron Sci 1951 p 685.
 - b) British Efforts, ARC RM 2596, 2819, 3116.
 - c) Lomax, Slender Wing Theory, NACA T Rpt 1105 (1952).
 - d) Spreiter, Slender Configurations, MACA T Rpt 962 (1950).
 - e) Sacks, Derivatives, NACA TN 3283 (1954), as in (1).
- (4) Analysis of non-linear lift in small A'ratios:
 - k) Bollay, Zero A'Ratio, ZaMM 1939 p 21; also J Aeron Sci 1936/37 p 294.
 - l) NACA, Statistical Interpretation, TN 2044 & 3430.
 - m) J Aeron Sci 1953 p 430; 1954 p 134, 212, 649.
 - n) Brown, NACA TN 3430; also J Aeron Sci 1954 p 690.
 - o) The non-linear problem is now claimed to have been solved; see Gersten, Non-Linear Theory, ZFW 1957 p 276 and Ybk WGL 1958 p 25. No explicit formulation seems to be available, however.
 - p) For “end-plate” principle, see (72) in the “wing” chapter.

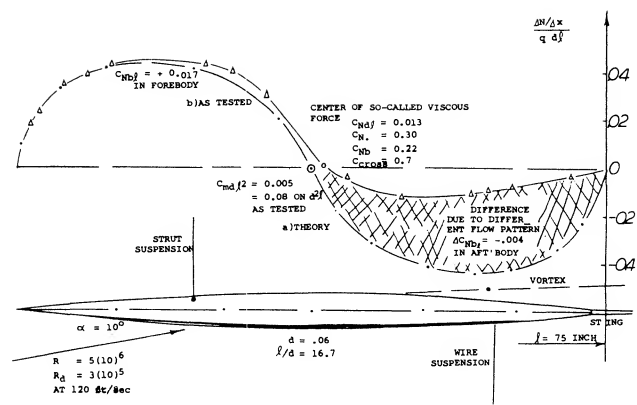


Figure 3. Normal force distribution on a slender streamline body, at $\alpha = 10^\circ$:

- a) as predicted by theory (1,c)
- b) as tested (7,b) by pressure distribution.

Load Distribution. As mentioned before, a complete body (with a tail reducing to a point) would have zero lift, in non-viscous fluid flow. The load distribution along the axis of a very slender streamline body is plotted in figure 3. As shown in (1,c) or (7,b) the change in surface pressure due to angle of attack (as against the distribution at $\alpha = 0$) is theoretically as follows:

- a) Along the sides of the body, the minimum pressure obtained corresponds to

$$C_p = -3 \sin^2 \alpha \quad (6)$$

as in a circular cylinder inclined against the flow (“2 alpha” cross flow).

- b) Along the plane of symmetry, the pressure variation due to thickness at $\alpha = 0$, is:

$$\Delta C_p = \sin^2 \alpha \pm \sin(2\alpha)(dd/dx) \quad (7)$$

where the first component represents the cross-flow stagnation pressure. The second component is due to the change in body diameter. The plus sign applies to the bottom, and the minus sign to the upper side. Since the variation of the diameter dd/dx is positive in the forebody, we obtain a lifting normal force there. In the afterbody, the theoretically expected normal force is negative (down) so that the resultant force is zero. The normal force loading is proportional to $(d_x/d)(dd/dx)$, where x = distance from the nose point of the body, and d_x = diameter at x .

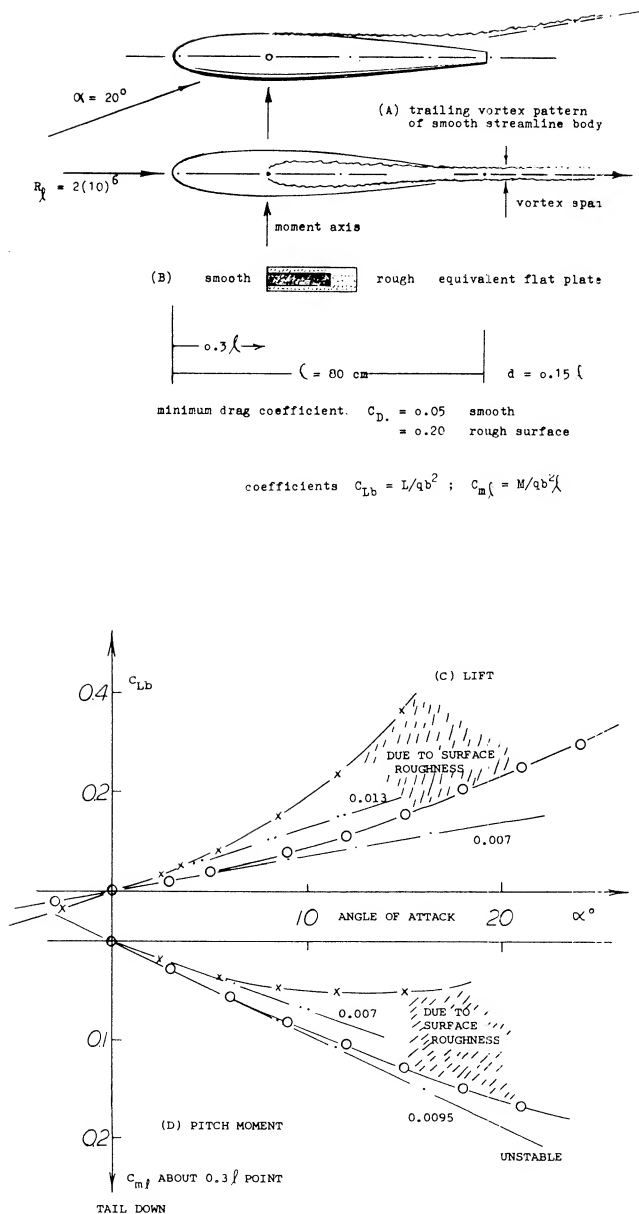


Figure 4. Characteristics (9,c) of streamline body as tested in open-jet wind tunnel:

- a) in smooth condition
 b) with sand-type roughness, corresponding to $k = 0.001l$.

"Viscous Lift." As demonstrated in figure 3, tested pressures and normal loads agree fairly well with theory, on the forebody. The corresponding lift is the same as indicated in equations 2 and 3 for cones. In the afterbody, theory expects negative loads. In reality, the pressure increase along the upper side of the afterbody, to the centerline pressure as in equation 7 does not take place. At the angle as tested, there is no positive lift in the afterbody. *The lift exists in the forebody.* However, the negative lift in the afterbody is reduced; the result is a net positive lifting or normal force.

"Edges." Although viscosity is the basic reason for the development of positive lift on a streamline body the boundary layer is not necessarily responsible for the deficiency of positive pressure at the upper side. In fact, there is "no" accumulation of B-layer material, and "no" separation. Rather, there is a change of flow pattern from that predicted by potential theory, to the real one as in figures 4, 5, & 6. Without friction, there would not be circulation and/or lift. However, the slightest trace of viscosity is sufficient to transform any "sharp" trailing edge into something similar to a stagnation line as in the case of airfoil sections. In the case of a streamline body, we do not have sharp edges. However, skin friction and the absolute refusal of the boundary layer to proceed against a strong positive pressure gradient, makes "edges" out of the lateral sides of the body. All this starts on a streamline body at roughly 50% of the length, where the negative pressure gradient due to thickness along the forebody and due to longitudinal flow, begins to change into a positive gradient. Therefore, the forebody retains a positive lifting load as approximately described by equation 3.

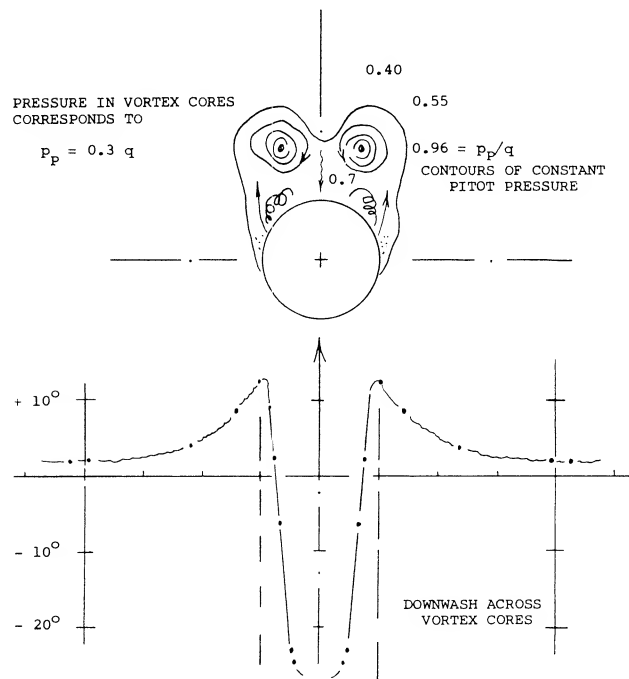


Figure 5. Pattern of the pair of vortices containing the circulation produced by an ogive-cylinder body (NACA Rpt 1371).

- (5) Slender delta wings, experimental:
- British ARC, RM 2518, 3077.
 - NACA, TN 1468 & 2674, T Rpt 1105.
 - Lange, ZWB UM 1023/5 (NACA TM 1176).
 - Truckenbrodt, 0012 Deltas ZFW 1956 p 236; also Swept and Deltas, ZFW 1954 p 185.
 - Fink, Delta Plates, ZFW 1956 p 247.

The flow pattern around lifting streamline bodies has been investigated by way of pressure distribution (7,b) (8), measuring boundary layer distribution (6), through visual means, such as smoke (7,a,c), and by surveying the wake (7,a) (12).

Important facts are as follows:

a) As shown in figure 6, the flow around the sides begins as in non-viscous fluid. The “2 alpha” type of flow is evident. It should also be noted that there is some flow around the forebody sides, *over the top* of the body (circulation).

b) The streamlines do not reach the body's plane of symmetry at the upper (suction) side, as expected by theory. In fact, there is a line (as in figure 6) beyond which the direction of the flow at and near the surface of the solid, is reversed.

c) While theory may consider the lift of wings and/or bodies, assuming that a cylinder or a sheet of air simply be deflected (downwash), in reality and by necessity, that stream of air starts immediately and vigorously rolling itself up into a pair of trailing vortices of the type as shown in figure 5.

Vortex Pair. As suggested above, it is not necessary or not even justified, to assume that the reversal of the flow as in (b) above, is “separation.” What we find in lifting bodies, is basically the same flow pattern as around slender (low-aspect-ratio) wings. Quoting from (7,b), “as soon as the incidence is increased from zero, a symmetrical pair of spiral vortex sheets form on the lee side.” At small angles of attack, the point along the body where the trailing pair can first be identified, may be at or possible behind the tail end of the body. As the angle of attack is increased, that point moves forward. As shown in (7,d) and (14,c) the location varies as x/d , $1/\alpha$ and it may reach a final position somewhat ahead of the maximum diameter. Figure 5 shows the flow pattern in the plane tangent to the base of an ogive-cylinder body. The lateral distance between the pair of trailing vortices is $\approx 2/3$ of the body's diameter. The fact that in figure 4, the vortex “span” is only $1/3$ of the maximum diameter, indicates that this body (tapering to a short vertical edge) is less effective in producing lift than the cylindrical body above.

- (6) Boundary layer on airship models tested: a) Klemperer, LZ-126 (“Los Angeles”); Aerody Inst TH Aachen 1932.
b) Freeman, “Akron” Model, NACA T Rpt 430 (1930).
c) ARC, British R-101, RM 1169 & 1268 (1929).

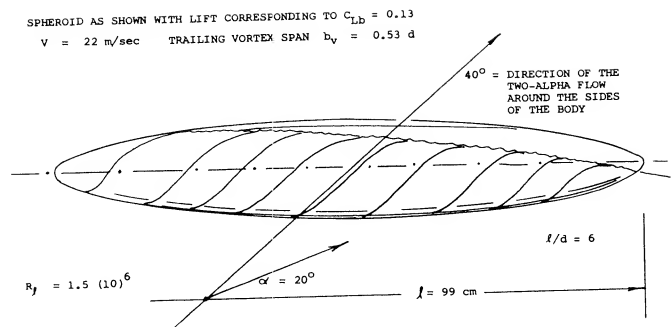


Figure 6. Flow pattern observed (7,a) directly at the surface of a streamline body of revolution similar to that of an airship.

Lift = f(Drag). In a closed streamline body with more or less round cross section, there is no geometrical definition, neither of the effective area, nor of the aspect ratio and/or the effective span. The only method of obtaining information of lift of such bodies, is statistical. Since the type of lift considered, originally stems from viscosity and boundary layer interference, it can be speculated that it is a function of the body drag. Normal force derivatives (obtained around zero angle of attack, or zero lift) are plotted in figure 7, as a function of the minimum drag coefficient, representing friction (boundary layer thickness) as well as the “resistance” of the lateral “edges” of the bodies tested, against the flow around them. Figure 4 presents direct proof for the fact that lift increases with drag produced by surface roughness.

- (7) The flow pattern around streamline bodies:
a) Harrington, Origin of Lift of Body, Guggenheim Airship Inst (Akron, Ohio) Pub 2 (1935); also J Aeron Sci 1934/1935 p 69.
b) Spence, Flow Structure, RAE Aero 2406 (1955).
c) Maltby, Vortex Suction, RAE TN Aero 2482 (1956).
d) Jorgensen, Vortex Pattern, NACA T Rpt 1371 (1958).
e) Gowen, Inclined Vortex Wakes, NACA RM A53117.
- (8) Pressure distribution on slender bodies:
a) Allen, Influence of Viscosity, NACA T Rpt 1048 (1951).
b) Fuhrmann, Ybk Motorluftschiff Studiengesellschaft, 1911; also ZFM June and July 1910; also ZFM 1911/12.
c) Cole, Bodies of Revolution, NACA RM L52D30.
d) Matthews, Theory and Experiment, NACA T Rpt 1155 (1953).

Appendages, a canopy on top of a fuselage or a windshield cut into the fuselage, also increase the lift-curve slope; see figure 8. A drastic example for this type of interference is shown in figure 9. The lift induced in the fuselage by the disk (simulating a very bluff windshield) is as high as that otherwise produced by an angle of attack between 10 and 20°. The lift is evidently obtained by preventing the increase of pressure along the upper side of the afterbody, thus *destroying* the *negative* lift originally produced.

Square Cross Section. The lifting characteristics of three bodies differing in cross-section shape, are plotted in figure 10. The left curve slope of these bodies and others are given in figure 11. Physical interpretation of the data is as follows:

- Plain, smooth and round streamline bodies have little lift, their flow pattern is closest to the ideal, without circulation.
- Lateral edges particularly in form of square cross section help to make streamline bodies lifting. Even the edges of polygonal airship hulls are sufficient possibly to double the lift-curve slope.
- A full shape of the afterbody, ending in a blunt base, does not directly contribute to circulation. A wide afterbody reduces or may even eliminate any negative loading, however, so that the resultant normal force is increased to two- or threefold compared to smooth and round streamline bodies ending in a point.

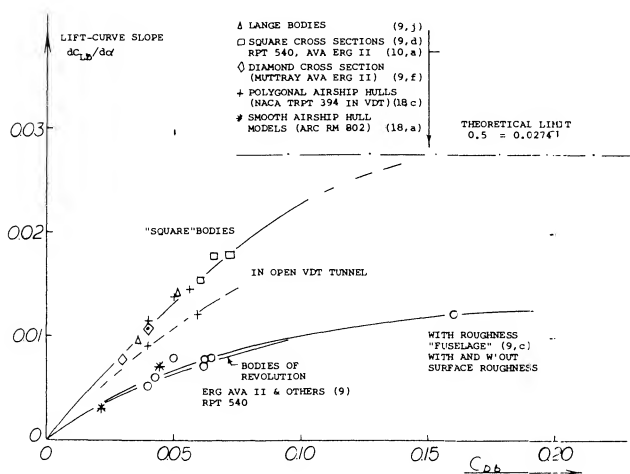


Figure 7. Lift-curve of streamline bodies as a function of their minimum drag coefficient.

FLUID DYNAMIC LIFT

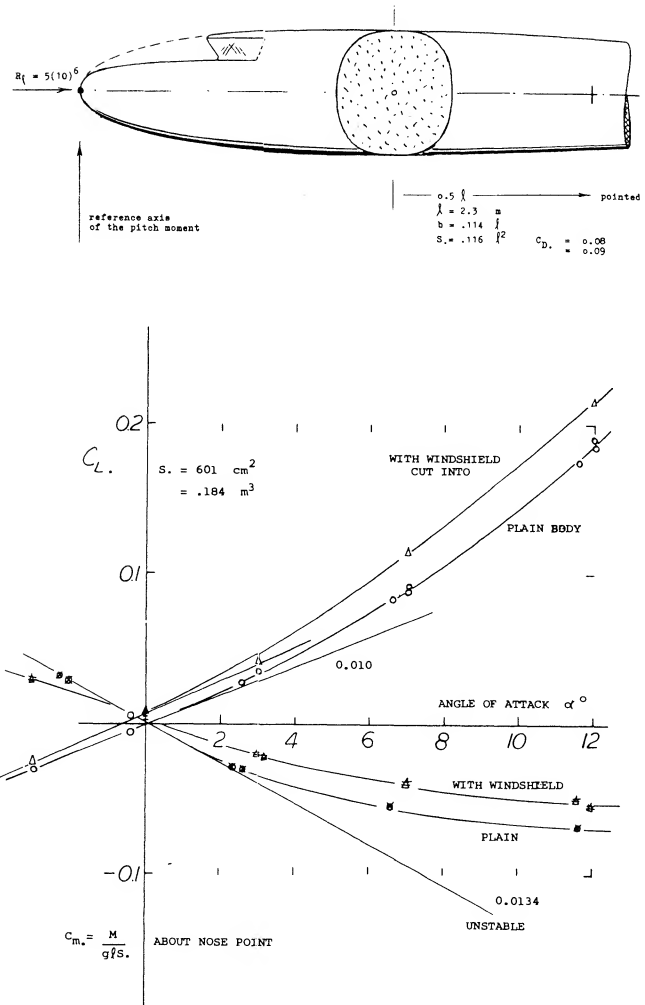


Figure 8. Longitudinal characteristics of a plain fuselage body (11,a) with and without a pilot's windshield.

"Parabolic" Bodies. The lift and moment of a series of bodies formed by parabolic arcs are shown in figure 12. Their afterbodies, which reduce in width to $\frac{1}{2}$ of the maximum at the blunt base, cause a reduction of the lift compared to that of equation 3. For example, the shapes with span/thickness ratio $b/h = 1.0$ and 1.5 have $dC_{Lb}/d\alpha$ values between 0.005 and 0.008, which is roughly $\frac{1}{4}$ of that of slender cones. As the span/thickness ratio is increased these bodies more and more develop into

- (9) Plain and round fuselage bodies:
 - Several Shapes, AVA Gottingen Rpt 1934/03.
 - Engelhardt, Roughness, TH Munich Aerody Lab Rpt 1/1943.
 - Goodman, Fineness Ratio, NACA T Rpt 1224 (1955).
 - Hollingsworth, Length Ratio, W'Rpts L-8,12,17 (1945).
 - Muttray, AVA Results, Lufo 1928/29 p 37; as (10,a).
 - NACA, Length Ratio, TN 2358 & 2587: T Rpt 1096.
 - Queijo, Length and Shape, T Rpt 1049 (1951).
 - Lange, Eight Shapes, ZWB FB 1516 (194); NACA TM 1194.
 - Gillespie, $M = 1.7$ & $l/d = 17$, NACA RM L54G28a.

“wings” with lateral edges. It should be noted that cross-section *shape*, rather than fineness ratio l/b (or any other of the parameters used in this analysis) determines lift and longitudinal moment. In fact, at $b/h = 3$, the lift derivative is already 0.024 which is close to that of equation 3. The moment derivative (about the 0.58 point) is comparatively constant (around -0.01) and it fits sufficiently well into figure 13.

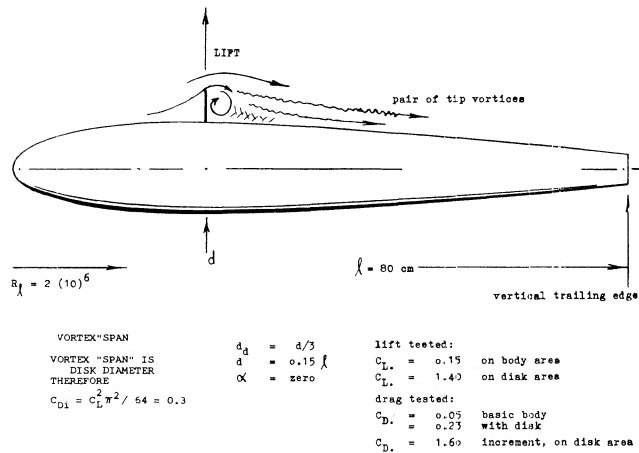


Figure 9. Flow pattern around, and lift “induced” by a circular disk attached to the streamline body as shown (9,c).

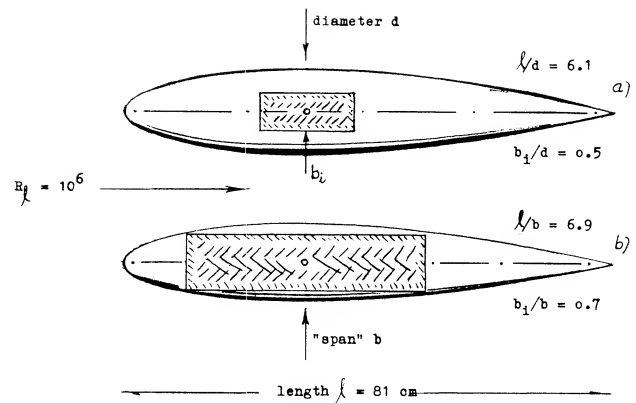
Boundary Layer. In an ogive plus cylinder combination, the afterbody is theoretically not expected to produce any lift, particularly not at small angles of attack. There is consistent evidence (8,a) (14,a,c), however, to the effect that such bodies have linear lift derivatives larger than indicated by equation 3. An explanation may be found in the growth of the boundary layer (displacement) and/or the mass of air within boundary layer and wake added to that originally deflected by the body. The effect seems to be in the order of

$$\Delta (dC_{Lb} / d\alpha) = (0.0001 \text{ to } 0.0002) \sqrt{l/d} \quad (8)$$

In the shapes with cylindrical afterbodies, as in figures 12 and 15, for example, the increment is in the order of 10% of the lift indicated by equation 3. Experimental results are assembled in figure 16.

(10) Fuselage bodies with various cross-section shapes:

- Square Cross Section, Erg AVA Go Vol II (1923).
- Bates, Various Shapes, NACA TN 3429 (1949).
- House, Elliptical Cross Section, NACA T Rpt 705 (1941).
- Letko, Cross Section Shape, TN 3551 & 3857 (1956).



a) body of revolution
b) with square cross section
c) same body at 45 degrees
The bodies have all the same size cross-section area, corresponding to $S_c/d^2 = 0.021$.
The coefficients are based on this area.
Moments are not reported.

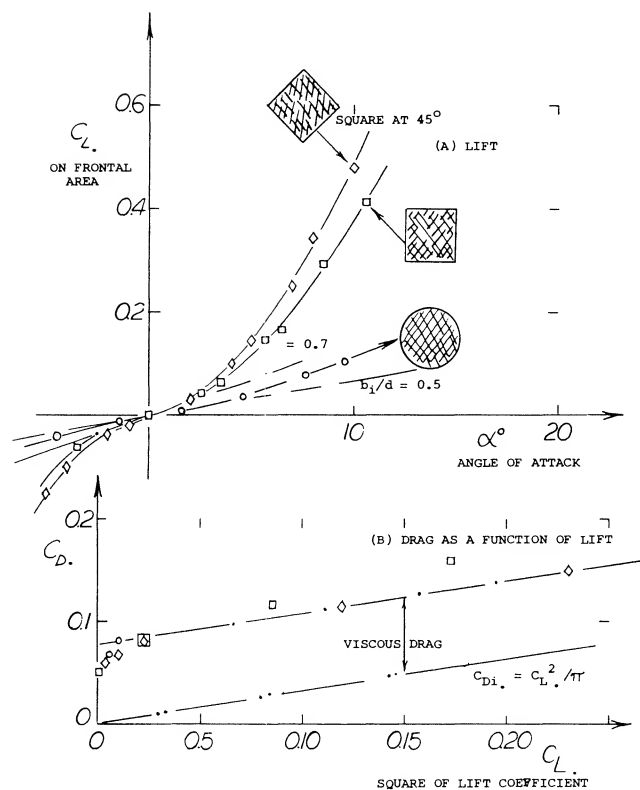


Figure 10. Lifting characteristics of streamline bodies of differing cross section, tested by AVA (10,a).

(11) Airplane fuselages, experimental:

- Brennecke, Fuselage Shapes, AVA Gottingen Rpt 1935/41.
- Gruenling, Me-109 in AVA Tunnel, ZWB Dct UM 7857 (1944).
- Imlay, Yaw Derivatives, NACA TN 636 (1938).
- Hoerner, Correlation, Ybk D'Lufo 1944, Rpt IA,022.

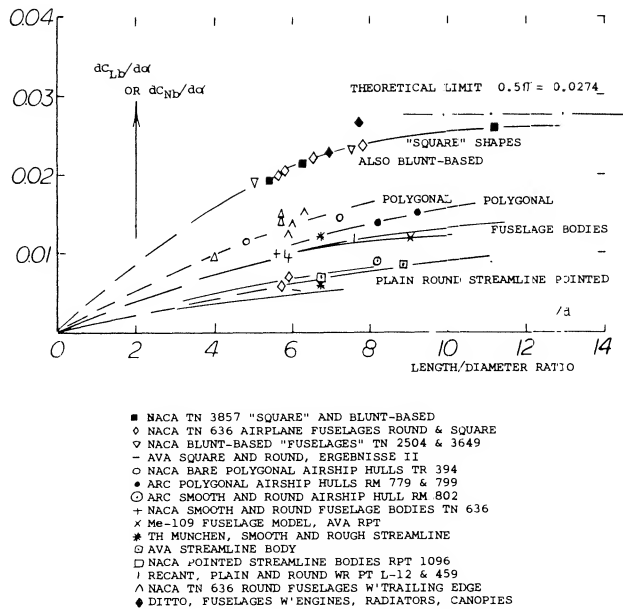


Figure 11. Lift-curve slope of various types of streamline bodies as a function of their fineness ratio.

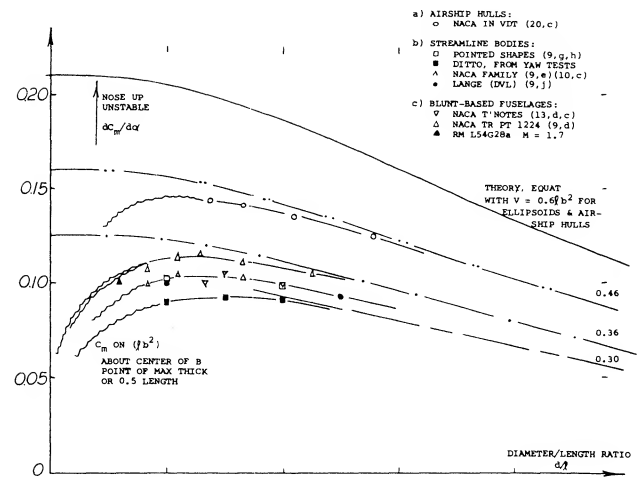


Figure 13. Longitudinal pitch or yaw moments of plain streamline bodies, as a function of their diameter/length ratio.

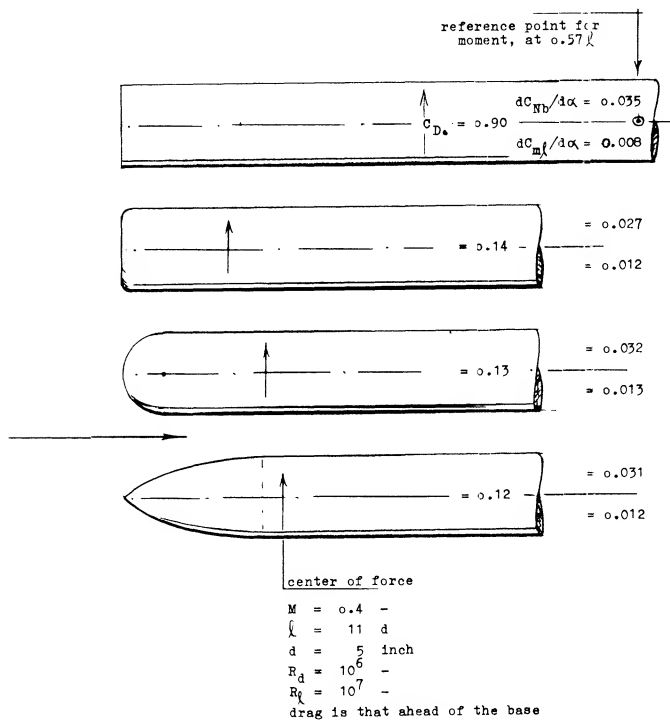


Figure 12. Lifting characteristics of a series of four bodies (13,e) with elliptical cross section shape. TN 4362.

(12) Influence of appendages:

- Jaquet, Fuselage with Ducts, NACA TN 3481 (1955).
- AVA Gottingen, Windshields, Test Rpts 1934/03 & 1935/41.

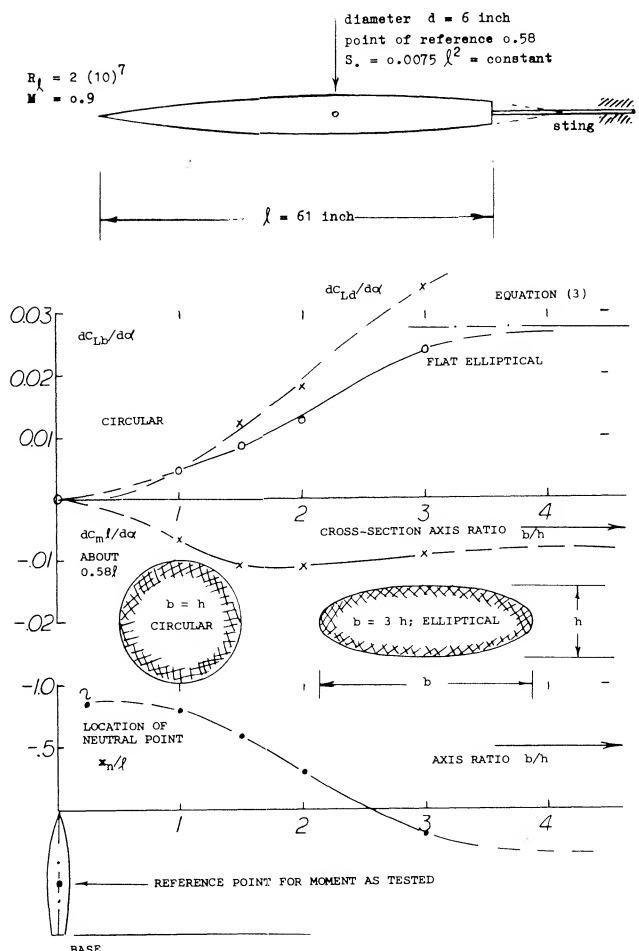


Figure 14. Lifting characteristics of four different shapes forming the nose of a circular cylinder when at an angle of attack (18,c).

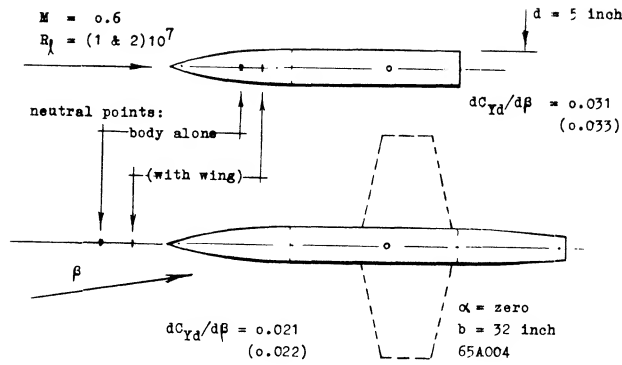


Figure 15. Directional characteristics of a fuselage body with and without boat-tailed afterbody (19,b).

2. CROSS FLOW FORCE

In the previous section the linear circulation-type component of the lift of streamline bodies was covered. As the angle of attack and/or the fineness ratio is increased, a second and non-linear component of lift or normal force originates. This component of lift is similar.

Circular Cylinder. Within the range of very small angles of attack, the rear end of a low aspect ratio rectangular wing does not contribute anything to lift. However, as the angle of attack is increased above a few degrees, the component of flow normal to the wing becomes significant in magnitude. As a consequence, a “second” and non-linear lift or normal-force component develops. The mechanism producing this component can be better understood, when first considering a long circular cylinder (with aspect ratio $A = d/l \rightarrow \text{zero}$) inclined against the oncoming fluid flow. The experimental results of such cylinders, presented in figure 9, apply to Reynolds numbers below the critical (which is around $R_d = 3(10)^5$). Disregarding a small component of skin friction drag in longitudinal flow (at small angles of attack) there are only *normal forces*; and the resultant force is split up geometrically into:

$$\begin{aligned} D &= N \sin \alpha \\ L &= N \cos \alpha \end{aligned} \quad (9)$$

(13) Blunt-based fuselage bodies:

- Loving, Boat-Tail Comparison, NACA RM L52J01.
- See references (9,d)(10,b)(10,e).
- Goodman, Configurations, NACA TN 2504 (1951).
- Wolhart, Various Configurations, NACA TN 3649.
- McDevitt, Family of Streamline Bodies, NACA TN 4254, 4280, 4362.

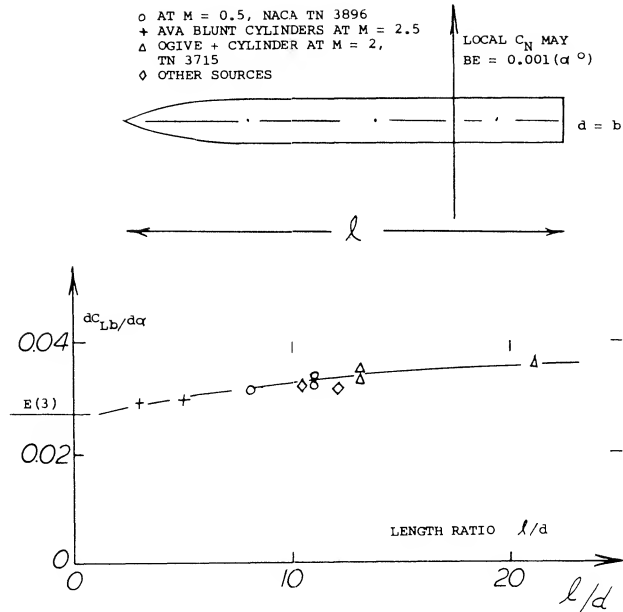


Figure 16. Experimental results showing the increase (due to viscosity) of the lift-curve slope of cylindrical bodies with their length ratio.

Cross Flow. At the angle of attack $\alpha = 90^\circ$, the drag coefficient of the cylinder is

$$C_{D_o} = C_{Nq_o} = C_C \quad (10)$$

based on cross-flow area (ld). For the cylinders as in figure 17, this coefficient is between 1.1 and 1.2. When the angle of attack is less than 90° , it is now speculated that the normal force corresponds to the cross-flow dynamic pressure

$$q_w = 0.5 \rho w^2 = 0.5 \rho (w/V)^2 V^2 \quad (11)$$

where the component of the speed V normal to the cylinder axis is $w = V \sin \alpha$, and $(w/V)^2 = \sin^2 \alpha$. The velocity component parallel to the cylinder axis, $V \cos \alpha$, does not contribute to the cross-flow pattern around the body. Using now the cross-flow coefficient C_C , the cylinder's normal force corresponds to

$$C_N = N/q \, dl = C_C \sin^2 \alpha \quad (12)$$

Using equation 9 the two components of this coefficient are then

$$C_D = C_C \sin^3 \alpha \quad (13)$$

$$C_L = C_C \sin^2 \alpha \cos \alpha = C_C \sin(2\alpha) \quad (14)$$

Figure 17 confirms these functions fairly well.

Below the critical Reynolds number, see for example in Chapter III of "Fluid-Dynamic Drag", the cross-flow coefficient of the circular cylinder is fairly constant ($C_c \approx 1.2$). Above $R_d = 4(10)^5$, cylinder drag coefficients are known to be much lower; at the level of $C_{Dc} = 0.3$. Within the transition range, it must be realized that the "effective" Reynolds number varies with the angle of attack. While at $\alpha = 90^\circ$, R_d (on diameter) is the proper indication for the flow conditions within the boundary layer, the length of the cylinder would rather be responsible at angles of attack near zero. Experimental results within the critical range, as in figure 18 demonstrate complications as follows:

a) Due to friction and boundary layer growth in tangential direction, the cross-flow coefficient at lesser angles of attack, is in between the sub- and supercritical level; it is in the order of $C_c = 0.6$.

b) As the angle of attack is increased, the effective R' number may reduce to below the critical. As a consequence, the cross flow coefficient increases in one set of experimental results to $C_c = C_{Dc} = 1.2$.

c) Within the range of sufficiently high Reynolds numbers, the cross flow coefficient reduces to $C_c = C_{Dc} = 0.2$. This very low value is supercritical.

Evidently, in round bodies, the cross-flow mechanism produces the highest lift at higher angles of attack (above $\alpha = 60^\circ$) and/or at Reynolds numbers definitely below the critical.

Transition. At small angles of attack, there will be a perfectly symmetrical slender-wing-type flow pattern as in figures 4 and 5. It is also well known that at very high angles of attack (say at $\alpha = 90^\circ$) and at Reynolds numbers below the critical (say below $3(10)^5$ on body diameter), the flow pattern is that of the alternating (in side and time) Karman vortex street. Between the two extremes, a transition takes place in two steps. Experiments on slender streamline bodies reported in (19) describe the first of these. At a certain angle of attack, the magnitude depending on Reynolds number, the flow pattern past the nose of a slender streamline body ceases to be symmetrical. The critical angle may, for example, be 20° (decreasing as the R' number is increased). Above the critical angle, the flow "separates" from one side of the nose, thus giving rise to a steady yaw moment to the other side. As the flow progresses along the length of the body,

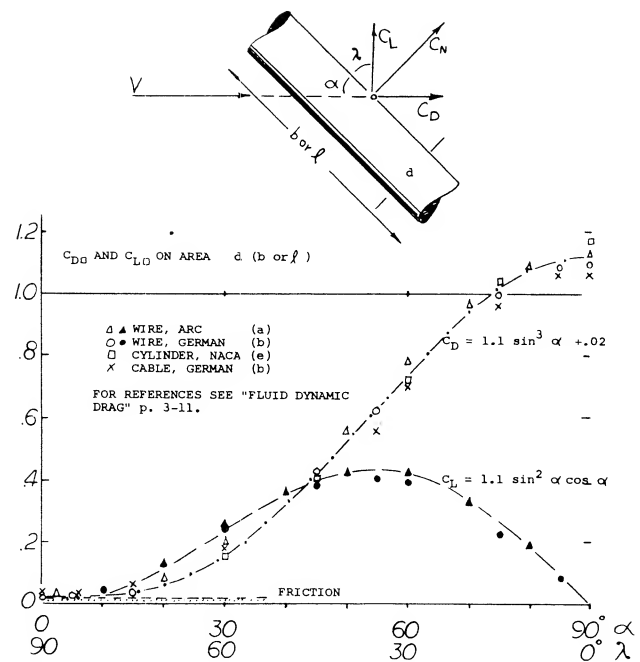


Figure 17. Lifting characteristics of circular cylinders at Reynolds numbers below the critical (where $C_{cross} = 1.1$) as a function of their angle of inclination.

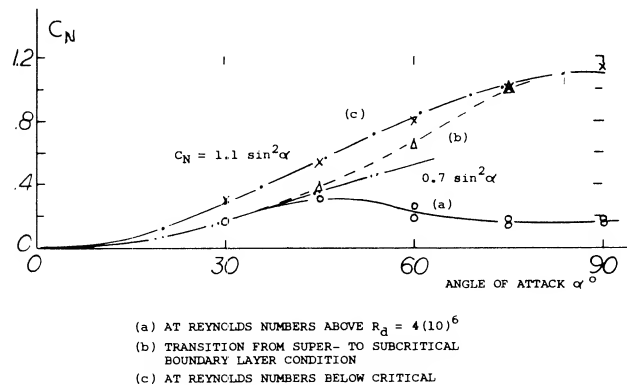


Figure 18. Normal force coefficients of circular cylinders tested (17,c) between walls at various angles of attack, within the critical range of the Reynolds number:

- a) at Reynolds above $R_d = 4(10)^6$
- b) transition from super- to subcritical boundary layer condition
- c) at Reynolds numbers below critical.

a second vortex forms at the other side; and the “separation” switches to that side. At the same station, the first vortex detaches itself from the body. The resultant values of lift and drag do not seem to depend on the type of symmetric or unsymmetric vortex formation. The pattern described is still “static” (no fluctuations). It seems, however, that here is the beginning of the second step, the alternating type of vortex street as we know it to prevail at higher angles of attack. Fluctuating values are connected with this flow pattern, of drag and lateral forces, and most likely of lift and yaw moments.

Pyramidal Shape. Since cones can be used as lifting devices, the delta-type body as in figure 19, having triangular cross sections will also develop lift. The shape was tested both with the flat side forming the top and the bottom. Note that the angle of attack is defined as against the ridge line. The flat top or bottom is evidently more effective, however, than the “V” shaped side since,

a) The lift-curve slope is higher in the flat-bottom configuration. The derivative (near zero) is practically equal to the theoretical value, (equation 3, with C_L based on projected “wing” area.

b) The non-linear component of lift or normal force corresponds somewhat more to the angle of attack of the flat side than of the ridge line.

Drag. Assuming that the non-linear force really varies as $C_{N2} \sim \sin^2 \alpha$, an average cross-flow coefficient can be evaluated in the order of $C_c = 1.0$.

Extrapolation to $\alpha = 90^\circ$, suggests on the other hand:

$$\begin{aligned} C_{D\infty} &= 0.9 && \text{for the flat-top configuration} \\ &= 1.3 && \text{for the flat-bottom shape} \end{aligned}$$

The linear component of lift (equation 2) is supposed to reach a maximum at 45° , and to reduce to zero at 90° . Between 40 and 45° , there is some discontinuity; it seems that the flow “separates”, or that the flow pattern changes into the alternating type mentioned above. We may speculate that the circulation type of lift breaks down at this point.

(14) Characteristics of ogive-cylinder bodies:

- Perkins, Normal Forces at $M = 2$, NACA TN 3715 & 3716 (1956).
- Jorgensen, Flow Pattern, NACA Rpt 1371 (1958).
- Tinling, Pressure and Wake, NASA TN d-1297 (1962).

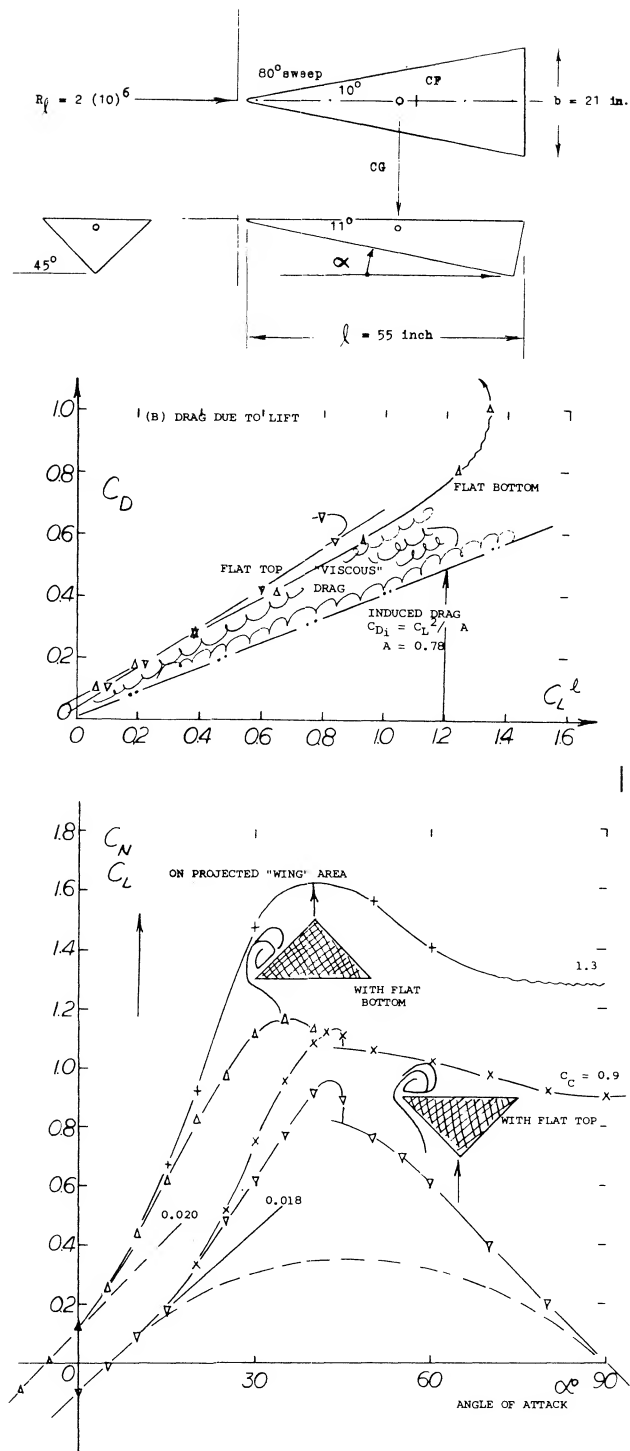


Figure 19. Aerodynamic characteristics of a basic reentry vehicle body as tested (43,b)(2,c) at 60 ft/sec.

(A) Lift and normal force as a function of the angle of attack.

(15) Characteristics of ducted bodies:

- Theory, see (62) on “ring wings” in the “wing” chapter.
- Fletcher, 5 Annular Foils, NACA TN 4117 (1957).
- Brown, Open-Nose Bodies, NACA T Rpt 808 (1945).
- Brown, At Supersonic Speeds, NACA W Rpt L-720 & -728 (1946).

(16) Ganslen, Aerodynamics of the Javelin, Univ of Arkansas Rpt 1960.

Within the range of lesser angles of attack, say to 30 or 40°, the drag is compared to the lift, figure 19. Although there is a considerable amount of drag due to viscous vorticity, the experimental functions show some similarity to that of the theoretical induced drag. Optimum lift/drag ratios of the "vehicles" are found at comparatively small lift coefficients:

$$\begin{aligned} L/D &= 2.9 \text{ at } C_L = 0.3 \text{ for the flat top,} \\ &= 2.6 \quad = 0.2 \text{ for the flat bottom.} \end{aligned}$$

A *Javelin* is basically a streamline body with extremely high fineness ratio. Typical data as for a type used in competitions, are as follows:

$$\ell = 100 \text{ inch length}$$

$$d = 1 \text{ inch } \ell/d = 100$$

$$S = 1.35 \text{ ft} \quad \text{wetted area}$$

$$W = 1.75 \text{ lb} \quad \text{weight}$$

$$V \approx 60\text{-}80 \text{ ft/sec speed}$$

$$x = 38\% \quad \text{center of gravity}$$

$$x = 45\% \quad \text{center of area}$$

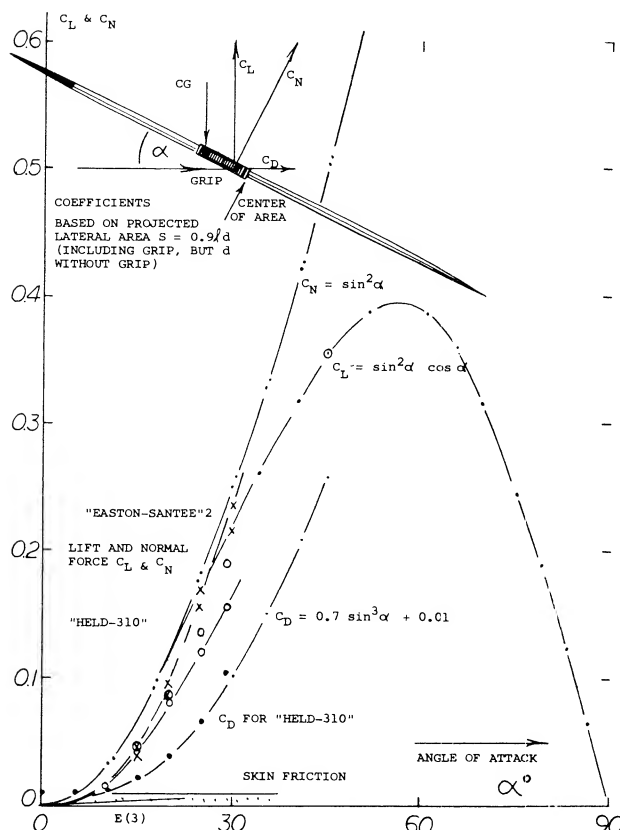


Figure 20. Forces in a javelin as tested (16) in a wind tunnel.

Lift and normal forces as tested in a wind tunnel are shown in figure 20. Evaluation yields a cross-flow coefficient between 0.6 and 0.7. Near $\alpha = 0$, where the Reynolds number on length, is $R_\ell = 5(10)^6$, boundary layer conditions must be turbulent, possibly 1 foot from the point. However when operating at $\alpha = 90^\circ$, the Reynolds number based on the diameter rather than length is no higher than $R_d = 5(10)^4$. Therefore, the cross-flow coefficient must be expected to increase from the 0.6 level near $\alpha = \text{zero}$, to between 1.1 and 1.2 at $\alpha = 90^\circ$. In fact, at $\alpha = 30^\circ$, one of the javelins tested, appeared to have a $C_c = 0.9$. The minimum drag/lift ratio is found (16) at $\alpha = 25^\circ$, in the order of $D/L = 0.60$. For comparison, equation 9 suggests a value of $D/L = \sin \alpha / \cos \alpha = 0.47$. The difference must be due to tangential forces skin friction and the drag of the grip protruding from the otherwise smooth surface. When throwing javelins, average angles of attack somewhat above 25° seem to be best.

Airship Hull. The lateral force characteristics of the bare hull of an airship are plotted in figure 21, where the normal force coefficient is based on the "lateral" area ($d\ell$); subscript " ℓ ". Although this hull was only tested up to the angle of sideslip $\beta = 20^\circ$, extrapolation to 90° is possible in the following manner:

a) Near $\beta = 0$, the linear (circulation-type) component of the normal force coefficient (on ℓ) seems to be

$$C_{N_0} = 0.0015 \beta^2 ; dC_{N_b}/d\alpha = 0.0015 (\ell/d) = 0.012$$

For the minimum drag coefficient (on b^2) $C_{D_b} = 0.06$, the corresponding value in figure 7, reflects the fact that the airship has a polygonal cross section (with a number of longitudinal edges).

b) Equation 2 indicates that the circulation reduces to zero when approaching the angle $\beta = 90^\circ$. It may be assumed, however, that the circulation-type of lift discontinues far below this angle as a consequence of separation.

c) The non-linear component is assumed to be as in equation 8. Using the value at $\beta = 20^\circ$, the cross flow coefficient is found to be $C_{c90} = 0.35$, so that:

$$\Delta C_{N_\ell} = 0.35 \sin^2 \alpha$$

At higher angles of attack, we have plotted this component, assuming that the linear type of lift would be zero.

The value 0.35 (on $b\ell$) represents a cross-flow coefficient on projected lateral area $C_{Co} = 0.41$, which is very reasonable for the polygonal shape considered, at Reynolds numbers *above* the critical. However, if one would really have tested the airship hull at $\beta = 90^\circ$, its proper R-number (on diameter) would have been a little above 10^5 , (instead of 10^6 , on length when near $\beta = 0$). The cross-flow coefficient would then have been in the order of unity.

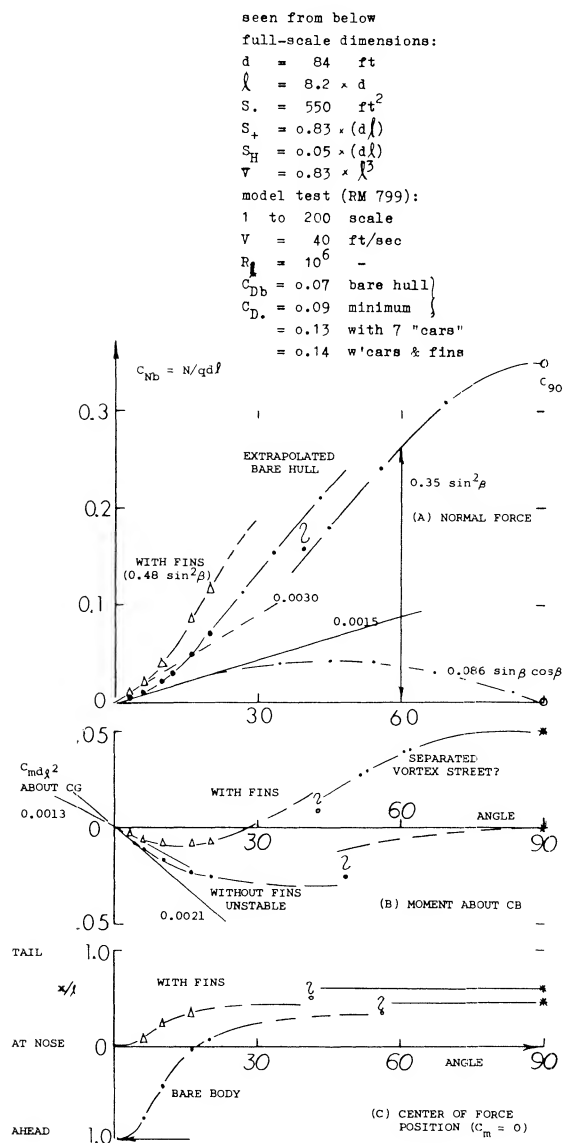
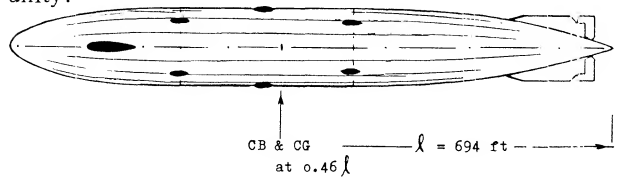


Figure 21. Characteristics in pitch and/or yaw of the hull of the British airship R-38 (ZR-2) as tested (20,b) on a 1/200 scale model.

(17) Characteristics of inclined circular cylinders:

- Relf, Inclined Wires, ARC RM (1917).
- Mustert, Lift and Drag, ZWB Doct FB 1690.
- Bursnall, Critical R-Number Range, NACA TN 2463 (1951).
- See "Fluid-Dynamic Drag", Chapter III.
- Allen, Cross-Flow Characteristics, NACA RM A50L07.

Drag characteristics of the hull may add to the understanding of the flow pattern. The coefficient (on d^2) is approximately:

$$C_{Dd} = 0.06 \text{ within } \alpha = \text{plus/minus } 7^\circ$$

$$= 0.22 \text{ at } \alpha = 20^\circ, \text{ almost 4-fold}$$

$$= 2.90 \text{ at } \alpha = 90^\circ, \text{ see above}$$

Roughly, the pressure drag and the second component of the normal force, grow in proportion to each other.

The cores of the pair of trailing vortices shown in figures 4 and 5, contain the momentum losses corresponding to the viscous drag of the body. The downwash of the flow field and/or the circulation of the vortices represent the induced drag of the body. As explained in Chapter VII of "Fluid-Dynamic Drag", this type of drag can be expected to correspond to

$$C_{Di b} = C_{Lb}^2 / \pi$$

which is the basic equation for wings regardless of their aspect ratio. The slope of the experimental values in part (B) of figure 10, shows fair agreement with this equation. The low drag coefficients near zero lift, are believed to be the consequence of a more laminar flow, particularly along the upper side of the bodies tested.

Equivalent Wing. Considering the square shape in figure 10, its lift-curve slope (around zero angle of attack) is $dC_{Lb}/d\alpha = 0.014$. In comparison to equation 3 this value corresponds to the ratio

$$(b_i/b)^2 = 0.014/0.0274 \approx 0.5$$

so that the effective span is found to be $b_i = \sqrt{0.5} b$. This span is shown in the drawing of the body. The chord of the equivalent "wing" is estimated on the basis of the tested "second" component of lift, corresponding to

$$\Delta C_{Lb} = 8 \sin^2 \alpha$$

Assuming that a flat plate would produce $\Delta C_L = 2 \sin^2 \alpha$, the chord of the equivalent rectangle as shown in the illustration, can then be calculated. In comparison to the body of revolution (having the same volume) the square shape is seen to have about twice the lift-curve slope, and 3.6 times the non-linear lifting capacity.

(18) Nose and Tail shape on cylindrical bodies:

- Loving, 4 Different Shapes, RM L52J01.
- Boat-Tailed "Fuselages", NASA TN D-217 & 950.
- Polharmus, Four Nose Shapes, RM L57F25.

3. THE LONGITUDINAL MOMENTS OF STREAMLINE BODIES

Every slender streamline body has theoretically an unstable "free" moment. Because of viscosity and the flow pattern of the type as found with slender wings, the moment is reduced, however. Therefore, in this section we will discuss the longitudinal moments including the neutral point of various types of streamline bodies. It should also be noted that in an isolated body of revolution, forces and moments due to an angle of sideslip β , are of the same magnitude as those due to a same-size angle of attack α .

Theory. The load distribution of a slender streamline body is shown in figure 3. There are positive lifting or normal forces in the forebody and as predicted by theory, forces equal in magnitude, but directed downward (negative) in the afterbody. The corresponding free moment (no resultant force) is

$$M = -0.5 \rho V^2 k V \sin(2\alpha) \quad (15)$$

where $k = 1$, for fineness ratios ℓ/d above 20. The minus sign indicates in this text, that the body is unstable, that the moment tends to turn the body away from the longitudinal direction of the flow. "V" indicates the effective volume of the air clinging to the body, so to speak, in lateral motion. In case of a body of revolution, this volume happens to be equal to that of the solid itself. Within the range of small angles of pitch or yaw, equation 15 thus reduces to 44:

$$M = -2 k q V \alpha; \text{ and to}$$

$$C_m = M/qV = -2k \alpha \text{ radians} \quad (16)$$

Streamline Bodies. As indicated by theory, the free moment of streamline bodies reduces with their fineness ratio. The corresponding factor in equation 16 may be approximated by

$$k = (1 - b/\ell) \quad (17)$$

For $b/\ell = d/\ell = 1$ (suggesting the shape of a sphere) the moment thus reduces to zero.

(19) Slender bodies at high angles of attacks:

- a) Letko, Lateral Characteristics, NACA TN 2911 (1953).
- b) Polhamus, Directional Stability, TN 3896 (1956).
- c) Maltby, Smoke Studies, RAE TN Aero-2482 (1956).

(20) Model investigations of bare airship hulls:

- a) Jones, New Shape, R-33 Model, ARC RM 802 (1922).
- b) Jones, Model R-38 Airship, ARC RM 799 (1923).
- c) Abbott, Models in VDT, NACA T Rpt 394 (1931).
- d) Jones, R-101 Airship Model, ARC RM 1168 (1929).

Pressure Distribution. The pressure distribution of the ellipsoidal body in figure 22 is shown as tested along the meridian, both at the bottom (at 0°) and on the top side (at 180°). It should be noted that the distribution as predicted by theory is symmetrical. In other words, if reversing the direction of flow, the pressure distribution of this or any other streamline body would theoretically be the same. The tested distribution agrees fairly well with theory, along the forebody. Approximately at $3/4$ of the body length, the pressure reduction, suction, expected by theory to take place on the lower side, begins to be deficient. This means that negative circulation around the tail end is reduced. At the upper side, divergence starts roughly one diameter ahead of the maximum thickness. All along this side of the afterbody, the theoretical increase of the pressure toward a rear stagnation point, fails grossly, although both lower and upper side reach together a positive pressure level in the order of $C_p = +0.1$. The area enclosed between the distributions on upper and lower side is an indication for lift or normal forces. While in the forebody, the force is up, essentially as described by equation 3, the normal force in the afterbody is almost zero (at $\alpha = 20^\circ$ as tested). The consequence is a resultant lifting force, and a reduction of the unstable moment (about the point at 0.5 of the length) to roughly half the theoretical value.

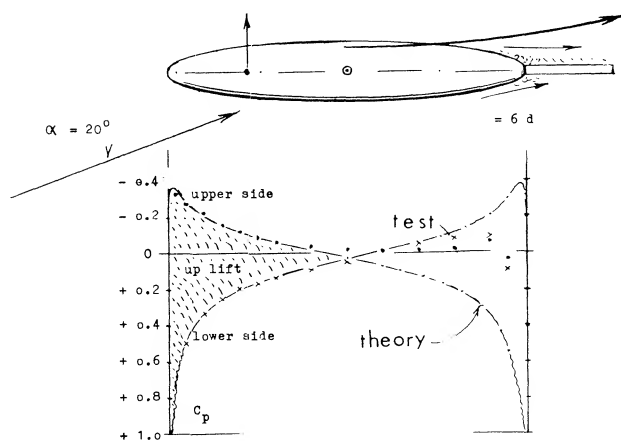


Figure 22. Pressure distribution along the meridian of a slender streamline body of revolution (8,c). RM L52d30.

(21) Analysis in NACA T Rpt 808 predicts, and experimental results in RM A52E22 and A54B15 prove, that the lift derivative of slender bodies increases with supersonic speed.

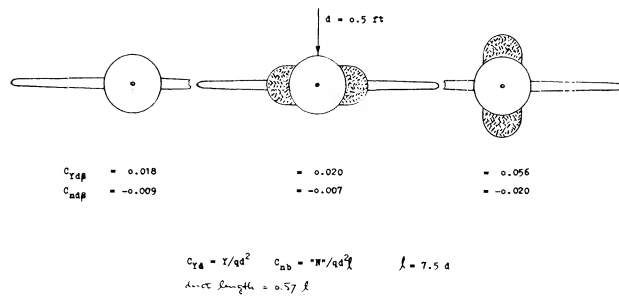


Figure 23. Directional characteristics of a wing-fuselage configuration as affected by a pair of "ducts" (12,a).

Elliptical Cross Section. The volume of air affected by a streamline body when at an angle of attack or sideslip, corresponds to its thickness measured normal to the plane of angular displacement (to the "span" when at an angle of attack). For example, a fuselage body with elliptical cross section will exhibit different moments depending on whether the body is placed at an angle of attack or of sideslip. Tentatively, lift and moment will be proportional to the square of the respective "span". Therefore, and since the volume may not always readily be known, the most appropriate moment coefficient will be:

$$C_{m\ell} = M/q b^2 \ell \quad (18)$$

where b is meant to be the "span" or "beam" when at an angle of pitch, or the height or thickness of the body when at an angle of yaw. As stated in the beginning of this chapter, in conventional streamline bodies, the so-called block coefficient may roughly be:

$$"B" = V/(\ell b h) = \text{between } 0.5 \text{ and } 0.6$$

where b = breadth or beam and h = height. In bodies of revolution $h = b = d$. Referring the moment above, to the nominal volume ($b^2 \ell$) of the body, we obtain the coefficient

$$C_{m\ell} = M/q b^2 \ell = - (2\pi/180) k "B" \propto -0.035 k "B" \propto \quad (19)$$

(22) Aerodynamic characteristics of seaplane floats:

- a) Liddell, Edo Floats, NACA W Rpt L-722 (1942).
- b) Parkinson, Hydro- and Aerodynamic, NACA TN 656 & 716 (1938).

(23) For some reason, the neutral points in figure 22 are less forward than those in figures 27 and 28.

EXPERIMENTAL RESULTS. In streamline bodies whose displacement volume is directly "useful" such as in airships, the center of buoyancy, tentatively identical with the center of gravity, is a convenient reference point for all moments. Moment derivatives of bare airship hulls, as tested about this point, are presented in figure 13. The tested values are between 70 and 75% of the theoretical function using equation 19 with "B" = 6. In typical streamline bodies (with volume concentrated more forward) the theoretical pressure distribution (1,h) changes from "positive" to "negative" at the position of the maximum thickness. Thus, the corresponding point on the body axis, is the natural reference point. Experimental results of such bodies are also given in figure 13. Within the range of higher diameter/length ratios, agreement with equation 19 is obtained when using "B" between 0.30 and 0.35, instead of the geometrical block coefficient for such bodies (which is in the order of 0.5). In other words, the moments are between 0.6 and 0.7 of the theoretical function. However, at diameter/length ratios approaching zero, higher fineness ratios, experimental moments are smaller. It appears that the boundary layer along the afterbody grows with the body length, thus reducing the negative normal forces developing along the afterbody; see figures 3 and 22. In fact, we might speculate that the moment may only be half the theoretical at $d/\ell \approx \text{zero}$.

"Ducts". When adding external stores, canopies or similar, essentially "streamlined" volumes to the outside of a fuselage, the changes in normal force and moment due to angle of attack or sideslip, can be predicted or estimated using the principles and equations presented above. A pair of "ducts" (simulating the presence of jet engines, but without openings and without any flow through them) was added to a plain fuselage body (12,a). The pitch moments and the yaw moments of the configuration are presented in Chapters XI and XIII. In sideslipping motion (where the wings may be assumed not to interfere very much), the tabulation in figure 23 demonstrates:

a) With the ducts at the sides of the fuselage, the yaw derivatives remain basically unchanged. Small differentials are due to viscous interference.

b) When placing the ducts on top and below the fuselage, lateral forces and yaw moments are considerably increased.

On the basis of equation 3 and test data the lateral force increases in proportion to $(h/d)^2 = 1.75^2 \approx 3$. The value of the negative, unstable, yaw moment is increased to a lesser degree, evidently because the force-producing volume of the ducts is concentrated near the CG of the configuration.

Ducted Body (15). We do not have suitable experimental results at hand, at this time, showing the influence of an axial duct upon lift and longitudinal moment of a *slender* body. Considering an open cylinder with unobstructed axial flow through its length, the deflection of the volume of air produces theoretically

$$C_{L_o} = 2 \hat{\alpha} = (\pi/180) \alpha^\circ = 0.035 \alpha^\circ \quad (20)$$

where the coefficient is based upon frontal area. Assuming that the turning takes place at or near the rim of the inlet, the pitch moment corresponds to the arm to the point of reference. If this point is a $x = 0.5\ell$, the maximum of the increment corresponds to the coefficient (based on body length ℓ)

$$C_{m_\ell} = -\hat{\alpha} = -0.0175 \alpha^\circ \quad (21)$$

Considering a streamline body with a duct smaller than cross section, and with a velocity through the duct lower than the ambient speed, the values above have to be reduced in proportion to velocity and area ratio. The lift differential can be appreciable (100%); the moment due to duct flow is destabilizing.

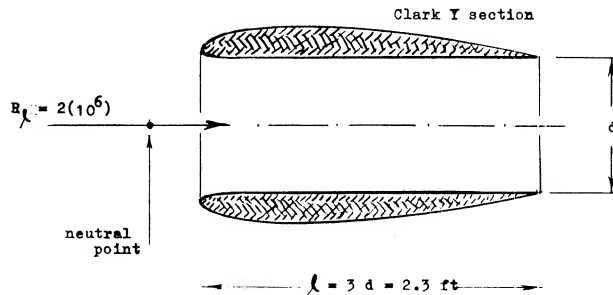


Figure 24. Longitudinal characteristics of a ring-shaped wing or ducted body (TN 4117).

The ring wing shown in figure 24 can be considered to be a ducted slender body:

a) The unobstructed duct is expected to provide a lift component corresponding to equation 28. Based upon nominal duct area d^2 equation 3 is obtained, $dC_{L_b}/d\alpha = 0.0274$.

(29) ARC, aerodynamic load distribution on airships:

- Jones, Pressure Distribution R-33 Model, RM 801 (1922).
- Bairstow, Aerodynamic Bending R-38, RM 794 & J'RAS July 1921.
- Distribution on fins and rudders, RM 779,808,911 (1921).
- Jones, Aerodynamic Loading in Turns, RM 780 (1922).
- As reported in ARC RM 775, the airship R-38 (Zeppelin Reparation "2") broke in two, while turning at a speed of some 50 kts. As deduced from experiments in (a) & (b) lateral forces are concentrated in the bow (equation 3) and in the stern (due to fins and rudders).

b) The outside shape is that of a streamline body with cut-off rear end boat tail. Theory suggests that lifting forces on that outside correspond to equation 3.

c) The combined lift coefficient (based on the square outlet or base diameter) is theoretically

$$dC_{L_b}/d\alpha = 2(0.0274) = 0.055 \quad (22)$$

The tested value is practically the same.

Assuming that the lift derivatives of ring wings with other aspect ratios $A = d/c$ or d/ℓ , also tested in (21,c), also be twice that of solid bodies (having same base area) the half values of the resulting derivatives have been plotted in figure 6. Agreement with other results in that graph is excellent if doubling the fineness ratio (ℓ/b).

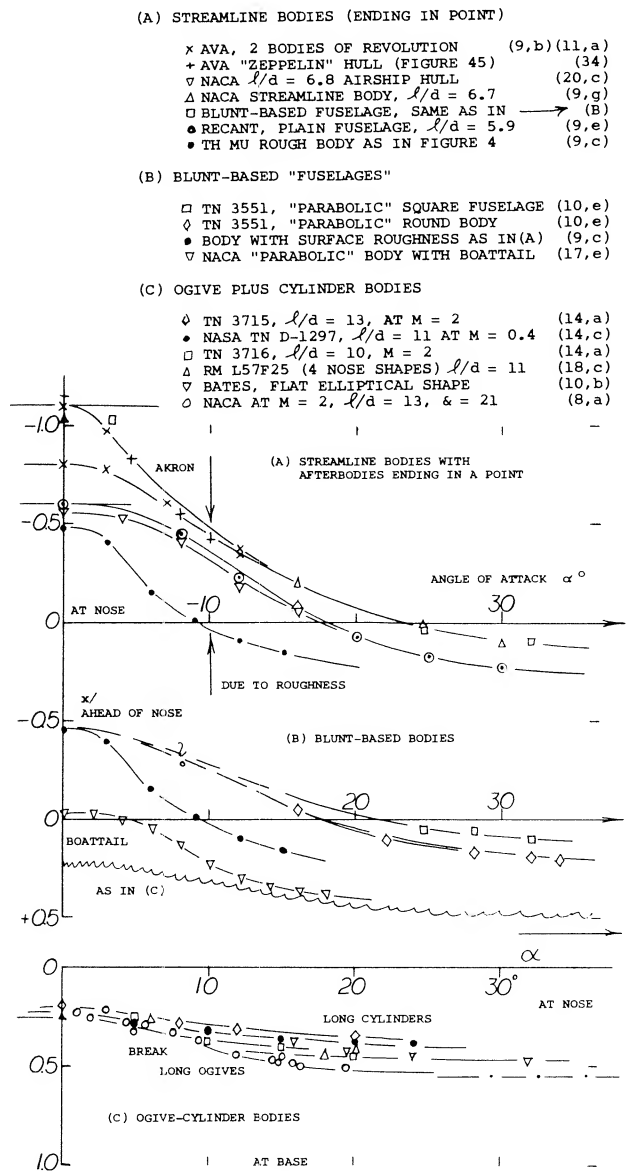


Figure 25. Longitudinal trim points (where moment = zero) of various types of streamline bodies, as a function of their angle of attack.

Neutral Point. The ideal moment of streamline bodies (without any resultant force) is “free” (independent of the point of reference). Since in real, viscous fluid flow, every body does develop lift (or a lateral force) when at an angle of attack (or of yaw) the longitudinal moment depends upon the axis of reference. To say it in different words, the resultant force produces a moment about the center of gravity or whatever axis is used. The location of the resultant force can only be obtained from pressure distribution tests, as for example in figure 3. Usually, therefore, its moment contribution is not known. Another method of describing the combined moment, is to quote the point on the axis of the body, for which the combined moment is zero. For small angles of attack (where both lift and moment vary in linear proportion) the moment reduces to zero at the *neutral point*, the location of which is away from the axis about which the moment was tested, by

$$\Delta x/\ell = dC_{m\ell}/dC_L = (dC_{m\ell}/d\alpha)/(dC_L/d\alpha) \quad (23)$$

For example, the neutral point of the bare airship hull in figure 21, is approximately at $x = -\ell$, ahead of the body's nose.

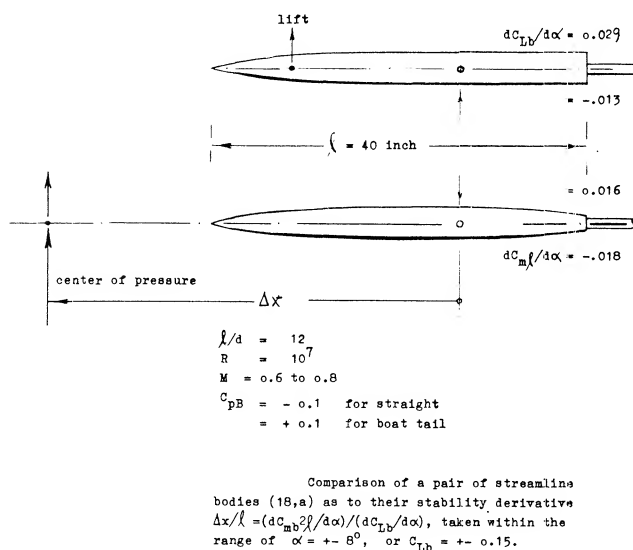


Figure 26. Influence of afterbody shape on the longitudinal (or directional) characteristics of a fuselage body.

(30) Aerodynamic characteristics of airships:

- Klemperer, Stalling, J Aeron Sci 1934 p 113.
- Freeman, "Akron" Pressure Distribution, NACA T Rpt 443.
- Frazer, "Full Scale Experiments", J. RAS Sept 1925.
- References appended to Jones, J RAS Feb 1924.
- Rizzo, Static Stability, NACA TN 204 (1924).
- Arnstein and Klemperer, Aerodynamics and Stability of Airships, see Durand's "Aerodynamic Theory", Volume VI.

Zero Moment. The location x for the zero moment is determined by

$$\Delta x/\ell = C_{m\ell}/C_L \quad (24)$$

In such points, the body is in trimmed condition, which does not mean that it would be stable. The point for zero moment changes in the manner as shown in figure 25. The most forward location of every particular body is around zero angle of attack, as defined by equation 23. In "typical" streamline bodies (with a tail tapering to a point) the neutral point is far ahead of the nose. As the angle of attack is increased, the point moves back, it reaches the body nose at angles around 20° . Depending upon the location of maximum thickness, the point may then approach a position between $1/4$ and $1/2$ the length of the body.

Cylindrical Streamline Bodies. An ogival or conical streamline body can be expected to produce the circulation-type linear lift component. This lift force acts within the length of the nose shape. Characteristics of one such body are presented in figure 26. As the second, non-linear normal-force component develops, the center of the combined force will move downstream. If the linear lift component is located at 0.4 of the nose length, and the cross-flow component assumed to be centered at $1/2$ the length of the cylindrical afterbody, the combined center of pressure is found to be as tested, for example near 50% of the length at angles of attack between 16 and 20° .

Nose Shape. Results of a cylindrical body are presented in figure 14, for several shapes of the forebody:

- As soon as a small rounding radius is provided (as small as 10% of the diameter) the drag coefficient C_{D0} drops from 0.9 to less than 0.2.
- The normal-force derivative is roughly independent of nose shape. The experimental values are slightly higher than the $dC_{Nb}/d\alpha = 0.0274$ as indicated by equation 3; see equation 8.
- Disregarding the really blunt shape, the pitch moment derivative is approximately independent of nose shape. On the average, the aerodynamic center is at

$$\Delta x/\ell = dC_{m\ell}/dC_{Nb} = 0.012/0.030 = 0.4$$

ahead of the reference point. In other words, the center of lift within the range of small angles of attack (say to plus/minus 4°) is at $x/\ell = 0.57 - 0.40 = 0.17$, or at $x/d = 1.6$, behind the nose point.

Afterbody. The experimental results in figure 15 give a perfect illustration of slender body aerodynamics:

- the ogival forebody produces the theoretically expected lateral force (equation 3).
- a cylindrical afterbody may produce a small component of force, of the type as described in context with equation 8.
- a boat-tailed afterbody produces a negative component of lift, in the manner if not magnitude, as predicted by theory.

Cylindrical Middle Body. There are streamline shapes such as possibly in airship hulls or fuselages, where a considerable part of the length is cylindrical. Basic theory expects destabilizing lifting or normal forces to originate in the bow and the stern, while the cylindrical middle body is not supposed to contribute to force or moment as far as small angles against the wind are concerned. Since the bow and stern have a considerable moment (about the center of buoyance or the CG) such partly cylindrical bodies may have larger moments than truly streamline shapes (with the same fineness ratio).

Cross Section. A series of four "fuselages" differing in the shape of their cross section are reported in 14,a. As shown in figure 12 of Chapter XI, the lift and pitch moment essentially a function of the body width. A fuselage with a flat and wide shape has considerably larger pitch moments, accordingly, while a "deep" and narrow body has reduced moments, defined about the point at $x/\ell = 0.54$. As series of 4 blunt-based bodies is presented in figure 12, differing in the span/thickness ratio of their cross sections. The pitch moment about the point at $x = 0.58\ell$, properly referred to b^2 and ℓ , reduces from 0.007 to 0.003, as the span ratio is increased to 3. The neutral point moves downstream from $x/\ell = -0.8$ (ahead of the body's nose, for the body of revolution) to $x/\ell = +0.2$ for $b/t = 3$.

Seaplane Float. Not all streamline bodies are rotationally or otherwise symmetrical. Aerodynamic characteristics of a float are presented in figure 27. Lift and moment seem to vary in the same manner as in other bodies. There is an irregularity, however, in the moment function, within the range of negative angles of attack. It is suggested that the flow separates here from the bottom of the float, behind the step.

Curvature. An airship or a submarine when turning, moves into a curved stream. As illustrated in figure 28, geometric conditions may then be such that nose and forebody are at an angle of yaw close to zero, while at the stern and the tail fins, the angle is in the order of 37° . This condition can roughly be simulated by testing a curved or cambered body in a straight stream of air or water. There are also bodies which are cambered naturally, such as the float in figure 25, or certain fuselages.

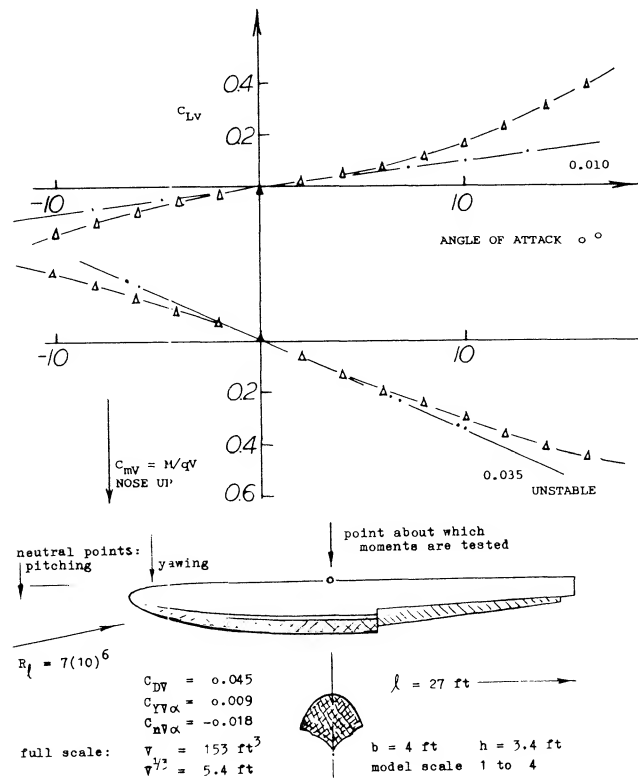


Figure 27. Aerodynamic characteristics of an airplane float (22,a).

Camber. Characteristics of a cambered body are presented in figure 29. For the linear circulation type of lift, the zero angle of attack corresponds to the tangent at about $3/4$ of the forebody length (near the point where the forebody lift may be centered). The slope is the same as that for the straight body. For the non-linear lift component, the average angle of attack of the afterbody can be expected to be responsible. This angle is $(\alpha + \Delta \alpha)$ and the non-linear normal-force component may be

$$N_2 \sim (\alpha + \Delta \alpha)^2$$

$$\Delta C_L \sim (\alpha - 3^\circ + 4^\circ)^2$$

where 3° = zero-lift angle of attack, and 4° = similar to the 5° corresponding to camber. For example, at $\alpha = 19 - 3 + 4 = 20^\circ$ (as in part C of the graph), the non-linear component is approximately the same as at $\alpha = -19 - 3 + 4 = -18^\circ$ (as plotted in the form of $+18^\circ$ in part A of the graph).

$$\Delta C_L \sim (\alpha - 3^\circ + 4^\circ)^2$$

where 3° = zero-lift angle of attack, and 4° = similar to the 5° corresponding to camber. For example, at $\alpha = 19 - 3 + 4 = 20^\circ$ (as in part C of the graph), the non-linear component is approximately the same as at $\alpha = -19 - 3 + 4 = -18^\circ$ (as plotted in the form of $+18^\circ$ in part A of the graph).

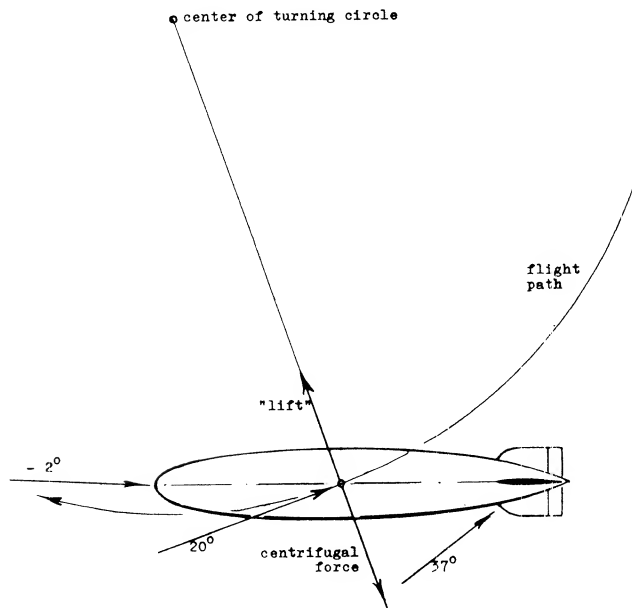


Figure 28. Geometry and lateral forces of an airship (or of a submarine) during a turn. Dimensions are assumed in such a manner that the stream curvature corresponds to the camber of the body in figure 29.

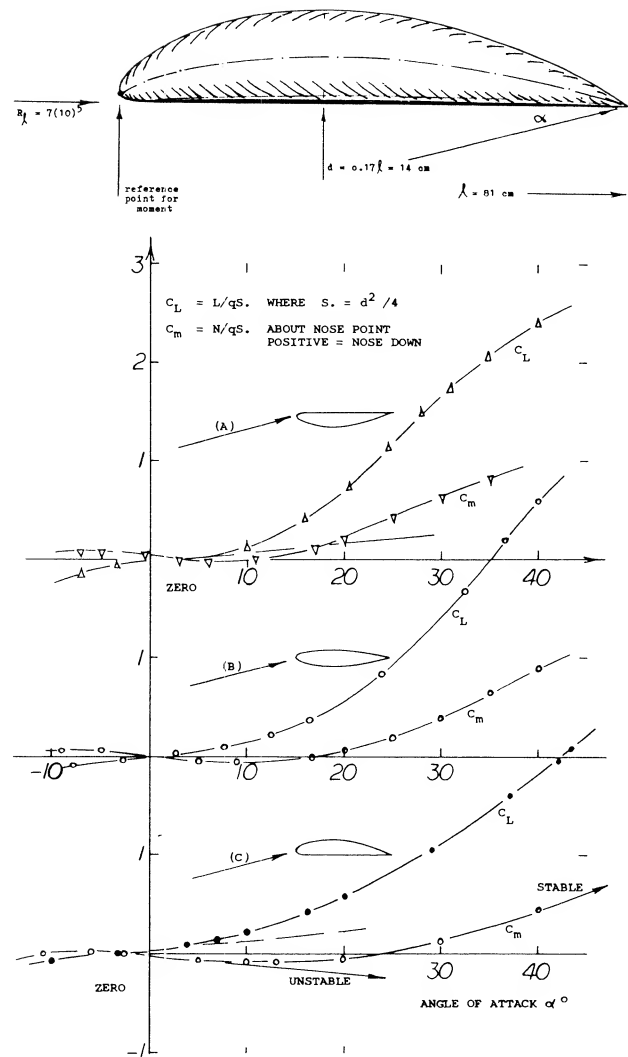


Figure 29. Longitudinal characteristics of a "cambered" streamline body (39,c) obtained from the body of revolution in figure 33, by curving the mean line, or center line.

4 . STABILITY OF STREAMLINE BODIES

Typical streamline bodies are unstable. Devices such as missiles, bombs, airships and fuselages can be stabilized by adding fins to their rear end.

Static Stability. As stated in context with equation 22 there is a range of the angle of attack (or yaw) around zero, where lift or lateral force and moments vary in linear proportion, so that $dC_m/dC_L = \text{constant}$. This derivative represents *the minimum of the static stability* (33). When using a moment coefficient referred to the bodies length (subscript l) the neutral point (where the moment is zero, and/or about which the static stability parameter may be constant) is located at

$$\Delta x/\ell = dC_m/dC_L \quad (25)$$

- (31) Characteristics of airship fins:
- a) ARC, Model Results, RM 714, 799, 802, 1168.
 - b) NACA, Technical Reports 215, 394, 432.
 - c) Pressure distributions, ARC RM 808, 811, 1169.
 - d) Pressure distributions, NACA T Rpts 213, 324, 443.

where Δx = distance measured from the center of gravity or the reference point about which the moment is tested, positive when downstream. Since stability of bare streamline bodies is usually "negative", the neutral point is forward accordingly. In fact, it may be located far ahead of the body's nose, such as $x = -\ell$, for example.

The Cones as in figure 1, have a fairly constant center of pressure, equal to neutral point (or aerodynamic center), located between 64 and 65% of their length. Cones thus behave in the same manner as slender delta wings. Placing the CG slightly ahead of 64% of the length, conical bodies could thus provide stable lifting "vehicles". The circular type in figure 24 has a maximum $L/D = 2.4$, at $C_{L0} = 0.4$, i.e. based on base area. The L/D ratio could be improved by giving the cone a flat (elliptical) cross-section shape, of the type as included in figure 2, for example.

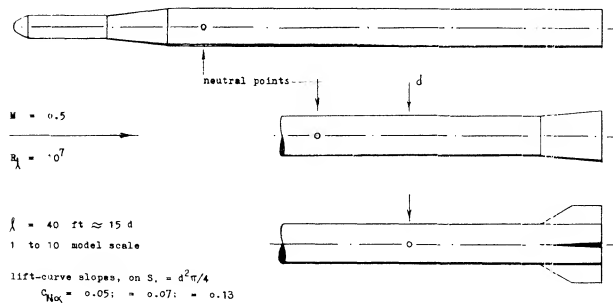


Figure 30. Stability (position of neutral point) of the essentially cylindrical "scout" rocket vehicle (38,a) for three different conditions of the tail end.

Cylindrical bodies with some type of "streamline" nose, could be expected to have their neutral point within the length of the nose; roughly as follows:

- at 2/3 of nose length, for conical shape
- at 1/2 of length, for ogive (as in figure 15)

Because of the "viscous" type of lift developing in the cylindrical afterbody (see equation 8) the neutral point may be further aft, however. For example in the shape at the bottom of figure 14, the point is at or slightly behind the juncture between nose and cylinder.

A *Flared Tail End* as in the second configuration in figure 30, is theoretically expected to provide a stabilizing force the magnitude of which corresponds to equations 1 and 3,

$$dC_{L_D}/d\alpha = (S_B/S_D - 1) 0.0274 \quad (26)$$

where "B" indicates the base area. The tested differential $\Delta C_{N0} = 0.02$ agrees with this equation sufficiently well. Moment and neutral point can be calculated as they were tested.

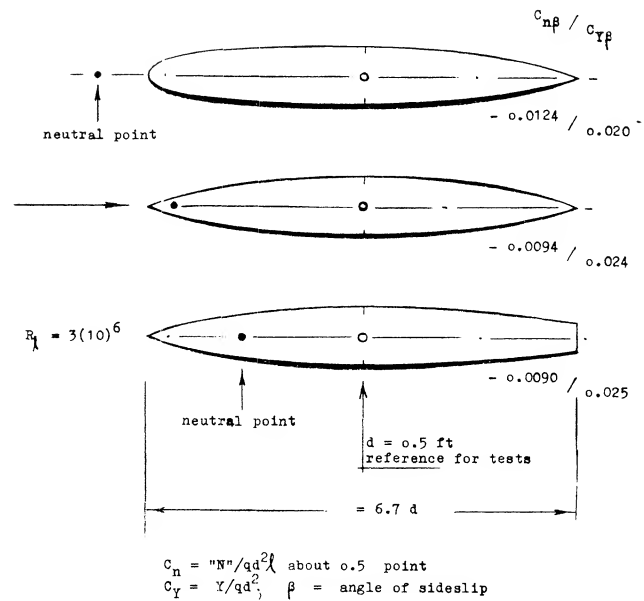


Figure 31. Longitudinal characteristics of three streamline bodies of revolution (9,h) differing in the shape of fore-and afterbody.

Boat Tail. As soon as the afterbody is made tapering, it begins to produce a negative lift force, thus making the moment more unstable (tail down, nose up) and causing the neutral point to move forward. Figure 15 is an example, where the addition of a boat tail results in a neutral point location ahead of the body's nose. The shape with the cylindrical afterbody in figure 26, will be stable if placing the CG ahead of $x = 0.2$. Boat-tailing (reducing the width of the afterbody) reduces stability. In fact, stability of the second shape in the illustration (still having a blunt base) is almost as poor as that of any pointed tail shape (such as an airship hull, for example). This result is confirmed in figure 31 where characteristics of three same-size bodies are listed, differing in shape. The blunt-based body has nearly the same derivatives as the slender double-pointed type.

Streamline Bodies. Although the results in figure 31 may quantitatively be deficient (23) they nevertheless demonstrate how stability deteriorates when "streamlining" the shape:

When reducing the afterbody to a point, the neutral point moves forward.

when giving the forebody a fuller shape, the point moves still further forward.

As a consequence, "perfect" streamline shapes such as in figures 32, 33, 34 have neutral points up to about once their length ahead of the nose.

Thickness Ratio. Characteristics of two streamline bodies differing in thickness ratio, are presented in figure 32. While, this time based on area ($b\ell$), the lift-curve slopes are roughly the same, the fatter body is much more unstable than the thin one. Neutral points of various types of bodies are plotted in figure 35, evaluated from tested pitch and/or yaw derivatives show:

- round streamline bodies with a tapering afterbody ending in a point are most unstable.
- airship hulls (bare, without fins, but with polygonal edges) still have a position of the neutral point more than half of their length ahead.
- sufficiently blunt-based “fuselage” shapes are the least unstable; their neutral point may be at their nose point.

The mechanism of negative lift in the afterbody (see figure 1) evidently deteriorates as the boundary layer grows with the length ratio ℓ/d . At $d/\ell \rightarrow 0$, we may speculate that the center of whatever linear lift component might still exist, is somewhere within the nose part.

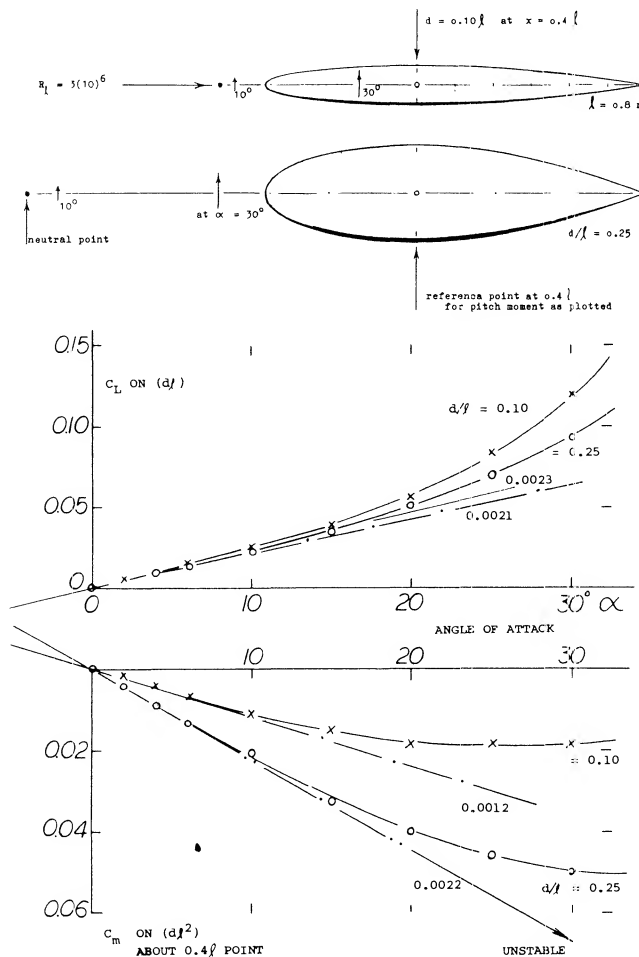


Figure 32. Longitudinal characteristics of a pair of streamline bodies (9.j) differing in fineness ratio.

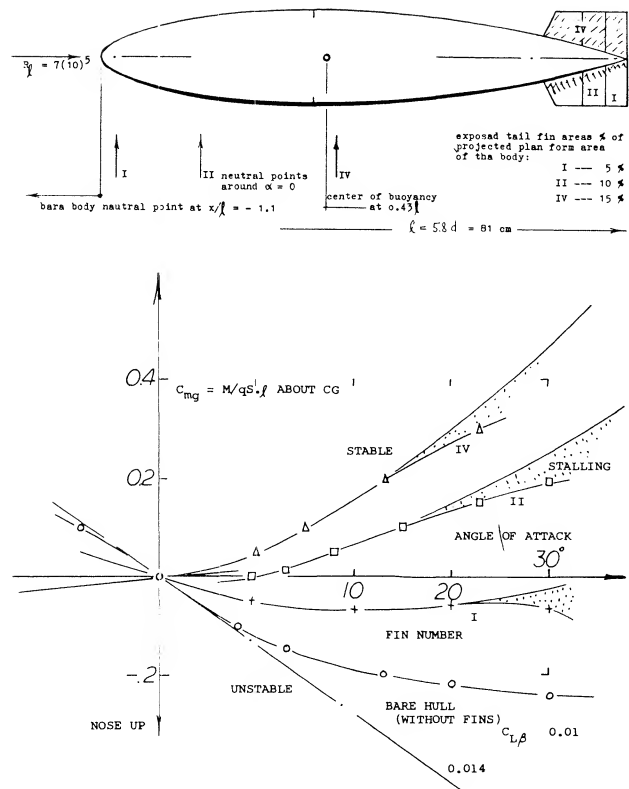


Figure 33. Longitudinal moments and neutral points of streamline body of rotation (39,c) with and without tail fins attached, tested in water towing tank.

Neutral Points of various types of bodies are marked in figures 26, 31, 32 and 36; and they are indicated in figure 27 by limiting horizontal lines around zero angle of attack. The distance from the nose point, is on the average 23.

- $x_n = -1.0 \ell$ for “perfect” streamline bodies
- $= -0.5 \ell$ in turbulent air, or with surface roughness
- $= -0.3 \ell$ for blunt-based parabolic-arc bodies
- $= -0.1 \ell$ for boat-tailed cylindrical shapes
- $= +0.2 \ell$ for cylindrical afterbody shapes

It seems that laminar boundary layer flow (around the nose) results in more unstable characteristics, while surface roughness is stabilizing. Stability about a given point such as the center of gravity, corresponds to

$$dC_{m\ell} / dC_L = (x_n/\ell - (x_g/\ell)) \quad (27)$$

where x_g = downstream of the CG from the nose of the body. A body is stable when the derivative is positive, i.e. when the CG is ahead of the neutral point.

Wedge Shape. Without fins, streamline bodies are hopelessly unstable. For example, the derivative of the bare and smooth airship hull in figure 37, about the CG at $x = 0.45l$, is $dC_{m\ell}/dC_L = -1.55$, which means that the neutral point is 1.1 body lengths ahead of the bow. From efforts to improve the hull shape, the configuration as in figure 38 was investigated and indicated:

a) When giving the tail end a wedge shape, with a vertical trailing edge, both the basic linear and the "second" non-linear lateral force components are increased.

b) Analysis confirms that the additional forces originate in the rear end, approximately at a "center" as indicated in the drawing.

c) As a consequence of (a) and (b) bodies with a flat tail end are less unstable. When making the trailing edge, $h = d$, the hull might obtain a stability similar to that of ogive-cylinder combinations.

The yaw-moment derivative of the airship hull and those of a few other "fuselage" bodies having a wedge-like afterbody shape, are plotted in figure 39. The results correlate with equation 3. A modification similar to that in figure 37, is shown in figure 38 of Chapter XIII. In that case, the neutral point is located ahead of the body's nose, at

$$\begin{aligned} x/l &= -1.2 \quad \text{for plain body of rotation} \\ &= -1.0 \quad \text{ending in edge with } h = 0.5 d \\ &= -0.6 \quad \text{with fins ending in } b = 0.5 d \end{aligned}$$

The second shape has a tail end with elliptical shape (with round top and bottom). It is thus found to be important to have sharp lateral edges as in fins and not just a trailing edge.

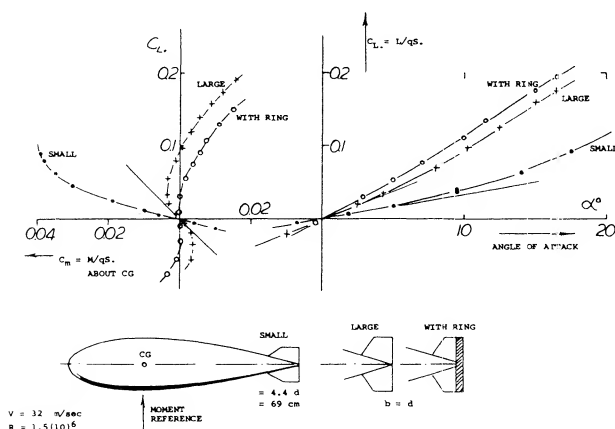


Figure 34. Stability characteristics of a fin-stabilized streamline body (fuel tank) as tested (39,a) in the Junkers wind tunnel. Model scale 1 to 5.

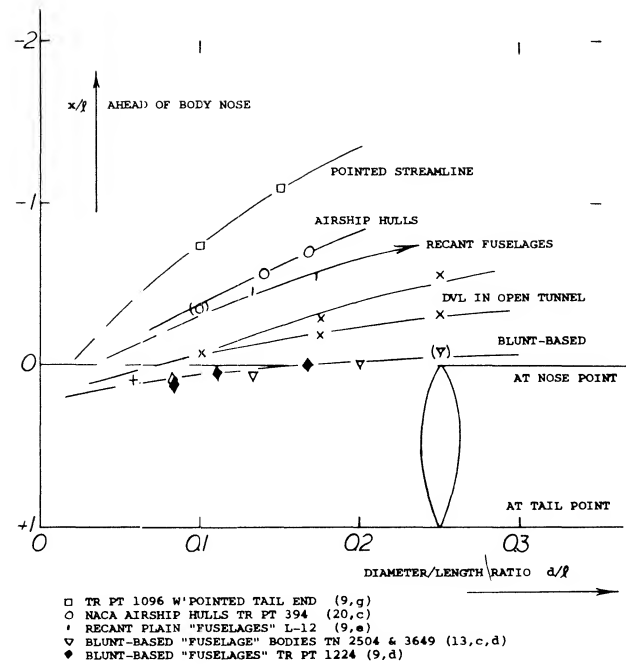


Figure 35. Position of the neutral point (at angles of attack near zero) of various types of streamline bodies, as a function of their diameter-length ratio.

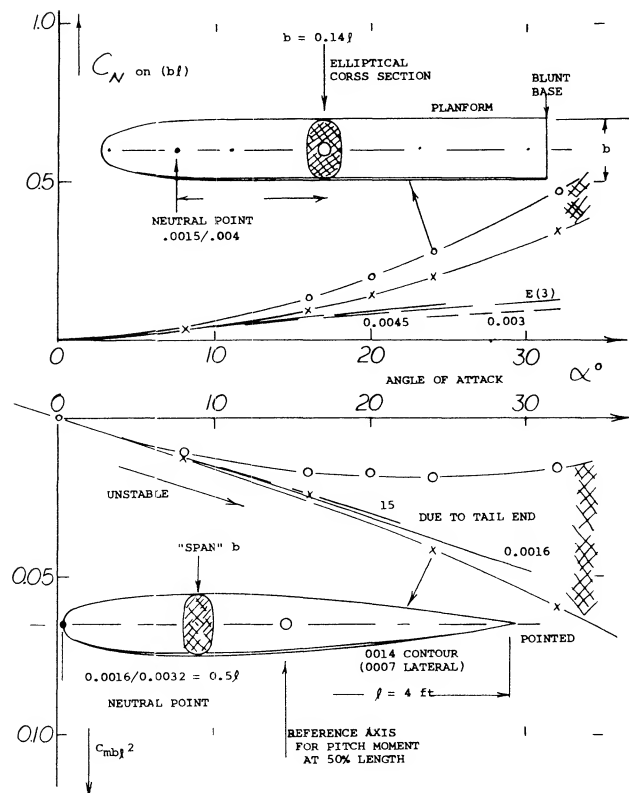


Figure 36. Longitudinal characteristics of a pair of fuselage bodies differing in the shape of the afterbody (TN 3429), (10,b).

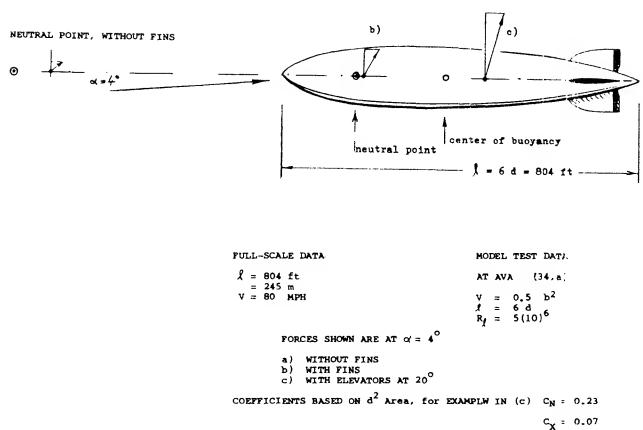


Figure 37. Longitudinal stability characteristics, with and without fins, of LZ-128 "Graf Zeppelin" airship (34,a).

Dorsal Fins are usually meant to be comparatively narrow surfaces attached to the tail end (or possibly the front end) of fuselages. Forces and moments of a plain "fuselage" model are shown in figure 40, without and with such fins (strips of metal) attached to the afterbody. With these strips there is a modest influence upon lift and moment near zero angle of attack. Also the non-linear lift or normal-force component is considerably increased along with improved stability at the higher angles of attack.

In conclusion, "dorsal" strips are primarily effective at higher angles of attack. The normal-force increment is roughly $\Delta C_N \sim \sin^2 \alpha$. In figure 40, the cross flow coefficient of the part of the afterbody "covered" by the fins (on projected lateral area S_F) is in the order of

$$C_C = (dC_{N_f} / d(\sin^2 \alpha)) (b_l / S_F) = 3$$

Tail Fins. A body with the round and full forebody such as shown in figure 30 is the most unstable kind. There is evidently no "support" in the afterbody; and the forebody force is located comparatively far ahead. The only aerodynamic means of stabilizing such streamline shapes, are fins attached to their tail end. The longitudinal (pitch or yaw) moment of a streamline body (similar to the hull of an airship or a submarine) is plotted in figure 33. Static stability about the center of buoyancy or gravity, is only obtained after adding the largest fin shown (number IV). The stabilizing moment of the tail fins (subscript "T") corresponds to

$$dC_{m_T} / d\alpha = (dC_{L_T} / d\alpha) (l_T / l) (S_T / S_o)$$

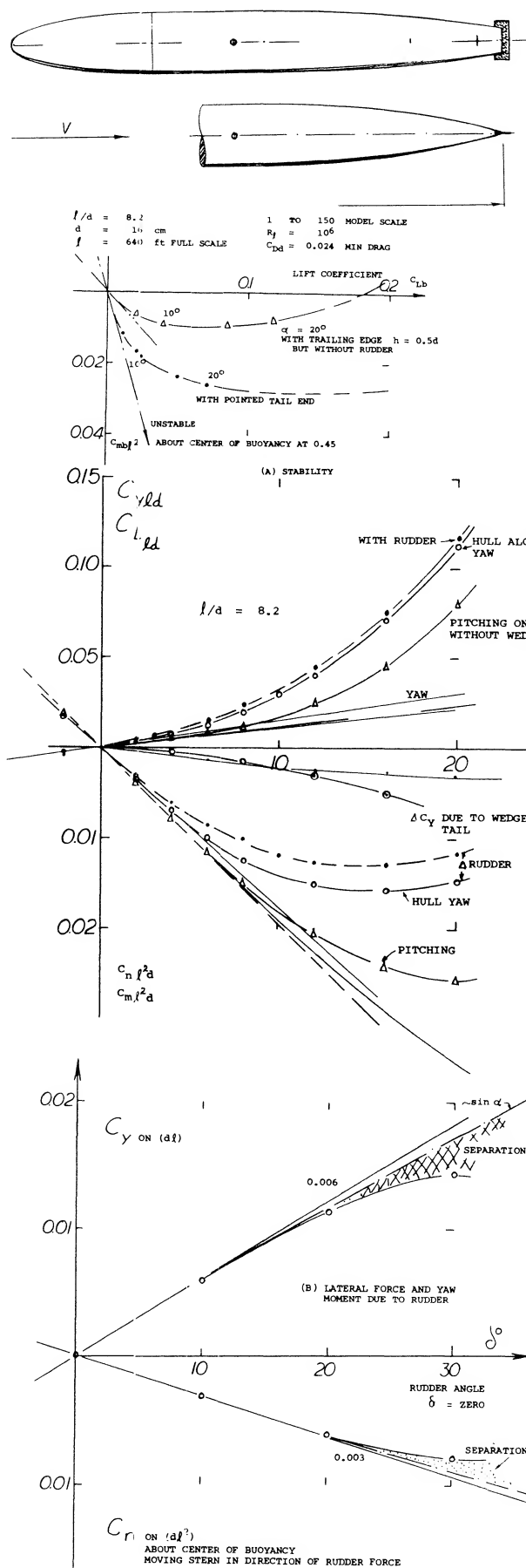


Figure 38. Airship hull with wedge-shaped afterbody (with a vertical trailing edge) R-33 tested (20,a) in yaw and in pitch.

The lift curve slope might be predicted for two extreme cases:

a) For small aspect ratios, equation 3 suggests a $dC_{Lb}/d\alpha = 0.0274$. The contribution of tail number IV is some 10% larger than this, possibly because of favorable 2-alpha type body interference.

b) In the range of larger fin aspect ratios, it can be assumed that the effective ratio is $\frac{1}{2}$ the geometrical one (36). Using equations of Chapter III, the lift-curve slope can thus be obtained. The contribution of tail number I (with $A = 4.4$) agrees well with this type of estimate.

Fin Size. When adding fins to a streamline body, the neutral point moves aft, say from $x/\ell = -1$ (ahead of the nose) possibly to $x/\ell = +0.5$ (half way between nose and tail point). The difference $\Delta x/\ell = 1.5$ is the length stabilized by means of the fins. In figure 33, it is seen how stability (position of the neutral point) varies as the chord length of the fins is increased. The configurations shown in figure 34 demonstrate how stability increases with the span of the fins. It may be speculated that the stabilizing forces originating in the fins grow in proportion to their chord length and to the square of their span. Neutral-point positions were, therefore, plotted in figure 41 as a function of the tail-size parameter $(b/d)^2 (c/\ell)$. The functions thus obtained can empirically be interpolated by

$$\Delta x/\ell = (dC_m/dC_L) = 2.5 \sqrt[3]{(b/d)^2 (c/\ell)} \quad (28)$$

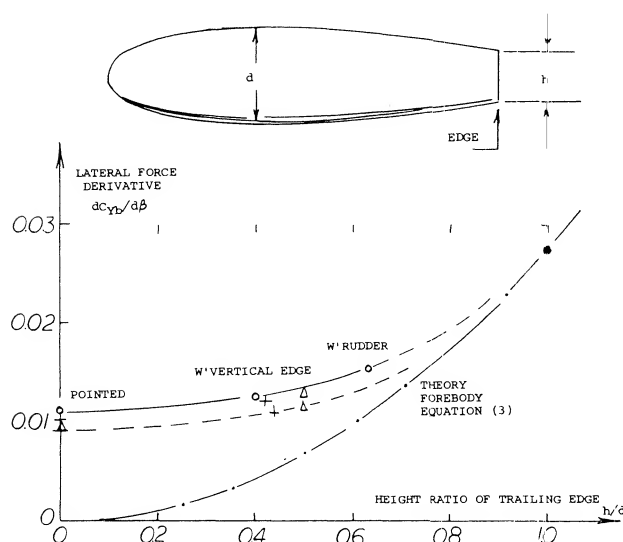


Figure 39. Lateral force derivatives of streamline bodies, as a function of the height of the trailing edge (if any).

(32) ARC, Characteristics of airships, pitching and turning:

- a) Pannell, R-32 Turning, RM 668 & 812 (1921).
- b) Simons, Stability and Turning, RM 713 (1919).
- c) Jones, Stability, RM 751 & 799 (1922).
- d) Jones, Equilibrium in Turns, RM 716,749,781,782 (1922).

Ring Surface. Lift and moment (about the CG as indicated) of a streamline fuel tank (to be dropped when necessary) are presented in figure 34. The “small” set of fins is evidently not sufficient to stabilize the body. Neutral stability is only obtained after adding a small “ring” to the larger set of fins. The model of a 1000 kg bomb was tested with two different tail surface configurations. As shown in figure 42, addition of a ring around the four fins, increases stability. The neutral point is moved aft on account of the ring by $\Delta x = 0.16\ell$. It can be assumed that the increment of the stabilizing forces in the tail surfaces are obtained on three counts:

- 1) the ring serves as an end plate, thus increasing the effectiveness of the fins;
- 2) the ring surface develops stabilizing forces of its own (see equation 20);
- 3) the ring reaches out into the flow outside the body’s boundary layer (wake).

In the configurations as in figures 34 and 42, the stabilized length is increased by the addition of a ring, roughly by 10 and 20%, respectively. This small change can make the difference between stable and unstable configuration.

Airship. Stability characteristics of an airship are shown in figure 37. Without fins, the slope near zero angle of attack (or sideslip) $dC_{m\ell}/dC_L = -1.4$ means that the neutral point is roughly one length ahead of the nose. After adding the set of fins, that point is brought back as indicated, roughly half way between nose and the center of buoyancy. The airship is not stable in this condition. The speed of these vehicles is evidently low in comparison to their mass; which means that their Froude number is comparatively low. As a consequence, the deviation from their direction of motion takes place at such a slow rate that correction by manual or automatic control (rudder and/or elevator) deflection) can easily be accomplished. As shown in 30,f one particular airship needs alternating rudder deflections of plus/minus 4° to keep it on course. Although it would be possible to make the airship in figure 37, stable by increasing the size of the fins, it was evidently concluded that this would not “pay”. Larger fins would add to drag and weight. As we will see later, the maneuverability (turning) would also be reduced when increasing stability.

(33) For a discussion of the dynamic stability of airships see (30,f) and (32,e), for example.

(34) Investigations in AVA wind tunnel:

- a) Kohler, “Zeppelin” Airships, Ringbuch D’Lufo Rpt IA15 (1940).
- b) Kohler, Airplane Skis, Luftwissen 1937 p 6.

Tail Fins. When attaching fins to the stern of the airship hull as in figure 21, they first produce some circulation-type lift. The linear normal-force slope is doubled; $dC_{Nb}/d\alpha = 0.003$. Based on various areas, the increment (due to fins) has the derivative:

$\Delta (dC_N/d\alpha) = 0.003$	on lateral hull area (d)
$= 0.024$	on hull diameter area d
$= 0.055$	on exposed fin area
$= 0.026$	on fin plus “covered” area

The most reasonable definition is the last one, on “total” fin area, including the part of the hull between them. The slope somehow corresponds to the geometric aspect ratio $A_F = 0.7$. There are interference effects involved, however:

a) At the sides of the hull, the angle of attack of the fins is possibly doubled, on account of “2 alpha” cross flow.

b) As explained for horizontal tail surfaces, in Chapter XI, the boundary layer (wake) developing along the hull interferes with the circulation around the fin plus stern configuration.

The stabilizing moment due to the lifting forces in the stern, corresponds to

$$dC_m/d\alpha = (dC_N/d\alpha)(\ell_T/\ell) \quad (29)$$

where ℓ_T = moment arm of the “tail” to the axis of reference. Solving the results as in figure 21 for that arm, it is found that the location of the stabilizing tail force is at

$$x/\ell = (dC_{m0}/d\alpha)/\Delta (dC_N/d\alpha) = 0.0013/0.0015 = 0.89$$

which is as expected, somewhat forward within the area of the, and covered by the fins.

(35) Dorsal and other fins on fuselages:

- see Bates in reference (10,b).
- Hoggard, Around Plain Body, TN 785 (1940).
- Recant, Fighter Model, NACA W'Rpt L-779 (1943).

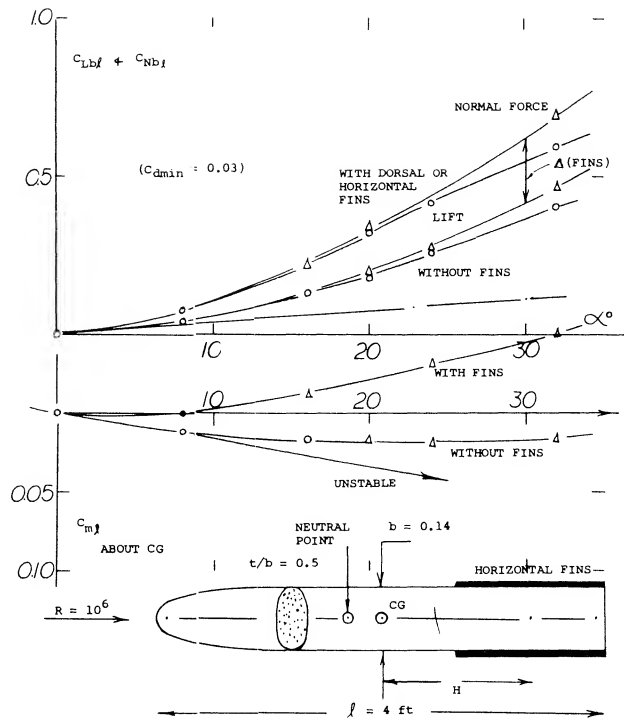


Figure 40. Influence of horizontal narrow “fins” upon lift and pitch moment of a flat “fuselage” body (35,b). TN 3429.

Stability. The center of gravity of an airship is or has to be identical with that of the buoyancy. In the example as in figure 21, the center is at 46% of the length. The stabilizing effect of the fins at the end of the hull corresponds to a moment arm $\ell_F/\ell = 0.47$. When shifting the axis of reference to the nose point, $dC_N/d\beta$ is just about zero. For practical purposes, this means that the airship would be stable if it would pitch about the axis through the nose point. Stability (33) improves, however, when reaching higher angles of attack, where the fins provide a “second” and non-linear normal-force component. Extrapolating corresponding to equation 14 the ΔC_N due to fins as in figure 21 (A) to $\beta = 90^\circ$, the following cross-flow values are obtained:

C_C	$= 0.13$	on lateral hull area (d ℓ)
	$= 1.0$	on hull diameter area (d 2)
	$= 2.3$	on exposed fin area
	$= 2.0$	on hull area covered by fins
	$= 1.1$	on fin plus covered area

The last definition yields a very reasonable value for the fin configuration considered.

5. CONTROL OF STREAMLINE BODIES

Any rocket-powered vehicle can be controlled by proper deflection of the jet exhausting from the base. All other streamline bodies have to be steered by means of flaps (rudders, elevators, ailerons) attached to their tail end.

Flap Theory, as presented in the “control” chapter is based upon the concept of two-dimensional circulation. In slender wing and/or body shapes, circulation is obtained through a different flow pattern, id est around the lateral edges. Therefore, an approach to the effectiveness of a trailing-edge flap is required, different from the two-dimensional type as in conventional control surfaces. In a small-aspect-ratio wing, downwash is “complete” and maximum, at and past the trailing edge. Deflection of a flap from that edge is the equivalent of placing a same-size flap behind the “wing” (at some small distance) within a field of flow having a downwash angle $\varepsilon = -\alpha$. The lift produced by the flap is thus expected to be

$$\Delta C_L = (S_f/S)(dC_L/d\alpha)_f \delta \quad (50)$$

where “f” indicates “flap”, and where the flap’s lift-curve slope corresponds to its aspect ratio b_f/c_f . If someone objects to this concept saying that a flap linked to the trailing edge of a body does not permit circulation to develop, it can be said that circulation does get around the *lateral* edges of the body (and of the flap).

Airplane Ski. There is very little information available regarding the effect of what we may call trailing-edge flaps used in combination with streamline or other slender bodies. The bent-up trailing edge of the airplane ski in figure 43, can be considered to be a flap, however. Interpretation is as follows:

a) The linear lift curve slope cannot very well be higher than indicated by equation 3. Based on plan-form area, the slope may thus be

$$dC_L/d\alpha = 0.2 (0.0274) = 0.0055$$

where 0.2 = aspect ratio.

b) On the basis of (a) the non-linear component is found to be in the order of

$$C_{N2} = 3.3 \sin^2 \alpha$$

c) Combining the moment derivative $dC_{m\ell}/dC_L = 0.0020$ with the lift curve slope as in (a), the neutral point is found to be $0.0020/0.0055 = 0.36$ of the length ℓ , ahead of the hinge axis.

The cross force coefficient as in (b) may seem to be very high. There is a number of similar values presented, however, in Chapter VII of “Fluid-Dynamic Drag”. It appears that low-aspect-ratio sharp-edge flat plates (and similar shapes) are very effective in producing the cross-flow type of lift. As mentioned before in this chapter, the coefficient should not be expected to be identical with the drag coefficient at $\alpha = 90^\circ$, which is $C_{D0} \approx 2$.

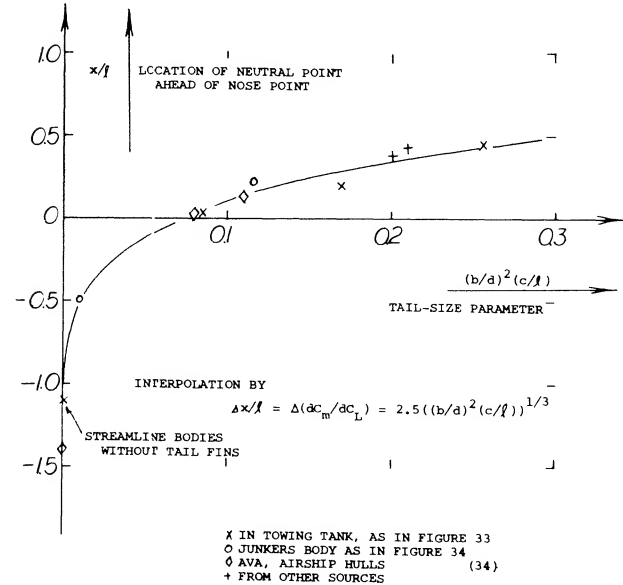


Figure 41. Statistical evaluation of the stabilizing effectiveness of fins attached to the end of streamline bodies.

Bent-Up Trailing Edge. For all practical purposes, bending up the trailing end of the ski, does not affect the non-linear lift component. The constant lift increment as seen in figure 42, can be expected to be the same as that due to a flap. Depending upon the flap’s aspect ratio b/c_f , its contribution to the lift of the ski will be

$$\Delta C_L = (c_f/\ell) (dC_L/d\alpha) \delta = (h/\ell) (dC_L/d\alpha) \quad (55)$$

where c_f = chord length of the flap, and $h = c_f \delta$ = height to which the trailing edge is bent up. The lift-curve slope of the flap can be approximated by

$$d\alpha/dC_L = 11 + 20/A_f$$

$$dC_L/d\alpha = 1/(11 + 20 c_f/b) \quad (56)$$

For the ski in figure 43, the equivalent flap chord is approximately $c_f = 0.5 b$, so that $dC_L/d\alpha = 0.048$. For $h/\ell = 0.062$, a $\Delta C_L = 0.062 (0.048) 180/\pi = 0.17$, is thus obtained, while the experimental differential is between 0.15 and 0.16.

(36) As explained in the first longitudinal chapter, the horizontal tail of an airplane is cut in two (so to speak) by the fuselage wake.

A *Radio-Controlled Bomb* is shown in figure 44. Deflection of the rudder produces differentials of lateral force and yaw moment, essentially independent of the angle of sideslip (plus/minus 20°) and the Mach number ($M \approx 0.2$ to 0.5). For practical purposes, the variations are also linear in β and δ , so that the derivatives tabulated in the illustration, give a full description of the aerodynamic characteristics.

Analysis is as follows:

a) The moment arm of the lateral force due to rudder deflection is $0.007/0.0015 = 0.47$ of the body length, aft of the CG. The center of force coincides with the geometric center of the flaps.

b) Assuming the effective aspect ratio of the rudder flaps (behind hinge line) to be $A_f = b_T/c_f = 5.3$, the lift curve slope may be $(dC_L/d\alpha)_f = 0.07$. Using equation 50 the effectiveness may then be

$$dC_{Y_0}/d\delta = (S_f/S_0)(dC_L/d\alpha)_f = \frac{0.22}{0.22(0.07)} = 0.015 \quad (57)$$

which is as tested.

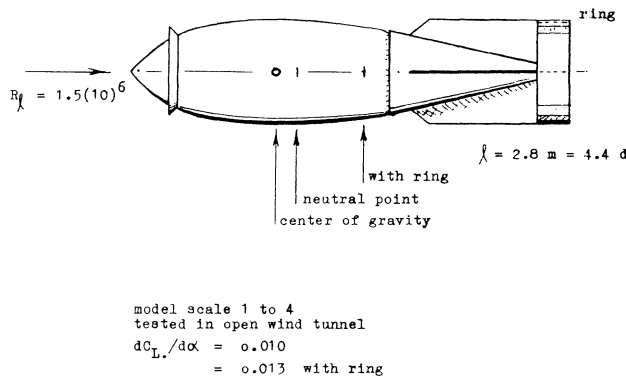


Figure 42. Static stability (position of neutral point) of 1000 kg bomb, tested in the Junkers wind tunnel (39,b).

There are certain assumptions in (b) which have not been confirmed yet by experiment or analysis. The advantage of equation 57 over the usual method of calculating effectiveness (as presented in the “control” chapter) is the fact that the tail contribution to $dC_Y/d\beta$ does not have to be known. The fins are considered to be part of the body.

(38) Lifting characteristics of rocket vehicles:

- Kelly, “Scout” with Flare, NASA TN D-794 & 945 (1961).
- Potter, Multiple Fins, J Aeron Sci 1955 p 511.

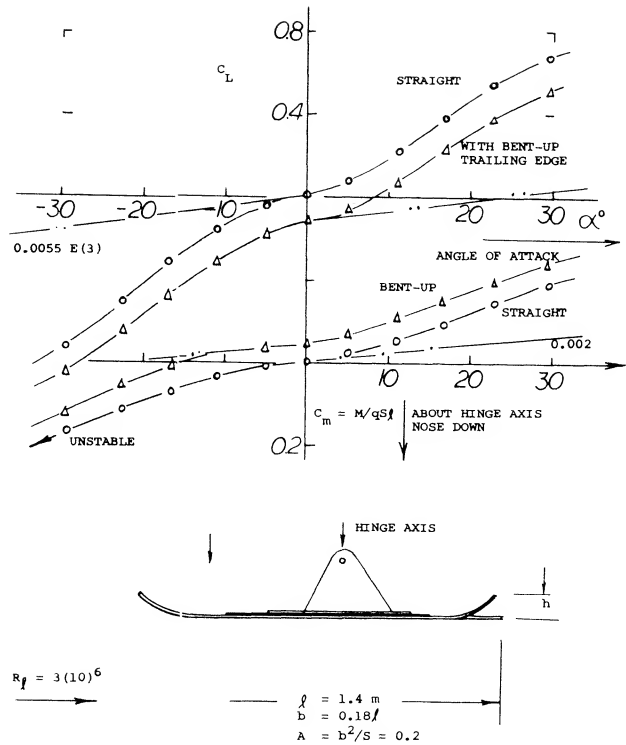


Figure 43. Longitudinal characteristics of the model of an airplane ski (34,b).

Airship Rudder. Directional characteristics of the experimental hull shape in figure 38 are discussed in the section dealing with “stability”. As far as the rudder is concerned, its deflection changes the yaw moment by a constant amount (independent of the angle of yaw); thus $\Delta(dC_Y/d\delta)$ and $\Delta(dC_Y/d\delta) \approx \text{constant}$. This means that the rudder changes the body’s basic circulation; regarding cross flow, the rudder area is too small to show an effect. As seen in part C of the illustration, force and moment increase in proportion to $\sin \delta$, up to some 20° deflection. The center of force, corresponding to $\Delta x/l = 0.003/0.006 = 0.50$, is as indicated in the drawing, somewhat ahead of the rudder, with the wedge-shaped tail end of the hull. Considering the body to be a low-aspect-ratio wing, the rudder is a “flap”. Deflection of this flap evidently increases the longitudinal circulation around the body. As in flapped control surfaces (such as a horizontal tail, for example) we have an effectiveness ratio based on the linear derivative $(dC_Y/d\beta)$:

$$(dC_Y/d\delta)/(dC_Y/d\beta) = d\beta/d\delta = 0.36$$

This looks like a very high value for the rudder area ratio $S_f/(d \cdot l) = 1.3\%$. However, it is shown in Chapter IX, that the effectiveness ratio increases as the aspect ratio is reduced. Considering the hull’s thickness ratio $d/l = 0.12$, to be the aspect ratio, the ratio of 0.36 can be understood.

“Akron”. Another example for this method of analysis, is the airship “Akron”:

$$\begin{aligned} \lambda &= 785 \text{ ft} && \text{length overall} \\ \nabla &= 7.4(10)^6 \text{ ft}^3 && \text{displacement volume} \\ d &= 130 \text{ ft} && \text{maximum diameter} \\ S_H &= 7400 \text{ ft}^2 && \text{exposed horizontal fins} \\ S_F &= 1100 \text{ ft}^2 && \text{elevator, aft of hinge line} \\ b_H &= 1.09 d && \text{span of fins} \end{aligned}$$

The lift derivatives (based on d^2) as tested on a 1/40 scale model (TR 432) are:

$$dC_{L_d}/d\alpha = 0.026 \text{ due to angle of attack}$$

$$dC_{L_d}/d\delta = 0.006 \text{ due to elevator deflection}$$

For the flap-area ratio $S_F/d^2 = 1100/130^2 = 6.5\%$, for $b_H/c_F = 10$, and a lift-curve slope $(dC_L/d\alpha)_F = 0.085$, equation 50 yields a $dC_{L_d}/d\sigma = 0.065 (0.085) = 0.0055$, which is close to that which was tested around zero angle of attack.

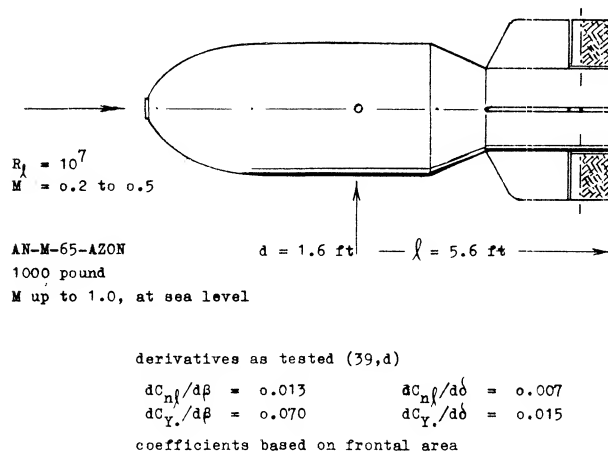


Figure 44. Directional characteristics of a radio-controlled bomb, tested (39,d) full scale in a wind tunnel.

(39) Fin-stabilized “flying” bodies:

- Junkers, Fin-Stabilized Tank, Dct D-6548 (1940).
- Junkers, Bombs, Dcts D-6549 & 6573 (1940).
- Kempf, In Towing Tank, NACA TM 1227.
- Pearson, 1000 Pound Bomb, NACA W’Rpt L-131 (1944).

(43) Control of reentry-type vehicles:

- Paulson, Cruciform Delat, NACA W’Rpt L-734.
- Paulson, Trailing Edge Control, NASA Memo 4-11-59L.

- (44) Comparison between equations (2) and (21) indicates that in a spheroid (or ellipsoide) the positive force in the forebody and the negative force in the afterbody, each has a moment arm equal to 1/3 of the body length.

Turning. It is described in the section dealing with “stability”, that airships are not really stable. The plot of $C_m(C_L)$ as in figure 38, shows that balance and stability of the airship (with control surfaces kept neutral) both in pitch and in yaw, is obtained at C_{L_b} or $C_{Y_b} = 0.18$, where α or $\beta = 26^\circ$. Conditions of an airship hull when turning are different, however, as explained in context with figure 28. For a difference in the angle of wind against body axis, between the center of buoyancy and the stern, say of 15° , the force in stern and fins may be doubled. This means a tremendous “resistance” against turning.

CHAPTER XX

LIFT OF AIRPLANE CONFIGURATIONS

The lift of a complete airplane is determined by the characteristics of all its components and their mutual interactions as discussed throughout the previous chapters of this book. The total lift of the complete airplane determines its performance, especially with regard to takeoff, landing, maneuver, climb, stability and safety. This lift characteristic effects the capability of the airplane with regard to maximum gross weight and range and is determined by the configuration, the flaps and gear position. Since we are interested in the overall performance, the complete airplane is considered in this chapter. The methods and equations needed for determining the performance characteristics of the airplane are given in Chapter I as these concepts are used throughout the book. While we are interested in the complete airplane system we will not attempt to present detailed procedures for establishing the total design. The complete aircraft can only be designed by considering all the factors discussed in the preceding chapters as well as drag as presented in the book "Fluid Dynamic Drag" (1,a) and the type of data given in (1,b). Of course, the propulsion system and mission are also important considerations in the design of the complete airplane.

1. CONFIGURATION TYPES

To arrive at the best airplane configuration to satisfy a given requirement there are hundreds of possibilities to be considered. Of these, the actual configurations that have been used and considered are numerous and varied. These include aircraft with various wing arrangements including single wings, biplanes, triplanes (2,a), swept wing, delta wings, full flying wings, swing wings and no wings at all. The type of wing, fuselage and empennage configuration that is best depends on many factors such as the powerplant, mission speed and payload. As a result it appears that to meet certain requirements the configuration selected by various designers are remarkably similar. For this reason a few typical airplane configurations with examples, as given on Table 1, are presented. The characteristics of any specific airplane can usually be found in (2,b,c).

* Maximum height of airplane with nose gear depressed, all tires and nose strut properly inflated, and optional flashing beacon installed.

** Maximum wing span if optional conical camber wing tips and optional strobe lights are installed. If standard wing tips without strobe lights are installed, wing span is 32'-8 1/2".

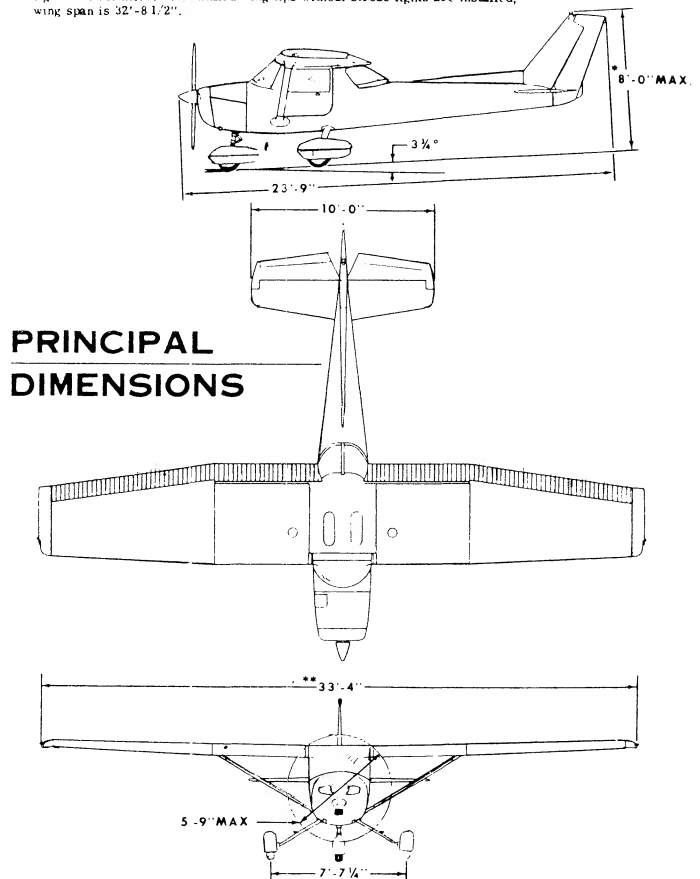


Figure 1. Typical high wing general aviation aircraft-Cessna 150.

- (1) Complete aircraft design:
 - a) Hoerner, Fluid Dynamic Drag.
 - b) Wood, Aerospace Vehicle Design, Vol. 1.
- (2) Airplane configurations:
 - a) Triplanes. As reported in "Heroes and Aeroplanes" (Grosset, New York 1966) a famous triplane was the 'Sopwith' flown in WWI (1917) using a 120 HP rotary engine. There was also a Fokker triplane, with a maximum speed of 100 mph and the Curtiss Model S-3 "Wasp" with a speed of 160 mph (1919).
 - b) Janes All World Aircraft, published yearly.
 - c) Mil A/C Specification Sheets.

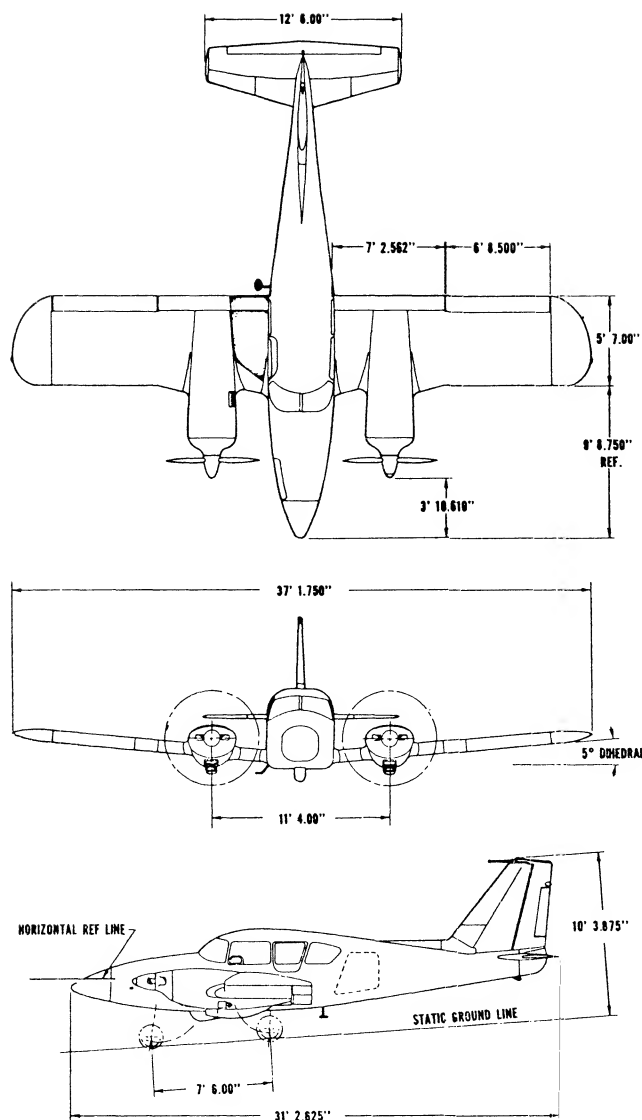


Figure 2. Low wing twin engine light airplane-Piper.

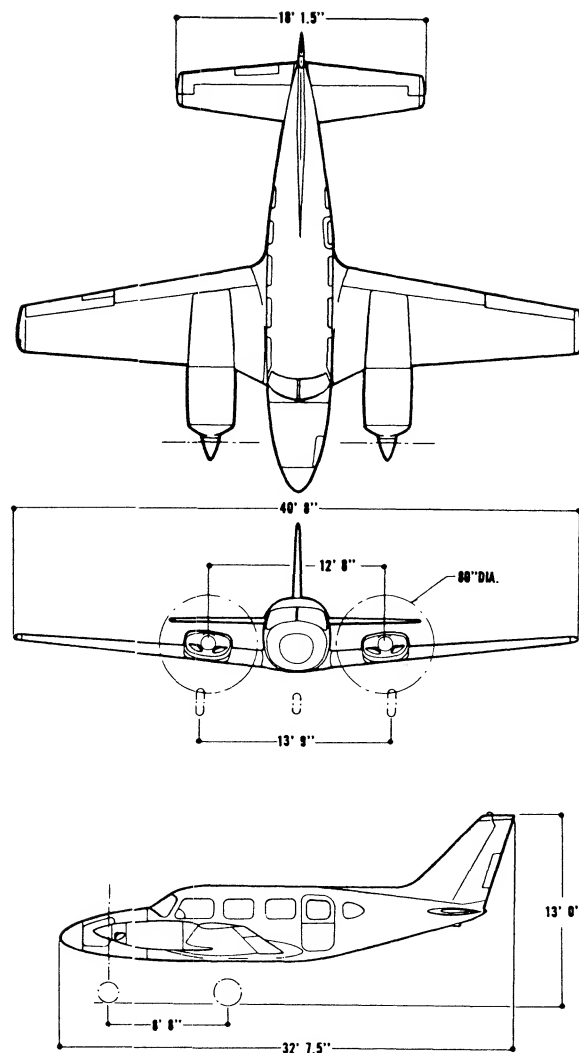


Figure 3. Twin engine low wing airplane-Piper Navajo.

General Aviation Aircraft. The characteristics of typical general aviation aircraft types are listed in Table 1, (2,b). These are generally fairly simple one or two engine aircraft with a single forward wing attached to a central fuselage with stability provided with a horizontal and vertical tail, as illustrated on figures 1 to 4. Both high and low wing configurations are found. In most cases, tractor propellers are used to provide thrust for overcoming drag, although both underwing and aft jet engines are also used. General aviation aircraft are generally designed for speeds under 300 MPH with stalling speeds under 70 MPH for single engine airplanes of 6000 pounds or less. Also considered under the general aviation heading are business jets which have nearly the speed capability of transport aircraft.

- (3) Aircraft design considerations:
 - a) Swihart, Jet Transport Design, AIAA Selected Reprints VIII.
 - b) Olason, Performance of 747 Airplanes, JofA/C, Vol. 6 No. 6 '69
 - c) Olason, Aerodynamic Design Boeing 737, JofA/C, Nov., Dec. 1966.
- (4) Special aircraft:
 - a) Strong, Sky Surfing with Low-speed Wings, Scientific American, Dec. 1974. See also, Fink, Sailing of A = 5.9 NASA TN D-5047.
 - b) Motorless Flight Research, NASA CR-2315, 1973.
 - c) Mitovich, "Man-Powered Flight: Achievements to Date" J A/C Vol. 7, No*3.
 - d) Gilbert, "Grunts, Groans & Gossamer Wings", Air Progress, Apr. 1973.

TABLE 1

A/C TYPE	EXAMPLE	NO. ENGINES	G.W.	W.E.	b FT.	A	S	Δ_c	MAX HP or T PER ENG.	V _S KTS	V _{CRUISE} KTS	V _{MAX} KTS	FIGURE NO.
GENERAL AVIATION													
LIGHT SINGLE ENGINE	CESSNA 150	1	1,600	990	33.5	7	160	0	100'	34	106	109	1
TWIN ENGINE	PIPER AZTEC	2	5,200	3,042	37.2	6.7	206	0	250	61*	66	181	2
MEDIUM TWIN ENGINE	PIPER NAVAJO	2	6,500	3,900	40'8"	7.3	229	0	310	63*	70	218	3
JET TWIN ENGINE	CESSNA	2	11,650	6,454	43.9	7.4	260		2200		347	347	4
TRANSPORT													
LIGHT	DOUGLAS DC-9-40	2	114,000	55,500	93.4				14,500	124	490		5
MEDIUM	BOEING 727-200	3	191,000	96,600	108	7.2	1560		14,500	129	449	521	6
HEAVY	LOCKHEED L-1011	3	426,000	234,300	155				42,000	139	498	538	7
	BOEING 747	4	710,000	355,700	195.7	6.96	5500		47,000	140	503	556	8
MILITARY													
FIGHTER - F16	GD - F16	1	21,500	13,800	31.8	3.6	280					M=2+	9
BOMBER	BOEING B-52H	8	488,000		185	8.6	4000	35°	17,000			577 @ 20,000'	10
CARGO	LOCKHEED C-130	4	155,000	70,140	132.6	10	1745	0	4591		296	336	11
	LOCKHEED C-5A	4	728,000	327,000	222.8	8.	6200	25°			460-480		12
SAILPLANE	CALIFORNIA a14	0	954	617	66.9	25.	173		0	34			13

' = HP

* FLAPS & GEAR DOWN

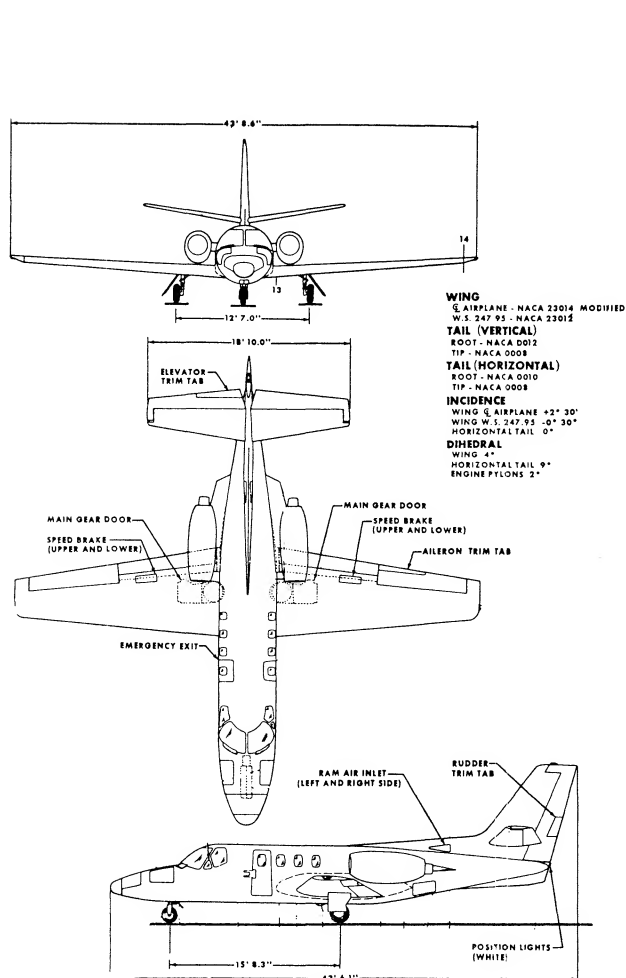


Figure 4. Twin jet airplane for general aviation-Cessna.

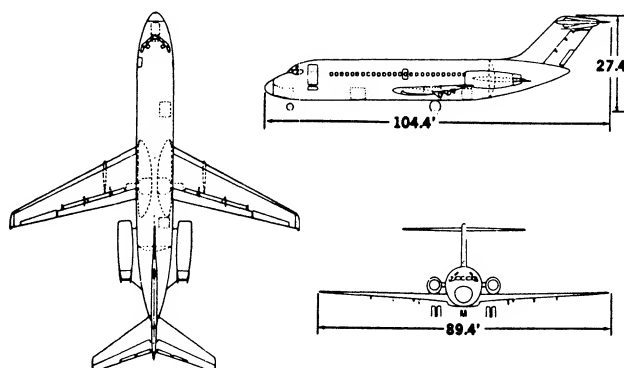


Figure 5. Twin engine transport aircraft-DC-9.

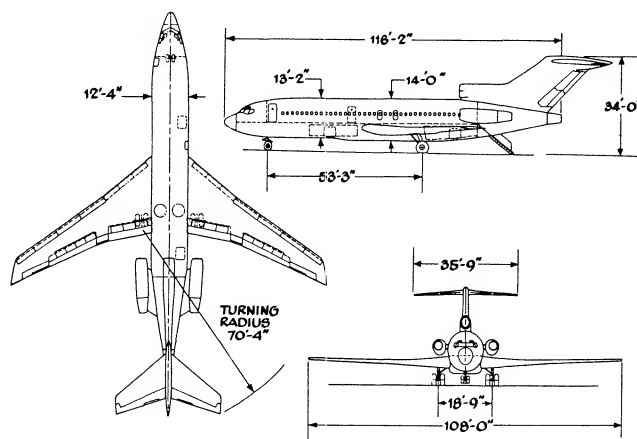
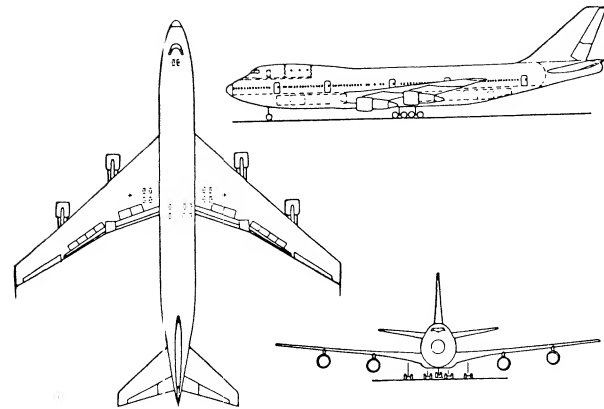


Figure 6. Three engine transport airplane-BAC 727.

Transport Aircraft. Nearly all commercial transport aircraft use turbine engines and most of these use jet engines with various ratios of engine to bypass air. It is convenient to classify the aircraft in terms of low, median and long range types with typical characteristics as given on Table 1. The short range transport types may use propellers; however, increasing numbers of aircraft are now powered with turbo fan engines. Almost all the median and long range transport aircraft have a large single swept wing forward and a normal type empennage for stability and control. The jet engines are generally placed below the wing or aft on the fuselage. Some examples of transport aircraft are given on figures 5 to 8.

The details of the philosophy used in the design of transport aircraft are given in (3,a,b,c). Here, reasons are given for the selection of the engine location, horizontal tail position, high lift devices and other factors that make up a successful transport type aircraft. The selection, design and evaluation of the wing and its flap systems for aircraft in this class are covered in Chapters XV and XVI as well as throughout this book.



PRINCIPAL DIMENSIONS

WING		AILERON	
AREA	5500 Sq.Ft.	AILERON AREA (INBD)	71.8 Sq.Ft.
SPAN	195 Ft. 8 In.	(OUTBD)	153.4 Sq.Ft.
BASIC ROOT CHORD	449.68 In.	HORIZONTAL TAIL	
TIP CHORD	160.00 In.	AREA	1470 Sq.Ft.
TAPER RATIO	.356 (Basic)	SWEEPBACK c/4	37.5°
DIHEDRAL	.245 (Ref)	SPAN	72 Ft. 9 In.
SWEEPBACK c/4	37.5°	VERTICAL TAIL	
ASPECT RATIO (REF)	6.96	AREA	830 Sq.Ft.
FLAP		SWEEPBACK c/4	45°
LEADING EDGE AREA		SPAN (HEIGHT)	32 Ft. 3 In.
(RETRACTED)	448 Sq.Ft.	BODY	
TRAILING EDGE AREA		LENGTH	228 Ft. 6 In.
(RETRACTED)	847 Sq.Ft.		

Figure 8. Heavy four engine transport-BAC 747.

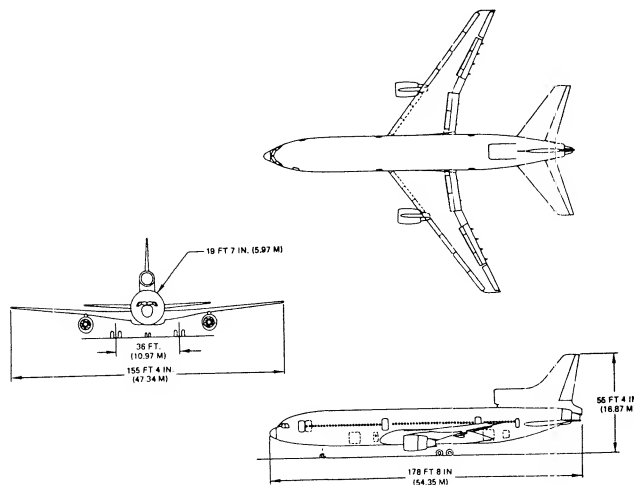


Figure 7. Three engine air bus type-LAC 1011.

Military Aircraft. Examples of the characteristics of various types of military aircraft are also given on Table 1. These aircraft range in size and type with their performance capability being established by the requirements of specific missions, figures 9 to 12. These aircraft are designed for such missions as training, low level attack, reconnaissance, interception, bombing and cargo.

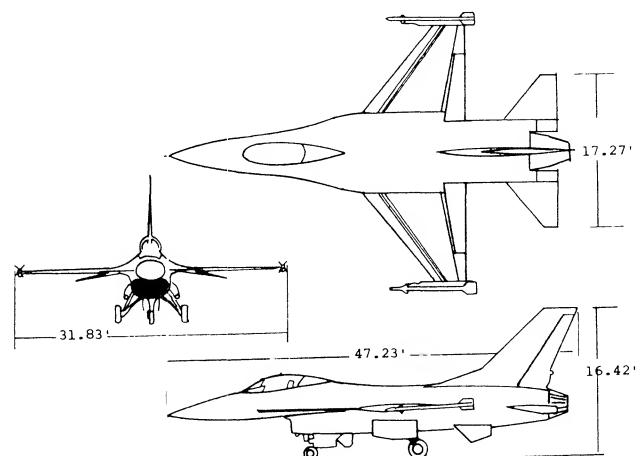


Figure 9. General arrangement and dimensions-F-16.

Lift and its characteristics are of primary importance in the design of military aircraft. For instance, the maximum lifting characteristic is of primary concern in flight because of the need for high maneuverability. The need for high lift is thus of primary importance in the design of attack interceptor type aircraft. In the case of bomber and military transport type the requirement for high lift is similar to that of conventional aircraft, as discussed in Chapters I, VII and VIII.

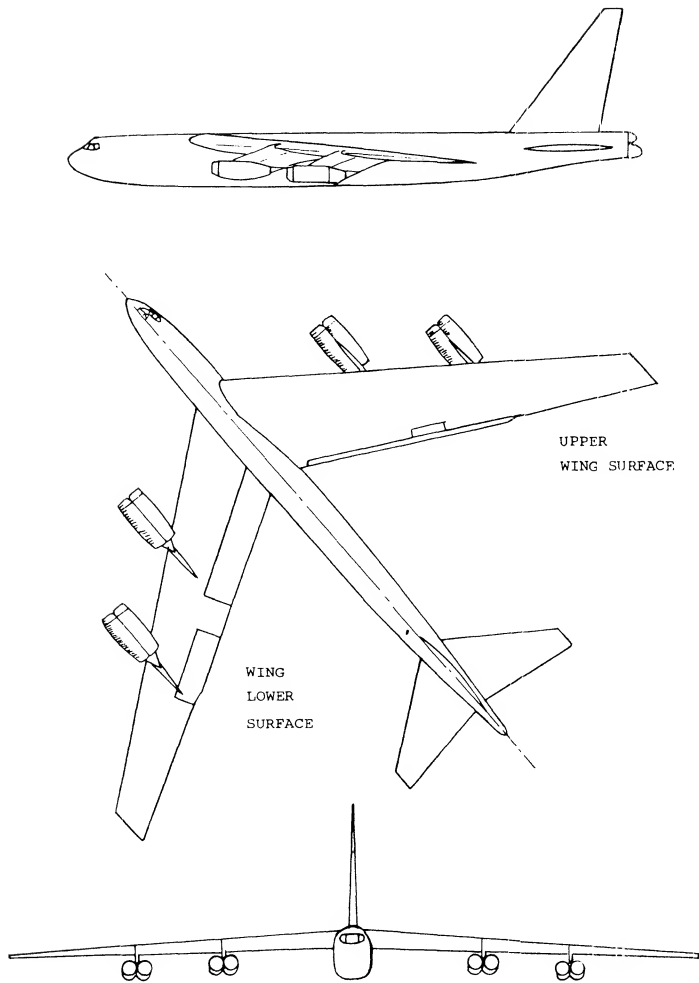


Figure 10. Heavy bomber-B-52.

Special Aircraft. There are many other aircraft types to be considered and these can lead to some very unusual types of configurations. Such aircraft can range from configurations designed to operate at extremely high altitude to vehicles designed to operate only in ground effect. These special aircraft include: gliders for sport, sky surfing (4,a), high performance sailplanes with lift drag ratio as high as 45, (4,b). Also, man powered airplanes may be considered (4,b,c).

- (5) Variable geometry aircraft:
- Baals & Polhamus, Variable Sweep Aircraft, A & A Engr., June 1963.
 - Jones, R.T., New Shape for SST, A&A Engr. Dec. 1972.

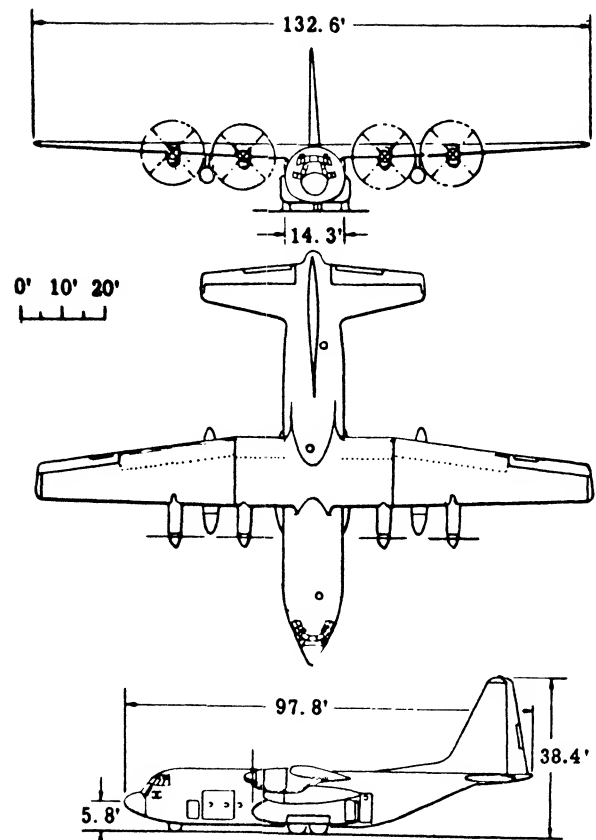
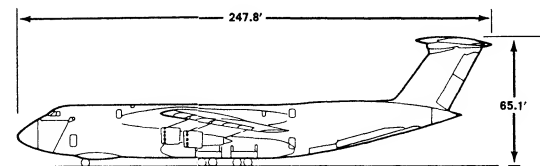


Figure 11. Median weight turbo prop cargo plane-C-130.



General Arrangement

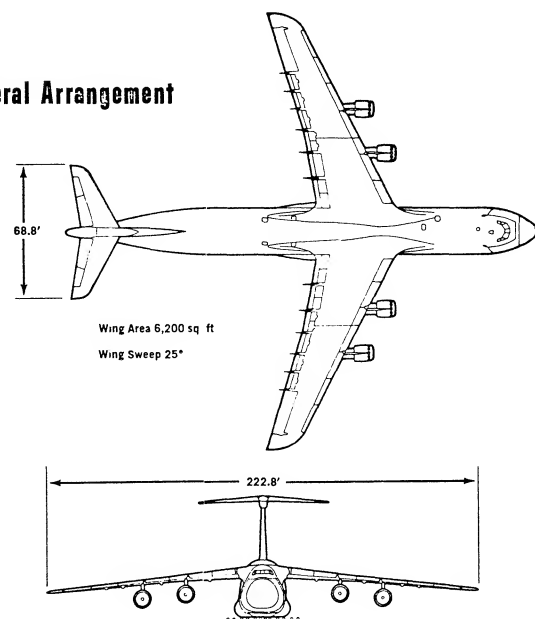


Figure 12. Heavy cargo airplane-C-5A.

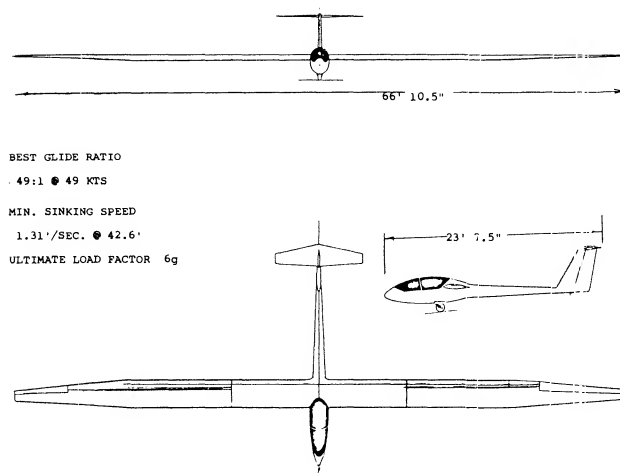


Figure 13. Sail plane - California a-14, general arrangement.

Sailplane Design. The design of high performance sailplanes such as are illustrated in figure 13 requires extreme attention to detail to achieve lift drag ratios in the 40 range with corresponding low rates of sink, since for a glider

$$\tan \delta = D/L \quad (1)$$

Where δ is the gliding angle and must be kept as low as possible for good performance. The drag is, of course, equal to the total profile and induced value. High performance sailplanes now use very high aspect ratio wings with airfoils designed especially for low drag and high lift coefficients (4,b). The frontal area is reduced to an absolute minimum by having the pilot in nearly a prone position. With these design features and attention to design details as discussed in (1,a), very high lift drag ratios are obtained.

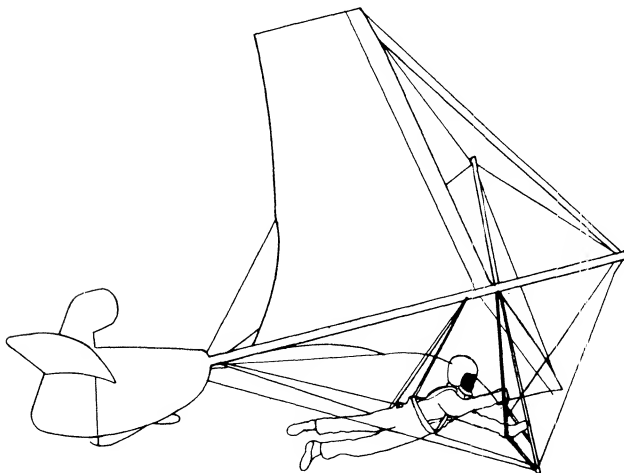


Figure 14. Hang type glider.

Hang Gliders. There is a growing sport in the use of hang type gliders such as are illustrated on figure 14. Although hang type gliders date back to the beginning of aviation, the development of the light weight Rogallo delta type wing, as discussed in Chapter XVIII, and similar wings (4,a) covered with sail cloth has made possible a new and exciting sport. In the design of hang gliders the lift drag ratio is on the order of 5 with the low aspect ratio delta wing, and up to approximately 10 with the more advanced configurations using sail type wings. The importance of aspect ratio in reducing the induced drag is well illustrated here.

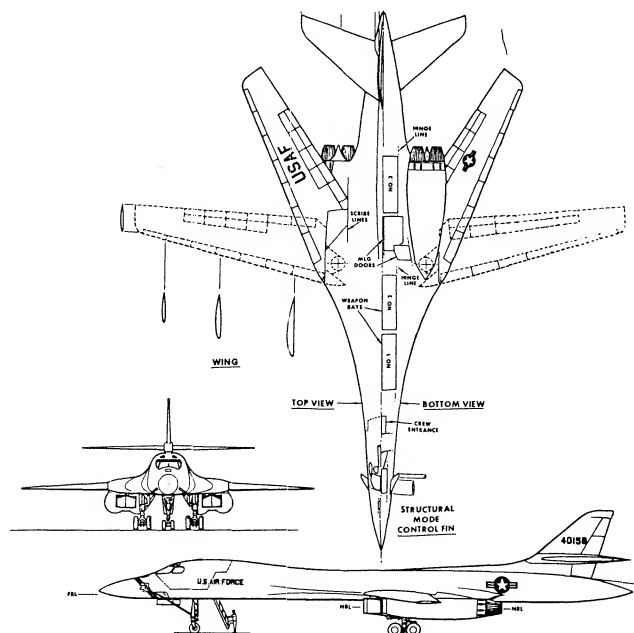


Figure 15. Swing wing bomber airplane-B-1.

Variable Geometry Configurations. Most of the airplane types listed in Table 1 have at least trailing edge flaps and may thus be considered to be variable geometry type aircraft. Some of the vehicles listed have extensive systems of flaps and slats, so much so that it often appears that the wing is coming apart especially during landing. Because of extensive demands for lift and drag, especially between the high speed and landing conditions, even greater differences in the aircraft configuration are required. As a result, aircraft have been designed with wings that pivot in such a way that we effectively have a variable sweep wing. An example of such an aircraft is given in figure 15 and the theory and reasons for such configurations are given in (5,a). A further unusual variable geometry concept is given in figure 16. Here the entire wing swings. This concept is discussed in (5,b) and offers some solid advantages in overall performance.

2. VARIOUS WING ARRANGEMENTS

In the case of most single wing aircraft, the lift and performance are determined by analyzing the wing operating in the flow field as generated by the fuselage, and the tail operating in the wake of the fuselage and wing. A pair (or any number) of wings can be arranged so that they interfere or combine with each other. Configurations of this kind, such as biplane or tandem wings in particular, and related characteristics are considered as follows.

Tip-to-tip Coupled. When putting together two airplanes in flight, joining them by means of some mechanism at their wing tips, it can be speculated that their effective aspect ratio might be doubled and their range be increased, possibly to the $\sqrt{2}$ -fold. Actually, to keep each of these airplanes balanced without straining the coupling it will be necessary to deflect the ailerons, thus reducing the lift distribution approximately to that as when flying alone. Only when joining three airplanes together, as in figure 17, might the one in the middle really benefit. Considering what is said and presented quantitatively in Chapter VII of "Fluid Dynamic Drag" about flying in swept formation (as migratory birds do), it might be better to do just that, thus eliminating physical contact. The lateral stability problems described in (6) would then also be avoided. Of course, to transfer fuel two or more airplanes have to make physical contact somehow, but not for any long duration of time.

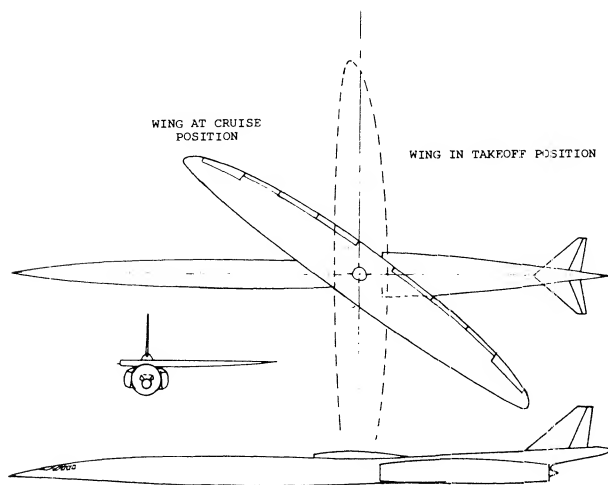


Figure 16. Oblique-winged configuration of a supersonic transport airplane.

- (6) Bennett, Tip-to-Tip coupled wings:
- a) Bomber with Two Fighters, NACA RM L1951A12.
 - b) With Floating Fuel Tanks, NACA RM L1951E17.

DYNAMIC (FORMATION-FLYING) MODEL
OF A POSSIBLE TIP-TO-TIP COMBINATION
OF A BOMBER WITH A PAIR OF FIGHTER
AIRPLANES.

$$\begin{aligned}b_0 &= 1.1 \text{ m} \\b_3 &= 1.7 \text{ m} \\A_0 &= 5.1 \\A_3 &= 9.4\end{aligned}$$

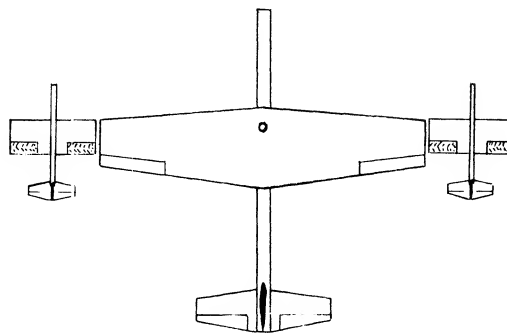


Figure 17. Arrangement of a bomber and two fighters coupled to each other.

Biplane. In the early years of aviation, hundreds of biplane-type airplanes were designed and built and they reached the peak of their development as fighter airplanes, particularly in England, between 1915 and 1925. Their aerodynamic characteristics were studied as a function of gap or height ratio, span ratio, stagger and so-called decalage (difference in angular setting as against each other). The optimum biplane (providing maximum L/D) has equal-size pannels. Many biplanes were developed, however, with a larger upper and a smaller lower wing (7,g). Theory indicates that in such configurations, aerodynamic efficiency is highest when the geometric aspect ratio of the upper wing is smaller and that of the lower wing is larger than the average. Since biplanes are hardly built any longer, except as sport or special purpose types, we will limit our presentation to that of the simple identical-panel type.

- (7) Theory and results of biplanes (multiplanes):
- a) Prandtl, NACA T'Rpt 116, also Erg AVA Go III.
 - b) Munk, Bi- & Triplanes, NACA T'Rpts 151 and 256.
 - c) Knight, At High Angles of Attack, NACA T'Rpt 317 (1929), also TN 310, 325, 330 (1929).
 - d) Diehl, Engineering Aerodynamics, 1928 and 1936.
 - e) Griffith, Triplanes, ARC RM 250 (1916); many results as a function of height and stagger.
 - f) Noyes, Various Configurations, NACA T'Rpt 417.
 - g) Pressure distribution on one upper and $\frac{1}{2}$ lower wing panel is reported in NACA T'Rpt 271 (1927).
 - h) Diehl, Relative Loading, NACA T'Rpt 458 (1933).
 - i) NACA, Load Distribution, Rpts 445 & 501 (1932/34).

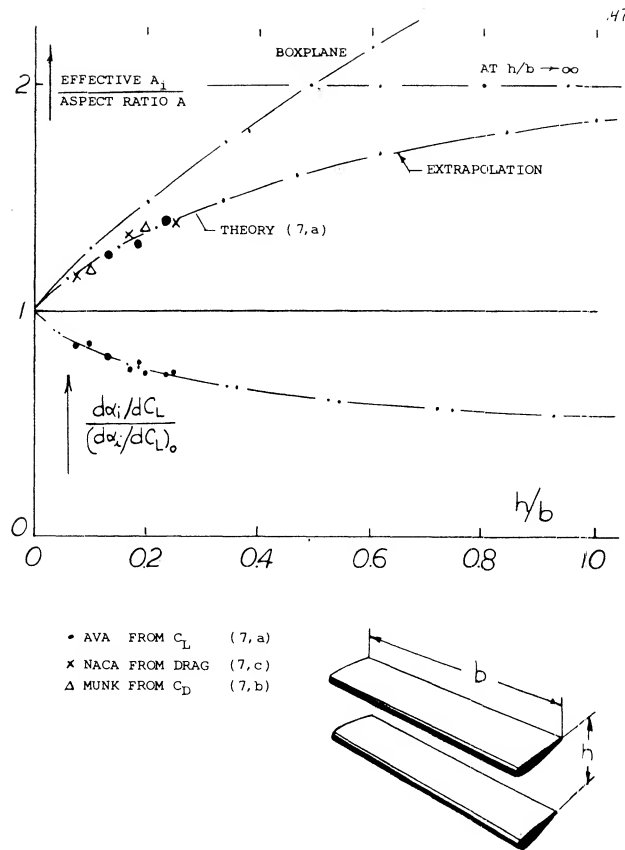


Figure 18. Effective aspect ratio of simple biplane configurations (7).

Effective Aspect Ratio. The average induced lift angle of a monoplane wing is a function of the deflected volume of air and that volume corresponds to a cylinder of air having a diameter equal to the span 'b' of the wing. Two identical wings far enough apart from each other have together two such cylinders, twice the volume and twice the lift, for a certain angle of attack but at the same induced angle of attack. Bringing the two wings together, in the form of a biplane, we may roughly assume that the cross section of the cylinder of air affected is that of two half circles with a diameter equal to 'b', plus twice the area between the two panels equal to $2(hb)$, where h = height or gap. We thus obtain tentatively

$$A_i/A = 1 + (8/\pi) (h/b) \quad (2)$$

where $A = b^2/S$, and S = combined area of the two panels. Note that the value $h/b = 0$ represents a monoplane wing with twice the chord of the panels assumed. A more accurate analysis and experimental results are plotted in figure 18. The function can be approximated by

$$A_i/A = (1 + 3.6(h/b))/(1 + 1.4(h/b)) \quad (3)$$

A "boxplane" (having a pair of end plates connecting upper and lower lateral edges) has even higher ratios. Note that the upper limit (for $h/b \dots \infty$) is $A_i/A = 2$ for the biplane, while for the "boxplane" $A_i/A \dots \infty$.

Lift Distribution. In part (a) of figure 19 a pair of lifting lines is shown representing a biplane. At the location of the lower vortex, the upper one induces a component of velocity against the oncoming flow. Vice versa there is such a component in the direction of the flow at the upper vortex. The average dynamic pressure is changed, accordingly. As a consequence, the lower wing of a biplane tends to exhibit somewhat less and the upper wing somewhat more lift, provided that both are set to the same angle of attack. Evidence for the difference is found in (7,b) where the combination of two panels each with $A = 6$ is tested at a gap ratio $h/b = 0.1$. The drag due to lift in the upper panel is found to be almost 20% higher, and that of the lower panel 20% lower than the average. For a certain lift coefficient, the loading can be made uniform by giving the lower wing a somewhat higher angle of attack (negative decalage). Another method is to give the lower panel a somewhat larger aspect ratio in a manner similar to that mentioned above. There are other considerations involved, however, in the design of biplanes, such as stalling for example.

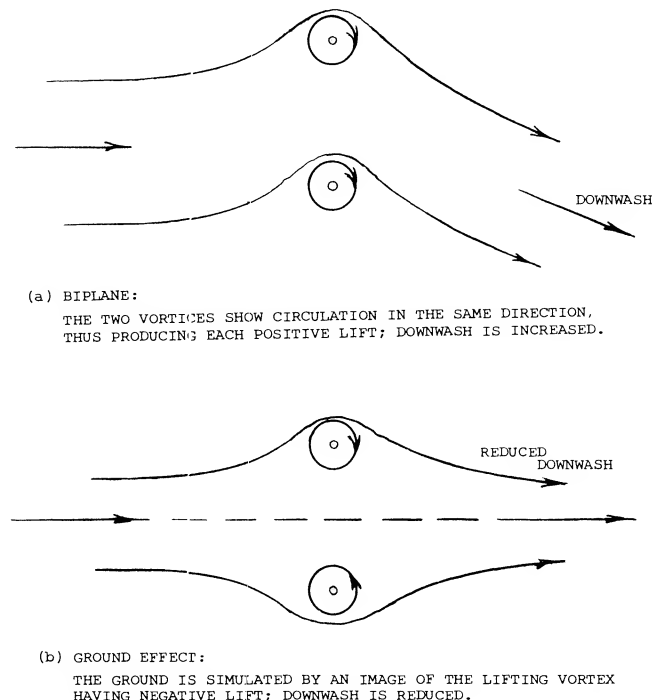


Figure 19. Representation of a biplane and of a wing near the ground, each by a pair of lifting lines.

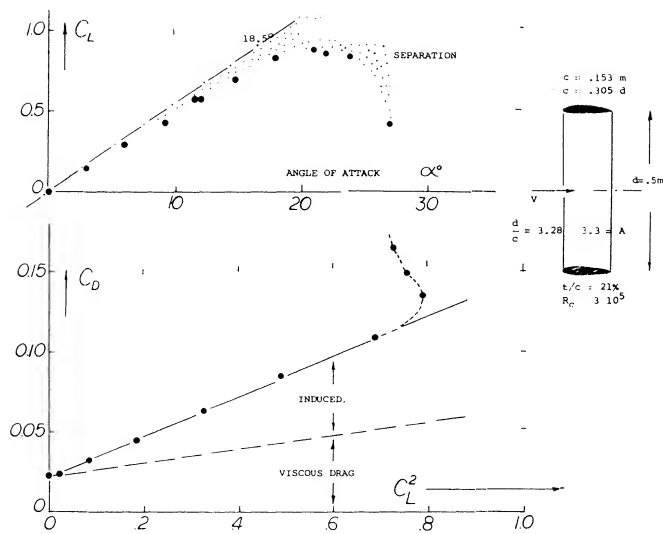


Figure 20. Lift characteristics of a ring-shaped airfoil (8,e).

Multiplanes. On the basis of constant span the induced efficiency increases not only as the height 'h' is increased, but also as the number of panels placed within that height is increased. Theoretically, the effective aspect ratio thus increases to that of the "boxplane" as in figure 18. The practical incentive for building biplanes or multiplanes is or was structural, compactness and maneuverability (rolling). A number of triplanes have actually been built and flown (2,a) over 50 years ago. Aerodynamic characteristics are reported in (7,e).

- (8) Characteristics of ring-shaped foils:
- Analysis by Ribner, J Aeron Sci 1947 p 529.
 - Muttray, Experiments, ZWB FB 824/3 (1941).
 - See also in the "small aspect ratio" chapter.
 - Dickmann, Axial Theory, Ing Arch 1940 p 36; see Brooklyn Poly Dpt. Aero Engg PIBAL Rpt 353 (1956).
 - Fletcher, 5 Annular Foils, NACA TN 4117 (1951).
 - Milla, Lift and Drag Characteristics Biannular Wing Aircraft, JofA/C, Nov., Dec. 1966.
 - Carmichael, Finite Element Methods for Wing Body Combination, NASA SP-228, 1969.
- (9) Influence of ground on wings, theoretical:
- Wieselsberger, AVA Gottingen Ergeb II (1923).
 - Datwyler, Wings Close to Ground, Mitteilung Aerody Inst., TH Zurich 1934; see ZFM 1933 p 442.
 - Analysis by Meyer, Hydrofoil Rpts 1950/51; and by Wu, Caltech Hydromechanics Rpt 26-8 (1953).

Ring Foil. A ring-shaped "wing" such as in figure 20 is somewhat similar to a biplane. Analysis (8,a) concludes that the effective wing area of a ring is

$$S' = 0.5 \pi d c \approx 1.6 d c \quad (4)$$

where $(0.5 \pi d)$ = half of the circumference. The equivalent stream of fluid deflected by such a wing is twice the cylinder defined by the diameter 'd' = $\pi d/2$. According to this theory, the induced angle of attack is less than half of that of a plane wing having the same span and developing the same lift. The effective aspect ratio is

$$A_i = 2 d^2 / S' = 4 d / (\pi c) \quad (5)$$

The induced angle is

$$d\alpha / dC_L = 1 / (\pi A_i) = 0.25 c / d \quad (6)$$

where C_L is based upon the area S' as in equation (4). The lift angle is

$$d\alpha / dC_L = (0.5 / \pi \bar{a}) + (1 / \pi A_i) \quad (7)$$

The experimental results in figure 20 confirm this function when using the efficiency factor of the foil section $\bar{a} = 0.8$. It must be noted, however, that the coefficients as plotted are based upon the area $2(d/c)$. Ring-shaped surfaces are sometimes used as stabilizing tails for bombs and similar devices. Ring foils are also discussed in the chapter on "small aspect ratios". Accurate theoretical methods have been developed (8,g) for calculating the lifting characteristics. This method is based on the finite element method and given good correlation with experiment.

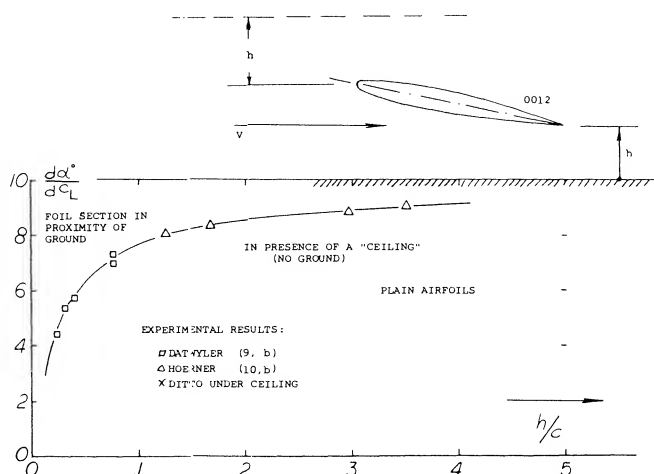


Figure 21. Influence of the ground on the lift angle of airfoil sections in two dimensional flow.

GROUND EFFECT. As far as the lift of an airplane wing is concerned, there are two effects through which the ground (of an airfield) affects the angle of attack necessary to produce a certain lift coefficient: the circulation of the airfoil section in two-dimensional flow is changed, and downwash and induced angle of attack are reduced. In case of the first effect, the height of the trailing edge above the ground is the parameter to be considered. Theory (9,b) predicts that roughly below $C_L = 1.5$ lift will be increased in proximity of the ground, while above that coefficient with wing flaps deflected, for example, there will be a *reduction* of the sectional lift. Figure 21 presents results obtained in the range of lift coefficients (up to $C_L = 1$, where $C_L(\alpha)$ is still linear). The lift angle $d\alpha/dC_L$ reduces considerably when approaching the ground, below $h/c = 0.1$. It must be realized, however, that there has to be a limit to the function plotted imposed by the fact that the trailing edge of the wing eventually touches the ground. When this happens, the pressure on the lower side is equal to the dynamic pressure (9,b) so that theoretically $C_L \approx 1$, at $\alpha \rightarrow 0$.

Induced Effect. Wings of conventional airplanes may never get close enough to the ground where the sectional effect as described above would become noticeable. For practical purposes, only the influence upon the induced angle of attack will then be left. The lifting-line equivalent to this ground effect is shown in part (b) of figure 19. While in a biplane the two vortices turn in the same direction, the ground is replaced by a mirror image of the lifting vortex. The plane of symmetry is characterized by the fact that no transport of air takes place across, as in the case of a solid plate. The influence of the ground upon the induced angle of attack (and drag) is presented in figure 22 in the form of the ratio

$$A/A_i = (d\alpha_i/dC_L)_h / (d\alpha/dC_L)_\infty \quad (8)$$

where h = height over ground measured to the wing's quarter chord axis, and where ' ∞ ' indicates conditions at $h = \infty$. Note that the tangent near $h/b = 0$ in part (a) of figure 22 indicated by $d(A/A_i)$ is twice that in figure 18 indicated by $d(A/A_i)$. The two derivatives would be alike if defining for the ground effect 'h' as the distance between the two lifting lines as in figure 19. The function as in figure 22 might be interpolated by

$$A/A_i = (33(h/b)^{3/2}) / (33(h/b)^{3/2} + 1) \quad (9)$$

For conventional airplanes, when near the ground (taking off or landing), the height ratio can be between $h/b = 0.1$ and 0.2 , (10,h) Figure 22 shows that at $b/h = 10$ the induced angle of attack is reduced to half. As to the spread of the experimental results in figure 23 (end plates), it can be said that on the average the more favorable points reflect the induced lift angle, while the less favorable ones indicate the drag due to lift. In this drag, there is usually a parasitic component involved due to interference on top of the viscous component of the airfoil section $\Delta C_D \approx C_{\min} C_L^2$, which was always subtracted when evaluating experimental results.

The reduction of the induced angle due to the ground may affect longitudinal stability and control of the airplane during the landing maneuver. In airplanes landing tail-down, the ground must also be expected to affect the horizontal tail surface directly. The ground effect will resist the effectiveness of the elevator in getting the tail down. The drag due to lift may not be of particular concern during landing. It is interesting, however, to speculate upon the reduction of drag to be expected when flying as close as possible to the surface. At an assumed $h/b = 0.25$ or $b/h = 4$ the reduction of the induced drag is some 20% and that of the total drag (when flying at maximum L/D) is possibly 10%.

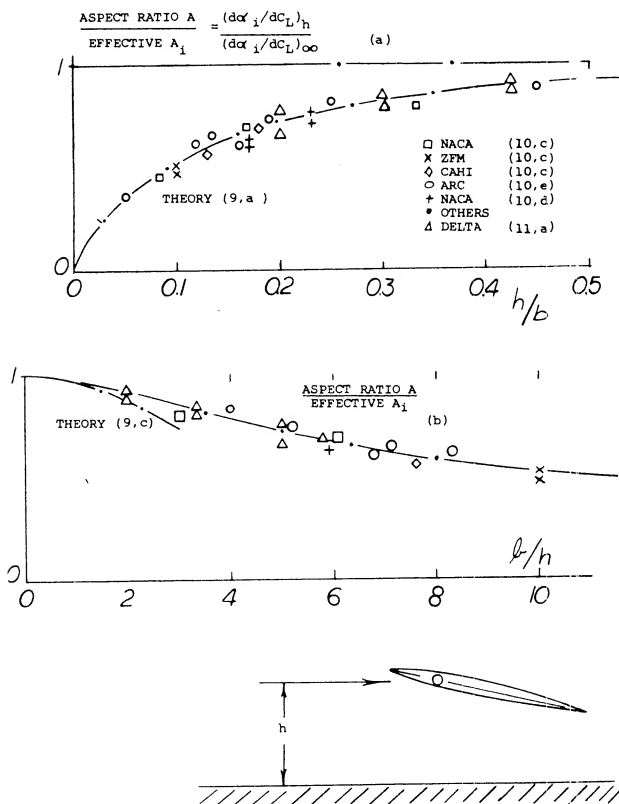


Figure 22. Induced angle of attack of wings operating near the ground.

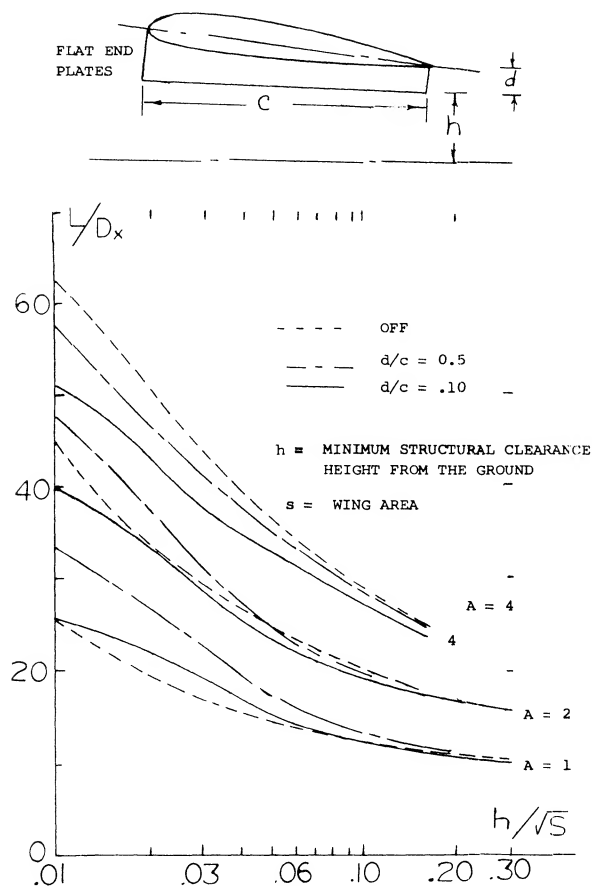


Figure 23. Lift drag characteristics of a "ram wing" as a function of height above the ground.

Landing Flaps. As in swept wings where the wing tips are closest to the ground, Chapter XV, landing flaps can bring some portion of the trailing edge down to a small distance 'h'. Here, as in wings, it might be better to define that distance from the 3/4 point of the "mac". There is a good reason for selecting the three-quarter axis of the wing as the level of reference. Analysis (11,a,b) shows that the effective angle of attack of the airfoil sections at the three-quarter point of the chord is really responsible for the lift produced.

Ram Wings. So-called "Ground Effect Machines" or "Air Cushion Vehicles" have been investigated and built. One version of these vehicles, called "Ram Wing", uses one or more wings with end plates or skegs attached to the lower side, thus coming very close to the ground or even slicing through the water surface. Figure 23 shows typical test results (12,e) of wings with aspect ratios of 1, 2 and 4 with and without end plates. Analysis of the induced angle is not readily possible because of the close proximity to the ground. The improvement with aspect ratio of the L/D_x is apparent from figure 23. The L/D_x also improves rapidly as the ground is approached and the end plates allow the main wing to operate further from the ground while maintaining high lift drag ratios.

To provide longitudinal stability, two wings in tandem are used in (12,c). Analysis of pitching characteristics is simple, insofar as downwash (behind the first wing) is practically zero. When pitching, the height over ground of the first wing increases while that of the second one reduces. Within the small values of ground clearance investigated in (12,b,c) the section characteristics (such as the angle of attack for zero lift) change considerably. Also, when these vehicles are to be used over water the deformation of its surface (due to the pressure below the wings) must be taken into account.

- (10) Influence of ground on wings, experimental:
- a) See some references under (7).
 - b) Hoerner, Fieseler Water Tunnel Rpt 9 (1939).
 - c) See "due to lift" chapter "Fluid-Dynamic Drag".
 - d) Reid, Full Scale Flight, NACA TRpt 265 (1927).
 - e) ARC, Experimental Results, RM 1847 and 1861.
 - f) Buell, On Delta Wings, NACA TN 4044 (1957).
 - g) Fink, 22% Thick A = 1 to 6, NASA TN D-926.
 - h) Baker, Ground Effect Low-aspect-ratio Airplanes, NASA TN D-6053.
 - i) Lockwood, Ground Effect Ogee Wing, NASA TN D-4329.

- (11) Wing theory:
- a) Weissinger, Yrbk D Lufo 1940 p I-145; ZWB Rpt FB 1553 (1942) see NACA TM 1553; Tech Berichte ZWB 1943; ZWB Rpt UM 1392 (1944); Math Nachrichten 1949 p 46; ZFW 1956 p 225; see NACA T Memo 1120 and TN 3476.
 - b) Pistolesi, 3/4 Chord Principle, Conf Rpt Lilienthal Ges Lufo 1937 p 214; applied by Weissinger (43,b).

- (12) Longitudinal characteristics of "ram wings":
- a) Foshag, Ground Bibliography, DTMB Rpt 2179.
 - b) Harry, With End Plates, DTMB Rpt 1979 (1965).
 - c) Harry, Tandem Wings, DTMB Rpt 2259-1 (1966).
 - d) Low Aspect Ratios, See Chapter on this subject.
 - e) Lockheed study, Single and Tandem Low-Aspect Ratio Wings in Ground Effect, U.S. Army Trecom TR63-63.

Tandem Wings. Little attention has been given to wings arranged in tandem. Experimental results of a pair of such wings, each having an aspect ratio of 7, are presented in figure 24. It is seen that the forward wing is comparatively little affected by the presence of the second wing. For practical purposes, we will thus disregard the upwash theoretically coming from the second wing. This wing works, on the other hand, in the much stronger downwash field of the first wing. Its lift angle is composed of four components:

- the angle of attack as in two-dimensional flow
- the final downwash angle behind the first wing
- downwash due to the first wing's bound-vortex circulation
- the induced angle due to the second wing's lift.

Regarding downwash see Chapter XI dealing with "longitudinal stability and control". The lift angle of the rear wing (in radians) is theoretically

$$\begin{aligned} (d\alpha/dC_L)_2 = & 1/(2\pi) + (d\alpha_i/dC_L) (1 - (\epsilon/\alpha_i) C_{L1}/C_{L2}) \\ & - (d'\epsilon'/dC_{L1}) (C_{L1}/C_{L2})/(x/c) \end{aligned} \quad (10)$$

where ϵ = final downwash angle (having a negative sign), where subscript '1' indicates the first and '2', the second wing, and where x = distance as indicated in the illustration. Note that in a tandem system using equal angles of attack C_{L1} is larger than C_{L2} . The last term of the equation covers the downwash component due to the first wing's circulation. Replacing that wing by a bound vortex, the circulation velocity at the radius $r = x$ is

$$w/V = -(0.25/\pi) C_{L1}/(x/c) = -0.08 C_{L1}/(x/c) = \epsilon' \quad (11)$$

where ϵ' in quotation marks to distinguish this angle from the permanent or final downwash angle. When considering the lift angle of the second wing, the angle ϵ' has to be multiplied with (C_{L1}/C_{L2}) . Therefore, in degrees:

$$d'\epsilon'/dC_{L2} = -0.08 (180) (C_{L1}/C_{L2})/\pi(x/c) \quad (12)$$

Also in degrees, the angle of the rear wing can be approximated by

$$\begin{aligned} (d\alpha^\circ/dC_L)_2 = & 11 + (20/7) (1 + 1.8 C_{L1}/C_{L2}) \\ & + (d'\epsilon'/dC_{L2}) \end{aligned} \quad (13)$$

where '7' = aspect ratio and '1.8' = downwash factor. This analysis is confirmed by the experimental results in figure 24. At the end of this analysis, it should be mentioned that according to theory (7,b) and (13,a) a pair of tandem wings is expected to have together a lift-curve slope equal to that of one wing having twice the chord and half the aspect ratio. In reality, lift is up to 10% less in the configuration as in figure 24, on account of the rolling-up process of the vortex sheet.

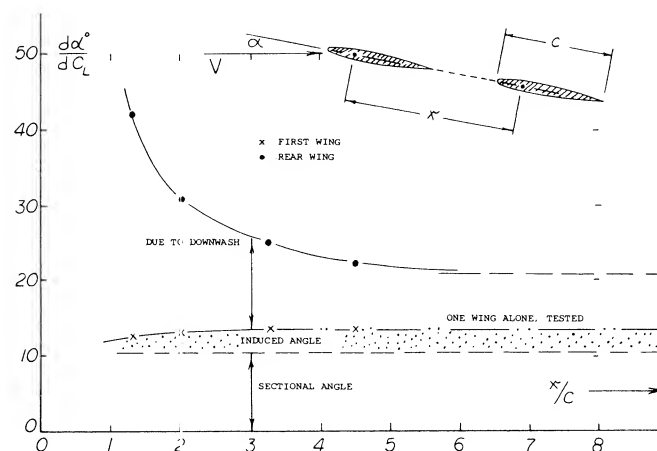


Figure 24. Interaction between a pair of wings operating in tandem (13,b).

Tandem Wings - Refueling. Except for some special VTOL aircraft, few vehicles have been built with tandem wings. Thus, the mechanism given above becomes of interest only during special cases such as the refueling operation. One example is illustrated in figure 25. In this case the airplane being refueled is almost directly behind and is effected to a considerable degree by the downwash produced by the lead or tanker aircraft. In some cases where the tanker is large as compared to the refueled airplane, the downwash is the major factor. Refueling can also take place from a relatively small airplane such as the KC-135, figure 9 Chapter I, to a very large cargo airplane such as the C-5, figure 12. In this case the aft airplane can have a large effect on the tanker and the refueling boom. The supersonic velocity around the nose of the airplane can be particularly troublesome as the refueling boom must "fly" through this field to make contact with the airplane. The upwash produced by the aft airplane also gives a problem to the tanker, causing a nose-up change in trim (13,g). This can be a problem during the initial contact and breakaway maneuver.

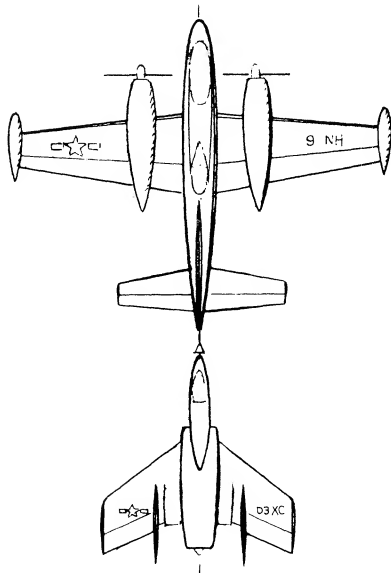


Figure 25. A practical example of three lifting surfaces (wings) flying in tandem formation.

Canard Arrangement. Some experiments in (13,c) give more insight into the mechanism of tandem systems. A rectangular wing with $A = 6$ has a $d\alpha/dC_L = 14^\circ$ when flying alone, and about 26° when in the rear position of a tandem system as in figure 26 (with an equal-span wing ahead). In the case of the "canard" arrangement (with the smaller wing forward) the rear wing is evidently receiving not only downwash, but also upwash (outboard the first wing's span). As a consequence, its lift angle may possibly be as low as when flying alone. As tested, it is somewhat increased, id est to 15° , probably because of non-uniformity of the flow meeting the rear foil.

The effect of canard surfaces with variations of leading sweep angle, dihedral and vertical position (13,f) shows the mutual interference effects of the two wings. As

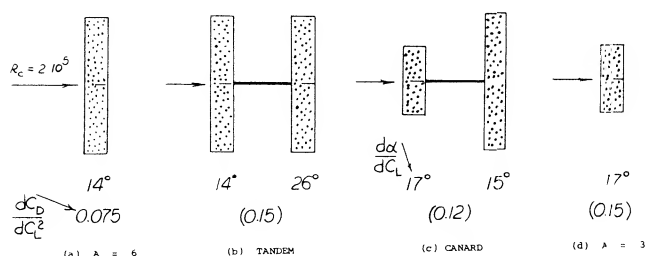


Figure 26. Lift angle of tandem, and canard wing arrangements.

shown on figure 27, there is little difference between lift curves for both the high and the mid vertical position canard arrangements up to an angle of attack of 16° . Above 16° the canard surfaces with increased leading-edge sweep develop higher values of lift with a corresponding increase in the total lift. When the wing and canard surface are on the same level the lift decreases. This reduction is due to the mutual interference of the two wings. On figure 27 the lift of the fore portion of the body without the canard surface is given. This was made possible by the dual balance system used. Characteristics of an airplane with a "canard" type of horizontal surface ahead of the wing are also presented in Chapter XI on "longitudinal stability".

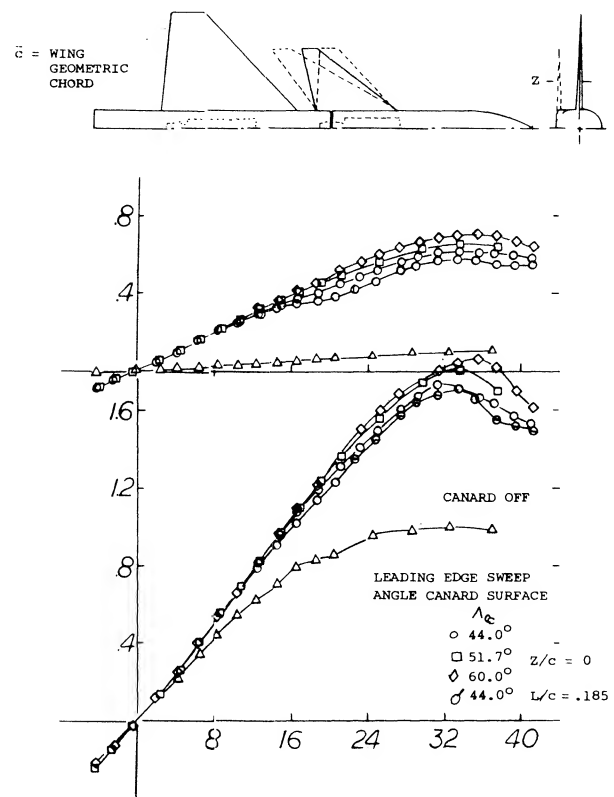


Figure 27. Effect of sweep and dihedral on the total lift of a canard airplane configuration.

(13) Characteristics of wings in tandem:

- Glauert, Tandem Theory, ARC RM 949 (1923).
- Luetgebrune, Wind-Tunnel Tests, ZWB FB 1677.
- Eiffel, Resistance de l'Air & Aviation, 1919.
- Cover picture, Aeron Engg Review Nov. 1955.
- LePage, "Wing" plus "Flap", ARC RM 804 & 886.
- Gloss, Effect of Canard Leading-edge Sweep and Dihedral on Close Coupled Aircraft, NASA TN D-7814 d.
- Aviation Week, Jan. 13, 1975.

3. LIFT OF WING-BODY COMBINATIONS

When a wing fuselage and/or engine nacelle are combined the lift of the combination is different than would be found by summing the lift of each body alone. The difference in the total lift is a result of the mutual interference due to the flow fields of each body. Until recently the mutual interference effects of wing-body combinations could only be determined by test. With the development of the vortex lattice technique, progress has been made in calculating the lift of the combination (15,g).

Alpha Flow. The interference of wing-body combinations can be determined by considering a circular cylinder inclined at some small angle of attack. At this condition then a component of the flow corresponding to $(V \sin \alpha)$ crosses the cylinder. This component is zero at the windward "stagnation" line of the body. At least theoretically, it reaches the maximum value of $(2V \sin \alpha)$ at the sides of the cylinder. As a result, the angle of the flow relative to the body axis is doubled. Placing now a wing across the cylinder, its angle of attack at the roots is equal to "2 α ". This type of upwash is illustrated in figure 6, Chapter XIX. The resultant lift distribution of a mid-wing fuselage configuration is shown in figure 28. At the roots a pair of peaks is evident.

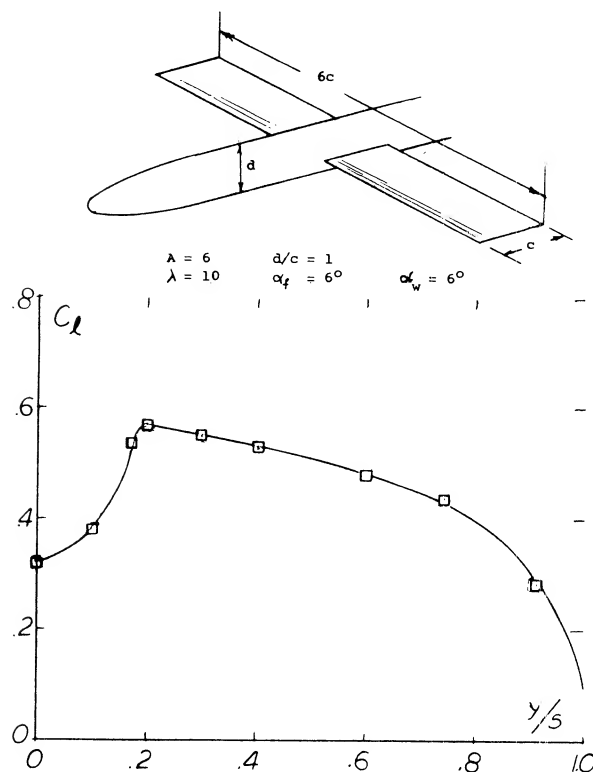


Figure 28. Lift distribution of a wing-fuselage combination.

Body Lift. Circulation and pressure distribution around the roots of a wing are transferred to a certain degree upon the fuselage. To understand this phenomenon, we may consider the two wing panels to be end plates prohibiting any flow around the sides of the body (at least within the length of the root chord). For example, in the configuration as in figure 28 the aspect ratio of the center part of the wing covered by the fuselage is $A_o = d/c = 1.0$. The "height" of the "end plates" each is $h'/d = 3.0$. According to the function presented in Chapter III, the effective aspect ratio of the fuselage is then $A_i = 5.7A_o = 5.7$. The coefficient of the lift on area (dc) induced upon the body by the wing is then 95% of the average of the wing panels. A more accurate analysis is presented in (15,d). The lift induced by a wing rotated to an angle of attack against a long cylindrical fuselage with $d = 0.36c$, kept at zero angle of attack, is indicated by the differential based on area (dc) :

$$\Delta C_{Ld} = k C_L \quad (14)$$

where C_L = average lift coefficient in the panels of the two-dimensional rectangular wing, and k is a constant to be discussed in the next paragraph. At any rate, the lift is less in this case than that of the wing alone. A situation similar to this one is obtained when deflecting trailing-edge wing flaps, such as in (16,c) for example.

(14) Airplanes using tandem wings, as the once-famous French "Pou du Ciel" ("Sky Flea"), were more a combination of biplane and tandem system.

(15) Analysis of the lift of wing-body combinations:
 a) Multhopp, Alpha Flow, Lufo 1941; NACA TM 1036.
 b) See NACA RM A1951G24, L1951J19, L1952J27a.
 c) Weber, Spanwise Loading, ARC RM 2872 (1956).
 d) Cross Flow, see also "slender body" chapter.
 e) Hoerner, T'Rpt F-TR-1187-ND WP AFB (1948).
 f) Vladen, Fuselage and Engine Nacelles Effects on Airplane Wing, NACA TM 736.
 g) Ashley, Wing-body Aerodynamic Interaction, Annual Review of Fluid Mechanics, Vol. 4, 1972, p 431.
 h) Flax, Simplification of the Wing-Body Problem, J of A, Oct. 1973.
 i) Mendenhall, Vortex Shedding on Aero Characteristics of Wing-Body Tail, NASA CR-2473, 1975.

(16) Wing-body combinations, experimental:
 a) Jacobs, 209 Combinations, NACA T'Rpt 540 (1935).
 b) Sherman, 28 Combinations, NACA T'Rpt 575 (1936).
 c) Sherman, With Split Flaps, NACA TN 640 (1938).
 d) Gimmmler, Pressure Distribution on Wing-fuselage Combination, German ZWB FB 1710 (1942).
 e) Goodman, Wing-body Position with reference to interference NACA TN 2504.

Wing With Body. When rotating wing and fuselage together the lift induced on the body, ΔC_{Ld} corresponds to

$$\Delta C_{Ld} = 2kC_L \quad (15)$$

where $k \cong 0.2$. However, considering a wing with conventional aspect ratio and possibly elliptical lift distribution, the proper factor might be $k = (4/\pi)0.2 = 0.25$. At least the same amount of lift is added to that of the wing panels so that the combined lift is somewhat increased. For example, in the combination as in figure 29 where $d/b = 0.1$, the increment is in the order of 4%. Figure 30 shows the increase of total lift as a function of the diameter/span ratio. As derived in (15,f) the three components of lift in larger aspect ratios are approximately as follows:

the lift increment of the exposed portions of the wing

$$L_w^* = L_{wB} (1 - \sigma)^{5/3} \quad (16)$$

due to cross flow or alpha flow

$$L_w = L_{wB} \sigma (1 - \sigma)^{5/3} \quad (17)$$

lift induced on the body by the wing

$$L_B = L_{wB} \sigma (1 + \sigma) (1 - \sigma)^{2/3} \quad (18)$$

where σ is the body diameter d over the full span b , $\sigma = d/b$ and L_{wB} is the lift of the complete body system. The interference effects of the wing and body have also been given in (15,g) as

$$L_{wB} = L_w^* (1 + \sigma)^2 \text{ -- Total lift @ } \alpha \quad (19)$$

$$L_w = L_w^* (1 + \sigma) \text{ -- Lift wing alone} \quad (20)$$

$$L_B = L_w^* \sigma (1 + \sigma) \text{ -- Body lift} \quad (21)$$

The lift given in equations 19 and 20 include the interference effects.

For small (d/b) ratios we find approximately

$$(dc_L/d\alpha)/(dC_L/d\alpha) = 1 + 0.2 (d/b) \quad (22)$$

Fuselage Shape. Not all fuselages are circular in cross section. Shapes as in figure 7, Chapter XI have been investigated. In general it can be said that bodies with a more or less flat bottom, adjoining the wing roots, tend to produce higher lift-curve slopes. Minimum drag and drag due to lift of such shapes are not necessarily higher than for the circular cross section.

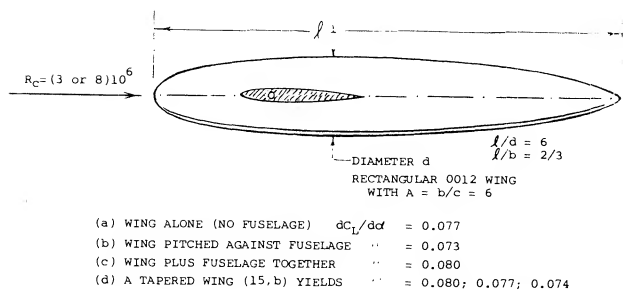


Figure 29. Influence of a fuselage and wing on the lift slope.

(17) Influence of fuselage cross-section shape:

- Muttray, Erg AVA IV; Lufo 1928 p 33; Ringbuch 1A4.
- Sherman, 30 Combinations, NACA TN 1272 (1947).

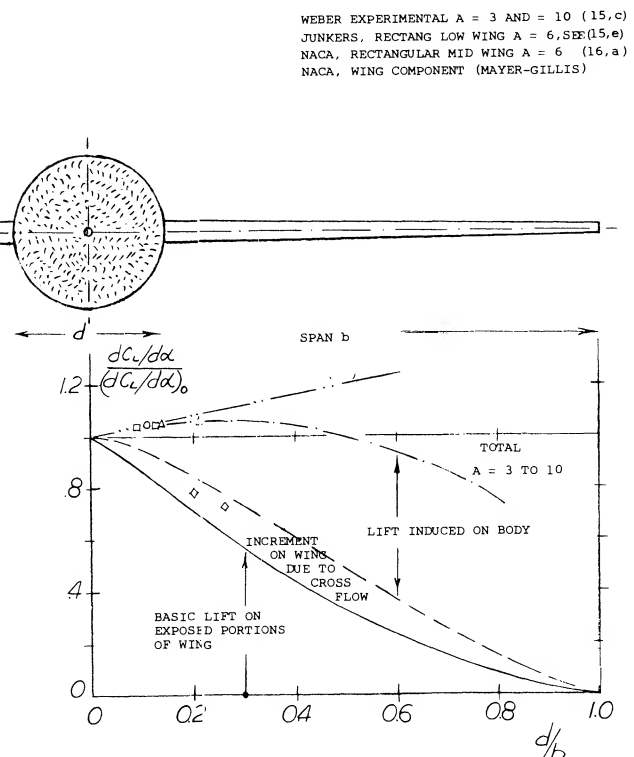


Figure 30. The lift-curve slope of wing-fuselage combinations as a function of the diameter ratio d/b .

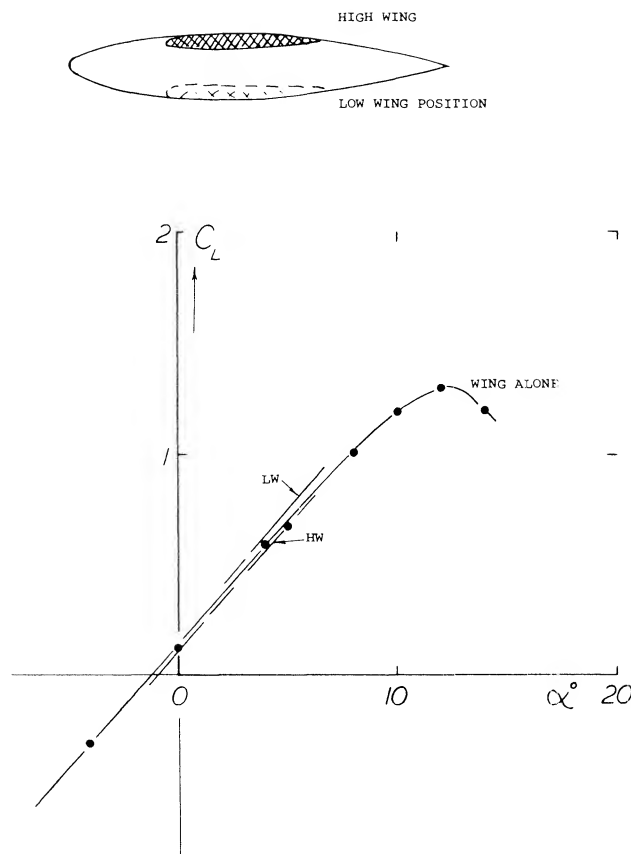


Figure 31. Lift differentials caused by typical high- and low-wing engine nacelle bodies.

Fillets. Of course, viscosity (skin friction, boundary layer, flow separation) reduced any peak in the lift distribution which may theoretically be predicted for the wing roots. Fillets used to fill out the corners between the upper side of the wing roots and the fuselage walls (18,a) are only effective when extending downstream, somewhat beyond the trailing edge. Their benefits are found at higher angles of attack and in the maximum lift coefficient. A disadvantage of fillets can be increased downwash and reduced longitudinal stability. Bending up the trailing ends of the root sections is a possible method of reducing downwash without causing separation.

Displacement. A fuselage or an engine nacelle displaces the flow around it (perturbation). This effect becomes particularly evident in high-wing or low-wing combinations. To explain the consequences of displacement, we may assume that in one strip of an airfoil the velocity may be reduced 50% and in another strip increased 50%. While the average velocity thus remains constant, the average of the dynamic pressure is now $0.5 (0.5^2 + 1.5^2) = 1.23$ times that of the undisturbed flow. A pair of round nacelle bodies (with a length $l = 1.5 c$) are shown in figure 31. For practical purposes the lift-curve slope remains unchanged. However, the low-wing type (with the nacelle above the wing) exhibits an increment of the lift coefficient, based on the covered area ($d c$), of $\Delta C_L = +0.18$ while the underslung nacelle shows a differential of -0.17 . The signs of these differentials can be explained by displacement, as above. In regard to drag, it should be noted that the low-wing configuration evidently suffers from interference along the roots (on the upper side of the wing).

Engine Nacelles. The wing position on the streamline body as in figure 32 was systematically varied. In an underslung forward position (with the body nose at x/c 100% of the wing chord ahead of the leading edge) a displacement flow develops, resulting in $\Delta C_{L_d} = -0.5$. For $x/c = -30\%$ (aft position investigated) the lift coefficient is not affected. As a function of height (low wing and high wing), ΔC_{L_d} varies as shown in the illustration.

Induced Drag. The influence of the angular setting of the nacelle against the wing chord results in $dC_{L_d}/di = 0.036$. At least half of this lift originates on the wing panels. As pointed out in Chapter VIII of "Fluid-Dynamic Drag", a certain amount of induced drag results from any lift differential. In the low-wing or high-wing position, as in figure 31, the induced component of the nacelle corresponds to $C_{D_i} = 0.01$, while the total drag (body, interference, induced) is in the order of $C_{D_t} = 0.04$. It is suggested that the variations of the forces are similar to those due to the deflection of a trailing-edge flap over a part of the span equal to the diameter of the body, as described in (22). This approach accounts for constant differentials of lift and induced drag.

(18) Wing-fuselage junctures (fillets):

a) Sherman, NACA TN 641 & 642, T'Rpt 678 (1939).
b) Muttray, see NACA TM 517 and 764 (1935).

(19) Influence of engine nacelles on lift:

a) McLellan, Nacelle Position, NACA TN 1593 (1948).
b) Becker, Twin-engine Model NACA T'Rpt 750 (1942).
c) Pepper, Fuel Tanks, NACA W'Rpt L-371 (1942).

4. INTERRUPTIONS OF SPAN

In the practical design of an airplane the need for data on the physical interruptions of the span may be encountered. This is particularly true in the application of all movable surfaces, such as might be encountered with tilt wing aircraft or the structural mode control fin illustrated on figure 33.

With Longitudinal Gap. Really cutting a wing in two eventually means reducing its aspect ratio to one half. The effective ratio decreases as a function of the gap between the two halves of such a wing. Theory (22,a), considering two lifting lines (having no physical chord), expects a rapid decrease of A_i/A . Experimental results (22,b) of a rectangular wing (presented in Chapter VII of "Fluid Dynamic Drag") show, however, that chord and thickness of the square and blunt wing ends are obstructions for the flow through the gap, at least for ratios of y/b below 0.03, or $y/c = 0.2$. The induced characteristics of a pair of wings or airplanes flying side by side can be derived from this information. A real gap is found between an all-movable control surface (fin or rudder, as on submarines in particular) and the adjoining "wall" of the vehicle.

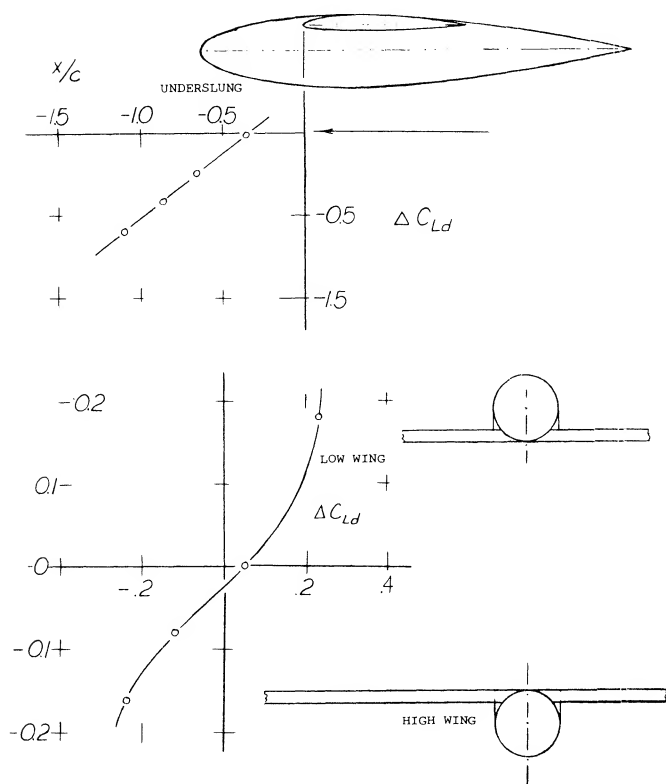


Figure 32. Influence of vertical position of a wing nacelle body combination on the lift.

Theoretically, the aspect ratio of the fin as in figure 33 is doubled through reflection in the wall. The lift angle, however, increases as the gap is opened from that for $A = 2$ to that corresponding to an $A = 1$. The increase is steady but not at all as sudden as theory (permitting infinitely high velocities without losses) would expect. It should be noted that in reality (as for instance at the end of a fuselage) the boundary layer can be appreciably thicker than that found on the wall of the wind tunnel in which the rudder, as in figure 33, was tested.

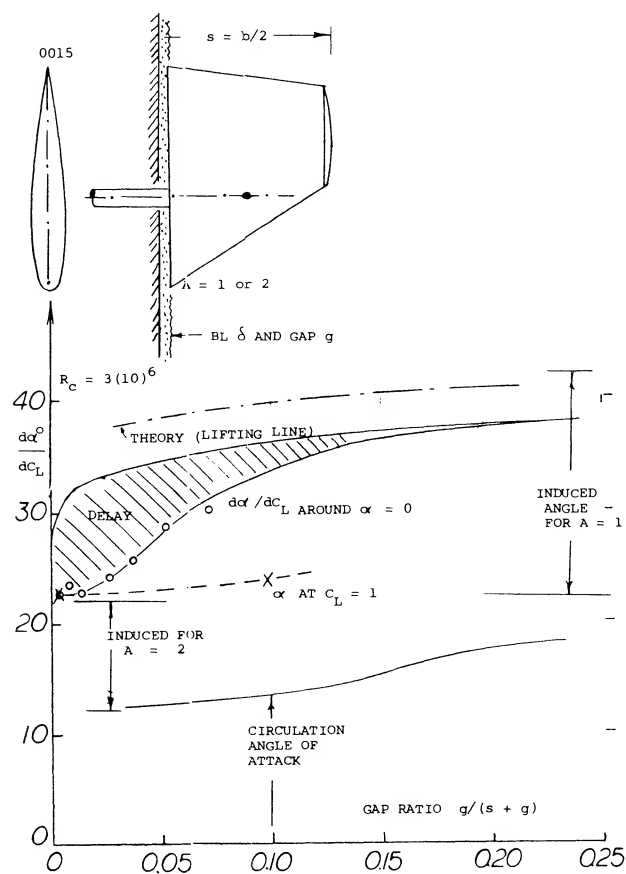
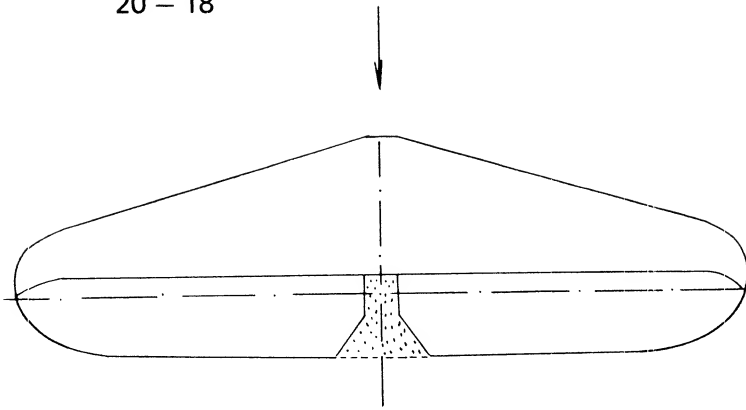


Figure 33. Influence of a wall gap upon the lift angle of a control surface.

- (20) Pearson and Anderson, Wings with Partial-span Flaps, NACA Tech Rpt 665 (1939).
- (21) Characteristics of wings with cutouts:
 - a) Ergebnisse AVA Gottingen Vol. III (1928) p 92.
 - b) Muttray, Zts Flugtechnik Motorluft 1929 p 161.
 - c) Sherman, Cut-Outs, NACA T'Rpt 480 (1934).
 - d) Smith, Wing Cut-Outs, NACA T'Rpt 266 (1927).



THE TAIL SURFACE SHOWN IS ONE EXAMPLE OF THOSE REPORTED IN (23,a) AND SHOWN ON THIS FIGURE; $t/c = 13\%$ IN CENTER, $= 10\%$ AT TIPS; ELEVATOR WITH OVERHANGING-NOSE BALANCE (INTERRUPTION OF SURFACE) AND GAP $= 0.5\% c$; $R_c = 5(10)^5$. WITH THE COEFFICIENTS BASED ON ACTUAL AREAS, EXPERIMENTAL CHARACTERISTICS ARE AS FOLLOWS:

WITHOUT CUT-OUT		WITH CUT-OUT
4.3	A	4.4
.055	$dC_L/d\alpha$.055
0.35	S_f/S	0.33
0.59	$d\alpha'/d\delta$	0.53
.0014	C_{Ho}	.0009
.0050	C_{Ho}	.0040

THE SIZE OF THE CUT-OUT CORRESPONDS TO $S/S = -3.3\%$ AND $S/S_f = -9.5\%$; THE MAXIMUM LIFT (NOT AFFECTED BY CUT-OUT) CORRESPONDING TO $C_{Lx} = 0.7$ FOR $\alpha = 0$ AND $C_{Lx} = 0.6$ FOR $\alpha = 0$.

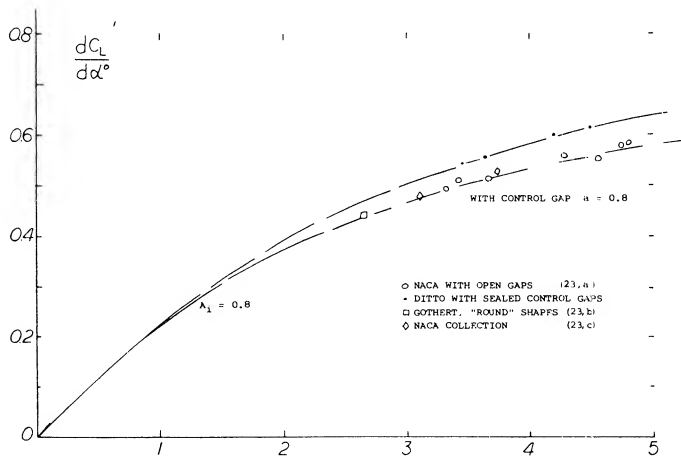


Figure 34. Lift-curve slope of horizontal tail surfaces tested without fuselage as a function of aspect ratio.

Horizontal Tail. Surfaces are an example of "wings" with moderate aspect ratio. The type, as in figure 34, has a more or less rounded planform, has a cut-out for the rudder, and has gaps to permit deflection of the elevator. The effective aspect ratio as well as the section efficiency are reduced, accordingly. Regarding cut-outs, the experiments reported in (23,a) do not show any influence upon the lift curve slope, provided that the lift is referred to the reduced area. The lift-curve slope of typical horizontal surfaces are plotted in figure 34. The difference between the tail surfaces and the "round" wings, figure 2, Chapter III, can be accounted for by reducing A from 0.9 to 0.8. This difference is primarily due to the open gaps along the hinge lines of the elevator flaps. In comparison to sharp-edged and rectangular wings the lift-curve slope is appreciably reduced, roughly between 16 and 19%.

Influence of Fuselage. When testing a half wing at the wall of a wind tunnel or mounted on a suitable end plate, the boundary layer developing along the wall can noticeably reduce the lift of that wing. In combination with an adverse pressure gradient, boundary-layer interference is particularly strong at the end of a fuselage. The B' layer developing reaches such proportions that at the location of the tail surfaces it fills a circle roughly equal in diameter to that of the fuselage. As pointed out in Chapter VIII of "Fluid Dynamic Drag", the horizontal tail is thus cut in half, so to speak; and its induced drag can be doubled. The lift of the combination reported in (16,b) is shown in figure 2 of Chapter III. The lift deficiency is largest at small angles of attack, where the lift-curve slope is but 11% of that of the isolated tail surface. At some angle of attack corresponding to $C_L = 0.7$, the maximum value of (C_L/α) is still 11% below the isolated slope. As indicated in "Fluid Dynamic Drag" the effective aspect ratio reduces according to

$$A_i/A = 1 - 12 C_{fH} \quad (25)$$

where the coefficient represents the fuselage drag (including everything attached to it and wing-root interference) and is referred to the total planform area of the tail surface (subscript H).

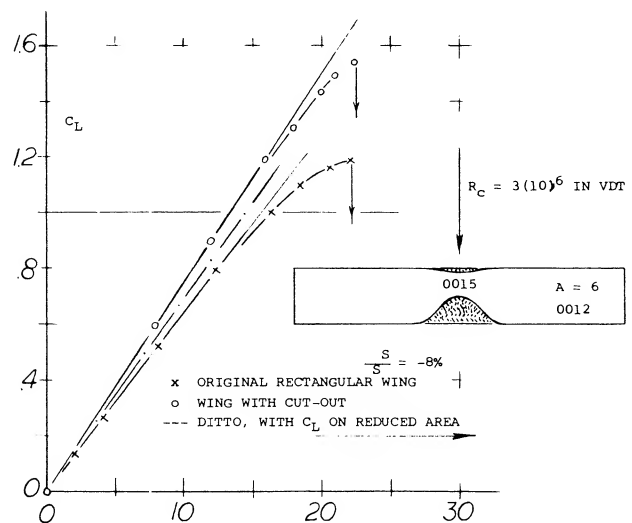


Figure 35. Lift characteristics of a wing with faired cutouts. Coefficient based on the original wing area.

Cutouts. Figure 35 presents the influence of a well profiled cutout as it was used many years ago in the upper wings of biplanes (to give the pilot a better view). Disregarding lift coefficients above 0.9, the effect is that of lift distribution (with a dent in the center). Some possible reductions in chord in the center of a wing are shown in figure 36. Because of flow separation the leading edge is more sensitive than the trailing edge. A lot of lift can also be lost, however, on account of a cutout from the rear. While the reduction of wing area in part (c) of the illustration is only 8%, that of the lift is 15%. Analysis shows that the effective aspect ratio is reduced to 82%. Any disturbance of the high-speed flow along the upper side of the wing roots may thus produce the equivalent of a gap or cutout in the wing span. In fact, cutouts have sometimes been used at the trailing ends of the wing roots to reduce downwash and improve longitudinal stability.

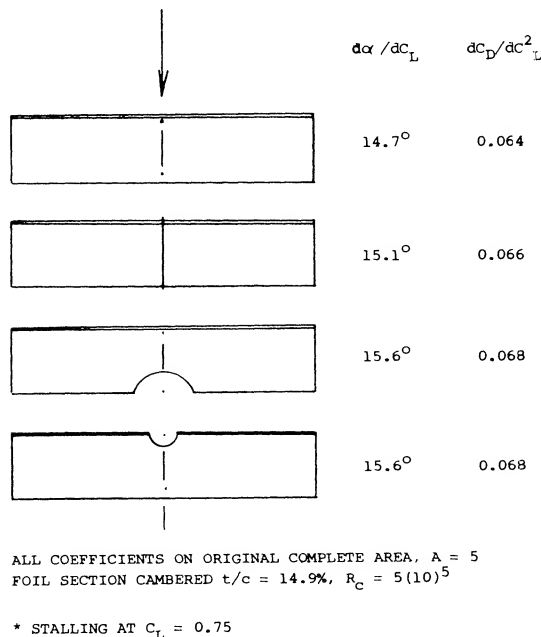


Figure 36. Influence of cutouts in the center of a wing on the induced characteristics.

5. TOTAL AIRCRAFT LIFT

Throughout the preceding chapters we have considered the lift of the various components of the airplane and how it is predicted. The ultimate object of all this is to determine the lift of the complete airplane system for any condition and configuration. To evaluate the performance of a given airplane the lift is needed as a function of attitude and power. In particular the maximum lift is needed as a function of operating flap settings and center of gravity for the complete airplane as this directly influences overall capability of the airplane. The variation of the lift and its maximum value also is needed to determine the stalling characteristics and stalling speed (25,b,c,d).

Stalling Speed. The stalling speed is of primary concern as it determines the capability of the airplane and is, of course, the minimum speed at which the airplane can be operated. The stall of an airplane may be defined by the unpreventable nose drop or an unmistakable manifestation of stall, such as a severe buffeting or oscillation (25,c). The speed at which stalling takes place is determined by the maximum lift coefficient and is expressed by the equation

$$V_S = \sqrt{2W/C_{LX} \rho S}$$

where C_{LX} is the maximum lift coefficient for the airplane configuration in the trimmed condition. The actual demonstration of the stalling speed of the airplane is a dynamic maneuver and depends on the rate of approach to the stall angle and the inertia of the airframe. If the dynamic approach angle to stall is large C_{LX} will be larger than that based on static tests as noted in Chapter IV.

- (22) Wings with longitudinal gap:
- Munk, Tech Berichte Flug Meist, Vol. I (1917) p 219.
 - Windsor, Streamwise Gap, Univ. Md. Rpt. 453 (1965).
 - Dugan, Theory of a Gap Between Wing and Body, NACA TN 3224 (1954).
- (23) Lift of horizontal tail surfaces:
- Bates, Horizontal Tails, NACA TN 1291 (1947).
 - Goethert, Aspect Ratio, Control Surfaces Ybk D Lufo 1940, P.I, 542.
 - Silverstein, Horizontal Tail Collection, NACA TR 688, 1940.
- (24) H'tails with disturbance in the center:
- Jacobs, 0012 With Protuberances, NACA Rpt 446 & 449.
 - Engelhardt

Stalling Characteristics. The stalling speed and characteristics of an airplane are a matter of safety as well as performance. For instance, if the stall is sudden and without warning, severe loss in altitude could be encountered during landing if the landing speed were not sufficiently high to eliminate gust effects. Stalling of certain types of airplanes has been found to be insidious and dangerous. This stalling problem is caused by the loss of rolling stability near maximum lift which causes the airplane to roll or possibly flip into a spiral dive, and incipient spin. Recovery from the spin can only be accomplished after some loss of altitude, which becomes critical when stalling takes place near the ground as during takeoff and landing.

If stalling can not be made safe (stable) the pilot should be forewarned by an indication of buffeting of the airplane and/or control column as well as its behavior: sagging, swaying, reduction of control response. When the stall is too dangerous it must be completely avoided by such devices as restricting longitudinal control in such a manner that the angle of attack needed for stall can not be obtained. While this appears to be a suitable approach, problems at other flight conditions may make it unsuitable.

In modern airplanes, the wings (airfoil section) are basically designed for high speed (low drag). Thin sections with small camber, and with the maximum thickness at 40% chord have a small nose radius and influence stalling as follows:

- a) the angles of attack are lower
- b) the stall is more sudden and more pronounced in manner
- c) little warnings, such as gentle stick buffeting, occur.

Higher wing loadings, that is increased take-off and landing speeds, also make any stall more dangerous. The pilot may be forewarned of the impending stall as follows:

- a) position and force of the elevator control column, also attitude of the airplane nose up.
- b) vibration and sound of the airplane as a function of engine, propeller and structure
- c) lateral behavior (rolling, swaying aileron response).
- d) by instruments: speed, sinking or climbing.

Unfortunately, the angle of attack (against air) cannot easily be measured and indicated.

Desired Stall Characteristics. An airplane with good stall characteristics will generally have a gentle stall that starts inboard on the wing. This type of stall will reduce the downwash on the tail which results in a stabilizing moment tending to eliminate the stall. Buffeting will be encountered on the tail from this as a warning. As the stall is approached there should be no loss of lateral control and the airplane should have no tendency to fall off on one wing or the other. Recovery from the stall should be easy to accomplish with a push of the control column.

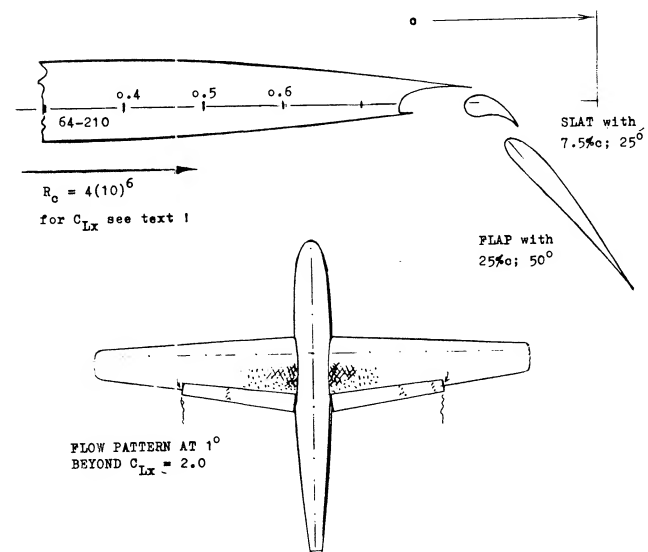


Figure 37. Aircraft configuration (25,a) with part-span double-slotted flaps.

- (25) Lift characteristics of complete aircraft:
 - a) Sweberg, Summary Maximum Lift Coefficients and Stalling Characteristics of Airplanes, NACA WR L-145.
 - b) Fink, Full-Scale Wind Tunnel Test Single Engine Airplane, NASA TN D-5700.
 - c) Wimpenny, Low-Speed Stalling Characteristics, AGARD Report 356.
 - d) Kier, Minimum Flying Speed for a Large Subsonic Jet Transport, NASA D-5806.
- (26) Maximum lift of flapped sections:
 - a) Sivells, 64/75-210 Wings with Flaps, NACA TR 942.
 - b) Serby, Review of Full-Scale Landing Flaps, ARC RM 1921 (1937).
 - c) Sherman, 18 Wing-Fuselage Combinations, NACA TN 640 (1938).
 - d) Abbott-vonDoenhoff-Stivers, Airfoil Data, NACA TR 824 (1945).

Prediction of Aircraft Maximum Lift. The determination of C_{LX} for the complete airplane with straight wings starts with finding the area of local stalling of the various wing sections employed as described in Chapter IV. If the wing has high lift devices Chapters VI and VII are also used. For moderate or high aspect ratio straight wings the local variation of C_{LX} can be chosen to give the desired stalling pattern. Even with flaps the secondary effects are such that the desired stall can be predicted (25,c). In the case of swept wings the C_{LX} is influenced to a large degree by the boundary layer flow as discussed in Chapters XV and VI. Here C_{LX} is increased inboard and reduced outboard making the prediction difficult.

The effect of the fuselage, nacelles and the moments needed for trim must also be considered in determining C_{LX} . These are discussed throughout this book. Unfortunately, interference effects, gaps and associated effects make the prediction of C_{LX} for the complete airplane somewhat inaccurate. This is true even with complete model wind tunnel test results, as there are many factors that influence the results including:

- Differences in Reynolds number between test and full scale.
- Effect of extremely low pressures in the slots of the flaps and leading-edge devices leading to Mach number problems in the wind tunnel tests that change the results compared to full scale.
- Trim and c.g. changes not properly measured.
- Poor simulation of full scale airplane by model due to lack of representation of such items as flap tracks, inlets, exits, landing gears, gun openings and gaps.
- Change in wing stalling pattern, due to Reynolds number.
- Changes in lift due to simulation of power effects.

It has been found that generally the model test results have a C_{LX} 10 to 15% higher than would be measured on the full scale airplane. These higher values of C_{LX} , determined from model test results, illustrate the difficulty in accurately predicting the maximum lift of full scale airplanes. Generally, the model results are reduced by 15% when making the final prediction for these reasons.

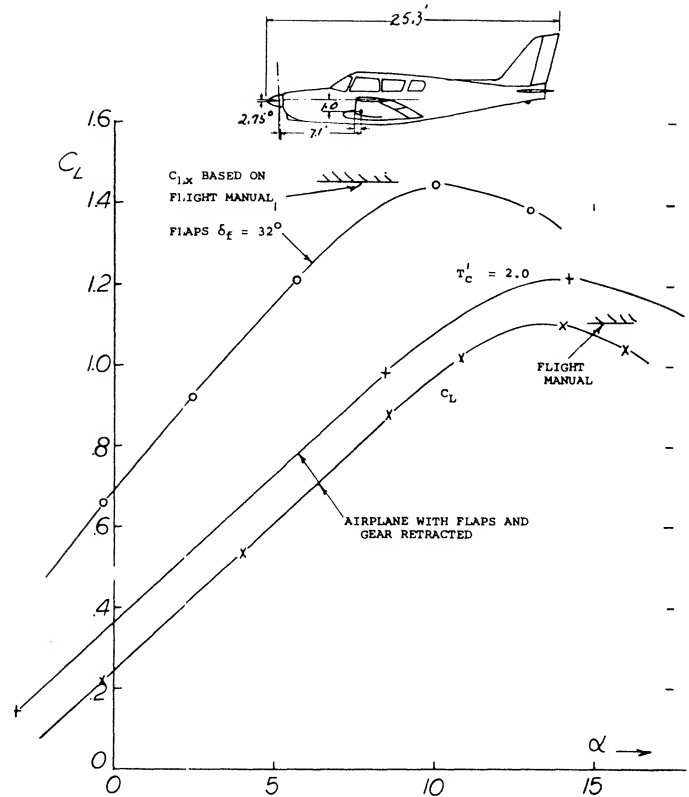


Figure 38. Full scale wind tunnel test of a low wing aircraft (25,b).

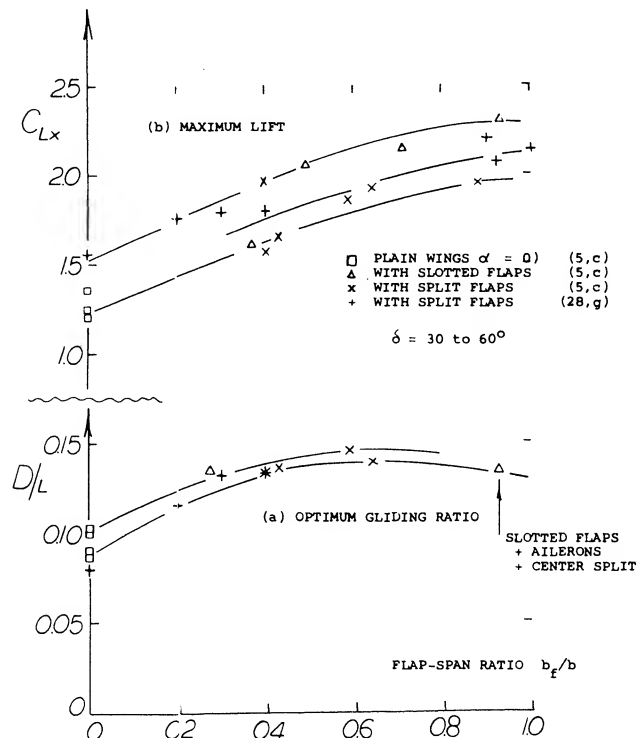


Figure 39. Flight test results of small airplane with various types of wing flaps as a function of span ratio.

Maximum Lift Build Up. In determining the maximum lift of the complete airplane for any given configuration the value of each component is found as a function of angle of attack. Starting with the wing, C_{Lx} is found for the clean configuration; then the effect of flap deflections, fuselage, tail, engines and their mutual interferences are determined. Equations and data are provided throughout this book to accomplish this. A typical buildup of C_{Lx} is given on figure 37 to illustrate the effect of the various components.

The airplane configuration as in figure 37 was tunnel tested (30,d) among others with double-slotted flaps. The maximum lift coefficient varies as follows:

$C_{Lx} = 2.76$	wing with full-span flaps
$= 2.41$	wing with 60% span flaps
$= 2.09$	after adding the fuselage
$= 1.94$	after adding a horizontal tail
$= 1.35$	for the plain wing alone
$= 1.18$	airplane with flaps neutral

While it thus might be claimed (on the basis of two-dimensional wind tunnel tests) that lift is increased 100% through the use of flaps, the realistic increase corresponds to $1.94/1.18 = 1.64$ or to $1.94/1.35 = 1.45$ only when including the fuselage. As far as gliding and climbing is concerned, the sinking speed is roughly doubled with the part-span flaps down ($C_{L_{opt}} = 1.9$) as against the condition with flaps neutral (where $C_{L_{opt}} = 1.1$). The illustration also shows the stall pattern. On account of inboard flaps and fuselage, stalling begins in the parts of the wing adjoining the fuselage while the wing tips reserved for the ailerons have a completely undisturbed flow.

Another example of the variation of lift with angle of attack and C_{Lx} for an airplane with and without flaps is given on figure 38. The maximum lift coefficient of the complete full scale airplane as tested agrees with flight results, thus showing that when the exact conditions and configuration are duplicated in the wind tunnel reliable results are obtained. The increase in C_{Lx} with power is also shown on figure 38. This would be expected based on the increased velocity in the propeller wake that impinges on the wing. In Chapter XII the procedures for calculating this increase are presented.

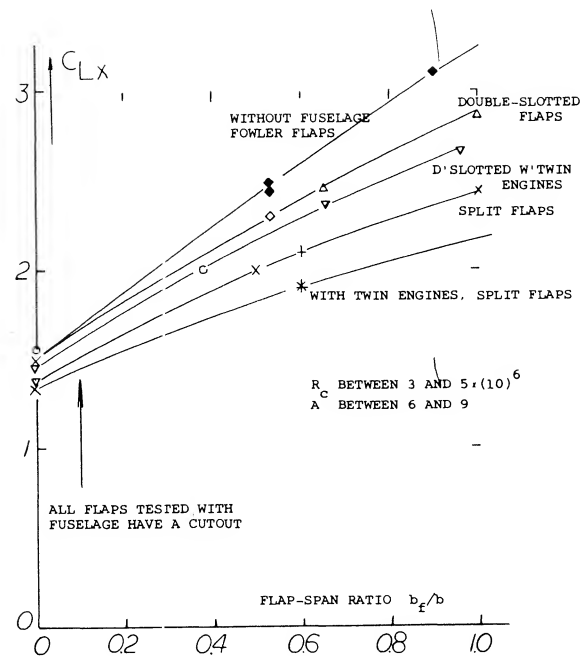


Figure 40. Statistical evaluation of the maximum lift on airplane configurations with trailing-edge flaps.

Effect of Flap Design. Wing flaps are presented in detail in Chapter V. The effect of the application of these flaps as a function of flap-span ratio for the complete airplane are given on figure 39. These are data from flight test results of a series of small aircraft. The drag lift ratio D/L presented shows the characteristics for evaluating landing and takeoff. At the higher values of D/L the approach angle is increased, which is usually an advantage when landing. Since Fowler and similar flaps have less drag during takeoff, the best flap system might be this type, providing it could be deflected to a very high angle when landing so that the approach angle would be large due to the high D/L . The effect of flaps on C_{Lx} can also be evaluated from the data given on figure 40, an evaluation of wind tunnel test results.

CHAPTER XXI — LIFT OF BLUNT BODIES

Lift can be developed on bodies with blunt shapes that have no resemblance to wings. In this case the lift on the bodies is defined as that force acting normal to the direction of the relative wind motion. Any lateral force may then be considered to be a lift force, although in the strict sense the force is side force. Since these forces are of interest in the design of land vehicles, they are included in this chapter.

1. IN TWO-DIMENSIONAL FLOW

Any structural beam or cylindrical elements (cables, pipes for example) exposed to wind, or in water, will usually react as in two-dimensional flow.

Flat Plate. A flat plate produces lift like an airfoil or wing when at small angles of attack. Long before reaching $\alpha = 90^\circ$ the flow is completely separated, however. A review of forces and pressures in this condition is given in (1,a). According to theory the normal force on the forward side of the plate is given by the coefficient

$$C_N = 2 \pi \sin \alpha / (4 + \pi \sin \alpha) \quad (1)$$

This average pressure and its variation is of interest in stalled airfoil sections and in cavitating flow. At $\alpha = 90^\circ$ the result is $C_N = 0.88$. However, in real flow there is a negative rear-side pressure $C_P = -1.1$, so that the total drag coefficient is 1.98, as found in Chapter III of "Fluid-Dynamic Drag". On the basis of tests (1,b) it is suggested that the value of the rear-side C_P varies in the same manner as the forward-side normal force. Multiplying equation (1) by $(1.98/0.88) = 2.25 = (9/4)$, the following equation is found:

$$1/C_N = 0.222 + (0.283/\sin \alpha) \quad (2)$$

- (1) Flat plates with separated flow pattern:
- Wick, Inclined Plate Between Walls, NACA TN 3221 (1954).
 - Fage, Experimental Between Walls, ARC RM 1104 (1927); also Proceedings Royal Society London Vol 116 (1927).
 - Flachsbart, Disk and Rectangular Plates, Erg AVA Göttingen IV (1932).

This function, plotted in figure 1, agrees well with experimental points. Splitting up the normal force in drag and lateral or lift components, $C_L = C_N \cos \alpha$ is obtained. Around $\alpha = 90^\circ$ (that is between 80 and 100) the "lift"-curve slope is negative:

$$(dC_L/d\alpha) \approx -C_D \approx -2/\text{rad}; -0.035 \text{ per degree} \quad (3)$$

where $2 \approx 1.98$, as above, and the second value per degree. It must be realized, however, that all these forces are by no means steady. Because of a Karman-type vortex street (discussed later in connection with circular cylinders) drag and particularly lift are fluctuating around the mean measured values. As shown in "Fluid-Dynamic Drag", pressures and forces also decrease considerably when the aspect ratio of the plate is reduced from infinity to say below $A = 10$. Around $\alpha = 90^\circ$ they are then similar to those of a square plate or disk, to be discussed later.

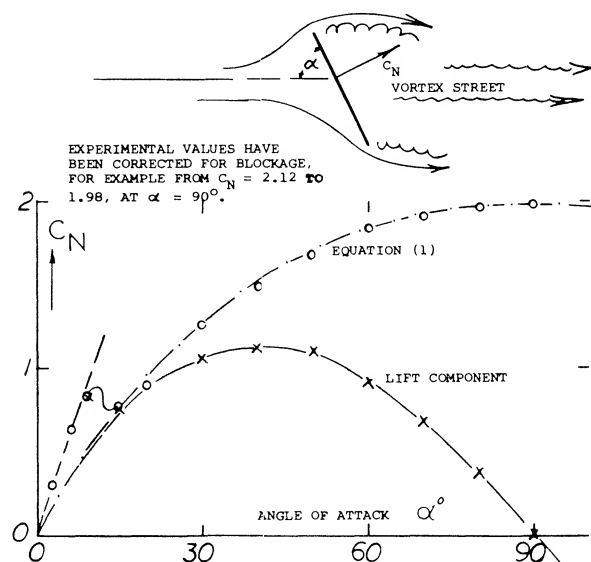


Figure 1. Normal force and lift component of a flat plate in two-dimensional flow (equation 1) and as tested between tunnel walls.

Circular Cylinders. The flow characteristics around circular cylinders are given in Chapter II in conjunction with the explanation of circulation. At Reynolds numbers below $R_d = 10^5$, the flow pattern past cylindrical elements such as cables, pipes, periscopes, smoke stacks and even rocket vehicles on their launching pads is that of the well-known Karman vortex street; see Chapter III of "Fluid-Dynamic Drag". Corresponding with the wake swinging up and down (or from one side to the other) there is a fluctuating lifting or lateral force in the cylinder. In fact, the vortex street originates because of a circulation around the cylinder, alternating between the two possible directions, once right or up and once left or down, respectively. As reported in (2,d) the point of separation fluctuates between 60 and 150° , measured on the circumference, from the ideal forward stagnation point that is roughly by $(+ \text{ and } -) 45^\circ$ around an average point. The maximum of the lateral force C_y is in the order of $(+ \text{ or } -) 1.0$ in this example, while C_D varies by $(+ \text{ or } -) 0.1$. The Strouhal number is

$$S = f_s D/V \quad (4)$$

Where f_s is the frequency of vortex shedding, D is the cylinder diameter and V the free stream velocity.

The frequency of vortex shedding is dependent on the Reynolds number for a stationary cylinder, no lateral motion, and varies between 0.2 and 0.3 as illustrated on figure 2. At Reynolds numbers between 6×10^5 and 4×10^6 there appears to be a region where the vortex shedding frequency is not definite (2,j) with much higher values of Strouhal numbers obtained. Measurement problems may have led to the high values shown on figure 2 at $R = 10$

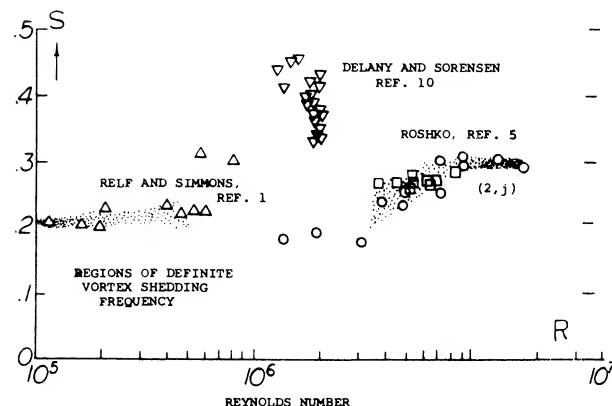


Figure 2. Variation of Strouhal number with R-number for unsteady lift on stationary cylinder.

FLUID DYNAMIC LIFT

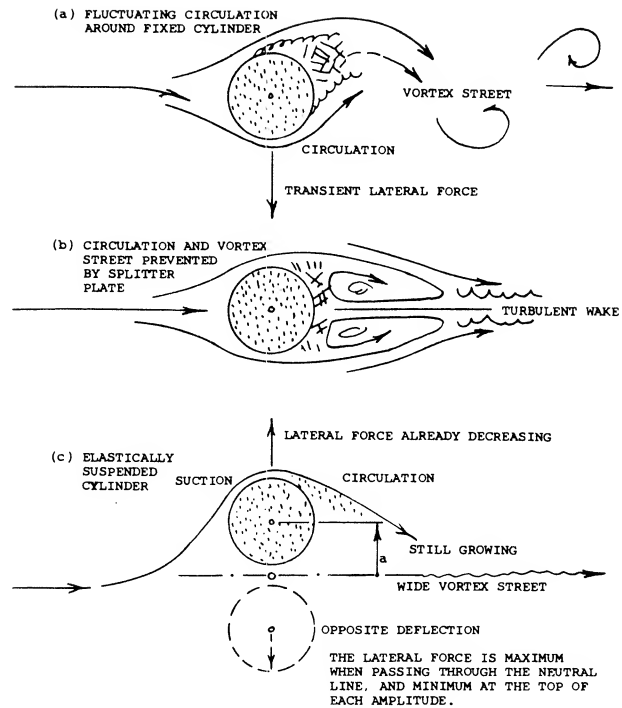


Figure 3. Sketches, showing the flow pattern around a circular cylinder (at R ' numbers between 10^4 and 10^5) under three different conditions.

Unsteady Lift. Although the steady state lift on a non-rotating cylinder is zero, the vortex shedding leading to the Karman vortex street results in an oscillating lift force. If all the vortex-street circulation were developed without skin friction theory (2,b) predicts a maximum transient force coefficient of $+3.6$. For a fixed cylinder, part (a) figure 3, operating between $R_d = 10^4$ to 10^5 the force coefficients reported are

$$\begin{aligned} C_y &= +0.6 \text{ to } 1.3 \\ C_{Dx} &= .05 \text{ to } .10 \end{aligned}$$

and the Strouhal number is $S \approx .205 = C$.

The RMS lift coefficient $C_{L, \text{rms}(o)}$ for cylinders with no lateral motion is on figure 4 as a function of Reynolds number. This unsteady lift or side force can, depending on the natural frequency of the structure, cause lateral motions which will produce further force changes.

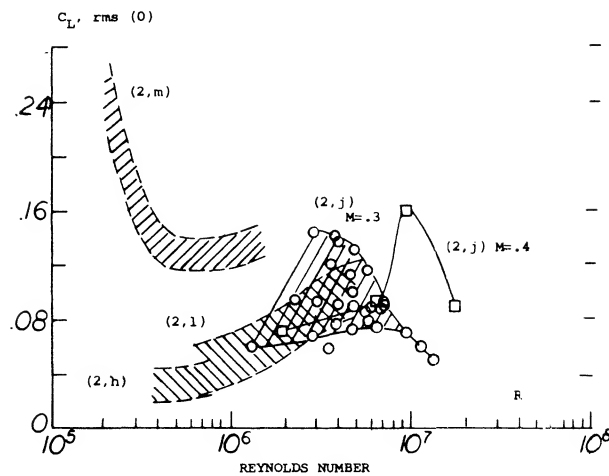


Figure 4. Unsteady lift coefficient on stationary cylinder.

Lateral Motion. The unsteady lift force on an elastically suspended cylinder as a result of lateral motion can either be stabilizing or destabilizing depending on the Strouhal number (2,c). The unsteady lift due to cylinder motion will increase with the motion when the cylinder is operating at a frequency near the Strouhal frequency for the stationary cylinder, figure 2. Below the Strouhal number for the stationary cylinder the unsteady lift force is destabilizing; while above, the unsteady lift force is stabilizing. Thus, if the natural frequency of the cylinder and its mounting is above the Strouhal number, the system will be aerodynamically damped.

Lateral motions (vibrations) of cylinders are caused by the force fluctuations discussed above, and these motions in turn amplify transient circulation and lateral forces. The amplitude of the vibrations is then maximum under conditions of resonance. As suggested in (2,f) drag may correspond to the ratio $(d + 2a)/d$, where a = value of the half amplitude of displacement, as indicated in part (c) of figure 3. As reported in (2,1) the lateral coefficient may, for example, increase from $C_{Yx} = 0.5$ to 1.0 when the cylinder displaces itself by $a = (+ \text{ and } -)d$.

Splitter Plates. As indicated in "Fluid-Dynamic Drag" splitter plates behind the cylinder will reduce the drag. Tests (3,c) have shown that splitter plates also reduce the unsteady lift and the transverse oscillations. This occurs as the strength of the shed vortices and their frequency are reduced, figure 3. Test showed that a splitter plate with a chord equal to the diameter of the cylinder to be effective.

Magnus Force. By rotating the cylinder about its axis the boundary layer that causes the periodic separation discussed above is changed. If the stream is moving from left to right and the cylinder is rotating in the clockwise direction, separation is delayed on the upper surface while the lower side of the cylinder separation occurs earlier, figure 5. As a result of the cylinder rotation the velocity is much higher on the upper surface, thus giving a lift force. This lift force would be expected to vary with the relative rotational speed of the cylinder, the free stream velocity and the Reynolds number. At a U/V equal to 4 the stagnation point front and rear coincide and theory (4,a) indicates that in two dimensions the lift per unit length is

$$L = 4\pi q d \quad (5)$$

where d is the cylinder diameter and q the dynamic pressure.

Equation 5 leads to

$$C_L = 4\pi$$

As noted in figure 1, Chapter IV this is the ideal maximum lift coefficient in two dimensional flow.

Experimental results of tests with rotating cylinders are given on figure 5 for a range of Reynolds numbers. These data indicate that after the rotational to forward speed ratio exceeds ~ 1.0 the lift increases linearly up to a speed ratio of 3.0. Above this ratio the cylinder does not appear to stall in the sense that it loses lift. In the critical Reynolds number range of 10^5 to 5×10^5 the data of (4,c) indicates a negative magnus lift. This occurs at a low speed ratio of 0.2 and appears to be caused by a bubble on the lower surface which reattaches resulting in negative lift.

- (2) Circular cylinders, vortex streets, fluctuating forces:
 - a) Cylinders, Smoke Stacks, Cables, Power Lines; Chapter IV "Fluid-Dynamic Drag".
 - b) Landweber, Analysis of Lateral Forces, TMB RPT 485 (1942).
 - c) Gerrard, Evaluation of Various Results, AGARD Rpt 463 (1963); AD-431, 328.
 - d) Drescher, Transient Pressures, Z. Flugwissenschaften 1956 page 17.
 - e) Macovsky, (Periscope) Vibrations, TMB Rpt 1190 (1958).
 - f) Boorne, Vibrations of Tall Stacks, IAS Paper 851 (1958).
 - g) Goldman, Vanguard Rocket, Vibration Bull Part II Nav Res Lab (1958).
 - h) Schmidt, Fluctuating Loads at High R'Numbers, J. Aircraft 1965 p 49.
 - i) Petrikat, Vibrations of Round Struts, W'Tunnel Rpt TH Hannover (1938).
 - j) Jones, Oscillating Circular Cylinder at High R'No., NASA TR R-300.
 - k) Tulio, Oscillating Rigid Cylinder, NASA CR-1467.
 - l) Schmidt, Fluctuating Force on Circular Cylinder, NASA June 1966 Conference.
 - m) Fung, Cylinder at Supercritical R'Number, IAS No. 60-6

Power and Drag. The power per unit length to rotate a cylinder in two dimensional flow due to the aerodynamic forces can be estimated from the equation

$$HP = C_{Df} \rho (U)^2 \pi d N / 21,000 \quad (6)$$

where C_{Df} is the skin friction drag coefficient at a Reynolds number corresponding to the tangential rotational speed and the cylinder parameter, πd . In equation 6 N is the rpm. Added to the above power, must be the mechanical power requirements due to bearings, gears, etc. As noted on figure 5, the drag coefficient is somewhat less than a cylinder at a corresponding Reynolds number. As a result of the required power for rotation and drag losses, the effective lift drag ratio of the rotating cylinder is low.

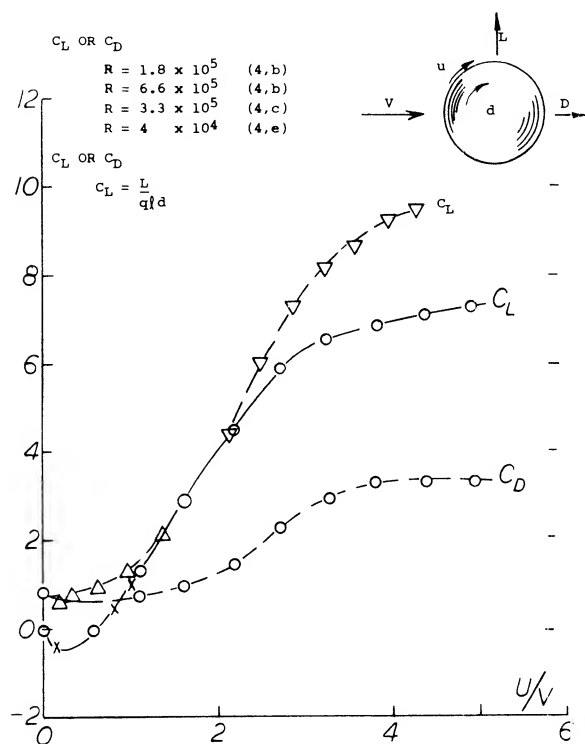


Figure 5. Lift and drag of a rotating cylinder as function of relative rotational speed, Magnus force.

Cylinders With Flaps. The addition of a flap to a non rotating cylinder has a large influence on the cylinder lift as illustrated on figure 6. Even with relatively low flap to diameter ratios as illustrated, a flap at 90° to the flow results in lift coefficient as high as 1.75. Thus, if a splitter were used to change the frequency of the vortex and severity of the fluctuating lift forces and the wind changed by 90° large values of lift could be generated as illustrated on figure 6.

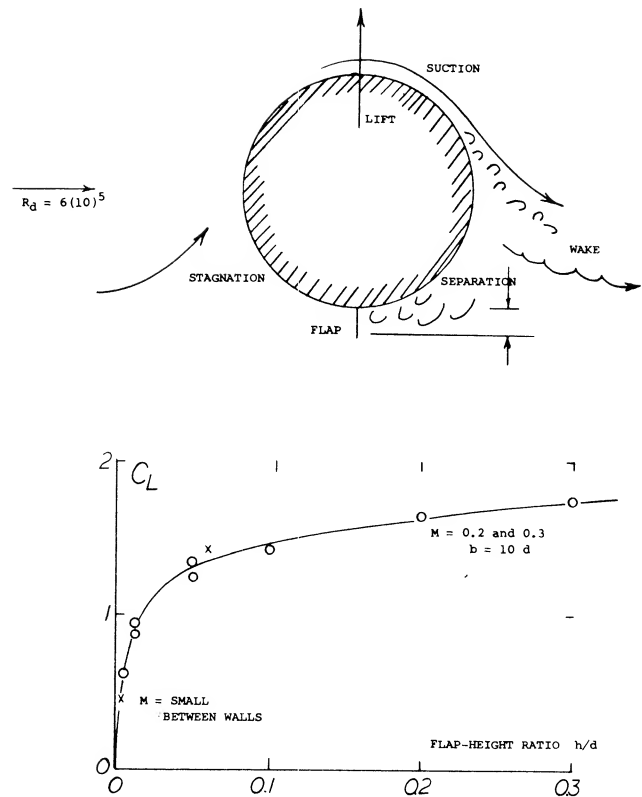


Figure 6. Lift of a circular cylinder in cross flow, induced by a small flap, extended from the lower side.

TWO DIMENSIONAL SHAPE VARIATIONS. The lift of sections in two dimensional flow other than cylinders and sections designed for good performance are often needed, as well as the lift of circular cylinders discussed previously.

Non-circular Cylinders. The flattening of the sides of circular cylinders influences the lift (5,c) as illustrated on figure 7 for variations of corner radius at $\alpha = 10^\circ$. Peak lift is obtained at a radius width ratio of 0.25 to 0.375 depending on the Reynolds number. When RN is above the critical and the radius ratio is 0.25 the lift of the cylinder approaches that for a flat plate, $2 \pi \sin \alpha$.

On figures 8 and 9 the variation of the side force coefficient C_Y with RN is given for square shapes with rounded corners, triangular and elliptical sections. The side force coefficient in this case is equivalent to the lift coefficient by the

$$C_L = -C_Y \cos \alpha$$

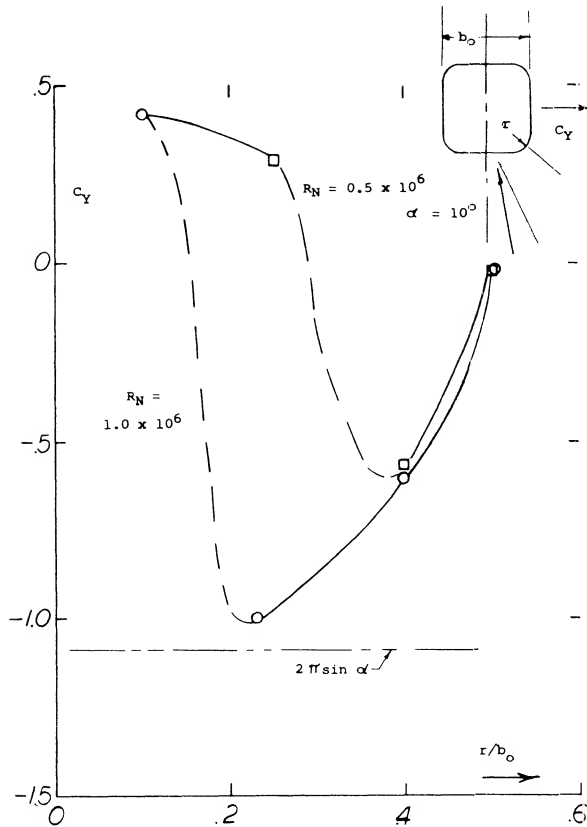


Figure 7. Side force variation of square section with rounded corners operating at $\alpha = 10^\circ$.

These coefficients are based on the width b normal to the body axis per unit length. The R_N is based on the depth of the section C_D . Below the critical Reynolds number the side forces variation is large. This large variation tends to be eliminated at R_N 's above 1.5×10^6 . The importance of separation and the corresponding formation of vortices which have a large influence are illustrated from these results.

Wedge Shape Sections. With their sharp edge leading, wedges develop lift in a manner similar to airfoils, as long as their base (thick trailing edge) is small. However, as shown in figure 10, the lift-curve slope is considerable as thickness ratio and apex angle are increased beyond a point where the geometrical similarity with any airfoil section ceases to exist. "Lift" is then again a component of drag, and its slope changes sign above $\epsilon = 50^\circ$. Considering a triangular cross section (with four included angles of $60^\circ = 2(30^\circ)$ in each corner) it is clear that within 360° there will be three angles of attack, around which the lift-curve slope is positive, and three angles where it has a maximum negative value.

- (3) Circular culinders with devices affecting circulation:
- Pankhurst, Cylinder With Thwaites Flap, ARC RM 2787 (1953).
 - Grimminger, Various Guide Vanes, TMB Rpt 504 (1945).
 - Welsh, Splitter Plate Reducing Transverse Oscillations, U.S. Navy USL Report No. 759, 1966.

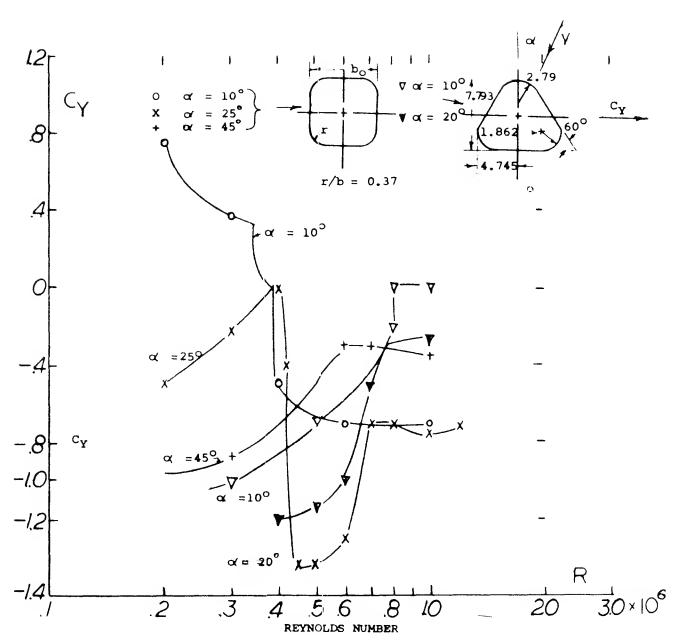


Figure 8. Side force variation with R -number for square and triangular sections for range of angles of attack.

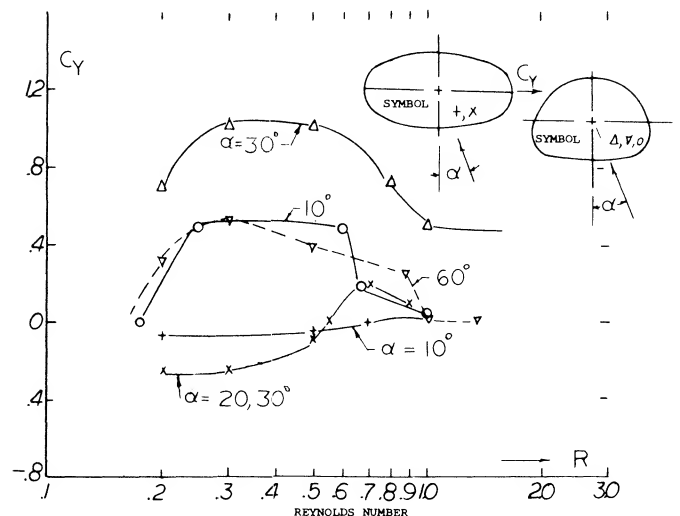


Figure 9. Variation of side force with R -number for sections with elliptical shapes.

(4) Magnus effect circular cylinders:

- Prandtl, Applied Hydro & Aeromechanics, Dover, N.Y. 1957.
- Mathews, Lift & Drag Rotating Cylinder, DTMB Report 977, 1960.
- Fletcher, Negative Magnus Forces in M Range, J of A/C Dec. 1972.
- Platou, Rotating Cylinder in Transonic Cross Flows, BRL Report No. 1150.
- Reid, Rotating Cylinders, NACA TN 209.

(5) Wedges and other prismatic shapes in cross flow:

- Lindsey, Simple Cylindrical Shapes, NACA Rpt 619 (1938).
- Polhamus, Non-circular Cylinders, NASA TR R-29 (1959).
- Polhamus, Pressures, Side Forces, Theory; NASA TR R-46 (1959).
- Tanner, Lifting Wedge Flow, German DLR FB 1965-14.
- Neilhouse, Spin Research, Fuselage Shape; NASA Rpt R-57 (1960).
- Flachsbart, Forces of Plates as a Function of Aspect Ratio and Camber, AVA Gottingen Ergebnisse Bol IV (1932).

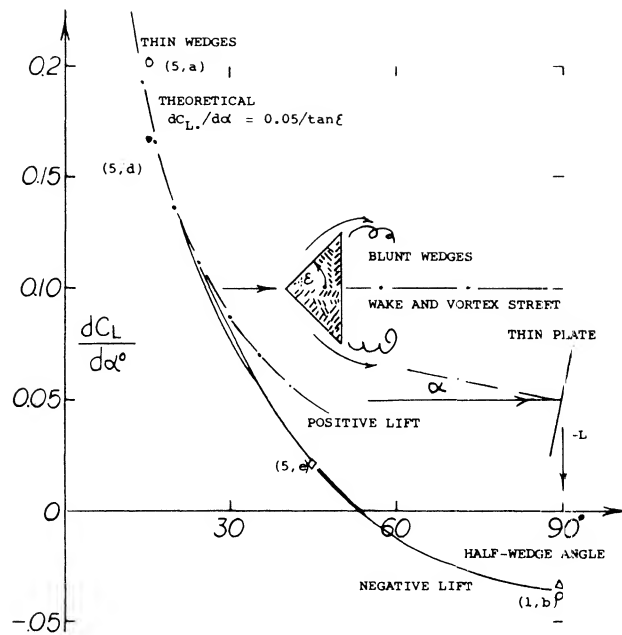


Figure 10. The lift-curve slope of sedges (in two-dimensional flow) as a function of their half-vertex angle.

Round Corners. The square cross section in figure 10 at $\epsilon = 45^\circ$, might be assumed to have the same lift-curve slope as the corresponding wedge shape. Then rounding the lateral edges of these shapes, different values are obtained, however. Pressure distributions of various more or less sharp-cornered cross-section shapes are presented in (5,b) and (5,c). Depending upon the Reynolds numbers employed, the flow tends to get around rounded corners and to produce suction forces of considerable magnitude. Prismatic shapes and their forces can be of interest in the field of structures exposed to wind. As far as airplanes are concerned, drag and lateral forces of fuselages can be important during spinning (5,e) if they get into this undesirable condition of cross flow.

Thick Airfoil. If considering a negative lift-curve slope to be the criterion for lift due to drag of blunt bodies, the 70% thick 0070 airfoil section in Chapter II must be included in this discussion. The derivative as found between tunnel walls, at $R = 6(10)$, is $dC_L / d\alpha^\circ = -0.08$, almost up to $\alpha = +10^\circ$. The flow pattern shown in figure 13 of that chapter explains this result. The minimum lift corresponds to $C_{Lx} = -0.8$. The graph also shows how unstable the flow pattern is, with fluctuations up to $\Delta C_L = (+ \text{ and } -) 0.1$.

2. THREE-DIMENSIONAL DRAG BODIES

Among drag devices in three-dimensional flow, parachutes in particular are gaining more and more importance as decelerators for high-speed vehicles.

Plates. Since the invention of sails and kites, and certainly since Newton (1643-1727), flat obstacles were known to have a force normal to the direction of the wind, which we now call "lift". The normal forces of disk and a square plate are shown in Chapter III of "Fluid-Dynamic Drag" up to angles of attack of 90° . The coefficient is constant between $\alpha = 50^\circ$ and 140° ; thus $C_N = 1.17$ and $C_L = 1.17 \cos \alpha$, which reduces to zero at $\alpha = 90^\circ$. Lift fluctuations, while irregular, are not as severe as those of cylinders or plates in two-dimensional flow. The lateral-force or lift derivative of rectangular plates (6) around $\alpha = 90^\circ$ is negative; it varies with aspect ratio and camber, as follows:

Aspect Ratio	Camber	C_D	$dC_L / d\alpha^\circ$
0.2	flat	1.20	-0.025
1.0	flat	1.16	-0.021
5.0	flat	1.20	-0.023
5.0	10%	1.22	-0.029

It might be expected that the value of the derivative corresponds to the drag coefficient. As pointed out in (10,c) the lift-curve slope of flat "wings" around $\alpha = 90^\circ$ may approximately be

$$dC_L / d\alpha = -C_D = (\pi/180) C_D \quad (7)$$

where α first in radians, and $C_{D\perp}$ = drag coefficient on frontal area. The results tabulated above show lift derivatives some 10% higher. Camber (10%, with the concave side against the wind) increases the lateral force considerably. This may be a consequence of shape, rather than drag.

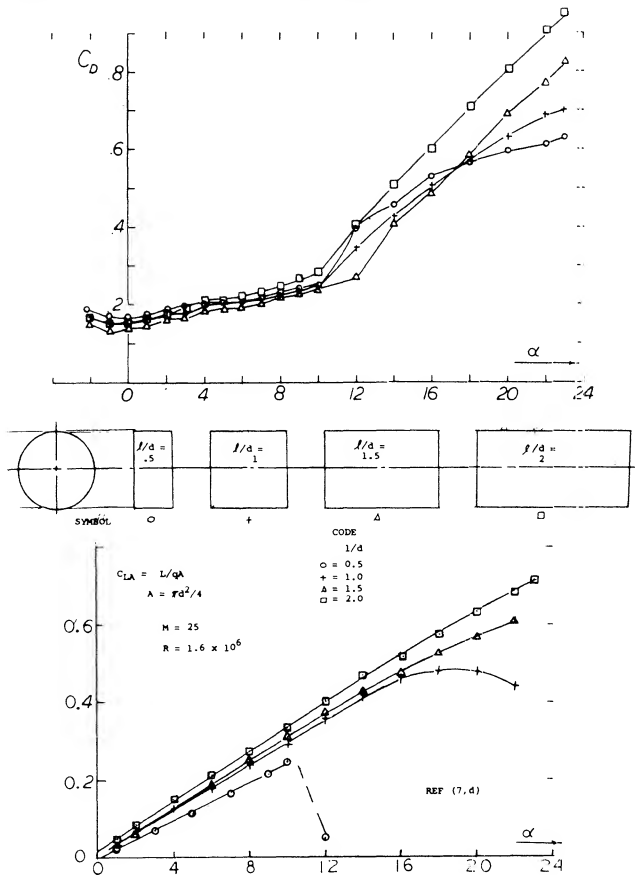


Figure 11. Lift and drag variation of bodies of revolution for range of diameter to length ratio and leading edge radius ratio.

Bodies of Revolution. The lift of bodies of revolution with a blunt nose for length diameter ratios from .5 to 2.0 (7,d) show an increase in lift slope with increasing length, figure 11.

Here

$$C_{LA} = L/qA$$

where A is the maximum cross section of the model $\pi d^2/4$. This trend is opposite to that expected based on the aspect ratio for rectangular wings, Chapter XVII, and illustrates the importance of 2α flow discussed in the streamline body chapter. For nose radius ratios of .05 to .2, $dC/d\alpha$ is essentially constant. For the body with an l/d of 0.5 the small nose radius ratio of .05 gives $C_L = -.2$ throughout angles of attack range. For the low nose radius ratio of 0.05 and l/d of 1.0 negative values of lift are also obtained. Increasing to l/d to 1.5 and above results in a positive lift as with the very blunt leading edge. Effects of other leading edge shapes on finite bodies revolution are given in Chapter XIX.

(7) Blunt ballistic reentry vehicles:

- Satellite Capsules, see Chapter XVIII of "Fluid-Dynamic Drag".
- Phillips, Blunt-faced Around $\alpha = 90^\circ$, Nasa TM x-315 (1960).
- Mugler, Lenticular Vehicle, NASA TM X-423 (1960).
- Hayes, Effects of Nose Bluntness, Fineness Ratio of Bodies of Revolution, NASA TN D-650.
- Flachsbort, Disk and Rectangular Plates, AVA Gottingen IV (1932).

Parachutes Parachutes of the old and simple type (a fabric canopy with a man hanging underneath) were not really stable. Depending upon shape, porosity and dynamic conditions (mass, size, speed, Froude number) they had a tendency of moving in an irregular pattern of swinging, coning, circling and gliding. Lift and drag coefficients of half-spherical sheet-metal models (8,b,c,d) are plotted together in (8,a). When using these "caps" as parachute canopies, a configuration as in figure 12 is obtained. At angles of attack (wind against the plane of the rim) between 70 and 100 the lift coefficient C_L . (in any direction normal to that of the wind) varies between plus and minus 0.6. The lift-curve slope is negative:

$$dC_L/d\alpha^\circ = -0.024$$

Assuming that man or load be the center of gravity of the configuration, the negative lateral-force derivative as in the equation, readily explains that the system is not stable statically. In aerodynamic language, the moment derivative (dC_m/dC_L) is positive. The same goes for a drag chute as they are used to decelerate high-speed airplanes after touching ground when landing. However, since the man below a parachute descending through the air begins to move sideways as soon as the canopy assumes an angle of deflection, a complicated system of dynamic stability is set in motion involving mass and damping of man and canopy. On top of it the flow pattern in the wake of the parachute is not steady. It exhibits fluctuations of pressures and directions, at irregular frequencies. The only stable position at which the parachute might arrive is as in figure 12. At angles of attack between 40 and 50° the flow gets around the leading edge, thus producing suction and a maximum lift coefficient in the order of -1.2 . It should be noted that V is larger than the sinking velocity U, and that the resultant force is larger (1.6) than the original drag (1.4). To say it in different words, the parachute is stably gliding, approximately at an angle of 45 corresponding to a ratio $(L/D) = 1$.

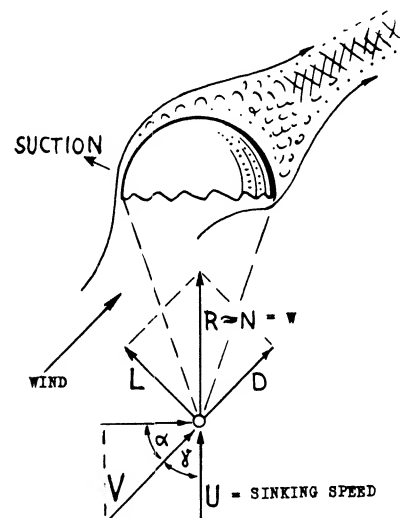


Figure 12. Sketch of flow pattern and forces acting upon a parachute when gliding; see also Chapter XIII of "Fluid-Dynamic Drag".

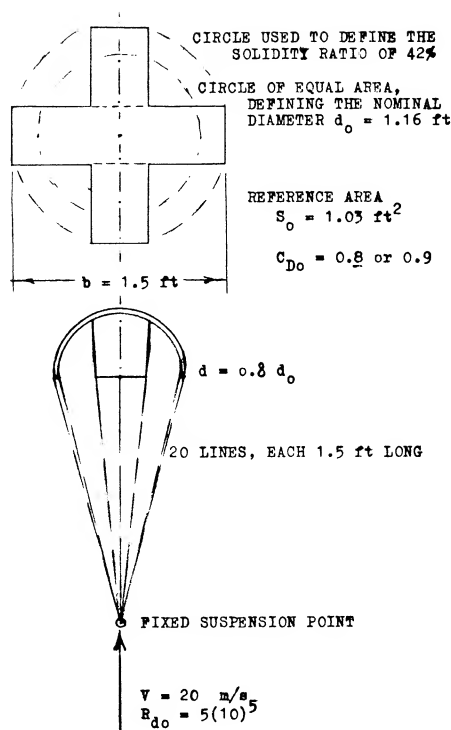


Figure 13. Shape of a special, cross-shaped parachute providing static stability between wind angles (3 and -) 15° away from vertical.

Cross Parachute. The basic fluctuations of the wake and the instability of a parachute can be minimized by porosity of the canopy (using more or less loose fabric or a network of ribbons). Another way is shown in figure 13. The cross shape (9,b) gives the wake a regulated pattern. The moment coefficient C_{m_o} is based on developed cloth area S_o and the nominal diameter $d_o = \sqrt{4 S_o / \pi}$, derived from $S_o = d_o^2 \pi / 4$. Sufficient stability about the point as in the illustration is obtained with some 30% of geometric solidity (ratio of material to open areas, "inflated" condition). The derivatives are then

$$dC_{m_o} / d\alpha^\circ = -0.011$$

$$\text{for } C_{D_o} = 0.840$$

$$dC_{Y_o} / d\alpha^\circ = +0.007$$

$$dC_{m_o} / dC_{Y_o} = -0.160$$

where Y indicates the lateral force in the canopy. This state of static stability discontinues, however, at (plus and minus) 15° away from the position corresponding to straight and vertical sinking.

Steerable Parachutes. Parachute jumping has been developed with skydiving to the point where an experienced jumper can land within a one-meter circle from 1000's of meters of altitude. The parachutes used for this purpose are steerable by means of an open sector (gore). The opening causes gliding; the rate of gliding depends upon the size of the opening. An adjustment of the two gore edges against each other makes the parachute turn. Both of the motions are controlled by the "pilot" with the help of his arms and hands through a pair of lines. The cross-type parachute as in figure 13 could also be steered by controlling one of the four gores. However, while one of these schemes (10,a) provides only a maximum $L/D = 0.6$, a more complicated configuration was developed (10,c) having an L/D ratio of 2, which is twice as high as found in optimum single-canopy designs. What we really have in this parachute is an inflated wing (made out of cloth) with an aspect ratio in the order of 2. Such devices are discussed in Chapter XVII.

Man in Free Fall. The forces and moments of a parachutist in free fall have been determined from wind tunnel tests (11,a,b). These tests indicate that during "sky diving" trim is obtained only at fairly high values of angle of attack, which appears to agree with the actual results. At these high angles the best L/D of approximately 0.61 is obtained at an angle of attack of 40 to 45° with the arms along side of the body, the legs spread at an angle of 16° and the legs bent at the hip so as to give the body camber with a negative angle with respect to the back of approximately 60°, figure 14. At this condition the lift coefficient is approximately 0.35. The lift drag ratio for the trimmed condition is 0.55.

The coefficients

$$C_L = L/qS, \quad C_D = D/qS, \quad \text{and} \quad C_M = M/qSl$$

where S is the area based on the man's height l and shoulder width. The reference length noted in the moment equation is the height. The wind tunnel test results are given on figure 14 for the man in the best position to give peak L/D as well as other typical positions of possible interest.

Based on the drag the effective aspect ratio is about one half the apparent value. The lift curve corresponds to the function $1.6 \sin^2 \alpha \cos \alpha$. This value is somewhat less than would be predicted in Chapter XIX.

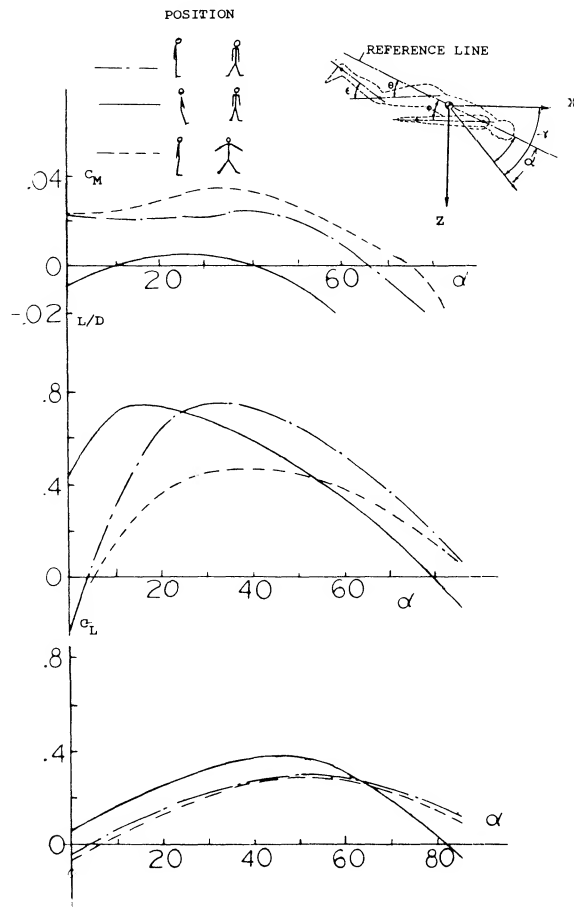


Figure 14. Lift, moment and L/D of a man in a free fall for various positions of arms and legs.

- (8) Characteristics of "cups" and "caps":
 - a) See in Chapter XIII of "Fluid-Dynamic Drag".
 - b) Hansen, Sheet-metal Caps, AVA Gottingen Ergebnisse Vol IV (1932).
 - c) Breevort, Forces on Anemometer Cupt, NACA TN 489 (1934).
 - d) Doetsch, Sheet-metal Parachute Models, Luftforschg 1938 p 577.
 - e) Babish, Two-dimensional Flow Pattern, FDL-TDR-1964-136, AD-461, 342.
- (9) Lateral forces and stability of parachutes:
 - a) See references in Chapter XIII of "Fluid-Dynamic Drag".
 - b) Niccum, Cross-type Parachutes, U/Minn Rpt FDL-TDR-1964-155, AD-460, 890.
- (10) Experiments with steerable parachutes:
 - a) Gamse, Parachutes With "Flaps", NASA TN D-1334 (1962).
 - b) Kinzy, Gliding Parachute, Northrop Venutra Rpt 2818 (1960).
 - c) Riley, Gliding & Turning, Northrop Rpt FDL-TDR-1964-81, AD-453, 219.

Radar Screens. Radar screens are structures similar in aerodynamic shape to parachutes. They are usually very porous; that is, their solidity ratio is small (for example, in the order of 40%). However, the parabolic reflector shown in figure 15 is solid. As a function of the yaw angle β (measured against the center axis of the circular screen) maximum forces correspond to the coefficients (based on total frontal area, at $\beta = 0$).

$$C_{D0} = 1.08 \quad \text{at } \beta = 0^\circ$$

$$C_{Y0} = -.41 \quad \text{at } \beta = 40^\circ$$

The lateral force is negative in comparison to a positive angle of yaw. Considering flow in the opposite direction (against the convex side) maximum values are

$$C_{D0} = 0.85 \quad \text{at } \beta = 0^\circ$$

$$C_{Y0} = -.14 \quad \text{at } \beta = 30^\circ$$

The lateral force is negative again, evidently on account of negative "base" pressure and some suction, as indicated in the illustration.

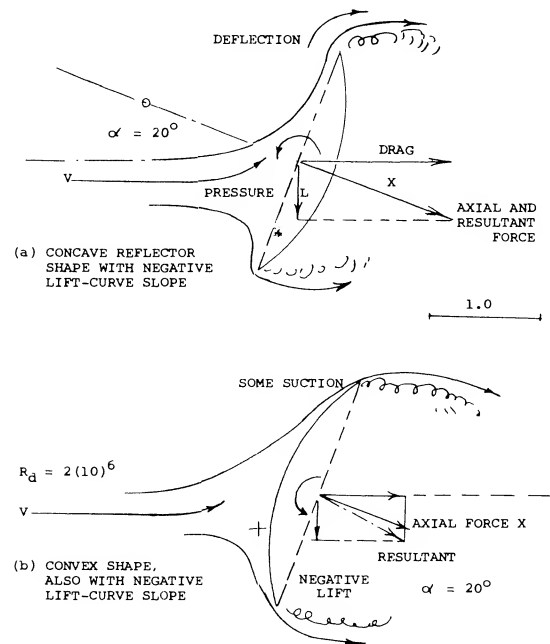


Figure 15. Forces on a reflector "dish", tested (12,b) at $\alpha = 20^\circ$, both with the concave and the convex side ahead.

- (11) Wind Tunnel test on human beings:
 - a) Oehlert, Trajectory Control, Parachutist in Free Fall, Wichita State Univ, Report AR 67-1 (1967).
 - b) Schmitt, Air Loads on Humans, David Taylor, Report 892, Aero 858 (1954).

Half Sphere. When reversing the direction of flow against a "cap" we obtain the flow pattern around a half sphere, as in figure 16. Drag and lift coefficients are plotted in polar form. The lift-curve slope is negative; between (+ and -) 10 (in the definition as shown) it is found:

$$dC_{L_s}/d\alpha^\circ = -0.01 \quad (8)$$

Lift also remains negative up to angles above 85° . The moment around $\alpha = 0^\circ$, about the center of the sphere, is given by

$$dC_{m_d}/d\alpha^\circ = -0.0007 \quad (9)$$

$$dC_{m_d}/dC_L = +0.700$$

Lift and moment are thus "unstable". Drag may correspond to $C_D = 0.4$, plus $C_{Di} = C_L^2/\pi A = C_L/4$. For practical purposes $C_D = 0.4$ for α between (+ and -) 20° . The open cup (hollow half sphere) also plotted in figure 16 shows somewhat different coefficients, in particular less drag at α between +20 and -20° . Besides the open base (bottom) the Reynolds numbers is likely to have an effect upon the flow pattern.

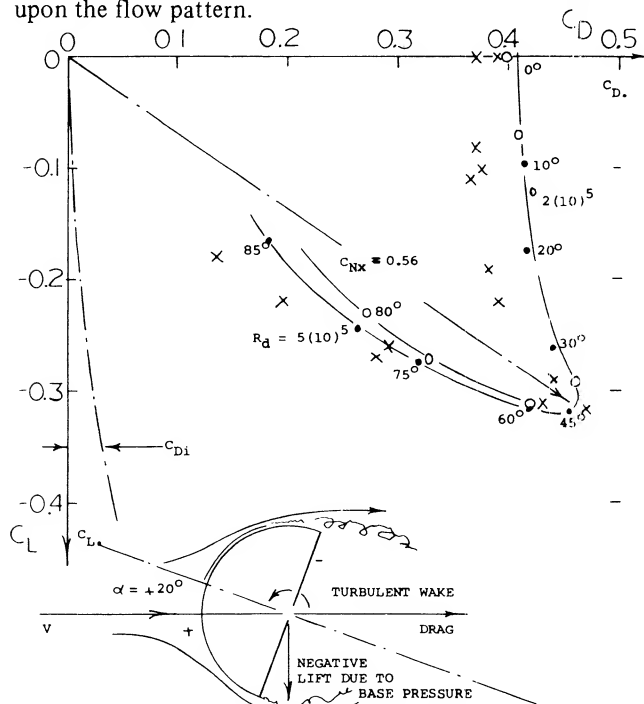


Figure 16. Drag and negative lift of a half sphere (8,b) at positive angles of attack, in the definition as shown, between zero and 80° .

(12) Experiments on radar antenna models:

- a) Bicknell, Parabolic Antenna, MIT Lincoln Lab Rpt 71-G-5 (1962).
- b) Fox, Series of Porous Reflector Antennas, CalTech Jet Prop Lab Memo Rpt CP-3 & 4 (1962); see also CP-6 and NY Acad Sci Antenna Conf Proceedings (1963).
- c) Sherwood, Two Full-size Radar Antennas, TMB Rpt 322 (1947).
- d) Williams, Radar Reflectors, ARC-NPL Rpt Aero-250 (1961).

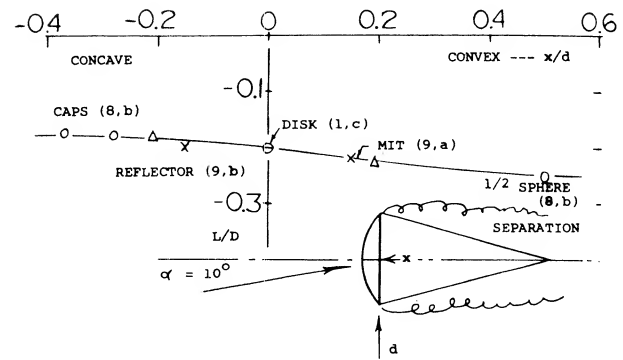


Figure 17. Lift/drag ratio of a hypothetical "capsule", as a function of the curvature of its blunt face (similar to the heat shield of a ballistic vehicle).

Gliding. Satellite capsules such as those developed in the United States (7) can also be steered when re-entering, in longitudinal and/or lateral direction, by means of the high pressure forces on their blunt heat shield. This happens at supersonic speeds; the principle is the same, however, as in figure 15,b. Some kind of diving capsule could also be designed to be used in deep water. The gliding angle could be controlled either by shifting a weight inside, or by adjusting the angle of attack (against the water with the help of a flap, for example). Some (L/D) values are plotted in figure 17. This value is approximately proportional to the angle of attack as against the body axis. There would be a limiting angle, however, where the flow gets attached to one side of the afterbody assumed to be conical. It should also be noted that with the CG behind or above the blunt front end, vehicles of this type are likely to be stable.

Cones. In a manner similar to the lift of the wedges in figure 10 the normal-force derivative of cones (with their point against the wind) reduces as the cone angle is increased. The experimental data plotted in figure 18 have been extended. For small cone angles, equation (3) in (12,b) can be applied. At $\epsilon = 90^\circ$, we have a thin disk as in (7,e). Its force normal to the axis is zero. The center of forebody pressure is roughly obtained as indicated in the sketch. It moves from $x/d = 0.97$ (ahead of the base) for $\epsilon = 10^\circ$, to -0.47 (behind the base) for $\epsilon = 50^\circ$. In reality, the cones also have a negative base pressure, contributing to drag, and providing a negative component of lift (at right angle to the direction of the wind) similar to that in figure 10 at larger angles.

Rotating Spheres. The motion of spinning tennis, golf and base balls show that lateral forces are developed that cause them to curve in flight. For instance, it has been shown (14,b) that a regulation baseball as used in the National or American Legues which weighs between 5 and 5¼ ounces and is 9 to 9¼ inches in circumference will move as shown

speed $V = 100$ ft/sec
 spin $n = 1200$ rpm
 distance $x = 60$ ft
 "curve" $y = 1$ foot

The spin of 1200 rpm means a speed ratio of $w/V = 0.15$. The speed corresponds to a Reynolds number based on diameter of $R_D = 5.7(10)^5$ which would result in a flow pattern above the critical.

Test data (14,a,c) on the lift and drag coefficients measured on smooth rotating spheres is given on figure 19. These data essentially confirm the results given in "Fluid Dynamic Drag" and show a C_{Lx} of between 0.4 and 0.45.

As in the case of a rotating cylinder, the lift and drag coefficients are dependent on the rotational speed ratio w/V . This ratio is important as it effects the separation on the cylinder and thus the lift. Since the lift is dependent on the separation points on the upper and lower surfaces it would be expected that surface roughness and Reynolds number would effect the results. Qualitative data is not available for an evaluation.

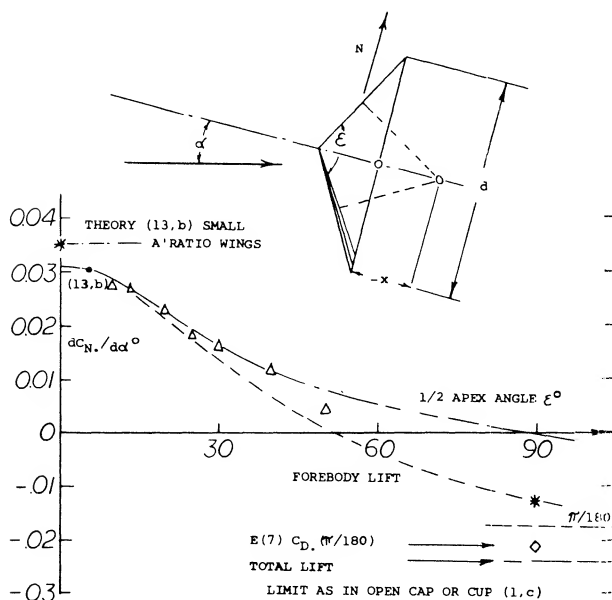


Figure 18. The variation of the normal force of cones (13.a) between $\alpha = \text{plus and minus } 10^\circ$, as a function of the half-apex angle.

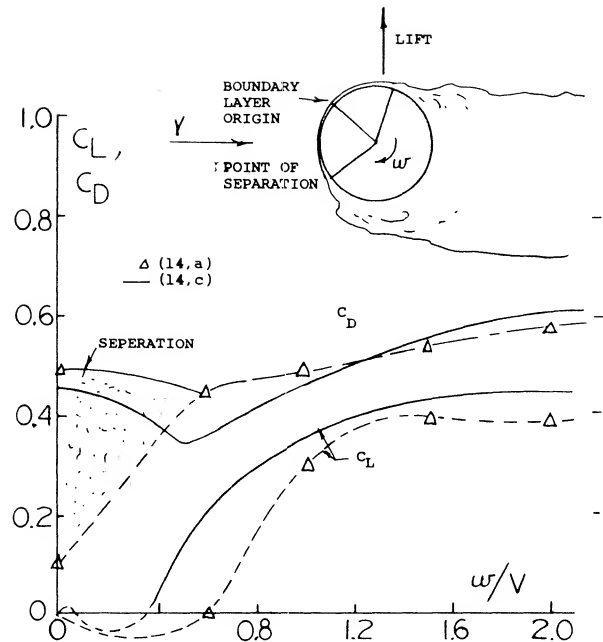


Figure 19. Lift and drag variation of spheres as a function of their relative velocity.

3. LIFT IN GROUND VEHICLES

Normally when considering the forces acting on ground vehicles the drag force is of primary concern, as this effects the power required. The variation of the drag force of representative vehicles with variations of shape are covered in "Fluid-Dynamic Drag" and (15,a). The lift forces produced by a vehicle can be important, especially if we consider the side force to be lifted as in the case of a vehicle operating in a cross wind. In this case, the side force will effect the stability and handling characteristics of the vehicle.

(13) Lifting characteristics of cones moving point-first:

- a) Owens, Large of Cones $M = 0.5$ to 5.0 , NASA TN D-3088 (1965).
- b) See results in the "wing and body" chapter.

(14) Lateral forces on revolving spheres:

- a) See "Drag Due to Lift" in Chapter VII of "Fluid-Dynamic Drag".
- b) Briggs, Deflection (curve) of a Baseball, NBS Rpts 1945 and later, NY Times "Sports" 29 Mar 1959.
- c) Niccum, Lift and Drag of a Rotating Sphere, Dept of Aero & Mech, U of Minn. 1964.

Automobile Lift. The lift coefficient of the conventional passenger car is given on figure 20 as a function of angle of attack. Here, the lift force, L , is that tending to decrease the weight of the vehicle on the road

$$C_L = L/qS_f \quad (10)$$

where S_f is frontal area of the car.

Even at an angle of attack of zero automobiles have a positive lift coefficient of 0.3. This is due to their basic shape, which is effectively cambered. The lift curve slope is high and shows the importance of ground effect. Although the lift coefficients for the automobile are high, the actual lift is very small in comparison with the weight of the basic car. For instance, even at 90 MPH and a lift coefficient of 1.0 the actual lift force is only of the order of the weight of one passenger. This is small considering automobiles in the 3 to 4000 weight class.

The more important lift force on an automobile is that produced in a cross wind. Although the side force coefficient is the same order of magnitude as the lift force, figure 21, it is more significant as it will effect the directional control of the car. It should also be noted that the actual lift coefficient of the car increases with yaw angle. An increase up to 0.5 due to a yaw of 25° (15,c). The importance of the side force is due to the variation of the force due to sudden changes. For instance, when operating a light weight car or trailer in a cross wind, the passing of a large truck can cause a sudden side force change of 50 to 200 pounds. This can cause sudden unwanted direction change, which can be dangerous. Thus, automobile shapes which minimize the side force are desirable. The large side force produced by trucks causes a side-wash change in the direction of the air, which is also a safety problem.

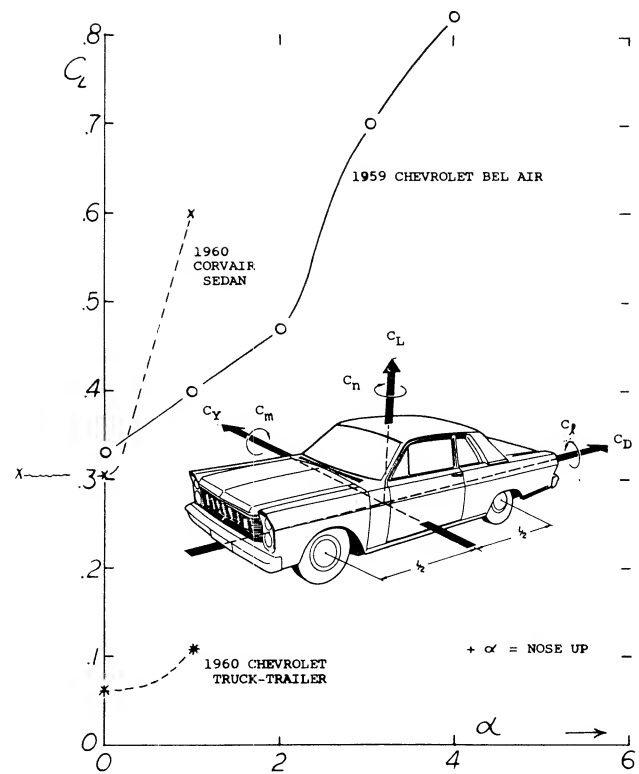


Figure 20. Lift coefficient of standard type automobiles as a function of angle of attack.

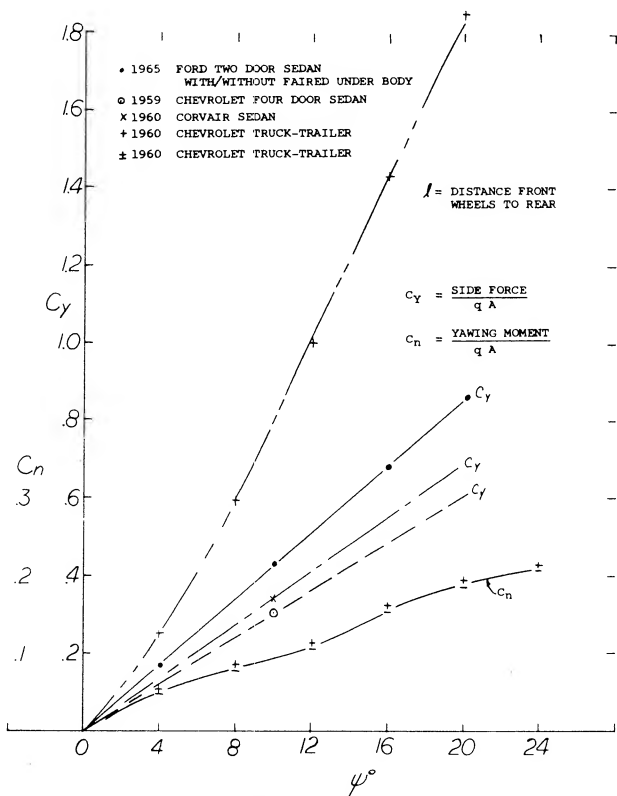


Figure 21. Side force coefficient of standard type automobiles as function of yaw angle.

(15) Ground vehicles lift and side force:

- Turner, Automobile Test Moving-belt, NASA TN-D-4229.
- Flynn, Truck Aerodynamics, SAE Preprint 284A, 1961.
- Whitcomb, Aero Forces on Critical Speed of Automobiles, CAL Report No. YM-2262-F-1 (1966).

4. LIFT FORCES ON STRUCTURES

The drag force produced on fixed buildings or structures is considered in Chapter IV of "Fluid-Dynamic Drag". The lift force generated on the structure is also an important design element, especially in the design of roofs and structural overhangs. Also, the lift force produced on smaller objects is important as these can become airborne and cause damage under certain conditions.

Ambient Wind Characteristics. To determine the wind generated loads on buildings, the worst ambient conditions that would occur in a given time span are used. These would be, for instance, the worst mile of wind over a period of say 50 years and would not necessarily include the winds generated as a result of tornados or hurricanes. In certain instances it is necessary to consider the forces and pressures generated as a result of tornados and hurricanes where a large loss of lift might be involved.

Fastest Mile Wind. The average speed of one mile of air passing an anemometer is defined as the fastest mile wind. This definition is used as a basis for design so that the effects of gusts that are small with respect to the structure will be eliminated. Charts of the occurrence of the fastest mile-speed are given for the United States at a height of 30 feet above the ground (16,b). In calculating the loads due to the fastest mile wind corrections are made for the exposure, wind profile gradient as a function of terrains and gusts, figure 22. The velocity at any height is determined from the equation

$$V_Z = V_G (Z/Z_G)^{1/\alpha} \quad (11)$$

where V is the velocity at any height Z and V_G and Z_G are standard values adopted (16,a) for various terrains, figure 22, and are given in the table

Terrain	Z_G (ft)	$1/\alpha$
Open Country	900	1/7
Suburban	1200	1/4.5
City	1500	1/3

At altitudes above Z_G the gradient velocity is assumed to be constant.

The effect of the direction of the exposure and gusts are covered by various standards (16,a,b) and should be used to find the true speed for finding the loads on a given structure.

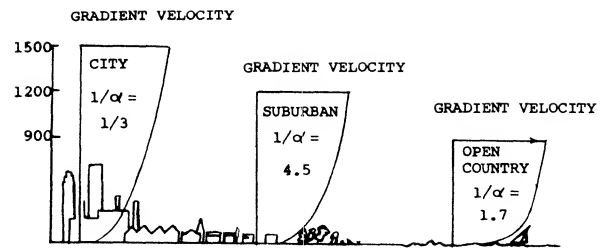


Figure 22. Wind profile variation with height for city, suburban and open country locations.

The characteristics of hurricanes and tornados are needed for the design of structures such as atomic power plants, and associated structures.

Hurricanes (16,b). Hurricanes are defined as tropical cyclones with a speed of at least 74 mph. The wind field is a function of the radius of maximum winds, the central pressure difference and forward speed. The strongest winds occur along the rim of the eye near the wall cloud. The wind speed will often reach a speed of 100 to 135 mph with winds of over 200 mph occurring in severe storms. The damage on structures produced by such high winds where the dynamic pressure can exceed 50 is usually severe.

Tornados. One of nature's most violent phenomena is the tornado. Although its horizontal extent is small it is characterized by a visible funnel, which contains dust and debris extending downward from the base of a cumulonimbus cloud of a thunderstorm. The winds and motion of air in a tornado vortex can be divided in four components: translational, rotational, vertical and radial. At the ground level the translational and rotational components are most significant. The translational speed of a tornado is anywhere from 0 to 70 mph with the usual speed being 40 to 45 mph. The maximum rotational speeds are believed to be based on wind damage estimates from 200 to 300 mph. With q 's up to 230 psf widespread damage is certain. In the core of the tornado the pressure can be 3 psi below the ambient. With this low pressure and the high winds, large objects can become airborne and cause large amounts of damage when striking stationary structures.

(16) Lift in buildings and structures:

- American National Standards Institute, Standard Building Code Requirements, ANSI A58.1-1972.
- Defense Civil Preparedness Agency, "Multi Protection Design" TR-20 (Vol 6) Dec 1973.
- Ackeret, "Aerodynamics in Structural Engineering" RAE LT 1185 (1965).

Lift in Structure Design. The lift forces generated on the various parts of a building must be determined and considered in their structural design. These forces can be as important as the drag forces discussed in "Fluid-Dynamic Drag" and generally are more poorly understood (16,c). The lift forces on a structure generally effect the roof design as large negative pressures in combination with positive pressures, as illustrated on figure 23, produce high loads. Based on the effective pressure as determined based on the fastest mile wind corrected for height, terrain and exposure as discussed previously, the effective dynamic pressure is calculated from the equation:

$$\begin{aligned} q_F &= K_Z G q \\ q_P &= K_Z G q \end{aligned} \quad (12)$$

where q is the basic wind pressure based on the fastest mile of wind at a height of 30 feet. K_Z is the velocity pressure coefficient at height Z from equation (12) and G is a gust factor (16,b). The subscripts F and P correspond to the effective velocity pressure for the full building or a part.

Based on q_F or q_P above, the standards have been generated (16,a) for establishing the pressure coefficients. These depend on the type of roof. A C_P of -0.7 is typical of gable roofs on the leeward slope. At ridges, eaves and sharp corners the C_P varies from -1.7 to -5.0 . In addition to (16,c) estimates of C_P can be estimated from the data given in Chapters II, III and XVII.

Tall Buildings, Towers, Stacks. Structures that are tall where the height exceeds the base by a factor of 5 or greater can be subjected to dynamic effects. For instance, round smoke stacks can have a natural frequency near the vortex shedding frequency as determined using figure 2&4. Similar problems are found with other tall structures and should be checked.

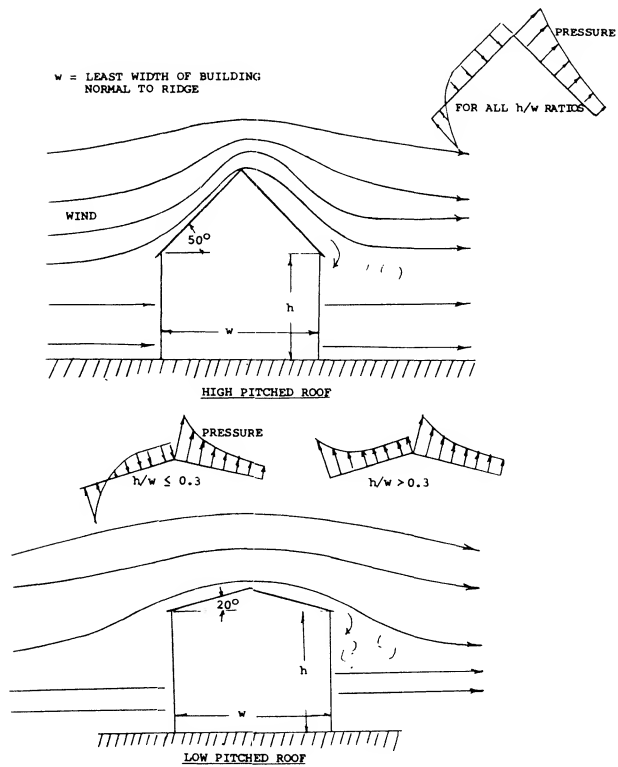


Figure 23. Wind pressure distribution on low and high pitched roofs.

SYMBOLS

SYMBOLS IN EQUATIONS AND GRAPHS. With some exceptions, the symbols employed throughout this book are those accepted or recommended by the NACA, NASA, and the American Standards Association (1).

“Fluid-Dynamic” Dimension

A	area
b	wing span (or width of a body)
c	chord of airfoil section
d	diameter of a body of revolution
δ	total boundary-layer thickness
f	camber height
h	height of a body; also TE thickness
k	diameter of sand grain (also other meanings)
l	length of a body (in x-direction)
S	area (“wing” area if without subscript)
t	maximum foil-section thickness
Δ	momentum thickness of boundary layer
x	length of forebody (to max. thickness)
x	dimension in direction of flow
Y	lateral distance
Z	altitude above sea level
Z	vertical distance

“Fluid-Dynamic” Ratios and Factors

A	$= b/S$ = aspect ratio of wings
λ	$= l/A$ = length ratio = “c”/b
e	indicating effective aspect ratio
f/c	camber ratio of foil sections
k	specific heat ratio in gasdynamics
k	constant or factor (used in many definitions)
K	constant or factor (used in many definitions)
l/d	fineness ratio of body revolution
σ	indicating solidity ratio
t/c	thickness ratio of sections

Terms Associated With Speed

a	speed of sound
V	flow- or flight speed (between body and fluid)
w	local velocity at specified point of a body
w	downwash velocity (behind wings)
w	internal velocity (in ducts)
M	$= V/a$ = Mach number, with ‘a’ = sonic speed
R	Reynolds number (always with subscript)
ρ	$= \mathcal{V}/g$ = mass density of the fluid
q	dynamic pressure
“q”	impact pressure
“P”	Prandtl factor (see chapter XV)
P	engine power (usually in HP)
T	absolute temperature (in degrees “Kelvin”)
T	thrust of propeller or jet engine
p	absolute static pressure in
f	vortex frequency (per second)
“S”	Strouhal number = $f l/V$
μ_o	viscosity of air

Fluid-Dynamic Coefficients & Forces

D	drag (or resistance), in “x” direction
C_{Di}	for induced drag (of wings)
C_{Ds}	for profile or section drag (of wings)
$C_{D\bullet}$	based on frontal area of body
$C_{D\sigma}$	on circumscribed area
$C_{D_{wet}}$	on wetted surface area of a solid
C_f	skin friction drag (on wetted area)
L	lift (in “y” or “z” direction)
C_L	lift coefficient = L/qS
N	normal force
C_N	normal force coefficient N/qS
C_p	$= \Delta p/q$ = pressure coefficient
Γ	$= 0.5 C_L V c$ = circulation about foil section
T	thrust force
T_c	thrust coefficient T/qS
C	momentum coefficient psw/qS
Y	lateral force
C_Y	lateral force coefficient Y/qS

Fluid-Dynamic Moment Coefficients & Moments

C	flap hinge moment
"L"	rolling moment
C	rolling moment coefficient
M	pitching moment
C _m	pitching moment coefficient M/qbs
C _{m/4}	pitching moment about quarter chord
N	yawing moment
C	yawing moment coefficient N/qbs

Geometrical and Other Angles

α°	angle of attack wings bodies, etc. — degrees
α	angle of attack, radian
β	angle of sideslip
Γ	angle of dihedral (of wings) (tail)
Λ	angle of sweep (of wings)
δ	angle of deflection of flaps
ϵ	half vertex of cone or wedge shapes
ϵ	downward angle
ψ	angle of yaw

In Shipbuilding and Vehicles

l	water-line length of a ship
l	average wetted length of planing surface
b	beam of the hull
h	draft or submergence
D	resistance = drag
W	weight
Δ	displacement in long tons (2240 lb each)
C	prismatic coefficient
F	Froude number (see equation 1-41)
σ	cavitation number
	displacement (volume)

General Subscripts and Exponents

amb	indicating ambient condition
av	indicating mean "average"
crit	critical (Reynolds or Mach number)
eff	or "e" = "effective"
min	indicating "minimum"
n	a general exponent
o	original condition
opt	= optimum, as defined in text
x	or "max" for "maximum"
x	for distance from L'edge or nose

Specific Subscripts

a	indicating "added" or "attached"
b	indicating reference area b
B	for "base" (also propeller blade)
c	indicating reference area c
comp	=compressible or compressive
Δ	indicating displacement
f	for "frictional" (also for "fuselage")
H	for horizontal tail
i	indicating "induce" (also "effective")
inc	indicating "incompressible"
lam	= laminar (boundary layer)
lat	for "lateral" forces
m	indicating main body (also as exponent)
M	for momentum (internal flow)
N	indicating "normal" force
O	on "developed" parachute area
p	for pressure, also indicated by "P"
P	propeller
t	indicating reference area t
turb	= turbulent (boundary layer)
w	pertaining to speed "w"
W	indicating "weight" or "wave"
wet	= wetted area (in contact with fluid)
x	or "ext" for external
•	indicating frontal area of body
\square	on circumscribed area

ALPHABETICAL SUBJECT INDEX

- Aerodynamic center 1-4, 2-22, 11-21, 18-8
 Aerodynamic chord 11-4, 11-5
 Aileron characteristics:
 effectiveness 10-2, 10-6, 10-7
 lift curve 10-4
 stick force 10-5, 10-7
 types 10-2, 10-6, 10-7
 Ailerons — swept wings 10-7
 Aircraft control flaps 9-1
 Airfoil characteristics
 basic geometry 2-1
 circulation 2-5
 efficiency 2-12, 4-18
 leading edge effects 2-8
 lift 2-1
 lift — angle 2-13
 moment characteristics 2-21
 stability 11-34
 stall 4-2
 symmetrical types 2-2, 2-15
 testing 2-4
 thickness influence 2-9, 2-16
 trailing edge shape 2-10
 Airfoils:
 at low Reynolds number 2-17
 British types 2-4
 computer designed 2-17, 2-18
 German types 2-5
 in cascade 2-19
 mean camber line 2-1, 2-14
 NACA 4-digit series 2-2
 NACA 5-digit series 2-3
 NACA 6-digit series 2-4
 Whitcomb type 2-19
 Wortman type for sailplanes 2-18
 Airplane configurations 20-1
 Airplane performance 1-17
 Airplane total lift 20-1
 Airship lift 19-12
 Airship lift — with/without fins 19-21
 Airspeed — equivalent 1-18
 Akron airship 19-28
 Alpha flow-two 3-12, 19-3, 19-5, 20-14
 Angle of attack 1-8
 Aspect ratio characteristics:
 effective 20-8
 effects on maximum lift coefficient 17-15
 effects swept wings 15-9
 flaps 9-9
 hydrofoil struts 8-17
 Augmentation by jets 5-25
 Augmentation — wing lift 12-13
 Automobile lift 21-11, 21-12
 Auxiliary airfoils 6-2
 Biconvex airfoil 6-14
 Biplane — wing design 20-9
 Block coefficient 19-15
 Blowing — boundary layer control:
 flaps 5-30
 over flaps 5-26, 5-30
 rate 5-28
 upper surface 12-14
 Blunt trailing edge airfoils 2-9
 Boat tail 19-20
 Body axis — reference 1-7
 body induce lift 16-8
 body lift 20-14
 Boeing KC-135 airplane 1-19
 Boeing 727 transport aircraft 20-3
 Boeing 747 transport aircraft 20-4
 Boundary layer characteristics:
 airfoils 2-11
 control 5-24, 5-26, 6-1, 6-18, 6-25
 control rain effects 6-21, 6-22
 control — suction 6-19, 6-24, 6-26
 separation 4-2
 thickness 4-5
 transition 4-4
 transition airfoils 2-13
 transport — swept wings 16-5
 Boxplane 8-9
 British airfoils 2-4
 Bubble bursting 4-4
 Buffeting — swept wings 16-15

Camber characteristics:		
effects — delta wings	18-11	
effects on C_{Lx}	4-9, 4-11, 4-12, 4-17, 4-21	
effects — wing tunnel	4-9	
reflexed — moment	2-22	
Canard aircraft:	20-13	
delta wings longitudinal stability	11-32	
principles — longitudinal stability	11-27	
stability	11-30	
Cargo aircraft	20-5	
Cascade effects	2-20	
Cavitation	1-13, 8-18	
Cessna 150	20-1	
Chord extension flaps	5-12	
Circulation:		
airfoils	2-6	
arc section	4-5	
lift	2-6, 18-10, 19-1	
Climb and descent performance	1-17	
C_{Lx} , Maximum lift — wedge	4-3	
C_{Lx} , NACA 63 — 64 sections	4-17	
Coanda effect	6-28	
Compressibility:		
effects	7-1	
effects lift curve	7-4	
effects-moments	7-6	
effects — wings & tail	7-7	
flow — delta wings	18-19	
low aspect ratio wings	17-12, 17-13	
Cones — elliptical	19-2	
Cones — lift	21-10	
Control characteristics:		
aircraft flaps	9-1, 9-13	
delta wing flaps	18-16	
hydrofoil flaps	8-10	
Control tabs	9-23	
Cooper ratings	14-16	
Corrugated surface	4-21	
Cranked wings	15-10	
Critical Mach number	7-3, 15-20	
Critical Reynolds number	4-12	
Critical sweep angle — stability	16-6	
Critical velocity	7-2	
Curvature streamline bodies	19-19	
Cutlass aircraft	13-15	
Cylinders lift characteristics:		
cross flow	19-9, 19-10	
rotating	21-3	
with flap	21-4	
Delta wings — double slotted flaps	18-16	
Delta wings with bodies	18-13	
Descent — climb performance	1-17	
Design lift coefficient	2-15	
Diamond wings	18-2	
Dihedral — wing and tail:		
effects in roll and yaw	14-6	
lateral force	14-5	
“V” shape	3-3	
Directional characteristics:		
aircraft	13-1	
control	13-27	
fuselage	13-4, 13-6	
Discus — performance	17-8	
Displacement — hydrofoils	8-12	
Dornier flap	5-21, 5-22	
Dorsal fin	13-24, 19-23	
Double edge airfoil	4-2	
Double slotted flaps	5-21, 5-22	
Douglas DC-9	20-3	
Downwash:	3-2, 5-37, 11-16	
at horizontal tail — propellers	12-19	
flaps	5-36	
jets	12-21	
wing	11-15	
Drag divergence	7-4	
Drag flaps	5-14	
Drag streamline bodies	19-11	
Drag — wing tips	3-8	
Duct Stall, Moments	12-6	
Duct streamline bodies	19-15	
Ducted fan lift	12-6	
Ducted propeller	12-12	
Dutch roll	14-14, 14-15	
Dynamic lift stall	4-24, 4-25	
Dynamic pressure	7-2	
Dynamic stability:	1-16	
lateral	14-11	
longitudinal	11-3	
Effective aspect ratio	20-17, 20-19	
Effective span	3-13	
Effectiveness flaps	9-2	
Effectiveness — tail	13-8	
Efficiency — intake jet engines	12-23	
Efficiency jet flaps	5-33	
Ellipsoid	17-8	
Elliptical lift distribution	3-2	
Elliptical sections	2-6	
Elliptical wing shape	3-6	
End plate effect — fuselage — tail	13-8	
End plates — wings	3-9, 3-10	
Endurance — Performance	1-20	
External flaps	5-11	
Deep stall — “T” tail aircraft	16-20	
Deflection angle flaps plain	5-5	
Delta wings	18-1	
Delta wings double	18-12, 18-18	

- Fastest mile wind 21-13
 Fences — swept wings 16-12
 Fighter aircraft 20-4
 Figure of merit — takeoff 1-17, 5-17
 Fillets 20-16
 Fillets — wing fuselage 11-8
 Flap characteristics:
 angle critical — stall 5-20
 chord ratio 5-5, 5-27
 deflection angle 5-5
 double slotted — $C_{L\alpha}$ 5-21, 5-22
 effectiveness 5-4
 for takeoff — setting and selection 5-18
 full span 5-20
 hinge moments 5-24, 9-4, 9-6
 increment, slope 5-5, 5-8
 load distribution 5-42
 loading 5-39
 part span inboard 5-15
 part span outboard 5-16
 selection angle, takeoff and landing 5-18, 5-19
 size influence on lift 5-27
 slot lip 5-14
 small aspect ratio wings 17-9
 theory 6-11
 thick wings 5-17
 trailing edge 5-1
 triple slotted — $C_{L\alpha}$ 5-22
 types 5-2
 vortex generators 5-6
 Flat plate lift 21-1, 21-6
 Flow pattern flaps 5-16
 Fluid properties 1-9, 1-12
 Flying qualities 14-16
 Foil sections — hydro 8-4
 Fowler flaps:
 hinge moments 5-43
 pitching moment 5-35
 Frequency — vortex shedding 21-2
 Fressler stork airplane 6-2
 Frise ailerons 10-8, 10-9, 10-10
 Froude, number 1-14, 8-1
 Froude, William 1-1
 Fuselage:
 boundary layer 20-18
 characteristics — directional 13-6
 free moment 11-7
 jet flap interaction 5-31
 lift 11-5, 11-6, 11-7
 shape 20-15
 Gaps in flaps 5-21
 General aviation — airfoils 2-19
 General aviation aircraft 20-2
 German airfoils 2-3
 Gothic wings 18-9
 Gradual stall 4-5
 Gross engine thrust 12-12
 Ground effects 20-10
 Flap moments 5-38
 Induced angle 20-10
 Jet flaps 5-32
 Swept wings 15-13
 Half sphere — lift 20-10
 Handley page — flaps 5-3
 Handley page — slat 6-4
 Handling qualities 14-16
 Hang type gliders 20-6
 High altitude 1-15
 High lift devices 6-27, 6-28
 High speed airfoils $C_{L\alpha}$ 4-16
 Hinge moments
 Ailerons 10-5
 Derivatives 9-6
 Flaps 5-42, 9-12, 9-13, 9-14, 9-16, 9-17
 Reversal 9-9
 Horseshoe vortex — lateral distance 3-2
 Horizontal tail 9-1, 9-3, 17-9, 20-18
 Horizontal tail position 11-22
 Hull lift 8-15
 Hull stability and wake 8-4, 8-5
 Hurricanes 21-13
 Hydrofoil 1-4, 8-14, 8-15
 Hydrofoils 8-6, 8-11
 Hydroskiis 8-8
 Hysteresis — stall 4-19, 4-25
 Icing 1-11, 4-22
 Impact pressure 7-2
 Induced flow effects:
 angle 3-2, 3-3
 camber 11-4
 drag 3-4, 20-16
 drag — jet flaps 5-33, 5-34
 drag — part span flaps 5-18
 drag swept wings 15-7
 propellers 12-4
 Interference on:
 flap and fuselage 5-31
 fuselage and tail 11-9
 swept wing — fuselage 15-8, 15-18
 wing — fuselage 20-14
 Irrotational flow 1-5

Javelin lift	19-12
Jet engine — interference @ tail	12-13
Jet flap	5-24, 5-25, 5-27
Efficiency	5-33
Slot size	5-31
Theory	5-29
Jet propulsion	12-21
Jet sheets	5-27
Joukowski, N.E.	1-1
Joukowski-airfoil	2-2
 Karman, T.	1-1
Karman vortex street	17-4, 19-10
Kruger flap	6-14, 6-16, 6-17
Kruger flap swept wing	16-19
Kutta-Joukowski — airfoil	2-7
 Laminar flow:	
airfoils	2-16
separation	4-4, 6-18
Lanchester, F.W.	1-1
Landing characteristics:	5-19
flaps	5-14, 20-11
maximum lift	5-19
performance	1-19
Langley, S.	1-1
Lateral force:	
derivatives	14-4
stability — swept wings	16-8
stability — theory	14-11
Laval nozzle	7-3
Leading edge characteristics:	
blowing	6-28
camber	4-12, 4-14
devices	6-1
flap angle — C_{LX}	6-16
flap hinge moment	6-17
flap pitching moment	6-15
flap pressure distribution	6-16, 6-17
flap — stalling	6-15
nose shape effects	6-11
radius effects on C_{LX}	4-12
separation at leading edge	4-2, 4-4
shape effects on C_{LX}	4-6
sharp leading edge	6-13
slot	6-2, 6-20
slots and flaps — swept wings	16-19
stall	4-2, 4-10, 4-15
strakes	6-19
suction	4-23, 6-21, 17-7
suction analogy	18-5
trailing edge flaps	6-13

Lift characteristics:

above stall	4-22
angle	1-4, 3-2
angle data two-dimensional	2-12
angle — hydrofoils	8-7
angle — low aspect ratio wings	17-3
center	2-21
coefficient	2-8
distribution — biplanes	20-8
distribution — with flaps	5-16
divergence	7-4
engines	12-7
Fowler flaps	5-13
hysteresis	4-19
increment due to blowing	5-28
increment of flaps	5-5, 5-12
maximum full span split flaps	5-20
overshoot	4-24, 4-25
stall type	4-2
to 90° — delta wings	18-4
total airplane	20-19
Lifting angle straight wings	3-2, 3-3
Lifting line	2-6, 3-1, 3-3
Lifting surface	3-2
Lifting surface theory low aspect wings	17-1
Lilienthal, Otto	1-1
Load distribution — flaps	5-40, 5-43
Load distribution — swept wings	16-10
Lockheed 1011	20-4
Longitudinal stability	11-1
Longitudinal stability — swept wings	16-7
Low Reynolds number airfoil data	2-17
Low-turbulence — wind tunnel	4-8
 “M” type wings	15-10
Mach number characteristics:	
critical	7-3, 15-17
on C_{LX}	4-17, 4-18
one	7-12
Magnus effect	2-5
Magnus force — cylinder	21-3
Man in free fall	21-8
Maximum aircraft lift	20-21
Maximum camber location	4-12
Maximum lift:	4-1, 4-14, 4-16
boundary layer control	6-24
divergence	4-19
landing — with flaps	5-19
swept wings	16-2, 16-17
theoretical	4-1
with end plates	3-11

- Maxwell slat 6-3
 Mean aerodynamic chord 1-4, 11-4
 Mean camber line airfoils 2-1
 Mechanism of stall 4-2
 Messerschmitt slat 6-19
 Metracentric height 8-10
 Metric system 1-7
 Military aircraft 20-4
 Moments developed by:
 double slotted flaps 5-36
 extended lip flaps 5-36
 flaps in ground effect 5-38
 jet flaps 5-37
 part span flaps 5-36
 swept wing flaps 5-37
 trailing edge flaps 5-7
 with boundary layer control 6-25
 Momentum definition 1-5
 Momentum lift 5-30
 Mustang P-51 aircraft 11-26
- NACA Airfoils,
 0012-Reversed 2-7
 4-digit airfoils 2-3
 6-series airfoils 2-3
 Negative pressure 1-6
 Neutral point 11-15, 11-20
 Neutral point — streamline bodies 19-17
 Newton, I. 1-3
 Nose camber 4-12, 4-14
 Nose radius airfoils 2-9
 Nose radius — C_{Lx} 4-10, 4-11, 4-16
 Nose radius flaps 5-23
- Ogee wings 18-9
 Optimum flap — setting 5-16
- Parachutes 21-6
 Parawings 18-20
 Part span flaps 5-15, 18-17
 Part span flaps — induced drag 5-18
 Perforated flaps 5-8
 Pilot opinion a/c ratings 14-16
 Piper Navajo airplane 20-2
 Pitching moment — wing fuselage 11-7
 Plain flaps 5-10
 Planform effects on stall 4-26
 Plates — lift 21-6
- Plug aileron 10-16
 Positive taper — swept wings 16-13
 Potential flow 1-5
 Potential flow lift delta wings 18-6, 18-9
 Powered lift 5-24, 5-25, 5-27
 Prandtl, L. 1-1
 Prandtl — Glauert rule 7-2
 Pressure 1-5
 Pressure distribution 1-6
 Pressure distribution airfoils 2-15
 Propeller characteristics
 Lift 12-5
 Normal forces, moment 12-2
 Slipstream 12-9
 Slipstream effects @ tail 12-18
 Thrust 12-2
 Wing lift 12-10
 Directional characteristics 13-23
 Dual rotation 13-21
 Propulsion lift 12-1
- Radar screens — lift 21-9
 Rain, fog 1-11
 Ram wing 20-11
 Range 1-20
 Rectangular wings 3-2, 3-5, 3-6
 Reduced frequency 4-25
 Refueling interference 20-12
 Reversed airfoil, lift of 2-7
 Reynolds, O. 1-1
 Reynolds number effects 1-2
 Airfoils 2-13
 C_{Lx} 4-6, 4-9, 4-13, 4-14
 Critical 19-10
 Effective 4-8
 Flaps 5-22
 Ring airfoil 20-9
 Ring wings 17-10, 17-11
 Roach, definition of 8-13
 Roll characteristics
 Control, damping 10-2, 10-6
 Damping 14-12
 Yaw coupling 10-2, 10-6, 10-7
 Derivatives 14-12
 Moment 10-5, 10-6
 Moments — Dihedral 14-6
 Rotating cylinder flaps 5-24, 6-27
 Rotating flaps 5-24, 5-27
 Rotor thrust 12-2
 Roughness
 Allowable 4-19
 Effecting C_{Lx} 4-18, 4-19
 Effects — airfoils 2-13
 Full scale 4-20
 NASA standard — C_{Lx} 4-20

Sailplanes	20-6	flutter	4-24
Satellite — gliding	21-10	hysteresis	4-24
Seaplane float	19-18	leading edge	4-2
Separation bubble — long type	4-3	prediction	4-10
Servo control	9-26	types	4-2, 4-21
Shape of airfoil on $C_{L\alpha}$	4-9	warning — mechanical	16-21
Sharp edge stall	4-2	with leading edge devices	6-27, 6-28
Sharp leading edge airfoils	2-8	Stalled wings	4-23
Sheared wings	15-2	Stalling characteristics:	
Shock stall	7-10	aircraft	20-20
Shock wave — swept wings	16-16	leading edge flaps	6-13
shock waves	4-18	low aspect ratio wings	17-16
Side force automobiles	21-12	mechanism	4-2
Similarity laws	1-7	speed	20-19
Skiis — lift of	19-26	straight wings	4-23, 4-26
Skydiving	21-8	swept wings	16-2
Slat size	6-2, 6-3, 6-4	Static stability — directional	13-2
Slats — leading edge	6-1, 6-5	Stick free	9-18
Slipstream effects wings	12-8	STOL	1-15
Slot characteristics:		STOL — control power	1-16
fixed leading edge	6-2, 6-20	Stream turbulence	4-8
for roll control	10-17	Streamline body lift	17-8, 19-1
forces — loads	6-7, 6-8, 6-9	Streamline body moments	19-14
leading edge	6-1, 6-4	Strouhal number	21-2
pitching moment	6-6, 6-7	Structures — lift of	21-13, 21-14
Reynolds number	6-4	Strut section	2-9
size — jet flaps	5-31	Suction	5-27
Slotted flaps — single	5-11, 5-21	Supersonic aircraft longitudinal stability	11-31
Small aspect ratio wing	17-2	Supersonic flow	7-11
Span load distribution	3-4	Supersonic transport aircraft	18-12
Span loading — flaps	5-41	Surface roughness airfoils	2-20
Speed break flaps	5-35	Sweep forward longitudinal stability	11-34
Speed of sound	1-10, 7-1	Swept wing characteristics:	
Speed ratio — rotating cylinders	21-11	forward sweep	15-5
Sphere — rotating lift	21-11	geometry	15-1
Spiral instability	14-14	lateral characteristics	14-8
Split flaps:		rolling moment	14-9
$C_{L\alpha}$	5-22	stalling	16-3
delta wings	18-16	theory	15-2
pitching moment	5-35	Symmetrical airfoil — $C_{L\alpha}$	4-10
position	5-6, 5-7		
section shape	5-9		
Splitter plates — cylinders	21-3		
Spoilers:	10-2, 10-6, 10-7		
stick force	10-19		
time delay	10-16	"T" tail	11-23, 11-24
Spring tab	9-28	Tabs — control	9-23
Square — cube law	1-13	Tail:	
Stability:		all movable	9-27
axis	14-2	lateral force	13-15
directional	13-1	load distribution	11-10
lateral	14-1	volume	13-13
longitudinal	11-1	Tailless aircraft longitudinal stability	11-34
stick free	9-7, 9-8, 9-18	Takeoff — aircraft:	
Stagnation point	1-6	figure of merit	6-26
Stall characteristics:		performance	1-17
ducted fans	12-6	with flaps	5-17

- Tandem configuration 11-28
- Tandem wing lift 20-12
- Taper ratio swept wing 15-5, 16-13
- Tapered wing 3-5
- Terms — Glossary 1-3
- Theory:
 - C_{Lx} 4-15, 4-23
 - delta wings 18-5
 - flap loading 5-39
 - jet flaps 5-29
 - low aspect ratio wings 17-2, 17-5
- Thick airfoils 2-9
- Thick wing sections 5-17
- Thickness:
 - effects C_{Lx} 4-13, 4-16, 4-21
 - effects — Low Reynolds number 2-17
 - ratio effects 2-16
 - ratio effects — flaps 5-22, 5-23
- Thin airfoil stall 4-10, 4-14
- Tip flow delta wings 18-3
- Tip shape effects 3-7, 3-8
- Tip tanks 3-12
- Tip tanks — swept wings 15-11
- Tornadoes 21-13
- Trailing edge characteristics:
 - airfoil 2-7
 - angle — airfoils 2-10
 - effects — moments 2-23
 - flap types 5-3
 - stall 4-2, 4-4, 4-5, 4-10
- Trailing vortex 3-7, 3-14
- Trailing wedge angle — flaps 5-10
- Transonic flight 7-12
- Transport aircraft 20-3
- Trim tabs 9-24
- Triple slotted flaps 5-21
- Triple slotted flaps C 5-22
- Turbulence characteristics:
 - effects at low Reynolds number 2-17
 - effects on C_{Lx} 4-7
 - effects on flaps 5-6
 - factor 4-8
 - simulation 4-21
 - wind tunnels 4-7
- Twist swept wings 16-11
- Two alpha flow 3-12
- Two dimensional airfoil C_{Lx} 4-6
- United States steam ship 8-12
- “V” tail 11-14
- Venetian blind split flaps 5-9
- Vertical tail characteristics 13-6
 - effective aspect ratio 13-6
 - slipstream effects 13-26
- Vertical wings plates 3-13
- Viscosity — air 1-9
- Viscosity — water 1-12
- Vortex effects 1-5
 - breakdown — delta wings 18-3, 18-15
 - core diameter 3-1, 3-2
 - leading edge — swept wings 16-16
 - lift 17-6
 - lift delta wings 18-7, 18-10
 - lift — streamline bodies 19-4
 - roll-up 3-2, 11-16, 11-17
 - sheet 3-1, 11-16
 - trailing 3-1
- Vortex generators 5-6
- Vortex generators — C_{Lx} 6-18, 6-19
- V/stol aircraft — with normal force 12-5
- “W” type wings 15-10
- Wake — fuselage 11-11
- Wake — wing propeller 11-21
- Washout effects on stall 4-26
- Water properties 1-12
- Water tunnels 1-12
- Wave angle 8-13
- Whitcomb airfoil 2-19
- Wind tunnel wall effects 4-9
- Wind tunnels 1-1
- Windshields — effect on bodily lift 19-6
- Wing body lift 20-15
- Wing cut-outs 11-19, 20-19
- Wing dihedral 3-13
- Wing flap performance 5-14
- Wing mounted engines 12-2
- Wing — ring 2-24
- Wing root stalling 11-9, 11-18
- Wing shape distribution 3-4
- Wing tip effects 3-6, 3-8
- Wing tip tanks 3-12
- Wings — low aspect ratio 17-2
- Wortman airfoils 2-18
- Wright brothers 1-1
- Wright brothers airfoil section 2-2
- X-15 Airplane 11-25
- “Y” tail 13-13
- Yaw low aspect ratio wing 17-13
- Yaw moments
 - dihedral effects 14-6
 - derivative directional 13-19
 - fuselage 13-2
 - typical aircraft 13-6
 - vertical tail 13-8
- Yawed airfoil 15-3
- Yawing moment — ailerons 10-9
- Zap flaps 5-2, 5-7, 6-28
- Zap flaps moments 5-35
- Zero lift angle — airfoils 2-14
- Zero — lift moment 2-21